PROCEEDINGS

10th
Symposium on Engineering Applications of Mechanics

Mechanics of Mobility

May 27 - 30, 1990

COMPTES RENDUS

10^{e}
Symposium sur les applications techniques de la mécanique

La Mécanique et la mobilité

du 27 au 30 mai 1990

P.H. Oosthuizen & J. Jeswiet
Editors

Queen's University
Kingston, Ontario, Canada

92-06721/

Additional copies available from:

Publication Sales and Distribution
National Research Council Canada
Ottawa, Ontario, Canada
K1A 0R6

Price: $50.00

DSS: NR15-13/1990
ISBN: 0-660-55780-0
CNRC: 31579

On pourra se procurer des exemplaires en s'adressant à:

Vente et diffusion des publications
Conseil national de recherches du Canada
Ottawa, Ontario, Canada
K1A 0R6

Prix: 50$

DSS: NR15-13/1990
ISBN: 0-660-55780-0
CNRC: 31579

PREFACE

The Tenth Symposium on Engineering Applications of Mechanics was held at Queen's University in May, 1990. It was held in conjunction with the Second International Specialist Meeting on Major Hazards in the Transport and Storage of Pressure Liquefied Gases. The general theme of the symposium was "Mechanics of Mobility" but papers covering all aspects of the application of mechanics were presented at the symposium. In accordance with the general aims of this symposium series, the basic objective was the promotion of communication and transfer of technology in the field of mechanics between industry, governmental agencies and universities. The wide range of affiliations of those presenting papers at the symposium indicates that this objective was met. In addition to the general papers, three keynote addresses were featured at the symposium, one of which is published in these Proceedings. All general papers were reviewed within Queen's University.

The success of the Tenth Symposium on Engineering Applications of Mechanics was largely the result of the hard work of the Organizing Committee and of the generosity of our sponsors: Faculty of Applied Sciences and School of Graduate Studies and Research, Queen's University; Transportation Development Centre, Transport Canada; Alcan International; and Canadian Airlines International. These contributions and those of the participants in the symposium is gratefully acknowledged.

P.H. Oosthuizen
J. Jeswiet
Editors of Proceedings.

SYMPOSIUM ORGANIZING COMMITTEE/COMITÉ ORGANISATEUR DU SYMPOSIUM

T.N. Moore *(Co-Chairperson/coprésident)*
P.H. Oosthuizen *(Co-Chairperson/coprésident)*
A.M. Birk *(Vice-Chairperson/vice-président)*
J. Jeswiet *(Vice-Chairperson/vice-président)*
C. Small *(Vice-Chairperson/vice-président)*

COMMITTE MEMBERS/MEMBRES DU COMITÉ

P. Bussieres
Y. Caron
G. English
Z.I. Johannes
W. Montasser
A. Teitsma
J. Tjong
D. Turke

STANDING COMMITTEE ON EAM SYMPOSIA/COMITÉ PERMANENT SUR LES SYMPOSIUMS ATM

D.S. Weaver *(Chairman/président)*
McMaster University
A.M. Garlicki *(Vice-Chairman/vice-président)*
National Research Council Canada
W.H. ElMaraghy
The University of Western Ontario
B. Tabarrok
University of Victoria

SPONSORED BY/PARRAINÉ PAR

Faculty of Applied Sciences, Queen's University, Kingston
School of Graduate Studies and Research, Queen's University, Kingston
Transportation Development Centre, Transport Canada
Alcan International
Canadian Airlines International
National Research Council of Canada

TABLE OF CONTENTS

Preface iii

Committees iv

Keynote Address

Condition Monitoring of Manufacturing Machinery
Z.F. Reif 1

Biomechanics

Metacarpophalangeal Joint Kinematics: Surface Markers Versus Bony Landmarks
C.F. Small, D.R. Pichora 11
High Heel Gait
U.P. Wyss, I. McBride, J.T. Bryant, T.D.V. Cooke 17
Three-dimensional Display and Manipulation of Medical Objects
C.H. Tuan, J.D. Chan, T. Caohuu, H. Rémy 21
A Biomechanical Study of Stability of Uncemented Femoral Stems
T.W. Phillips, S.D. Munro, L.T. Nguyen 27
A Biomechanical Test of Interfacial Shear Characteristics in Cementless Prosthetic Fixation
T.W. Phillips, L.T. Nguyen, D.R. Rao, J.L. Snel 33
A Biomechanical Test of Fixation of Proximal Humeral Endoprostheses
T.W. Phillips, L.T. Nguyen 39
Actuator Control by Extended Physiological Proprioception
C. Kirtley 43
Computer Modelling of Occupant Crash Dynamics in Child Restraint Devices
S. Basile, B.K. Latouf, R.G. Gaspar 49

Dynamics

A Cartesian Tensor Methodology for the Study of Classical Newtonian Dynamics
(Part I: Cartesian Tensor Analysis)
C.A. Balafoutis, R.V. Patel 55
Simulation dynamique des solides par la méthode des reseaux vectoriels
M.J. Richard, I. Bindzi 61
An FEM Approach for Robot Path Planning under Dynamic Conditions
S. Ramachandran, T. Nagarajan, N. Sivaprasad 67
The Application of Modern Systems Techniques to Helicopter Modelling and Control
R. Srinivasan, K.R. Goheen 73
Symbolic Closed-Form Dynamics of Rigid/Flexible Hybrid Multibody Systems Subject to Control
J. Lieh, I. Haque 79
A Cartesian Tensor Methodology for the Study of Classical Newtonian Dynamics
(Part II: Applications to Rigid Body Motion)
C.A. Balafoutis, R.V. Patel 85
One-Step Approach to Solving Nonlinear Problem of Beam-Column
Y. Yu 91
A Variable Order Runge-Kutta Method for Problems in Applied Mechanics
R.C. Quirt, R.J. Anderson 95

Synthesis of Cam Curve in Line with Complex Boundary and Interior Constraints
L. Xue, J. Pei 101
A Method of Smoothing and Synthesis and Optimization of Cam Curve Using Spline Functions
L. Xue, J. Pei 109

Evaluation Techniques

Performance of Abrasive Disk Dehullers
M.W. Bassey, H.M. Mbengue 115
Multiaxial Creep Damage and Fatigue Life Evaluation Using the Gloss Plot
R. Seshadri, R.K. Kizhatil 121
Novel Techniques for the Surface Evaluation of Paper
D.C.S. Kuhn, P. Whiting 129

Fluid Mechanics

Numerical Simulation of Liquid Sloshing in a Baffled Rectangular Tank
G. Popov, S. Sankar, T.S. Sankar 135
Gas Flow in a Vertical Chemical Vapour Deposition (CVD) Reactor
W. Montasser 141
Field Panel Method for Transonic Flows with Body Fitted Grids
Z. Fang, I. Paraschivoiu 145
Modélisation des forces aérodynamiques sur une éolienne darrieus avec un sillage tri-dimensionnel
K. Héon, B. Massé, A. Laneville 151
Some Observations of the Flow Regimes around a NACA 0018 Aerofoil in Circular Translation
A. Benmeddour, F. Bouak, A. Laneville, P. Vittecoq 157
Drag Reduction and the Turbulent Flow of Micropolar Fluids in a Pipe
N.H. Aydemir, J.E.S. Venart 163
The Measurement of Wood Fibre Flexibility
D.C.S. Kuhn, P.H. Oosthuizen, P. Whiting 169
Heat Transfer and Fluid-Flow Characteristics of Arrays of Impinging, Round Air Jets
P. Hrycak, D.M. Kaya, S. Sethi, C. Wei 175
Natural Convection Generated by Conjugate Heat Transfer in Rectangular Enclosures
F.L. Bello-Ochende, I.O. Ogunleye 181
Investigation of Pressure Distribution around a Cylinder near an Endwall
P.H. Oosthuizen, P.C.C. Tong 187
Pressures in a Horizontal Cylindrical Tank Due to Impact Induced Accelerations
D.B. Chidley, A.M. Birk 191
Flow Visualization in a Planar Transonic Turbine Cascade
W.E. Carscallen 199

Heat and Mass Transfer

Turbulent Convective Heat Transfer in a Three Dimensional Square Duct
G. Yang, M.A. Ebadian 207
A Preliminary Study of Combined Modes of Convection Air Cooling of Electronic Components
R.A. Showole, J.D. Tarasuk 213
Thermoeconomic Optimization of Energy Conversion System Working on Heat Recovery
J. Wang, H. Zhang 219

Free Convection Heat Transfer from a Finite Horizontal Plate
P. Hrycak, D.J. Sandman, K.E. Tsouras 225
An Experimental and Numerical Investigation of Natural Convection and U-Value Determination of Sealed Window Glazing Units
R.A. Showole, E.S. Nowak 231
Application of Digital Image Processing to Interferogram Analysis
D. Naylor, J.D. Tarasuk 237
Effects of Ambient Humidity on the Thermal Behavior of Porous Building Materials
F. Kallel, N. Galanis 243
Convective Heat Transfer for Simultaneously Developing Flow in Ducts of Rectangular and Equilateral Triangular Cross-Section
G. Yang, M.A. Ebadian 249
Influence of Slab Thickness on Responses of Concrete Walls under Fire
G.N. Ahmed, C.L.D. Huang 255
Heat Transfer in Forced Non-Newtonian Fluids with Viscous Dissipation Past a Horizontal Flat Plate
F.L. Bello-Ochende, C.D. Obiajunwa 261
Study of Finned Heat Transfer under the Condition of Radiation and Convection
Y. Xiangxiang, L. Liangbin 267
Rotary Dryer for Flash Drying Paddy in Developing Countries
A.R. Elepaño, P.H. Oosthuizen 273
Assisting and Opposing Mixed Convective Heat Transfer to a Cylinder in a Porous Medium with Freezing
P.H. Oosthuizen, J.T. Paul 279
Modelling of an Indirect Natural Convective Solar Rice Dryer with a Thermal Storage Bed
P.H. Oosthuizen, H.M. Bashagur 285

Manufacturing

Time Based Signal Analysis for the Detection of Intermittent and Impact Noise and Vibration
J.S.Y. Tjong, H.W. Miller, Z. Reif, R. Gaspar 291
The Determination of Milling Cutter Tool Condition Using Vibration Signals
T.N. Moore, J. Pei 297
The Analysis of Fault Occurrences in an FMS
J. Jeswiet 303
Nonisothermal Metal Flow Simulations for the Die Casting Process
C.A. Loong, V.V. Kappel, G. Salloum 309
A Flexible Internal Defect Detector for 12 Inch Pipelines
A. Teitsma 313
Design of Single Stage Pipeline Inspection Tools
L.A. Davies, A. Teitsma 317
A Friction Sensor for Sheet Metal Rolling
C. Nyahumwa, J. Jeswiet, T.N. Moore 321
Design, Development, and Testing of a Real-Time Impedance Control System for Deburring Operation
M.S. Ali, M. Noori, J. Turi 327

Robotics

A Dexterity Measure for the Design Evaluation of Redundant Robot Manipulators
R.V. Mayorga, B. Ressa, A.K.C. Wong 333
Dynamique des mécanismes et robots manipulateurs
T.B. Wang, M. Dahan 341
An Approach for the Design and Dynamic Analysis of Light Weight Robotic Manipulators Using Finite Element Method
S. Ramachandran, T. Nagarajan, N. Sivaprasad 347
Economic Evaluation of a Cement Floor Finishing Robot
O. Moselhi, P. Fazio, S. Hason 353
The Operation of a Gantry Robot in a Turning FMC
J. Jeswiet 359
Error Analysis for the Automatic Visual Inspection of a 2D Shape with a Laser Range-Finder Camera
P. McComber, M. Galopin, A. Paradis, A. Royal 365
Computer Graphics Simulation of an Industrial Robot
A. Meghdari 371
Control Algorithm for a Planar Five Bar Mechanism Used as Robotic End Effector for Precision Buffing Operation
S. Srinivas.V, T. Nagarajan 377

Transportation

The Transportation Development Centre's Rail R&D Program Related to Heavy Haul Transportation
D.W. Dibble, W.S.C. McLaren 383
Optimisation of Road Vehicle Power Systems
A.S. Davies 389
Étude de la stabilité des véhicules articulés par la méthode de Lyapunov
M. Khan, P. Bourassa, M. Brezina 395
Dynamic Performance of Logging Trucks
M. El-Gindy, J.H.F. Woodrooffe 403

Vibrations

Free Vibration Analysis of Simply Supported Rectangular Plates with Internal Point Supports
D.J. Gorman, H.L. Ohman 409
A Modified Lévy Type Solution for the Free Vibration Analysis of Simply Supported Isosceles Triangular Plates
H.T. Saliba 415
Free Vibration of a Thick-walled Vessel
D. Redekop 421
Nonlinear Parametric Vibration of Fully Clamped Rectangular Plates
S.D. Yu, D.J. Gorman 427

Late Submission (Fluid Mechanics)

On the Design of Vehicle Engine Coding Systems
S.F. Bloomer, T.E. Base, H.N. Charles 433

Author Index 439

CONDITION MONITORING OF MANUFACTUIRNG MACHINERY

Z.F. Reif

Department of Mechanical Engineering
University of Windsor, Windsor, Ontario, Canada N9B 3P4

ABSTRACT

The general aspects of the application of predictive and preventive maintenance systems in industry are discussed. The advances, which are currently made in enlarging the knowledge base in this area and in developing dedicated expert systems, suggest that in the near future significant increases in productivity and industrial safety will be achieved by the application of such procedures. Condition monitoring of machine elements in automated machining systems, such as transfer lines, is discussed in more detail, with particular reference to rolling element bearings and tool wear. It is concluded that although this type of application is inherently more complex, predominantly because of the cyclic mode of operation, the rewards are potentially higher and hence justify the additional effort required for the development of fully effective monitoring systems.

INTRODUCTION

One of the consequences of the competitive pressures to improve productivity and product quality is increased emphasis on improved machinery and process maintenance procedures. Significant decreases of operating cost can not only be achieved by reducing the wear of machine components and by preventing catastrophic failures, but also, perhaps more importantly, by reducing machine down-time. These advantages may be further improved by being able to predict developing failures well before the event, thus preventing serious damage and permitting planned repairs without interference with production schedules. The effectiveness of these procedures is enhanced by the application of fast, inexpensive and compact computers with large storage capacities. A less obvious, but very important by-product of automated data storage and analysis, is the availability of the true costs of less efficient production maintenance, which often turns out to be significantly higher than previously assumed by the management.

The general terms, which are used to define these relatively new procedures, are preventive and predictive maintenance, and sometimes, more directly, machinery condition diagnostics and prognostics. Such systems are generally based on a sensing medium to provide input data, which is then appropriately analysed for indications of the deteriorating condition of machine elements. The results can be used directly to progressively monitor their condition or, by comparison with previously investigated trends, to predict the approximate time of failure. In most cases the time history of the condition of a machine element, as indicated by the progressive changes of the sensing medium, follows a characteristic shape, generally referred to as the bathtub curve", as shown in Fig. 1,(1). Phase I, the infant mortality, which is caused by original manufacturing faults or material imperfections, has to be appropriately allowed for when establishing baseline values for later comparisons with measurements in the wearout phase. This final section of the curve is the most important monitoring range because maintenance decisions, such as for example an automatic shut-down of a computer controlled system, are generally made on the basis of the magnitude of changes from baseline values. Perhaps the most important aspect of condition monitoring is the choice of the sensing medium and of the analysing procedure to provide greatest and most consistent changes of the indicators of the progressing wear and approaching failure.

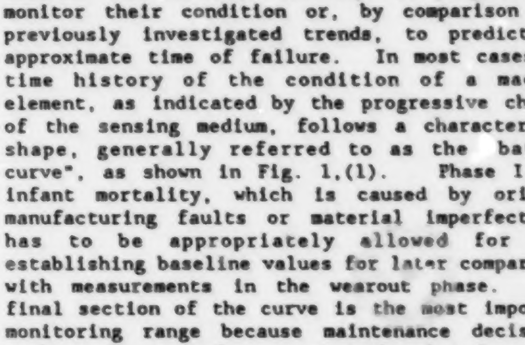

Fig. 1 Component Life Characteristic (1)

In some industries condition monitoring has been applied successfully in its simpler forms for several decades. The rapid development of automation in recent years, together with significant advances in computer hardware and software, have significantly broadened the scope of application and the complexity of monitoring systems. The greatest need and, because of the current reduction of capital investments, also the greatest potential for the adoption of monitoring systems is in retrofit applications on existing machinery. Monitoring systems are generally more sophisticated than the host machinery. Their functioning is not uniformly effective, often because some important practical aspects are overlooked in their design. Coupled with some reluctance to adopt new technology, the introduction of monitoring systems in industry is slower than it should be. Decisions on their adoption are generally made by production managers on a predominantly commercial basis. It is, for example, quite important that their operation is sufficiently "user friendly" to be efficiently managed by the existing maintenance staff and that it can be repaired quickly and locally. The viability of a system is significantly increased if it is capable of performing several different monitoring functions. Of particular importance in that respect is the ability to control the manufacturing process itself (2).

The general requirements of a monitoring system may vary significantly. To determine the condition of fans and pumps in a manufacturing plant, for example, it may be only necessary to take manual readings at daily or weekly intervals. On a large, automated manufacturing system, on the other hand, continuous monitoring under computer control and with automatic shut-downs may be necessary. To be effective and commercially acceptable, the design of a condition monitoring system or procedure must thus satisfy many requirements and in more advanced applications on large machinery it must be customised to a degree on the basis of appropriate initial measurements and a thorough study of operating conditions. Most of the currently available systems are of a standard type, with virtually no scope for adjustments. In some applications their performance is very good, in others it is less satisfactory.

Ultimately the main criterion, which predominantly determines the adoption of condition monitoring for industrial applications, is cost viability. The reported financial advantages vary significantly. The cause is often excessive optimism on the one hand and an incomplete assessment of the gains on the other. The advantages of condition monitoring do not accrue only from its maintenance costs. In addition appropriate allowance must be made for the broader implications of preventable catastrophic failures, improvements of productivity by reductions of machinery downtime, increases of product quality and control of other manufacturing aspects (1,2,3,4).

There are four basic types of failure in industrial processes: mechanical, chemical, electrical and electronic. A variety of procedures and sensing media are used for condition monitoring although each group has its best performers. Some of the most common are: vibration, noise, temperature, force, power and debris analysis. Because of its functioning effectiveness and generally greater scope of application, vibration is emerging as the best sensing medium in the majority of condition monitoring procedures. Most of the required hardware components have been fully developed for other applications and are therefore readily available and relatively cheap. The corresponding sensors are compact and can be very simply mounted. Output signals contain much information, and several distinct descriptors can be extracted by appropriate analysis.

The main topic of this paper is the application of vibration for condition monitoring of metal cutting machines, with particular reference to transfer lines. These systems are used extensively in the automotive and construction machinery industries, and account for the majority of metal cutting work in North America. Because of the untended mode of operation and the hostile working environment, there is a well defined need for fully automated condition monitoring procedures.

TRANSFER LINES

Transfer lines consist of several automated machine tools, sometimes as many as fifty, which are connected by means of a common guide way. On it the work pieces are moved in a continuous stream from one machining station to the next. For example, internal combustion engine blocks enter a transfer line system as rough castings and emerge completely machined at an approximate rate of two hundred units per hour. The process is completely untended and the working environment is very hostile, such that human inspection during operation is impossible and most instruments are quickly damaged. The value of production can exceed $20,000 per hour. The average machine down-time is approximately 25%. It is predominantly caused by unexpected component failures, with tool breakages, bearing and drive failures as the most common types. If, in addition, the cost of damaged work pieces and catastrophic machine failures is allowed for, an effective monitoring system, which is capable of predicting the majority of developing faults, has obviously good potential for significant cost savings. Economic studies have indicated that for best results on transferlines it should combine several different monitoring functions and that it must be fully automated by computer control. Because of the cyclic mode of operation, the noisy and hostile working environment and lighter structures, the required monitoring procedures are more complex, and in some basic aspects different to those used in other applications. On the other hand, the rewards of a successful system are proportionally greater.

VIBRATION AS THE SENSING MEDIUM

As mentioned previously, vibration is one of the most useful sensing media for machinery condition monitoring. Several descriptors with different characteristics and varying degrees of effectiveness can be extracted from a particular vibration signal, such as for example: maximum value, RMS, crest factor, shock pulse, spike energy, several properties of the frequency spectrum, some statistical parameters and acoustic emission. A single accelerometer, which is mounted on the spindle casing of a machining head, can provide information on the condition of bearings, cutting tools, drive belts and electric motors. It can also indicate the degree of tool wear, the onset of machining chatter, excessive rotational unbalance of the spindle assembly and the approximate quality of the surface finish. Inclusion of these monitoring functions requires the knowledge of their basic relationships with corresponding changes in vibration and the addition of the appropriate control software for the additional analysis of the common signal. In reference (5) several techniques of vibration analysis are discussed, and in (6) some interesting applications of vibration for on-line condition monitoring in advanced manufacturing are described.

In many respects it is the old "screwdriver to the ear" method, which has been refined and made respectable by the application of computers. It must, however, be admitted that some signal characteristics, cannot yet be reliably detected with sophisticated instrumentation and algorithms, whereas an experienced tester can sometimes pick them up by ear.

BALL BEARINGS

A typical transfer line is likely to contain several hundred rolling element bearings. This bearing type has extremely small clearances, hence the characteristic forces, which are generated by developing faults, are efficiently transmitted to the outer casing. Measurement of vibration on the outer surfaces of bearing or spindle covers generally provides satisfactory results.

Some vibration will be generated even with new bearings as a result of their compliance, which varies with rotation, and of some possible manufacturing imperfections (7). Developing failures can significantly increase the amplitude and alter the frequency distribution of this vibration. These changes will depend to some degree on the type of the evolving damage and the method of monitoring will have to be adjusted for best performance under the existing conditions.

At least thirteen different modes of failure have been identified (8). The two most common types are caused by spalling fatigue and by abrasive wear. Their development is accelerated by insufficient lubrication.

Spalling fatigue generally starts around a microscopic slag inclusion, cracks propagate then to the surface where minute metal flakes are broken off and a surface indentation is formed. This type of damage produces several relatively large vibration components at low discrete frequencies, which are related to the speed of rotation, the configuration of the bearing components and their dimensions. Generally, the subsequent bearing rotation produces a self-peening effect which tends to reduce the indentation and hence the resulting vibration response.

Ball bearings have a mixed rolling and sliding motion and are therefore more prone to abrasive wear, which is particularly sensitive to inadequate lubrication. In this case the increase of vibration is dominated by broad band vibration in he high frequency range.

From measurements on bearings in predominantly large rotating installations, such as steam turbines, it is concluded that the most reliable indication of incipient bearing failure is obtained from discrete frequency components at well below 1 KHz (9). This is referred to as the Prime Spike region and extends over the first seven harmonics of the bearing element passage frequencies. In the presence of faults, one or more of these harmonics are amplified. It is also stated in this paper that occasionally early warning of failure is provided by significant vibration increases in the much higher frequency range of 5 KHz to 25 KHz. Self-peening, however, generally causes a reduction of this vibration component and the bearing will operate satisfactorily for some time beyond this stage. It is recommended that the high frequency region should only be used as an early warning of developing failure and the timing of bearing replacement should be determined by the vibration levels in the Prime Spike region.

In contrast, in another investigation of predicting bearing failures on electric motors (10), high frequency resonances of the bearing assembly and of the supporting structure were found to dominate the vibration and are consequently recommended as indicators for monitoring purposes. The high frequency signal of this type of vibration, which is excited by impacts from fault irregularities, is then filtered and modulated at the rolling element passing frequencies. It is suggested in this paper that by this method a more reliable indication of the developing failure is obtained, with significantly less interference from other machinery vibration.

A more general discussion of using vibration for bearing condition monitoring (11) describes several possible methods of evaluation. It also suggests that in many cases the vibration response to impulsive fault excitation is dominated by structural resonances. There is a clear indication that an effective monitoring system must be based on a careful evaluation of the manufacturing system, on which it is to be mounted.

Pattern recognition is one of the more recent techniques, which are used to evaluate the condition of bearings (12, 13). In its simple form, it involves plotting of two monitoring properties against each other and then mapping areas of safe operation. The boundaries are derived by correspondence and discriminant analysis or by a simple inspection of previously obtained measurements.

One of the important decisions in designing a monitoring system is the choice of the most suitable descriptor, or sets of descriptors for a particular application, and the selection of their limit values to indicate the timing for replacement. On the one hand the objective is to prevent a catastrophic failure, with possible damage to the machine, on the other it is to make the best possible use of the component. In the operation of transfer lines the first consideration is more important. The limits are selected on the basis of past experience and the specific requirements of a particular application. A more systematic approach (14) may be provided by appropriate statistical analysis.

The hostile working environment on transferlines makes necessary the use of the most robust transducers and the small space in the working area restricts severely their size. Vibration from the numerous sources within the machine is likely to interfere with and make the analysis of low frequency vibration difficult. All these conditions indicate that on transferlines accelerometers have the best potential for applications as vibration sensors.

The results presented here form part of a general research project to determine basic relationships between developing failures of machine components and the resulting changes in vibration. In order to establish the feasibility of bearing state monitoring, trial test sequences were performed on transfer lines in a manufacturing plant (15). A three spindle machining head was selected for this purpose. Accelerometers were attached at three positions on the spindle casing, as shown in Fig. 2. The time intervals between measurements were approximately one week. It can be seen that for all three accelerometer positions, the same trend is exhibited, but the most sensitive indication is from the accelerometer near the bearing.

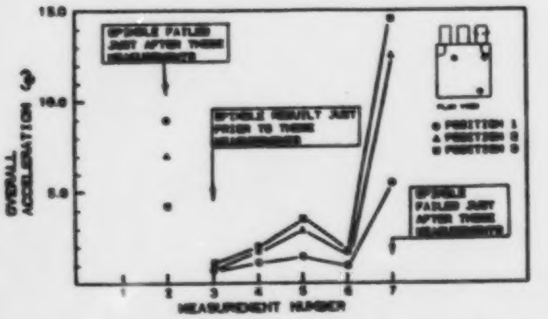

Fig. 2 Bearing Failure Trends on Machining Head of a Transferline

These results were typical of measurements obtained from other stations of the same production machine and on this basis it was concluded that vibration offered good potential for predicting bearing failures. Subsequently a testing program was developed for obtaining more detailed information on incipient bearing failures. A study of such defects occurring on production transfer lines showed that the most common causes were rotational unbalance, failure of lubrication and the ingression of coolant and grit. The results presented in this paper were obtained from a machining station test rig, which was operating in a laboratory environment, under rotational unbalance loading with the lubricant progressively washed out of the bearing by means of a cleaning fluid.

In a preliminary test sequence small indentations were cut in the inner and outer raceways and balls. The resulting vibration changes were characterized by distinct discrete components at the fault passing frequencies and their higher harmonics. In every case it was easy to identify the particular fault from the low frequency vibration spectrum. Even incorrect mounting of a bearing in the axial direction was clearly indicated, as can be seen from Fig. 3. It could be argued that, when measuring on a production machine, the evaluation of the spectrum in this frequency range would be difficult because of the masking effect of vibration from other sources. This quite valid concern does not, however, arise on transfer lines. The primary requirement of monitoring is a sufficiently early warning of an incipient bearing failure, to permit changing of the whole spindle unit during the next break between operating shifts. Identification of a particular type of fault, or even of the specific bearing damage, are of no concern. The spindle is replaced by a reworked unit, in which all bearings were changed, irrespective of their actual degree of wear or damage. The cost of this approach is significantly less in the long run and for similar reasons there is no interest in trying to extend the use of a particular bearing by taking it closer to the failure point. These aspects influence significantly the design of a condition monitoring system. Specifically, accelerometers are preferred as the transducers and the higher frequency range of vibration has the best potential of providing the required information.

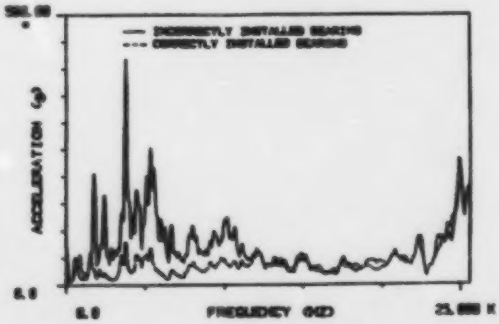

Fig. 3 Frequency Spectra for Bearing Installation

A large number of ball bearings, of a size normally used on high speed machine tool spindles, was run on the test rig until failure. Comparisons with vibration displacement and velocity measurements have indicated that acceleration provided best results and consequently it was selected as the sensing medium for all subsequent tests. The measurements were obtained from accelerometers, which together with the signal conditioning equipment had a linear frequency response of up to 20 kHz and were mounted by means of a screw stud on the top casing of the test bearing. The output was recorded either on an instrumentation type tape recorder, or after digitisation, on computer discs. The test procedure was fully automated under the control of a computer. The recordings were subsequently evaluated for the whole range of useful vibration descriptors. For this application it was found that the RMS value of vibration acceleration in frequency bands above 6 KHz consistently provided the most effective indication of developing bearing failures.

Typical results are shown in Figure 4, where the overall RMS value of acceleration is plotted against normalized life. The latter was obtained by dividing the running time at a particular measurement by the time to failure for that bearing. Although very significant differences in endurance existed between the nominally identical new bearings, when normalized the characteristics are almost coincident and exhibit a consistent trend. A well defined indication of impeding failure is evident, without any intermediate early warning changes.

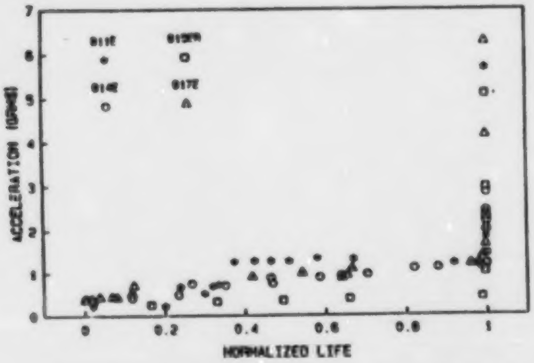

Fig. 4. Change of Acceleration RMS with Normalised Life for Four Bearings

Statistical analysis provided several descriptors of which Kurtosis appeared to offer best trends. It is the fourth moment of the statistical distribution curve about the mean value. Typical results are shown in Fig. 5. The consistent characteristic of this curve is that near failure it approaches a value of 3, which represents completely random distribution. It has the advantage as a secondary descriptor of decreasing in magnitude towards the failure point which is opposite to the trend of other indicators. Components at the bearing element passing frequencies were generally observed, but were relatively weak and without a significant increase towards failure. Although they were judged to be unsuitable for monitoring purposes in this case, it was recognized that the particular failure mode, which was induced by eliminating lubrication, favoured the high frequency range.

To obtain some indication of the effect on the vibration changes by the second common mode of failure, which is caused by spalling fatigue, small notches were cut on the raceways of several separate test bearings by means of a dental drill. The indentations were approximately 0.2 mm deep and 0.4 mm wide (16).

Typical results of such tests are shown in Figs. 6 to 8 for a bearing which was first given one notch and later a second notch on the outer raceway. Fig. 6 shows the vibration acceleration distribution in the time and frequency domains. The bearing was run for 24 hours from new and without any interference. Subsequently a notch was cut in the outer race. The effect of this fault is shown in Fig. 7 for a total operating time of 27 hours. The pulses in the time domain are at the race passing frequency, although the presence of much higher frequency components is evident. This is confirmed by the frequency spectrum. In addition to an approximately tenfold increase in acceleration amplitude, it is clear that most of this increase is concentrated in the higher frequency range of approximately 16 to 25 KHz.

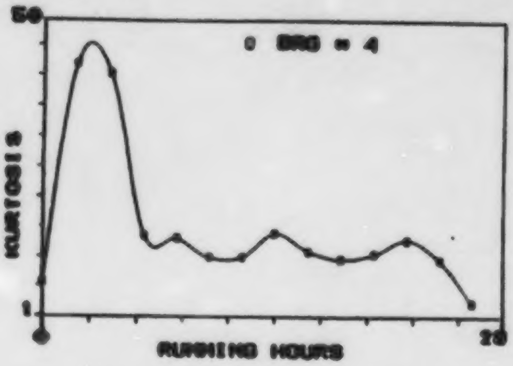

Fig. 5 Change of Kurtosis with Running Time

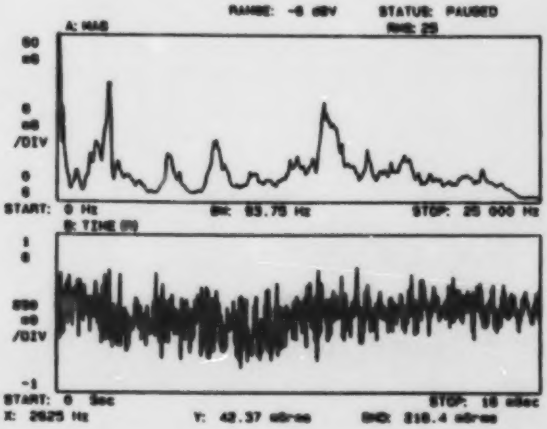

Fig. 6 Frequency Spectrum and Acceleration Waveform for New Bearing After 24 Hours of Operation

After 60 hours of operation the removal of lubricant was started by regular four hourly injections of cleaning fluid. After 120 hours a second notch was cut in the surface. Figure 8 shows the results after 126 hours of operation. Other than a slight overall increase in

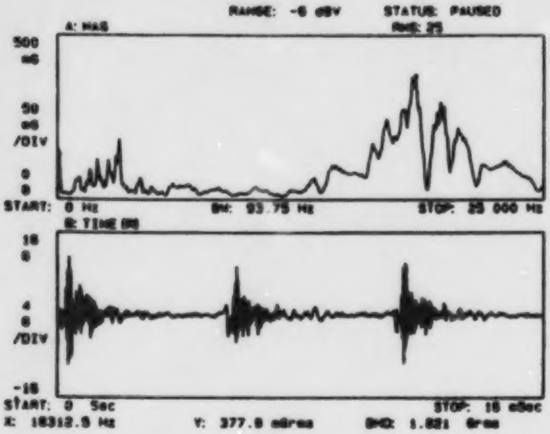

Fig. 7 Frequency Spectrum and Acceleration Waveform for Bearing with One Notch in Outer Race after 26 Hours of Operation

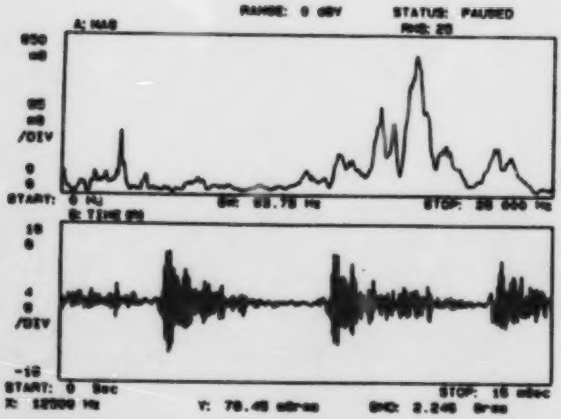

Fig. 8 Frequency Spectrum and Acceleration Waveform for Bearing with Two Notches in Outer Race and Reduced Lubrication After 126 Hours of Operation

magnitudes, predominantly in the high frequency range, very little difference from the results shown in Figure 7 can be observed. In the time base trace an increase of the high frequency components is also evident. The bearing failed after approximately another fifteen hours of operation and failure was preceded by a large amplitude increase in both frequency regions of interest.

The frequency of the predominant spike in the low range was approximately one hundred times that of the fundamental shaft rotation and sixteen times the outer race passing frequency. From some other experimental results it was also observed that the order number of the predominant spike was changing and hence to capture it a fairly wide frequency band has to be monitored. For the limited number of bearings tested in this mode it was found that this band had to include at least the first twenty harmonics of the fault pass frequency. If the RMS levels of the frequency bands are used, it is obvious that, because of the much greater density of components in addition to their higher amplitudes, the high frequency range gains further advantage for monitoring purposes. The complete results for a bearing with notches cut and lubricant eliminated are shown in Figure 9. RMS values of acceleration, which are expressed in terms of g's (GRMS) over the specified frequency bands, are plotted against the normalized life. Very little qualitative difference can be observed between the two curves. It can be, however, observed that in the 10 kHz to 20 kHz frequency range the acceleration levels are significantly higher than those in the band corresponding to the initial twenty harmonics. This is very important in respect of reducing the masking and interference effects of other, structure borne vibration, which did not exist in the laboratory environment.

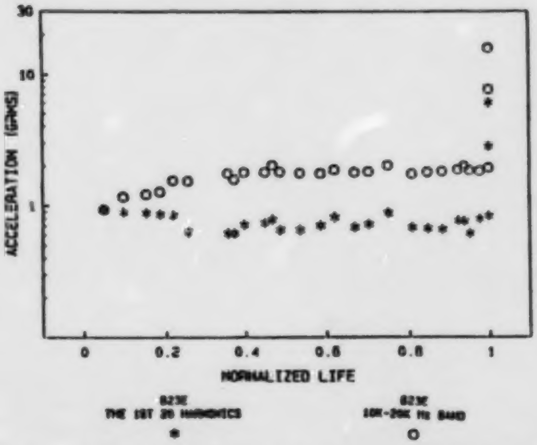

Fig. 9 RMS Levels in Frequency Bands

Some measurements were performed with special equipment which provided directly indications of spike energy. Similar trends were obtained as with the RMS acceleration in the higher frequency range. On the other hand crest factor, maximum acceleration amplitude, cepstrum and several statistical descriptors were less suitable for condition monitoring. Acoustic emission provided reasonably good results, but because of the significantly higher cost of the associated hardware and larger size of transducers, it does not appear to be a viable alternative on transferlines.

TOOL CONDITION MONITORING

Tool condition monitoring is relatively new in predictive maintenance, consequently the required background knowledge and application experience are less developed. However, because of the significantly higher incidence of failures it is likely to become the most important condition monitoring function on large machining systems, such as transferlines.

Several different procedures and sensing media can be used for tool condition monitoring, but in recent years monitoring systems, which are based on vibration and force measurements, have attracted most attention. In some, feed, radial and tangential cutting forces are detected by means of force transducers; appropriate algorithms are then used to primarily determine tool wear and breakage. The systems are generally self contained with an internal microprocessor or computer (17,18). Acoustic emission has good potential for tool condition monitoring (19), particularly because its high frequency range eliminates any possible interference from other vibration sources. On the other hand, this characteristic makes necessary the use of much more expensive hardware, which is also more susceptible to damage from the working environment. In another application (20) vibration displacement probes, which are attached to the bush plate of a multispindle drill head just above the protruding tools, are used to measure tool wear and detect tool damage. A somewhat more complex procedure (21), which may be applied for the prediction of developing tool damage by means of vibration or other types of inputs, it based on pattern recognition. One of the newest, commercially available monitoring systems (22) uses as the sensing medium a combination of vibration acceleration characteristics, which is referred to as spike energy. Vibration is also used to determine the condition of cutting inserts in face milling cutters (23).

Perhaps the most important advantage of using vibration for tool condition monitoring on large machining systems is that the same transducer can also provide the necessary information for other diagnostic functions for tool spindle unit. A transfer line often employs over a hundred drills, taps and reamers. Because of their relative slenderness and mode of operation, these types of tools are much more prone to damage and consequently the need for their condition monitoring is greatest. To study the basic relationships between the progressing wear of drills and the resulting changes of vibration, a large number of representative tools were operated until failure (24,25). The progressing wear was measured by means of a travelling microscope and the vibration output was analysed for a number of different descriptors. Vibration acceleration was again found to provide best overall results.

The simplest approach, in terms of the required hardware and data treatment, is to use maximum values of the vibration acceleration. This approach gives satisfactory results for detecting tool breakages or severe damage. From Fig. 10 it is evident that drill breakage produces sufficiently large changes in the vibration response to be reliably recognised by the monitoring computer software. On the other hand, this method is unsatisfactory for determining wear and predicting developing failure of tools. Figure 11 shows vibration acceleration changes for a particular drill with several levels of wear. It can be seen that maximum values of acceleration alone would not provide a good measure of tool wear and that the density of the signal is much better in that respect. It follows that a vibration descriptor, which allows for both the amplitude and density, such as for example the RMS value of the acceleration signal, would produce better results. This was confirmed by the obtained results. Another procedure with reasonably good application potential is the counting of spikes, which exceed a certain specified level. This function can be performed relatively easily by electronic methods.

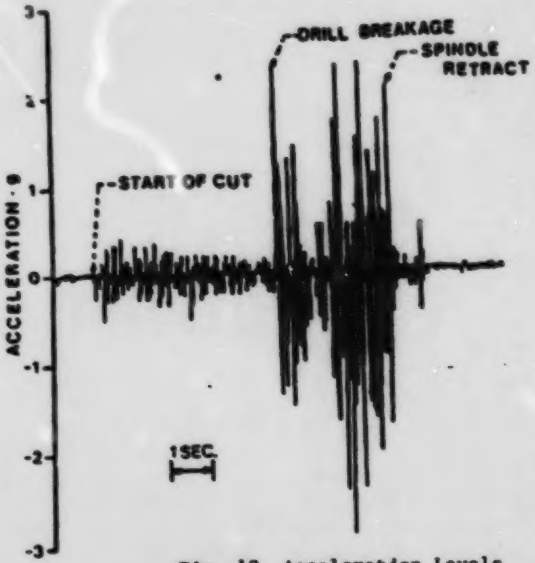

Fig. 10 Acceleration Levels for Drill Breakage

Figure 12 shows frequency spectra of the vibration acceleration during cutting sequences with one drill. The traces represent in ascending order a sharp, 30% and 60% worn drill. It was found that power or RMS levels within the frequency bands, which correspond to the distinct peaks in the spectra, provided slightly better measures of the progressing tool wear than the overall level. The location of these frequency bands, however, changed with some operating parameters and with machine tools. Although this variation was small, the use of band power levels for monitoring would require relatively frequent base line measurements.

Several statistical properties can also be extracted from the vibration signal. In this particular investigation, best results were obtained with standard deviation and variance. A typical set of results is shown in Fig. 13, where standard deviation is plotted against normalised wear. The latter is obtained by dividing a wear value by its magnitude at failure for the same drill. This was necessary in order to eliminate the significant variations in endurance of nominally identical new drills. It can be seen from Fig. 13 that, as wear progresses, a well defined trend exists with this descriptor and that, when normalised, the curves for the four drills are practically coincident.

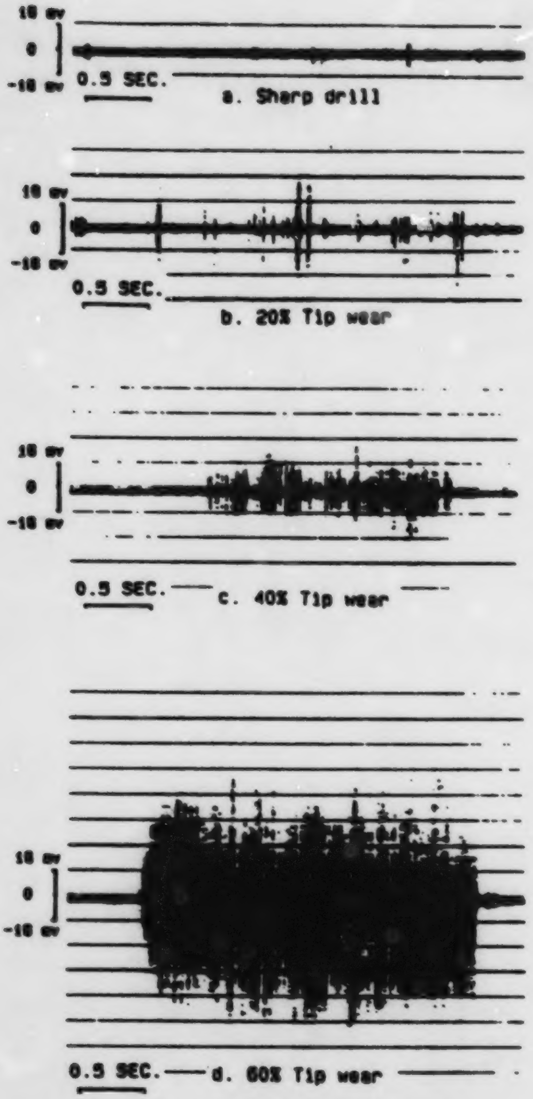

Fig. 11 Acceleration Levels for Progressing Stages of Drill Wear

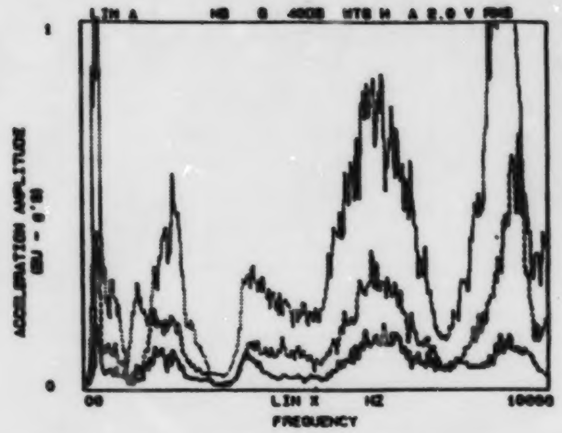

Fig. 12 Change of Acceleration Frequency Spectra with Drill Wear

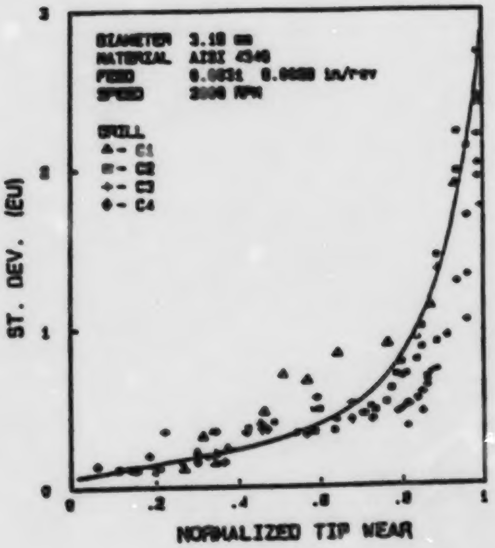

Fig. 13 Variation of Standard Deviation with Drill Wear

Most of several other vibration characteristics, which were investigated, showed satisfactory if not outstanding monitoring performance. Their relative effectiveness can, however, change with different working environments.

SUMMARY

Because of their cost and management advantages, and as a direct consequence of growing automation, the demand for predictive and preventive maintenance systems will continue to increase. The potential of extending their functioning to the control and management of manufacturing processes will provide an additional stimulus. Although the performance of presently used monitoring systems is not uniformly successful, gradual improvement will be achieved, predominantly because of the growing knowledge base. The developing application of expert systems (26,27) will eventually significantly improve the functioning of computer controls. The range of operational requirements is very wide; there is not a "fix-all" solution and the design of a monitoring system should be based on appropriate preliminary measurements and a thorough study of the machinery and the manufacturing processes. One of the basic considerations is to adjust the sophistication of the system to the requirements of the particular application. Not only is such a system more viable and has a better potential of functioning effectively, it is also more likely to be adopted by the production management. On the other hand, computer control is necessary with fully automated manufacturing systems. It provides continuous monitoring of any number of control points with almost instantaneous response to any emergency. It permits combinations of several different monitoring functions and its reliability is improved by using multiple tests and by reducing errors due to subjective judgment. Further development is encouraging the application of expert systems for the control of many of the monitoring processes.

REFERENCES

1. Khurasia, H.B., Telang, A.D., Reliability Through Maintenance: Some Aspects, Proceedings of the 1st International Machinery Monitoring & Diagnostics Conference, Las Vegas, Nevada, Sept. 1989, pp. 222-229.

2. Lyon, R.H., The Monitoring and Diagnostics of machines and Processes, Proceedings of the 1st International Machinery Monitoring & Diagnostics Conference, Las Vegas, Nevada, Sept. 1989, p. XI-XIII.

3. Reeves, C.W., Vibration Monitoring on Chemical Process Plant - the Justification, Proceedings of the 2nd International Conference on Condition Monitoring, London, England, May 1988, pp. 1-15.

4. Rao, B.K.N., Condition Monitoring & Diagnostic Engineering Management (COMADEM) - A Novel Problem Solving Holistic Discipline, Proceedings of the 1st International Machinery Monitoring & Diagnostics Conference, Las Vegas, Nevada, Sept. 1989, pp. 202-209.

5. Baines, N.C., and Fisher, C., Incorporation of Modern Vibration Analysis Techniques in Condition Monitoring Systems, Company Publication SHL 408, Stewart Hughes Limited, Southhampton S09 1XB, England, March 1987.

6. Rix, L.G. and Ludwig, B.W., Computer Aided Quality Control, International Conference on Condition Monitoring, Brighton, England, May 1986, pp. 257-278.

7. Sunnersjo, C.S., Rolling Bearing Vibrations - The Effects of Geometrical Imperfections and Wear, Journal of Sound and Vibration, Vol. 98, No. 4, 1985, pp. 455-474.

8. Tallian, T., Rolling Contact Failure Control Through Lubrication, Institution of Mechanical Engineers, 182, (3A), 1967.

9. Sandy, J., Monitoring and Diagnostics for Rolling Element Bearings, Sound and Vibration, June 1988, pp.16-20.

10. Prasad, H., Malay Ghosh and Biswas, S., Diagnostic Monitoring of Rolling-Element Bearings by High-Frequency Resonance Technique, ASLE Transactions, Vol. 28, No. 4, pp. 439-448.

11. Bearing Fault Diagnosis, Technology Brochure SHL 135, Stewart Hughes Limited, Southampton S09 1XB, England, August 1984.

12. Cortina, E., Engel, H.L. and Scott, W.K., Pattern Recognition Techniques Applied to Diagnostics, SAE, Publication 700497, Detroit, May 1970.

13. Pipe, K., Application of Advanced Pattern Recognition Techniques in Machinery Failure Prognosis for Turbomachinery, Proceedings of the 2nd International Conference on Condition Monitoring, London, England, May 1988, pp. 199-208.

14. Cempel, C., The Vibration Symptom Limit Value in Condition Monitoring, Proceedings of Condition Monitoring 84, Swansea, England, April 1984, pp. 328-339.

15. Tjong, J.S. and Reif, Z., Feasibility of Applying Vibration Monitoring to High Volume, Multistation Transfer Machines, Proceedings of the Eighth Machinery Dynamics Seminar, NRC, Halifax, October 1984, pp. 7.01-7.16.

16. Reif, Z. and Lai, M.S., Detection of Developing Bearing Failures by Means of Vibration, ASME DE-Vol.18-1, 1989, pp. 231-236.

17. Stockline, L.E., New Developments in Tool Condition Inspection Systems, Proceedings of the 1987 Eastern Manufacturing Technology Conference, Springfield, Massachusetts, November 1987, Vol 1, pp. 179-196.

18. Beyer, P.J., Tool Condition Sensor for Automated Manufacturing, Proceedings of the 1987 Eastern Manufacturing Technology Conference, Springfield, Massachusetts, November 1987, Vol 4, pp. 206-226.

19. Suzuki, I., Inasaki, I. and Koshimizu, S., Acoustic Emission Detection of Cutting Tool Chipping, Proceedings of the 1987 Eastern Manufacturing Technology Conference, Springfield, Massachusetts, November 1987, Vol 1, pp. 197-216.

20. Kuhbauch, P. and Quante, F., A New System for Tool Wear and Failure Monitoring in Multispindle Drilling Heads, VDI Berichte Nr. 644, 1987 Proceedings of the 5th International Symposium on Technical Diagnostics, Paderborn, F.D.R., October 1987, pp. 275-282.

21. Monostori, L., Computer Aided Generation of Monitoring Strategy for Complex Machine Tool Monitoring Systems, VDI Berichte Nr. 644, 1987, Proceedings of the 5th International Symposium on Technical Diagnostics,Paderborn, F.D.R., October 1987, pp. 323-331.

22. Kincaid, H.R., Machine Tool Action Monitoring Systems, Proceedings of the 10th Machinery Dynamics Seminar, N.R.C., Calgary, September 1988, pp. 349-372.

23. Moore, T.N. and Pei, J., The Determination of Milling Cutter Tool Condition Using Vibraiton Signals, EAM 90, Kingston, 1990.

24. Moore, T. and Reif, Z., Detection of Tool Breakage Using Vibration Data, SME Manufacturing Transactions 1985, pp. 45-50.

25. Reif, Z., Lau, H.K., Monitoring the Condition of Drills by Means of Vibration, Proceedings of the 7th International Modal Analysis Conference, Las Vegas, February 1989, Vol II, pp. 1022-1027.

26. Petrie, A.M., Sihra, T.S., Ismail, A., The Development of an Automated System for On-Line Tool Wear Monitoring, Proceedings of the 1st International Machinery Monitoring & Diagnostics Conference, Las Vegas, Nevada, Sept. 1989, pp. 546-552.

27. Bernhard, D.L., A Knowledge Based Automatic Machinery Diagnostic System, Proceedings of the 1st International Machinery Monitoring & Diagnostics Conference, Las Vegas, Nevada, Sept. 1989, pp. 651-654.

METACARPOPHALANGEAL JOINT KINEMATICS: SURFACE MARKERS VERSUS BONY LANDMARKS

C.F. Small[1] and D.R. Pichora[2]

(1) Department of Mechanical Engineering, Queen's University
(2) Division of Orthopedic Surgery and Department of Medicine,
Queen's University and Kingston General Hospital, Kingston, Ontario

ABSTRACT

In preparation for a kinematic study of the function of the hand and wrist in progressive rheumatoid arthritis patients, tests were done to assess the suitability of using surface marker positional data to estimate metacarpophalangeal flexion. Stereoradiographs of the hands of two volunteers were made in flat and flexed positions, and the 3D positions of landmarks in the bony anatomy and of lead balls fixed to the hand and fingers were obtained. Kinematic analyses were made according to Euler angle and equivalent screw displacement axis methods, and rotation angles were compared for a number of different landmark and markers combinations. Results suggest that strict surface marker placement is not necessary for good agreement with true (bony) joint angle; markers over the heads of M2 and M3 and near the base of M2 or M3 give good results. Wide separation of the markers must be balanced against ensuring that the rigid body assumption holds.

NOMENCLATURE

abduction - motion away from a median or middle line; in the fingers, away from a line through the middle (third) finger and third metacarpal bone (opposite: adduction)
articulation - a joining together loosely so as to allow motion
carpal - pertaining to the wrist (carpus)
distal - farther away from the trunk of the body (opposite: proximal)
dorsal - pertaining to the back (dorsum) surface (opposite: volar or palmar in the hand and fingers)
flexion - bending of a joint in such a direction as to bring together the two parts the joint connects; in the wrist and fingers refers to motion palmarward (opposite: extension)
metacarpal - pertaining to the five bones of the hand between the wrist and the fingers, i.e. the metacarpus
metacarpophalangeal joint - articulation between a metacarpal bone and the proximal phalanx (knuckle joint)
phalanx - bone of the finger; each finger has three phalangeal bones; the fingers are numbered from one (thumb) through five
pronation/supination -rotation of the forearm about its long axis
proximal - nearer to the trunk of the body
proximal phalanx - most proximal of the three phalangeal bones of a finger
radial deviation - wrist joint movement towards the thumb side of the hand (opposite: ulnar deviation)
radius - long bone of the forearm which articulates with the carpal bones and the ulna at the wrist
ulna - long bone of the forearm which articulates with the radius at the wrist on the side opposite the thumb
x,y,z - orthogonal coordinate system imbedded in a rigid body moving with respect to another
X,Y,Z - orthogonal coordinate system imbedded in a rigid body taken as a "fixed" reference
ϕ - first Euler angle, corresponding to MCP flexion-extension (FEM)
θ - second Euler angle, corresponding to MCP radial-ulnar deviation (RUD)
ψ - third Euler angle (about the long axis of the phalanx); assumed zero
Φ - equivalent screw axis rotation angle

INTRODUCTION

Rheumatoid arthritis is a crippling disease estimated to affect 1 - 2 % of Canadians, and causing inability to work in some 20 - 30% of RA patients. The hand, wrist, and fingers are involved in nearly all cases, but ideal therapy is hampered by the lack of a quantitative, reproducible, and cost-effective method of functional assessment to document disease progression and response to treatment. Researchers at Queen's hope to identify a simple standardized kinematic method of assessment by studying motion of the wrist and metacarpophalangeal (MCP) joints in progressive RA using data obtained from a three-dimensional motion analysis system. However, the accuracy of using markers fixed to the surface of the skin to measure three-dimensional joint motion must first be established. Using a stereoradiographic technique developed at Queen's, the positions of surface markers attached to the hands and fingers of volunteers and the positions of bony landmarks on their metacarpals and phalanges were determined in three dimensions.

THREE-DIMENSIONAL JOINT KINEMATICS

The motions of the wrist and MCP joints are fundamentally three-dimensional and cannot be adequately modelled using conventional planar motion techniques (such as instant centre of rotation) unless the joint is physically constrained. Kinematic analysis of wrist motion and estimation of biomechanical parameters is relatively new [1,2,3,4,5] and the models most often used for the wrist and other non-planar joints are those borrowed from classical dynamics: characterization by use of Euler or Cardan angles [2,10] or by equivalent screw displacement axis [5]. These methods assume that an unknown mechanism connects two rigid bodies, and require that the location of at least four non-colinear points be known on each body; a set of six parameters describes the relative motion.

Euler or Cardan Angles

Euler and Cardan angle descriptions of motion are very similar; by imbedding orthogonal coordinate systems in each of two rigid bodies, relative orientation may be described by a vector connecting the origins and a set of three ordered rotations [6,10]. The differences are in the sequence of rotations and the axes about which the rotations are made. Yet another possible set of rotations (and translations) may be defined wherein the first axis is fixed in the reference body, the third is fixed in the moving body, and the second "floats" mutually orthogonal to them [11]. It may be shown that this body-fixed reference system is equivalent to an Euler angle system if the imbedded coordinate systems are aligned with the body-fixed axes [12]. In this study we have used Euler angles [6] and have chosen a coordinate system such that the first Euler angle ϕ corresponds to MCP flexion-extension (FEM) and the second Euler angle θ is MCP radial-ulnar deviation (RUD) (Fig. 1). The third rotation Ψ about the long axis of the phalanx)is assumed to be zero; this assumption is necessary when only two markers can be placed on the phalanx.

Equivalent Screw Displacement Axis

If the locations of four points in one rigid body before and after a movement are known in terms of a coordinate system imbedded in another, the relative motion between them may be expressed as equivalent to a rotation about and a translation along some axis in space [7]. This axis is known as the equivalent screw displacement or helical axis. The motion is parametrized by the direction cosines of the axis in space, the point of intersection of the axis with some known plane, and magnitudes of the translation and rotation. While magnitudes of the parameters necessarily depend on the orientation of the "fixed" coordinate system, the ESDA method of analysis has the advantage that the physical location of the axis relative to the reference body is system-invariant.

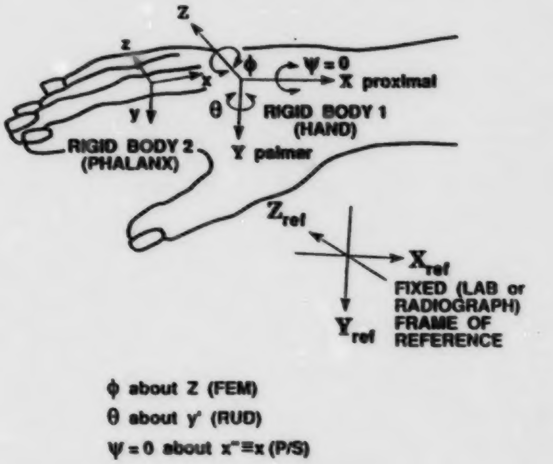

FIGURE 1. JOINT COORDINATE SYSTEMS

Bony Landmarks versus Surface Markers

Stereoradiography can be used to obtain good estimates of the orientations of bones in 3-space [8]; inaccuracies due to the "headland" effect in different views can be minimized by the choice of stereo angle and the separation between calibration planes [9]. However, if continuous kinematic analyses are desired without great expense or X-ray exposure, surface markers must be used. As a first step towards determining the correlation between Euler angle and ESDA calculations made from bony landmarks measurements and surface measurements, a small series of stereoradiographs of hands in flat and flexed positions were made.

METHOD

A number of 1.5 mm diameter lead spheres were fixed to the dorsal surface of the hands of two volunteers (Figure 2). Radiographs were taken from two angles using a standardized calibrated frame (Figure 3), first with the hand flat and then with the MCP joints flexed. The locations of the lead markers and those of prominent bony landmarks on the second and third phalanges and metacarpal bones from the stereo pairs were digitized using a light table interfaced to a personal computer, and the data was used to compute 3D coordinates for each point of interest. A program was written to calculate Euler angles and ESDA parameters for the phalanges with respect to the dorsum of the hand, and various combinations of surface markers were analyzed for comparison with the results obtained from bony landmarks. Tolerances for the program were such that the in-plane locations of points was known to within 0.2 mm, and depth (anteroposterior direction) was known to 0.5 mm.

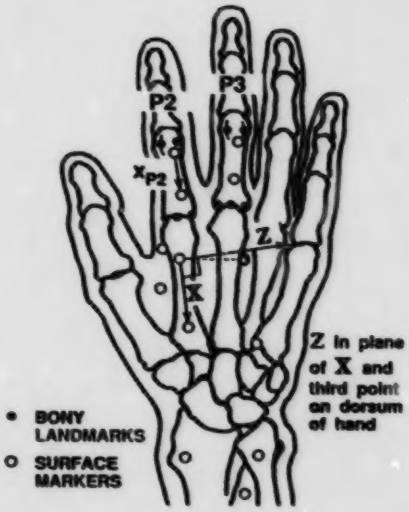

FIGURE 2. TYPICAL RADIOGRAPH

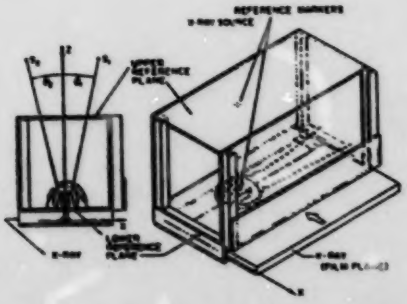

FIGURE 3. STEREORADIOGRAPH APPARATUS

Anatomical Frame - Bony Landmarks

The motions of the second and third phalangeal bones (P2, P3) with respect to the metacarpals (M2, M3) were taken as the reference for true joint motion. M2 and M3 undergo little motion relative to each other and may be considered to be a rigid body. The distal margins of M2 and M3, together with the proximal junction of M2/M3 (Figure 2) formed the basis for the reference body. The origin of the coordinate system was taken in the distal tip of one of the metacarpal bones. The imbedded coordinate system was defined such that X ran proximally to the M2/M3 junction, Z lay in the same plane as X and the distal tip of the other metacarpal bone, and Y was palmarward. This results in a Z axis directed ulnarward in right hands and radially in left hands. The four points used in the calculations of kinematic parameters were thus the origin of coordinates and the tips of the unit vectors.

Three points on each phalanx were identified: the medial and lateral margins of the base of each proximal phalanx, and the prominences just proximal to the attachment of the interphalangeal collateral ligaments at the heads. There is no identifiable "distal-most" point of the phalanges of the hand due to the central articular grooves. A line connecting the head to the midpoint of the base of each phalanx, directed proximally, defined the longitudinal x axis for the phalanx. The assumption of no rotation about the long axis was made for consistency with the surface analysis.

Surface Markers

Two surface markers were placed near the proximal and distal ends of each of P2 and P3 on each subject and secured with medical-grade double-sided tape. A number of markers were taped to the dorsum of the hand of each subject; one objective of the study was to determine the sensitivity of the analysis to marker placement. In both subjects, markers were placed roughly over the heads of M2 and M3, and near the base of M2 (in subject 2 the marker was seen on x-ray to be over the carpus). Other markers were placed around the head of M2 and near M5. A total of 7 markers on the dorsum of the hand were placed for one subject and five for the other.

For each analysis, three markers on the dorsum of the hand were chosen to define the hand segment. One marker near the head of M2 was chosen as the origin of coordinates, and the X axis was directed proximally between it and another marker. Z lay in the plane of X and the third marker selected, and Y was palmarward. A line directed proximally joining the two phalangeal surface markers defined the x axis for the finger.

ANALYSIS

Let the coordinates of a point in the second body be expressed both relative to the moving frame of reference (MFR) and to the fixed frame of reference (FFR) imbedded in the first body. The unit vectors for the MFR expressed in terms of the FFR are given by:

$$\begin{bmatrix} i \\ j \\ k \end{bmatrix} = \begin{bmatrix} i.I & i.J & i.K \\ j.I & j.J & j.k \\ k.I & k.J & k.K \end{bmatrix} \begin{bmatrix} I \\ J \\ K \end{bmatrix} = [B] \begin{bmatrix} I \\ J \\ K \end{bmatrix} \qquad (1)$$

With coordinate systems defined as described, and the assumption that there is negligible rotation of the phalanx about its long axis (third Euler angle zero), the transformation matrix between coordinate systems may also be expressed as:

$$\begin{bmatrix} i \\ j \\ k \end{bmatrix} = \begin{bmatrix} \cos\theta\cos\phi & \cos\theta\sin\phi & -\sin\theta \\ -\sin\phi & \cos\phi & 0 \\ \sin\theta\cos\phi & \sin\theta\sin\phi & \cos\theta \end{bmatrix} \begin{bmatrix} I \\ J \\ K \end{bmatrix} \qquad (2)$$

The "no rotation" assumption also permits the definition of a complete coordinate system in the finger from only two points. Note that the cross product of K (hand) and i (finger) gives the direction of j for the finger:

$$\begin{aligned} K \times i &= K \times (\cos\theta\cos\phi I + \cos\theta\sin\phi J - \sin\theta K) \\ &= \cos\theta(-\sin\phi I + \cos\theta J) \\ &= \cos\theta j \end{aligned} \qquad (3)$$

The k vector for the finger is given by the crossproduct $k = i \times j$.

Comparing the form of [B] in (2) with that in (1) allows us to calculate Euler angles from the unit vectors:

$$\begin{aligned} b_{13} &= k.I = -\sin\theta \\ \text{and} \quad \theta &= \sin^{-1}(-k.I) \end{aligned} \qquad (4)$$

$$\begin{aligned} b_{21} &= j.I = -\sin\phi \\ \phi &= \sin^{-1}(-j.I) \end{aligned} \qquad (5)$$

Notice that conventions for positive Euler rotations (given by the right hand rule) result in a negative sign for MCP flexion relative to the hand coordinate system in both right and left hands. The assumption that the hand segment is rigid means that Euler angles for the finger after flexion may be subtracted from the corresponding Euler angle before motion. Translation of the origin of coordinates was not considered in this analysis.

Equivalent screw axis calculations may be performed using essentially the same transformation matrix, "augmented" to the 4x4 form by including vector $(s_x\ s_y\ s_z)^T$ connecting the origins [7]:

$$\begin{bmatrix} 1 \\ P_X \\ P_Y \\ P_Z \end{bmatrix} = \begin{bmatrix} 1 & 0 & 0 & 0 \\ s_x & b_{11} & b_{12} & b_{13} \\ s_y & b_{21} & b_{22} & b_{23} \\ s_z & b_{31} & b_{32} & b_{33} \end{bmatrix} \begin{bmatrix} 1 \\ p_x \\ p_y \\ p_z \end{bmatrix} \qquad (6)$$

where $(P_X\ P_Y\ P_Z)^T$ are the coordinates of a point P expressed relative to the FFR, and $(p_x\ p_y\ p_z)^T$ are the same point's coordinates relative to the MFR. This augmented form of [B] is denoted [B']. If the location of a point relative to the FFR is known before and after a motion, the final position may be expressed in terms of the starting position by an equation of a similar form:

$$\{P\}_2 = [A]\{P\}_1 + \{T\} \qquad (7)$$

where [A] is a rotational matrix and {T} is a translation vector. This equation can also be expressed as an augmented matrix [A']. If the coordinates of four points (such as the origin of coordinates and the tips of the unit vectors of the MFR) are known in both systems before and after a motion, their augmented column vectors may be assembled and three systems of equations result:

$$[P']_2 = [A'][P']_1 \qquad (8)$$

$$[P']_2 = [B_2'][p'] \qquad (9)$$

$$[P']_1 = [B_1'][p'] \qquad (10)$$

It follows from (8), (9), and (10) that

$$[A'] = [B_2'][B_1']^{-1} \qquad (11)$$

The EDSA parameters can be calculated from the coefficients of [A'] [17]; it can be shown [12] that for "no phalangeal rotation the relationship between change in Euler FEM angle $(\phi_2-\phi_1)$ involves only the helical rotation Φ and the projection of the screw axis in the Y direction (direction cosine u_Y):

$$u_Y^2 + (1-u_Y^2)\cos\Phi = \cos(\phi_2-\phi_1) \qquad (12)$$

For coordinate axes aligned with the functional axes of motion, good agreement would be expected between helical and Euler rotations for an essentially planar motion, except for the sign of the angle for MCP flexion, as ESDA analysis defines rotation angle to be always positive with the direction cosines giving the sense.

RESULTS

Subject 1

Excellent agreement was obtained between Euler and ESDA rotations for bony landmark data for both P2 and P3 (Table 1), and for X axes directed either along M2 or M3; this corresponded to values of u_Y of 0.150 or less. Surface marker data also showed good agreement between Euler FEM and ESDA rotation for combinations of markers roughly over the heads of M2 and M3 and the base of M3 (5,6,9) and (5,7,9). Combinations where two of the markers were very close together (6,7,9) or the X axis was diagonally across the back of the hand rather than roughly proximally (5,6,8) gave poorer agreement and corresponded to u_Y values greater than 0.23. However, for all surface marker combinations involving a proximally directed X axis, rotations calculated from surface markers agreed with bony landmark calculations to within 5.5°.

TABLE 1 ROTATION RESULTS - SUBJECT 1

	SECOND MCP JOINT			THIRD MCP JOINT		
	EULER ANGLES		SCREW	EULER ANGLES		SCREW
	ϕ (FEM)	θ (RUD)	ROT'N	ϕ (FEM)	θ (RUD)	ROT'N
Bony landmarks						
7,8,9	-32.89	1.22	32.91	-37.22	5.92	37.46
8,7,9	-31.10	1.41	31.13	-37.76	-3.37	37.46
Surface markers						
5,6,9	-32.12	3.48	32.30	-31.66	5.86	32.19
5,7,9	-34.33	7.87	35.20	-36.07	10.52	37.52
6,7,9	-32.38	15.60	35.85	-32.66	18.54	37.44
5,8,9	-37.72	13.23	39.89	-38.12	16.35	41.36

Subject 2

In all cases where the choice of surface markers included the base of M2, giving an X axis directed roughly proximally, the MCP Euler FEM angles and ESDA rotations agreed within 5° (Table 2). This suggests that strict measures for setting up the proximal axis of the hand and finger markers is not necessary for reproducible results in this sensitivity range.

However, the angles calculated from surface marker data underestimated the bony angle in both MCP joints, whether the reference bony system was aligned with M2 or M3. In this subject, the proximal marker for the dorsum of the hand was seen on xray to be proximal to the base of M2; that is, over the wrist joint. A small amount of wrist dorsiflexion between "MCP flat" and "MCP flexed" stereopairs may be included in this measurement.

TABLE 2 ROTATION RESULTS - SUBJECT 2

	SECOND MCP JOINT			THIRD MCP JOINT			
	EULER ANGLES		SCREW	EULER ANGLES		SCREW	
	FEM	RUD	ROT'N	FEM	RUD	ROT'N	NOTES
Bony landmarks							
7,8,9	-36.66	-4.23	36.89	-31.14	-1.83	31.19	X along M2
8,7,9	-34.87	-9.44	36.08	-31.97	4.88	32.33	X along M3
Surface markers							
8,6,11	-24.53	-5.42	25.11	-28.35	-2.91	28.50	
8,9,11	-20.99	-.76	21.00	-25.98	.99	26.00	
5,6,11	-22.30	2.31	22.42	-27.73	3.43	27.94	
5,7,11	-20.96	6.64	21.97	-27.09	8.59	28.39	
5,9,11	-20.23	5.87	21.06	-26.91	6.52	27.67	
8,7,11	-21.69	.35	21.69	-26.72	2.25	26.81	
5,7,9	-32.01	-.29	32.01				(7-9) close
5,6,8	-37.44	25.31	44.94	-56.78	27.33	62.52	X diagonal
6,9,10	-28.00	14.32	31.39	-41.33	16.42	44.34	X diagonal

As will be seen from the last two lines in Table 2, misalignment of the proximal axis results in large RUD angles and poor agreement between methods; they correspond to large values of helical axis direction cosines u_Y.

Error analyses based on a box technique for uncertainty in spatial locations from the digitizing procedure was performed, and resultant errors in the magnitudes of FEM and ESDA rotation are in the order of 2.3°; that in RUD is less than 1°. A more detailed analysis of error propagation is underway.

CONCLUSION

The results indicate that calculations based on surface markers should provide the same information on joint rotations as do the bony landmarks within the accuracy of the measurements, if reasonable care is taken with marker placement. The results are insensitive to marker placement, with the exception that one axis on the dorsum of the hand must be directed proximally in order to validate the "no rotation" assumption. Minor misalignments of the proximal axis with respect to the bony anatomy result in overestimation of the radial-ulnar component of motion, but the magnitude of FEM angle calculated by the Euler method agrees well with the helical rotation. Underestimation of joint angle was observed in one of the two subjects tested, likely due to placing the marker too near the next joint. The phenomenon requires further investigation, as maximal separation of markers is desired to reduce error propagation.

ACKNOWLEDGEMENTS

This work was supported by a grant from the Advisory Research Committee of Queen's University at Kingston, ONtario. The assistance of members of the Clinical Mechanics Group at Queen's is gratefully acknowledged.

REFERENCES

1) Youm Y et al (1978) Kinematics of the Wrist: An Experimental Study of Radial-Ulnar Deviation and Flexion-Extension. J Bone Jt Surg 60-A:423-431

2) Youm Y and Yoon YS (1979) Analytical Development in Investigation of Wrist Kinematics J Biomechanics 12:613-621

3) Linscheid RL (1986) Kinematic Considerations of the Wrist. Clin Orthop 202:27-39

4) Tolbert JR et al (1985) Kinetics of Normal and Prosthetic Wrists J Biomech 18:887-897

5) Evans JS et al (1986) The In Vivo Kinematics of the Rheumatoid Wrist. J Orthop Res 4:142-151

6) Chao EYS (1980) Justification of the Triaxial Goniometer in the Measurement of Joint Rotation. J Biomech 13:989-1006

7) Kinzel GL et al (1972) Measurement of the Total Motion Between Two Body Segments - I. Analytical Development. J Biomech 5:93-105

8) Wevers et al (1982) A quantitative method of estimating malalignment and joint space loss of the human knee. J Biomed Eng 4:319-24

9) Runciman JR et al (in preparation) Standardized Stereoradiographic Technique for Estimating Alignment of the Metacarpophalangeal Joint.

10) Tupling SJ, Pierrynowski MR (1987) Use of cardan angles to locate rigid bodies in three-dimensional space. Medical and Biological Engineering and Computing 25:527-32

11) Grood ES and Suntay WJ (1983) A joint coordinate system for the clinical desription of three-dimensional motions: application to the knee. J Biomecanical Eng 105:136-144

12) Small, CF (in preparation) On rigid body kinematics of the wrist and finger joints.

HIGH HEEL GAIT

U. P. Wyss, I. McBride, J. T. Bryant, T. D. V. Cooke

Clinical Mechanics Group, Apps Medical Research Center
Kingston General Hospital, Kingston, Ontario K7L 2V7

ABSTRACT

Our way of life is influenced to a great deal by habits. One particular part of female fashion that comes and goes over time is the wearing of high heel shoes. It is generally accepted that high heel shoes are not healthy for the feet, but not much objective information is available. This paper focuses on the loading conditions at the first metatarsophalangeal (MTP or big toe) joint. Eleven young normal females participated in this study. Each subject walked three times along a raised walkway while wearing high heel shoes. Sagittal kinematic and force plate data were collected simultaneously. Subsequently, a lateral and a dorsoplantar radiograph were taken with radiopaque markers at the location of the kinematic markers. These data were used in a biomechanical model to analyze the forces acting at the great toe joint. The normalized peak resultant force, FRES, was found to have values which were about two times greater than walking in low level heel shoes. The mean angle at which FRES is applied relative to the anterior shaft of the first metatarsal (MT) bone was observed dorsal to the longitudinal axis of the bone. This is approximately four degrees further dorsal than the mean data obtained by barefoot walking, indicating that wearing high heel shoes alters the location of loading at the MTP joint. This may shift the sesamoids to a location that is beyond the ridge that separates and guides these two bones, which increases the possibility of subluxation and the development of osteoarthritis.

INTRODUCTION

Few articles have been written to describe the forces at the first MTP joint. Stokes et al. (1979) determined that approximately 40 per cent of body weight was exerted on the toes during the push-off phase of gait and that the majority of this was applied on the great toe. These authors also calculated that the joint reaction force at the first MTP joint was about 80 per cent of body weight during gait. On the other hand, Hutton and Dhanendran (1981) found maximum forces at the first MTP joint of approximately body weight during bare foot walking. In more recent articles, Sussman and D'Amico (1984) presented the influence of heel height on the dorsiflexion angle at the first MTP joint, whereas Shereff et al. (1986) described the kinematics of this joint. However, the effect of heel height has not been considered with regard to its influence on the first MTP joint reaction forces. In addition, Yoshioka et al. (1988) and Wyss et al. (1989) have described the importance of the sesamoids in this region with respect to geometric features and alignment. Only one other study has included the joint reaction forces between the metatarsal head during gait as a part of their analysis (Wyss, 1989). The purpose of this study was to examine the effect of heel height on the joint reaction forces at the first MTP joint and at the metatarsal-sesamoid joint at toe-off during gait.

MATERIALS AND METHODS

Eleven young normal females participated in this study. Age, height, weight and other subject data are summarized in table one. Prior to the walking trials, reflective markers were placed on the medial side of the left knee, ankle, heel, MTP joint, and toe. The subjects were filmed with a LOCAM camera as they walked along a raised walkway to obtain sagittal kinematics. Force plate data were collected simultaneously. Three acceptable trials were collected for each of barefoot and high heel walking for a total of six

Table 1. Summary of subject data.

	Number of Subjects	Age (years)	Height (cm)	Mass (kg)	Heel Height (cm)
Mean	11	26.8	162.8	64.1	6.8
S.D.		6.7	6.2	9.1	0.8

trials. For each trial a footprint was obtained by placing an inked rubber mat over an accurately positioned piece of paper on the force platform providing a good correlation of the footprint with the course of the ground reaction forces. Subsequently, a lateral and a dorsoplantar radiograph were obtained with radiopaque markers at the locations of the kinematic markers. The lateral radiographs were taken with the subjects' bare foot while the dorsoplantar radiograph involved the subjects wearing their high heel shoes. A footprint was obtained during the dorsoplantar radiograph using the same method as during the recording of the kinematics, while the subjects stood on the X-ray cassette. As well, two lead markers, which were visible on the radiograph, were attached to this sheet of paper. This enabled a drawing to be made on a transparency of the bones of the foot together with the footprint obtained during radiography with an accuracy of plus/minus 0.5 mm as shown in figure one. On the overhead were marked the centers of curvature of the first and second MT, the joint centers of the distal interphalangeal joints, and the end of the first and second toes. By accurately aligning the outline of the radiographic footprint of the overhead with the footprint obtained during the gait study, and by indicating the force plate center on the piece of paper, it was possible to determine the location of the center of pressure (ground reaction force) relative to the force plate center, the centers of rotation, joint centers, and ends of the first and second toes.

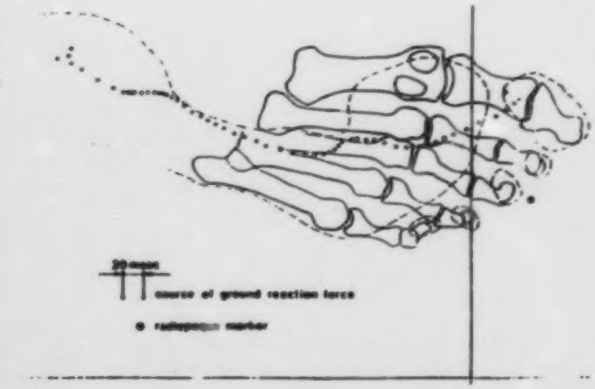

Figure 1. A footprint of a subject (dashed line), the relative positions of the bones in the distal aspect of the foot, and the course of the ground reaction force (dots) throughout the stance phase of gait. The positions of the two oval sesamoid bones may be observed in relation to the first metatarsal bone.

Various bone dimensions, angles of the bones relative to the radiopaque markers, and angles of the muscles and tendons also were obtained from the radiographs and were corrected for parallax error. These data, together with the x and z coordinates, were used in a simple biomechanical model to analyze the forces acting at the first MTP joint.

Biomechanical Model

The model used to calculate the various parameters in this study is similar to the model developed by Stokes et al. (1979). This model, as shown in figure two, is based on subject specific measurements about the geometry, kinematics, and forces acting on the first MT. The relative position of the ground reaction force between the first and second toes provided a ratio of the forces that act directly on the first MT. When the ground reaction force was lateral to the second toe and posterior to the centre of curvature of the MT head then the load was assumed to be zero. Once the ground reaction force was distal to the centre of curvature of the first MT head, it was possible to calculate the various forces. FTS was the relative proportion of the total force that acted directly on the first MT in the sagittal (xy) plane. The pulling force of the flexor hallucis longus muscle, FM, also was determined, as well as the corresponding lever arms for FTS and FM, t and m, respectively. This provided values for FM and the x and y components of the joint reaction force, FJ, between the MT head and the proximal phalanx. Assuming the situation of a frictionless pulley, with FM pulling away from the sesamoids in both directions, it was possible to calculate the resultant force, FS, acting between the

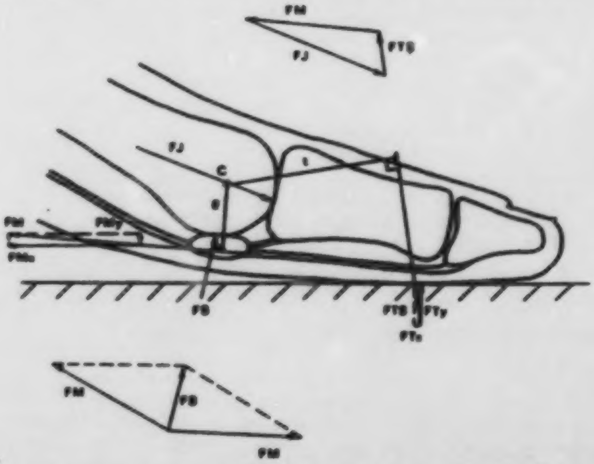

Figure 2. Biomechanical Model of the first MTP joint in the sagittal plane. The accelerations during push-off are small and allowed to use a static approach.

sesamoids and the MT head. FS and FJ were combined to give a resultant force, FRES, which acts at the MT head. These forces were calculated for each cine frame (sampling rate of 50 Hz), and expressed relative to the anterior ridge of the shaft of the MT providing an angle PHI between FRES and the anterior ridge.

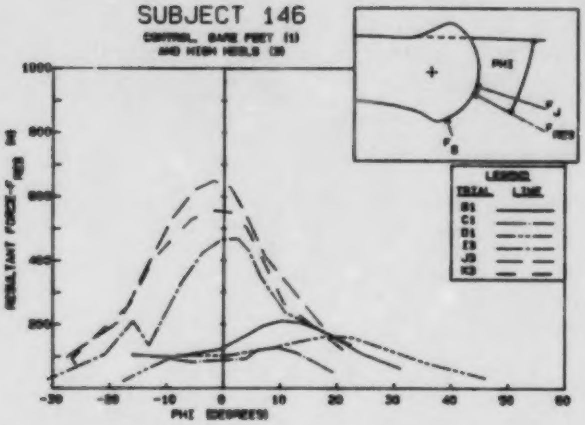

Figure 3. This figure displays the resultant forces, FRES, that act on the first metatarsal during toe-off and the angle PHI that FRES makes relative to the anterior shaft of the metatarsal (see inset). It shows the results when the subject walked in bare feet and in high heeled shoes.

RESULTS

A typical example of the influence of high heels is shown in figure three for one subject. The heel height of 5.5 cm for this subject was below the average height of 6.8 cm for the whole group, but the difference in the resultant loading of the first MT is still significant as can be seen in the figure. Also noticeable is a twenty degree shift of the orientation of the maximum forces dorsally. The loading of the MT's two articulations is shown for another subject in figure four A and B. It shows the same pattern with the resultant forces during the high heel gait trials moving dorsally. The graph in the lower right corner indicates to which degree the joint reaction forces are transmitted through the first toe. Figure 4b shows that most of the push-off phase is almost entirely carried by the first toe, while the transition to the first toe is more gradual during barefoot walking.

The characteristic features during high heel gait are summarized in tables two and three. The average velocity is almost identical for the high heel and barefoot walking trials. All other values in the tables are for the moment of the maximum resultant forces, which were normalized per kg body mass. The forces during high heel gait are approximately twice as large as during barefoot walking. These forces are significant as they represent more than one time body weight, especially when keeping in mind the relatively small size of the joint. The forces between the first MT and the two small sesamoid bones are about half of those between the MT and the proximal

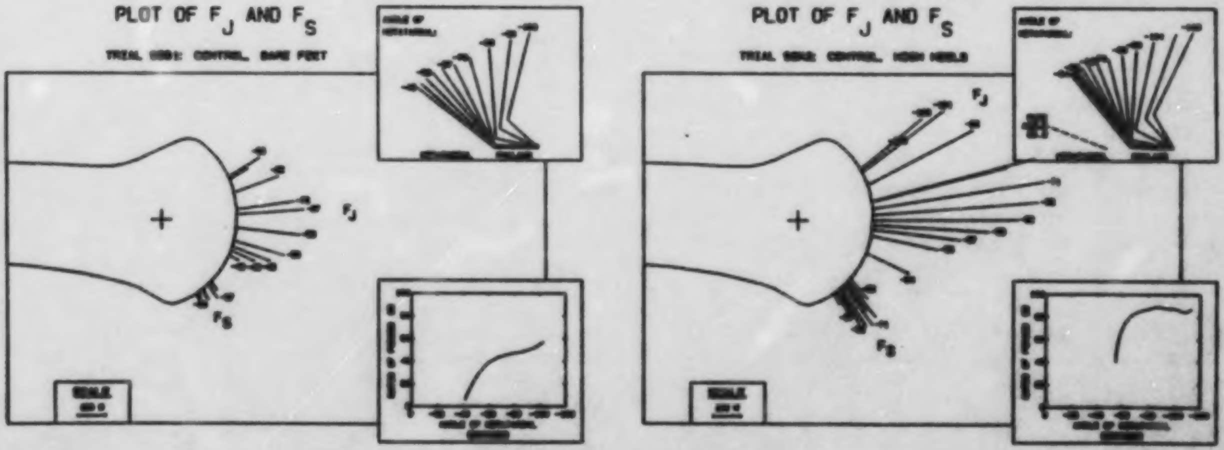

A

B

Figure 4. Figures 4A and 4B show FJ and FS. The FS data act at an inferior angle to the metatarsal and are smaller in magnitude than the FJ results. The increased magnitude of forces and ratio of forces during high heeled walking can be seen.

phalanx. The absolute value of META represents the angle between the MT and the horizontal. The average of this angle is about eight degrees larger at maximum resultant forces as one would expect with the higher heels. The angle PHI is measured between the resultant force and the anterior shaft of the first MT. Wearing high heel shoes shifted PHI dorsally by approximately 4 degrees.

DISCUSSION

The purpose of this study was to determine the effects of footwear on the loading patterns at the first MTP joint during the push-off phase of gait for a young female population wearing high heels. The results obtained clearly show that the forces are approximately twice as large during the high heel trials. This fact alone must be considered a potential risk factor for earlier development of a pathological first MTP joint. Furthermore, it has been shown by Yoshioka et al. (1988), that even small changes of the orientation of the bones to each other within this joint may have serious consequences. In particular, the location of the sesamoid bones with respect to the MT is very sensitive. The sesamoids are running in grooves that are separated by a central ridge. The depth of the groove varies, but it is only in a small region deep enough to keep the sesamoids from being "pulled out". The change in this articulation is affected by both, META and PHI, and both change for the worse during high heel gait.

In conclusion it can be stated, that from a biomechanical perspective, high heel gait should be avoided.

Table 2. Normalized parameters during maximum loading of the metatarsal head during barefoot walking.

	Velocity (m/s)	Heel Ht (cm)	FRES (N/kg)	FS (N/kg)	FJ (N/kg)	PHI (Deg)	META (Deg)
Mean	1.34	0.0	6.12	2.93	5.18	2.24	-63.67
S.D.	0.16	0.0	4.66	2.66	4.00	6.17	13.36

Table 3. Normalized parameters during maximum loading of the metatarsal during high heel gait.

	Velocity (m/s)	Heel Ht (cm)	FRES (N/kg)	FS (N/kg)	FJ (N/kg)	PHI (Deg)	META (Deg)
Mean	1.31	6.60	12.26	6.69	10.34	-1.86	-71.63
S.D.	0.18	0.77	6.63	5.13	6.50	6.15	10.76

ACKNOWLEDGEMENTS

The authors would like to acknowledge financial support by the Physician's Services Incorporated and the Ontario Ministry of Health.

REFERENCES

1. Hutton, W. C., and Dhanendran, M. 1981, The mechanics of normal and hallux valgus feet - a quantitative study, Clin. Orthop., Vol. 157, pp. 7-13.
2. Shereff, M. J., Bejjani, F. J., and Kummer, F. J. 1986, Kinematics of the first metatarsophalangeal joint, J. Bone Surg., Vol. 68A, pp. 392-398.
3. Stokes, I. A. F., Hutton, W. C., and Stott, J. R. R. 1979, Forces acting on the metatarsals during normal walking, J. Anat., Vol. 129 (3), pp. 579-590.
4. Sussman, R. E., and D'Amico, J. C. 1984, The influence of the height of the heel on the first metatarsophalangeal joint, J. Am. Podiatry Assoc., Vol. 74 (10), pp. 504-508.
5. Wyss, U. P., McBride, I., Murphy, L., Olney, S. J., and Cooke, T. D. V. Joint reaction forces at the first MTP joint in an elderly population, J. Biomech., accepted 1989.
6. Wyss, U. P., Cooke, T. D. V., Yoshioka, Y., Bryant, J. T., Siu, D. 1989, Alignment of the First Metatarsal-phalangeal Joint: Important Criteria for a New Joint Replacement, J. Biomed. Eng., Vol. 11, pp. 19-24.
7. Yoshioka, Y., Siu, D. W., Cooke, T. D. V., Bryant, J. T., and Wyss, U. 1988, Geometry of the first metatarsophalangeal joint, J. Orthop. Res., Vol. 6, pp. 878-885.

Three–dimensional Display and Manipulation of Medical Objects

Cao H Tuan, Joaquin D Chan, T. Caohun and Hélène Rémy

Department of Mechanical Engineering, Concordia University
Department of Computer Science, Texas A & M University
Department of Diagnostic Radiology, Montreal General Hospital

Three-dimensional (3D) imaging in medicine is a new discipline that offers the unique possibility of interactive manipulation and quantitative location of anatomical structures for display, measurement and analysis. The framework for the three–dimensional reconstruction of an anatomical object from serial cross-sections is: data acquisition, image processing, reconstruction, and display. For most 3D methodologies, the three-dimensional reconstruction of an organ from serial cross-sections has three basic operators. Subregioning provides a subset of the total data volume. Interpolation is required to reconstruct the image of an embedded element when the serial cross–sections are not closely spaced. Interpolation is also required for rendering. Thresholding simplifies an image by redistributing the data spectrum into a binary volume. It is a simple, direct method to intensify the organ's shape and geometric structure while reducing the computational requirements. In this article we will describe the techniques of linear and B-spline interpolation and illustrate several specific clinical examples that can be readily appreciated by non-specialists.

Introduction

---

1. FUNDAMENTAL REQUIREMENTS

Medical imaging imposes a different set of display and processing requirements from those in high–performance graphics systems such as in CAD/CAM for the following reasons:

(a) Medical objects, composed of multiple tissues, are extremely complex and irregular. Medical imaging systems process an enormous amount of data (an average of 5 megabytes per patient for a routine head scan, where each pixel requires 12 to 16 bits of storage) to be displayed without loss of detail. Representing medical objects by curved surface patches, planar polygons, or constructive solid geometry is computationally expensive [1,8].

(b) The data on which the images are built are obtained under machine control from real objects, rather than generated from mathematical or computer models. In order to understand the structural and functional characteristics of a medical object, interactive manipulation must be supported in real-time.

(c) Real-time display is also necessary to provide a high patient throughput for maximum therapeutic efficiency.

Even though three-dimensional imaging is a new discipline, various points of view have already been proposed [1,4,5,8] which include the use of software on existing hardware that is a part of the standard configuration for modern scanners, special–purpose computer architecture, and hardware assist devices. The following requirements and improvements for 3D medical imaging systems have been recently reviewed and formulated [8], see Figure 1.

(a) Accurate and reliable display and quatitative location of structures for analysis and measurement of **distance, area and volume.**

(b) Depiction of both soft and hard tissues.

(c) The ability to generate various translucencies in order to display depth and organ topology and to examine the interior of the organ.

(d) High speed generation of multiplanar, reprojected and shaded surface images.

(e) 3D rotation, translation, scaling, tissue segmentation, and object editing.

(f) Display of 3D objects over time.

(g) 3D *multimodal* imaging. The ability to interregister data sets from anatomical, spatial (CT and NMR), physiological and morphological (PET and SPECT) sources will contribute greatly to therapeutic efficiency. For example, as in the case of cardiac imaging, multimodal imaging can simultaneously: (1) assess regional blood flow, (2) evaluate cardiac function under pharmacological stress and at rest, (3) sharpen indications for surgery or angioplasty by distinguishing viable, reversibly injured myocardium from necrotic tissue, (4) assess the major postinfarction prognostic indicators of infarct size, ejection fraction and end-systolic left ventricular volume.

2. 3D BINARY SCENE PROCESSING

CT data sets are usually obtained with an inter-slice distance no thinner than 1 mm, which is significantly greater than the inter-pixel distance. To obtain a good quality image, we need the inter-slice distance to be equal to the distance between pixels, we use interpolation to obtain cube-shaped volume elements or voxels (that is, through interpolation we increase the axial resolution by adding new slices between old slices to obtain an isotropic data set). We had considered two other alternatives: one is to increase the dimension of the pixel to that of the inter-slice distance, the other is to decrease the voxel size to that of the pixel. Both are rejected, the former for lack of accuracy and the latter due to the occurrence of artifacts and aliasing. Interpolation is also needed for rendering. Thresholding (or binarization) simplifies an image while intensifying its shape and geometric structure. This operator produces a binary scene by assigning the value 1 to all voxels within a certain user-defined range of values (radiological densities) and 0 to all other voxels. This is a direct, simple method for extracting an object but it has served us well since our initial interest [9] in the problem of 3D surface reconstruction arose from the need to evaluate patients with midfacial fracture gaps which follow predictable lines of intrinsic fragility. In X-ray tomography, since the photoelectric and compton effects conveniently separate bone from soft-tissue by a CT density threshold (similar arguments apply to NMR and PET although the mechanisms are different), it is easy to redistribute a continuous CT data spectrum into a binary volume.

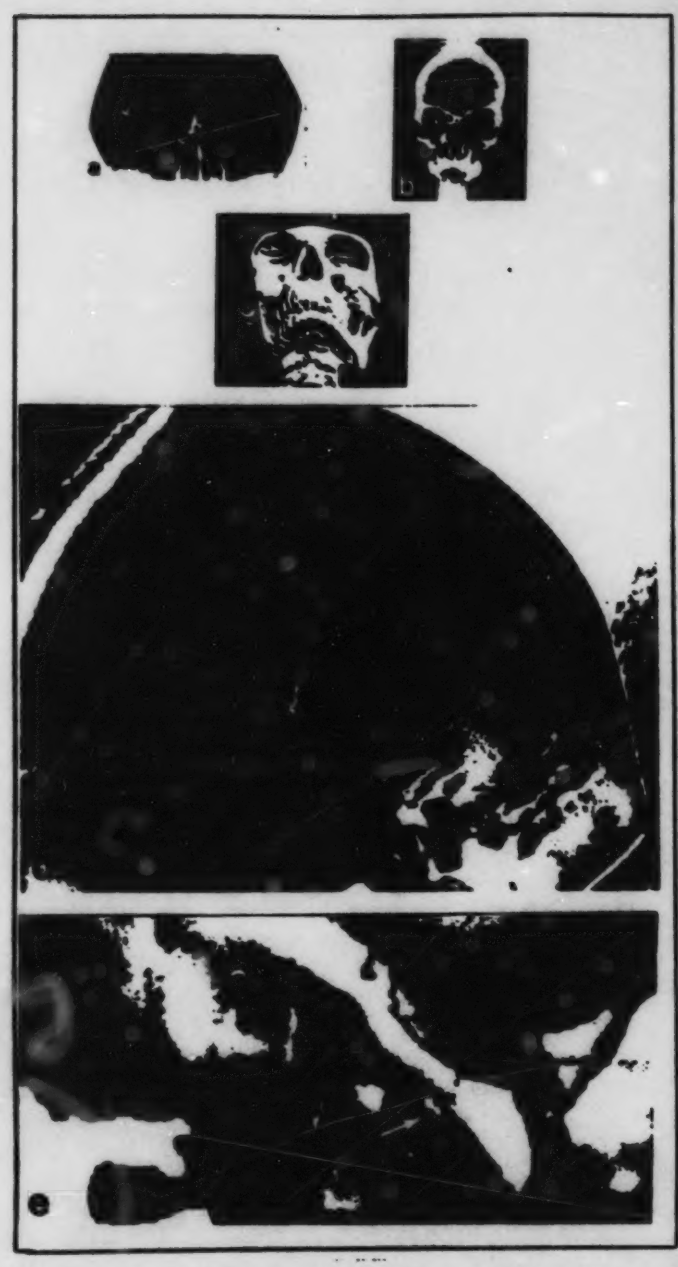

Figure 1. (a,b, c) Conventional X-Ray, 3D CT scan, 3D image of the skull (cranium) for comparison, (d) Interactive manipulation: 3D rotation, translation, scaling to zoom in on the object, and object editing to simulate surgery such as to drill a hole or to move bone from one place to another, (e) 2D CT may entirely fail to detect hair-line fracture between 0.1 – 0.3 mm. 3D Images provide a superior understanding and shows a small break (arrow) at the temporo-mendibular joint.

Display Process: Object Representation ↦ Geometric Coordinate Transformation ↦ Hidden Surface Removal ↦ Smooth Surface Shading.

3. SURFACE AND VOLUME RENDERING

In surface rendering, an edge-detecting algorithm will explicitly determine the object's surface. This information is stored as piecewise linear representations or contours for eventual processing and display.

In volume rendering, object surfaces are not explicitly computed. A process of cumulative projection of voxels or ray-traycing generate interfaces, surfaces, and pseu-do surfaces. Computational ease and efficiency, powerful data structure and access will determine reliability, accuracy, easy and speed of display and interactive manipulation. Data storage can be achieved by octree encoding, set of cube faces, or contours [1,8].

4. 3D RECONSTRUCTION ALGORITHMS

We wish to reconstruct the surface S(x,y,z) from a given set of oriented closed curves in k planar cross-sections. 3D reconstruction algorithms can be formulated in an analogous manner to those used in 2D tomography where real space algorithms, either convolution back-projection or iterative methods are most commonly used. The basis of many real space reconstruction algorithms is back-projection, which can be simply thought of as `smearing back` the density from each pixel of the projection image, along the projection direction, into the higher dimension image or volume to be reconstructed. In iterative algorithms, it is also necessary to project forward . Back and forward projection are essentially inverse operations. Several basic approaches to the problem of surface reconstruction have been proposed in the literature. The first approach is the cuberrille representation [1,5,8] in which an object is represented by sets of cubes or voxels (volume elements). A cuberille is defined to be a face of the voxel [1], and the focus is on extracting and following the cuberilles at the boundary surface between the object and its background. Interpolation is used to reconstruct the contours between the adjacent cross-sections. The second approach is the polygon tiling technique which approximates a solid object by determining a polyhedral structure between parallel contours. The polygons are then rendered to generate a 3D scene. The general steps are: shape detection, contour representation, 3D scan conversion and surface approximation from the triangulation process which can be achieved through either heuristic or graph methods [5]. The polygon tiling technique is generally suitable only for simple surfaces. If the distance beween adjacent contours is large, errors of representation may occur. Another promising approach has recently been proposed and developed [9]. This approach is independent of inter-slice distance. We wish to determine a unique surface from a set of closed, oriented curves based on `equality-constrained` functional optimization [9]. The mathematical idealization of the problem of surface reconstruction is to determine the constrained optimization which is a surface that minimizes a functional measuring surface consistency [6]. The constraint that we chose is that the sum of all curvatures of the surface S must be minimum. This means that the surface should be as flat (smooth) as possible. Our approach is also a good smoothing technique. It satisfies several of the fundamental criteria that we outlined in the section that follows. The Euler equations of the interpolation problem are then derived and solved using nonlinear mathematical programming (NLP) [9].

> **We wish to determine a unique surface from a set of closed, oriented curves based on equality-constrained functional optimisation [9]. The mathematical idealisation of the problem of surface reconstruction is to determine the constrained optimisation which is a surface that minimises a functional measuring surface consistency [6].**

5. IMAGE SPACE SHADING

Shading `models` classify the surface as smooth, faceted, textured, diffuse, shiny or colored. Shadows and multiple light sources are to be simulated for improved realism. Shading `algorithms` achieve the desired effects by assigning the appropriate intensities to the pixels. Almost all display methodologies comprise of the following steps: object representation, geometric coordinate transformation, hidden surface removal, and smooth surface shading (Figure 2). Several shading models have been proposed. The simplest shading model uses `distance only` and the more sophisticated ones use a combination of distance and light illumination and reflection effects. The intensity of a reflected light at a point on a visible surface can be given [3] as the integral over the hemisphere above the reflecting surface of an illumination function, $\mathbf{L}(t,x,y,z,\phi,\theta,\lambda)$ and the reflectance function $\mathbf{R}(t,x,y,z.\phi,\theta,\lambda)$:

$$\mathbf{I}(x,y,z) = \int_{-\infty}^{+\infty}\int_{580}^{760}\int_{0}^{\frac{\pi}{2}}\int_{0}^{2\pi} \mathbf{L}(t,x,y,z,\phi,\theta,\lambda)\cdot \mathbf{R}(t,\phi,\theta,\lambda)\,d\theta\, d\phi\, d\lambda\, dt. \qquad (6\text{-}1)$$

Where ϕ and θ are polar coordinates of illumination direction vectors, t is time, λ is the wavelength of incidence and reflected light and (x,y,z) are the coordinates at the reflection point.

For a perfectly diffuse surface, the same brightness can be observed from all directions and the reflected light intensity is given by,

$$\mathbf{I} = \mathbf{I}_a + \sum_{i=1}^{N} k_d \mathbf{I}_{L_i}(\mathbf{N} \cdot \mathbf{L}_i) \qquad (6\text{-}2)$$

where I is the intensity of the reflected light, $\mathbf{I}_a$ is a constant intensity due to reflected ambient light.

Eqn (6-2) implies that all surfaces are assumed to be polygons. As such, intensity discontinuities are introduced at the joints between two polygons. Gouraud solved this problem by interpolating intensities across the polygonal surface to achieve the effect of a smoothly curving surface. Phong took into consideration the specular reflection. He computed a resultant normal vector at each of the vertex that joints the two polygons. These resultants are then interpolated across the polygon. Phong proposed a shading function that includes a specular term. His scheme turned out to be much less susceptible to the `mach` band effect as Gouraud's.

$$\mathbf{I} = \mathbf{I}_a + \sum_{i=1}^{N} k_d \mathbf{I}_{L_i}(\mathbf{N} \cdot \mathbf{L}_i) + k_s \sum_{i=1}^{N} \mathbf{I}_{L_i} R_s \qquad (6\text{-}3)$$

Interpolation Techniques

1. THE CONCEPT OF INTERPOLATION

We wish to reconstruct the `volume` of a medical object from a set of volume elements (voxels) whose typical size is no smaller than 0.5 mm × 0.5 mm × 1 mm, the third dimension indicates the thickness of the slice. The interpolation schemes are chosen according to the following `criteria`: applicability to existing hardware, image quality, consistency with human perception, reliability and accuracy, scale invariance, rotational and translational invariance, computational ease and efficiency, ease and speed in interactive manipulation, and other functionalities.

We have experimented with simple interpolation schemes such as first-order linear, B-spline cubic and more sophisticated interpolation functions. Our experience has shown that the more sophisticated functions, other than linear and B-spline interpolations, are not necessary since image quality is not improved because of artifacts due to limitations in numerical precision.

2. LINEAR INTERPOLATION

On the real axis x, given two points s_i and s_{i+1} and $f(x_i)$ and $f(x_{i+1})$. Let $\mathbf{v}(x)$ be the linear interpolating function.

For $x_{i+1} - x_i = 1$, $\delta x = x - x_i$ and $0 \le \delta x \le 1$, we have:

$$\mathbf{v}(x) = f(x_i)(1 - \delta x) + f(x_{i+1})\delta x, \qquad (2\text{-}1)$$

Letting $u_0 = f(x_i)$, $u_1 = f(x_{i+1})$ and $s_1(u_O, u_1, \delta x)$ be an interpolated value of $\mathbf{v}(x)$.
Using the algorithmic function, one obtains:

`Bi-linear`: from 4 control points (u_0, u_1, u_2, u_3).

$$\mathbf{u}_{int} : s_1[s_1(v_0, u_1, \delta x), s_1(u_2, u_3, \delta x), \delta y] \qquad (2\text{-}2)$$

`Tri-linear`: from 8 points $(v_0, v_1, v_2, v_3, v_4, v_5, v_6, v_7)$.

$$\begin{aligned}\mathbf{u}_{int} : s_1[&s_1(s_1(u_0, u_1, \delta x), s_1(u_2, u_3, \delta x), \delta y),\\ &s_1(s_1(u_4, u_5, \delta x), s_1(u_6, u_7, \delta x), \delta y), \delta z] \qquad (2\text{-}3)\end{aligned}$$

3. B-SPLINE CUBIC INTERPOLATION

This is our preferred scheme due to the superior image quality and surface detail.
A B-spline cubic is a piecewise cubic defined by:

$$u_i(x) = 4 \sum_{i=0}^{4} \frac{(x - x_i)^3 \mathbf{p}(x - x_i)}{\mu(x_i)} \qquad (3\text{-}1)$$

where the function $\mathbf{u}\,(\mathbf{x})$, the first derivative $\frac{du}{dx}$ and the second derivative $\frac{d^2u}{dx^2}$ are continuous.
Where $\mu(x_i)$ and $\mathbf{p}(x - x_i)$ are given by:

$$\mu(x_i) = \prod_{\substack{k=0\\ k \ne i}}^{4} (x_i - x_k) \qquad (3\text{-}2)$$

$$\mathbf{p}(x - x_i) = \begin{cases} 1 & \text{if } x > x_i; \\ 0, & \text{otherwise.} \end{cases} \qquad (3\text{-}3)$$

The B-spline cubic that interpolates over four sample points (x_{-1}, x_0, x_1, x_2) is given as,

$$\mathbf{v}(x) = \sum_{i=-1}^{2} a_i u_i(x), \ \textit{where}\ (x_0 \le x \le x_1) \qquad (3\text{-}4)$$

and the coefficients a_i are given as in eqns. (3-9), (3-12).
Then,

$$\begin{aligned}\mathbf{v}(x) = &\frac{1}{6}\left[a_{-1}[(x - x_{-3})^3 - 4(x - x_2)^3 + (x - x_1)^3]\right]\\ &- \frac{1}{6}\left[4(x - x_1)^3 - 6(x - x_0)^3 - a_1(x - x_1)^3\right]\\ &- \frac{1}{6}\left[4a_1(x - x_0)^3 + a_2(x - x_0)^3\right] \qquad (3\text{-}5)\end{aligned}$$

Letting $x - x_0 = \gamma$, where $(0 \leq \gamma \leq 1)$ and

$$\mathbf{a} = [a_{-1}, a_0, a_1, a_2]^t \quad and \quad \Gamma = [\gamma^3, \gamma^2, \gamma, 1] \qquad (3\text{-}6)$$

$$\mathbf{C} = \begin{pmatrix} -1 & 3 & -3 & 1 \\ 3 & -6 & 3 & 0 \\ -3 & 0 & 3 & 0 \\ 1 & 4 & 1 & 0 \end{pmatrix}. \qquad (3\text{-}7)$$

We obtain,

$$g(v + x_0) = \Gamma \ \mathbf{C} \ \mathbf{a} \qquad (3\text{-}8)$$

where the vector **a** is the solution to the system:

$$\mathbf{v}(x_i) = f(x_i) = \sum_{j=-1}^{2} a_j u_j(x_i), \ i = -1, 0, 1, 2. \qquad (3\text{-}9)$$

We let:

$$\mathbf{f} = [f(x_{-1}), f(x_0), f(x_1), f(x_2)]^T \qquad (3\text{-}10)$$

$$\mathbf{M} = \begin{pmatrix} 4 & 1 & 0 & 0 \\ 1 & 4 & 1 & 0 \\ 0 & 1 & 4 & 1 \\ 0 & 0 & 1 & 4 \end{pmatrix} \qquad (3\text{-}11)$$

where **M** is symmetric and positive definite.
Then the solution of the system given in eqn. (3-9) is:

$$\mathbf{a} = \mathbf{M}^{-1}\mathbf{f} \qquad (3\text{-}12)$$

which depends on choices of interpolation points. Extension of this to 2D and 3D can be carried out similarly.

Results

Our interpolation schemes results in 3D images of remarkable detail and accuracy. These techniques are, however, very computationally expensive. Despite the use of efficient algorithms, the 3D display of medical object for measurement and analysis cannot be done in real-time. We carried out most of our computation on the local variables and we suggest its eventual implementation on parallel machines in order to achieve true real time interactive manipulation.

Acknowledgments

The CT and NMR scan raw data were obtained from the Montreal General Hospital and the Montreal Neurological Institute. This work was partially supported by MRC departmental grants. Data set generation, scene representation, surface extraction and display using B-spline interpolation have been developed by CHT in conjunction with Prof. T.S. Sankar of the Department of Mechanical Engineering, Concordia University. We thank Prof. J. McKay from the Department of Computer Science, Concordia University and B. Murray from the Department of Psychology (CSBN) for the careful proofreading of this manuscript. CHT thanks Linda and Ildiko from the audiovisual department, Montreal General Hospital for their professional help and their daily pleasant conversations during the completion of this work.

References

1. Chen L., Herman G.T., Reynolds R.A. and Udupa J.K. (1977). Surface shading in the cuberille environment. Comput. Graph. Applic. 5, 33–43.
2. Cook L.T. *et al* (1984). A 3D display system for diagnostic imaging application. IEEE Comput. Graphics Appl., 4, 13.
3. Cook L.T. *et al* (1984). Distributed Ray Tracing. Computer Graphics, 18, 3, 137–145.
4. Farrell E.J., Yang W.C., and Zappulla R.A. (1985). Animated 3D Imaging. IEEE Comp. Graph. Applic. 5, 26-32.
5. Fuch Z. Kedem and Uselton S.P. (1977). Optimal surface reconstruction from planar contours. Commun: ACM 20, 10, 693-702.
6. Grimson W.E.L. (1983). An implementation of a computational theory of visual surface interpolation. Computer Vision, Graphics, and Image Processing 22, 39–69.
7. Harris L.D. it et al (1979). Display visualization of 3D reconstructed anatomic morphology. Experience with the thorax, heart, and coronary vasculature of dogs. J. Comp. Assist. Tomogr. 3, 439.
8. Udupa J.K. (1983) Display of 3D information in discrete 3D scenes produced by computerized tomography. Proc. IEEE, 71(3), 420.
9. Cao H. Tuan and Joaquin D Chan (1989). Three-dimensional Imaging in Medicine. Proc. Cancam'89 12, 896–897.
10. Cao H. Tuan *et al.* (1990). Surface Interpolation Methods for the 3D Display and Manipulation of Anatomical Objects. Proc. of the International Symposium on Applied Informatics, IASTED'90, Innsbruck, Austria. February 1990. Submitted for publication to IASTED/ISMM International Journal of Robotics and Automation.

A BIOMECHANICAL STUDY OF STABILITY OF UNCEMENTED FEMORAL STEMS

T.W. Phillips, B.A.Sc. (Engineering), M.D., F.R.C.S.(C), S.D. Munro, B.A.Sc.,
and L.T. Nguyen, B.A.Sc., M.H.Sc., P.Eng.

The Orthopaedic Research Laboratory, St. Joseph's Health Centre of London
268 Grosvenor Street, London, Ontario, N6A 4V2

ABSTRACT

Cementless implants must have immediate secure fixation to be clinically successful. Unfortunately the magnitude and consistency of immediate fixation provided by cementless stems remains unknown. Twelve pairs of human cadaveric femora were implanted and cyclically loaded in a worst case simulation of a patient getting up from a chair. Each femur was secured to the table of a servohydraulic testing machine in a horizontal position, and the prosthetic head loaded in a vertically downward direction. The offset of the prosthetic head resulted in a combined torsional and compressive load being applied to the stem within the proximal femur. Loosening was found to consistently occur and rapidly accelerate when the head subsided more than 0.2 mm during 100 cycles. The loosening loads ranged from 62 to 171% of body weight for a 70 kg patient. Combining all specimens there was a statistically insignificant right vs. left difference ($p > 0.05$). The differences in loosening load within each pair showed an average of 2.6% (± 5.4% S.E.) from the mean for that pair. Now that we have shown right vs. left consistency, the methodology may now be used to compare different types of stems right vs. left within pairs.

INTRODUCTION

A multitude of different types of cementless total hip arthroplasties are being developed and used around the world. It is generally accepted that immediate secure fixation must be obtained [7]. Unfortunately it is being found that thigh pain occurs more frequently with cementless than cemented stems, and that this pain is most pronounced when the femur is loaded in positions approaching horizontal [15]. Here the gravitational force of body weight pushes downward on the offset prosthetic head. This tends to twist the stem into retroversion. Studies have shown that rotational loading is required to demonstrate loosening [12,17]. Evidence from fractured stems retrieved from patients at revision surgery shows metallurgic defects and plastic deformation patterns clearly demonstrating torsional overloading as a major mode of failure [8]. However, other than a recent report showing that posteriorly directed forces during stair climbing are in the neighbourhood of 500 Newtons [4], we have been unable to find any human biomechanical studies to measure this type of loading. In addition, it has been suggested that fit and fill is important in securing permanent implant stability [19]. The purpose of this study is to quantify the rotational fixation of the AML porocoat stem (DePuy) immediately following implantation, to determine right vs. left consistency within cadaveric pairs, and to determine the relationship between the tightness of fit as scored radiologically and the loosening load.

MATERIALS AND METHODS

Preparation of Specimen

Twelve pairs of human cadaveric femora previously fixed in formalin, were stripped of all soft tissue, transected above the femoral condyles and stored in sealed plastic bags until use. The femora were x-rayed simulating the technique used with patients on a clinical x-ray unit resulting in 15% magnification. None of the femora had any abnormality due to arthritis, previous fracture, deformity, tumour nor previous implant.

All femora were implanted with the AML 5/8 porocoat prosthesis, all in the 32 mm head and medium (+5) neck configuration. Templating, sizing, bone preparation, and prosthetic implantation were performed following the technique recommended by the manufacturer [6]. Following implantation, anteroposterior and lateral x-rays were taken in order to score the quality of implantation as per the system described by Engh [5].

Loading Protocol

All femora were potted in a metal box fixture with methacrylate up to the inferior aspect of the lesser trochanter. The fixture was then secured to the table top of an MTS 880/858 servohydraulic testing machine as detailed elsewhere [11] and shown in Fig. 1. The femur was positioned with its long axis horizontal and its anterior aspect facing upward. The cylindrical plunger of the MTS was positioned with its flat surface over the spherical head of the prosthesis. The plunger applied loads vertically downward resulting in a posterior force on the prosthetic head tending to twist the stem into retroversion.

The prosthetic head was loaded to an initial tare of 25 Newtons (N) to ensure the plunger stayed in contact with the prosthetic head. A superimposed

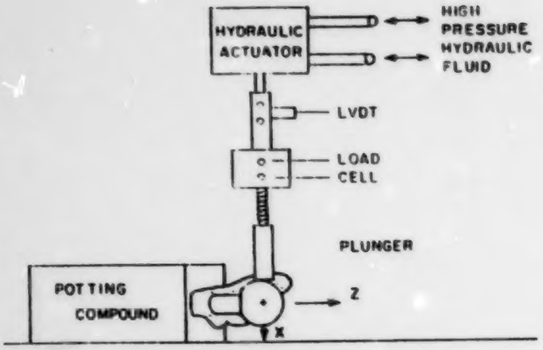

Figure 1:
SCHEMATIC DIAGRAM OF 90° FLEXION TEST CONFIGURATION

The direction x is vertically downwards with respect to the test position, and posterior with respect to the femur. The plunger of the MTS servohydraulic machine applies loads vertically downward on the horizontal femur resulting in a posterior force that presses the stem against the posterior intraosseous metaphysis of the proximal femur and a torsional moment that twists the stem into retroversion.

cyclical load in the form of haversine waves with an amplitude of 50 N and a period of 5 seconds was then applied. For the first 100 cycles, the cyclical load was 25 to 75 N. At the end of each 100 cycles, the peak load was incremented by 50 N while the tare load of 25 N was kept constant. Vertical displacement of the prosthetic head was measured with a LVDT transducer built into the MTS system and relayed to a Beckman strip recorder. The test was carried to ultimate failure defined as a femoral crack or subsidence of the prosthetic head by 5 mm or more.

From the strip recording the prosthetic head resting position at the end of each 100 cycles was measured. This was then used to formulate a summarized graph of prosthetic head resting position at the end of each 100 cycles versus load condition throughout the full range of the test. The graphs for all femurs were then analyzed for patterns which could be used to quantify and define a loosening load.

To detect any slippage of the femur within the potting compound, a second LVDT transducer was attached to the medial surface of the femoral neck 5 mm down from its level of transection. The displacement of this transducer was also relayed to the strip recorder. If a cumulative displacement greater than 0.5 mm occurred at any time during the test, slippage of the femur was defined to have occurred, and the test terminated.

RESULTS

Defining the Loosening Load

Throughout the first half of the loading range before ultimate failure, prosthetic head displacement amplitude remained close to constant throughout each 100 cycle load condition as shown in Fig. 2. Peak displacement increased in direct proportion to peak load and then returned to the original resting position after each cycle. However, in the second half of the loading range peak displacement continued to increase as always, but the prosthetic head began failing to return to its original resting position at the end of each cycle. This was the point of inelastic and irreversible subsidence.

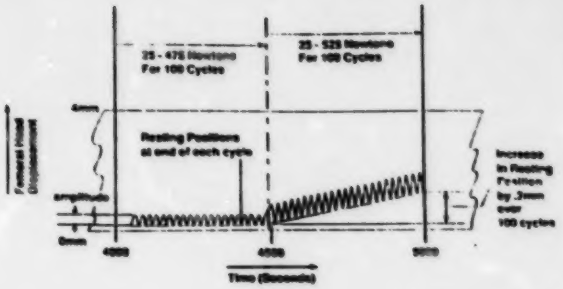

Figure 2:
STRIP RECORDING OF FEMORAL HEAD DISPLACEMENT

Time condensed strip chart recording of femoral head displacement versus time for specimen H58 - Left. The displacement amplitude is constant throughout a given load condition. When the peak load was increased from 475 N to 525 N, the femoral head resting position subsided by 0.2 mm over 100 cycles. The load at which this occurs, in this case 525 N, is defined as the loosening load.

A typical curve summarizing the results for a femoral pair is shown in Fig. 3. All tests produced this general shape of curve with almost no irreversible subsidence at low loads, followed by a rapid increase at high loads. This rapid increase always occurred at or close to a slope in the curve representing 0.2 mm of displacement per 100 cycles as also shown in Fig. 3. Soon after this point loosening always became rapidly progressive. This point was not detectable to the naked eye watching the implant/femur interface during the test. However, soon after, as the slope of the curve rapidly increased, loosening became visibly obvious also. This slope of 0.2 thus provided the first quantitative and consistent measure of loosening. The peak load condition producing this slope of 0.2 mm per 100 cycles was therefore defined as the loosening load.

Table 1 summarizes the data and statistical analyses for loosening loads and radiologic scores of all twelve femoral pairs. All cementless femoral prostheses loosened with posteriorly directed loads in the range of 425 to 1175 Newtons. This corresponds to 62 to 171% of body weight for a 70 kg patient. By Student's t-test paired analysis there were statistically insignificant right vs. left differences in loosening load and in radiologic score (both $p > 0.05$). The differences in loosening load within each pair showed an average of 2.6% (± 5.4% S.E.) from the mean for that pair.

Fig. 4 shows the scattergram of radiologic Engh score vs. loosening load, and that the correlation between the two was statistically insignificant ($r = 0.22$).

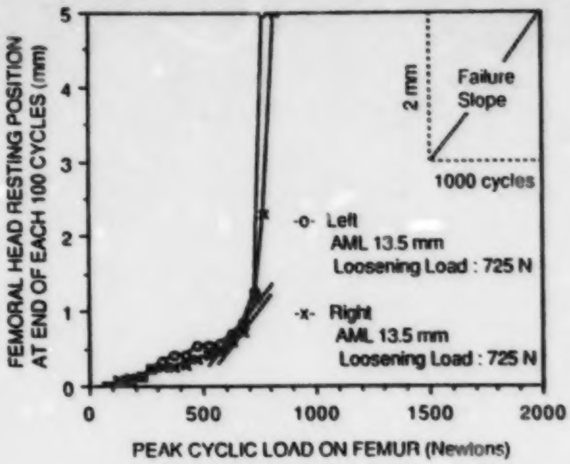

Figure 3:
RESTING POSITION vs. LOAD FOR PAIRED SPECIMEN NO. H28

Typical summarized test result of femoral head resting position at the end of each 100 cycles vs. peak load for paired specimens H28 - Left and Right. The straight line indicates the critical loosening slope of 0.2 mm change in femoral head resting position during 100 cycles. For clarity this slope is shown in the triangle insert in the upper right corner of the figure to a larger scale of 2.0 mm over 1000 cycles. The loading condition at which this slope was surpassed is the loosening load, and in this example was 725 N for both sides.

Table 1

FEMORAL LOOSENING LOAD (NEWTONS) AND RADIOLOGIC ENGH SCORE

Specimen	Loosening Load Left	Loosening Load Right	Radiologic Score Left	Radiologic Score Right
H47	825	875	16	14
H53	725	625	12	14
H48	775	575	18	16
H59	675	675	14	13
H49	575	525	11	13
H58	525	725	15	15
H44	925	1175	14	15
H22	1075	875	12	15
H23	425	475	14	11
H30	825	775	14	16
H28	725	725	14	13
H42	975	775	14	15
Mean	754.2	733.3	14.0	14.2
Std. Dev.	188.9	188.1	1.9	1.5
Std. Err.	54.5	54.3	0.5	0.4
p Value	0.633		0.772	

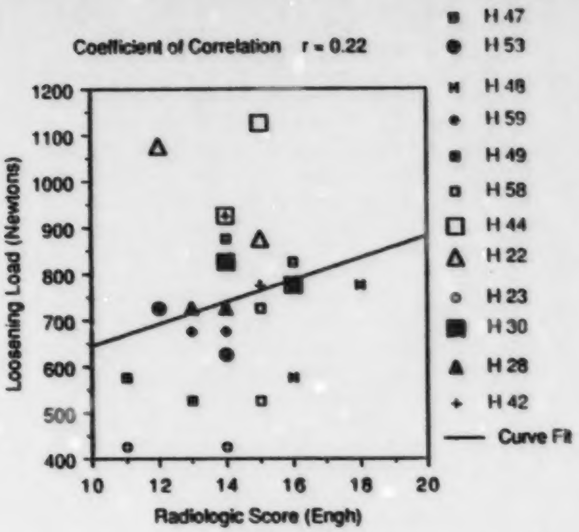

Figure 4:
SCATTERGRAM OF RADIOLOGIC SCORE (ENGH) vs. LOOSENING LOAD (Newtons)

The straight line indicates the least squares best fit correlation of the two variables (r = 0.22).

LOOSENING LOAD = 23.9 x RADIOLOGIC SCORE + 401.6

DISCUSSION

We have described a completely new methodology for assessing the fixation of femoral prostheses. In the past implant fixation has been studied by others using conventional axial loading [3,14]. However, this loading mode does not represent a worst case scenario in regards to stability of the implant [9]. Our technique assesses the worst case rotational instability of the femoral implant. Our incremented and cyclic torsional loading of the femoral implant produces a form of loosening akin to that which occurs in clinical practice - a gradual subsidence into the cancellous bone of the proximal metaphysis. For cementless porous-coated prostheses, micromovement should not approach the pore size to assure bone ingrowth [16]. Our loosening criterion of 0.2 mm (200 µm) subsidence per 100 cycles is thus well within the limits for optimal bone ingrowth established by Bobyn [2] of between 50 and 400 µm. The 0.2 mm refers to motion at the outer end of the offset neck. Motion along the stem would be even less.

While the simplification of loading to a worst case situation with the femur horizontal and the force vertical, in the absence of surrounding muscle attachment and forces, with continuous cycling of cadaveric bone, and with no provision for living bone repair or muscle action, all make the absolute value of the loosening loads impossible to apply directly to patients, the methodology does provide an excellent comparative test for different stems and implantation techniques. The results are easily understood and of relevance to both the surgeon and engineer.

While these femora were mostly from elderly patients, it is pointed out most patients receiving hip replacements are of this age group. Formalin fixation reduces the bone mechanical properties in compression by only 12% [10]. Postmortem changes before formalin fixation also have been shown to have little effect on the elastic mechanical properties of bone [1].

That some stems loosened after as few as 800 cycles, and at loads as low as 62% of body weight is concerning. The lack of predictability of loosening load as a function of radiologic Engh score is surprising and disturbing. In the Engh score, 19 out of 27 points (70%) are based on distal fit. However, in a recent study, Whiteside et al. [20] showed proximal micromotion was not significantly affected by the tightness of distal fit. Our results thus appear to be in agreement with Whiteside's finding.

Comparisons of different implants are best performed in pairs of femora from the same individual. Even here variations in bone quality, and surgical implantation point to the need for a reasonably large sample of specimens. One technique used in biomechanical testing of cemented implants has been to have each femur serve as its own control by reimplanting and testing different stems in the same femur [14]. Unfortunately this is not possible with cementless implants where a precise tight fit would be compromised with subsequent reimplantations. Also fatigue of the femur by the cyclic loading of previous tests could affect subsequent results [18]. A torsional loading configuration similar to ours was recently used to assess the advantage of preservation of the femoral neck [13]. Their study tested single femora and compared prosthetic displacements after 5 loading cycles of 400 N. The results therefore did not represent the clinical gradual subsidence into the cancellous bone of the proximal metaphysis. In addition, it was reported that bones with an uncemented smooth prosthesis fractured at loads only a little above 400 N with the neck intact, and that they often fractured at loads around 200 N when retested with the neck excised. This was probably affected by damage to the bone from the previous test (eg. irreversible crushing of the subcortical cancellous bone). The effect of the previous test could be eliminated by testing pairs of femora from the same individual. In our study, the right vs. left consistency within pairs provides the baseline to next directly compare different stems and implantation techniques within pairs of femora.

Acknowledgements:
Financial support for this project was provided by the Medical Research Council of Canada. The authors express thanks to Dr. Elias Gammal and Mr. Wayne Davis of the Anatomy School of the University of Western Ontario, to Dr. Ian Taylor and Mr. Steve Toussaint of the University of Toronto for assistance in obtaining the specimens, and to Miss. Jackie Snel for her assistance in our laboratory. We thank DePuy for providing the AML stems.

REFERENCES

1. Ashman, R.B. et al., Postmortem Changes in the Elastic Properties of Bone, Orthop Trans, Vol. 6(2), pp. 223-4, 1982.

2. Bobyn, J.D. et al., The Optimal Pore Size for the Fixation of Porous-Surfaced Metal Implants by the Ingrowth of Bone, Clin Orthop, Vol. 150, pp. 263-70, 1980.

3. Butler, C.A. et al., The Initial Implant Stability of Porous Coated Total Hip Femoral Components - A Mechanical Study, Orthop Trans, Vol. 12(2), page 423, 1988.

4. Davy, D.T. et al., Telemetric Force Measurements Across the Hip After Total Arthroplasty, J Bone Joint Surg [Am], Vol. 70, pp. 45-50, 1988.

5. Engh, C.A., Hip Arthroplasty With a Moore Prosthesis With Porous Coating: A Five Year Study, Clin Orthop, Vol. 176, pp. 52-66, 1983.

6. Engh, C.A. & Bobyn, J.D., Biological Fixation of the Porocoat AML Hip, Manual for Preoperative Planning and Recommended Surgical Technique. Technical Brochure #20M2840601-80. DePuy Inc., Warsaw, Indiana, 46580 U.S.A, 1984.

7. Engh, C.A. et al., Porous-Coated Hip Replacement. The Factors Governing Bone Ingrowth, Stress Shielding, and Clinical Results, J Bone Joint Surg [Br], Vol. 69, pp. 45-55, 1987.

8. Gallante, J.O., Causes of Fractures of the Femoral Component in Total Hip Replacement, J Bone Joint Surg [Am], Vol. 62, pp. 670-673, 1980.

9. Jasty, M. et al., Rotational Instability: The Achilles Heel of Cementless Femoral Total Hip Replacement, Proceedings of the 44th Annual Meeting of the Canadian Orthopaedic Association, Toronto, Ontario, Canada, pp. 83-4, 1989.

10. McElhaney, J. et al., Effect of Embalming on the Mechanical Properties of Beef Bone, J Appl Physiol, Vol. 19, 1234-6, 1964.

11. Messieh, SS., Torsional Loosening of Cementless Femoral Stems - A Biomechanical Study, Resident's Presentations, Paper Number 11. Proceedings of the 16th Clinical Seminar in Orthopaedic Surgery, University of Western Ontario, London, Ontario, Canada, May 4, 1988.

12. Mjorberg, B. et al., Instability of Total Hip Prostheses at Rotational Stress: A Roentgen Stereophotogrammetric Study, Acta Orthop Scand, Vol. 55, pp. 504-6, 1986.

13. Nunn, D. et al., Torsional Stability of the Femoral Component in Hip Arthroplasty Response to an Anteriorly Applied Load, J Bone Joint Surg [Br], Vol. 71, 452-5, 1989.

14. Oh, I. & Harris, W.H., Proximal Strain Distribution in the Loaded Femur, An In Vitro Comparison of the Distribution in the Intact Femur After Insertion of Different Hip Replacement Components, J Bone Joint Surg [Am], Vol. 60, pp. 75-85, 1978.

15. Phillips, T.W. & Messieh, S.S., Cementless Hip Replacement for Arthritis, J Bone Joint Surg [Br], Vol. 70, pp. 750-5, 1988.

16. Pilliar, R.M. et al., Observations on the Effect of Movement on Bone Ingrowth Into Porous-Surfaced Implants, Clin Orthop, Vol. 208, pp. 108-13, 1986.

17. Radin, E.L. et al., Changes in the Bone-Cement Interface After Total Hip Replacement, J Bone Joint Surg [Am], Vol. 64, page 1188, 1982.

18. Swanson, S.A.V. et al., The Fatigue Properties of Human Cortical Bone, Medical and Biologic Engineering, Vol. 9, page 23, 1971.

19. Walker, P.S. & Robertson, D.D., Design and Fabrication of Cementless Hip Stems, Clin Orthop, Vol. 235, pp. 25-34, 1988.

20. Whiteside, L.A. & Easley, J.C., The Effect of Stem Fit and Collar Seating on Micromotion of the Femoral Component in Uncemented Total Hip Replacement, Orthop Trans, Vol. 12(2),422-3, 1988.

A BIOMECHANICAL TEST OF INTERFACIAL SHEAR CHARACTERISTICS IN CEMENTLESS PROSTHETIC FIXATION

T.W. Phillips, B.A.Sc. (Engineering), M.D., F.R.C.S.(C), L.T. Nguyen, B.A.Sc., M.H.Sc., P.Eng.,
D.R. Rao, M.B.B.S., M.S. (Orth), and J.L. Snel, A.H.T.

The Orthopaedic Research Laboratory, St. Joseph's Health Centre of London
268 Grosvenor Street, London, Ontario, N6A 4V2

ABSTRACT

A new biomechanical methodology has been developed to directly compare and quantitate bone ingrowth of numerous porous surfaces. In group one, CoCr Porocoat (DePuy) test plugs were implanted in both the right and left iliac crests of ten adult female sheep to establish the right vs. left consistency of the test methodology. In group two of another ten sheep, Porocoat test plugs were implanted in one crest side, and Titanium Fibermesh (Zimmer) test plugs in the contralateral side. All animals were sacrificed at three months, and the plugs tested under torsional loading mode using a servohydraulic MTS testing system. On radiographic review, no lucencies were seen at the bone/implant interface. The results from the first group established equality between right and left bone ingrowth biomechanical characteristics within each animal ($p > 0.45$). Combining all 30 Porocoat specimens, the ultimate shear stress was 5.92 ± 3.72 MPa (mean ± 1 S.D.), compared with 8.83 ± 3.08 MPa for the ten Ti Fibermesh plugs ($p = 0.002$). Porous coating separation from the solid metal base has been a problem only with the Fibermesh plugs.

INTRODUCTION

Porous coated implants are being increasingly used in joint arthroplasty. Porous ingrowth characteristics of plugs of various materials and surfaces have been reported in the literature. Niles et al. was one of the first to biomechanically evaluate the cortical bone/porous implant interface in 1973 [11]. They found titanium cylinders with a pore size of 275 microns implanted in canine cortical bone for six weeks had an ultimate push out stress in the neighborhood of 15 MPa. Bobyn et al. studied optimal pore size to reach maximal interfacial shear strength in the shortest time [3]. They used Porocoat implants inserted into canine cortical bone and followed for periods of up to 16 weeks. They found implants having medium pore sizes (50 to 400 microns) reached the maximal strength of 17 MPa in eight weeks. Implants having a smaller pore size never reached this shear strength by 16 weeks. However, close inspection of their data shows at 16 weeks the shear strength of the medium and large pore size (400 to 800 microns) group was still increasing. Recently, Thomas et al. reported the effect of surface macrotexture and hydroxylapatite coating on the mechanical strengths and histologic profiles of titanium implant materials [16]. They implanted commercially pure titanium cylinders into canine femora. All implants had a machined groove surface approximately 750 microns in maximum depth, with one group hydroxylapatite coated, and the other uncoated. At ten weeks, the push-out interfacial shear stress was 11 and 14 MPa, and interfacial stiffness was 38 and 70 GPa/m, for uncoated and HA coated, respectively.

Several studies have examined porous ingrowth fixation in cancellous bone. Galante et al. studied titanium fiber mesh cylinders with pore diameters of 170 to 350 microns implanted into the trochanteric area of canine femora [9]. They found the average ultimate pull out shear stress was approximately 2 MPa at two weeks and remained constant thereafter at up to twelve weeks. Berry et al. described a comparison of Simplex bone cement and scintered cobalt chrome test plug shear strength in medullary bone of the canine ulna [2]. At twelve weeks the bond strength of the cement had decreased to 1.5 MPa, and that for the scintered metal increased to 4.5 MPa. Sauer et al. studied porous high density polyethylene with an average pore size of 210 microns coated on the stem of femoral head prostheses in canine femora [15]. All achieved an implant/bone shear strength of greater than 4.88 MPa beyond four weeks.

As can be seen, previous tests used different push or pull out tests, different animal models, different anatomical locations, different types of bone implant locations (cancellous vs. cortical bone), different follow-up periods, and different testing conditions. These may explain the widely varied results. A direct comparison between these results is impossible.

Many different types of prostheses are manufactured with different materials and geometries of porous coating. At the present in North America, cementless designs have mostly been of the microporous variety using either Cobalt-Chromium or Ti-6Al-4V alloys. The Porocoat by DePuy, the PCA by Howmedica, and the Fibermesh by Zimmer are the three most widely used systems. With funding from the Medical Research Council of Canada and collaboration from these three manufacturers, we are currently carrying out a study to comparatively evaluate ingrowth characteristics of these three types of porous surfaces and to single out which of the three provides the strongest fixation. This paper describes our new biomechanical torsional test methodology and summarizes the test results of the first two animal groups to establish the right vs. left consistency of the test methodology (group one) and to compare ingrowth between the DePuy's Porocoat and Zimmer's Fibermesh surfaces (group two) at three months. Ultimate shear stress, interface stiffness, and energy to failure were analyzed, compared, and correlated.

DePuy's Porocoat (CoCr)

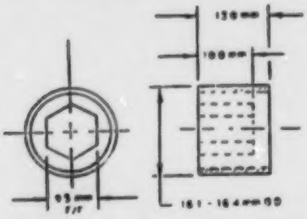

Zimmer's FiberMesh (Titanium)

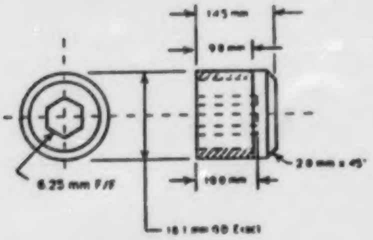

Figure 1:
DIMENSIONS OF TEST PLUGS

Shaded areas represent porous or fibermesh coatings. The hexagon hole is for attaching the plug to surgical insertion T-bar and to biomechanical testing fixture.

MATERIALS AND METHODS

Surgical Implantation and Follow-up

In group one, CoCr Porocoat (DePuy) test plugs were implanted in both the right and left iliac crest of ten adult female sheep to establish the right vs. left consistency of the test methodology. In group two of another ten sheep, Porocoat test plugs were implanted in one crest side, and Titanium Fibermesh (Zimmer) test plugs on the contralateral side. The dimensions of the Porocoat CoCr test plug are shown in Fig. 1; its outer coating diameter varied from 16.1-16.4 mm. The dimensions of the Titanium Fibermesh test plug are also shown in Fig. 1; the outer diameter was found to be consistent at 16.1 mm. The dimensions of these plugs were optimized from a combination of factors including iliac crest anatomy, no effect on gait nor activity, surgical insertion, length to diameter ratio, cancellous bone shear strengths, biomechanical fixturing, and histologic sectioning. These factors allow implantation of a maximum two test plugs per sheep, one in each iliac crest, as illustrated in Fig. 2.

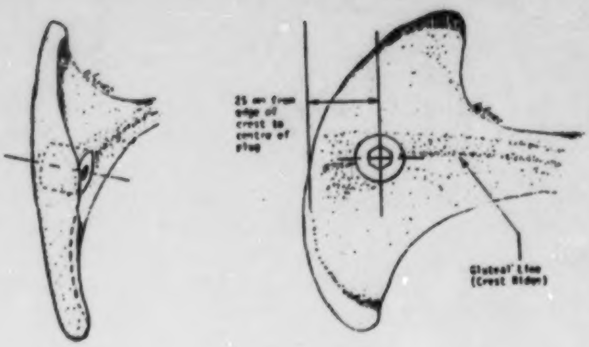
25 mm from edge of crest to centre of plug
Gluteal Line (Crest Ridge)

Figure 2:
ANATOMICAL SCHEMATIC DIAGRAM OF SHEEP ILIAC CREST & TEST PLUG IMPLANT LOCATION

All sheep were Suffolk breed, all females, all six to eight years of age, and all fifty to seventy kilograms. A 4.8 mm diameter pilot hole was drilled 25 mm below the iliac crest and perpendicular to the outer surface of the ilium. For the Porocoat plugs, a 15.6 mm diameter hole saw (0.8 mm smaller than the maximum outer plug diameter of 16.4 mm) with a 4.5 mm diameter smooth pilot was then used to cut a hole through the ilium. For the Fibermesh plugs, a 15.3 mm diameter hole saw (again, 0.8 mm smaller than the maximum outer plug diameter of 16.1 mm) was used. The 4.5 mm diameter smooth leading pilot of the hole saw kept the hole saw from wobbling or cutting eccentrically, and also assisted in cutting perpendicular to the outer surface of the ilium. The plug was then inserted manually with a T-bar insertion tool having a hex end fitting into the plug. Most DePuy Porocoat plugs and all Zimmer Fibermesh plugs were inserted to the same degree of interference fit obtained with prosthetic joints in clinical practice having a fit which was tight, but not so tight as to run the risk of cross wedging or damaging the bone. However, in five of the Porocoat plugs the outer diameter was smaller than the maximum 16.4 mm and a tight interference fit was not obtained.

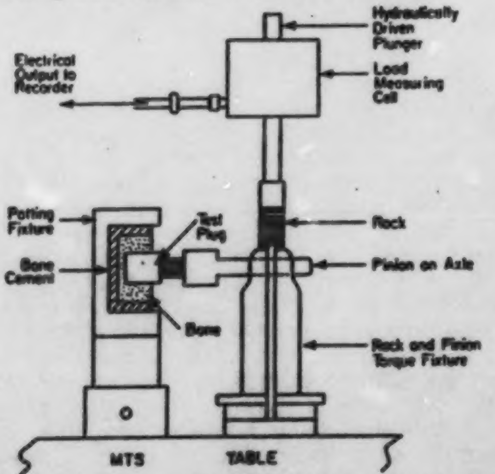
Hydraulically Driven Plunger
Electrical Output to Recorder
Load Measuring Cell
Potting Fixture
Test Plug
Rack
Bone Cement
Pinion on Axle
Bone
Rack and Pinion Torque Fixture
MTS
TABLE

Figure 3:
SCHEMATIC OF THE TORSIONAL TEST FIXTURE, POTTED SPECIMEN, AND MTS 880/858 MACHINE

The animals were maintained and allowed free activities on a farm for three months. At sacrifice, the iliac crests were excised, stripped free of soft tissue, cut down to a 51 mm diameter block, labelled, x-rayed, sealed and stored in a -70°C freezer.

Biomechanical Torsional Test

Mechanical testing was performed with a servohydraulic testing system (MTS Bionix Model 880/858). Provision for torsional testing of the implant was made by a rack and pinion test fixture as shown in Fig. 3. The specimens were thawed, centrally positioned in the test fixture, and potted in methyl methacrylate. Strain was applied at a rate of 4.5 degrees per minute (equivalent to 1 mm/min linearly). Output was plotted during the test with an X-Y recorder (MTS Model 431) scaled to provide direct reading of plug rotation in degrees versus torque in Newton-meters (Nm). From this plot, the ultimate interfacial shear stress (MPa) was calculated as the maximum torque on the plug divided by the outer cylindrical plug surface area; energy density to failure (KJ/sq.m) was measured as the area under the shear stress-strain curve normalized to plug surface area; and interfacial stiffness (GPa/m) was the slope of the initial linear portion of the shear stress-strain curve.

RESULTS

During implantation separation of the outer porous coating from the metal core occurred in one of the Fibermesh and none of the Porocoat plugs. All animals tolerated the operation well; all resumed normal activities just a few hours after surgery. At sacrifice, one sheep in group one was found to be infected on one side and so completely excluded and replaced with another animal. On radiographic review, no lucencies were seen at the bone/porous implant interface. The torsional test results in all animals yielded shear stress-angular deformation curves with a similar pattern as shown in Fig. 4. The curves began with an elastic (linear) portion followed by a plastic portion. After failure, 30 to 40% of the maximum torque was still required to rotate the plug further. All plugs failed during biomechanical testing at the bone/implant interface.

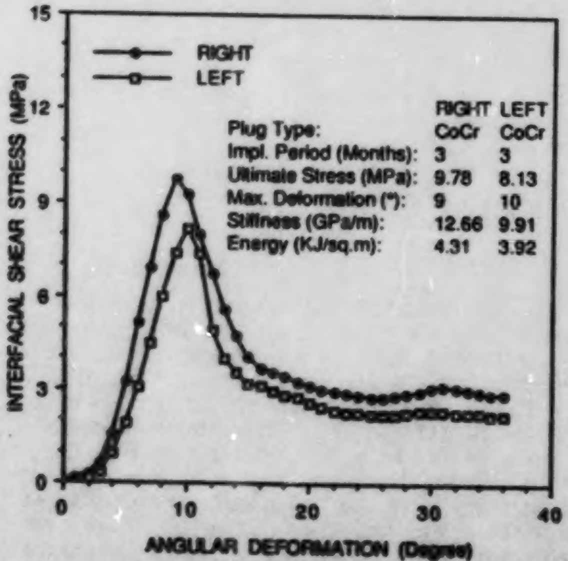

Figure 4:
SHEAR STRESS vs. ANGULAR DEFORMATION
POROCOAT PLUGS, RIGHT vs. LEFT
(Sheep No. 4)

Table 1

SUMMARY OF TORSIONAL TEST RESULTS OF ANIMAL GROUP ONE
POROCOAT TEST PLUGS (LEFT vs. RIGHT)

SHEEP NO	STRESS (MPa)		STIFFNESS (GPa/m)		ENERGY (KJ/sq.m)	
	Left	Right	Left	Right	Left	Right
1	9.653	13.083	11.879	10.047	4.419	11.244
2	8.256	7.240	12.107	11.429	3.552	2.993
3	4.954	1.270	8.929	2.536	1.884	0.492
4	8.129	9.780	9.914	12.664	3.920	4.306
5	2.173	5.335	4.036	9.143	0.659	2.449
6	11.971	11.241	14.500	14.150	6.528	4.817
7	4.308	3.430	8.214	6.857	1.655	1.330
8	2.032	2.223	4.214	5.000	1.102	0.935
9	1.080	1.379	1.134	2.126	0.780	0.623
10	6.414	9.145	9.889	13.518	2.713	4.027
Mean	5.897	6.413	8.428	8.747	2.721	3.322
S.D.	3.609	4.304	4.179	4.427	1.865	3.202
S.E.	1.141	1.361	1.322	1.400	0.596	1.013
p value*	0.486		0.801		0.456	

* Left vs. Right Student's paired t-test p value

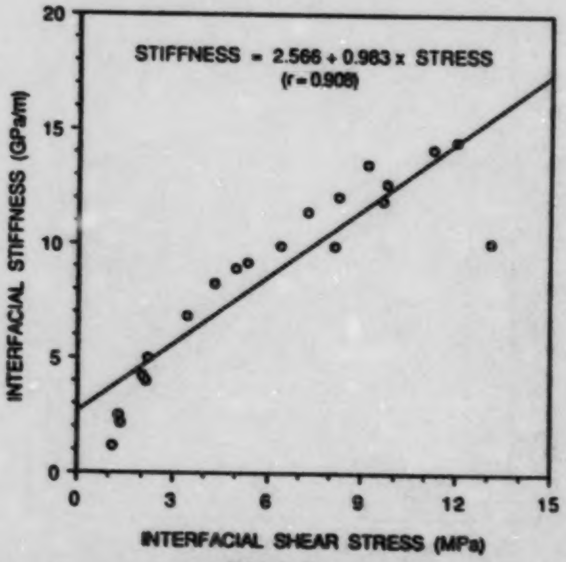

Figure 5:
STIFFNESS vs. ULTIMATE SHEAR STRESS
(Porocoat Plugs - Group One)

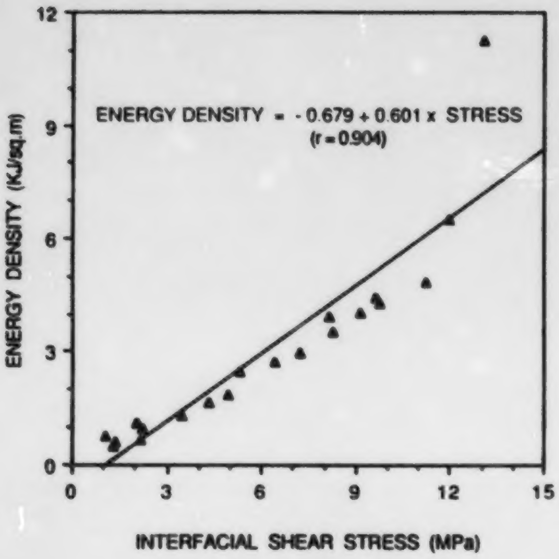

Figure 6:
ENERGY DENSITY vs. ULTIMATE SHEAR STRESS
(Porocoat Plugs - Group One)

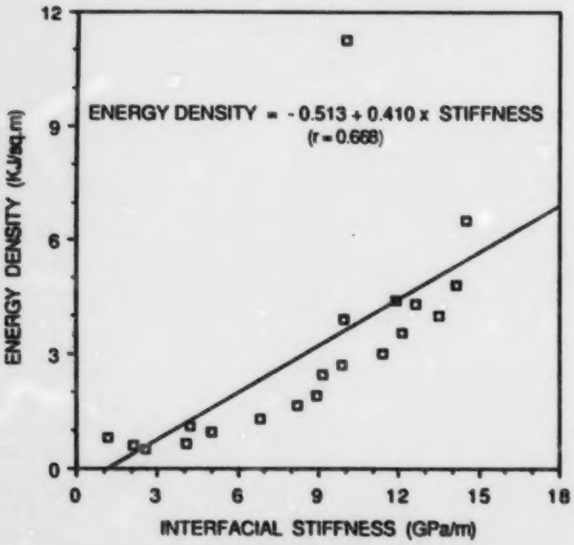

Figure 7:
ENERGY DENSITY vs. STIFFNESS
(Porocoat Plugs - Group One)

In animal group one comparing the Porocoat plugs left versus right, the ultimate interfacial shear stress, interfacial stiffness, and energy density for all plugs are summarized in Table 1 and Fig. 4. The overall mean values were 6.155 ± 3.875 MPa (mean ± 1 S.D.), 8.614 ± 4.192 GPa/m, and 3.021 ± 2.576 KJ/sq.m for stress, stiffness, and energy density, respectively. Statistically there was no significant right versus left difference in stress, stiffness, and energy density ($p = 0.486$, 0.801, and 0.456, respectively - all $p > 0.05$). The relationships between stiffness vs. stress and energy vs. stress were linear as shown in Figures 5 and 6 (coefficients of correlation $r = 0.908$ and 0.904, respectively). There was, however, a poor relationship between energy density and interfacial stiffness ($r = 0.668$), as shown in Fig. 7.

In animal group two comparing the Porocoat versus Fibermesh plugs, the ultimate interfacial shear stress, interfacial stiffness, and energy density for all plugs are summarized in Table 2 and Fig. 8. The mean values for the Fibermesh plugs were 8.833 ± 3.076 MPa, 8.097 ± 2.401 GPa/m, and 6.809 ± 3.409 KJ/sq.m, respectively. These results indicate a higher strength of the Titanium Fibermesh over the CoCr Porocoat ($p = 0.002$).

Combining all 30 Porocoat specimens, the ultimate shear stress, interfacial stiffness, and energy density to failure were 5.920 ± 3.720 MPa, 8.311 ± 4.209 GPa/m, and 2.903 ± 2.389 KJ/sq.m.

Table 2

SUMMARY OF TORSIONAL TEST RESULTS OF ANIMAL GROUP TWO
FIBERMESH vs. POROCOAT TEST PLUGS

SHEEP NO	STRESS (MPa)		STIFFNESS (GPa/m)		ENERGY (KJ/sq.m)	
	FM	Poro	FM	Poro	FM	Poro
11	10.342	9.463	8.521	12.006	7.761	5.021
12	10.429	5.104	10.145	8.869	6.519	1.680
13	8.430	3.170	9.585	6.622	4.033	1.052
14	8.865	7.729	9.149	12.077	5.876	3.806
15	1.769	1.032	2.281	0.985	1.071	0.753
16	11.559	10.039	10.208	10.596	10.437	5.833
17	7.474	1.334	7.656	2.001	5.424	0.577
18	10.081	2.223	8.927	3.184	8.506	1.036
19	6.692	4.763	5.913	7.732	5.204	1.688
20	12.688	9.653	8.581	12.963	13.258	5.212
Mean	8.833	5.451	8.097	7.704	6.809	2.666
S.D.	3.076	3.538	2.401	4.401	3.409	2.070
S.E.	0.973	1.119	0.759	1.392	1.078	0.655
p value*	0.002		0.740		< 0.001	

* Fibermesh vs. Porocoat Student's paired t-test p value

DISCUSSION

This torsional test model is effective in determining and comparing biomechanical characteristics of different porous ingrowth materials and surfaces. Traditionally, implant characteristics have been evaluated mechanically using push-out or pull-out tests [3,9,11,14]. These tests have been shown to create uneven stress distribution at the bone-implant interface during load application, particularly at the boundary layer near the ends of the plug. This introduces an unknown variable into data interpretation. A torsional mode, as we use, employs a more appropriate loading mode since it applies more even shear stress to the bone-implant interface [10].

Our model assesses ingrowth characteristics in cancellous bone. Most other investigators studied

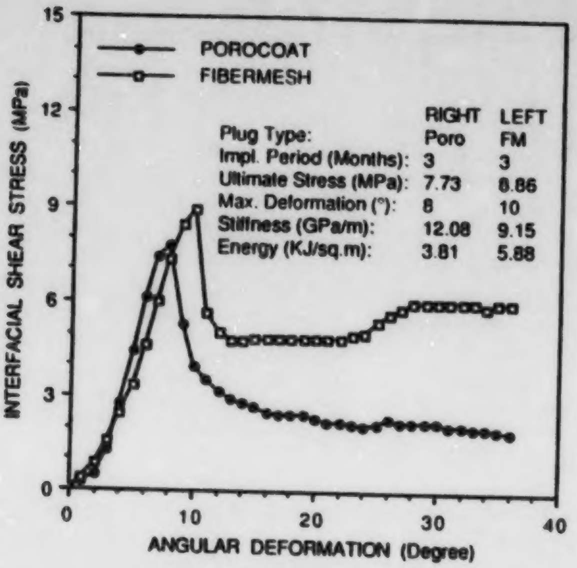

Figure 8:
SHEAR STRESS vs. ANGULAR DEFORMATION
POROCOAT vs. FIBERMESH PLUGS
(Sheep No. 14)

porous ingrowth in cortical bone [3,5,11]. The latter results do not apply to the predominantly cancellous environment where almost all porous surfaces are now used, such as the internal metaphysis of the femur at the hip and the prepared surfaces of the tibia and femur at the knee. From concerns about stress shielding and difficult extraction, many stems are now being coated only where they interface with cancellous bone of the metaphysis and not cortical bone of the diaphysis [7,17]. In addition, with our technique the contact of the bone with the implant surface is under our control, based only on the size of hole saw and careful alignment, such that we are able to achieve uniform contact around the entire perimeter of the test plug. This allows consistent controlled comparison of mechanical and histologic ingrowth characteristics, free from variables in long bone diaphyseal anatomy.

Most studies have been performed on canine models [2,3,9,11,14]. There are concerns about the consistently high rate of porous ingrowth in dogs, in comparison to the lack of ingrowth in some people [12]. Sheep allowed free activity on a farm more closely simulate the situation of active patients than do dogs housed in small enclosures in conventional research facilities [1]. Sheep, all Suffolk breed, all female, all six to eight years of age, and all fifty to seventy kilograms, are chosen because of their consistency from animal to animal, availability, low expense, ease of handling, and their ability to tolerate surgery.

Numerous studies have used "non-functional" or "non-loaded" implants rather than actual joint replacements to investigate porous ingrowth characteristics. Few directly compared different types of implants with rigorous control over the critical variables. Ideally, the implant should be loaded during the period of ingrowth, preferably physiologically like joint implants. The practical difficulty is that any method of practically accomplishing this introduces its own difficulties. Recently, Eschenroeder et al. [8] attempted to obtain physiological loading in a canine model by implanting a cylindrical rod into the femoral intramedullary canal, followed by a segmental femoral ostectomy. This model however resulted in only 50% useful animal retrieval rate due to complications after ostectomy. Wang et al. later undertook the same technique, and achieved only 16% animal retrieval rate [18]. The ideal solution might be to implant porous coated actual joint replacement prostheses. However, this necessitates a complex design with a multitude of sizes to come even close to fitting the varied anatomy, all of which becomes prohibitive for financial and practical reasons in an animal prototype project. In addition there would then be difficulties with more complex shaped implants in finding a way of isolating the interface for pure and consistent biomechanical studies. With the priority on achieving clear cut and as reproducible as possible results in cancellous bone, we selected the "non-functional" plug model. The plugs do accurately simulate the first two to three month period of weight protection as applied to most porous surfaced implants in clinical practice today. This initial period of weight protection is to minimize any movement at the bone/implant interface [4,6,13].

We have obtained a quantitative measure for porous ingrowth of CoCr Porocoat and Titanium Fibermesh plugs in terms of interfacial shear strength, interfacial stiffness, and energy density to failure. The fact that ultimate shear stress (USS) correlates well with both stiffness and energy density suggests that USS represents the best quantitative measure for ingrowth characteristics. The criterion of ultimate shear stress at three months is in agreement with Bobyn et al. as being one of the most important in selecting the optimal porous system for joint implants [3]. Implants should be strong enough for full weight bearing by three months to be acceptable for widespread use.

Some scattering of data was due to variations in bone quality, thickness, and surgical insertions. As mentioned in the materials and methods section, we have also encountered some difficulty with slight variation in the greatest outer diameter of the Porocoat plugs due to a few proud beads. Low strength values of some of the Porocoat plugs might have been due to the fact that some had outer diameters below the nominal maximum dimension, and thus didn't provide a tight fit. The methodology of implantation is very sensitive to this variation. The Zimmer Fibermesh plugs had an outer diameter which was very consistent due to the method of manufacture where a mould is used during pressure compaction and diffusion bonding of the mesh. As shown in Fig. 1, the Porocoat plugs in groups one and two also had an inferior square leading edge compared to the tapered Fibermesh. More consistent and easier straight implantation of the tapered Fibermesh plugs in group two may have favorably biased their results. We have designed a newer improved Porocoat test plug profile with a 45° leading edge similar to the Fibermesh. This should make surgical insertion and implant tightness of fit more consistent. DePuy has incorporated this new design and also tightened their quality control to assure more consistent outer diameter dimension. All further testing will use this improved test plug profile.

Nevertheless, even with the original Porocoat plug shape, the general consistency between right and left biomechanical ingrowth characteristics within each animal in group one reinforces our planned further protocol calling for a comparative analysis of different porous ingrowth materials and surfaces right vs. left within the same animal.

The preliminary results in group two show the Fibermesh to have an average 62% superiority over Porocoat in ultimate shear stress at three months. This requires verification with the newly designed Porocoat test plug. Porocoat performed better in having no separation at the porous metal/substrate interface.

Acknowledgement: The authors thank Mr. Gordon Young for his expert care of the animals. This project is financially supported by Medical Research Council of Canada Operating Grant No. MA-10375. We thank DePuy and Zimmer for providing the test plugs.

REFERENCES

1. Bergmann, G. et al., A Comparison of Hip Joint Forces in Sheep, Dog and Man, J Biomech, Vol. 17, page 907, 1984.

2. Berry, J.L. et al., Early Characterization of the Interface Between Medullary Bone and Porous Implant Coatings, Orthop Trans, page 32, 1981.

3. Bobyn, J.D. et al., The Optimal Pore Size for the Fixation of Porous Surface Metal Implants by the Ingrowth of Bone, Clin Orthop, Vol. 150, pp. 263-70, 1980.

4. Cameron, H.U. et al., The Effect of Movement of Porous Metal to Bone, J Biomed Mat Res, Vol. 7, pp. 301-11, 1973.

5. Cook, S.D. et al., Interface Mechanics and Histology of Titanium and Hydroxylapatite-Coated Titanium for Dental Implant Applications, J Oral and Maxillofacial Implants, Vol. 2(1), pp.15-22, 1987.

6. Ducheyne, P et al., Influence of a Functional Dynamic Loading on Bone Ingrowth Into Surface Pores of Orthopaedic Implants, J Biomed Mat Res, Vol. 11, pp. 811-38, 1977.

7. Engh, C.A. et al., Results of Cementless Revision for Failed Cemented Total Hip Arthroplasty, Clin Orthop, Vol. 235, pp. 91-110, 1988.

8. Eschenroeder, H.C. Jr et al., Cortical Versus Cancellous Bone Ingrowth Into a Porous Metal Surface Subjected Physiologic Loading, Trans 34th Annual Meeting, Orthop Res Soc, page 334, 1988.

9. Galante, J.O. et al., Scintered Fiber Metal Composites as a Basis for Attachment of Implants to Bone, J Bone Joint Surg, Vol. 53, pp. 101-14, 1971.

10. Harrigan, T.P. et al., Interface Failure Assessed Using Push-Out Tests - Example: The Cement-Prosthesis Interface, Trans of 34th Annual Meeting, Orthop Res Soc, page 501, 1988.

11. Niles, J.L. et al., Biomechanical Evaluation of Bone-Porous Material Interfaces, J Biomed Mater Res, Vol. 7, pp. 231-51, 1973.

12. Phillips, T.W. et al., Selection of an Animal Model for Hip Resurfacing, J Arthroplasty, Vol. 2(2), pp. 111-7, 1987.

13. Pilliar, R.M. et al., Observations on the Effect of Movement on Bone Ingrowth Into Porous Surfaced Implants, Clin Orthop, Vol. 208, pp. 109-13, 1986

14. Rivero, D.P. et al., Effects of Calcium Phosphates and Bone Grafting Materials on Bone Ingrowth in Titanium Fiber Metal, Trans of 31st Annual Meeting, Orthop Res Soc, page 191, 1985.

15. Sauer, B.W. et al., Long Term Stabilization of Canine Femoral Head Prostheses Using High Density Polyethylene Coatings, Ortho Trans IRS, page 173, 1981.

16. Thomas, K.A. et al., The Effect of Surface Macrotexture and Hydroxylapatite Coating on the Mechanical Strengths and Histologic Profiles of Titanium Implant Materials, J Biomed Mater Res, Vol. 21, pp. 1395-414, 1987.

17. Turner, T.M. et al., A Comparative Study of Porous Coatings in a Weight Bearing Total Hip Arthroplasty Model, J Bone Joint Surg [Am], Vol. 68-A, page 1396, 1986.

18. Wang, G.J. et al., Long Term Stability of Polysulfone or Hydroxyapatite Coated Prosthesis, Trans of 35th Annual Meeting, Orthop Res Soc, page 387, 1989.

A BIOMECHANICAL TEST OF FIXATION OF PROXIMAL HUMERAL ENDOPROSTHESES

T.W. Phillips, B.A.Sc. (Engineering), M.D., F.R.C.S.(C) and L.T. Nguyen, B.A.Sc., M.H.Sc., P.Eng.

The Orthopaedic Research Laboratory, St. Joseph's Health Centre of London
268 Grosvenor Street, London, Ontario, N6A 4V2

ABSTRACT

A new biomechanical test was developed to evaluate the fixation of humeral endoprostheses immediately following implantation. Phase one determined the loosening load of press-fit (cementless) humeral components and established the right vs. left consistency in paired humerii. Phase two compared loosening of press-fit vs. cemented implants. The prosthesis was implanted and cyclically loaded in a vertically downward direction, simulating the worst case 90 degree forward flexion position of the shoulder. For phase one the press-fit loosening load was 620 ± 155 Newtons (mean ± 1 S.D.). The right vs. left differences were not significant ($p > 0.15$). This established different fixation techniques could be compared right vs. left within each pair. For phase two the cemented side withstood loads of up to 2875 N. The mean loosening loads were 2539 ± 352 N for the cemented side and 489 ± 256 N for the press-fit side. The differences were significant ($p < 0.001$).

Clinical Relevance: Unless there are special reasons not to use cement, such as concern about the need for subsequent stem extraction, the results of this study indicate cement should be used for the strongest and most consistent fixation.

INTRODUCTION

Several studies have illustrated the excellent or satisfactory results of total shoulder replacement in the treatment of painful degenerative rheumatoid and traumatic diseases of the glenohumeral joint [2,7,9,14,15]. However, there is controversy over the need for cement to fix humeral endoprostheses, a lack of data on the relative tendency of press-fit versus cemented to loosen, and uncertainty about which of the press-fit stem designs is best. Complications that occur after shoulder replacement are varied, including rotator cuff tears, dislocations, subluxation, and loosening. A high incidence of radiolucent lines about the humeral component has been reported: Bade 26% [2], Post 33% [13], and Kelly 47% [7]. In a follow-up assessment of 71 total shoulder replacements, Settergren and Cofield reported that one half of the 66 press-fit humeral components showed a shift in position [14]. We feel these are related to loosening of the stem within the humerus. To our knowledge, loosening of humeral prostheses has not been studied by biomechanical testing.

Forward flexion is the most important functional aspect of movement of the shoulder. In 90 degree forward flexion of the shoulder, the acromion acts as a fulcrum pushing down on the humeral head to offset the muscles pulling up on the humerus. This results in a downward force on the head of a prosthesis that presses the stem against the posterior intraosseous metaphysis of the proximal humerus. Through the offset of the humeral head from the longitudinal axis of the stem, this force also produces a torsional moment that tends to twist the stem into retroversion. Studies of hip implants have shown that a component of torsional loading most clearly demonstrates loosening [1,5,8]. We have developed a methodology for testing the tendency to loosen of hip implants [11]. In the present study we utilize similar techniques to assess proximal humeral endoprostheses.

Phase one of the present study was to evaluate the feasibility of taking our test methodology as developed in the hip [11], and applying it to the shoulder. We also had to establish the right vs. left consistency in paired humerii. Phase two was to compare loosening of press-fit vs. cemented implants. The Neer II proximal humeral endoprosthesis was selected for its popularity [3,7,9,15] using the exact same design in both the press-fit and cemented modes.

MATERIALS AND METHODS

Fourteen pairs of human cadaveric humerii were stripped of all soft tissue, transected directly proximal to the elbow condyles, and stored in sealed plastic bags until use. None of these humerii had any abnormalities due to arthritis, previous fracture, deformity, tumor, nor implant. In phase one, seven humeral pairs were press-fit bilaterally with a Neer II proximal humeral prosthesis. Bone preparation and implantation was performed following the technique recommended by the manufacturer [10]. In phase two, seven additional pairs were implanted with one side press-fit, and the other cemented.

Each humerus was potted in a metal box fixture with methacrylate up to ten millimeters (mm) below the anatomic neck. The fixture was then secured to the table top of a model 880/858 MTS servo-hydraulic testing machine. The humerus was positioned with its long axis horizontal, and its anterior aspect facing upward as shown in Fig. 1.

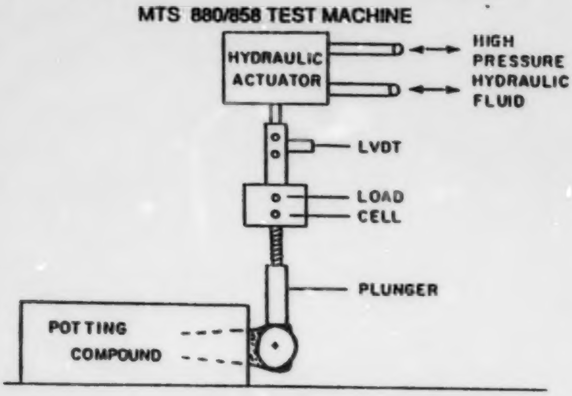

Figure 1:
SCHEMATIC DIAGRAM OF
90° FLEXION TEST CONFIGURATION

The plunger of the MTS servohydraulic machine applies loads vertically downward on the horizontal humerus resulting in a posterior force that presses the stem against the posterior intraosseous metaphysis of the proximal humerus and a torsional moment that tends to twist the stem into retroversion.

The plunger of the MTS machine was positioned with its flat surface over the prosthetic head. This plunger applied loads vertically downward resulting in a posterior force on the humerus. This test configuration simulated the worst case loading condition in 90 degree forward flexion of the shoulder [4,12].

The prosthetic head was loaded to an initial resting tare of 25 N to ensure continuous contact with the plunger. A superimposed cyclical load in the form of haversine waves of amplitude 50 N and period five seconds was then applied. For the first 100 cycles, the cyclical load was cycled from 25 to 75 N. After each 100 cycles, the peak load was incremented by 50 N while the 25 N resting tare load was kept constant. Vertical displacement of the prosthetic head was measured with a LVDT transducer built into the MTS system, and relayed to a Beckman strip recorder. The test was carried to ultimate failure defined as the point at which there developed subsidence of the prosthetic head by five mm or more.

To detect any slippage of the bone within the potting compound, a second LVDT was attached to the medial surface of the humeral neck five mm down from its level of transection. The displacement of this transducer was also relayed to the Beckman strip recorder. If cumulative displacement reached 0.5 mm at any point during the test, slippage of the humerus within the potting was defined to have occurred and the test terminated.

From the strip recording, the prosthetic resting position at the end of every 100 cycles was measured. This was then used to formulate a summarized graph of prosthetic head resting position at the end of each 100 cycles versus cycle peak load for the full range of the test. The graphs for all humerii were then analyzed for patterns which could be used to quantify and define a loosening load.

RESULTS

At low loads, displacement increased in direct proportion to load, and returned to the original resting position after each cycle. However at higher loads, while displacement continued to increase in a similar manner, it failed to return to its original resting position. This indicated inelastic and irreversible subsidence of the prosthesis within the bone. A typical curve is shown in Fig. 2. All tests produced this shape of curve with almost no subsidence at low loads followed by a rapid increase at high loads.

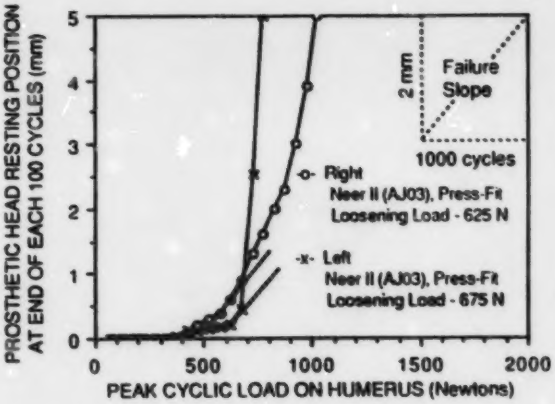

Figure 2:
RESTING POSITION vs. LOAD FOR
PAIRED SPECIMENS NO. H54
BOTH SIDES PRESS-FIT

Typical summarized test result of prosthetic head resting position at the end of each 100 cycles vs. peak load for paired specimens H54 - Both press-fit, Right vs. Left. The straight line indicates the critical loosening slope of 0.2 mm change in prosthetic head resting position during 100 cycles. For clarity, this slope is also shown in the triangle insert in the upper right corner of the figure to a larger scale of 2.0 mm over 1000 cycles. The loading condition at which this slope was surpassed is the loosening load. In this example, the loosening loads were 625 and 675 Newtons for the right and left sides, respectively.

This rapid increase always occurred close to a slope of the curve representing 0.2 mm of displacement per 100 cycles as also shown in Fig. 2. Soon after this point loosening became rapidly progressive first graphically and later visibly. This slope therefore provided a warning signal of imminent loosening, and the peak load producing this slope was thus defined as the loosening load. In all specimens, failure began with irreversible crushing of the subcortical cancellous bone in the region of the anatomic neck. In some specimens, this failure was followed immediately by a longitudinal fracture of the cortex of the posterior and/or medial neck. In all press-fit specimens, the bone crushing was also accompanied by a slight internal rotation of the prosthesis within the humerus.

Table 1 summarizes the loosening loads of seven press-fit humeral pairs tested in phase one. The loosening load was 620 ± 155 N (mean ± 1 S.D.). The right vs. left differences were not statistically significant ($p > 0.15$). This established a consistency in loosening load between right and left sides.

Table 1:

RIGHT vs. LEFT PRESS-FIT LOOSENING LOAD (Newtons)

PAIR	LEFT SIDE		RIGHT SIDE
H13	525		775
H20	575		475
H21	925		375
H22	875		575
H54	675		625
H56	625		475
H61	675		525
Mean	696		546
Std. Dev.	150		129
p Value		0.154	
Right and Left Combined			
Mean		620	
Std. Dev.		155	

(Prosthesis: 3M-AJ03, 12.7 mm stem dia., 150 mm length)

For phase two the cemented side withstood loads of up to 2875 N (Fig. 3 and Table 2), and even here, loosening occurred by implant stem metal fatigue rather than pure interface loosening. The cemented vs. press-fit differences were statistically significant ($p < 0.001$). The loosening loads of the cemented sides were superior by 520% on average. Their loosening load was 2539 ± 352 N compared to 489 ± 256 N for the contralateral press-fit side. Combining all press-fit specimens in phases one and two, the loosening load was 575 ± 200 N.

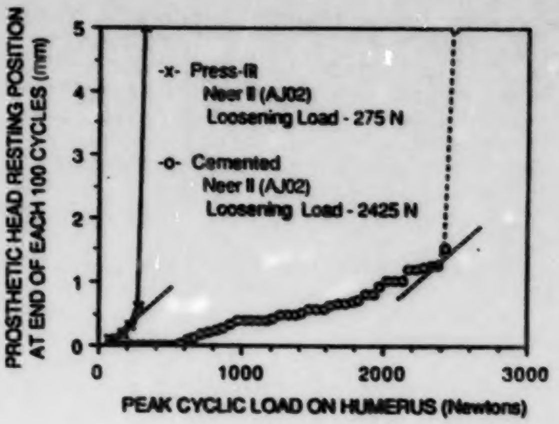

Figure 3:
RESTING POSITION vs. LOAD FOR PAIRED SPECIMENS NO. H26 PRESS-FIT vs. CEMENTED

Typical summarized test result of prosthetic head resting position at the end of each 100 cycles vs. peak load for paired specimens H26 - Cemented vs. Press-fit. The loosening loads were 2425 and 275 Newtons for the cemented and press-fit sides, respectively.

Table 2:

CEMENTED vs. PRESS-FIT LOOSENING LOAD (Newtons)

PAIR	CEMENTED SIDE		PRESS-FIT SIDE
H15*	1925		275
H26*	2425		275
H48*	2525		325
H50*	2875		375
H62**	2825		825
H63**	2875		475
H64**	2325		875
Mean	2539		489
Std. Dev.	352		256
p Value		< 0.001	

(Prosthesis: * 3M-AJ02, 9.5 mm stem dia., 150 mm length
** 3M-AJ03, 12.7 mm stem dia., 150 mm length)

DISCUSSION

We have described a methodology for biomechanically assessing fixation of humeral prostheses. We have picked one position of shoulder flexion and simplified loading to one known vertical force. There are no clear descriptions available of the magnitude or direction of individual physiologic muscle forces in this position, so we have not attempted to simulate them. In the shoulder as with the hip, simulations with a rotator cuff or abductor strap are technically difficult due to problems in securing a simulated tendon to bone especially with high cyclic loads. We studied only posterior subsidence and rotation of the stem. Axial subsidence of the humeral prostheses distally down into the medullary canal towards the elbow, is an additional important aspect of loosening in clinical practice. In the future this should also be tested using a position of zero degrees shoulder flexion as others [16] have done in the hip but with the exact same cyclic loading protocol and loosening criteria as we have described in the 90° flexed position. The two modes of loosening could then be directly compared. We feel the loading which occurs in the 90 degree flexed position is the worst case situation which initiates the loosening process. However, this would have to be substantiated with further studies. In summary our approach is not perfect in that it does not take into consideration and simulate all muscle insertions and forces. However, it follows the basic engineering principle of simplifying the situation to a few essential and reproducible features. It is a start for other subsequent test data to be built upon. The results are easily understood and of relevance to both the practicing surgeon and design engineer. It has the great advantage of providing some indication of the relative performance of various types of new prostheses, before embarking on widespread clinical trials.

We have shown that the humeral press-fit loosening loads were in the range of 275 to 925 N. This corresponds to approximately 40 to 135% (mean 84%) of body weight for a 70 kilogram patient. In the classical study of Inman et al [4], the maximum compressive force acting on the glenohumeral joint was calculated to be approximately 90% of body weight at 90 degrees of abduction. Poppen and Walker [12] found that the resultant force on the glenohumeral joint for elevation of the arm in the scapular plane to be almost 90% of body weight at 90 degrees of elevation. Our mean loosening load of 84% of body weight is therefore within the physiological maximum joint force.

Analyses of different prostheses and techniques are best performed in pairs of humerii from the same individuals. The consistency between left and right loosening load of paired humerii which we found in this study has reinforced this method. Our methodology thus provides an excellent comparative test for future comparisons of other prostheses and implant techniques.

The results of this study are of clinical importance since there have not been clear indications of whether to cement or press-fit humeral components. Some investigators (eg. Neer [9]) recommend cement , while others (eg. Thornhill [15]) press-fit the humeral endoprostheses in place without cement. In our study, cemented implants invariably withstood more than five times the loads of press-fit implants before loosening. Therefore, patients who receive a press-fit stem have a dangerously low margin of safety in resisting loosening. Unless there are special reasons not to use cement such as concern about the need for subsequent stem extraction, the results of this study indicate cement should be used for the strongest and most consistent fixation. This is in agreement with the clinical experience recommending the cementing technique if there are any doubts as to the initial press-fit stability of the prosthesis [3,6].

Acknowledgement: The authors express thanks to 3M Canada for providing the Neer II endoprostheses and to Miss Jackie Snel for her assistance in our laboratory.

REFERENCES

1. Allen, J. et al., Mechanical Analysis of the Rotational Fixation of Cementless Femoral Stems, Orthop Trans, Vol. 10(1), pp. 89-90, 1986.

2. Bade, H.A. et al., Long-term Results of Neer Total Shoulder Replacement, in Surgery of the Shoulder, ed. Bateman, J.E. & Welsh, R.P., Decker and Mosby, St. Louis, 1984.

3. Clayton, M.L. et al., Prosthetic Arthroplasties of the Shoulder, Clin Orthop, Vol. 164, pp. 184-91, 1982.

4. Inman, V.T. et al., Observations on the Function of the Shoulder Joint, J Bone Joint Surg [Am], Vol. 26, pp. 1-30, 1944.

5. Jasty, M. et al., Rotational Instability - The Achilles Heel of Cementless Femoral Total Hip Replacement. Proceedings of the 44th Annual Meeting of the Canadian Orthopaedic Association, Toronto, Ontario, Canada, pp. 83-4, 1989.

6. Kay, S.P. & Amstutz, H.C., Shoulder Hemiarthroplasty at UCLA, Clin Orthop, Vol. 228, pp. 42-8, 1988.

7. Kelly, I.G. et al., Neer Total Shoulder Replacement in Rheumatoid Arthritis, J Bone Joint Surg [Br], Vol. 69, pp. 723-26, 1987.

8. Mjorberg, B. et al., Instability of Total Hip Prostheses at Rotational Stress - A Roentgen Stereophotogrammetric Study, Acta Orthop Scand, Vol. 55, pp. 504-6, 1986.

9. Neer, C.S. II et al., Recent Experience in Total Shoulder Replacement, J Bone Joint Surg [Am], Vol. 64, pp. 319-37, 1982.

10. Neer, C.S. II, Surgical Protocol, Neer II Proximal Humerus Prosthesis, Arthroplasty of the Shoulder, Neer Technique, Technical brochure, #70-2008-3281-7 (38.1)II, 1982.

11. Phillips, T.W. et al., Hip Replacement Femoral Stem Fixation - A Biomechanical Comparison of Cementless vs. Cemented, J Bone Joint Surg [Br], Vol. 72, 1990.

12. Poppen, N.K. & Walter, P.S., Forces at the Glenohumeral Joint in Abduction, Clin Orthop, Vol. 135, pp. 165-70, 1978.

13. Post, M. et al., Total Shoulder Replacement with a Constrained Prosthesis, J Bone Joint Surg [Am], Vol. 62, pp. 327-35, 1980.

14. Settergren, C.R. & Cofield, R.H., Total Shoulder Arthroplasty, Five to Ten Year Assessment, Orthop Trans, Vol. 11(2), page 238, 1987.

15. Thornhill, T.S. et al., Total Shoulder Arthroplasty: The Brigham Experience, Orthop Trans, Vol. 7(3), page 497, 1983.

16. Whiteside, L.A. & Easley, J.C., The Effect of Collar and Distal Stem Fixation on Micromotion of the Femoral Stem in Uncemented Total Hip Arthroplasty, Clin Orthop, Vol. 239, pp. 145-53, 1988.

ACTUATOR CONTROL BY EXTENDED PHYSIOLOGICAL PROPRIOCEPTION

Dr. C Kirtley

Bioengineering Unit, University of Strathclyde,
Glasgow G4 0NW, UK.

ABSTRACT

The use of Functional Electrical Stimulation (FES) of muscle for locomotion in paraplegia, and grasp augmentation in tetraplegia, is limited by the variability of muscle force output in response to electrical stimulation. Moreover, some form of sensory feedback to the user, via the appropriate kinaesthetic pathways, is also required so that obstacles can be negotiated and stimulation hardware faults can be detected.

This paper describes the implementation of a technique known as Extended Physiological Proprioception (EPP) to meet these objectives. In the experimental system described, a paraplegic subject controlled the extension of his paralysed knee by shoulder protraction. A Bowden cable linked the two joints, and a dynamometer in this cable was used to derive the control signal for a computer-controlled stimulator which delivered surface stimulation to the quadriceps muscle group. System modelling was performed by analysis of the open-loop step response, and the controller synthesised by dominant pole-cancellation.

In a series of joint positioning tests with vision occluded the EPP system showed good compensation for muscle response variability, and improvement in joint positioning precision over conventional closed-loop position-servo control.

EPP is suggested as a method for control in both the rehabilitation and industrial fields.

INTRODUCTION

Functional Electrical Stimulation (FES) of paralysed muscle has enabled standing and walking of paraplegics in the laboratory [1-2], and grasp augmentation for tetraplegics [3]. However, in order for these systems to be practical for use in the home and street environment, a number of problems related to the control of the stimulation need to be addressed [4].

Firstly, the force output (and hence joint position achieved) by stimulation of a muscle varies over a considerable range as a result of many internal and external influences, such as temperature, fatigue, and relative movement between the stimulating electrode and the motor point of the muscle [5]. One solution to such a problem is to implement closed-loop position-servo control, in which the joint position is monitored by an electrogoniometer and compared with a reference to give the controller input. The reference signal to the controller may be obtained from a potentiometer moved by a normal joint [6-7], EMG from a normal muscle [6], or from a predefined sequence stored in the computer [8].

Position-servo control methods have been shown to function satisfactorily in laboratory conditions, in which the paralysed joint is free to move. However, practical walking systems will need to negotiate obstacles, stairs and kerbs; and grasp force as well as finger position will need to be controlled in tetraplegic systems. It is therefore necessary that there be some means by which the user can detect obstacles and modify the stimulation accordingly.

In laboratory systems so far implemented, the sensory feedback function has usually been implemented by relying on the patient's vision. This is far from satisfactory since it demands the continuous attention of the patient. It has been suggested that supplemental sensory feedback (in the form of electrocutaneous stimulation) might be employed to lessen this reliance on vision [8]. However, many such systems have been tried in conjuction with both upper and lower-limb prostheses [9-11], with disappointing results in terms of practical impact [12]. This may be because the sensory information is transmitted along inappropriate nervous pathways, which are not part of the body's normal sensorimotor system [13]. Thus the information must be presented in a form which can be accepted, and skin vibration or pain receptors are unlikely to make a satisfactory substitute for kinaesthetic receptors [14].

A better approach is to feed back joint angle information directly to a normally innervated joint[15]. This principle is called Extended Physiological Proprioception (EPP) or Control Interface Feedback[17], and has been successfully applied to the control of several upper-limb prostheses[15-18]. By constraining the motion of the control joint according to that of the slave joint a consistent relationship between force, position and velocity of the two joints is created: the so-called "unbeatable servo". This constraint can be most easily effected by forming a mechanical linkage between control and slave joint, for example by means of a Bowden cable. The tension in this cable can then be used to control the prosthetic or orthotic actuator. In this way, proprioceptive sensations arising from the slave limb are transmitted to the control joint in a physiological manner, via the normal proprioceptive pathways[17], and the actuator may be conceptualised as operating in a power-assist mode.

The purpose of this study was to investigate the possibility of controlling electrically stimulated muscle by EPP, with a view to applying such a technique to the control of FES hybrid neuroprostheses. This paper discusses the basic problems encountered when attempting to implement EPP control of an actuator, and includes an assessment of the method compared to open-loop and closed-loop position servos. Although the work described concentrates on the use of stimulated muscle as the actuator, the principles involved should be applicable to systems using other actuators, such as DC-motors, pneumatics, hydraulics, etc.

MATERIALS AND METHODS

In order to develop and test the concept of controlling stimulated muscle by EPP, the experimental apparatus shown in Fig. 1 was designed, in which a paraplegic subject controls his paralysed knee joint by FES applied to the quadriceps muscle group.

A trans-scapular harness similar to that used to control upper-limb prostheses was worn, and a nylon-in-steel (Perlon) Bowden cable linked shoulder protraction to knee-joint extension by its attachment to a pulley on the joint of a knee brace. The arrangement was such that shoulder protraction caused tension in the cable to rise and the knee to tend to extend. Actual extension was difficult without stimulation because of the small mechanical advantage given by the pulley radius, which was 25 mm. Tension in the cable was monitored by a strain-gauged proof-ring dynamometer in series with it at the knee. The amplified signal was input to the Analogue-Digital converter of an IBM-PC Compatible microcomputer, and used to generate the control signal to a constant-current stimulator developed at this site. The stimulation train was pulse-width modulated at a constant inter-pulse-interval (40 ms), between the threshold level of the muscle (typically 50 - 100 μs) and a limit, arbitrarily set at 500 μs, and applied using "Pals +" surface electrodes (Axelgaard Manufacturing Co. Ltd., Fallbrook, California). Current level was adjusted to give full extension at this limit, and the force transducer was calibrated for cable tensions produced when comfortable levels of force were applied through the harness.

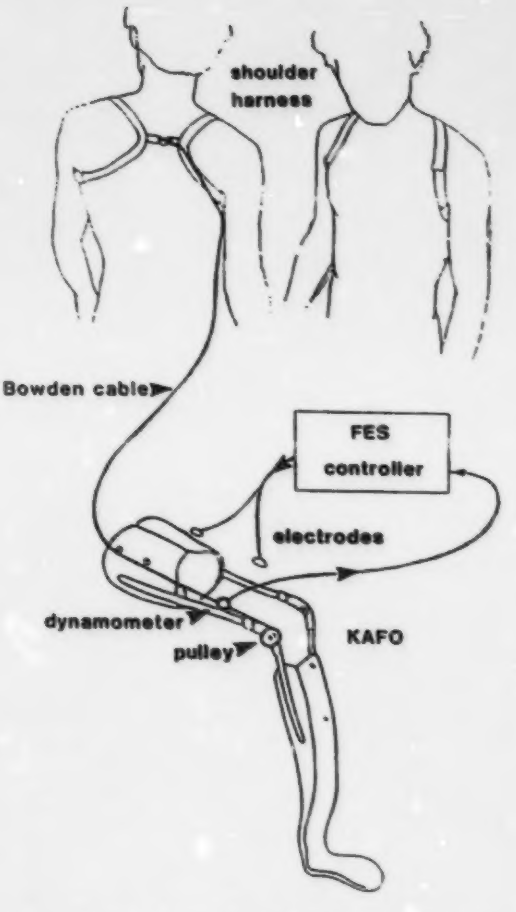

Fig. 1. Experimental apparatus for investigation of EPP control of FES.

A block diagram of the system is shown in Fig. 2, which is modified from an EPP control system used for an upper-limb prosthesis[18]. The force sensed by the dynamometer is denoted by $T_{x,m}(t)$, which is a function of the difference between the user's intended position, x(t), and the actual position of the control joint y(t). In a single cable system such as this, in which the action of gravity is

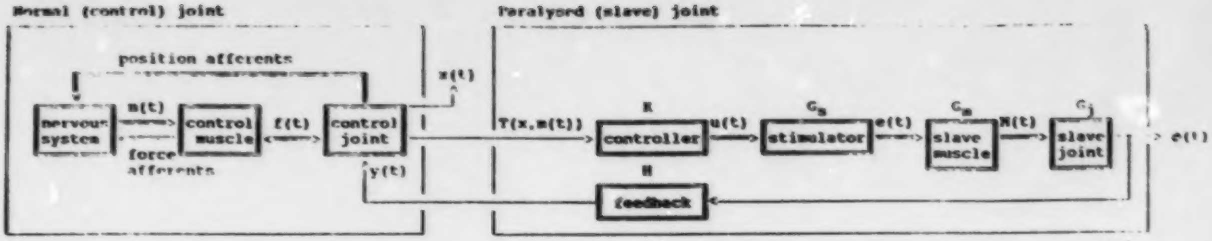

$$T(x, m(t)) = F_T \left[X_d \, (m(t) - x(t)) \right]$$

Fig. 2. Schematic diagram of the EPP-FES control system. The user's motor intent, m(t), modifies the cable tension, T(x, m(t)), which controls the muscle-joint-limb system. The output of the system is fed back (by the cable and harness) to the controlling joint, where it can be sensed by the user. The position of the control joint is constrained by that of the paralysed joint, although it should be noted that position does not explicitly enter into the control scheme.

used to provide a restoring antagonistic force, a 1:1 relationship between the control and paralysed joints will exist only whilst the cable remains taught. It is, of course, possible for the cable to become slack should the limb move faster than the control joint, in which case the proprioceptive advantages of the linkage would be lost. In practice this limitation of single cable systems is not a serious one, since the user can feel that the cable has become slack and, by moving the control joint accordingly, can reestablish the linkage. If necessary a second cable can be added to control the antagonist muscle.

Controller Synthesis

Using a simple proportional relation between transducer output and pulse-width, it was found that the system as described was unstable, with unacceptably large oscillations ocurring at around 1.4 Hz (Fig. 3). This might have been expected, since in linking input and output joints by the cable a closed-loop system is created, with a large dead-time caused by the inertial effects of the limb together with muscle excitation-force coupling delays [5].

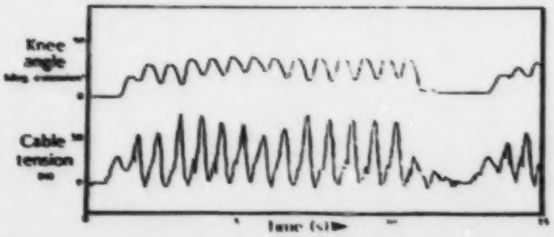

Fig. 3. Closed-loop step response of the system with proportional control.

The step response characteristics of the muscle-knee system (Fig. 4) show that the system is lightly damped, espacially at low muscle activation levels (narrow pulse widths). Input-output analysis, by curve fitting a critically-damped second-order Laplace equation to the muscle frequency response [19], and the product of this together with another second-order equation to the most lightly-damped response, revealed the following discrete model after bilinear transformation:

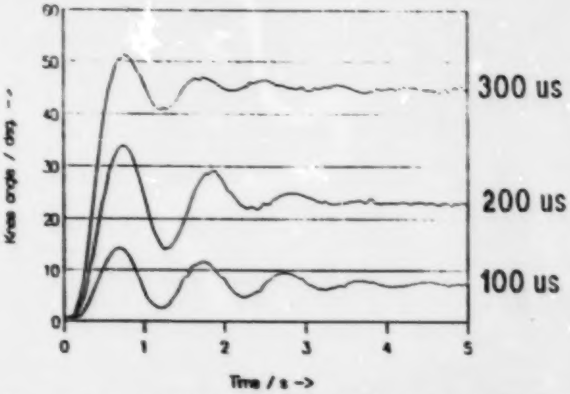

Fig. 4. Open loop step response of the muscle-joint-limb system to stimulation with three different pulse-widths. IPI in each case is 40 ms, and current approximately 50 mA. All responses are underdamped, with damping increasing with increasing muscle activation (larger pulse-widths). In control terms, the least damped response is most likely to cause instability, and this was therefore used to generate the plant model.

$$G(z) = \frac{K_o\ (z+1)^4}{\underbrace{(z^2-1.78z+0.15)}_{\text{muscle}}\ \underbrace{(z^2-1.86z+0.92)}_{\text{joint-limb}}}$$

where K_o is a measure of the overall loop-gain (highly variable) and z is the unit delay operator (sampling interval = 40 ms). The root locus of this equation (Fig. 5) exhibits two dominant poles very close to the unit-circle, which rapidly cross this into the unstable zone as the loop is closed and gain increased from zero. In order to stabilize the system, a controller was designed [20], in which two zeros cancel these poles and draw the locus away from the unit circle to increase gain margin (Fig. 6). Additionally, since muscle, unlike a DC motor for instance, does not include an integrating function in its transfer function, this was incorporated by placing a pole at (z = 1). To make the controller realisable a further pole was placed at (z = 0). The resulting algorithm was as follows:

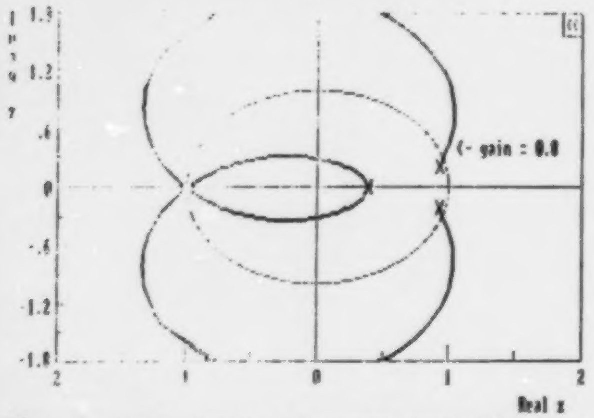

Fig. 5. Root locus of normalised discrete system model. Two open-loop poles lie very close to the Unit Circle, and a point of instability (locus passing outside the circle) is reached at a closed-loop gain of only 0.8.

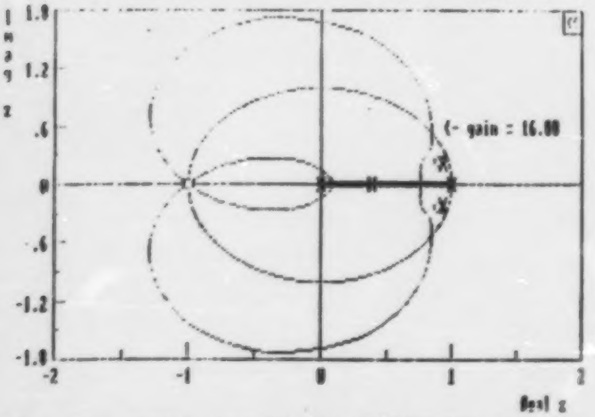

Fig. 6. Root locus of discrete system model with z-transform controller.

Open-loop poles (desired controller zeros) at (z = 0.9 ± 0.25j)

$$\text{Controller} = K\ (z) = \frac{u(z)}{e(z)}$$

$$= \frac{(0.8725 * z^{-2} - 1.8 * z^{-1} + 1)}{(1 - z^{-1})}$$

Thus,

$$u(k) = u(k-1) + K_o\ (e(k) - 1.8 * e(k-1) + 0.8725 * e(k-2))$$

where u(k) = controller output at k'th time interval;
K_o = velocity gain (tuned for optimum performance)
and e(k) = error signal at k'th time interval

Unlike a conventional closed-loop servo, an EPP controller does not have a distinct reference or output, since these are dimensionless and implicitly defined by the user's nervous system. For instance, the same controller can be used for position or velocity control when the limb is free to move, or for force control when the limb is restrained, using the same force sensor. The cable tension signal is thus an aggregate of reference and output signals, and the error signal to the controller must therefore be derived from it. This was done by subtracting from it the previous output from the controller:

$$e(k) = T(k) - u(k-1)$$

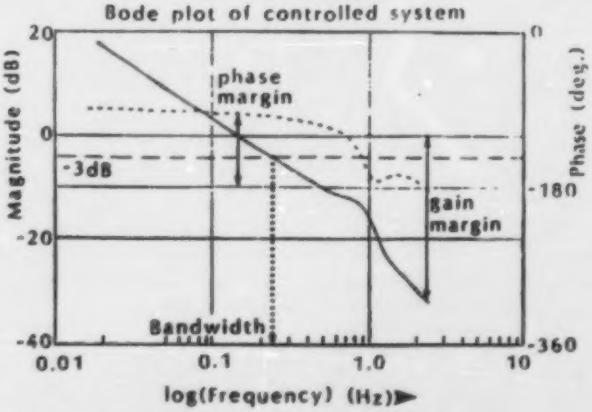

Fig. 7: Bode-plot of controller

Using this controller, it was found that stability was achieved with loop gain sufficient for an adequate response speed: bandwidth approximately 1.4Hz, rise time 1.2s. Moreover, the controller was robust, with a gain margin of 30 dB and a phase margin of 85° (Fig. 7). The same controller parameters were used in tests with three different subjects with no observed deterioration in stability or transient response.

System Assessment

In order to assess the control of limb position using the EPP-FES controller, the apparatus shown in Fig. 8 was constructed, which is a modified version of that used to assess kinaesthetic sensing with the Boston arm[10]. The controlled limb was hidden behind a screen on which were mounted Light-Emitting Diodes at five equidistant points around a quadrant whose centre was approximately co-linear with the subject's knee-joint axis. These target indicators were switched on at random by the controlling computer, and the subject instructed to move his leg (using the FES controller) to a point at which he felt the shank was opposite the illuminated LED. He then pressed a switch and the computer recorded the position achieved by a electro-goniometer on the knee. A three second rest period ensued, after which another LED was illuminated. This process was repeated until all five LEDs had been selected five times each. In order to give the subject a reference with which to estimate leg position, a two minute practice period was allowed before each test, during which the LED nearest to the shank position was illuminated, and the subject instructed to move the leg freely in order to "get the feel of the system".

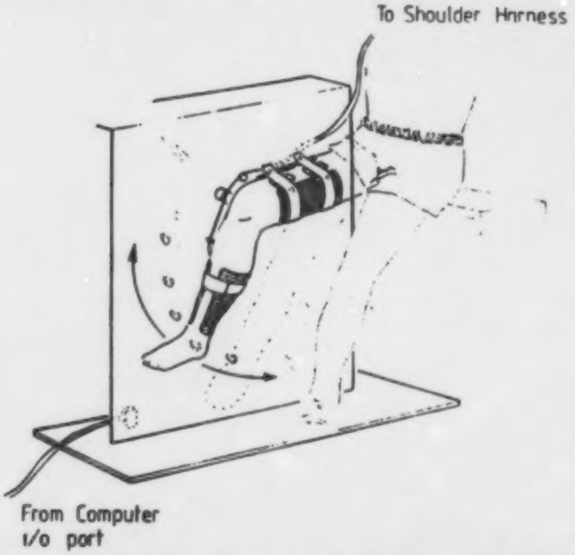

Fig. 8. Apparatus for assessment of limb-positioning performance. Goniometer measures knee extension, calibrated with the rest position (90° flexion) = 0°.

The performance of EPP control against conventional open and closed-loop control was compared. For these latter two methods the control cable was detached from the pulley and made to operate a rectilinear-action sprung potentiometer. In the open-loop case the signal from this potentiometer alone provided the input to the controller, whilst in the closed-loop case the difference between this and the goniometer output was used. The assessment was performed on three subjects, who had sustained complete thoracic-level lesions. For each subject at each test position two measures of performance were calculated: accuracy, being the mean error between limb position and target position; and precision, the mean error between limb position and the mean of the five attempts at each target position. The former provides a measure of systematic error in joint positioning, whilst the latter is a measure of the repeatability of the controller.

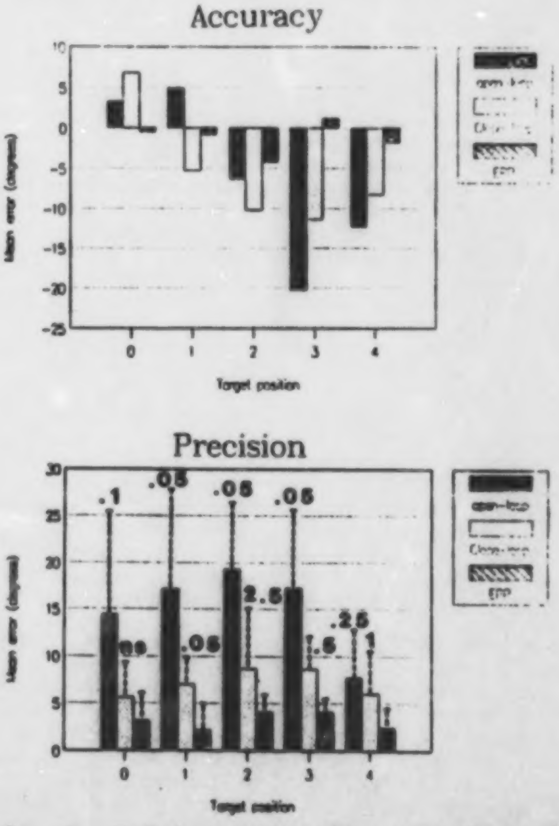

Fig. 9. Joint-positioning accuracy and precision for the three control methods

RESULTS

The results of the assessment are displayed in Fig. 9. Results of Student's t-tests (one-tail, N=30) of the EPP controller versus the open-loop and conventional closed-loop controllers are displayed next to the appropriate bar.

CONCLUSIONS

The first finding to note in the results of the joint-positioning tests is the large variability (around 20°) in joint position achieved using the open-loop controller. This confirms previous work, and highlights the need for some form of closed-loop control in FES-powered orthoses. In contrast, the mean error in joint positioning measured while using the EPP controller was consistently small (around 5°), showing the effectiveness of transmission of proprioceptive feedback.

Such an improvement might also have been expected from closed-loop position-servo control. In fact, errors in joint-positioning were only partially reduced, to values (around 10°) which are still significant. The reasons for such an improvement are not obvious. Position-servo control, by eliminating the variability in muscle response might have been expected to perform equally as well. Its relatively poorer performance must therefore have been due to the patient forgetting his reference position and therefore losing the mapping between shoulder and knee position [21]. The continual refreshment of this mapping by the feel of the motion of the paralysed extremity may be responsible for the improvements observed with EPP control, and the inclusion of the user in the control loop may thus enable the potential of the natural motor control system to reduce variability to be more fully exploited.

At targets in the outermost portions of the movement range errors were smaller, and the improvement shown by the EPP controller not so marked. This may be because the subject received proprioceptive clues to joint position from the end-stop of the potentiometer in these positions. Accuracy measurements confirm the previously noted finding of a progressive over-estimation of limb position with increasing target position [10], characteristic of cable-controlled systems without sensory feedback.

In the design of an interface for manipulator control, whether for rehabilitation or industrial use, as little cognitive demand as possible should be placed on the user's attention [18]. By interfacing directly with the patient's natural motor control pathways, EPP shows advantages over systems which do not give proprioceptive feedback. The presence of this proprioceptive feedback in EPP control might be expected to enable the user to detect unexpected obstacles and so take appropriate action. Moreover, it may be noted here that proprioception has been found to be important in the generation of a favourable emotional response [22], and the effective restoration of this sense may therefore improve compliance with control systems. Although in these experiments muscle was utilised as the actuator for shoulder-knee control, the technique of EPP is versatile, and could in principle be applied to the control of any manipulator. The more natural control achieved by EPP should facilitate subconscious operation of such devices and improve efficiency.

ACKNOWLEDGEMENTS

The author wishes to acknowledge collaboration with Mr. GH Creasey & Mr. D Gow, Bioengineering Unit, Princess Margaret Rose Hospital, Edinburgh, in formulating the ideas behind this work; Drs. L Wang & Mr. J Guan, Department of Dynamics and Control, University of Strathclyde, in designing the controller; Prof. JP Paul & Dr. BJ Andrews for supervision of the work; Dr. G Phillips, Mr. R Barnett and Mr. B Heller for their invaluable assistance generally; and the kind co-operation of Dr. M Delargy and the patients of Philipshill Hospital. The project was funded by the Scottish Home & Health Department, and the author was supported by a UK Medical Research Council Training Fellowship.

1. Kralj A, Bajd T, Turk R, Krajnik J, Benko H. Gait restoration in paraplegic patients: a feasibility demonstration using multichannel surface electrode FES. J. Rehab Res. & Dev. 1983, 20:3-20.

2. Vodovnik L, Bajd T & Kralj A. Functional Electrical Stimulation for control of locomotor systems. CRC Crit. Rev. 1981, CRC Press Inc., Boca Raton, Florida.

3. Peckham PH. Functional electrical stimulation: current status and future prospects of application to the neuromuscular system in spinal cord injury. Paraplegia 1987, 25: 279-288.

4. Stanic U & Trnkoczy A. Closed-loop positioning of hemiplegic patient's joint by means of functional electrical stimulation. IEEE Trans. Biomed. Eng. 1974, BME-21: 365-370.

5. Crochetiere WJ, Vodovnik L & Reswick JB. Electrical stimulation of skeletal muscle - a study of muscle as an actuator. Med. Biol. Eng. 1967, 5: 111-125.

6. Vodovnik L, Crochetiere WJ & Reswick JB. Control of a skeletal joint by electrical stimulation of antagonists. Med. Biol. Eng. 1967, 5: 97-109.

7. Crago PE, Mortimer JT & Peckham PH. Closed-loop Control of Force During Electrical Stimulation of Muscle. IEEE Trans. Biomed. Eng. 1980, BME-27: 306-312.

8. Petrofsky JS, Phillips CA, Douglas R & Larson P. A computer-controlled walking system: the combination of an orthosis with functional electrical stimulation. J. Clin. Eng. 1986, 11 (2), 121-133.

9. Beeker TW, During J & Den Hertog. Artificial touch in a hand prosthesis. Med. Biol. Eng. 1967, 5:47-49.

10. Mann RW & Reimers SD. Kinesthetic sensing for the "Boston arm". Proc. 3rd. Int. Symp. Advances in External Control of Human Extremities, ETAN, Belgrade, Yugoslavia, 1970: 231-243.

11. Clippinger FW, Seaber AV, McElhaney JH, Harrelson JM & Maxwell GM. Afferent sensory feedback for lower extremity prosthesis. Clin. Orth. Rel. Res. 1982, 169: 202-206.

12. Childress DS. Closed-loop control in prosthetic systems: historical perspective. Ann. Biomed. Eng. 1980,8: 293-303.

13. [illegible]

14. Simpson DC & Kenworthy G. The design of a complete arm prosthesis. Biomed. Eng. 1973 (Feb.) 56-59.

15. Simpson DC. The choice of control system for the multimovement prosthesis: Extended Physiological Proprioception (EPP). In: The control of upper-limb prostheses and orthoses, ed. P Herberts P, CC Thomas, Springfield, Illinois, 1974: 146-150.

16. Carlson LE & Primmer KR. Extended Physiological Proprioception for electric prostheses. Proc. 6th Int. Symp. on Advances in External Control of Human Extremities, ETAN, Belgrade, Yugoslavia, 1978: 301-311.

17. Doubler JA & Childress DS. An analysis of Extended Physiological Proprioception as a prosthesis control technique. J. Rehabil. Res. & Dev. 1984, 21 (1): 5-18.

18. Doubler JA & Childress DS. Design and evaluation of a prosthesis control system based on the concept of Extended Physiological Proprioception. J. Rehabil. Res & Dev. 1984, 21 (1): 19-31.

19. [illegible] Effects of elastic loads on the contractions of cat muscles. Biol. Cybern. 1976, [illegible]

20. DiStefano JJ, Stubberud AR & Williams IJ. Theory and problems of feedback and control systems. p 333. Schaum's outline series, McGraw-Hill, New York, 1976.

21. Mortimer JT, Bayer DM, Lord RH & Swanker JW. Shoulder position transduction for proportional two axis control of orthotic/prosthetic systems. In: The control of upper limb prostheses and orthoses, ed. P Herberts et al, CC Thomas, Springfield Illinois: [illegible], 1974.

22. Gellhorn E. Motion and emotion. The role of proprioception in the physiology and pathology of the emotions. Psychol. Rev. 1964, 71 (6): 457-472.

COMPUTER MODELLING OF OCCUPANT CRASH DYNAMICS IN CHILD RESTRAINT DEVICES

S. Basile, B.K. Latouf, R.G. Gaspar*

Becker Transportation Safety Inc., *University of Windsor

ABSTRACT

A preliminary study involving the applicability of computer simulation of child occupant dynamics, as a performance evaluation tool, for child restraint devices was carried out. The occupant simulation model used, known as CAL3D, was originally developed by the Calspan Corporation and is currently administered by Wright Patterson Air Force Base (WPAFB) in the United States.

Full–scale sled and barrier crash tests are important aspects of child restraint safety design. CAL3D, a Fortran based computer program, has been used extensively in the automotive world to simulate occupant dynamics during barrier or sled impacts. By means of computer simulation, an indepth occupant safety analysis may be performed which is much more cost effective then current testing procedures.

This preliminary study involved applying the CAL3D computer program to child restraint occupant modelling. An important input requirement of the CAL3D child restraint model is the dynamic interaction between the occupant and the child seat. A finite element analysis was performed to establish the force–deflection stiffness characteristics of a dynamically loaded child restraint seat. High speed film analysis was used to establish an acceleration time history for a typical sled test.

By providing flexibility and cost savings, the CAL3D approach allows for a design environment condusive to product enhancement. Based on this preliminary study it appears that computer modelling of occupant dynamics is a feasible method for performance evaluations of child restraint devices. The integration of other computer methods, such as finite element analysis, further augments the flexibility and capability of the occupant simulation model.

INTRODUCTION

In most industrialized nations, motor vehicle accidents have been the leading cause of death among children between 1 and 14 years of age [1]. In a motor vehicle accident, there are two kinds of collisions. The first is the car's collision when it impacts another object and then procedes to crush as it is decelerated. The second is the "human collision", which occurs when an occupant impacts the vehicle interior and/or other occupants. It is this secondary action which is the main cause of injury. Unrestrained child occupants, standing on a seat, leaning out of a window, or sitting on someone's lap are in danger. A sudden stop or impact will slam an unrestrained child against the vehicle interior or eject the child onto the roadway. Since adult restraints do not provide a child with sufficient protection, several child restraint devices have been introduced. It has been clearly shown that the proper use of child restraint devices would preclude a majority of fatalities and injuries that occur among children in automotive impacts [2].

For a child restraint device to be sold in Canada it must first meet Federal Safety Standards. Manufacturers of child restraint devices must comply with Canadian Motor Vehicle Safety Standards (CMVSS) 213, which evaluates the performance of child restraint devices during sled tests. The present lack of computer modelling of these restraint devices, requires manufacturers to perform expensive and time consuming staged sled tests to evaluate changes in child restraint design.

The objective of this study is to establish an effective and inexpensive means of evaluating the performance of child restraint devices, by incorporating mathematical models and computer simulations. The crash victim simulation (CVS) program used is the CAL3D gross motion simulator. It is also an objective of this study to demonstrate the utility of finite element analysis when integrated with the simulation process.

OCCUPANT SIMULATION USING CAL3D

Simulation of occupant dynamics is a challenging analytical task. Several Fortran–based computer programs are currently available to determine the dynamics of a victim in a crash environment. The CAL3D model is one such code, which can predictively simulate human body dynamics. The equations of motion are formulated by a Newtonian–Eulerian approach and assembled in block matrix form. The resulting system of equations is solved numerically using a variable time step, vector exponential integrator.

In the model, the vehicle interior is described as a series of connected planes that can be used to represent components such as the seat, floor or dashboard. In this study, three–dimensional planes have been assembled to form a child restraint system. The occupant consists of an ellipsoidal, segmented, rigid body tree structure as shown in Fig. 1. Through interactions with the various contact surfaces, the occupant undergoes a rapid change in its dynamic state of motion. The relative rotations of the segments (ellipsoids) between links are characterized by non–linear torsional springs, dampers, and Coulomb friction effects. Contact forces on the various segments are determined by the amount and rate of penetration into the different vehicle planes from user specified force–deflection curves.

Model Inputs

Within the CAL3D program there are three main modelling categories, namely; occupant anthropometry, vehicle crash pulse, and the energy characteristics of occupant–vehicle interaction.

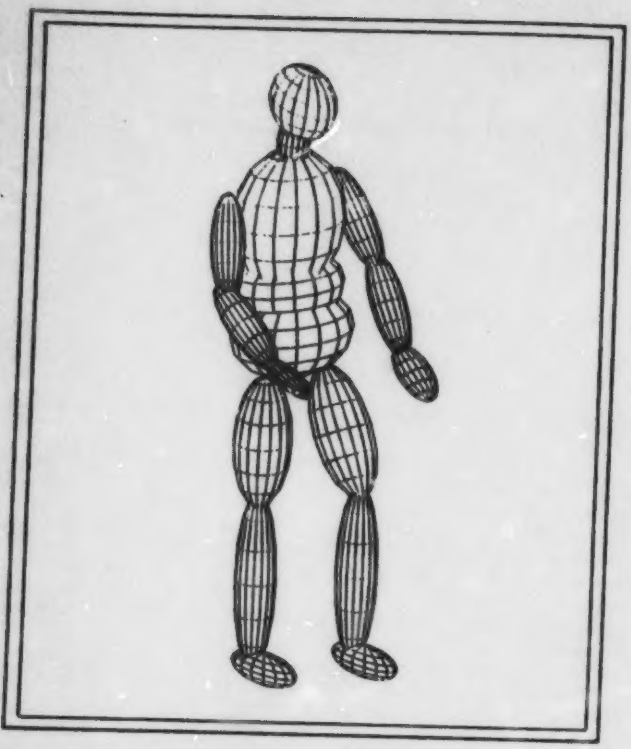

Figure 1 Representation of Human Body as an Ellipsoidal tree structure.

In the CAL3D model, to mathematically represent the anthropometry, the human is subdivided into segments that are connected by joints. The program features a "tree structure" for defining the segments. Once a reference segment has been established each succeeding segment must be connected to a previously defined segment. To each connection a restoring function which describes the induced torque, for relative rotation of two segments, must be provided. A scaled anthropometric body data set was used since data for child dummies was not available. The scaling was done using GEBOD, a supplement to CAL3D, which gives ellipsoid size, weight, and inertial properties based on age, sex, height, and weight. This program does not however, provide the connectivity characteristics (i.e., joint restoring functions) between segments. For this purpose the WPAFB Hybrid III dummy set [2], which is published for adults, was adapted.

The crash pulse input for this study consisted of two acceleration–time histories. The first is the acceleration of the vehicle with respect to fixed space reference and the second is the acceleration, both linear and angular, of the child restraint device with respect to the vehicle. For the former, a standard 30 mph crash pulse was taken. The child restraint crash pulse however, was achieved by high speed film analysis. A sled test film was analyzed and a trace of particular points, frame by frame, provided the position and angular displacement time histories. This data was subsequently differentiated by CAL3D to arrive at the appropriate crash pulse.

During occupant–vehicle interaction, the calculation of forces is related to the extent of penetration by a segment into a plane. The resulting contact force is determined by a force–deflection routine which allows for frictional effects, energy losses, permanent offset (hysteresis), and impulse loading. Care must be taken when establishing the force–deflection characteristics for a given contact. In this study, the finite element method is introduced as a method of ascertaining this information.

Finite Element Analysis

A finite element analysis was used to acquire the force–deflection characteristics of the child seat. Two main modelling tasks were involved in this part of the study. The first, is that of geometrical description and descretization of the complex 3–D surface that comprises the child restraint device and the second is the choice of appropriate boundary conditions.

The description of complex surfaces, in mathematical terms acceptable for digital input, can be achieved by parametric graphic models. The dominant form used to model surfaces is the parametric or vector valued function [3, 4]. A point on a surface is represented as a vector:

$$\bar{p}(u,v) = \Big(x(u,v), y(u,v), z(u,v) \Big) \qquad (1)$$

Many techniques exist for establish–ing polynomial parametric equations for surfaces, given the coordinates for the control points. For application to this study, Bezier surfaces are most appropriate.

Bezier defines the surface p(u,v) as a cartesian product of two curves, in terms of n + 1 control points Pij (points which are measured from the seat) to give a grid (nxm) across the surface:

$$p(u,v) = \sum_{i=0}^{n} \sum_{j=0}^{m} \bar{P}_{ij} \, B_{in}(u) B_{jm}(v) \qquad (2)$$

where B(u) and B(v) are a set of polynomials called blending functions, defined as:

$$B_{in} = c(n,i) u^{i} (1-u)^{n-i}$$

$$B_{jm} = c(m,j) v^{j} (1-v)^{m-j} \qquad (3)$$

C(n,i), C(m,j) are the bionomial coefficients, given by:

$$c(n,i) = \frac{n!}{(i!(n-i)!)}$$

$$c(m,j) = \frac{m!}{(j!(m-j)!)} \qquad (4)$$

This formulation was coded into Fortran and the output was directed in a format intelligible to most finite element packages. The data was transferred to the Algor Supersap finite element software and the grid was further descretized to triangular elements for this plane stress problem. Fig. 2 depicts the computer generated drawing of the child restraint device.

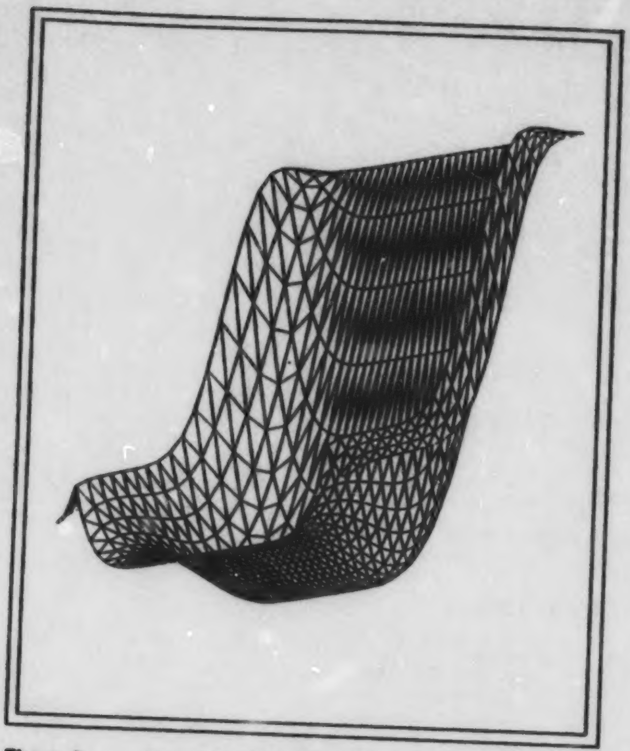

Figure 2 Descretized Bezier Surface representing Child Restraint Device.

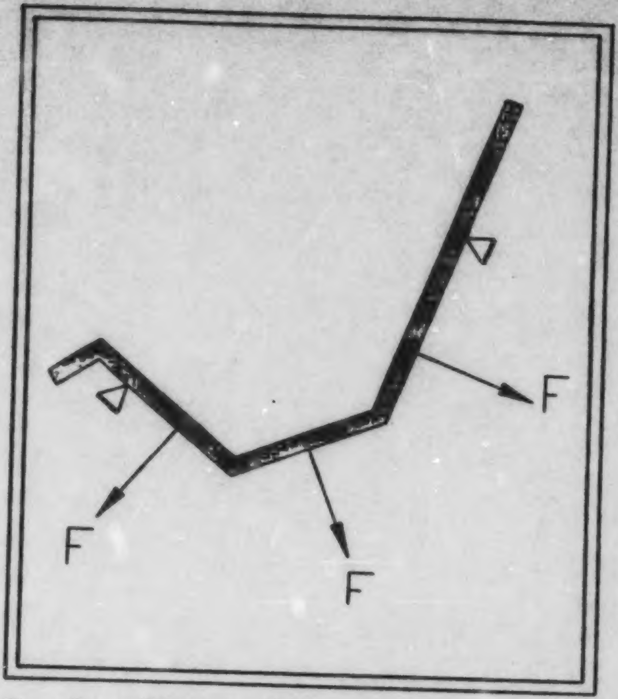

Figure 3 Schematic Diagram Depicting Boundary Conditions Used for Finite Element Analysis.

The film data revealed that three main areas of the child restraint are loaded during a sled test. These areas are the in the leg support, seat pan and seatback areas of the child restraint as shown schematically in Fig. 3. A dynamic ramp load of amplitude 500 lbs. (2230 N) with a period of 50 msec was used as the forcing function for the finite element analysis, at each of these locations. To constrain the seat from rigid body motion, appropriate support conditions had to be provided to the child seat. The support conditions shown in Fig. 3 coincide with positions on the seat which were observed to essentially remain fixed in space during the sled test films.

Having established the geometry and boundary conditions for the finite element model, a dynamic loading analysis was performed. The results of this analysis are shown in Fig. 4, which gives the force deflection characteristic at the three positions of interest. These linear functions were used as direct input for the CAL3D model.

RESULTS OF SIMULATION

The results of the occupant crash simulations are best appreciated by computer graphics which depict the kinematic state of the occupant. The child occupant kinematics are shown in Fig. 5 at 20 msec intervals up to 100 msec. Table 1 is a summary of the significant crash victim injury criteria in the context of this study.

From Table 1, it can be seen that the crash victim data indicates compliance with CMVSS No. 213. The HIC number, which is used to predict the potential for head injury of adult occupants in the case where contact of the head or neck is prevelant, is not as significant, in this case. The child's head and neck were free from contact. However, a separate head injury criteria for children should be established and might be addressed in future legislation.

Table 1
Summary of Salient Crash Victim Data

Item	Simulation Result	CMVSS Limit
Head Excursion	15.4 in.	28.4 in
Sustained Acceleration*	47.5 g	60.0 g
Peak Acceleration	53.6 g	–
Head Injury Criterion HIC	762	1000**

* For a period of more than 3 msec

** A value of 1000 is usually considered as an injury threshold for adult occupants.

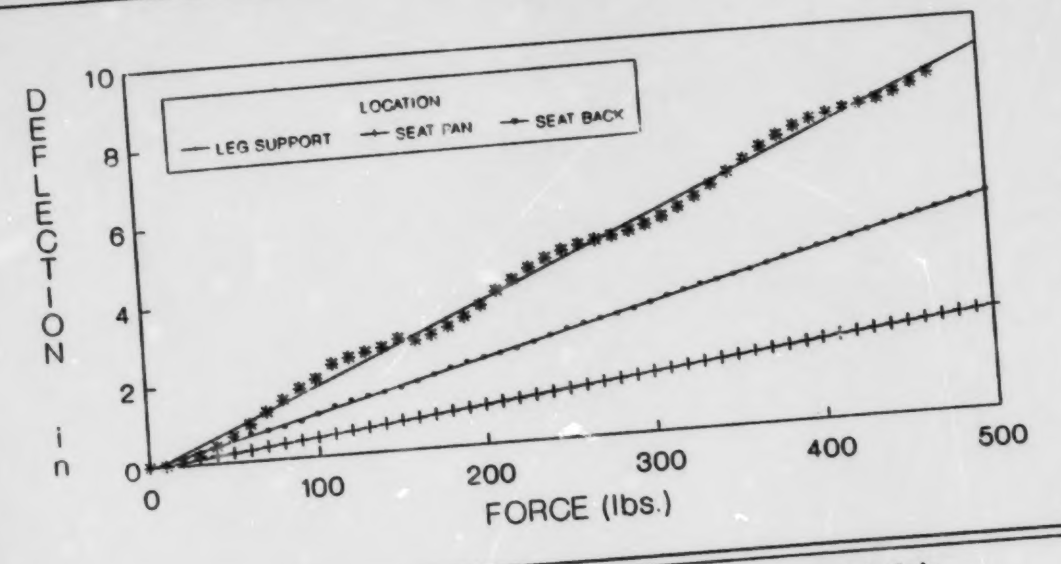

Figure 4 Force Deflection Results Derived From Finite Element Analysis

CONCLUSIONS

While this study is of a preliminary nature, and extensive model refinements were not undertaken, a general conclusion appears to be warranted. Simulation of occupant dynamics appears to be a feasible method for performance evaluations of child restraint devices. Furthermore, the use of computer based methods, such as finite element analysis, may be used to construct more sophisticated force–deflection models improving on the limited capabilities of the current CVS force–deflection models.

One future implementation of computer modelling is as a design/parameter optimization tool. Such a method would require an initial crash test which would be used for model calibration. Once a correlated model has been obtained, various design parameters may then be studied with respect to occupant performance. After an optimum design has been achieved, a final check, to asert compliance with CMVSS No. 213, is done by incorporating an actual sled test. In this scheme, the need for intermediate sled tests, has been eliminated and prototype development and design have been facilitated considerably.

ACKNOWLEDGEMENTS

This study was supported in part by a NSERC undergraduate scholarship.

REFERENCES

1. Dalmotas, D.J., Dance, D.M., Gardner, W.T., Gutoskie, P.A. & Smith, G.A., Current Activities in Canada Relating to the Protection of Children in Automobile Accidents, Proc. Advances in Belt Restraint Systems: Design, Performance and Usage, Detroit, SAE 840529, 1984.

2. Kaharne, C.J., Kossar, J., Chi, G.Y.H., Evaluation of the Effectiveness of Child Safety Seats in Actual Use, Proc. SAE Child Injury and Restraint Conference, San Diego, SAE 831656, 1983.

3. Kaleps, I., Hybrid III Geometrical and Inertial Properties, Proc. SAE International Congress and Exposition, Detroit, SAE 880638, 1988

4. Newman, W.N. & Sproull, R.F., Principles of Interactive Computer Graphics, 2nd Edition, pp. 315 – 320, McGraw – Hill, New York, 1979

5. Hearn, D., Computer Graphics, pp. 195 – 203, Prentice Hall, New Jersey, 1986

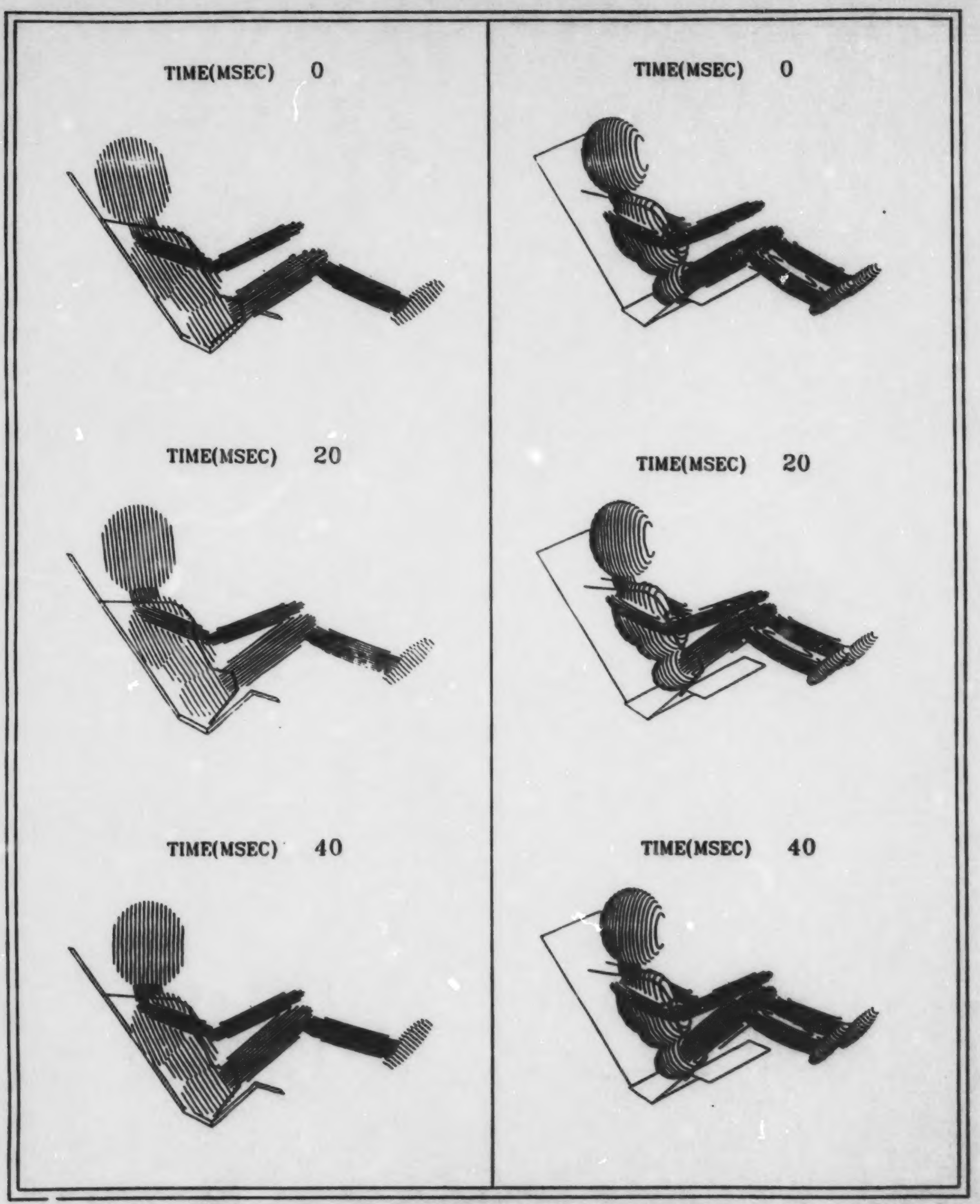
TIME(MSEC) 0
TIME(MSEC) 20
TIME(MSEC) 40
TIME(MSEC) 0
TIME(MSEC) 20
TIME(MSEC) 40

Figure 5 Child Occupant Kinematics, Time 0 msec.– 40 msec, a) Side View b) Oblique View (Note: Camera view point is fixed with respect to child restraint device)

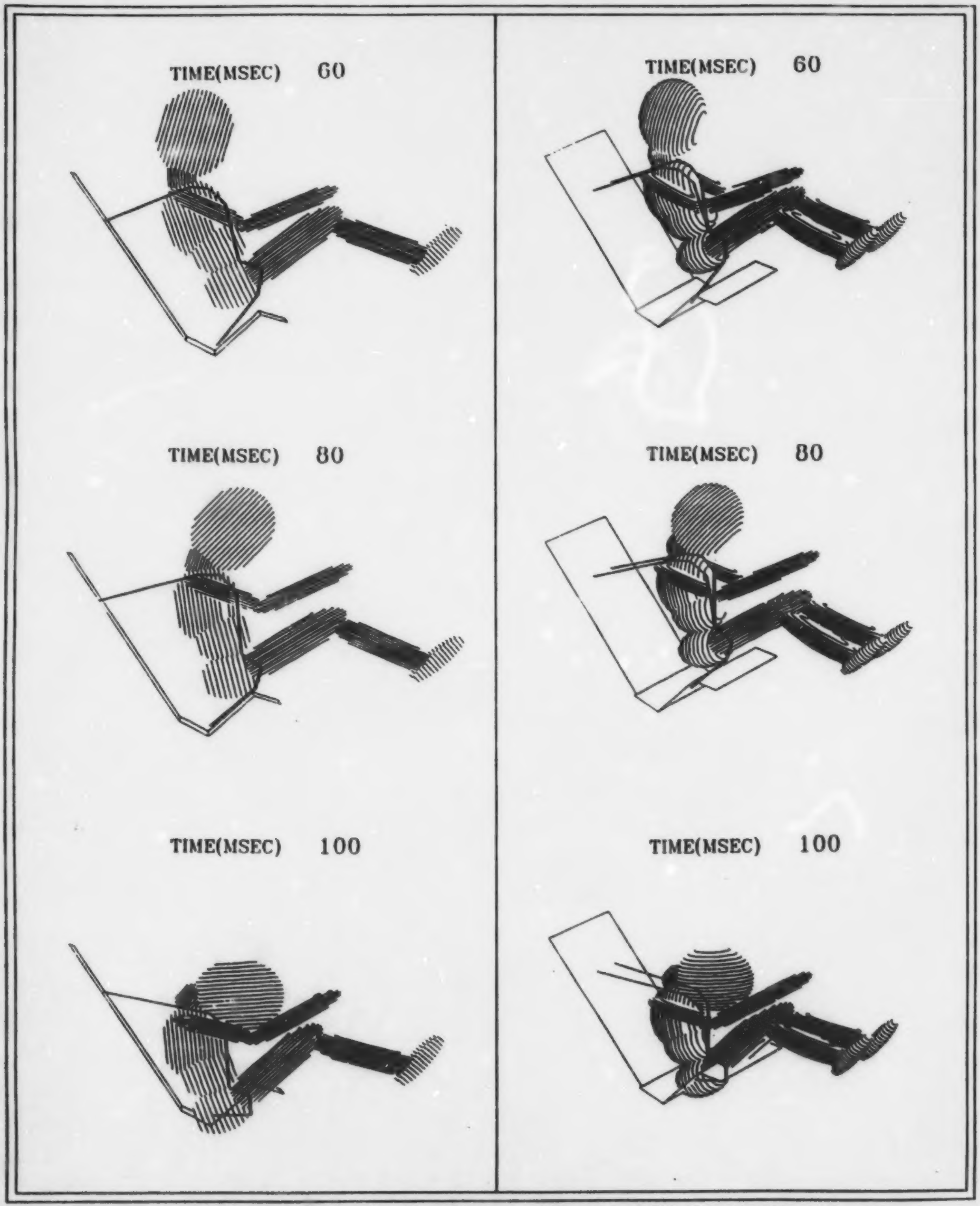
TIME(MSEC) 60
TIME(MSEC) 60
TIME(MSEC) 80
TIME(MSEC) 80
TIME(MSEC) 100
TIME(MSEC) 100

Figure 6 Child Occupant Kinematics, Time 60 msec.– 100 msec, a) Side View b) Oblique View (Note: Camera view point is fixed with respect to child restraint device)

A CARTESIAN TENSOR METHODOLOGY FOR THE STUDY OF CLASSICAL NEWTONIAN DYNAMICS

PART I : CARTESIAN TENSOR ANALYSIS †

C. A. Balafoutis and R. V. Patel

Electrical and Computer Engineering Department
Concordia University, Montreal, Quebec
CANADA H3G 1M8

ABSTRACT

In this paper, we provide a brief analysis of second-order Cartesian tensors which will be used in an accompanying paper (Part II) for the study of classical Newtonian dynamics. In particular, in this paper, by exploring various relationships between second-order skew-symmetric Cartesian tensors and their vector invariants (defined in a 3-D Euclidean space), we state and prove a number of propositions which define important tensor identities. These identities enable one to manipulate effectively (and thus simplify) complex tensor equations. They will be used in Part II for deriving a computationally efficient Cartesian tensor formulation for the dynamic equations of rigid body motion.

I INTRODUCTION

Conventionally, in the classical Newtonian formulation of rigid body dynamics, vectors are normally used to represent basic physical quantities and, therefore, vector analysis is used [1,3] for deriving the equations of rigid body motion. In particular, vector analysis is imposed on classical Newtonian dynamics from the consideration that *angular rates* (i.e., linearly independent rates of change of a rigid body orientation) constitute the components of a vector quantity, the *angular velocity vector*. This consideration also assigns a vector character to other physical quantities which are defined in terms of the angular velocity vector, such as *angular acceleration, angular momentum, external torque*, etc. However, as is well known [1-12], angular velocity can also be described by a second-order skew-symmetric Cartesian tensor, the *angular velocity tensor*. This obviously indicates that besides vector analysis, Cartesian tensor analysis [5-10,12] can also be applied in rigid body dynamics and this raises the following question : Which of the two representations of the angular velocity describes more efficiently the angular motion of a rigid body? In order to answer this question, we shall concentrate in this paper on Cartesian tensor analysis, and in an accompanying paper, we shall show that rigid body motion can be described more efficiently using Cartesian tensor analysis than vector analysis.

As we mentioned above, certain physical quantities have a dual description, i.e., they can be described in a Cartesian coordinate system by using either a 3-D vector or a second-order Cartesian tensor. Moreover, it is well known [4,12], that for angular velocity or angular acceleration, which can both assume this dual description, the two descriptions are very closely related. In particular, it is well known [4,12], that the 3-D vector which describes the quantity in question is the *vector invariant* of the corresponding second-order Cartesian tensor. Therefore, in order to provide a computationally efficient Cartesian tensor formulation of the equations of rigid body motion, a better understanding and an efficient mathematical description of the relationship which exists between second-order Cartesian tensors and their vector invariants is essential. In general, in tensor analysis the relationship between a second-order Cartesian tensors and their vector invariants is usually expressed by using the third-order Levi-Civita tensor ϵ. However, this results in a computationally inefficient formula with no obvious physical insight. In this paper, to describe this relation between second-order skew-symmetric Cartesian tensors and their vector invariants, we introduce a 1-1 operator which makes the relationship transparent and which can be implemented with no computational cost. Furthermore, by using this 1-1 operator, we explore the relationships between second-order Cartesian tensors and their vector invariants, and state and prove a number of propositions which define important tensor identities. These identities enrich the theory of Cartesian tensor analysis and enable one to manipulate effectively (and thus simplify) other complex tensor equations.

Also, it is well known [3-5,12] that second-order orthogonal Cartesian tensors constitute a linear algebra which is isomorphic to the matrix algebra. Thus, based on this isomorphism, in many applications the well-established matrix algebra is usually used to carry out not only calculations for various operations with tensors but also to perform the mathematical analysis for the problem at hand. Since matrix elements are scalars, matrix algebra has the advantage of reducing all such calculations to addition and multiplication of real numbers. However, it has the disadvantage of requiring that a basis be introduced. This defines an isomorphism between tensors and matrices and may be quite irrelevant to the problem at hand. This often obscures the physical or geometrical meaning of the tensor involved in the mathematical formulation of a problem. Moreover, this matrix representation may lead us to perform irrelevant and unnecessary calculations. Therefore, it is important in practical applications to be able to work with Cartesian tensors directly without resorting, at an early stage of our analysis, to their matrix representations. Therefore, in this paper, all tensor identities are stated and proved in a coordinate-free manner.

---

† This research was supported by the Natural Sciences and Engineering Research Council of Canada under Grant A1345 and by the Fonds pour la Formation de Chercheurs et l'Aide a la Recherche of Quebec under Grant 88AS25A.

The rest of this paper, is organized as follows : Section II defines the notation used in this paper and briefly discusses some basic tensor operations. Section III presents possible useful decompositions for second-order Cartesian tensors. We introduce a 1-1 operator between second-order skew-symmetric Cartesian tensors and their vector invariants which are defined in a 3-D Euclidean space. A geometric characterization for second-order skew-symmetric Cartesian tensors is also given. Section IV contains some propositions which define important tensor identities and Section V concludes the paper.

II NOTATION AND BASIC TENSOR OPERATIONS

In this paper, boldface lower case roman letters are used to denote vectors. Upper case boldface roman letters are used to denote second-order Cartesian tensors. A second-order skew-symmetric Cartesian tensor associated with a vector (see Section III) will be denoted with a tilde (˜) above the boldface lower case roman letter denoting this vector. The *coordinate matrix*, associated with a second-order Cartesian tensor (or a vector), will be denoted by the corresponding upper (or lower) case italic letter.

In order to use tensors in an efficient manner we define algebraic structures on them by introducing some algebraic operations. Thus, as is well known [1-8,12], the following tensors and algebraic operations are well defined.

The *zero* and *unity (identity)* tensors are denoted and defined, respectively, by

$$\mathbf{0v} = \mathbf{0} \quad , \ \forall \mathbf{v} \qquad (2.1)$$

$$\mathbf{1v} = \mathbf{v} \quad , \ \forall \mathbf{v} \qquad (2.2)$$

The algebraic operations of *addition* and *scalar multiplication* can be defined as usual. Thus the addition of two second-order tensors **T** and **S** is defined by

$$(\mathbf{T} + \mathbf{S})\mathbf{v} = \mathbf{T}\,\mathbf{v} + \mathbf{S}\,\mathbf{v} \quad , \ \forall \mathbf{v} \qquad (2.3)$$

and the multiplication of **T** by a scalar λ is defined by

$$(\lambda\mathbf{T})\mathbf{v} = \lambda(\mathbf{T}\,\mathbf{v}) \quad , \ \forall \lambda \qquad (2.4)$$

Note : It is well known [7,12], that the set of second-order Cartesian tensors, together with the two algebraic operations of addition and scalar multiplication, constitutes a vector space over a scalar field. Here, this scalar field is assumed to be the field of real numbers.

Besides the addition (or subtraction) and scalar multiplication defined above, the following algebraic operations are also well defined [7.12].

Tensor product : Let **T** and **S** be two second-order tensors whose components, referred to an orthogonal Cartesian coordinate system, are t_{ij} and s_{kl}. Then it can be shown that the 3^4 scalars

$$u_{ijkl} = t_{ij}\, s_{kl} \qquad (2.5)$$

form the components of a tensor **U**, say, of order 4. We call **U** the tensor product of **T** and **S** and we write $\mathbf{U} = \mathbf{T} \otimes \mathbf{S}$.

Contraction : Given a tensor of order $r \geq 2$, we may select a pair of indices and replace them by two identical indices. This action by virtue of Einstein's convention implies summation over the possible values of the identical indices. This process is known as contraction and the quantities obtained by contraction constitute the components of a tensor of order $r - 2$.

Note : In the special case where $r = 2$, the contraction operator is synonymous with the familiar *trace* operator since, as we can see, the contraction of the two indices produces a tensor of order zero, i.e., a scalar. Note, also, that the algebraic operations of tensor product and contraction can be performed on any tensor not necessarily Cartesian.

The dot product : Let T and S be coordinate matrices, relative to the same coordinate system, of second-order tensors **T** and **S**, respectively. Then the equation

$$U_{ij} = T_{il}\, S_{lj} \quad . \qquad (2.6)$$

defines the components of the second-order tensor **U** which we call the *dot product* or *multiplication* of **T** and **S**, and we write

$$\mathbf{U} = \mathbf{T} \cdot \mathbf{S} \equiv \mathbf{T}\,\mathbf{S} \qquad (2.7)$$

The double dot or inner product : The double dot product of two second-order tensors **T** and **S** is given by

$$\mathbf{T} : \mathbf{S} = tr(\mathbf{T} \cdot \mathbf{S}) \qquad (2.8)$$

where tr denotes the trace operator and produces a scalar.

The left and right dot product : Let **T** be a second-order tensor and **v** be a vector, with coordinate matrices T and v relative to coordinate systems $\{ \mathbf{e}_i \otimes \mathbf{e}_j \}$ and $\{ \mathbf{e}_i \}$, respectively. Then the equation

$$u_i = T_{ij}\, v_j \qquad (2.9)$$

which is computed by considering first the tensor product of **T** and **v** and then contracting the second index for the components of **T** and the index for the components of **v**, defines the *right dot product* or *post-multiplication* of **T** and **v**. Similarly using the equation

$$w_i = v_j\, T_{ji} \qquad (2.10)$$

we can define the vector **w**. Equation (2.10) defines the *left dot product* or *pre-multiplication* of **v** and **T**. In tensor form, (2.9) and (2.10) are written as

$$\mathbf{u} = \mathbf{T} \cdot \mathbf{v} \equiv \mathbf{T}\,\mathbf{v} \qquad (2.11)$$

$$\mathbf{w} = \mathbf{v} \cdot \mathbf{T} \equiv \mathbf{v}\,\mathbf{T} \qquad (2.12)$$

respectively. We can use the transpose operation to reorder the factors in the dot products defined above. Thus, for example, we can write

$$\mathbf{w} = \mathbf{v} \cdot \mathbf{T} = \mathbf{T}^T \cdot \mathbf{v} \qquad (2.13)$$

Remark 2.1 : Strictly speaking some operations introduced above are defined by using coordinate matrix representations of second-order tensors and vectors. However, once these operations have been established, the actual coordinate matrices used to represent the tensors or vectors are of no consequence and we can speak of these operations as being defined on the tensors themselves without any ambiguity.

Remark 2.2 : The double dot product of two second-order Cartesian tensors is a generalization of the familiar vector dot product, and this allows us to define a norm for a tensor and the "angle" between two tensors. In particular, we define the *Frobenius norm* of a tensor **T** as followis

$$\| \mathbf{T} \|_F \triangleq \sqrt{\mathbf{T} : \mathbf{T}^T} . \qquad (2.14)$$

This is called the Frobenius norm since, when we use a coordinate matrix T of a tensor **T** to evaluate (2.14), we end up with the familiar Frobenius matrix norm [14]

$$\| T \|_F \triangleq \sqrt{tr(TT^T)}. \tag{2.15}$$

Now, using the double dot product and the Frobenius norm, we can define the cosine of the "angle" θ between two non-zero tensors, $\mathbf{T}$ and $\mathbf{S}$ as follows

$$\cos(\theta) = \frac{\mathbf{T} : \mathbf{S}^T}{\| \mathbf{T} \|_F \| \mathbf{S} \|_F}. \tag{2.16}$$

Equation (2.16) is a generalization [12] of the following familiar definition for the cosine of the angle θ between two non-zero vectors $\mathbf{t}$ and $\mathbf{s}$

$$\cos(\theta) = \frac{\mathbf{t} \cdot \mathbf{s}}{| \mathbf{t} | | \mathbf{s} |}. \tag{2.17}$$

Note also that based on this definition for the angle between two tensors, we can say [4] that two tensors $\mathbf{T}$ and $\mathbf{S}$ are *orthogonal* if and only if their double dot product is zero.

III PROPERTIES OF SECOND ORDER CARTESIAN TENSORS

In this section we review the structural symmetries of second-order Cartesian tensors by considering their *Cartesian* and *Spectral decompositions*. Moreover, for second-order *skew-symmetric* or *pseudo*-tensors, defined on a 3-D Euclidean space, very important dual correspondences between them and vectors of the same 3-D Euclidean space are defined and a geometric characterization is given.

3.1 Cartesian and Spectral Decomposition of Second-Order Cartesian Tensors.

An arbitrary Cartesian tensor $\mathbf{T}$ defined on an 3-D Euclidean space may always be decomposed into the sum of a symmetric and a skew-symmetric tensor, as follows

$$\mathbf{T} = \mathbf{T}_s + \mathbf{T}_w \tag{3.1}$$

where, $\mathbf{T}_s$ is symmetric and $\mathbf{T}_w$ is skew-symmetric. These terms are given by

$$\mathbf{T}_s = \frac{1}{2}\left(\mathbf{T} + \mathbf{T}^T\right) , \quad \mathbf{T}_w = \frac{1}{2}\left(\mathbf{T} - \mathbf{T}^T\right). \tag{3.2}$$

We usually refer to (3.1) as the *Cartesian decomposition* of a tensor. The *projection tensor* along the direction of a vector $\mathbf{e}$ is defined [6] by the equation

$$\mathbf{P}_e = \mathbf{e} \otimes \mathbf{e} \tag{3.3}$$

Now, based on projection tensors, we can define another important decomposition for symmetric tensors. As is well known [6], any symmetric tensor $\mathbf{T}$ has real eigenvalues (λ_i) with a complete set of orthogonal eigenvectors. Therefore, if $\mathbf{P}_k$ is the projection tensor along the unit direction of the k-th eigenvector, we can write [6] the following *canonical form* or *spectral decomposition* for $\mathbf{T}$.

$$\mathbf{T} = \lambda_i \mathbf{P}_i \equiv \lambda_1 \mathbf{P}_1 + \lambda_2 \mathbf{P}_2 + \lambda_3 \mathbf{P}_3 \tag{3.4}$$

3.2 Dual Vectors and Dual Tensors

As is well known [5-12], every Cartesian tensor $\mathbf{T}$, defined on a 3-D Euclidean space, has a *vector invariant* which is defined component-wise by the equation

$$t_i = \frac{1}{2} \epsilon_{ijk} t_{kj} \tag{3.5}$$

where ϵ_{ijk} and t_{kj} are the components of the *Levi-Civita* tensor ϵ and the tensor $\mathbf{T}$ respectively. We denote the vector invariant $\mathbf{t}$ of a tensor $\mathbf{T}$ by writing

$$\mathbf{t} = vect(\mathbf{T}) \tag{3.6}$$

where, $vect(\cdot)$ denotes the *tensor valued vector operator* which is defined by (3.5).

The *vect* operator, as defined above, is not a 1-1 operator. This follows from the fact that its *kernel* (or *null space*) is a subspace of the symmetric tensors which is not an empty set. Therefore, if we are seeking a 1-1 correspondence between tensors and their vector invariants we have to consider the restriction of the *vect* operator onto the subspace of the skew-symmetric tensors. As we can see from (3.6), to each skew-symmetric tensor there corresponds a vector, its vector invariant. Conversely, as we shall show, to any vector $\mathbf{t}$ in an 3-D Euclidean space there corresponds a skew-symmetric tensor, which we shall denote by $\bar{\mathbf{t}}$. Moreover, the skew-symmetric tensor $\bar{\mathbf{t}}$ has the important property that its vector invariant is the vector $\mathbf{t}$ from which the tensor $\bar{\mathbf{t}}$ has been generated. To see this, given a vector $\mathbf{t}$, we define the tensor $\bar{\mathbf{t}}$ by considering the tensor product of the Levi-Civita tensor ϵ with the vector $\mathbf{t}$ and contract the first index of ϵ with that of $\mathbf{t}$, i.e., we consider the equation

$$t_{kj} = \epsilon_{ijk} t_i . \tag{3.7}$$

The tensor $\bar{\mathbf{t}}$ is skew-symmetric, since the Levi-Civita tensor is antisymmetric with respect to the indices j and k. Moreover, if we multiply (3.7) by ϵ_{rjk} we can write

$$\epsilon_{rjk} t_{kj} = 2\delta_{ri} t_i .$$

which, by using the definition of the Kronecker tensor δ_{ri}, can also be written as

$$t_r = \frac{1}{2} \epsilon_{rjk} t_{kj} .$$

This equation is equivalent to (3.5) and therefore, $\mathbf{t}$ is indeed the vector invariant of the skew-symmetric tensor $\bar{\mathbf{t}}$.

From the foregoing, we can see that by considering the restriction of the vect operator onto the subspace of the skew-symmetric tensors, (3.5) (together with (3.7)) defines a 1-1 correspondence between skew-symmetric tensors and vectors. To express this 1-1 correspondence between skew-symmetric tensors and vectors, we introduce the following tensor-valued tensor operator.

$$dual(\cdot) \triangleq vect(\cdot)\Big|_{\left\{\text{second order skew-symmetric tensors}\right\}} \tag{3.8}$$

The dual operator can also be defined in a componentwise manner, as follows :

Definition 3.1 : The *dual operator* is a 1-1 *tensor-valued tensor operator* which has the following property : when this operator is evaluated at a tensor of order one (i.e., a vector) we get a skew-symmetric tensor of order two, and when it is evaluated at a second-order skew-symmetric tensor we get a tensor of order one. We define the action of the dual operator on a vector or a skew-symmetric tensor, component-wise, using the following 1-1 correspondence

$$\begin{bmatrix} u_1 \\ u_2 \\ u_3 \end{bmatrix} \Leftrightarrow \begin{bmatrix} 0 & -u_3 & u_2 \\ u_3 & 0 & -u_1 \\ -u_2 & u_1 & 0 \end{bmatrix}. \tag{3.9}$$

Symbolically, we denote the action of the dual operator on a vector $\mathbf{u}$ by writing

$$\hat{\mathbf{u}} \triangleq \mathit{dual}(\mathbf{u}). \qquad (3.10)$$

and, similarly

$$\mathbf{u} \triangleq \mathit{dual}(\hat{\mathbf{u}}) \qquad (3.11)$$

denotes the action of the dual operator on a skew-symmetric tensor $\hat{\mathbf{u}}$.

Here, for simplicity, we write *dual*(·) to denote both, the vector-valued and the tensor-valued dual operators. We shall rely on the argument to distinguish between the two cases (i.e., the "direct" or the "inverse" operator), and we shall referred to the tensor $\hat{\mathbf{u}}$, defined by (3.10), as the *dual tensor* of the vector $\mathbf{u}$. Similarly, we shall refer to the vector $\mathbf{u}$, defined by (3.11), as the *dual vector* of the tensor $\hat{\mathbf{u}}$.

Note : Obviously, the 1-1 correspondence, which has been established above, is not the only possible 1-1 correspondence between vectors and skew-symmetric tensors in a 3-D Euclidean space. For example, if instead of (3.9), we consider the following correspondence

$$\begin{bmatrix} u_1 \\ u_2 \\ u_3 \end{bmatrix} \Leftrightarrow \begin{bmatrix} 0 & u_3 & -u_2 \\ -u_3 & 0 & u_1 \\ u_2 & -u_1 & 0 \end{bmatrix}. \qquad (3.12)$$

we can define, as in Definition 3.1, another operator which also establishes a 1-1 correspondence between vectors and skew-symmetric tensors in the 3-D Euclidean space.

The tensor-valued tensor operator which describes, mathematically, this new 1-1 correspondence between vectors and skew-symmetric tensors will again be referred to as a dual operator. But, to express it symbolically, we shall use a different notation from that used for the dual operator given by Definition 3.1. In particular, to denote the action on a vector or a skew-symmetric tensor of the dual operator, which is introduced here by the correspondence (3.12), we shall write

$$\bar{\mathbf{u}} \triangleq (\mathbf{u})\mathit{dual}. \qquad (3.13)$$

and

$$\mathbf{u} \triangleq (\bar{\mathbf{u}})\mathit{dual}. \qquad (3.14)$$

respectively. In the following, we shall rely on the notation or the context to make clear which correspondence, i.e., (3.9) or (3.12), has to be used for the dual operator.

Now, as we can see from the correspondence (3.9), the coordinate matrix of the skew-symmetric tensor $\hat{\mathbf{u}}$ has the following structure,

$$\hat{\mathbf{u}} = \begin{bmatrix} 0 & -u_3 & u_2 \\ u_3 & 0 & -u_1 \\ -u_2 & u_1 & 0 \end{bmatrix}. \qquad (3.15)$$

i.e., the signs of its components follow a special pattern. Similarly, from the correspondence (3.12), we have that the coordinate matrix of the dual tensor $\bar{\mathbf{u}}$ is given by the following equation

$$\bar{\mathbf{u}} = \begin{bmatrix} 0 & u_3 & -u_2 \\ -u_3 & 0 & u_1 \\ u_2 & -u_1 & 0 \end{bmatrix}. \qquad (3.16)$$

To emphasize the fact that the coordinate matrices of the tensors $\hat{\mathbf{u}}$ and $\bar{\mathbf{u}}$ have special sign patterns, we shall say that the tensors $\hat{\mathbf{u}}$ and $\bar{\mathbf{u}}$ are *oriented* relative to their dual vector $\mathbf{u}$, or simply, that they are *relatively oriented*. In particular, we shall say that the dual tensor $\hat{\mathbf{u}}$ has a *positive* or a *right-handed* orientation relative to $\mathbf{u}$. Similarly, we shall say that the tensor $\bar{\mathbf{u}}$ has a *negative* or *left-handed* orientation relative to the vector $\mathbf{u}$. This terminology and characterization for the relative orientation will become clear shortly when we assign a geometric meaning to the skew-symmetric tensors $\hat{\mathbf{u}}$ and $\bar{\mathbf{u}}$.

Based on the relative orientation of the two tensors $\hat{\mathbf{u}}$ and $\bar{\mathbf{u}}$, it would be more informative if we call *right dual* and *left dual* the two dual operators which are defined by the correspondences (3.9), and (3.12) respectively. We shall do this if we need to emphasize which of the two dual operators is involved in the correspondence between vectors and skew-symmetric tensors.

3.3 A Geometric Characterization for Second Order Skew-symmetric Cartesian Tensors

It is well known, from spatial intuition, that in three dimensional space an unambiguous distinction can be made between two *orientations* of a plane relative to a normal vector. These are the *positive* or *right-handed* (or *counter-clockwise*) orientation and the *negative* or *left-handed* (or *clockwise*) orientation. Geometrically, we can describe these two oriented planes, relative to a normal vector, as follows,

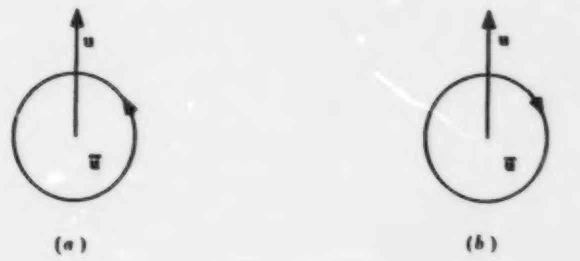

Figure 1 : Relatively oriented planes and skew-symmetric tensors.

and we shall refer to them as *relatively oriented planes*.

Now, as is often the case most, geometric ideas are more useful in applications if we describe them algebraically. Therefore, to describe algebraically what Figure 3.1 shows geometrically, or to express in mathematical symbols the words "relatively oriented plane", we first note the following important points.

- *a*) Any non-zero second-order skew-symmetric tensor, defined in 3-D Euclidean space, has rank 2 [6,11,12]. This implies that to any non-zero skew-symmetric tensor we can associate two linearly independent directions, or equivalently, a plane in the 3-D physical space.
- *b*) As we saw before, given a vector $\mathbf{u}$, there correspond to it two relatively oriented skew-symmetric tensors, namely, the tensors $\hat{\mathbf{u}}$ and $\bar{\mathbf{u}}$.

Therefore, just as we consider vectors to represent the geometric notion of directed line segments in vector analysis, we can consider in 3-D Cartesian tensor analysis, skew-symmetric tensors to represent the geometric notion of *directed plane segments* (i.e., *directed plane areas*) or more precisely, we can use skew-symmetric dual tensors to represent *relatively* *oriented planes.* In particular, given a vector $\mathbf{u}$, we can use its right-handed dual tensor $\hat{\mathbf{u}}$ to represent the positively oriented (relative to $\mathbf{u}$) plane area which is normal to $\mathbf{u}$ and is shown in Figure 1(a). Similarly we can use its left-handed dual tensor $\bar{\mathbf{u}}$ to represent the negatively oriented (relative to $\mathbf{u}$) plane area which is shown in Figure 1(b). Thus, according this convention the spatial intuition of relative orientation is expressed mathematically with the correspondence (3.9) or (3.12). However, the correspondences (3.9) and (3.12) alone do not describe completely the geometry shown in Figure 1 because they fail to express clearly the orthogonal relationship between the vector $\mathbf{u}$ and the dual skew-symmetric tensors $\hat{\mathbf{u}}$ and $\bar{\mathbf{u}}$.

To express algebraically this orthogonal relationship, we can use either of the following well known [1-12] equations

$$\hat{\mathbf{u}} \cdot \mathbf{u} \triangleq \hat{\mathbf{u}}\,\mathbf{u}\ (\equiv \mathbf{u} \times \mathbf{u}) = 0 \tag{3.17}$$

and

$$\mathbf{u} \cdot \hat{\mathbf{u}} = \hat{\mathbf{u}}^{T} \cdot \mathbf{u} = \bar{\mathbf{u}} \cdot \mathbf{u}\ (\equiv -\,\mathbf{u} \times \mathbf{u}) = 0, \tag{3.18}$$

since an orthogonal relation is independent of the relative orientation. The fact that both equations (3.17) and (3.18) define an orthogonal relationship is supported from the following arguments

As is well known [8,12], second-order Cartesian tensors can be viewed as linear operators. Then, based on (3.17) (or (3.18)) and using relevant terminology from the theory of linear operators, we can say that the vector $\mathbf{u}$ spans the *null* space of the linear operator $\hat{\mathbf{u}}$ (or $\hat{\mathbf{u}}^{T} = \bar{\mathbf{u}}$). Furthermore, since the rank of a skew-symmetric tensor is 2, we can identify the *range* space of the linear operator $\hat{\mathbf{u}}$ (which has dimension 2) with the plane $\hat{\mathbf{u}}$ or the plane $-\hat{\mathbf{u}}$, since both planes define the same vector space. Now, based on this identification and the well known fact that the null space of a linear operator is an orthogonal complement to its transpose operator, we can say that (3.17) (or (3.18)) indeed express the fact that the vector $\mathbf{u}$ is orthogonal to the plane $\hat{\mathbf{u}}$ (or the plane $\bar{\mathbf{u}}$).

From the foregoing discussion, the dual vector $\mathbf{u}$ is normal to both tensors $\hat{\mathbf{u}}$ and $\bar{\mathbf{u}}$. Obviously then, the vector $\mathbf{u}$ remains normal, and thus invariant, when the plane $\hat{\mathbf{u}}$ (or $\bar{\mathbf{u}}$) rotates in space. Thus, the terminology "vector invariant" which has also been assigned to the dual vector $\mathbf{u}$ becomes clear.

IV CARTESIAN TENSOR ALGEBRAIC IDENTITIES

In the following, by exploring the relationships between second-order Cartesian tensors and their vector invariants, we shall prove three propositions which define important tensor equations. These equations will allow us to manipulate second-order tensors very efficiently as abstract objects, without the need to resort to coordinate bases [12,13]. Moreover, the transition, when needed, from these tensor equations to the corresponding coordinate matrix equations is effortless. This is because the basic Cartesian tensor algebraic operations are formally the same as the basic algebraic operations in matrix theory [7,12].

To prove these propositions we need the following equations which are derived in [12].

$$\mathit{dual}(k\,\mathbf{u}) = k\,\hat{\mathbf{u}} \tag{4.1}$$

$$\mathit{dual}(\mathbf{u} + \mathbf{v}) = \hat{\mathbf{u}} + \hat{\mathbf{v}} \tag{4.2}$$

$$\hat{\mathbf{u}}\,\mathbf{v} = -\,\hat{\mathbf{v}}\,\mathbf{u} \tag{4.3}$$

$$\hat{\mathbf{u}}\,\mathbf{u} = \mathbf{u}\,\hat{\mathbf{u}} = 0 \tag{4.4}$$

$$\hat{\mathbf{u}}\,\hat{\mathbf{v}} = \mathbf{v} \otimes \mathbf{u} - \mathbf{u} \cdot \mathbf{v}\,\mathbf{1} \tag{4.5}$$

$$\mathbf{v} \otimes \mathbf{u} = \hat{\mathbf{u}}\,\hat{\mathbf{v}} + (\mathbf{v} \cdot \mathbf{u})\mathbf{1} \tag{4.6}$$

$$\mathit{dual}(\hat{\mathbf{u}}\,\mathbf{v}) = \hat{\mathbf{u}}\,\hat{\mathbf{v}} - \hat{\mathbf{v}}\,\hat{\mathbf{u}} \tag{4.7}$$

$$\mathit{tr}\,[\hat{\mathbf{u}}\,\hat{\mathbf{v}}] = -\,2\mathbf{u} \cdot \mathbf{v}\,. \tag{4.8}$$

where, k is a scalar and $\mathbf{u}$, $\mathbf{v}$ are vectors.

The first proposition enables us to reorder the terms in dot products between dual tensors.

Proposition 4.1 :

$$\hat{\mathbf{u}}\,\hat{\mathbf{v}}\,\hat{\mathbf{u}} = \hat{\mathbf{v}}\,\hat{\mathbf{u}}\,\hat{\mathbf{u}} + \hat{\mathbf{u}}\,\hat{\mathbf{u}}\,\hat{\mathbf{v}} - \frac{1}{2}\mathit{tr}\,[\hat{\mathbf{u}}\,\hat{\mathbf{u}}]\hat{\mathbf{v}} \tag{4.9}$$

Proof : By using (4.3), (4.5) and (4.8), the first two terms on the right-hand side of (4.9) can be written as

$$\begin{aligned}
\hat{\mathbf{v}}\,\hat{\mathbf{u}}\,\hat{\mathbf{u}} + \hat{\mathbf{u}}\,\hat{\mathbf{u}}\,\hat{\mathbf{v}} &= \hat{\mathbf{v}}\,(\mathbf{u} \otimes \mathbf{u} - \mathbf{u} \cdot \mathbf{u}\,\mathbf{1}) + \hat{\mathbf{u}}\,(\mathbf{v} \otimes \mathbf{u} - \mathbf{v} \cdot \mathbf{u}\,\mathbf{1}) \\
&= (\hat{\mathbf{v}}\,\mathbf{u}) \otimes \mathbf{u} - (\mathbf{u} \cdot \mathbf{u})\hat{\mathbf{v}} + (\hat{\mathbf{u}}\,\mathbf{v}) \otimes \mathbf{u} - (\mathbf{v} \cdot \mathbf{u})\hat{\mathbf{u}} \\
&= -(\hat{\mathbf{u}}\,\mathbf{v}) \otimes \mathbf{u} - (\mathbf{u} \cdot \mathbf{u})\hat{\mathbf{v}} + (\hat{\mathbf{u}}\,\mathbf{v}) \otimes \mathbf{u} - (\mathbf{v} \cdot \mathbf{u})\hat{\mathbf{u}} \\
&= -\,(\mathbf{u} \cdot \mathbf{u})\hat{\mathbf{v}} - (\mathbf{v} \cdot \mathbf{u})\hat{\mathbf{u}} \\
&= \frac{1}{2}\mathit{tr}\,[\hat{\mathbf{u}}\,\hat{\mathbf{u}}]\hat{\mathbf{v}} - (\mathbf{v} \cdot \mathbf{u})\hat{\mathbf{u}}
\end{aligned}$$

Therefore, the right-hand side of (4.9) becomes

$$\hat{\mathbf{v}}\,\hat{\mathbf{u}}\,\hat{\mathbf{u}} + \hat{\mathbf{u}}\,\hat{\mathbf{u}}\,\hat{\mathbf{v}} - \frac{1}{2}\mathit{tr}\,[\hat{\mathbf{u}}\,\hat{\mathbf{u}}]\hat{\mathbf{v}} = -\,(\mathbf{v} \cdot \mathbf{u})\hat{\mathbf{u}}$$

The left-hand side of (4.9) can be written as

$$\begin{aligned}
\hat{\mathbf{u}}\,\hat{\mathbf{v}}\,\hat{\mathbf{u}} &= \hat{\mathbf{u}}\,(\mathbf{u} \otimes \mathbf{v} - \mathbf{v} \cdot \mathbf{u}\,\mathbf{1}) \\
&= (\hat{\mathbf{u}}\,\mathbf{u}) \otimes \mathbf{v} - (\mathbf{v} \cdot \mathbf{u})\hat{\mathbf{u}} \\
&= -\,(\mathbf{v} \cdot \mathbf{u})\hat{\mathbf{u}}\ . \quad [\text{since}\ \ \hat{\mathbf{u}}\,\mathbf{u} = 0]
\end{aligned}$$

completing the proof. ▯

Proposition 4.2 : The dual tensor $\mathit{dual}(\hat{\mathbf{u}}\,\hat{\mathbf{u}}\,\mathbf{v})$ can be written in terms of the dual tensors $\hat{\mathbf{u}}$ and $\hat{\mathbf{v}}$ as

$$\mathit{dual}(\hat{\mathbf{u}}\,\hat{\mathbf{u}}\,\mathbf{v}) = -\,[\hat{\mathbf{v}}\,\hat{\mathbf{u}}\,\hat{\mathbf{u}} + \hat{\mathbf{u}}\,\hat{\mathbf{u}}\,\hat{\mathbf{v}}] + \mathit{tr}\,[\hat{\mathbf{u}}\,\hat{\mathbf{u}}]\hat{\mathbf{v}} \tag{4.10}$$

Proof : The left-hand side of (4.10) can be expressed as

$$\mathit{dual}(\hat{\mathbf{u}}\,\hat{\mathbf{u}}\,\mathbf{v}) = \mathit{dual}(\hat{\mathbf{u}}\,(\hat{\mathbf{u}}\,\mathbf{v}))$$

Using (4.7), the above equation becomes

$$\begin{aligned}
\mathit{dual}(\hat{\mathbf{u}}\,(\hat{\mathbf{u}}\,\mathbf{v})) &= \hat{\mathbf{u}}\,\mathit{dual}(\hat{\mathbf{u}}\,\mathbf{v}) - \mathit{dual}(\hat{\mathbf{u}}\,\mathbf{v})\hat{\mathbf{u}} \\
&= \hat{\mathbf{u}}\,(\hat{\mathbf{u}}\,\hat{\mathbf{v}} - \hat{\mathbf{v}}\,\hat{\mathbf{u}}) - (\hat{\mathbf{u}}\,\hat{\mathbf{v}} - \hat{\mathbf{v}}\,\hat{\mathbf{u}})\hat{\mathbf{u}} \\
&= -\,2\hat{\mathbf{u}}\,\hat{\mathbf{v}}\,\hat{\mathbf{u}} + \hat{\mathbf{u}}\,\hat{\mathbf{u}}\,\hat{\mathbf{v}} + \hat{\mathbf{v}}\,\hat{\mathbf{u}}\,\hat{\mathbf{u}}\,.
\end{aligned}$$

Finally, using (4.9), we can simplify the above equation to get (4.10). ▯

Proposition 4.3 : Let $\mathbf{I}$ be a symmetric tensor. Then the dual tensor $\mathit{dual}(\mathbf{I}\,\mathbf{v})$, where $\mathbf{v}$ is any vector, satisfies the following equation

$$\mathit{dual}(\mathbf{I}\,\mathbf{v}) = -\,[\mathbf{I}\,\hat{\mathbf{v}} + \hat{\mathbf{v}}\,\mathbf{I}] + \mathit{tr}\,[\mathbf{I}]\hat{\mathbf{v}} \tag{4.11}$$

Proof : Since $\mathbf{I}$ is a symmetric tensor, it has a complete set of eigenvectors [1,6]. Let us denote the unit directions of these eigenvectors by $\mathbf{x}$, $\mathbf{y}$ and $\mathbf{z}$. Then, using (3.3) and (3.4), we can write $\mathbf{I}$ in its spectral decomposition form as

$$\mathbf{I} = \lambda_1 \mathbf{x} \otimes \mathbf{x} + \lambda_2 \mathbf{y} \otimes \mathbf{y} + \lambda_3 \mathbf{z} \otimes \mathbf{z}$$

where, λ_i, $i = 1, 2, 3$ are the eigenvalues of $\mathbf{I}$. Moreover, using (4.6) and the equation

$$\mathit{tr}\,[\mathbf{I}] = \lambda_1 + \lambda_2 + \lambda_3.$$

we can write the spectral decomposition of $\mathbf{I}$ in terms of the dual tensor of its eigenvectors, i.e., we can write

$$\mathbf{I} = \lambda_1\tilde{\mathbf{x}}\,\tilde{\mathbf{x}} + \lambda_2\tilde{\mathbf{y}}\,\tilde{\mathbf{y}} + \lambda_3\tilde{\mathbf{z}}\,\tilde{\mathbf{z}} + tr\,[\mathbf{I}]\,\mathbf{1} \tag{1.12}$$

Then, the right dot product $\mathbf{I}\,\mathbf{v}$ becomes

$$\mathbf{I}\,\mathbf{v} = \lambda_1\tilde{\mathbf{x}}\,\tilde{\mathbf{x}}\,\mathbf{v} + \lambda_2\tilde{\mathbf{y}}\,\tilde{\mathbf{y}}\,\mathbf{v} + \lambda_3\tilde{\mathbf{z}}\,\tilde{\mathbf{z}}\,\mathbf{v} + tr\,[\mathbf{I}]\,\mathbf{v}$$

Now, using (1.2) and (1.10), we can write

$$\begin{aligned} dual\,(\mathbf{I}\,\mathbf{v}) = -\Big\{ &\tilde{\mathbf{v}}\,[\lambda_1\tilde{\mathbf{x}}\,\tilde{\mathbf{x}} + \lambda_2\tilde{\mathbf{y}}\,\tilde{\mathbf{y}} + \lambda_3\tilde{\mathbf{z}}\,\tilde{\mathbf{z}}] \\ &+ [\lambda_1\tilde{\mathbf{x}}\,\tilde{\mathbf{x}} + \lambda_2\tilde{\mathbf{y}}\,\tilde{\mathbf{y}} + \lambda_3\tilde{\mathbf{z}}\,\tilde{\mathbf{z}}]\,\tilde{\mathbf{v}} \Big\} \\ &+ \big(\lambda_1 tr\,[\tilde{\mathbf{x}}\,\tilde{\mathbf{x}}] + \lambda_2 tr\,[\tilde{\mathbf{y}}\,\tilde{\mathbf{y}}] + \lambda_3 tr\,[\tilde{\mathbf{z}}\,\tilde{\mathbf{z}}]\big)\,\tilde{\mathbf{v}} + tr\,[\mathbf{I}]\,\tilde{\mathbf{v}} \end{aligned}$$

Then, from (1.8), for unit vectors, we get

$$tr\,[\tilde{\mathbf{x}}\,\tilde{\mathbf{x}}] = tr\,[\tilde{\mathbf{y}}\,\tilde{\mathbf{y}}] = tr\,[\tilde{\mathbf{z}}\,\tilde{\mathbf{z}}] = -2$$

Therefore, we can write

$$\begin{aligned} dual\,(\mathbf{I}\,\mathbf{v}) = -\Big\{ &\tilde{\mathbf{v}}\left[\lambda_1\tilde{\mathbf{x}}\,\tilde{\mathbf{x}} + \lambda_2\tilde{\mathbf{y}}\,\tilde{\mathbf{y}} + \lambda_3\tilde{\mathbf{z}}\,\tilde{\mathbf{z}} + tr\,[\mathbf{I}]\,\mathbf{1}\right] \\ &+ \left[\lambda_1\tilde{\mathbf{x}}\,\tilde{\mathbf{x}} + \lambda_2\tilde{\mathbf{y}}\,\tilde{\mathbf{y}} + \lambda_3\tilde{\mathbf{z}}\,\tilde{\mathbf{z}} + tr\,[\mathbf{I}]\,\mathbf{1}\right]\tilde{\mathbf{v}} \Big\} + tr\,[\mathbf{I}]\,\tilde{\mathbf{v}} \end{aligned}$$

from where, using (1.12), we get (1.11). ||

With this analysis for Cartesian tensors at our disposal, in an accompanying paper, we provide a Cartesian tensor formulation for the kinematic and dynamic equations of rigid body motion. This tensor formulation is computationally far more efficient than the equivalent vector formulation.

V CONCLUSIONS

In this paper, by exploring relationships between second-order Cartesian tensors and their vector invariants, we stated and proved a number of propositions which define important tensor identities. These identities enable one to manipulate effectively (and thus simplify) complex tensor equations. Moreover, in this paper, by using the *dual* operators we proposed a geometric characterization for second-order skew-symmetric Cartesian tensors and their vector invariants which are defined in a 3-D Euclidean space. The geometric characterization of second-order skew-symmetric Cartesian tensors which is proposed here is currently under investigation for providing an efficient mathematical representation for the orientation of a rotation tensor.

VI REFERENCES

[1] Wittenburg, I. J., Dynamics of Systems of Rigid Bodies. B. G. Teubner, Stuttgart, 1977.

[2] Goldstein, H., Classical Mechanics, 2nd Ed., Addison-Wesley, Reading, MA : 1980.

[3] Konopinski, E. J., Classical Descriptions of Motion. W. H. Freeman and Company, San Francisco, 1969.

[4] Angeles, J., Rational Kinematics. Springer-Verlag, New York, 1988.

[5] Jeffreys, H., Cartesian Tensors. Cambridge University Press, Cambridge, 1961.

[6] Temple, G., Cartesian Tensors : An Introduction . John Wiley & Sons, New York, 1960.

[7] Goodbody, A. M., Cartesian Tensors: With Applications to Mechanics, Fluid Mechanics and Elasticity . Ellis Horwood, England, 1982.

[8] Simmonds, J. G., A Brief on Tensor Analysis. Springer-Verlag, New York, 1982.

[9] Synge, J. L. and Schild, A., Tensor Calculus . University of Toronto Press, Toronto, 1949.

[10] Brand, L., Vector and Tensor Analysis . John Wiley & Sons, New York, 1947.

[11] Heading, J., Matrix Theory for Physicists . Longmans, London, 1958.

[12] Balafoutis, C. A., Dynamic Analysis of Rigid-Link Open-Chain Robot Manipulators Using Cartesian Tensor Methods, Ph. D. thesis, Dept. of Elec. & Comp. Engineering, Concordia University, Montreal, Quebec, Canada, 1989.

[13] Balafoutis, C. A., Patel, R. V. and Misra, P., Efficient Modeling and Computation of Manipulator Dynamics Using Orthogonal Cartesian Tensors in IEEE J. Robotics and Automation. Vol. 4, No. 6, pp 665-676, 1988.

[14] Stewart, G. W., Introduction to Matrix Computations . Academic Press, New York, 1973.

SIMULATION DYNAMIQUE DES SOLIDES PAR LA METHODE DES RESEAUX VECTORIELS

Marc J. Richard et Isaac Bindzi

Dép. de génie mécanique, Université Laval, Ste-Foy, Québec, G1K 7P4

RESUME

Cet article présente une méthode de dérivation des équations du mouvement de systèmes mécaniques de n corps rigides reliés entre eux par des joints sphériques, universels et/ou rotoïdes, l'ensemble ayant une structure d'arbre. Les équations dynamiques et cinématiques sont construites à partir du modèle du réseau vectoriel. L'approche par le réseau vectoriel est un modèle mathématique pour la formulation systématique des équations non-linéaires de mouvement d'un système de corps rigides interconnectés par des joints cinématiques. La procédure entière du réseau vectoriel est une application des concepts de base de la théorie des graphes dans laquelle les lois vectorielles de la dynamique ont été intégrées. En partant des lois de Newton et d'Euler, des équations différentielles non-linéaires sont dérivées pour décrire les mouvements des n corps rigides du système mécanique. Dans cet article, nous ne considérons que le cas où le système mécanique a une structure d'arbre et où ce système contient un corps dont le mouvement est spécifié (corps appelé "corps meneur"), relié à un unique corps du système mécanique.

INTRODUCTION

La plupart des systèmes mécaniques peuvent effectivement être modelisés par des systèmes de corps rigides reliés entre eux par des joints (cinématiques ou non). L'analyse dynamique de tels systèmes peut être faite par des méthodes analytiques ou numériques. Les méthodes analytiques ont considérablement élargi leur champ d'application pendant les dernières années mais les difficultés théoriques et analytiques sont telles que la seule alternative réside dans les méthodes numériques. Le raffinement des techniques de formulation, comparable à celle présentée dans cet article pour l'analyse dynamique des systèmes mécaniques a conduit au développement de programmes d'ordinateur à usage général [1]. Nous citerons en exemples les programmes IMP de Sheth et al [2], DRAM et ADAMS de Chace et Orlandea [3,4], DYMAC de Paul [5], DADS de Haugh et Nikravesh [6], NEWELL de Schiehlen et Kreuser [7] et naturellement, des programmes basés sur la méthode du réseau vectoriel, tel RESTRI de Richard [1]. Il en existe sûrement beaucoup d'autres et leur nombre va en croissant.

Le présent travail se révèle ainsi une amélioration des précédents travaux basés sur la méthode des réseaux vectoriels [1,8] car il fournit une formulation générale et systématique des équations de mouvement des systèmes mécaniques.

LA METHODE DU RESEAU VECTORIEL

Pour extraire les propriétés cinétiques d'un système mécanique donné, le modèle du réseau vectoriel propose de discrétiser le système en un diagramme schématique composé de noeuds (ou sommets) représentant des points particuliers du système mécanique et d'arcs orientés (ou vecteurs) identifiant les éléments du système. La combinaison des arcs orientés et des noeuds constitue le "diagramme du réseau vectoriel" du système mécanique. Dans le cas le plus général, un système mécanique peut contenir les huit groupes d'éléments suivants :

N_1: Elément représentant un corps rigide (masse ayant une inertie en rotation et/ou en translation.

N_2: Elément représentant un "bras-de-levier". Cet élément permet de localiser le point de connexion d'un corps rigide au reste du système, par rapport au centre de masse de ce corps rigide.

N_3: Elément représentant un point dans le système dont les positions et vitesses (linéaires et/ou de rotation) sont spécifiées. Le point considéré appartient donc au corps meneur.

N_4: Elément représentant le couple dû aux forces internes s'exerçant à un joint donné. Cet élément enregistre donc le moment, par rapport au centre de masse du corps rigide considéré de la force interne au joint considéré.

N_5: Elément représentant les forces et/ou moments externes s'exerçant sur un corps rigide donné. (La force externe aura toujours sa droite d'action passant par le centre de masse du corps rigide.)

N_6: Elément représentant un ressort (en tension, compression ou torsion) et/ou un amortisseur.

N_7: Elément représentant un joint cinématique.

N_8: Elément représentant un actuateur à un joint cinématique.

Dans le modèle du réseau vectoriel, deux concepts importants sont ceux d'"arbre" et de "co-arbre" (complémentaire de l'arbre) [8] et il est crucial de bien choisir, pour un système mécanique donné, les éléments qui appartiennent à chacun des deux sous-ensembles. Il a été montré [1] que les éléments N_1, N_2, N_3 forment toujours l'arbre du système mécanique et donc que les éléments N_4, N_5, N_6, N_7, N_8 forment le co-arbre. Pour un système mécanique donné, la sélection ci-dessus fournit une procédure systématique de dérivation des équations de mouvement et assure par conséquent une modélisation réussie du problème dynamique.

DIAGRAMME SCHEMATIQUE DU RESEAU VECTORIEL

Considérons le système mécanique représenté par la figure 1. En appliquant la procédure ci-dessus, nous obtenons le diagramme schématique représenté sur la figure 2.

Il est évident que, plus le nombre de corps dans le système mécanique devient important, plus le diagramme schématique devient complexe et donc peu utile pour les renseignements qu'il devrait fournir. Cette difficulté est contournée en construisant plutôt des diagrammes schématiques élémentaires pour chaque corps rigide, diagrammes qui représentent une sorte de "Diagramme du corps libre" des solides considérés. Ces diagrammes élémentaires permettent tout aussi bien d'obtenir les informations nécessaires pour installer le modèle du réseau vectoriel du système mécanique.

MATRICES DU RESEAU VECTORIEL

Le diagramme du réseau vectoriel peut être représenté par une matrice incidente qui spécifie l'ordre d'interconnection des éléments du système. Une ligne de cette matrice représente un noeud du diagramme et une colonne représente un vecteur du même diagramme. A l'intersection d'une ligne et d'une colonne on a un "1" ou un "-1" ou un "0" suivant que le vecteur considéré admet le noeud pour extrémité, pour origine, on ne passe pas par le noeud, respectivement.

La matrice dynamique [A] est construite à partir de la matrice incidente, ses lignes sont toutes les branches du diagramme schématique (respecter l'ordre des arcs imposé dans la construction de la matrice incidente) et ses colonnes, tous les arcs. Les éléments d'une ligne de cette matrice sont obtenus, à partir du diagramme schématique, en supprimant (effaçant) la branche considérée et en faisant, à partir de la matrice incidente, la somme des lignes correspondant aux noeuds qui restent reliés au reste du système mécanique par des cordes du co-arbre. La matrice dynamique est mieux représentée sous la forme :

$$[A] = \begin{bmatrix} U_1 & & & \lambda_{14} & \cdots & \lambda_{18} \\ & U_2 & & \lambda_{24} & \cdots & \lambda_{28} \\ & & U_3 & \lambda_{34} & \cdots & \lambda_{38} \end{bmatrix} \qquad (1)$$

dans la notation λ_{ij} : i indique l'élément de l'arbre (i = 1,2,3) et j indique l'élément du co-arbre (j = 4,...,8). Les matrices U_i désignent des matrices vectorielles unitaires d'ordre n_i (avec n_i nombre d'éléments de type N_i dans le système, i = 1,2,3) ou des matrices scalaires unitaires d'ordre $3n_i$. Les matrices λ_{ij} sont des matrices vectorielles de dimension $n_i \times n_j$ et représentent la relation directe entre les éléments des types N_i et N_j (en supprimant la branche N_i, la corde N_j permet de relier le sous-système correspondant au reste du système).

En appliquant le principe d'orthogonalité [1], on obtient directement la matrice de boucle, qui est mieux représentée sous la forme :

$$[B] = \begin{bmatrix} B_{41} & B_{42} & B_{43} & U_4 & & \\ B_{51} & \cdot & \cdot & & & 0 \\ B_{61} & \cdot & \cdot & & & \\ B_{71} & \cdot & \cdot & & 0 & \\ B_{81} & B_{82} & B_{83} & & & U_8 \end{bmatrix} \qquad (2)$$

$$\text{avec } B_{ji} = -\lambda_{ij}^{T} \ (i = 1,2,3 \ ; \ j = 4,5,\ldots,8) \qquad (3)$$

ENSEMBLE D'EQUATIONS DU MODELE DU RESEAU VECTORIEL

La stratégie dynamique consiste ainsi à supprimer toutes les branches reliées à un élément inertiel et qui exercent des forces et/ou moments et à les remplacer par les cordes adjacentes exerçant leurs forces ou moments sur le système réduit. On peut ainsi subdiviser l'équation dynamique en deux équations : une équation dynamique en translation et une en rotation, en considérant les propriétés physiques liées aux différents types d'éléments et en posant à zéro les variables directes n'ayant pas de justification physique. Ainsi, nous aurons:

. Equation dynamique en translation :

$$\begin{bmatrix} U_1 & 0 & & \lambda_{15} & \cdots & \lambda_{18} \\ & U_2 & & \lambda_{25} & \cdots & \lambda_{28} \\ 0 & & U_3 & \lambda_{35} & \cdots & \lambda_{38} \end{bmatrix} \begin{matrix} \{F_1\} \\ \{F_2\} \\ \{F_3\} \\ \{F_5\} \\ \vdots \\ \{F_8\} \end{matrix} = \{0\} \qquad (4)$$

(Dans cette équation, on a supprimé λ_{14} et $\{F_4\}$, car $\{F_4\} = \{0\}$.)

. Equation dynamique en rotation :

$$\begin{bmatrix} U_1 & 0 & \lambda_{14} & \lambda_{15} & \lambda_{16} & \lambda_{17} & \lambda_{18} \\ 0 & U_3 & \lambda_{34} & \cdot & \cdot & \cdot & \lambda_{38} \end{bmatrix} \begin{matrix} \{T_1\} \\ \{T_3\} \\ \vdots \\ \{T_8\} \end{matrix} = \{0\} \qquad (5)$$

Pour une écriture correcte des équations (4) et (5), les matrices $\{F_i\}$, $\{T_i\}$ devraient être ordonnées de la même manière que les arcs du diagramme schématique l'ont été pour la construction des différentes matrices.

Un postulat directeur du réseau vectoriel est le "postulat de boucle" qui établit que la somme algébrique des variables cinématiques (longueur, vitesses, accélérations) correspondant à tous les éléments compris dans une boucle fermée est identiquement nulle.

De même que pour l'équation dynamique, l'équation cinématique peut être subdivisée en une équation cinématique en translation et une équation cinématique en rotation. Ainsi donc, nous aurons :

- Equation cinématique en translation :

$$\begin{bmatrix} B_{61} & B_{62} & B_{63} & U_6 & & 0 \\ B_{71} & B_{72} & B_{73} & & U_7 & \\ B_{81} & B_{82} & B_{83} & & & U_8 \end{bmatrix} \begin{array}{lcc} \{\dot{r}_1\} & \text{ou } \{\ddot{r}_1\} & \text{ou } \{r_1\} \\ \{r_2\} & - & - \\ \{r_3\} & - & - \\ \{r_6\} & - & - \\ \{r_7\} & - & - \\ \{r_8\} & - & - \end{array} = \{0\} \tag{6}$$

- Equation cinématique en rotation :

$$\begin{bmatrix} B_{61} & B_{63} & U_6 & & 0 \\ B_{71} & B_{73} & & U_7 & \\ B_{81} & B_{83} & 0 & & U_8 \end{bmatrix} \begin{array}{lc} \{\gamma_1\} & \text{ou } \{\dot{\gamma}_1\} \\ \{\gamma_3\} & - \\ \{\gamma_6\} & - \\ \{\gamma_7\} & - \\ \{\gamma_8\} & - \end{array} = \{0\} \tag{7}$$

Pour une écriture correcte des équations (6) et (7), les matrices-colonnes $\{r_i\}$ et $\{\gamma_i\}$ doivent être ordonnées de la même manière que les arcs du diagramme schématique l'ont été pour la construction des différentes matrices.

En dynamique, les équations terminales expriment les caractéristiques empiriques des éléments du réseau vectoriel et sont basées sur différentes lois. Nous présentons ici les équations terminales des éléments les plus rencontrés en dynamique:

Eléments de type N_1 :

$$\{F_1\} = -[m]\{\ddot{r}_1\} \tag{8}$$

De même, nous avons

$$(T_1)_i = -\dot{I}_i(\omega_1)_i + [(\underline{\omega}_1)_i]\, I_i\, (\omega_1)_i \tag{8a}$$

avec $(T_1)_i$: dérivée absolue par rapport au temps du moment angulaire absolu, dans le référentiel lié à i.

I_i : tenseur principal d'inertie du corps rigide i par rapport à son centre de masse, dans le référentiel qui lui est lié.

et sous forme matricielle, nous avons l'expression :

$$\{T_1\} = -([I]\{\dot{\omega}_1\} + [\{\underline{\omega}_1\}]\,[I]\{\omega_1\}) \tag{8b}$$

Eléments de type N_2 :

$$(\ddot{r}_2)_{ia} = (\dot{\gamma}_1)_i \times (r_2)_{ia} + (\gamma_1)_i \times (\gamma_1)_i \times (r_2)_{ia} \tag{9}$$

Eléments de type N_3 :

$$(r_3) = f(t)_i,\ (\dot{r}_3) = \dot{f}(t)_i,\ (\ddot{r}_3) = \ddot{f}(t)_i \tag{10}$$

$$(\gamma_3)_i = g(t)\ ,\ (\dot{\gamma}_3)_i = \dot{g}(t) \tag{10a}$$

Eléments de type N_4 : compte tenu de la topologie du diagramme schématique, sachant qu'un moment est positif s'il impose une rotation dans le sens anti-horaire au solide, et en adoptant la convention que les forces aux joints sont dans le même sens que les arcs symbolisant les joints, on peut écrire (pour des joints cinématiques n'autorisant aucun déplacement relatif) :

$$(T_4)_{ia} = -(r_2)_{ia} \times (F_2)_{ia} \tag{11}$$

Eléments de type N_6 :

$$(F_6)_{ij} = -\xi_6\,(\|(r_6)_{ij}\| - \|(r_6)^{\circ}_{ij}\|)\,(\hat{r}_6)_{ij} - \eta_6\,[(\dot{r}_6)_{ij}\cdot(\hat{r}_6)_{ij}]\,(\hat{r}_6)_{ij} \tag{12}$$

avec :
- $\|(r_6)^{\circ}_{ij}\|$: longueur du ressort à l'instant initial.
- ξ_6 : constante de raideur en tension /compression du ressort
- η_6 : constante d'amortissement

$$(T_6)_{ij} = -k_6\,(\gamma_6)_{ij} \tag{12a}$$

avec : k_6 : constante de raideur en torsion du ressort.

MODELE DYNAMIQUE D'UN SYSTEME MECANIQUE AVEC JOINTS SPHERIQUES

Nous considérons dans ce modèle des joints idéaux : pas de frottements au joint et aucun déplacement relatif du centre de rotation au joint. De même, dans un premier temps, nous considérons que le système mécanique ne contient pas d'éléments de type N_8 (pas d'actionneurs aux joints). Le système mécanique est formé de n corps rigides reliés entre eux par des joints sphériques, et un seul de ces corps relié au corps meneur, l'ensemble ainsi formé ayant une structure d'arbre (pas de chaine cinématique fermée de corps rigides). Si plusieurs corps du système mécanique sont reliés au corps meneur, on peut se ramener au cas étudié dans ce modèle en considérant autant de sous-systèmes qu'il y a de corps reliés au corps meneur.

Pour le cas d'un système mécanique composé essentiellement de joints sphériques, les trois ensembles d'équations suivantes, combinées avec les équations terminales des différents éléments, sont nécessaires et suffisantes.

A partir de l'équation (4), nous tirons l'équation :

$$U_1\{F_1\} + A_{15}\{F_5\} + A_{17}\{F_7\} = \{0\} \tag{13}$$

Cette équation est l'écriture de la 2^e loi de Newton pour chacun des corps rigides du système mécanique, à partir du diagramme du corps libre correspondant.

A partir de l'équation (5), nous tirons l'équation :

$$U_1\{T_1\} + A_{14}\{T_4\} + A_{15}\{T_5\} + A_{17}\{T_7\} = \{0\} \quad (14)$$

Cette équation est l'écriture de la loi d'Euler pour chacun des corps rigides à partir de leur diagramme du corps libre. De l'équation (6), nous tirons l'équation :

$$B_{71}\{\ddot{r}_1\} + B_{72}\{\ddot{r}_2\} + B_{73}\{\ddot{r}_3\} + U_7\{\ddot{r}_7\} = \{0\} \quad (15)$$

Pour un joint sphérique, nous avons les équations terminales :

$$(\dot{r}_7)_a = (\ddot{r}_7)_a = (r_7)_a = 0 \quad (16)$$

$$(T_7)_a = 0 \quad (16a)$$

En projetant l'équation (14) sur les référentiels liés aux différents corps rigides, nous avons, en considérant la relation (16a) :

$$U_1\{T_1\} + [D]\, A_{14}\, \{T_4\} + [D]\, A_{15}\, \{T_5\} = \{0\} \quad (17)$$

où $[D]$ est la matrice quasi-diagonale :

$$D = \begin{bmatrix} D_1 & \\ & 0 \\ 0 & D_n \end{bmatrix}$$,avec D_i $(i = 1,\ldots,n)$ matrice de transformation du référentiel inertiel au référentiel lié au corps rigide i ($a = D_i\, a$).

Pour un système mécanique avec un corps meneur relié à un seul corps du système mécanique, la matrice A_{17} est carrée (le nombre de corps rigides est égal au nombre de joints cinématiques).

Nous avons donc à partir de l'équation (17):

$$\{F_7\}^{-1} = - A_{17}\, (U_1\{F_1\} + A_{15}\{F_5\}) \quad (18)$$

Par définition, $\{T_4\} = - \{r_2\} \times \{F_2\}$ (19)

De l'équation (4), nous tirons :

$$U_2\{F_2\} + A_{25}\{F_5\} + A_{27}\{F_7\} = \{0\} \quad (20)$$

Toutes les forces et moments externes étant ramenés aux centres de masses des différents corps rigides, la matrice A_{25} est toujours identiquement nulle. En substituant l'équation (18) dans l'équation (20) et en tirant $\{F_2\}$ de cette expression, l'équation (19) devient :

$$\{T_4\} = - \{r_2\} \times A_{27}^{-1}\, A_{17}\, U_1\{F_1\} - \{r_2\}$$

$$\times A_{27}^{-1}\, A_{17}\, A_{15}\{F_5\}(21) \quad (21)$$

L'équation (21) peut être mise sous la forme matricielle suivante :

$$\{T_4\} = - [\{\underline{\underline{r}}_2\}\, A_{27}^{-1}\, A_{17}\, U_1\{F_1\}$$

$$- [\{\underline{\underline{r}}_2\}\, A_{27}^{-1}\, A_{17}\, A_{15}\{F_5\} \quad (21a)$$

avec $[\{\underline{\underline{r}}_2\}]$ qui représente le produit vectoriel.

En remplaçant, dans l'équation (21a), $\{F_1\}$ par sa valeur donnée par l'équation (8a) nous obtenons, en combinant les équations (15) et (16) pour tirer $\{r_1\}$ (en utilisant le principe d'orthogonalité pour les matrices dynamique et cinématique) :

$$\{T_4\} = - [\{\underline{\underline{r}}_2\}]\, A_{27}\, A_{17}^{-1}[m]\, (A_{27}\, A_{17}^{-1})^T\, \{\ddot{r}_2\} + \{w_1\} \quad (22)$$

avec

$$\{w_1\} = - ([\{\underline{\underline{r}}_2\}]\, A_{27}\, A_{17}^{-1}[m]\, (A_{37}\, A_{17}^{-1})^T\, \{\ddot{r}_3\}$$

$$+ [\{\underline{\underline{r}}_2\}]\, A_{27}^{-1}\, A_{17}\, A_{15}\{F_5\}) \quad (22a)$$

Pour l'ensemble du système mécanique, en considérant la topologie du diagramme schématique, nous avons :

$$\{\ddot{r}_2\} = - [\{\underline{\underline{r}}_2\}]\, ([D]\, A_{14})^T\, \{\dot{\omega}_1\} + \{w_2\} \quad (23)$$

avec $\{w_2\} = [\{\dot{\underline{\underline{r}}}_2\}]\, B_{41}[D]^T\, \{\omega_1\}$ (23a)

et $[\dot{D}]_1^T\, \{\omega\ \} = [D]^T\, [\{\underline{\underline{\omega}}_1\}]\, \{\omega_1\} = \{0\}$ (23b)

or, nous savons que $- [\{\underline{\underline{r}}_2\}] = [\{\underline{\underline{r}}_2\}]^T$

L'équation (23) devient donc :

$$\{\ddot{r}_2\} = ([D]\, A_{14}[\{\underline{\underline{r}}_2\}])^T\, \{\dot{\omega}_1\} + \{w_2\} \quad (23c)$$

En substituant l'équation (23c) dans l'équation (22), nous obtenons :

$$\{T_4\} = -[\{\underline{\underline{r}}_2\}]\, A_{27}A_{17}^{-1}[m]\, ([D]\, A_{14}[\{\underline{\underline{r}}_2\}]\, A_{27}A_{17}^{-1})^T$$

$$\{\dot{\omega}_1\} + \{w_3\} \quad (24)$$

avec $\{w_3\} = [\{\underline{\underline{r}}_2\}]\, A_{27}\, A_{17}^{-1}[m]\, \{w_2\} + \{w_1\}$ (24a)

En substituant l'équation (24) dans l'équation (17), nous obtenons, en remplaçant $\{T_1\}$ par son équation terminale (8b), l'équation finale devient :

$$[J]\ \{\dot{\omega}_1\} = \{M\} \quad (25)$$

avec $[J] = [I] + [K][m][K]^T ,$ (25a)

$[K] = [D]\, A_{14}[\{\underline{\underline{r}}_2\}]\, A_{27}^{-1}\, A_{17}$ (25b)

et $\{M\} = [D]\, A_{14}\{w_3\} + [D]\, A_{15}\{T_5\} - [\{\underline{\underline{\omega}}_1\}[I]\{\omega_1\}$

(25c)

La matrice [J], est une matrice vectorielle d'ordre n, symétrique et définie positive similaire à une matrice globale d'inertie pour le système mécanique. L'équation (25) est un système de n équations différentielles non-linéaires, de premier ordre en $\{\omega_1\}$.

A ces n équations vectorielles (3n équations scalaires), on devrait ajouter 3n autres équations scalaires qui relient les vitesses angulaires $(\omega_1)_i$ aux dérivées premières par rapport au temps des coordonnées généralisées ϕ_i, θ_i, ψ_i $(i = 1,\ldots,n)$.

SYSTEME MECANIQUE AVEC JOINTS SPHERIQUES, UNIVERSELS ET/OU ROTOIDES

Nous prenons comme coordonnées généralisées les angles par rapport aux axes de rotation $e'_{a\ell}$ $(\ell = 1,\ldots\rho_a$, avec ρ_a nombre de degrés de liberté en rotation) du joint a.

Pour les trois types de joints considérés, nous avons toujours :

$$\{r_7\} = \{\dot{r}_7\} = \{\ddot{r}_7\} = \{0\} \qquad (26)$$

Par définition, $(\gamma_7)_a$ est le vecteur-vitesse de rotation du joint a, c'est-à-dire la vitesse relative de rotation d'un des corps relié à ce joint par rapport à l'autre. Ainsi dans le référentiel mobile lié au corps rigide pour lequel le joint a est receveur, nous avons :

$$(\omega_7)_a = \sum_{\ell=1}^{\rho_a} \hat{e}'_{a\ell}\, \dot{\phi}_{a\ell} \quad (a = 1,\ldots,n) \qquad (27)$$

Les vecteurs $\hat{e}'_{a\ell}$ sont fonction des $\phi_{a\ell}$.

Soit $(\overset{\circ}{\omega}_7)_a$ la dérivée par rapport au temps, dans le référentiel mobile considéré, de $(\omega_7)_a$; nous avons :

$$(\overset{\circ}{\omega}_7)_a = \sum_{\ell=1}^{\rho_a} \hat{e}_{a\ell}\, \ddot{\phi}_{a\ell} + (\mu_7)_a \qquad (28)$$

$$\text{avec} \quad (\mu_7)_a = \sum_{\ell=1}^{\rho_a} \sum_{m=1}^{\rho_a} \frac{\partial\, \hat{e}'_{a\ell}}{\partial\, \phi_{am}}\, \dot{\phi}_{a\ell}\, \dot{\phi}_{am} \qquad (28a)$$

Aussi, nous avons, pour un joint donné a_i (joint receveur associé au corps rigide i) :

$$(\dot{\omega}_7)_{ai} = (\overset{\circ}{\omega}_7)_{ai} + (\omega_1)_i \times (\omega_7)_{ai} \quad (i = 1,\ldots,n) \qquad (29)$$

Ainsi, pour l'ensemble du système mécanique, nous avons la relation :

$$\{\dot{\omega}_7\} = \{\overset{\circ}{\omega}_7\} + [\{\underset{=}{\omega}_1\}]\{\omega_7\} = [\{\hat{e}'_a\}]\, \{\ddot{\phi}_a\} + \{\beta_7\} \qquad (30)$$

$$\text{avec} \quad \{\beta_7\} = \{\mu_7\} + [\{\underset{=}{\omega}_1\}][\{\hat{e}'_a\}]\, \{\dot{\phi}_a\} \qquad (30a)$$

$$\text{et nous avons} \quad [\{\hat{e}'_a\}] = \begin{bmatrix} \{\hat{e}'_1\}^T & \\ & 0 \\ 0 & \{\hat{e}'_n\} \end{bmatrix} \qquad (31)$$

$[\{\hat{e}'_a\}]^T$ est une matrice scalaire de dimension

$$\left(\sum_{a=1}^{n} \rho_a \times 3n\right).$$

Pour le cas du système mécanique considéré, $\{T_7\} \neq \{0\}$. L'équation (25) devient donc :

$$[J]\{\dot{\omega}_1\} = \{M\} - [D]\, \Lambda_{17}\{T_7\} \qquad (32)$$

A partir de l'équation (7), nous tirons l'équation :

$$B_{71}\{\gamma_1\} + B_{73}\{\gamma_3\} + U_7\{\gamma_7\} = \{0\} \qquad (33)$$

et nous tirons :

$$\{\omega_1\} : [D]^T \{\omega_1\} = -(\Lambda_{17}^{-1})^T [D]^T \{\omega_7\} + \{\alpha_1\} \qquad (34)$$

$$\text{avec} \quad \{\alpha_1\} = -(\Lambda_{37}^{-1}\, \Lambda_{17}^T)\ \{\gamma_3\} \qquad (34a)$$

Dérivons par rapport au temps, dans le référentiel inertiel, l'équation (34), nous obtenons:

$$[D]^T \{\dot{\omega}_1\} = \{\dot{\alpha}_1\} + (\Lambda_{17}^{-1})^T [D]^T \{\overset{\circ}{\omega}_7\} + (\Lambda_{17}^{-1})^T [D]^T [\underset{=}{\omega}_1\}]\ \{\omega_7\} \qquad (35)$$

En substituant l'équation (30) dans l'équation (35), nous tirons de celle-ci :

$$\{\dot{\omega}_1\} = [D]\ (\Lambda_{17}^{-1})^T\ [D]^T[\{e'_a\}]\ \{\ddot{\phi}_a\} + [D]\ \{\beta_1\} \qquad (36)$$

$$\text{avec} \quad \{\beta_1\} = \{\dot{\alpha}_1\} + (\Lambda_{17}^{-1})\ [D]^T\ \{\beta_7\}\ . \qquad (36a)$$

En remplaçant, dans l'équation (32), $\{\dot{\omega}_1\}$ par sa valeur donnée parl'équation (36) ci-dessus, nous obtenons :

$$[J][D](\Lambda_{17}^{-1})^T\ [\{\hat{e}'_a\}]\ \{\ddot{\phi}_a\} = \{M\} - [J]\{\beta_1\} - [D]\ \Lambda_{17}\{T_7\} \qquad (37)$$

(équation dans laquelle nous avons remplacé $[D]\ [\{\hat{e}'_a\}]$ par $[\{\hat{e}'_a\}]$)

En tirant $\{T_7\}$ de l'équation (37) (avec $[D]^{-1} = [D]^T$), nous obtenons :

$$\{T_7\} = -\Lambda_{17}^{-1}[D]^T[J][D](\Lambda_{17}^{-1})^T[\{\hat{e}'_a\}]\{\ddot{\phi}_a\}$$

$$-\Lambda_{17}^{-1}[D]^T\{M\} + \Lambda_{17}^{-1}[D]^T[J]\{\beta_1\} \qquad (38)$$

Pour tout joint a, le vecteur $(T_7)_a$ est orthogonal au vecteur e'_a, nous avons donc :

$$[\{\hat{e}'_a\}]^T\{T_7\} = \{0\} \qquad (39)$$

En multipliant l'équation (38), à gauche, par $[\{e'_a\}]^T$ et en substituant dans l'expression obtenue l'équation (39) ci-dessus, nous obtenons l'équation finale :

$$[J^*]\{\ddot{\phi}_a\} = \{M^*\} \qquad (40)$$

avec $$[J^*] = ([\{\hat{e}'_a\}]^T\Lambda_{17}^{-1}[D]^T)[J]$$

$$([\{\hat{e}'_a\}]^T\Lambda_{17}^{-1}[D]^T)^T \qquad (40a)$$

$$\{M^*\} = [\{\hat{e}'_a\}]^T\Lambda_{17}^{-1}[D]^T(\{M\} - [J]\{\beta_1\}) \qquad (40b)$$

l'équation (40) représente ainsi un système de $N_a = \sum_{a=1}^{n} \rho$ équations différentielles nonlinéaires de 2^e ordre, scalaires en $\phi_{a\ell}$ $(a = 1,\ldots,n, \ell = 1,\ldots,\rho_a)$.

CONCLUSION

Cet article présente une amélioration des fondements analytiques de la modélisation dynamique basée sur la méthode du réseau vectoriel. Les résultats des simulations basées sur le programme RESTRI sont ainsi justifiées par le modèle présenté dans cet article et, de plus, le présent modèle permet d'élargir le champ d'application du modèle du réseau vectoriel. Le modèle dynamique présenté dans cet article trouve une application simple et directe dans le domaine de la robotique (modélisation dynamique des bras manipulateurs à structure de chaine ouverte ou arborescente). L'avantage de la méthode du réseau vectoriel réside dans le fait que toutes les grandeurs dynamiques du système mécanique peuvent être connues à chaque instant, en exploitant entièrement les équations dynamiques (4) et (5). Le présent modèle est en train d'être développé pour permettre d'étudier les systèmes mécaniques avec des joints quelconques (holonomes, non holonomes, ...), de même que les systèmes mécaniques contenant des chaines fermées.

REFERENCES

1. Richard, M.J., "Dynamic Simulation of Constrained Three-Dimensional Multi-Body Systems Using Vector-Network Techniques", Ph.D. Thesis, Queen's University, [illegible]ston, Ontario, 1985.
2. Sheth, P.N., and Uicker, J.J., "IMP (Integrated Mechanisms Program), A Computer-Aided Design Analysis System for Mechanisms and Linkage", ASME Journal of Engineering for Industry, Vol. 94, 1972, p. 454.
3. Orlandea, N., "Node-Analogous, Sparsity-Oriented Methods for Simulation of Mechanical Dynamic Systems", Ph.D. Thesis, University of Michigan, Ann Arbor, Mich. 1973.
4. Orlandea, N., Chace, M.A. and Calahan, D.A., "A Sparsity Oriented Approach to the Dynamic Analysis and Design of Mechanical Systems - Part 1", ASME Journal of Engineering for Industry, Vol. 99, 1977, p. 773.
5. Paul, B., and Krajcinovic, D., "Computer Analysis of Machines with Planar Motion - Part 1", ASME Journal of Applied Mechanics, Vol. 37, 1970, p. 697.
6. Haug, E.J., Nikravesh, P.E., Sohoni, V.N., and Wehage, R.A., "Computer-Aided Analysis of Large-Scale, Constrained, Mechanical Systems", Proceedings, NATO Advanced Study Institute on Computer-Aided Analysis of Mechanical System Dynamics, University of Iowa, 1983.
7. Schiehlen, W., and Kreuzer, E.J., "Symbolic Computerized Derivation of Equations of Motion", IUTAM Symposium on Dynamics of Multibody Systems, K. Magnus, Springer-Verlag, 1978.
8. Andrews, G.C., "The Vector-Network Model; A Topological Approach to Mechanics", Ph.D. Thesis, University of Waterloo, Waterloo, Ontario, 1971.

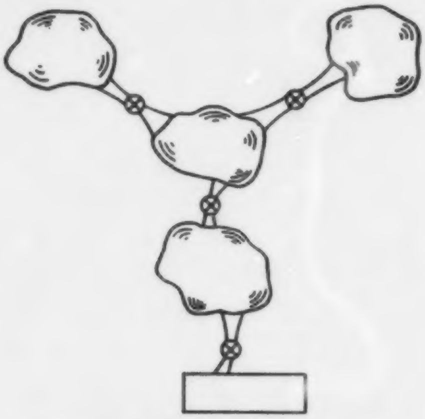

Figure 1. Système mécanique tridimensionnel.

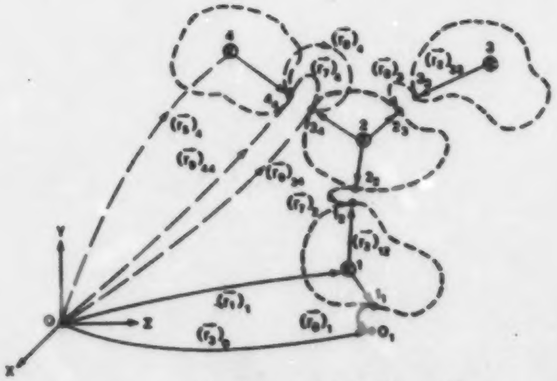

Figure 2. Réseau vectoriel du système mécanique de la figure 1.

AN FEM APPROACH FOR ROBOT PATH PLANNING UNDER DYNAMIC CONDITIONS

Ramachandran S.   Nagarajan T.   Sivaprasad N.

Dept. of Mechanical Engineering, Indian Institute of Technology
Madras 600 036, India.

ABSTRACT

Path planning of robot end effector is an important area of design for efficient dynamic performance of the system. Forward and inverse kinematic analyses of the system provide details about the end effector path without considering the forces and torques experienced by the system. When the forces and the torques experienced by the system are considered robot path can be planned under dynamic conditions. Analytical derivation of a closed form solution for robot forward and inverse kinematics is tedious especially for inverse analysis which can be made available for particular geometries only. Numerical methods are preferred for the dynamic analysis of the manipulators. In the present work, an approach for robot path planning under dynamic condition is presented using Finite element method. For this purpose both forward and inverse analyses of the geometry of the manipulator are made using finite element method. Finite element applications in robot structure analysis is a limited area of research due to the difficulties in modeling the kinematic pairs. 3D beam elements with 6 DOF for each end and direct stiffness formulation of FEM are used with consistent mass approach. The method considers kinematic pair modeling and inertial forces and torques experienced due velocities and accelerations of the links of the manipulator. The method has been illustrated with examples of two manipulators, one having 6R pairs and the other having 5R and 1P pairs. The task chosen for the analysis produces a straight line motion for the end effector as experienced in welding or in machining.

NOMENCLATURE :

Finite Element Parameters :

$[Ae]$	Element statics matrix
$[Ae]^T$	Transpose of $[A]$
$[Cg]$	Global damping matrix
$\{Fe\}$	Vector containing element end forces and moments
$\{Fg\}$	Global load vector
$[Ke]$	Element stiffness matrix
$[Kg]$	Global stiffness matrix
$[Mg]$	Global mass matrix
$\{Fg(t)\}$	Global load vector varying with time
$[Se]$	Element internal stiffness matrix
$\{Xg\}$	Global displacement vector
$\{\dot{Xg}\}$	First derivative of global displacement vector
$\{\ddot{Xg}\}$	Second derivative of global displacement vector

Link Parameters (pertaining to link i) :

A_i	Acceleration of link
F_i	Inertial force of link
I_i	Mass moment of inertia of link
T_i	Inertial torque of link
α_i	Angular acceleration of link
w_i	Angular velocity of link

INTRODUCTION

In an industrial environment using robot for assembly, parts handling, welding or painting, it is essential to plan the path the manipulator should take between the defined goal points. Several automatic path planning algorithms have been developed to decide about the collision free paths to be followed using robot's configuration on joint space. Difficulties arise when attempts are made to use the programs for planning paths considering complex geometries of the manipulators and characteristics of robot controllers. Dynamic workspace environments are difficult for automatic path planning. In a typical work station environment, path planning is done off-line, to improve the effective utilization of robot's capabilities. A systematic and an easy path planning method for various tasks is required for fully utilizing the advantages of automation. For a thorough analysis for a new task, an industrial engineer is expected to have a clear knowledge about the parameters which interact among themselves to affect the path following performance.

A path following performance can successfully be predicted only by understanding the various motion criteria of the robot. Parameters which affect the motion of the robot manipulator are ,
a) Kinematic parameters
b) Operating language facilities
c) Operating system facilities.

Kinematic parameters which affect the system performance are,
a) Overshoot and undershoot which are functions of the moment of inertia of the links of the manipulator and that of the control system. This means the desired position is not reached and the robot is either above or below the desired position.
b) Hunting is an estimate of the oscillating motion of the end effector experiences when the robot is not commanded to move.
c) Ripple is the wave motion superimposed on a straight line motion.

Operational parameters which affect the path planning are ,
a) Acceleration which will ascertain how quickly the robot will reach the designated speed and how quickly the robot will be able to respond to changes in speed and path
b) Accuracy which is the error estimate between the actual and desired position where the desired position is already programmed
c) Repeatability which estimates the precision of robot's ability to arrive at a desired position.

Industrial robots in general have 6 degrees of freedom for the end effector to perform various tasks. High production levels demand high speed of operation for robots and robot path is planned off-line to reduce the down time. When the operating speeds are low static analysis would be sufficient to predict the dynamic performance. However, when the operating speeds are high it is very essential to have an accurate prediction about the dynamic performance of robots. A simple way of planning a robot path would be to record the joint variables by teaching the path and try to produce the same motion. Robot path planning is usually done by performing both forward and inverse kinematics without considering the various torques and forces that act on the system. Flexibilities of links,joints and the severe dynamic conditions under which the robot works impair the dynamic performance of the robot resulting in poor positioning performance. Hence, it is very essential to perform both forward and inverse dynamic analysis to predict the path under actual working conditions of the robot. Analyses using rigid body dynamics provide less accurate results.

In the present work,a generalized approach is presented for predicting the robot's path under dynamic conditions using finite element method. The method considers modeling of kinematic pairs and flexibility of links. 3D beam elements, direct stiffness formulation of FEM and consistent mass approach have been used for the modeling of the robot manipulators. The method has been illustrated by a practical problem of producing a straight line path using two manipulators one having 6R pairs-Model I and the other having 5R and 1P pairs - Model II.

Problem Selection

In a robot operation the following motions exist
a) Single joint motion
b) Joint interpolation motion
c) Straight line motion
d) Circular motion
e) Mathematical interpolation motion

A straight line motion for end effector has been selected for the present work for the following reasons though it requires mathematical interpolation along the desired path:
a) Most of the motion paths are either a single straight line or consist of several straight line segments
b) Straight line paths are the shortest and are easily visualized
d) Inertial effects on the end effector are less since there is uniform motion in a straight line path
e) Techniques used for producing a straight line path can be used for other paths

As are well known, a few definitions are presented as in [1] will be useful for the present problem. Forward dynamic analysis is performed by defining the end effector motion and obtaining the torques and forces required to produce the desired motion. Inverse dynamic analysis is performed by knowing the input torque and force values that are required to drive the system to produce the desired motion. In both the cases a time step is assumed to consider the dynamic forces involved in the system.

ANALYSIS PROCEDURE

Robot path under dynamic operating conditions is estimated by analyzing the finite element model of the robot manipulator based on the kinematic model.

Kinematic Model

Robot manipulators have pairs like prismatic, cylindrical, revolute, spherical and combinations of pairs to achieve the various desired motions. Physical models of the manipulators under investigation are shown in Figs(1,2). Kinematic models of the manipulators indicating the various motions are shown in Figs(3,4).

FE Model

Finite element model of the manipulator is made using 3D beam elements having constant cross sectional properties, by specifying 6 DOF for rotations and translations in the three axes. Inner and outer elements of a pair will be specified with separate DOF numbers order to model the kinematic pair. For example, a prismatic pair will have one different translatory DOF for its outer element. A revolute pair will have one rotation and one translation DOF different for its outer element. Fig(5) shows DOF number specifications for prismatic and revolute pairs. Modeling of the robot manipulator is done by DOF specifications considering the practical working conditions. In modeling a robot manipulator each link is considered as a finite element. However, more number of elements can be used for obtaining better results. This more so when higher order elements such as plate elements are used. A node is specified,

a) where a joint exists
b) where the cross section varies
c) depending on the end fixity conditions.

Procedure for finite element modeling has been presented in [1,2,3].

In a finite element model active DOF numbers are specified first depending on the pairs used in the manipulator and fixed DOF assumes one number more than the active DOF. Finite element models of the manipulators with separate DOF numbers specified for inner and outer elements of pairs are shown in Figs(6,7). Model I having 6R pairs has 9 elements and 61 active DOF numbers. Model II has 7 elements and 49 active DOF numbers.

Kineto-elasto-dynamic Analysis

KED analysis is performed on the finite element models to predict the robot path under dynamic conditions by performing forward and inverse dynamic analysis.

Forward analysis

In the forward analysis a time varying displacement equation is assumed for the end effector. Forces experienced by the end effector are used as the load vector for the finite element model. First the static analysis is performed by solving for [xg] from equation .....

$$[kg]\,[xg] = [fg] \qquad (1)$$

On computing the displacement vector[xg] and implementing the co--ordinates in the appropriate DOF numbers the new geometry of the manipulator is obtained. Driving forces and torques are obtained by restraining the DOF numbers at the input end of the input link and allowing the DOF at the other end. Under this condition, the reaction forces and the reaction moments for the input links provide the input drive requirements. By assuming a small time step velocities , accelerations and inertial effects of the links are computed and are specified as loads at the appropriate DOF numbers for the new geometry of the model. In performing a kineto-elasto-dynamic analysis, the robot structure is considered as an instantaneous structure in equilibrium under the action of these forces. This is performed till the task is completed or till a time limit is reached. The values of driving torques and forces for a particular period of operation.

Inverse analysis:

Input forces and torques obtained earlier from the forward analysis are approximated to a function of time and used as the load vector for the finite element model , trying to produce the same required motion. In this analysis the same time step is assumed as in the forward analysis and the analysis is carried out in the similar manner till the time limit is reached. The end effector path is described based on the deflections obtained from the inverse dynamic analysis, representing them as corrections to be applied at the end effector.

Equations used for the analyses are presented in Appendix. Details of cross section of materials used are provided in Table 1.

COMPUTER PROGRAMS

Computer programs have been developed in FORTRAN 77 coding for performing the forward and inverse dynamics of any type of manipulator having beam elements and or plate elements. The programs are run on SIEMENS 7580E system and require the following as input values:

1 Element numbers,DOF for inner and outer elements of pairs,co-ordinates of the terminal end of links
2 Material and cross sectional properties of the elements
3 Load details

RESULTS AND DISCUSSION

Joint actuator force and torque values obtained from the forward analysis are approximated using curve fitting available algorithms and are presented in Figs(8,9). Paths generated by the two models and the path required are shown in Figs(10,11). Table II presents the necessary corrections to be applied to the end effector to obtain a straight line path. Load details used for the FE models are presented in Fig(12).

CONCLUSION

Finite element method has been used in the present work by illustrating two examples of a 6R manipulator and 5R and 1P pair manipulator. Though examples of open loop manipulators have been presented the method can be effectively used for the analysis of closed loop, constrained and unconstrained manipulator mechanisms. The method is expected to provide accurate results than other methods used for the dynamic analysis. By assuming a very small time step it is possible to predict the system behavior exactly. The method can be used for any type of manipulator and for any task.

REFERENCES:

1. Dado,M., Soni,A.H., A generalized approach for the forward and inverse analysis of elastic manipulators, Proc. of 1986 IEEE International Conf. on Robotics and Automation, Vol.1, pp.359-364, 1986.

2. Bagci,C., Methods of elastodynamics of mechanical,structural and industrial robotic systems using finite elements, ASME Paper No. 83-wa/dsc-7

3. Nagarajan,T.,Sivaprasad,N.,Ramachandran, Determination of minimum deflection path for assembly robots using FEM, Accepted for publication in AMSE Journal on control, France, Winter 1990.

TABLE I- Section details
Material - Steel
E = 2.10e06 Kgf/sq.cm
G = 1.15e06 Kgf/sq.cm

Model I

Element No	Section
1	100 mm OD , 65 mm ID tube
2	10 mm Dia rod
3	85 mm OD , 65 mm ID tube
4	10 mm Dia rod
5	85 mm OD , 65 mm ID tube
6	10 mm Dia rod
7	85 mm OD , 65 mm ID tube
8	20 mm Dia rod
9	20 mm Dia rod

Model II

1	100 mm OD , 65 mm ID tube
2	75 mm OD , 60 mm ID tube
3	75 x 75 x 12.5 mm thick rectangular tube
4	50 x 50 x 15 mm thick rectangular tube
5	20 mm Dia rod
6	20 mm Dia rod

TABLE II End effector positions

Time(sec)	X axis(cm)	Z axis(cm)
MODEL I		
0.00	15.000	21.000
0.10	15.005	20.952
0.20	15.020	20.826
0.30	15.037	20.670
0.40	15.052	20.540
0.50	15.057	20.493

MODEL II

Time(sec)	Y axis(cm)	Z axix(cm)
0.00	96.500	21.000
0.10	96.505	21.055
0.20	96.512	21.119
0.30	96.537	21.377
0.40	96.552	21.520
0.50	96.557	21.575

APPENDIX

Finite element formulation in general has a stiffness matrix, a mass matrix, a damping matrix and load vector. Deflection analysis is performed by the solution of equation....

$$[K_g]\ \{x_g\} = \{F_g\} \qquad (1)$$

Global Mstiffness matrix of the structure is obtained by assembling the element stiffness matrix [Ke] of each element. Element stiffness matrix in any orientation is obtained by equation......

$$[K_e] = [A_e]\ [S_e]\ [A_e]^T \qquad (2)$$

End forces and moments are computed from the equation ......

$$\{f_e\} = [S_e]\ [A_e]^T\ \{X_e\} \qquad (3)$$

Elasto-dynamic analysis is performed by obtaining the solution of the equation..

$$[M_g]\{\ddot{X}_g\}+[C_g]\{\dot{X}_g\}+[K_g]\{X_g\}=\{F_g(t)\} \qquad (4)$$

Resonant frequencies of vibration are obtained by the solution of the equation..

$$[M_g]\{\ddot{X}_g\}+[C_g]\{\dot{X}_g\}+[K_g]\{X_g\}=\{0\} \qquad (5)$$

Damping matrix is not considered in the present analysis.
Inertial forces and torques are computed using equations......

$$F_i = M_i A_i \qquad (6)$$

$$T_i = I_i \alpha_i + I_i w_i^2 \qquad (7)$$

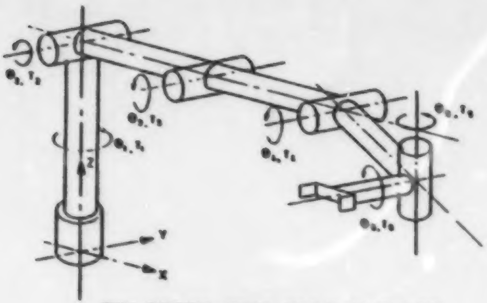

θ2, T2
θ3, T3
θ1, T1
θ4, T4
θ6, T6
θ5, T5
Z
Y
X

FIG.1 PHYSICAL MODEL OF 6-R MANIPULATOR

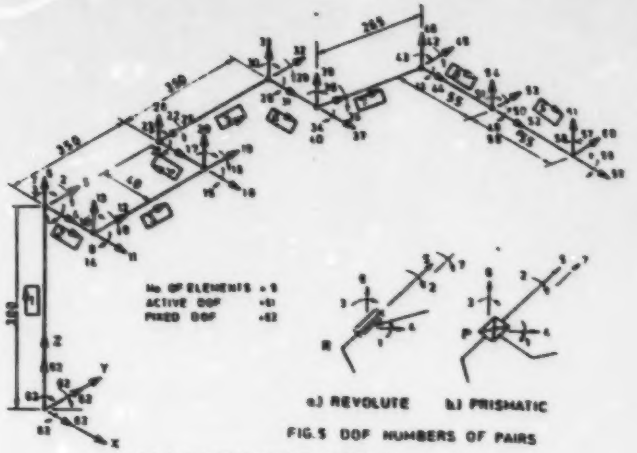

285
350
350
300
No OF ELEMENTS = 9
ACTIVE DOF = 61
FIXED DOF = 62
Z
Y
X
R
P

a) REVOLUTE b) PRISMATIC

FIG.5 DOF NUMBERS OF PAIRS

FIG 6 FINITE ELEMENT MODEL - I

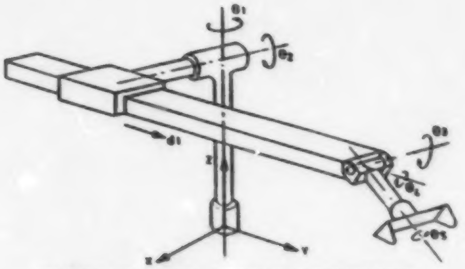

θ1
θ2
d1
θ3
θ4
θ5
Z
X
Y

FIG.2 PHYSICAL MODEL OF 5 AND 1P MANIPULATOR

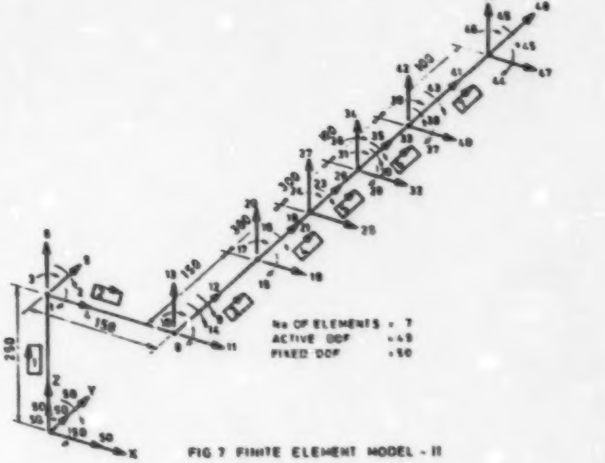

100
300
300
150
150
250
No OF ELEMENTS = 7
ACTIVE DOF = 43
FIXED DOF = 50
Z
Y
X

FIG 7 FINITE ELEMENT MODEL - II

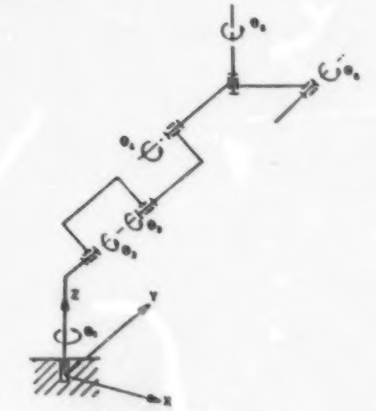

θ6
θ5
θ4
θ3
θ2
θ1
Z
Y
X

FIG.3 KINEMATIC MODEL I

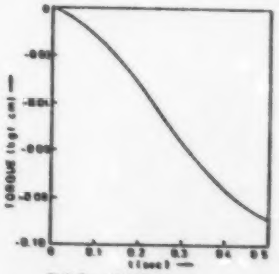

FIG 8a. JOINT 1

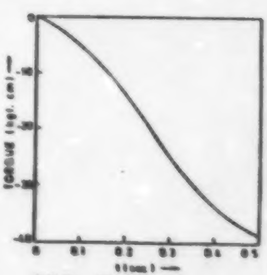

FIG.8b. JOINT 2

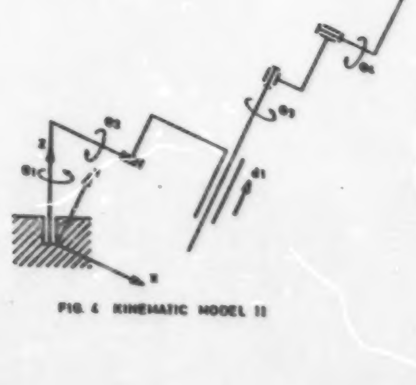

θ5
θ4
θ3
θ2
θ1
d1
Z
X

FIG. 4 KINEMATIC MODEL II

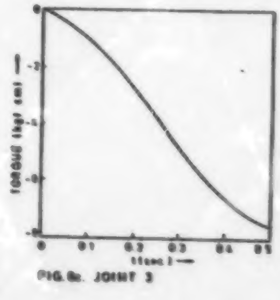

FIG.8c. JOINT 3

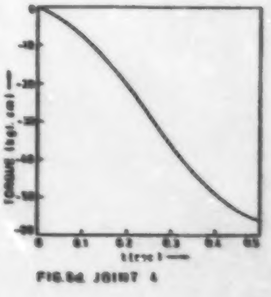

FIG.8d. JOINT 4

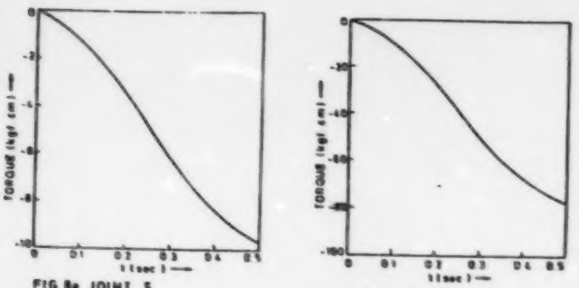

FIG 8e JOINT 5

FIG. 8f JOINT 6

FIG.8 JOINT INPUT PARAMETERS- MODEL I

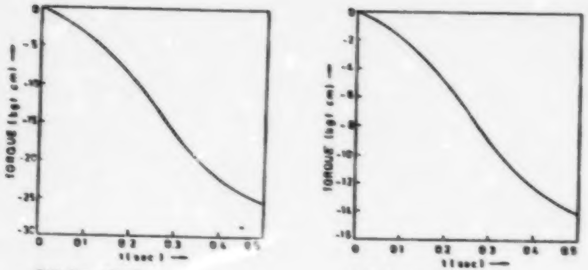

FIG 9a JOINT 1

FIG. 9b JOINT 2

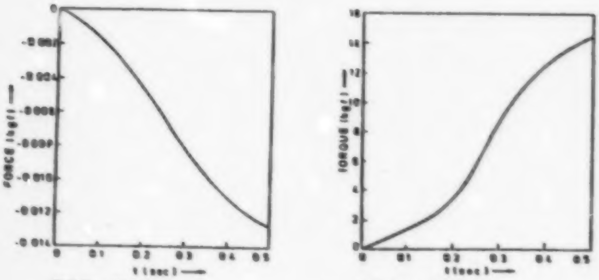

FIG.9c JOINT 3

FIG. 9d JOINT 4

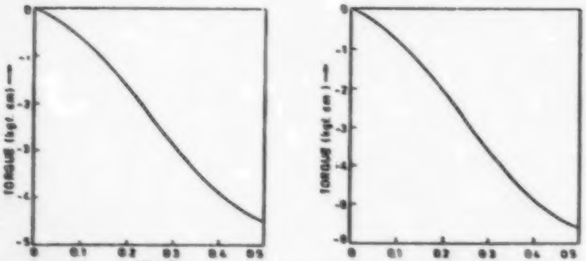

FIG.9e JOINT 5

FIG.9f JOINT 6

FIG.9 JOINT INPUT PARAMETERS- MODEL II

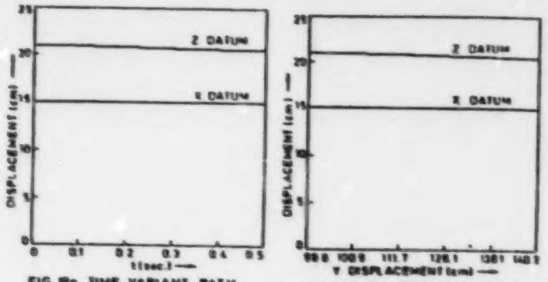

FIG. 10a. TIME VARIANT PATH

FIG. 10b. CO-ORDINATE VARIANT PATH

FIG. 10 PATH REQUIRED AND GENERATED-
MODEL I

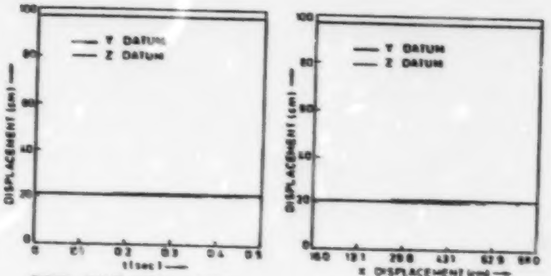

FIG 11a. TIME VARIANT PATH

FIG. 11b. CO-ORDINATE VARIANT PATH

FIG. 11 PATH REQUIRED AND
GENERATED - MODEL II

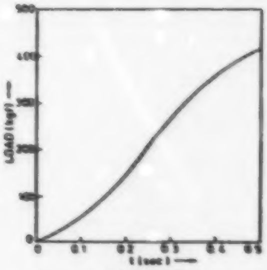

FIG 12 LOAD DIAGRAM

THE APPLICATION OF MODERN SYSTEMS TECHNIQUES TO HELICOPTER MODELLING AND CONTROL

Mr. R. Srinivasan
Graduate Student

Dr. K. R. Goheen
Assistant Professor

Department of Mechanical and Aerospace Engineering,
Carleton University, Ottawa, Ontario, CANADA - K1S 5B6.

ABSTRACT

This paper presents research-in-progress from a joint project between the Department of Mechanical and Aerospace Engineering, Carleton University and the Flight Research Laboratory at the National Aeronautical Establishment of the National Research Council. The initial stage of the project is concerned with the application of System Identification (SI) and Parameter Estimation (PE) techniques to helicopter modelling.

SI algorithms are related to PE methods, but since they are usually formulated in a recursive manner, their computer hardware requirements are much less. SI models can be used as a replacement for PE models, or as an accurate "first-guess" to start off the PE algorithm.

The framework of these algorithms is described along with their extension to multi-input/multi-output (MIMO) estimation. A simulation of the Bell-205 and its navigation system is used to produce data for PE and SI. The performance of an SI algorithm is compared to PE. Statistical methods, including Akaike's Information Criteria and F-statistics, are used to calculate the optimal model complexity.

INTRODUCTION

The large numbers of helicopters now flying with the world's armed forces and rescue service corps have necessitated an extensive study of helicopter dynamics. Though the dynamic and aerodynamic characteristics of helicopters have been investigated for some time now, the areas of their modelling and control have received relatively less attention, at least until recently.

With the emergence over the last two decades of several new applications for such models, such as new helicopter designs, flight-simulators for pilot training and certification and regulation, the need for new methods to develop quick and accurate helicopter models has increased dramatically. To fill this need an increasing use of systems techniques is being made. In the past, these techniques have been applied very successfully to fixed-wing aircraft modelling; and as such have come to be recognized as reliable tools for aircraft - or in general, dynamic systems - modelling.

However, the highly non-linear and coupled nature of the dynamic equations of a helicopter and the vibration noise associated with the rotor that always corrupts flight-test measurements, makes the application of the same systems techniques to helicopters more challenging. In spite of this, Parameter Estimation (PE) techniques have been successfully applied to develop accurate models based on the input-output data obtained from actual flight tests [1,2,3].

In order to simulate helicopter motion on a digital computer, aerodynamic stability and control derivatives are required. In this study, these derivatives were obtained from the National Research Council's Flight Research Laboratory (FRL) for their fully instrumented, fly-by-wire Bell-205 helicopter. The FRL has compiled this data on the basis of extensive flight testing of the Bell-205, and subsequent PE studies using a large NASA-developed computer program "MMLE3" which implements a third generation version of the Modified Maximum Likelihood Estimation technique. MMLE3 however, suffers from the disadvantages of large memory and time resource requirements, even on a mainframe computer. This paper describes the use of System Identification (SI) techniques, as both an alternative and a supplement to PE.

THE MATHEMATICAL MODEL

The equations of motion which describe the dynamics of a helicopter are a good deal more complex than those for fixed-wing aircraft. The primary difficulty arises due to the nature of the higher order system of helicopter dynamics. Whereas two uncoupled sets of three degree-of-freedom (DOF) equations can be used to describe fixed-wing aircraft dynamics adequately, it has been shown that at least a 6 DOF model is required for helicopters [2]. This is due to the considerable degree of inter-axis coupling that exists, as well as the coupling between fuselage, main-rotor and the tail-rotor.

In disturbed flight, the rotor is assumed to behave as if the motion were a sequence of steady conditions, i.e. the accelerations of the helicopter are small enough to have a negligible effect on the rotor response [4]. This assumption stems from the fact that the rotating blade can be represented by a second order system having a natural frequency which is the same as the rotor angular frequency. Typical disturbed motion then corresponds to forcing the blade at a very low frequency ratio, so that the rotor responds as if an instantaneous disturbance were being applied steadily. A more detailed description of the reasons for this fully coupled and non-linear nature of the helicopter model equations can be found in reference [3].

A complete derivation of the equations of motion for fixed-wing aircraft may be found in any text book on flight dynamics [5]. Following a similar method and employing suitable simplifying assumptions, Kobiersky [3] has developed the following set of equations for the small-perturbation motion of the linearised 6 DOF, 8th order model of the Bell-205 helicopter (Fig. 1).

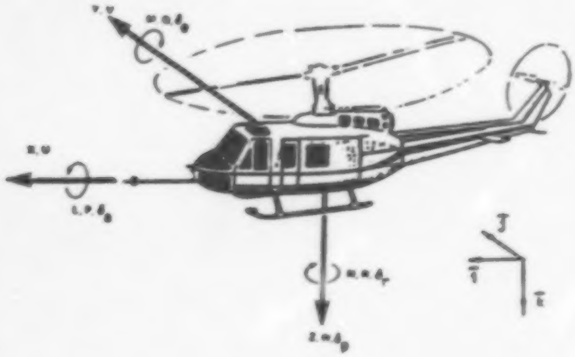

Fig.1 Body-fixed Helicopter Coordinate System

$$\dot{u} = g[\sin(\Theta_0) - \sin(\Theta_0 + \theta)] + V_0 r + vr - W_0 q - wq$$
$$+ X_u u + X_v v + X_w w + X_p p + X_q q + X_r r$$
$$+ X_{\delta e}\delta e + X_{\delta a}\delta a + X_{\delta r}\delta r + X_{\delta p}\delta p$$

$$\dot{v} = g[\cos(\Theta_0 + \theta)\sin(\Phi_0 + \phi) - \cos(\Theta_0)\sin(\Phi_0)]$$
$$+ W_0 p + wp - U_0 r - ur$$
$$+ Y_u u + Y_v v + Y_w w + Y_p p + Y_q q + Y_r r$$
$$+ Y_{\delta e}\delta e + Y_{\delta a}\delta a + Y_{\delta r}\delta r + Y_{\delta p}\delta p$$

$$\dot{w} = g[\cos(\Theta_0 + \theta)\cos(\Phi_0 + \phi) - \cos(\Theta_0)\cos(\Phi_0)]$$
$$+ U_0 q + uq - V_0 p - vp$$
$$+ Z_u u + Z_v v + Z_w w + Z_p p + Z_q q + Z_r r$$
$$+ Z_{\delta e}\delta e + Z_{\delta a}\delta a + Z_{\delta r}\delta r + Z_{\delta p}\delta p$$

$$\dot{p} = L_u u + L_v v + L_w w + L_p p + L_q q + L_r r$$
$$+ L_{\delta e}\delta e + L_{\delta a}\delta a + L_{\delta r}\delta r + L_{\delta p}\delta p$$

$$\dot{q} = M_u u + M_v v + M_w w + M_p p + M_q q + M_r r$$
$$+ M_{\delta e}\delta e + M_{\delta a}\delta a + M_{\delta r}\delta r + M_{\delta p}\delta p$$

$$\dot{r} = N_u u + N_v v + N_w w + N_p p + N_q q + N_r r$$
$$+ N_{\delta e}\delta e + N_{\delta a}\delta a + N_{\delta r}\delta r + N_{\delta p}\delta p$$

$$\dot{\phi} = p + q\sin(\Phi_0 + \phi)\tan(\Theta_0 + \theta)$$
$$+ r\cos(\Phi_0 + \phi)\tan(\Theta_0 + \theta)$$

$$\dot{\theta} = q\cos(\Phi_0 + \phi) - r\sin(\Phi_0 + \phi) \tag{1}$$

where:

u, U_0	are the perturbation and steady-state forward speeds, respectively (fps)
v, V_0	are the perturbation and steady-state lateral speeds, respectively (fps)
w, W_0	are the perturbation and steady-state normal speeds, respectively (fps)
p	is the perturbation roll rate (rad/s)
q	is the perturbation pitch rate (rad/s)
r	is the perturbation yaw rate (rad/s)
g	is the gravitational acceleration (fps^2)
θ, Θ_0	are the perturbation and steady-state pitch angle (radians)
ϕ, Φ_0	are the perturbation and steady-state roll angle (radians)
X_u...N_r	are the various (linear and angular) stability derivatives
$X_{\delta e}$...$N_{\delta p}$	are the various (linear and angular) control derivatives
δ_e	is the main rotor longitudinal cyclic control perturbation
δ_a	is the main rotor lateral cyclic control perturbation
δ_r	is the tail rotor collective control perturbation
δ_p	is the main rotor collective control perturbation

PARAMETER ESTIMATION

Ljung and Soderstrom [6] show that models can be derived by two methods. The first, called appropriately, "modelling", determines the parameter values of the physical mechanisms which all together make up the system. Examples would be finding the values of mass, damping and stiffness in a second order system or conventional aerodynamic modelling of an aircraft. An alternative is "identification" or "estimation" where measured signals produced by the system are used to construct the model. If a mass/spring/dashpot system is set oscillating and the frequency and log decrement of the vibrations noted from the output, then the model has been derived by identification.

Parameter Estimation (PE) and System Identification (SI) are both techniques for inferring the numerical values of the parameters of a mathematical model which describes any dynamic system from input-output data. As well, SI also considers questions of model structure and model complexity; PE is usually useful when the structure of the mathematical model (i.e. the equations in parametric form) are already known, leaving only the numerical values of the parameters to be estimated.

A helicopter, at a specified flight condition, can be described by non-linear, time-dependant, differential equations, which are almost always contaminated with non-Gaussian, non-stationary correlated noise. For example, during flight-testing, the system states are perturbed by process or state noise comprised of unmeasured inputs from wind gusts, control backlash and modelling imperfections. In addition, there is also measurement noise, made up of quantization noise and vibration, which corrupts measured responses with higher frequency noise components.

Based on the above two main types of noise, there have also developed two methods of doing PE; the output error method and the equation error method. Output error methods are based on the assumption that there is no state noise (wind gusts or other disturbances) during the data-collection stage of the flight testing. These methods, which yield unbiased values for the coefficients, if only measurement noise is present; use iterative Newton_Raphson techniques, often in conjunction with Maximum Likelihood (ML) algorithms. Equation error methods, on the other hand, are based on some form of Least Squares (LS) regression; and can account for state noise, but not for measurement noise. These methods are described in greater detail in a later section on SI.

The Maximum Likelihood estimation approach, which gives good results in practice, has the following useful properties:

- Parameter errors have an unbiased Gaussian distribution, and
- Estimates are efficient and consistent.

Here, PE takes place on Maine and Iliff's formulation for a linear time-invariant (LTI) continuous state-space model [7]:

$$\dot{x}(t) = Ax(t) + Bu(t) + Fn(t) \tag{2}$$

When discretized, this gives:

$$x_{i+1} = \Phi x_i + \Gamma u_i + Q_d^{0.5} n_i \tag{3}$$

The measurement equation, in discrete form then becomes:

$$z_i = Cx_i + Du_i + g\eta_i \tag{4}$$

where:

$x(t)$ = state at time t
z_i = measured output at time t_i
A = continuous system dynamics matrix
B = control distribution matrix
F = square root of the state noise spectral density FF^T
$n(t)$ = Gaussian white noise process
n_i, η_i = Gaussian random sequences
C = state measurement matrix
D = discretized transmission matrix
g = square root of the measurement noise covariance matrix
Q_d = discrete state noise covariance approximation
Φ = e^{AT_s}, T_s = sampling period
Γ = discrete control distribution matrix

ML methods are one of the so-called Bayesian approaches to parameter estimation. The parameters, here the elements of A, B, F, C, D and g, are assumed to be unknown random constants distributed according to Gaussian probability distributions. The measurements z_i are used to determine those values of the parameters with the highest probability given the experimental data. Special computer codes such as MMLE3 [7], which was originally developed to run on large mainframe computers, implement the ML method. MATLAB, a numerical methods software package for microcomputers, includes an implementation of MMLE3 called the State-Space Systems Identification Toolbox (SSSIT) [8]. A complete description of the MMLE3 formulation is given in references [7,8,9]. The ML method also provides an indicator of the estimated accuracy by calculating a Cramer-Rao bound for each parameter. Under most circumstances, the Cramer-Rao bound represents the standard deviation of a parameter.

The type of PE algorithm is only one decision that needs to be made. Two other choices of particular interest are the experimental conditions and the input signals. Issues to consider with the former includes the sampling rate, what exactly to measure and how to prefilter the raw data. The input signal also affects the experiment. A poor choice can lead to numerical difficulties or even more dangerous, poor estimates without any indication of numerical difficulty. The input must be "persistently exciting", a term which can be defined mathematically; suffice it to say that over the course of the experiments, all modes of the system and all combinations of parameters must be perturbed. Since the tests are often driven by computer, a good choice for the inputs is often a Pseudo Random Binary Sequence (PRBS), where the signal randomly switches between two levels at a given clock period. For helicopter flight testing, PRBS signals cannot be employed, as they may cause unsafe operating conditions. For example, while running a computer simulation of the simplified longitudinal dynamics of a helicopter in hover, simulation results showed the helicopter getting into a dangerously unstable phugoid mode. It is for this reason that various control input strategies have been proposed for helicopter PE. The most widely used is the DFVLR '3211' and now the 'M3211' developed at the NAE of NRCC [1,2]. This modified 3211 sequence effectively reduces the tendency for an aircraft to depart from the trimmed flight condition by reducing the magnitude of the initial pulse.

SYSTEM IDENTIFICATION

MMLE3 is a batch processing technique, i.e. the algorithm operates on the entire data set simultaneously. Data is first collected to time 't' and then a "single-shot" estimate is made. MMLE3 does this a number of times in order to iterate to an accurate estimate of the model parameters. The difficulty with batch processing is that computer memory and time increases with the length of the data set:

$$z_t = [\ z(t), z(t-1) \ldots z(1)\ ] \tag{5}$$

which is the entire data record up to time t. The solution to the memory constraint problem is to condense z_t into an auxiliary memory quantity S(t) of fixed dimensions. Recursive SI algorithms are of the form:

$$\theta'(t) = F(\ \theta'(t-1),\ S(t),\ z(t)\ )$$

$$S(t) = H(\ S(t-1),\ \theta'(t-1),\ z(t)\ ) \qquad (6)$$

$$y'(t+1) = M(\ \theta'(t),\ S(t)\ )$$

where ' denotes an estimate of the true value and y is the output of the system. Since the current parameter estimate θ'(t) is found from the previous estimates, the current auxiliary variable and current measurement, there is only the need to store θ'(t) and S(t), arrays that do not increase in size over time.

The recursive SI problem is simply to choose i) the model M in eq.(6), ii) the experimental conditions, including the input signal and iii) the functions F and H in eq.(6). However, the general opinion in the engineering community is that recursive SI is a "bag of tricks" [6] or "a fiddler's paradise" [10]. It is more constructive to take the view of [6]; "...There is only one recursive identification algorithm. It contains some design variables to be chosen by the user."

The first choice that has to be made is the model set which will represent the true system. If the data is sampled in discrete time, a natural selection would be a linear difference equation or ARMAX model:

$$A(z^{-1})\ y(t) = B(z^{-1})\ u(t) + C(z^{-1})\ e(t) \qquad (7)$$

Here, y is the value of the output variable (or vector of variables if a MIMO system), u, the control variable, e, uncorrelated or "white" noise and z is the backward shift operator such that:

$$z^{-1}\ y(t) = y(t-1) \qquad (8)$$

If the system is MIMO, as in the case of the helicopter, A, B and C are z matrix polynomials and eq.(7) can also be written as:

$$\begin{aligned} \underline{y}(t) &= \theta(t)\ \phi(t) + \underline{e}(t) \\ &= [A_1 \ldots A_n,\ B_1 \ldots B_m,\ C_1 \ldots C_r]\ x \\ &\quad \{-\underline{y}(t-1)^T \ldots -\underline{y}(t-n)^T,\ \underline{u}(t-1)^T \ldots \underline{u}(t-m)^T, \\ &\quad \underline{e}(t-1)^T \ldots \underline{e}(t-r)^T\} + \underline{e}(t) \end{aligned} \qquad (9)$$

With the chosen model set, there are different ways of calculating the "best" estimate of θ. Least Squares (LS) strives to minimize the equation error:

$$V(\theta) = \frac{1}{N} \sum^{N} a_t\ [y(t) - \theta(t)\ \phi(t)]^2 \qquad (10)$$

Here, $C(z^{-1})$ is chosen to be the identity matrix and a_t is a factor which changes the weights given to different measurements. If the actual noise model is not unity then LS can give biased estimates of the parameters. LS has a criterion function which is quadratic in θ and so, can be minimized analytically. In general, this is not the case with other Recursive Prediction Error Methods (RPEM), and so approximations must be made in minimizing the equation error, V(θ). The approximations are dependent on the choice of model. An example of RPEM is Extended Least Squares (ELS) where the noise model is estimated along with $A(z^{-1})$ and $B(z^{-1})$.

A compromise between a good description of the data and complexity is required when choosing model order. Soderstrom [11] reviews many model order determination techniques, two of which will be used here. Both give a measure of the trade-off between the modelling error and the number of model parameters. As the model order increases, the loss function $V_n(\theta)$ decreases. Statistical tests can be used to determine whether this loss is significant. If $V_n(\theta)$ is achieved for a model with n parameters and $V_m(\theta)$ by a model whose number of parameters has been increased to m, then the statistic:

$$F_{n-m} = \frac{V_n - V_m}{V_m} \cdot \frac{N - m}{m - n} \qquad (11)$$

is F(m-n, N-m: α) distributed, where N is the number of sampling points and α is the risk of error, typically chosen to be between 0.005 and 0.1.

This compromise may also be described by a figure of merit or "criterion function". The most widely used is Akaike's Information Criteria (AIC) [12], given by:

$$AIC = -2 \log L + 2\ v \qquad (12)$$

AIC represents a compromise between the maximum of the likelihood function, L, and the number of model parameters, v, and should be minimum for a correct model. The likelihood function is defined as:

$$\begin{aligned} L = -\exp(\ & N \log 2\pi + N \log R_v \\ & + R_v\ \Sigma^N\ e^2(k)) \end{aligned} \qquad (13)$$

where $R_v = 1/n\ \Sigma^N\ e^2(k)$ is the variance of the equation error.

RESULTS

The algorithms are tested by using the nonlinear Bell-205 simulation to generate the raw trials data. The simulation was run at a sampling rate of 10 Hz. A single cycle sine wave of magnitude ±10% to the main rotor longitudinal cyclic and collective control was used as the input series.

A preliminary result of helicopter PE is illustrated in Fig. 2. Here, estimation is limited to the so-called "longitudinal" dynamics of the Bell-205 helicopter; this consists of the surge, heave and pitch motions. A continuous LTI model is proposed:

$$\begin{bmatrix} \dot{u} \\ \dot{w} \\ \dot{q} \\ \dot{\theta} \end{bmatrix} = \begin{bmatrix} p_1 & p_2 & 0 & k_1 \\ p_3 & p_4 & p_5 & k_2 \\ p_6 & p_7 & p_8 & 0 \\ 0 & 0 & 1 & 0 \end{bmatrix} \begin{bmatrix} u \\ w \\ q \\ \theta \end{bmatrix} + \begin{bmatrix} p_9 & p_{10} \\ p_{11} & p_{12} \\ p_{13} & p_{14} \\ 0 & 0 \end{bmatrix} \begin{bmatrix} \delta_e \\ \delta_p \end{bmatrix} \qquad (14)$$

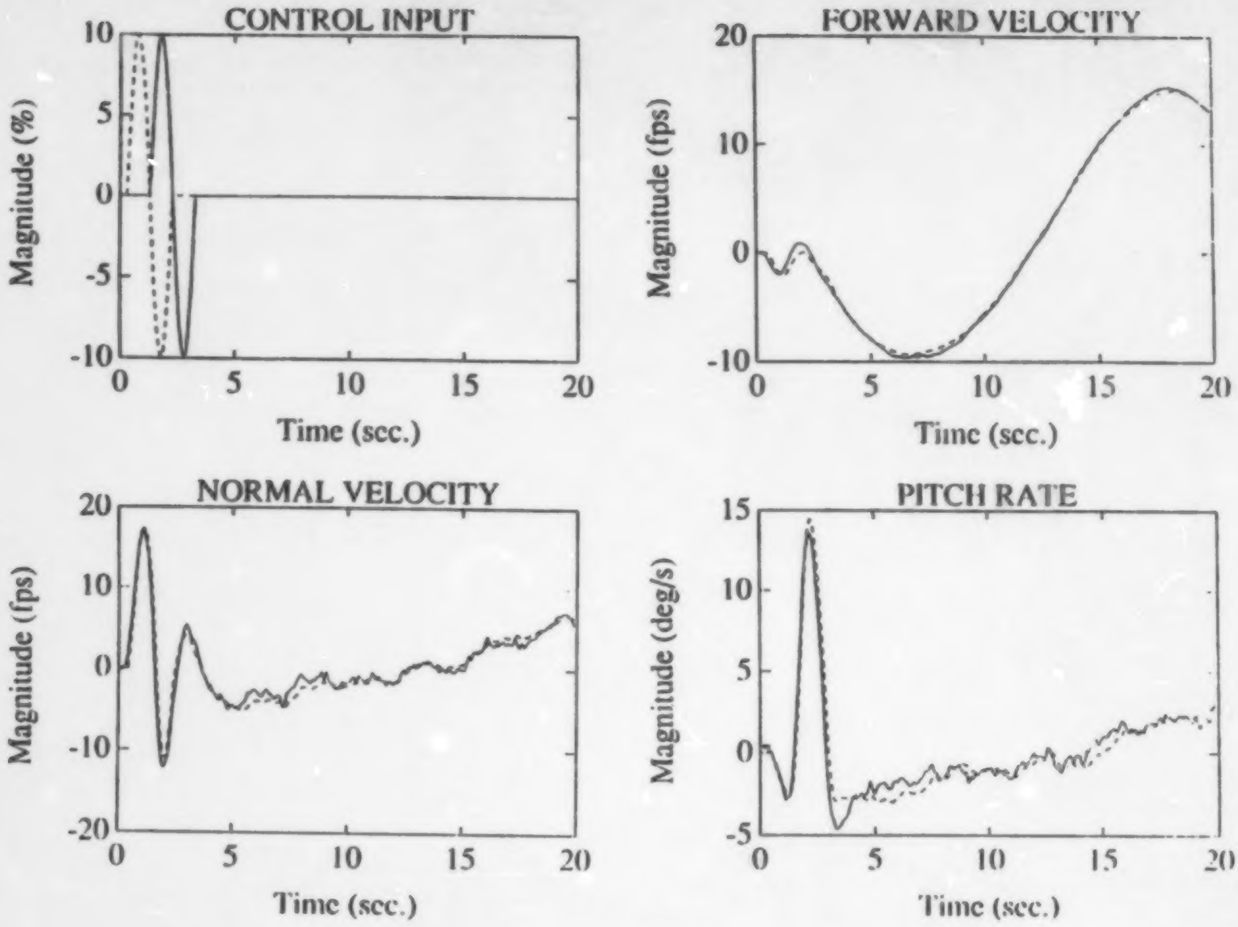
CONTROL INPUT

FORWARD VELOCITY

NORMAL VELOCITY

PITCH RATE

Fig.2 PE Results (— = simulated, - - - = estimated)

The results of SI, illustrated in Fig. 3, show that the non-linear simulation is characterised very well. The orders of $A(z^{-1})$ and $B(z^{-1})$ were increased together starting from 1 until the optimal order was determined.

Though not listed here, the criterion functions' minima shows that surge, heave and pitch rate are adequately represented by first order descriptions. The F statistics also indicate these model orders are best.

CONCLUSIONS

Preliminary studies indicate that multi-input/multi-output recursive SI can be applied advantageously to the problem of modelling helicopter dynamics.

Modelling helicopter flight dynamics by these methods compared with the conventional batch PE approach can result in great computational savings. These savings occur because the SI algorithms are cast in a recursive form, allowing them to be run on low cost personal computers.

The Least Squares method was used for SI. Statistical tests indicated that all of the nonlinear dynamics which are thought to be essential in modelling a helicopter's flight performance are conveniently lumped into low order linear models about given operating points.

Once a reliable and efficient method for helicopter model derivation by SI is established, it is planned to use the model for control system experimentation and design. One potential area of research will be the integration of a predictor of the heaving motion of a ship's flight deck with the autopilot, in order to aid in helicopter operations at sea. In addition, real-time, recursive SI is a requirement for adaptive closed-loop control, where the performance of the helicopter is estimated continuously and the controller gains adjusted accordingly.

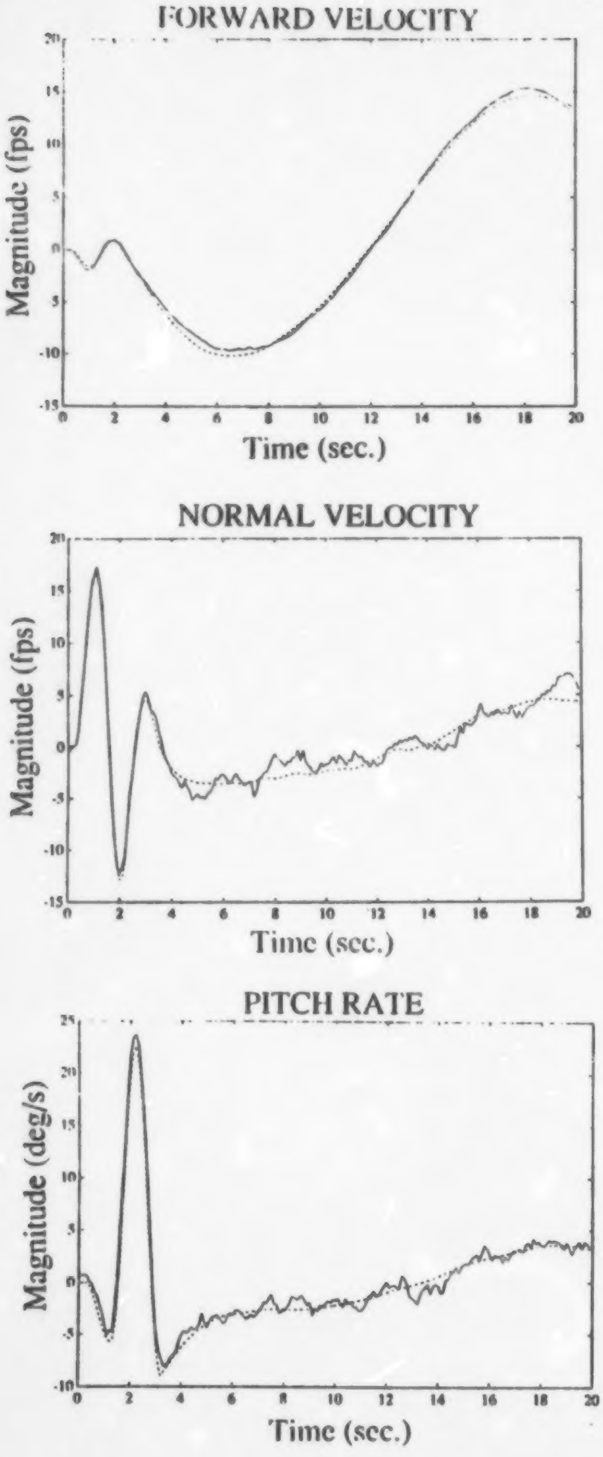

Fig.3 SI Results (— = simulated, - - - = identified)

ACKNOWLEDGEMENTS

The work described here was supported by the Natural Sciences and Engineering Research Council of Canada. The NRC Flight Research Laboratory kindly gave us access to the flight test data.

REFERENCES

[1] Kobierski, R. D. & Sattler, D. E., Flight Test and Data Analysis Techniques for Helicopter Parameter Estimation, CASI Journal, Vol.34,no.4,pp.213-223,1988.

[2] deLeeuw, J. H. & Hui, K., The Application of Linear Maximum Likelihood Estimation of Aerodynamic Derivatives for the Bell-205 and Bell-206. NAE-AN-48, NRC # 28442, National Research Council Canada, Ottawa, October 1987.

[3] Kobiersky, R. D., Flight Test Techniques for Helicopter Parameter Estimation, M.Eng. thesis, Carleton University, Ottawa, Canada, 1988.

[4] Bramwell, A. R. S., Helicopter Dynamics, Edward Arnold Publishers Ltd., London, 1976.

[5] Etkin, B., Dynamics of Flight - Stability and Control, John Wiley & Sons, second edition, 1982.

[6] Ljung, L. & Soderstrom, T., Theory and Practice of Recursive Identification, MIT Press, Cambridge, Mass., 1983.

[7] Maine, R. E. & Iliff, K. W., Users Manual for MMLE3, a General FORTRAN Program for Maximum Likelihood Parameter Estimation. NASA Technical Paper 1563, 1980.

[8] Milne, G. W., State-Space Identification Tool: User's Guide, The MathWorks, Inc., MA., 1988.

[9] Iliff, K. W., Maine, R. E. & Montgomery, T. D., Important Factors in the Maximum Likelihood Analysis of Flight Test Maneuvers, NASA Technical Paper 1459, 1979.

[10] Astrom, K. J. & Eykoff, P., System identification - a Survey, Automatica, Vol. 7, pp. 123 - 162, 1971.

[11] Soderstrom, T., On Model Order Testing in System Identification, Int. J. Control, Vol. 26, pp. 1 - 18, 1977.

[12] Akaike, H., Use of an Information Theoretic Quantity for Statistical Model Identification, Proc. 5th Hawaii Int. Conf. System Science, pp. 249 -250, 1972.

Symbolic Closed-Form Dynamics of Rigid/Flexible Hybrid Multibody Systems Subject to Control

J. Lieh and I. Haque

Mechanical Engineering Department
Clemson University
Clemson, South Carolina 29634

ABSTRACT

An efficient symbolic algorithm of equation formulation for rigid and flexible bodies is developed from the principle of virtual work. The algorithm is cast in a form that facilitates computer programming and simplifies matrix computation. Principal body coordinates and an accelerating reference frame are used in the formulation. Euler-Bernoulli beam theory and the assumed-mode method are adopted to represent elastic members. The integration of shape function related expressions of elastic modes are performed symbolically. The output linear/nonlinear symbolic equations may be obtained either in syntactically correct FORTRAN form or in the form as derived by hand. The equations are linearized symbolically through a subroutine developed by authors. Several examples are used to validate the program. Included are an elastic pendulum on vibrating foundation and a flexible manipulator with link and joint flexibility. Simulation results of the flexible manipulator with step input are presented.

INTRODUCTION

General-purpose programs to model multibody system such as robots, spacecrafts, mechanisms and vehicle systems has greatly attracted the attention of those who have been working in the field. Computer implementation of these schemes requires that they be recast in a form that makes them computationally attractive. A great deal of research has been involved in developing numerical programs based on several approaches [1-9]. The drawbacks of the numerical method of equation generation [10-14] include: 1) the algorithm needs to repeatedly set up the equations of motion for each computation or integration, 2) it is difficult to implement the control strategies in numerical equations, and 3) numerical expressions do not provide the physical insight into a system. Symbolic formulation overcomes these problems. Several symbolic programs based on various dynamic formulations have been developed in past decade [15-25]. However, they have been restricted to the dynamics of rigid mechanical systems with open chain topology. Symbolic programs for flexible mechanical systems can be found in [26-27]. These have been more or less limited in application to robotic manipulators.

The need for research in the dynamics of flexible systems was first stimulated by the higher operating speed and better positioning accuracy requirement of mechanisms [28-29] and flexible spacecrafts [30] in 1970s. Traditional analysis using rigid-body models was considered inadequate to predict and control the dynamic behavior of such systems. Instead, mathematical models assuming deformable bodies were deemed necessary. More recently, increasing research in the dynamics and controls of flexible manipulators has renewed interest in these areas [31-37]. This was due to the increasing application of robots in hazardous or unpleasant environments, factory automation and space. Requirements for safety, accuracy, productivity and mobility or other improved conditions are becoming important because of legislation, higher quality and lower cost performance for international competition, and applications in space. Long term success in domestic and international competitive environments depends on these high performances. To meet these requirements, much attention has been paid to the design, simulation and control of high speed and light manipulators. Thus the ease and efficiency with which one can formulate a mathematical model for rigid/elastic mechanical systems such that it may facilitate computer programming, and increase formulation and computational efficiency became important.

In this paper, computerized symbolic closed-form dynamics of constrained multibody systems subject to control is presented. The formulation considered here is for rigid/elastic hybrid multibody systems with flexible bodies undergoing large rigid body motions and small elastic deformations. Separation of variables technique is adopted to represent the solution of elastic deformation of flexible beams. The assumed-mode method containing a finite number of the lower modes is used to approximate the deformation.

Methods of Equation Formulation

The most commonly used methods for deriving the dynamic equations include Newton-Euler method [38-39], d'Alembert's principle [40], Lagrange's method [41-42], Lagrange-Euler equations [43], Hamilton's canonical equations and Hamilton's principle [44]. Each method possesses its own merits because of its specific procedure of constructing dynamic equations. The choice of algorithms, kinematic frames and system variables may also influence the efficiency of formulation as well as the computation in simulation and control. These methods are considered inefficient either in eliminating the workless forces, Lagrange's multipliers or redundant coordinates, or in differentiating the energy functions for complex constrained mechanical systems. The other methods being relatively less familiar include Boltzmann-Hamel (Lagrange's quasi-coordinate) equations, Gibbs-Appell's equations [45] and Lagrangian form of d'Alembert's principle [46]. The Gibbs-Appell's equations are derived from Gibbs' function which is defined by kinetic energy of acceleration. This method is considered less laborious than the previously mentioned approaches because there are no momenta generated. The differentiation is very straightforward and workless constraint forces do not appear in the procedure.

The principle of virtual work [46] states that the work done by a system in static equilibrium undergoing an arbitrary virtual displacement vanishes. The use of inertia forces in d'Alembert's principle makes a dynamic system equivalent to being in static equilibrium. From this standpoint, the work done by all forces/torques including inertia forces/torques in an arbitrary virtual displacement vanishes. It is salient that the workless constraint forces can be dropped out from the virtual work equation. This method is also called Lagrangian form of d'Alembert's principle. By collecting the coefficients of independent virtual displacements, one obtains the dynamic equations in the form as proposed by Kane et al [47-48].

Representation of Elastic Members

An elastic system requires infinite degrees of freedom to describe its dynamic deformation behavior and finite number degrees of freedom to describe the nominal rigid motion. The governing equations of a hybrid rigid and elastic dynamic model are coupled, nonlinear partial-ordinary mixed differential equations in integral-differential form. Since it is not possible to analysis a system consisting of infinite degrees of freedom, simplified models with finite coordinates have always been assumed. In order to discretize a continuous system, several methods such as finite element method (FEM) [29,34-36] including stiffness method and force matrix method, finite difference method (FDM) [9,28], and the assumed-mode method (AMM) [7-8,33] have been used to represent the transient response of elastic members. The FEM uses the corners or ends as nodes which form the field variables. In the stiffness method, the nodal displacements are assumed to be unknowns. On the other hand, the force matrix method utilizes internal forces as field variables. The nodes for

FDM (or sometimes called lumped-parameter method) are usually located at the geometric center of its lump. This method assumes that the entire lump has the same property. In general, the mode shapes are transcendental functions that consist of infinite number of natural frequencies and normal modes, which are solved through given boundary conditions. Not only will the boundary conditions influence natural frequencies and shape functions but also the material density, cross section and shape of the body. The assumed-mode method assumes that only some lower modes dominate the transient response and truncates the higher modes. Hastings and Book [32] showed that a dominant portion of the response of a flexible manipulator is adequately characterized by as few as two modes.

PRINCIPLE OF VIRTUAL WORK

The procedure for obtaining equations of motion using principle of virtual work is recognized as one of the most powerful tools because of its efficiency, less labor, and suitability to computers. The construction of energies, complex differentiation, and elimination of multipliers and workless constraint forces may be avoided. The formulation presented here is based on an improved algorithm for multibody systems derived by Lieh and Haque [49]. The advantage of this algorithm is that it simplifies the procedure of formulation and is highly suitable for computer programming. It also automatically eliminates the workless constraint forces and redundant coordinates and gives the equations in closed-form. Another advantage is that the formulation is in expanded form thus eliminating some of the tedious matrix computation.

The conventional form of principle of virtual work can be written as follows,

$$\sum_{i=1}^{n_r}\left\{\delta\vec{R}_i\cdot(m_i\vec{a}_i-\vec{F}_i)+\delta\vec{\pi}_i\cdot(\dot{\vec{H}}_i-\vec{T}_i)-\delta W_i\right\}$$

$$+\sum_{i=1}^{n_f}\left(\int_0^{L_i}\delta\vec{R}^f_i\cdot(\vec{a}^f_i dm_i-d\vec{F}^f_i)-\delta W^f_i\right)=0 \qquad (1)$$

where i represents the i^{th} body and superscript ^{f} represents a flexible body. $\delta\vec{R}_i$ and $\delta\vec{\pi}_i$ are virtual linear and angular displacements, m_i is the mass, $\vec{a}_i$ is the linear acceleration, $\vec{H}_i$ is the angular momentum, $\vec{F}_i$ and $\vec{T}_i$ are external force and torque, W_i is the work not done by $\vec{F}_i$ and $\vec{T}_i$, and n_r and n_f are the number of rigid and elastic bodies.

Rigid Bodies - Order Reduction and Closed Form Dynamics

The algorithm for rigid bodies can possibly be simplified by the choice of body-fixed principal coordinate systems. In this case the time derivative of angular momentum of i^{th} body can be expressed as:

$$\dot{\vec{H}}_i=\vec{\vec{I}}_i\cdot\dot{\vec{\omega}}_i+\vec{\omega}_{fi}\times\vec{\vec{I}}_i\cdot\vec{\omega}_i \qquad (2)$$

where $\vec{\vec{I}}_i$ is the principal inertia tensor, $\vec{\omega}_i$ and $\vec{\omega}_{fi}$ are the angular velocity of i^{th} body and body frame. To convert the dot product of the vector-dyadic into matrix-vector manipulation to facilitate programming, it is intended to express each term of equation (1) in terms of a set of arbitrarily chosen virtual displacements $\delta\underline{q}$, Jacobian matrices $\underline{J}_{vi}$ and $\underline{J}_{\omega i}$, and principal unit direction vector $\vec{\underline{\varepsilon}}_i$. This results in matrix-vector manipulation since $\vec{\underline{\varepsilon}}_i\cdot\vec{\underline{\varepsilon}}_i^T$ is a 3 by 3 identity matrix and can be dropped from equation, i.e.,

$$\delta\underline{q}^T\sum_{i=1}^{n_r}\left\{\underline{J}_{vi}^T(m_i\underline{a}_i-\underline{F}_i)+\underline{J}_{\omega i}^T(\dot{\underline{H}}_i-\underline{T}_i)-\underline{F}_{qi}\right\} \qquad (3)$$

The dynamic equations are obtained by collecting the coefficients for each virtual variable. The coefficients will not vanish unless all the virtual variables are independent. To achieve this, the constraint equations are introduced,

$$\underline{f}(\dot{\underline{q}},\underline{q},t)=\underline{0} \qquad (4)$$

By use of generalized coordinate partitioning technique [12, 49] to partition $\underline{q}$ into $[\underline{x}^T,\underline{q}_d^T]^T$, it is possible to express the dependent variables $\dot{\underline{q}}$ in terms of independent variables $\dot{\underline{x}}$.

$$\dot{\underline{q}}=\underline{C}_v(\underline{q},t)\,\dot{\underline{x}}+\underline{D}_v(\underline{q},t) \qquad (5)$$

$$\delta\underline{q}=\underline{C}_v(\underline{q},t)\,\delta\underline{x} \qquad (6)$$

The absolute linear velocity of the i^{th} body with respect to its own body frame can be expressed by,

$$\underline{V}_i=\underline{J}_{vi}(\underline{q},t)\dot{\underline{q}}+\underline{V}_{ti}(\underline{q},t) \qquad (7a)$$

By substituting the constraint equations (5) into the velocity vector, one expresses the velocity in independent space $\dot{\underline{x}}$ as

$$\underline{V}_i=\underline{J}_{vi}(\underline{C}_v\dot{\underline{x}}+\underline{D}_v)+\underline{V}_{ti}=\underline{J}_{vci}\dot{\underline{x}}+(\underline{J}_{vdi}+\underline{V}_{ti}) \qquad (7b)$$

The absolute angular velocities of i^{th} body and body frame with respect to the body frame can also be found as follows,

$$\underline{\omega}_i=\underline{J}_{\omega ci}\dot{\underline{x}}+(\underline{J}_{\omega di}+\underline{\omega}_{ti}) \qquad (8)$$

$$\underline{\omega}_{fi}=\underline{J}_{fci}\dot{\underline{x}}+(\underline{J}_{fdi}+\underline{\omega}_{fti}) \qquad (9)$$

The linear acceleration of i^{th} rigid body is derived by differentiating velocity in (7b).

$$\underline{a}_i=\underline{J}_{vci}\ddot{\underline{x}}+\dot{\underline{J}}_{vci}\dot{\underline{x}}+\tilde{\underline{\omega}}_{fi}(\underline{J}_{vci}\dot{\underline{x}}+\underline{J}_{vdi}+\underline{V}_{ti})+\dot{\underline{J}}_{vdi}+\dot{\underline{V}}_{ti} \qquad (10)$$

Analogously, the time derivative of angular momentum becomes,

$$\dot{\underline{H}}_i=\underline{I}_i\underline{J}_{\omega ci}\ddot{\underline{x}}+\underline{I}_i\dot{\underline{J}}_{\omega ci}\dot{\underline{x}}+\tilde{\underline{\omega}}_{fi}\underline{I}_i(\underline{J}_{\omega ci}\dot{\underline{x}}+\underline{J}_{\omega di}+\underline{\omega}_{ti})$$

$$+\underline{I}_i(\dot{\underline{J}}_{\omega di}+\dot{\underline{\omega}}_{ti}) \qquad (11)$$

where $\underline{I}_i$ is the diagonal principal inertia matrix and $\tilde{\underline{\omega}}_{fi}$ is the skew-symmetric matrix of angular velocity of body frame $\underline{\omega}_{fi}$.

Substitution of (6), (10) and (11) in (3) will result in a simplified algorithm. The dynamic equations for rigid bodies are therefore obtained by collecting the coefficients of independent virtual displacement vector $\delta\underline{x}^T$, i.e.,

$$\sum_{i=1}^{n_r}\Big\{m_i\underline{J}_{vci}^T[\underline{J}_{vci}\ddot{\underline{x}}+\dot{\underline{J}}_{vci}\dot{\underline{x}}+\tilde{\underline{\omega}}_{fi}(\underline{J}_{vci}\dot{\underline{x}}+\underline{J}_{vdi}+\underline{V}_{ti})+\dot{\underline{J}}_{vdi}+\dot{\underline{V}}_{ti}]$$

$$+\underline{J}_{\omega ci}^T[\underline{I}_i\underline{J}_{\omega ci}\ddot{\underline{x}}+\underline{I}_i\dot{\underline{J}}_{\omega ci}\dot{\underline{x}}+\tilde{\underline{\omega}}_{fi}\underline{I}_i(\underline{J}_{\omega ci}\dot{\underline{x}}+\underline{J}_{\omega di}+\underline{\omega}_{ti})$$

$$+\underline{I}_i(\dot{\underline{J}}_{\omega di}+\dot{\underline{\omega}}_{ti})]-\underline{J}_{vci}^T\underline{F}_i-\underline{J}_{\omega ci}^T\underline{T}_i-\underline{F}_{xi}\Big\} \qquad (12)$$

$\dot{\underline{J}}_{vci}$, $\dot{\underline{J}}_{\omega ci}$, $\dot{\underline{J}}_{vdi}$, $\dot{\underline{J}}_{\omega di}$, $\dot{\underline{V}}_{ti}$ and $\dot{\underline{\omega}}_{ti}$ can be expanded as partial derivatives with respect to $\underline{q}$ and t. As before, the dependent variables $\dot{\underline{q}}$ are to be substituted by independent variables $\dot{\underline{x}}$ from (5), which results in,

$$\dot{\underline{J}}_{vci}=\left[\frac{\partial J_{vcijk}}{\partial\underline{q}}\underline{C}_v\dot{\underline{x}}\right]+\left[\frac{\partial J_{vcijk}}{\partial\underline{q}}\underline{D}_v+\frac{\partial J_{vcijk}}{\partial t}\right] \qquad (13a)$$

$$\dot{\underline{J}}_{\omega ci}=\left[\frac{\partial J_{\omega cijk}}{\partial\underline{q}}\underline{C}_v\dot{\underline{x}}\right]+\left[\frac{\partial J_{\omega cijk}}{\partial\underline{q}}\underline{D}_v+\frac{\partial J_{\omega cijk}}{\partial t}\right] \qquad (13b)$$

where j=1 to 3, k=1 to DOF and DOF represents degrees of freedom.

$$\dot{\underline{J}}_{vdi}+\dot{\underline{V}}_{ti}=\frac{\partial}{\partial\underline{q}}(\underline{J}_{vdi}+\underline{V}_{ti})\underline{C}_v\dot{\underline{x}}+\frac{\partial}{\partial\underline{q}}(\underline{J}_{vdi}+\underline{V}_{ti})\underline{D}_v$$

$$+\frac{\partial}{\partial t}(\underline{J}_{vdi}+\underline{V}_{ti}) \qquad (13c)$$

$$\dot{\underline{J}}_{\omega di}+\dot{\underline{\omega}}_{ti}=\frac{\partial}{\partial\underline{q}}(\underline{J}_{\omega di}+\underline{\omega}_{ti})\underline{C}_v\dot{\underline{x}}+\frac{\partial}{\partial\underline{q}}(\underline{J}_{\omega di}+\underline{\omega}_{ti})\underline{D}_v$$

$$+\frac{\partial}{\partial t}(\underline{J}_{\omega di}+\underline{\omega}_{ti}) \qquad (13d)$$

The dynamic equations represented by (12) are therefore in order-reduced form. The equations can be put in closed-form by substituting (9) into the skew-symmetric matrix, $\tilde{\omega}_{fl}$, and (13a-d) into (12) and formulating the inertia term, centrifugal/coriolis and other terms separately. Details of the expanded closed-form equations can be found in [49].

Elastic Bodies - Assumed Mode Method and Closed Form Equations

In order to obtain the formulation, elastic deformations consisting of transverse bending, longitudinal and torsional deformations are considered. $U_{xl}(r_l,t)$ and $U_{yl}(r_l,t)$ represent the transverse deformations. $U_{rl}(r_l,t)$ and $U_{tl}(r_l,t)$ represent the longitudinal and torsional deformations. Consider there are n_m lowest assumed modes dominating the system, thus,

$$U_{xl}(r_l,t) = \sum_{p=1}^{n_m} U_{xlp}(r_l)\,\xi_{lp}(t); \quad U_{yl}(r_l,t) = \sum_{p=1}^{n_m} U_{ylp}(r_l)\,\psi_{lp}(t)$$

$$U_{rl}(r_l,t) = \sum_{p=1}^{n_m} U_{rlp}(r_l)\,\zeta_{lp}(t); \quad U_{tl}(r_l,t) = \sum_{p=1}^{n_m} U_{tlp}(r_l)\,\alpha_{lp}(t) \tag{14}$$

where U_{xlp}, U_{ylp}, U_{rlp} and U_{tlp} are shape functions, and ξ_{lp}, ψ_{lp}, ζ_{lp} and α_{lp} represent the time dependent generalized coordinates. The strain energy of the elastic beam is expressed in the following general form,

$$W_l^f = \frac{1}{2}\int_0^{L_l}\Big[E_l I_{xl}\Big(\frac{\partial^2 U_{xl}}{\partial r_l^2}\Big)^2 + E_l I_{yl}\Big(\frac{\partial^2 U_{yl}}{\partial r_l^2}\Big)^2 + E_l A_l\Big(\frac{\partial U_{rl}}{\partial r_l}\Big)^2 + G_l I_{pl}\Big(\frac{\partial U_{tl}}{\partial r_l}\Big)^2\Big]dr_l \tag{15}$$

where E_l and G_l are the moduli of elasticity and rigidity; I_{xl} and I_{yl} are the area moment of inertia, I_{pl} is the polar moment of inertia, and A_l is the area of cross section.

The general form of the shape function for transverse deformations of a beam is,

$$U_{lp}(r_l) = A_{lp}\cos(\lambda_{lp} r_l) + B_{lp}\sin(\lambda_{lp} r_l) + C_{lp}\cosh(\lambda_{lp} r_l) + D_{lp}\sinh(\lambda_{lp} r_l) \tag{16a}$$

and for longitudinal and torsional deformations,

$$U_{lp}(r_l) = E_{lp}\cos(\eta_{lp} r_l) + F_{lp}\sin(\eta_{lp} r_l) \tag{16b}$$

If the beam contains rigid body modes, the shape function will be replaced by polynomial functions of r_l. The eigenvalues and the coefficients may be found by a given set of boundary conditions. The integration of mode shape related functions may be simplified by applying the orthogonal property of shape functions. However, this may not be achieved if the boundary conditions are dependent on eigenvalues or are time-varying.

As shown in Figure 1, the position vector of an arbitrary point p_l located between o_l and L_l of l^{th} flexible body is given by:

$$\vec{R}_l^f = \vec{R}_{lo} + (r_l + U_{rl})\vec{e}_{rl} + U_{xl}\vec{e}_{xl} + U_{yl}\vec{e}_{yl} = \vec{R}_{lo} + \vec{\underline{e}}_l^T \underline{U}_l \tag{17}$$

The velocity is obtained by differentiating (17) with respect to time. By dropping the unit directional vector, the velocity of point p_l becomes,

$$\underline{V}_l^f = (\dot{\underline{R}}_{lo} + \tilde{\omega}_{fl}\,\underline{R}_{lo}) + (\dot{\underline{U}}_l + \tilde{\omega}_{fl}\,\underline{U}_l) \tag{18}$$

or in the form similar to (7b),

$$\underline{V}_l^f = (\underline{J}_{rl}(\underline{q},t) + \underline{J}_{ul}(\underline{q},t))\dot{\underline{q}} + \underline{V}_{tl}^f(\underline{q},t) = \underline{J}_{vcl}^f\dot{\underline{x}} + \underline{J}_{vdl}^f + \underline{V}_{tl}^f \tag{19}$$

The acceleration is then obtained by differentiating (19),

$$\underline{a}_l^f = \underline{J}_{vcl}^f\ddot{\underline{x}} + \dot{\underline{J}}_{vcl}^f\dot{\underline{x}} + \tilde{\omega}_{fl}(\underline{J}_{vcl}^f\dot{\underline{x}} + \underline{J}_{vdl}^f + \underline{V}_{tl}^f) + \dot{\underline{J}}_{vdl}^f + \dot{\underline{V}}_{tl}^f \tag{20}$$

Similar to (3), the dot product is converted in matrix-vector form. Using the procedure from (4) to (12) and dropping the independent virtual displacement vector $\delta\underline{x}^T$, one gains the dynamic equations of elastic bodies as follows,

$$\sum_{l=1}^{nf}\Big\{\int_0^{L_l}\rho_l \underline{J}_{vcl}^{f\,T}\big(\underline{J}_{vcl}^f\ddot{\underline{x}} + \dot{\underline{J}}_{vcl}^f\dot{\underline{x}} + \tilde{\omega}_{fl}(\underline{J}_{vcl}^f\dot{\underline{x}} + \underline{J}_{vdl}^f + \underline{V}_{tl}^f) + \dot{\underline{J}}_{vdl}^f + \dot{\underline{V}}_{tl}^f\big)dr_l - \int_0^{L_l}\underline{J}_{vcl}^{f\,T}d\underline{F}_l^f - \underline{F}_{xl}^f\Big\} \tag{21}$$

The derivatives $\dot{\underline{J}}_{vcl}^f$, $\dot{\underline{J}}_{vdl}^f$ and $\dot{\underline{V}}_{tl}^f$ in (21) are expanded in independent space $\dot{\underline{x}}$, i.e.,

$$\dot{\underline{J}}_{vcl}^f = \Big[\frac{\partial}{\partial \underline{q}}(J_{vcljk}^f)\underline{C}_v\dot{\underline{x}}\Big] + \Big[\frac{\partial}{\partial \underline{q}}(J_{vcljk}^f)\underline{D}_v + \frac{\partial}{\partial t}(J_{vcljk}^f)\Big] \tag{22a}$$

$$\dot{\underline{J}}_{vdl}^f + \dot{\underline{V}}_{tl}^f = \Big[\frac{\partial}{\partial \underline{q}}(\underline{J}_{vdl}^f + \underline{V}_{tl}^f)\Big]\underline{C}_v\dot{\underline{x}} + \Big[\frac{\partial}{\partial \underline{q}}(\underline{J}_{vdl}^f + \underline{V}_{tl}^f)\Big]\underline{D}_v + \frac{\partial}{\partial t}(\underline{J}_{vdl}^f + \underline{V}_{tl}^f) \tag{22b}$$

where j=1 to 3 and k=1 to DOF. The equations, summation of (12) and (21), are therefore in order-reduced form. They are further expanded by substituting (9), (13a-d) and (22a-b) into the summation, and formulating the inertia term, centrifugal and coriolis term and other terms separately, i.e.,

$$\underline{M}(\underline{q},t)\ddot{\underline{x}} + f_1(\dot{x}_k^2, \dot{x}_k\dot{x}_n, \underline{q}, t) + f_2(\underline{q},t)\dot{\underline{x}} + f_3(\underline{q},t) - \underline{F}_e = \underline{0} \tag{23}$$

where the first term is inertia term, the second is centrifugal and coriolis term, the third corresponds to the relative velocities of bodies and the prescribed velocity of reference frame, the fourth corresponds to the prescribed acceleration of reference frame, and the last is the generalized force.

The formalism obtained above has been implemented in MAPLE [50] by the authors. The algorithm is derived for constrained rigid/elastic hybrid mechanical systems undergoing 3D motion based on an accelerating reference frame. This closed-form dynamic equation formulation lends itself well to symbolic processing and will contribute a significant step forward in saving formulation and computational time and ease of linearization of equations. Another advantage is that the formulation is in expanded form thus eliminating some of the tedious matrix computation.

The closed-form equations expressed in (23) are a complete set of nonlinear equations and are ready for nonlinear analysis and simulation. However, the analysis and control of full nonlinear problems of many degrees of freedom is a difficult task not only because the nonlinear equations are rather complex but also because general control subroutines are mainly available for linear systems. Within acceptable accuracy, particularly for systems undergoing small motion, it is certainly easier to solve linearized equations than nonlinear ones. Since the algorithm is of closed-form, the formulation of centrifugal/coriolis term can be omitted. The details of symbolic linearization can be found in [49].

STATE-SPACE EQUATIONS WITH CONTROL

In order to perform simulation of the linearized equations with control, a subroutine is provided to compute the matrices of the system state equations. The procedure first symbolically linearizes the dynamic equations and then obtains a set of second order differential equations.

$$\underline{M}\ddot{\underline{x}} + \underline{B}\dot{\underline{x}} + \underline{K}\underline{q} + \underline{B}_1\underline{u} + \underline{F}_1(t) = \underline{0} \tag{24}$$

where $\underline{u}$ and $\underline{F}_1$ are the control and environmental inputs. $\underline{q}$ can be replaced by a set of linearized constraint equations.

$$\underline{q} = \underline{C}_L\underline{x} + \underline{D}_L \tag{25}$$

One finally obtains the equations in state-space form using symbolic or numerical matrix manipulation, i.e.,

$$\dot{\underline{z}} = \underline{A}_m\underline{z} + \underline{B}_{m1}\underline{u} + \underline{F}_m$$

$$\underline{y} = \underline{C}_m\underline{z} \tag{26}$$

where

$$\underline{z} = \begin{vmatrix} \underline{x} \\ \dot{\underline{x}} \end{vmatrix} \qquad \Delta_m = \begin{vmatrix} \underline{0} & \underline{I} \\ -\underline{M}^{-1}\underline{K}\,\underline{C}_L & -\underline{M}^{-1}\underline{B} \end{vmatrix}$$

$$B_{m1} = \begin{vmatrix} \underline{0} \\ -\underline{M}^{-1}\underline{B}_1 \end{vmatrix} \qquad E_m = \begin{vmatrix} \underline{0} \\ -\underline{M}^{-1}(\underline{E}_1 + \underline{K}\,\underline{D}_l) \end{vmatrix}$$

$$\underline{u} = [u_1, u_2, u_3, \ldots]^T$$

EXAMPLES

In order to validate the symbolic formulation program, symbolic equations of an elastic pendulum on a vibrating foundation and a flexible manipulator have been formulated. These symbolic equations are the same as those obtained from Lagrange's method. The linearized system equations were converted symbolically by the developed subroutine into the form of (24). The system state equations were then obtained through the procedure of (26). Dynamic behavior of the flexible manipulator with step input is presented.

Example-1: Simple Flexible Pendulum on Vibrating Foundation

The schematic of a simple flexible pendulum on a vibrating foundation is shown in Figure 2. One end of the uniform flexible beam is clamped to a shaft of negligible mass that is free to rotate on the vibrating foundation and the other end is free. The foundation is assumed to vibrate with a velocity of S_0 w cos(wt). The configuration gives the boundary conditions as,

$$U_x(o,t) = \ddot{U}_x(o,t) = 0 \quad \text{and} \quad \ddot{U}_x(l,t) = \dddot{U}_x(l,t) = 0 \tag{27}$$

The lowest four eigenvalues obtained from these boundary conditions are,

$$\lambda_1 L = 1.875104069 \qquad \lambda_2 L = 4.694091133$$
$$\lambda_3 L = 7.854757438 \qquad \lambda_4 L = 10.99554073 \tag{28}$$

and the corresponding shape functions are found as follows,

$$U_{xp}(r) = A_p\left[\cos(\lambda_p r) - \cosh(\lambda_p r)\right] + \sin(\lambda_p r) - \sinh(\lambda_p r) \tag{29}$$

where $A_1 = -1.3622206$, $A_2 = -0.98186754$, $A_3 = -1.0007761$ and $A_4 = -0.9999964$. Rewriting (19) and taking the first two flexible modes, the vector of generalized speeds is therefore $\dot{\underline{q}} = \dot{\underline{x}} = [\dot{\xi}_1, \dot{\xi}_2, \dot{\theta}]^T = [\dot{q}_1, \dot{q}_2, \dot{q}_3]^T$. The symbolic nonlinear and linearized equations formulated by program are listed below.

Nonlinear Equations of Flexible Pendulum

```
0.1855645E1*Lfl*mfl*ddq1+0.7748661E0*Lfl**2*mfl*ddq3-
0.1855645E1*Lfl*mfl*q1*dq3**2-0.1066607E1*Lfl*mfl*So
*w**2*sin(w*t)*cos(q3)+0.1066607E1*Lfl*mfl*g*sin(q3)
+0.2294016E2*E1*Ix1*q1/Lfl**3 = 0
```

```
0.9640631E0*Lfl*mfl*ddq2+0.8912096E-1*Lfl**2*mfl*ddq3-
0.9640634E0*Lfl*mfl*q2*dq3**2-0.4260676E0*Lfl*mfl*So
*w**2*sin(w*t)*cos(q3)+0.4260676E0*Lfl*mfl*g*sin(q3)
+0.4680712E3*E1*Ix1*q2/Lfl**3 = 0
```

```
0.7748661E0*Lfl**2*mfl*ddq1+0.8912096E-1*Lfl**2*mfl*ddq2+
(0.3333333E0*mfl*Lfl**3+0.9640631E0*Lfl*mfl*q2**2+0.185564
5E1*Lfl*mfl*q1**2)*ddq3+0.3711290E1*Lfl*mfl*q1*dq1*dq3+0.1
928126E1*Lfl*mfl*q2*dq2*dq3+0.1066607E1*Lfl*mfl*So*w**2*s
in(w*t)*sin(q3)*q1+0.4260676E0*Lfl*mfl*So*w**2*sin(w*t)
*sin(q3)*q2-0.5000000E0*mfl*So*w**2*sin(w*t)*cos(q3)*Lfl**2
+0.1066607E1*Lfl*mfl*g*cos(q3)*q1+0.4260676E0*Lfl*mfl*g
*cos(q3)*q2+0.5000000E0*mfl*g*sin(q3)*Lfl**2 = 0
```

where Lfl = length of the pendulum (L) and mfl = mass per unit length (ρ).

Linearized Equations of Flexible Pendulum

```
0.7748661E0*Lfl**2*mfl*ddq3+0.1855645E1*Lfl*mfl*ddq1-
0.1066607E1*Lfl*mfl*So*w**2*sin(w*t)+0.1066607E1*Lfl*mfl*g*
q3+0.2294016E2*E1*Ix1*q1/Lfl**3 = 0
```

```
0.8912096E-1*Lfl**2*mfl*ddq3+0.9640631E0*Lfl*mfl*ddq2-
0.4260676E0*Lfl*mfl*So*w**2*sin(w*t)+0.4260676E0*Lfl*mfl*g*
q3+0.4680712E3*E1*Ix1*q2/Lfl**3 = 0
```

```
0.8912096E-1*Lfl**2*mfl*ddq2+0.3333333E0*mfl*Lfl**3
*ddq3+0.7748661E0*Lfl**2*mfl*ddq1-0.5000000E0*mfl*So
*w**2*sin(w*t)*Lfl**2+0.1066607E1*Lfl*mfl*g*q1
+0.4260676E0*Lfl*mfl*g*q2+0.5000000E0*mfl*g*q3*Lfl**2 = 0
```

Example 2: Flexible Manipulator with Link and Joint Flexibility

The schematic of a one-link flexible robot with link and joint flexibility is shown in Figure 3. The elastic robot consists of two rigid bodies: hub and tip payload, a complaint joint between hub and the clamped end of the link, and an elastic link. A torque is applied to the hub. From the configuration in Figure 3, the following boundary conditions are obtained.

$$U_x(o,t) = \dot{U}_x(o,t) = 0 = \ddot{U}_x(L,t) = 0 \quad \text{and}$$

$$EI\dddot{U}_x(L,t) = m_p\left(\ddot{U}_x(L,t) + L(\ddot{\theta}_h + \ddot{\theta}_k) - U_x(L,t)(\dot{\theta}_h + \dot{\theta}_k)^2\right) \tag{30a}$$

The fourth boundary condition can be simplified by using the partial differential equations obtained from Hamilton's principle, i.e.,

$$\dddot{U}_x(L,t) + \frac{m_p}{\rho}\ddddot{U}_x(L,t) = 0 \tag{30b}$$

These boundary conditions result in an eigenexpression,

$$1 + \cos(\lambda L)\cosh(\lambda L) + \frac{M_p}{\rho}\lambda\left[\cos(\lambda L)\sinh(\lambda L) - \sin(\lambda L)\cosh(\lambda L)\right] = 0 \tag{31}$$

where ρ is the mass per length. By specifying a set of parameters, for example $\frac{M_p}{\rho} = 1$ and L = 1 m, the lowest four eigenvalues are computed.

$$\lambda_1 L = 1.24791741 \qquad \lambda_2 L = 4.031139437$$
$$\lambda_3 L = 7.13413224 \qquad \lambda_4 L = 10.25662107 \tag{32}$$

The shape functions, in the same form as (29), can then be computed from the eigenexpression (31). However for this elastic manipulator, $A_1 = -1.15616025$, $A_2 = -0.9940172$, $A_3 = -1.00014631$ and $A_4 = -0.9999054$. Figure 4 show the mode shapes of the first four elastic modes.

Taking the first two flexible modes and arranging the vector of generalized speed as $\dot{\underline{q}} = \dot{\underline{x}} = [\dot{\theta}_h, \dot{\theta}_k, \dot{\xi}_1, \dot{\xi}_2]^T = [\dot{q}_1, \dot{q}_2, \dot{q}_3, \dot{q}_4]^T$, the symbolic nonlinear equations are generated from program accordingly. Assuming small motion, the equations are linearized. The symbolic equations from program are listed below.

```
(0.3333333E0*mfl*Lfl**3+113+m2*Lfl**2)*ddq1+(0.3333333E0
*mfl*Lfl**3+m2*Lfl**2)*ddq2+(0.3218716E0*Lfl**2*mfl
+0.1162957E1*m2*Lfl)*ddq3+(0.4239200E0*Lfl**2*mfl-
0.3015801E0*m2*Lfl)*ddq4-u1 = 0
```

```
(0.3333333E0*mfl*Lfl**3+m2*Lfl**2)*ddq1+(0.3333333E0*mfl
*Lfl**3+m2*Lfl**2)*ddq2+(0.3218716E0*Lfl**2*mfl+0.1162957E1
*m2*Lfl)*ddq3+(0.4239200E0*Lfl**2*mfl-0.3015801E0*m2*Lfl)
*ddq4+0.10E1*k1*q2 = 0
```

```
(0.3218716E0*Lfl**2*mfl+0.1162957E1*m2*Lfl)*ddq1
+(0.3218716E0*Lfl**2*mfl+0.1162957E1*m2*Lfl)*ddq2+(
0.3223548E0*Lfl*mfl+0.1352469E1*m2)*ddq3+(0.3507246E0*Lfl
*mfl-0.3507246E0*m2)*ddq4+0.4061744E1/Lfl**3*E1*Ix1*q3 = 0
```

```
(0.4239200E0*Lfl**2*mfl-0.3015801E0*m2*Lfl)*ddq1
+(0.4239200E0*Lfl**2*mfl-0.3015801E0*m2*Lfl)*ddq2
+(0.3507246E0*Lfl*mfl-0.3507246E0*m2)*ddq3
+(0.9198573E0*Lfl*mfl+0.9095053E-1*m2)*ddq4
+0.2669192E3/Lfl**3*E1*Ix1*q4 = 0
```

where m2 = m_p, Lfl = L and mfl = ρ.

SIMULATION

In order to illustrate the usefulness of the symbolic closed-form algorithm developed in this paper, simulation of the one-link elastic manipulator is presented. A comparison of various joint compliances is made to demonstrate the dynamic behavior of the manipulator. Simulation is based on the model developed previously and is performed using a commercially available numerical package. The input torque is assumed to be a step function. The beam is assumed to be of uniform 5 cm x 0.2 cm cross section, 1 meter length, Young's modulus $EI = 7.1 \times 10^{10}$ N/m^2 and mass per length $m/l = 0.277$ kg/m. The payload mass, $m_p = 0.277$ kg and the moment of inertia of hub, $I13 = 0.8$ kg-m^2. Three values of joint compliance, $k1=5$, 10 and 20 N-m/rad are considered here.

Figure 5 shows the angular displacements of the hub. Small differences are found for three different values of the joint compliance. However, the joint angles in Figure 6 show that the amplitude of joint motion is significantly influenced by joint stiffness. Figure 7 represents the time response of generalized coordinate of mode 1 and Figure 8 represents the time response of generalized coordinate of mode 2. The higher mode has much smaller amplitude than the lower mode, however, it possesses much higher natural frequency. The natural frequency of this elastic manipulator is found to be serial combination of joint frequency and the fundamental frequency of the beam. The beam deflection is computed based on the summation of two modes, $U_x(r, t) = U_{x1}(r)\, q_3(t) + U_{x2}(r)\, q_4(t)$. The deflection of the tip away from the nominal motion of the beam is shown in Figure 9. These results show that the responses are dominated by the joint stiffness and fundamental mode of the beam.

CONCLUSIONS

The paper discusses the state-of-the-art in equation generation for rigid/flexible hybrid multibody systems. The symbolic closed-form algorithm represents the first effort to date and will contribute a significant step forward in saving computation time and ease of linearization of equations. The examples are shown to illustrate the use of principle of virtual work to generate the equations of motion. The closed-form algorithm presented above has been successfully implemented in a symbolic program. It is in an expanded form that simplifies programming and avoids tedious matrix manipulation. The closed-form algorithm improves the formulation efficiency and facilitates symbolic linearization. It also provides a clearer representation of the physics due to the nature of closed-form equations and can easily be implemented with control laws. This is a 3D general-purpose formalism derived with respect to an accelerating reference frame and can be applied to both holonomic and nonholonomic constrained systems. Linearization was easily accomplished as was the implementation of a control algorithm. The first example, an elastic pendulum, has successfully demonstrated the ease and efficiency of the algorithm when applied to elastic systems attached to a vibrating foundation. The second example shows the applicability of this algorithm to the dynamics of elastic robots. Dynamic behavior of the elastic manipulator to step input is easily obtained from the output symbolic equations. The results of this study indicate that the method of equation formulation holds promise in modeling and analysis of rigid/elastic hybrid mechanical systems.

REFERENCES

1. Hooker, W.W., "A Set of r Dynamical Attitude Equations for an Arbitrary n-Body Satellite Having r Rotational Degrees of Freedom", AIAA J., July, 1970, pp. 1205-1207.
2. Magnus, K. Edited, Dynamics of Multibody Systems, IUTAM Sym., Munich, Germany, 1977, Springer-Verlag.
3. Bianchi, G. and Schiehlen, W. Edited, Dynamics of Multibody Systems, IUTAM/IFToMM Sym., Udine, Italy, 1985, Springer-Verlag.
4. Haug, E.J. Edited, Computer Aided Analysis and Optimization of Mechanical Systems Dynamics", NATO ASI Series F: Computer and Systems Sci., Vol. 9, Springer-Verlag, 1984.
5. W. Kortum and W. Schiehlen, "General Purpose Vehicle System Dynamics Software Based on Multibody Formalisms", Veh. Sys. Dynamics, 14, 1985 pp. 229-263.
6. Sunada, W.H. and Dubowsky, S., "On the Dynamic Analysis and Behavior of Industrial Robotic Manipulators with Elastic Members", J. Mech., Trans., and Auto. in Design, Mar. 1983, Vol. 105, pp. 42-51.
7. Book, W.J., "Recursive Lagrangian Dynamics of Flexible Manipulator Arms", Int. J. Robotics Research, Vol. 3, No. 3, Fall 1984, pp. 87-101.
8. Low, K.H. and Vidyasagar, M., "A Lagrangian Formulation of the Dynamic Model for Flexible Manipulator Systems", J. Dyn. Sys., Meas., and Control, 1988, Vol. 110, pp. 175-181.
9. Huang, H. and Lee, C.S.G., "Generation of Newton-Euler Formulation of Dynamic Equations to Nonrigid Manipulators", J. Dyn. Sys., Meas., and Control, Vol. 110, Sept. 1988, pp. 308-315.
10. Sheth, P.N. and Uicker, J.J. Jr., "IMP (Integrated Mechanisms Program), A Computed-Aided Design Analysis System for Mechanisms and Linkage", J. Eng. for Ind., 1972, pp. 454-464.
11. N. Orlandea, M.A. Chace and D.A. Calahan, "A Sparsity-Oriented Approach to the Dynamic Analysis and Design of Mechanical Systems", J. Eng. for Ind., Aug. 1977, pp. 773-784.
12. Wehage, R. A., Generalized Coordinate Partitioning in Dynamic Analysis of Mechanical Systems, Ph.D. Thesis, Univ. of Iowa, 1980.
13. Richard, M.J., Dynamic Simulation of Constrained Three Dimensional Multibody Systems Using Vector Network Techniques, Ph.D. Thesis, Queen's University, Canada, 1985.
14. A. Jaschinski, W. Kortum, and O. Wallrapp, "Simulation of Ground Vehicles with the Multibody Program MEDYNA", Symp. Simul. and Contr. of Gr. Veh. and Trans. Sys., AMD-Vol. 80 DSC-Vol. 2, Dec. 1986.
15. Macala, G. A., "SYMBOD: A Computer Program for the Automatic Generation of Symbolic Equations of Motion for Systems of Hinged-Connected Rigid Bodies", Paper No. AIAA-83-0013, AIAA 21th Aero. Sc. Meeting, Jan. 1983/Reno, Nevada.
16. Kreuzer, E. J. and Schiehlen, W. O., "Computerized Generation of Symbolic Equations of Motions of Motion for Spacecraft", J. Guidance, V.8, 1985, pp. 284-287.
17. Wittenburg, J. and Wolz, U., "MESA VERDE: A Symbolic Program for Nonlinear Articulated Rigid Bodies Dynamics", ASME Paper No. 85-DET-151, 198
18. Rosenthal, D.E. and Sherman, M.A., "High Performance Multibody Simulation Via Symbolic Equation Manipulation and Kane's Method", J.Astronaut. Sc., V.34,1986, pp. 223-239.
19. G. Cesareo, F. Nicolo and S. Nicosia, "DYMIR: A Code for Generating Dynamic Model of Robots", Int. Conf. on Robots, Atlanta, Mar. 13-15, 1984, pp. 115-119.
20. Neuman, C.P. and Murray, J.J., "Symbolically Efficient Formulations for Computational Robot Dynamics", J. Robotics Systems, 4(6), 743-769, 1987.
21. Burdick, J.W., "An Algorithm for Generation of Efficient Manipulator Dynamic Equations", Proc. 1986 IEEE Int. Conf. Robotics and Auto., pp. 212-218.
22. Sreenath, N. and Krishnaprasad, P.S., "DYNAMAN: A Tool for Manipulator Design and Analysis", Proc. 1986 IEEE Int. Conf. Robotics and Auto., pp. 836-842.
23. Leu, M.C. and Hemati, N., "Automated Symbolic Derivation of Dynamic Equations of Motion for Robot Manipulators", J. Dyn. Sys., Meas. and Control, V.108, Sept. 1986, pp. 172-179.
24. Hoplik, J and Leu, M.C., "Computer Generation of Robot Dynamics Equations and the Related Issues", J. Robotic Sys., 3(3), 301-319, 1986.
25. Faessler, H., "Computer-Assisted Generation of Dynamical Equations for Multibody Systems", Int. J. Robotics Res., V.5, No.3, 1986.
26. Cetinkunt, S. and Book, W.J., "Symbolic Modeling of Flexible Manipulators", Proc. 1987 IEEE Int Conf. on Robotics and Auto., pp. 2074-2080.
27. A.P. Tzes, S. Yurkoviah, F.D. Langer, "A Symbolic Manipulator Package for Modeling of Rigid or Flexible Manipulators", 1988 Int. Conf. on Robotics and Auto., pp. 1526-1531.
28. J.P. Sadler, "On the Analytical Lumped-Mass Model of an Elastic Four-Bar Mechanism", J. Eng. for Ind., 1975, pp. 561-565.
29. A. Midha, A.G. Erdman and D.A. Frohrib, "Finite Element Approach to Mathematical Modeling of High-Speed Elastic Linkages", Mech. and Mach. Theory, Vol. 13, 1978, pp. 603-618.
30. Likins, P.W., "Analytical Dynamics and Nonrigid Spacecraft Simulation", NASA Technical Report 32-1593, 1974.
31. Cannon, R.H. and Schmitz, E., "Initial Experimental on the End-Point Control of a Flexible One-Link Robot", Int. J. Robotics Research, Vol. 3, No. 3, Fall 1984.

32. Hastings G.G. and Book, W.J., "A Linear Dynamic Model for Flexible Robotic Manipulators" IEEE Control Systems Magazine. Feb. 1987, pp. 61-64.

33. Yang, G.-B. and Donath, M., "Dynamic Model of a Two-Link Robot Manipulator with Both Structural and Joint Flexibility", Symp. on Robotics, 1988 WAM of ASME, pp. 37-44.

34. Naganathan, G. and Soni, A.H., "Nonlinear Modeling of Kinematic and Flexible Effects in Manipulator Design", J. Mech., Trans., and Auto. in Design, 1988, Vol. 110, pp. 243-254.

35. P.B. Usoro, R. Nadira and S.S. Mahil, "A Finite Element/Lagrange Approach to Modeling Lightweight Flexible Manipulators", J. Dyn. Sys., Meas., and Control, Vol. 108, 1986, pp. 198-205.

36. Changizi, K. and Shabana, A.A., "A Recursive Formulation for the Dynamic Analysis of Open Loop Deformable Multibody Systems", J. Appl. Mech., Sept. 1988, pp. 687-693.

37. E. Bayo, G.D. Jalonand M.A. Serna, "A Modified Lagrangian Formulation for The Dynamic Analysis of Constrained Mechanical Systems", Comp. Meth. in Appl. Mech. and Eng., 71 (1988) 183-195.

38. J.Y.S. Luh, M.W. Walker and R.P.C. Paul, "On-Line Computational Scheme for Mechanical Manipulators", J. Dyn. Sys., Meas., and Control, June 1980, V.102, pp. 69-76.

39. Gupta, S.G. and Townsend, M.A., "On the Equations of Motion for Robot Arms and Open Kinematic Chain", J. Mech., Trans., and Auto. in Design, 1988, Vol. 110, pp. 287-294.

40. Greenwood, D.T., Principle of Dynamics, Prentice-Hill, 1965.

41. Wang, T. and Kohli, D., "Closed and Expanded Form of Manipulator Dynamics Using Lagrangian Approach", J. Mech., Trans., and Auto. in Design, V.107, 1985, pp. 223-225.

42. Hollerback, J.M., "A Recursive Lagrangian Formulation of Manipulator Dynamics and a Comparative Study of Dynamics Formulation Complexity", IEEE Tran. Sys., Man, and Cyber., V. SMC-10, 1980.

43. Li, C.J., "A New Method of Dynamics for Robot Manipulators", IEEE Trans. Sys., Man, and Cyber., V.18, No.1, 1988.

44. Goldstein, H., Classical Mechanics, second edition, Addison-Wesley, 1980.

45. Kane, T.R. and Levinson, D.A., "Formulation of Equations of Motion for Complex Spacecraft", J. Guid. and Cont., V.3, 1980.

46. Greenwood, T.D., Classical Dynamics, Prentice-Hall, 1977.

47. Kane, T.R. and Wang, C.F. "On the Derivation of Equations of Motion", J. Soc. Ind. Appl. Math., V.13, No.2, 1965.

48. Kane, T.R. and Levinson, D.A., Dynamics: Theory and Applications, McGraw-Hill, 1985.

49. Lieh, J. and Haque, I., "Symbolic Formulation and Linearization of Equations of Multi-body Systems Subject to Control Using Principle of Virtual Work", Proc. 1st Nat. Conf. on Appl. Mech. and Robotics, Nov. 1989, Cincinnati, Ohio.

50. B.W. Char, K.O. Geddes, G.H. Gonnet and S.M. Watt, MAPLE User's Guide, 4th Ed., WATCOM Pub. Waterloo, Canada, 1988.

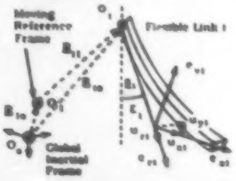

Figure 1. Deformation of Elastic Link i

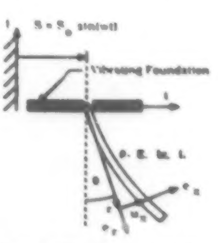

Figure 2 Simple Flexible Pendulum on Vibrating Foundation

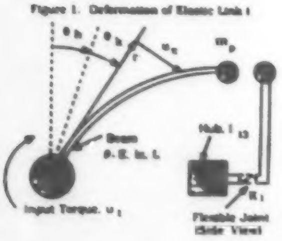

Figure 3 Dynamic Model Of Flexible Manipulator

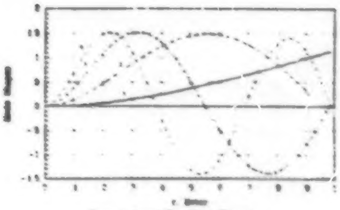

Figure 4 Lowest Four Mode Shapes

Note for Figures 5 to 9:

Line	Joint Compliance
———	K1 = 5 N-m/rad
- - - - -	K1 = 10 N-m/rad
- · - · -	K1 = 20 N-m/rad

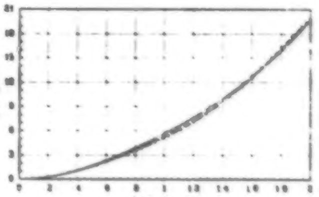

Figure 5. Angular Displacement of Hub

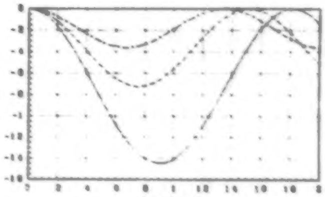

Figure 6 Time Response of Joint Compliance

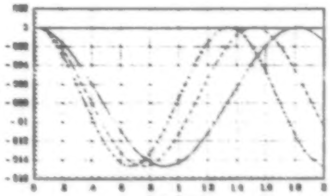

Figure 7 Time Response of Generalized Coordinate of Beam 1

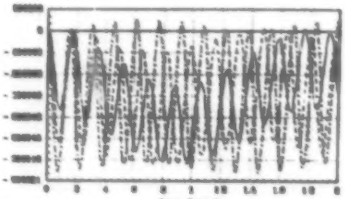

Figure 8 Time Response of Generalized Coordinate of Mode 2

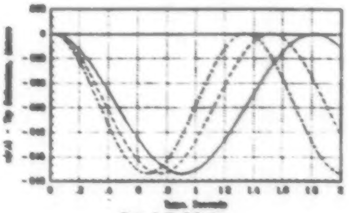

Figure 9 Tip Deflection

A CARTESIAN TENSOR METHODOLOGY FOR THE STUDY OF CLASSICAL NEWTONIAN DYNAMICS

PART II : APPLICATIONS TO RIGID BODY MOTION †

C. A. Balafoutis and R. V. Patel

Electrical and Computer Engineering Department
Concordia University, Montreal, Quebec
CANADA H3G 1M8

ABSTRACT

In this paper, we propose a new, computationally efficient, approach for the study of classical Newtonian dynamics. In particular, we propose a Cartesian tensor methodology for the dynamic analysis of rigid body motion which is conceptually simple, easy to implement and computationally efficient. Based on this methodology, we derive a new tensor formulation for Euler's equation. In this tensor formulation, Euler's equation has a simpler structure than its classical vector formulation and can therefore be implemented computationally in a far more efficient manner. Moreover, in this paper it is shown that by using Cartesian tensors, we can evaluate the dynamic equations of rigid body motion (i.e., Newton and the Euler equations) with only 27 scalar multiplications and 24 scalar additions.

I INTRODUCTION

Application of Cartesian tensor analysis (within the framework of the Newtonian approach) in rigid body dynamics requires that all basic physical quantities of motion (*angular velocity, angular acceleration, angular momentum*, etc.) be treated as Cartesian tensors instead of vectors. Besides the well known angular velocity tensor, tensor representations for the angular momentum and the external or resultant torque have appeared in the literature since 1931 in the work of Jeffreys [1]. Jeffreys introduced the angular momentum and torque tensors in his Cartesian tensor description for the Newtonian formulation of rigid body motion. But his formulation for the equations of motion fell short of producing any significant computational advantages over the classical vector formulation. Therefore, in the Newtonian approach to classical dynamics, Jeffreys' work has been largely ignored, and almost exclusively, the equations of rigid body motion are formulated following the vector approach [2-6].

Jeffreys approach did not succeed in improving the computational efficiency of the equations of motion, mainly because he followed a component-wise approach in his analysis and did not use a tensor representation for the angular acceleration. This resulted in rather complex expressions for the computation of the linear acceleration and the torque vector. In this paper, following Jeffreys' ideas and using the Cartesian tensor identities which have been derived in an accompanying paper (Part I), we develop a new tensor formulation for one of the basic equations of rigid body motion, namely, the Euler equation. In this tensor formulation, Euler's equation has a simpler structure than its classical vector formulation, and therefore, it can be implemented computationally in a far more efficient manner. Moreover, in this paper, it is shown that by using Cartesian tensors we can evaluate the dynamic equations of rigid body motion (i.e., Newton and Euler equations) with only 27 scalar multiplications and 24 scalar additions. From a computational point of view, this is a considerable improvement over the classical vector formulation of these equations which requires a total of 45 scalar multiplications and 30 scalar additions. This tensor treatment of rigid body motion can be used [10,11] to obtain in a computationally efficient manner, the dynamic behavior of complex rigid body systems (e.g., robot manipulators).

The rest of this paper is organized as follows : Section II defines the notation used in this paper. Section III introduces the angular velocity and angular acceleration tensors and describes their use in the kinematic analysis of rigid body motion. Section IV is the main section of the paper where Cartesian tensor analysis is applied to rigid body dynamics. This leads to a new formulation of Euler's equation. Also, in this section, the computational complexity of the proposed tensor formulation are examined and compared to that of the classical vector formulation.

II NOTATION

Throughout the text, boldface lower case roman letters are used to denote position vectors. Upper case boldface roman letters are used to denote second order tensors or vectors of forces and moments. From the context it will be clear if a tensor or a vector is considered. A second order skew-symmetric Cartesian tensor associated with a vector (see Part I) will be denoted with a tilde (˜) above the boldface lower or upper case roman letter denoting this vector. The *coordinate matrix*, associated with a second order Cartesian tensor or a vector, will be denoted by the corresponding lower or upper case italic letter.

III ON KINEMATIC ANALYSIS OF RIGID BODY MOTION

The main objectives of this section are to introduce two very important second order Cartesian tensors,

---

† This research was supported by the Natural Sciences and Engineering Research Council of Canada under Grant A1345 and by the Fonds pour la Formation de Chercheus et l'Aide a la Recherche of Quebec under Grant 88AS25A.

namely, the angular velocity and angular acceleration tensors and to demonstrate their use in the kinematic analysis of rigid body motion.

3.1 The Angular Velocity Tensor

It is well known [1-11] that the angular rates (or linear independent rates of change of rigid body orientation) constitute the components of a tensor quantity, the *angular velocity tensor*. But this is not reflected in the applied literature. Even in the cases where the angular velocity tensor is mentioned, its vector invariant or dual vector, i.e., the familiar *angular velocity vector*, is usually used in applications instead of the tensor itself. This does not mean that the angular velocity vector is more important than the angular velocity tensor. On the contrary, as we shall see in this paper, the angular velocity tensor is more suitable for kinematic and dynamic analysis of rigid body motion.

Perhaps the easiest way to introduce the angular velocity tensor is by using a corollary of the following theorem [5,7,11].

Theorem 3.1 : Any differentiable orthogonal tensor $\mathbf{Q} \equiv \mathbf{Q}(t)$ satisfies the following first order differential equation

$$\dot{\mathbf{Q}} = \mathbf{\Phi}\mathbf{Q} \tag{3.1}$$

where, $\mathbf{\Phi}$ is a second order skew-symmetric tensor.

A simple proof of this theorem can be found in [5]. Now, since a rotation tensor is an orthogonal tensor, it satisfies Theorem 3.1 and we can state the following corollary.

Corollary 3.1 : A rotation tensor $\mathbf{R}$ satisfies a first order differential equation given by

$$\dot{\mathbf{R}} = \mathbf{\Phi}\mathbf{R} \tag{3.2}$$

where, $\mathbf{\Phi}$ is a second order skew-symmetric tensor.

From this Corollary we can derive the definition of the angular velocity tensor as follows : When the rotation tensor $\mathbf{R}$ is defined in a 3-D Euclidean space, it describes the orientation of a rigid body. In this case, we denote the skew-symmetric tensor $\mathbf{\Phi}$ by $\tilde{\omega}$, i.e., we write eq. (3.2) as

$$\dot{\mathbf{R}} = \tilde{\omega}\mathbf{R}\,. \tag{3.3}$$

and refer to $\tilde{\omega}$ as the *angular velocity tensor*. Equation (3.3), which is sometimes referred to as *Poisson's equation*, can also be written in the form

$$\tilde{\omega} = \dot{\mathbf{R}}\,\mathbf{R}^{T} \tag{3.4}$$

and can be used as the definition of the angular velocity tensor. Moreover, since the skew-symmetric tensor $\tilde{\omega}$ is defined in a 3-D Euclidean space, it has a unique dual vector or vector invariant. The dual vector ω, of $\tilde{\omega}$, is the familiar *angular velocity vector*. Therefore, eq. (3.4) and the dual tensor operator provide a simple definition for the angular velocity vector.

3.2 The Angular Acceleration Tensor

Let us now consider the second time derivative $\ddot{\mathbf{R}}$, relative to an inertial frame, of a rotation tensor $\mathbf{R}$. The functional relationship between $\mathbf{R}$ and $\mathbf{R}$ follows from the following theorem.

Theorem 3.2 : Any differentiable orthogonal tensor $\mathbf{Q} \equiv \mathbf{Q}(t)$ satisfies the following second order differential equation

$$\ddot{\mathbf{Q}} = \mathbf{\Psi}\mathbf{Q} \tag{3.5}$$

where, $\mathbf{\Psi}$ is a second order tensor defined by

$$\mathbf{\Psi} = \dot{\mathbf{\Phi}} + \mathbf{\Phi}^{2}\,, \tag{3.6}$$

$\mathbf{\Phi}$ satisfies (3.1) and $\mathbf{\Phi}^{2} = \mathbf{\Phi}\cdot\mathbf{\Phi} \equiv \mathbf{\Phi}\mathbf{\Phi}$.

Proof : Differentiation of (3.1) gives

$$\ddot{\mathbf{Q}} = \dot{\mathbf{\Phi}}\mathbf{Q} + \mathbf{\Phi}\dot{\mathbf{Q}}$$

and substituting for $\dot{\mathbf{Q}}$ we get

$$\begin{aligned}\ddot{\mathbf{Q}} &= (\dot{\mathbf{\Phi}} + \mathbf{\Phi}\mathbf{\Phi})\mathbf{Q}\\ &= \mathbf{\Psi}\mathbf{Q}\end{aligned}$$

where $\mathbf{\Psi} = \dot{\mathbf{\Phi}} + \mathbf{\Phi}^{2}$. This complete the proof. ∎

Corollary 3.2 : A second order rotation tensor $\mathbf{R}$ satisfies the following second order differential equation

$$\ddot{\mathbf{R}} = \mathbf{\Psi}\mathbf{R} \tag{3.7}$$

where, $\mathbf{\Psi}$ is a second order tensor defined by

$$\mathbf{\Psi} = \dot{\mathbf{\Phi}} + \mathbf{\Phi}^{2}, \tag{3.8}$$

$\mathbf{\Phi}$ is the angular velocity tensor which corresponds to $\mathbf{R}$ and $\mathbf{\Phi}^{2} = \mathbf{\Phi}\mathbf{\Phi}$.

Theorem 3.2 and its Corollary are obviously valid for orthogonal tensors defined in an n-D Euclidean space, but here we shall be concerned only with the case where $n = 3$. In this case, we introduce the notation $\mathbf{\Omega}$ to denote the tensor $\mathbf{\Psi}$ and write (3.7) as

$$\ddot{\mathbf{R}} = \mathbf{\Omega}\mathbf{R}\,. \tag{3.9}$$

Also, using $\tilde{\omega}$, we write (3.8) as

$$\mathbf{\Omega} = \dot{\tilde{\omega}} + \tilde{\omega}\tilde{\omega} \tag{3.10}$$

and we refer to the tensor $\mathbf{\Omega}$ as the *angular acceleration tensor*. Obviously, using (3.7), we can also define the angular acceleration tensor $\mathbf{\Omega}$ by the equation

$$\mathbf{\Omega} = \ddot{\mathbf{R}}\,\mathbf{R}^{T} \tag{3.11}$$

where $\mathbf{R}$ is a rotation tensor in 3-D Euclidean space.

The tensor $\mathbf{\Omega}$ is neither symmetric nor skew-symmetric. Actually, since $\dot{\tilde{\omega}}$ is skew-symmetric and $\tilde{\omega}\tilde{\omega}$ is symmetric, equation (3.10) represents the *Cartesian decomposition* of $\mathbf{\Omega}$. Moreover, since the tensor $\tilde{\omega}\tilde{\omega}$ is symmetric we have

$$vect(\mathbf{\Omega}) = vect(\dot{\tilde{\omega}}) \equiv dual(\dot{\tilde{\omega}}) = \dot{\omega} \tag{3.12}$$

i.e., the vector invariant of the angular acceleration tensor $\mathbf{\Omega}$ is the familiar *angular acceleration vector*. This obviously justifies the name given to the tensor $\mathbf{\Omega}$.

The angular acceleration tensor has only recently been reported in the literature [7,9-11]. This is probably due to the fact that applications of the angular acceleration tensor to rigid body dynamics is not obvious and researchers fail to recognize that the dynamic analysis of rigid body motion can be simplified when the angular acceleration tensor is properly used. Thus, for example in [9], although the formulation of the angular acceleration is stated, this tensor is not used in the dynamic analysis of the equations of motion and is not, in practice, used in the kinematic analysis either. Thus, since the dynamic analysis of rigid body motion is carried out based on vector analysis, the angular velocity and angular acceleration tensors even if mentioned are not in general used in applications. In this paper, we shall show that the use of the angular velocity and acceleration tensors in the dynamic analysis of rigid body motion leads us to computationally more efficient formulations. However, first we shall demonstrate how the angular velocity and angular acceleration tensors can be used in the kinematic analysis of rigid body motion.

3.3 Linear Velocity and Acceleration in Rigid Body Motion

The concepts of angular velocity and angular acceleration tensors provide powerful tools for describing the motion of a rigid body since they enable us to derive equations with very simple structure. To see this, let us consider some arbitrary vector involved in a mechanical problem, such as the position vector $\mathbf{r}$ of a point on the rigid body. Usually such a vector will vary in time as the body moves. Therefore, it is important that its linear velocity and acceleration relative to an inertial coordinate system can be determined in a computationally efficient manner. To solve problems of this type, we proceed as follows.

As is usually the practice in rigid body motion, we consider two coordinate systems. An inertial and a body coordinate system, which we denote by $\{ \mathbf{e} \}$ and $\{ \mathbf{e}' \}$ respectively. The body coordinate system is rigidly attached to the rigid body and so moves with it. Suppose, now, that a point P on the body has a position vector $\mathbf{r}_1$ relative to the origin o of the inertial coordinate system and a position vector $\mathbf{r}_2$ relative to the origin o′ of the moving coordinate system. Let also $\mathbf{a}$ be the vector from o to o′. Then, as we can see in the following Figure

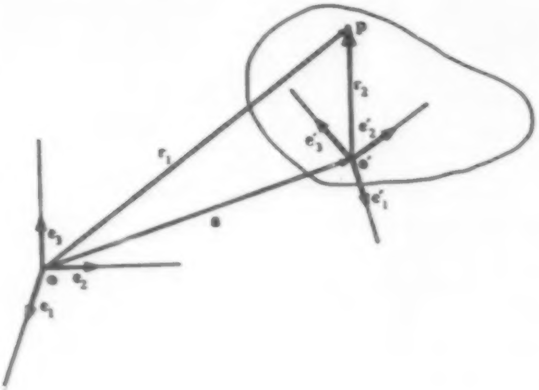

Figure 1 : Position vectors and coordinate systems in rigid body motion.

the three vectors, expressed in the inertial system coordinates, are related by the equation

$$\mathbf{r}_1 = \mathbf{a} + \mathbf{r}_2. \tag{3.13}$$

Moreover, let $\mathbf{R}$ be the rotation tensor which specifies the orientation of the moving coordinate system relative to the inertial one. Then, if $\mathbf{r}'_2$ denotes the position vector of the point P relative to o′ when it is expressed in the moving coordinate system, premultiplication by the rotation tensor $\mathbf{R}$ expresses it relative to the inertial coordinate system, i.e., we can write

$$\mathbf{r}_2 = \mathbf{R}\,\mathbf{r}'_2 \tag{3.14}$$

Therefore, (3.13) can also be written as

$$\mathbf{r}_1 = \mathbf{a} + \mathbf{R}\,\mathbf{r}'_2 . \tag{3.15}$$

Now, from (3.15) we have

$$\dot{\mathbf{r}}_1 = \dot{\mathbf{a}} + \dot{\mathbf{R}}\,\mathbf{r}'_2 . \tag{3.16}$$

since the vector $\mathbf{r}'_2$ is time independent. Moreover, substituting for $\mathbf{R}$ from (3.3) and using (3.14), we finally have for the absolute velocity of the point P

$$\dot{\mathbf{r}}_1 = \dot{\mathbf{a}} + \tilde{\omega}\,\mathbf{r}_2 \tag{3.17}$$

where $\tilde{\omega}$ is the angular velocity tensor of the moving body. Also, for the absolute linear acceleration of the point P we have

$$\ddot{\mathbf{r}}_1 = \ddot{\mathbf{a}} + \ddot{\mathbf{R}}\,\mathbf{r}'_2$$

which can be simplified to

$$\ddot{\mathbf{r}}_1 = \ddot{\mathbf{a}} + \Omega\mathbf{r}_2 \tag{3.18}$$

where Ω is the angular acceleration tensor of the moving body.

Let us recall, at this point, that in the classical vector description of rigid body dynamics, the vectors of the absolute linear velocity and acceleration of the same point P are computed from the following vector equations

$$\dot{\mathbf{r}}_1 = \dot{\mathbf{a}} + \omega \times \mathbf{r}_2 \tag{3.19}$$

and

$$\ddot{\mathbf{r}}_1 = \ddot{\mathbf{a}} + \dot{\omega} \times \mathbf{r}_2 + \omega \times (\omega \times \mathbf{r}_2) \tag{3.20}$$

respectively. Obviously, (3.17) and (3.18) are equivalent to (3.19) and (3.20) respectively. However, as we can see, (3.17) and (3.18) are more compact, and thus simpler, than (3.19) and (3.20).

IV ON DYNAMIC ANALYSIS OF RIGID BODY MOTION

In this section we shall be concerned with the Newtonian formulation of the equations of rigid body motion and we shall provide a new formulation for Euler's equation. As is well known [1-6], a general motion of a rigid body can be considered as resulting from the superposition of two independent motions, namely a pure translational motion of a point (usually its center of mass) and a pure rotational motion about that point. The Newton-Euler procedure for describing rigid body motion uses exactly this decomposition. In particular, in the Newtonian formulation of the equations of rigid body motion, the translational motion is described by Newton's equation (or Newton's second law) which symbolically is stated as follows

$$\mathbf{F}_c = m\,\ddot{\mathbf{r}}_c \tag{4.1}$$

where $\mathbf{F}_c$ is the total external (or resultant) force acting on the rigid body, m is the mass of the rigid body and $\ddot{\mathbf{r}}_c$ is the absolute linear acceleration of its center of mass. The rotational motion is described by Euler's equation which is symbolically stated as

$$\mathbf{M}_c = \mathbf{I}_c \cdot \dot{\omega} + \omega \times \mathbf{I}_c \cdot \omega \tag{4.2}$$

where $\mathbf{M}_c$ is the total external (or resultant) torque about the center of mass, $\mathbf{I}_c$ is the inertia tensor of the body about its center of mass and ω ($\dot{\omega}$) is the angular velocity (acceleration) of the body. Now, before we proceed to analyze these vector equations, we need to review some relevant facts about the rigid body inertia tensor.

4.1 The Rigid Body Inertia Tensor

As is well known [2,3], the *inertia tensor* of a rigid body characterizes the mass distribution of the body relative to a point, and is usually defined by the equation

$$\mathbf{I}_o = \int_m (\mathbf{r} \cdot \mathbf{r}\, \mathbf{1} - \mathbf{r} \otimes \mathbf{r}\,)dm = - \int_m \tilde{\mathbf{r}}\, \tilde{\mathbf{r}}\; dm \qquad (4.3)$$

where o denotes a point of the body and $\mathbf{r}$ denotes the position vector of a point mass relative to the point o.

For a treatment of the dynamic analysis of rigid body motion based on Cartesian tensors, this definition for the inertia tensor needs to be modified. As we shall see later, the proper definition for a Cartesian tensor formulation of rigid body rotational dynamics is provided by the equation

$$\mathbf{J}_o = \int_m \mathbf{r} \otimes \mathbf{r}\; dm \qquad (4.4)$$

where o is a point on the rigid body, $\mathbf{r}$ is the position vector of a point mass relative to point o and $\mathbf{r} \otimes \mathbf{r}$ denotes the tensor product of $\mathbf{r}$ with itself. We shall refer to the inertia tensor $\mathbf{J}_o$ as the *pseudo-inertia* tensor of a rigid body.

Obviously, the two inertia tensors $\mathbf{I}_o$ and $\mathbf{J}_o$ describe the same physical property of a rigid body and, therefore, they are equivalent. Actually, it can be shown [11], that the following equivalence relationships exists between the two tensors $\mathbf{J}_o$ and $\mathbf{I}_o$.

$$\mathbf{J}_o = \frac{1}{2} tr\,[\mathbf{I}_o]\mathbf{1} - \mathbf{I}_o \qquad (4.5)$$

and

$$\mathbf{I}_o = tr\,[\mathbf{J}_o]\mathbf{1} - \mathbf{J}_o. \qquad (4.6)$$

Next, we consider the *parallel axis theorem* which is probably the most important theorem concerning the inertia tensor and is usually stated in the following form

$$\mathbf{I}_o = \mathbf{I}_c + m\left(\mathbf{r}_c \cdot \mathbf{r}_c \mathbf{1} - \mathbf{r}_c \otimes \mathbf{r}_c\right) \qquad (4.7)$$

where $\mathbf{I}_c$ is the rigid body inertia about its center of mass, $\mathbf{r}_c$ is the position vector of the center of mass relative to point o, and m is the mass of the body. Note that (4.7) can also be written [11] in a compact tensor form as follows

$$\mathbf{I}_o = \mathbf{I}_c - m\, \tilde{\mathbf{r}}_c \tilde{\mathbf{r}}_c. \qquad (4.8)$$

Obviously, the parallel axis theorem is also valid for the pseudo-inertia tensor $\mathbf{J}_o$. For this tensor, the parallel axis theorem is expressed [11] by the equation

$$\mathbf{J}_o = \mathbf{J}_c + m\, \mathbf{r}_c \otimes \mathbf{r}_c \qquad (4.9)$$

where $\mathbf{r}_c$ is the position vector of the center of mass relative to point o and m is the total mass of the body. Also, it can be shown [11], that the absolute derivative of the inertia tensor $\mathbf{I}_o$ and pseudo-inertia tensor $\mathbf{J}_o$ are defined by the equations

$$\dot{\mathbf{I}}_o = \tilde{\omega}\mathbf{I}_o - \mathbf{I}_o \tilde{\omega}. \qquad (4.10)$$

and

$$\dot{\mathbf{J}}_o = \tilde{\omega}\mathbf{J}_o - \mathbf{J}_o \tilde{\omega}. \qquad (4.11)$$

respectively.

In the following, we shall use the two inertia tensors $\mathbf{I}$ and $\mathbf{J}$ to compute other basic physical quantities in rigid body motion such as the angular momentum and the external (or resultant) torque.

4.2 The Angular Momentum Tensor

In the classical vector treatment of rigid body dynamics, angular momentum is represented by a vector which is defined [2] by the equation

$$\mathbf{L}_o = \mathbf{s} \times \left(\dot{\mathbf{s}} + \omega \times \mathbf{r}_c\right) m + \mathbf{r}_c \times \dot{\mathbf{s}}\, m + \mathbf{I}_{o'} \cdot \omega \qquad (4.12)$$

where o is the origin of the inertial coordinate system, o' is a point fixed on the rigid body, $\mathbf{s}$ is the position vector of o' relative to o, $\mathbf{r}_\rho$ is the position vector of the center of mass relative to o', $\mathbf{I}_{o'}$ is the rigid body inertia tensor about the point o' and ω is the vector of the angular velocity. When the inertial coordinate system has its origin at the point o', since $\mathbf{s} = 0$, (4.12) takes the form

$$\mathbf{L}_o = \mathbf{I}_o \cdot \omega \equiv \mathbf{I}_o \omega. \qquad (4.13)$$

Obviously, when the center of rotation is at the center of mass, (4.13) becomes

$$\mathbf{L}_c = \mathbf{I}_c \omega. \qquad (4.14)$$

The angular momentum can also be defined in terms of the pseudo-inertia tensor $\mathbf{J}_o$. To see this we need only to substitute $\mathbf{I}_o$ in (4.13) by $\mathbf{J}_o$. For this, we use (4.6) and get

$$\mathbf{L}_o = - \mathbf{J}_o \omega + tr\,[\mathbf{J}_o]\omega \qquad (4.15)$$

Besides its vector description, the angular momentum can also be described by a second order skew-symmetric Cartesian tensor. To see this, we apply the dual operator (see Part I) to the angular momentum vector $\mathbf{L}_o$. This gives a dual skew-symmetric tensor $\tilde{\mathbf{L}}_o$ which we express by writing

$$\tilde{\mathbf{L}}_o = \boldsymbol{dual}(\mathbf{L}_o) \qquad (4.16)$$

We refer to the dual skew-symmetric tensor $\tilde{\mathbf{L}}_o$ as the ***angular momentum tensor*** about the point o.

The dual operator provides an indirect definition of the angular momentum tensor. However, as the following theorem shows, it is possible to define the angular momentum tensor $\tilde{\mathbf{L}}_o$ directly in terms of the inertia tensor $\mathbf{I}_o$ and the angular velocity tensor $\tilde{\omega}$, i.e., without the need to first compute the angular momentum vector.

Theorem 4.1 : The angular momentum tensor of a rotating rigid body about a point o, satisfies the equation

$$\tilde{\mathbf{L}}_o = \left(\tilde{\omega}\mathbf{I}_o\right)^T - \left(\tilde{\omega}\mathbf{I}_o\right) + tr\,[\mathbf{I}_o]\tilde{\omega} \qquad (4.17)$$

where $\mathbf{I}_o$ is the inertia tensor of the rigid body about the center of rotation o and $\tilde{\omega}$ is the angular velocity tensor.

Proof : Using (4.13) we can write (4.16) as

$$\tilde{\mathbf{L}}_o = \boldsymbol{dual}(\mathbf{I}_o \tilde{\omega})$$

Further, since the inertia tensor $\mathbf{I}_o$ is symmetric, by using Proposition (4.3) in Part I, we get

$$\begin{aligned} \tilde{\mathbf{L}}_o &= - \left(\mathbf{I}_o \tilde{\omega} + \tilde{\omega}\mathbf{I}_o\right) + tr\,[\mathbf{I}_o]\tilde{\omega} \\ &= \mathbf{I}_o \tilde{\omega}^T - \tilde{\omega}\mathbf{I}_o + tr\,[\mathbf{I}_o]\tilde{\omega} \\ &= \left(\tilde{\omega}\mathbf{I}_o\right)^T - \tilde{\omega}\mathbf{I}_o + tr\,[\mathbf{I}_o]\tilde{\omega} \end{aligned}$$

and this completes the proof. ▯

Theorem 4.1 can also be written in terms of the pseudo-inertia tensor $\mathbf{J}_o$. First we notice that from (4.6) we have

$$tr\,[\mathbf{I}_o] = 2tr\,[\mathbf{J}_o]. \tag{4.18}$$

Therefore, if we substitute (4.6) and (4.18) in (4.17), we have

$$\begin{aligned}\tilde{\mathbf{L}}_o &= \left(tr\,[\mathbf{J}_o]\tilde{\omega} - \tilde{\omega}\mathbf{J}_o\right)^T - \left(tr\,[\mathbf{J}_o]\tilde{\omega} - \tilde{\omega}\mathbf{J}_o\right) + 2tr\,[\mathbf{J}_o]\tilde{\omega} \\ &= \mathbf{J}_o\tilde{\omega} + \tilde{\omega}\mathbf{J}_o\end{aligned}$$

or, finally

$$\tilde{\mathbf{L}}_o = \mathbf{J}_o\tilde{\omega} - \left(\mathbf{J}_o\tilde{\omega}\right)^T. \tag{4.19}$$

Obviously, when a rigid body is rotating about its center of mass, the angular momentum tensor is defined by the equation

$$\tilde{\mathbf{L}}_c = \left(\tilde{\omega}\mathbf{I}_c\right)^T - \left(\tilde{\omega}\mathbf{I}_c\right) + tr\,[\mathbf{I}_c]\tilde{\omega} \tag{4.20}$$

or the equation

$$\tilde{\mathbf{L}}_c = \mathbf{J}_c\tilde{\omega} - \left(\mathbf{J}_c\tilde{\omega}\right)^T \tag{4.21}$$

As we can see from (4.13) and (4.15), the angular momentum vector has a simpler expression when it is written in terms of the inertia tensor $\mathbf{I}_o$. But this is not true for the angular momentum tensor. Equations (4.17) and (4.19) show that the angular momentum tensor has a simpler expression when it is expressed in terms of the pseudo-inertia tensor $\mathbf{J}_o$.

In the following, we shall use the angular momentum, in its vector or tensor representation, to describe the dynamic behavior of a rotating rigid body.

4.3 The Torque Tensor

As is well known [2], the absolute time derivative of angular momentum defines the *resultant torque* or *moment of force*. This derivative expresses the basic law governing the rotational motion of a rigid body and is written in vector form as

$$\mathbf{M}_o = \dot{\mathbf{L}}_o = \mathbf{I}_o\cdot\dot{\omega} + \tilde{\omega}\mathbf{I}_o\cdot\omega \tag{4.22}$$

Obviously, when the point of rotation is the center of mass of the rigid body, (4.22) takes the form of (4.2). Sometimes, in the literature on classical dynamics, (4.2) is referred to as the *generalized Euler equation* for rigid body rotational motion. Here, we shall refer to (4.2) as the *vector* formulation of the generalized Euler equation.

Equation (4.22) has been stated in terms of the inertia tensor $\mathbf{I}_o$. If we use (4.6) to substitute for $\mathbf{I}_o$ in terms of $\mathbf{J}_o$, (4.22) becomes

$$\mathbf{M}_o = -\left(\mathbf{J}_o\cdot\dot{\omega} + \tilde{\omega}\mathbf{J}_o\cdot\omega\right) + tr\,[\mathbf{J}_o]\dot{\omega}. \tag{4.23}$$

Similarly, for $\mathbf{M}_c$ we can write

$$\mathbf{M}_c = -\left(\mathbf{J}_o\cdot\dot{\omega} + \tilde{\omega}\mathbf{J}_c\cdot\omega\right) + tr\,[\mathbf{J}_c]\dot{\omega}. \tag{4.24}$$

Now, as with angular momentum, the torque can be described by a second order skew-symmetric Cartesian tensor, which we shall refer to as the *torque tensor* . Using the dual operator we define the torque tensor as follows

$$\tilde{\mathbf{M}}_o = \mathit{dual}(\mathbf{M}_o). \tag{4.25}$$

This definition for the torque tensor requires the computation of the torque vector $\mathbf{M}_o$. Another definition for the torque tensor in terms of the inertia and the angular acceleration tensors is given by the following theorem.

Theorem 4.2 : The torque tensor about the center of rotation o, is defined as the absolute time derivative of the angular momentum tensor about the point o and satisfies the equation

$$\tilde{\mathbf{M}}_o = \left(\Omega\mathbf{I}_o\right)^T - \Omega\mathbf{I}_o + tr\,[\mathbf{I}_o]\dot{\tilde{\omega}} \tag{4.26}$$

where Ω is the angular acceleration tensor of the rotation and $\mathbf{I}_o$ is the rigid body inertia tensor about the point o.

Proof : By definition, we have

$$\tilde{\mathbf{M}}_o = \frac{d}{dt}\tilde{\mathbf{L}}_o.$$

Further, using (4.17), we get

$$\tilde{\mathbf{M}}_o = \left(\dot{\tilde{\omega}}\,\mathbf{I}_o + \tilde{\omega}\dot{\mathbf{I}}_o\right)^T - \left(\dot{\tilde{\omega}}\,\mathbf{I}_o + \tilde{\omega}\dot{\mathbf{I}}_o\right)^T + tr\,[\mathbf{I}_o]\dot{\tilde{\omega}}\ ,$$

since the time derivative of the scalar invariant $tr\,[\mathbf{I}_o]$ is zero. Now, using (4.10), we have

$$\begin{aligned}\tilde{\mathbf{M}}_o &= \left(\dot{\tilde{\omega}}\,\mathbf{I}_o + \tilde{\omega}\tilde{\omega}\mathbf{I}_o\right)^T - \left(\dot{\tilde{\omega}}\,\mathbf{I}_o + \tilde{\omega}\tilde{\omega}\mathbf{I}_o\right) + tr\,[\mathbf{I}_o]\dot{\tilde{\omega}} \\ &= \left(\Omega\mathbf{I}_o\right)^T - \Omega\mathbf{I}_o + tr\,[\mathbf{I}_o]\dot{\tilde{\omega}} \qquad \square\end{aligned}$$

The torque tensor $\tilde{\mathbf{M}}_o$ can also be defined in terms of the pseudo-inertia tensor $\mathbf{J}_o$ and the angular acceleration tensor Ω. To see this, we can consider the time derivative of (4.19) or use (4.6) to substitute for $\mathbf{I}_o$ in (4.26). In both cases after a few manipulations we arrive at the following equation

$$\tilde{\mathbf{M}}_o = \Omega\mathbf{J}_o - \left(\Omega\mathbf{J}_o\right)^T. \tag{4.27}$$

Obviously, when a rigid body is rotated about its center of mass (4.26) and (4.27) are written as

$$\tilde{\mathbf{M}}_c = \left(\Omega\mathbf{I}_c\right)^T - \Omega\mathbf{I}_c + tr\,[\mathbf{I}_c]\dot{\tilde{\omega}} \tag{4.28}$$

and

$$\tilde{\mathbf{M}}_c = \Omega\mathbf{J}_c - \left(\Omega\mathbf{J}_c\right)^T. \tag{4.29}$$

respectively. We shall refer to (4.29) as the *tensor* formulation of the generalized Euler equation of a rigid body rotational motion.

As we can see from (4.2) and (4.24), the torque vector $\mathbf{M}_c$ has a simpler expression when it is defined in terms of the inertia tensor $\mathbf{I}_c$. But, as in the case of the angular momentum tensor, the pseudo-inertia tensor $\mathbf{J}_o$ leads to a simpler equation for the definition of the torque tensor $\tilde{\mathbf{M}}_c$. This implies that for a vector formulation of the equations of rotational rigid body motion, the proper definition for the inertia tensor is given by (4.3). But, when a tensor formulation for the equations of rotational rigid body motion is required, then the proper definition for the inertia tensor is given by (4.4).

4.4 Computational Considerations

In the following, we shall assume that the angular velocity vector ω, the angular acceleration vector $\dot{\omega}$, and the angular acceleration tensor Ω are available, and we shall examine the computational cost of computing the vectors $\mathbf{F}_c$ and $\mathbf{M}_c$ which describe the motion of a rigid body.

To compute the vector $\mathbf{F}_c$ we need to evaluate (4.1). It is obvious that the computational burden of evaluating this equation results mainly from the computation of the vector $\ddot{r}_c$. From a computational point of view, most of the time, computing the vector $\ddot{r}_c$ is similar of computing the vector $\ddot{r}_1$ which is defined by (3.18) or (3.20). Thus, to compute the vector $\ddot{r}_c$, we can use (3.20) or (3.18). In the former case, we need to perform three vector cross product operations and two vector additions. This requires a total of 18 scalar multiplications and 12 scalar additions. In the latter case, we need to perform a matrix-vector multiplication and a vector addition. This requires a total of 9 scalar multiplications and 9 scalar additions. To compute the torque vector M_c we can use (4.2) or (4.29) which computes the skew-symmetric torque tensor $\tilde{M}_c$ from which we can extract, with no computational cost, its dual vector M_c by using the correspondence (3.9) in Part I. In the first approach, i.e., using (4.2), we need to perform two matrix-vector multiplications, a vector cross product operation and a vector addition which requires a total of 24 scalar multiplications and 18 scalar additions. In the second approach, we can evaluate the torque vector M_c with only 15 scalar multiplications and 15 scalar additions. This is so because there is no need to compute the complete matrix-matrix multiplication, which is involved in (4.29), since the tensor $\tilde{M}_c$ is skew-symmetric and the extraction of its dual vector requires no computations.

From the foregoing, when vectors are used to describe the Newtonian formulation of rigid body motion, i.e., equation (3.20), (4.1) and (4.2), to compute the vectors F_c and M_c, we require a total of 45 scalar multiplications and 30 scalar additions. On the other hand, when Cartesian tensors are used to describe the Newtonian formulation of rigid body motion, i.e., equation (3.18), (4.1) and (4.29), we require a total of only 27 scalar multiplications and 24 scalar additions for evaluating the same vectors. Therefore, the tensor treatment of rigid body motion which is presented in this paper considerably reduces the computational cost of evaluating the equations of rigid body motion. This, obviously, has very important implications in many practical problems of mechanics. For example, it has been shown in [10,11] that based on this tensor treatment of rigid body motion, we can solve in a computationally very efficient manner, the dynamic equations of rigid-link robot manipulators. It is therefore natural for one to expect that the proposed tensor methodology will yield similar reductions in computational cost for many other problems of mechanics, where rigid body dynamics play an important role.

V CONCLUSIONS

In this paper, based on Cartesian tensor analysis, a conceptually simple, easy to implement, and computationally efficient methodology is proposed for studying classical rigid body dynamics. In particular, by using the angular acceleration tensor, a new tensor formulation has been given for one of the basic equations of rigid body motion, namely, the Euler equation. Moreover, it has been demonstrated that the use of the angular acceleration tensor also simplifies the computation of the linear acceleration of various position vectors which are important in studying rigid body motion. Thus, based on this new tensor methodology we have provided a new and efficient approach for the study of classical Newtonian dynamics.

VI REFERENCES

[1] Jeffreys, H., Cartesian Tensors, Cambridge University Press, Cambridge, 1961.

[2] Wittenburg, I. J., Dynamics of Systems of Rigid Bodies, B. G. Teubner, Stuttgart, 1977.

[3] Goldstein, H., Classical Mechanics, 2nd Ed., Addison-Wesley, Reading, MA : 1980.

[4] Konopinski, E. J., Classical Descriptions of Motion, W. H. Freeman and Company, San Francisco, 1969.

[5] Bottema, O. and Roth, B., Theoretical Kinematics, North-Holland Publishing Co., Amsterdam, 1978.

[6] Angeles, J., Spatial Kinematic Chains : Analysis, Synthesis, Optimization, Springer-Verlag, New York, 1982.

[7] Angeles, J., Rational Kinematics, Springer-Verlag, New York, 1989.

[8] Casey, J., A Treatment of Rigid Body Dynamics, J. Appl. Mech., Vol. 50, pp 905-907, 1983.

[9] Casey, J. and Lam, V. C., A Tensor Method for the Kinematical Analysis of Systems of Rigid Bodies, Mechanism and Machine Theory, Vol. 21, No. 1, pp 87-97, 1986.

[10] Balafoutis, C. A., Patel, R. V. and Misra, P., Efficient Modeling and Computation of Manipulator Dynamics Using Orthogonal Cartesian Tensors, IEEE J. Robotics and Automation, Vol. 4, No. 6, pp 665-676, 1988.

[11] Balafoutis, C. A., Dynamic Analysis of Rigid-Link Open-Chain Robot Manipulators Using Cartesian Tensor Methods, Ph. D. thesis, Dept. of Elec. & Comp. Engineering, Concordia University, Montreal, Quebec, Canada, 1989.

ONE-STEP APPROACH TO SOLVING NONLINEAR PROBLEM OF BEAM-COLUMN

Yongxi Yu

Mechanical Engineering Dept. -Shanghai Jiao Tong University
Shanghai, 200030, P. R. of China

ABSTRACT

In this paper a new method of solution of nonlinear beam-column problem is presented. The relation between the lateral deflections of the beam-column and the bending moments caused by both of lateral and axial compressive loads is developed. The geometrical nonlinearity and linearly elastic material behavior are presumed. Given problem is reduced to formulation of a set of linear algebraic equations in terms of undeterminded lateral deflections of the beam-column. Numerical examples for uniform and nonuniform beam-columns are illustrated. Obtained results are in good agreement with those given by well-known formulas in [1].

INTRODUCTION

It is known that the solution of the problem of the beam-column with uniform and piecewise nonuniform cross section is given in reference [1]. However, there is no efficient method to analyze the beam-column with variable cross section. Here we provide a method of solution of this kind of problems. Employing the Castigliano's second theorem and Simpson's integration rule, a set of linear equtions with desired lateral deflections can be formulated. We assume that the axial deformations of the beam-column are so negligible in comparison with its lateral deformations that the complementary strain energy consists only of that due to bending deformations.

MATRIX FORM OF COMPLEMENTARY STRAIN ENERGY

The complementary strain energy of the beam-column shown in Fig. 1 is

$$U = \frac{1}{2}\int_{l}\frac{M^2dx}{EI} \qquad (1)$$

where M is the bending moment caused by both of lateral and axial loads; I is the moment of inertia, which could be variable; l is the length of beam-column. Let the beam-column be divided into s segments. The eq. (1) becomes

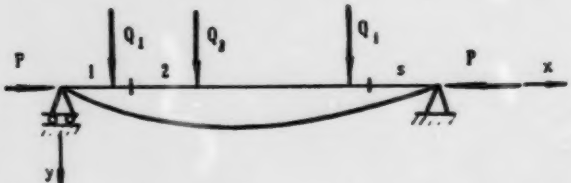

Fig. 1

$$U = \sum_{i=1}^{s}\int_{l_i}\frac{1}{2}\frac{M^2dx}{EI} \qquad (2)$$

The length of i-th segment is l_i (Fig. 2). Suppose the bending moments applied at the left end, the midpoint and the right end of the segment are given. By Lagrange interpolation the bending moments applied at points 1' and 2', which are the midpoints of the left and right halves of the segment should be

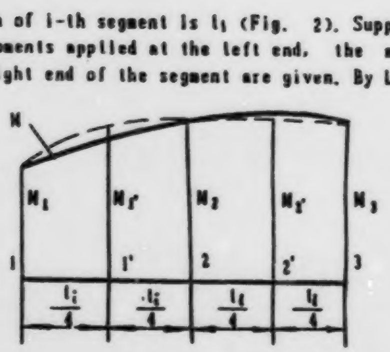

Fig. 2

$$M_{1'} = \frac{1}{8}(3M_1+6M_2-M_3) \qquad (3)$$

$$M_{2'} = \frac{1}{8}(3M_3+6M_2-M_1) \qquad (4)$$

According to Simpson's integration rule we have

$$\int_{l_i}\frac{M^2dx}{EI} = \frac{l_i}{12E}\left(\frac{M_1^2}{I_1}+\frac{4M_{1'}^2}{I_{1'}}+\frac{2M_2^2}{I_2}+\frac{4M_{2'}^2}{I_{2'}}+\frac{M_3^2}{I_3}\right) \qquad (5)$$

where I_i, $i = 1, 1' \ldots 3$, are the moments of inertia of the corresponding cross sections, on which they act. Letting $r_i = I_{max}/I_i$, $i = 1, 1' \ldots 3$, where I_{max} is the largest moment of inertia of the beam-column, substitution of $M_{1'}$ and $M_{2'}$ from eqs. (3) and (4) into eq. (5) gives

$$\int_{l_i} \frac{M^2 dx}{EI} = (M_i)^T [C_i] (M_i) \tag{6}$$

where

$$(M_i) = (M_1\ M_2\ M_3)^T \tag{7}$$

is bending moment vector for the segment and

$$[C_i] = \frac{l_i}{192 E I_{max}} \begin{bmatrix} 16r_1+9r_{1'}+r_{2'} & 18r_{1'}-6r_{2'} & -3r_{1'}-3r_{2'} \\ & 36r_{1'}+32r_2+36r_{3'} & -6r_{1'}+18r_{2'} \\ \text{symm.} & & r_{1'}+9r_{2'}+16r_3 \end{bmatrix} \tag{8}$$

is the costitutive matrix of this segment. Substituting eq. (6) into eq. (2), we can acquire the complementary strain energy of the beam-column

$$U = \frac{1}{2} (M)^T [C] (M) \tag{9}$$

where

$$(M) = (M_1\ M_2 \ldots M_n)^T \tag{10}$$

is the bending moment vector for the beam-column and

$$[C] = \begin{bmatrix} [C_1] & & & & \\ & [C_2] & & 0 & \\ & & \cdot & & \\ & & & \cdot & \\ & 0 & & \cdot & \\ & & & & [C_S] \end{bmatrix}, \tag{11}$$

is the constitutive matrix for the whole beam-column. It is noted that [C] is a symmetrical matrix. During forming [C], the element $(c_{33})_i$ of $[C_i]$ must be added to the element $(c_{11})_{i+1}$ of the successive submatrix $[C_{i+1}]$.

BENDING MOMENTT AND DEFLECTION VECTORS

The bending moment m_i acting on the cross section at any point i consists of m_{iq} and m_{ip} due to lateral loads Q and axial load P, respectively, i.e.

$$m_i = m_{iq} + m_{ip} \tag{12}$$

So the bending moment vector will be

$$(M) = (M_q) + (M_p) \tag{13}$$

where (M_q) is contributed only by lateral loads Q and

$$(M_p) = P[S](Y) \tag{14}$$

In eq. (14) P is an axial load.

$$[S] = \begin{bmatrix} 0 & 0 & . & . & . & . & 0 & 0 \\ 0 & 1 & . & . & . & . & 0 & 0 \\ . & . & 1 & . & . & . & . & . \\ . & . & . & 1 & . & . & . & . \\ . & . & . & . & . & . & 1 & 0 \\ 0 & 0 & . & . & . & . & 0 & 0 \end{bmatrix} \tag{15}$$

and

$$(Y) = (y_1\ y_2 \ldots y_n)^T \tag{16}$$

is a deflection vector. Matrices [S] for beam-columns having different kind of supports are listed in the Appendix. In order to apply Castigliano's second theorem, we are to discuss the expression of bending moment m_{ji} at any point i, when an auxiliary lateral load f_j is superposited at point j. It is easily to obtain

$$m_{ji} = m_i + (1 - \frac{x_j}{l}) f_j x_i - f_j (x_i - x_j), \quad j < i \tag{17a}$$

$$m_{ji} = m_i + (1 - \frac{x_j}{l}) f_j x_i, \qquad j \geq i \tag{17b}$$

where x_i and x_j are the distances from left end to points i and j, respectively. Then we have the vector of bending moments, caused by original loads and the auxiliary load f,

$$(M_j) = (m_{j1}\ m_{j2} \ . \ . \ . \ m_{jn})^T \tag{18}$$

When $f_j = 0$, we have

$$(M) = (M_j) \tag{19}$$

Utilizing Castigliano's second theorem and considering eq. (19), the deflection at point j is

$$y_j = \frac{\partial U}{\partial f_j}\bigg|_{f_j=0} = (M)^T [C] (J_j)\bigg|_{f_j=0} \tag{20}$$

where

$$(J_j) = \left(\frac{\partial m_{j1}}{\partial f_j}\ \frac{\partial m_{j2}}{\partial f_j} \ldots \frac{\partial m_{jn}}{\partial f_j}\right)^T_{f_j=0} \tag{21}$$

The element of vector (J_j) is given by

$$\frac{\partial m_{ji}}{\partial f_j} = x_i - \frac{x_i x_j}{l}, \quad j > i \tag{22a}$$

$$\frac{\partial m_{ji}}{\partial f_j} = x_j - \frac{x_i x_j}{l}, \quad j < i \tag{22b}$$

The expressions of the element $\partial m_{ji}/\partial f_j$ for different kind of beam-column supports are summarized in the

Appendix. Collecting all the deflections in one vector (Y), we have following expression

$$(Y) = [J]\ [C]\ (M) \qquad (23)$$

where

$$[J] = \begin{bmatrix} \frac{\partial m_{11}}{\partial I_1} & \frac{\partial m_{12}}{\partial I_1} & \cdots & \frac{\partial m_{1n}}{\partial I_1} \\ \frac{\partial m_{21}}{\partial I_2} & \frac{\partial m_{22}}{\partial I_2} & \cdots & \frac{\partial m_{2n}}{\partial I_2} \\ \vdots & \vdots & \cdots & \vdots \\ \frac{\partial m_{n1}}{\partial I_n} & \frac{\partial m_{n2}}{\partial I_n} & \cdots & \frac{\partial m_{nn}}{\partial I_n} \end{bmatrix} \qquad (24)$$

and [C] is calculated according to eq. (11). Considering eqs. (13) and (14), we can obtain an expected system of linear equations

$$[A]\ (Y) = (B) \qquad (25)$$

where

$$[A] = [I] - P[J][C][S] \qquad (26)$$

$$[B] = [J][C](M_q) \qquad (27)$$

In equations (26), (27) [I] is an identity matrix, but [J], [C] and [S] are given by eqs. (24), (11) and (15) respectively. (M_q) is calculated, as mentioned previously, by considering only lateral loads Q. The solution of eq.(25) provides the deflection vector (Y), while from the eigenvalue of [A] we can obtain the buckling load of beam-column.

EXAMPLES

The fact that many of examples have been solved to verify the accuracy of the proposed method exhibits the efficiency and reliability of the method. Three of them are demonstrated here.

1. A simply supported beam-column (Fig. 3) with uniform cross section has a length of 200 cm. The axial load P is 3000 kg. At the midpoint a lateral load Q = 2000 kg is applied. Young's modulus E is 2.1×10^6 kg/cm². The moment of inertia I is 20 cm⁴. The beam-column is divided into two segments of equal length.

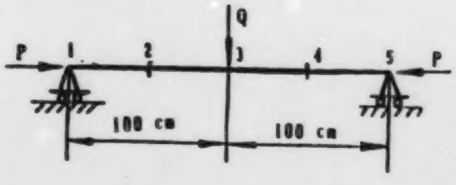

Fig. 3

$$[C] = \frac{1}{192 \times 2.1 \times 10^6} \begin{bmatrix} 130 & 60 & -30 & 0 & 0 \\ 60 & 520 & 60 & 0 & 0 \\ -30 & 60 & 260 & 0 & -30 \\ 0 & 0 & 60 & 520 & 60 \\ 0 & 0 & -30 & 60 & 130 \end{bmatrix} \text{kg}^{-1}\text{cm}^{-1}$$

$$[J] = \begin{bmatrix} 0 & 0 & 0 & 0 & 0 \\ 0 & 37.5 & 25.0 & 12.5 & 0 \\ 0 & 25.0 & 50.0 & 25.0 & 0 \\ 0 & 12.5 & 25.0 & 37.5 & 0 \\ 0 & 0 & 0 & 0 & 0 \end{bmatrix} \text{cm}$$

$$(M_q) = (\ 0\ 50000\ 100000\ 50000\ 0\ )\ \text{kgcm}$$

Substituting above matrices into eq. (25), we obtain the deflection vector

$$(Y) = (\ 0\ 8.6119\ 11.3365\ 8.6119\ 0\ )\ \text{cm}$$

and the buckling load Pcr = 9808.3 kg. The analytical formulas in [1] give the deflection at point 3 (Fig. 3) y_3 = 11.1269 cm and the buckling load Pcr = 10363.0 kg. If the beam-column is divided into 8 segments, we shall have y_3 = 11.14574 cm and Pcr = 10319.5 kg.

2. A piecewise variable beam-column, which is divided into 3 segments, has a length of 200 cm (Fig. 4). The middle segment being 80 cm long has I_2 = 50 cm⁴. The left and right segments have the same I_1 = 20 cm⁴. Obtained deflection vector under loads Q and P is

$$(Y) = (\ 0\ 2.786\ 4.404\ 5.500\ 4.404\ 2.786\ 0\ )\ \text{cm}$$

and Pcr is 17002.9 kg. The Pcr given by [1] is 17535.0 kg.

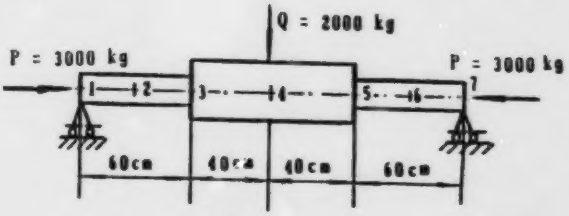

Fig. 4

3. A crane jib shown in Fig. 5 has a total length 38 m. Its overhanging span is 22 m. Young's modulus E is 2.1×10^6 kg/cm². The jib is divided into two segments. The moments of inertia at the points indicated in Fig.5 are $I_1 = 1.0590 \times 10^6$ cm⁴, $I_2 = 1.6776 \times 10^6$ cm⁴, $I_3 = 2.4858 \times 10^6$ cm⁴, $I_4 = 5.0317 \times 10^6$ cm⁴, $I_5 = 7.7900 \times 10^6$ cm⁴, $I_6 = 6.3875 \times 10^6$ cm⁴, $I_7 = 5.0512 \times 10^6$ cm⁴, $I_8 = 1.9862 \times 10^6$ cm⁴ and $I_9 = 0.8249 \times 10^6$ cm⁴. The compressive load is P = 10000 kg and lateral load is Q = 2500 kg at the free end.

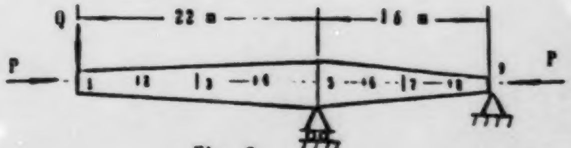

Fig. 5

Proposed method gives the deflection vector {Y} = {20.5 7.30 0 -1.6 0} cm and the buckling load Pcr =2.52 x 10^6 kg.

CONCLUSION

Presented method provides a general technique to solve the problem of beam-columns with variable cross-section. The method reduces the given problem to solving a system of linear equations, giving adequate results for engineering practices. Formulation of such a system of linear equations is simple and may be easily programable. In general, if a beam-column is divided into 2--4 segments, obtained results (deflections and buckling load) will possess sufficient accuracy for practical engineering purposes.

REFERENCES

1. Timoshenko S. P. & Gere J. M., Theory of elastic Stability, 2nd ed., pp. 1-15 & 110-130, McGraw-Hill, New York, 1961.
2. Reddy J. N., Energy and Variational Methods in Applied Mechanics, pp. 160-170, John Wiley & Sons, New York, 1984.

APPENDIX

The matrices [S] listed in Tab. 1 are derived only for the beam-columns that are divided into 2 segments.

Table 1. The values of $\frac{\partial m_{ji}}{\partial f_j}$ when f_i = 0 and matrices [S]

Type of beam-column	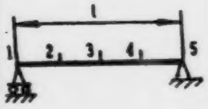	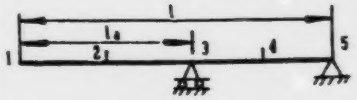		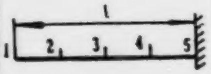
		$x_i \leq l_a$	$x_i > l_a$	
$\frac{\partial m_{ji}}{\partial f_j}$ =	$x_i - \frac{x_i x_j}{l}, j \geq i$ $x_j - \frac{x_i x_j}{l}, j < i$	$0, \ j \geq i$ $x_j - x_i, j < i$	$\frac{l-x_j}{l-l_a}(x_i - l_a), j \geq i$ $\frac{l-x_j}{l-l_a}(x_i - l\ ) + x_j - x_i, j<i$	$0, \ j \geq i$ $x_j - x_i, j < i$
[S] =	$\begin{bmatrix} 0&0&0&0&0\\ 0&1&0&0&0\\ 0&0&1&0&0\\ 0&0&0&1&0\\ 0&0&0&0&0 \end{bmatrix}$	$\begin{bmatrix} 0&0&0&0&0\\ -1&1&0&0&0\\ -1&0&0&0&0\\ -.5&0&0&1&0\\ 0&0&0&0&0 \end{bmatrix}$		$\begin{bmatrix} 0&0&0&0&0\\ 1&-1&0&0&0\\ 1&0&0&0&0\\ 1&0&-1&0&0\\ 1&0&0&0&0 \end{bmatrix}$

A VARIABLE ORDER RUNGE-KUTTA METHOD FOR PROBLEMS IN APPLIED MECHANICS

R. C. Quirt and R. J. Anderson

Department of Mechanical Engineering,
Queen's University, Kingston,
Ontario, Canada

ABSTRACT

Many problems in engineering yield a set of simultaneous differential equations that must be solved numerically. These equations can be efficiently solved by either Variable Order Linear Multistep Methods (LMM) or Runge-Kutta (RK) methods provided the equations are not overly stiff. Efficient differential equation solvers all implement some form of error control. However, when these solvers are applied to problems where the frequency of state variable output constrains the step size their performance degrades. The variable order LMMs can reduce their order to deal with this but the Runge-Kutta codes are in general fixed in order and this constraint can significantly reduce their efficiency.

Runge-Kutta methods are often the method of choice for a problem since they are self starting and can deal more efficiently with discontinuities than can LMMs. It is desirable then to develop a variable order RK method for application to these situations. This paper presents a variable order Runge-Kutta code, RKV. RKV is based upon a family of imbedded Runge-Kutta methods of order up to eight developed by Verner [5].

For test problems taken from mechanical dynamics RKV demonstrates similar performance to some widely used fixed order RK methods when the step size is not constrained and superior performance when it is.

1.0 INTRODUCTION

Many problems in Applied Mechanics result in a set of nonlinear ordinary differential equations for which a closed form solution cannot be found. Therefore, a numerical ordinary differential equation (ODE) solver must be used to obtain a solution. A numerical method to solve these equations should achieve a solution of desired accuracy as efficiently as possible. For efficiency, only numerical methods of reasonably high order that implement some sort of error control can be used. There are a wide variety of such methods available but it is important that the method be matched to the type of problem under consideration.

When selecting an ODE solver, one must consider three principal factors. First, the nature of the equations. Often, equations arising from problems in Mechanics are not very stiff, contain some discontinuities from piece-wise linear models or other sources, and are not very expensive to evaluate. Secondly, one must consider the desired accuracy of the solution. For example equations including parameters that have been measured to a moderate level of accuracy should be solved to a corresponding degree of accuracy. Finally, the interval between output data points is important. Usually the desired solutions are continuous functions and some kind of graphical output is desired. For this reason the interval between output data points is frequently small thereby constraining the allowable step size.

When choosing or developing an efficient program to solve these types of problems, linear multistep and Runge-Kutta methods should be considered. Both of these methods can be efficient if the order is matched properly to the problem and the frequency of output [1,2].

1.1 Linear Multistep Methods

Programs implementing variable order linear multistep methods (LMM) such as Shampime and Gordon's STEP [1,2] have received wide acceptance in software libraries. These codes obtain their efficiency through changing both the step size and the order of the method used. The overall philosophy is to keep the step size fairly constant and change the order to deal with a problem's changing dynamics. For maximum efficiency they utilize the lowest order LMM which will meet the desired error tolerance. A fairly constant step size is necessary to allow simplification of the error estimation since LMMs use past information to propagate the solution and to estimate the error in the present step [1]. Higher order estimates of the function are achieved by combining additional past information about the derivative function to that used by the lower order LMM. Since the previous points are the same for the different orders, it is quite inexpensive to propagate error estimates for the solutions of different order simultaneously. At each successful step, the error in each lower order method is tested to see if the method could meet the error requirement. If the method fails to meet the error requirement during a step, then higher order methods are evaluated to see if they could successfully propagate the solution. If an order or step size change is indicated, a fair amount of work is required to change the order or step size before the solution can be propagated. This overhead tends to decrease the overall efficiency of LMMs.

LMMs are not usually used to solve the types of problems considered here, because they are difficult to code and, since they use past information, they are hard to start and do not deal well with discontinuities. Their high overhead also makes them inefficient when the derivative evaluations are simple. They have however an inherent ability to deal with frequent output by simply interpolating between solution points using a polynomial of an order similar to the method.

1.2 Runge-Kutta Methods

The other major family of codes in widespread use are based on the Runge-Kutta (RK) methods. The most salient difference between Runge-Kutta methods and linear multistep methods is that the former use function evaluations only at points within the step. The use of points within the step make RK methods both self starting and inherently better suited to dealing with discontinuities. Unlike LMM codes, RK codes are usually of fixed order. They can be equally as efficient as LMM codes if a proper order is used [2] provided the derivative evaluations are not very expensive.

RK methods of order greater than four (the classical) which implement error control have been developed. They estimate the local error in the solution by propagating two solutions that differ by an order of one. The difference between these solutions is an estimate of the local error in the lower order method. Higher order is achieved by using more derivative evaluations within the step. For example the minimum number of evaluations or stages for a fourth order method with local error estimation is six, and for a sixth order method is eight [10]. The number of stages equals the number of derivative evaluations per step. In general high order RK codes (which require more evaluations per step) are suitable when a high degree of accuracy is desired, and low order when less accuracy is required [2,7]. RK codes cannot interpolate the function to achieve output at intermediate points but instead must step to the desired output point. This can limit the step size to a value less than that required to achieve the desired accuracy, especially when a high order method is used.

To achieve optimum performance over a wide range of tolerances and to avoid unnecessary work when frequent output is requested, a variable order RK code is appropriate. Shampime and Gordon, and Shampime and Wisniewski [2,3] have developed two such codes, RKSG and RKSW. RKSG uses three pairs: a 3(4)13 (order(order+1)stages) pair derived from the Fehlberg [4] 7(8)13 pair, the 7(8)13 pair itself, and an unrelated 3(4)4 pair. The 3(4)13 pair uses the same function evaluations as the 7(8)13 and thus it is possible to calculate an estimate of the error in the fourth order solution with little additional overhead when propagating with the 7(8)13 method. The 3(4)13 pair is used to determine if a fourth order pair would be able to meet the requested tolerance at the present step size. The solution is propagated, however with the 3(4)4 pair. The 3(4)4 method has minimal stages and is much more efficient than the 3(4)13 pair. RKSG has many features which increase the overhead and makes this code not particularly efficient.

RKSG has been superseded by RKSW because the latter is very efficient [2,3]. RKSW utilizes two efficient unrelated methods. The selection of order is based solely upon the observation that the low order pair is most efficient at relative tolerances below about 10^{-3}. This simple criterion is very easy to implement, and the entire RKSW code has been kept as simple as possible to minimize overhead.

2.0 THE PROPOSED METHOD

The method presented in this paper uses methods selected from a Complete Set of Imbedded Runge-Kutta (CSIRK) methods of order one to eight. This complete imbedding means that all of the orders use the same function evaluations such that it is simple to change order dynamically.

The general Runge-Kutta method can be written as:

$$f(x,y) = \frac{dy}{dx}$$

$$y_{n+1} = y_n + h \sum_{r=1}^{s} b_r k_r$$

$$k_1 = f(x_n, y_n)$$

$$k_r = f(x_n + hc_r, y_n + h \sum_{j=1}^{r-1} a_{rj} k_j) \quad r = 2, \ldots, s$$

The parameters a, b and c must satisfy certain constraints if a method of order p is to be achieved [10]. A method of order p greater than q must satisfy all the constraints of q as well as some additional constraints to achieve the higher order. In general these constraints can be met with a few free parameters. These parameters can then be used to produce some desirable property such as a minimum principal error term. In [5] Verner derives complete sets of imbedded methods from imbedded pairs of orders $p-1$ and p for p greater than 5. This is achieved by determining a set of weighting factors b^q for each method of order q such that only the constraints necessary for order q are met. The c vector and the a array are common to all the methods and thus the function evaluations are common to all the imbedded methods.

In this investigation two complete sets of imbedded methods were considered; a CSIRK(8,6) (stages,maximum order), and a CSIRK(13,8). They can be found in tables A.3 and A.5 of [5]. In order to determine which of these methods to use, each of the pairs of methods in the CSIRKs were evaluated as a fixed order pair.

To evaluate the efficiency of the fixed order methods each was coded into an identical program that utilized the error estimation and step size control discussed in sections 2.1 and 2.2. In order to select the most efficient methods, a number of tests were performed using the vehicle model test problem introduced in section 3.0. From this analysis, the following conclusions were made: 1) the CSIRK(13,8) contains the two best methods, 2) when the step size is not constrained by the need for frequent output the 6(7)12 pair is the most efficient at any error tolerance, 3) when the step size is constrained by the output the 3(4)6 pair is the most efficient at low tolerances, and 4) since the 6(7)12 and the 3(4)6 pairs are more efficient than all of the other orders it does not appear fruitful to consider a code that would continuously vary order. Accordingly it was decided to go ahead with a code that switches between the 3(4)6 and the 6(7)12 pair of the CSIRK(13,8).

2.1 Error Estimation

All efficient codes for solving ODEs use some type of error estimation scheme to control the step size and/or order. The most popular and reliable schemes estimate the error by the difference between two estimates of the function of order $p+1$ and p, y^{p+1} and y^p. The code developed here uses this estimation. Writing this difference in terms of the Taylor series expansion of the RK methods of order p and $p+1$ [6]

$$\begin{aligned} EE^p &= h^{p+1}\sum_{i=1}^{N_p} T_p^{p+1} D_i^{p+1} + \\ &\sum_{q=p+2}^{\infty} h^q \sum_{i=1}^{N_q}\left(T^q_{p,i} - T^q_{p+1,i}\right) D^q_i \end{aligned} \tag{1}$$

where EE^p is the estimate of the error in the p order solution, and the T_p's are the constants from a Taylor series expansion of the p order method, the T_{p+1}'s similarly for the p+1 order method, h is the step size, the D^q's are the elementary differentials of order q of the function and the summation is over the number of principal derivatives. The magnitude of the T's determine how accurate a method is, and are set by the parameters a, b, and c of the method. The first term of (1) is the principal local truncation error term of the p order method. If EE is to be an effective estimator of the local truncation error, then the method should be designed to minimize the second term of (1) with respect to the first term [6,8,10]. As a further constraint for a method to be efficient it is necessary to have the principal local truncation error term as small as possible for the p order method [6,8,10]. Also note that the actual magnitude of the two terms of (1) are a function of the problem since the principal derivatives, the D's, of the function are involved.

The maximum T values for the imbedded methods were not published in [5] so it was not possible to evaluate each method from this perspective. Instead, tests using the selected problems were performed as described earlier to quantitatively evaluate their efficiency.

2.2 Step Size Control

A step size control strategy can be developed based on the assumption that the principal local truncation error dominates the error estimate. Then equation (1) becomes

$$EE^p = h^{p+1}\sum_{i=1}^{N_p} T_p^{p+1} D_i^{p+1} \tag{2}$$

from which it is seen that EE^p is proportional to h^{p+1}. In this code a further attempt was made to adjust the step size to control global error which is proportional to h^p [10]. The resulting formula [1,8] is;

$$h_{n+1} = h_n\left(V\left\|\frac{tol}{\max\frac{EE}{y_n}}\right\|\right)^{1/p} \tag{3}$$

where tol is the desired tolerance, and $max(EE/y_n)$ is the largest relative error estimate calculated from the difference of two solutions of order p and $p+1$ to the vector valued function y. Inherent in this approach is the assumption that the constant of proportionality is independent of h, and is therefore constant. For RK methods the principal local truncation error term is a function comprised of a linear combination of the fundamental derivatives of the function and is thus a function of h, x, and y. Also the scaling factor used to change the step size in the $n+1^{st}$ step is based upon the behavior of the function in the n^{th} step. The term V is introduced to account for these inadequacies and equals 0.5 after [1]. As a further safeguard the change in the step size is limited.

The user specifies two parameters for the error control; a relative tolerance and a base value. The base value is used to clamp the function value to some non-zero level. Thus, the actual error control is relative when the function value exceeds base, and absolute when it is less than base.

2.3 Order Selection

Since the 6(7)12 method is in general the most efficient, it is prudent to always start with this order and only switch if the 3(4)6 would be more efficient. Since the derivative evaluations are the same for both the 6(7)12 and the 3(4)6 methods no additional derivative evaluations are necessary to determine the error in a third order estimate when propagating with the 6(7)12 method. Since many of the b terms for the 3(4)6 method are zero it costs only eight multiplications to form a third order estimate and error. The approach used is to calculate an error estimate for the third order method while propagating the solution with the 6(7)12 method. Then if the third order method meets the tolerance requirements for this and the previous step the code switches to the 3(4)6 method.

Once using the 3(4)6 method, the code will continue to do so until a step fails. At that point, rather than scrapping the step the code switches to the 6(7)12 method. It is only necessary to calculate six additional function evaluations to implement this transition to the 6(7)12 method. Then only if the 6(7)12 method fails will it scrap the step and start over with the 6(7)12 method and a new smaller step size.

This scheme has been designed to 1) minimize the overhead associated with order selection, 2) try to salvage the six evaluations necessary for the 3(4)6 method by switching to the 6(7)12 if the 3(4)6 fails a step, and 3) if in doubt favour the more efficient 6(7)12 method.

2.4 Stability

The interval or region of absolute stability was not published for the imbedded methods in [5] and time precludes any attempt to determine them. In general the region of absolute stability for the 6(7)12 method will be considerably larger than for the 3(4)6. However if the regions are scaled for equal work ie. the 6(7)12 region scaled down by a factor of two, then the 3(4)6 method will probably show a larger stability region [10]. No attempt was made to detect a stability problem in the code. This is not a major limitation since the types of systems to which RK codes should be applied are not very stiff. Typically when trying to solve a stiff problem the tolerance is set fairly low which will favour the lower order method if frequent output is requested. This will give improved efficiency but it will remain the responsibility of the user to be sure that the step size is small enough to prevent any stability problems.

3.0 TEST MODELS

Problems in dynamics yield sets of second-order, nonlinear ordinary, differential equations. These arise from Newton's or Lagrange's equations which relate accelerations, the second derivative of position with respect to time, to the sum of the forces. In vehicle dynamics small displacement models are very popular and effective. The small displacement assumption allows the linearization of the trigonometric functions and this significantly reduces the computational effort involved in solving these problems. While geometric linearization is often justifiable, linearization of the component constitutive relation is not. Since many of the force components are nonlinear functions of the state variables the corresponding equations of motion are nonlinear. Piecewise linear functions are frequently used to approximate the nonlinear constitutive relations which introduce into the equations a number of mild discontinuities.

The first test problem chosen to evaluate the variable order method is of this type. It is a simple but surprisingly accurate handling model of a typical large North American automobile. A cubic saturation model is used for the tire forces and a ramped steering input is used to represent a typical manoeuver. The discontinuities in both the cubic saturation model and the ramped steering are common in many of the models used in vehicle dynamics. The equations used are a derivative of those used by Anderson and Kurtz [11].

The second model is of a simple harmonic oscillator with damping. This problem was chosen because a closed form solution could be obtained to check the numerical solution.

3.1 Test Result

Most testing was performed using the vehicle dynamics model. This was done since it was more representative of a typical problem than is the damped oscillator. The first maneuver studied was a ramped turn to two degrees of front wheel steer in one second. This was held for three seconds and then returned to neutral. A two degree front wheel steer corresponds to a steering wheel rotation of about twenty degrees. This maneuver was performed at forty four feet per second (thirty miles per hour). One hundred output points was selected as typical to achieve smooth graphical output.

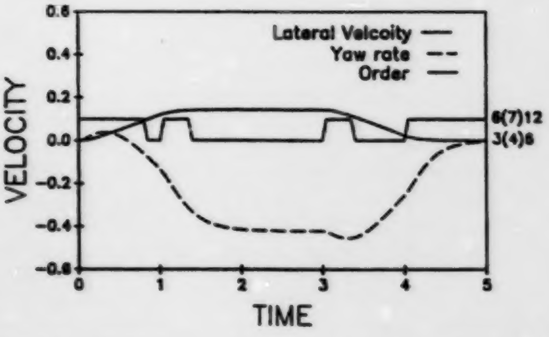

Figure 1: Lateral velocity, Yaw rate and RKV order for *tol* = 10^{-5}.

Figure 1 shows the lateral velocity, yaw rate and order of the method over the five seconds required to complete the maneuver. It is apparent that the order changing logic performs well, switching to high order when the rate of change of the derivative function is high in order to meet the desired error tolerance.

Table 1 summarizes some important performance indicators over a range of error tolerances. First it should be noted that the code takes almost the minimum number of steps (100) over the entire tolerance range. The average number of evaluations per step is seen to range smoothly from the minimum of approximately six to a maximum of twelve. No failed steps occurred which indicates that when the code switched up from the 3(4)6 to the 6(7)12, method the higher order method successfully salvaged the existing step. A few results for fifty output points are included in Table 1 and verify these findings.

Table 1: The performance of RKV on the vehicle dynamics model with 100 output points (50 output points).

TOL	STEPS	EVALUATIONS	EVALS./STEP	FAILURES
1(-9)	101	1212	12	0
1(-8)	102	1206	11.8	0
1(-7)	102	1146	• 11.2	0
1(-6)	107(52)	912(588)	8.5(11.3)	0
1(-5)	104(55)	768(546)	7.4(10.0)	0
1(-4)	102(54)	636(402)	6.2(7.4)	0
1(-3)	101	624	6.2	0

A second series of tests was performed to compare the performance of RKV to either of its component methods as fixed order methods. A slightly sharper turn of three degrees in one second was used and only the turn into the constant radius curve was considered. Table 2 summarizes the results which shows RKV to be a superior performer when frequent output is requested at all but the slackest tolerance when compared to its component fixed order methods.

Table 2: A comparison of RKV to the imbedded methods used in RKV as fixed order methods.

	100 OUTPUT POINTS			1 OUTPUT POINT		
TOL	3(4)6	6(7)12	RKV	3(4)6	6(7)12	RKV
1(-8)	3012	1296	1332	2700	468	468
1(-7)	1902	1248	1086	1632	360	492
1(-6)	1266	1272	894	912	276	336
1(-5)	906	1248	768	558	276	216
1(-4)	726	1212	666	354	180	180
1(-3)	660	1212	642	240	156	132
1(-2)	606	1212	624	126	96	144

The second test problem was a simple damped oscillator. Table 3 summarizes the maximum relative error at the output points. With one step to the end point the error shows the desired smooth progression with the tolerance. With one hundred output points the error changes abruptly at a tolerance of 10^{-5}. This is a result of having only two orders from which to choose in RKV. Inclusion of more orders would produce a smoother relationship but in doing so the efficiency at intermediate error tolerances would be lower.

As a final effort to validate RKV and to establish it's efficiency solutions to the vehicle dynamics model for a three degree steering angle were obtained using four other Runge-Kutta methods: V5(6) and V7(8) fifth and seventh order methods from [6], and D5(6) and D7(8) from [8]. Figures 2 and 3 summarize the number of function evaluations for a single, and one hundred output points respectively. It is apparent that RKV is competi-

Table 3: Maximum relative error for RKV on spring/damper model *base* = 10^{-3}.

TOL	1 OUTPUT POINT	100 OUTPUT POINTS
1(-8)	1.2(-7)	1.4(-8)
1(-7)	9.6(-7)	1.4(-8)
1(-6)	5.6(-6)	1.4(-8)
1(-5)	1.9(-5)	1.4(-8)
1(-4)	3.9(-5)	3.4(-2)
1(-3)	2.1(-3)	4.8(-2)
1(-2)	1.1(-2)	5.1(-2)

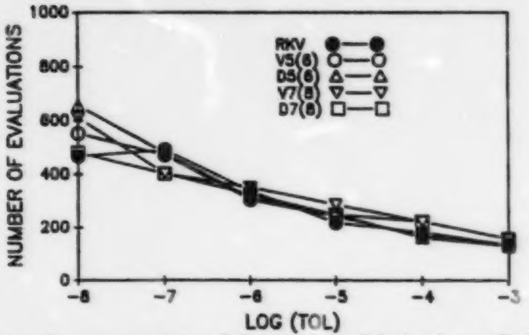

Figure 2: A comparison of the number of derivative evalutions for a single output point.

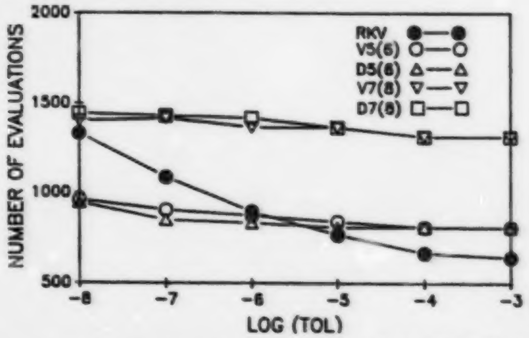

Figure 3: A comparison of the number of derivative evalutions for 100 output points.

tive with the other methods and shows superior performance at low tolerances ($< 10^{-5}$) and frequent output.

4.0 CONCLUSION

Based on the results of tests conducted on these typical problems, RKV shows definite promise when frequent output is desired. In particular RKV is more efficient than either of its constituent methods for the test problems chosen. It performs well with respect to some of the popular efficient fixed order codes. It shows superior performance to the fixed order codes at low tolerances.

A further improvement may be obtained by using local extrapolation on at least the 3(4)6 method to obtain higher accuracy.

One further benefit to the imbedding scheme is the possibility of detecting discontinuities and better dealing with them. The 3(4)6 method in RKV uses function evaluations only in the first half of the step while the 6(7)12 covers the entire step. If, then, the 3(4)6 method fails and the 6(7)12 also fails, it may be because of a discontinuity near the half way point of the step. This information could be used to step up to the discontinuity and then to continue on from it. It is important however to keep the overhead to an absolute minimum if RKV is to be efficient.

ACKNOWLEDGEMENT

The authors are indebted to the Natural Science and Engineering Research Council of Canada for support provided by way of a postgraduate Scholarship and an Operating grant.

REFERENCES

1. Shampine L. F., Gordon M. K., "Computer Solution of Ordinary Differential Equations -The Initial Value Problem", W. H. Freeman and Company, San Francisco 1975.

2. Shampine L. F., Wisniewski J. A.,"Variable Order Runge-Kutta Codes", Proc. of IMA conference, Computional Techniques for Ordinary Differential Equations, Manchester, England, Dec. 1978.

3. Shampine L. F., Wisniewski J. A.,"The Variable Order Runge- Kutta Code RKSW and its Performance", SAND78-1347, Sandia Laboratories, Albuquerque, 1978.

4. Fehlberg, E.,"Classical fifth-, sixth-, seventh-, and eighth-order formulas with stepsize control", NASA Tech. Rep. NASA TR R-287, George C. Marshall Space flight Centre, Huntsville, 1968.

5. Verner J. H.,"Families of Imbedded Runge-Kutta Methods", SIAM J. Numer. Anal., Vol. 16 No. 5 ,pp. 857-875, Oct. 1979.

6. Verner J. H.,"Explicit Runge-Kutta Methods with Estimates of the Local Truncation Error", SIAM J. Numer. Anal., Vol. 15 NO. 4, pp. 772-790, Aug. 1978.

7. Jackson K. R., Enright W. H. and Hull T. E.,"A Theoretical Criterion for Comparing Runge-Kutta Formulas", SIAM J. Numer. Anal., Vol. 15 No. 3, pp. 618-641, June 1978.

8. Prince P. J., Dormand J. R.,"High order embedded Runge-Kutta formulae", J. Comp. and Appl. Math., Vol. 7 No. 1, pp. 67-75, 1981.

9. Dormand J. R., Prince P. J.,"A reconsideration of some embedded Runge-Kutta formulae", J. Comp. and Appl. Math., Vol. 15, pp. 203-211, 1986.

10. Lambert, J. D., "Computational Methods in Ordinary Differential Equations", Wiley, 1973.

11. Anderson, R. J., Kurtz, E. F.,"Handling-Characteristics Simultaion of Car-Trailer Systems", Trans. Society of Automotive Engineers, Paper No. 800545, pp2097-2113, 1980.

SYNTHESIS OF CAM CURVE IN LINE WITH COMPLEX BOUNDARY AND INTERIOR CONSTRAINTS

L. Xue
Assistant Professor
Department of Mechanical Engineering
Shaanxi Mechanical Engineering Institute
Xian, Shaanxi, P.R. of China

J. Pei
Research Assistant
Department of Mechanical Engineering
Queen's University
Kingston, Ontario, Canada

ABSTRACT

This paper is concerned with the method of general synthesis of cam motion using spline functions in which not only complex boundary conditions can be satisfied but also the complex interior constrains. It is easily applied the method to the synthesis of cam curves which have the variety of requirements with displacement, velocity and acceleration through controlling the interior shape of the curves and boundary conditions. Yet, a local adjustment can be used to improve the performance of cam curve while still satisfying the constraints. Several examples is presented to illustrate application of the method and to compare it to more traditional techniques.

INTRODUCTION

Most of contour design in engineering, such as cam profile , can be contributed to the following problem.

Suppose Y=f(x) is a curve to be approximated. With a simple and calculable curve Y=s(x) to approximate Y=f(x) is a common approach. The premise which Y=s(x) can represent Y=f(x) approximately is:

.Y=s(x) should keep the convex-concave of Y=f(x);
.s(x) should be uniform approximation f(x) in [a,b].

When spline function is used to fit cam curve, it well satisfies above conditions.

Based on the author's paper [1], a general, systematic approach for motion synthesis of cam using spline functions is presented. It overcomes difficulties associated with some previous approaches, such as polynomial approach. The method with spines can satisfy not only the complex boundary conditions but also the complex interior constraints. Also, the spline method in the paper can insure continuity of the derivatives of displacement since the spline can be made to have continuous derivatives up to any order [2] [3].

However, the continuity in the second derivative is usually enough for the requirement of cam systems. The splines describe in the paper is only up to cubic function. The local adjustment can be used to improve the curve performance through adjusting the motion parameters such as acceleration while still satisfying the constraints. Several examples are presented in the paper.

ZERO ORDER DUMMY TREATMENT

Similar to polynomial interpolation function, polynomial splines can easily used to satisfy boundary conditions through selecting the proper coefficients and degrees of the polynomial. But it is more important to control interior kinematic parameters such as displacement, velocity and acceleration to satisfy the variety requirements of cam motions rather than only satisfy the boundary conditions in cam system.

Traditional method is to fit acceleration curve first based on some typical conditions or principles. And then adjust the acceleration curve to satisfy the boundary conditions. Finally the displacement and velocity curves can be obtained [4].

This method is well satisfied the cam system which only has the requirement on acceleration. In the synthesizing motion for actual cams, designers is often faced with variety of problems. There are usually specific displacement, velocity and acceleration constraints to be satisfied. When the cam system has requirements of displacement or velocity as well this traditional method may only provide few points (such as the points at boundary) which can satisfy the displacement or velocity conditions.

It is very common in actual cam systems that major kinematic requirement is displacement or velocity, in which displacement or velocity is not only required at boundary points but also at interior knots. Acceleration for such a cam system only becomes the dynamic requirement. In this case, using splines may be a proper way because it can be used to satisfy the boundary conditions and interior kinematic parameters (displacement, velocity and acceleration).

As a example, we consider a cam profile design which should satisfy the following constraints.

1) interior conditions (displacement)

$$S_3(X_i)=R_i \quad i=1,2,\ldots,n-1;$$

where

S_3 - displacement of the follower

X - cam rotational angle

R - displacement required

i - knot locations in sequence 1,...,n-1

2)boundary constraints

$$S_3^{\alpha}(X_0)=S_3^{\alpha}(X_n)=R_n^{\alpha} \qquad \alpha=0,1,2;$$

where

α - derivative order of displacement in sequence 0,1,2

0, n - knot locations at 0, n

Obviously, there are n+3 interpolation knots and n+5 constraint equations. We need to find out two more knots. X_p and X_q are given as the two knots where the p and q must be follow the relation of equation (1)

$$2<p<q<n-2 \tag{1}$$

to remain the boundary conditions.

The corresponding function values should be

$$S_3(X_p)=R_p \quad \text{and} \quad S_3(X_q)=R_q$$

From n+3 basic constraints, we have

$$\begin{bmatrix} 4&1&0&0&0&0&0&0&0&0&0&1\\ 0&1&4&1&0&0&0&0&0&0&0&0\\ 0&0&1&4&1&0&0&0&0&0&0&0\\ 0&0&0&\cdot&\cdot&\cdot&0&0&0&0&0&0\\ 0&0&0&0&\cdot&\cdot&\cdot&0&0&0&0&0\\ 0&0&0&0&0&1&4&1&0&0&0&0\\ 0&0&0&0&0&0&\cdot&\cdot&\cdot&0&0&0\\ 0&0&0&0&0&0&0&1&4&1&0&0\\ 0&0&0&0&0&0&0&0&\cdot&\cdot&\cdot&0\\ 0&0&0&0&0&0&0&0&0&1&4&1\\ 1&0&0&0&0&0&0&0&0&0&4&1 \end{bmatrix} \begin{bmatrix} C_1\\ C_2\\ C_3\\ \cdot\\ \cdot\\ C_p\\ \cdot\\ C_q\\ \cdot\\ C_{n-1}\\ C_n \end{bmatrix} = \begin{bmatrix} 6R_1\\ 6R_2\\ 6R_3\\ \cdot\\ \cdot\\ 6R_p\\ \cdot\\ 6R_q\\ \cdot\\ 6R_{n-1}\\ 6R_n \end{bmatrix} \tag{2}$$

$$\text{and} \qquad C_1=C_{n+1} \qquad C_0=C_n \qquad C_{-1}=C_{n-1} \tag{3}$$

where C_i = constant coefficients

(i=0,1,2,...,n)

The two boundary constraints added in are

$$\frac{1}{2}C_1-\frac{1}{2}C_{n-1}=R_n'$$

$$C_1+C_{n-1}-2C_n=R_n''$$

in addition,

$$\frac{1}{6}C_1+\frac{1}{6}C_{n-1}+\frac{2}{3}C_n=R_n$$

Using Cramer's rule, we obtain

$$C_1=\Delta_1/\Delta \qquad C_{n-1}=\Delta_{n-1}\ /\Delta \qquad {}_nC_n=\Delta\ /\Delta \tag{4}$$

where

$$\Delta=\begin{vmatrix} 1/2 & -1/2 & 0\\ 1 & 1 & -2\\ 1/6 & 1/6 & 2/3 \end{vmatrix} \qquad \Delta_1=\begin{vmatrix} R_n' & -1/2 & 0\\ R_n'' & 1 & -2\\ R_n & 1/6 & 2/3 \end{vmatrix}$$

$$\Delta_{n-1}=\begin{vmatrix} 1/2 & R_n' & 0\\ 1 & R_n'' & -2\\ 1/6 & R_n & 2/3 \end{vmatrix} \qquad \Delta_n=\begin{vmatrix} 1/12 & -1/2 & R_n'\\ 1 & 1 & R_n''\\ 1/6 & 1/6 & R_n \end{vmatrix}$$

From equations (3), (4), the coefficients C_i mentioned above completely satisfy the six boundary conditions as required. Substituting (4) into (2) and eliminating C_1, C_{n-1}, C_n, we obtain

$$\begin{bmatrix} 1&0&0&0&0&0&0&0&0&0&0&0\\ 0&4&1&0&0&0&0&0&0&0&0&0\\ 0&1&4&1&0&0&0&0&0&0&0&0\\ 0&0&\cdot&\cdot&\cdot&0&0&0&0&0&0&0\\ 0&0&0&\cdot&\cdot&\cdot&0&0&0&0&0&0\\ 0&0&0&0&1&4&1&0&0&0&0&0\\ 0&0&0&0&0&\cdot&\cdot&\cdot&0&0&0&0\\ 0&0&0&0&0&0&1&4&1&0&0&0\\ 0&0&0&0&0&0&0&\cdot&\cdot&\cdot&0&0\\ 0&0&0&0&0&0&0&0&1&4&1&0\\ 0&0&0&0&0&0&0&0&0&0&1&4\\ 0&0&0&0&0&0&0&0&0&0&0&1 \end{bmatrix} \begin{bmatrix} \\ C_2\\ C_3\\ \cdot\\ \cdot\\ C_p\\ \cdot\\ C_q\\ \cdot\\ C_{n-3}\\ C_{n-2}\\ \\ \end{bmatrix}$$

$$= \begin{bmatrix} 6R_1-4C_1-C_n\\ 6R_2-C_1\\ 6R_3\\ \cdot\\ \cdot\\ 6R_p\\ \cdot\\ 6R_q\\ \cdot\\ 6R_{n-3}\\ 6R_{n-2}-C_{-1}\\ 6R_{n-1}-4C_{n-1}-C_n \end{bmatrix} \tag{5}$$

We present equation (5) as the form

$$\bar{A}\,\bar{C}=\bar{R} \tag{6}$$

With recurrence formula, there are

$$\bar{C}_i=\bar{R}_{i-1}-4\bar{C}_{i-1}-\bar{C}_{i-2} \quad i=2,3,\ldots,p; \tag{7}$$

$$C_1=C_0=0$$

and

$$\bar{C}_j=\bar{R}_{j-1}-4\bar{C}_{j+1}-\bar{C}_{j+2}$$

$$j=n-1,n-2,\ldots,q; \tag{8}$$

$$\bar{C}_n=\bar{C}_{n+1}=0$$

R_p and R_q are undetermined values and should satisfy the following relations.

$$C_{p-1} + 4C_p + C_{p+1} = 6R_p \qquad (9)$$

$$C_{q-1} + 4C_q + C_{q+1} = 6R_q$$

Where C_{p-1}, C_p, C_q, and C_{q+1} have been solved from the equation (7) and (8). Hence equation (9) can be rewritten as

$$\begin{aligned} C_{p-1} + 4C_p &= 6R_p - C_{p+1} \\ C_{q-1} + 4C_q &= 6R_q - C_{q-1} \end{aligned} \qquad (10)$$

The rest coefficients (from C_{p+1} to C_{q-1}) can be obtained by next equation.

$$\begin{bmatrix} 6 & -1 & 0 & 0 & 0 & 0 & 0 & 0 & 0 & 0 \\ 0 & 0 & 4 & 1 & 0 & 0 & 0 & 0 & 0 & 0 \\ 0 & 0 & 1 & 4 & 1 & 0 & 0 & 0 & 0 & 0 \\ 0 & 0 & 0 & . & . & . & 0 & 0 & 0 & 0 \\ 0 & 0 & 0 & 0 & . & . & . & 0 & 0 & 0 \\ 0 & 0 & 0 & 0 & 0 & . & . & . & 0 & 0 \\ 0 & 0 & 0 & 0 & 0 & 0 & 1 & 4 & 1 & 0 \\ 0 & 0 & 0 & 0 & 0 & 0 & 0 & 1 & 4 & 0 \\ 0 & 0 & 0 & 0 & 0 & 0 & 0 & 0 & -1 & 6 \end{bmatrix} \begin{bmatrix} R_p \\ C_{p+1} \\ C_{p+2} \\ . \\ . \\ . \\ C_{q-2} \\ C_{q-1} \\ R_q \end{bmatrix} = \begin{bmatrix} 4C_p + C_{p-1} \\ 6R_{p+1} - C_p \\ 6R_{p+2} \\ . \\ . \\ . \\ 6R_{q-2} \\ 6R_{q-1} - C_q \\ 4C_q + C_{q+1} \end{bmatrix}$$

Write it as the form

$$\bar{A}\,\bar{C} = \bar{R} \qquad (11)$$

Where $\bar{A}$ is symmetric triple diagonal matrix. The coefficient matrix (C_i) and R_p, R_q can be solved by speedup method. The procedures to solve (11) are as following:

1) to determine the proper interpolation knot X_p, X_q and p, q in terms of interior knot conditions;

2) using formulae (3), (4) to obtain coefficient C_i ($i=-1$, 0, 1, n-1, n, n+1) which are at boundary points;

3) using formulae (7), (8) to determine C_i which are outside of p, q (including p, q);

4) using equation (11) to determine coefficient C_i which are inside of p, q;

5) After determined all coefficient C_i we can substitute all C_i into

$$S_3(X) = \sum_{j=-1}^{n+1} C_j\, \Omega_3\,[(X-X_0)/h] \qquad (12)$$

where $\Omega_3[(X-X_j)/h]$ = third spline function
h = $X_j - X_{j-1}$
j = knot locations in sequence -1, 0, 1, 2, ..., n, n+1;

Then the profile of cam required is obtained.

It is necessary to point out that selections of p and q is very flexible. They can be located at any point except two boundary points. If p and q are two consecutive points equation (11) can be omitted. In most cases, the displacement constraints given at some positions do not need to be satisfied strictly. A certain error is allowed. Therefore, the points of p and q can be selected directly from the given displacement constrains. If the error of calculation is exceeding the error required, "excess and deficiency correction" can be used to correct error based on iteration rules.

From equation (12) we can see that the equation can be easily used to do differentiation, integration and approximation. This method is called "zero order (displacement) dummy treatment". That is, in order to satisfy the extra boundary conditions, the same number of knots should be inserted to compensate the extra constraints. Since the method is based on the satisfaction of interior knots to adjust the function shape to satisfy the variety of boundary conditions, it is same as the general numerical methods and geometric figure control in the aspect of the satisfaction boundary conditions. But it provides an advantage in which the interior knots can be satisfied as well rather than only boundary conditions. This can not be done by the general numerical methods and geometric figure control.

FIRST AND SECOND ORDER DUMMY TREATMENT

In this portion we consider the design of cam curve which should satisfy following conditions:

1) interior conditions (velocity)

$$S_3'(X_i) = R_i' \quad i=1,2,\ldots,n-1;$$

2) boundary conditions

$$S_3^{\alpha}(X_0) = S_3^{\alpha}(X_n) \qquad \alpha=0,1,2$$

Assume the cam curve is given as

$$S_3(X) = \sum_{j=-1}^{n+1} C_j\, \Omega_3\,[(X-X_j)/h] \qquad (13)$$

According to interior conditions, there is

$$S_3'(X) = \sum_{j=-1}^{n+1} C_j\, \Omega_3'\,[(X-X_j)/h] \qquad (14)$$

The number of interpolation knots and of constraints are (n+3). Based on the boundary conditions we have

$$C_1 = C_{n+1}, \quad C_0 = C_n, \quad C_{-1} = C_{n-1}$$

and notice that

$$\Omega_3'(X) = \delta\, \Omega_2(X) = \Omega_2(X+1/2) - \Omega_2(X-1/2)$$

where $\Omega_2(X)$ = second spline function δ is the coefficient obtained from the first derivative of third spline.

hence

$$\Omega_3'(0)=0, \quad \Omega_3'(\pm1)=\mp1/2, \quad \Omega_3'(X)=0 \quad (|X|\geq2)$$

Equation (13) can be rewritten as:

$$\begin{bmatrix} 0 & 1/2 & 0 & 0 & 0 & 0 & -1/2 \\ -1/2 & 0 & 1/2 & 0 & 0 & 0 & 0 \\ 0 & . & . & . & 0 & 0 & 0 \\ 0 & 0 & . & . & . & 0 & 0 \\ 0 & 0 & 0 & . & . & . & 0 \\ 0 & 0 & 0 & 0 & -1/2 & 0 & 1/2 \\ 1/2 & 0 & 0 & 0 & 0 & -1/2 & 0 \end{bmatrix} \begin{bmatrix} C_1 \\ C_2 \\ . \\ . \\ . \\ C_{n-1} \\ C_n \end{bmatrix} = \begin{bmatrix} R_1'h \\ R_2'h \\ . \\ . \\ . \\ R_{n-1}' \\ R_n' \end{bmatrix} \tag{15}$$

The N*N matrix in equation (15) is a symmetric triple diagonal matrix. The coefficient matrix $\{C_i\}$ can be solved by speedup method. Substituting $\{C_i\}$ into equation (13) interpolation $S_3(X)$ can be obtained.

If the boundary conditions mentioned above are changed to following:

$$S_3^{\alpha}(X_0)=S_3^{\alpha}(X_n)=R_n^{\alpha} \qquad \alpha=0,1,2$$

Then

$$\begin{aligned} &C_1+C_{n-1}-2C_n=R_n'' \\ &\frac{1}{6}C_1+\frac{1}{6}C_{n-1}+\frac{2}{3}C_n=R_n \\ &\frac{1}{2}C_1-\frac{1}{2}C_{n-1}=R_n'' \end{aligned} \tag{16}$$

Using Cramer's rule, C_1, C_{n-1}, and C_n can be solved. Then the values of first derivative of R_p and R_q should satisfy the following relations.

$$\begin{aligned} &\frac{1}{2}C_{p+1}-\frac{1}{2}C_{p-1}=R_p' \\ &\frac{1}{2}C_{q+1}-\frac{1}{2}C_{q-1}=R_q' \end{aligned} \tag{17}$$

The rest procedures to solve equations using "First Order Dummy Treatment" are same as the ones using in "Zero Order Dummy Treatment".

The procedures of second order dummy treatment method are similar to first order dummy treatment. As an example, we consider the design of cam profile which should satisfy the following conditions.

1) interior conditions (acceleration)

$$S_3''(X_i)=R_i'' \quad i=1,2,\ldots,n-1;$$

2) boundary conditions

$$S_3^{\alpha}(X_0)=S_3^{\alpha}(X_n)=R_n^{\alpha} \quad \alpha=0,1,2$$

From the interior conditions, we can have following equation

$$S_3''(X_0)=\sum_{j=-1}^{n+1} C_j\,\Omega_3''[(X-X_j)/h] \tag{18}$$

With basic boundary conditions and

$$\Omega_3''(X_0)=-2, \quad \Omega_3''(\pm1)=1$$

we have

$$\begin{bmatrix} -2 & 1 & 0 & 0 & 0 & 0 & 1 \\ 1 & -2 & 1 & 0 & 0 & 0 & 0 \\ 0 & . & . & . & 0 & 0 & 0 \\ 0 & 0 & . & . & . & 0 & 0 \\ 0 & 0 & 0 & 1 & -2 & 1 & 0 \\ 1 & 0 & 0 & 0 & 0 & 1 & -2 \end{bmatrix} \begin{bmatrix} C_1 \\ C_2 \\ . \\ . \\ C_{n-1} \\ C_n \end{bmatrix} = \begin{bmatrix} R_1''h^2 \\ R_2''h^2 \\ . \\ . \\ R_{n-1}''h^2 \\ R_n''h^2 \end{bmatrix} \tag{19}$$

and $C_0=C_n \qquad C_{-1}=C_{n-1} \qquad C_1=C_{n+1}$

The rest procedures to solve problem will be same as the ones used in "Zero Order Dummy Treatment".

From the discussion above, for the interior conditions under second order, the procedures to solve problems are exact same except the difference of coefficients (C_i) of N*N matrix under the same complex boundary conditions.

CONTROL OF INTERIOR STATUS OF CURVE

It is possible that the requirements of the interior conditions in actual cam design could be the displacement, velocity and acceleration or any combination of them. The requirements can be one of following discussions.

1) There is only one type of constrains at each knot position of curve. That is

$$S(X_i)=R_i, \quad S'(X_j)=R_j', \quad S''(X_k)=R_k''$$

where $i\neq j\neq k$
These three conditions can be presented as following equations.

$$\frac{1}{6}C_{i-1}+\frac{2}{3}C_i+\frac{1}{6}C_{i+1}=R_i$$

$$\frac{1}{2h}(-C_{j-1}+C_{j+1})=R'_j \qquad (20)$$

$$\frac{1}{h^2}(C_{k-1}-2C_k+C_{k+1})=R''_k$$

with the basic boundary conditions, also

$$S_3^{\alpha}(X_0)=S_3^{\alpha}(X_n) \quad \alpha=0,1,2$$

There are n+3 constraints altogether. So the equation is unisolvent one.

2) There are two types of constraints in an interior knot position of curve. That is

(a) $S(X_i)=R_i \quad S'(X_i)=R'_i$

These two constrains can be presented as

$$\frac{1}{6}C_{i-1}+\frac{2}{3}C_i+\frac{1}{6}C_{i+1}=R_i$$

$$\frac{1}{2h}(-C_{i-1}+C_{i+1})=R'_i$$

The number of constraints is one more than the number of knots. We need to dummy a knot X_p at a position of cam curve (coefficient C_p and R_p are undetermined). It is easy to dummy such a knot because it is not necessary to satisfy the every position strictly and also not every position has constraints in cam design. Therefore, after omitting first order conditions, we can obtained

$$C_j=C_j(R_p) \quad j=1,2,...p,...,n+1 \qquad (21)$$

then using first order conditions again

$$\frac{1}{2h}\left[-C_{i-1}(R_p)+C_{i+1}(R_p)\right]=R'_i$$

From this equation, R_p can be obtained. Substituting R_p into equation (21), the all coefficient $\{C_j\}$ can be solved.

So far, spline which satisfies interior conditions has been completed. The position of X_p is flexible. It can be located at either original or a new knot. If the R_p value obtained is not ideal (for example the difference of R value between X_p and close knot is not satisfied, which causes the changes of velocity and acceleration acutely), we may set up knot again to repeat the above procedures until satisfaction.

(b) $S(X_i)=R_i \quad S''(X_i)=R''_i$

(c) $S'(X_i)=R'_i \quad S''(X_i)=R''_i$

These two case are same as first case mentioned in (a). We do not need discussion them again.

3) There are three constraints at an interior knot position.

$$S(X_i)=R_i \quad S'(X_i)=R'_i \quad S''(X_i)=R''_i$$

They can be presented as

$$\frac{1}{6}C_{i-1}+\frac{2}{3}C_i+\frac{1}{6}C_{i+1}=R_i$$

$$\frac{1}{2h}(-C_{i-1}+C_{i+1})=R'_i \qquad (22)$$

$$\frac{1}{h^2}(C_{i-1}-2C_i+C_{i+1})=R''_i$$

Hence coefficient C_{i-1}, C_i and C_{i+1} can be determined through equation (22). But for whole problem, there are two extra constraints. Two more dummy knots of X_p and X_q must be set up in order to satisfy the two extra constraints. Again, the procedures to solve this case be will same as the ones mentioned above.

Of course, we may use piecewice Hermite interpolation to get unique and exact solution directly. But the formulae and procedures are much more complex.

THIRD ORDER DUMMY TREATMENT

The same boundary conditions shared in zero, first and second order dummy treatment as mentioned above can be defined as following

$$S^{\alpha}(X_0)=S^{\alpha}(X_n)=R^{\alpha} \quad \alpha=0,1,2$$

It means that the derivative values of zero, first and second equal each other and also equal to a value at boundary points. In fact, we could extend the boundary points to third derivative. That is $\alpha=0,1,2,3$. The Cubic Spline is represented by

$$S_3(X)=\sum_{j=-1}^{n+1} C_j\,\Omega_3\left[(X-X_j)/h\right]$$

The third derivative is

$$S_3^{(3)}(X)=\sum_{j=-1}^{n+1} C_j\,\Omega_0\left[(X-X_j)/h\right] \qquad (23)$$

where

$$\Omega_0(X)=\begin{cases}0 & \text{when } |X|>1/2\\ 1 & \text{when } |X|\le 1/2\end{cases}$$

then

$$S_3^{(3)}(X)=\begin{cases}C_j & \text{when } X_j-\frac{h}{2}<X\le X_j+\frac{h}{2}\\ 0 & \text{when } X>X_j+\frac{h}{2} \text{ or } X<X_j-\frac{h}{2}\end{cases}$$

$$j=0,1,2\ldots n$$

From the extra boundary conditions there are

$$S_3^{(3)}(X_0) = C_0 = R_n^{(3)}$$

$$S_3^{(3)}(X_n) = C_n = R_n^{(3)}$$

That is $C_0 = C_n = R_n^{(3)}$ (24)

From the equation (24), we can see that the $C_0 - C_n$ obtained from the basic boundary conditions has already included in third derivative implicitly. This boundary condition is only equivalent as a constraint. Therefore, we can dummy a knot to solve the problem. The procedures are same as the ones mentioned in the second order dummy treatment. Considering $C_n = \Delta_n/\Delta$ in equation (4), we can adjust the magnitudes of R_n, R'_n, R''_n $R_n^{(3)}$ to satisfy $C_n = \Delta_n/\Delta = R_n$ in certain accuracy. It is easy to adjust these values because the accuracy requirements for second and third derivatives are not strict.

CAM PERFORMANCE IMPROVEMENT

After designed a cam system, one probably find cam performance is not very satisfactory in some positions compared with some other positions. For instance, the acceleration is greater at a certain range. We should make some adjustments which still remain constraints to improve the cam performance. Since the linear combination of spline coefficients are directly related with the kinematic parameters of cam (displacement, velocity and acceleration), the adjustments of cam performance are easy and direct. This local adjusting method is illustrated by a following example.

The performance data of cam to be adjusted are shown as Table 1.

TABLE 1

angle°	vector radius	coeff-icient	velo-city	accle-ration.
300	32.2043	34.2030	-.2303	.0073
309	34.0586	34.0487	-.2285	.0115
310	33.0264	33.8253	-.2213	.0030
311	33.6078	33.6061	-.2147	.0101
312	33.3988	33.3964	-.2026	.0142
313	33.1967	33.2010	-.2003	-.0257
314	33.0023	32.9799	-.1538	.1347
315	32.8615	32.8934	-.1822	-.1959
316	32.6377	32.6155	-.2113	.1332
317	32.4665	32.4708	-.1576	-.0257
318	32.3035	32.3004	-.1610	.0183
319	32.1490	32.1488	-.1509	.0013
320	32.0002	31.9985	-.1452	.0101

From the Table, it is clear that the acceleration values among 314°-316° are much greater than others. They should be adjusted.

The rough adjusting method is to make the rate of velocity become smooth through change the values of displacement so that the rate of velocity can be fairly distributed over each position. It can be done manually and, therefore, is simple and direct. The acceleration values can be reduced greatly by this method.

The accurate adjustment is to use "excess and deficiency correction" method. From the Table 1, we have

$$(C_{i-1} - 2C_i + C_{i+1} = R''_i$$

$$i=311^0,\ 312^0,\ldots,\ 318^0$$

There are eight equations and ten coefficients. Because the further away from the adjusting points, the less effect for the adjusting. Therefore, the magnitudes of C_{310} and C_{319} remain unchanged and let $R''_i = [R''_i]_{\max}$. That is the magnitudes of acceleration can not exceed the value expected. Of course, if do so the precision of displacement will be reduced. We should check weather the magnitudes of displacement exceed the error range allowed. This can be done directly by obtaining $\bar{R}_i$ from $\tilde{C}_i$. The error to be checked is ΔR.

$$\Delta R = \bar{R}_i - R_i \tag{25}$$

If the value of ΔR exceeds the value allowed, there are two compensation methods.

1) Increase the $[R''_i]_{\max}$ or adjust the rest values of $[R]_{\max}$.

2) Enlarge the range of positions adjusted so that the finite error can be distributed in wider range.

CONCLUSIONS

The method using spline function to fit, design and improve cam curves has been presented. It is more accurate and flexible than the general numerical solution such as finite difference method since general numerical solution is only equivalent to zero order spline by which the precision is lower within same interval compared with cubic spline and the error of first and second difference are larger. Zero spline does not provide the continuity for discrete quantity realistically, and therefore, to control of boundary conditions and interior shape of curve are limited. If geometric figure is used to adjust the curve, the control of interior shape is also limited after boundary conditions are satisfied.

Using cubic spline to control the interior shape of curve and boundary conditions can overcome these disadvantages. The number of knots controlled are unlimited theoretically as long as the conditions are under second order (sometimes third order). Also, it can insure continuity of the derivatives of displacement, at least through the second derivatives. The local adjustment method to reduce the acceleration peaks is also provided for the improvement of performance of cam curve. The third spline is versatile enough for variety of requirements of the motion synthesis of actual cam. If higher order conditions are needed, higher spline such as quartic spline can be used.

Various calculations of spline such as integral and derivative are also simple. And it does not need to involve in iterative process. Therefore, the method using spline in analysis and synthesis of cam system is very useful tool.

REFERENCE

1 Xue, L., and Pei, J., " A Method of Smoothing and Synthesis and Optimization of Cam Curve Using Spline Functions", The Proceedings of 10th Symposium on Engineering Applications of Mechanics, 1990.
2 Bellman, R. E. and Roth, R. S., "Methods in Approximation", D.Reidel Press, 1986.
3 Xue, L., "Analysis and Synthesis of Cam Curve — B-Spline", Xian Press, 1988.(in Chinese)
4 Kong, W., "High speed Cam System", Beijing Press, 1986.(in Chinese)

A METHOD OF SMOOTHING AND SYNTHESIS AND OPTIMIZATION OF CAM CURVE USING SPLINE FUNCTIONS

L. Xue
Assistant Professor
Department of Mechanical Engineering
Shaanxi Mechanical Engineering Institute
Xian, Shaanxi, P.R. of China

J. Pei
Research Assistant
Department of Mechanical Engineering
Queen's University
Kingston, Ontario, Canada

ABSTRACT

A method for cam curve smoothing, dynamic cam design and optimization design using spline functions is presented. The models obtained by spline functions are of universal significance. The results achieved so far show that the method is applicable for most of general and special cam systems. The spline method is versatile enough to complete many tasks which ordinarily require a variety techniques.

INTRODUCTION

A major effort in cam curve smoothing, dynamic cam design and optimization design is to meet the needs of high performance and high quality. As a result, many approaches have been proposed. In the cam curve smoothing, and dynamic cam design a wide spectrum of the standard motions can be used such as constant acceleration, harmonic, modified harmonic, cycloidal, trapezoidal, polynomial functions. In order to reduce or shift acceleration peaks, sometimes they are combined into piecewise functions or are otherwise modified as the conditions requires [1]. The combination and modification of standard curve family used in a cam design is often a possibility but suffers from lack of generality.

The cam curve optimization is certainly not a new concept as it has been performed by many researchers over the past twenty years [2-4]. The major effort has been directed toward specific cases using a selected acceleration profile form for the follower motion. However, a variety of optimization techniques can not be applied because the design of the cam curves usually have special assumptions for the typical applications. And it is also not ideal for cam curve optimization when general discrete variable methods are employed such as finite difference unless the interior relations of curve can be denoted.

The method presented in the paper provides a general, systematic approach to cam curve smoothing, dynamic cam and optimization designs.

The smoothing spline can provide arbitrary order smoothing for the displacement (or velocity, acceleration) curves if it is necessary in the actual cam curve design. The curve smoothed by spline function has the advantages in both properties, the smoothness and approximation.

In the synthesis and analysis of dynamic cam , spline function can provide the continuous approximate solution (as the solution from global analysis) and the process involving is simple (same as difference method). On the other hand, The spline method is versatile enough to complete many tasks which ordinarily require a variety techniques.

The spline function also provides a very general environment for optimization of cam design. It can overcome the disadvantages in optimization process when traditional approaches are employed as mentioned above. The total number of design variables can be reduced since some variables can satisfy the boundary conditions directly. If designers face the contradictory requirements of design in a complex cam system in which designers may have difficult to determine which function can de used as the objective function, two methods presented in the paper can be used to handle the problems. The final non-constraint objective function is formulated by an interior penalty function method and solved by Powell method.

SMOOTHING OF CAM CURVES

One of major studies in cam design is cam curve smoothing. In order to avoid shock and vibration which increase the operating forces and noise at high cam speed, the motion with acute change of acceleration is not appropriate for cam system. However, such a motion can not be avoided in some cases. An unit-rise dwell-rise-dwell (D-R-D) motion, or cosine acceleration (at the both ends) motion is a typical example in actual cam application. General method of solving the problems is to modify cam curve by using the combination of standard motion curves, which are called family of profiles, to reduce the acceleration peaks.

Smoothing spline functions for such a motion of cam follower system provides a very convenient tool. As an example, we consider the design of step function given by

$$F(X)=\sum_{j=0}^{n} Y_j \, \Omega_0[(X-X_j)/h] \qquad (1)$$

Its first order smoothing spline is polygonal function.

$$F_1(X)=\sum_{j=0}^{n} Y_j\,\Omega_1[(X-X_j)/h] \qquad (2)$$

And its smoothing spline of order k is

$$F_k(X)=\sum_{j=0}^{n} Y_j\,\Omega_k[(X-X_j)/h] \qquad (3)$$

where

F =kinematic parameters of the follower (displacement or velocity or acceleration)

X =cam rotational angle

Y_j =constant coefficient $(j=0,1,\ldots,n)$

$\Omega_k[(X-X_j)/h]$ =spline of order k

h $=X_j-X_{j-1}$

The various subscripts on j (X_1, X_j, etc.) signify specific knot locations in the sequence $X_1, X_2, \ldots, X_n$.

It is possible to carry out arbitrary order smoothing for the displacement (or velocity, acceleration) curves if it is necessary in the actual cam curve design. Obviously, the higher the order of smoothing spline functions, the smoother the cam curves.

In addition, the smoothing spline curve has the advantages in both properties, the smoothness and approximation. It is ideal fitting curves.

ANALYSIS AND SYNTHESIS OF DYNAMIC CAM

The objective of a cam-follower system design is to obtain a cam which generates the desired output motions. The cam-follower systems can be modeled by lumped-parameter model consisting of masses, springs and dashpots.

The following cam system has single degree freedom consisting lumped parameters such as mass(m), the spring(k). In first step of the discussion, external and internal damping, and workload are omitted to make the problem simple. After obtaining the solutions for first model, the external and internal damping as well as workload will be added into the model to be discussed.

The differential equation of first model is

$$m\ddot{Y} + k(Y-Y_e)=0 \qquad (4)$$

where Y, Y_e denote the displacements of the mass (output) and follower.

When cam curve is given in the form of discrete variables, such as data or table, two general methods are available to solve it.

1) discrete approximation such as numerical integration or numerical differentiation etc..

2) global analysis approximation such as series expansion as undetermined function (curve).

where $X\in[a,b]$ and assume

$$X_{-1}=a-h, \quad X_{n+1}=b+h.$$

There are n+3 periodic conditions. Therefore, the undetermined coefficient matrix (C_j) $(j=-1, 0, 1, 2, \ldots n+1)$ is unisolvent system. Substituting Y and Y_e into equation (5), we have

$$\sum_{j=-1}^{n+1} C_j\,\ddot{\Omega}_3[(X-X_j)/h]+\omega\sum_{j=-1}^{n+1} C_j\,\Omega_3[(X-X_j)/h]$$

$$=\omega\, S_{3e}(X) \qquad (5a)$$

where $\ddot{\Omega}_3(X)=\Omega_1(X)$

Hence me obtain

$$\frac{1}{h^2}(C_{i-1}-2C_i+C_{i+1})+\frac{\omega}{2h}(C_{i+1}-C_{i-1})=\omega\, S_{3e}(X)$$

After sorting and merging above two equations, we can have

$$\alpha\, C_{i-1}+\beta\, C_i+\gamma\, C_{i+1}=\bar{Y}_i \qquad (6)$$

$$(i=0,\ 1,\ \ldots.n) \ (6)$$

where $\alpha=\dfrac{1}{h^2}-\dfrac{k}{2hm}$ $\qquad \beta=-\dfrac{2}{h^2}$

$$\gamma=\frac{1}{h^2}+\frac{k}{2hm}$$

$$\bar{Y}_i=\omega\, S_{3e}(X_i)$$

Part of the solutions of periodic problem are

$$C_{-1}=C_{n-1} \qquad C_0=C_n \qquad C_1=C_{n+1}$$

Equation (6) can be rewritten as

$$\begin{bmatrix} \beta & \gamma & 0 & 0 & 0 & 0 & \alpha \\ \alpha & \beta & \gamma & 0 & 0 & 0 & 0 \\ 0 & \alpha & \beta & \gamma & 0 & 0 & 0 \\ 0 & 0 & . & . & . & 0 & 0 \\ 0 & 0 & 0 & . & . & . & 0 \\ 0 & 0 & 0 & 0 & \alpha & \beta & \gamma \\ \gamma & 0 & 0 & 0 & 0 & \alpha & \beta \end{bmatrix} \begin{bmatrix} C_1 \\ C_2 \\ C_3 \\ . \\ . \\ C_{n-1} \\ C_n \end{bmatrix} = \begin{bmatrix} Y \\ Y_2 \\ Y_3 \\ . \\ . \\ Y_{n-1} \\ Y_n \end{bmatrix} \qquad (7)$$

The undetermined coefficients (C_i) can be solved using speedup method. Then displacement of the mass Y_i can be obtained. The precision of this solution is higher than the one of Euler polygon method (first spline) and Trapezoidal method (second spline).

It is possible to improve the precision of this solution. If the function value Y_j in second order numerical derivative is substituted by the functional value at knot X_j which is obtained in first order numerical derivative. Then using interpolation again to get coefficients $\{C_j'\}$. Then use following equation

$$S_3''(X) = \sum_{j=-1}^{n+1} C_j' \, \Omega_3'[(X-X_j)/h] \qquad (8)$$

as the formula of second order number derivative. The precision is higher than one using second order numerical derivative directly.

In above discussions a single degree of freedom consisting of lumped parameters without considering dashpot and workload. In the actual cam system, the external and internal damping as well as the workload must be considered. The following model which includes the external, internal damping and workload has the controlling equation as

$$Y'' = k(Y_e - Y) + c\,(Y_e - Y) - (F + P_0) \qquad (9)$$

where c = linear damping ratio
F = spline preload
P_0 = workload

If unknown function Y and its derivatives are moved to the same side of the equation the procedures to solve the equation (9) are same as ones of the equation (4). Its responsive function is given by

$$\Delta Y = Y - Y_e \qquad (10)$$

The model can be used to analyze the motion and response of the mass. If employed for design of cam mechanism the model should be only applied in state-steady design because it can not insured to satisfy the requirements of the motion of cam follower at higher speed. However, the method of excess and deficiency correction can be utilized to approximate Y_e. The error of coefficients between the motion of mass, denoted as $Y=S_3(X)$, and the motion of the follower, denoted as $Y_e=S_{3e}(X)$, is defined as

$$e_i = C_i - C_{ei} \qquad i = -1,\ 0,\ 1, \ldots,\ n,\ n+1;$$

Use e_i to correct the coefficients $\{C_{ei}\}$, we have

$$\tilde{C}_{ei} = C_{ei} - C_i$$

Substituting $\tilde{C}_{ei}$ into $S_{3e}(X)$, there is

$$\tilde{S}_{3e}(X) = \sum_{j=-1}^{n+1} \tilde{C}_{ej} \, \Omega_3[(X-X_j)/h] \qquad (11)$$

Where $\tilde{S}_{3e}(X)$ is displacement curve of the follower.

The precision required can be satisfied after several corrections using excess and deficiency correction method. In the computer program this correction can be completed using the program of the first model (without considering the damping and workload) including equation (11). Actually, the program of second model, which is the program of first model with equation (11), can be considered as dynamic design of cam curve.

It is possible to consider the motion of mass, denoted as $Y=S_3(X)$, as known function and the desired motion, denoted as $Y_e=S_{3e}(X)$, as undetermined motion to do the dynamic design of cam curve. This is a more direct approach than above. From the equation (5a), we have

$$\omega \, S_{3e}(X_j) = Y_j \qquad (12)$$

where

$$Y_j = \sum_{j=-1}^{n+1} C_j \, \Omega_3'' \, [(X-X_j)/h] + \omega \, C_j \, \Omega_3[(X-X_j)/h]$$

Then a system of linear equation as equation (7) is obtained. Using the speedup method undetermined coefficients $\{C_j\}$ can be solved.

Although the second approach is simpler, the first approach is still recommended. A series of useful solutions can be obtained in the processes of the first approach and one of them might be chosen as the solution. As we see there are so many factors which could affect the design of cam curves and usually the cam designed is only based on a certain speed range, it is necessary to compare the solutions and choose the best one to meet the requirements of the cam system. This is the reason that the first approach is recommended in the dynamic design of cam curves.

OPTIMIZATION DESIGN OF CAM CURVE

To meet the requirement of high cam speed, a wide spectrum of cam curves have been contributed including constant acceleration, polynomial dynamic cam and combinational curve. However, a variety of optimization techniques can not be applied because the design of the cam curves usually have special assumptions for the typical application. And it is also not ideal for cam curve optimization when general discrete variable methods such as finite difference are employed unless the interior relations of curve can be denoted.

The spline function provides a very general environment for cam curve optimization.

Cam Curves and Boundary Conditions

In order to avoid some unnecessary limits some researchers proposed that function family of combinational power can be used for lift cam curve. It is

$$Y(X) = \alpha_0 + \sum_{j=1}^{n} \alpha_j X^{\beta_j} \qquad (13)$$

where β_j – design variables

α_j – coefficients (can be solved by boundary conditions and β_j)

j – the number of knots

j=1,2,...,n

The curve (13) extends the selective range of cam curves. Obviously the method to search the cam profiles with the equation (13) is better than the polynomial function. But the number of undetermined coefficients should not be more than 4 or 5 based on the limits of boundary conditions with the function family of combinational power. Therefore, its generality is also limited. The spline function can be used to overcome this limitation.
Now use third spline again as cam curve

$$Y(X) = S_3(X) = \sum_{j=-1}^{n+1} C_j \Omega_3[(X-X_j)/h] \qquad (14)$$

where $\{C_j\}$ is design variables.

a) If boundary conditions are given as

$$S_3(X) = Y_0 \qquad S_3^{(\alpha)}(X_n) = S_3^{(\alpha)}(X_0) \qquad \alpha = 0,1,2$$

then $C_{-1} = C_{n-1} \qquad C_0 = C_n \qquad C_1 = C_{n+1}$

b) If boundary conditions are extended to

$$S_3'(X_0) = Y_0' \qquad S_3''(X_0) = Y_0''$$

then $C_{-1} = C_{n-1} = \Delta_{n-1}/\Delta_n \qquad C_0 = C_n = \Delta_n/\Delta$

$C_1 = C_{n+1} = \Delta_1/\Delta$

c) If the boundary conditions are extended to

$$S_3^{(3)}(X_0) = S_3^{(3)}(X_n) = Y_0$$

then have $C_0 = C_n = Y_0''$

Certainly, the number of boundary conditions added in should be same as the the number of knots which are dummied [6]. The rest coefficients $\{C_i\}$ which are not determined by the boundary conditions, therefore, can be considered as the design variables in the optimization design.

Application of Optimization Design

To concentrate on the optimization process of cam design some of constraints are not considered in the following discussion although they are important such as the return force of spring must be greater than maximum initial force in vibration circumstance.

From the previous work [7], if the working speed of cam system is 10 percent higher than its designed speed the vibration amplitudes of cam system become much greater. The objective in this example is to optimize the cam follower system to satisfy the requirement of acceleration in which the acceleration amplitude A is less than or equal to A_{max} within the certain cam speed range $[\omega_a, \omega_b]$. To complete such cam design the following optimization model is employed.

1) objective function

$$I(c,m,k) = \sum_{i=1}^{n} \omega_i A_{mi} \qquad (15)$$

2) constraints $\quad m_{max} \geq m \geq 0$

$k_{max} \geq k \geq 0$

$A_i \leq [A_{imax}]$

where

A_{mi} – the amplitude acceleration of cam system at certain speed ω_i

ω_i – weight factor at speed ω_i

A_i – the maximum acceleration at speed ω_i

$[A_{imax}]$ – the maximum acceleration required

For the actual cam design there may are more constraints than mentioned above. An final non-constraint objective function is formulated by an interior penalty function method and solved by Powell method. The analysis process of spline is only recurrence rather than iterative process. Therefore, Optimization program with spline on computer will take less time than the others mentioned earlier.

In many cases, we often face with a variety of problems in the optimization program of cam system. And it is possible that design requirements are contradictory in a complex cam system or it may be difficult to determine which function can be used as the objective function. If we face such design situations, the following approaches can be used.

a) Trade-off study

For a certain number of design requirements, which are contradictory each other, we define them as

$F_1(X), F_2(X), \ldots, F_r(X)$

If the design requires that all of them are as small as possible, first step for such a problem is to obtain a serial trial values from the calculation. After reviewing these values, designer can decide to lower the design requirements for some $F_j(X)$ which are less important than the others in order to optimize the some $F_i(X)$ to meet the major requirements of the cam. It is, certainly, that the performance of the cam designed by using this method also depends on the experience of designer.

The interior penalty function can be used for this optimization design. After giving an acceptable point a certain number of acceptable results, which are improved step by step, can be generated. The trade-off method provides very efficient tool for the design of complex cam system which has contradictory design requirements.

b) Another available method for such problem is "Coordinated Curve Method" or "Homaloidal Objective Function". When designer has difficult to determine which function can be chosen as the objective function, these two methods can be employed to deal with the problems. The optimization design of timing cam of internal combustion engine is an typical example. The design requirements of the timing cam are as following:

a) The value of "section-time" $\left|\frac{A_{max}}{-A_{max}}\right|$ should be as large as possible.

b) The maximum positive and negative accelerations should be as small as possible.

Obviously these two requirements are important for timing cam. The traditional method for this design is use one requirement as objective function and the other one as subjective function to optimize them. The author used the two methods mentioned above in timing cam optimization design and found these two methods also possible means for timing cam.

When spline is used in optimization design of cam curve some coefficients C_i which are located at boundary knots can be obtained directly from the boundary conditions. We do not need to treat them as the constraints into the optimization. If function values of some knots are not important for objective function the coefficients C_i of these knots do not need to consider as design variables too.

CONCLUSIONS

As has been presented above, the methods using spine functions for cam curve smoothing, synthesis and optimization design has been discussed. The spline method is versatile enough to complete many tasks which ordinarily require a variety of techniques. It can be conveniently used to satisfy the requirements of common cam curve smoothing, synthesis, and optimization design while remaining versatile enough to deal with some cases that are very difficult by any other means.

In cam curve smoothing, the performance of cam curve that is obtained by smoothing spline is much better than the one obtained by any other means since it is possible to carry out arbitrary order smoothing for the displacement (or velocity, acceleration) curves. It has the advantages in both properties, the smoothness and approximation.

In analysis and synthesis of dynamic cam, the third spline employed can provide continuous approximate solution such as the solution given out by global analysis approximation method and the process involving to solve the equations are almost as simple as discrete approximation method such as numerical differentiation. On the other hand, it overcome the limitations of global analysis approximation and discrete approximation methods. The precision of solution is higher than Euler Polygon and Trapezoidal methods and can be improved by the further treatment.

When spline is used in optimization design of cam the total number of design variables can be reduced since some variables can satisfy the boundary conditions directly. Designers do not need to treat them as the constraints in the optimization process. The two possible methods are also presented in the paper for the contradictory requirements of design in a complex cam system in which designers may have difficult to determine which function can be used as the objective function. The results of the applications using splines in cam curve smoothing, synthesis and optimization will be presented soon.

REFERENCES

1 Chen, F. Y., Mechanics and Design of Cam Mechanisms, Pergamon Press, 1982.

2 Kanzaki, K., and Itao, K., "Polydyne Cam Mechanisms for Typehead Positioning", ASME Journal of Engineering for Industry, Vol. 94, Feb. 1972, pp 250-254.

3 Wiederrich, J. L., and Roth, B., "Dynamic Synthesis of Cam sing Finite Trigonometric Series", ASME Journal of Engineering for Industry, Vol. 97, 1975, pp. 287-293.

4 Chew, M., Freudenstein, F., and Longman, R. W., "Application of Optimal Control Theory to Synthesis of High Speed Cam Follower Systems: Part 2 – System Optimization", ASME Journal of Mechanical Design, Vol. 105, 1983, pp. 584-591.

5 Chen, L. Z., The Method of Mechanical Optimization, Shanghai Press, 1982. (in Chinese)

6 Xue, L., "Analysis and Synthesis of Cam Curve — B-Spline", Xian Press, 1988. (in Chinese)

7 Kong, W., "High Speed Cam System", Beijing Press, 1986. (in Chinese)

PERFORMANCE OF ABRASIVE DISK DEHULLERS

M. W. Bassey* and H. M. Mbengue**

* International Development Research Centre (Canada), BP 11007 CD Annexe, Dakar, Senegal
* * Centre Nationale de Recherches Agronomiques, B.P. 53, Bambey, Senegal.

ABSTRACT

Traditional dehulling of cereal grains is a time consuming, labor intensive, but important task performed by women in rural areas in developing countries. Dehulling separates the outer envelop, which contains both anti-nutritional and organoleptically unacceptable factors, from the edible portion of the grain.

This paper discusses the performance of dehullers which use vertically rotating abrasive disks embedded in the grains being processed. Results of various studies are used to explain the effects of several parameters on the dehulling performance of the machines.

The performance of the dehullers depend on the speed of rotation of the disks, the disk's surface characteristics, the quantity of grain in the dehuller, the spacing between disks, the disk diameter, the physical characteristics of the grain, the duration of dehulling and the physical characteristics of the internal surface of the dehuller barrel. In the absence of detailed studies, in some cases, certain hypotheses are used to explain the operation of the dehuller.

It is concluded that even though the performance of abrasive disc dehullers are satisfactory, significant improvement may be obtained through studies aimed at understanding the mechanics of disk/grain, grain/grain and grain/wall interactions, during the dehulling process.

INTRODUCTION

Need for Dehulling

Semi-arid regions in developing countries in, e.g., Africa can only support the cultivation of cereals such as sorghum, millet and maize. As a result, a significant percentage of the population in many countries in Western, Central, Eastern and Southern Africa, depend on sorghum and millet for their daily meal. Other crops such as barley and quinoa contribute to the daily diets of populations in other parts of the world.

Rural women have traditionally improved the organoleptic quality of foods prepared from cereals by processing the grains to remove the outer layers (the pericarp and testa). The pericarp (bran) contains mainly fibre whereas the testa contains anti-nutritional substances, such as polyphenols, which give a bitter taste to the grain and inhibit the digestion of protein from the grain [1]. Phytic acid, which is present in the bran and germ of sorghum and millet, combines with mineral elements such as calcium, iron, sodium, zinc and magnesium, to form insoluble compounds (phytates), thus making them unavailable for human nutrition [2]. The presence of high concentrations of C-glycosylflavones in undehulled millet has been linked to the incidence of goitre in Sudan [3,4]. All of these various anti-nutritional factors can be substantially reduced by dehulling.

Description of Traditional Dehulling

Traditional dehulling, which is done by women, involves pounding the wet grain in a mortar with a pestle. Wetting reduces damage to the grain and facilitates the removal of the bran. Once the required degree of dehulling has been achieved, the grain is washed to remove excess bran, dried to reduce its moisture content and then pounded into flour. This moist flour cannot be kept for more than 24 hours as it ferments.

Dehulling Equipment for Grains

Technologies that can be used for dehulling include roller milling equipment, rice dehulling equipment, attrition-type dehullers and abrasive-type dehullers [5]. Roller milling equipment do not appear to be very useful in dehulling sorghum or millet; the high degree of dehulling and color of the flour obtained are unacceptable to the consumer. Rice milling equipment do not generally work well on these cereal grains. Abrasive-type dehullers use rotating abrasive surfaces to abrade the grain. Various types such as the Bavaria Record, the Wondergrain Jaybee, the FAO (Fondateur de l'atelier de l'ouest) and the Decomatic dehullers have been described in [5].

Some of disadvantages of various dehullers for village use are: their large capacities, often greater than 1000 kg/day; lack of spare parts; inability to dehull different grains without adjustment or mixtures of grains; and, the need to wet the grains.

Aim of Paper

The purpose of this paper is to discuss the performance of the abrasive-disk dehuller which has been developed at various research institutions in Canada and in Africa, for use on cereal grains and grain legumes. Both lab and field results and observations are used to explain the effect of various parameters on the performance of this dehuller. It is anticipated that the discussion will serve as a basis for further work aimed at improving the understanding of the operation of the dehuller, ultimately leading to an improvement of its performance.

DESCRIPTION OF ABRASIVE DISK DEHULLERS

General Features and Operating Principle

The basic features of the abrasive disk dehuller are shown in Fig. 1. It consists of several abrasive disks, rigidly mounted on a horizontal shaft rotating on bearings mounted on the ends of a trough-shaped barrel made of mild steel sheet. In operation, the disks are rotated in the grain at speeds ranging from 800 to 2500 rpm depending on the type of disk and abrasive surface being used.

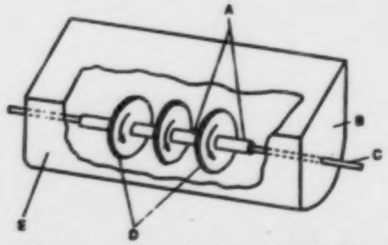

Figure 1. Basic features of the abrasive disk dehuller. A, spacers; B, end plate; C, shaft; D, abrasive disks; E, barrel.

Several models of the this dehuller have been developed and have been fully described in [6]. They have been developed to take into account specific dehulling needs and available technical skills in various countries. They are: PRL and Mini-PRL dehullers, developed at the Prairie Regional Laboratory of the National Research Council in Canada (now the Plant Biotechnology Institute); the RIIC dehuller manufactured by the Rural Industries Innovation Centre in Botswana and being used extensively in that country; the NUHULL dehuller manufactured by a Canadian manufacturer, Nutana Machine Ltd; the Mini-CRS dehuller developed by the Catholic Relief Services in the Gambia and manufactured by local artisans; the Mini-SISMAR/ISRA I and II dehullers developed by the Centre Nationale de Recherches Agronomiques and a large manufacturing company SISMAR in Senegal; and, the Mini-ENDA dehuller developed by ENDA in Zimbabwe.

The PRL, RIIC and NUHULL dehullers are larger machines with aspiration systems for bran removal, whereas the Mini dehullers have lower capacities and operate in the batch mode. Typical features of these two sizes of machines are shown in Figs. 2 and 3. Abrasive surfaces used in the dehullers are in the form of carborundum stones or lightweight resinoid discs. Some of the main features and specifications of the dehullers are shown in Tables 1 and 2.

Some of the advantages of the abrasive disc dehuller over others mentioned earlier are: its operating principle is simple; it can be easily manufactured; it is potentially lower in price; it can be easily operated by persons with little technical skills; it can effectively dehull the grains in their dry state; it can dehull a wide variety of cereal grains and grain legumes without adjusting the geometry of the machine; it can dehull an assorted mixture of grains in the same batch.

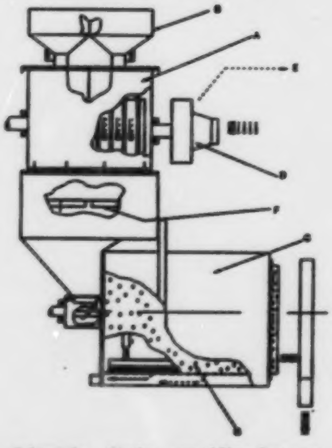

Figure 2. Schematic showing specific features of the Mini-SISMAR/ISRA II dehuller (courtesy of SISMAR, Senegal). A, dehullers; B, feed box; C, separator; D, aspirator; E, to cyclone; F, two trap doors; G, sieve. Solid arrows, movement of grains; broken arrows; bran.

ASPECTS OF DEHULLER'S PERFORMANCE

Laboratory and field studies indicate that the performance of abrasive disk dehullers depend on [6]: speed of rotation of the disks; physical characteristics of the disks surface such as roughness and hardness; number and diameter of disks in the barrel, reflecting the total surface

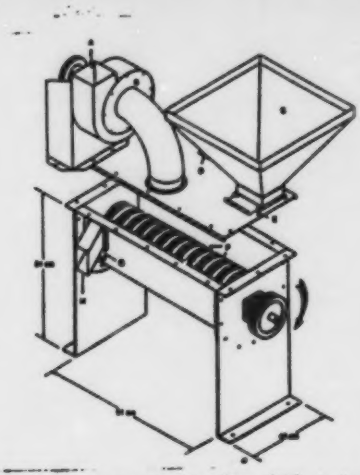

Figure 3. Exploded view of the PRL dehuller (from [6]). A, bran to cyclone; B, fan; C, grain hopper; D, air inlet; E, feed gate; F, abrasive disks; G, adjustable gates; H, overflow outlet for dehuller grains.

Table 1. Typical disc types, speeds, and power for the abrasive disc dehullers.

Dehuller Type	Discs Type	Disc Speeds rpm	No. of discs	Power of Electric Motor, HP
PRL	Stones	800-1300	13	8
RIIC	Stones	2000	13	8
NUHULL	Stones	1500-2000	4	10
Mini-PRL	Resinoid	1500-2000	4	3
Mini CRS	Resinoid	1500-2000	6	3
SISMAR/ISRA I	Resinoid	1500-2000	10	3
SISMAR/ISRA II	Resinoid	1500-2000	8	3
Mini-ENDA	Stones	1500-2000	10	3

Table 2. Mode of operation and quantity of grains processed

Dehuller Type	Through put kg/hr	Mode of Operation	Batch Size kg	Aspiration of Bran
PRL	250-500	Cont.*	-	yes
RIIC	<800	Cont./Batch	5-15	yes
NUHULL	200-500	Cont./Batch	5-15	yes
Mini-PRL	80	Batch	7	no
Mini-CRS	80	Batch	7	no
SISMAR/ISRA I	80	Batch	7	no
SISMAR/ISRA II	80	Batch	2-8	no
Mini-ENDA	100	Batch	15	no

* "Cont." means continuous mode.

area available for dehulling; spacing between disks and their angle of inclination to the shaft; distance between the end disks and the end plates of the barrel; clearance between the periphery and the barrel; presence or absence of aspiration during dehulling; roughness of the inner surface of the barrel; rate at which grains are fed into the dehuller in the continuous mode, and the quantity of grain in the dehuller in the batch mode; residence or retention time of the grain in the dehuller; and, physical characteristics of the grain being dehulled. Available results are discussed in this section.

Effect of Speed of Rotation of Disks

Results of studies on three models of abrasive disk dehullers, using barley, sorghum and millet, have been reported in [7]. The dehullers used were: a Graham Hill Thresher containing 13 Carborundum stones 30.5 cm in diameter and 3.2 cm thick; an experimental Resinoid Disk Dehuller containing 27 resinoid steel cut-off disks, 30.5 cm in diameter and 0.64 cm thick; an RIIC dehuller containing 13 carborundum stones 25.4 cm in diameter and 1.9 cm thick [7]. Typical results obtained are shown in Fig. 4 for disk speeds of 1300, 1700 and 2000. The degree of dehulling increases with the duration of dehulling (the retention time), for a given disk speed. Increasing this speed increases the degree of dehulling. For a given machine, therefore, optimum dehulling can be obtained using disk speed as a variable parameter. Similar results have been obtained with all the other dehuller models mentioned earlier using other cereals and grain legumes [6].

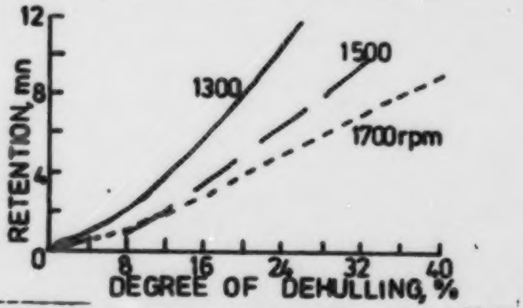

Figure 4. Effect of disk speed on Resinoid Disk Dehuller performance.

Configuration of Disks in Barrel

The gap between disk surfaces range from 1.5 to 3 cm [6] depending on the dehuller model. Obviously, the smaller the gap between the disks, the larger the number of disks and the higher would be the degree of dehulling for a given operating condition. However, the quantity of grain dehulled would be reduced as the distance between the disks is decreased, and the energy consumption would increase. Thus for economical operation, the disk spacing should be maximized. Systematic studies have not been carried to facilitate the choice of the optimum distance between disks.

Laboratory [7] and field [9] observation indicate that inclining the lightweight disks at the end of the dehuller to the vertical, improves the uniformity of dehulling. The angle of inclination of the disks have ranged from 9 degrees [7], to 5 degrees which eliminated disk breakage [9], probably due to the reduction of rotational stresses. Inclining all the disks is expected to reduce dehulling time and improve the degree of dehulling but results are not available to confirm the benefits of this arrangement. Improvement of the uniformity of dehulling has also been achieved by reducing the gap between the disks at the end of the shaft and the end plates of the dehuller [10].

Effect of Type of Grain

The performance of the dehuller depends both on the type and variety of the grain being dehulled. Factors that influence dehulling, have been discussed in [6]. They are the pericarp thickness and hardness of the grain.

Effect of Mass of Grain in Dehuller

In practice the mass of grain dehulled in mills varies from 0.5 to over 20 kg. The speed of rotation of the disks, which is usually fixed for a given mill, depends on whether grinding stones or resinoid disks are used. The retention time is thus the parameter used to control the degree of dehulling of the grains.

Detailed studies on the effect of mass of grain used on dehuller performance are available for several Mini dehullers [8, 10, 11]. Results for quantities of millet between 2 and 8 kg, which is similar for other grains, is shown in Fig. 5 for various disk speeds. Holding all other parameters constant, the degree of dehulling increases as the mass of grain in the dehuller barrel is increased.

Typical results for quantities ranging from 0.5 to 8 kg in the Mini-SISMAR/ISRA I machine using resinoid discs [10] is shown in Fig. 6. The degree of dehulling decreases with increasing mass of grain for loads less than 2 kg. The following explanation can be given for the results in Fig. 6 using Fig. 7. At very low loads the grain at level 1 in Fig. 7 is not in contact with the disc; there is no motion of grain, hence no dehulling. As the grain reaches level 2, the air motion caused by the rotating disks entrains grains which are then flung against the walls of the barrel. They break into fine particles, giving the impression that the grain is being dehulled. This effect increases significantly as the mass of grain increases between level 2 and 3, a maximum being attained at level 3 where the disk now touching the grain imparts more kinetic energy to the grains. Between levels 3 and 4, the disks now embedded in the grain abrade the lighter envelop of the grains, giving an apparent decrease in the degree of dehulling. Above level 4, the degree of dehulling increases as the grains continue to be abraded.

It is hypothesized that the dehulling that occurs when the grain is between level 3 and 4 is predominantly due to friction between the rotating disks and the grains. As level 4 is surpassed, it is suggested that the dehulling is a contribution of the abrasion between disks and grain and between grain and grain. (Bran in the barrel is considered to be part of the grain). The responsibility of the disk/grain and grain/grain interaction for the dehulling after level 4 may be supported by the fact that the degree of dehulling is decreased in practice if the bran is aspirated during dehulling. Observations of dehulling in the PRL dehuller indicates that this machine, which has aspiration, gives dehulled products with significant percentage of broken grains, whereas the Mini dehuller, which dehulls before separation of the grain and bran occurs, produces less broken grains.

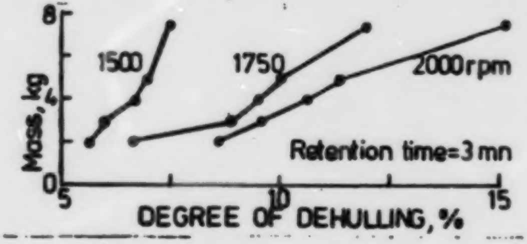

Figure 5. Effect of mass of grain on degree of dehulling for large quantities of grain in a Mini-PRL dehuller using carborundum stones.

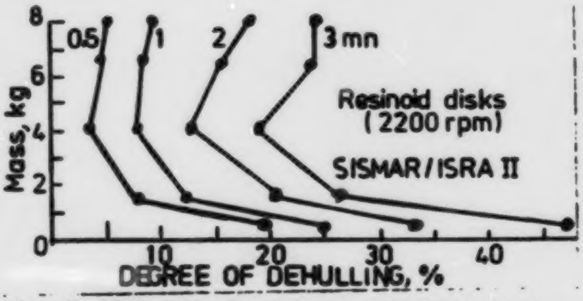

Figure 6. Effect of mass of grain on degree of dehulling of grain in a Mini-PRL dehuller using resinoid disks.

The above discussion implies that in practice, the dehuller should operate, as best as possible, above level 4. This has been incorporated in the design of the Mini-SISMAR/ISRA II and in a Mini-CRS model so that the grain is above level 4 when about 0.5 kg is being dehulled.

Disk Wear

Disk wear is also related to the

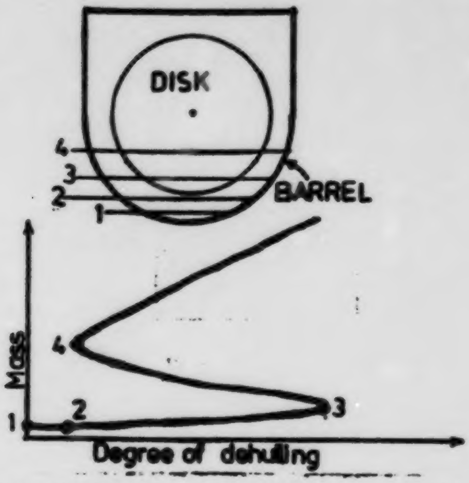

Figure 7. Diagram used to explain the effect of mass of grain on the degree of dehulling.

Table 3. Wear experienced by resinoid disks at village mills in Senegal.

	Bignona (24 t dehulled)#			Ndandallaye Tessanb## (4 t dehulled)		
Disk No.	Diameter (mm)	Thickness (mm)	Mass (g)	Diameter (mm)	Thickness (mm)	Mass (g)
1	229	34	287.6	202	31	215.4
2	230	32	275.1	159	30	130.9
3	232	33	299.7	164	33	142.7
4	233	33	295.7	162	33	140.0
5	230	32	289.1	166	33	149.9
6	325	30	287.1	174	33	163.4
7	225	31	246.2	174	33	162.4
8	228	32	274.3	175	34	167.6
9	228	30	266.4	180	35	160.2
10	224	31	249.0	227	32	276.1
Av.**	229	32	277.0	178	33	173.1
%wear*	9.7	11.7	25.2	29.8	9.2	53.3

** Average values for all 10 disks.

* Percentage wear with respect to new disks: diameter = 25.4 cm thickness = 3.6 cm; mass = 370.3 g.

# Each batch dehulled greater than 6 kg.

## Each batch dehulled between 2 and 3 kg.

mass of grain being processed in the dehuller, although there are as yet no conclusive results on this aspect of dehuller performance. Results of field tests in Senegal [11] indicated that substantial disc wear occurred in machines installed in villages where batch dehulling of between 2 to 3 kg was done, compared to villages where batches were greater than 6 kg. Table 3 shows typical results of disk wear in two villages using similar grains and operating conditions, but using different batch sizes. The average wear as reflected in the diameter, thickness and mass of the disks is significantly greater in the village where 4 tonnes were processed (in batch sizes less than 3 kg), compared to the village where 24 tonnes being processed (in batch sizes greater than 6 kg).

Effect of Grinding Surface

Studies in Senegal [10] and in Canada [7] indicated that resinoid disks, which are smoother than carborundum stones, give better performance as indicated by degree of dehulling, uniformity of dehulling and power consumption. Mechanical aspects of the dehulling action between grinding stones and grain have been discussed in [6]. Important characteristics of grinding stones for the dehullers appear to be grit size, the grade (proportion of bonding material) and the surface dressing. Examples of abrasive discs that have been used are: carborundum stones made of coarse grit silicon carbide abrasives (85% of the total composition) with vitrified clay bonds; resinoid disks made of medium-grit aluminum oxide abrasive (67%), cured phenol formaldehyde resin bond (14%), and Fluorspar (10.6%) and reinforced with fibreglass (7%) to improve their strength.

The comparative performance of lightweight disks and grinding stones can be summarized as follows:

- Coarse grit stones abrade grains much faster than the smoother-faced resinoid disks but the color of the resulting flour indicates that the resinoid disks produce more uniform dehulling as demonstrated by reflectance measurements.
- Grinding stones with coarse grit should be rotated at lower speeds in order to produce dehulling comparable to resinoid disks.
- Grinding stones consume more energy compared to lighter weight disks. Results for the dehulling of maize using a Mini-PRL dehuller using 5 carborundum disks (3 kg each) and 8 resinoid disks (0.15 kg each) [10] are shown in Fig. 8. The carborundum stones consume more fuel to achieve a given degree of dehulling due to their weight and surface friction effect.

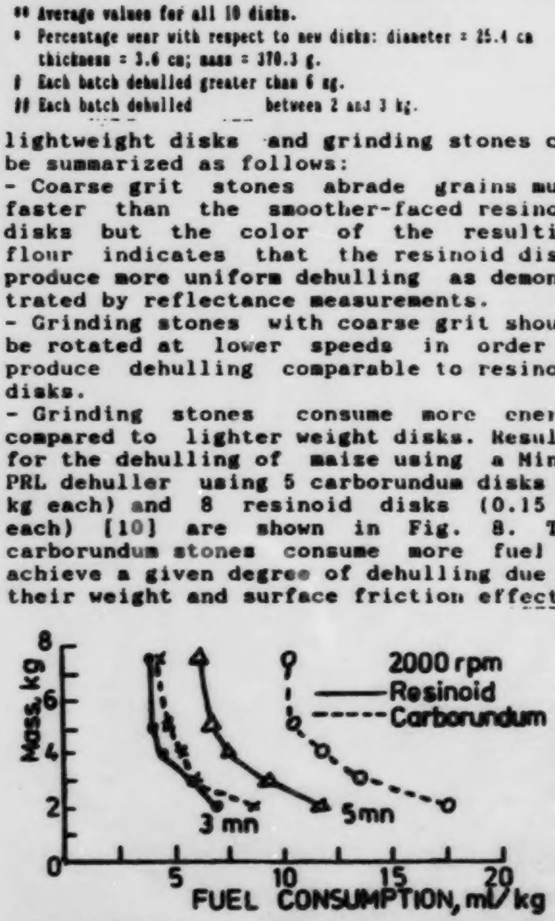

Figure 8. Comparison of the effect of abrasive disk types on power required by Mini-PRL dehuller.

Effect of Internal Lining in Barrel

The interaction between disks and grain, grain and grain, and grain and barrel wall is complex and not well understood. Observations made during the development of the RIIC dehuller, for example, indicated differences between results for bare wall and one lined with rubber. The degree of dehulling was improved when the wall was lined with a rubber material; the dehulling was less uniform, and power consumption was increased [7] as shown in Table 4.

Power consumption is increased due to the restricted motion of the grains by the lining, and the resulting increased resistance to the rotation of the disks. This is because the lining restricts the motion of the grains near the wall, causing higher resistance to the rotation of the disks. In general the grains near the wall are less dehulled than those near the disks.

Table 4. Effect of liner in RIIC dehuller on power consumption, throughput and degree of dehulling for a given flour color for sorghum.

Internal surface	Disk speed (rpm)	Throughput (kg/hr)	Power input hp-hr/t	Degree of dehulling (%)
Without liner	1300	518	7.26	14
	2000	1273	4.4	13
With liner	1300	636	8.58	14
	2000	1053	6.16	20

Source [7].

Areas for Further Studies

Although the mechanical performance of abrasive disc dehullers is satisfactory, the socio-economic viability of their operation is very often in question mainly due to the inability of rural women to pay for dehulling services, which is less than US$ 0.1/kilo of grain. Thus any changes in the design and/or operating conditions of the dehuller aimed at reducing its capital and operating costs would allow it to be more widely used. These technical changes can be obtained by improving the understanding of the performance of the dehuller.

There is need to describe the mechanics of the interaction between the abrasive discs, the grain and the internal wall of the barrel. In such an investigation, it would be informative to determine the optimum spacing between discs and how to maximize the mixing of the grain so that uniform dehulling is obtained. Results of such a study should lead to the proper sizing of dehullers for given loads, reduction of energy consumption and minimization of disk wear, with the ultimate reduction of capital and operating costs.

Since the major component of the dehuller is the abrasive disks, it is of interest to investigate the effects of various types of discs on the dehulling of grains. Emphasis should be placed on longevity of disc surfaces and techniques for local manufacture.

CONCLUSIONS

Abrasive disk dehullers have several features which make them superior to other dehullers for use in developing countries. Their performance is dependent on the types of grains, the physical arrangement and speed of rotation of the disks, the retention time, the internal surface of the dehuller barrel, mass of grain being dehulled and the presence or absence of aspiration of the bran.

Their performance can be improved by studies aimed at understanding the mechanics of the dehulling process, i.e., the interaction between rotating disks, grain and the internal surface of the barrel. The development of appropriate abrasive surfaces that are durable and cheaper would encourage the wide spread use of the dehullers.

ACKNOWLEDGEMENTS

Results discussed in this paper were obtained by research institutions in Canada and Africa with funding provided by the International Development Research Centre (Canada).

REFERENCES

1. Hulse, J.H., Laing, E.M. and Pearson, O.E., Sorghum and the millets: their composition and nutritive value. Academic Press, Toronto, Canada.
2. Doherty, C., Rooney, L.W. & Faubion, J.M., Phytin content of sorghum and sorghum products, Proc. Int. Sym. on Sorghum Grain Quality, 28-31 Oct. 1981, Patancheru, India. ICRISAT, Patancheru, India. pp 329-333.
3. Osman, A.K., Bulrush millet (Pennisetum typhoides) - a contributory factor to the endemicity of goitre in Western Sudan. Ecology of Food and Nutrition, 11, pp 121-128, 1981.
4. Gaitan E. et al, C-glycosylflavones: goitrogens in millet, in Frontiers in thyroidology, eds. Medeiros-Neto, G., Gaitan, E., vol. 2. Plenum Medical Book Company, New York, 1986.
5. Reichert, R.D., Sorghum Dry Milling, Proc. Int. Sym. on Sorghum, 2-7 Nov. 1981, Patancheru, A.P., India. ICRISAT, Patancheru, A.P., India. pp 547-563.
6. Bassey, M.W. & Schmidt, O.G., Abrasive-disk dehullers in Africa: from research to dissemination. International Development Research Centre, Ottawa, Canada. 1989.
7. Oomah, B.D., Reichert, R.D. & Youngs, C.G., Quantitative Comparison Between Carborundum Stones and Resinoid Disks in Dehulling Cereal Grains, Cereal Chemistry, vol. 58, no. 6, pp 492-496, 1981.
8. Mbengue, H.M., Création d'un décortiqueur au Sénégal, Premier Rapport Intérimaire, Projet 3-P-84-0016-02, Septembre 1986. Centre Nationale de Recherches Agronomiques de Bambey, Sénégal.
9. Nance, J.P., Gambian Grain Dehuller, Final Report Phase one. December 1987. Catholic Relief Services, The Gambia.
10. Mbengue, H.M., Création d'un décortiqueur au Sénégal, Deuxieme Rapport Intérimaire, Projet 3-P-84-0016-02, Septembre 1987. Centre Nationale de Recherches Agronomiques de Bambey, Senegal.
11. Mbengue, H.M., Création d'un décortiqueur au Senegal, Troisième Rapport Intérimaire, Projet 3-P-84-0016-02, October 1988. Centre Nationale de Recherches Agronomiques de Bambey, Senegal.

MULTIAXIAL CREEP DAMAGE AND FATIGUE LIFE EVALUATION USING THE GLOSS PLOT

R. SESHADRI R.K. KIZHATIL

Industrial Systems Engineering
University of Regina
Regina, Saskatchewan

ABSTRACT

A simple and systematic method for evaluating multiaxial creep damage and fatigue life of notched members in industrial components is discussed in this paper. Central to the development of the prediction methods is the study of the inelastic component response on the "Generalized Local Stress-Strain (GLOSS) plot". The underlying theory of "generalized relaxation" essentially relates multiaxial stress redistribution due to plastic flow or creep-relaxation to a uniaxial relaxation model.

The elevated temperature component is divided into "local" and "remainder" systems. The local system essentially experiences high inelastic strain concentrations, while the remainder system operates at nominal levels of stresses and strains. The relaxation of stress in the local system is characterized by a constraint parameter which is determined using linear finite element analysis. The constraint parameter is then used to relate multiaxial relaxation and damage to the uniaxial model. The theory developed is validated by considering a cantilever beam undergoing creep.

The inelastic response of notched members is also studied using the GLOSS plot of the high strain-concentration "local" region at the notch root. From the estimated values of the elastic-plastic stresses and strains fatigue level can be easily determined. Examples of notched members are also considered, and their inelastic response obtained using the GLOSS plot.

INTRODUCTION

In many elevated temperature components, that undergo creep, regions of high inelastic strain concentration are present. In such components the elastic strain energy of the bulk of the structure maintains a high magnitude of stress in the localized regions that are prone to strain concentration. The less stressed portions act as a "spring" on the highly stressed parts resulting in the accumulation of creep deformations. Fig. 1 shows some typical component configurations that come under this category.

The relaxation of stress in such components could be evaluated using time-consuming and expensive non-linear finite element analysis. Alternately, a simplified method of estimating the relaxation response of the local region of high strain-concentration is available [1,2]. In this simplified method, the relaxation response of the local region is obtained by studying the GLOSS (Generalized Local Stress Strain) plot, which is essentially a plot of the normalized equivalent stress versus normalized equivalent strain for the local region under consideration.

This paper briefly describes the theory that relates multiaxial stress relaxation to a uniaxial model (Fig. 1). It shows how the "constraint parameter", $\bar{\lambda}$, which characterizes multiaxial relaxation can be determined from the GLOSS plot. The theory developed is applied to the problem of a cantilever beam undergoing creep.

This paper also attempts to point out that the GLOSS plot technique is not restricted to predicting stress relaxation due to creep alone, but can also be used to predict any kind of inelastic response of a local high strain-concentration region. In this context, the elastic-plastic response of notch root is considered, which is a region of local high strain-concentration. Two examples of notched specimens are considered, and the result obtained by the simplified method is compared with other methods.

THEORETICAL CONSIDERATIONS

It is possible to characterize generalized relaxation of a local region

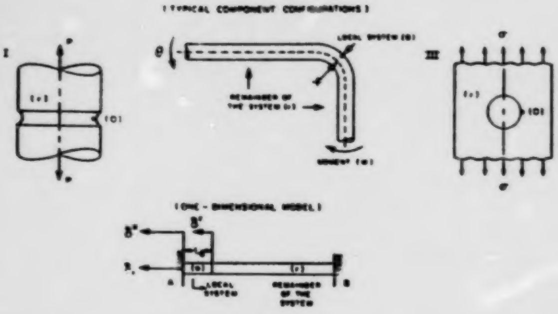
(TYPICAL COMPONENT CONFIGURATIONS)
I
P
(r)
(O)
LOCAL SYSTEM (O)
REMAINDER OF THE SYSTEM (r)
MOMENT (M)
III
σ
(ONE - DIMENSIONAL MODEL)
A
(o)
(r)
LOCAL SYSTEM
REMAINDER OF THE SYSTEM
B

Fig. 1: **One-Dimensional Generalized Relaxation Model**

using certain "constraint parameters". This section deals with the systematic determination of these parameters and the theoretical considerations required to relate multiaxial stress-relaxation to uniaxial stress-relaxation.

Relationship Between Multiaxial and Uniaxial Stress Relaxation

Seshadri and Mikulcik [3] have described the relationship between multiaxial and uniaxial stress-relaxation. For a steady-state creep relationship of the form $\dot{\epsilon}_C = \beta\sigma^n$, the multiaxial stress-relaxation model can be expressed as

$$\frac{d\sigma_e}{d\tau} + \bar{\lambda} B E_o \sigma_e^{\ n} = 0 \qquad \ldots(1)$$

where $\sigma_e = \frac{1}{\sqrt{2}}\left[(\sigma_1 - \sigma_2)^2 + (\sigma_2 - \sigma_3)^2 + (\sigma_3 - \sigma_1)^2\right]^{\frac{1}{2}}$

is the Von-Mises equivalent stress.

In equation (1), $\bar{\lambda}$ is the constraint-parameter characterizing multiaxiality and B, n and E_o are material constants.

For a time-hardening primary creep relationship of the form $\dot{\epsilon}_C = A\tau^m \sigma^n$, the multiaxial stress relaxation model can be expressed as

$$\frac{d\sigma_e}{d\tau} + \bar{\theta}[mAE_o\ \tau^{m-1}\ \sigma_e^{\ n}] = 0 \qquad \ldots(2)$$

where $\bar{\theta}$ is the primary creep constraint-parameter.

It has been shown by Seshadri and Mikulcik [3] that the constraint parameters $\bar{\lambda}$ and $\bar{\theta}$ are equal. Making the substitution

$$\tau' = \frac{A\tau^m}{B}$$

equation (2) can be expressed as

$$\frac{d\sigma_e}{d\tau'} + \bar{\theta}(BE_o\sigma_e^{\ n}) = 0 \qquad \ldots(3)$$

Equations (1) and (3) are identical since $\bar{\lambda} = \bar{\theta}$.

Further if

$$\tau^* = \bar{\theta}\tau'$$

then the uniaxial stress relaxation equation

$$\frac{d\sigma_e}{d\tau^*} + BE_o\sigma_e^{\ n} = 0 \qquad \ldots(4)$$

is obtained.

Thus it can be seen that multiaxial relaxation involving primary or steady creep can be converted to uniaxial relaxation using suitable time-scale corrections.

Generalized Stress-Relaxation

The constraint parameter $\bar{\lambda}$ in equation (1) has been determined for two and three-dimensional constraints [3]. For a two-dimensional constraint,

$$\bar{\lambda} = \frac{(2.5-2\nu)(1+\alpha^2) + (5\nu-4)\alpha}{2(1-\nu^2)(1-\alpha+\alpha^2)} \qquad \ldots(5)$$

where $\alpha = \sigma_2/\sigma_1$ is the stress ratio.

For a three-dimensional constraint

$$\bar{\lambda} = \frac{3}{2(1+\nu)} \qquad \ldots(6)$$

In obtaining these expressions for $\bar{\lambda}$, it has been assumed [3] that the stress-ratio α is a constant during relaxation. This assumption of constancy is required for the development of the generalized relaxation model, which is discussed next.

The elevated temperature component under consideration is divided into "local" and "remaining" systems, Fig. 1. The local system experiences large inelastic strain concentrations, and the variables pertaining to it are denoted by the superscript '0'. The remaining system variables are designated by the superscript 'r'. When dealing with multiaxial stress problems, equivalent stress and strain are used to relate them to the uniaxial model in Fig. 1.

If δ^0 and δ^r in Fig. 1 denote respectively the displacement of the local and remaining system, then the total displacement of end A is

$$\delta_t = \delta^0 + \delta^r \qquad \ldots(7)$$

Defining parameters β and ϕ as

$$\beta = \frac{\delta_e^{\,r}}{\delta_e^{\,o}}, \quad \phi = \frac{\delta_c^{\,r}}{\delta_c^{\,o}} \qquad \ldots(8)$$

The total displacement of the system, δ_t, is the sum of elastic, plastic and creep displacements in general, i.e.

$$\delta_t = \delta_e^{\,o} + \delta_p^{\,o} + \delta_c^{\,o} + \delta_e^{\,r} + \delta_p^{\,r} + \delta_c^{\,r} \qquad \ldots(9)$$

From equations (8) and (9)

$$\delta_t = (1+\beta)\delta_e^{\,o} + (1+\phi)\delta_c^{\,o} + \delta_p^{\,o} + \delta_p^{\,r} \qquad \ldots(10)$$

Now end A is subjected to a displacement δ_t and then fixed, and the stresses are allowed to relax. Also, the plastic components $\delta_p^{\,o}$ and $\delta_p^{\,r}$ are time-independent. Hence

$$\dot{\delta}_t = 0 = (1+\beta)\dot{\delta}_e^{\,o} + (1+\phi)\dot{\delta}_c^{\,o} \qquad \ldots(11)$$

Dividing (11) by the length of the local system L_o,

$$\dot{\varepsilon}_e^{\,o} + \frac{(1+\phi)}{(1+\beta)}\dot{\varepsilon}_c^{\,o} = 0 \qquad \ldots(12)$$

Since $\dot{\varepsilon}_e^{\,o} = \frac{1}{E_o}\frac{d\sigma}{d\tau}$ and $\dot{\varepsilon}_c^{\,o} = B\sigma^n$

$$\frac{d\sigma}{d\tau} + \bar{\lambda} B E_o \sigma^n = 0 \qquad \ldots(13)$$

where

$$\bar{\lambda} = \frac{1+\phi}{1+\beta} \qquad \ldots(14)$$

By letting $\tau^* = \bar{\lambda}\tau$ in equation (13), the uniaxial relaxation model, equation (4) results. Thus in the presence of multiaxiality, the time taken for a given initial stress σ_i to relax to a prescribed level σ would be $1/\bar{\lambda}$ times the uniaxial relaxation, i.e.

$$\tau = \frac{1}{\bar{\lambda}}\left[\frac{1}{BE_o(n-1)}\left(\frac{1}{\sigma^{n-1}} - \frac{1}{\sigma_i^{\,n-1}}\right)\right] \qquad \ldots(15)$$

Equation (15) characterizes the well observed phenomenon that in regions of high local strain concentration, stresses take a longer time to relax due to the elastic "spring" effect of the remaining region [4]. If β and ϕ are determined for a "local" region in a general component undergoing multiaxial relaxation, then using equation (20), the relaxation of stress in the "local" region can be predicted.

The Generalised Local Stress-Strain (GLOSS) Plot

The values of β and ϕ can be obtained by studying the relaxation of stresses in the local system. The mixed-mode relaxation modulus is

$$E_r = \frac{d\sigma}{d\varepsilon_t^{\,o}} \qquad \ldots(16)$$

where ε_t, the total strain in the local system is the sum of elastic, plastic and creep components. By re-arranging equation (12) it can be shown that

$$\dot{\varepsilon}_t^{\,o} = -\beta\dot{\varepsilon}_e^{\,o} - \phi\dot{\varepsilon}_c^{\,o} \qquad \ldots(17)$$

Using $\dot{\varepsilon}_e^{\,o} = \frac{1}{E_o}\frac{d\sigma}{d\tau}$ and $\dot{\varepsilon}_c^{\,o} = B\sigma^n$ and equation (13) the following expression is obtained;

$$\dot{\varepsilon}_t^{\,o} = \frac{1}{E_o}\left(\frac{\phi}{(1+\phi)}(1+\beta) - \beta\right)\frac{d\sigma}{d\tau} \qquad \ldots(18)$$

from which

$$E_r = \frac{1}{\dot{\varepsilon}_t^{\,o}}\left(\frac{d\sigma}{d\tau}\right) = \frac{E_o}{\left(\frac{\phi(1+\beta)}{1+\phi} - \beta\right)} \qquad \ldots(19)$$

Simplifying (19) leads to

$$\phi\left[\left(\frac{E_r}{E_o}\right) - 1\right] - \beta\frac{E_r}{E_o} = 1 \qquad \ldots(20)$$

Introducing the non-dimensional quantities

$$\bar{\sigma} = \frac{\sigma}{\sigma_i}, \quad \bar{\varepsilon}_t^{\,o} = \frac{\varepsilon_t^{\,o}}{\varepsilon_i} \text{ and } \bar{E}_r = \frac{d\bar{\sigma}}{d\bar{\varepsilon}_t^{\,o}} = \frac{E_r}{E_o} \qquad \ldots(21)$$

where σ_i and ε_i are the initial values at time t = 0,

$$\phi(\bar{E}_r - 1) - \beta\bar{E}_r = 1 \qquad \ldots(22)$$

In cases where the remainder system has no significant creep, $\phi = 0$ from equation (8) which leads to

$$\beta = -\frac{1}{\bar{E}_r} \qquad \ldots(23)$$

Equation (23) is valid in elevated temperature components that have a local region of very high stress levels and remainder region of low nominal stresses. This leads to insignificant creep deformation occurring in the remainder system. In such cases the constraint parameter $\bar{\lambda}$ is obtained from equation (14) simply as

$$\bar{\lambda} = \frac{1}{1+\beta} \qquad \ldots(24)$$

Determination of Generalized Relaxation Modulus E_r

For a practical elevated temperature component undergoing creep and subject to local regions of high strain-concentration, the determination of E_r allows the constraint parameter $\bar{\lambda}$ to be obtained using equations (23) and (24). For this the Generalized Local Stress Strain (GLOSS) plot is constructed for the local region using linear-elastic finite element analysis alone.

A linear finite element analysis of the component is first carried out, and the location of the highest stressed region is determined. The elastic modulus for this region alone is now changed from its initial E_o by an amount ΔE and once again a linear finite element analysis is performed. This leads to a drop in the stress level by $\Delta\bar{\sigma}$, and an increase in the total strain by $\Delta\epsilon_t$, for the local region. The relaxation modulus is then given to a good approximation by

$$\bar{E}_r = \frac{\Delta\bar{\sigma}}{\Delta\bar{\epsilon}_t^{\,o}} \qquad \ldots(25)$$

where $\bar{\sigma}$, $\bar{\epsilon}_t^{\,o}$ and E_r are normalized values as defined earlier. Fig. 2 shows a typical GLOSS plot on normalized stress-strain co-ordinates.

Using equations (23) and (24), $\bar{\lambda}$ can be evaluated.

This method of obtaining generalized relaxation for multiaxial components by using a suitable scaling factor to a uniaxial model is in a sense similar to the "reference stress method". In the reference stress method, the creep response of a complex structure is obtained by studying the creep response of a uniaxial model subjected to the appropriate reference stress value [5].

Multiaxial Creep Damage

From the solution of equation (1), the relaxation of equivalent stress with time for steady-state creep is given by

$$\sigma_e(\tau) = \frac{1}{\left[\frac{1}{\sigma_i^{\,n-1}} + \bar{\lambda}BE_o(n-1)\tau\right]^{\frac{1}{n-1}}} \qquad \ldots(26)$$

where σ_i is the initial equivalent stress.

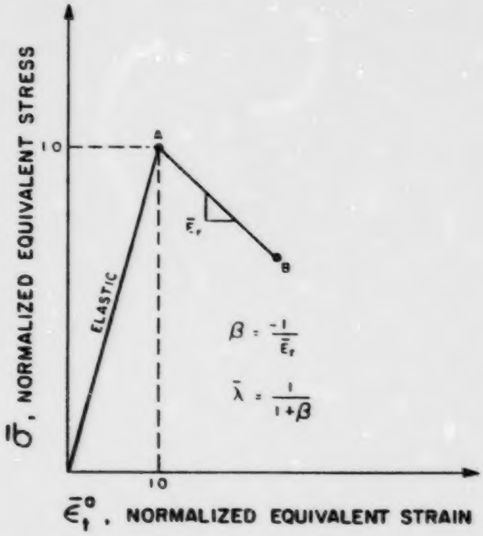

Fig. 2: A Typical GLOSS Plot

Since $\bar{\lambda}$ can be evaluated for practical cases, as previously described, equation (26) can estimate the relaxation of stress with time in high strain concentration local regions. If a time-hardening primary creep relationship of the form $\dot{\epsilon}_c = A\tau^m\sigma^n$ is used, then

$$\sigma_e(\tau) = \frac{1}{\left[\frac{1}{\sigma_i^{\,n-1}} + \bar{\lambda}AE_o(n-1)\tau^m\right]^{\frac{1}{n-1}}} \qquad \ldots(27)$$

The creep damage fraction or the life usage fraction during generalized relaxation can be obtained from

$$D(\tau) = \int_{\tau_1}^{\tau_2} \frac{d\psi}{L(\psi)} \qquad \ldots(28)$$

where ψ is a dummy variable for τ and $L(\psi)$ is the time to rupture for a given stress level. Rupture parameters p and q have been determined experimentally for pressure component materials such that the time to rupture at a given stress level is given by

$$L(\sigma) = \frac{p}{\bar{\sigma}} \qquad \ldots(29)$$

Substituting equations (26) and (29) into (28) gives the multiaxial creep damage fraction as

$$D(\tau) = \frac{1}{(q+1-n)p\bar{\lambda}BE_o}\left[\bar{\sigma}_i^{\,q+1-n} - \left\{\bar{\sigma}_i^{\,1-n} + \bar{\lambda}BE_o(n-1)\tau\right\}^{\frac{q+1-n}{1-n}}\right] \qquad \ldots(30)$$

NOTCH STRAINS AND FATIGUE LIFE EVALUATION

This section describes how the theory of the generalized local stress-strain (GLOSS) plot can be extended to predict the inelastic response at notch root locations. Neuber [6], and more recently Molski and Glinka [7] and Ellyin and Kujawski [8] have developed analyses which enable determination of the inelastic behaviour of notches. Detailed non-linear finite element analysis such as by Mowbray and McConnelee [9] can also be used to predict notch stresses and strains. Result obtained using the GLOSS plot method is compared with the above mentioned methods wherever possible.

From a linear-elastic analysis, the pseudo-elastic stress and strain at the notch can be calculated from nominal values of stress and strain as

$$\sigma_i = K_t \sigma_n$$

and

$$\epsilon_i = K_t \epsilon_n \qquad \ldots(31)$$

where K_t is the theoretical stress concentration factor. Eq. (31) is applicable only within the elastic range since plastic redistribution at the notch causes the actual stress value to drop and the strains to increase. The stress-strain behaviour deviates from linear-elastic beyond the yield point and the problem now is to determine the values of stress and strain on the actual stress-strain curve from the pseudo-elastic values.

The curve connecting the pseudo-elastic stress and strain to the actual values on the material σ-ϵ curve, such as Neuber's hyperbola, can be looked upon as some kind of "generalized relaxation" of stress. Of course, in this case, there is no time variable involved, as in creep, and the "relaxation" is instantaneous. The "local" system, in this case, is the region around the notch that has a high strain-concentration.

The "local" system can be identified by a linear elastic finite element analysis as the most highly stressed element at the notch root. Merely modifying the elastic modulus of this element alone, as in the case of creep, has shown to be insufficient in predicting notch root inelastic behaviour accurately. This is because the "local" system is influenced by the plastic constraint of the "remainder" systems. The "remainder" system undergoes plastic deformation by an amount proportional to its stress level above yield as an approximation. Two slightly different procedures, referred to as method I and method II in Fig. 6 and Fig. 7 are used to obtain the notch inelastic response. Both methods are based on linear-elastic finite element analysis.

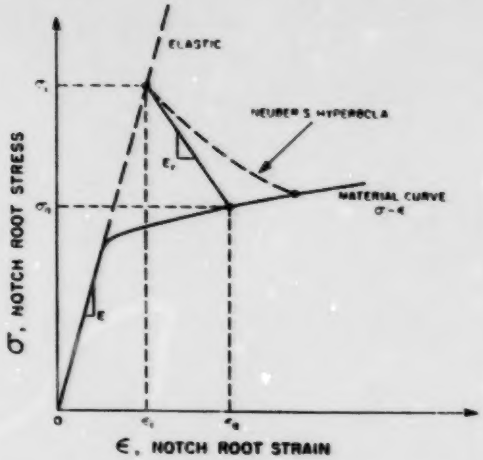

Fig. 3: Determination of Inelastic Notch Response

In method I, a linear finite element analysis is carried out, and all elements that are above yield identified. The elastic modulii of all these elements are reduced to, say 90% of the original value and the linear finite element analysis carried out again. New values of stress and strain, $\sigma_i - \Delta\sigma$ and $\epsilon_i + \Delta\epsilon$, are obtained for the "local" system viz. the most highly stressed element at the notch root. The "relaxation" trajectory is approximated by a straight line of slope E_r passing through the pseudo-elastic point (σ_i, ϵ_i), and the new values ($\sigma_i - \Delta\sigma$, $\epsilon_i + \Delta\epsilon$). The intersection of this "relaxation" trajectory of slope E_r with the material stress-strain curve gives the elastic-plastic values of stress and strain.

In method II, the procedure is more or less the same. All elements above yield are identified from a linear elastic FEM, and the elastic modulus of each of them modified to

$$E_s = E \frac{\sigma_y}{\sigma_e} \qquad \ldots(32)$$

where E_s is the new "secant" modulus, σ_y the yield stress and σ_e the equivalent stress level in a particular element. Eq. (32) is prompted by the physical observation that higher the equivalent stress in an element, the more it has to be softened to simulate plastic flow. Fig. 3 illustrates the determination of the elastic-plastic notch root stress, σ_a and strain ϵ_a from the pseudo-elastic values σ_i and ϵ_i using the relaxation

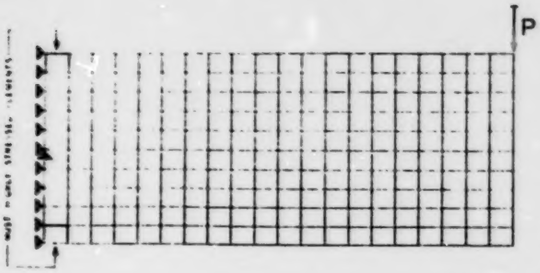

Fig. 4: Numerical Example - Cantilever Beam

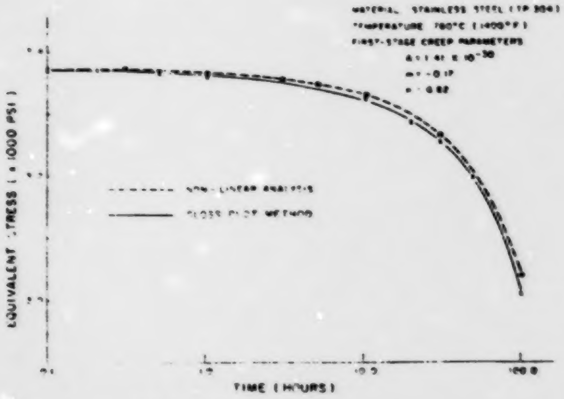

Fig. 5: Relaxation of Stress For Cantilever Beam

modulus E_r and the material stress-strain curve.

Once the actual stress or strain range at the notch root is determined, the fatigue life of the notched member can be obtained from stress versus life or strain versus life plots obtained from smooth specimen tests.

NUMERICAL EXAMPLES

a) Cantilever Beam Undergoing Creep

A cantilever beam of length 254.00 mm (10 inches), depth 101.60 mm (4 inches) and thickness 25.40 mm (1 inch) subjected to an end load P = 15,123 N (3400 lbs) as shown in Fig. 4 is considered. The most highly stressed elements are shown in Fig. 4. These elements alone are subjected to a time-hardening primary creep relationship of the form $\dot{\epsilon}_{cr} = At^m\sigma^n$ where $A = 1.41 * 10^{-30}$, $m = 0.17$ and $n = 6.82$. The rest of the elements in the beam are not allowed to creep, so that a "local" region of high strain concentration along with $\phi = 0$ is obtained. A GLOSS plot for the "local" region is constructed using two linear elastic finite element analyses. The value of β is found to be 1.824 which is substituted in eq. (26) and eq. (27) to obtain the relaxation of stress with time. A non-linear finite element creep analysis using ANSYS [10] is also carried out. Fig. 5 shows the relaxation predicted using the GLOSS plot to be in excellent agreement with the non-linear finite element analysis results.

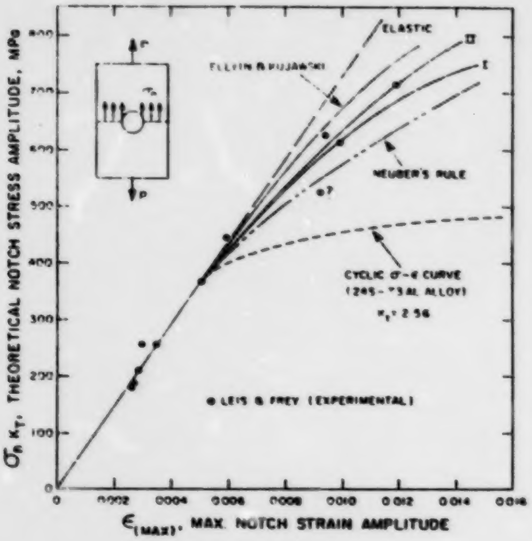

Fig. 6: Theoretical Notch Stress Amplitude vs Maximum Notch Strain Amplitude For a Circular Notch

b) Strain Concentration for Notched Components

Fig. 6 shows the results obtained for a plate with a circular hole in tension by both method I and II. Method I overpredicts the notch root strain as some of the elements are excessively softened when the elastic modulii of all the elements above yield are reduced by, say 10%. Both methods are compared with those of Ellyin and Kujawski [8], Neuber [6] and experimental results obtained by Leis and Frey [11]. Another example of a circumferentially notched bar is considered in Fig. 7, and results compared with an elastic - plastic finite element analysis using ANSYS [10]. Here again method I is seen to overpredict notch root strain. Method II gives good results, as can be seen from the figures.

CONCLUSIONS

A simple and systematic method, that uses only linear-elastic finite element analysis, for predicting generalized relaxation in elevated temperature components and thereby assessing creep

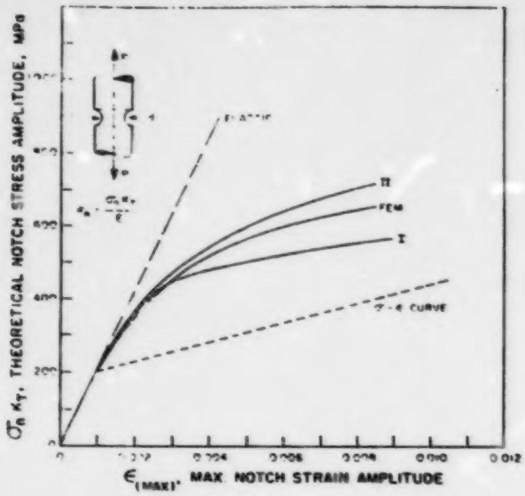

Fig. 7: Theoretical Notch Stress Amplitude vs Maximum Notch Strain Amplitude For A Circumferentially Notched Round Bar

damage is presented in this paper. The underlying theory is validated by considering the case of a simple cantilever beam undergoing creep.

This concept of generalized "relaxation" in a "local" high strain-concentration region is extended to predict the inelastic response of notch stress and strain. Two specific examples of notched members are considered and results obtained using the much simpler GLOSS plot method is found to be in good agreement with other methods.

The GLOSS plot method is understandably approximate, and yields approximate results, unlike a detailed non-linear finite element analysis. However, the results of non-linear finite element analysis are themselves in many cases questionable due to the use of unreliable material data, particularly for the creep phenomenon. In such situations the simpler technique proposed can prove useful and time-saving particularly for preliminary design or analysis.

ACKNOWLEDGEMENT

The authors gratefully acknowledge the support provided by the Natural Sciences and Engineering Research Council of Canada which made it possible to carry out the research reported in this paper.

REFERENCES

1. Seshadri, R., "The Effect of Multiaxiality and Follow-up on Creep Damage, The 1989 ASME Pressure Vessels and Piping Conference, Honolulu, PVP-Vol. 161, pp. 13-23, 1989.

2. Vaidyanathan, S., Kizhatil, R.K. and Seshadri, R., GLOSS Plot-Validation and Application to Elevated Temperature Component Design, The 1989 ASME Pressure Vessels and Piping Conference, Honolulu, PVP-Vol. 161, pp. 25-31, 1989.

3. Seshadri, R. and Mikulcik, E.C., On Relating Multiaxial and Uniaxial Stress Relaxation in Pressure Components, Transactions of the CSME, Vol. 13, No. 1/2, pp. 11-16, 1989.

4. Robinson, E.L., Steam Piping Design to Minimize Creep Concentration, Trans. ASME, Vol. 77, pp. 1147-1162, 1955.

5. Kraus, H., Creep Analysis, John Wiley and Sons, 1980.

6. Neuber, H., Theory of Stress Concentration for Shear-Strained Prismatical Bodies with Arbitrary Non-linear Stress-Strain Law, Journal of Applied Mechanics, Vol. 28, pp. 544-550, 1961.

7. Molski, K., and Glinka, G., A Method of Elastic-Plastic Stress and Strain Calculation of Notches, Material Science and Engineering, Vol. 50, pp. 93-100, 1981.

8. Ellyin, F., and Kujawski, D., Notch Root Stress/Strain Prediction for Elastic-Plastic Loading, Res Mechanica, Vol. 20, pp. 177-190, 1989.

9. Mowbray, D.F. and McConnelee, J.E., Applications of Finite Element Stress Analysis and Stress-Strain Properties in Determining Notch Fatigue Specimen Deformation and Life, Cyclic Stress-Strain Behaviour - Analysis, Experimentation and Failure Prediction, ASTM Spec. Tech. Pubication 519, pp. 151-169, 1971.

10. DeSalvo, G.J. and Gorman, R.W., ANSYS Engineering Analysis System User's Manual, Swanson Analysis Systems, Inc., Houston, Penn., June 1987.

11. Leis, B.N. and Frey, N.D., Cyclic-Inelastic Deformation and Fatigue Resistance of Notched-Thin Aluminum Plates, Proc. of the Society for Experimental Stress Analysis, Vol. 39, pp. 287-295, 1982.

NOVEL TECHNIQUES FOR THE SURFACE EVALUATION OF PAPER

D.C.S. Kuhn and P. Whiting

Abitibi-Price Inc., Central Research Division, Mississauga, Ontario

ABSTRACT

Paper quality is primarily a function of the runnability and printability of the paper. The relationship between paper surface topology and its printability is discussed in this paper. The surface profile of paper samples was recorded using a Surtronics 3P profilometer and digitized using a Dash 16 A/D board. A number of different roughness measures were then determined over sampling lengths of between 32 μm and 8.134 mm. The results were compared to Parker Print Surface results (air-leak method) and visual assessment results.

Abitibi-Price Inc. has further used the digitized surface profiles in a number of novel ways: to investigate confusing roughness versus printability results; to determine relevant sampling lengths for roughness determination; and to develop relevant surface topology parameters to characterize the printability of paper.

INTRODUCTION

In the press room, there are two main paper quality concerns: runnability and printability. Runnability describes the efficiency of the paper in the press room, while printability describes the achievable print quality in the press room. The runnability and printability of a sheet are difficult to quantify since both describe a wide range of properties as well as being dependant on the printing method. Runnability encompasses the following factors: frequency of web breaks, linting, picking, paper curl and misregister of colour. Factors described by printability include: gloss, print uniformity, ink requirement, print density, print through, setoff and ruboff. An extensive review of printability concepts is given by Aspler (1990). Printability assessment methods are described by Mangin and Geoffroy (1989), Parker (1965, 1981) and Mittelstaedt (1987), and a review of ink-paper interactions in printing is given by Lyne and Aspler (1982).

Printability is predicted by a combination of roughness, sheet compressibility, porosity, air permeability, formation, surface chemistry, ink holdout, printing, surface strength and subjective quality tests. The results of some of these tests are a function of the surface topology of the paper. However, the surface topology of paper is difficult to characterize since a single parameter does not adequately describe the surface, e.g. sheet roughness measures only the deviation of the surface profile from a flat plane. Presently, the surface topology of paper is quantified using air-leak roughness devices, optical smoothness testers, and profilometers.

In the present study the surface profiles of paper samples were recorded using a Surtronics 3P profilometer and digitized using a Dash 16 A/D board. A number of different roughness measures were then determined over sampling lengths of between 32 μm and 8.134 mm. Different sampling lengths are of interest depending on the printing process. The results were compared to Parker Print Surface results (an air-leak method) and visual assessment results.

The profilometer was used as a tool to investigate confusing press results. Strips of paper were printed with a laboratory IGT press. The inking unit was charged only once and therefore successive prints received less ink. The mass of the ink layed down, Parker Print Surface roughness, gloss, and optical density of these strips were subsequently measured. The Parker Print Surface results showed roughness increasing with increasing gloss. The profilometer was used to investigate this unusual phenomenon. The roughness of the strips were first assessed visually based on SEM photographs of the surfaces. The variation of the Parker Print Surface roughness, the profilometer measured roughness and the Walsh roughness factor with gloss was then considered.

Another area considered was the relationship between the paper surface topology and its printability. The paper surface profile was characterized by two roughness measures, a peak to valley measure and a surface valley density; while the printability was characterized by mottle, an Abitibi-Price Printability Index, formation, and a subjective printability ranking. Paper surface valley density has been considered previously, notably by Aschan et al. (1986). They showed that the total number of valleys with widths between 75 and 175 μm has a pronounced effect on gravure printability. The present study considered the influence of valley density on flexo news printability.

SURFACE ROUGHNESS

Roughness is a measure of some average departure of the surface profile from a flat plane. The profilometer measures the arithmetic mean of the deviation of the surface profile from the mean plane. The Walsh roughness factor, to be discussed below, essentially measures the root mean square (RMS) of the deviation of the surface from the mean plane. A RMS average would give more weight to a large deviation from the mean plane than the arithmetic mean. Air-leak methods, e.g. Parker Print Surface Tester (PPS), measure the cubed root of the mean cube of the deviation of the surface profile from a flat plane lying on the surface (Parker, 1965). The cube root of the mean cube average would be even more strongly influenced by large deviations than a RMS average. The above three roughness measures, therefore, weight the importance of a deviation from a flat plane differently.

Visual Assessment

The surface of paper samples was visually assessed using a scanning electron microscopic (SEM). Three sets of photographs were taken at 100x, 150x and 500x magnification.

Parker Print Surface Roughness Tester

The Parker Print Surface (PPS) roughness tester is an air-leak roughness tester. An annulus of smooth, hard material (metering land) is pressed against the paper surface. A differential pressure is applied across this annulus, and a measurement is made to indicate the rate of flow through the gaps provided by the roughness of the paper. The metering land of the instrument is 10.0 cm in circumference and its breadth is 51 μm.

Profilometer Roughness Factor

Profilometer Roughness values, Ra_p, were recorded directly from the LCD display on the profilometer. Ra_p is the average of five Ra values measured over consecutive sampling lengths. The mean plane was averaged over the entire assessment length (i.e. over the five consecutive sampling lengths).

Digitized Roughness Factors

The surface roughness of the samples was characterized using two methods. The surface profile was first recorded by a Surtronics 3P profilometer and then digitized using a Dash 16 A/D board. A standard Ra roughness, Ra_m, (the arithmetic mean of the deviation of the surface profile from the mean plane) over each sampling length was then determined from the digitized profile. The second roughness measure, Ra_l, was defined as the arithmetic mean of the deviation of the surface profile from the line of best fit of the profile. The mean plane was averaged over each sampling length.

"PPS-Like" Roughness Evaluation

Parker Print Surface like (PPS-like) roughness values, Ra_s, based on different sampling lengths, were determined from the digitized surface. The "PPS-like" values were weighted as the cubed root of the deviation of the surface profile from a flat plane. The cubed area above the plane was subtracted from the cubed area under the plane. The flat plane was set at a position 80% of the distance from the lowest profile position to the highest profile position. This plane position was chosen to simulate conditions measured by the PPS tester. Some compression of the paper by the PPS metering head is to be expected.

Walsh Roughness Factor

The Walsh roughness factor, μ, is essentially a RMS average determined from the digitized surface profile. To compute a Walsh roughness factor the profile is first resolved into a series of 15 component Walsh waveforms of decreasing wavelengths (see Fig. 1). The amplitude of each roughness wavelength is then determined and the Walsh roughness factor is determined as follows:

$$\mu = \sum_{k=1}^{k=15} A_k^2 k^2 \qquad (1)$$

where A_k is the amplitude of the Walsh function k. The Walsh function analysis gives information on wavelengths ranging from 1/2 of the sampling length to 1/8 of the sampling length. Walsh functions rather than sine waves have been used since the former are better suited to processing of digitized data (Smith and Walmsley, 1979; Kent et al., 1981; Gane, 1989).

SURFACE CHARACTERIZATION

The surface texture was further characterized with a maximum peak to valley height measurement and a paper surface valley density.

Maximum Peak to Valley Height Measurement

The maximum peak to valley height, Ry, was determined over each sampling length from the digitized surface profile.

Paper Surface Valley Density

The valley density, V, was defined as the number of valleys of a given width over the profilometer trace length times the valley width divided by the assessment length, l_t. Valleys were characterized not only by their width, W, but also by a minimum required depth, D.

The valley count was determined by an ASYST program as follows:

1. the digitized profile was divided into sections, S_n, of length equal to the valley width, W.
2. the mean height, h_n, of all sections was determined.
3. a section S_n was defined to contain a valley if the mean height of the section to the right, h_{+1}, and the mean height of the section to the left, h_{-1}, were greater than the mean height of the section, h_n, by at least the minimum depth selected, i.e. if $h_{-1} > h_n < h_{+1}$, and $| h_n - (h_{-1} + h_{+1})/2 | > D$.
4. the sections containing valleys were summed to give the valley count, $N_{w,D}$.

The valley density, V, is therefore determined as follows:

$$V = N_{w,D} * D / l_t \qquad (2)$$

SURFACE EVALUATION OF IGT PRINTED PAPER

Strips of value added paper were printed with the IGT apparatus with blue ink of #8 tack at Abitibi-Price's research facilities in Kenogami. The inking unit was charged only once and therefore successive prints received less ink. Visual inspection of the samples showed that picking decreased with decreasing ink lay down. The Parker Print Surface roughness, Ra_p, results showed roughness increasing with increasing gloss (ink lay down). This set of printed samples was therefore studied in more detail, since as sheet roughness increases gloss is usually found to decrease. To further investigate the influence picks have on PPS measurements a "PPS-like" roughness, Ra_λ, was determined from the digitized profilometer results.

Standard Printability Evaluation and Visual Assessment

The IGT printed samples (26 in total) were subjected to electron microscopic (SEM) examination. Three sets of photographs were taken at 100x, 150x and 500x magnification. The first few samples showed severe surface ruptures over nearly the whole samples which gradually became less frequent so that by strip #17 ruptures were beginning to become infrequent, e.g. see Figs. 2 and 3.

The SEM photographs of the IGT samples are of particular interest when considering the variation of roughness with gloss. SEM photographs of the high gloss samples (lower numbered samples) showed frequent and severe surface ruptures resulting from picking. SEM photographs of samples with lower gloss values showed less frequent and less severe surface ruptures. The visual assessment was based on SEM photographs selected to show "typical" surface failures rather than to give a representative picture of the surface scanned. It is recalled that the higher gloss samples were assessed to be rougher than the lower gloss samples. However, the surface between ruptures on high gloss samples appears smoother than the surface between ruptures on lower gloss samples, e.g. compare strip #3 and #17 at 500x magnification. More representative photographs of the surface scanned would have focused more attention on the surface area between the ruptures and less on the ruptures.

Surface Evaluation

The surface roughness of the IGT printed samples was assessed with a Parker Print Surface (PPS) tester and a Surtronics 3P profilometer and visually assessed as described above. Each approach showed a different variation of surface roughness with gloss and ink optical density. The variation of roughness with gloss was essentially the same as the variation of roughness with ink optical density for the respective test methods, e.g. if PPS roughness increased with increasing gloss then PPS roughness also increased with increasing ink optical density. Hence, the following discussion will be limited to the variation of roughness with gloss.

The PPS roughness results (see Fig. 4) showed roughness increasing with gloss. The visual roughness assessment also found that roughness increased with gloss. The profilometer results showed, however, that either there is no clear variation of roughness with gloss or that roughness decreased with increasing gloss, e.g. see Fig. 5. The roughness variation is dependent on the roughness sampling and assessment lengths. Note that the sampling length is defined as the length over which a single roughness value is determined, and the assessment length is the distance over which a series of roughness values are averaged.

As sheet roughness increases gloss is usually found to decrease. However, the PPS measurements as noted above indicate the opposite trend. The roughness increase with gloss can be attributed to the increased number of picks found in samples with higher gloss values and the strong weighting the PPS tester gives to these deep disruptions of the surface profile.

Ra_p values (LCD profilometer Ra value), based on a sampling length of 0.8 mm, showed no distinct variation with gloss. This was also true of Ra_D (digitized Ra value) values based on sampling lengths of greater than 0.5 mm. This implies that small scale roughness changes observed in the SEM photographs have little influence on the Ra values at longer sampling lengths (> 0.5 mm). At shorter sampling lengths picks have only a weak influence on the roughness value and small scale roughness changes begin to influence the Ra_D value. As a consequence, the roughness decreased with increasing gloss at shorter sampling lengths, e.g. see Fig. 5. This results is in agreement with earlier observations of the SEM photographs.

The Walsh analysis of the samples was conducted based on a sampling length of 256 μm, i.e. the analysis centred on a wavelength range from 32 μm to 128 μm. The Walsh roughness factor, μ, was found to decrease with increasing gloss. This is not unexpected at this sampling length since the Ra_D values at short sampling lengths and visual inspection of the areas between ruptures both showed that roughness decreased as the gloss increased.

"PPS-Like" Roughness

To determine whether the "PPS-like" roughness measure, Ra_λ, is a good approximation of PPS roughness, Ra_p, the regression equations of PPS roughness at a number of sampling lengths were determined. Linear regression results show that there is a significant linear relationship at the shorter sampling lengths. However at the lower sampling lengths the residuals exhibit a distinctive nonlinear variation suggesting a higher order relationship. Hence a linear model does not adequately describe the relationship between the Ra_p and Ra_λ results.

The degree of linear relationship was also determined between Ra_D values at different sampling lengths and Ra_p values. A comparison of these results with the Ra_λ versus Ra_p results indicates that the Ra_λ results account for more of the variation in the Ra_p data than the Ra_D results.

FLEXO NEWS PRESS ROOM TRIAL

Samples from a flexo news press room trial were used to investigate the relationship between the paper surface topology and its printability. The trial was run at the Washington Post on their Goss Flexo press to investigate the comparative printing properties of newsprint and groundwood products.

The printability ranking of the flexo news press room trial samples was based on visual inspection of ANPA offset test form printed paper. Printability was also characterized by mottle (PMN), an Abitibi-Price Inc. Letterpress Printability Index (LPI) and formation (NUI). All of these parameters were compared with paper surface parameters. These results are summarized in Table 1. Only a marginal difference in printability was observed among the newsprint products in the flexo news trial.

Surface Roughness

The Ra_D and Ra_p roughness results are average values based on ten traces each of 16.396 mm length. A t-test at 95% probability level was used to determine the least significant roughness difference between samples, it being assumed the roughness results were normally distributed. An average standard deviation based on the standard deviation of each of the nine samples was used in this analysis.

The least significant roughness difference varies with sampling length and is different for Ra_s and Ra_p results. Significant Ra_p differences exist between groundwood samples up to a sampling length of 0.800, while none of the newsprint Ra_p results are significantly different.

Significant Ra_s differences exist between newsprint and groundwood samples up to sampling lengths of 0.032 and 2.048 mm respectively. At longer sampling lengths there was no significant difference between samples. An important implication of the significant roughness difference results is that fewer traces are required to distinguish a minimum Ra_s difference than a minimum Ra_p difference. Large Ra_p differences between samples are not unexpected since little printability differences were noted during the flexo news trial.

Ra_s and Ra_p results were compared to determine if these two roughness measures describe the same surface features. The degree of linear relationship between Ra_s and Ra_p was determined at all sampling lengths. The line of best fit between Ra_s and Ra_p was determined at all sampling lengths and the resulting residuals were plotted. A strong linear relationship exists at short sampling lengths, becoming increasingly less correlated at longer sampling lengths. As discussed in the previous section, at longer sampling lengths there is little or no significant difference between Ra_s or between Ra_p results. Hence, a poor linear relationship at longer sampling length does not necessarily imply Ra_s and Ra_p describe different roughness features. Hence, the following discussion of the roughness results will centre on Ra_p results since Ra_s and Ra_p describe the same roughness features.

Ra_p results have been compared with the overall printability rankings. The newsprint and groundwood samples were ranked separately. Ra_p roughness, at short sampling lengths, is in good agreement with the printability ranking of the groundwood samples but not in as good agreement with the printability ranking of the newsprint samples. The good agreement is not unexpected for the groundwood samples since the Ra values cover a large range. The newsprint samples, however have very similar Ra_p values and surface roughness does not appear to have a pronounced effect on the printability.

Ra_p has been compared with LPI, PMN and NUI results to examine the relationship between Ra and other printability indicators. Correlation results indicate that PMN and NUI are only weakly linearly correlated with Ra at all sampling lengths. LPI is moderately linearly correlated with Ra_p at sampling length less than 1.024 mm. The residuals, however are only well distributed at sampling lengths of 0.512 and 1.024 mm. The highest correlation between Ra_s and Ra_p occurs at the same sampling length as between LPI and Ra_p. This can be attributed to the fact that LPI is determined, in part, from the PPS roughness of the sample.

Maximum Peak to Valley Height

The Ry results are listed in Table 2. The values listed in this table are averaged values based on ten traces each of 16.396 mm length. A similar analysis carried out for Ra_p was used for Ry. No significant Ry differences exist between newsprint or groundwood samples. An analysis of the variance of the Ry results indicated that an order of magnitude (~ 100) more traces of each sample would be required to significantly distinguish between samples.

Valley Density

Valley density results were determined for minimum valley depths of 0 and 4 μm (0 depth implies that the surface depression is less than or equal to the surrounding surface), and for valley widths between 0.032 and 8 mm. Tables 3 and 4 list valley density averages based on 10 traces (each of length 16.384 mm) of each sample.

The within sample valley density variance over the 10 traces was determined for all samples. The minimum valley density difference which would indicate a significant difference between samples was also determined. These results imply that a significant difference exists between samples at valley widths of 2.048 and 8.192. However, a significant difference exists only between the highest and lowest valley density samples. Similar results were found for the zero minimum valley depth cases.

The lack of significant difference between valley density results is not unexpected since the flexo news trial indicated little printability differences between samples. An analysis of the variance of the valley density results indicated that an order of magnitude more traces (~ 100) of each sample would be required to significantly distinguish between samples at short valley widths. Samples with greater printability differences than those considered here would be expected to have significantly different valley density values at fewer traces. Further analysis of the valley density results was not carried out since there was little between sample difference.

CONCLUSIONS

Surface Evaluation of IGT Printed Paper

The higher gloss I.G.T. printed strips have more severe and frequent surface ruptures resulting from picking than lower gloss strips. However, the area between surface ruptures is smoother for higher gloss strips.

The assessment of the roughness of the I.G.T. printed strips was found to be very dependent on the sampling method. These differences are a results of the different sampling lengths used by each method and the different methods of averaging the deviation of the surface profile from a flat reference plane. The PPS tester is very sensitive to picking. The profilometer weights the entire surface equally, hence it is less sensitive to picking. The walsh roughness factor is a very sensitive measure of roughness and weights the importance of picks between that of the profilometer and the PPS tester.

"PPS-like" roughness measurement results linearly correlate more closely with PPS results than Ra roughness with PPS results. The residuals suggest a higher order relationship exists between the data.

The Parker Print Surface instrument weights the large deviations of a paper surface from a flat plane more strongly than the cubed power as has been suggested in the literature.

Flexo News Press Room Trials

Ra_s and Ra_p describe the same roughness features and fewer traces are required to obtain a least significant roughness difference between Ra_s values than between Ra_p values.

Significant valley density differences of the newsprint and groundwood samples were evident at sampling lengths of 2.048 mm and 8.192. However, a significant difference existed only between the highest and lowest valley density samples.

No significant peak to valley (Ry) differences exist between newsprint or between groundwood samples. As was the case in the valley density results approximately 100 traces would be required to significantly distinguish between samples.

ACKNOWLEDGEMENTS

The authors wish to thank Dr. T.A. Duever for his valuable assistance in evaluating the experimental data, Mr. T.W.A. Dwars for his SEM photography and Kenogami Research for sample testing.

REFERENCES

Aschan, P.-J., Makkonen, T. and Pauko, J. 1986, Board Surface Structure and Gravure Printability, Paperi Ja Puu, Vol. 68, No. 1, p. 30.

Aspler, J.S. 1990, Testing and Predicting Print Quality, in Pulp and Paper Manufacture, ed. M.J. Kocurek, Vol. 10, Joint Textbook Committee of the Pulp and Paper Industry of the United States and Canada.

Gane, P.A.C. 1989, Mottle and the Influence of Coating and Binder Migration, Paper Technology, Vol. 30, No. 4, p. 34.

Kent, H.J., Climpson, N.A., Coggon, L., Hopper, J.J. and Gane, P.A.C. 1986, Applications of Novel Techniques for Quantitatively Characterization of Coating, 1986 TAPPI Coating Conference Proceedings, p. 103.

Lyne, M.B. and Aspler, J.S. 1982, Ink-Paper Interactions in Printing: A Review, in ACS Symposium, No. 200: Colloids and Surfaces in Reprographic Technology, ed. M. Hair and M.D. Croucher, p. 385, American Chemical Society.

Mangin, P.J. and Geoffroy, P. 1989, Printing Roughness and Compressibility: A Novel Approach Based On Ink Transfer, in Fundamentals of Papermaking, Trans. of the Ninth Fundamental Research Symposium, ed. C.F. Baker, p. 951, Mechanical Engineering Publications Ltd., London.

Mittlestaedt, M. 1987, Non-Destructive Testing, Photonics Spectra, Vol.21 No.10, p. 121.

Parker, J.R. 1965, An Air Leak Instrument to Measure Printing Roughness of Paper and Board, Paper Technology, Vol. 6, No. 2, p. 126.

Parker, J.R. 1981, The Measurement of Printing Roughness, TAPPI, Vol. 64, No. 12, p. 56.

Smith, E.H. and Whalsley, W.M. 1979, Walsh Functions and their Use in the Assessment of Surface Texture, Wear, Vol. 57, p.157.

Table 1: Washington Post Ra,, PMN, NUI and overall printability results

Sample	Ra, (μm)	PMN	LPI	NUI	Ranking
1	3.7	198	149	9	9
2	3.2	222	65	16	4
4	3.2	186	112	8.1	4
6	3.6	198	181	9.3	8
8	3.4	283	217	9.5	6
12	3.5	206	115	7.7	7
13	2.4	236	-31	7.3	2
15	2.1	259	-46	7.5	1
17	2.9	139	97	5	3

Table 2: Maximum Peak to Valley Height, Ry (μm)

	Sampling Length (mm)						
	0.032	0.128	0.512	1.024	2.048	8.192	0.8000
Sample							
1	18.0	23.5	27.6	30.7	33.0	40.1	29.8
2	16.0	23.0	26.9	28.1	29.6	37.8	26.7
4	16.0	20.4	26.1	28.4	33.3	36.4	28.5
6	16.4	21.9	26.0	29.6	36.6	38.9	27.2
8	15.9	20.9	25.8	27.2	30.5	39.6	27.0
12	17.4	22.9	27.9	30.4	31.6	36.3	28.5
13	13.4	17.3	20.9	25.3	29.4	35.2	22.9
15	12.9	16.4	20.5	24.8	29.7	35.1	22.7
17	16.9	25.7	27.8	31.2	33.3	38.9	28.3

Table 3: Valley Density (D=0)

	Sampling Length (mm)						
	0.032	0.128	0.512	1.024	2.048	8.192	0.800
Sample							
1	0.246	0.298	0.259	0.238	0.250	0.050	0.244
2	0.252	0.278	0.231	0.244	0.225	0.100	0.244
4	0.246	0.288	0.266	0.263	0.313	0.050	0.225
6	0.249	0.277	0.247	0.250	0.275	0.000	0.249
8	0.251	0.284	0.231	0.225	0.263	0.000	0.190
12	0.246	0.294	0.225	0.256	0.263	0.050	0.229
13	0.240	0.274	0.228	0.206	0.275	0.000	0.200
15	0.252	0.273	0.219	0.225	0.250	0.050	0.195
17	0.246	0.281	0.250	0.250	0.275	0.050	0.264

Table 4: Valley Density (D=4 μm)

	Sampling Length (mm)						
	0.032	0.128	0.512	1.024	2.048	8.192	0.800
Sample							
1	0.055	0.098	0.072	0.106	0.150	0.000	0.088
2	0.035	0.060	0.063	0.056	0.100	0.100	0.063
4	0.029	0.074	0.053	0.081	0.038	0.000	0.068
6	0.035	0.073	0.078	0.075	0.125	0.100	0.088
8	0.046	0.086	0.063	0.088	0.225	0.150	0.073
12	0.051	0.087	0.047	0.125	0.150	0.050	0.098
13	0.019	0.040	0.047	0.106	0.188	0.050	0.103
15	0.019	0.037	0.044	0.063	0.113	0.150	0.063
17	0.049	0.096	0.097	0.113	0.150	0.050	0.122

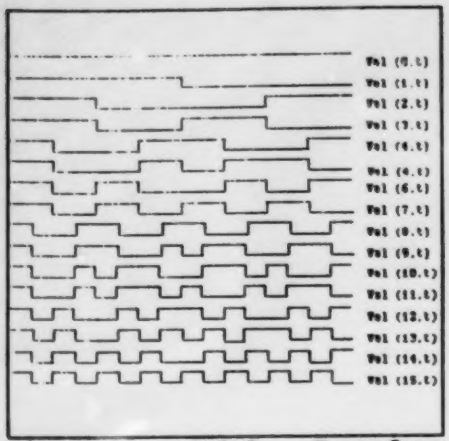
Wal (0,t)
Wal (1,t)
Wal (2,t)
Wal (3,t)
Wal (4,t)
Wal (5,t)
Wal (6,t)
Wal (7,t)
Wal (8,t)
Wal (9,t)
Wal (10,t)
Wal (11,t)
Wal (12,t)
Wal (13,t)
Wal (14,t)
Wal (15,t)

Figure 1: Walsh Transform Function

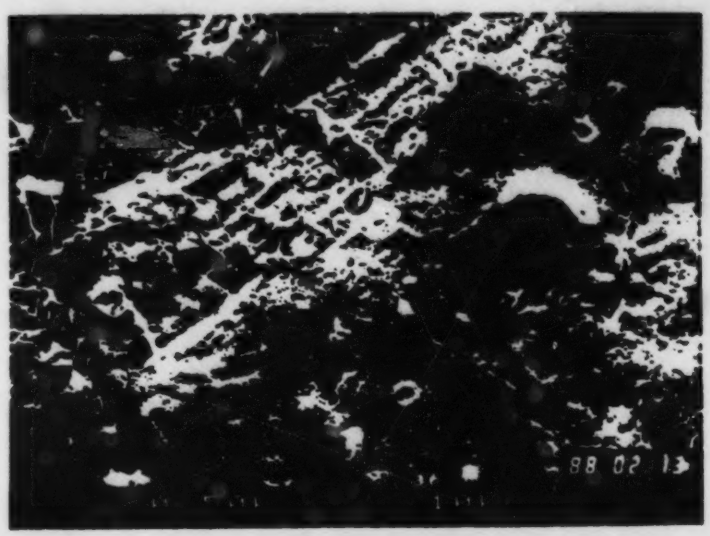

#3

Figure 2: Sample #3, 500X

#17

Figure 3: Sample #17, 500X

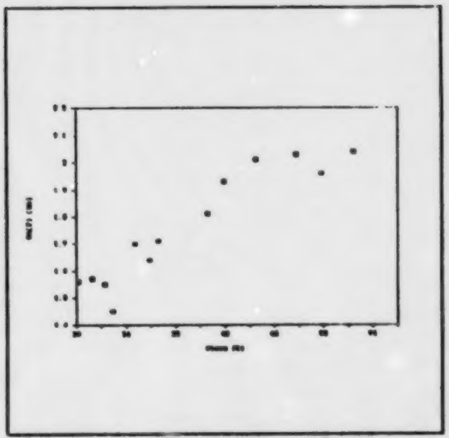

Figure 4: Ra, versus Gloss

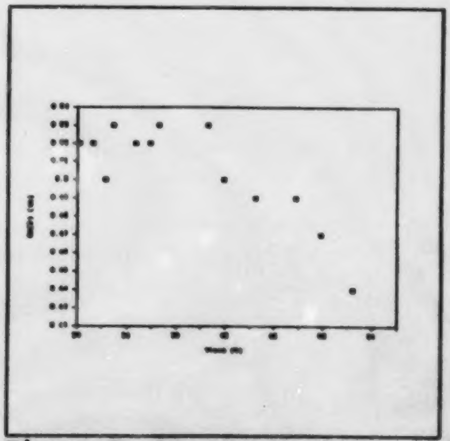

Figure 5: Ra, versus Gloss, 32 μm sampling length

NUMERICAL SIMULATION OF LIQUID SLOSHING IN A BAFFLED RECTANGULAR TANK

G. Popov
Research Associate

S. Sankar
Professor

T.S. Sankar
Professor

CONCAVE Research Centre,
Dept. of Mechanical Engineering
Concordia University
Montreal, Canada

INTRODUCTION

The transportation of liquid cargos is characterized by the movement of loads relative to the vehicle and by more frequent road accidents comparing with solid cargos. The common method to reduce the sloshing effect is the use of separating walls both solid or containing some orifices, the latter is often called baffles. The modern design of road tankers widely uses the separating walls, however, there is no general theory, or at least a unique approach, predicting their effect neither in dynamics nor in statics. The design concepts are rather based on the tank walls strength analysis then on sloshing characteristics of liquids.

A number of investigations in this area deals mostly with a coupling effect of liquid-elastic walls interaction [1,2] while the influence of the number of walls and their locations is presented only in a few works, for example in [3] and [4]. In the last reference, Strandberg investigated the dependence of dynamic liquid forces on the number and type of partitions in an elliptical cross-section tank using a hybrid methodology. The simplified vehicle model was simulated by an analogue computer while the liquid forces were determined experimentally and recorded. Then, the recorded data was used as input to the vehicle model in order to couple the vehicle-liquid system. Although this methodology loses the feedback between the two coupled elements, it, however, gives a sufficiently good understanding of the complicated coupling sloshing phenomena. Another drawback of this study is that it requires as many experimental trials as the number of cases is studied.

The purpose of this investigation is to create a sufficiently accurate mathematical model of the sloshing and to study the effects of the separating walls basing on the numerical solution. The steady-state solution for compartmented tanks is carried out analytically and it is found for the liquid heights, forces and moments of forces in terms of the basic non-dimensional parameters: relative height of the tank, *h*, filling of the tank, *f*, lateral acceleration, G_x, and number of compartment, *n*. The transient solution is studied for two types of a vehicle manoeuvres: braking and cornering basing on the rectangular cross-section of a tank both in longitudinal and transversal direction. The liquid sloshing is modeled by the Navier-Stokes equations together with the free-surface equation and the boundary conditions along the walls and the free surface. The 2-D governing equations are discretized in an Eulerian mesh and solved by modified Marker-and-Cell technique. A special attention is given to the boundary conditions imposition, the subject is discussed on the corresponding section below.

STEADY-STATE SOLUTION. COMPARTMENT TANK

The assumptions made for the steady-state response include the following: the separating walls are distributed evenly, the initial filling is the same in each compartment, all walls are rigid, and unit body force, due to the input acceleration, is constant and uniform. The set of the non-dimensional parameters characterizing the problem is given by the four quantities:

n: number of compartments, integer; (n-1) is the number of separating walls

$h = \frac{H_0}{L_0}$: geometrical parameter, H_0 is the tank height, and L_0 is the length or the width of the tank.

$f = \frac{H_{in}}{L_0}$: filling parameter, H_{in} is the initial fill level

$G_x = \frac{a}{g}$: unit body force, a is the lateral acceleration and g is the gravity acceleration

The schematic of a compartmented tank is given in Fig. 1.

The free surface of the liquid can take different positions, depending on the combination of the four parameters, defined here as configurations, which are

Configuration 1, when the free surface intersects two side walls of the compartment
Configuration 2, when the intersection happens at the upper and one of the side walls
Configuration 3, when the liquid intersects the bottom and one of the side walls
Configuration 4, when the upper and bottom walls are crossed by the free surface

The existence of either of those configurations is defined by the following general conditions:

$$\text{Conf.1}\quad \begin{cases} G_x \geq 0 \begin{cases} Y(X_{K-1}) & \geq 0 \\ Y(X_K) & \leq h \end{cases} \\ G_x \leq 0 \begin{cases} Y(X_{k-1}) & \leq h \\ Y(X_K) & \geq 0 \end{cases} \end{cases}$$

$$\text{Conf.2}\quad \begin{cases} G_x \geq 0 \begin{cases} Y(X_{K-1}) & \geq 0 \\ Y(X_K) & \geq h \end{cases} \\ G_x \leq 0 \begin{cases} Y(X_{k-1}) & \geq h \\ Y(X_K) & \geq 0 \end{cases} \end{cases}$$

$$\text{Conf.3}\quad \begin{cases} G_x \geq 0 \begin{cases} Y(X_{K-1}) & \leq 0 \\ Y(X_K) & \leq h \end{cases} \\ G_x \leq 0 \begin{cases} Y(X_{k-1}) & \leq h \\ Y(X_K) & \leq 0 \end{cases} \end{cases}$$

$$\text{Conf.4}\quad \begin{cases} G_x \geq 0 \begin{cases} Y(X_{K-1}) & \leq 0 \\ Y(X_K) & \geq h \end{cases} \\ G_x \leq 0 \begin{cases} Y(X_{k-1}) & \geq h \\ Y(X_K) & \leq 0 \end{cases} \end{cases}$$

where K is the number of compartment counting from left to right in Fig. 1.

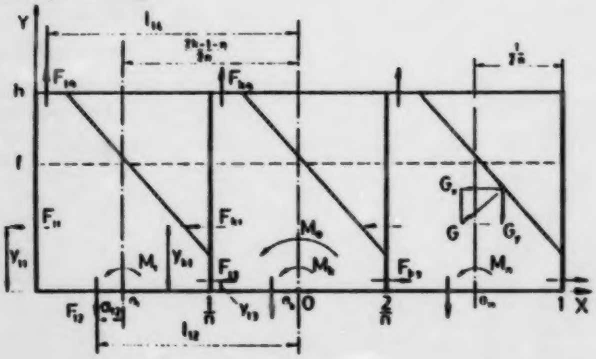

Fig. 1 Schematic of compartmented tank

The free-surface equations are found separately for each configuration by integrating the differential equation of isobars

$$G_x\,dX + G_y\,dy = 0 \qquad \text{with } G_y = -1,$$

by using the condition at the free surface

$$Y(X_K) - Y(X_{K-1}) = \frac{G_x}{n},$$

by maintaining the mass conservation, and by taking into account that the spacing of each compartment from the centre of the tank is

$$\frac{2K - n - 1}{2n}$$

The resulting expressions for the free surface and the conditions of their existence are summarized in the Table 1.

Table 1. Free surface equations

Conf.	Free-Surface equations	Conditions
1	For $G_x \gtrless 0$ $Y = G_x X + f - \frac{2k-1}{2n} G_x$	$f - \frac{G_x}{2n} \geq 0$ $f + \frac{G_x}{2n} \leq h$
2	$Y = G_x X + h - \frac{K-1}{n} G_x - A;\ G_x > 0$ $Y = G_x X + h - \frac{K}{n} G_x - A;\ G_x < 0$ where $A = \sqrt{\frac{2(h-f)\lvert G_x \rvert}{n}}$	$h - A \geq 0$ $\frac{\lvert G_x \rvert}{n} - A \geq 0$
3	$Y = G_x X - \frac{K}{n} G_x + B;\ G_x > 0$ $Y = G_x X - \frac{K-1}{2} G_x + B;\ G_x < 0$ where $B = \sqrt{\frac{2f\,\lvert G_x \rvert}{n}}$	$B - \frac{\lvert G_x \rvert}{n} \leq 0$ $B - h \leq 0$
4	$Y = G_x X + \frac{h}{2} - (\frac{K}{n} - \frac{f}{nh}) G_x;$ $G_x > 0$ $Y = G_x X + \frac{h}{2} - (\frac{K-1}{n} + \frac{f}{nh}) G_x;$ $G_x < 0$	$\frac{h}{2} - \frac{\lvert G_x \rvert}{2} (1 - \frac{f}{h}) \leq 0$ $\frac{f \lvert G_x \rvert}{nh} - \frac{h}{2} \geq 0$

The total horizontal force at steady-state is equal to the algebraic sum of the forces exerted on vertical walls and it must be equal to the force of inertia of the liquid and the total vertical force is equal to the liquid weight, that in the non-dimensional form may be expressed as

$$F_{HSS} = G_X \,, \qquad F_{VSS} = G_y = -1$$

for the unit width of the tank and the both values are the ratios of their dimensional values to the liquid weight. Thus, the separating walls have no influence on the magnitudes of forces at the steady-state, but they obviously affect the overturning moments, since the arms of forces depend on n. The overturning moment, M_{ss}^{c}, taken around the middle bottom point is computed as the sum of moments of all forces for each configuration separately. Their expressions are given in the Table 2 together with those of forces and their arms.

The behaviour of the moment with variation of number of compartments and the level of acceleration for fixed values of h and f is illustrated in Fig. 2 and 3 for two different geometries of the tank and for the same filling of 60% with respect to the h. In particular, Fig. 2 is referred to a long tank (13.5 m x 2 m) and Fig. 3 to a short one (2.56 m x 1.83 m). It can be seen that the magnitudes of M_{ss}^{c} rapidly drop from those of uncompartmented tanks and tend asymptotically to $fG_x/2$. The reducing effect of separating walls is significantly stronger for long tanks. This effect is even better illustrated in Fig.

Table 2. Overturning moments and forces

Conf.	Moments, Forces, and Forces Arms
1	$M^c_{SS} = \frac{G_x}{2}\left(f + \frac{G_x^2}{12\,n^2 f} + \frac{1}{6\,n^2 f}\right)$ $F_H = G_x \,.\, Y_H = \frac{f}{2} + \frac{G_x^2}{24\,n^2 f}$ $F_V = -1 \,.\, E_V = \frac{G_x}{12\,n^2 f}$
2	$M^C_{SS} = G_x \frac{h-f}{f}\left[-h + \frac{1}{2\,n\,G_x} + \frac{h^2}{2(h-f)} - \frac{A}{3}\left(\frac{1}{G_x^2} - 1\right)\right]$ $F_H = G_x \,.\, Y_H = \frac{h-f}{f}\left[-h + \frac{h^2}{2(h-f)} + \frac{A}{3}\right]$ $F_V = -1 \,.\, E_V = G_x \frac{h-f}{f}\left(\frac{1}{2n\lvert G_x\rvert} - \frac{A}{3\,G_x^2}\right)$
3	$M^C_{SS} = G_x\left[\frac{1}{2nG_x} - \frac{B}{3}\left(\frac{1}{G_x^2} - 1\right)\right]$ $F_H = G_x \,.\, Y_H = \frac{B}{3}$ $F_V = -1 \,.\, E_V = G_x\left(\frac{1}{2n\lvert G_x\rvert} - \frac{B}{3G_x^2}\right)$
4	$M^C_{SS} = G_x\left[\frac{1}{2n\lvert G_x\rvert} + \frac{h}{2} - \frac{f}{2nh\lvert G_x\rvert} - \frac{nh^3}{12f\lvert G_x\rvert} - \frac{nh^3}{24f\lvert G_x\rvert^3}\right]$ $F_H = G_x \,.\, Y_H = G_x\left(\frac{h}{2\lvert G_x\rvert} - \frac{n\,h^3}{12fG_x^2}\right)$ $F_V = -1 \,.\, E_V = G_x\left(\frac{h-f}{2nh\lvert G_x\rvert} - \frac{nh^3}{24f\lvert G_x\rvert^3}\right)$

4 through Fig. 8, where the ratios of the moments of the uncompartmented tank to those of the compartmented ones are plotted against f, or G_x, or h. The ratios M_{SS} / M^c_{SS} for a long tank are given in Fig. 4, from where one can read that four separating walls, n=5, can reduce the moment by 12 times for sufficiently small value of G_x, however this effect decreases with increasing of G_x. The dotted lines in Fig. 4 define the region of configurations. The similar plot for a short tank, h = 0.713, Fig. 5, displays the smaller influence of partitions. Thus, for the same n = 5 the gain in the moment reduction is slightly above 2 times. The Figures 6 and 7 show the same reduction factor as a function of the f for two tank geometries. The functions have strongly pronounced maxima occurring at some optimal values of the f which decrease with increasing of the n. The reduction factor also depends on the geometric parameter h, Fig. 8. It can be seen that the effectiveness of separating walls is significantly greater for long tanks, besides, for very long tanks it decreases again. For short tanks, h=0.6 ÷ 0.8, the reduction is still essential; for example, for h=0.7 one separating wall reduces the moment by 1.6 times for G_x = 0.3 and f = 0.6 h. Relating to the lateral stability of a tanker, the 1.6 times reduction is considerable.

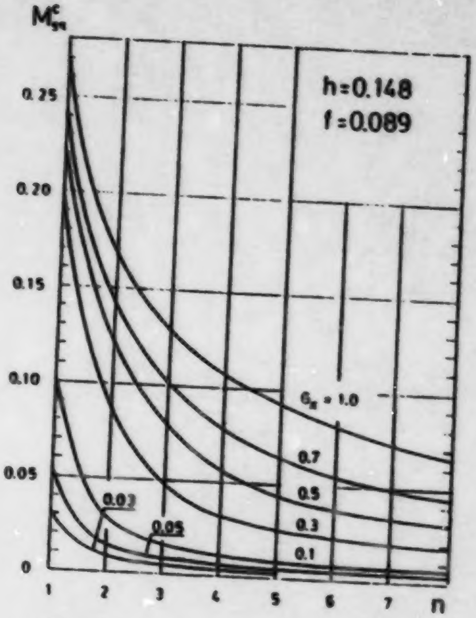

Fig. 2 Static overturning moment for a long tank as function of compartments number

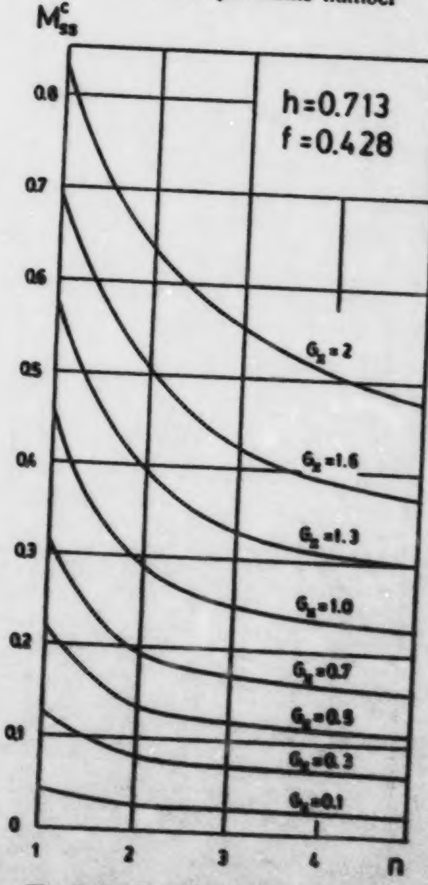

Fig. 3 Static overturning moment for a short tank as function of compartments number

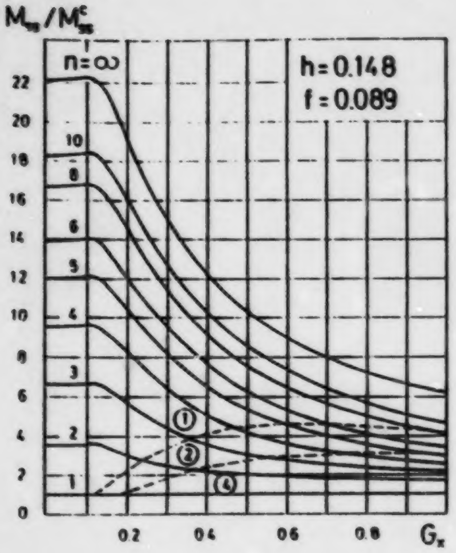

Fig. 4 Moment reduction factor for a long tank as function of acceleration level

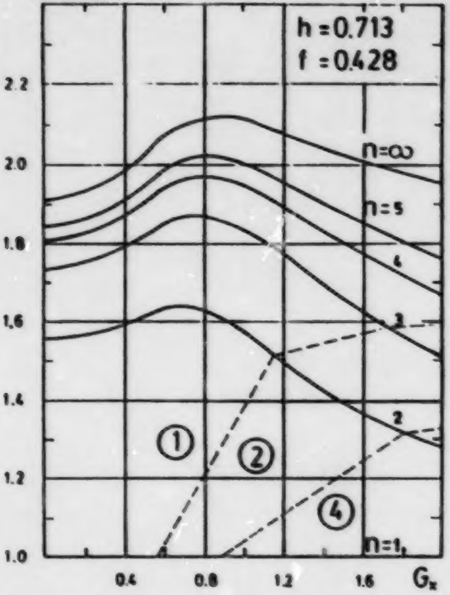

Fig. 5 Moment reduction factor for a short tank as function of acceleration level

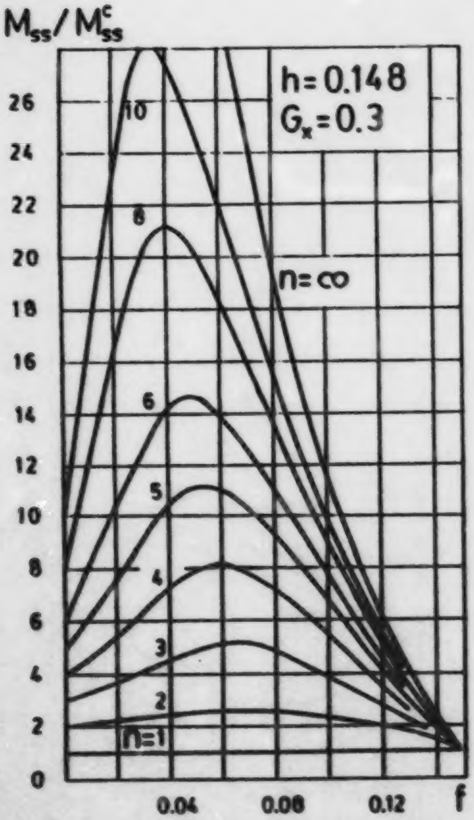

Fig. 6 Influence of fill level on moment reduction factor for a long tank

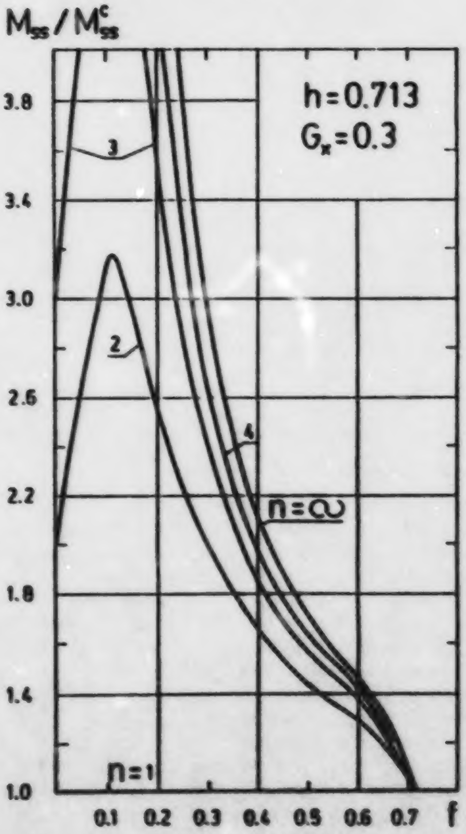

Fig. 7 Influence of fill level on moment reduction factor for a short tank

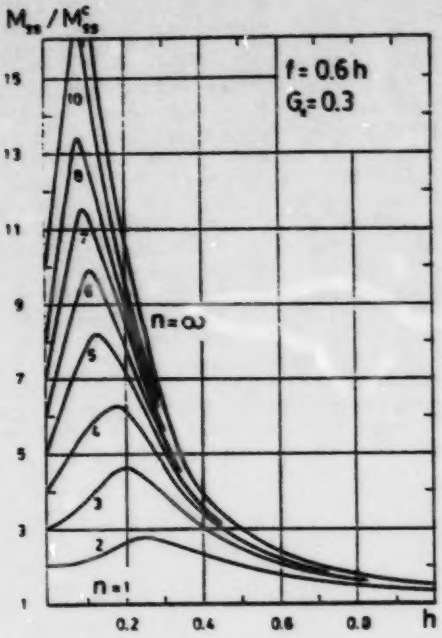

Fig. 8 Influence of tank geometry parameter on moment reduction factor

TRANSIENT SOLUTION

The transient response of the liquid is found by the numerical solution of the Navier-Stokes equations, free-surface equation, and the associated boundary conditions. The governing equations are discretized by finite differences in an Eulerain mesh [5]. The inhouse modified Marker-and-Cell technique with a special treatment of boundary conditions along the rigid walls, solid partitions or baffles, and along the free surface was developed for this particular case. The details of the computational procedure are described in reference [5], except those that are related to the baffles. For the latter, the 3-D array for the velocities and pressures and the 2-D array for liquid heights were used in order to avoid a confusion between the boundary and working values of the flow parameters. Thus, the horizontal velocity array is expressed in the code as U(k,i,j), where k referred to a compartment and i and j to the number of the cell in horizontal and vertical directions. If however, the free surface passes through the baffle orifice, then the boundary values are defined as for a continuous flow.

The numerical model of sloshing was validated experimentally. For this purpose, a special experimental set-up was created. The small scale plexiglass tank, 800 mm x 580 mm, mounted on the Thompson table with low friction bearings, was horizontally actuated by an electro-hydraulic shaker. The displacement and acceleration of the tank were recorded as well as the force between the tank and the shaker. The free surface of the liquid, water in the case, was also recorded with a video-camera. The real motion of the liquid, seen as the free surface displacement, was compared with a computed one for some arbitrary input disturbance. The best correlation was found for the coefficients of upstream differencing equal to 1, for both the momentum and the free-surface equations, and for the reflection type boundary conditions. Those quantities were kept throughout the computations.

The study of liquid sloshing includes compartmented tanks, plain and with full partitions, and baffled tanks, with different size of the baffle orifice and different number of baffles; all this for a constant value of input acceleration G_x = 0.3. The separating walls in compartmented tanks are evenly distributed and therefore the liquid vibrations in different compartments are identical. In baffled tanks, because of the liquid flow from one section to another, the vibrations are not the same. The size of the baffle orifice was varied from 5 to 20% of its area with respect to the area of the cross-section. It has been found that even small orifice has a significant effect on the character of liquid motion. A small opening between two sections, of the order of 5%, decreases the magnitude of the overturning moment at the first overshoot comparing with the plane tank by the amount of 27%, and increases the same value comparing with the 2-compartmented tank by 6%. The following overshoots increase slowly with time and reach the steady value at 6th cycle, after which the interflowing of the liquid is practically ceases. The further increase in the orifice area has a very small additional effect with the same trend. Thus, for areas of 10 and 20% the stabilizing of the moment magnitude happens at the 5th cycle. The magnitude of the horizontal force is not as sensitive to the area variation as the moment is, and its behaviour in the baffled tank is much closer to that of the associated compartmented tank.

The comparison of the horizontal forces F_H, and moments, M, for plane, compartmented, and baffles tanks is given in Fig. 9, where n is the number of sections that corresponds to (n-1) separating walls or baffles. It can be seen that baffles give a small loss in force comparing with full partition, and this loss tends to decrease with increasing of the number of compartment. After n > 4 the peak values of the forces are practically identical. The difference in moments for the two cases is significant. The shaded area shows the maximum peak values of the moment and the minimum peak values that correspond to the first overshoot. The band becomes more narrow with increasing of n and asymptotically tends to the line of a compartmented tank. This indicates that a large number of baffles has such a strong damping that orifices have no longer their negative effect and the entire flow behaves like full partition are installed instead of baffles.

The natural damped frequencies diagram in given in Fig. 10, where the upper lines show the natural frequencies resulting from the linearized theory and the columns represent the damped frequencies. In compartmented tanks frequencies increase with refining of the tank by separating walls. In baffled tanks the trend is rather inverse: frequencies decrease with increasing of the number of baffles. This is due to the coupling between the baffled compartments and to the damping effect of the baffles, the greater is the number of baffles, the slow are the liquid oscillations.

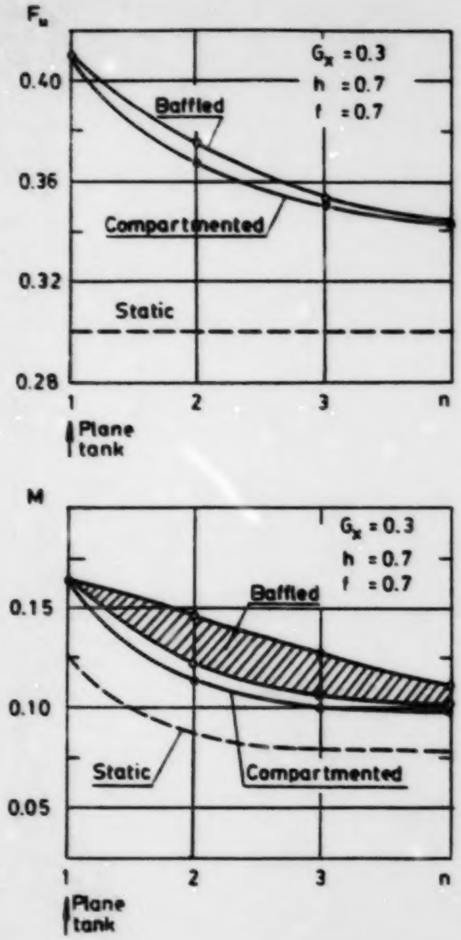

Fig. 9 Dynamic horizontal force and moment for compartmented and baffled short tank

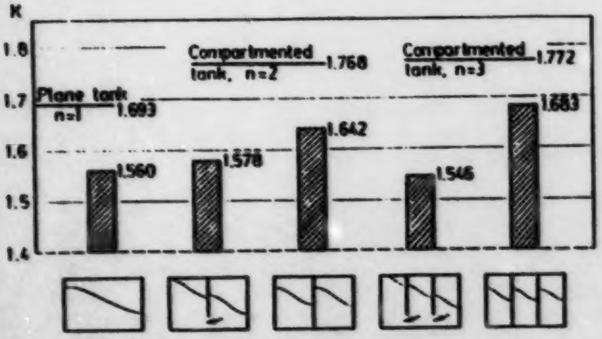

Fig. 10 Damped natural frequencies for compartmented and baffled short tanks

SUMMARY

The present study aimed to investigate the role of the separating walls and baffles in reducing of the sloshing forces and moment in road containers during the cornering or braking manoeuvres. The effect of full partitions is tremendous, while that of the baffles is somewhat less because of the coupling between the compartments. Thus, the requirement to keep baffles orifices closed during the transportation is important since it can reduce the overturning moment up to 30% for a tank with one baffle. Moreover, if the number of baffles is greater than the gain is smaller.

The methodology used in this investigation allows to significantly enlarge the fields of study in the sense of the ranges of input parameters comparing with the linearized theory of sloshing. In many cases it can give the only solution to the sloshing problem when the linearized theory does not work, i.e. in the cases of very small or very high fill levels and for high values of the input acceleration.

REFERENCES

1. Miles, J.W., "On the sloshing of liquid in a flexible tank", J. of Applied Mech., 25, 1958, p. 277.
2. Bauer, H.F., "Dynamic behaviour of an elastic separating wall in vehicle container", Part 1, Int. J. of Vehicle Design, Vol. 2, no. 1, 1981, p. 44.
3. Partom, I.S., "Numerical calculation of equivalent moment of inertia for a fluid in a cylindrical container with partitions", Int. J. for Numerical Methods in Fluid, Vol., 5, 1985, p. 25.
4. Strandberg, L., "Lateral stability of road tanker", Nat. Road and Traffic Res. Institute, Sweden, Report no. 138 A, 1978.
5. Popov, G., Vatistas, G.H., Sankar, S., and Sankar T.S., "Liquid sloshing in arbitrary shape containers", Proc. of CANCAM 89, Carleton University, Ottawa, Canada, 1989, Vol. 2, p. 590.

GAS FLOW IN A VERTICAL CHEMICAL VAPOUR DEPOSITION (CVD) REACTOR

W. Montasser

Alcan International Limited
Kingston Research and Development Centre
P.O. Box 8400, Kingston, Ontario, Canada, K7L 5L9

The use of thin films in solid state device is pervasive. As the name Chemical Vapour Deposition (CVD) indicates, this process uses chemically reacting vapours to deposit a film. A CVD system is simply a chemical reactor. As such, flow rates and flow patterns of reactant vapours, along with substrate temperature, must be carefully controlled if uniform film layers are to be obtained. In turn, prediction of deposition rates and uniformity requires detailed understanding of fluid flow phenomena.

A steady, laminar, axisymmetric gas flow in a vertical-type reactor was modelled using Version 1.3 of the Phoenics Code. The effects of gas flow rate, reactor operating pressure and temperature of the substrate on the flow pattern were examined.

Results were obtained for the velocity and temperature fields. Flow circulation resulting from entrance, reactor geometry and natural convection has been shown to exist at some operating conditions. The obtained flow patterns show areas on the substrate where film layer uniformity is realizable.

Nomenclature

C_p	specific heat
g	gravitational acceleration
P	pressure
P_o	reactor operating pressure
Q	gas flow rate
R	gas constant
T	temperature
T_s	susceptor temperature
T_w	reactor wall temperature
V	velocity
ρ	density
μ	dynamic viscosity

INTRODUCTION

Chemical vapour deposition (CVD) is an important technology in electronic materials processing. A good overview of the technology is given in reference [1]. In the CVD reactor a mixture of gases flows over the hot wafer surface. The gas mixture is made of a carrier gas, usually hydrogen and small fractions of different reactant gases. The type of reactant gases used depends on the kind of layer to be deposited. In the present work, only flow of hydrogen gas will be considered. Susceptors in CVD reactors are usually made of graphite, into which wafers are recessed. The walls of the reactors are often water cooled and susceptors are heated to about 600-700°C. The heated susceptors in some reactors rotate at high speeds of about 1500-2000 rpm, such as rotating disk reactors. In these reactors the rotation provides driving force for the gases to flow radially outward over the disk, where wafers are placed. Flow modelling of such arrangements are demonstrated by Evans [2] and Makarov [3]. In another type of vertical CVD reactor gases flow over stationary or low speed (<3 rpm) rotation susceptors. The model here deals with the latter kind of reactor where susceptors are stationary.

The object of the present work is to examine the effect of changing reactor operating conditions, such as reactor inlet flow rate, reactor operating pressure and susceptor temperature, on the flow uniformity over the susceptor surface. This work is a continuation of the previous model development and experimental work which was reported in references [4] and [5] respectively.

ANALYSIS

The problem considered in the present work is modelling of hydrogen gas flow in a vertical, commercial type CVD reactor, the schematic view of which is shown in Fig. 1. The reactor height is about 25 cm, and the diameter is about 10 cm at the bottom and 1.5 cm at the flow inlet near the top of the reactor. The gas flow exits from an annular gap of about 3.5 mm. The model solves the continuity, momentum and energy equations. Also the equation of state for ideal gas is solved simultaneously with the previous equations to calculate density as a function of pressure and temperature. The governing equations were solved using the Phoenics code, details of which are given in reference [6]. Only laminar axisymmetric flow conditions were examined in the present study. The conditions considered are flow rate of 5, 10 and 15 SLPM, susceptor temperature of 300 K-900 K and reactor operating pressure of 1.0 atm, 0.6 atm and 0.3 atm. Temperatures of reactor wall and inlet gas were assumed to be constant at 300 K. A no slip velocity boundary condition was adopted throughout the study. The inlet gas velocity and reactor exit pressure were also specified for each case. The governing equations are given below:

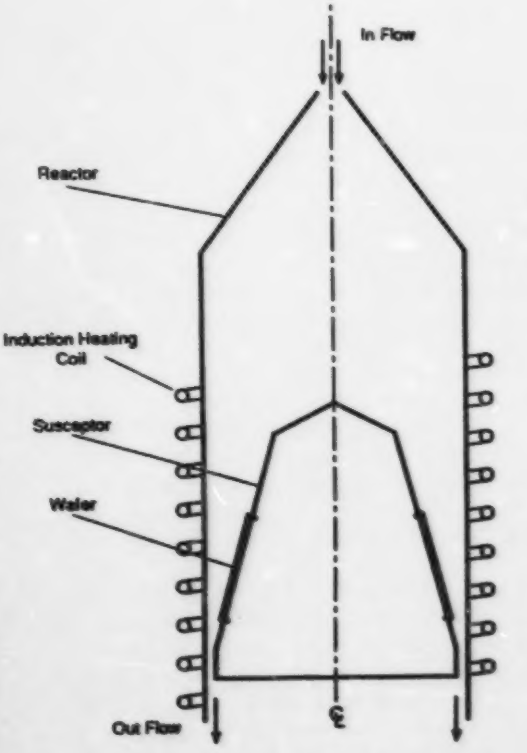

Fig. 1: Schematic View of the CVD Reactor

Governing Equations

Continuity equation:

$$\nabla \rho \bar{V} = 0 \qquad (1)$$

Momentum equation:

$$\rho \bar{V} \nabla \bar{V} = -\nabla P + \nabla(\mu \nabla \cdot \bar{V}) + g\rho i_z \qquad (2)$$

Energy equation:

$$\rho C_p \bar{V} \nabla T = \nabla \cdot (k \nabla T) \qquad (3)$$

Ideal gas equation of state:

$$\rho = \frac{P}{RT} \qquad (4)$$

RESULTS AND DISCUSSION

As mentioned before, the Phoenics code was used to solve the governing equations given in the previous section. The influences of flow rate, susceptor temperature and operating pressure on the flow field were examined for a wide range of reactor operating conditions. Temperature and velocity results for these flow fields are discussed here. The results are presented as plots of temperature contours and velocity vectors.

Effect of Susceptor Temperature, T_s:

As the susceptor temperature, T_s , increases, the temperature difference T_s-T_w increases which in turn increases the driving force for buoyant convection in the reactor. Velocity and temperature results for flow fields at Q = 5 SLPM, P_e = 1.0 atm and T_s = 300, 500, 700 and 900 K are shown in Fig. 2. At T_s = 300 K, i.e, at T_s - T_w = 0.0 a counter-clockwise circulation cell over the susceptor is shown to exist because of the reactor geometry. As T_s increases from 300 K a buoyancy-driven, clockwise vortex develops above the susceptor. This vortex grows as T_s increases, and pushes against the geometrically generated vortex. The upward motion of the hot gas at the center of the reactor forces the inlet cold gas to move outward and then down along the reactor wall. Another interesting observation is that at the surface of the susceptor, there exists a stagnation region separating the upward and downward flows. Presence of such a stagnant region will adversely affect uniformity of deposition.

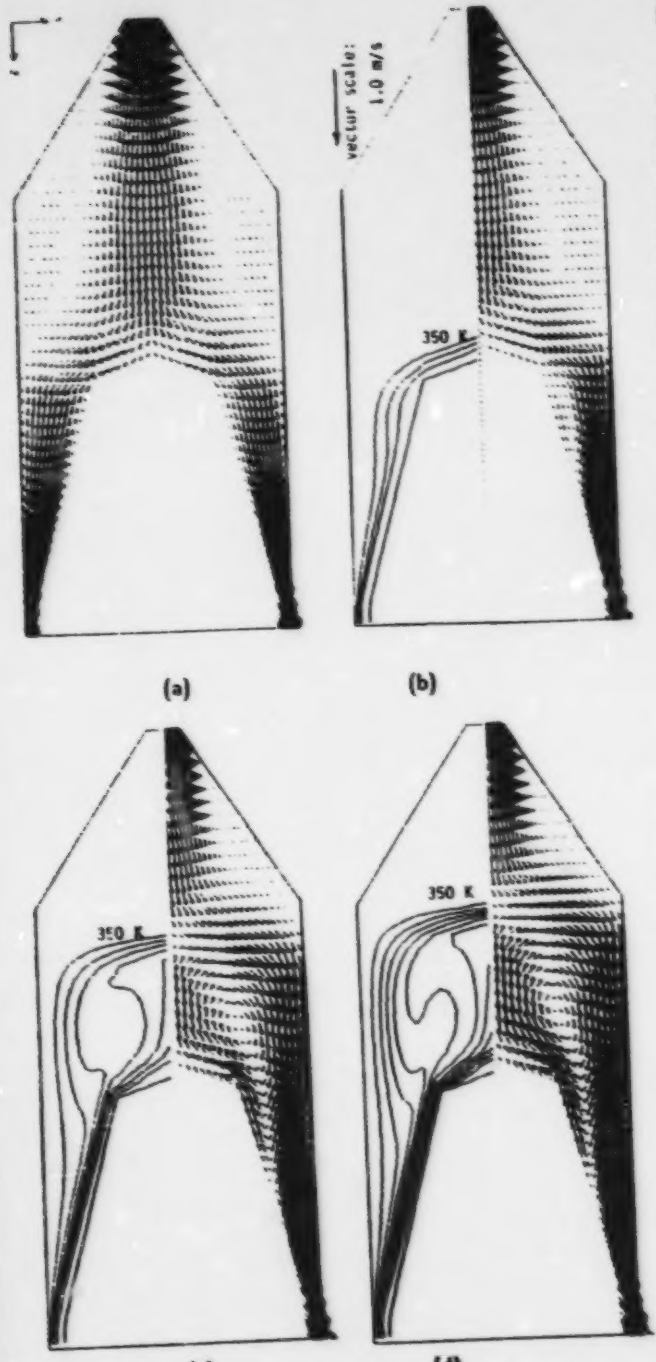

(a) (b)

(c) (d)

Fig. 2: Temperature Contours and Velocity Vectors for Flow Fields at Flow Rate, Q, of 5 SLPM and Reactor Pressure, P_e, of 1 atm at Susceptor Temperatures, T_s, of: (a) 300 K; (b) 500 K; (c) 700 K; (d) 900 K.

Effect of Reactor Operating Pressure, P_e:

The reactor operating pressure, P_e, has a large effect on the flow pattern as it determines the intensity of buoyancy force by decreasing the density differences caused by temperature variations. The effect is evident in Figs. 2(a) and 3, where velocity and temperature fields are shown for H_2 flow rate of 5 SLPM, T_s of 900 K and reactor operating pressure of 1.0, 0.6, 0.3 atm respectively. At $P_e = 1.0$ atm the buoyancy dominates the flow motion where a clockwise rotating vortex convects heat away from the susceptor. This vortex occupies more than two-thirds of the space above the susceptor. As the operating pressure is reduced to 0.6 atm the size of the buoyancy driven recirculating cell is reduced significantly. At a lower pressure of $P_e = 0.3$ atm the forced convection dominates the flow. The reduced pressure limits the buoyant driving force and suppresses the buoyant convection motion even though a large temperature difference of 600 K exists in the reactor.

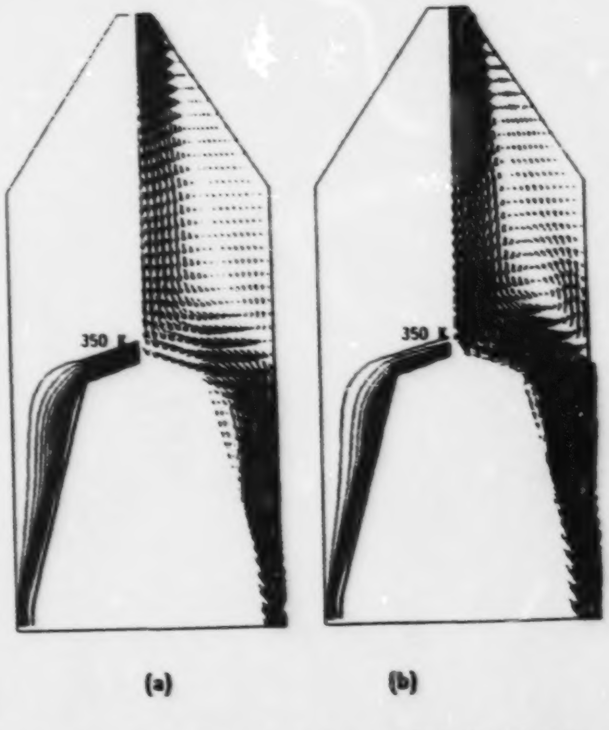

(a) (b)

Fig. 3: Temperature Contours and Velocity Vectors for Flow Fields at Flow Rate, Q, of 5 SLPM and Susceptor Temperature, T_s, of 900 K at Reactor Pressure, P_e, of: (a) 0.6 atm; (b) 0.3 atm.

Effect of Gas Flow Rate, Q:

The flow patterns at a reactor pressure of 1.0 atm and a susceptor temperature of 900 K for flow rates of 5, 10 and 15 SLPM are shown in Fig. 4. It is clear that as the gas flow rate increases, the size of the buoyancy circulation cell decreases. This is due to the fact that the inertia force increases relative to the buoyancy force and hence weakening the buoyancy driven convection flow. The weakening of the buoyancy driven convection results in confining of the hot gas to an area close to the susceptor. This enhances the reactor performance since the reactant gases now decompose near the wafer surface. As the size of the circulation cell decreases, the gas residence time decreases leading to certain benefits such as abruptness of interfaces between layers of different composition. These layers are produced by changing the composition of the reactant gases during the operation of the reactor. It is also obvious that the deposition rate would change as the flow rate increases. However, in the present study such an effect has not been studied since that would require the incorporation of mass balance equation for the various reactants.

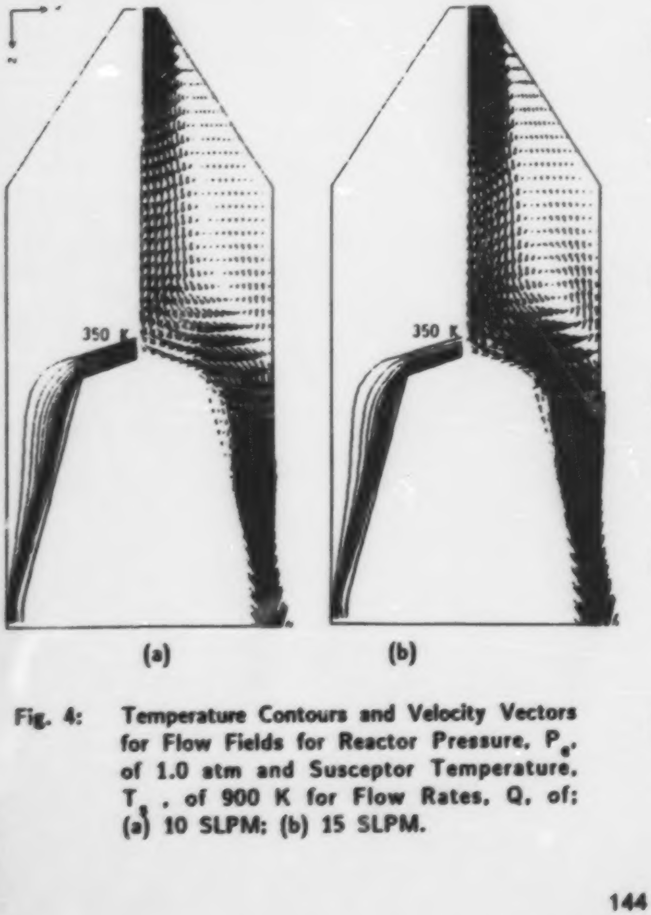

(a) (b)

Fig. 4: Temperature Contours and Velocity Vectors for Flow Fields for Reactor Pressure, P_e, of 1.0 atm and Susceptor Temperature, T_s, of 900 K for Flow Rates, Q, of: (a) 10 SLPM; (b) 15 SLPM.

CONCLUSIONS

The gas flow patterns in a vertical CVD reactor are modeled by numerical solution of the Navier-Stokes equations, continuity equation and the energy equation. The buoyancy-driven recirculations as well as other secondary flows caused by reactor geometry which are detrimental to uniformity of deposition and interface abruptness were shown to exist mainly when operating the reactor at a pressure of 1.0 atm and a flow rate of 5 SLPM. The buoyancy-driven recirculations cause the upward motion of the hot reactant gases away from the susceptor, leading to an increase in the amount deposited on the reactor wall, hence lowering the reactor efficiency. It also leads to an increase in the residence time of reactant gases which in turn adversely affects the interface abruptness. These flows can be eliminated by appropriate choice of reactor operating conditions such as gas flow rate and reactor pressure. Also, at any operating condition, the location of wafers on the susceptor should be carefully determined to avoid flow stagnation regions.

REFERENCES

[1] Amundson, N.R. and Luss, D., Reviews in Chemical Engineering, Vol. 3 No. 2, pp. 97-186, 1985.

[2] Evans, G. and Greif, R., Effects of Boundary Conditions on the Flow and Heat Transfer in a Rotating Disk CVD Reactor, Numerical Heat Transfer, Vol. 12, pp. 243-252, 1987.

[3] Makarov, Yu.N and Zhmakin, A.I., On the Flow Regimes in VPE Reactors, J. Crystal Growth 94, pp. 537-550, 1989.

[4] Montasser, W., Modelling of Gas Flow in a Vertical Chemical Vapour Deposition (CVD) Reactor, Proc. 3rd Int. Phoenics User Conference, Dubrovnik, pp. 442-465, August, 1989.

[5] Raghavan, N.S., Montasser, W., Timsit, R.S., Adams, R.L. and Fjarlie, E.J., Gas Flow in a Vertical MOCVD Reactor, 16th Int. Sym. on Gallium Arsenide and Related Compounds, Karuizawa, Japan, Paper 203, September, 1989.

[6] Rosten, H.J. and Spalding, The Phoenics Reference Manual, CHAM TR/200, Document Revision 06, October 1987.

FIELD PANEL METHOD FOR TRANSONIC FLOWS WITH BODY FITTED GRIDS

Z. Fang and I. Paraschivoiu

Department of Mechanical Engineering
Ecole Polytechnique de Montreal
Montreal, Quebec, Canada

ABSTRACT

A field panel method based on Green function theory has been developed to solve the full potential equation for subsonic and transonic flows. In this field panel method, potential values in the flow region are determined by potential values represented by boundary integrals and a volume integral. The boundary potential values are obtained by implementing the boundary integrals along boundary segments where a linear potential relation is assumed. The volume integral is evaluated in a grid generated by finite element discretization. The volume integral is evaluated only outside the body. Therefore, there is no extra boundary treatment required for evaluation of the volume integral. The source term is assumed to be constant in a finite integral volume. The volume integral needs to be evaluated only once and can be stored in computer memory for further usage.

INTRODUCTION

The field panel method for solving partial differential equations is a very useful tool in computational fluid dynamics. This method provides an alternative approach to finite difference and finite element methods for solving transonic potential flows. One of the advantages with field panel method is that it can be easily applied to solve flow problems with complex configurations. A major technical obstacle involved with other methods seems to be the difficulty in generating suitable grids for flows with complex configurations.[1] In field panel method, computational grids include two part: boundary grids and field grids. Boundary grids are used for implementation of the boundary integrals while field grids are used for evaluation of certain volume integrals instead of the conventional purpose of replacing partial differential equations. Therefore, many kinds of grids can be adopted for field grids required by field panel method.

Another advantage of the field panel method is that solutions can be obtained by using only surface panels and solutions everywhere else can be represented by solutions on surface panels. For nonlinear equations only a system equations for surface points are solved in iterative solution procedures. Generally, grid points on surfaces are much less than those in the field. Thus, the field panel method could take less computer CPU time.

Computational schemes based on integral formulation have been developed for linear Prandtl-Glauert equation[2-3]. More recently, full potential equation has been solved using integral method.[4-12] Applying field panel method to solve unsteady potential equation has been studied.[13-14] The full potential equation has also been solved using field panel method for flow over multi-element airfoils[15] and over the entire aircraft.[16-17] For transonic flows, some method combines the field panel method with finite volume method[5] and some other methods use the field panel method coupled with finite difference method.[7] It is not clear that how they treat the shock integrals resulting from the Green function transformation.

In this work, the field panel method is applied to solve the full potential equation for compressible flows. The boundary linear potential integral method is applied in this work[18]. The coefficient matrix is formulated on body grid points only. The nonlinear full potential equation is solved by Newton-Raphson iteration procedure. In each iteration the influence matrix does not change and is decomposed only once. Only the source term in the volume integral needs to be evaluated in each iteration. After potential values on the body have been solved, potential values anywhere else can be calculated. For transonic flows, shock integrals are calculated and contributions are added to the right hand side of the discretized simultaneous equations. Our results show that shock integrals are necessary for catching sharp shock jumps.

In this work, two dimensional flows over NACA0012 airfoil are calculated. Numerical results are compared with experimental data[19]. Good agreement between numerical results and experimental data shows that the boundary linear potential integral method provides an alternative tool for analytical and design purposes in aeronautical engineering.

GOVERNING EQUATION AND BOUNDARY CONDITIONS

In the Cartesian coordinates, the conservative form of the full potential equation is

$$\nabla\cdot(\rho\nabla\Phi) = 0 \qquad (1)$$

where Φ is the full potential, ρ is the density, and ∇ is defined by

$$\nabla = \frac{\partial}{\partial x}\,\hat{i} + \frac{\partial}{\partial y}\,\hat{j} + \frac{\partial}{\partial z}\,\hat{k}. \tag{2}$$

The full potential equation given by Eq. (1) is not well suitable for integral representation because the left hand side of Eq. (1) is not a Laplacian operator. However, the full potential equation can be written in another form

$$\nabla^2 \Phi = \sigma \tag{3}$$

where

$$\sigma = M^2 \Phi_{ss}, \tag{4}$$

M is the Mach number, Φ_{ss} is the rate of velocity change along the stream line direction and σ is called the source term.

Boundary condition of Eq. (1) at the infinity is given by

$$\Phi_\infty = V_\infty \,(x \cos\alpha + y \sin\alpha). \tag{5}$$

The surface boundary conditions for inviscid flows are tangential flow conditions given by

$$\mathbf{n} \cdot \nabla \Phi = 0 \tag{6}$$

where **n** is the normal direction of the body surface. Kutta condition is also implemented, which requires that the flow leaves the trailing edge smoothly.

The Poisson equation can be solved iteratively. Solutions are assumed to be obtained when the iterative procedure converges.

INTEGRAL FORMULATION

Using Green's theorem, solution Φ can be represented by the sum of boundary integrals and a volume integral

$$\Phi(x_p, y_p) = \oint \left[(\mathrm{n}\cdot\nabla\Phi)\Phi_L - \Phi(\mathrm{n}\cdot\nabla\Phi_L) \right] \mathrm{ds} + \int_V \sigma\, \Phi_L \mathrm{dV} \tag{7}$$

where the surface integral is on boundaries of a single connected region and the volume integral is inside the region. $\Phi(x_p, y_p)$ is the potential value at an arbitrary location p inside the region or on the boundary. For two dimensional problems Φ_L is given by

$$\Phi_L = \frac{1}{2\pi} \ln\left[(x - x_p)^2 + (y - y_p)^2 \right]^{0.5}. \tag{8}$$

In Eq. (7), boundary integrals include those at the infinity. When a numerical solution procedure is employed, it is inconvenient to perform the integrals at infinity directly. However, integrals at the infinity can be transformed into a simple solution called undisturbed potential by using Green function theory. The undisturbed potential is defined by

$$\Phi_r = V_\infty \,(x \cos\alpha + y \sin\alpha). \tag{9}$$

The undisturbed potential satisfies Laplace equation $\nabla^2\Phi = 0$ everywhere and also satisfies the boundary condition at the infinity. Considering a region surrounded by a boundary at the infinity and applying Green function theory to the undisturbed potential, we have

$$\Phi_r(x_p, y_p) = \oint_\infty \left[(\mathrm{n}\cdot\nabla\Phi_r)\Phi_L - \Phi_r(\mathrm{n}\cdot\nabla\Phi_L) \right] \mathrm{ds}. \tag{10}$$

Thus, integrals at the infinity in Eq. (7) can be represented by the undisturbed potential Φ_r. Substitute the undisturbed potential into Eq. (7) solutions can be expressed by

$$\Phi(x_p, y_p) = \int_{B+C+SH} \left[(\mathrm{n}\cdot\nabla\Phi)\Phi_L - \Phi(\mathrm{n}\cdot\nabla\Phi_L) \right] \mathrm{ds} + \Phi_r + \int_V \sigma\, \Phi_L \mathrm{dV} \tag{11}$$

where B represents body surfaces, C denotes wakes or cuts between region boundaries, and SH are shock surfaces. On body surfaces and wakes, we have

$$\int_{B+C} (\mathrm{n}\cdot\nabla\Phi)\Phi_L \,\mathrm{ds} = 0 \tag{12}$$

because of the tangential boundary conditions. Across shocks, we have

$$\int_{SH} \Phi(\mathrm{n}\cdot\nabla\Phi_L) \,\mathrm{ds} = 0 \tag{13}$$

since the tangential velocities are assumed to be equal across shock waves. Thus, Eq. (7) becomes

$$\Phi(x_p, y_p) = -\int_B \Phi(\mathrm{n}\cdot\nabla\Phi_L)\,\mathrm{ds} - \Gamma \int_C (\mathrm{n}\cdot\nabla\Phi_L)\,\mathrm{ds} + \int_{SH} (\mathrm{n}\cdot\nabla\Phi)\Phi_L \,\mathrm{ds} + \Phi_r + \int_V \sigma\, \Phi_L \mathrm{dV} \tag{14}$$

where

$$\Gamma = \Phi_+ - \Phi_- \tag{15}$$

with Φ_+, Φ_- potential values across the wake. The circulation Γ is determined from the solutions.

NUMERICAL SOLUTION PROCEDURE

In Eq. (14) potential values are represented by boundary integrals plus an extra volume integral. For incompressible flows, the source term σ is zero and there is no shock. The incompressible potential depends only on boundary integrals on body surfaces and wake. After potential values on body surface are determined, potential solutions everywhere can be determined by those on body surface. For compressible flows the source term has to be evaluated and if supersonic flow appears, shock integrals have to be performed.

To determine potential solutions on body surface, Eq. (14) is implemented on body surface only. Therefore, the body surface needs to be cut into many pieces of small panels. Applying the surface integrals to each panel will result a group of simultaneous equations. Potential solutions on body surface are obtained from these simultaneous equations. Within a boundary segment, a linear potential formulation is assumed

$$\Phi = \Phi_i + \frac{\xi}{l}(\Phi_{i+1} - \Phi_i) \tag{16}$$

where l is the segment length and ξ varies from zero to l. Applying integral equations on body surfaces and introducing this linear potential relation into these boundary integrals, a set of linear simultaneous equations result

$$\left[A_{i,j} \right] \left[\Phi_i \right] = \left[F_i \right] \tag{17}$$

where

$$i = 1, \cdots\cdots m. \text{ and } j = 1, \cdots\cdots m. \tag{18}$$

with m the total number of nodes on boundaries. The matrix [A] is identical in every iteration. Thus, this matrix is only decomposed once.

For compressible flows, the source term must be evaluated throughout the volume. For transonic flows, the integral for shocks is needed because the normal derivatives of potential across shock wave is discontinuous. In this work, potential values across shock wave are assumed to be continuous because the tangential velocities across shock are equal.

The volume integral in Eq. (14) is evaluated in a discretized field obtained by finite element discretization. In each element volume the source term inside the volume integral is assumed to be a constant. Thus,

$$\int_V \sigma \, \Phi_L \, dV = \sum_{i}^{M} \sigma_i \int_{V_i} \Phi_L \, dV. \tag{19}$$

Integral $\int_{V_i} \Phi_L \, dV$ can be calculated analytically. Assume the finite integral volume boundaries can be represented by

$$y = at + bt\, x \tag{20}$$

The limit function of the volume integral is

$$F(\bar{x}) = (AT\, \bar{x} + 0.5\, BT\, \bar{x}^2) \ln\left[(1 + BT^2)(\bar{x} + 2\, B\, \bar{x} + C)\right]$$

$$+ \bar{x}^2 \tan^{-1} \frac{AT + BT\, \bar{x}}{\bar{x}}$$

$$- \frac{BT(C + 2B^2) - 2\, AT\, B\, D}{2} \ln(\bar{x}^2 + 2\, B\, \bar{x} + C)$$

$$+ \frac{AT(C - 2\, B^2)D + 2\, BT\, B^3}{E} \tan^{-1} \frac{\bar{x} + B}{E}$$

$$- 1.5\, BT\, \bar{x}^2 + (BT\, B - 2\, AT)\bar{x} - AT\, D\, \bar{x} \tag{21}$$

where

$$\bar{x} = x - x_p, \tag{22}$$

$$AT = at - y_p + bt\, x_p \tag{23}$$

$$BT = bt \tag{24}$$

$$B = \frac{AT\, BT}{1 + BT^2} \tag{25}$$

$$C = \frac{AT^2}{1 + BT^2} \tag{26}$$

$$D = \frac{1 + 2\, BT^2}{1 + BT^2} \tag{27}$$

$$E = \frac{AT}{1 + BT^2} \tag{28}$$

If $AT = 0$, the singularity location (x_p, y_p) is on the line represented by $y=at+btx$ as shown in Figure 1. The limit function becomes

$$F(\bar{x}) = 0.5\, BT\, \bar{x}^2 \ln\left[(1 + BT^2)\, \bar{x}^2\right]$$

$$- 1.5\, BT\, \bar{x}^2 + \bar{x}^2 \tan^{-1}(BT) \tag{29}$$

If the singularity location (x_p, y_p) is on the node point of the finite integral volume, $x=x_p$ and $y=y_p$ Thus, the limit function value becomes zero.

The value of a volume integral is obtained by calling the limit functions. In Figure 2, a typical finite integral volume is shown. The integral region is divided into three regions. In region 1, the integral value is

$$I_1 = F_{AU}(\bar{x}_D) - F_{AD}(\bar{x}_D) - \left[F_{AU}(\bar{x}_A) - F_{AD}(\bar{x}_A)\right] \tag{30}$$

In region 2, we have

$$I_2 = F_{AU}(\bar{x}_U) - F_{DB}(\bar{x}_U) - \left[F_{AU}(\bar{x}_D) - F_{DB}(\bar{x}_D)\right] \tag{31}$$

and in region 3,

$$I_3 = F_{UB}(\bar{x}_B) - F_{DB}(\bar{x}_B) - \left[F_{UB}(\bar{x}_U) - F_{DB}(\bar{x}_U)\right] \tag{32}$$

The integral value in this integral volume is

$$I = I_1 + I_2 + I_3 \tag{33}$$

Special care should be taken, when the finite integral volume appears to be different.

RESULTS AND DISCUSSION

The solution procedure discussed in above sections is applied to compressible flows over the NACA-0012 airfoil for a range of Mach numbers from subsonic to transonic flows. Solution results are compared with experimental data[19].

Numerical solutions are obtained in a grid generated by finite element discretization with 1176 element and 1275 nodes. Boundary grid consists 30 panels on the upper surface and 30 panels on the lower surface with more panels near the leading and trailing edges. A wake network consisting of two panels in the boundary grid is appended to the trailing edge of the airfoil. The wake is aligned with the chord bisector. The wake panels are divided into 11 smaller grid segments when building up the field grid. The boundary of the field grid is located at a distance of six chord length around the airfoil. Beyond that the source distributions are small thus, can be neglected.

The nonlinear potential equation is solved in a iterative solution procedure. First, the linear Laplace equation for incompressible flows is solved. Thus, the source distribution can be evaluated. With the first evaluated source distribution, the iterative solution procedure is performed. In each iteration, a system simultaneous equations on the boundary grid are solved and then the source distribution is evaluated inside the field grid. If supersonic flows appears, shock integrals are calculated. The contributions of the volume and shock integrals are added in the right hand side of the system equations. Because the matrix of the system equations does not change in iteration loops, the matrix is decomposed in advance only once to speed up the solution. The iteration number for subsonic flows is between 7 to 10 for the system residual to reach the order of 10.0E-07. For transonic flows, more iterations are needed for the same system residual order. For flows with Mach number 0.8 at the infinity, angle of attack 0.0°, the number of iterations is about 40.

In Fig. 3 and Fig. 4, pressure coefficients for flows over NACA0012 airfoil with Mach number at the infinity 0.5 and 0.7, angle of attack 0.0° are presented. Good agreement between numerical results and experimental data in these cases are shown. In Fig. 5, pressure coefficient for flow over NACA0012 airfoil with Mach number 0.5 at the infinity, angle of attack 2.0° is presented. Numerical results predicte lower pressure coefficients along the upper surface of the airfoil. Pressure coefficients for flow over NACA0012 with Mach number 0.8 and 0.83 at the infinity, angle of attack 0.0° are shown in Fig. 6 and Fig. 7 respectively. Numerical solutions agree well with experimental data in these cases. Pressure coefficients for Mach number 0.75 at the infinity, angle of attack 1.0° and 2.0° are shown in Fig. 8 and Fig. 9 respectively. In the lifting case, numerical solutions predict lower pressure coefficients on the upper surface of the airfoil. In Fig. 10 and Fig. 11, iso-Mach lines for Mach number 0.8 and 0.83, angle of attack 0.0° are presented. Iso-Mach lines for Mach number 0.75, angle of attack 1.0° and 2.0° are shown in Fig. 12 and Fig. 13. In these figures the shock regions are relatively thick because of the grid size near the shock. In this work, there is no grid clusting used near the shock regions.

REFERENCES

1. Holst, T. L., Slooff, J. W., Yoshihara, H., and Ballhaus, W. F. Jr., "Applied Computational Transonic Aerodynamics," edited by B. M. Spee and H. Yoshihara, AGARD-AG-266, pp. 86, 1982.

2. Tseng, K., Morino, L., "Nonlinear Green's Function Methods for Unsteady Transonic Flows," *Transonic Aerodynamics*, edited by D. Nixon, AIAA, New York, pp. 565-603, 1982.

3. Piers, W. J., Slooff, J. W., "Calculation of Transonic Flow by Means of A Shock-Capturing Field Panel Method," Proceedings of AIAA Computational Fluid Dynamics Conference, paper No. 79-1459, pp. 147-156, 1979.

4. Johnson, F. T., James, R. M., Bussoletti, J. E., Woo, A. C., "A transonic Rectangular Grid Embedded Panel Method," AIAA paper No. 82-0953, presented at AIAA/ASME 3rd Joint Thermophysics, Fluids, Plasma and Heat Transfer Conference, St. Louis, Missouri, June 7-11, 1982.

5. Oskam, B., "Transonic Panel Method for the Full Potential Equation Applied to Multicomponent Airfoils," *AIAA Journal*, Vol. 23, No. 9, pp. 1327-1334, 1985.

6. Crown, J. C., "Calculation of Transonic Flow Over Thick Airfoils by Integral Methods," *AIAA Journal*, Vol. 6, No. 3, pp. 413-423, 1968.

7. Sinclair, P. M., "An Exact Integral (Field Panel) Method for the Calculation of Two-Dimensional Transonic Potential Flow Around Complex Configurations," *Aeronautical Journal*, June/July, pp. 227-236, 1986.

8. Kandil, O. A., Hu, H., "Full-Potential Integral Solution for Transonic Flows with and without Embedded Euler Domains," *AIAA Journal*, Vol. 26, No. 9, pp. 1079-1086, 1988.

9. Masson, C., "Panel Method for Transonic Flows," MSc. Thesis, Ecole Polytechnique of Montreal, August, 1989.

10. Erickson, L. L., Strande, S. M., "A Theoretical Basis for Extending Surface-Paneling Methods to Transonic Flow," *AIAA Journal*, Vol. 23, No. 12, pp. 1860-1867, 1985.

11. Chu, L., Yates, E., Kandil, O., "Integral Equation Solution of the Full Potential Equation for Transonic Flows," AIAA paper No. 89-0563, presented at AIAA 27th Aerospace Sciences Meeting, Reno, Nevada, January 9-12, 1989.

12. Wilson, D. E., "A New Singular Integral Method for Compressible Potential Flow," AIAA paper No. 85-0481, presented at AIAA 23rd Aerospace Sciences Meeting, Reno, Nevada, January 14-17, 1985.

13. Hounjet, M. H. L., "Transonic Panel Method to Determine Loads on Oscillating Airfoils with Shocks," *AIAA Journal*, Vol. 19, No. 5, pp. 559-566, 1981.

14. Hounjet, M. H. L., "A Field Panel/Finite Difference Method for Potential Unsteady Transonic Flow," *AIAA Journal*, Vol. 23, No. 4, pp. 537-545, 1985.

15. Halsey, N. D., "Calculation of Compressible Potential Flow About Multielement Airfoils Using a Source Field-Panel Approach," AIAA paper No. 85-0038, presented at AIAA 23rd Aerospace Sciences Meeting, Reno, Nevada, January 14-17, 1985.

16. Erickson, L. L., Madson, M. D., Woo, A. C., "Application of the TranAir Full-Potential Code to the F-16A," *Journal of Aircraft*, Vol. 24, No.8, pp. 540-545, 1987,

17. Sinclair, P. M., "A Three-Dimensional Field-Integral Method for the Calculation of Transonic Flow on Complex Configurations-Theory and Preliminary Results," *Aeronautical Journal*, pp. 235-243, June/July, 1988.

18. Moran, J., *Theoretical and Computational Aerodynamics*, John Wiley & Sons, 1984.

19. Thibert, J. J., Grandjacques, M., Ohman, L. H., "NACA-0012 Airfoil, An Experimental Data Base for Computer Program Assessment," AGARD-AR-138, pp. A1.1-A1.10, May, 1979.

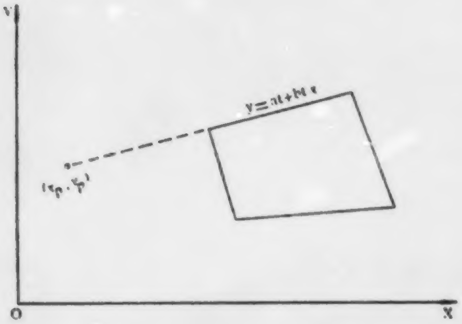

Figure 1. Volume integration when AT = 0.

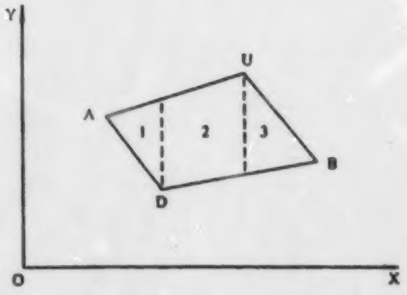

Figure 2. Volume integration by subregions.

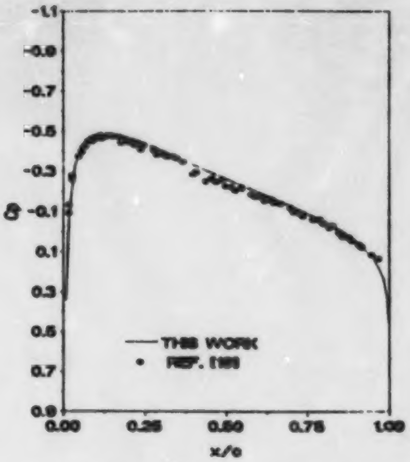

Figure 3. Pressure coefficient for NACA0012 airfoil $M_\infty = 0.5$, $\alpha = 0.0$

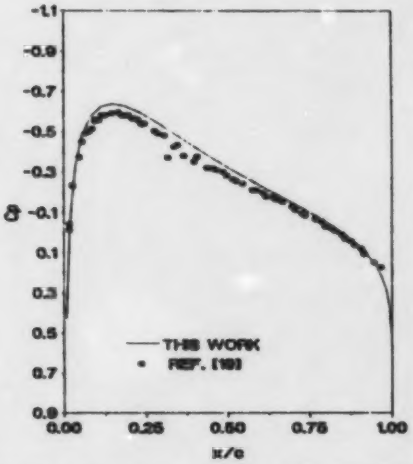

Figure 4. Pressure coefficient for NACA0012 airfoil $M_\infty = 0.7$, $\alpha = 0.0$

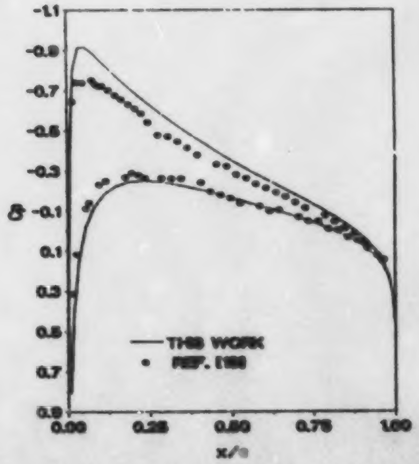

Figure 5. Pressure coefficient for NACA0012 airfoil $M_\infty = 0.5$, $\alpha = 2.0$

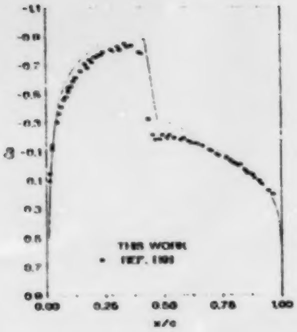

Figure 6. Pressure coefficient for NACA0012 airfoil $M_\infty = 0.8$, $\alpha = 0.0$

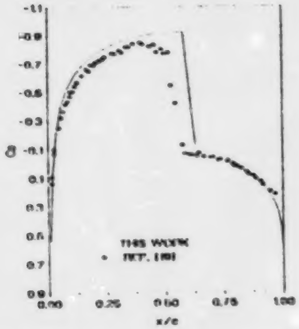

Figure 7. Pressure coefficient for NACA0012 airfoil $M_\infty = 0.83$, $\alpha = 0.0$

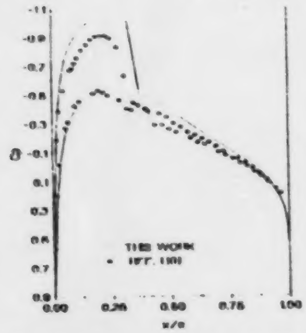

Figure 8. Pressure coefficient for NACA0012 airfoil $M_\infty = 0.75$, $\alpha = 1.0$

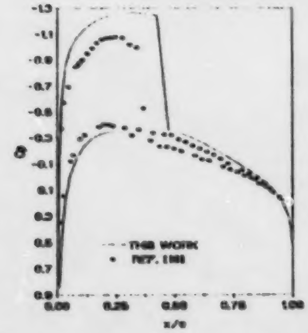

Figure 9. Pressure coefficient for NACA0012 airfoil $M_\infty = 0.75$, $\alpha = 2.0$

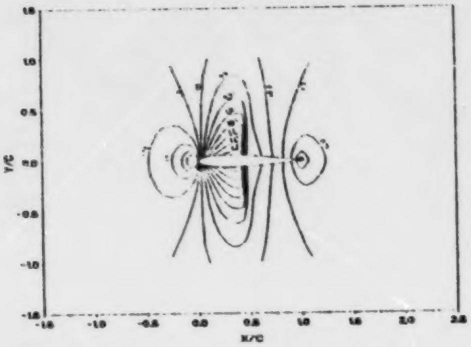

Figure 10. Iso-Mach lines, $M_\infty = 0.8$, $\alpha = 0.0$

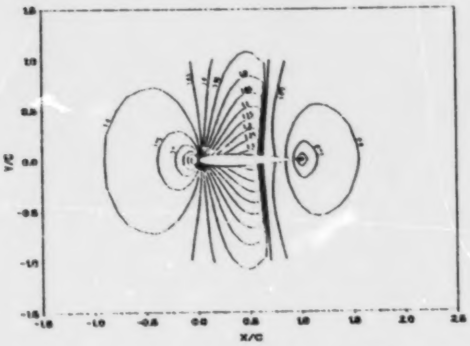

Figure 11. Iso-Mach lines, $M_\infty = 0.83$, $\alpha = 0.0$

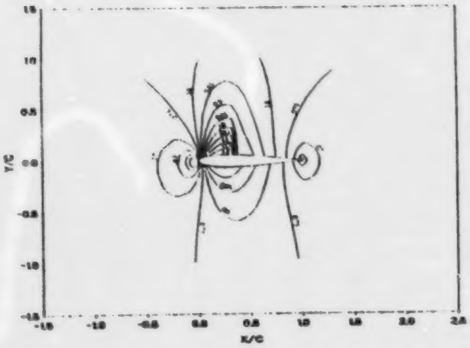

Figure 12. Iso-Mach lines, $M_\infty = 0.75$, $\alpha = 1.0$

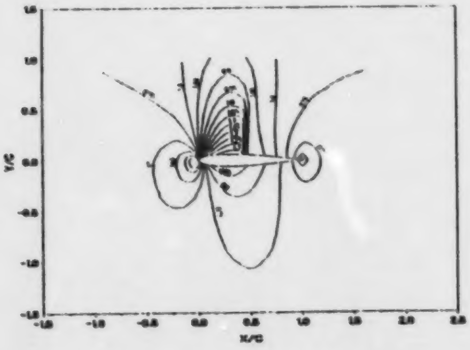

Figure 13. Iso-Mach lines, $M_\infty = 0.75$, $\alpha = 2.0$

MODÉLISATION DES FORCES AÉRODYNAMIQUES SUR UNE ÉOLIENNE DARRIEUS AVEC UN SILLAGE TRI-DIMENSIONNEL

Katéri Iléon
Étudiante graduée

Génie mécanique
Univ. de Sherbrooke

Bernard Massé
Chercheur

Hydro-Québec
Varennes

André Laneville
Professeur titulaire

Génie mécanique
Univ. de Sherbrooke

Sommaire

Cet article traite de la simulation numérique de l'écoulement autour des pales d'un aérogénérateur à axe vertical par la méthode de la circulation locale avec un nouveau modèle de sillage en trois dimensions. La vorticité émise par les pales est représentée par des "vortex verticaux" dont l'intensité varie en fonction de la vorticité attachée au temps d'émission. Les résultats numériques se comparent bien avec les résultats expérimentaux.

Nomenclature

A	surface projetée du rotor
c	corde du profil
C_L	coefficient de portance
CP	coefficient de performance puissance/$\frac{1}{2}\rho A V^3$
L	portance aérodynamique
ℓ	cote longitudinale sur la pale
s	demi-longueur de la pale
r	cote radiale de l'aérogénérateur
v	vitesse induite par le rotor
V	vitesse de l'écoulement amont
V_{ind}	vitesse induite par le sillage
V_r	vitesse résultante de l'écoulement
X	vitesse spécifique $\omega r/V$
Z	cote verticale
θ_1, θ_2	angle associé à l'interaction du vortex avec un point sur la pale
θ	cote azimuthale
Γ	vorticité
Γ_0	vorticité au point central de l'écoulement
ρ	densité de l'air

Introduction

La prédiction des forces aérodynamiques sur les pales d'un aérogénérateur en rotation consiste à évaluer le champ des vitesses (la vitesse résultante et l'angle d'incidence en particulier) autour des pales puis à calculer les forces exercées sur ces pales à partir des données expérimentales obtenues pour le profil utilisé. Ce champ des vitesses peut être représenté en suivant trois approches, l'approche des tubes de courants, l'approche tourbillonnaire et l'approche hybride.

L'approche des tubes de courant(1,2) utilise un bilan momentum linéaire sur chacun des tubes définissant l'aérogénérateur et permet le calcul des forces agissant sur les pales à partir de la réduction de momentum linéaire. Comme chaque tube de courant est une entité indépendante, cette approche néglige les interactions entre les tubes adjacents et n'inclut pas de modélisation du sillage.

Les approches de type tourbillonnaire calculent les interactions en intégrant dans le sillage les vitesses induites par le rotor. Un modèle du sillage est donc requis et la distribution de la vorticité dans ce dernier doit être évaluée pour une position donnée des pales.

L'approche de type hybride, dont fait partie la méthode de la circulation locale s'apparente à l'approche tourbillonnaire mais utilise un modèle de sillage dont la géométrie est approximative. La géométrie du sillage peut être admise fixe(3,4) ou laissée libre de se déformer(5). De plus, le rotor est représenté sous la forme d'une superposition de solutions simples, ce qui permet une réduction substantielle des temps de calcul.

Cette communication traite de l'utilisation de la méthode de la circulation locale avec un modèle nouveau du sillage en trois dimensions et de son application à l'éolienne Darrieus de 17 m des laboratoires SANDIA.

Méthode de la circulation locale

Le calcul des forces aérodynamiques sur une pale par cette méthode consiste à déterminer la circulation sur chacun des éléments de cote (θ, Z) et constituant la pale. Ainsi, pour un élément de pale dont l'intensité de la circulation attachée est $\Gamma(\theta, Z)$, il s'en suivra selon la loi de Kutta-Joukowski, une portance $L(\theta, Z)$

$$L(\theta, Z) = \rho\, V_r(\theta, Z)\, \Gamma(\theta, Z) \qquad (1)$$

et dont l'intensité s'exprime aussi, selon l'analyse dimensionnelle, par

$$L(\theta, Z) = C_L \times \frac{c}{2} \rho V_r^2(\theta, Z) \qquad (2)$$

La simple comparaison de ces deux expressions permet d'établir la base de la méthode de la circulation locale

$$\Gamma(\theta, Z) = \frac{C_L}{2} c V_r(\theta, Z). \qquad (3)$$

Dans l'équation (3), le coefficient de portance dépend de plusieurs paramètres tels que le profil de la pale, le nombre de Reynolds, la fréquence réduite, l'angle d'attaque effectif et la rugosité du profil. La méthode consistera donc à évaluer toutes les composantes de vitesses agissant au point (θ, Z) et à déterminer la vitesse résultante $V_r(\theta, Z)$, son angle d'attaque effectif par rapport à la corde, le nombre de Reynolds et la fréquence réduite de l'écoulement pour enfin trouver la valeur expérimentale appropriée du coefficient de portance C_L. La figure 1 montre les triangles de vitesses. Dans le plan de rotation, les trois principales composantes sont la vitesse tangentielle de rotation ωr, la vitesse de l'écoulement en amont, V et la vitesse induite par le sillage V_{ind}.

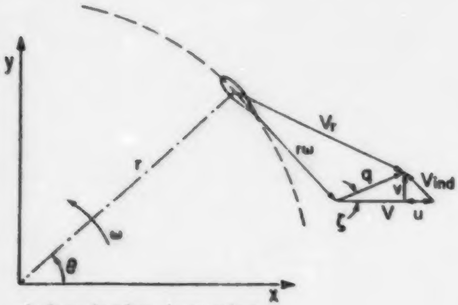

a) dans le plan de rotation

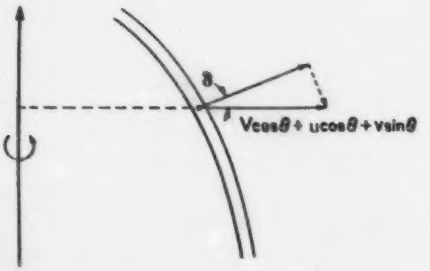

b) dans le plan du rotor

Figure 1: Triangles des vitesses

En faisant abstraction de l'interférence de la pale sur elle-même et en admettant qu'à l'azimuth θ, l'évolution antérieure du sillage (sa forme géométrique et la distribution de sa vorticité) est connue, il est possible de déterminer $\omega r(Z)$, V(Z) et $V_{ind}(Z)$, et par conséquent $\Gamma(Z)$. C'est le premier palier du modèle. La distribution de la vorticité le long de la pale, $\Gamma(Z)$, peut ainsi être quelconque. La connaissance de $\Gamma(Z)$ permet ensuite d'évaluer, pour chacun des éléments de pale, l'interférence due au reste de la pale, d'où l'ajout de la vitesse induite par le rotor, v_Z. Ce second palier de la méthode ramène une valeur corrigée de la vitesse résultante de même que de la distribution $\Gamma(Z)$. Il s'agit donc d'une méthode itérative.

Modélisation de la pale

Dans la méthode de circulation locale$^{(4)}$, la pale du rotor dont la distribution de la vorticité est quelconque est représentée par une superposition de pales imaginaires de longueurs différentes mais chacune ayant une distribution elliptique de vorticité (Figure 2). Ceci permet de fragmenter le système en autant d'équations que de points contrôles et ainsi produire un ensemble d'équations de solution plus simple.

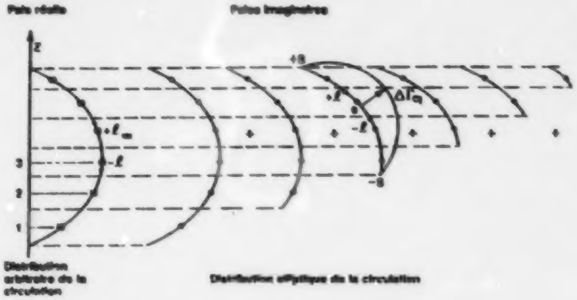
Pale réelle
Pales imaginaires
z
+s
$\Delta\Gamma_{oi}$
+ℓ
-ℓ
$+\ell_m$
3
2
1
-s
Distribution arbitraire de la circulation
Distribution elliptique de la circulation

Figure 2: Modélisation de la pale

Pour un azimuth θ du rotor, la circulation en un point de la pale est la somme des circulations sur les k pales imaginaires ayant la même ordonnée:

$$\Gamma(Z) = \sum_{i=1}^{k} \Delta\,\Gamma_i(Z)$$

Comme la distribution de la circulation sur les pales imaginaires est admise elliptique, il s'ensuit selon la figure 2 que

$$\Delta\Gamma_i(Z) = \Delta\Gamma_{oi}\left[1 - (\ell / s)^2\right]^{1/2}$$

où $\Delta\Gamma_{oi}$ est la circulation au centre ($\ell = 0$) de la ième pale et s est la demi-longueur de la pale imaginaire. Les termes $\Delta\Gamma_o$ sont les inconnus et le point controle i sur la pale réelle sert à évaluer $\Delta\Gamma_{oi}$.

Vitesses induites par le rotor

Pour tenir compte de l'interférence produite par le rotor sur un élément de pale, la vitesse induite, v_Z est déterminée$^{(4)}$ en représentant chaque élément de pale en une vorticité attachée qui se transforme en une vorticité émise du bord de fuite de la pale jusqu'à l'infini aval. La figure 3 montre cette représentation pour un élément de la pale situé à la cote ℓ' et dont la vorticité émise est $d\Gamma(\ell')$. Cette vorticité aura une influence sur un autre élément de la même pale situé situé à la cote ℓ et séparé par la distance $Z_{\ell\ell'}$ de l'élément initial, influence calculée en terme de vitesse induite. Sachant que l'intensité de $d\Gamma(\ell')$ est déterminée par la pente de la distribution de la circulation $\Gamma(\ell)$

$$d\Gamma(\ell') = \frac{d\Gamma(\ell')}{d\ell'}\, d\ell'$$

on peut démontrer que la vitesse induite par le rotor entier en sa position ℓ est

$$\vec{v} = -\frac{1}{4\pi}\int_{-S}^{S} \frac{1}{Z_{\ell\ell'}} \frac{d\Gamma(\ell')}{d\ell'}\, d\ell'$$

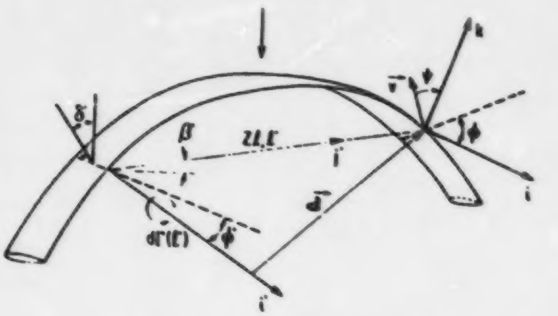

Figure 3: Vitesses induites par une pale courbe

Définissant l'angle β' entre l'axe j' et la parallèle à l'axe de rotation du rotor, la vitesse induite exprimée au point ℓ dans les axes i,j et K se calcule par

$$\begin{bmatrix} v_x \\ v_y \\ v_z \end{bmatrix} = \begin{bmatrix} \cos(\phi' - \phi) & \sin(\phi' - \phi)\sin(\delta - \beta) & -\sin(\phi' - \phi)\cos(\delta - \beta) \\ 0 & \cos(\delta - \beta) & \sin(\delta - \beta')) \\ \sin(\phi' - \phi) & -\cos(\phi' - \phi)\sin(\delta - \beta') & \cos(\phi' - \phi)\cos(\delta - \beta') \end{bmatrix} \begin{bmatrix} 0 \\ 0 \\ v \end{bmatrix}$$

Modélisation du sillage

Afin de simuler le sillage, un lien sera établi entre la vorticité distribuée sur la pale et les vorticités émise et libre. En consultant la figure 4, il est possible de postuler la formation d'un sillage tridimensionnel. Ainsi pour trois éléments adjacents de temps dt, communes à l'élément central, on retrouvera les vorticités suivantes:

la vorticité attachée au temps t, $\Gamma_i(t)$

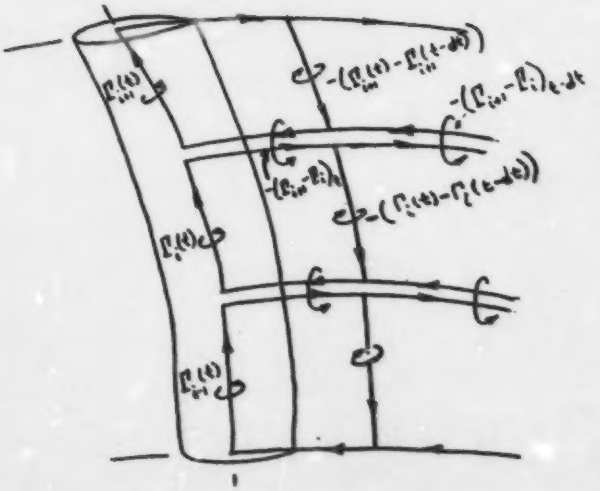
$\Gamma_{i+1}(t)$
$-(\Gamma_{i+1}(t)-\Gamma_{i+1}(t-dt))$
$-(\Gamma_{i+1}-\Gamma_i)_{t-dt}$
$-(\Gamma_{i+1}-\Gamma_i)_t$
$-(\Gamma_i(t)-\Gamma_i(t-dt))$
$\Gamma_i(t)$
$\Gamma_{i-1}(t)$
t

Figure 4: Représentation des vorticités

les vorticités émises, $-(\Gamma_{i+1} - \Gamma_i)_t$
et $-(\Gamma_i - \Gamma_{i-1})_t$

la vorticité libre, $-(\Gamma_i)_t + (\Gamma_i)_{t-dt}$.

Les deux vorticités émises ont tendance à annuler les vitesses induites qu'elles produisent de sorte que la vorticité libre devient la plus influente. Le sillage est donc représenté par de longs vortex courbes qui relient la vorticité libre émise au même temps par chaque élément. Chacun de ces longs vortex a donc une distribution quelconque, à l'image de la vorticité attachée de la pale. En négligeant les vorticités émises, le sillage ressemble maintenant à une série de longs vortex ayant une forme similaire au rotor à l'émission mais qui se déforme à mesure qu'ils se déplacent en aval. En admettant une variation linéaire de la vorticité libre entre deux points contrôles i.e. les points 1 et 2, la vitesse induite pour un élément droit de vortex qui relie chacun de ces points contrôles devient

$$v = \frac{1}{4\pi h}(\cos\theta_1 - \cos\theta_2) + (\Gamma_2 - \Gamma_1)\left(\frac{\sin\theta_2(1 - \cos(\theta_1 - \theta_2))}{\sin(\theta_2 - \theta_1)}\right)$$

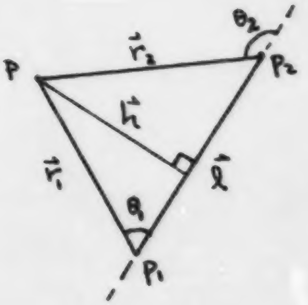

Figure 5: Schéma de l'emplacement d'un segment par rapport à un point contrôle

Pour trouver la vitesse induite par un de ces longs vortex sur un point de la pale, cette équation est évaluée (n-1) fois si n représente le nombre de points contrôles sur le "vortex vertical". Pour bien représenter la continuité d'un long vortex, la fonction de ces (n-1) vitesses est intégrée par la règle de Simpson. D'autre part, le sillage de la pale contient 180 longs vortex. Ce nombre vient du fait que le pas de temps correspond à un déplacement angulaire de 10° et que les vortex sont conservés pour cinq tours du rotor qui a deux pales.

Il s'ensuit que l'équation précédente est calculée 3040 fois pour un seul point de la pale. Puisqu'il est de plus désiré de représenter le sillage comme deux feuilles contenant chacune de longs vortex distribués de façon continue dans la direction de l'écoulement, les vitesses induites obtenues pour les 180 vortex sont intégrés suivant la règle de Simpson. Enfin, comme chaque pale est représentée par 15 éléments ou points contrôles, la même équation sera calculée 151200 fois pour chaque pas de temps.

Simulation d'une éolienne Darrieus de 17 M

Le calcul des forces aérodynamiques et de la puissance à l'arbre fournie a été réalisé pour l'éolienne Darrieus de 17 m des laboratoires Sandia. Trois modélisations furent employées et leurs résultats, comparés aux résultats expérimentaux des figures 6 et 7.

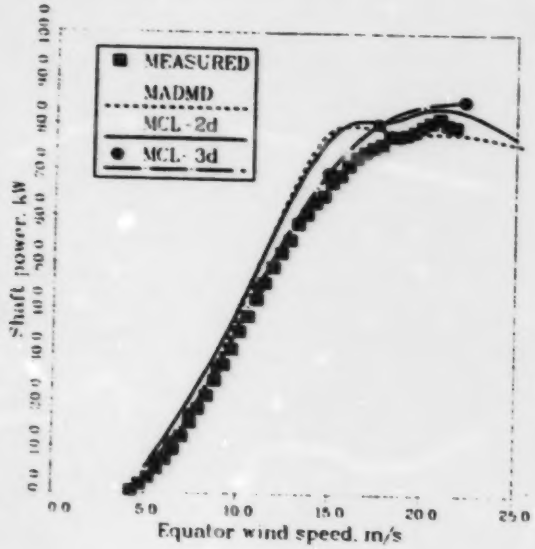

Figure 6: Puissance à l'arbre fournie en fonction de la vitesse équatoriale du rotor

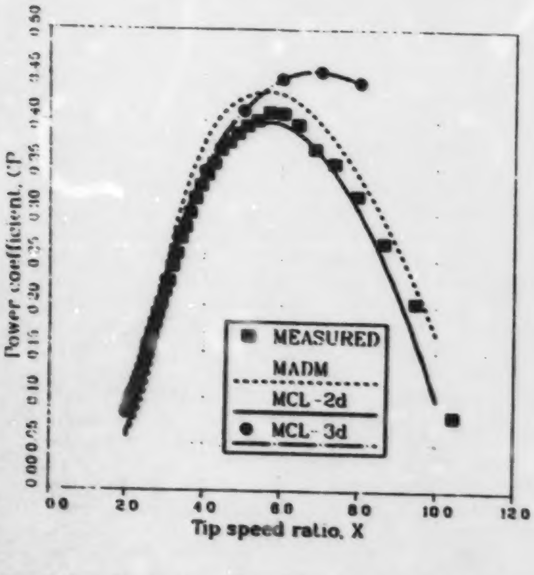

Figure 7: Coefficient de puissance en fonction de la vitesse spécifique

À la figure 6, on constate que la modélisation avec des tubes de courant (MADMD) de même que le modèle de circulation locale avec sillage bidimensionnel (MCL-2d) ont tendance à surestimer la puissance fournie dans la plage de vitesses allant de 10 m/s à 20 m/s. Le modèle de circulation locale avec sillage tridimensionnel a pour sa part tendance à surestimer la puissance légèrement aux grandes vitesses tout comme le modèle MCL-2d. Comme l'éolienne qui a servi aux essais ne devait pas avoir un fini de surface lisse, une augmentation du coefficient de traînée de 0.003 a été introduite

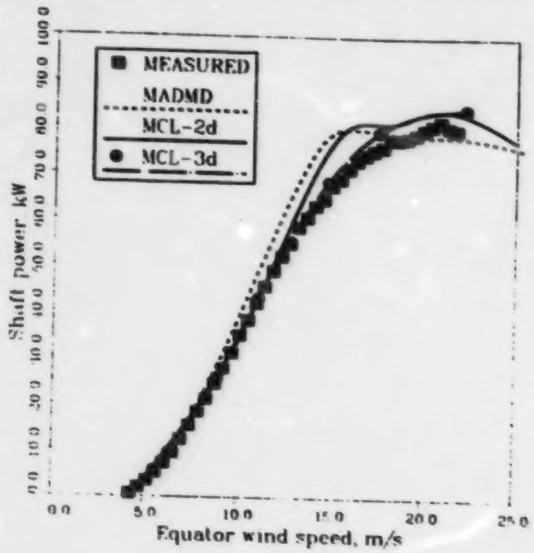

Figure 8: Puissance à l'arbre fournie en fonction de la vitesse équatoriale du rotor, avec effet de rugosité

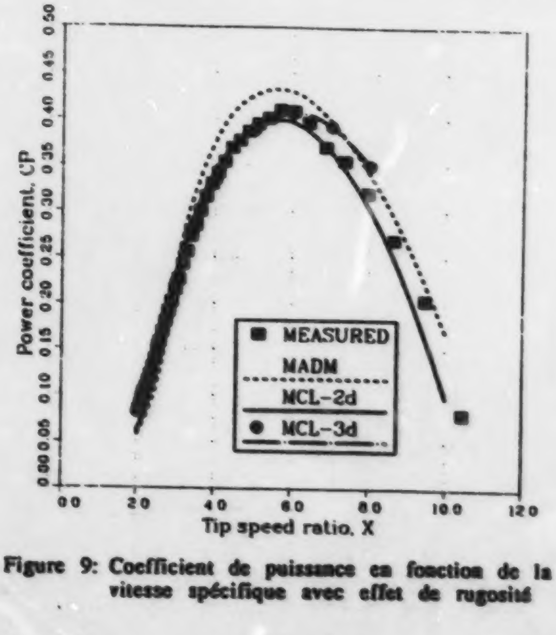

Figure 9: Coefficient de puissance en fonction de la vitesse spécifique avec effet de rugosité

dans les données pour simuler l'effet de rugosité. Les résultats obtenus sont comparés aux figures 8 et 9.

On constate donc que les modèles à circulation locale comme tous les modèles aérodynamiques, sont très sensibles à la valeur du coefficient de traînée à des valeurs de X supérieures à 5. L'effet de la turbulence atmosphérique pourrait produire des effets similaires additionnels.

L'avantage des méthodes à circulation locale réside dans l'obtention des forces aérodynamiques locales tenant compte du sillage et de l'interférence du rotor. Les figures 10 et 11 montrent les forces calculées par les modèles de circulation locale et qui ont servi à trouver la puissance fournie.

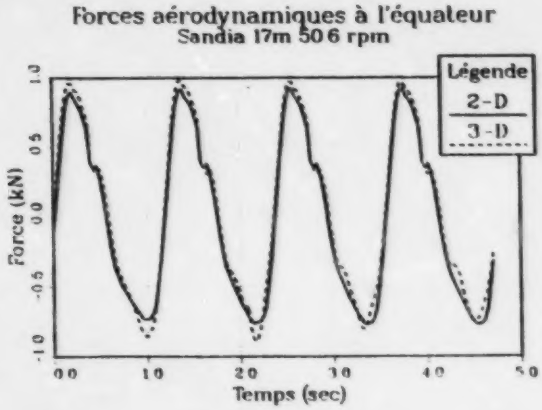

Figure 10: Force normale

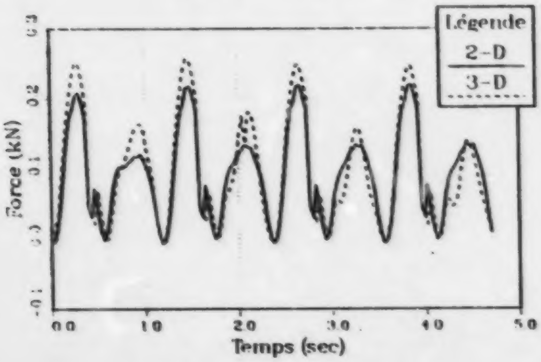

Figure 11: Force tangentielle

Pour les simulations des figures 6 à 9, chacun des points obtenus par le nouveau modèle a coûté 45 minutes de temps d'ordinateur CPU sur un IBM 3090.

Conclusion

Un modèle amélioré de la méthode de circulation locale pour calculer les forces aérodynamiques sur un aérogénérateur à axe vertical a été présenté. L'amélioration a été apportée au niveau de la modélisation du sillage qui se fait par des "vortex verticaux" dont l'intensité varie en fonction de la vorticité attachée au temps d'émission. La forme de ces "vortex verticaux" au départ suit celle du rotor.

Dans une simulation du rotor Darrieus de 17 m des laboratoires SANDIA, ce nouveau modèle donne des résultats en accord avec les résultats expérimentaux. L'obtention d'une condition d'opération exige 45 minutes de CPU sur un ordinateur IBM 3090.

Remerciements

Les auteurs tiennent à remercier le CRSNG et Hydro-Québec pour leur support de même que madame P. Jutras et Luc Marcouiller, pour leur collaboration.

Bibliographie

[1] Templin, R.J., "Equations and Flow Chart for the Double-Multiple Stream Tube Wind Turbine Performance Theory", notes manuscrites non publiées, mai 1979 - fév. 1980.

[2] Paraschivoiu, I., "Double-Multiple Streamtube Model for Darrieus WT's", Paper presented at 2nd DOE/NASA Workshop, Cleveland, Ohio, fév. 1981.

[3] Holme, O., "A Contribution to the Aerodynamic Theory of the Vertical Axis Wind Turbine", International Symposium of Wind Energy Systems, Cambridge, England, sept. 1976.

[4] Massé, B., "A Local-Circulation Model for Darrieus Vertical-Axis Wind Turbine", Journal of Propulsion and Power, AIAA, Vol. 2, no. 2, mars-avril 1986.

[5] Massé, B., Laneville, A. et P. Vittecoq, "Numerical Simulation of the Unsteady Aerodynamic Forces for a Rotating Aerofoil: Application to the Darrieus Wind Turbine", Numerical Methods in Laminar and Turbulent Flow, Volume 5, Part 2, pp. 1652-1664, 1987.

SOME OBSERVATIONS OF THE FLOW REGIMES AROUND A NACA 0018 AEROFOIL IN CIRCULAR TRANSLATION

A. Benmeddour*
Graduate Student

F. Bouak*
Graduate Student

A. Laneville*
Professor

P. Vittecoq*
Associate Professor

*Mechanical Engineering Department
Université de Sherbrooke

ABSTRACT

This paper presents the results of an experiment investigation of the aerodynamic loads and a flow visualization for a NACA 0018 aerofoil moving in a circular translation. The aerofoil is exposed to an upstream smooth flow with different preset angles of incidence and with tip speed ratios (λ) varying between 2 and 12. For large values of λ, the airloads are quasi-static and as the value of λ is reduced, different types of dynamic stall are observed. In the case of $\lambda = 2$, the lift coefficient, as the incidence is reduced, has a larger value than the one at the same incidence but in the increasing phase. The presence of a standing vortex is deduced in this case.

NOMENCLATURE

c : aerofoil chord
C_L : lift coefficient = lift force/q.c.ℓ
C_p : pressure coefficient = $(P - P_\infty)/q$
K : reduced frequency
ℓ : blade length
M : Mach number
P : surface static pressure
P_∞ : undisturbed upstream static pressure
q : dynamic pressure = $1/2\ \rho\ U^2_{rel}$
r : circle radius for blade motion
Rey : mean Reynolds number = $U_\infty\ c/\nu$
U_{rel} : relative airspeed
U_∞ : undisturbed upstream airspeed
α : kinematic angle of incidence
$\dot{\alpha}$: $d\alpha/dt$
α_0 : preset angle of incidence
α_{ss} : static stall angle of incidence
θ : azimuthal blade's position = ωt (azimuthal angle)
λ : tip speed ratio
ν : air kinematic viscosity
ω : blade angular speed

INTRODUCTION

Most of the observations dealing with the dynamic stall phenomenon are related to the case of an aerofoil in a sinusoidal pitching motion. Helicopter blades are essentially submitted to such a motion. In this case, the independent variables of similitude are, for a given profile, the Reynolds number, Rey, the Mach number, M, the reduced frequency, K, the amplitude of oscillation, α_{max} as well as the preset angle of incidence. Each of these parameters can be modified independently[1]. In some other applications, such as the case of a vertical axis wind turbine, V.A.W.T., the motion may also bring the blades into a dynamic stall situation but in this case some of the independent variables become coupled.

It is only recently that dynamic stall has been given due consideration for wind turbine applications. The search for an acceptable quantitative description of this phenomenon has been difficult and, although good progress has been made much remains to be determined.

In order to contribute to the understanding of this phenomenon, this article presents some experimental results obtained for a NACA 0018 aerofoil exposed to a circular translation, a motion equivalent to the V.A.W.T. The tests were performed in the wind tunnel laboratories of the Université de Sherbrooke.

EXPERIMENTAL SET UP

Figure 1 shows a schematic of the experimental set up. A NACA 0018 vertical blade with a 35.6 cm chord was mounted on top of an oscillating mechanism in the wind tunnel. The test section is 1.2 m wide with a false ceiling located within 2 mm of the top of the blade and with vertically slotted lateral walls (40% open area ratio) to reduce the blockage effects.

As the blade was in motion, the surface pressure distributions were measured using 40 pressure taps. A Scanivalve was mounted inside the blade to link each pressure tap to a Setra differential pressure transducer. Its analog output as well as the ones from the angular position transducer and the electronic manometer (upstream Pitot static tube), were fed to a data acquisition and treatment system. For each pressure tap, the time history of the static pressure were recorded during 5 cycles and averaged. The pressure distribution at a given azimuthal position was generated by comparing the signals of all taps and then integrated over the chord to calculate the pressure lift, drag and pitching moment coefficients. The Reynolds number in the tests was varied between 0.75×10^5 and 5×10^5 but only those of 1.5×10^5 with a preset angles of 0° and 10° are reported here.

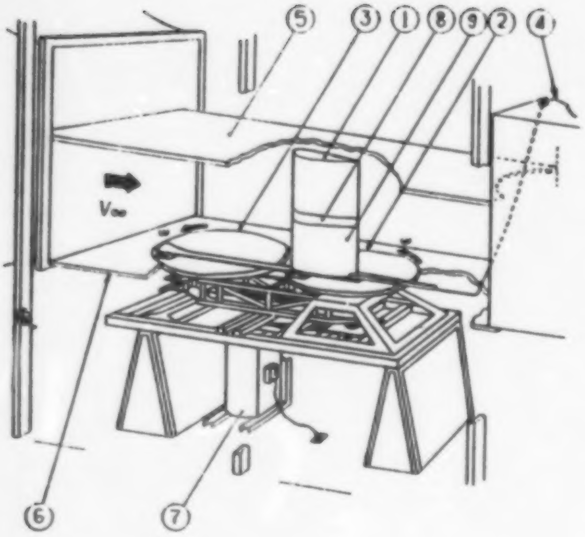

Fig. 1: Schematic of the experimental set up

1 : blade's upper section
2 : downstream disk
3 : upstream disk
4 : wires connection
5 : false ceiling
6 : false floor
7 : Eaton dynamic motor
8 : pressure taps
9 : blade's lower section

KINEMATICS OF THE MOTION

In order to produce a circular translation, the aerofoil was mounted on an arm attached to two synchronized rotating disks (see figure 1). Ball bearings on the attachments to the disks allowed for the rotation. Figure 2 shows the aerofoil trajectory attached to the downstream disk.

The radius of rotation, r, for the quarter chord location was 30 cm and the angular speed, ω, maintained constant for a given test. The preset angle of incidence, α_0, in the results presented here, was 0° and 10°.

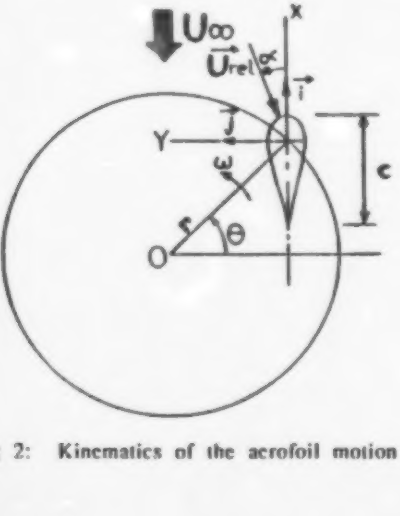

Fig 2: Kinematics of the aerofoil motion

For a given undisturbed upstream velocity, U_∞, the tip speed ratio is defined as:

$$\lambda = U_\infty / \omega r \qquad (1)$$

The relative air velocity for the aerofoil, and the kinematic angle of incidence, become:

$$U_{rel} = U_\infty [1 + (1/\lambda^2) + (2 \cos(\omega t))/\lambda]^{1/2} \qquad (2)$$

$$\alpha = \alpha_0 + \tan^{-1} [(\sin(\omega t))/(\lambda + \cos(\omega t))] \qquad (3)$$

The reduced frequency, K, defined[2] as the ratio of the pitching velocity $c\,\mathring{\alpha}_{max}/(\alpha_{max} - \alpha_{min})$ and the upstream velocity U_∞, is for a circular translation motion:

$$K = c/(2\,\lambda\, r(\lambda-1)\, \tan^{-1} [\,(\lambda^2-1)^{-1/2}]\,) \qquad (4)$$

As shown by (3) and (4), a variation of the independent variable λ produced a simultaneous variation of the reduced frequency and the amplitude of motion α.

The tests conditions λ and α_0, are summarized in Table 1 with their consequent effect on α and K.

Tests conditions		Consecutive coupling		
α_0	λ	K	α_{max}	α_{min}
+10°	12	0.054	+ 14.8°	+ 5.2°
	7	0.098	+ 18.2°	+ 1.8°
	4.9	0.151	+ 21.8°	- 1.8°
	3.8	0.209	+ 25.3°	- 5.3°
	3.3	0.254	+ 27.6°	- 7.6°
	2.6	0.341	+ 32.6°	- 12.6°
	2	0.567	+ 40°	- 20°
0°	5	0.147	+11.54°	-11.54°
	4	0.195	+14.48°	-14.48°
	3	0.29	+19.47°	-19.47°
	2	0.565	+ 30°	- 30°
	1.5	1.081	+41.8°	- 41.8°

Table 1

RESULTS AND THEIR INTERPRETATION

Figures 3 and 4 show the pressure lift coefficient as a function of the angle of attack for all the dynamic test conditions (see Table 1). In each case the pressure lift coefficient measured at the equivalent static angle of attack is indicated by the dash line.

For both preset angles imposed, it can be observed that the dynamic $C_L(\alpha)$ curve has the same slope as the static $C_L(\alpha)$ curve for increasing angle of attack. For large tip speed ratios ($\lambda > 3$ for $\alpha_0 = 0°$ and $\lambda > 5$ for $\alpha_0 = 10°$), the motion forced the blade to angles of attack smaller than the static stall angle (+ 20.5° in this case) and the general behavior of the dynamic $C_L(\alpha)$ is quasi-static. For smaller tip speed ratios, the aerofoil does not experience a static stall.

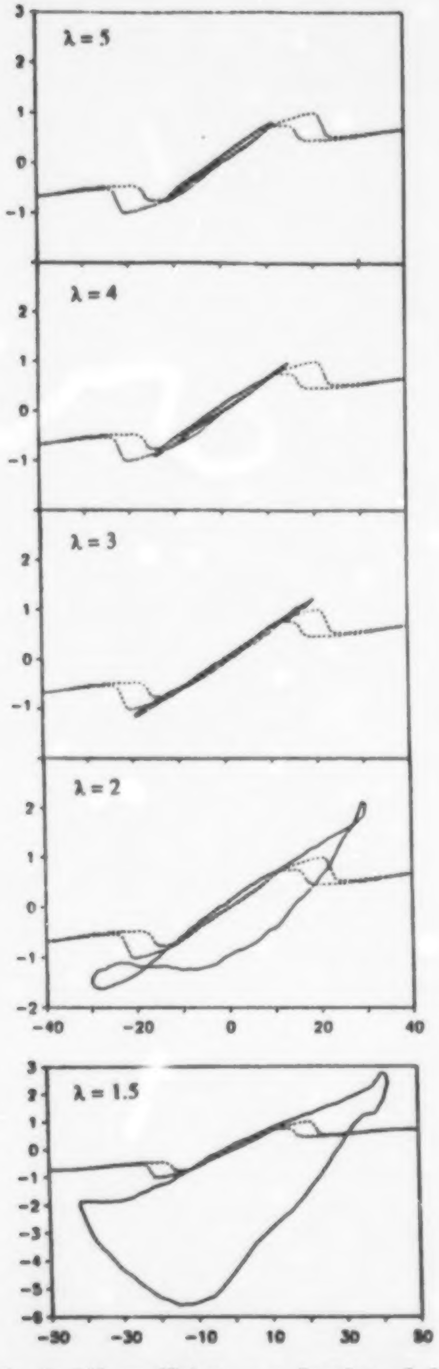

Fig. 3: Lift coefficient as a function of the kinematic angle of incidence for different values of λ ($\alpha_0 = 0°$)

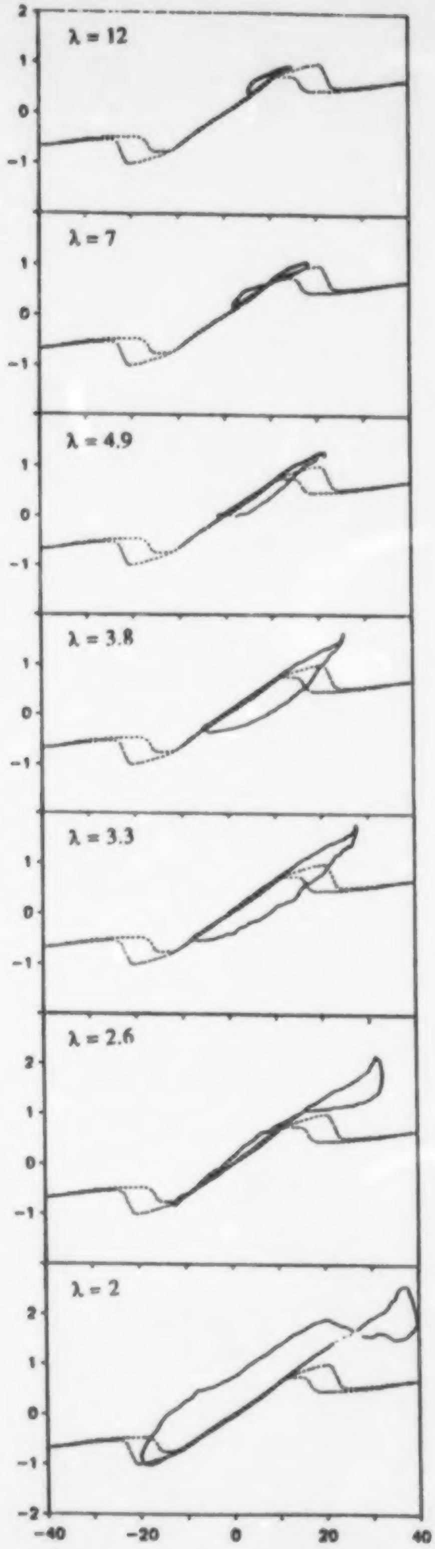

Fig. 4: Lift coefficient as function of the kinematic angle of incidence for different values of λ ($\alpha_0 = 10°$)

As α is increased, the lift coefficient continues increasing to reach a value up to 2.9 (case of $\lambda = 1.5$ and $\alpha_0 = 0°$) and $\alpha = 40°$ before stalling. This behavior is a characteristic of dynamic stall, as well as the post-stall $C_L(\alpha)$ that differs from the pre-stall $C_L(\alpha)$ at the same α. Most of the time, for a given α, the pre-stall $C_L(\alpha)$ is larger than the post-stall $C_L(\alpha)$. However, it should be observed that in two cases ($\alpha_0 = 10°$ and $\lambda \leq 2.6$), for a given positive incidence, the post-stall $C_L(\alpha)$ may be larger than the pre-stall $C_L(\alpha)$. Three regimes can be deduced and with the upper surface pressure distributions, they will be qualified. Figures 5 and 6 show these distributions as a function of the azimuth angle ($0 \leq \theta \leq 180°$) for the two preset angles and different tip speed ratios.

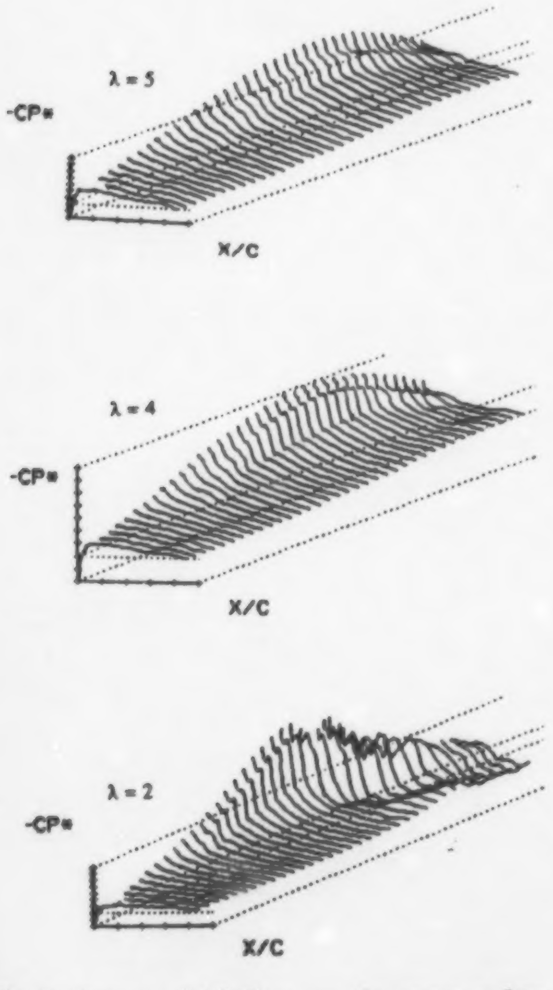

Fig. 5: Pressure distributions on the upper surface as θ progresses from 0° to 180° by step of 5°, ($\alpha_0 = 0°$)

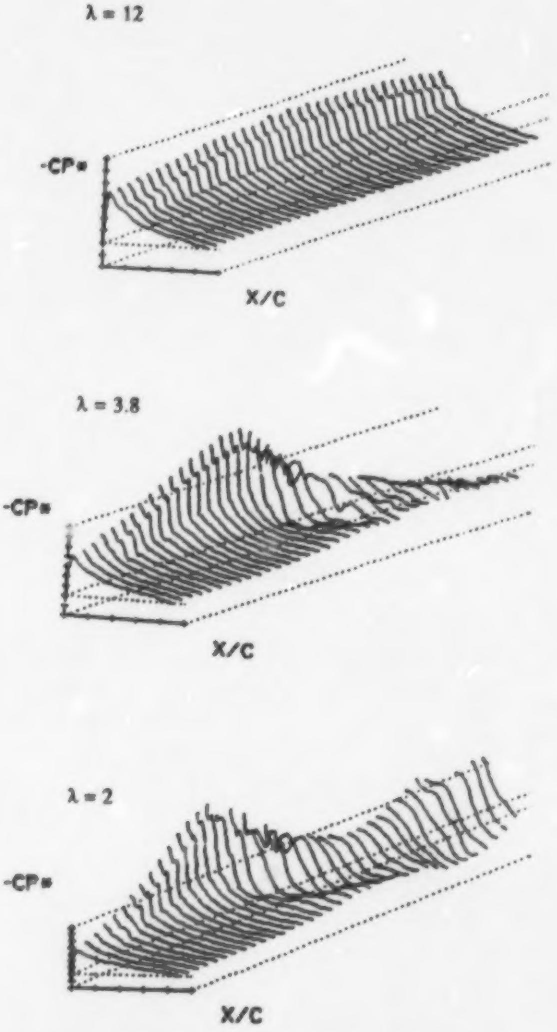

Fig. 6: Pressure distributions on the upper surface as θ progresses from 0° to 180° by step of 5° ($\alpha_0 = 10°$)

The first regime can be observed for $(\alpha_0, \lambda) = (0°, 5)$, $(0°, 4)$ and $(10°, 12)$. It is a quasi-static regime with a laminar separation bubble from the leading edge to 20% of the chord. The bubble is stationary in the case $(\alpha_0, \lambda) = (10°, 12)$ while in the case $(\alpha_0, \lambda) = (0°, 5°)$ it develops at the azimuth angle $\theta = 75°$.

The second regime can be identified for $(\alpha_0, \lambda) = (0°, 4)$, $(0°, 2)$, $(10°, 3.8)$. In the case $(10°, 3.8)$, a separation bubble is formed at $\theta = 20°$ and transformed at $\theta = 90°$ ($\alpha = 24.7°$) into a vortex that moves over the upper surface ($\theta = 100°$), producing lower local pressures, and that is finally shed in the wake (post-stall) at $\theta = 155°$ ($\alpha = 18.31°$). This second regime is a typical deep dynamic stall regime.

The third regime can be observed on the pressure distribution curves for $(\alpha_o, \lambda) = (10°, 2)$. This regime, at first, has common points with the second regime: the formation of a separation bubble and its transformation into a vortex. However, in this regime, the vortex remains on top of the upper surface in the post-stall region, if the term "stall" can be used. The presence of this vortex causes the already observed $C_L(\alpha)$ that is larger in the post-stall for a given angle of attack.

CONCLUSION

An experimental investigation of the aerodynamic loads for a NACA 0018 aerofoil in circular translation has indicated that:

- during its motion, the aerofoil experiences several regimes, from a quasi-static one to a deep dynamic stall one, regimes that are function of the tip speed ratio λ;
- in the case of tip speed ratios less than 2.6, the lift coefficient at a given incidence is larger in the post-stall region;
- as the aerofoil is undergoing dynamic stall, the vortex generated at the leading edge moves downstream to be shed completely in some cases ($\lambda = 3.3$ and 3.8) and in some other cases to be recaptured in the aerofoil path ($\lambda = 2$ and 2.6).

ACKNOWLEDGMENTS

This research project was supported by a N.S.E.R.C. grant as well as by I.R.E.Q. and the "Ministère des Études Supérieures" of Algeria.

REFERENCES

1. Lawrence W. Carr, Kenneth W. McAlister and William J. McCroskey, "Analysis of the Development of Dynamic Stall Based on Oscillating Airfoil Experiments". NASA-TN-D-8382. January 1977.

2. A. Laneville, P. Vittecoq and J. Côté, "Étude expérimentale de l'effet de la turbulence sur le décrochage dynamique". AGARD-CP-386, 6-9 May 1985; pp. S5-1 - S5-7.

DRAG REDUCTION AND THE TURBULENT FLOW OF MICROPOLAR FLUIDS IN A PIPE

N.H. Aydemir* and J.E.S. Venart**

* NSERC Government Laboratories Visiting Fellow, WNRE, Pinawa, Manitoba ROE 1LO
** Department of Mechanical Engineering, University of New Brunswick,
Fredericton, New Brunswick E3B 5A3

ABSTRACT

A theoretical study of drag reduction in the turbulent flows of dilute polymer solutions is presented. The fluid is conceived as a structured continuum similar to that considered in theories of micromorphic media. The microstructure within the fluid possesses internal degrees of freedom for spin and arbitrary deformation in addition to inertia associated with its shape and mass. The field equations of a simpler sub-class of micromorphic fluids known as microstretch fluids are given and the averaged equations of turbulence are derived; terms responsible for transfer of energy between microstretching, microrotation and the mean flow are identified. The equations are solved for the simple case of a fluid with microrotation using Prandtl's hypothesis for mixing length. An explicit function for the effective shear viscosity near the wall is derived from the field equations and is used in a van Driest type expression for mixing length. Friction factors corresponding to various flow conditions and polymer concentrations are calculated and compared with experimental data.

NOMENCLATURE

f	friction factor
J_1	modified Bessel function
j	microinertia
l	mixing length
P	pressure
R	pipe radius
Re	Reynold's number
r, x_k, z	coordinate variables
t	time
t_{kl}	stress tensor
U_{av}	average velocity
$\bar{u}_z, u_k, \bar{u}$	velocity
y	$R - r$
β, γ, κ	microstructure viscosities
λ, μ	Newtonian fluid viscosities
θ	azimuthal angle of pipe
$\delta_{kl}, \epsilon_{klr}$	Kronecker delta, alternating tensor
ν_k, ν	gyration vector and scalar microstretch
$\sim$	fluctuating port
$-$	time averaged port

INTRODUCTION

The Toms' phenomenon [1] describes the turbulent pipe flow of dilute polymer solutions. It was discovered that polymeric additives often reduce skin friction relative to pure solvents. Considerable experimental information has now accumulated on the turbulent flow of weak polymer solutions in tubes. A recent review by Pazwash [2] also presented experimental data based on the flow of Polyox WSR-301 solutions in capillary tubes. Friction drag correlations for the turbulent flow of polyethylene oxide in channels of different diameters, polymer concentration and molecular mass are given by Mironov and Shishov [3].

Several attempts were made to explain this phenomena from a different point of view. Virk [4,5] approximated the flow in three zones: a viscous sublayer, an elastic sublayer and an outermost region with a constant Newtonian mixing length. The use of the eddy viscosity concept has been quite successful, for example, as presented by Edwards and Smith [6]. An interesting analysis has been given by Mizushina et al. [7], who used a Maxwell model to represent the constitutive equation of the solution. This presentation, however, is suspect since the concentration of the additives is usually insufficient to yield viscoelastic solutions. A computational attempt to model the reduction in skin friction via bubble injection is presented in [8] where a simple mixing-length model is used for the turbulence. The density and viscosity were assumed to be a function of the void profile.

Although these theoretical studies are successful in explaining certain aspects of the phenomenon, such as reduced friction coefficients and enhanced velocities, they do not, however, shed any light into the physical mechanisms involved. Many of the constants required are adjusted to fit the experimental data and usually lack direct physical meaning.

An alternative explanation of drag reduction is presented in this paper using Eringen's [9] theory of micromorphic fluids. Micromorphic fluids have been used to model the flow of blood, nematic liquid crystals and Newtonian turbulence. They contain structures that can independently rotate and translate in the flow, giving rise to internal body couples, microstresses, microdeformations and microstress moments. The theory can also accommodate particle spin inertia, which obviously cannot be neglected if the structures are of significant size and mass within the fluid.

In accordance with the experimental studies in the literature, the present study assumes that the concentration is distributed uniformly in the pipe, a fact verified by Goren and Norbury [10]. We have used a modified expression for the van Driest mixing length where the fluid viscosity near the wall is replaced by an effective shear viscosity that takes into account the stresses due to the rotation of the microstructures. This effective viscosity also turned out to be a function of the rate of microrotation or the rotation of the macromolecules of the polymer additive. Plots of friction factor versus the Reynold's number closely resemble the experimental results [11].

ANALYSIS

The mechanism of drag reduction due to polymeric additives is quite complex. However, it has been proven that, in general, drag reduction increases by the polymer chain length and molecular weight. The proposed mechanism is that entangled balls of polymer chains break down turbulent eddies of comparable size and store this as elastic energy. This mechanism of turbulent dissipation reduces the effective eddy size near the wall, thus reducing the amount of turbulent fluctuation. This in turn, reduces the wall friction. The theory of microstretch fluids [12][1] allows for microstructure within the fluid. These structures can stretch and contract in addition to undergoing rigid body rotations. The governing field equations are given by [12]:

Balance of Linear Momentum:

$$\rho\left(\frac{\partial v_k}{\partial t} + v_l \frac{\partial v_k}{\partial x_l}\right) = -\frac{\partial P}{\partial x_k} + \lambda_0 \frac{\partial \upsilon}{\partial x_k}$$

$$+ (\mu_v + \kappa_v)\frac{\partial^2 v_k}{\partial x_l \partial x_l} + \kappa_v \epsilon_{klm} \upsilon_{m,l} \qquad (1)$$

Balance of Moment of Momentum:

$$\rho j\left(\frac{\partial \upsilon_k}{\partial t} + v_l \frac{\partial \upsilon_k}{\partial x_l}\right) = (\alpha_v + \beta_v)\frac{\partial^2 \upsilon_l}{\partial x_l \partial x_k}$$

$$+ \gamma_v \frac{\partial^2 \upsilon_k}{\partial x^2{}_l} + \kappa_v \epsilon_{klm}\frac{\partial v_m}{\partial x_l} - 2\kappa_v \upsilon_k \qquad (2)$$

$$\tfrac{1}{2}\rho j\left(\frac{\partial \upsilon}{\partial t} + v_l \frac{\partial \upsilon}{\partial x_l}\right) = a_0 \frac{\partial^2 \upsilon}{\partial x^2{}_l} - (\mu_0 - \lambda_0)\,\upsilon \qquad (3)$$

Conservation of microinertia: (for microisotropic case)

$$\frac{\partial j}{\partial t} + v_l \frac{\partial j}{\partial x_l} - 2\,\upsilon j = 0 \qquad (4)$$

Conservation of mass:

$$\frac{\partial v_k}{\partial x_k} = 0 \qquad (5)$$

We have assumed that

1) The fluid is incompressible
2) Body couples and moments are negligible.

If we follow the standard procedure to derive the averaged equations for turbulence and substitute

$$v_k = \bar{v}_k + \tilde{v}_k, \text{ ... etc. in Eqs. (1 - 5)}$$

we obtain

$$\rho\left(\frac{\partial \bar{v}_k}{\partial t} + \bar{v}_l \frac{\partial \bar{v}_k}{\partial x_l}\right) = -\frac{\partial \bar{P}}{\partial x_k} + \lambda_0 \frac{\partial \bar{\upsilon}}{\partial x_k}$$

$$+ (\mu_v + \kappa_v)\frac{\partial^2 \bar{v}_k}{\partial x^2{}_l} + \kappa_v \epsilon_{klm}\frac{\partial \bar{\upsilon}_m}{\partial x_l}$$

$$- \rho \frac{\partial\, \overline{(\tilde{v}_k\ \tilde{v}_l)}}{\partial x_l} \qquad (6)$$

$$\rho j\left(\frac{\partial \bar{\upsilon}_k}{\partial t} + \bar{v}_l \frac{\partial \bar{\upsilon}_k}{\partial x_l}\right) = (\alpha + \beta)\frac{\partial^2 \bar{\upsilon}_l}{\partial x_l \partial x_k}$$

$$+ \gamma_k \frac{\partial^2 \bar{\upsilon}_k}{\partial x^2{}_l} + \kappa_v \epsilon_{klm}\frac{\partial \bar{v}_m}{\partial x_l} - 2\kappa_v \bar{\upsilon}_k$$

$$- \frac{\partial}{\partial x_l}\overline{(\tilde{v}_l\ \tilde{\upsilon}_k)\ \rho j} \qquad (7)$$

$$\tfrac{1}{2}\rho j\left(\frac{\partial \bar{\upsilon}}{\partial t} + \bar{v}_l \frac{\partial \bar{\upsilon}}{\partial x_l}\right) = a_0 \frac{\partial^2 \bar{\upsilon}}{\partial x^2{}_l} - (\mu_0 - \lambda_0)\,\bar{\upsilon}$$

$$- \frac{\partial}{\partial x_l}\overline{[(\tilde{v}_l\ \tilde{\upsilon})]\ \tfrac{1}{2}\rho j} \qquad (8)$$

$$\text{since}\quad \overline{\tilde{v}_l \frac{\partial \tilde{\upsilon}}{\partial x_l}} = \frac{\partial\,\overline{(\tilde{v}_l\ \tilde{\upsilon})}}{\partial x_l} - \underbrace{\overline{\tilde{\upsilon}\frac{\partial \tilde{v}_l}{\partial x_l}}}_{0}$$

It can easily be shown from Eq. (6) that the mean stress tensor is given by:

$$\bar{t}_{kl} = -\bar{P}\delta_{kl} + \lambda_0\,\bar{\upsilon}\delta_{kl} + (\mu_v + \kappa_v)\frac{\partial \bar{v}_k}{\partial x_l}$$

$$+ \kappa_v \epsilon_{klm}\bar{\upsilon}_m - \rho\,\overline{\tilde{v}_k \tilde{v}_l} \qquad (9)$$

The kinetic energies of mean flow for velocities, microrotation and microstretches can be obtained when equations (6), (7) and (8) are multiplied by $\bar{v}_k$, $\bar{\upsilon}_k$ and $\bar{\upsilon}$. Similarly, multiplying them by v_k, υ_k and υ gives the kinetic energy of instantaneous motion. When these equations are compared, we obtain the expressions for the kinetic energy of total and mean flows associated with v_k, υ_k and υ. These are very lengthy calculations, therefore we give only one example:

---

[1] Microstretch fluids is a sub-class of micromorphic fluids. Here, the particles are not allowed arbitrary deformations. The resulting field equations are significantly easier to handle.

Kinetic energy of total and mean flow associated with microrotation:

Total KE

$$\tfrac{1}{2}\rho j \frac{\partial}{\partial t} (\bar{\upsilon}_k \bar{\upsilon}_k) + \tfrac{1}{2}\rho j \frac{\partial}{\partial t} (\bar{\upsilon}_k \bar{\upsilon}_k) = -\tfrac{1}{2}\rho j \frac{\partial}{\partial x_l} (\bar{v}_l \ \bar{\upsilon}_k \ \bar{\upsilon})$$

$$- \tfrac{1}{2}\rho j \frac{\partial}{\partial x_l} (\bar{v}_l \ \overline{\tilde{\upsilon}_k \ \tilde{\upsilon}_k}) + (\alpha + \beta) \frac{\partial}{\partial x_k} (\bar{\upsilon}_k \frac{\partial \bar{\upsilon}_l}{\partial x_l})$$

$$+ (\alpha + \beta) \frac{\partial}{\partial x_k} (\overline{\tilde{\upsilon}_k \frac{\partial \tilde{\upsilon}_l}{\partial x_l}}) - (\alpha + \beta) \frac{\partial \bar{\upsilon}_l}{\partial x_l}$$

$$- (\alpha + \beta) \overline{\frac{\partial \tilde{\upsilon}_l}{\partial x_l} \frac{\partial \tilde{\upsilon}_k}{\partial x_k}} + \gamma \frac{\partial}{\partial x_l} (\bar{\upsilon}_k \frac{\partial \upsilon_k}{\partial x_l})$$

$$+ \gamma \frac{\partial}{\partial x_l} (\overline{\tilde{\upsilon}_k \frac{\partial \tilde{\upsilon}_k}{\partial x_l}}) - \gamma \frac{\partial \bar{\upsilon}_k}{\partial x_l} \frac{\partial \bar{\upsilon}_k}{\partial x_l} - \gamma \overline{\frac{\partial \tilde{\upsilon}_k}{\partial x_l} \frac{\partial \tilde{\upsilon}_k}{\partial x_l}}$$

$$+ \kappa \ \epsilon_{klm} \frac{\partial \bar{v}_m}{\partial x_l} + \kappa \ \epsilon_{klm} \overline{\tilde{\upsilon}_k \frac{\partial \tilde{v}_m}{\partial x_l}} - 2 \ \kappa \ \bar{\upsilon}_k \ \bar{\upsilon}_k$$

$$- 2 \ \kappa \ \overline{\tilde{\upsilon}_k \ \tilde{\upsilon}_k} - \tfrac{1}{2}\rho j \frac{\partial}{\partial x_l} (\overline{\tilde{\upsilon}_l \ \tilde{\upsilon}_k \ \tilde{\upsilon}_k})$$

$$- \rho j \frac{\partial}{\partial x_l} (\overline{\tilde{\upsilon}_l \ \tilde{\upsilon}_k} \ \bar{\upsilon}_k) \tag{10}$$

Mean KE

$$\tfrac{1}{2}\rho j \frac{\partial (\bar{\upsilon}_k \ \bar{\upsilon}_k)}{\partial t} = -\tfrac{1}{2}\rho j \frac{\partial}{\partial x_l} (\bar{\upsilon}_l \ \bar{\upsilon}_k \ \bar{\upsilon}_k)$$

$$+ (\alpha + \beta) \frac{\partial}{\partial x_k} \left(\bar{\upsilon}_k \frac{\partial \bar{\upsilon}_l}{\partial x_l}\right) - (\alpha + \beta) \frac{\partial \bar{\upsilon}_k}{\partial x_k} \frac{\partial \bar{\upsilon}_l}{\partial x_l}$$

$$+ \gamma \frac{\partial}{\partial x_l} (\bar{\upsilon}_k \frac{\partial \bar{\upsilon}_k}{\partial x_l}) - \gamma \frac{\partial \bar{\upsilon}_k}{\partial x_l} \frac{\partial \bar{\upsilon}_k}{\partial x_l} + \kappa \ \epsilon_{klm} \ \bar{\upsilon}_k \frac{\partial \bar{v}_m}{\partial x_l}$$

$$- 2 \ \kappa \ \bar{\upsilon}_k \ \bar{\upsilon}_k - \frac{\partial}{\partial x_l} (\rho j \ \bar{\upsilon}_k \ \overline{\tilde{v}_l \ \tilde{\upsilon}_k})$$

$$+ \rho j \ \overline{\tilde{v}_l \ \tilde{\upsilon}_k} \frac{\partial \bar{\upsilon}_k}{\partial x_l} \tag{11}$$

KE of Turbulence

$$\tfrac{1}{2}\rho j \frac{\partial (\overline{\tilde{\upsilon}_k \ \tilde{\upsilon}_k})}{\partial t} = -\tfrac{1}{2}\rho j \frac{\partial}{\partial x_l} (\bar{v}_l \ \overline{\tilde{\upsilon}_k \ \tilde{\upsilon}_k})$$

$$+ (\alpha + \beta) \frac{\partial}{\partial x_k} \left(\overline{\tilde{\upsilon}_k \frac{\partial \tilde{\upsilon}_l}{\partial x_l}}\right) - (\alpha + \beta) \overline{\frac{\partial \tilde{\upsilon}_l}{\partial x_l} \frac{\partial \tilde{\upsilon}_k}{\partial x_k}}$$

$$+ \gamma \frac{\partial}{\partial x_l} (\overline{\tilde{\upsilon}_k \frac{\partial \tilde{\upsilon}_k}{\partial x_l}}) - \gamma \overline{\frac{\partial \tilde{\upsilon}_k}{\partial x_l} \frac{\partial \tilde{\upsilon}_k}{\partial x_l}} + \kappa \ \epsilon_{klm} \overline{\tilde{\upsilon}_k \frac{\partial \tilde{v}_m}{\partial x_l}}$$

$$- 2 \ \kappa \ \overline{\tilde{\upsilon}_k \ \tilde{\upsilon}_k} - \tfrac{1}{2}\rho j \ (\overline{\tilde{v}_l \ \tilde{\upsilon}_k \ \tilde{\upsilon}_k}) - \rho j \ \overline{\tilde{v}_l \ \tilde{\upsilon}_k} \frac{\partial \bar{\upsilon}_k}{\partial x_l} \tag{12}$$

Similar equations can be written for the turbulence energies associated with velocity v_k and microstretching υ. The following terms were identified as responsible for the transfer of energy between mean and turbulence energies:

$$\text{KE of } v_k\text{:} \quad \rho \ \overline{\tilde{v}_k \ \tilde{v}_l} \frac{\partial \bar{v}_k}{\partial x_l}$$

$$\text{KE of } \upsilon_k\text{:} \quad \rho j \ \overline{\tilde{v}_l \ \tilde{\upsilon}_k} \frac{\partial \bar{\upsilon}_k}{\partial x_l}$$

$$\text{KE of } \upsilon \text{ :} \quad \tfrac{1}{2}\rho j \ \overline{\tilde{v}_l \ \tilde{\upsilon}} \frac{\partial \bar{\upsilon}}{\partial x_l} \ . \tag{13}$$

The full solution of the equations of motion (eqns. (6) to (8)) coupled with a $\kappa - \epsilon$ model of turbulence is now possible. Obviously this task is very difficult as much as it is rewarding. We will leave this for future workers and give a simpler solution here, analogous to a mixing-length approach. We will also assume that the stretching or contraction of the macromolecules do not significantly affect the dissipation. This point is certain to spark criticism and stimulate future research.

For a one-dimensional pipe flow coupled with the assumption of steady turbulent flow, the equations of motion simplify considerably. Choosing z as the direction of flow and r as the radial distance, equations (6) and (7) can be written as:

$$- \frac{\partial \bar{P}}{\partial z} + (\mu + \kappa) \left[\frac{1}{r} \frac{\partial}{\partial r} \left(r \frac{\partial v_z}{\partial r}\right)\right] + \kappa \frac{1}{r} \frac{\partial}{\partial r} (r \upsilon_\theta)$$

$$- \frac{1}{r} \rho \frac{\partial}{\partial r} (\overline{\tilde{v}_r \ \tilde{v}_z \ r}) = 0 \tag{14}$$

$$\gamma \frac{\partial}{\partial r} \left[\frac{1}{r} \frac{\partial}{\partial r} (r \upsilon_\theta)\right] - \kappa \frac{\partial v_z}{\partial r} - 2 \ \kappa \ \upsilon_\theta = 0 \tag{15}$$

and the stress tensor is given by

$$t_{rz} = \mu \frac{\partial \bar{v}_z}{\partial r} + \kappa \frac{\partial \bar{v}_z}{\partial r} + \kappa \bar{\upsilon}_\theta - \rho \overline{\tilde{v}_r \tilde{v}_z}. \qquad (16)$$

Clearly, in one dimension, $\upsilon_z = \upsilon_r = 0$ and υ_θ denotes microrotation on a constant θ plane. We do not give here the expressions for turbulent couple stresses and moments since they are not used in this simple analysis. A mixing length given by:

$$l = 0.4\, y\, [1 - \exp(-y^+/A^+)]\ ,\ y^+ = y\sqrt{\rho\tau_w/\mu}\ ,$$
$$A^+ = 26 \qquad (17)$$

will now be introduced. Clearly, l approaches $0.4\,y$ as y^+ increases. This is necessary since fluids with polymeric additives behave like Newtonian fluids when the centre of the pipe is approached [4]. Assuming that t_{rz} is a linear function of r near the wall, equation (16) can be written as

$$-\frac{\tau_w}{\rho}\frac{r}{R} = \frac{\mu_{app}}{\rho}\frac{d\bar{v}_z}{dr} \pm l^2 \left(\frac{d\bar{v}_z}{dr}\right) \qquad (18)$$

where we assumed that $\overline{\tilde{v}_r\ \tilde{v}_z} \approx l^2 \left|\frac{d\bar{v}_z}{dr}\right| \frac{d\bar{v}_z}{dr}$.

The term μ_{app} can be shown to be given by

$$\mu_{app} = \mu \left[1 + \frac{\kappa}{\mu}\left(\frac{\bar{\upsilon}_\theta}{\frac{d\bar{v}_z}{dr}}\right)\right]. \qquad (19)$$

Equation (18) can be integrated to give

$$v_z(r) = \int_R^r \frac{-4\,\frac{\tau_w}{\rho}\,\frac{r^2}{R^3} \Big/ \left(\frac{\mu_{app}}{\rho}\right) dr}{1 + \sqrt{1 + 4\,l^2\,\frac{\tau_w}{\rho}\,\frac{r}{R} \Big/ \left(\frac{\mu_{app}}{\rho}\right)^2}} \qquad (20)$$

The ratio $\left(\bar{\upsilon}_\theta \Big/ \frac{d\bar{v}_z}{dr}\right)$ in equation (19) can be obtained from the analytical solution of equations (14) and (15) with the assumption that the fluctuation terms are negligible. Equation (19) can now be written as

$$\mu_{app} = \mu \left[1 + \frac{\kappa}{\mu}\left\{\frac{\frac{J_1(K\varsigma)}{J_1(K)}\,H + P\left[\frac{J_1(K\varsigma)}{J_1(K)} - \varsigma\right]}{\frac{\kappa}{\mu+\kappa}\,\frac{(H+P)}{J_1(K)}\,K\,J_1(K\varsigma) - 2P\varsigma}\right\}\right] \qquad (21)$$

where $\varsigma = r/R,\ K = kR,\ k^2 = \frac{2\mu + \kappa}{\mu + \kappa},$

$$P = \frac{R^2}{2(2\mu + \kappa)}\frac{dP}{dz}\ ,\ H = \upsilon_\theta(1).$$

Equation (21) is similar to Einstein's effective viscosity expression $\mu = \mu_1\ (1 + 2.5\,\phi)$ where ϕ is the concentration of particles.

Equation (21) is more general and takes into account parameters such as the particle gyration gradient viscosity, γ, particle rotation and vortex viscosity, κ. This work showed the vortex viscosity to be related to the concentration of the additives.

RESULTS AND CONCLUSIONS

In Fig. 1, the friction factor is plotted against the Reynold's number for two values of k and pure water. The choice of k seems to represent the 50 and 100 ppm data in [11] closely. Here,

$$Re = 2\rho R\,\frac{U_{av}}{\mu}\ ,\ U_{av} = \int_0^1 2\,v(s)\,s\,ds$$

and $$f = 8\,\frac{dP}{dz}\,\frac{R}{2\rho\,U_{av}^2}$$

The corresponding velocity profiles shown in Fig. 2 display the expected behaviour: they are blunt near the centre line and the profiles for different concentrations cross over close to r = 0 as observed in the experiments.

Obviously, more research is needed to determine the roles of several microstructure parameters and their relations to macromolecular solutions. This work shows that the parameter k is related to concentration of the additives.

REFERENCES

1. Toms, B.A., Proc. 1st Int. Congress on Rheology, Vol. 2, p. 134, North Holland Publishing Co., Amsterdam, Holland, 1948.

2. Pazwash, H., Reduction of Friction Drag in Pipes by Polymers: A Review, J. Trans. Eng., Vol. 110, No. 2, pp. 223-234, 1984.

3. Mironov, B.P., Shishov, V.J., Friction Drag Correlation for a Turbulent Flow of Polymer Solutions, Heat Transfer, Soviet Research, Vol. 15, pp. 131-144, 1985.

4. Virk, P.S., An Elastic Sublayer Model for Drag Reduction by Dilute Solutions of Linear Macromolecules, J. Fluid Mech., Vol. 45, pp. 417-440, 1971.

5. Virk, P.S., Mickley, H.S., Smith, K.A., The Ultimate Asymptote and Mean Flow Structure in Toms' Phenomenon, Trans. ASME, June, pp. 488-493, 1970.

6. Edwards, M.F., Smith, R., the Use of Eddy Viscosity Expressions for Predicting Velocity Profiles in Newtonian, Non-Newtonian and Drag-Reducing Turbulent Pipe Flow, J. Non-Newtonian Fluid Mech., Vol. 7, pp. 153-169, 1980.

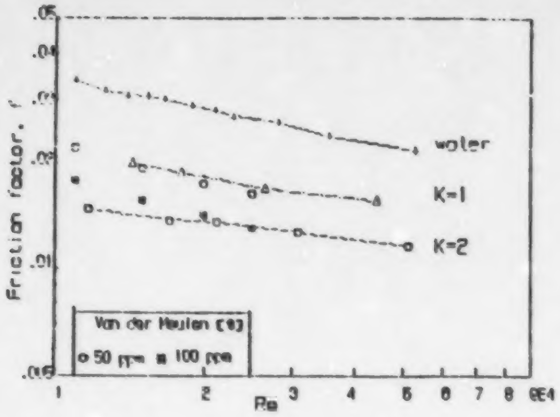

Fig. 1: Reduction of Drag when k = 1 and k = 2; k = Microgyration Viscosity/Solvent Viscosity

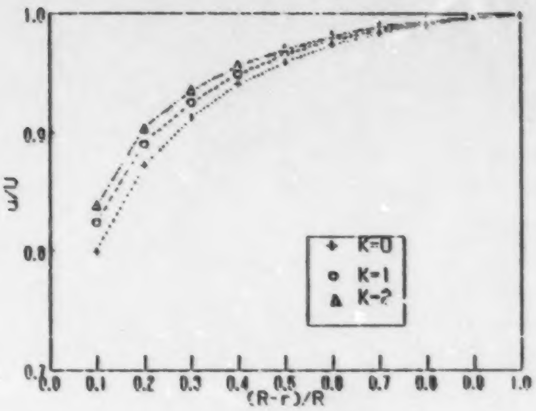

Fig. 2: Normalized Velocity Profiles as Functions of Radius

7. Mizushina, T., Hiromoto, W., Yoshida, T., Turbulent Pipe Flow of Dilute Polymer Solutions, J. Chem. Eng. Japan, Vol. 7, No. 3, pp. 162-167, 1974.

8. Madavan, N.K., Merkle, C.L., Deutsch, S., Numerical Investigations into the Mechanisms of Microbubble Drag Reduction, Trans. ASME, Vol. 107, pp. 370-377, 1985.

9. Eringen, A.C., Simple Microfluids, Int. J. Eng. Sci., Vol. 2, pp. 205-216, 1964.

10. Goren, Y., Norbury, J.F., Turbulent flow of Dilute Aqueous Polymer Solutions, Trans. ASME, December, pp. 814-822, 1967.

11. Van der Meulen, J.H.J., Friction Reduction and Degradation in Turbulent Flow of Dilute Polymer Solutions, Appl. Sci. Res., Vol. 29, pp. 161-174, 1974.

12. Eringen, A.C., Micropolar Fluids with Stretch, Int. J. Eng. Sci., Vol. 7, pp. 115-127, 1969.

THE MEASUREMENT OF WOOD FIBRE FLEXIBILITY

D.C.S. Kuhn[1], P. H. Oosthuizen[2] and P. Whiting[1]

[1] Abitibi-Price Inc. [2] Queen's University

ABSTRACT

An apparatus is being developed using a combination of numerical and experimental work to rapidly measure the wet fibre flexibility of a large sample of pulp. The method is based on the principle that when a fluid containing fibres flows on a curved path, the flow path of the fibres will depend on their flexibility. Past methods and existing methods for measuring fibre flexibility are reviewed in this paper.

The apparatus currently under development consists of a tank containing a dilute pulp suspension connected to a rectangular channel with a slot in its wall. The pulp suspension flows from the tank through the channel and some of the water, together with some of the fibres, flows out of the channel through the slot in the wall, the remaining water and fibres flow down the channel into a downstream collection tank. The fraction of the fibres that pass through the slot is a measure of the average flexibility of the fibres.

A two-dimensional numerical model has been developed to simulate the fluid flow within the channel and slot portion of the apparatus. Reynold numbers of between 100 and 500, non-dimensional slot widths of 0.025 to 0.1 and slot volume flow to entrance channel flow ratios of 0.025 to 0.2 have been considered.

INTRODUCTION

Wet fibre flexibility is an important parameter in determining the suitability of the pulp for the manufacture of paper. It determines the ability of fibres to deform and entangle during the consolidation process and thus affects floc formation, drainage characteristics and retention characteristics. Following the initial consolidation stage the degree of fibre entanglement affects the strength of the wet fibre network, and hence paper machine runnability. Also the degree of entanglement and floc formation during the consolidation process strongly affects the optical, surface and strength properties of the final paper product. Although fibre flexibility is recognized as an important fibre property, an accepted method for rapidly measuring the wet flexibility of a large sample does not exist.

This paper will discuss past methods for measuring fibre flexibility and a method currently being jointly developed by Abitibi-Price Research and the Heat Transfer Laboratory at Queen's University. The flexibility measurement apparatus under development consists of a channel through which a pulp suspension flows. The channel has a slot in its lower wall through which some of the fibres pass. The fraction of the fibres that pass through the slot will be largely dependent on flexibility and fibre length. Hence by measuring the fraction of the fibres passing through the slot, a measure of the average flexibility of the fibres is obtained. The apparatus is being developed using a combination of experimental and numerical work to determine flow rate values and geometric parameters that give the best results. This flexibility apparatus should provide a method for rapidly measuring the wet flexibility of a large sample of pulp.

EXISTING MEASUREMENT METHODS

A number of methods for determining fibre flexibility have been proposed in the past. These may be conveniently grouped into five categories: cantilever loading methods, simply supported beam loading methods, fibre deformation in a shear flow methods, conformability methods and screening methods.

Single Fibre Tests

The cantilever loading methods, simply supported beam loading methods and conformability methods are all single fibre test methods.

In cantilever loading methods, a fibre is supported as a cantilever and a bending load is applied, eg. see Fig. 1. The fibre flexibility is derived from bending beam theory:

$$F = \frac{1}{EI} = \frac{3v}{WL^3} \qquad (1)$$

where E = modulus of elasticity
I = moment of inertia
v = deflection of the free end
W = load applied to the fibre
L = length of the fibre

Seborg and Simmons (1941) used the hooked end of a quartz spiral spring to bend a dry fibre until the hook began to slip along the fibre. The deflection of the fibre and the expansion of the spring (i.e. applied force) were measured before slippage to determine the flexibility of the fibre. Samuelsson (1963) fixed a fibre to the wall of a channel through which water was flowing. The hydraulic drag force acting on the fibre caused it to deflect, and this deflection was measured using a microscope. In this case, of course, the load is applied along the full length of the fibre. Other methods used to apply a load on a fibre are by a torsion wire (Haugen and Young, 1969) and by a strong sonic vibration (Nethercut, 1957).

The cantilever loading methods suffer from a number of problems, including non random selection of fibres, minimum fibre length requirements, induced plastic deformation and, in particular, tediousness. These methods require the non random selection of "good" fibres, i.e. relatively long, unkinked and undamaged fibres. The results are sensitive to fibre surface irregularities, non uniform fibre cross sections, to rough handling and the methods tend to be time consuming and tedious. The selection of "good" fibres excludes a large portion of most mechanical pulps, hence the average flexibility of fibres tested will not be representative of the pulps. Nethercut (1957) argued that many of the methods exceeded the fibre plastic deformation limit, hence static flexibility analyses do not apply. The most serious problem is the tediousness and time consuming nature of these methods. Fibres of approximately 1 mm to 5 mm in length and of order 30 μm diameter must be individually and delicately clamped.

Tam Doo and Kerekes (1981) developed a simply supported beam loading method where the fibre is supported across a notched capillary tube and a hydrodynamic load is applied to the fibre by a flow through the tube. The fibre deflection is measured to determine fibre flexibility. Tam Doo and Kerekes's approach is limited by some of the same problems as the cantilever methods, however their method is partially automated and has weaker constraints on the type of fibre that can be tested.

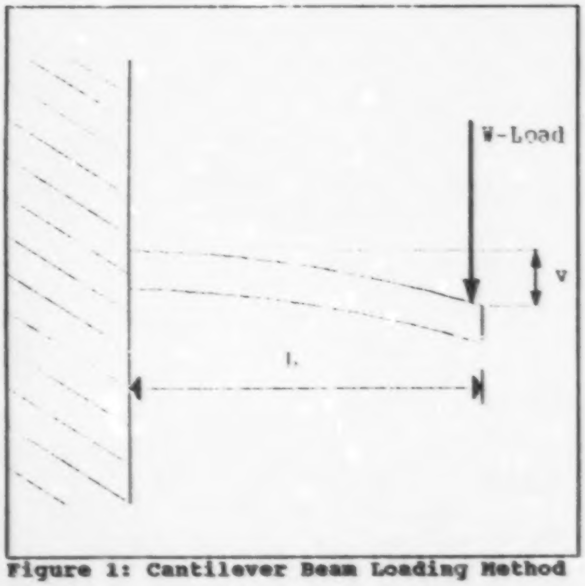

Figure 1: Cantilever Beam Loading Method

A number of conformability methods have been developed, including a method by Mohlin (1957). Here a wet standard hand sheet is pressed against a glass slide which has stainless steel wires attached to it and fibres are allowed to dry to the slide across the wires, see Fig. 2. The flexibility of a fibre crossing a wire is then determined from the distance between the contact point on the glass and the wire. This method, of course, determines the conformability of a fibre not its flexibility and the correlation between conformability and flexibility has not been established, conformability being influenced by the other fibre properties as well as flexibility making the results difficult to interpret (Jones, 1963; Elias, 1967).

Multi-Fibre Tests

The fibre deformation in a shear flow and screening methods are multi-fibre test methods. In fibre deformation in a shear flow methods, the fibres are suspended in a liquid flow field in which there is a strong shear. The shape of the fibres in this flow field is used to determine their flexibility. Robertson, Meindersma and Mason (1961), for example, suspended fibres in a liquid contained in a annulus between two coaxial cylinders, one of which rotated relative to the other, thus subjecting the liquid to a shear. The fibres were then classified into three groups according to the orbit they described in the flow, the form of this orbit depending on the fibre flexibility. The first group included fibres that rotated in the shear field but did not bend, the second group included fibres that were bent while rotating in the shear field, and the third and most flexible group included fibres that rolled on top of themselves in response to the shear field. The major disadvantage of this method is that it does not give a direct measure of flexibility but only allows the fibres to be classified into one of three flexibility groups.

Shallhorn and Karnis (1981) developed a screening method for measuring fibre flexibility. Here fibres of uniform length obtained using a Bauer-McNett classifier are screened, the fibres with higher flexibility passing more readily through the screen when a fixed pressure difference is maintained across the screen. This method does not provide a direct measurement of flexibility, a flexibility index being determined. The initial fibre length classification obtained using the Bauer-McNett classifier also gives a wide fibre length distribution and fractionates partially on the basis of flexibility and so influences the results obtained.

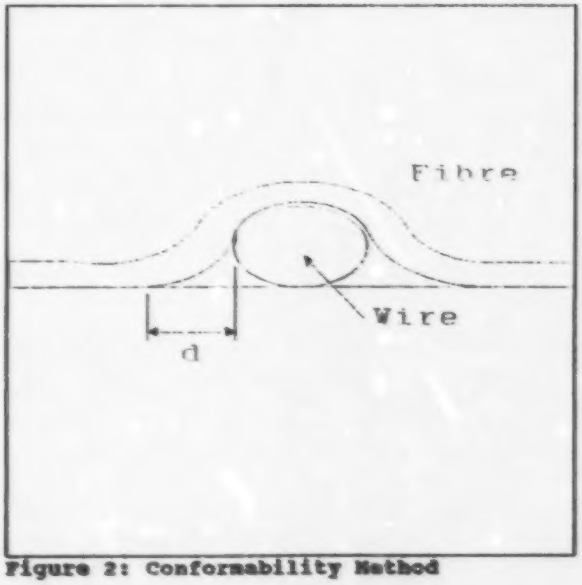

Figure 2: Conformability Method

BASIC CONCEPT

When a fluid containing fibres flows on a curved path, the flow path of the fibres will depend on their flexibility. A perfectly flexible fibre would conform to the flow path. This concept is being used in the developing of a single slot apparatus that will allow a relatively rapid description of the flexibility of a large number of fibres.

The working section of the flexibility measurement apparatus is shown in Figure 3. Basically, it consists of a bifurcation flow, i.e. a main channel flow with a portion of the flow leaving through a slot. Gooding (1986) observed that the fraction of fibres flowing out of a channel through a slot in a channel is dependent on the flexibility of the fibres. Also fibres in a simple shear flow will preferentially orientate along the axis of flow (Mason, 1950). Hence fibres flowing out of a channel through a slot will attempt to conform to the streamlines of the exiting fluid flow (see Figure 4). It is therefore expected that the more flexible the fibre the more able it will be to conform to the streamlines. In contrast, stiff fibres are not flexible enough to bend and flow through the slot, i.e. stiff fibres are unable to conform to the streamlines of the exiting flow.

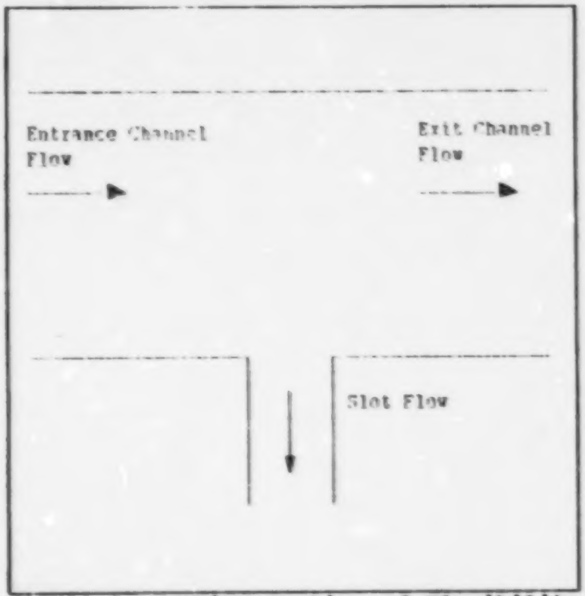

Figure 3: Working Section of Flexibility Measurement Device

FIBRE FLEXIBILITY CLASSIFIER

The flexibility apparatus under development at Abitibi-Price Research and the Heat Transfer Laboratory at Queen's University is shown in Figures 5 and 6. The apparatus consists of a tank containing a dilute pulp suspension connected to a rectangular channel of varying cross sectional area. The channel has a slot in its wall at some distance downstream of the channel inlet. The pulp suspension will flow from the tank through the channel and some of the water, together with some of the fibres, will flow out of the channel through the slot in the wall, the remaining water and fibres flowing down the channel into a downstream collection tank. Low flow rates are maintained to ensure a laminar flow situation, since a turbulent flow situation tends to destroy the preferred orientation (Mason, 1950).

The inlet and outlet tanks are 40 cm by 30 cm wide and 40 cm high, and the channel is centred on the 40 cm by 30 cm side of both tanks 8 cm from the bottom of the tanks. This size of tank was chosen to provide uniform inlet condition to the channel flow. A constant head is maintained in the channel by a flow inlet at the bottom of the inlet tank and an overflow exit set 26 cm from the bottom of the exit tank. The inlet flow is disturbed upon entering the inlet tank by an open ended flow distribution box. This is to reduce the chance of coherent structures and disturbance in the inlet flow to the inlet tank from being transferred to the channel flow. The inlet flow may be reduced to as low as 10 ml/s using a bypass valve.

The channel consists of two parts: an entrance channel which connects to the inlet tank and an exit channel with a slot in the wall which connects to the exit tank (see Figure 6). The entrance channel has a rounded inlet, a 4 cm by 2 cm cross sectional area and is 30 cm long. The channel is rounded to reduce the chance of flow instabilities developing at a sharp channel entrance. The exit channel is a converging section reduced from a 4 cm by 2 cm cross sectional area to a 2 cm by 1 cm cross sectional area at the exit to the exit tank. A channel with a varying cross sectional area was chosen since it has been observed that fibre alignment in the direction of flow is more prominent in accelerating flows (Moss and Bryant, 1938).

The slot is 50 cm from the inlet tank and 10 cm from the exit tank and is 0.5 mm wide. The slot discharge angle is swept back at 23° from the vertical, i.e. in the upstream direction. This will emphasize the fractionation of the fibres based on flexibility. A slot-accepts tank fits around the slot allowing the exit slot pressure to be controlled.

Varying the flow rates, slot size, slot discharge angle nad other geometric parameters of the apparatus will change the flow patterns within the channel. Hence the minimum fibre flexibility required for a fibre to flow through the slot may be varied.

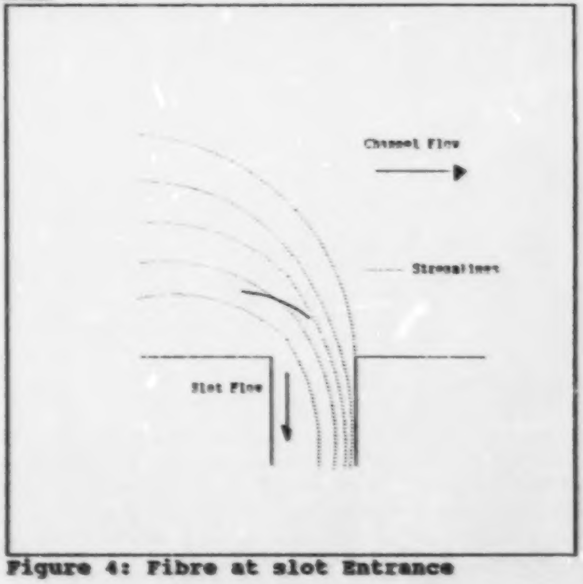

Figure 4: Fibre at Slot Entrance

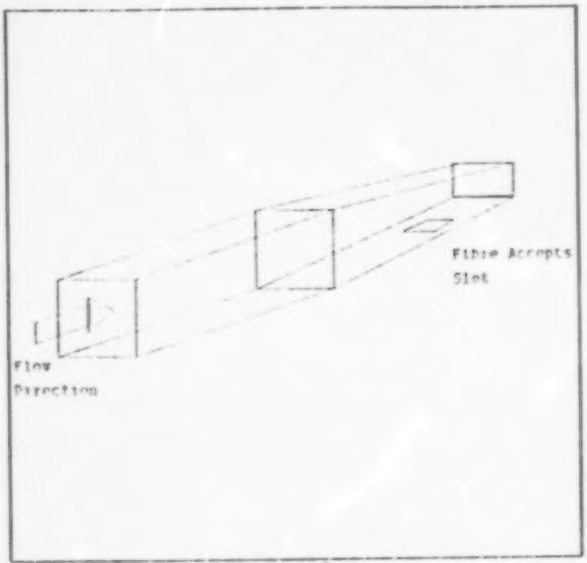

Figure 5: Channel Section

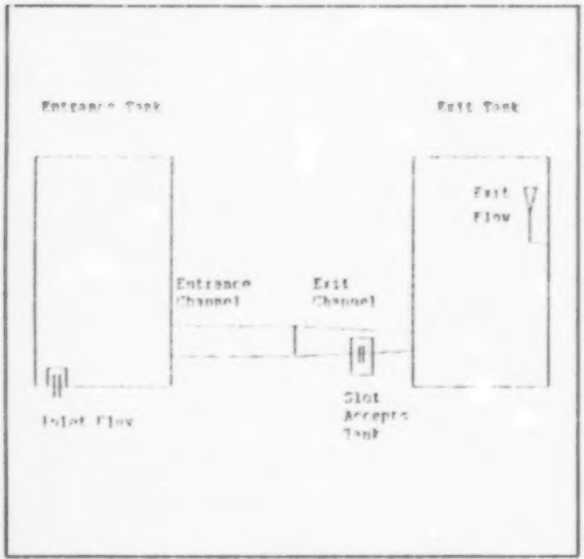

Figure 6: Flexibility Classifier

FIBRE LENGTH

The fraction of the fibres that pass through the slot is not only a function of fibre flexibility but also fibre length. Hence, the fibre length distribution of the fibre accepts must be know to accurately determine fibre flexibility. A Kajaani FS-100 fibre length analyzer will, therefore be used to determine the fibre length distribution of the fibre accepts.

OBSERVED FLOW PHENOMENA

Some initial tests were conducted to establish that the flexibility classifier fractionates fibres based on fibre flexibility. The motion of TMP fibres was observed for a main channel flow rate of 1 l/s. The slot flow volume to main channel flow volume ratio was approximately 0.3, i.e. the flow rate into the slot was 0.3 l/s. A very dilute pulp suspension was introduced into the entrance tank (see Figure 6), little fibre to fibre interaction was observed.

Two main fibre deformation and flow patterns were observed near the slot, only fibres in the flow stream exiting through the slot were considered here. The first flow pattern is illustrated in Figure 7. Here, the fibres begin to bend and accelerate just upstream of the slot. The fibres then continue to bend and move into the slot. As the fibres enter the slot they straighten and align themselves with the exit flow. A stiff fibre reacts very differently at the slot entrance as illustrated in Figure 8. Here, as the fibres nears the slot they bend, but less than more flexible fibres, and begin to enter the slot. However, as the fibres enters the slot the top of the fibres begin to be acted upon by the main channel flow. This flow causes the top of the fibres to accelerate downstream in the main channel direction. The fibres pivots, and are pulled out of the slot and downstream towards the exit tank.

Fibre alignment in the channel was observed. As the fibre entered the converging channel (exit section, see Figure 6), more fibre alignment with the main channel flow was observed. Further fibre alignment was observed close to the slot entrance, where the flow accelerates to exit through the slot.

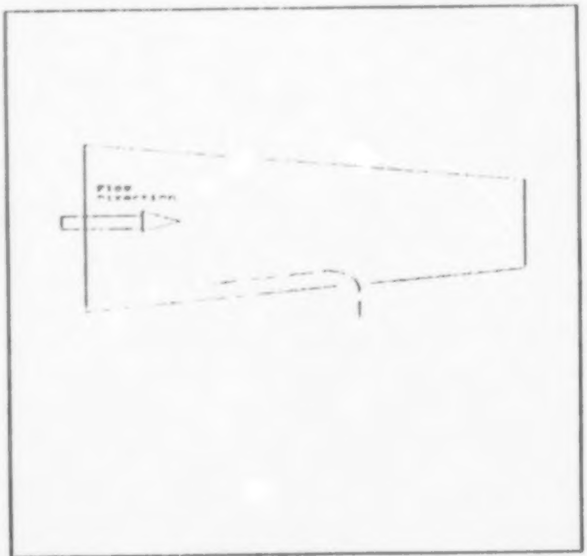

Figure 7: Accepted Fibre

NUMERICAL FLOW SIMULATION

A model of water flow from the inlet tank through the channel and the slot has been developed, the finite element method being used. The flow conditions considered are such that the flow can be assumed to be steady and laminar.

The study is based on the two-dimensional Navier-Stokes and continuity equations. The equations have been solved in a non-dimensional stream function - vorticity form, the equations being non-dimensionalized in terms of the channel height at the slot and the mean channel velocity at the slot. Hence, the flow and boundary conditions include: the Reynolds number at the slot, Re, the slot volume flow to entrance channel volume flow ratio, channel length, channel entrance height to exit height ratio, slot width, distance to slot from channel entrance and slot angle. The flow at the channel entrance and exit and the flow at the slot exit are assumed fully developed.

A rectangular channel with a slot perpendicular to the channel flow has been considered, and Reynold numbers of between 100 and 500, non-dimensional slot widths of 0.025 to 0.1 and slot volume flow to entrance channel flow ratios of 0.025 to 0.2.

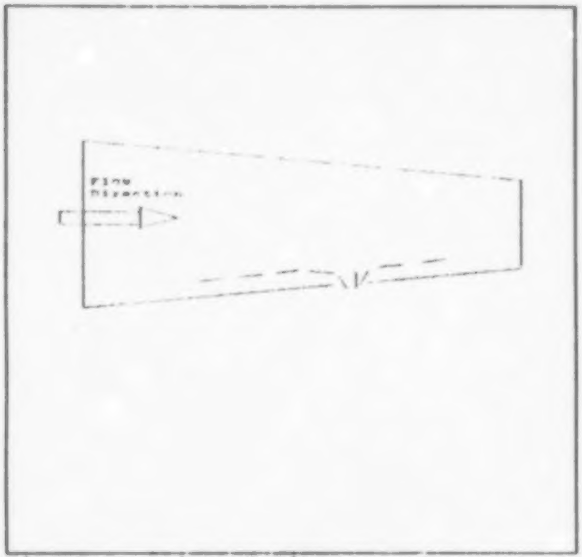

Figure 8: Rejected Fibre

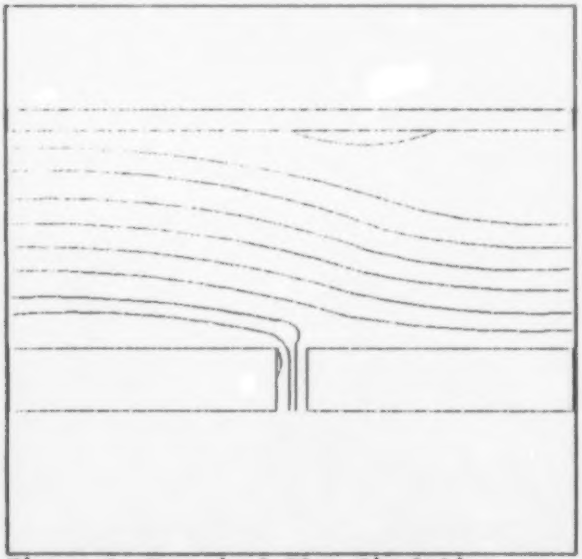

Figure 9: Numerical Flow Simulation

A representative flow field is given in Figure 9. A rectangular channel was considered with a slot width 0.05 of the channel width, a slot perpendicular to the channel and far downstream from the channel entrance, Reynolds number of 300, slot volume flow rate to channel flow rate ratio of 0.025. A number of interesting flow phenomena occur in bifurcation flow including the two separation regions that can be seen in Figure 9. The separation zone on the top surface of the channel is due to the large portion of the flow exiting through the sot, while the separation zone in the slot on the downstream facing wall is due to a sharp change in flow direction. This separation zone will effectively reduce the slot width thereby requiring the fibres to be more flexible to exit through the slot.

A model of a fibre flowing in the flow field is currently being developed. In the initial model it will be assumed that the fibres have the same density as the fluid and inertial effects are negligible. The flow field and fibre motion will be solved separately.

CONCLUSIONS

A flexibility classification device is being developed using a combination of experimental and numerical work. A single slot screen apparatus has been developed to fractionate fibres on the principle that a fibre in a curved flow field will attempt to follow the flow stream, its ability to follow the flow stream being dependent on the fibre's flexibility. Initial flow test show that fibres must bend to enter the slot from the main channel flow.

A numerical model of the flow situation has been developed based on the finite element method. This model has predicted two separation zones at the slot area, one in the slot on the downstream facing wall and the other on the top channel wall above the slot. These separation zones will effect the fibre fractionation.

Initial numerical and experimental results suggest that the device being developed will provide a rapid method for measuring the wet flexibility of a large sample of pulp.

ACKNOWLEDGEMENTS

The portion of this work conducted at Queen's University was supported by the Natural Sciences and Engineering Council of Canada under the Research Partnerships Program. The portion of this worked conducted at the Central Research Division of Abitibi-Price Inc. was funded by Abitibi-Price Inc.

REFERENCES

Elias, T.C. 1967, Investigation of the Compressive Response of Ideal Unbonded Fibrous Structures, TAPPI , Vol. 50, No. 3, p. 125.

Gooding, R.W. 1986, The Passage of Fibres Through Slots in Pulp Screens, M.Sc. thesis, University of British Colombia, Vancouver, British Colombia.

Haugen, P. and Young, J.H. 1969, in The Physics and Chemistry of Wood Pulp Fibers , TAPPI STAP No. 8, p. 542, New York.

Jones, R.L. 1963, The Effect of Fiber Structural Properties on Compression Response of Fiber Beds, TAPPI , Vol. 46, No. 1, p. 20.

Mason, S.G. 1950, The Motion of Fibres in Flowing Liquids, Pulp and Paper Magazine of Canada , Vol. 51, No. 3, p. 93.

Mohlin, U.-B. 1975, Cellulose Fibre Bonding: Part 5. Conformability of Pulp Fibres, Svensk Papperstidning , Vol. 78, No. 11, p. 412.

Moss, L.A. and Bryant, E.O. 1938, Photographic Study of the Motion of Fibers and Water in Flowing Fiber Suspensions, TAPPI Technical Association Papers, Series XXI , p. 250.

Nethercut, P.E. 1957, A Fundamental Study of the Softening Mechanism of Paper Plasticizerse, TAPPI , Vol. 40, No. 1, p. 39.

Robertson, A.A., Meindersma, E. and Mason, S.G. 1961, The Measurement of Fibre Flexibility, Pulp and Paper Magazine of Canada , Vol. 62, No. 1, p. T3.

Samuelsson, L.-G. 1963, Measurement of the Stiffness of Fibers, Svensk Papperstidning , Vol. 66, No. 15, p. 541.

Seborg, C.O. and Simmons, F.A. 1941, Measurement of the Stiffness in Bending of Single Fibers, Paper Trade Journal , Vol. 113, p. 225.

Shallhorn, P.M. and Karnis, A. 1981, A Rapid Method for Measuring Wet Fibre Flexibility, Trans. Tech. Sec. CPPA, Vol. 7, No. 4, p. TR69.

Tam Doo, P.A. and Kerekes, R.J. 1981, A Method to Measure Fiber Flexibility, TAPPI , Vol. 64, No. 3, p. 113.

HEAT TRANSFER AND FLUID-FLOW CHARACTERISTICS OF ARRAYS OF IMPINGING, ROUND AIR JETS

P. HRYCAK, D.M. KAYA, S.SETHI, and C. WEI

New Jersey Institute of Technology
Newark, New Jersey 07102, U.S.A.

ABSTRACT

Heat transfer and fluid flow patterns of square arrays of submerged, turbulent, round air jets, impinging normally on a flat plate, have been studied experimentally. Jets issued from an array of five to nine nozzles, 3.18 mm to 9.52 mm in diameter. The nozzle exit Reynolds numbers ranged from 14 000 to 54 000, while the ratio of the nozzle-to-the test plate distance to the nozzle diameter was varied from three to fifteen. The resulting fluid-flow patterns have been studied systematically, since local heat transfer intensities are determined by the interaction between jet fluids and the target plate. The present investigation has been carried out as a continuation of earlier work done with a single-jet nozzle and rows of round nozzles, and was focussed here on the interaction between the centrally located nozzle in the array and the jets at the periphery. The experiments carried out indicate that, by using properly clusters of jets, a great enhancement of the average heat transfer intensity can be achieved, in comparison with the single jet results. Eventually, these results can be optimized, with respect to nozzle-to-nozzle and nozzle-to-target plate spacings.

INTRODUCTION

Among the first authors concerned with heat transfer from arrays of jets (without considering specifically the effects of cross-flow) we find Gardon and Cobonpue [1] and Livingood and Hrycak [2], and, more recently, Behbahani and Goldstein [3]. A related topic is heat transfer from a row of jets (cf. Koopman and Sparrow [4] and Hrycak [5]). Sethi [6] investigated systematically the fluid flow patterns generated by arrays of impinging jets, and Kaya [7] the resulting heat transfer. Earlier results on heat transfer from impinging jets have been summarized, e.g., by Martin [8],Hrycak [9]. It is seen that there are still many factors essential for successful application of impinging jets arrayed in clusters that have not been fully clarified. This is the information on the extent of area of maximum heat transfer intensity at the stagnation point, and the effect of interference between the adjacent jets due to the mutual "crowding out", related to the inability to draw freely on supply of the ambient air, that characterizes a typical single developing jet.

Of concern for multi-jet systems is the ability to get rid of "spent" air that becomes useless as heat transfer agent and must be efficiently ducted away. Thus, it appeared interesting to see to what extent the performance of a single jet impinging on a flat surface can differ from the characteristics of a jet performing as a part of an array of jets. Since in typical applications, substantial, finite areas are to be cooled/heated by arrays of jets, the study of the effects of arraying of jets has been taken up here as the subject of a separate, experimental and analytical investigation. The general experimental test-set up and the instrumented heat transfer plate are shown in Figs. 1 and 2. The nozzles were arranged symmetrically one diameter apart ($C_n/D = 2$), to three diameters apart ($C_n/D = 5$); they all could be reproduced with the same plenum chamber to which an exchangeable orifice plate with the proper number of holes and C_n/D could be attached. The clusters of jets, with one jet located at the center, were located at the center of symmetry of the heat transfer plate by means of a suitable centering device. This appeared to be the simplest way to test the effects of two-dimensional arraying of jets on the particular jet located at the center of cluster. Flow from the individual nozzles was equalized by means of internal baffles and screens in the common plenum chamber. A grease imprint of a jet cluster is seen in Fig. 3. A rectangular ridge has formed in the center of cluster, around the center jet, on the lucite plate used in fluid flow measurements, those of velocity distribution and velocity decay along the centerline and in the wall-jet zone (cf. Fig. 4), from which the wall friction coefficients were then calculated by Clauser's method [10]. From the magnitude of the wall-friction coefficient, and from the intensity of the maximum wall-jet velocity decay, it was possible to draw conclusions about heat transfer intensity at the wall in question.

EXPERIMENTAL TEST SET-UP AND PROCEDURE

The experiment was to be carried out in the steady state, requiring that all stay constant during data acquisition. Steam, condensing at the atmospheric pressure was used as the heating medium, while, e.g., the following readings were taken: 1. Barometric pressure and all pressure differentials of interest, 2. Rotameter setting, 3. Room temperature and all temperatures of interest, including thirty-plus thermocouple readings for the calorimeters, and the water, steam, and the plenum chamber temperature, obtained with calibrated copper-constantan thermocouples, on K-5 L&N potentiometer, with an error margin of less than 0.3 K.

At the heart of the present investigation lies the effectiveness of the heat flux-measuring devices used, the "calorimeters" (cf. Fig. 3), precision -turned cylinders made of metal of a well-known thermal conductivity with two small holes drilled in to accommodate two thermocouples [11], to measure T (top) and T(bottom) at a distance N from each other. The distance from the bottom hole to the surface of calorimeter is M. Temperature distribution in the calorimeter will be linear, if the effect of the holes is small ($D_{hole} \ll D_{cyl.}$); the thermocouple lead conducting error is eliminated if fine gage wire is used, carried at the right angle to heat flux vector. Then the Nusselt number can be calculated directly from the expression below:

$$Nu_D = hD/k = \frac{k_{cal} D}{k_{air} N} \left[\frac{T_b - T_\infty}{T_b - T_t} - \frac{M}{N}\right]^{-1} \qquad (1)$$

Here, k_{cal} is to be evaluated at mean temperature, $(T_t+T_b)/2$, and k_{air} at the mean film temperature.

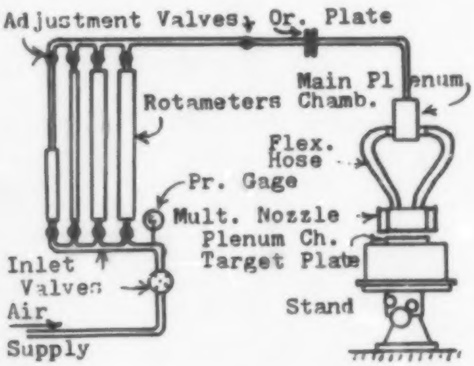

Fig. 1 Experimental Test Set-Up

As T_∞ may well serve the plenum chamber temperature. Also, the calorimeter is insulated against lateral heat leaks and any distortion of the measured heat transfer in a fashion similar to a guarded hot plate and does not require any additional calibration in principle. Some details are shown in Fig. 3. The distribution of a total of fourteen calorimeters is shown in Fig. 2 below.

Fig.2 Heat Transfer Plate during Overhaul

FLUID FLOW INTERACTIONS

One of the primary concerns in investigation of fluid-flow patterns in arrays of jets is the interaction between the maximum nozzle velocity, u_{oc}, and the maximum wall-jet velocity, V_m. It is interesting to note that in the single-nozzle generated wall jet [12], we have, for r = distance from the center of symmetry, and $\alpha = 1.12$ (cf. Fig. 4)

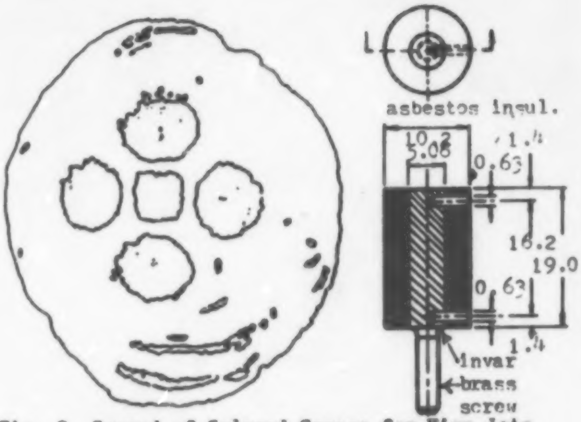

Fig. 3 Spread of Colored Grease for Five Jets Calorimeter Detail

$$V_m/u_{oc} = 1.4\,(D/r)^\alpha \qquad (2)$$

while for the center jet of a multiple jet cluster [6] eq. (2) still applies, only the exponent α changes to 1.162; in the radial fan jet, resulting from collision of two axially opposing jets of equal strength, $V_m = K(D/r)$. Therefore, we can expect $\alpha > 1$ to be indicator of wall friction. Thus, in the multiple jet, the effect of wall friction is somewhat larger than in a single-jet generated wall jet, which can be expected to lead to some improvement in heat transfer. Actual wall-jet velocity and temperature profiles can be deduced from a similar argument.

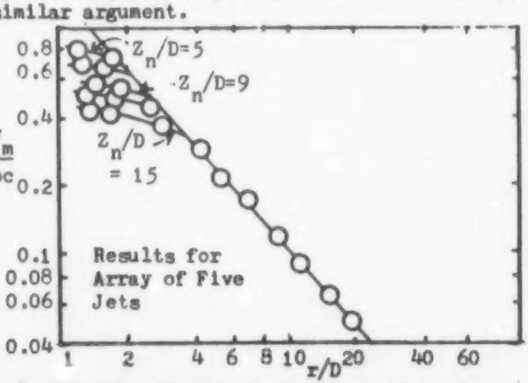

Fig. 4 Maximum Velocity Decay along Flat Plate

Some additional information on the behavior of impinging jets may be obtained through analysis employing the concept of mixing length, ℓ, for turbulent flow. For a fan-jet of initial diameter D, a half-width $b = Br$, $\ell = \beta b$, $V_m = K(D/r)$, B, β, and K being suitable constants, and a similarity variable $\Omega = z/b$, where the local radial velocity is approximated as $v = V_m f(\Omega)$, the momentum equation becomes

$$w\partial v/\partial z + v\,\partial v/\partial r = -2\,\beta^2 b^2\,\partial v/\partial z\;\partial^2 v/\partial z^2 \qquad (3)$$

Since $w \ll V_m$, the first term in eq. (3) may be neglected, and it may be transformed into an integrable combination, if we also let $v\partial v/\partial r \approx V_m \partial v/\partial r$:

$$f + \Omega f' = 2\,(\beta^2/B)\,f'\,f'' \qquad (4)$$

with the first integral

$\Omega f = (\beta^2/B)\, f'^2 + C_1$; because at $\Omega = 0$, $f' = 0$, C_1 is also zero. The second integration yields

$f^{\frac{1}{2}} = B^{\frac{1}{2}}/(3\beta)\, \Omega^{3/2} + C_2$; at $\Omega = 1$, $f = 0$, and $C_2 = -B^{\frac{1}{2}}/(3\beta)$. As β is a free constant, $\beta = B^{\frac{1}{2}}/3$, and

$$v = K(D/r)\,(1 - \Omega^{3/2})^2 \tag{5}$$

Equation (5) is very useful in a variety of problems related to jets, and in particular, it describes very well the velocity distribution in the outer layer of a radial wall jet, where the half-width changes to $b + \delta$. b becomes now the outer boundary layer, and δ the inner boundary layer, and $\Omega = (z - \delta)/b$; also, $V_m = K(D/r)^{\alpha}$, and $b = Br^{\lambda}$. Here, $1 < \alpha < 1.16$, and $0.9 < \lambda < 1$, represent the effects of wall friction. If, additionally, we let $\ell = \beta b^N$, where $2N = (3\alpha - 1)/\lambda$, it may be shown that eq. (5) again results, with Ω unchanged, but D/r term appears now as $(D/r)^{\alpha}$. It is also useful to realize that $\alpha = f(n)$, n being here the exponent in the expression for the inner boundary-layer wall-jet velocity profile, $v = V_m(z/\delta)^{1/n}$. The values of n, determined by Sethi [6] are not larger than those mentioned in Ref. 12. Also, Sethi's values of the wall friction coefficient are similar to those available in the literature [13], generated by a single jet, and his stagnation point flow measurements do not appear to be much influenced by the presence of the other jets.

Therefore, it appears that the main reason for the very substantial contribution that multiple impinging jets, arranged in an array make to the average heat transfer, lies in the effect of superposition. As the individual jets (at least in the arrays investigated) affect relatively little each other, their total contribution may be seen to consist of two parts. (1) Each jet in the array extends the area of high heat flux near the stagnation point and its immediate neighborhood, to additional four to eight locations, and (2), the entire mass flow is enhanced five to nine times, depending on the number of jets in the array. For a plate of finite dimensions (as the one used in the present experiments), this translates into an improvement of the average heat transfer coefficients of up to fifty percent, for clusters consisting of five jets. Experiments on heat transfer from nine-jet clusters have been carried out only partially. Another interesting flow parameter that has been found of influence on heat transfer from impinging jets is the theoretical dimensionless potential core length [1,2,11,12]. Sethi [6] found it to be $C \approx 3$, vs. $C \approx 6.5$ mentioned in [1,12]. A shorter C indicates a higher level of turbulence in the mixing cone of the center jet in the cluster, and indicates also the approximate location of of the peak of heat flux intensity with respect to the orifice plate here.

STAGNATION POINT HEAT TRANSFER

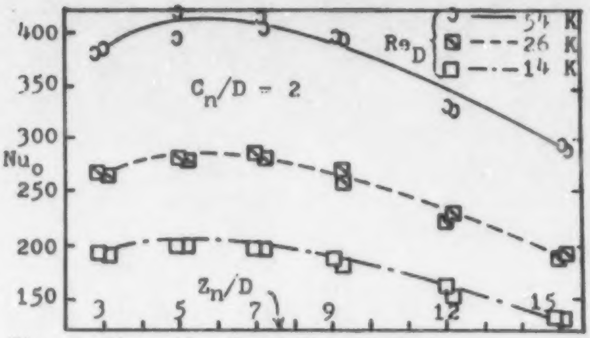

Fig. 5 Stagnation Point Nusselt Number as a Function of Nozzle-to-Plate Distance, Z_n/D, and of Nozzle Reynolds Number

In this section, highlights of the present investigation are described. A few additional details may be found in Refs. 6 and 7. Characteristics of heat transfer from impinging jets will be analyzed by considering the order of magnitude of various pertinent parameters in their effect on heat transfer coefficients and the results of existing theory [10]. Thus, for the local value of the Nusselt number, Nu, one can expect a relation involving Re_D, Pr, and n characteristic linear dimensions, or

$$Nu_D = K\, Re_D^a\, Pr^b (Z_n/D)^c (D/D_{pl})^d (C_n/D)^e \ldots (L/D)^n \tag{6}$$

where K, a, b, c, etc., are ordinarily considered as constants valid for suitably restricted ranges of the independent variables; e.g., $a = 0.5$ has a justification in the boundary-layer theory [11,10], and $b = 0.4$ is justified experimentally and theoretically for stagnation flow [2,11], while $a = 0.7$ and $b = 1/3$ are in the same fashion found applicable in the the turbulent boundary-layer flow.

When Nusselt number is plotted vs. Z_n/D at the stagnation point (cf. Fig. 5) it is seen that Nu at first rises as Z_n/D is increased up to ≈ 5, and then begins to decrease. Similar trends were reported in the earlier literature [1,2,11]. Centerline velocity of the jet remains constant within the potential core (here ≈ 3), but starts to decay outside of it. The resulting effect of turbulence and velocity of the center jet in the first place is to increase the stagnation point Nusselt number with increasing Z_n/D within the potential core, and to reduce the same with increasing Z_n/D outside of it. Also, stagnation point heat transfer was found to increase for larger diameter nozzles, as an explicit function of the diameter size. This may also be found in the literature [1,9,11] and may be justified by dimensional analysis as, e.g., $(D/D_o)^n$ according to eq. (6). where D is the variable diameter, and D_o the fixed part of the experimental test set-up, with $n > 0$ for $D > D_o$. Therefore, based on the experimental results outlined above (cf. also [5, 11], we can write for the stagnation point the following relation, valid for $3 \leq Z_n/D \leq 5$, $Nu_o = hD/k$,

$$Nu_o = 1.61\, Re_D^{0.5} Pr^{0.4} (Z_n/D)^{0.14} (D/D_o)^{0.4} F(C_n/D) \tag{7}$$

where $D_o = 6.35$ mm. In the text below, $Z_n/D = \underline{Z}$, $C_n/D = \underline{C}$. Equation (7) is based on data from Fig. 6; as the data were all normalized for the nominal $Re_D = 14K$, by scaling from 26/35/54K, some horizontal spread of the data in Fig. 6 does not indicate any deviation from the nominal Z_n/D value, but illustrates coexistence of multiple data points with the same abscissa, but different ordinates. The same remarks also apply for Fig. 7 below.

In eq. (7), for D = 9.52 mm, $\underline{C}$-dependence may be shown by $F = 1.0643\ \underline{C}^{-0.09}$, and for D = 6.35 mm by $F = 0.943\ \underline{C}^{0.08}$. Outside of the potential core for $\underline{Z} \geq 7$, and D = 9.52 mm, the applicable relation is

$$Nu_o = 2.842\ Re_D^{0.5755} Pr^{0.4} \underline{Z}^{-0.545} (D/D_o)^{0.25} F \quad (8)$$

with $F = 0.953\ \underline{C}^{0.07}$, whereas for D = 6.35 mm, there results the expression, valid for $\underline{Z} > 5$,

$$Nu_o = 0.984\ Re_D^{0.5755} Pr^{0.4} (D/D_o)^{0.25} (1.155 - 0.031 \underline{Z}) F \quad (9)$$

with $F = 0.946\ \underline{C}^{0.07}$; note here a linear $\underline{Z}$ dependence. For D = 3.18 mm, for $\underline{Z} \leq 7$, the formula is

$$Nu_o = 1.47\ Re_D^{0.5} Pr^{0.4} \quad (10)$$

and for $\underline{Z} > 7$, we have, as an average for all $\underline{C}$'s,

$$Nu_o = 4.52\ Re_D^{0.5} Pr^{0.4}, \pm 10\ \% \quad (11)$$

From the above relations that describe the experimental results shown in Fig. 6, we see as characteristic features of heat transfer at the stagnation point: the dependence on $Re^{\frac{1}{2}}$ power, and on $Pr^{0.4}$ power, both supported by theory [10,11]. The effect of dimensionless orifice-to-plate spacing, $\underline{Z}$, is expressed either by a power relationship, of the $\underline{Z}^n$ type, or by a linear relationship, like $a + b\underline{Z}$. The effect of dimensionless orifice-to-orifice spacing is complex and difficult to describe by simple power-law expressions. Therefore, Nusselt number $\underline{C}$-dependence here is acknowledged by terms like $F = K\ \underline{C}^n$, wherever an appropriate distinction of this type could be made. For $\underline{Z} > 5$, the exponent of the Reynolds number, 0.5755, indicates already the beginning of turbulent flow regime even at the stagnation point itself.

Correlations above show Nu_o a fairly strong function of Re_D and D/D_o, but a rather weak function of $\underline{Z}$ and $\underline{C}$, for $3 < \underline{Z} < 5$, and $2 < \underline{C} < 5$ at least. As D is here an experimental variable, scaling with $D_o = 6.35$ mm appeared appropriate. Because of the "tunneling" problem with 3.18 mm dia. orifice (flow constricted to a narrow space between the bottom of the plenum chamber and the target plate), it had to be treated separately. At the stagnation point there appears to be a unique combination of highly turbulent flow in the impinging jet stream, and a laminar sublayer at the target plate. The theoretical solution according to Sibulkin (cf. [10,11]) yields results that are nearly 45 % too low, as only laminar heat transfer is considered. The highest Reynolds number, for D=9.52 mm, obtained with the present set up was 35 000 (35K), for five jets in array. Some experiments were carried out, for D = 3.18 mm, with nine-jet arrays. Also, most experiments with this diameter were carried out with a reduced-diameter plenum chamber: from the original dia. of 237 mm to 68 mm, to eliminate tunneling flow.

AVERAGE NUSSELT NUMBER

Average Nusselt numbers were calculated by subdividing the plate into six segments centered around the embedded calorimeters. The center segment had one, second and third had two, and the remaining segments had three heat-flux measuring calorimeters each, located in their midpoints. To calculate the average Nusselt number, the following formula was used

$$\overline{Nu} = \overline{h}D/k' \quad (12)$$

where $\overline{h}$ = average heat transfer coefficient for the entire surface, and k' = thermal conductivity of air at mean film temperature, $\overline{T} = (T_{ch} + T_s)/2$, for T_s= surface temperature of individual plate segments. The interaction between jets occurs along the Zn distance, and is also a function of the Reynolds number. It is essentially a mixing process that generates a great deal of turbulence, which has an appreciable effect on heat transfer rates. The air from the jet at the center picks up heat as it moves outward from the stagnation point. The temperature of this air is affected by turbulent mixing with the relatively cold air from the screening jets. It is not possible to determine accurately the actual temperature of this air experimentally due to the complexity of the local turbulence. Therefore, the area-averaged Nusselt number was calculated instead, based on the air temperature in the plenum chamber, T_{ch}, rather than the actual local temperature of air which varied along the heat transfer surface. Since, as a matter of fact, it is the actual local temperature difference that is instrumental in forced convection heat transfer, local values of Nusselt numbers would be somewhat different for other experimental arrangements. It is believed, however, that the present approach gives results that are representative, and at the same time conservative enough for practical applications.

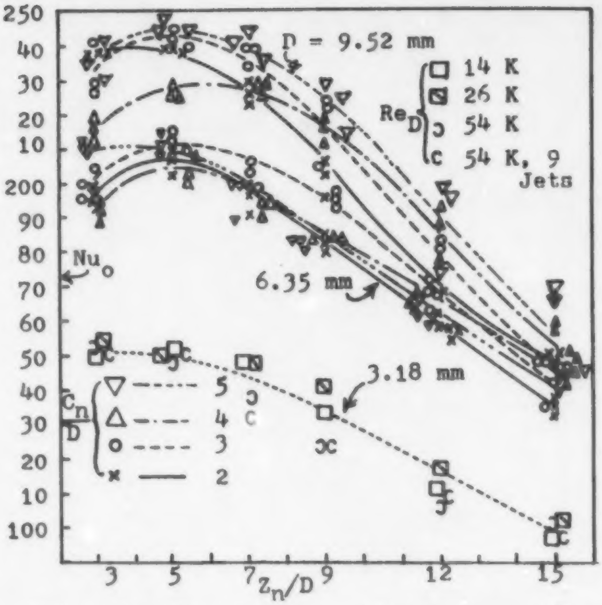

Fig. 7 Stagnation Point Nusselt Number vs. Z_n/D

The experimental data for the average Nusselt number, $\overline{Nu}$, are plotted in Fig. 7. They are well correlated by the expression (for $\underline{Z} < 7$)

$$\overline{Nu} = 5.084\ Re_D^{0.7} Pr^{1/3} (D/D_{pl})^{1.226} F \quad (13)$$

where for D = 9.52 mm, $F = 1.012\ \underline{C}^{-0.03}$, and for D = 6.35 mm, $F = 0.946\ \underline{C}^{0.08}$. For $\underline{Z} \geq 7$, D=9.52 mm,

$$\overline{Nu} = 5.284\ Re_D^{0.7} Pr^{1/3} (1.19 - 0.027\ \underline{Z}) (D/D_{pl})^{1.226} F \quad (14)$$

with $F = 1.082\ \underline{C}^{-0.055}$, while for D = 6.35 mm, eq. (14) still applies, but $F = 1.18\ \underline{C}^{-0.08}$.

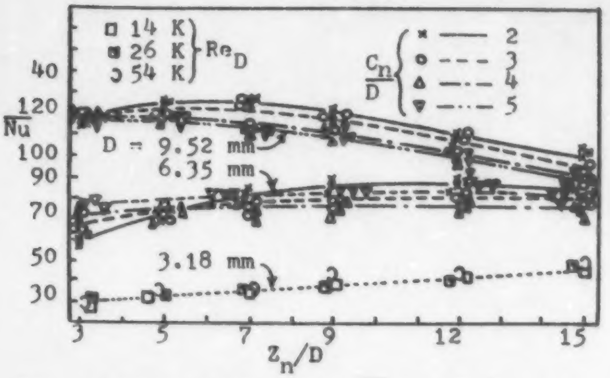

Fig. 7 Average Nusselt Number $\overline{Nu}$ vs. Z_n/D

For D = 3.18 mm, a relation valid for $3 \leq \underline{Z} \leq 15$ is the formula

$$\overline{Nu} = 17.3\, Re_n^{0.58} Pr^{1/3}(0.858 + 0.047\,\underline{Z})\left(\frac{D}{D_{pl}}\right)^{1.278} \quad (15)$$

that represents an average, valid for all $\underline{C}$'s here. In Fig. 7, data for 26K/35K/54K Reynolds numbers have been reduced to Re_D = 14 K by scaling to 0.7 power (D = 9.52 and 6.35 mm), and 0.58 power (D=3.18 mm). In eq. (13) and (14), the term $Pr^{1/3}$ is taken over from the turbulent boundary-layer theory [10]. Also, the power of the Reynolds number, 0.7, is actually lower than the corresponding power, 0.8, for turbulent heat transfer on a flat plate [10]. One has to consider that in the case of an impinging jet, we start with $Re^{\frac{1}{2}}$ at the stagnation point, and then the power of the Reynolds number gradually increases, till an average of 0.7 is built up.

The exponent of the nozzle Reynolds number here is identical to that obtained for a single jet in Ref. 11, and is very nearly the average of the results for arrays of jets by Behbahani and Goldstein [3], a = 0.78, and a = 0.625 by Gardon and Cobonpue [1].

It is interesting to note that the experimental relation for D = 6.35 mm shows no noticeable $\underline{Z}$-dependence. Consequently, for D = 6.35 mm eq. (12) is valid for the entire range of $3 \leq \underline{Z} \leq 15$ here investigated. As an explanation for this phenomenon, one should perhaps consider here again the effect of the bottom of the plenum chamber (the orifice plate here) on the overall heat transfer on the heat transfer plate. Evidently, the flow becomes more channel-like for the relatively small absolute Z_n values associated with smaller diameter nozzles. Actually, for D = 3.18 mm, $\overline{Nu}$ values measured were even smaller than those obtained previously with a single jet nozzle (cf. Datta [14]) of the tube type, described in Ref. 11. In Fig. 7, a few data points are shown, for comparison, for D = 3.18. Equations (13) and (14) show dependence on the plate diameter D_{pl} = 1.54mm here, in the form $(D/D_{pl})^{1.226}$, which is justified by eq. (6), as D_{pl} is a fixed parameter, and D the experimental variable. Similar dependence of $\overline{Nu}$ on D/D_{pl} has been observed earlier in Refs. 5 and 11, and is the natural result of integration over the entire plate area, $\pi D_{pl}^2/4$.

As expected, the average heat transfer from arrays of jets rises with the Reynolds number faster than heat transfer at the stagnation point (cf. Fig. 6 here). The effect of arraying, as expressed by the power of $\underline{C}$, shows a similar tendency. In Reference 2, results of six earlier investigators of arrays of jets have been compared. After extrapolation to the range of Re_D used in this work, they are summarised in Table 1 below. It is seen from Table 1 that the results of the present measurements are realistic. A direct comparison is not always possible, because of a variety of ways the individual authors chose to array their jets and to represent their data, however.

Table 1 Average Heat Transfer From Arrays of Jets

	$Re_D \times 10^{-3}$	14	26	54	67
$\overline{Nu}_D$	high	95	150	290	350
"	average	65	105	190	260
"	low	46	64	135	160
"	this work*	95	150	245	284

* Results represent an average for D = 6.35 and 9.52 mm, and are extrapolated to the required Re_D when needed. The present orifice plate: 273x6.35 mm

Figure 8 shows the radial variation of the local heat transfer coefficient due to multiple jets, and shows also, for the sake of comparison, corresponding results for a single jet. It is seen that the screening jet produced a secondary maximum of heat transfer intensity several diameters away from the center of plate. This in contrast to the behavior of a single jet that, with exception for a small secondary maximum near r = 0, for small $\underline{Z}$ values (not shown in Fig. 8), shows a uniform decrease with r. As an increase in $\underline{C}$ would tend to spread the area of high heat transfer intensity over a larger area, $\overline{Nu}$ is expected to correlate negatively with a power of $\underline{C}$. This can be seen from eqs. (13) and (14), and may be associated with high, but reasonably uniform heat transfer intensity over the plate. Similarly, we can expect within the limits of the potential core, only a small dependence of the average results on $\underline{Z}$, which is going to become much more pronounced outside of the potential core, where the original jet velocity is decreasing. Thus, it appears that average heat transfer from array of five jets can be, in most respects, predicted from the behavior of its single jet components in a qualitative fashion. Yet the final results, by showing an improvement in heat transfer intensity of the order of only 20 to 50 %,

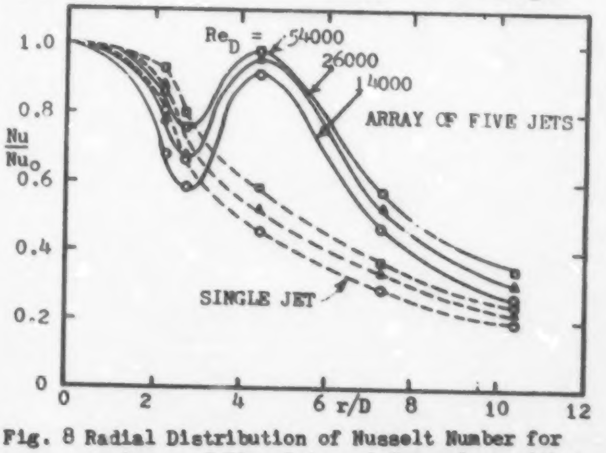

Fig. 8 Radial Distribution of Nusselt Number for an Array of Five Jets and Comparison with a Single Jet. D = 6.35 mm. Area under a Curve, Weighted with r/D, is Proportional to $\overline{Nu}$.

indicate that the principle of superposition applies here only in a limited way. Therefore, the calculation of average heat transfer from multiple jets, based on such local parameters like local maximum velocity, boundary-layer thickness and the friction coefficient, is much more complicated than that for a single jet, as has been carried out, for example, in Ref. 11, using Colburn's analogy and Ludwieg-Tillmann wall-friction coefficient. This is also evident from inspection of Fig. 8.

CONCLUSIONS

This work appears to be the first systematic investigation of the interaction between the jet at the center of an array and four/eight screening identical jets as a single unit, without any noticeable cross-flow effect. There appeared already many interesting investigations of arrays of jets (cf. [3, 9,15], with cross-flow effects included, or with other ways of disposing of the spent air. The present study was centered entirely around an investigation of heat transfer aspects of a single, self-contained, square array, that could be interpreted and explained by the measured fluid flow patterns of the associated turbulent, impinging jets, observed in- and outside of the potential core, in the stagnation region, and in the wall-jet region.

ACKNOWLEDGMENT

This work has been supported by the National Science Foundation under Grant NGR-81-19471. V. Hlinka and O.W. Hrycak helped with collection and processing of data.

NOMENCLATURE

b = wall jet width, m
C_n/D = distance between jet centers in array, $\underline{C}$
Nu = hD/k, Nusselt number
Pr = $c_p\mu/k$, Prandtl number
Re_D = $\overline{u}D/\nu$, Reynolds number
T_{ch} = plenum chamber temperature, K
v, V = wall jet velocity, m/s
Z_n/D = nozzle-to-target plate distance, $\underline{Z}$

Subscripts

m = condition where velocity is maximum
oc = condition at center of nozzle
s = condition at plate's surface
pl = refers to target plate

Greek symbols

β = free constant in eq. (3)
δ = (inner) boundary-layer thickness, m

REFERENCES

1. Gardon, R., & Cobonpue, J., Heat Transfer Between a Flat Plate and Jets of Air Impinging on It, International Developments in Heat Transfer, ASME, pp. 454-460, 1963.
2. Livingood, J.N.B., & Hrycak, P., Impingement Heat Transfer from Turbulent Air Jets to Flat Plates - a Literature Survey, NASA TM X-2778, 1973.
3. Behbahani, A.I., & Goldstein, R.J., Local Heat Transfer to Staggered Arrays of Impinging Circular Air Jets, J. of Engineering for Power, ASME, Vol. 105, pp. 354-360, 1982.
4. Koopman, R.N., & Sparrow, E.M., Local and Average Heat Transfer Coefficients Due to an Impinging Row of Jets, Int.J. Heat Mass Transfer, Vol.19, pp. 673-687, 1976.
5. Hrycak, P., Heat Transfer from a Row of Impinging Jets to Concave Cylindrical Surfaces, Int. J. Heat Mass Transfer, Vol. 24, pp. 407-419, 1981.
6. Sethi, Samir, Experimental Investigation of Submerged Turbulent Array of Air Jets Impinging on a Flat Plate, M.S. Thesis, N.J.I.T., Newark, N.J., 1984.
7. Kaya, D.M., Experimental Investigation of Heat Transfer from an Array of Jets Impinging Normally on a Flat Plate, M.S.Thesis, N.J.I.T., Newark, N.J., 1985.
8. Martin, H., Heat and Mass Transfer between Impinging Jets and Solid Surfaces, in Advances in Heat Transfer, ed. by J.P. Hartnett & T. F. Irvine, Jr., Vol. 13, pp. 1-60, Acad.Press, New York, 1977.
9. Hrycak, P., Heat Transfer from Impinging Jets-A Literature Review, AFWAL-TR-81-3054, Fl.D.L., Wright-Patterson AFB, Ohio 45433, 1981.
10. Schlichting, H., Boundary-Layer Theory, (7th edn.), Mc Graw-Hill, New York, 1979.
11. Hrycak, P., Heat Transfer from Round Impinging Jets to a Flat Plate, Int. J. Heat Mass Transfer, Vol. 26, pp. 1857-1865, 1983.
12. Hrycak, P., Lee, D.T., Gauntner, J.W., & Livingood, J.N.B., Experimental Flow Characteristics of a Single Turbulent Jet Impinging on a Flat Plate, NASA Technical Note D-5690, 1970.
13. Tanaka, T., & Tanaka, E., Experimental Studies of a Radial Turbulent Jet, Bulletin of JSME, Vol. 20, pp. 209-215, 1977.
14. Datta, C.S., Cooling Characteristics of a Turbulent Round Jet Impinging Normally on a Heated Flat Plate, M.S. Thesis, Newark College of Engineering, Newark, N.J., 1970.
15. Metzger, D.E., & Florschuetz, L.W., Heat Transfer Characteristics for In-Line and Staggered Arrays of Circular Jets with Crossflow of Spent Air, J. of Heat Transfer, ASME, Vol. 101, pp. 526-531, 1979.

NATURAL CONVECTION GENERATED BY CONJUGATE HEAT TRANSFER IN RECTANGULAR ENCLOSURES

F.L. Bello-Ochende and I.O. Ogunleye

Department of Mechanical Engineering, Faculty of Engineering and
Technology, University of Ilorin, Ilorin, Nigeria.

ABSTRACT

A numerical study of steady two-dimensional conjugate heat transfer problem incorporating conduction and free convection within rectangular enclosures is presented. The enclosure is bounded at the top and bottom by adiabatic walls and by two differentially-heated vertical walls; one cold and the other thick, hot and conductive. For the convection domain, the conservation equations of mass, momentum and energy are solved using the vorticity-stream function formulation. Series of numerical experiments performed document the effect of the geometric aspect ratio, $\mathbb{R}$, the temperature ratio, θ^* of the faces of the thick conductive wall and the conjugation parameter, λ^* on heat transfer for a given Rayleigh number, Ra. The range of interest for each parameter is: $0.5 \leq \mathbb{R} \leq 2.0$; $0.2 \leq \theta^* \leq 0.8$, $100 \leq \lambda^* \leq 1100$ and $0 \leq Ra \leq 2 \times 10^{12}$. Computed heat transfer coefficients were extrapolated to zero grid size for a given set of $\mathbb{R}$ and Ra, and the mean Nusselt number, $\overline{Nu}$ decreases both as the conjugation parameter and as the aspect ratio increase. Using the continuation procedure, the critical value of Ra was established for transition from uncellular to bicellular flow regime.

NOMENCLATURE

$\mathbb{R}$	Aspect ratio of the enclosure (L/H).
Gr	Grashof number (= Ra/Pr).
h^*	Grid size ratio (= h_f/h_s).
h_f	Nondimensional horizontal grid size in the fluid domain (ΔX_f).
h_s	Nondimensional horizontal grid size in the solid domain (ΔX_s).
H	Height of the vertical conducting wall.
K	Nondimensional vertical grid size (the same for both solid and fluid domain, ΔY).
L	Length of the enclosure.
N_f	Number of divisions in the x-direction of the fluid domain.
N_s	Number of divisions of the solid matrix in the x-direction.
$\overline{Nu}$	Mean Nusselt number.
Nu_L	Local Nusselt number.
Pr	Prandtl number.
$\mathbb{B}$	Inverse of the fourth root of the Rayleigh number (= $1/Ra^{1/4}$).
Ra	Rayleigh number.
T_c	Temperature of isothermal cold surface.
T_f	Temperature of fluid.
T_s	Temperature of solid.
T_1	Temperature of isothermal hot surface of the conducting wall.
T_2	Interface temperature.
U	Nondimensional horizontal component of velocity.
V	Nondimensional vertical velocity component.
W	Width of the vertical conducting wall.
X	Nondimensional horizontal coordinate for the fluid domain.
X^*	Nondimensional horizontal coordinate for the solid domain.
Y	Nondimensional vertical coordinate.

Greek symbols

α	Thermal diffusivity.
β	Coefficient of volumetric expansion.
∇_*^2	2-D nondimensional operator (= $Ra^{\frac{1}{2}}\frac{\partial^2}{\partial X_f^2} + \frac{\partial^2}{\partial Y^2}$).
λ_f	Thermal conductivity of fluid.
λ_s	Thermal conductivity of solid.
λ^*	Conductivity ratio (= λ_s/λ_f).
μ	Dynamic viscosity.
ν	Kinematic viscosity of fluid.
Ω^*	Nondimensional vorticity.
θ^*	Nondimensional wall temperature ratio, (= θ_{s1}/θ_{s2}).
θ_f	Nondimensional temperature of fluid.
θ_s	Nondimensional temperature of solid.
ψ^*	Nondimensional stream function.

INTRODUCTION

A conjugate heat transfer problem arises when the temperature field within a conducting wall, which may either be vertical, inclined or horizontal, is coupled to that within a reservoir of fluid next to the wall. The basis for the coupling is the interface matching conditions that exist between conducting wall and the fluid domain. These conditions are the continuity of heat flux and equal wall and fluid temperatures at the interface. Literatures abound on conjugated heat transfer problems. Brosh et al [1] worked on conjugated heat transfer in a laminar layer with heat source located at the fluid-solid interface. They presented numerical results for forced convection for temperature profiles as functions of the source strength and of the properties of the fluid and solid. Zinnes [2] investigated the effect of coupling of conduction with laminar natural convection from a vertical flat plate with arbitrary surface heating using finite-difference technique. He found that the degree of coupling between conduction in the plate and natural convection in the fluid was strongly influenced by the plate-fluid conductivity ratio. Also, Rotem [3] investigated the effect of thermal conduction of the wall upon convection from a surface in a laminar boundary layer flow. Davis and Gill [4] investigated the transfer of heat from a thick block of conducting material to a plane poiseuille-Couette flow. Conjugate heat transfer has received considerable attention from some other investigators [5-12].

The objective of the present work is the study of the effect of various parameters on steady conjugate conduction-convection heat transfer in rectangular enclosures bounded by a pair of horizontal adiabatic walls and sideways by a hot thick vertical conducting wall and an isothermal cold surface.

Lower critical Rayleigh number Ra_L^* below which there is no convection for a given set of parameters were computed analytically, a priori. Results also predict the existence of upper critical Rayleigh numbers Ra_u^* at which the single cell structure breaks into two cells for various aspect ratios. These upper critical Rayleigh numbers were obtained by a continuation procedure which involves the bisection method following Tomcej and Nandakumar [6]. At higher Rayleigh numbers, multicellular regimes develop.

PROBLEM FORMULATION AND ANALYSIS

The physical model, coordinate system and wall conditions are depicted in Fig. 1. Conduction through the hot wall is assumed one-dimensional. The fluid within the convection domain is Newtonian. The fluid motion is assumed to be steady, laminar, incompressible and two-dimensional. The Boussinesq approximation is invoked.

The systems of governing equations are:

(a) Solid domain: (with temperature invariant thermal conductivity)

$$\frac{d^2\Theta_s}{dX^{*2}} = 0 \tag{1}$$

subject to the following thermal boundary conditions,

(i) At $X^* = 0$, $\Theta_s = 1.0$

(ii) At $X^* = \frac{W}{H}$, $\Theta_s = \frac{T_2 - T_c}{T_1 - T_c}$. (2)

The normalised form of temperature distribution obtained after integration and appropriate simplifications is,

$$\Theta_s = 1 - BX^* \tag{3}$$

where $B = (\frac{T_1 - T_2}{T_1 - T_c})\frac{H}{W} = \Theta^*\frac{H}{W}$.

(b) Fluid domain:

The Mass Conservation Equation:

$$\frac{\partial U}{dX_f} + \frac{dV}{dY} = 0. \tag{4}$$

Energy Transport Equation:

$$U\frac{\partial\Theta_f}{\partial X_f} + V\frac{\partial\Theta_f}{\partial Y} = \frac{1}{Pr}\nabla_*^2\Theta_f. \tag{5}$$

Vorticity Transport Equation:

$$U\frac{\partial\Omega^*}{\partial X_f} + V\frac{\partial\Omega^*}{\partial Y} = \nabla_*^2\Omega^* + \frac{Ra^{5/4}}{Pr}\frac{\partial\Theta_f}{\partial X_f} \tag{6}$$

Poisson Equation of the Stream Function:

$$\Omega^* + \nabla_*^2\psi^* = 0 \tag{7}$$

where ∇_*^2 is a non-dimensional 2-D operator defined as

$$\nabla_*^2 = (Ra^{\frac{1}{2}}\frac{\partial^2}{\partial X_f^2} + \frac{\partial^2}{\partial Y}).$$

The velocity components, vorticity and stream functions are related by

$$\Omega^* = Ra^{1/4}\frac{\partial V}{\partial X_f} - Ra^{-1/4}\frac{\partial U}{\partial Y}$$

$$U = Ra^{1/4}\frac{\partial\psi^*}{\partial Y}$$

$$V = -Ra^{1/4}\frac{\partial\psi^*}{\partial X_f} .$$

The normalised boundary constraints are:

(i) At the rigid boundaries,
$U = V = 0$ (No-slip condition)
and $\psi^* = 0$
$\Omega^* \neq 0$.

(ii) At $X_f = 0$; $\Theta_f = \Theta_2$
At $X_f = \frac{L}{H}$: $\Theta_f = 0$ (8)
At $Y = 0, 1$: $\frac{\partial\Theta_f}{\partial Y} = 0$.

(iii) Conjugation Interface Conditions are:

$$\Theta_f\Big|_{\text{interface}} = \Theta_s\Big|_{\text{interface}} = \Theta_s$$

$$\frac{\partial\Theta_f}{\partial X_f} = (\frac{\lambda_s}{\lambda_f})(-\frac{1}{Ra^{1/4}})\frac{\partial\Theta_s}{\partial X^*} . \tag{9}$$

To solve the conjugated heat transfer problem, a rectangular grid system is used and it is always ensured that the discretization is much finner in the fluid domain than it is in the solid domain. The discretised forms of the transport equations are:

$$\Theta_{f\,i,j} = A_{i,j}\Theta_{f\,i+1,j} + B_{i,j}\Theta_{f\,i-1,j} + C_{i,j}\Theta_{f\,i,j+1} + D_{i,j}\Theta_{f\,i,j-1} \tag{10}$$

where $A_{i,j} = (\frac{Ra^{\frac{1}{2}}}{Pr\,h_f^2} - \frac{U_{i,j}}{2h_f})$.

$B_{i,j} = (\frac{U_{i,j}}{2h_f} + \frac{Ra^{\frac{1}{2}}}{Pr\,h_f^2})$; $C_{i,j} = \frac{1}{D^*}(\frac{1}{Pr\,k^2} - \frac{V_{i,j}}{2k})$

$D_{i,j} = \frac{1}{D^*}(\frac{1}{Pr\,k^2} + \frac{V_{i,j}}{2k})$; $D^* = \frac{1}{Pr}(\frac{2Ra^{\frac{1}{2}}}{h_f^2} + \frac{2}{k^2})$

$$h_f = \Delta X_f \; ; \quad k = \Delta Y$$

$$i = i_w+2, \; . \; . \; . \; . \; , N_f$$

$$j = 3,4, \; . \; . \; . \; . \; , M-2$$

Vorticity:

$$\Omega^*_{i,j} = S_{i,j}\Omega^*_{i+1,j} + R_{i,j}\Omega^*_{i-1,j} + P_{i,j}\Omega_{i,j+1} + Z_{i,j}\Omega^*_{i,j-1} + E(\theta_{f\,i+1,j} - \theta_{f\,i-1,j}) \qquad (11)$$

where,

$$S_{i,j} = \left(\frac{Ra^{1/2}}{h_f^2} - \frac{U_{i,j}}{2h_f}\right); \quad R_{i,j} = \left(\frac{U_{i,j}}{2h_f} + \frac{Ra^{1/2}}{h_f^2}\right)$$

$$P_{i,j} = \frac{1}{S^*}\left(\frac{1}{k^2} - \frac{V_{i,j}}{2k}\right); \quad Z_{i,j} = \frac{1}{S^*}\left(\frac{V_{i,j}}{2k} + \frac{1}{k^2}\right)$$

$$E = \frac{Ra^{5/4}}{2Pr\, h_f S^*} \quad ; \quad S^* = \frac{2Ra^{1/2}}{h_f^2} + \frac{2}{k^2}$$

$$i = i_w+1, \; . \; . \; . \; . \; , N_f$$

$$j = 2,3, \; . \; . \; . \; . \; , M.$$

The boundary vorticities are:

$$\Omega^*_{i_w,j} = \frac{Ra^{1/4}}{h_f} V_{i_w+1,j}; \quad \Omega^*_{N_f+1,j} = -\frac{Ra^{1/4}}{h_f} V_{N_f,j}$$

$$\Omega^*_{i,M+1} = \frac{Ra^{-1/4}}{k} U_{i,M} \; ; \quad \Omega^*_{i,1} = -\frac{Ra^{-1/4}}{k} U_{i,2} \qquad (12)$$

where,

$$j = 1, \; 2, \; . \; . \; . \; . \; , M$$

$$i = i_w, \; . \; . \; . \; . \; , N_f+1.$$

Poisson Equation of the Stream Function:

$$\psi^* = A^*(\psi^*_{i+1,j} + \psi^*_{i-1,j}) + B^*(\psi^*_{i,j+1} + \psi^*_{i,j-1}) \; C^*\Omega^*_{i,j} \qquad (13)$$

where,

$$A^* = \frac{Ra^{1/2}}{S^* h_f^2} \; ; \quad B^* = \frac{1}{S^* k^2} \; ; \quad C^* = \frac{1}{S^*}$$

$$i = i_w+1, \; . \; . \; . \; . \; , N_f$$

$$j = 2, \; 3, \; . \; . \; . \; . \; , M.$$

The corresponding discretized forms of velocity components are:

$$U_{i,j} = \frac{Ra^{1/4}}{2k}(\psi^*_{i,j+1} - \psi^*_{i,j-1})$$

$$V_{i,j} = -\frac{Ra^{1/4}}{2h_f}(\psi^*_{i+1,j} - \psi^*_{i-1,j}).$$

LIMITING CASE

The computation of Ra for onset of thermal convection goes thus: the discretized form of the interface or conjugation condition is given by:

$$\theta_{f\,i_w+1,j} = (1+h^*\lambda^*R)\theta_2 - (h^*\lambda^*R)\theta_{s\,i_w-1,j}$$

where,

$$h^* = \frac{h_f}{h_s} \; ; \quad \lambda^* = \frac{\lambda_s}{\lambda_f} \; ; \quad R = 1/Ra^{1/4}$$

$$\theta_2 = \theta_{f\,i_w,j} = \theta_{s\,i_w,j}$$

$$i_w = \text{interface node}$$

$$j = 1, \; . \; . \; . \; . \; , M.$$

Since $\theta_{f\,i_w+1}$ must be positive within the fluid domain, for the limiting case of no convection, $\theta_{f\,i_w+1,j} = 0$. Thus, for no convection

$$R = \frac{\theta_{s\,i_w,j}}{h^*\lambda^*(\theta_{s\,i_w-1,j} - \theta_{s\,i_w,j})}$$

and hence for the onset of convection

$$Ra^*_L > \left[\frac{\theta_{s\,i_w,j}}{h^*\lambda^*(\theta_{s\,i_w-1,j} - \theta_{s\,i_w,j})}\right]^4$$

DISCUSSION OF RESULTS AND CONCLUSION

Fig. 1 shows the coordinate axes, the physical model and the thermal boundary constraints.

The mean Nusselt number for various aspect ratios at several finite grid-sizes were extrapolated to zero grid-size with reasonable confidence following Ozoe et al [12]. Typical extrapolation graph for aspect ratio 1.5 is presented in Fig. 2.

The effect of conductivity ratio on the heat transfer coefficient for various aspect ratios is illustrated in Fig.3. The mean Nusselt number decreases as the conductivity ratio increases. This is well pronounced at the least wall temperature ratio.

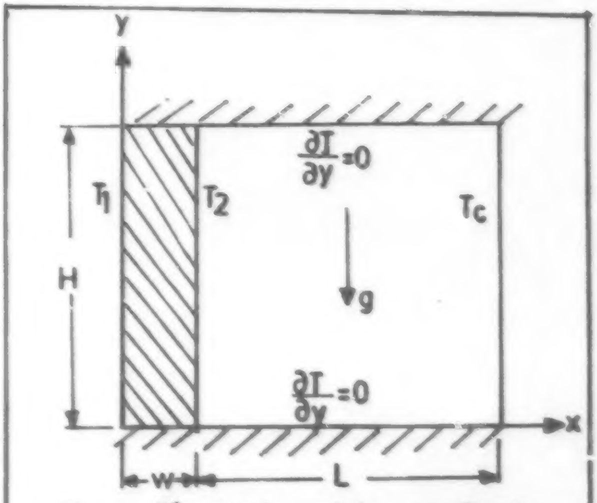
y
$\frac{\partial T}{\partial y}=0$
T_1
T_2
T_c
H
g
$\frac{\partial T}{\partial y}=0$
x
w
L

Fig.1. Physical model, coordinate system and thermal boundary constraints.

The Rayleigh number evaluated by a bisection method at the neighbourhood of the upper critical Rayleigh number at which a bicellular flow regime is observed is plotted against the aspect ratio for two extreme wall temperature ratios and two extreme conductivity ratios. This is illustrated in Fig. 4. This critical Rayleigh number increases as the aspect ratio increases and as the wall temperature ratio decreases.

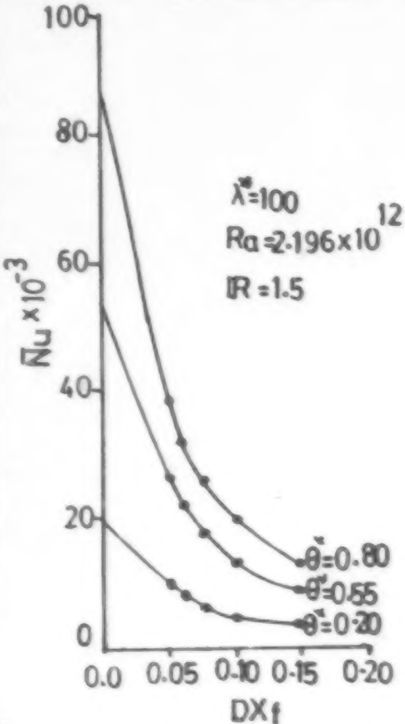

Fig.2. Typical extrapolation graphs

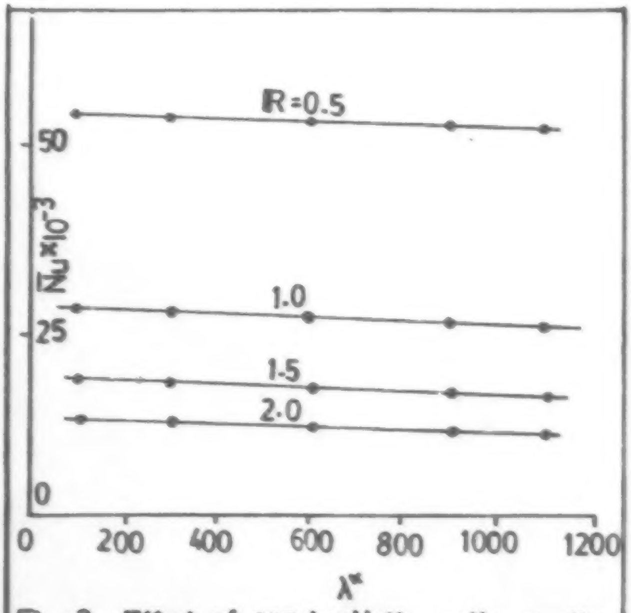

Fig.3. Effect of conductivity ratio on the mean Nusselt number for various aspect ratios; $\theta^* = 0.2$, $Ra = 2.196 \times 10^{12}$

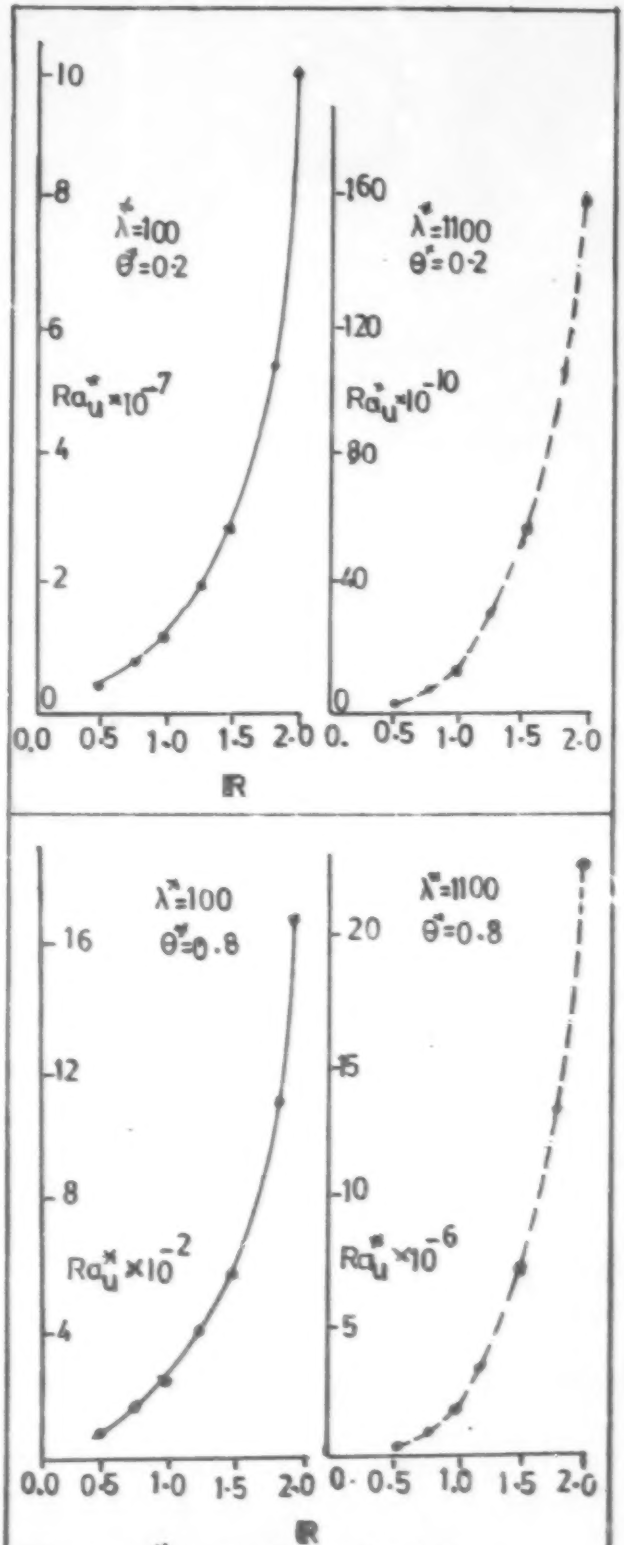

Fig.4. $\bar{Ra}_u$ vs. IR for the two extreme values of θ^* and λ^*

Conclusively,a physical model with high conduction and convection coupling rate requires less heating to set up convection in the fluid domain.

ACKNOWLEDGEMENT

The authors are grateful to the University of Ilorin for sponsoring the research through the Senate Research Grant No.8.303.11.

REFENCES

1. Brosh,A., Degani,D.& Zalmonovich,S., Conjugated Heat Transfer in a Laminar Layer with Heat Source at the Wall,ASME Journal of Heat Transfer, Vol.104,pp.90-95,1982.
2. Zinnes,A.E., The Coupling of Conduction with Laminar Natural Convection fron Vertical Flat Plate with Arbitrary Surface Heating, ASME Journal of Heat Transfer,Vol.92,pp.528-535,1970.
3. Rotem,Z., The Effect of Thermal Conduction of the Wall Upon Convection from a Source in a Laminar Boundary Layer,Int. J. Heat Mass Transfer Vol.10, pp.461-466,1967.
4. Davis,E.J. & Gill,W.N., The Effect of Axial Conduction in the Wall on Heat Transfer with Laminar Flow, Int.J.Heat Mass Transfer,Vol.13, pp.459-470,1970.
5. Faghri,M.& Sparrow,E.M., Simultaneous Wall and Fluid Axial Conduction in Laminar Pipe Flow Heat Transfer, ASME Journal of Heat Transfer, Vol.102, pp. 58-63,1980.
6. Tomcej,R.& Nandakumar,K., Mixed Convection Flow of a Power Law Fluid in Horizontal Ducts, The Canadian Journal of Chemical Engineering, Vol. 64. pp. 746, 1986.
7. Barrozzi,G.S. & Pagharini,G., A Method to Solve Conjugate Heat Transfer Problems; The Case of Fully Developed Laminar Flow in a Pipe , ASME Journal of Heat Transfer,Vol.107,pp.77-83 1985.
8. Shelyag,V.R., Calculation of Temperature Fields in a Laminar Gas Flow in Flat Slots Channel Journal of Engineering Physics,Vol.12,pp.227-234,1967.
9. Mori,S. Shinke,T.,Sakakibara,M.& Tanimoto,A., Steady Heat Transfer to Laminar Flow between Parallel Plates with Conduction in Wall, Heat Transfer,Japanese Research,Vol.5.No.4,pp.17-25 1976.
10. Mori,S.,Sakakibara,M.& Tanimoto,A.,Steady Heat Transfer to Laminar Flow in Circular Tube with Conduction in Tube Wall, Heat Transfer,Japanese Research,Vol. 3,No.2, pp.37-46,1974.
11. Aleksashenko,V.A., Conjugate Stationary Problem of Heat Transfer with a Moving Fluid in a Semi-infinite Tube Allowing for Viscous Dissipation ,Journal of Engineering Physics,Vol. 14,pp. 55-58, 1968.
12. Ozoe,H. Samaya,H. & Churchill,S.W., Natural Convection in an Inclined Square Channel,Int. J.Heat Mass Transfer,Vol.17,pp. 401-406,1974.

INVESTIGATION OF PRESSURE DISTRIBUTION AROUND A CYLINDER NEAR AN ENDWALL

P.H. Oosthuizen and P.C.C. Tong

Dept. of Mechanical Engineering
Queen's University
Kingston, Ontario
Canada K7L 3N6

ABSTRACT

An experimental investigation of the pressure distribution over a cylinder near an endwall and of the surface flow pattern on the endwall has been undertaken. The cylinder diameter used was 5.4cm and tests were undertaken with natural and artificially thickened turbulent boundary layers. Tests were conducted at $Re=1.4\times10^4$ and 2.8×10^4 with turbulent boundary layer.

NOMENCLATURE

D	cylinder diameter
S	upstream distance to saddle point
x	distance upstream from cylinder's axis
z	distance along cylinder from endwall
δ	boundary layer thickness
P	pressure at any point on the cylinder
P_o^*	pressure at stagnation point on the cylinder far from the endwall
P_∞	pressure at far upstream of the cylinder
β	angle from stagnation point on cylinder
C_p	pressure coefficient, $(P-P_\infty)/(P_o^*-P_\infty)$
Re	Reynolds number, $\rho U_\infty D/\mu$

INTRODUCTION

When a cylinder placed in a fluid flow intersects an endwall at right angles to the axis of the cylinder, a complex flow pattern develops in the region where the surfaces intersect. The flow in this vicinity is three dimensional and often leads to the formation of complex vortices as shown in Fig. 1. Flow approaching the cylinder adjacent to the surface is in a region of adverse pressure gradient. This flow stagnates on the cylinder and is curled towards the end wall due to the velocity gradient in the boundary layer. This flow is now reversed and eventually looses its momentum due to the in-coming flow leading to a formation of a vortex upstream of the cylinder. The vortex is swept around the base of the cylinder by the in-coming flow, hence forming a horseshoe vortex. Shown in Table 1 are some practical applications of horseshoe vortices in engineering.

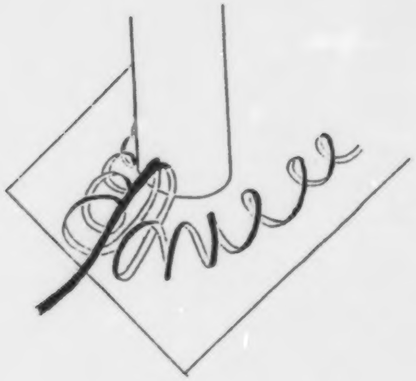

Fig. 1 Horseshoe Vortex

Area		Applications
Turbomachinery	-	achieving better designs at turbine blade and roots junction.
Aerodynamics	-	wing-fuselage junction of an aircraft.
Hydrodynamics	-	local scour on the erodible bed of a river adjacent to a bridge support.
Heat Transfer	-	heat exchanger tubes.

Table 1 Horseshoe vortex applications

Some practical effects of horseshoe vortices are experienced in everyday life. After a blizzard the way the snow is scooped out on the windward side of trees and telephone poles may be noticed. This is evidence of horseshoe vortex formations resulting when the boundary layer on the ground encounters an obstruction. These beautiful snow patterns have their counter parts underwater near bridge piers in streams.

Flow near a bluff body and wall

junction has been investigated by researchers dating back to the time of Leonardo da Vinci, this early work being reviewed by Belik [1973]. Shown in Table 2 is a brief summary of previous work on horseshoe vortices. In reviewing the following work, x is defined as the distance upstream of the cylinder. D is the cylinder diameter and Reynolds number is based on the cylinder diameter. Other related studies at horseshoe vortices are as follows, Blair [1984], Ireland and Jones [1986], Moore and Forlini [1984], Moore and Moore [1984], Langston et al. [1977], Barber [1978], Gupta [1987] and Sharma and Gupta [1989] to name a few.

The present study concentrates on the pressure distribution on a high aspect ratio cylinder near an end wall. Experiments were performed with a natural boundary layer thickness and at an artificially thickened boundary layer. Some supplementary studies of the "surface flow" pattern were also undertaken.

Author	Findings
Belik [1973]	-at $0.36\times10^5<Re<2.2\times10^5$, a minimum pressure point was found at $x/D=0.715$. -concluded that the minimum pressure point is the vortex core.
Baker [1979]	-at $Re<5000$, minimum pressure point was found for $0.75<x/D<0.85$. -at $Re>5000$, no minimum pressure point was found -found that the number of vortices present was dependent on Re and the boundary layer thickness
Baker [1980]	-for $4400<Re<71800$, minimum pressure point was found at $x/D=0.8$. -concluded that the minimum pressure point is the vortex core.
Eckerle and Langston [1987]	-at $Re=5.5\times10^5$, minimum pressure point was found at $x/D=0.72$. -from flow visualization, a saddle point was found at $x/D=0.9$. -concluded that only one one vortex exist.

Table 2 Previous Work

EXPERIMENTAL APPARATUS AND PROCEDURE

In the present experiment, an open-circuit, low speed wind tunnel was used. Pressure measurements on the cylinder near an end wall were made using a Datametrics Barocel pressure sensor and in conjunction with a scani-valve.

A cylinder with a diameter of 5.4cm and a length of 97cm was used. This cylinder had eight pressure taps along its length spaced at distance of 5, 10, 15, 20, 25, 30, 50, 100 and 356mm from the end wall, the pressure taps were spaced 45 degrees to each other in a helical fashion up the cylinder. The pressure was attained by rotating the cylinder, thus placing the pressure taps at various angles to the stagnation point.

Counihan's [1973] method of thickening the boundary layer utilizing a "LEGO" base board was used. This base board was mounted 94.18cm upstream of the cylinder. Boundary layer thicknesses were derived from velocity profiles measured at $x/D=7.09$ upstream of the cylinder.

Pressure measurements over the cylinder near the end wall and "surface flow test" were conducted at two Reynolds numbers based on the cylinder diameter (see Table 3). The upstream boundary layers under these conditions were, of course, turbulent.

Re	Velocity	δ
1.4×10^4	4.27m/s	3.8cm
1.4×10^4	4.27m/s	3.8cm
2.8×10^4	8.54m/s	2.4cm
2.8×10^4	8.54m/s	2.5cm

Table 3 Testing conditions

"Piecemeal" horizontal surface flow tests were performed using the technique of Langston and Boyle [1982] with the addition of a very thin layer of water applied between the wall and the polyester drafting film to keep the drafting film adhered to the wall surface and to prevent fluttering.

RESULTS AND DISCUSSION

Typical measured pressure distributions are shown in Fig. 2-5. In general, it was found that the pressure distributions far from the wall under all conditions agreed well with Schlichting [1979]. As can be seen from Fig. 2-5 for distances close to the end wall, the pressure distributions over the cylinder at the frontal region of the cylinder has a lower C_p than that far from the end wall. This can be explained in the following manner. The flow near the wall surface is curled towards the end wall as it encounters the cylinder, due to the

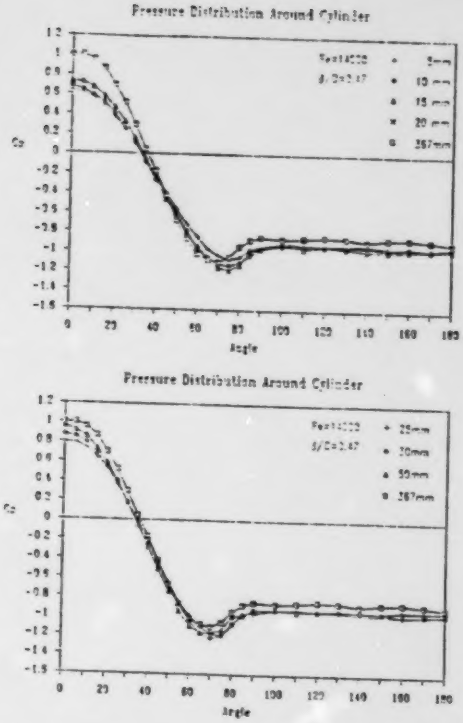

Fig. 2 Pressure distribution on cylinder near end wall: Re=14000, natural boundary layer

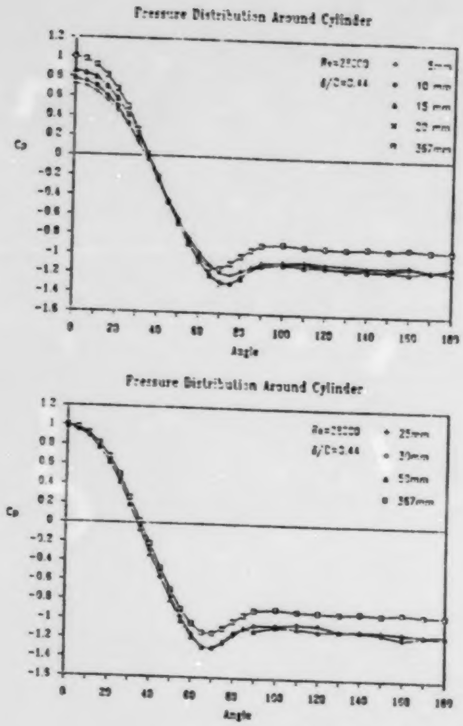

Fig. 3 Pressure distribution on cylinder near end wall: Re=28000, natural boundary layer

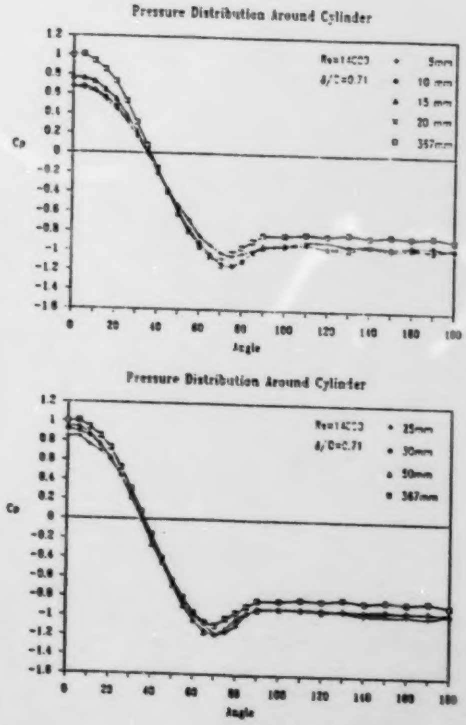

Fig. 4 Pressure distribution on cylinder near end wall: Re=14000, thickened boundary layer

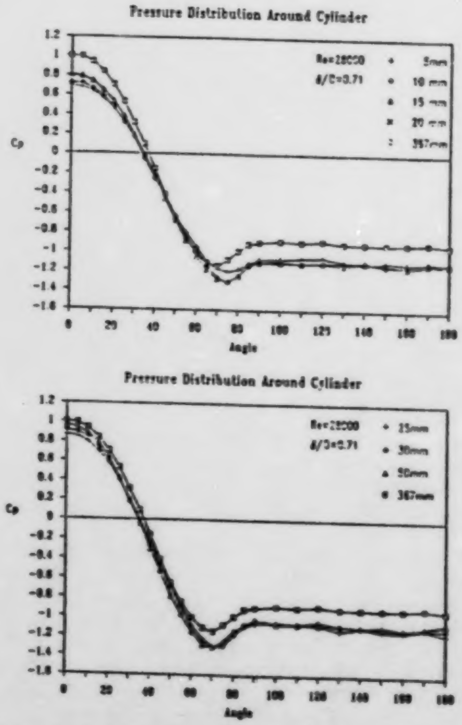

Fig. 5 Pressure distribution on cylinder near end wall: Re=28000, thickened boundary layer

presence of the boundary layer upstream of the cylinder. This flow towards the wall is associated with a decreasing pressure. Very close to the wall, e.g. the pressure tends to level off and will ultimately rise again. This is assumed to be associated with a vortex. The difference in C_p at $\beta=0°$ for $5mm<z<10mm$ is very small and is interpreted as a small corner vortex at the cylinder endwall junction. The C_p near end wall in the wake region was found to be lower than that far from the wall.

The surface flow tests showed that a saddle point exists at $S/D=1.1\pm5\%$. A sketch of the surface flow is shown in Fig. 6, from such flow patterns it was found that S did not vary with the test conditions and it was observed that the solvent dried in a horseshoe shape.

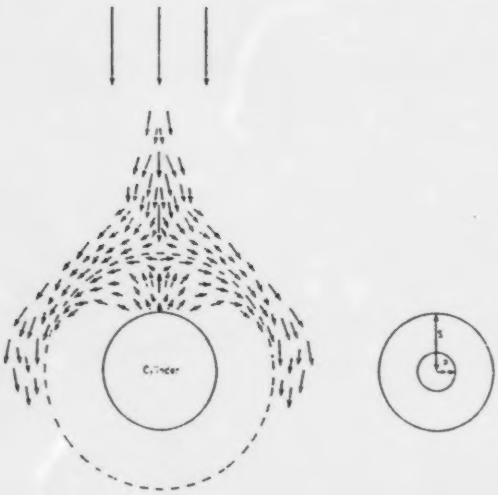

Fig. 6 Surface Flow

CONCLUSION

The present study indicates the following:

1. The pressure at the frontal region of the cylinder is lower than that far from the end wall while the pressure far from the wall in the wake region is lower.
2. A vortex system is present upstream of the cylinder.
3. There exist a corner vortex at the cylinder and endwall junction.
4. A single saddle point was observed at $x/D=1.1\pm5\%$ upstream of the cylinder from surface flow tests.

REFERENCES

Baker, C.J. 1979: "The Laminar Horseshoe Vortex" J. Fluid Mech., Vol. 95, pp. 347-367.

Baker, C.J. 1980: "The Turbulent Horseshoe Vortex" J. Wind Engineering and Industrial Aerodynamics, Vol. 6, pp. 9-23.

Barber, T.J. 1978: "An Investigation of Strut-Wall Intersection Losses" J. Aircraft, Vol.15, No. 10, pp. 676-681.

Belik, L. 1973: "The Secondary Flow about Circular Cylinders Mounted Normal to a Flat Plate" Aero Quarterly, Vol.24, pp. 47-54.

Blair, M.F. 1984: "Heat Transfer in the Vicinity of a Large-Scale Obstruction in a Turbulent Boundary Layer" AIAA 19th. Thermophysics Conference, June 25-28/ Snowmass, Colorado. AIAA-84-1723.

Counihan, J. 1973: "Simulation of an Adiabatic Urban Boundary Layer in a Wind TUnnel" Atmospheric Environment, Vol.7, pp. 673-689.

Eckerle, W.A. and Langston, L.S. 1987: "Horseshoe Vortex Formation Around a Cylinder" J. Turbomachinery, Vol.109, pp. 278-285.

Gupta, A.K. 1987: "Hydrodynamic Modification of the Horseshoe Vortex at a Pier Junction with Ground" Phys. Fluids 30(4), pp. 1213-1215.

Ireland, P.T., and Jones, T.V. 1986: "Detailed Measurements of Heat transfer on and Around a Pedestal in Fully Developed Passage Flow" Proc. Eighth International Heat Transfer Conference, San Francisco, August 1986.

Langston, L.S. and Boyle, M.T. 1982: "A New Surface-Streamline Flow-Visualization Technique." J. Fluid Mech., Vol. 125, pp. 53-57.

Langston, L.S., Nice, M.L. and Hooper, R.M. 1978: "Three-Dimensional Flow Within a Turbine Cascade Passage" J. Engineering for Power, Vol. 99, pp.21-28.

Moore, J. and Forlini, T.J. 1984: "A Horseshoe Vortex in a Duct" J. Engineering for Gas Turbine Power, Vol. 106, pp.668-676.

Moore, J.G. and Moore, J. 1984: "Calculation of Horseshoe Vortex Flow Without Numerical Mixing" ASME Paper No.84-GT-241, 1984

Schlicting, H. 1979: Boundary Layer Theory, 7th. ed., Mcgraw Hill, New York.

Sharma, S.C. and Gupta, A.K. 1989: "Horseshoe Vortex Modification on a Vertical Circular Cylinder Junction With Ground" Proceedings CANCAM 89, Vol.2, pp.614-615.

PRESSURES IN A HORIZONTAL CYLINDRICAL TANK DUE TO IMPACT INDUCED ACCELERATIONS

D. B. Chidley
A. M. Birk

Department of Mechanical Engineering
Queen's University
Kingston, Canada

ABSTRACT

An experimental study investigating pressures generated on the ends of cylindrical tanks by the contained fluid when the tank was suddenly accelerated was undertaken. An experimental apparatus had to be designed and built to accommodate repeated violent impact forces and the associated vehicle motion reliably and in a safe environment. The following paper gives a description of the apparatus including significant aspects of design, construction and instrumentation. Results obtained for various test configurations are presented.

NOMENCLATURE

a	vehicle acceleration	
c	speed of sound in water	
d	diameter of tank	
E^*	liquid bulk modulus	
Fr	Froude number u^2/gh	
g	acceleration due to gravity	
h	liquid height in tank	
K	constant	
m_g	mass of gas	
m_l	mass of liquid	
P	pressure	
P_u^*	ullage pressure	
P_{uv}^*	vapour pressure	
P^*	pressure coefficient	$P/(0.5\rho u^2)$
P^{**}	pressure coefficient	$P/(\rho gh)$
Re	Reynolds number	$(\rho ud)/\mu$
u	initial vehicle velocity	
We	Weber number	$(\rho u^2 d)/\sigma$
ρ_g	density of gas	
ρ_l, ρ	density of liquid	
σ	liquid surface tension	

INTRODUCTION

The effects of fluid sloshing and fluid pressures are observed in many common situations. Fluid pressures account for the difference in handling of road going or railway tanker vehicles when empty and when fully laden with liquid. Fluid sloshing is also of importance in cargo, ballast or fuel tanks of large ships, fuel and cargo tanks of aircraft and aerospace vehicles, and offshore storage containers. Vessels used to transport liquids are typically exposed to varying types of impacts or sudden accelerations which tend to cause fluid motion and resulting pressures of interest to this study.

The subject of fluid pressures occurring in vessels as a result of a single impact force of a relatively high magnitude has received very little attention. Numerous studies have examined resonant sloshing induced by vibrational excitation, refns. (3),(4),and (8), and although not directly related to the present study, the fluid theory and treatment of data is.

Brooks (4) presented an overview of various experimental techniques for the simulation of liquid sloshing used by NASA when studying space vehicle motion. For the purpose of designing control systems for launch vehicles that can accommodate slosh forces, the magnitude of these forces must be determined. To accomplish this, a tank was first oscillated at a selected frequency and amplitude to generate the desired fluid motions and then it was 'quick stopped' at a point of zero velocity in the cycle. The fluid forces applied to the tank were then measured. The advantage of this method over the normally used forced-response technique was that since the apparatus had been brought to rest, there was no need to subtract the tare forces associated with the tank support system.

Two experimental methods for studying dome impact caused by a sudden acceleration of a fluid were also described by Brooks. This particular problem arises in space vehicles during engine shutdown of a launch vehicle in motion. For acceleration substantially greater than 1g, a pressure-activated carriage was used to accelerate a partially liquid filled tank in a downward direction. The resulting pressures were measured by an array of pressure cells. To examine smaller accelerations, a second method was described. A tank was accelerated upwards by a cable passing over a system of pulleys attached to a drop weight. After the drop weight came to rest, a braking force applied by another cable attached to the tank brought the tank to rest. This braking force induced a fluid impact on the dome of the tank.

A test described by Dalzell (5) involved a suddenly accelerated vessel partially filled with liquid in which the vessel could be positioned at various angles to vertical. Figure (1) presents the measured pressures on the spherical tank end as a function of acceleration and sensor position. As can be seen from the data, the pressure varied slightly over the tank end and was directly proportional to the tank acceleration. The proportionality was a function of tank angle. Other conclusions made by Dalzell were that slosh forces or pressures did not depend on vapor pressure, surface tension, or fluid viscosity.

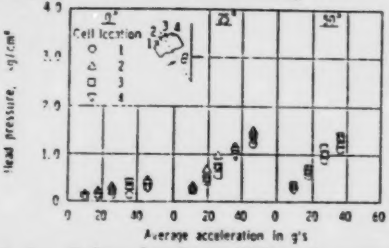

Figure 1: Spherical bulkhead pressure data in a half-full tank as a function of acceleration and for three angles of inclination. ref. (5)

Forces in ships holds due to sloshing can be very large and resulting damages have been documented by R. L. Bass (1), (2), and others. The incidents reported concerned the commercial transportation of liquefied natural gas (LNG) in large cargo ships. Sloshing related damage usually occurred when ocean wave motion closely matched the resonant sloshing period of the cargo. Later, reference (6), Bass described scale model testing of sloshing in ship hulls represented by geometrically similar liquid filled tanks. These tanks were translated and rotated to simulate ship motions. Since it was found that peak pressure at a given location in the tank had a random nature, large number of motion cycles were used to measure peak pressure. A typical pressure-time history, as recorded by Bass is given in fig (2).

An American Association of Railroads (AAR) report (7) considering horizontal tanks undergoing impact accelerations investigated stresses in tank car ends due to sloshing during impacts. The tests did not include the measurement of pressures but it was found that stresses in the tank ends were considerably reduced when the tank fill level was below 100%, indicating that tank end stress are related to fill level. These tests were performed because of a concern that sloshing during impact could cause tank end failure. The results of these tests appear to have ended those concerns. Other AAR tests (8) performed later, using tank cars for sloshing studies, usually investigated lateral sloshing effects on train handling and did not involve detailed measurement of longitudinal slosh pressures on tank ends.

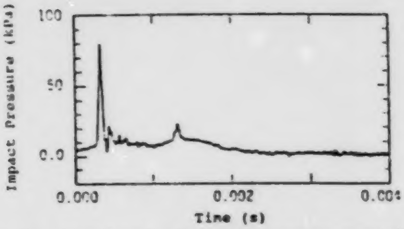

Figure 2: Typical impact pressure-time history. ref. (6)

THE PRESENT STUDY

The objectives of the present study were as follows:

1. To construct an apparatus to facilitate the study of single impact acceleration-induced fluid motion in a horizontal cylindrical tank.
2. To measure pressure versus time, initial impact velocity, and initial tank acceleration for a fixed geometry tank with varying fluid fill levels. Pressures were to be measured at several locations on the tank ends. The tank was to be exposed to an impact by a second body of fixed mass with varying impact velocities.
3. To develop a possible relationship between fluid pressure, tank acceleration, and fluid fill level.

DIMENSIONAL ANALYSIS

A dimensional analysis of a fluid sloshing in a tank with out boiling at the vessel wall will give the following expression:

$$P^* = f\,(\,Fr,\ Re,\ We,\ P^*_v,\ P^*_{uv},\ E^*,\ \rho_l/\rho_g,\ m_l/m_g\,,\ h/d,\ l/d,\ a/g,\ \text{tank wall properties}\,) \qquad (1)$$

Bass (6) described sloshing tests that were performed with air in the ullage space at 1 atm. Two different model liquids with different compressibilities were used and it was found that liquid compressibility, E^*, was not a significant factor and therefore can be eliminated as a variable. Since the fluids were air and water in all tests, the density ratio remained constant. As stated previously, vapor pressure, surface tension and viscous effects were not significant and since a single tank was used the l/d ratio remained constant.

With the above assumptions, eq'n (1) reduces to:

$$P^{*} = f\ (\ h/d,\ Fr\ ) \qquad (2)$$

$$P^{**} = f\ (\ h/d,\ a/g\ ) \qquad (3)$$

The above equations apply only for the specific geometry in this work.

APPARATUS AND TEST PROCEDURE

The basic test rig that was built, as described in ref. (9), consisted of a cylindrical tank mounted on a chassis with wheels, a section of track to guide the vehicle, a pendulum hammer to provide the necessary sudden acceleration, a stationary barrier to simulate vehicle collision with an immovable object, and a data acquisition system. An illustration of the above test rig is given in fig. 3.

The length of the test track was approximately 12 metres, with the final 3 metres of the track being used as a friction brake to stop the test vehicle. Due to the magnitude and unknown nature of the impact and sloshing forces that might have resulted, a 'captive rail' type of track was used. This design ensured that the tank-car would not leave the test track if strong vertical forces occurred. Lateral motion was prevented by utilizing 'vee' shaped lower rails and appropriately grooved wheels on the vehicle. A cross-sectional view of the track is given in fig. 4. With future experimentation being considered, the track was designed to be stiff enough to allow the track to be inclined.

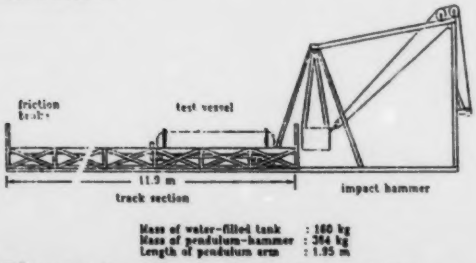
friction
brake
test vessel
11.9 m
track section
impact hammer
Mass of water-filled tank : 160 kg
Mass of pendulum-hammer : 364 kg
Length of pendulum arm : 1.95 m

Figure 3: Slosh Test Apparatus

To provide the impact acceleration that was applied to the test vehicle, a large hammer that would contact the bumper on the tank-car was built. A supporting structure and a hoist mechanism were built to allow various magnitudes of impact accelerations to result by varying the initial height that the hammer was raised to. The hammer was designed to meet two main criteria: It was to be able to propel the test vehicle to a maximum velocity of approximately 10 m.p.h. or 4.7 m/s; and, the point of contact between the tank-car and the hammer was to be at the centre of percussion of the pendulum hammer. With this criterion satisfied, there would be no normal forces transmitted to the bearings of the hammer upon impact, thus improving bearing life and safety of operation. To ensure that the contact point was at the centre of percussion, a slight radius was pressed into the steel plating that made up the otherwise flat face of the hammer. The total mass of the hammer could be varied from approximately 100 to 364 kg by adding or removing lead weights that filled the lower section. For this study the mass of the hammer remained constant at 364 kg.

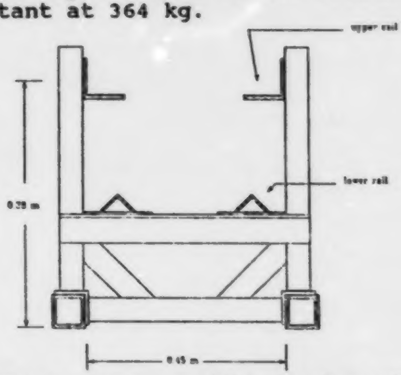

Figure 4: Cross-sectional view of test track

The cylindrical tank that was mounted on the test vehicle had a diameter of 0.25 metres, was 1.5 metres in length, and had a wall thickness of 9.5 mm. The end caps of the tank were ellipses with a major to minor axes ratio of 2:1. The material used for construction of the entire vehicle, with the exception of the axles, bumper plates, wheels, and bearings was aluminum. This material was chosen to aid in minimizing vehicle mass thereby simplifying other components of overall apparatus. The lower v-notched aluminum wheels prohibited lateral vehicle motion while the upper rubber wheels prevented vertical motion. The chassis for the vehicle was a ladder frame design consisting of two pieces of aluminum channel joined with 13 mm aluminum plates for added stiffness. The bumper plates were made of 19 mm thick aluminum which were covered with 9.5 mm carbon steel plates so that the hammer impact would be steel against steel thereby reducing losses on impact. The test vehicle is shown in fig. 5. Pressure inside the

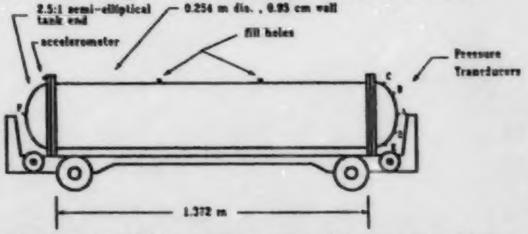

Figure 5: Scale tank car for measuring slosh pressures

vessel was measured at six different locations as indicated by the letters A-F in fig. 5. Since vehicle motion was restricted to a single axis, a single accelerometer was mounted on the flange of the end cap at the front of the vessel.

A transient pressure transducer manufactured by PCB Piezotronics Inc. model S111A26 was used to measure pressures resulting in the test vessel. The transducer had a calibrated range of 0-3.5 MPa with a useful overrange up to 6.9 MPa and a maximum allowable pressure of 13.8 MPa. The acceleration sensitivity is 1.4 Pa/m/s^2, a resonant frequency of 400 kHz, and a rise time of 1 µs. The accelerometer used to measure vehicle acceleration was also made by PCB Piezotronics Inc., model 303A02. The device was calibrated over a frequency range of 0.7-20000Hz. The range was ±4905 m/s^2, the resonant frequency was 100 kHz, and the maximum allowable shock was 19620 m/s^2. The signals from the above devices were relayed to the data acquisition system by long cables carried on cars strung along a suspension wire mounted alongside the test track. In addition, a velocity sensor was mounted on the track at the point of impact and was used to measure the initial tank velocity after impact. The velocity sensor was a light beam interruption type.

For all of the tests conducted, water was used in equilibrium with air at room temperature (approx. 20 - 25°C). The tank pressure was 1 atm during all tests. The tests that were performed were divided into six groups according to instrument location, type of impact and tank motion, and type of instrument used. A summary of the six test groups is given in table 1. A typical test consisted of the following steps. The empty tank was filled to the desired level and sealed with a threaded plug. the vehicle was then positioned precisely at the starting point located at the hammer end of the track. The hammer was raised to the desired height and released. The tests conducted covered a range of Froude numbers of 2.5 to 14.

Table 1: Summary of the six test groups

Group No.	Transducer Location	Accelerometer	Impact Type	Variables	
				# of fill levels	# of hammer heights or velocities
1	A	NO	HAMMER	14	5
2	A,B,C,D,E	NO	HAMMER	7	2
3	F	NO	HAMMER	7	2
4	NONE	YES	HAMMER	5	3
5	A	NO	BARRIER	8	3
6	F	NO	BARRIER	7	3

RESULTS AND DISCUSSION

The results of a representative sampling of tests conducted, (ref. 10), are presented giving a pressure-time history along with the corresponding frequency domain plot for fill levels (h/d) of 1.00, 0.60, and 0.45 given in figs. 6 to 11. For the case of a completely liquid filled tank (h/d = 1.00), a water hammer effect, rather than fluid sloshing was expected. Water hammer would be characterized by a pressure pulse travelling through the liquid medium at approximately the sonic velocity. For water at 20°C, the sonic velocity is 1400 m/s. With a tank length of 1.372 m, the time for a pressure wave to traverse the tank twice would be approximately 2 ms and the frequency that this corresponds to is 500 Hz. The plot given in fig. 7 showed evidence that a wave was propagating at the above frequency, and consequently, a water hammer effect did occur. As fill level was decreased, a significant reduction in peak pressure generated was observed due to the accompanying increase in wave action inside the vessel associated with an increase in Froude number. The increased wave motion also caused a longer transient signal and less clearly defined pressure spike to be evident.

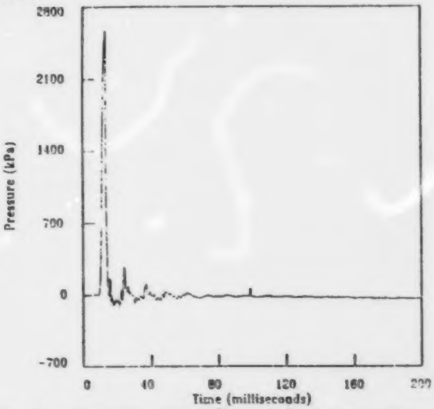

Figure 6: Pressure-time history for h/d = 1.00, u = 3.5 m/s

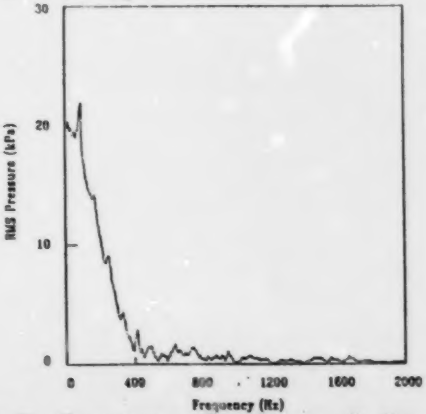

Figure 7: Frequency domain graph for h/d = 1.00, u = 3.5 m/s

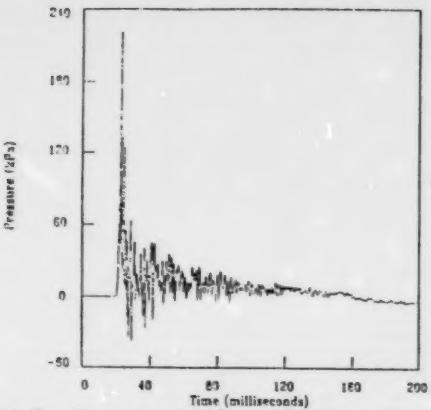

Figure 8: Pressure-time history for h/d = 0.60, u = 3.24 m/s

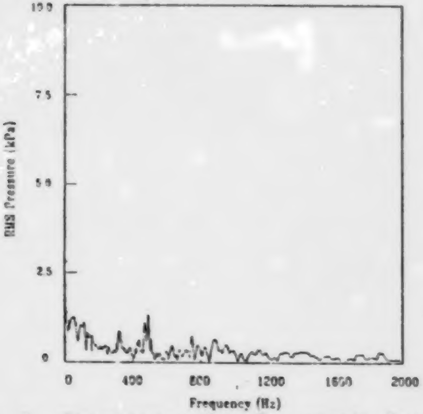

Figure 9: Frequency domain graph for h/d = 0.60, u = 3.24 m/s

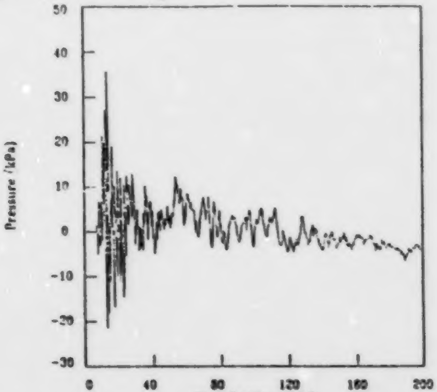

Figure 10: Pressure-time history for h/d = 0.45, u = 3.38 m/s

In fig. 12, pressure coefficient, P/ρgh, versus acceleration is presented along with pressure rise due to water hammer, P = ρcu₀, and the pressure that would result if the liquid behaved as a solid mass, P = ρaL for comparison with the case where h/d = 1.00. As can be seen, the slopes of the three curves are similar, giving further support to the fact that a water hammer effect occurred for a fully liquid filled tank. The magnitude of the pressure generated at a given acceleration from experimentation and from the equations was not equal indicating that this phenomenon needs further investigation.

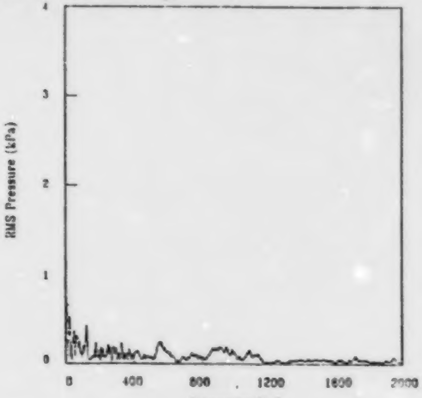

Figure 11: Frequency domain graph for h/d = 0.45, u = 3.38 m/s

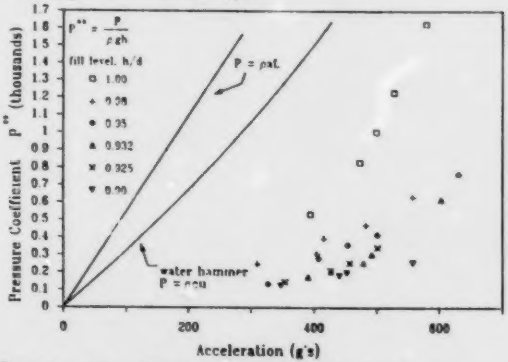

Figure 12: Pressure coefficient vs. acceleration for h/d between 1.00 and 0.90 and for water hammer

In the early stages of this experimental study, an accelerometer was not available. To accommodate for this, instantaneous velocity of the vehicle was measured for every test and since acceleration and velocity can be related, the peak acceleration of the vehicle for earlier test could be determined. To establish a relationship, an accelerometer was acquired and tests measuring acceleration and velocity for a representative number of impacts and fill levels were completed. At this time, the sensitivity of the results to a variation in the initial start position of the vehicle was investigated. The results for the tests with an identical start position along with the derived relationship between acceleration and velocity are given in fig. 13. It was seen that the relationship was fairly consistent. When the test vehicle's initial start position was randomly varied by ± 0.005 metres, considerable error was introduced, as is shown in fig. 14. These tests emphasized

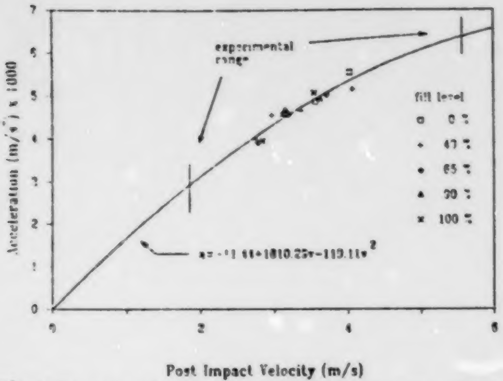

Figure 13: Tank acceleration vs. post impact velocity for cases with identical vehicle start location on track

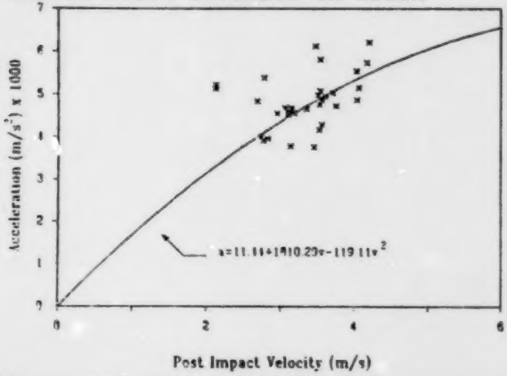

Figure 14: Tank acceleration vs. post impact velocity showing the effect of small errors in initial vehicle position

the importance of accurate placement of the vehicle prior to testing.

A possible relationship between the pressure coefficient ($P^{**}=P/\rho gh$), fill level (h/d), and acceleration (a/g) was to be determined. A relationship of the form:

$$P^{**} = C * (a/g)^{n} \tag{4}$$

was investigated by plotting P^{**} versus a/g on a log-log scale, as is shown in figs. 15 and 16, for all fill levels. The slope, n, was found to have a constant value of n = 2.824, while the value for C was found to vary uniformly with a discontinuity at h/d = 0.90. The value for C is given by:

$$C = K * (h/d)^{n_1} \tag{5}$$

where

- for h/d < 0.90, n_1=3.7011, K=7.8968x10^{-6}

- for h/d ≥ 0.90, n_1=14.7397, K=2.6918x10^{-5}

The observed discontinuity at h/d = 0.90 is likely indicative of a transition of the dominant fluid motion from a water hammer effect to wave generation and propagation. Combining equations (4) and (5) gave the desired relation between

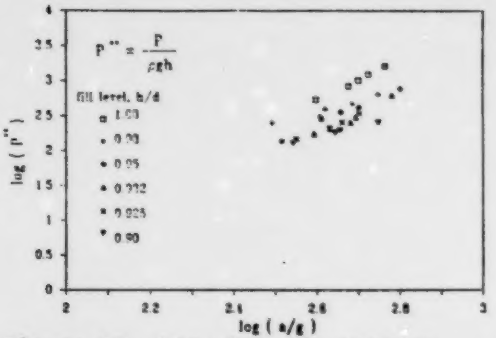

Figure 15: Log plot of pressure coefficient vs. acceleration for h/d between 1.00 and 0.90

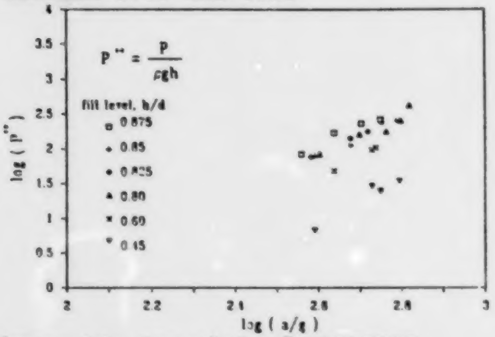

Figure 16: Log plot of pressure coefficient vs. acceleration for h/d between 0.875 and 0.45

pressure, acceleration and fill level given below.

$$\left(\frac{P^{**}}{K(a/g)^{n}}\right)^{\frac{1}{n_1}} = \frac{h}{d} \tag{6}$$

The plot of this relation is given in fig. 17 and, as can be seen, the relationship given in equation (6) was reasonably consistent with the experimental data with significant error only resulting at fill levels below h/d = 0.45.

A plot of pressure versus angle of transducer location is presented in fig. 18. It was observed that, on average, the magnitudes of pressures from largest to smallest always occurred at the same transducer locations. The locations of pressures in order of largest to smallest was seen to be: -45°, -60°, 0°, 60°, 45°. Since flow visualization was not possible for the present study, only speculations can be made concerning the reason for the above order. One explanation was that for a partially liquid filled horizontal tank at rest, the fluid occupies the bottom portion of the tank due to the effect of gravity. Upon impact, the centre of pressure would then be located on the lower part of the tank as observed. A swirling type of fluid motion around the tank end could then have occurred resulting in the other pressures measured. Since flow visualization was beyond the

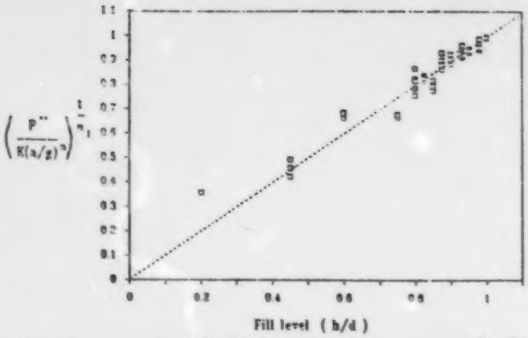

Figure 17: Modified pressure coefficient vs. fill level, h/d, for all vehicle accelerations

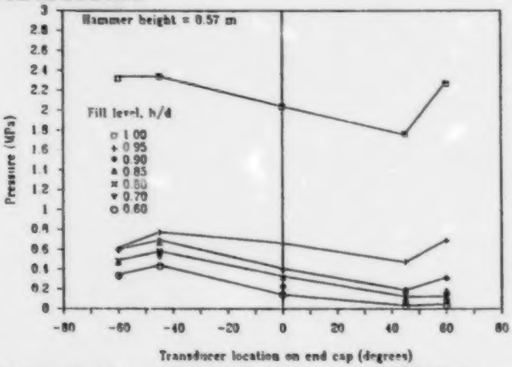

Figure 18: Pressure vs. transducer location angle for group 2 tests

scope of this study, the exact fluid motion cannot be determined.

CONCLUSIONS

The results obtained in this study and the conclusions drawn are summarized as follows:

1. The apparatus that was built was effective in measuring fluid pressures during severe impacts.
2. Impact pressures increase with an increase in fill level, acceleration, and initial velocity of the vessel.
3. The resulting vehicle acceleration, and therefore, pressures, were highly sensitive to the initial start position of the test vehicle.
4. A correlation was developed from the experimental data relating peak pressure, liquid fill level and vessel acceleration and was found to have a 15% error for h/d ≥ 0.45 and a 50 % error for h/d < 0.45.
5. The induced pressures appeared to have been caused by a water hammer effect above h/d = 0.90 and by a surface wave motion or sloshing effect below this fill level.
6. While the magnitude of pressure variation across the tank end was relatively small, it was found to follow a definite pattern.

Further studies of pressures arising from single impact forces are needed to gain a more complete understanding of this phenomenon. Recommendations for future experimentation are that tests with a clear tank should be undertaken to allow for flow visualization and that tanks of differing length to diameter ratios and the effect on resulting pressures should be investigated.

REFERENCES

1. Bass, R. L. 'Dynamic Slosh Induced Loads on Liquid Cargo Bulkheads.' SNAME. Tech. and Research Report R-19, 1975.

2. Bass, R. L. et al. 'Liquid Dynamic Loads in LNG Cargo Tanks.' SNAME. Vol. 88, 1980. pp. 103-126

3. Kobayashi, N. et al. 'A Study of the Liquid Slosh Response in Horizontal Cylindrical Tanks.' Journal of Pressure Vessel Technology. Vol. 111, 1989. pp. 32-38

4. Brooks, G. W. 'Simulation and Experimental Techniques, Part II. Experimental Techniques and Apparatus.', Chapter 5, The Dynamic Behaviour of Liquids in Moving Containers., Ed. H. N. Abramson, NASA SP-106., 1966. pp. 170-197

5. Dalzell, J. F. 'Special Topics, Part I. Liquid Impact on Tank Bulkheads.', Chapter 10, The Dynamic Behaviour of Liquids in Moving Containers., Ed. H. N. Abramson, NASA SP-106., 1966. pp. 353-372

6. Bass, R. L. et al. 'Modelling Criteria for Scaled LNG Sloshing Experiments.' Journal of Fluids Engineering. Vol. 107, 1985. pp. 272-280

7. AAR Report 'Investigation of Stresses in Tank Car Tank Heads During Lading Surge Due to Impact.' AAR Research Centre Report MR-209., 1954.

8. Phillips, E. 'Lading Sloshing in Partially Loaded Tank Cars.' AAR Research Centre Report. File: Phase II., 1977.

9. A. M. Birk and D. Chidley, 'Slosh Pressures in Cylindrical Tanks Undergoing Impact Induced Accelerations.',ASCE/ASME Mechanics, Fluids Engineering and Biomechanics Conference, San Diego, California, 1989.

10. D. Chidley, Fluid Pressures in Cylindrical Tanks Undergoing Impact Induced Accelerations., Master's Thesis, Queen's University, 1989.

FLOW VISUALIZATION IN A PLANAR TRANSONIC TURBINE CASCADE

W.E. CARSCALLEN

Senior Research Officer
Gas Dynamics Laboratory
National Research Council, Canada
Ottawa, Ontario, Canada K1A 0R6

SUMMARY

A transonic planar turbine cascade of the exhauster type was designed and constructed at the National Research Council of Canada (NRC) to investigate the redistribution of gas stream total temperature as it passed through a turbine nozzle. Flow visualization techniques were employed during the initial shakedown test to ensure that downstream pitchwise distributed static pressure taps were not adversely affected by the trailing edge shock waves. Results of these flow visualization studies and of unintentional flow visualization studies which were realised upon disassembly of the facility at the end of the first phase of experiments are reported on. Both sets of results demonstrated that flow visualization represents a very powerful tool which may be employed in the understanding of highly three dimensional flows within a transonic planar turbine cascade.

INTRODUCTION

A joint research program between National Research Council of Canada (NRC) and Pratt and Whitney Canada (P&WC) was initiated in the early 1970's. This program studied an aggressive design of a highly loaded, low-wheel-speed gas generator turbine stage of a typical P&WC aviation gas turbine engine of about 600 shaft horsepower. The objectives of this experimental and theoretical research program were to explore design rules for highly loaded turbines and evaluate and improve current design and analysis methods. In support of this work a highly loaded turbine test rig (HLTTR) was constructed in which a three times engine size stage (stator and rotor or stator alone) could be operated at representative Reynolds and Mach numbers. A description of the facility and some results of the research program have been published by Moustapha [1,2], Williamson [3,4,5] and Schaub [6].

Unpublished results of this joint research program indicated that there was a redistribution of the gas stream total temperature profile as it passed through the stator blade row, and an increase in the area weighted average of total temperature. In order to investigate these phenomena an experimental program was initiated on a separate transonic planar turbine cascade. The goals of this new research program were to reproduce the redistribution of total temperature in a highly loaded, high turning angle planar cascade, and to study the effect of secondary flows on local heat transfer coefficients at representative engine Mach and Reynold's numbers. A description of the facility and preliminary results pertaining to the redistribution of the total temperature profile of the gas stream as it passed through the stator blade row has been published by Carscallen [7].

The purpose of this paper is to describe flow visualization studies and results obtained during the initial shakedown tests of the planar cascade and unintentional flow visualization results realised upon disassembly of the planar cascade at the end of the experimental program.

TEST FACILITIES AND TEST METHODS

Transonic Planar Cascade.

A schematic representation of the planar cascade is given in Figure 1. The planar cascade constructed for this experimental investigation was an exhauster type with six blades and five nozzle passages. The highly loaded, transonic turbine stator blades were scaled to 4.3 times engine size and employed the mid-span profiles of the blades used in the NRC HLTTR. The distinguishing feature of this transonic planar cascade, versus the traditional two-dimensional cascade, was the requirement for three-dimensional flow within the nozzle passages. Though spanwise pressure gradients could not be simulated, the use of an extended inlet bellmouth of 6.67:1 aspect ratio allowed endwall boundary layers to be grown to one-tenth blade span in height, resulting in the classic horseshoe vortices and the associated three-dimensional flows as outlined by Sieverding[8]. Adjustable boundary layer bleeds were installed on both sidewalls adjacent to and upstream of the first and sixth blades to remove sidewall boundary layers and corner vortices. Variation in flow periodicity between the centre nozzle passage and the two bounding nozzles was less than 0.5 % for the range of cascade operating pressure ratios of 1.07 to 3.0. An adjustable, porous, aluminum tail board allowed fine adjustment in periodicity between nozzle passages and the elimination of shock wave reflection. Tailboard porosity was 23.0 percent with a hole depth to diameter aspect ratio of 1.0. The cascade was operated by a 2680 horse power exhauster facility, capable of continuously drawing 10 pounds of air per second at 2 psia.

Major specifications and design conditions of the planar cascade are as follows:

Blading	
Blade chord	C=8.032 in
Axial blade chord	Cx=3.33 in
Blade pitch	S=5.817 in
Blade span	H=4.44 in
Blade aspect ratio	H/C=.871
Solidity	C/S=.876
Design turning angle	76 deg
Nozzle throat width	1.215 in
Number of blades	6
Design conditions	
Inlet total temperature	70 F
Inlet total pressure	14.7 psia
Pressure ratio	2.3
Inlet Mach Number	.112
Exit Mach Number	1.2
Mass flow rate (total)	8.5 lb/s
Reynolds Number (axial)	213000

EXPERIMENTAL PROCEDURE

Introduction

Initial shakedown tests of the planar cascade were carried out with minimal instrumentation. Provision for visual inspection of the internal elements of the planar cascade under operational conditions was provided by having the right hand endwall constructed from clear plexiglass, the left hand endwall was aluminum. There was one static pressure tap installed in the planar cascade to measure the operating pressure ratio. This static tap was located at the planar cascade exit, half way between the trailing edge of the tailboard and the trailing edge of the blade incorporated in the boundary layer bleed. Wool tufts were taped to the end walls upstream of the boundary layer bleed knife edges allowing a visual indication of the streamline approaching the knife edge.

Shakedown tests of the planar cascade were carried out at the following pressure ratios 1.045, 1.11, 1.88, 2.30 (design pressure ratio), 2.64.

Flow Visualization

Flow visualization was carried out during the initial shakedown test to locate the trailing edge shock waves and thus allow the specific position of pitchwise oriented static pressure taps, located downstream of the nozzle passages, to be determined such that their location was not coincident with trailing edge shocks at the design pressure ratio. This flow visualization was realised by sucking lamp black from an oxyacetylene welding torch burning only acetylene through the bellmouth into the planar cascade. The adhesion of the lamp black to the internal surfaces was enhanced by the presence of a vaseline film on the internal surfaces. Vaseline having been used to seal the mating surfaces of the planar cascade during assembly.

The visualization of blade surface streamlines was carried out by dotting the surface to be studied with machinist's blue. Unfortunately, the viscosity of the machinist's blue was too high and no flow visualization took place. Varsol was sprayed into the bellmouth in an effort to dissolve the machinist's blue and allow flow visualization to commence. This was unsuccessful in allowing visualization of the blade surface streamlines, but, the varsol flowing along the endwalls did leave some traces of the limiting streamlines on the endwall.

Unintentional flow visualization was realised at the end of the complete experimental program upon disassembly of the planar cascade. This unintentional flow visualization was a result of oil mist from the main bearings of the Brown Bovari exhauster becoming airborne in the compressor bay in which both the planar cascade and exhauster were located. This oil mist was inhaled by the planar cascade over a period of months as various test were run and was deposited on the internal surfaces leaving very extensive flow visualization records.

RESULTS AND DISCUSSION

Intentional Flow Visualization

Figure 2 is an annotated photograph of the dark lines left on the right plexiglass endwall by the trailing edge shock waves and their reflections from the suction surface of the adjacent blade interacting with the endwall boundary layer. Also shown is an indication of the flow through holes in the porous tailboard at the tailboard/endwall junction as affected by the trailing edge shock waves and their reflections. The cancellation of shock waves by the porous tailboard is indicated by the lack of dark lines reflecting from the tailboard adjacent to the location of the dark lines associated with the trailing edge shock waves striking the tailboard.

The dark lines on the endwall are caused by oblique trailing edge shock waves. These impose an adverse pressure gradient on the entire nozzle gas stream. As the endwall boundary layer flow has been retarded by viscous effects within, the boundary layer has insufficient momentum to over-come the adverse pressure gradient associated with the shock wave. A reverse flow results in the lower boundary layer region between the end of the shock wave and the endwall surface. This reverse flow causes a separation of and a thickening of the endwall boundary layer. The stagnation region between the reverse flow and boundary layer flow are indicated by the dark lines on the plexiglass endwall. This picture of the boundary layer/shockwave interaction implies that the endwall edge of the shock waves and their reflections are located downstream of the dark lines.

The pitchwise oriented endwall static pressure taps, downstream of the nozzle passage were located to the upstream side of the dark lines of the shock wave system.

Flow through the porous tailboard at the tailboard/endwall junction is manifested as a series of dark lines of varying length and intensity at the porous tailboard/endwall junction. The varying length and intensity of the lines are attributed to the effect on the flow through the porous tail board by the trailing edge shock waves and their reflections on the pressure gradient across the tailboard. The longer darker lines are always located just downstream of the shockwave or a shockwave reflection where there is a local increase in gas stream static pressure and thus an increase in pressure gradient across the tailboard.

Unintentional Flow Visualization

The unintentional flow visualization records are the result of cascade operation over extensive periods of time and at varying pressure ratios. These records are thus both time and pressure ratio averaged records and they indicate the long term mean three dimensional flow behaviour.

Figure 3 is an annotated photograph of visualized flow on the endwall of the centre nozzle passage.

The generation of the secondary flow phenomena called the horseshoe vortex at the blade/endwall junction is attributable to the pressure variation at the leading edge/endwall intersection. The pressure variation being due to the turbulent endwall boundary layer velocity distribution and the stagnation pressure distribution on the blade leading edge. This pressure difference forces the flow down the leading edge towards the endwall. The flow in moving down the leading edge towards the endwall separates from the leading edge just prior to the blade/endwall junction and generates a small corner vortex. This occurs just prior to the pressure distribution on the endwall and the proximity of the blade leading edge force the flow to turn upstream. The flow in turning upstream causes the lower regions of the approaching downstream directed endwall boundary layer to separate, roll up and form a vortex system. The ends of this vortex system when swept downstream assume the characteristic horseshoe shape. As the endwall boundary layer separates, a region between the boundary layer separation line and the liftoff line of the horseshoe vortex results in a region of low momentum gas and the dark deposit denoting the horseshoe vortex separation region. Development of both the horseshoe and corner vortices are illustrated in Figure 4.

From the trajectory of this separation region it may be seen that the suction surface side of the horseshoe vortex is pushed towards the suction surface blade/endwall junction after merging with the corner vortex stagnation line. This is in contrast to Sieverding [8] who states that in the accelerating front part of the nozzle passage the vortex moves away from the endwall but stays close to the suction surface. The pressure surface side of the horseshoe vortex migrates from the pressure surface towards the suction surface of the adjacent blade and finally contacts the adjacent blade suction surface just upstream of the nozzle throat. As there is no discontinuity in the pressure side leg of the horseshoe vortex separation line one might presume as has Langston [9] and Sieverding that the pressure surface side of the horseshoe vortex merges with and becomes part of the passage vortex. The migration of the pressure surface side of the vortex is attributable to the pressure gradient between the pressure and suction surfaces of the nozzle passage generated by the turning of the mainstream flow by the blades. As the passage vortex traverses the endwall, the endwall boundary layer is lifted off the endwall and wrapped onto the passage vortex. As a result, a new endwall boundary layer forms downstream of the passage vortex. The transition region of this new endwall boundary layer from laminar to turbulent is seen to be that endwall area where a 'flyspeck' and endwall static pressure tapping will trip the boundary layer. The wakes from the 'flyspecks' and static pressure tappings are readily identifiable. Complete transition of the new endwall boundary layer seems to be indicated in Figure 3 by the dark area just upstream of the trailing edge shock waves.

The corner vortex stagnation line as shown in Figure 5 is produced on the endwall at the blade/endwall junction where both the corner vortex and the horseshoe vortex flow field develop a mutual stagnation line. This corner vortex stagnation line is seen to be pushed into the corner of the pressure surface blade/endwall junction were it can be seen in Figure 3 to extend to the trailing edge, while on the suction surface the corner vortex stagnation line separates from the suction surface blade/endwall junction as it rounds the blade leading edge prior to it's becoming indistinguishable from the horseshoe vortex separation line. Note, the passage vortex separation line from the adjacent blade ultimately blends into both the corner vortex stagnation line and suction surface passage vortex separation line. This may be seen in Figure 3.

Figure 6 shows the relationship between the corner vortex and the leading edge stagnation region which is denoted as a spanwise dark strip on the blade leading edge. The darkness of this deposit varies from heavy in the central region to lighter at the edges. The corner vortex is closest to to the blade leading edge at the position of heaviest deposit, indicating that the position of the leading edge stagnation line is spanwise invariant. The flow angle between the gas stream and the blade may be derived by measuring the position of the heaviest deposit on the leading edge. The flow angle is 31.0 degrees.

Figure 7 shows an area of spanwise distributed 'flyspeck' wakes on the suction surface of the blades. This area is nominally bounded by the blade trailing edge locating dowel and the blade trailing edge. These 'flyspeck' wakes indicate the transition zone of the blade pressure surface boundary layer from laminar to turbulent. The black band just upstream of the blade trailing edge may be the result of the machining process of the blade as are the distinctive spanwise black bands upstream of the 'flyspeck' wakes and the faint black bands in the 'flyspecked' area.

Figure 8 is an annotated photograph of the blade suction surface. The wake from the midspan static pressure tap 'R' is distinctive. The static tap causes transition of the suction surface boundary layer. The trailing edge shockwave stagnation line resulting from the interaction of the oblique planar trailing edge shock wave with the static pressure tap wake and the vortex system located at the blade/endwall junction is readily identifiable. The cause of this type of stagnation line has been previously discussed. What are presumed to be the passage vortex separation line and the separation line of the suction surface leg of the horseshoe are seen as dark bands originating where the corner vortex, suction surface leg of the horseshoe vortex and the passage vortex merge. These lines then extend downstream to the blade trailing edge. Similar lines have been observed by Marchal and Sieverding [10] and were attributed to the passage vortex riding up on the suction leg of the horseshoe vortex as the two vortices moved along the blade suction surface. The work of Goldstein and Spores [11] and Gregory-Smith and Graves [12] also supported this explanation of the flow. Unfortunately, in the present work there is insufficient data available to allow any discussion reguarding the interaction of the leading edge corner vortex and the horseshoe vortex as they migrate through the nozzle passage.

CONCLUSIONS

Flow visualization results have allowed the placement of downstream, pitchwise oriented, static pressure taps on the endwall of a transonic planar cascade such that the taps are uneffected by unsteady pressure gradients associated with trailing edge shockwaves.

Unintentional flow visualization has indicated that two vortices are dominant, the leading edge horseshoe and corner vortices and that these two vortices stay adjacent to the endwall in their passage through the cascade. There are no indications that the pressure surface side of the horseshoe vortex may be differentiated from the passage vortex. The roll up of the endwall boundary layer by the pressure surface side of the horseshoe vortex is supported by the development of a new endwall boundary layer downstream of the pressure surface side of the horseshoe vortex. Along the blade suction surface the pressure surface side of the horseshoe vortex rides up upon the suction surface side of the horseshoe vortex from the forward section of the blade to the trailing edge. Flow visualization records of the blade leading edge corner vortex and stagnation line show that the gas stream flow angle is spanwise invariant.

REFERENCES

1 Moustapha, S.H. and Williamson, R.G., 1986, "Investigation of the Effect of Two Endwall Contours on the Performance of a Annular Nozzle Cascade", AIAA Journal.

2 Moustapha, S.H., Okapuu, U., and Williamson, R.G., 1987, "The Influence of Rotor Blade Aerodynamic Loading on the Performance of a Highly Loaded Turbine Stage", ASME Journal of Turbomachinery.

3 Williamson, R.G., and Moustapha, S.H., 1986, "Three-Dimensional Cascade Testing of Turbine Nozzles at High Exit Mach Number", ASME Journal of Fluids Engineering.

4 Williamson, R.G., and Moustapha, S.H., 1986, "Annular Cascade Testing of Turbine Nozzles at High Exit Mach Numbers" Journal of Fluids Engineering

5 Williamson, R.G., and Moustapha, S.H. and Huot, J.P., 1986, "The Effect Of a Downstream Rotor on the Measured Performance of a Transonic Nozzle", ASME Journal of Turbomachinery.

6 Schaub, U.W., Williamson, R.G., Huot, J.P. and Moustapha, S.H. "An Experimental Assessment of the Influence of Downstream Conditions on the Performance of a Transonic Turbine Nozzle", ASME Gas Turbine and Aeroengine Congress and Exposition, June 4-8, 1989, Toronto, Ontario, Canada.

7 Carscallen, W.E., and Oosthuizen, P.H., "The Effect of Secondary Flow on the Redistribution of the Total Temperature Field Downstream of a Stationary Turbine Cascade", AGARD-CPP-468/469, 1989.

8 Sieverding, C.M., 1985, "Recent Progress in the Understanding of Basic Aspects of Secondary Flow in Turbine Blade Passages", ASME Journal of Engineering for Gas Turbine and Power.

9 Langston, L.S., Nice M.L., Hooper, R.M., "Three Dimensional Flow within a Turbine Nozzle Passage", Journal for Engineering Power", January 1977, Pages 21-28.

10 Marchal P., Sieverding, C.H., "Secondary Flows within Turbomachinery Blading", AGARD Conference Proceedings CP 214, 1977, Pages 11-1 to 11-19.

11 Goldstein R.J., Spores R.A., "Turbulent Transport on the Endwall in the Region Between Adjacent Turbine Blades", The American Society of Mechanical Engineers, Vol. 110, November 1988, Pages 862 to 869.

12 Gregory-Smith D.G., Graves C.P., "Secondary Flows and Losses in a Turbine Cascade", Viscous effects in Turbomachinery, AGARD CP 351,1983.

ACKNOWLEDGMENTS

The authors are indebted to Drs. R.G. Williamson and M.K.Y. Lai for their valuable input and encouragement in the evaluation of these results, and to Messrs. P.S. Hunt, M. McMullin and B.J. Day for their assistance in the design, assembly and operation of the facility and to Mr. M. Klein for his assistance in securing the experimental data and in the preparation of the graphics.

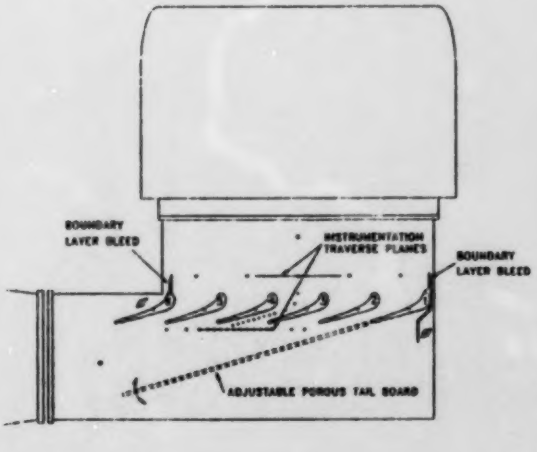

Schematic Drawing of Planar Cascade

Figure 1

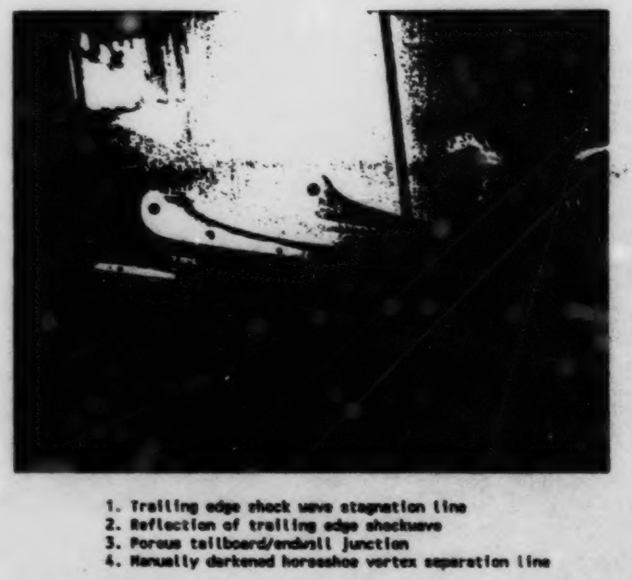

1. Trailing edge shock wave stagnation line
2. Reflection of trailing edge shockwave
3. Porous tailboard/endwall junction
4. Manually darkened horseshoe vortex separation line

Photograph of Endwall Flow Visualization

Figure 2

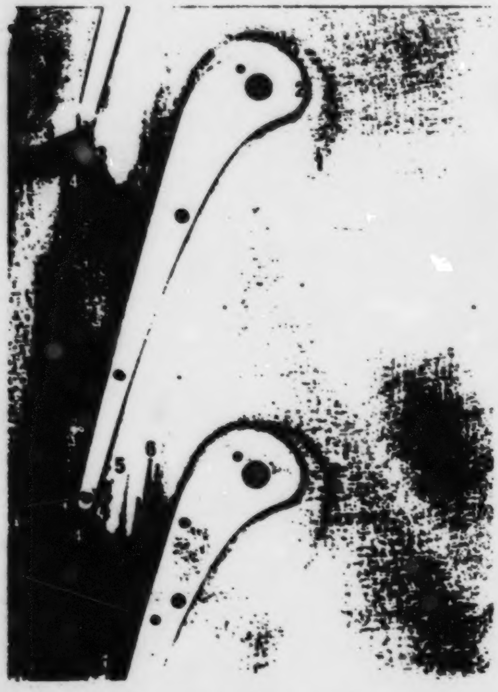

1. Horseshoe vortex separation region
2. Corner vortex stagnation line
3. Trailing edge shock wave stagnation region
4. Nozzle blade wakes
5. 'Flyspeck' wake
6. Static pressure tap wakes

Endwall Flow Visualization

Figure 3

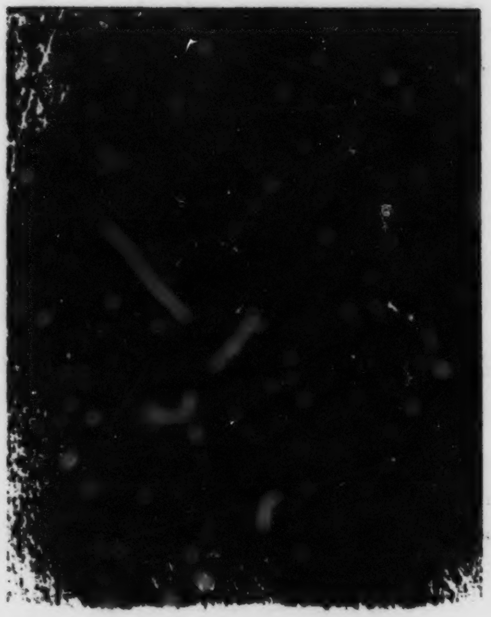

Corner Vortex Flow Visualization

Figure 5

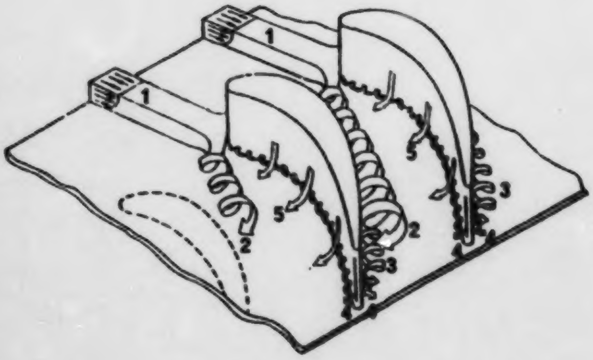

1. Inlet boundary layer
2. Horseshoe vortex pressure surface leg
3. Horseshoe vortex suction surface leg
4. Corner vortex
5. Endwall crossflow

Horseshoe and Corner Vortex Development

Figure 4

Leading Edge Flow Visualization

Figure 6

Pressure Surface Flow Visualization

Figure 7

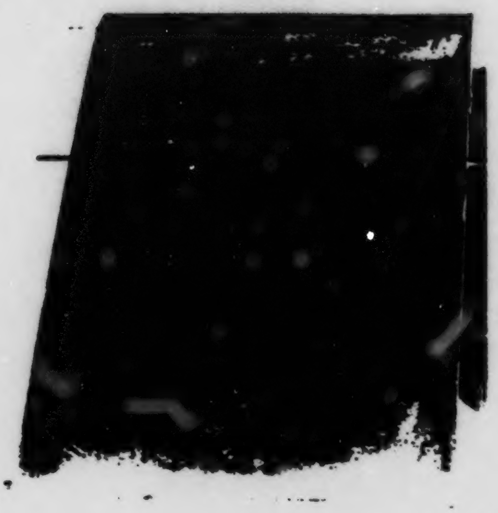

1. Static pressure tap wake
2. Trailing edge shock wave stagnation line
3. Suction surface leg of horseshoe vortex separation line
4. Passage vortex separation line

Blade Suction Surface Flow Visualization

Figure 8

TURBULENT CONVECTIVE HEAT TRANSFER IN A THREE DIMENSIONAL SQUARE DUCT

G. Yang and M. A. Ebadian

Department of Mechanical Engineering
Florida International University
The State University of Florida at Miami
Miami, Fl. 33199 U.S.A.

ABSTRACT

This paper presents the numerical prediction of thermal developing processes in a square, cross-section duct for turbulent flow with isothermal walls. The algebraic stress model has been employed to predict the fully developed turbulent flow. The three dimensional energy equation was discretized and solved by the Method of Lines (MOL). The effects of Prandtl and Reynolds numbers on the thermal behaviors in the entrance region is investigated. The computed results for the fully developed region are shown to be in good agreement with the measured data published in open literature.

NOMENCLATURE

a	duct half-width [m]
c_D	turbulance constant
c_p	specific heat at constant pressure [J kg^{-1} K^{-1}]
c_μ	turbulence constant
D_h	hydraulic diameter [m]
k	molecular thermal conductivity [W m^{-1} K^{-1}]
k_t	turbulent thermal conductivity [W m^{-1} K^{-1}]
K	turbulent kinetic energy
$\dot{m}$	mass flow rate [kg s^{-1}]
Nu	Nusselt number
p	pressure [N m^{-2}]
P	production rate of kinetic energy
P'	pressure correction [N m^{-2}]
P^*	estimate pressure [N m^{-2}]
Pe	Peclet number, RePr
Pr	Prandtl number
Pr_t	turbulent number
Q_T	total heat rate, equation (14) [J]
q_w	total wall heat flux, equation (15) [w]
Re	Reynolds number, u/D_h
St	Stanton number, Nu/Pe
S_ϕ	source term
T	absolute temperature [K]
T_b	mean bulk temperature [K]
T_o	entrance temperature [K]
T_w	wall temperature [K]
u	streamwise velocity
v, w	transverse velocities
x	streamwise coordinate
y, z	transverse coordinates

Greek Symbols

α	heat diffusivity [m^{-3} s^{-1}]
ϵ	rate of kinetic energy dissipation [J]
κ	Von Karman constant
Γ_ϕ	diffusion coefficient [m^{-2} s]
ν	molecular kinematic viscosity [m^{-2} s^{-1}]
ν_t	turbulent kinematic viscosity [m^{-2} s^{-1}]
ρ	density [kg m^{-3}]
σ_k	effective Prandtl number of k
σ_ϵ	effective Prandtl number of ϵ
ϕ	dimensionless temperature
ψ	general dependent variable

Subscripts

eff	effective
o	initial value
w	wall

INTRODUCTION

Straight ducts of square cross-section are widely used in designs of compact heat exchangers, gas cooled nuclear reactors, aircraft propulsion systems, and air conditioning systems. Turbulent forced convection in the thermally developing region of this geometry is of great interest for designer and practitioner working in these fields. It has been proven experimentally by Nikuradse (1962) that the turbulent flow in a duct of square cross-section is three dimensional even for the case of a fully developed condition. The velocity of the secondary flow (normal flow) is approximately 1% of the magnitude of the mean velocity of primary flow (axial flow). However, even this small percentage exerts a measurable effect in distorting the axial velocity profile, increasing the friction coefficients in the ducts, and augmenting the heat transfer rate. A number of papers has been published in the open literature containing the results for the hydrodynamically or simultaneously developing turbulent heat transfer in square ducts. Unfortunately, none of those experimental/numerical results deal with the thermal developing process for a square cross-section (Kakac, et al. 1987). This paper is an effort to study the effects of Reynolds and Prandtl numbers on the thermal developing process in the entrance region of square ducts.

The early stages of the study of turbulent flow in a square duct relied heavily on experimental tests [Leutheusser (1963), Brundrett and Baines (1964), Brundrett and Burroughs (1967)]. These experimental observations demonstrate that secondary flows are normally attributed to the presence of Reynolds-stress gradients in the cross-stream direction of the main flow. In recent years, a significant effort has been devoted toward the computation of turbulent secondary flows using the algebraic turbulent stress model. The first attempt to predict fully developed flow in a square duct was made by Launder and Ying (1973) using a one-equation model for k and adopting Buleev's method (1963) to select the turbulent length, ℓ. In the case of the mean velocity field, they obtained good agreement with the experimental data reported by (Brundrett and Burroughs, 1967). The algebraic stress model originally developed in Launder and Ying (1973) later evolved into an explicit expression by Gessner and Emery, (1976). This modified version of the model was coupled by Nakayama, et al. (1983), with a two equation model (K-ϵ) to study fully developed velocities in square ducts. Their numerical prediction of the friction coefficients compared satisfactorily with the experimental observations reported by Leutheusser (1963) and Hartnett, et al. (1962), respectively. Additionally, Speziale (1986) has examined the usefulness of various turbulence models in predicting the secondary flows in non-circular ducts.

Presently, there are many experimental data available in the literature for the fully developed Nusselt number in square ducts. Brundrett and Burroughs (1964) measured the temperature profile and the Nusselt number in a square duct. Novotny, et al. (1964) measured the Nusselt numbers for turbulent flow using air as a fluid (Pr = 0.7) in a square duct with two insulated and two uniform heat flux walls. Recently, there have been several numerical studies to predict the fully developed Nusselt numbers in square ducts using a variety of turbulence closure models. Patankar and Archarya (1984) developed a simple mixing-length turbulence model which neglects the effect of secondary flow. Their predicted results are in good agreement with the test data. Launder and Ying (1973) considered the effects of secondary flow and slightly improved the results. The developing process for the velocity and temperature profiles were computed by Emery, et al. (1979) for a square duct with constant wall temperature, based on an algebraic closure model. The computed local and fully developed shear stresses and heat transfer are shown to be in good agreement with measured data and with predictions using the K-ϵ model.

This paper investigates numerically the thermal entrance problem in a straight square duct subjected to constant wall temperature with a fully developed turbulent flow. Two steps have been taken in this investigation; 1.) finding the turbulent flow pattern in a square duct by a simplified algebraic turbulent model, and 2.) solving the energy equations by the Method of Lines (MOL). In light of the foregoing, the effects of Prandtl and Reynolds numbers on turbulent flow in a square duct are also calculated and discussed.

MATHEMATICAL DEVELOPMENT

The geometry and coordinate system of a square duct is shown in Fig. 1. The incompressible fluid enters steadily through the ducts with a fully developed velocity profile and a uniform temperature φ_o at x = 0. The surface of the duct is maintained at uniform temperature $\varphi_w = 0$.

Momentum Transfer and Turbulence Model

In Cartesian coordinates (x along the axis and y and z in the cross-sectional plane of the square ducts), the conservation equation for a fully developed turbulent flow of a constant property gas is

$$v \frac{\partial\phi}{\partial y} + w \frac{\partial\phi}{\partial z} - \frac{\partial}{\partial y}\left(\Gamma_\phi \frac{\partial\phi}{\partial y}\right) - \frac{\partial}{\partial z}\left(\Gamma_\phi \frac{\partial\phi}{\partial z}\right) = S_\phi \qquad (1)$$

where the general dependent variable ϕ, the diffusion coefficient Γ_ϕ and the source term S_ϕ are defined in Table 1 for each transport equation.

TABLE 1. Variable in the Transport Equations

Transport Equation	ϕ	Γ_ϕ	S_ϕ
Continuity	1	0	0
u-momentum	u	$\nu + \nu_t$	$-\frac{P_x}{\rho}$
v-momentum	v	ν	$-\left[\frac{p}{\rho} - \frac{c' c_D K^3 u_y^2}{\epsilon^2} + c_k' K\right]_y$ $+ \frac{c' c_D K^3 u_y u_z}{\epsilon^2}$
w-momentum	w	ν	$-\left[\frac{p}{\rho} - \frac{c' c_D K^3 u_z^2}{\epsilon^2} + c_k' K\right]_y$ $+ \frac{c' c_D K^3 u_y u_z}{\epsilon^2}$
Turbulent Kinetic Energy	K	$\nu + \frac{\nu_t}{\sigma_k}$	$P - \epsilon$
Rate of Dissipation	ϵ	$\nu + \frac{\nu_t}{\sigma_\epsilon}$	$\frac{(c_1 P - c_2 \epsilon)\epsilon}{K}$

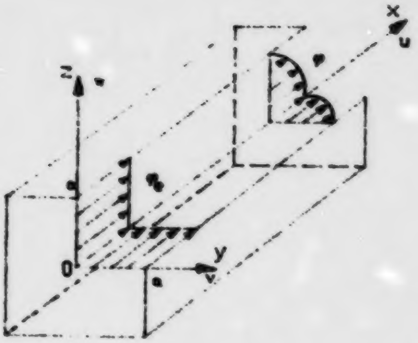

Figure 1: Geometry and Coordinate System.

In the preceding equations, the subscripts x, y, and z in the source terms denote partial derivatives and the symbols are defined in the Nomenclature.

The longitudinal pressure gradient, p_x, in the u-momentum equation can be assumed as uniform over a cross-section and can be found by considering the mass-conversion in the axial direction (Patanker and Spalding, 1972) as:

$$p_x = p_x^{*} + p_x'$$

where p_x^{*} presents the results of the previous iteration, and p'_x the correct value of p_x from the local continuity equation:

$$p_x' = \frac{\dot{m} - \sum \rho\, u^{*}\, \Delta y \Delta z}{\sum \rho\, D_u \Delta y\ \Delta z} \tag{2}$$

the $\dot{m}$ indicates the total mass flow rate, and u^{*} is the estimated axial velocity (the calculated results from the previous iteration). The initial value of p_x in the u-momentum equation is given by:

$$-\frac{p_x}{\rho} = 4\,\frac{c_D^{1/2} K_{av}}{D_h} \tag{3}$$

where K_{av} is the mean value of kinetic energy in the "near-wall" region (average over the periphery. Moreover, turbulence viscosity is modeled by introducing an effective kinematic viscosity (the sum of the laminar and the turbulent kinematic viscosity),

$$\nu_{eff} = \nu + \nu_t \tag{4}$$

Here, the turbulent kinematic viscosity, ν_t, is related to K and ϵ through the near-wall constant c_D, as

$$\nu_t = \frac{c_D\, K^2}{\epsilon}\,. \tag{5}$$

In addition to this, the production rate of kinetic energy, P, was calculated by the relation

$$P = \nu_t \left[\left(\frac{\partial u}{\partial y}\right)^2 + \left(\frac{\partial u}{\partial z}\right)^2 \right] \tag{6}$$

The constants in the K-ϵ model are chosen according to Launder and Spalding (1972), and are given in Table 2.

Table 2. Constants for K-ϵ Model

c_D	c'	c_k'	c_1	c_2	σ_k	σ_ϵ
0.09	0.0185	0.552	1.44	1.92	0.9	1.3

To complete the system of equations, the boundary conditions for K and ϵ at the duct wall are derived from the logarithmic wall function for forced convection (Launder and Spalding, 1972).

Heat Transfer

The time-average energy equation in the thermal entrance region of an isothermal square duct is:

$$u\frac{\partial T}{\partial x} + v\frac{\partial T}{\partial y} + w\frac{\partial T}{\partial z} = \frac{\partial}{\partial y}\left[\alpha\frac{\partial T}{\partial y} - \overline{T'v}\right] + \frac{\partial}{\partial z}\left[\alpha\frac{\partial T}{\partial z} - \overline{T'w}\right]. \tag{7}$$

By introducing the concept of eddy diffusivity, α_t, one can write:

$$\overline{T'v'} = -\alpha_t\frac{\partial T}{\partial y}$$
$$\overline{T'w'} = -\alpha_t\frac{\partial T}{\partial z} \tag{8}$$

Therefore eq. (7) can be simplified as

$$u\frac{\partial T}{\partial x} + v\frac{\partial T}{\partial y} + w\frac{\partial T}{\partial z} = \frac{\partial}{\partial y}\left[\alpha_{eff}\frac{\partial T}{\partial y}\right] + \frac{\partial}{\partial z}\left[\alpha_{eff}\frac{\partial T}{\partial z}\right] \tag{9}$$

where

$$\alpha_{eff} = \alpha + \alpha_t \tag{10}$$

and α_t will be

$$\alpha_t = \frac{\nu_t}{Pr_t} \tag{11}$$

The turbulent Prandtl number, Pr_t, can now be found based on the molecular Prandtl number Pr of the calculated fluid [Reynolds (1975), Malhotra and Kang (1984)]. Also, the wall function has been used to determine the turbulent heat diffusivity, α_t, near the solid wall.

$$\alpha_t = \left(c_\mu^{\frac{1}{4}} k^{\frac{1}{2}} y_p\right) \Bigg/ \left\{ \frac{Pr_t}{\kappa} \ln\left[\epsilon\,\frac{y_p\left(c_\mu^{\frac{1}{4}} k^{\frac{1}{2}}\right)}{\nu}\right] + 9.24\left(\frac{Pr_t}{P_r} - 1\right)\left(\frac{Pr}{Pr_t}\right)^{-\frac{1}{4}} \right\} \tag{12}$$

where the Von Karman constant, κ, and ϵ are 0.41, and 9.26, respectively.

NUMERICAL PROCEDURE

The finite difference method used to solve the descriptive equations entails subdividing the calculation domain into a number of control volumes. First, the velocity profile of fully developed turbulent flow in the square duct was solved. The algorithm solution was embodied in a version of the Teach Program (Gosman, et al., 1976) with a 22x22 mesh. Convergence was achieved when the normalized residuals were less than 10^{-6} for each equation.

The results of the momentum equations u, v, w, k, and ϵ are then used to calculate the energy equation. The Method of Lines (Liskovets, 1965) has been used to solve the energy equation. According to this method, the transversal derivatives are replaced by finite difference formulations and, correspondingly, the region of integration is divided into a collection of lines parallel to the axial coordinate of the duct. The partial differential equation comprising the set of conservation equations is replaced by a system of ordinary differential equations of first order (the independent variable is the axial coordinate), coupled to a system of algebraic equations. The solutions of these equation systems are obtained numerically using Runge-Kutta algorithms. A non-uniform grid of 8x8 nodes was used for calculating the temperature profile at each cross-section. Furthermore, the mean bulk temperature has been computed from the discrete temperature data by a two-dimensional tensor-product interpolation/integrate subroutine from the IMSL Library Subroutine Package (IMSL, Inc., 1984).

PARAMETERS OF INTEREST

The main results that will be extracted from the numerical solutions are the mean bulk temperature and the rate of heat transfer from the gas flowing in the square ducts. The mean bulk temperature at a streamwise station, x, is usually defined by

$$T_{bx} = \frac{\int_A u\, T\, dA}{\int_A u\, dA} \qquad (13)$$

In this sense, if $\dot{m}$ denotes the mass flow rate, then the total rate of heat transfer for the region between $x = 0$ and any x (a downstream station), is given by

$$Q_T = \dot{m}\, c_p (T_{bx} - T_o) \qquad (14)$$

where T_{bx} is obtained from eq. (13) and is normally presented graphically as T_{bx} versus x.

Alternatively, the Stanton number may also be computed as follows:

$$St = \frac{Nu}{Pe} = \frac{q_w\, D_h}{k(T_w - T_b)\, Pe} \qquad (15)$$

RESULTS AND DISCUSSION

Based on the mathematical modeling proposed, the effects of Prandtl and Reynolds numbers on heat transfer behaviors in square ducts are studied.

The previous studies showed that the Prandtl number of fluid is one of the most important parameters to affect the process of heat transfer (Kakac, et al., 1987). Three different fluid mediums (air, water, and ethylene glycol) with the different Prandtl numbers have been calculated. The major properties of these mediums are listed in Table 3.

Table 3. The Major Properties of Three Mediums

	Air	Water	Ethylene glycol
Density $[kg/m^3]$	1.20	1000	1111.40
Specific heat $[J\ kg^{-1}\ K^{-1}]$	1.01	4.18	2.41
Thermal Conductivity $[w\ m^{-1}\ K^{-1}] \times 10^3$	0.02	0.61	0.25
Kinematic Viscosity $[m^{-2}\ S^{-1}] \times 10^6$	15.40	0.80	14.10
Prandtl number	0.70	5.83	151.00

Fig. 2 shows the comparison of predicted results with the results of Deissler and Taylor (1959). It can be seen that fully developed Nusselt numbers enhances significantly when the Prandtl number increases. The present data are in good agreement with previous work.

Fig. 3 illustrates the fully developed dimensionless temperature profiles for different Prandtl numbers. The temperature gradients for the large Pr is steeper compared with the smaller one, due to the turbulent effect.

The dimensionless Nusselt number during thermal developing processes in the square duct is presented in Fig. 4. For low Prandtl number fluids ($Pr = 0.7$ and 5.03), the processes follow the same trend. That is the Nu/Nu_{∞} drops very quickly at the beginning, then slows down to the fully thermal developed condition. However, the developing process of a high Pr is much faster than that of a low Pr. The behavior of the thermal developing process for a high Pr is much different than that of a low Pr. The Nusselt number undergoes a small drop at the beginning, then it slowly increases as seen from the curve of ethylene glycol.

Fig. 5 shows the comparison between the predicted and measured fully developed Stanton numbers for a square duct with isothermal walls. The tested data are obtained by Brundrett and Burroughs (1967). The solid line is the calculated results in this investigation with $Pr = 0.7$, which is in good agreement with the measured results.

Fig. 6 shows the calculated axial variation of the Stanton number for four different Reynolds numbers. All the curves in this figure follow the classical patterns where higher heat transfer rates occur at the vicinity of the entrance $x = 0$. Then the Stanton number decreases gradually until reaching a state of thermal equilibrium. The thermal entry length associated with this thermal equilibrium is 20 to 30 times of the hydraulic diameter of the square duct.

CONCLUSION

This paper has examined the effects of Prandtl and Reynolds numbers on the thermal developing process of turbulent flow at the entrance of the square duct. The algebraic stress model is used to predict the fully developed velocity profiles and turbulent viscosity.

The thermal developing process is discretized and solved by the Method of Lines. Three kinds of fluid mediums with large ranges of Pr and Re have been calculated. The predicted results are in a excellent agreement with the results published in the literature.

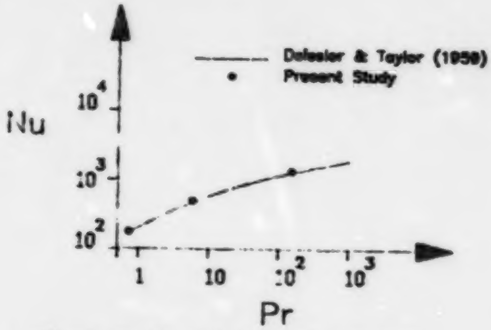

Figure 2: Nusselt Number for Fully Developed Turbulent Flow in Square Duct.

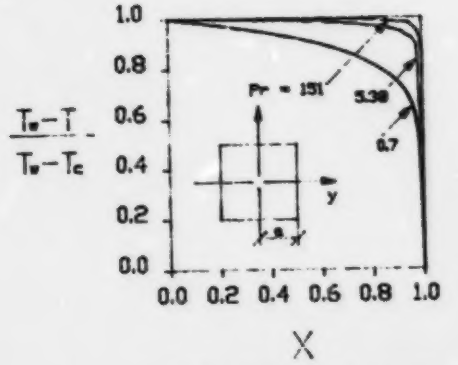

Figure 3: Fully Developed Turbulent Temperature Distribution in Square Duct.

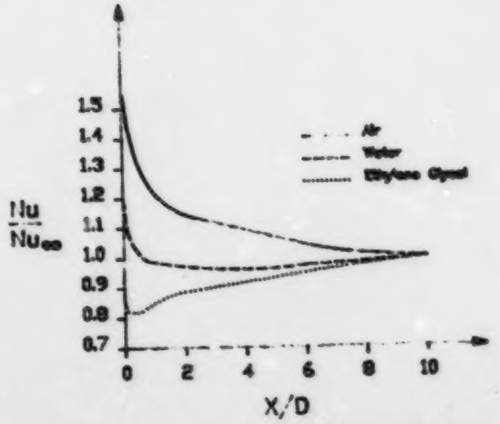

Figure 4: Thermal Developing Process in Square Duct.

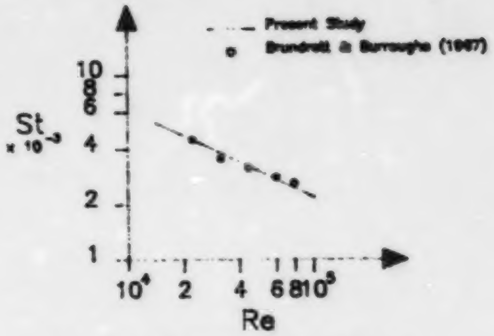

Figure 5: Comparison of Predicted Results with Experimental Data.

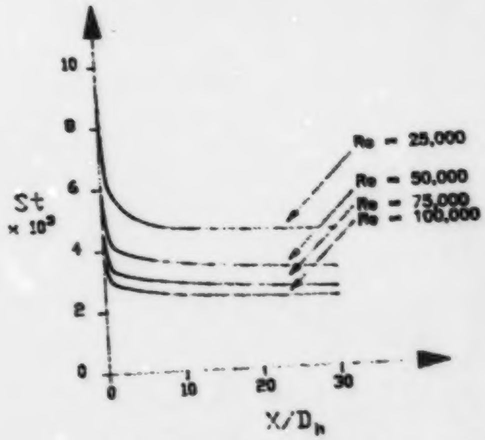

Figure 6: Thermal Developing Process for Different Reynolds Number.

ACKNOWLEDGEMENT

The results presented in this paper were obtained in the course of research, sponsored by the Department of Energy under Subcontract No. 19X-SE133V.

REFERENCES

Brundrett, E. & Baines, W. D. 1964, The Prediction and Diffusion of Vorticity in Duct Flow, J. Fluid Mech., 19, pp. 374-394.

Brundrett, E. & Burroughs, P. R. 1967, The Temperature Inner-Law and Heat Transfer for Turbulent Air Flow in a Vertical Square Duct, Int. J. Heat Mass Transfer, 10, pp. 1133-1142.

Buleev, N. I. 1963, Theoretical Model of Mechanism of Turbulent Exchange in Fluid Flow, AERE Translation, pp. 957-1063.

Deissler, R. D. & Taylor, M. F. 1959, Analysis of Turbulent Flow and Heat Transfer in Non-Circular Passages, NASA TR, R-31.

Emery, A. F., Neighbors, R. K. & Gessner, F. B. 1979, Numerical Prediction of Developing Turbulent Flow and Heat Transfer in a Square Duct, ASME Paper 79-WA/HT-12.

Gessner, F. B. & Emery, A. F. 1976, A Reynolds Stress Model for Turbulent Corner Flows - Part I: Development of the Model, J.Fluids Engineering, 98, pp. 261-268.

Gosman, A. D., Humphrey, J. A. C. & Vlachos, N. S. 1976, TEACH-3E: A General Computer Program of Three-Dimensional Recirculating Flows, Imperial College, England, U.K.

Hartnett, J. P., Koh, J. C. & McComas, S. 1962, A Comparison of Predicted and Measured Friction Factors for Flow Through Rectangular Ducts, J. Heat Transfer, 84, pp. 82-88.

IMSL library Subroutine Package 1984, IMSL Inc., Houston, Texas.

Kakac, S., Shah, R. K & Aung, W. 1987 *Handbook of Single-Phase Convective Heat Transfer*, pp. 4-83, John Wiley of Sons, N.Y.

Launder, B. E. & Spalding D. B. 1972, Mathematical Models of Turbulence, Academic Press, New York, N.Y.

Launder, B. E. & Ying, W. M. 1973, Prediction of Flow and Heat Transfer in Ducts of Square Cross-section, Int. J. Heat Fluid Flow, 3, pp. 115-121.

Leutheusser, H. J. 1963, Turbulent Flow in Rectangular Ducts, J. Hydraulics Division, ASCE 89, pp. 1-19.

Liskovets, D. A., 1965, The Method of Lines (review) Differential Equations, 1, pp. 1308-1323.

Malhotra, A. & Kang, S. S. 1984, Turbulent Prandtl Number in Circular Pipes, Int. J. Heat Mass Transfer, 27, No. 11, pp. 2158-2161.

Nakayama, A., Chow, W. L. & Sharma, D. 1983, Calculation of Fully Developed Turbulent Flow in Ducts of Arbitrary Cross-section, J. Fluid Mechanics, 28, pp. 199-217.

Nikuradse, J. 1962 Untersuchungeu Über die Geschwindigkeitsverteilung in Turbulruten Strömungen, VDI - Forschungshett, No. 281, Bhatti, M. S. & R. K. Shah, Turbulent and Transition Flow Convective Heat Transfer in Ducts.

Novotny, J. L., McComas, S. T., Sparrow, E. M. & Eckert, E. R. G. 1964, Heat Transfer for Turbulent Flow in Rectangular Ducts with Two Heated and Two Unheated Walls, AICHE Journal, 10, pp. 446-470.

Patankar, S. V. & Archarya, S. 1984, Development of Turbulence Model for Rectangular Passages, Trans. CSME, 8, pp. 146-149.

Patankar, S. V. & Spalding, D. B. 1972, A Calculation Procedure for Heat, Mass and Momentum Transfer in Three-Dimensional Parabolic Flows, Int. J. Heat Mass Transfer, 15, pp. 1787-1805.

Reynolds, A. J. 1975, The Prediction of Turbulent Prandtl and Schmidt numbers, Int. J. Heat Mass Transfer, 18, pp. 1055-1069.

Speziale, C. G. 1986, The Dissipation Rate Correlation and Turbulent Secondary Flows in Non-Circular Ducts, J. Fluids Eng., 108, pp. 118-120.

A PRELIMINARY STUDY OF COMBINED MODES OF CONVECTION AIR COOLING OF ELECTRONIC COMPONENTS

R.A. Showole J.D. Tarasuk

Department of Mechanical Engineering
The University of Western Ontario
London, Ontario, Canada, N6A 5B9

ABSTRACT

Natural and mixed convection flows in the space between two horizontal rectangular blocks were studied numerically using a finite difference technique and experimentally by Mach-Zehnder interferometry. The rectangular blocks were used to simulate electronic components. The space between them has an aspect ratio, h/W of 1 and was considered to be isothermal. Air was the test medium with a Prandtl number of 0.7. Solutions have been obtained for a Rayleigh number range of $10^3 < Ra < 5\times10^5$ and Gr/Re² of 4.46. All the dimensionless numbers were based on the width of the notch between the rectangular blocks. Experimental interferograms and numerical isotherms of the temperature fields in the notch, the local Nusselt number distributions, and the average Nusselt numbers were presented. The experimental and the numerical results obtained in this study show good agreement and compare favourably with results presented in literature for rectangular cavities.

NOMENCLATURE

g = acceleration due to cavity (m/s^2)
Gr = Grashof number
h = Local heat transfer (w/m^2k); height of cavity
H = Height of wind tunnel duct
k = Thermal conductivity
L = Length of cavity walls
n = normal coordinate to the wall
Nu = Local Nusselt number
Nu = Average Nusselt number
Pr = Prandtl number
Ra = Rayleigh number (Gr.Pr)
Re = Reynolds number
T = Temperature
T* = Dimensionless temperature, $(T-T_\infty)/(T_w-T_\infty)$
W = Width of cavity; charateristic dimension
x* = x/W
y* = y/W
Ψ = Stream-function
ω = Vorticity

Subscripts
m = mean
w = wall
∞ = free stream or room condition

INTRODUCTION

An electronic system such as a computer utilizes electrical energy to process various information supplied to it. The larger the system, the higher the electrical energy consumption. Most of the electrical energy fed to such machine is converted into heat. The heat must be removed from the machine in order to secure the machine's reliability and to obtain performance at its peak. In new electronic machines, the thermal properties of the materials selected for the integrated circuit (IC) components are such that the resistance to heat flows are due mostly to convective resistance of the fluid between the IC components. The fundamental physical understanding of the convective heat resistance of the fluid between the IC components is essential in order to effectively remove the generated heat. The present study was motivated by the problem of over-heating which often occurred in electronic systems. As a preliminary investigation, we considered a two-dimensional model of a rectangular cavity between two rectangular blocks representing two IC components, as illustrated in Fig. 1. This study was limited to the natural and mixed convection situation often experienced in a passively or actively cooled electronic machine.

A number of papers have been published on the general area of steady separated flows with heat transfer in rectangular cavities, for example, Jacobs et al (1974), Jacobs and Mason (1976), Penot (1982), Le Quere et al (1981), and Chan and Tien (1985). These studies in the exception of Jacob et al (1974) were not designed to simulate convection cooling of electronic components. The work of Jacob et al (1974) was limited also to natural convection over an array of rectangular blocks. Several papers have also been published on various aspects of convective cooling of electronic components. Jaluria (1985) has published a bibliography on natural convection cooling. However, some factors affecting the convection cooling have not been covered in detail. In the present study attention is focused on the natural and mixed convection in the space between two electronic IC components where heat generated by the electronic components is removed.

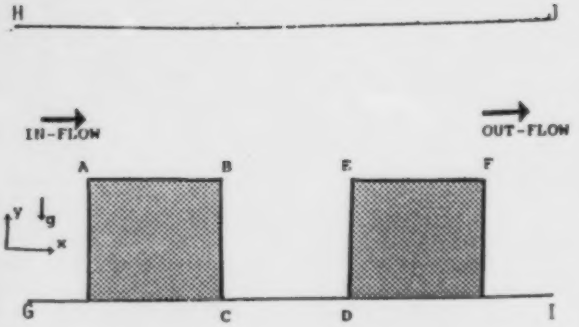

Figure 1. Schematic showing the space between two rectangular blocks representing electronic components

MATHEMATICAL MODEL AND NUMERICAL APPROACH

The problem consists of flow between parallel plates with two rectangular blocks representing electronic components, as shown in Fig.1. In the case of the mixed convection, the approaching flow is fully developed with parabolic profile, leaving at the other end of the plates carrying the heat dissipated between the blocks. For the free convection, the top plate is assumed removed or placed over the rectangular blocks at a considerable distance far away from the blocks. The two-dimensional governing equations for incompressible elliptic flow under consideration is written in cartesian coordinates for the stream-function and vorticity formulation as follows:

Poisson:

$$\frac{\partial^2\psi}{\partial x^{*2}} + \frac{\partial^2\psi}{\partial y^{*2}} = -\omega \qquad (1)$$

Free Convection

Vorticity:

$$\frac{\partial\psi}{\partial y^*}\frac{\partial\omega}{\partial x^*} - \frac{\partial\psi}{\partial x^*}\frac{\partial\omega}{\partial y^*} = Ra\,Pr(\frac{\partial T^*}{\partial y^*}) + Pr\,(\frac{\partial^2\omega}{\partial x^{*2}} + \frac{\partial^2\omega}{\partial y^{*2}}) \qquad (2)$$

Energy:

$$\frac{\partial\psi}{\partial y^*}\frac{\partial T^*}{\partial x^*} - \frac{\partial\psi}{\partial x^*}\frac{\partial T^*}{\partial y^*} = \frac{\partial^2 T^*}{\partial x^{*2}} + \frac{\partial^2 T^*}{\partial y^{*2}} \qquad (3)$$

Mixed Convection

Vorticity:

$$\frac{\partial\psi}{\partial y^*}\frac{\partial\omega}{\partial x^*} - \frac{\partial\psi}{\partial x^*}\frac{\partial\omega}{\partial y^*} = \frac{Gr}{Re^2}\,(\frac{\partial T^*}{\partial y^*}) + \frac{1}{Re}(\frac{\partial^2\omega}{\partial x^{*2}} + \frac{\partial^2\omega}{\partial y^{*2}}) \qquad (4)$$

Energy:

$$\frac{\partial\psi}{\partial y^*}\frac{\partial T^*}{\partial x^*} - \frac{\partial\psi}{\partial x^*}\frac{\partial T^*}{\partial y^*} = \frac{1}{Re\,Pr}(\frac{\partial^2 T^*}{\partial x^{*2}} + \frac{\partial^2 T^*}{\partial y^{*2}}) \qquad (5)$$

Boundary Conditions

The boundary conditions which apply to free and mixed convection (see figure 1) are given as:

on AB, BC , CD .DE, EF; $\psi = \frac{\partial\psi}{\partial x} = \frac{\partial\psi}{\partial y} = 0$

on AB, CD, and EF, $\omega = -\frac{\partial^2\psi}{\partial y^2}$

on BC, DE $\omega = -\frac{\partial^2\psi}{\partial x^2}$

on GH, IJ, and HJ, $\omega = -(\frac{\partial^2\psi}{\partial x^{*2}} - \frac{\partial^2\psi}{\partial y^{*2}})$ (free convection)

For mixed convection fully developed inflow and outflow boundary conditions based on mean velocity in the duct, ψ and ω are given as:

on GH and IJ $\psi = -2(W/H)^2y^3 + 3\,(W/H)y^2$

$$\omega = 12\,(W/H)^2y - 6\,(W/H)$$

on GH, IJ, AB, and EF, $\frac{\partial T^*}{\partial x} = \frac{\partial T^*}{\partial y} = 0$

on BC, CD, and DE $T^* = 1.$
on HJ $T^* = 0.$

The vorticity eqs.(2 and 4) are not valid at the sharp corners B and E (see Fig.1) where singularity occurred. Several papers have dealt with the corner singularity problem in the past. The method developed by Moffat (1964) for solving the singularity problem was employed in this study.

Solution Procedure

Eq.(1) to (5) were approximated by a second order finite difference method which has been developed by Dennis and Hudson (1978). The difference equations are stable and the results were accurate to the order of h^2, where h is the grid size used.

A successive over-relaxation procedure was used to solve the algebraic equations derived from the difference equations. The sensitivity and stability of the numerical approximation were analyzed using the non-linear transformation technique developed by Shank (1955).

EXPERIMENTAL APPARATUS AND TECHNIQUE

The experimental set-up is shown in Fig.2. The rectangular blocks arrangement was located at the test-section of the open return wind tunnel. For free convection experiments, the wind tunnel was not operated, and the wind tunnel duct was blocked at both sides of the test-section to prevent air draft that could disturb the natural convection.

As seen in Fig.2, a Mach-Zehnder interferometer was integrated with the wind tunnel. The interferometer was used to obtain isotherms in the cavity between the rectangular blocks, as well as in the region above the cavity. A monochromatic light source from the

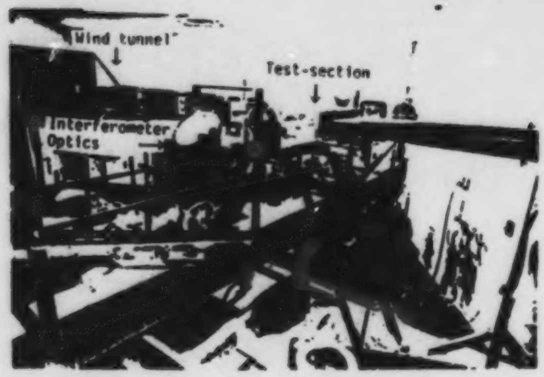

Figure 2. Experimental set-up

He-Ne laser of the interferometer was collimated by two lenses (not shown in Fig.2) and was made parallel by a parabolic mirror before being split into two identical beams by the first beam-splitter. The two beams traversed separate paths, one as a reference beam passing through the laboratory room, and the other through the cavity between the two rectangular blocks. The two beams recombined later at the second beam splitter to produce interference fringe patterns which represent isotherms in the cavity. The fringe shifts were analyzed to obtain the local Nusselt numbers and hence, the average Nusselt number. A detailed interferometer analysis technique has been reported by Showole (1988).

RESULTS AND DISCUSSION

Temperature distribution (free convection)

At low Rayleigh number, that is $Ra < 10^3$, heat transfer in the cavity between the rectangular blocks is by conduction and $Nu \simeq 1$. As Rayleigh number is increased to $Ra = 10^3$, the transition from conduction to convection heat transfer could be observed in the cavity as shown in Fig.3. The interferogram indicates that pure conduction dominates in the deeper region of the cavity, but convection occurred in the top corner region of the rectangular blocks. At $Ra = 5\times10^5$, the free convection in the cavity has become fully established. Rolls and secondary rolls have formed in the cavity as shown by the stream-function distribution and the interferogram in Fig.4. The flow in the cavity at $Ra = 5\times10^5$, the highest Ra considered in this study, is dominated by the boundary layer which has formed on the vertical walls of the cavity between the blocks. The isotherms indicate highest heat transfer rate at the top corners of the blocks. The heat transfer rate decreases from the highest value at the top corners to the lowest at the bottom corners of the cavity. The heat transfer from the base of the cavity exhibits a symmetrical nature. The isotherms and the stream-function also suggest that air was drawn into the cavity from both sides of the duct and hot air or plume exited through the central region of the cavity leading to the symmetrical profile of the flow inside the cavity.

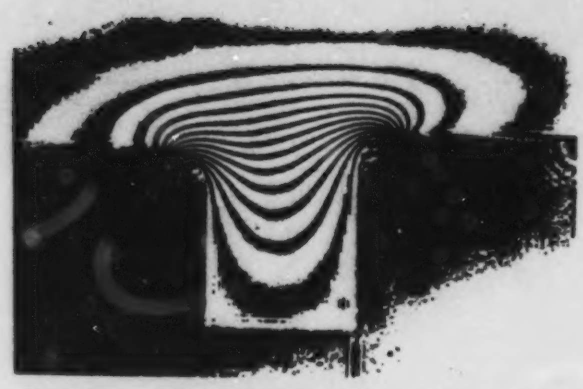

Figure 3. Interferogram of the conduction/free convection transition, $Ra = 10^3$

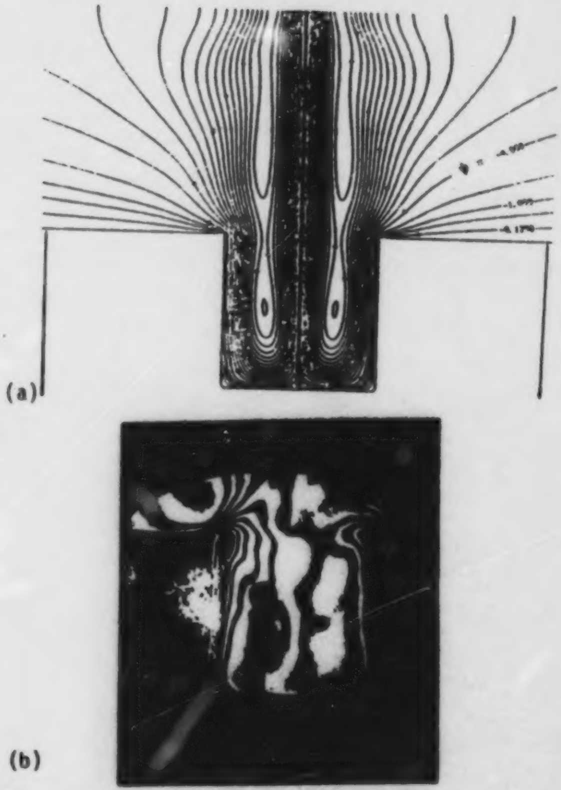

Figure 4. (a) Stream-function distribution and (b) interferogram of free convection, $Ra = 5\times10^5$

Temperature distribution (mixed convection)

The free convection situation shown in Fig.4 exhibits a high heat transfer rate which may lead to an over-heating of electronic components. To prevent over-heating, the cooling of electronic components subjected to a similar condition must be augmented with forced or mixed convection cooling. We considered in this study a mixed convection cooling as shown in Fig.5. The flow of air over the rectangular blocks was from left to right. The Reynold number of the flow based on the cavity width is 400 or $Gr/Re^2 = 4.46$ which falls within the range of mixed convection. The approaching flow separates at top corner of the left rectangular block and reattaches at the top corner of the right block. Flow recirculation occurs inside the cavity. Unlike the vertical plume of hot air observed in the free convection case, Fig.4, the plume in the mixed convection case was deflected downstream as shown in Fig.5. Low heat transfer rate occurs at the separation corner and higher rate of heat transfer occurs at the reattachment corner as shown in the isotherms.

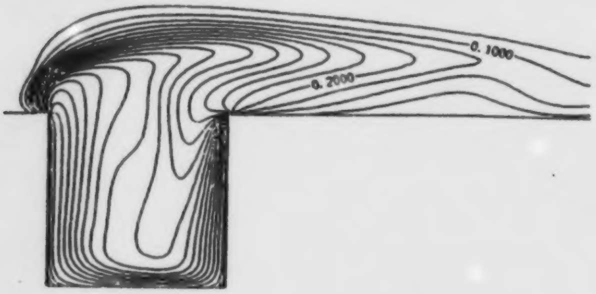

Figure 5. Mixed convection numerical isotherms $Ra = 5x10^5$, $Gr/Re^2 = 4.46$ (flow direction left to right)

Heat transfer result

The local and average Nusselt numbers based on the dimensionless temperatures obtained from the numerical or experimental procedure, and defined in the nomenclature, are calculated as follows:

$$Nu = \frac{h \cdot W}{K_m} = W \frac{dT^*}{dn} \Big|_W \qquad (6)$$

$$\overline{Nu} = \frac{1}{L} \int_0^L W \frac{dT^*}{dn} \Big|_W \, dL \qquad (7)$$

The local Nusselt number distribution for the free and mixed convection cases are shown in Fig.6. The average Nusselt numbers for all the Rayleigh numbers covered are shown in Table 1. Fig.6 depicts a similar charateristics we have observed on the isotherms. The free convection heat transfer curve shows the symmetrical nature of free convection which has been observed on the isotherms. The mixed convection curve also indicates lower heat transfer rates at the separation and higher at the reattachment zone of the cavity. The mixed convection average Nusselt number is lower than the free convection for the Gr/Re^2 value considered in this study.

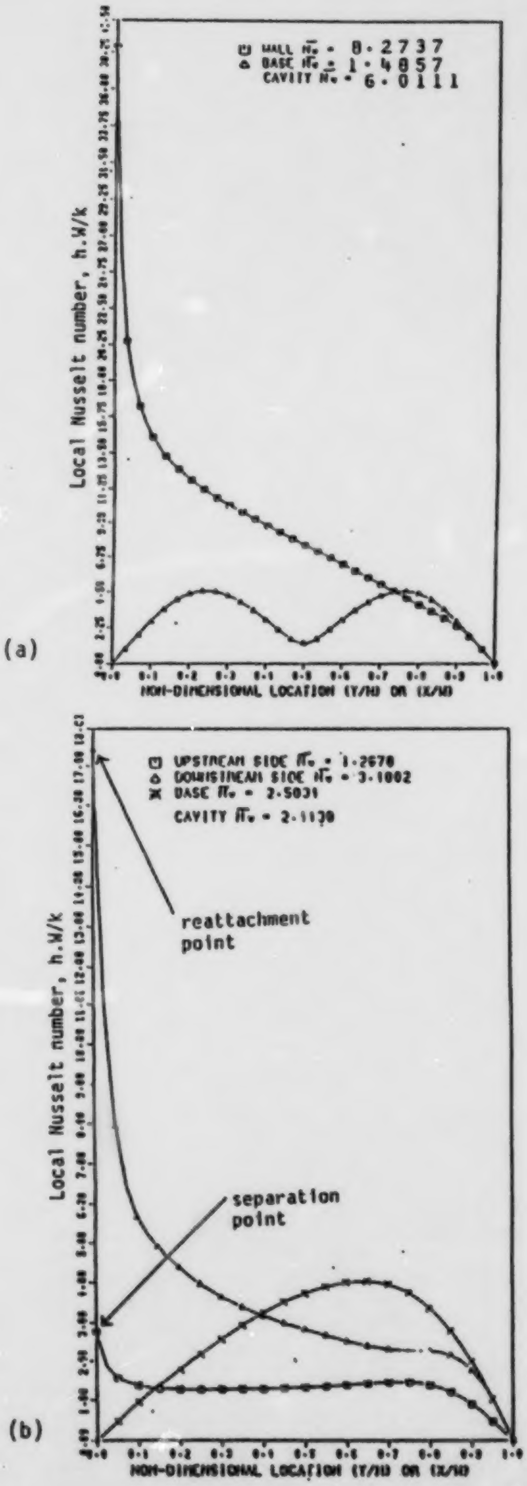

Figure 6. Local and average Nusselt number, (a) free convection; (b) mixed convection, $Ra = 5x10^5$, $Gr/Re^2 = 4.46$

Table 1

Heat Transfer Results

Ra	10^4	3.16×10^4	10^5	3.16×10^5	5×10^5
$\overline{Nu}$	1.7260	2.4130	3.7766	4.8544	6.3079

CONCLUSION

A Mach-Zehnder interferometer and a finite difference numerical technique were employed in this study designed to simulate free and mixed convection cooling of electronic components. For low Rayleigh number below a critical value of Ra = 10^3, heat transfer between the rectagular blocks is by conduction. However, as Ra is increased heat transfer by convection predominates. At moderate Ra, free convection cooling of electronic components may be adequate. At high Rayleigh number, for example, Ra = 5×10^5, the natural convection becomes very strong with rolls and secondary rolls formation in the cavity between the rectangular blocks. Boundary layers develop on the vertical walls of the cavity between the blocks. At this Rayleigh number, over-heating of electronic components may occur and forced or mixed convection cooling may be a proper remedy.

The mixed convection characteristics is distinctly different from the free convection situation. Flow separation and low heat transfer rate occurred at the upstream corner, and flow reattachment and high heat transfer rate at the downstream corner. The overall heat transfer was lower than in the free convection case. The mixed convection enhaces the dissipation of heat from the cavity. This is evident from the numerical isotherms (Fig. 5) which indicate a downstream deflection and outflow of hot air or plume from the cavity.

ACKNOWLEDGEMENT

This research was supported by the Natural Sciences and Engineering Research Council of Canada.

REFERENCES

Chan, Y.L., and Tien, C.L. 1985, A Numerical Study of Two-dimensional Natural Convection in Square Open Cavities, Numerical Heat Transfer, Vol. 8, pp. 65-80.

Dennis, S.C.R., and Hudson, J.D. 1978, A Difference Method for Solving the Navier-Stokes Equations, Proc. 1st Int. Numerical Methods in Laminar and Turbulent Flow Conf., Swansea, U.K., pp. 69-80.

Jacobs, H.R., Mason, W.E. Jr., and Hikida, E.T. 1974, Natural Convection in Open Rectangular Cavities, Proc. 5th Int. Heat Transfer Conf., Tokyo, Japan, Sept. 3-7, Vol. III.

Jacobs, H.R., and Mason, W.E. Jr. 1976, Natural Convectioon in Open Rectangular Cavities with Adiabatic Side Walls, Proc. Heat Transfer and Fluid Mechanics Institute, Stanford University Press, Stanford California, pp. 33-46.

Jaluria, Y. 1985, Natural Convection Cooling of Electronic Equipment, Technical Report, Dept. of Mechanical and Aerospace Engineering, Rutgers University, New Brunswick, New Jersey.

Le Quere, P., Humphrey, J.A.C., and Sherman, F.S. 1981, Numerical Calculation of Thermally Driven Two-dimensional Unsteady Laminar Flow in Cavities of Rectangular Cross-section, Numerical Heat Transfer, Vol. 4, pp. 249-283.

Moffat, H.K. 1964, Viscous and Resistive Eddies Near A Shapr Corner, J. Fluid Mech., Vol. 18, pp. 1-18.

Penot, F. 1982, Numerical Calculation of Two-dimensional Natural Convection in Isothermal Open Cavities, Numerical Heat Transfer, Vol. 5, pp. 421-437.

Shanks, D. 1955, Non-Linear Transformation of Divergent and Slowly Convergent Sequences, J. Mathematics and Physics, Vol. XXXIV, pp. 1-42.

Showole, R.A. 1988, An Interferometric And Numerical Study of Free and Mixed Convective Heat Transfer From Open Rectangular, Semi-cylindrical, and V-Shaped Isothermal Cavities, Ph.D. thesis, The University of Western Ontario, London, Ontario, Canada.

THERMOECONOMIC OPTIMIZATION OF ENERGY CONVERSION SYSTEM WORKING ON HEAT RECOVERY

Jiaxuan Wang Professor
Hengtian Zhang Lecturer

North China Institute of Electric Power
Baoding, Hebei Province, P. R. China

ABSTRACT

The paper studies a new method for estimation and optimal design of an energy conversion system working on low/intermediate temperature heat recovery. Making use of K. E. Nichols' investigation, combined with the consideration of the conditions of China, the cost equations of nation-made turbines and heat exchangers are deduced with the criterion geometric parameter calculated on the basis of mechanics. Some useful results are also analyzed.

INTRODUCTION

Large quantities of waste heat in numerous forms are generated daily in industries and commercial processes. How to utilize such kind of low-grade, large quantities, but scattered in different locations energy is a worldwide concerned problem of energy conservation. Under today's technical conditions, the problem is not much technical, as economical, and therefore, the trade-off should be made between the energy saving and capital cost of the equipment, which is, as saying goes in China, "the sparrow may be small, but it has all the vital organs."

The development of thermodynamic analysis provides a new approch named thermoeconomics which permits to make such trade-off. The essence of the approach is to combine thermodynamic analysis (including first law analysis and second law analysis) with an economic optimization. This new approach makes the estimation much faster and more reliable, and permits the estimation for life-time costing, and under variable price structure.

For deducing the cost equation, it is necessary to know the criterion geometric parater of the turbine. The diameter of last stage turbinecascade is taken as such parameter and its determination is a little bit complex, because it should be checked in its stresses.

PERFORMANCE OF THERMOECONOMIC ANALYSIS

The performance of the thermoeconomic analysis may be proceeded by following steps,

Step 1. Thermodynamic Analysis

The detailed mass, energy and exergy balances of the energy conversion system, as shown in figure-1 are conducted with the usually used method. It can be proceeded with the aid of computer program or by hand due to its simplicity. The point needing attention is that the cycle of such system as well as the maxmum work given by such cycle a little bit differ from the ordinary ones whose maximum work can be expressed by Carnot cycle.

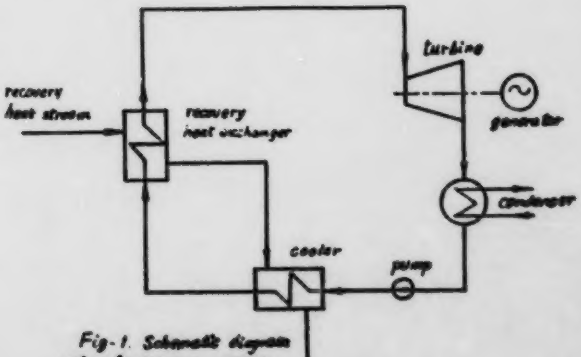

Fig-1. Schematic diagram of a heat recovery power system.

Because the high temperature heat source of such low-grade energy discharges only apparent heat, and therefore, its temperature can not keep constant during the heat discharge process. Denote the initial temperature by T_1, as shown in figure-2, and the ending temperature T_2, the temperature of the low temperature heat source is, no matter, keeps constant on the ambient temperature T_{e}. It can be seen from Fig-2, we may image there is a set of continuous differential Carnot cycles under the line T_1 and T_2, then the maximum work of such cycle will be the integration of all the differential Carnot cycles, as:

$$W_{max} = \int_{T_1}^{T_2} d\,W_j = C_p(T_1 - T_2) - T_e \ln\left(\frac{T_1}{T_2}\right) \qquad (1)$$

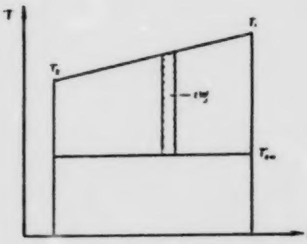

Fig-2 T-S diagram of apparent heat source cycle

Step 2 Economic Analysis

Making use of K. E. Nichols' cost equations, we put forward amendments with the statistic results from collecting and analyzing the data and other informations of nation-made turbines. The mathematical model is deduced as:

$$\Phi_t = a_0 (N_{t0}/N_t)^{b_0} n_s \sqrt{n_e} \cdot f_p \cdot f_\theta D_p^2 \qquad (2)$$

where Φ_t -the cost of turbine

N_{t0}-the selected reference output of the turbine

N_t-the real output of the turbine under consideration

a_0 and b_0-coefficients to be determined

n_s-the number of turbine stages

n_e-the number of turbine exhausts

f_p, f_θ -coefficients considering the effects of inlet pressure and the liner velocity of last turbine cascade top respectively. They are determined by following equations,

$$f_p = \begin{cases} 0.9667 + 0.7675\times10^{-3} P_0 & \text{when } P_0 > 34.5\,\text{bar} \\ 1.0 & \text{When } P_0 \leq 34.5\,\text{bar} \end{cases} \qquad (3)$$

$$f_\theta = \begin{cases} -1.70 + 1.95(\pi D_p n/100) - 0.50(\pi D_p n/100)^2 & \\ + 0.05(\pi D_p n)^3 & \text{When } \pi D_p n > 300(\text{m/s}) \\ 1 & \text{when } \pi D_p n \leq 300(\text{m/s}) \end{cases} \qquad (4)$$

In Eq-2. D_p is important. By chancing D_p, we can use the Eq. 2 through 4 for the nation-made turbines with diferent capacities. Meanwhile adjusting a_0 and b_0, we have the cost equation for the turbines with different working fluids, with the error not more than 10%. Diameter D_p is determined from steam rate with its properities calculated thermodynamically from which the effective section area of steam passage and hights of the moving blades are determined.

What important here is to check the stresses in the disc. Generally, disc of constant thickness is not suitable for large diameter stage since the stresses induced at the collar, i.e. where the disc meets the hub, are exceedingly high. Discs of conical form are used for these cases to reduce stress concentration at the collar. A thicker disc section at the hub and uniformly decreasing thickness towards the rim gives a very uniform stress distribution all along the lenhth of the disc. Fig-3 shows a disc of conical section.

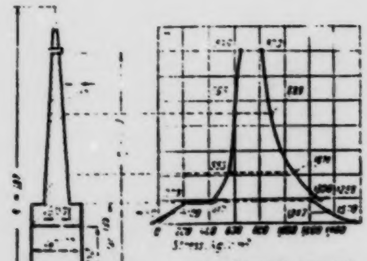

Fig -3 Stresses in a conical collared disc

The stresses deduced in the disc is mainly caused by the centrifugal force. The stress at any point in the conical portion of the disc may be determined from equations,

$$\sigma_r = \sigma_u P_0 + AP_1 + BP_2 \qquad (5)$$

$$\sigma_t = \sigma_u q_0 + Aq_1 + Bq_2 \qquad (6)$$

where A and B -contants of integration obtained from the boundary conditions

σ_a-stress in the thin ring of radius R(see Fig-3)

P and q -coefficients depending upon the ratio r/R=x

To determine the stresses σ_r and σ_t it is necessary to obtain from boundary conditions the values of the integration constants A and B.

The equations for the boundary conditions of the disc are:

1) for radial stress at radius r_2

$$\sigma_{r_2} = \sigma_u P_0 + AP_1 + BP_2 \qquad (7)$$

2) for radial and tengential stress at the collar,

$$\sigma_{r_1} = \sigma_u P_0 + AP_1 + BP_2 \qquad (8)$$

$$\sigma_{t_1} = \sigma_u q_0 + Aq_1 + Bq_2 \qquad (9)$$

3) for the hub portion:

$$\sigma_{r\,hub} = \frac{y_1}{y_2}\sigma_{r_1} \qquad (10)$$

$$\sigma_{r_0} = \ell^{\circ}\sigma_u' + \ell_1^{\circ}\frac{y_1}{y_2}\sigma_{r_1} + \ell_2^{\circ}\sigma_{t\,hub} \qquad (11)$$

$$\sigma_{t_1} = \sigma_{t\,hub} + \left(1 - \frac{y_1}{y_2}\right)\gamma\sigma_{r_1} \qquad (12)$$

The tangential and radial stresses in the thinner section the disc at a radius of $r_1 = r_{hub}$ may be determined by Eq.s :

$$\sigma_{t_1} = k\sigma_u + k_1\sigma_{r_2} + k_2\sigma_{t_2} \qquad (13)$$

$$\sigma_{r_1} = \ell\sigma_u + \ell_1\sigma_{r_2} + \ell_2\sigma_{t_2} \qquad (14)$$

From these equations, the four unknows σ_{t_1}, σ_{r_1}, σ_{t_2} and $\sigma_{t\,hub}$ are calculated with a given value of σ_{r_2}.

The radial stress σ_{r_2} is obtained from equation

$$\sigma_{r_2} = \frac{C_0 + xC_d}{2\pi r_2 y} \qquad (15)$$

and the stress σ_u from equation

$$\sigma_u = \frac{\gamma}{g} r^2 \omega^2 = \frac{\gamma}{g} U^2 \qquad (16)$$

where $U = \pi R n / 30$

Solving this set of equations, simultaneously, we obtain the values of the six unknowns, $\sigma_{r\,hub}$, $\sigma_{t\,hub}$, σ_{r_1}, σ_{t_1}, A and B.

Since A and B are known, it becomes very easy to calulate the stress σ_r and σ_t in the conical portion of the disc and the stresses in the hub.

After checking the stresses in the conical disc, the diameter of disc D_p' is determined. Adding the length of moving blades of this stage, we have D_p.

The cost equations for the condensing turbine generator under consideration is obtained, as

$$\phi_{tg} = C_0 N_g^{0.7} + \phi_t \qquad (17)$$

The first term on right hand of the Eq.(17) is the cost of generator which is proportional to its capacity raised to 0. 7 power, and C_0 is a coefficient to be determined. The second term is the cost of turbine itself.

The cost equation of heat exchanger mainly depends upon its heat transfer area, as

$$\phi_{he} = a_1 + a_2 A^b \qquad (18)$$

where a_1, a_2 and b -coefficients to be selected according to the construction and materials of the heat exchanger.

On the basis of themodynamic calculation and the cost equations. we have the total cost of the equipment in whole.

$$\Phi_e = (\Phi_{he} + \Phi_{tg})(1+f_i)(1+f_m) \qquad (19)$$

where f_i -coefficient considering the cost of auxiliaries

f_m -coefficient considering the operation cost other than the cost of equipment, such as the cost of overhauling and mainternance.

These coefficients may be expressed by f_e as the percentage of total cost then we have,

$$\Phi_{total} = f_e \Phi_e \qquad (20)$$

Denote the annual depreciation of the equipment by Z in %, then

$$C_z = z\Phi_{total} \qquad (21)$$

The total operation cost, $C = C_h + C_z + C_r$

where C_h -the annual cost of the heat stream from the heat recovery

C_z -annual depreciation of the equipment

C_r -the remainder cost including overhead

Step 3. Optimization

The annual profit Γ of the system is taken as the objective function which should be maxmized

$$\Gamma = P_e^\circ W_{net} - C \qquad (22)$$

where P_e° -the market price of electricity (Yuan Rmb/Kwh)

W_{net}-net output of the turbine-generator

C -the total operation cost

The decision variables are selected in such way, choosing the ones which have more effects on the objective function and they should be as much as having the same dimentions and independent each other.

In our case, the following parameters are selected as decision variables,

- The temperature difference at pinch point of heat transfer process;
- The temperature difference of heat transfer from recovery heat stream to the working fluid;
- The temperature difference at pinch point of heat transfer process in condenser;
- The temperature difference on the outlet side of recovery heat exchanger;
- The evaporation and condensation temperatures of the working fluid(in our case R_{114} is adaped)

A newly developed method of optimization, named "Method of Right Polyhedron" is adapted for solving our problem with the aid of computer program. That proves this method is very good in its simplicity and fast convergence.

Step 4 Results and Their Aanlysis

Two categories of results are obtained from computation, namely thermodynamic and thermo-economic parameters.

A comparison between these two categories of results are made under the conditions of the initial of the initial temperatures at 150 °C , 125 °C , and 100 °C . All the results are summarized in the following table,

initial temperature of the recovery heat (°C)	150	125	100
economically optimal condensing temperature(°C)	28.5	29.0	29.0
thermodynamically optimal condensing temperature(°C)	27.5	28.4	28.5
difference Δ_n (°C)	-0.7	-0.6	-0.5
economically optimal evaporation temperature(°C)	100.2	84.4	69.8
thermodynamically optimal evaporation temperature(°C)	97.2	82.3	68.5
difference Δ_n (°C)	-3.0	-2.1	-1.3

1) The economically optomal temperature difference

on the pinch point of heat exchanger will be $3 \sim 5\,^{\circ}C$ under the conditions, t_h=100–150 °C ; the cost of unit area of heat exchanger P_{he} =150–350 Yuan/m^2; coefficient of heat transfer u=500-1200W/($m^2 \cdot ^{\circ}C$); the cost of unit exergy of recovery heat P_h =0.0-0.013 Yuan/KWh; the market price of electricity P_e^* =0.08–0.12 Yuan/KWh.

2) The relation between thermodynamic optimum and thermoeconomic optimum ordinally can not be coincident, but for our case, because the low-grade energy coversion with camporative low efficiency, the thermodynamic optimum does not much differ from the thermoeconomic optimum. That may be one of the conclusions about the heat recovery energy convesion system.

3) The effect of heat recovery conditions upon the thermoeconomic efficiency are analyzed. Such conditions are the initial temperature t_h of the heat recovery stream and cooling water temperature t_o . Fig-4 and Fig-5 show the effect of t_h and t_o on energy efficiency of the system η_s, annual profit Γ and the economic life of the equipment S_e.

CONCLUSIONS

1. A lot of facorts should be considered for the economic optimization. What is important among them is to search the simple method which can be directly used for that optimization. The method and results of computation by this paper provide references for the thermal system analysis.

2) Under certain conditions, there is not much difference between the thermoeconomic optimum and thermodynamic optimum.

REFERENCES

(1) Nichols, K. E. "Turbine Price Mover Cost Model Empirical Equation P. O. 1/Y-4920V"

(2) Ministry of Electric Power, Electric Equipment Co. "Usually Used Equipment Handbook for Electric Insdustry" Electric Power Publishing Co.(1980)

(3) North China Electricity Design Institute "A Collection of Reference Materials for Nation-made Turbines" (1981)

(4) Hengtian Zhang, "Thermoeconomic Analysis and Optimization of Heat Recovery Power System" Master Thesis NCIEP (1985)

(5) Yu Yongxi, Zhou Zhongrong, "Introduction to a New Approach of Optimization of Right Polyhedron Method" Jourant of Shanghai Jiaotong University No.1, 1983.

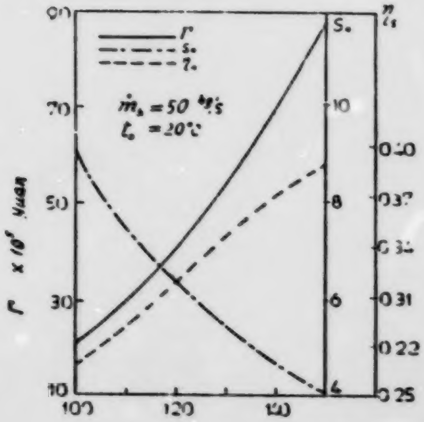

Fig-4. Effect of t_h on Γ. S_e and η_e

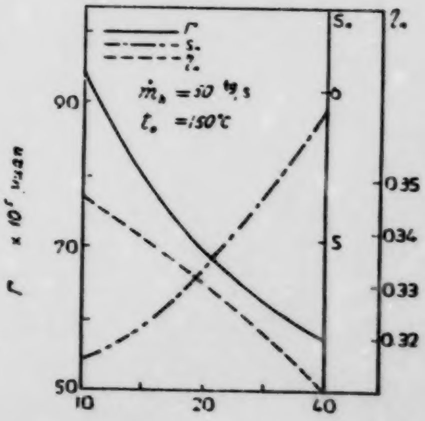

Fig-5. Effect of t_o on Γ, S_e and η_e

FREE CONVECTION HEAT TRANSFER FROM A FINITE HORIZONTAL PLATE

Peter Hrycak, D.J. Sandman, and K.E. Tsouras

New Jersey Institute of Technology
Newark, New Jersey 07102

ABSTRACT

An experimental and analytical investigation of heat transfer by free convection from a horizontal, square plate, with L = 76.2 mm, has been carried out. Experimental results have been obtained for both the upward-facing and the downward-facing sides of a heated plate. Heat transfer coefficients for the downward-facing side of plate were about half of those for the upward-facing side. The analysis is based on the integrated momentum and energy equations. The continuity equation is satisfied identically. For the constant surface temperature, there results a formula for an average Nusselt number applicable for an upward-facing, horizontal, heated plate. For a plate heated on both sides, this formula is adjusted to show the effect of simultaneous heating on both sides. Another formula has been proposed for turbulent free-convective heat transfer on an upward-facing, heated plate. These analytical results were then compared with our own experimental results, and those available from the literature, with a reasonably satisfactory agreement. Various analytical approaches were discussed.

INTRODUCTION

Heat transfer from horizontal, heated plates by far has not received the attention accorded to other geometries. There appears still to exist a general scarcity of representative experimental data, in particular in the turbulent regime. As heat transfer by free convection is of the same order of magnitude as that by radiation, for moderate temperature differentials, the need for radiation correction during experimentation cannot be disregarded. As the things stand today, the contributory effects of radiation are not always mentioned in description of experimental results. This, and other experimental error margins, make comparisons among the results of various investigators, and with analytical calculations, quite difficult. Therefore, the results of experimentation described below were carefully checked for the effects of radiation. Also, equations of the boundary-layer type are set up, describing free convection on a horizontal plate (heated electrically), facing upward, and of finite dimensions. Similarity is assumed for both the velocity and temperature profiles. The solutions obtained apply for laminar as well as for turbulent free convection. Due to highly sheltered conditions inside the chamber where the the present experiments were carried out, undesirable disturbances like uncontrollable small air movements were eliminated.

EXPERIMENTAL TEST SET-UP

In order to make the intended free-convective experiments reasonably accurate, it was decided to test the specimens, to be used as the horizontal plates in the tests, independently for emissivity under high-vacuum conditions. Therefore, a high-vacuum chamber had to be built first, that could contain pressures as low as 10^{-4} mm Hg, when the mean free path of molecules inside was long enough to eliminate convection, and to leave only radiation as the mode of heat transfer. Conduction along the specimen support wire, and the heater and the thermocouple wires was calculated to be less than 1% of the total heater input.

The vacuum chamber (Fig. 1) was constructed of high-strength aluminum plates 6.35 mm thick, by heliarc welding, forming a cube 305 mm on each side internally. It was sprayed on inside three times with a high-emissivity ($\epsilon_2 = 0.80 - 0.90$), low outgassing paint. The specimens to be tested consisted each of two similar plates, 76.2x76.2x1.6 mm, between which a patch heater and four copper-constantan thermocouples were sandwiched in - two monitoring the temperature of each specimen. The assembly was tested to make sure that in each plate there was dissipated one half of the total heat used. It was suspended on an insulated, hollow piano wire 1.6 mm thick, with the areas A_1 parallel to those of top and bottom of chamber, A_2. Top plate was sealed to chamber with high-vacuum thermal grease, and held down by threaded steel rods. Voltage across the heater, and the current in the heater leads were monitored, and recorded when the steady-state surface temperature of the specimens was reached. For emissivity measurements, the chamber was evacuated through the stopcock at the top plate. For free-convective measurements, atmospheric pressure inside of chamber was reestablished.

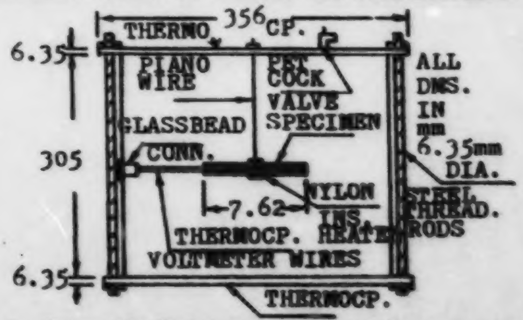

Fig. 1 Schematic Representation of Test Chamber and of Specimen Assembly

As the total area of the specimens represented only 2.1% of the area of the vacuum chamber, the required emissivity could be calculated from the formula

$$Q(\text{heater}) = \epsilon_1 \sigma A_1 (T_1^4 - T_2^4) \qquad (1)$$

The emissivities measured with this set-up are seen in Fig. 2. They all appear to be of the right order of magnitude, when compared with results from the literature, and are more than adequate for making radiative loss corrections in free-convective measurements more realistic. In most papers on the subject, when experimental results are discussed, there is very seldom any mention on how radiation correction has been carried out.

In the set-up described above, only the vacuum chamber and the specimens were home made. All other components were obtained commercially from specialty suppliers. The final results on free convection experiments are shown in Figs. 3 and 5.

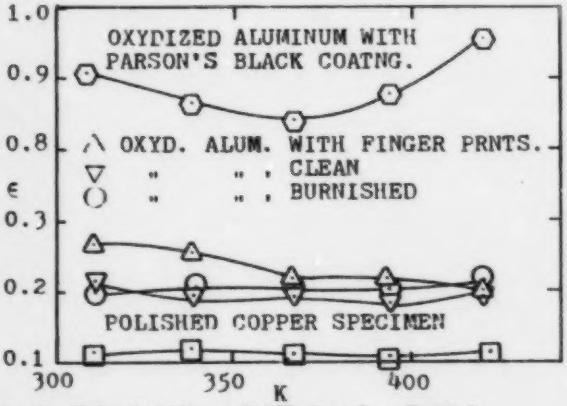

Fig. 2 Emissivities of All Samples Tested

THE BASIC EQUATIONS OF THE PROBLEM

Let's now consider natural convection flow of a Newtonian, single species fluid over a horizontal surface in an axisymmetric flow, with the coordinates r and z. The flow is in the steady state, the velocity field consists of u = dr/dt and w = dz/dt, and the corresponding temperature field is T = T(r,z). The acting surface force is the pressure, and the body force is the gravitational force, g, all acting on a horizontal plate 86.0 mm in diameter which, in turn, gives rise to convective flow considered positive in the direction towards the center of plate; at edge of plate, r = 0. In the steady state this flow exhibits characteristic instabilities and is difficult to treat analytically, but we assume it is amenable to analytical treatment using the boundary-layer theory approach, together with Boussinesq approximation towards the treatment of the variable physical properties. Also, there is assumed similarity of velocity and temperature profiles. Then the continuity, momentum, and the energy equations assume the form

$$\frac{\partial(ru)}{\partial r} + \frac{\partial(rw)}{\partial z} = 0 \qquad (2)$$

$$u\frac{\partial u}{\partial r} + w\frac{\partial u}{\partial z} = -\frac{1}{\rho}\frac{\partial P}{\partial r} + \nu\frac{\partial^2 u}{\partial z^2} \qquad (3)$$

$$0 = -\frac{1}{\rho}\frac{\partial P}{\partial z} + g\beta(T - T_\infty) \qquad (4)$$

$$u\frac{\partial T}{\partial r} + w\frac{\partial T}{\partial z} = a\frac{\partial^2 T}{\partial z^2} \qquad (5)$$

The pertinent boundary conditions are:

$$\text{at } z = 0: \quad u = w = 0, \quad T = T_w = \text{const} \qquad (6)$$

$$u = 0 \qquad T = T_\infty = \text{const}$$

$$\text{at } z = \delta \quad \frac{\partial u}{\partial z} = \frac{\partial T}{\partial z} = 0 \qquad (7)$$

On differentiating eq.(4) with respect to r, and integrating it with respect to z, we have

$$-\frac{1}{\rho}\frac{\partial P}{\partial r} = g\beta\int_z^\delta \frac{\partial}{\partial r}(T - T_\infty)\,dz \qquad (8)$$

The limits on integral in eq. (8) may be also taken as 0 and z, respectively, for the temperature profile chosen below. On solving the continuity equation for w, we have

$$w = -\int_0^z \left(\frac{\partial u}{\partial r} + \frac{u}{r}\right) dz \qquad (9)$$

Equations (8) and (9), on substitution in eq. (3), after partial integration, yield

$$\frac{1}{r}\frac{d}{dr}\left(r\int_0^\delta u^2\,dz\right) = g\beta\int_0^\delta\left[\int_z^\delta \frac{\partial}{\partial r}(T - T_\infty)dz\right]dz - \nu\left(\frac{\partial u}{\partial z}\right)_w \qquad (10)$$

Also, using eq. (8), eq. (5) may be transformed after partial integration, and on assuming that δ (hydrodynamic) ≈ δ(thermal), as well as letting $\theta = T - T_\infty$, there results

$$\frac{1}{r}\frac{d}{dr}\left(r\int_0^\delta u\theta\,dz\right) = -a\left(\frac{\partial\theta}{\partial z}\right)_w \qquad (11)$$

Letting the velocity and temperature profiles be

$$u = U(z/\delta)(1 - z/\delta)^2 \ ; \ \theta = \theta_w(1 - z/\delta)^2 \qquad (12)$$

as proposed by Eckert and Drake [1], and letting

$$U = C_1 r^m \ ; \ \delta = C_2 r^n \qquad (13)$$

one can proceed to a speedy solution of eqs. (10) and (11), as eqs. (12) and (13) satisfy all boundary conditions. Thus, the momentum and the energy equations transform first into (with β = 1/T)

$$\frac{1}{r}\frac{d}{dr}(rU^2\delta) = 17.5\,g\beta\theta\delta\,d\delta/dr - 105\,\nu(U/\delta) \qquad (14)$$

$$\frac{1}{r}\frac{d}{dr}(rU\delta) = 60\,a/\delta \qquad (15)$$

which, after eqs. (13) have been substituted, look as

$$(2m + n + 1)C_1^2 C_2 r^{2m+n-1} = 17.5\,g\beta\theta_w n C_2^2 r^{2n-1} - 105(C_1/C_2)\,r^{m-n} \qquad (16)$$

and

$$(m + n + 1)\, C_1 C_2\, r^{m+n-1} = 60\, a r^{-n}/C_2 \qquad (17)$$

For similarity solutions, both sides of these equations must be independent of r, or 2m+n-1 = 2n -1 = m-n, and m+n-1 = -n; this is true if m = 1/5, and n = 2/5, for the geometry at hand. Then, eqs. (16) and (17) reduce to expressions

$$(3/175) C_1^2 C_2 = (1/15) g\beta\theta_w C_2^2 - \nu C_1/C_2 \qquad (18)$$

$$C_1 C_2^2 = 37.5\, a \qquad (19)$$

Then, the values of C_1 and C_2 are obtained as

$$C_2 = 3.548\ Pr^{-2/5}(9/14 + Pr)^{1/5}(Gr^*)^{-1/5} \qquad (21)$$

$$C_1 = 2.978\, a\, Pr^{4/5}(9/14 + Pr)^{-2/5}(Gr^*)^{2/5} \qquad (20)$$

with $Gr^* = g\beta\theta_w/\nu^2 = Gr/L^3$.

Now the expressions for δ and U can be written as

$$\delta/r = 3.548\, Pr^{-2/5}(0.643 + Pr)^{1/5} Gr_r^{-1/5} \qquad (22)$$

$$rU = 2.978\, a\, Pr^{4/5}(0.643 + Pr)^{-2/5} Gr_r^{2/5} \qquad (23)$$

From this, we calculate

$$h_r = q_w/\theta_w = 2k/\delta \qquad (24)$$

and the average heat transfer coefficient becomes

$$\bar{h}_r = (1/A)\int_A h_r\, dA = 0.705\, k Pr^{2/5}(0.643 + Pr)^{-1/5} \cdot (Gr^*)^{1/5} R^{-2/5} \qquad (25)$$

In order to obtain a formula for the average heat transfer coefficient based on the side L of a square plate, we let $L^2 = \pi R^2$, so that L(equivlnt.) $= \pi^{1/2} R$, $\bar{h}_r = h_L\, \pi^{-1/5}$, and

$$Nu_L = (h_L L/k) - 0.886\, Pr^{2/5}(0.643 + Pr)^{-1/5} Gr_L^{1/5} \qquad (26)$$

For air (Pr = 0.72) this generates for Ra = RePr,

$$Nu_L = 0.780\, Ra_L^{1/5} \qquad (27)$$

for a horizontal square plate heated on the top side only. With the present choice of coordinates, $\delta = 0$ at the edge of plate. Since, in the case of a horizontal plate heated on both sides, $\delta \neq 0$ at the edges, we can accommodate this fact by increasing the actual area of the plate by some appropriate amount. It appears in the present case that increasing the area of plate by one fifth, an "effective area" is generated that shows realistically the effect of heating of the bottom side of the plate on heat transfer on the upper side,

$$A_{eff} = 1.20\, A_{act} \qquad (28)$$

that results in $R_{eff} = 1.095\, R_{act}$

$$h_{R,eff} = 0.8157\, k\, Pr^{2/5}(0.643 + Pr)^{-1/5} Gr_R^{1/5}/R \qquad (29)$$

$$Nu_L = 1.025\, Pr^{2/5}(0.643 + Pr)^{-1/5}\, Gr_L^{1/5} \qquad (30)$$

and, for Pr = 0.72

$$Nu_L = 0.902\, Ra_L^{1/5} \qquad (30a)$$

According to the literature, (cf. [2]) a plate that is heated on both sides has on its upper side heat transfer appreciably enhanced by formation of a warm air "bubble" on its lower side, for strictly horizontal inclination, as suggested in Fig. 4. Also, in an enclosure, the effect of restricted spacing alone causes an early transition (cf. Mc Adams [3], p. 182. This is explainable, for the case of heated, horizontal plates, by the destabilizing effect of the upward-directed buoyant force on the boundary layer formed by the fluid flowing in the direction tangential to plate. For developed turbulent flow, the last term in eq. (10) may be taken as

$$0.0228\, \rho U^2(\nu/U\delta)^{1/4} \qquad (31)$$

and the term on the right-hand side of eq. (11) may be defined as

$$0.0228\, \rho c_p U\theta_w(\nu/U\delta)^{1/4} Pr^{-2/3} \qquad (32)$$

while the velocity and temperature distributions (cf. Eckert and Jackson [1], p. 324), in analogy to forced convection, may be written as

$$u = U\, (y/\delta)^{1/7}(1 - y/\delta)^4 \qquad (33)$$

and letting

$$\theta = \theta_w[1 - (y/\delta_t)^{1/7}], \quad \delta_t = \lambda\delta \qquad (34)$$

With these substitutions, eqs. (10) and (11) yield after integrations required had been carried out, the relations (for $\lambda = 1$)

$$0.0523\, (1/r)\frac{d}{dr}(rU^2\delta) = 0.0667\, g\beta\theta_w \delta d\delta/dr - 0.0228\, U^2(\nu/U\delta)^{1/4} \qquad (35)$$

and

$$0.0367\, (1/r)\left(\frac{d}{dr}\right)(rU\delta) = 0.0228\, U(\nu/U\delta)^{1/4} Pr^{-2/3} \qquad (36)$$

Assuming, as before, the validity of eqs.(13), eqs. (35) and (36) yield, for similar flow,

$$0.0523(2m + n + 1) C_1^2 C_2 r^{2m+n-1} = 0.0667 g\beta\theta_w n C_2^2 r^{2n-1} - 0.0228\, C_1^{7/4} C_2^{-1/4} \nu^{1/4} r^{(7m-n)/4} \qquad (37)$$

and

$$0.0367(m+n+1) C_1 C_2 r^{m+n-1} = 0.0228\, Pr^{-2/3} \nu^{1/4} C_1^{3/4} \cdot C_2^{-1/4} r^{(3m-n)/4} \qquad (38)$$

In order to be independent of r, m = 4/11, and n = 8/11 are required in eqs. (37) and (38); then, the constants C_1 and C_2 may be determined from the relations

$$0.1284 C_1^2 C_2 = 0.0485 g\beta\theta_w C_2^2 - 0.0228\nu^{1/4} C_1^{7/4} C_2^{-1/4} \qquad (39)$$

and

$$C_1 C_2 = 0.2971\ Pr^{-2/3} \nu^{1/4} C_1^{3/4} C_2^{-1/4} \tag{40}$$

Equations (39) and (40), solved simultaneously, yield

$$C_1 = 0.4131\ Pr^{-8/33}(1 + 0.5965 Pr^{2/3})^{1/11}(Gr^*)^{5/11}\nu \tag{41}$$

and

$$C_2 = 0.4520\ Pr^{-16/33}(1 + 0.5965 Pr^{2/3})^{1/11}(Gr^*)^{-\frac{1}{11}}$$

when the ratio of boundary-layer thicknesses=1. (42)

Consequently, there results

$$Nu_r = h_r r/k \tag{43}$$

or, since here, for the turbulent flow regime,

$$Nu_r = 0.0228\ (\rho c_p/k)U(\nu/U\delta)^{1/4} Pr^{-2/3} r \tag{44}$$

which, when expressions for U and δ are substituted according to eqs. (13), yields here

$$Nu_r = 0.01433\ Pr^{-8/11}(1 + 0.5965 Pr^{2/3})^{-\frac{4}{11}}\ Gr_r^{\frac{4}{11}} \tag{45}$$

and, when integrated over the area of plate πR^2, results in

$$Nu_R = 0.01371\ Pr^{-8/11}(1 + 0.5965 Pr^{2/3})^{-4/11} Gr_R^{4/11} \tag{46}$$

and for air ($Pr = 0.72$) reduces to

$$Nu_R = 0.01510\ Ra_R^{4/11} \tag{47}$$

When L is used instead of R, eq. (47) yields

$$Nu_L = 0.01433\ Ra_L^{4/11} \tag{47a}$$

Here, eq. (47a) has the form $Nu = C\ Ra^p$, to describe turbulent free convection on an upward pointing, horizontal plate, with the analysis carried out along the lines presented in Ref. 1, but the constant C is too small to fit the experimental data in Fig. 3. However, by assuming a plume forming over the plate (cf. Fig. 4), with $\delta_t/\delta = 13.8$, together with the use of eq. (28), C_1 is increased, and C_2 is decreased in eqs. (41) and (42) so that $C = 0.109$ results, very close to C in eq. (55) below that fits the experimental data within ± 15%. This may serve as the justification for the polynomials used, that satisfy all the boundary conditions, and the governing D.E.'s on the average. For a similar problem, Levy [4] got $p = 4/11$. Thus, for the present geometry, solutions based on boundary-layer and integral methods seem realistic.

For the downward-facing, heated plate, Schulenberg [5] found for $Pr < 10^{-2}$ and a sufficiently large Grashof number, an approximate solution

$$Nu_R = C(Pr\ Ra_R)^{1/5} \tag{48}$$

where the exponent of Ra, $p = 1/5$, is the same as p found for the upward-facing, heated plate, and is found frequently in the literature on this subject, when integral methods are used. On the other hand, Sibulkin's exact solution of the governing D.E.'s may be written as (cf. [1], p. 249)

$$Nu_R = 0.540\ Pr^{0.4}\ Re_R^{\frac{1}{2}} \tag{49}$$

for stagnation heat flow on a sphere. As some analogy exists between the forced and free convection flow for the same geometry (ibid., p.324), one can also expect, for free-convective flow directed upward, relations like $Nu = C\ Ra^{\frac{1}{4}}$, as $Gr \sim Re^2$. Here Hrycak [6] solved exactly the governing D.E.'s assuming existence of a warm-air bubble in the center of the plate (cf. Fig. 4) as the driving force:

$$Nu_R = 0.519\ Pr^{0.07}(m Ra_R)^{\frac{1}{4}} \tag{50}$$

when the flow is laminar; $0.3 < m < 0.9$ is a constant to be determined experimentally, for the center of plate. With $L = R\ \pi^{\frac{1}{2}}$, the average Nusselt Nu. is then

$$Nu_L = 0.34\ Pr^{0.07} Ra_L^{\frac{1}{4}} \tag{51}$$

that represents the average of the data of Fishenden and Saunders [7] and Bosworth [8]. Some authors today prefer to represent data of Ref. 7 in a version adapted for $p = 1/5$. In general, approximate solutions, even when based on the exact boundary-layer theory, generate here formulas with $p = 1/5$ (cf. Ref. 5), while those based on the complete N-S equations and the energy equation, valid exactly for $r/R \ll 1$ (cf. ref. 6), tend to show $p = 1/4$. There are no known analytical solutions for the turbulent regime for this geometry.

DISCUSSION OF EXPERIMENTAL RESULTS

As mentioned in Ref. 3, in applications involving integrated momentum and energy equations, usually a reasonable relationship between the dependent and independent variables is realized, but often still a final adjustment of the constants may be required to reach a precise agreement with the experimental results. This applies here, in particular, to the results developed on turbulent free convection.

Our own experimental results on free convection on upward-facing, horizontal heated plate are shown in Fig. 3.

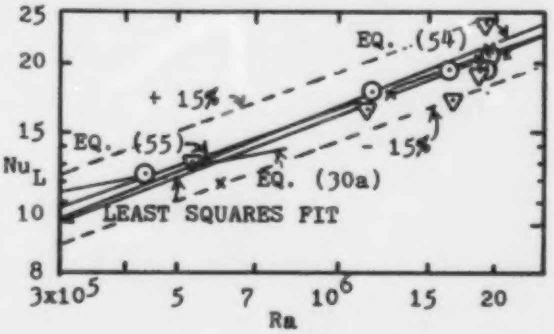

Fig. 3 Nusselt Number vs. Rayleigh Number for Three Specimens; Horizontal Plate Facing Upward (Please note L.S. fit with C=0.0799; p=0.384)

It is seen from Fig. 3 that, for $Ra < 10^6$, the experimental data show a reasonable agreement with eq. (30a) here; the number of experimental points available is not quite sufficient for a definitive finding, however, for an upward-facing, horizontal plate, heated on both sides. Recently, Lewandowski and Kubski [9] obtained from well-documented experiments, based both on heat-balance and temperature gradient methods, for a horizontal plate 100x60 mm, heated on one side only, the formula

$$Nu = 0.766\ Ra^{1/5} \tag{52}$$

good for $10^4 < Ra < 10^7$, with a ± 10% error margin. No information is available on how L was determined. Distilled water, glycerine, and soya-bean oil have been used as the fluids. Equation (52) is very close to our eq. (27) above.

Yousef et al. [10] obtained, using a Mach-Zehnder interferometer, for $10^5 < Ra < 2 \times 10^7$, in air,

$$Nu = 0.622\ Ra^{1/4} \tag{53}$$

for square plates with L = 100, 200, and 400 mm. The exponent of Rayleigh's number, p = 0.25, has been also obtained by Fishenden and Saunders [7], with the constant C = 0.54, by Bosworth [8], with C = 0.71, and by Al-Arabi and El-Riedi [11], with C = 0.70, for a similar range of Ra, and all for laminar flow and the same geometry. The discussion applies to average Nusselt numbers only.

Our turbulent flow formula, eq. (47a), shows the need for the adjustment of the constant C. It is seen from Fig. 3 that expressions

$$Nu_L = 0.065 Ra_L^{0.4} \tag{54}$$

and

$$Nu_L = 0.108\ Ra_L^{0.364} \tag{55}$$

show a reasonable agreement with our own experimental results in Fig.3 which apply to a plate heated on both sides, with a constant wall temperature, after constant adjustment in eq.(47a) to C= 0.109. In eq.(55) p = 0.364 is 4/11 rounded off; p = 0.4 occurs already in Ref. 1 for conditions applicable to a vertical plate. Otherwise, in experimental results below, p = 1/3 indicates already a turbulent flow.

Here Lewandowski and Kubski propose [9]

$$Nu = 0.173\ Ra^{1/3} \tag{56}$$

for $10^5 < Ra < 10^8$, while Yousef et al. [10] propose, for p = 1/3, C = 0.14 for $2 \times 10^7 < Ra < 10^{10}$, virtually identical with Fishenden and Saunders' result [7], while for p =1/3, Bosworth [8] proposes C = 0.17, which for Hassan and Mohamed [12] becomes 0.12, for Fujii and Imura [13], 0.16 ($Ra < 2 \times 10^8$), for Al-Arabi and El-Riedy [11], 0.155 ($4 \times 10^7 < Ra < 10^9$), and for Ishiguro, et al. [14] C is equal to 0.20, $Ra > 2 \times 10^5$.

From the review of the above results it appears that p = 1/3 is very common for situations where only one side was heated. For heat transfer on both sides, for a finite, horizontal plate as shown in Fig. 3, p increases somewhat, due to instabilities generated by heat transfer at the bottom of heat transfer plate, during transition.

For a horizontal plate facing downward, the results [7,8] show p = 1/4 for laminar flow, p =1/3 for the turbulent flow (experimental), while newer results indicate p = 1/5 [5,9], for laminar flow (anal. and experimental), p = 1/3 [12], turbulent flow, experimental. An explanation for this may be perhaps seen from Fig. 4, where near the stagnation point the streamlines are suggested by Fig. 4 of a paper by Singh and Birkebak [15]. The flow on a downward-facing, heated horizontal strip, in water, is visualised. It is seen that near the stagnation point a thin, boundary-layer like region exists. Then, farther away, the boundary layer becomes thicker, and that thickness is gradually decreasing as the edge of plate approached; cf. also Figs. 6 and 7 of the paper by Aihara et al. [16] whose results are based on air. There, the dual nature of the flow near the stagnation point may also be observed. Thus, the existence of a "bubble" formed by warmer fluid near the center of plate generates a kind of metastable situation, subject to a variety of interpretations.

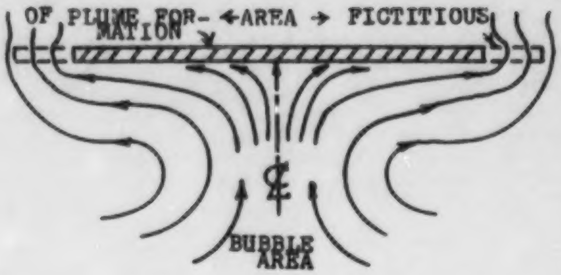

Fig. 4 Schematic Representation of Natural Convection near Stagnation Point

Our own experimental data are shown in Fig.5. It is seen from Fig.5 that the flow regime there must have been already turbulent for Ra as low as 6×10^5. There is a considerable scatter of the data, indicating a highly unstable flow. Heat transfer intensity, as represented by the corresponding Nusselt numbers, is roughly 50 % of that existing on the upward-facing side of plate.

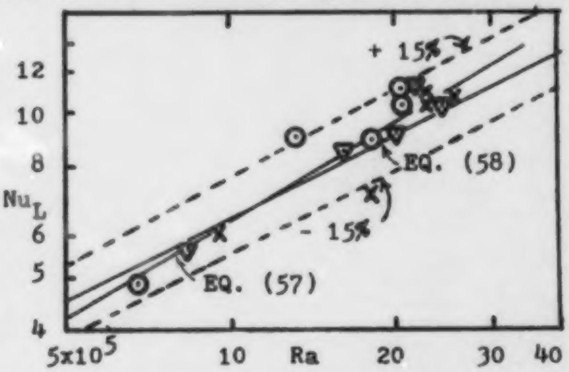

Fig. 5 Nusselt Number vs. Rayleigh Number for Three Specimens; Horizontal Plate Facing Downward

The results in Fig. 5 may be represented by either of the equations (eq. (57) is the L.S. fit)

$$Nu_L = 0.0017 Ra_L^{0.596} \tag{57}$$

or

$$Nu_L = 0.0064\ Ra_L^{0.5} \tag{58}$$

equally well. Few data for the present configuration are available for the turbulent regime, except those by Hassan and Mohamed [12], where such data are correlated simply by a formula that represents one-half of the results obtained with the heated flat plate facing upward, with p = 1/3, as

$$Nu = 0.068 Ra^{1/3} \tag{59}$$

Bosworth [8], for example, suggests here C=0.08. Obviously, more data for this configuration are still required, and our objective has been to fill this need at least partially.

CONCLUSIONS

Experimental data on free convection within an enclosure, from a square plate, heated on both sides, have been presented. Also, for an upward-facing, heated, horizontal plate, heat-transfer formulas have been derived (for both laminar and turbulent flow regime) that represent reasonably well own experimental data. A comparison of these data with results of several other authorities is shown in Fig.6. It is seen that the present data fall into the middle of the results obtained by other investigators cited, both for the laminar and the turbulent regime. It appears that the simultaneous convection at the bottom (from the downward-facing side of the plate) helps the convection on the top of the experimental plate. The data presented suggest an early onset of transition for the present set-up. For the downward-facing side of the plate, a formula is shown, based on the exact solution of the Navier-Stokes equations, for laminar flow only. In Fig.7, there is shown a comparison of the present experimental results for this geometry with the findings of other investigators cited. It is seen that the present experimental data indicate also an early transition (in view of the high power of the Ra realized), but otherwise fall into the middle of the known experimental results of others.

The present authors are aware of the fact that only a restricted number of references has been used, because of paper format requirements. Still, it is believed that the references selected are representative of the present subject's state of the art.

NOMENCLATURE

Gr_L; Gr^*	Grashof Nu., $g\beta\theta_w L^3/\nu^2$; Gr_L/L^3, m^{-3}
Nu_L	Nusselt Nu., hL/k
Pr	Prandtl Nu., $c_p\mu/k$; ν/a
P	pressure, N/m^2
Ra_L	Rayleigh Nu., $Gr_L Pr$
r; z	coordinates, parallel/perpendicular to pl.
R; L	radius of plate; significant length, m
u; w	velocities, dr/dt; dz/dt, m/s
δ; δ_t	boundary-layer thickn., hydr./thermal, m
θ	reduced temperature, $T - T_\infty$, K

Other symbols explained in text.

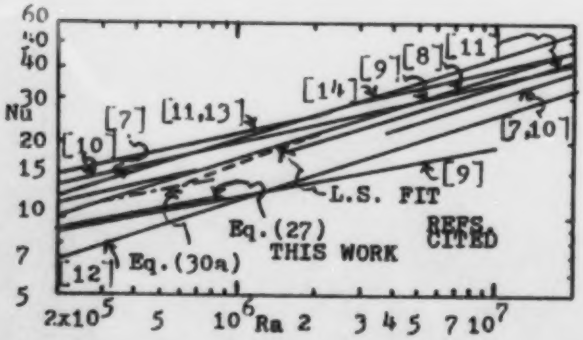

Fig. 6 Comparison of Results of Various Investigators, for Upward-Facing Horizontal Plate and the Results of this Paper

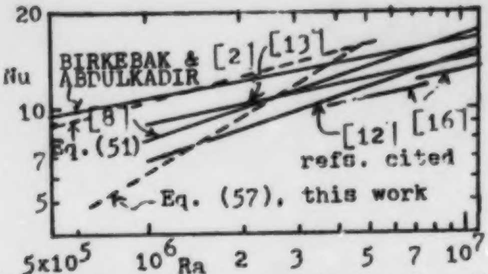

Fig. 7 Comparison of Results of Various Investigators, for Downward-Facing Horizontal Plate

REFERENCES

1. Eckert, E.R.G. & Drake, R.M.,Jr., Heat and Mass Transfer, Mc Graw-Hill, New York, 1959.
2. Bandrowski, J., & Rybski, W., Analysis of Heat Transfer in Free Convection on Horizontal Plates, Chemical Engineering, Vol. 1, pp. 3-16, 1975 (in Polish, English Abstract).
3. McAdams, W.H., Heat Transmission, McGraw-Hil, New York, 1954.
4. Levy, S., Integral Methods in Natural Convection, J. of Applied Mechanics (ASME), Vol. 22, pp. 515-522, 1955.
5. Schulenberg, T., Natural Convection Heat Transfer to Liquid Metals Below Downward Facing Horizontal Surfaces, Int. J. of Heat Mass Transfer, Vol. 27, pp. 433-441, 1984.
6. Hrycak, P., Calculation of Heat Transfer for a Downward-Facing, Heated Horizontal Plate, Proc. 12th Canadian Cong. of Applied Mechanics, Ottawa, Canada, Vol. 2, pp. 700-701, 1989.
7. Fishenden, M., & Saunders, O.A., An Introduction to Heat Transfer, Clarendon Press, Oxford,1952.
8. Bosworth, R.L.C., Heat Transfer Phenomena, Wiley, New York, 1952.
9. Lewandowski, W.M. & Kubski, P., Effect of the Use of the Balance and the Gradient Methods ... Natural Convection... , Wärme und Stoffübertragung, Vol. 18, pp. 247-256, 1984.
10. Yousef, W.W., Tarasuk, J.D. & McKean, Free Convection Heat Transfer from Upward-Facing Isothermal Horizontal Surfaces, J. of Heat Transfer (ASME), Vol. 104, pp. 493-500, 1982.
11. Al Arabi, M. & El-Riedy, M.K., Natural Convection Heat Transfer from Isothermal Horizontal Plates of Different Shapes, Int. J. Heat Mass Transfer, Vol. 19. pp. 1399-1404, 1976.
12. Hassan, K.E. & Mohamed, S.A., Natural Convection from Isothermal Flat Surfaces, Ibid., Vol. 13, pp. 1873-1886, 1970.
13. Fujii, T. & Imura, H., Natural Convection from Plate with Arbitrary Inclination, Ibid., Vol. 15, pp. 755-767, 1972.
14. Ishiguro, R., Abe, T., Nagase, H. & Nakanishi, S., Heat Transfer and Flow Instabilities of Natural Convection over Upward-Facing Horizontal Surfaces, Proc. 6th Int. Heat Transf. Conf., Toronto, Canada, Vol. 2, pp. 229-234, 1978.
15. Singh, S.N. & Birkebak, R.C., Laminar Free Convection from a Horizontal Infinite Strip Facing Downwards, Z.A.M.P., Vol. 20, pp. 954-961, 1969.
16. Aihara, R., Yamada, Y. & Endo, S., Free Convection along the Downward-Facing Surface of a Heated Horizontal Plate, Int. J. Heat Mass Transf., Vol. 15, pp. 2535-2549, 1972.

AN EXPERIMENTAL AND NUMERICAL INVESTIGATION OF NATURAL CONVECTION AND U-VALUE DETERMINATION OF SEALED WINDOW GLAZING UNITS

R.A. Showole E.S. Nowak

Department of Mechanical Engineering
The University of Western Ontario
London, Ontario, Canada, N6A 5B9

ABSTRACT

A preliminary investigation of natural convection in the air layer between a sealed double glazed window was undertaken experimentally using a Mach-Zehnder interferometer and a guarded Hot Box apparatus equipped with an isothermal baffle. The Hot Box apparatus was employed to obtain isothermal condition on the surfaces of the glazings. A finite difference technique was used in the supplementary numerical study. The range of Grashof number considered is $500 \leq Gr \leq 10000$. The dimensionless number was based on the air gap or the thickness of the air layer. Interferograms and numerical isotherms of the natural convection in the air layer are presented. At low Grashof numbers, heat is transfered mainly by conduction from the hot to the cold glazing. As Grashof number increases, convection sets in at the lower and upper corners of the air layer. Heat transfer by conduction prevails in the central region. At higher Grashof number, boundary layer begins to form on the inside surfaces of the glazings. Temperature variation occurs vertically, but remains constant across the horizontal plane of the air layer. In both the numerical and interferometric procedures, the R-value and U-value determination was based on the value obtained for the average Nusselt number.

NOMENCLATURE

g = acceleration due to gravity (m/s^2)

Gr= Grashof number, ($g\beta\Delta T W/\nu^2$)

h = Local heat transfer coefficient (w/m^2k)

Nu_y = Local Nusselt number

$\overline{Nu}$ = Average Nusselt number

x^* = x/W

y^* = y/W

t, T = Temperature ; $\Delta T = T_h - T_c$

T^* = Dimensionless temperature, $(T-T_c)/(T_h-T_c)$

SUBSCRIPTS

c = cold
D = Design
e = effective or apparent
h = hot
w = wall

INTRODUCTION

Natural convection occurring in the air gap between window glazings has been recognized as the major source of energy losses through window glazings. A fundamental understanding and accurate prediction of the complex heat transfer mechanism in the air gaps of sealed window glazings is essential in order to develop supper energy efficient windows for the cold climate.

The standard window design method has been based on the American Society of Testing Material standard (ASTM standard C177) which estimates energy transport and determines U-value based only on the window glazing boundary temperatures. This procedure has been used by Bowen (1985). The shortcoming of this procedure is that no consideration was given to the strong convection heat transport occurring in the lower and upper corner regions of the air layer between the glazings. This strong convection heat transport constitutes a major source of energy losses through window glazings and limits the insulating effect of the double glazed window. One reason for the omission of the convective heat transport mechanism in the analysis of heat losses through window glazings is the lack of a technique to measure the convective heat transport in the confined air layer. Therefore, the objective of the present paper is to discuss two techniques which could be employed to measure the convective heat transport in the confined air layer. This paper will also discuss the prediction of thermal transmittance of window glazings based on the natural convection in the air layer. A qualitative analysis of the preliminary result obtained using the interferometric and numerical techniques will be presented.

The problem of predicting the amount of heat transported through the air layer enclosed between two differentially heated vertical plates has received considerable attention in the past. Few examples are the works by Batchelor (1954), Eckert and Carlson (1961), and Hollands et al (1976). These studies employed numerical techniques or experimental procedures where the plates considered are metals, such as copper, and isothermality on the plates' surfaces can be easily obtained. In addition, these studies were not designed to predict thermal performance of window glazing system, hence no determination of R-value and U-value was considered. In the present study, we considered glass plates in our experimental study in order to accurately simulate window glazings. But the problem with the glass is that , unlike metals, isothermality cannot be easily obtained. To obtain isothermal condition, we employed a guarded Hot Box apparatus equipped with a constant temperature baffle. The determination of U-value based on the value of the heat transfer coefficients in the air layer between the glazings was discussed. The double glazed window model considered in this study is shown schematically in Fig. 1. The height-to-width aspect ratio of the air layer is 8. One side of the double glazed window was kept at typical room-side temperatures and the other at various weather-side temperatures. The Mach-Zehnder interferometer employed in the experimental study produced interferograms which give indications of the flow situation. The existence of boundary layers is clearly indicated. The interferograms can be analyzed to obtain temperature distributions, local and average heat transfer coefficients. All the information can provide the fundamental and physical understanding of the flow and heat transfer phenomena which could aid designers and manufacturers of windows in developing a more energy efficient window glazing system.

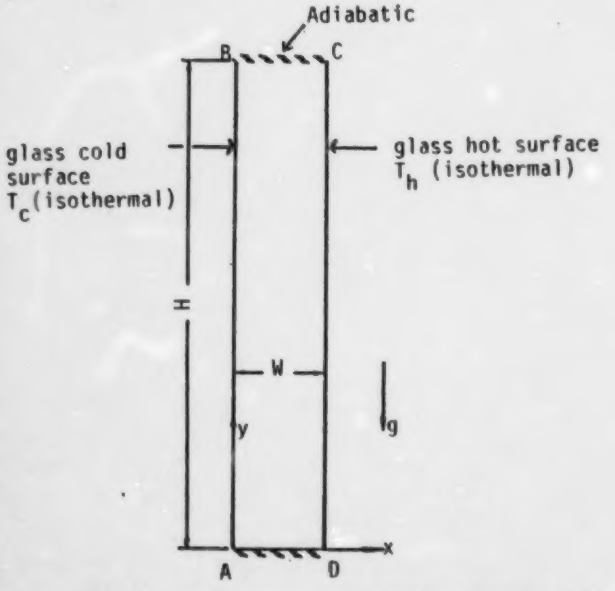

Figure 1 A schematic of the double glazed window with the boundary conditions

NUMERICAL PROCEDURE AND ANALYSIS

The schematic of the solution domain is shown in Fig. 1. The differentially heated vertical walls are considered isothermal. The upper and lower horizontal boundaries of the air layer are considered to be adiabatic. The height, H, and the width, W, are fixed for all experiments. The governing equations which applied to the physical problem under consideration are the conservation of mass, momentum and energy. In dimensionless form, they are written in cartesian coordinates for the stream-function and vorticity formulation as follows:

Poisson Equation:

$$\frac{\partial^2\psi}{\partial x^{*2}} + \frac{\partial^2\psi}{\partial y^{*2}} = -\omega \qquad (1)$$

Vorticity Equation:

$$\frac{\partial\psi}{\partial y^*}\frac{\partial\omega}{\partial x^*} - \frac{\partial\psi}{\partial x^*}\frac{\partial\omega}{\partial y^*} = Ra\,Pr\,(\frac{\partial T^*}{\partial y^*}) \qquad (2)$$

$$+ Pr\,(\frac{\partial^2\omega}{\partial x^{*2}} + \frac{\partial^2\omega}{\partial y^{*2}})$$

Energy Equation:

$$\frac{\partial\psi}{\partial y^*}\frac{\partial T^*}{\partial x^*} - \frac{\partial\psi}{\partial x^*}\frac{\partial T^*}{\partial y^*} = \frac{\partial^2 T^*}{\partial x^{*2}} + \frac{\partial^2 T^*}{\partial y^{*2}} \qquad (3)$$

Boundary Conditions

The boundary conditions for the governing differential equations are given as:

$\psi = \frac{\partial\psi}{\partial x^*} = \frac{\partial\psi}{\partial y^*} = 0$ on AB, BC, CD, and AD

$\omega = -\frac{\partial^2\psi}{\partial x^{*2}}$, on AB and CD

$\omega = -\frac{\partial^2\psi}{\partial y^{*2}}$, on BC and AD

$T^* = 1$ on CD; $T^* = 0$ on AB (isothermal)

$\frac{\partial T^*}{\partial y^*} = 0$, on AD and BC (adiabatic)

Solution Procedure

The governing differential equations discussed in the preceding paragraphs were approximated by a finite difference method following a procedure which has been outlined by Dennis and Hudson (1978). Matrices of the difference equations derived using this procedure are always diagonally dominant, and the results were accurate to the order of h^2, where h is the finite difference grid.

The algebraic equations derived from the difference equations were solved at the internal grid points of the solution domain using the successive over-relaxation procedure. Grid analysis was carried out to ensure the stability of the numerical approximation. This grid analysis technique was first introduced by Shank (1955).

Local and average Nusselt numbers based on the dimensionless temperature from the numerical calculation can be expressed as:

$$Nu_y = W(\partial T^*/\partial x^*) \tag{4}$$

$$\overline{Nu} = \frac{1}{H}\int_0^H W(\partial T^*/\partial x^*)\,dH \tag{5}$$

The average Nusselt number from eq.(5) can be related to the thermal conductivity, k, of the air layer and the effective or apparent thermal conductivity, k_e, as given by Holman (1981) and expressed as:

$$\overline{Nu} = k_e/k \tag{6}$$

The effective thermal coductivity can be related to the thermal resistance, R, by the following expression:

$$R = \delta/k_e \tag{7}$$

where δ is the thickness of the air layer between the glazings. The overall thermal transmittance, U, can be estimated as follows:

$$U = 1/R_U = 1/(R + R_h + R_c) \tag{8}$$

where R_h and R_c are the outside surface film resistances on the hot and cold sides of the double glazed window respectively, and can be obtained from the standard ASHRAE data or calculated as shown in a later section of this paper.

EXPERIMENTAL PROCEDURE

A Mach-Zehnder interferometer was employed to obtain the temperature distributions in the air layer between the glazings. This was accomplished by integrating a guarded Hot Box apparatus holding the double glazed window with the Mach-Zehnder interferometer. For clarity we show in Fig. 2, the integration of the double glazed window with interferometer. The schematic of the guarded Hot Box with the double glazed window in place is shown in Fig. 3. As mentioned above, the guarded hot box apparatus was employed to obtain isothermal condition on the surfaces of the glazings. As will be seen later, it is also used to obtain the surface film resistances on the outside surfaces of the hot and cold sides of the double glazed window. This procedure improves the accuracy of the overall thermal transmittance, U-value.

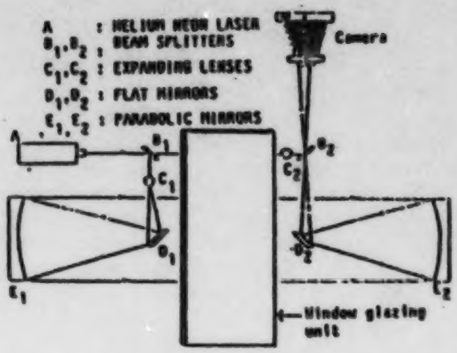
A : HELIUM NEON LASER
B_1, B_2 : BEAM SPLITTERS
C_1, C_2 : EXPANDING LENSES
D_1, D_2 : FLAT MIRRORS
E_1, E_2 : PARABOLIC MIRRORS
Camera
A
B_1
B_2
C_1
C_2
D_1
D_2
E_1
E_2
Window glazing unit

Figure 2 Mach-Zehnder Interferometer integrated with a Double-glazed Window Unit

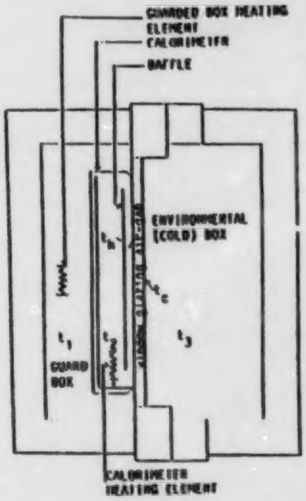

Figure 3. Schematic of A Guarded Hot Box Apparatus

A monochromatic light source from the He-Ne laser was collimated by two lenses (see Fig.2), and was made parallel by the parabolic mirror H before being split into two identical beams by the beam-splitter D. The two beams traversed separate paths, one as a reference passing through air in the laboratory and the other through the test medium. The two beams later recombined to produce interference fringe patterns. In this study, finite fringe shifts were obtained. The fringes were analyzed to obtain temperature distributions in the air layer. Temperature data obtained from the analysis were then used to calculate the local temperature gradients and hence the local and average Nusselt numbers as follows:

$$Nu_y = \frac{h \cdot W}{K_m} = W\,\frac{dT^*}{dx^*}\Big|_W \tag{9}$$

$$\overline{Nu} = \frac{1}{H}\int_0^H W\,\frac{dT^*}{dx^*}\Big|_W\,dH \tag{10}$$

The surface film resistances on the hot and cold sides of the glazing unit can be determined from the energy input to the hot box and the temperatures of the warm and cold chambers of the box as follows:

$$R_h = (t_2 - t_h)/q \tag{12}$$

$$R_c = (t_c - t_3)/q \tag{13}$$

The R-values and U-values can then be determined using the average Nusselt numbers and film resistances as discussed in the previous section.

RESULTS AND DISCUSSION

Few samples of the interferograms obtained during this study is shown in Figs. 4(a) to 4(f). A sample of the numerical isotherms corresponding to one of the interferograms is shown in Fig. 5. Since this study is a preliminary stage of an intensive research and development of advanced window glazing systems, the results to be presented in this paper will be limited to the qualitative analysis of the temperature field, flow characteristics and heat transfer phenomenon observed on the interferograms and the numerical isotherms. A more detailed heat transfer results will appear in subsequent publlications.

Temperature, Heat Transfer and Flow Characteristics

The interferograms shown in Figs. 4(a) to 4(f) were obtained by finite fringe settings. Prior to the heating and cooling of the glazings, the inteference fringes were horizontal as laser beam traversed the air layer of uniform density. The horizontal fringes indicates also that the temperature difference across the air layer is zero. As the heating and cooling of the glazings progressed, the horizontal fringes began to curve slightly as shown in Fig. 4(a). At higher Grashof numbers the fringes have become more distorted. Distortion is apparent in the top and lower corner regions of the air layer. An examination of the interferograms in Figs 4(c) to 4(f) and the numerical isotherms in Fig. 5, indicates a considerable distortion of the fringes at the top left corner of the cold plate and bottom right corner of the hot plate. This phenomenon indicates that heat is transported by coduction in the central region of the air layer, and by convection in the lower and upper corners. The flow recirculation in the air layer is by upward motion along the hot surface and downward motion along the cold surface with strong convection at high Grahsof number at the lower and upper corner regions. The flow characteristics indicate that fluid in the central region of the air layer does not contribute to energy transport across the air layer. But the strong convection at the corners constitutes a major source of heat transport. This is evident by the high temperature gradient which can be observed in the corner regions of the interferogram, Fig.4(f), the numerical isotherms, Fig.5, and the local Nusselt number distribution in Fig.6.

At higher Grashof number (Figs. 4(d) to 4(f)), longitudinal rolls began to form in the enclosure, and boundary layer developed on the vertical surfaces. This phenomenon results in high heat transfer rate as indicated by the closely spaced fringes in Figs 4(d) to 4(f). These figures also reveal temperature reversal as temperature gradient at some locations near the corners changes from negative at the hot plate to positive and then negative again at the cold plate. The temperature reversal is caused by the high velocities of the flow recirculating at the

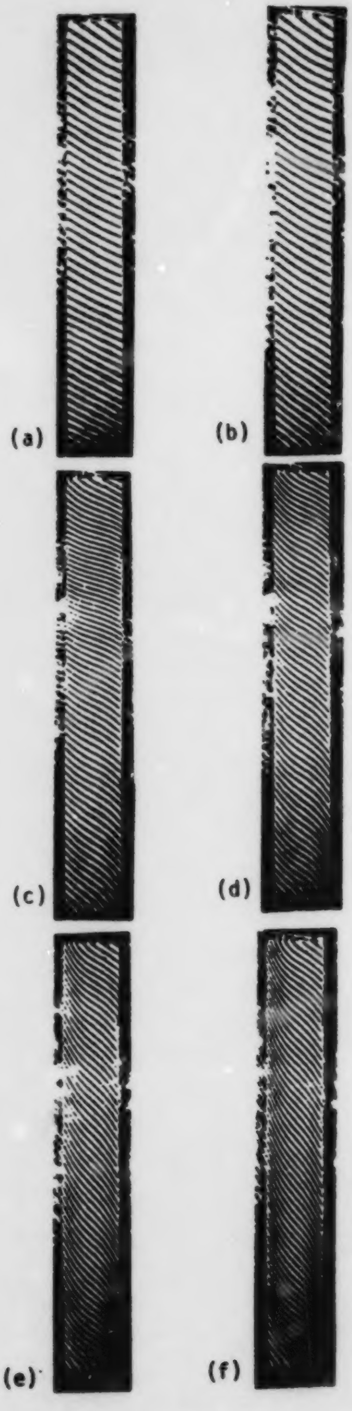

Figure 4. Interferograms

(a) Gr = 685; ΔT = 1.8 (b) Gr = 2771; ΔT = 7.3

(c) Gr = 4694; ΔT = 12.4 (d) Gr = 6826; ΔT = 18.1

(e) Gr = 8316; ΔT = 22.1 (f) Gr = 9282; ΔT = 24.7

corner region of the enclosure. This complex phenomenon calls for further heat transfer study and analysis in the corner region of the air layer.

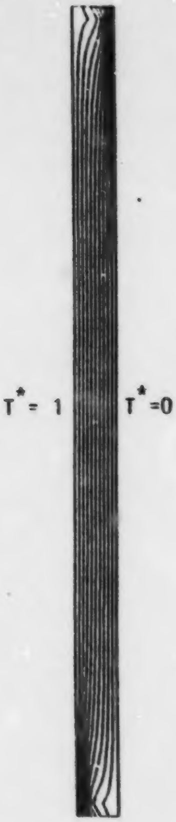

Figure 5. Numerical Isotherms (Gr = 5000)

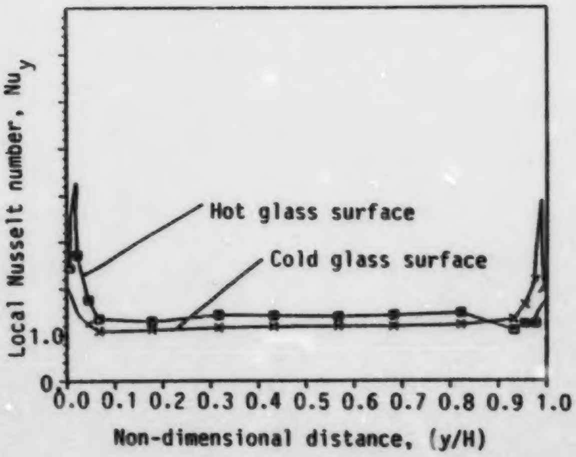

Figure 6. Sketch of Local Nusselt Number distribution along cold and hot glass

CONCLUSION

Interferometric and numerical techniques were employed to investigate the convective flow in the air gap of a double glazed window unit. This is the first time an interferometric technique was used to study heat tranport in an air layer enclosed by window glazings. The fluid circulation in the air gaps was from the hot to the cold plate. Heat transport by convection occured in the lower and upper regions of the air layer. Energy was transported by conduction in the central region. At high Grashof number, boundary layer developed on the vertical walls. The boundary layer formation contributes considerably to heat transfer rate as evident from the closely spaced fringes. Temperature reversal appear to occur near the corners due to high velocities of the flow recirculating in the enclosure. This phenomenon calls for further study and analysis. All the information provided indicate that the insulating effect of double glazed window could be improved if the convection activities in the corner regions are suppressed.

ACKNOWLEDGEMENT

This research was supported by the Natural Sciences and Engineering Research Council of Canada.

REFERENCES

Batchelor, G.K. 1954, Heat Transfer by Free Convection Across A Closed Cavity Between Vertical Boundaries at Different Temperatures, Quarterly of Applied Mathematics, Vol. XII, pp. 209-233.

Bowen, R.P. 1985, DBR's Approach for Determining the Heat Transmission Characteristics of Windows, National Research Council, Division of Building Research, Building Research Note 234, November.

Dennis, S.C.R. & Hudson, J.D. 1978, A Difference Method for Solving the Navier-Stokes Equations, Proc. 1st Int. Numerical Methods in Laminar and Turbulent Flow Conf., Swansea, U.K., pp. 69-80

Eckert, E.R.G. & Carlson, W.O. 1961, Natural Convection In An Air Layer Enclosed Between Two Vertical Plates With Different Temperatures, Int. J. Heat Mass Transfer, Vol. 2, pp. 106-120.

Hollands, K.G.T., Unny, T.E., Raithby, G.D., Konicek, L. 1976, Free Convective Heat Transfer Across Inclined Air Layers, Journal of Heat Transfer, Vol. 98, pp. 189-193.

Holman, J.P. 1981, Heat Transfer, pp. 286-288, McGraw-Hill, New York.

Shanks, D. 1955, Non-Linear Transformation of Divergent and Slowly Convergent Sequences, J. Mathematics and Physics, Vol. XXXIV, pp. 1-42.

APPLICATION OF DIGITAL IMAGE PROCESSING TO INTERFEROGRAM ANALYSIS

D. Naylor J.D. Tarasuk

The University of Western Ontario
Department of Mechanical Engineering
London, Ontario
N6A 5B9

ABSTRACT

A digital image processing system for the analysis of interferograms has been developed which greatly reduces processing time over standard manual methods. Image scanning to locate interference fringe centres has been semi-automated by means of interactive software. A fringe detection algorithm is presented which is insensitive to varying background intensity and noise in the image. Using the algorithm presented, precise fringe centre data can be obtained by either an integrated pixel intensity method or by locally averaging the maximum intensity data from several adjacent scans.

INTRODUCTION

Interferometry is widely used to analyze heat transfer and compressed fluid flows. Photographically recorded interference fringe patterns can be calibrated to yield the temperature or density fields; given the precise location of the fringe centres, local gradients of these properties can be calculated.

In the past, interference fringe centres have commonly been located by eye using a travelling microscope or densitometer. Both of these methods are time consuming and subject to human error. This paper describes the application of an IBM PC based digital image processing system to infinite fringe interferogram analysis. With minor software modifications, the system would be equally useful for analyzing finite (wedge) fringe interferograms.

Interferogram analysis by digital image processing has been used recently by several heat transfer researchers [1-3]. Problems of poor image resolution and low reliability/accuracy of the fringe centre detection algorithms have been reported. Hunter and Collins [2] found varying background light intensity to be a major problem. However, other "false fringes" can be produced by surface diffraction, imperfections in the optics or blemishes on the film. The simple algorithm presented here for analyzing infinite fringe interferograms largely overcomes these problems.

SYSTEM HARDWARE

In the present system the interference patterns are recorded photographically using Polaroid Land Film (4" x 5", type 55 positive/negative). Film negatives are analyzed since they have higher resolution (160 lines/mm) than the positives.

The image processing system is shown schematically in Fig. 1. A CCD camera (Cohu model 4815, 754 x 488 pixels) mounted directly on a travelling microscope supplies a video signal to a frame grabber board (Imaging Technology PCVISION) in an expansion slot of an IBM compatible (80286) personal computer. Rather than capturing the entire interferogram at once, it is stored as several separate images. Each image is digitized and stored in 640 x 480 x 8 bit frame memory (256 grey levels). In this way, excellent image resolution is achieved.

The overall scale factor of the system is measured by placing a reticule under the travelling microscope. The reticule has a scale 10 mm long with 0.1 mm divisions. The scale factors are determined by placing the reticule in both the horizontal and vertical scanning positions and recording the number of pixels between a known distance on the reticule. In Fig. 2 the horizontal scale factor is 3.62μm per pixel and the vertical scale factor is 3.66μm per pixel. Hence, images on the monitor are slightly distorted since the horizontal and vertical scale factors differ by approximately 1%. However, this difference does not introduce errors into the results since vertical and horizontal distances are scaled appropriately in the fringe analysis software.

In regions of low heat transfer, fringes are widely spaced and lower magnifications must be used to get the required fringes in the field of view. In these regions, the image resolution is lower.

FRINGE ANALYSIS ALGORITHM

On an infinite fringe interferogram as shown in Fig. 2a, fringe centres can be calibrated as lines of constant temperature. However, surface temperature gradients (i.e. local heat transfer coefficients) are of primary

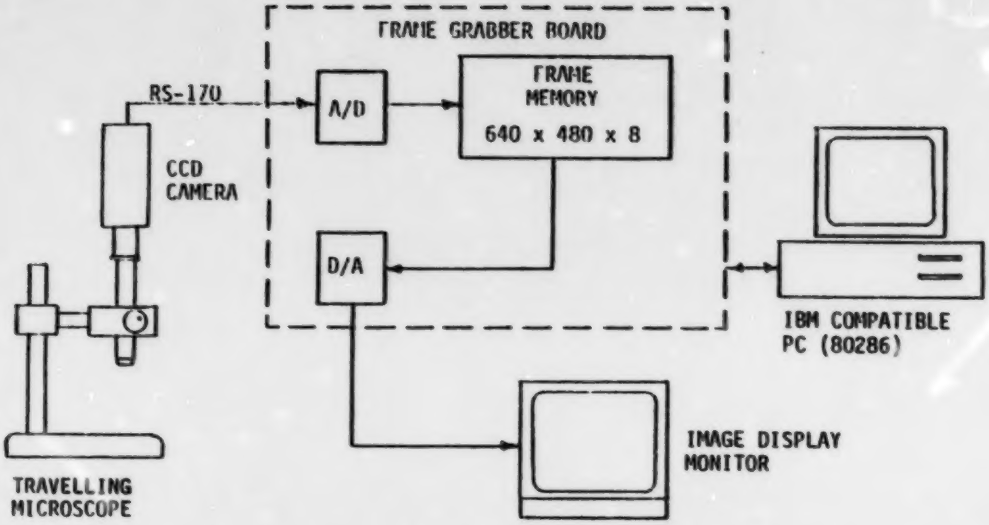

Fig. 1. Schematic diagram of the image processing system.

interest in heat transfer studies. To measure the surface temperature gradient, first a temperature profile perpendicular to the model wall is obtained from the closest three or four destructive interference fringe centres. The temperature profile is then extrapolated to the wall to obtain the surface gradient.

Interactive software has been developed which accurately locates the fringe centres in an image. The procedure is as follows: Initially, the interferogram image is aligned under the microscope (with the aid of software generated cross hairs) so that the model surface is vertical on the monitor as shown in Fig. 2a. Once the desired section of the interferogram has been captured into frame memory, the cursor is used to indicate the horizontal location of the wall on the interferogram. Then the user selects the start and end locations of the first horizontal scan using the cursor. Also, the vertical location of the last horizontal scan is selected as well as the number of pixels between each horizontal scan. Fig. 2b shows the image after scanning has taken place at a vertical increment of five pixels. White lines are displayed at each scan so that the user can verify the scanning locations. The complete scan and data processing of one image takes about 30 seconds after the desired image has been captured into frame memory.

A typical horizontal pixel intensity profile from frame memory is shown in Fig. 3. The three primary peaks represent destructive interference fringes. The "noise" which is superimposed upon the interference pattern is produced by surface diffraction, imperfections in the optics and blemishes on the film. For each horizontal scan the following simple algorithm is used to extract the fringe centre locations.

First, the mean pixel intensity ($\bar{I}$) for the scan is calculated. Next, the width of each peak (Δ_i) is calculated where it crosses the mean intensity line (Fig. 3). Each Δ_i represents a potential fringe. To eliminate the small noise "spikes" (Δ_1 and Δ_5 in Fig. 3) the width of each Δ_i is compared to the largest spacing (Δ_{max}). If $\Delta_i < 0.2\ \Delta_{max}$ the "spike" is discarded as noise.

Once only valid fringe peaks remain, the intensity data in each Δ_i range are processed to yield the fringe centres. Two different techniques have been used:

i) *Maximum pixel intensity fringe centre*:
In the range Δ_i, the location of maximum pixel intensity is found. If the data are completely free of noise this is the ideal technique, since there is exactly one fringe shift between each fringe maximum. Measured fringe spacings would not be in error by more than the width of one pixel.

ii) *Integrated intensity fringe centre*:
The integrated intensity fringe centre is found by locating the line which equally divides the area under each valid fringe peak. The area under the pixel intensity curve for a valid fringe peak is calculated numerically using the trapezoidal rule:

$$A = \Sigma(I - \bar{I}) \quad \text{summed over each pixel in the range } \Delta_i.$$

The fringe centre is taken to be the pixel location which corresponds to A/2. This method is a modification of a method used by McKeen [4,5] to extract fringe centres from the output of an automated scanning densitometer.

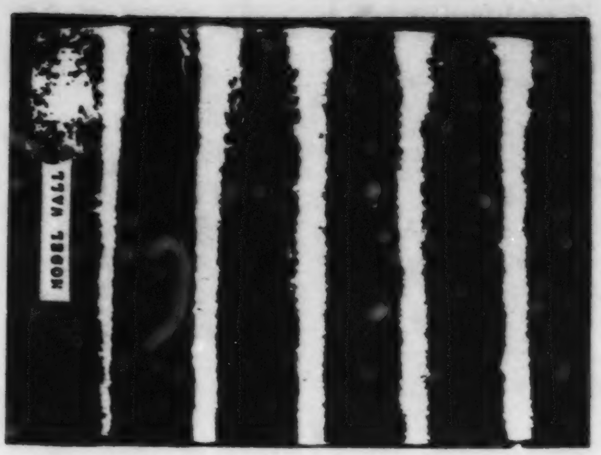

Fig. 2. (a) Section of an infinite fringe interferogram displayed on the monitor.

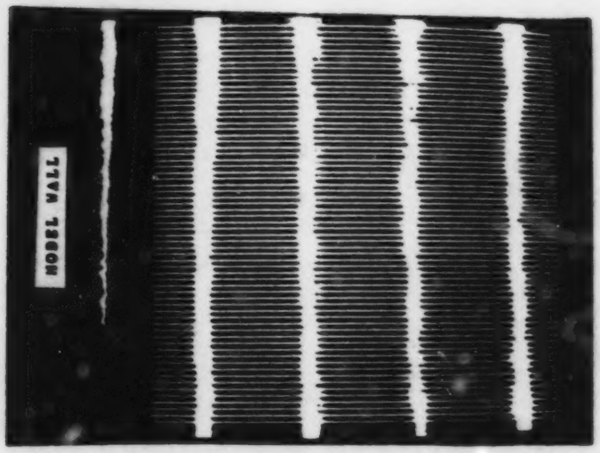

Fig. 2. (b) Interferogram showing horizontal scan lines.

The mean intensity value fluctuates from one horizontal scan to another due to noise and changes in the background intensity across the image. For this reason the sensitivity of the integrated intensity data to fluctuations in the mean intensity has been tested. The image shown in Fig. 2a was analyzed with the mean intensity line arbitrarily shifted by ± 20%. The maximum change in any measured fringe spacing did not exceed 1.7%. The average difference was 0.18%.

It should also be noted that this algorithm can also be extended to measure half fringe shifts simply by repeating the analysis for the data under the mean intensity line. It is clear from Fig. 3 that the *constructive* interference fringe peaks are not as well defined and the measured spacings will be less accurate. However, the ability to measure half fringe shifts could be very useful in regions where the fringe spacing is very large or where insufficient full fringe shifts exist.

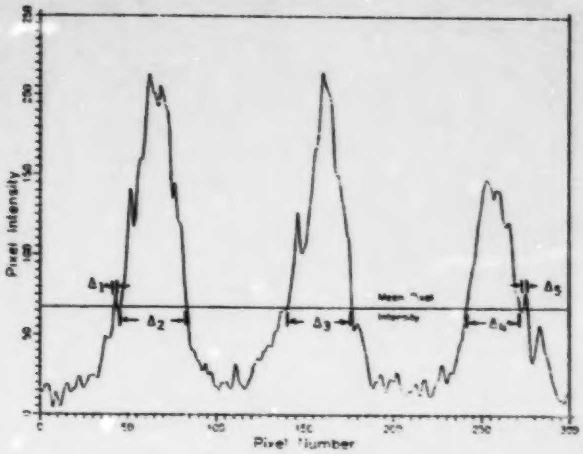

Fig. 3. Typical horizontal pixel intensity profile.

RESULTS AND DISCUSSION

Fig. 4 shows a fringe centre plot of the first two fringes obtained from scanning the image at five pixel increments (approx 0.018mm) as shown in Fig. 2b. From this plot it is evident that the maximum intensity fringe centres exhibit substantially more scatter than the integrated intensity fringe centres. Also, in general, the maximum intensity fringe centres appear to be uniformly scattered on both sides of the integrated intensity centres. Hence, it may be concluded that the integrated intensity fringe centre detection algorithm is superior for analyzing "noisy" interferograms.

For the fringe closest to the wall, the large amount of scatter in the maximum intensity fringe centres is primarily due to the surface diffraction fringes. This will always be the case. Hence, even in a high quality interferogram, in which noise is kept to a minimum, the integrated intensity fringe centre method will likely give more accurate results for the first fringe.

Another point of note in Fig. 4 is that data from the eleventh horizontal scan have been omitted (wall location of approx. 0.18mm). A dark imperfection in the image near the centre of the second destructive fringe caused an additional fringe centre to be detected. Data from this scan were automatically discarded by the software when it detected five fringes rather than four during the analysis.

In Fig. 5, the noise in the maximum intensity fringe centres has been "smoothed" using an averaging procedure. The horizontal distance between each data point in Fig. 5 is five pixels. However, each maximum intensity fringe centre represents the averaged fringe centre from eleven scans. The eleven scans comprise five scans at *one pixel* increments on each side of the data point location. The integrated intensity fringe centres have not been averaged.

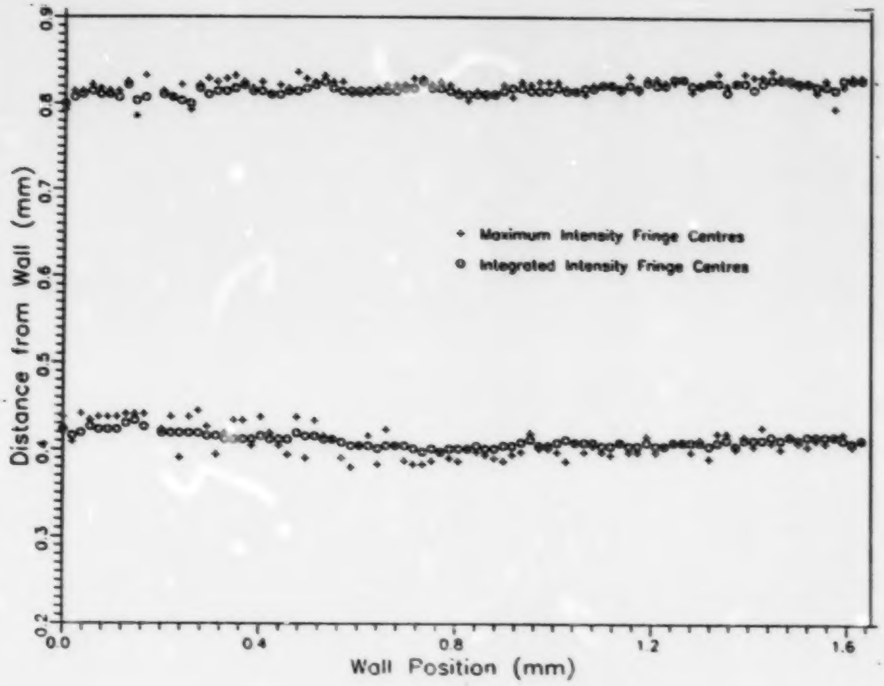

Fig. 4. Integrated intensity and maximum intensity fringe centre plot.

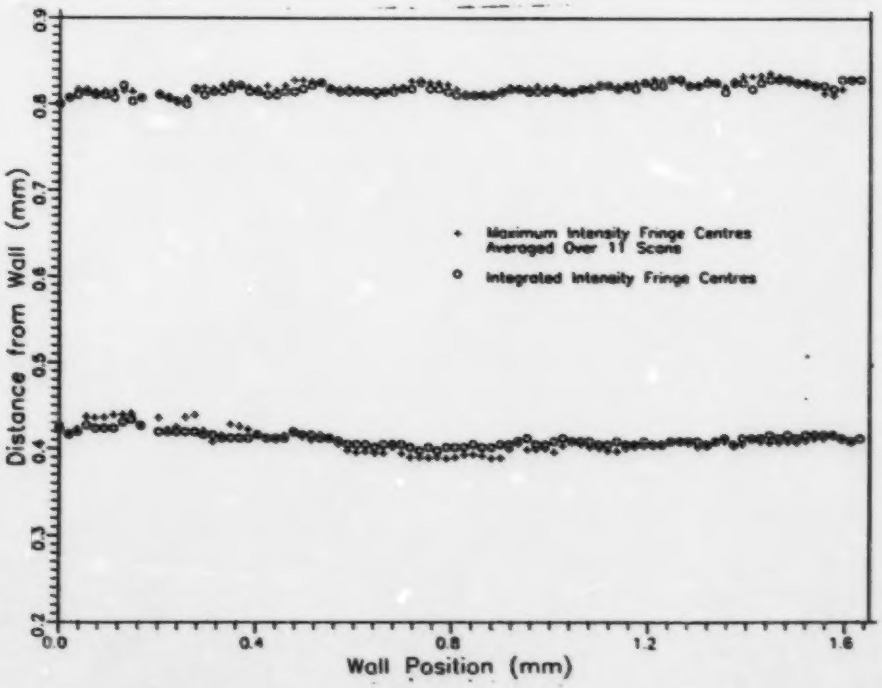

Fig. 5. Integrated intensity and averaged maximum intensity fringe centre plot.

It can be seen in Fig. 5 that this averaging procedure is a viable method of reducing the scatter in the maximum intensity fringe centres. The integrated intensity centres and the maximum intensity centres are in good agreement, particulary for the second fringe from the wall. The slight disagreement for the fringe closest to the wall is likely caused by surface diffraction.

CONLUSIONS

An IBM PC based digital image processing system has been developed for analyzing interferograms. An algorithm for detecting interference fringes has been implemented which is insensitive to noise in the image. Fringe centre data with a low amount of scatter can be obtained using either an integrated intensity method or by locally averaging the maximum intensity data from several adjacent scans.

ACKNOWLEDGMENTS

The authors wish to acknowledge the support of NSERC of Canada during the course of this study.

REFERENCES

1. Kato S. & Maruyama N., Holographic Interferometry Measurements of the Three-dimensional Temperature Field with Thermally Developing Flow in the Measuring Beam Direction, Proc. of the First World Conference on Experimental Heat Transfer, Fluid Mechanics and Thermodynamics, Dubrovnik, Yugoslavia, pp.425-432, 1988.

2. Hunter J. & Collins W.C., Problems in using Holographic Interferometry to Resolve the Four-Dimensional Character of Turbulence. Part II: Image and Data Processing, J. Optical Sensors, Vol. 1, pp.227-234, 1986.

3. Lehmann G.L., Experimental Investigation of Convective Heat Transfer in a Transitional Channel Flow with Periodic Cavity Induced Roughness, Ph.D. thesis, Clarkson University, Potsdam, New York, 1985.

4. McKeen W.J., The Development of a Technique to Measure the Location of Fringes on an Interferogram, M.Eng. thesis, The University of Western Ontario, London, Ontario, 1978.

5. McKeen W.J. & Tarasuk J.D., Accurate Method for Locating Fringes on an Interferogram, Review of Scientific Instruments, Vol. 52, pp.1223-1225, 1981.

EFFECTS OF AMBIENT HUMIDITY ON THE THERMAL BEHAVIOR OF POROUS BUILDING MATERIALS

F. KALLEL and N. GALANIS
Département de génie mécanique

Université de Sherbrooke Sherbrooke, Québec, J1K 2R1

ABSTRACT

A one-dimensional model for simultaneous heat and moisture transfer in porous building materials is formulated and validated by comparison with temperature and moisture content profiles measured in brick and mortar slabs. The model is then used to study the effect of decreasing ambient humidity on the thermal behavior of such slabs. For constant and variable temperatures and for symmetrical and unsymmetrical ambient conditions, the results show that a reduction of ambient relative humidity causes a decrease in slab temperature and corresponding heat fluxes which can not be predicted if mass transfer is neglected.

NOMENCLATURE

A	area normal to x
C_p	specific heat
D_m	isothermal mass transfer coefficient
D_T	non-isothermal mass transfer coefficient
H	enthalpy
h_c	convective heat transfer coefficient
h_m	convective mass transfer coefficient
J	mass flux
M	mass
m	rate of vapor condensation
q	heat flux
T	temperature
t	time
W	total moisture content, $W = w_l + w_v$
w	mass ratio, $w_i = M_i/M_o$
x	space coordinate
λ	equivalent thermal conductivity
ρ	density
ϕ	relative humidity

Indices

a	refers to the dry air
i	refers to any component (i = a, l, o, υ)
l	refers to the liquid
o	refers to the solid matrix
s	indicates conditions at the slab's surface
sat	indicates saturation conditions
υ	refers to the vapor
∞	refers to ambient conditions

INTRODUCTION

Simultaneous heat and moisture transfers occur under natural conditions (variable ambient temperature and/or relative humidity) and during the thermal treatment (drying, freezing, etc.) of porous materials such as soils, concrete, food products, textiles, paper, wood, etc. In both cases the quantities usually required (moisture content and temperature distributions in the material, moisture and heat fluxes at the surfaces, etc.) must be determined under unsteady conditions. Moreover, the transfer of mass and energy are strongly coupled. Indeed, moisture flux depends on the temperature gradient while the temperature field is influenced by the heat sources or sinks associated with phase changes and by the transport of energy by the moving moisture.

For building materials the presence of moisture in the liquid or solid phases is the source of thermal and structural degradation. Wood and other hygroscopic materials acting as seasonal moisture sources or sinks influence comfort conditions within the building by affecting both indoor humidity and heat fluxes at the interior building surface. Although some studies of combined heat and moisture transfers have been carried out for homogeneous building materials and composite walls (Andersson [1985] , Mitalas - Kumaran [1987] , Hedlin [1988]) the subject is far from exhausted and moisture effects have not been incorporated in any existing building energy analysis computer codes.

In this paper we present a one-dimensional model based on the continuum mechanics approach. It is assumed that temperatures are above freezing so that water is only present in the liquid and vapor phases. The model is validated by comparison with measurements and predictions from Luikov's model [1966] and is used to study the transient response of homogeneous brick or mortar slabs under variable ambient conditions.

MODELLING HEAT AND MASS TRANSFER

The model is based on the assumption that the spatial variation of all dependent variables is continuous. It also incorporates the assumption of local thermal equilibrium between the three coexisting phases under consideration: the solid matrix, the pure liquid (no dissolved gases) and the gaseous mixture of vapor and dry air. These same assumptions have been used by, among others, DeVries [1958] and Luikov [1966] .

For a one-dimensional system the principle of mass conservation for the three mobile components (vapor, liquid, dry air) is:

$$\frac{\partial w_i}{\partial t} = -\frac{\partial J_i}{\rho_o \partial x} \pm \frac{m}{M_o} \qquad (1)$$

A positive value of the source term m indicates that vapor is condensing. Therefore, the plus sign appears in the equation for liquid, the minus in the equation for vapor, while for the dry air the source term is zero. The density of the solid matrix has been assumed to be a fixed constant.

Several different ways of modeling the mass fluxes are found in the literature. The diffusion theory assumes that mass transfer depends on concentration gradients. The capillary theory considers that mass movement arises from the pressure difference between the liquid and gaz components caused by surface tension; since the latter depends on the temperature mass flows can be caused by temperature gradients. Finally, mass flow is also caused by pressure differences and by gravity. Both DeVries [1958] and Luikov [1966] use a combination of these driving forces. Andersson [1985] presents several equivalent expressions for the liquid and vapor fluxes in terms of different combinations of the total moisture content, the temperature and the corresponding partial pressures. In our case we neglected gravity (since we are considering one-dimensional horizontal flows) and expressed the fluxes in Eq. 1, as follows:

$$J_i = -\rho_o\left[D_{mi}\frac{\partial w_i}{\partial x} + D_{Ti}\frac{\partial T}{\partial x}\right] \qquad (2)$$

This approach is different from that of both DeVries and Luikov who assume that liquid and vapor fluxes are caused by the same potentials: the total moisture content and the temperature. Since in general $w_l >> w_v$, and therefore $W \approx w_l$, the difference between the two formulations is only significant when evaluating the vapor flux. We believe however that it is more appropriate to express the flux of each component in terms of its own concentration. The result is that the isothermal mass transfer coefficients are not the same in our model and in that proposed by Luikov [1966].

Replacing Eq. 2 in Eq.1 results in the following form for the continuity relations:

$$\frac{\partial w_v}{\partial t} = \frac{\partial}{\partial x}\left[D_{mv}\frac{\partial w_v}{\partial x} + D_{Tv}\frac{\partial T}{\partial x}\right] - \frac{m}{M_o} \qquad (3a)$$

$$\frac{\partial w_l}{\partial t} = \frac{\partial}{\partial x}\left[D_{ml}\frac{\partial w_l}{\partial x} + D_{Tl}\frac{\partial T}{\partial x}\right] + \frac{m}{M_o} \qquad (3b)$$

$$\frac{\partial w_a}{\partial t} = \frac{\partial}{\partial x}\left[D_{ma}\frac{\partial w_a}{\partial x} + D_{Ta}\frac{\partial T}{\partial x}\right] \qquad (3c)$$

Summing up the relations for vapor and liquid and applying the condition $w_l >> w_v$, we obtain:

$$\frac{\partial w_l}{\partial t} = \frac{\partial}{\partial x}\left[D_{ml}\frac{\partial w_l}{\partial x} + \left(D_{Tl} + D_{Tv}\right)\frac{\partial T}{\partial x}\right] \qquad (4a)$$

A comparison of Eqs 3b and 4a results in the following expression for the rate of vapor condensation

$$\frac{m}{M_o} = \frac{\partial}{\partial x}\left[D_{Tv}\frac{\partial T}{\partial x}\right] \qquad (4b)$$

The three differential equations 4a, 4b and 3c express the principle of mass conservation for the three mobile components and relate the four unknown quantities w_l, T, m/M_o and w_a.

A fourth equation is obtained from the principle of energy conservation applied to the system of Fig. 1. The following simplifications are made:

- viscous dissipation is neglected
- the pressure work term for the gaseous components is also neglected, and
- the internal energy of the liquid and solid components is identical with their enthalpy.

The energy equation is then written as:

$$\rho_o\frac{\partial}{\partial t}\left(\sum w_i H_i\right) = \frac{\partial}{\partial t}\left(\lambda\frac{\partial T}{\partial x}\right) - \frac{\partial}{\partial x}\left(\sum J_i H_i\right) \qquad (5a)$$

The summations in this expression include the four components, i.e. the solid, dry air, water vapor and liquid. The conduction term comprises heat transfer through all components by an appropriate definition of an equivalent thermal conductivity.

Substituting in Eq. 5a the gradient of the mass fluxes from Eq. 1 and neglecting the convective heat transfer term, which according to Luikov is small in comparison with the conductive component, results in the following expression:

$$C^*\frac{\partial T}{\partial t} = \frac{1}{\rho_o}\frac{\partial}{\partial x}\left(\lambda\frac{\partial T}{\partial x}\right) + \frac{m}{M_o}\left(H_v - H_l\right) \qquad (5b)$$

where

$$C^* = C_o + C_l\, w_l + Cp_v\, w_v \qquad (5c)$$

In the last expression the term $Cp_a w_a$, which is small compared with the specific heat of the solid matrix, has been neglected. This elimination means that the differential equations 4a, 4b, and 5b can be solved for w_l, m/M_o and T provided the various material properties are known and appropriate boundary conditions are specified.

BOUNDARY CONDITIONS AND SOLUTION PROCEDURE

It is assumed that the surfaces of the slab are exposed to air at atmospheric pressure. Its temperature T_∞ and relative humidity ϕ_∞ are known functions of time. Continuous transfers of vapor and heat take place between the air and the surface. These are normally expressed as follows:

$$J_\infty = h_m\left(\rho_{v\infty} - \rho_{vs}\right) \qquad (6a)$$

$$q_\infty = h_c\left(T_\infty - T_s\right) + J_\infty H_\infty \qquad (6b)$$

The conservation equations for the surface consistent with the simplifications used to obtain Eqs 4a, 4b and 5b are the following:

$$\frac{\partial w_l}{A \partial t} = J_\infty + \rho_o \left[D_{ml} \frac{\partial w_l}{\partial x} + \left(D_{Tl} + D_{Tv} \right) \frac{\partial T}{\partial x} \right] \qquad (7a)$$

$$\frac{m}{A} = J_\infty + \rho_o \, D_{Tv} \frac{\partial T}{\partial x} \qquad (7b)$$

$$\frac{M_o C^*}{A} \frac{\partial T}{\partial t} = h_c \left(T_\infty - T_s \right) + \lambda \frac{\partial T}{\partial x} + \frac{m}{A} \left(H_v - H_l \right) \qquad (7c)$$

All the derivatives in the last three equations are evaluated at the slab's surface.

The formulation of the external vapor flux in terms of a density difference (Eq. 6a) introduces a certain complexity in the model since density is not used to express moisture movement within the material (Eqs. 4a, 4b and 5b). This situation arises with all models treating convective boundary conditions. It is totally removed only when the boundary conditions are imposed directly on the surface in terms of specified time variations for the variables T_s and M_{ls}. In the more general case with both boundary conditions specified away from the surface, the difficulty is eliminated by writing:

$$J_\infty = h_m \left(\phi_\infty \rho_{sat,\infty} - \phi_s \rho_{sat,s} \right) \qquad (6c)$$

The relative humidity at the surface is related to the local temperature and moisture content through the experimental moisture content isotherm of the material. Additional experimental information necessary to complete the model includes:

- the specific heats of the solid, liquid and vapor which are readily available in standard tables,
- the convective coefficient of heat transfer which can be calculated from appropriate correlations,
- the convective mass transfer coefficient which must be determined experimentally or estimated from the heat and mass transfer analogy; for natural convection on a vertical surface the latter gives $h_m = 10^{-3} h_c$
- the equivalent thermal conductivity and the mass transfer coefficients for liquid and vapor which depend on temperature and moisture content; for mortar and brick these properties have been measured by Perrin [1985].

The formulation is now complete. The system of differential equations 4a, 4b, 5b can be solved from fixed initial conditions M_l (x), T (x), m(x) for given external conditions $T_\infty(t)$, $\phi_\infty(t)$ using the boundary conditions expressed by Eqs 7a, 7b, 7c where J_∞ is given by Eq. 6c and M_{ls} by the experimental moisture isotherm.

The numerical solution of the problem was realized through an implicit scheme discretisation of the partial differential equations applying within the slab. The discretisation of the boundary conditions uses an explicit formulation which calculates directly the new values of T_s, ϕ_s and m_s at each timestep from previous conditions within the slab and in the ambient air.

RESULTS AND DISCUSSION

The numerical solution has been obtained for several different conditions for brick and mortar slabs of thickness equal to 20 cm. In the results presented here the slab is considered to be initially at a condition of hydrothermal equilibrium and at t = 0 a sudden change of one, or both, of the ambient properties (T_∞, ϕ_∞) is imposed on one, or both, surfaces of the slab. The results presented here include comparisons with measured values, comparisons with numerical results obtained from Luikov's model and illustrate the influence of mass transfer on temperature profiles within the slab and heat fluxes across its surfaces. The effect of the convective coefficients on the solution are also discussed.

Validation - Effect of convective coefficients.

Perrin [1985] has measured the temperature and moisture content evolution for slabs at uniform initial conditions (T = 20°C, w_l = 0.07) which were suddenly put in contact with cold, humid air (T_∞ = 5°C, ϕ_∞ = 80%) on one side and with hot, dry air (T'_∞ = 23°C, ϕ'_∞ = 45%) on the other side.

For this case, the convective coefficients h_c, h_m have been fixed respectively at 40 W/m^{2}K, 0.00095 m/s for the cold side. For the warm side, two different sets of coefficients (A and B) have been considered. Their values are given in Fig. 1 which compares the measured and calculated equilibrium temperature distribution for the mortar slab. Fig. 2 compares the measured and calculated evolutions of moisture content near the warm surface of the mortar slab. The results calculated with the higher-value transfer coefficients agree on the whole better with the experimental results, although the values of set A are those suggested by Perrin for his experimental conditions. The steady-state temperature distribution calculated with the B coefficients shows good agreement with experimental results except at the surfaces of the slab where the measured values are quite close to the ambient temperatures. It is believed this temperature discrepancy at the surface may be due to poor contact between the temperature sensor and the slab. Fig. 1 suggests that even better agreement between calculated and measured temperatures could be obtained by increasing the value of the heat transfer coefficient on the cold side of the slab. Similarly, the results of Fig. 2 suggest that a variable value of h_m may give better calculated results than either of the constant values A and B. Both these remarks show the importance of the convective transfer coefficients which, unfortunately, can not be determined with accuracy. Indeed, the uncertainty in the values of h_c and, in particular, h_m may constitute the most important difficulty in obtaining accurate results for coupled heat and mass transfer in building materials.

Further calculated results for this case show that phase changes occur only at the surfaces where liquid evaporates and is transferred to the atmosphere. Within the slab moisture is transported towards the surfaces in the liquid phase. Fig. 3 plots the evolution of the temperature on the surfaces and at the mid-plane of the slab. These values have been calculated using the A set of transfer coefficients for the warm side (see Fig. 1). Also shown on the figure are the corresponding temperatures calculated for the simple heat transfer problem (i.e. without moisture transfer) with the value of the thermal conductivity for mortar with zero moisture content. The figure shows that the temperature difference between the two surfaces of the slab is smaller when mass transfer is taken into account. It also follows that the temperature differences between the surface and the ambiance is larger when mass transfer is considered. These results can be explained by the fact that the presence of moisture results in an increase of the effective thermal conductivity. Furthermore, since the difference between ambient and surface temperatures is larger when mass transfer takes place, this case results in higher heat fluxes between the ambient air and the surfaces.

For the case of brick slabs, the agreement between numerical and experimental results is similar to that shown in Figures 1 and 2 for mortar. Overall the model is therefore judged as satisfactory.

Comparisons with Luikov's model - Constant T_∞.

The slabs are initially at uniform conditions ($T = 20°C$, $w_l = 0.07$). The ambient conditions for $t \geq 0$ are symmetrical with $T_\infty = 20°C$, $\phi_\infty = 50\%$. The convective coefficients for heat and mass transfer are considered to be constant and respectively equal to 15 W/m^{2}K, 0.015 m/s.

Fig. 4 shows the evolution of calculated liquid mass content for brick slabs. The results obtained from our model are identical with those obtained from Luikov's model. As expected the distribution is symmetrical. At the surfaces, equilibrium is reached very quickly. The liquid content everywhere tends towards the same asymptotic value since the atmospheric conditions are symmetrical.

Further results show that, once again, phase changes occur only at the surfaces of the slab where liquid evaporates at an initially high but rapidly decreasing rate. After approximately 2×10^4 seconds the evaporation rate is negligible. By comparison with the results of Fig. 3, it is noted that the rate of evaporation becomes negligible at about the same instant that the surface liquid content reaches its asymptotic value.

Fig. 5 presents the evolution of temperature within the brick slab. Once again results from our model are identical with those from Luikov's model. We note, that although the ambient temperature is fixed at 20°C, the slab temperature decreases to a minimum of ~ 14°C. This cooling down of the slab is due to the evaporation process which acts as a heat sink. Since evaporation takes place only at the surfaces, the surface temperature decreases faster. It subsequently drives down the temperature within the slab by conduction. Throughout this cooling down period, which lasts approximately as long as the evaporation process of the previous figure, the temperature within the slab increases with distance from the surface. As the evaporation rate decreases, heat convection between the ambient air at 20°C and the surface takes over and starts heating the slab. From then on the temperature of the surface becomes higher than that of interior points which are heated by conduction. Throughout this warming up period, the temperature within the slab decreases with distance from the surface. The temperature of all interior points tends asymptotically to the equilibrium value of 20°C.

Analogous results were obtained for the mortar slab. In this case the minimum temperature is 16°C and is reached quicker than for brick.

During this entire process of moisture removal caused solely by a lowering of the atmospheric humidity, the slab (being at a lower temperature than the surrounding air) acts as a heat-sink. The associated heat fluxes can not be predicted by addressing the thermal problem alone which predicts a uniform, constant temperature distribution in the slab (20°C).

Unsymmetrical ambient conditions - Effect of ϕ_∞.

The slabs are initially at uniform conditions ($T = 20°C$, $w_l = 0.04$). The ambient conditions for $t \geq 0$ are $T_\infty = 20°C$, $\phi_\infty = 25\%$ and $T'_\infty = 20°C$, $\phi'_\infty = 75\%$. The convective coefficients for heat and mass transfer are considered to be constant and respectively equal to 15 W/m^{2}K, 0.015 m/s on both sides of the slab.

Fig. 6 shows the evolution of the mass fluxes at the two slab surfaces for these conditions. Vapor is transferred from the high humidity air to the slab surface at x = 20 cm where it condenses (see Fig. 7). The mass flux within the slab at x = 20 cm is negligible, so that the liquid content at x = 20 cm is increasing (see Fig. 8). At the other surface, in contact with the low humidity air, a small mass flux reaches the surface from within the slab (Fig. 6, continuous line for x = 0). There it evaporates (see Fig. 7) and is transferred towards the ambient air (Fig. 6, broken line for x = 0). At x = 0, since the amount of moisture transferred away from the surface is larger than that reaching it, the moisture content decreases (Fig. 8). The asymptotic values reached by these variables as $t \rightarrow \infty$ are:

	$x = 0$	$x = 20$ cm
M_l / M_0 (%)	1.06	4.00
$\dot{m}$ (kg/m^{3}s)	-0.21×10^{-4}	0.21×10^{4}
J_l (kg/m^{2}s)	-0.53×10^{-6}	0.53×10^{6}

The mass flux is directed from the high to the low humidity side. Vapor is condensing at x = 20 cm and liquid is evaporating at x = 0.

Fig. 9 shows the temperature evolution at the surfaces and within the slab. Once again, although the ambient temperatures remain constant and equal to the initial temperature of the slab, the material experiences considerable cooling. This is due to the evaporation taking place at x = 0 which results in a rapid decrease of the local temperature. The interior of the slab is then cooled down by conduction. For the surface at x = 20 cm, where according to Fig. 7 vapor is condensing at a very small rate, the temperature initially increases very slightly. However the conduction heat flux from x = 20 towards x = 0 is much more important and thus even the temperature at x = 20 eventually decreases. The temperature distributions shown in Fig. 9 indicate that the material acts as a heat sink all the time at x = 0 and most of the time at x = 20. The corresponding heat fluxes can not be predicted by addressing the thermal problem alone which predicts a uniform, constant temperature in the slab (20°C).

What is quite interesting in this unsymmetrical case is that even when equilibrium conditions are achieved, these heat fluxes do not become zero. A small heat flux is directed towards the surface at x = 0 from both the low humidity air and the interior of the slab. It serves to evaporate liquid at the rate of 0.21 X 10^{-4} kg/m^3s. Similarly a small heat flux is directed away from the surface at x = 20 cm towards the low humidity air and the interior of the slab.

CONCLUSIONS

The proposed model for one-dimensional heat and moisture transfer in porous building materials gives good agreement with measured temperature and moisture content profiles. However the results are quite sensitive to the values of the convective heat and mass transfer coefficients which are generally not accurately known. Results obtained with the model show the effect of decreasing ambient humidity on the thermal response of the slab. For constant and variable ambient temperatures and for symmetrical and unsymmetrical ambient conditions, the results show that a reduction in ambient relative humidity is followed by a decrease in slab temperature and corresponding heat fluxes which can not be predicted when mass transfer is ignored.

ACKNOWLEDGEMENTS

This study has been carried out with the financial assistance of NSERC and FCAR.

REFERENCES

Andersson, A.C., 1985: Verification of calculation methods for moisture transport in porous building materials. Swedish Council for Building Research, D6 1985, 223 p.

DeVries, D.A., 1958: Simultaneous transfer of heat and moisture in porous media. Trans. Am. Geo. Union, V. 39, no. 5 pp. 909-916.

Hedlin, C.P. 1988: Heat flow through a roof insulation having moisture contents between 0 and 1% by volume, in summer. ASHRAE Transactions, V. 94, pt. 2, pp. 1579-1593.

Luikov, A.V., 1966: Heat and mass transfer in capillary porous bodies. Pergamon Press.

Mitalas, G.P. and Kumaran, M.K., 1987. Simultaneous heat and moisture transport through glass fibre insulation: an investigation of the effect of hygroscopicity. ASME Winter annual meeting, Boston MA.

Perrin, B., 1985: Etude des transfers couplés de chaleur et de masse dans des matériaux poreux consolidés non saturés utilisés en génie civil. These d'Etat , Univ. Paul Sabatier, Toulouse, France.

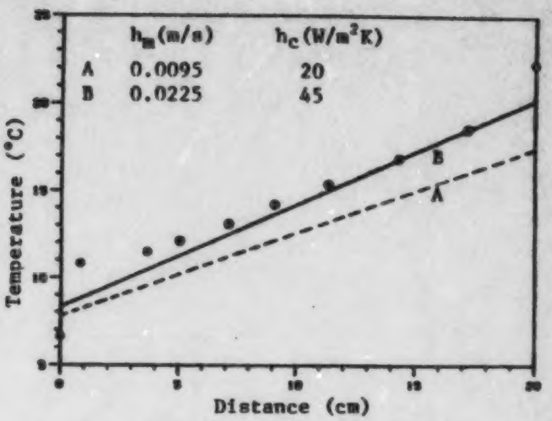

Fig. 1: Measured and calculated temperatures for mortar slab.

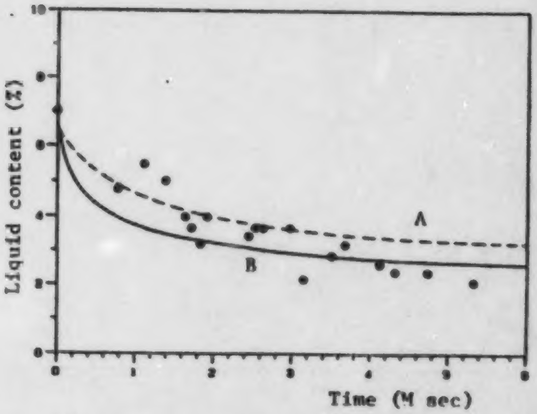

Fig. 2: Measured and calculated liquid content in mortar slabs.

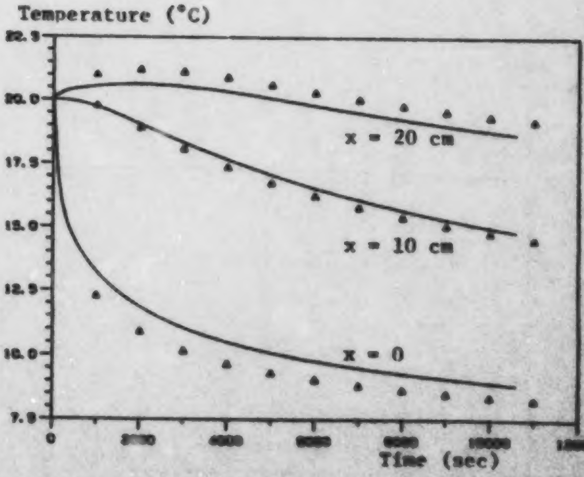

Fig. 3: Evolution of temperature in mortar slab with (-) and without (Λ) mass transfer.

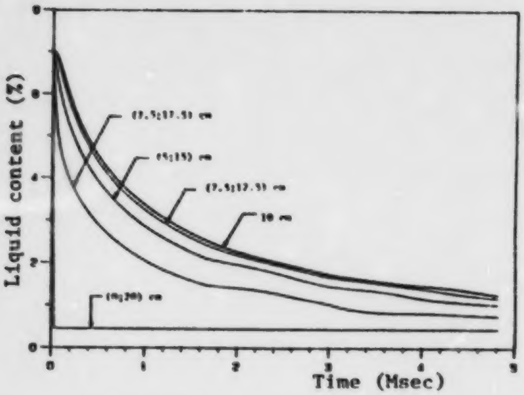

Fig. 4: Evolution of liquid content for brick slab.

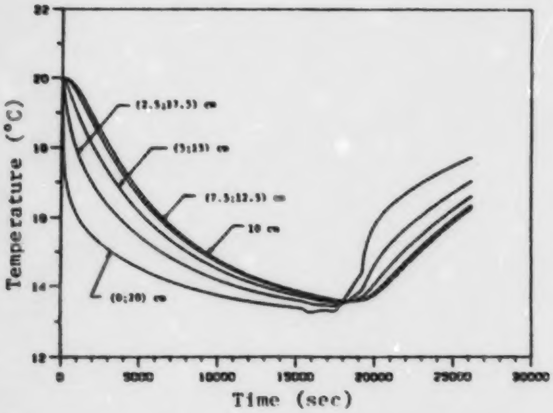

Fig. 5: Evolution of temperature for brick slab.

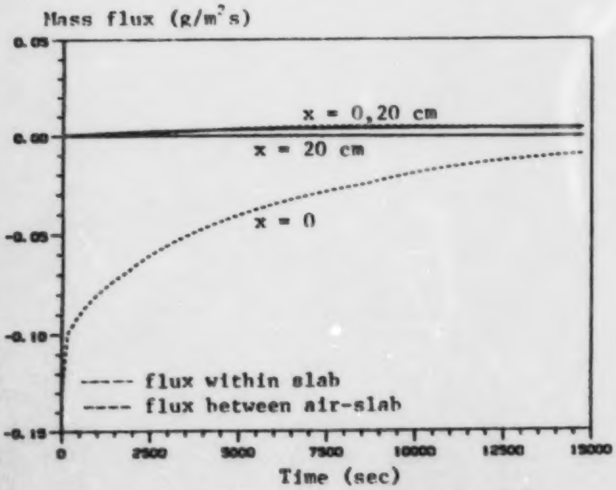

Fig. 6: Mass fluxes for the mortar slab (positive value for flux towards surface)

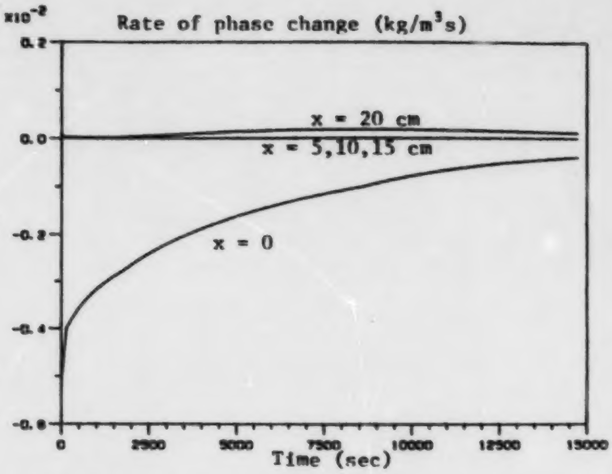

Fig. 7: Rate of phase changes for mortar slab (positive values indicate condensation).

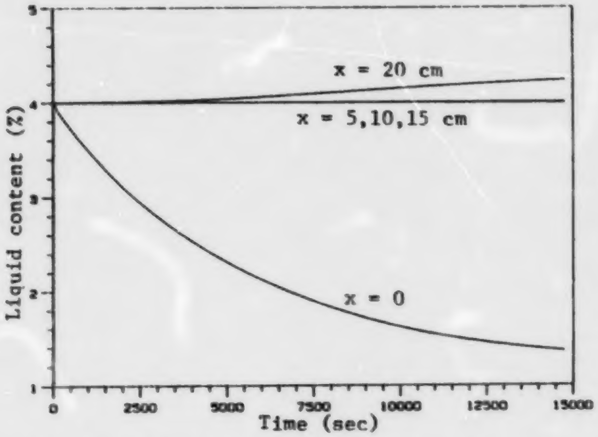

Fig. 8: Evolution of liquid content for mortar slab.

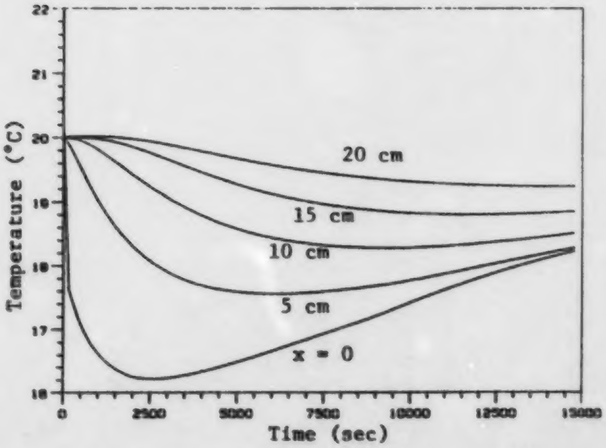

Fig. 9: Evolution of temperature for mortar slab.

CONVECTIVE HEAT TRANSFER FOR SIMULTANEOUSLY DEVELOPING FLOW IN DUCTS OF RECTANGULAR AND EQUILATERAL TRIANGULAR CROSS-SECTION

G. Yang and M.A. Ebadian

Department of Mechanical Engineering
Florida International University
The State University of Florida at Miami
Miami, FL 33199, USA

ABSTRACT

A numerical scheme is introduced in this paper to obtain the mean bulk temperature and mean Nusselt number for laminar flow in ducts of rectangular and equilateral triangular cross-section. The flow in these geometries is considered to be both, simultaneously developing velocity and temperature. The developing velocity and temperature field in these geometries are obtained analytically/numerically from the solution of the Navier-Stokes and energy equation respectfully employing the method of lines (MOL). These equations are reformulated by a system of first-order differential equations controlling the velocity and temperature along each line. The results based on sixteen lines or less are computed numerically using a Runge-Kutta subroutine. They are presented in terms of the axial distribution of bulk temperature and total Nusselt numbers for rectangular and equilateral triangular ducts. Furthermore, the computed results are compared against some analytical/numerical findings reported in the literature. In all cases, a satisfactory comparison is obtained.

NOMENCLATURE

A	Cross-sectional area [m^2]
a	Characteristic length [m]
C_p	Specific heat [$J\ kg^{-1}\ K^{-1}$]
D_h	Hydraulic diameter of duct [m]
f	Friction factor
k	Thermal conductivity of fluid [$W\ m^{-1}\ K^{-1}$]
L	Length of duct [m]
$\dot{m}$	Mass flow rate of fluid [$kg\ s^{-1}$]
$Nu_{m,T}$	Mean Nusselt number, eq. (16)
$Nu_{x,T}$	Local Nusselt number, eq. (15)
P	Perimeter [m]
p	Pressure [$kN\ m^{-2}$]
Pe	Peclet number, Re Pr
Pr	Prandtl number, ν/α
Q_T	Total heat transfer [W], eq. (13)
Q_{∞}	Ideal heat transfer [W], eq. (14)
Re	Reynolds number, $(\bar{u}D_h)/\nu$
T	Temperature [K]
T_b	Bulk temperature [K]
T_e	Entrance temperature [K]
T_w	Circumferential duct wall temperature [K]
u, U	Dimensional and dimensionless velocity of fluid, $U = u/\bar{u}$
$\bar{u}$, $\bar{U}$	Dimensional and dimensionless mean velocity of fluid
w	Generalized dependent variable
X	Dimensionless axial coordinate, $X = (D_h^2/a^2)\,x^*$
x, x^*	Dimensional and dimensionless axial coordinate, $x^* = x/(D_h Pe)$
y, Y	Dimensional and dimensionless transversal coordinates, $Y = y/a$
z, Z	Dimensional and dimensionless transversal coordinates, $Z = z/a$

Greek Symbols

α	Thermal diffusivity of fluid [$m^{-2}\ s^{-1}$]
α^*	Aspect ratio
ν	Kinematic viscosity of fluid [$m^2\ s^{-1}$]
μ	Dynamic viscosity of fluid [$kg\ m^{-1}\ s^{-1}$]
ρ	Density of fluid [$kg\ m^{-3}$]
θ	Dimensionless temperature
Ω	Heat transfer efficiency, eq. (14)
η	Generalized independent variable
w	Generalized dependent variable

INTRODUCTION

This paper is concerned with convective heat transfer in ducts of arbitrary cross-section with simultaneously developing temperature and velocity profile, subjected to constant wall temperature. Laminar flow heat transfer in ducts of various cross-sections has been catalogued by Kakac et al.[1] and Shah and London [2], for different types of boundary conditions. These references along with Eckert et al.[3-5], Soloukhin and Martynenko [6], and Martynenko [7], indicate that significant attention has been devoted in recent years to the investigation of simultaneous development of velocity and temperature in ducts with non-circular cross-sectional areas. In general, the geometries encountered in heat exchange equipment are complex in nature and consequently, computational predictions of the velocity and temperature fields need to be considered as three-dimensional.

Primarily, these investigations along with Chandrupatta et al. [8], Cook and Rahman [9], Haji-Sheikh et al. [10], Lakshminarayanan and Haji-Sheikh [11], Lyczkowski et al. [12], Marco and Han [13], are restricted to conditions of fully developed velocity profile. In addition, Nomura and Haji-Sheikh [14] have presented the solution to a fully developed velocity and temperature distribution for two different duct cross-sections, using symbolic algebra software (MACSYMA). The solution presented by Rajagopal and Sadegh [15] deals with a boundary integral solution to a fully developed velocity and temperature profile in elliptical and rectangular cross-section ducts. Therefore, a technical comparison cannot be obtained for either paper since the present paper deals with the simultaneously developing velocity and temperature fields.

The problem examined in this paper is concerned with the analysis of forced convective heat transfer in the entrance region of isothermal ducts having various cross-sectional areas. Therefore, the corresponding developing temperature in these non-circular ducts is determined by solving the three-dimensional energy equation via the method of lines (MOL), [cf. Liskovets, 16]. According to this method, the transversal derivatives in the three-dimensional energy equation are replaced by finite difference formulations while the axial derivative remains continuous. Correspondingly, the region of integration is divided into a collection of lines parallel to the axial coordinate of the duct. On the other hand, it is widely known that the retention of equal transversal intervals in the presence of irregular boundaries constitutes a complicating feature requiring special equations for nodes in its neighborhood. To prevent this complication and difficulty, the two-dimensional grid in the duct cross-section is constructed in such a manner that the dividing lines coincide with the irregular boundaries resulting in equal or unequal transversal intervals depending on the geometry under study. From a conceptual point of view, the partial differential energy equation is being replaced by a system of ordinary differential equations of first-order where the independent variable is the axial coordinate. The resulting linear system, accounting for extremely coarse grids in conjunction with the appropriate boundary conditions, constitutes an initial value problem. Accordingly, the temperature field provided by its solution may be readily obtained using either an eigenvalue subroutine or numerically, using a Runge-Kutta subroutine.

In this paper, the hybrid methodology (MOL), has been applied and tested for laminar flow in ducts of rectangular and equilateral triangular cross-sections. The analytical solutions of the resulting system of equations, via the eigenvalue approach, or the numerical solution, via the Runge-Kutta algorithm, have been presented in terms of the distributions of the mean bulk temperature and local Nusselt number in the region of thermal development of the duct. In addition, the same set of results is compared against some experimental and numerical findings reported in the literature. In all cases, satisfactory comparison is achieved.

BASIC EQUATIONS

In this paper, consideration is given to simultaneously developing velocity and temperature laminar flow in ducts of arbitrary cross-section. Based on a Cartesian coordinate system, the equations of conservation describing the steady simultaneous development of velocity and temperature through a non-circular duct are:

$$\operatorname{div} \vec{V} = 0 \tag{1}$$

$$\rho \frac{\partial \vec{V}}{\partial t} = - \nabla P + \mu \nabla^2 \vec{V} \tag{2}$$

$$\rho C_v \frac{\partial T}{\partial t} = k \nabla^2 T \tag{3}$$

where $\nabla^2 \vec{V}$ designates the velocity profile determined from the solution of eq. (2). Also, ρ is the density, C_v is the specific heat , k is the thermal conductivity and T is the temperature sought. The boundary conditions imposed on eq. (3) are: 1) Uniform entrance temperature, T_e, and 2) Isothermal wall temperature, T_w, with reference to Figs. 1 and 2, and upon introduction of the dimensionless variables

$$U = \frac{u}{u_m} \qquad \phi = \frac{T - T_w}{T_e - T_w}$$
$$Y = \frac{y}{b} \qquad Z = \frac{z}{b} \qquad X = \frac{x}{D_h \, Re \, Pr} \tag{4}$$

into energy eq. (3) can be rewritten as:

$$\frac{\partial \phi}{\partial x} = \frac{1}{U}\left[\frac{\partial^2 \phi}{\partial y^2} + \frac{\partial^2 \phi}{\partial z^2} \right] \tag{5}$$

The boundary conditions imposed on eq. (5) are expressed as

$$\phi = 1, \qquad x = 0$$
$$\phi = 0, \qquad \text{at all surfaces} \tag{6}$$

PARAMETERS OF INTEREST

The physical quantities of interest for practical applications of internal forced convection exposed to isothermal wall conditions are the dimensionless bulk temperature, $\phi_b(x)$

$$\phi_b = \frac{\int_A U \phi \, dA}{\int_A U \, dA} \, . \tag{7}$$

from here, the total heat transfer, Q_T, in a certain duct length L, may be easily calculated via an overall energy balance, wherein

$$Q_T = \dot{m} \, C_p \, [T_e - T_b(L)] \tag{8}$$

This expression may be rewritten in terms of an associated heat transfer efficiency, Ω, such that

$$\Omega = \frac{Q_T}{Q_{oo}} = 1 - \phi_b(L) \tag{9}$$

where Q_{oo} designates an ideal heat transfer for an infinitely long duct of similar characteristics.

Alternatively, the total heat transfer, Q_T, may also be computed from the mean Nusselt number

$$Nu_{m,T} = - \frac{1}{4X} \left[\frac{D_h^2}{a^2} \right] \ln \phi_b \tag{10}$$

At this stage, it should be emphasized that in this paper calculation of the Nusselt number has been performed with the sole purpose of comparing our results against other fully numerical solutions published in the literature.

NUMERICAL TECHNIQUE

In this paper, the transverse velocity components are considered to be zero and also, neglecting the effects of axial diffusion in eqs. (1), (2), and (5), the coupled problem may be reformulated by a system consisting of two parabolic equations. This will be achieved by the method of lines (MOL). This method [cf. Liskovets [16]), which takes advantage of a combination of differential and difference procedure. In general, the method (MOL) replaces a PDE of parabolic type in three independent variables by a system of first-order differential equations. Thus, the integration domain may be divided into the strips parallel to the axial coordinate. In this respect, the second-order derivatives for U and T at each strip are substituted by their finite difference formulations.

Correspondingly, upon specifying the sizes of Δy and Δz in the two-dimensional grid of Figs. 1 and 2, this mathematical approach generates a system of first-order linear ordinary differential equations for U_{IJ} and T_{IJ}. This may be solved either a) analytically, employing the eigenvalue subroutine [17], or b) numerically, utilizing a Runge-Kutta algorithm.

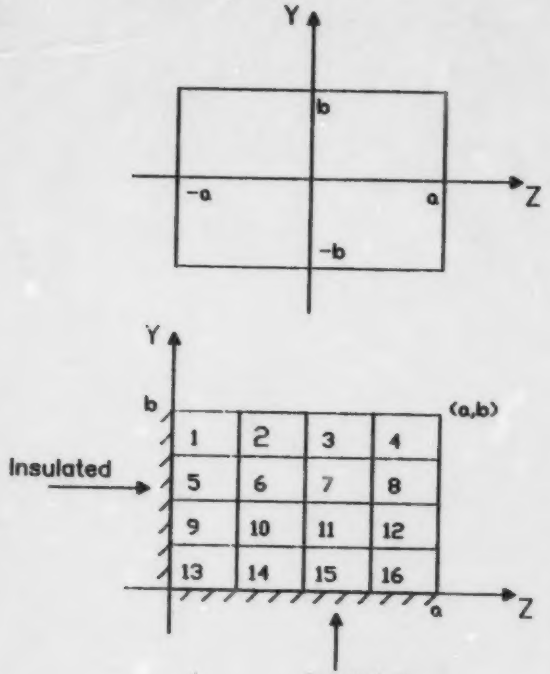

Figure 1: Coordinate System and Coarse Grid for Rectangular Duct.

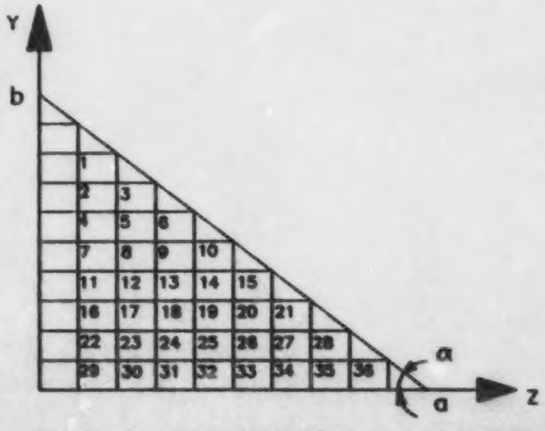

Figure 2: Coordinate System and Coarse Grid for Equilateral Triangular Duct.

RESULTS AND DISCUSSION

The mean bulk temperature distribution, ϕ_b, eq. (7) and the mean Nusselt number, eq. (10), have been calculated numerically in the development region of rectangular and equilateral triangular ducts, using the method of line (MOL). These are shown graphically in Figs. 3 and 4. The numerical solution for laminar thermal entrance region for the above specified ducts, has been carried out and the results are presented in Table 1. Comparison of tabulated values for the total Nusselt number indicates an excellent agreement with the published results given in the literature [18]. This agreement further supports the validity of the proposed methodology. Calculations of the velocity distribution and the temperature distribution for rectangular and equilateral triangular ducts are based on 16 and 36 lines, respectively. The following section is devoted to the discussion of each geometry.

Rectangular Duct

For this configuration, the calculations are performed in 1/4 of the duct cross-section utilizing equal intervals ($\Delta Y = 0.25$, $\Delta Z = 0.25$ for square duct, $\Delta Y = 0.25$, $\Delta Z = 0.5$ when $\alpha^* = 0.5$, and $\Delta Y = 0.25$, $\Delta Z = 0.1$ when $\alpha^* = 0.25$). The aspect ratios of $\alpha^* = 0.25$, 0.5, and 1.0 are chosen for the calculations related to this geometry. In all cases, a system having sixteen lines is used. From here, the numerical distributions of the mean bulk temperature and the mean Nusselt number are numerically calculated and graphically presented in Figs. 3 and 4.

Figure 3 represents the variation of the mean bulk temperature against the entrance region of the duct. The inspection of the curves for rectangular ducts in this figure indicates that the entrance region bulk temperature is unaffected by the aspect ratio. However, this deviation increases as the flow progresses toward the end of the channel.

Figure 4 represents the mean Nusselt number with the axial position for rectangular ducts. Inspection of the curves in this figure indicates that the Nusselt number increases with decreasing aspect ratio. Furthermore, comparison of these results with the one given by Wibulswas [18] indicates an excellent agreement. As it can also be observed from Table that the predicted values (via MOL) tend to slightly overestimate the Nusselt number in the region of thermal development. In terms of numbers, the errors are 0.7%, 1.03%, and 3.6% at $1/x = 200$ for $\alpha^* = 1.0$, 0.5, and .025, respectively.

Equilateral Triangular Duct

For this configuration, the calculations are performed on the entire equilateral triangular duct with thirty-six lines. Figures 3 and 4 also represent the mean bulk temperature and mean Nusselt number as a function of the entrance region, respectively. Figure 3 represents the mean bulk temperature, ϕ_b, as a function of the axial position, x. Inspection of the curve in this figure indicates a very small deviation at the entrance of the pipe compare with the square duct ($\alpha^* = 1$). However, this deviation vanishes rapidly as the flow moves in the duct. Figure 9 represents the mean Nusselt number versus the axial position for an equi-

Table 1. Comparison of the Total Nusselt Number for Laminar Forced Convection (N = 0)

		Square Duct		Rectangular Duct ($\alpha^* = 0.5$)		Rectangular Duct ($\alpha^* = 0.25$)		Equilateral Triangular Duct	
$\frac{1}{X^*}$	X^*	Wibulswas	Present Study	Wibulswas	Present Study	Wibulswas	Present Study	Wibulswas	Present Study
10	0.1	3.75	3.63	4.20	4.13	5.11	5.09	3.52	3.74
20	0.05	4.39	4.22	4.79	4.71	5.56	5.50	4.27	4.29
30	0.0333	4.88	4.75	5.23	4.71	5.93	5.85	4.88	4.80
40	0.025	5.27	5.21	5.61	5.60	6.27	6.17	5.35	5.25
50	0.02	5.63	5.61	5.95	5.98	6.61	6.48	5.73	5.61
60	0.01675	5.95	5.96	6.27	6.31	6.90	6.78	6.08	5.97
80	0.01275	6.57	6.58	6.89	6.89	7.47	7.32	6.68	6.54
100	0.01	7.10	7.19	7.42	7.47	7.98	7.91	7.21	7.09J
120	0.00875	7.61	7.67	7.91	7.82	8.48	8.36	7.68	7.41
140	0.00725	8.06	8.15	8.37	8.35	8.93	9.03	8.09	7.88
160	0.00625	8.50	8.29	8.80	8.86	9.36	9.61	8.50	8.29
180	0.00575	8.91	8.90	9.20	9.17	9.77	9.96	8.88	8.54
200	0.005	9.70	9.77	9.60	9.70	10.18	10.57	9.21	8.98

lateral triangular duct. The comparison of these results with [18] indicates an excellent agreement. However, at the entrance, as it can be seen from Table 1 and also Fig. 4, the predicted values (via MOL) tend to slightly underestimate the Nusselt number in the region of thermal development. In terms of numbers, the error associated with ref. [18] is -2.4%.

CONCLUDING REMARKS

In this paper, the effect of convective heat transfer in simultaneous development of velocity and temperature of fluid flow in the ducts of rectangular and equilateral triangular cross-section is analyzed. An explicit finite-difference procedure for laminar flow which takes advantage of the method of lines (MOL) was developed. The numerical scheme was found to be simple, accurate, and efficient. It is ideally suited for this type of problem. Furthermore, comparison of the mean Nusselt number with standard finite-difference solutions are satisfactory for the geometries tested.

ACKNOWLEDGMENT

The results presented in this paper were obtained in the course of research sponsored by the Department of Energy under Subcontract No. 19X-SE133V

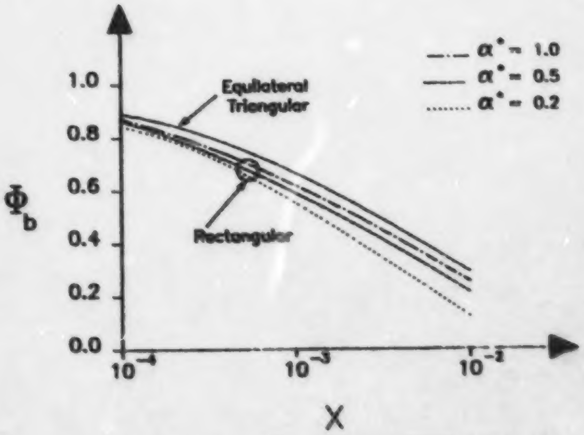

Figure 3: Distribution of Mean Bulk Temperature for Rectangular and Equilateral Triangular Duct.

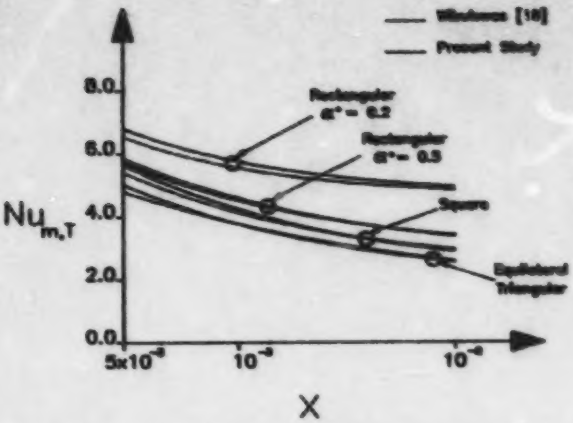

Figure 4: Distribution of Mean Nusselt Number for Rectangular and Equilateral Triangular Duct.

REFERENCES

1. Kakac, S., Shah, R.K. & Aung, W., Handbook of Single-Phase Convective Heat Transfer, Wiley Interscience, New York, 1987.

2. Shah, R.K. & London, A.L., Laminar Flow Forced Convection in Ducts, Academic Press, New York, 1978.

3. Eckert, E.R.G., Goldstein, R.G., Pfender, E., Ibele, W.E., Patanker, W.E., Ramsey, S.W., Simon, T.W., Decker, N.A., Kuehn, T.H., Lee, H.O. & Girshick, S.L., Heat Transfer - A Review of the 1985 Literature, Int. J. Heat Mass Transfer, Vol. 29, pp. 1767-1842, 1986.

4. Eckert, E.R.G., Goldstein, R.G., Pfender, E., Ibele, W.E., Patanker, W.E., Ramsey, S.W., Simon, T.W., Decker, N.A., Kuehn, T.H., Lee, H.O. & Girshick, S.L., Heat Transfer - A Review of the 1986 Literature, Int. J. Heat Mass Transfer, Vol. 30, pp. 2449-2523, 1987.

5. Eckert, E.R.G., Goldstein, R.G., Pfender, E., Ibele, W.E., Patanker, W.E., Ramsey, S.W., Simon, T.W., Decker, N.A., Kuehn, T.H., Lee, H.O. & Girshick, S.L., Heat Transfer - A Review of the 1987 Literature, Int. J. Heat Mass Transfer, Vol. 31, pp. 2401-2488, 1988.

6. Soloukhin, R.I. & Martynenko, O.G., Heat and Mass Transfer Bibliography - Soviet Literature, Int. J. Heat Mass Transfer, Vol. 26, pp. 1771-1781, 1983.

7. Martynenko, O.G., Heat and Mass Transfer Bibliography - Soviet Literature, Int. J. Heat Mass Transfer, Vol. 31, pp. 2489-2503, 1988.

8. Chandrupatta, A.R. & Sastri, V.M.K., Laminar Forced Convection Heat Transfer of a Non-Newtonian Fluid in Square Duct, Int. J. Heat and Mass Transfer, Vol. 20, pp. 1315-1324, 1977.

9. Cook, A.E. & Rahman, M., Temperature and Velocity Distribution in a Square Duct, Applied Math Modeling, Vol. 10, pp. 221-223, 1986.

10. Haji-Sheikh, A., Mashena, M. & Haji-Sheikh, M.J., Heat Transfer Coefficient in Duct with Constant Wall Temperature, Transaction of the ASME, J. of Heat Transfer, Vol. 105, pp. 878-883, 1983.

11. Laksminarayanan, R. & Haji-Sheikh, A., A Generalized Closed-Form Solution to Laminar Thermal Entrance Problems, The Eighth Int. Heat Transfer Conf., Vol. 3, pp. 871-876, 1986.

12. Lyczkowski, R.W., Solbrig, C.W. & Gidaspow, D., Forced Convection Heat Transfer in Rectangular Ducts-General Case of Wall Resistance and Peripheral Conduction, Int. Gas Technol., Chicago, Illinois, 1969.

13. Marco, S.M. & Han, L.S., A Note on Limiting Laminar Nusselt Numbers in Ducts with Constant Temperature Gradient by Analogy to Thin-Plate Theory, Trans. ASME, pp. 625-630, 1977.

14. Nomura, S. & Haji-Sheikh, A., Flow and Heat Transfer in Arbitrary-Shaped Ducts Using Symbolic Algebra, ASME/WAM HTD, Vol. 105, pp. 75-80, 1988.

15. Rajagopal, K.R. & Sadegh A.M., A Boundary Integral Equation Method for the Study of Some Laminar Forced Convection Problems, Numerical Heat Transfer, Vol. 8, pp. 485-496, 1985.

16. Liskovets, D.A., The Method of Lines (Review), Differential Equation, Vol. 1, pp. 1308-1323, 1965.

17. IMSL Library Reference Manual, IMSL Inc., Houston, Texas, 1982.

18. Wibulswas, P., Laminar Flow Heat Transfer in Non-Circular Ducts, Ph.D. thesis, London University, London, UK, 1966.

INFLUENCE OF SLAB THICKNESS ON RESPONSES OF CONCRETE WALLS UNDER FIRE

Gamal N. Ahmed and C. L. D. Huang

Dept. of Mechanical Engineering, Kansas State University
Manhattan, KS 66506

ABSTRACT

Predicting the response of concrete structures exposed to high temperatures in a short duration is of great concern in safety assessments of high temperature nuclear reactors and of tall buildings. For the purpose of fire safety, one-dimensional concrete walls with different thicknesses exposed, on both sides, to the fire course described by ASTM E119 and the following decay stage specified in ISO 834 standard have been considered. A mathematical model, simulating the coupled heat and mass transfer in concrete walls under time-dependent boundary conditions has been developed by the authors and numerically solved. The numerical results predict the pore pressure and temperature histories for different concrete wall thicknesses at various depth thickness ratios. As the results show for the thinner walls under fire, because of the rapid increases of pore pressure and temperature, the slabs are more vlunerable to the damages in ruptures than the thicker ones.

NOMENCLATURE

C_p	effective heat capacity, cm^2/sec^2 ·K
C_{pi}	specific heat of i-component at constant pressure, cm^2/sec^2 ·K
D'	diffusivity of gaseous mixture, cm^2/sec
e	effective emissivity
h_c	convective heat transfer coefficient, g/sec^3 ·K
h_D	mass transfer coefficient, $mole/cm^2$ sec
h_{es}	heat transfer coefficient of the side exposed to high temperatures, g/sec^3 ·K
h_{us}	heat transfer coefficient of the side exposed to atmospheric environment, g/sec^3 ·K
k	effective thermal conductivity of the porous medium, g cm/sec^3 ·K
k_g	thermal conductivity of the gaseous mixture, g cm/sec^3 ·K
K_D	Darcy's coefficient or coefficient of permeability, cm^3 sec/g
K_g	permeability of gaseous mixture, cm^2
m	volumetric moisture content per unit volume of the porous system, cm^3/cm^3
M	molecular weight of the gaseous mixture, g/mol
M_i	molecular weight of i-component of the gaseous mixture, g/mol
P	total pressure or pore pressure, $g/cm\ sec^2$
Q	latent heat of evaporation of free water, cm^2/sec^2
R	universal gas constant, gcm^2/sec^2mol K
t	time, sec
T	absolute temperature, ·K
V_g	bulk velocity of the gaseous mixture, cm/sec
x	space-coordinate

Greek

Γ	mass rate of evaporation per unit volume of the porous system, g/cm^3 sec
ϵ	porosity of the porous system
ϵ_g	volume fraction of the gaseous mixture, cm^3/cm^3
ρ	effective density of the porous system, g/cm^3
ρ_i	density of i-component, g/cm^3
σ	Stefan-Boltzman constant, g/sec^3 ·K^4
ϕ	mole fraction of water vapor of the gaseous mixture, mol/mol

Subscripts

atm	atmosphere
es	at the exposed surfaces to fire
f	fire
g	of gaseous mixture
i	i-component of the porous system
l	of liquid
o	initial condition
s	at the surface
us	at the unexposed surfaces to fire
v	of vapor in a gaseous mixture
w	of water
∞	ambient

INTRODUCTION

In recent analysis on high temperature drying of concrete and safety assessment of nuclear reactors or the behavior of materials subject of fires [1,2], mositure was modeled on the basis of the evaporation-condensation mechanism with pore pressure and concentration gradient terms.

Finite element models have been developed to study the coupled heat and mass transfer in concrete at high temperatures [3,4]. A condensed survey of the present state of knowledge in the field of high temperature properties of concrete, is reported [5-7]. The main features of concrete at high temperatures are summarized and discussed in these publications.

Modeling of concrete walls exposed to high temperatures, such as in fires, has met with many difficulties: First, strong coupling of pore pressure, temperature, and moisture content. Second, highly nonlinear dependence of various parameters of porous media, such as permeability, conductivity, etc. on the pressure, temperature, and moisture content. Finally, multi-phase mass transfer involved in concrete. To evaluate all aspects of the problem, the model needs to consider three distinct components: a correct description of fire exposure, the heat transfer from the fire to the concrete structures; and last, heat and mass transfer in the structure itself. The solution is definitely complicated by the many variables affecting the aforementioned components. With advances being made in all areas of design, a more realistic prediction of the concrete response to fire exposure can be made. A computational model now makes this approach practical.

In this contribution, a mathematical model describing the coupled heat and mass transfer in concrete under fire has been developed. A computational model employing fully implicit finite difference scheme along with quasi-linearization for the nonlinear coupled governing equations and boundary conditions has been constructed. Finally, an efficient solution algorithm using variable time steps has been used to yield a realistic prediction of concrete response under fire. Using this model, the attention is paid to the problem of one-dimensional concrete walls with different thicknesses exposed, on both sides, to the fire course, described by ASTM E119 and the following decay stage specified in ISO 834 standard. The numerical solutions obtained by this model predict the pore pressure and temperature histories for different concrete slab thicknesses at various depth-thickness ratios. In addition, the effect of concrete wall thickness on both pore pressure buildup and temperature has been demonstrated and analyzed.

GOVERNING EQUATIONS

Concerning the porous system and the transport porcess, the following assumptions can be introduced: multi-phase porous system is taken as a continuous medium, local thermodynamic equilibrium exists, a rigid solid matrix and incompressible liquid are assumed, mobility of liquid is assumed to be negligible as compared to that of gases; water vapor, air, and their mixture are ideal gases; and energy transferred by diffusion compared to that one by conduction is negligible. Given such assumptions and based on principles of irreversible thermodynamics, and conservation of mass, momenta, and energy equations, a set of three basic equations describing one-dimensional heat and mass transfer in a concrete slab is obtained as follows:

(a) Conservation of mass for water vapor,

$$\rho_v \epsilon_g \frac{\partial \phi}{\partial t} - (1-\phi)\Gamma =$$

$$-\rho_v \epsilon_g V_g \frac{\partial \phi}{\partial x} + \frac{\rho_g}{\rho_a} \frac{\partial}{\partial x} (\rho_g \epsilon_g D \frac{\partial \phi}{\partial x}) \quad (1)$$

(b) Conservation of mass for gaseous mixture,

$$\frac{\partial}{\partial t} (\rho_g \epsilon_g) + \frac{\partial}{\partial x} (\rho_g \epsilon_g V_g) = \Gamma \quad (2)$$

(c) Conservation of energy.

$$\rho C_p \frac{\partial T}{\partial t} + \rho_w Q \frac{\partial \epsilon_g}{\partial t} =$$

$$\frac{\partial}{\partial x} (k \frac{\partial T}{\partial x}) - \rho_g \epsilon_g C_{p_g} V_g \frac{\partial T}{\partial x} \quad (3)$$

The moisture content, m, is related to the pore pressure of gaseous mixture, P, temperature T, and mole fraction of water vapor in the gaseous mixture, ϕ, through a state equation, $m = m\ (P,T,\phi)$. This constitutive relation is given as a set of sorption isotherms for various temperatures of concrete through experimental techniques [3]. With the definition of the volume fraction of gaseous mixture, $\epsilon_g = \epsilon - m\ (P,\ T,\ \phi)$, a set of three coupled nonlinear second-order partial differential equations is given in the following form:

$$A_k \frac{\partial \phi}{\partial t} + B_k \frac{\partial P}{\partial t} + C_k \frac{\partial T}{\partial t} =$$

$$D_k \frac{\partial^2 \phi}{\partial x^2} + E_k \frac{\partial^2 P}{\partial x^2} + F_k \frac{\partial^2 T}{\partial x^2} + G_k \left(\frac{\partial \phi}{\partial x}\right)^2$$

$$+ H_k \left(\frac{\partial P}{\partial x}\right)^2 + I_k \left(\frac{\partial T}{\partial x}\right)^2 + J_k \left(\frac{\partial k}{\partial x}\right)$$

$$+ K_k \left(\frac{\partial \phi}{\partial x} \frac{\partial T}{\partial x}\right) + L_k \left(\frac{\partial P}{\partial x} \frac{\partial T}{\partial x}\right) \quad (4)$$

where the coefficients A_k, ..., L_k for k = 1,2,3 are functions of the dependent variables ϕ, P, and T. They are defined as follows:

$$A_1 = 1 - \left[\frac{(1-\phi)\rho_w}{(PM_w/RT)} \frac{1}{\epsilon_g} \frac{\partial \epsilon_g}{\partial \phi}\right]$$

$$B_1 = -\left[\frac{(1-\phi)\rho_w}{(PM_w/RT)} \frac{1}{\epsilon_g} \frac{\partial \epsilon_g}{\partial P}\right]$$

$$C_1 = -\left[\frac{(1-\phi)\rho_w}{(PM_w/RT)} \frac{1}{\epsilon_g} \frac{\partial \epsilon_g}{\partial T}\right]$$

$$D_1 = D'$$

$$E_1 = 0$$

$$F_1 = 0$$

$$G_1 = D'\left[\frac{1}{\epsilon_g} \frac{\partial \epsilon_g}{\partial \phi} - \frac{M_w - M_a}{M}\right]$$

$$H_1 = 0$$

$$I_1 = 0$$

$$J_1 = D'\left[\frac{1}{\epsilon_g} \frac{\partial \epsilon_g}{\partial P} + \frac{1}{P}\right] + K_D$$

$$K_1 = D'\left[\frac{1}{\epsilon_g} \frac{\partial \epsilon_g}{\partial T} - \frac{1}{T}\right]$$

$$L_1 = 0$$

$$A_2 = \left[1 - \frac{\rho_w}{PM/RT}\right]\frac{1}{\epsilon_g} \frac{\partial \epsilon_g}{\partial \phi} + \frac{M_w - M_a}{M}$$

$$B_2 = \left[1 - \frac{\rho_w}{PM/RT}\right]\frac{1}{\epsilon_g} \frac{\partial \epsilon_g}{\partial P} + \frac{1}{P}$$

$$C_2 = \left[1 - \frac{\rho_w}{PM/RT}\right]\frac{1}{\epsilon_g} \frac{\partial \epsilon_g}{\partial T} - \frac{1}{T}$$

$$D_2 = 0$$

$$E_2 = K_D$$

$$F_2 = 0$$

$$G_2 = 0$$

$$H_2 = \frac{\partial K_D}{\partial P} + K_D\left[\frac{1}{\epsilon_g} \frac{\partial \epsilon_g}{\partial P} + \frac{1}{P}\right]$$

$$I_2 = 0$$

$$J_2 = \frac{\partial K_D}{\partial \phi} + K_D\left[\frac{1}{\epsilon_g} \frac{\partial \epsilon_g}{\partial \phi} + \frac{M_w - M_a}{M}\right]$$

$$K_2 = 0$$

$$L_2 = \frac{\partial K_D}{\partial T} + K_D\left[\frac{1}{\epsilon_g} \frac{\partial \epsilon_g}{\partial T} - \frac{1}{T}\right]$$

$$A_3 = \rho_w Q \frac{\partial \epsilon_g}{\partial \phi}$$

$$B_3 = \rho_w Q \frac{\partial \epsilon_g}{\partial P}$$

$$C_3 = \rho_w Q \frac{\partial \epsilon_g}{\partial T} + \rho C_p$$

$$D_3 = 0$$

$$E_3 = 0$$

$$F_3 = k(\epsilon_g)$$

$$G_3 = 0$$

$$H_3 = 0$$

$$I_3 = k' \frac{\partial \epsilon_g}{\partial T}$$

$$J_3 = 0$$

$$K_3 = k' \frac{\partial \epsilon_g}{\partial \phi}$$

$$L_3 = k' \frac{\partial \epsilon_g}{\partial P} + K_D(\rho_g \epsilon_g C_{p_g})$$

$$\rho C_p = (1-\epsilon)\rho_s C_{p_s} + (\epsilon - \epsilon_g)\rho_w C_{p_w} + \rho_g \epsilon_g C_{p_g}$$

$$k' = \frac{dk(\epsilon_g)}{d\epsilon_g}$$

BOUNDARY CONDITIONS

Consider one-dimensional concrete slab of thickness 2L exposed to fire on both sides (x=0, 2L) as shown schematically in Fig. 1. The temperature course of the fire may be divided into two periods: developing period, and decay period. The fire temperature in the developing period

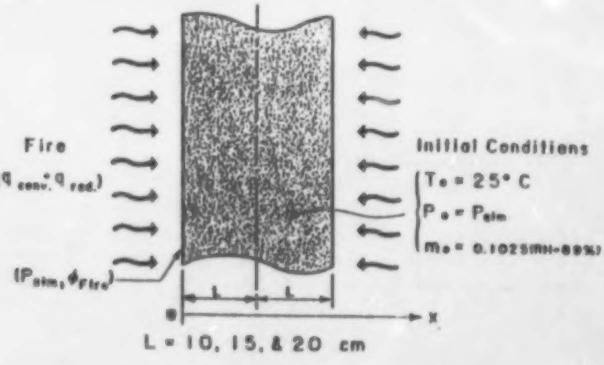

Fig.1 Concrete slab of thickness 2L exposed to fire on both sides

is assumed to follow that of the standard fire described in ASTM E-119 over a fire exposure duration of 3 hours. After the fire exposure, the fire temperature in the following decay period is assumed to decrease linearly to the atmospheric temperature, T_∞, according to the relations specified in ISO 834 standard [7,8]. The standard fire temperature-time curve for both the developing and following decay periods is shown in Fig. 3.

The spatial uniformity of the fire course introduces symmetry at the center of the slab with zero flux conditions, i.e., $\partial\phi/\partial x = \partial P/\partial x = (\partial T/\partial x)_{x=L} = 0$. Thus, the boundary conditions are described as,

$$\text{at } x = 0, \quad \phi = \phi_f = 0 \tag{5}$$

$$P = P_{atm} \tag{6}$$

$$-k\,\frac{\partial T}{\partial x} = h_{es}\,(T_f(t) - T) \tag{7}$$

where

$$h_{es} = h_{c,es} + e\sigma(T_f(t)+T)(T_f^2(t) + T^2)$$

$$\text{at } x = L, \quad \frac{\partial\phi}{\partial x} = 0 \tag{8}$$

$$\frac{\partial P}{\partial x} = 0 \tag{9}$$

$$\frac{\partial T}{\partial x} = 0 \tag{10}$$

Using uniform initial conditions as,

$$\phi(x,0) = \phi_0\ , \quad P(x,0) = P_{atm}\ ,$$

$$T(x,0) = T_\infty\ , \tag{11}$$

equations (4)-(11) form a complete mathematical model simulating the coupled heat and mass transfer in concrete walls under fire.

NUMERICAL MODELING

Equations (4)-(11) can be expressed in a general form in terms of a dependent variable, U_k, $k = 1,2,3$. U_1, U_2, and U_3, representing mole fraction of water vapor, ϕ, pore pressure, P, and temperature, T, are functions of time, t, and space, x. A fully implicit finite difference scheme incorporating quasi-linearization of the nonlinear coefficients, $A_k, \ldots, L_k$, and the mixed derivatives, $(\partial U_k/\partial x)(\partial U_j/\partial x)$ for $k,j = 1,2,3$ is employed and proceeded as,

$$\frac{\partial U_k}{\partial t} \simeq \frac{1}{\Delta t}\left(U_{k,i}^{n+1} - U_{k,i}^{n}\right) \tag{12}$$

$$\left(\frac{\partial U_k}{\partial x}\right)^{n+1} \doteq \frac{1}{2\Delta x}\left(U_{k,i+1}^{n+1} - U_{k,i-1}^{n+1}\right) \tag{13}$$

$$\left(\frac{\partial^2 U_k}{\partial x^2}\right)_i^{n+1} \doteq \frac{1}{(\Delta x)^2}\left(U_{k,i-1}^{n+1} - 2U_{k,i}^{n+1} + U_{k,i+1}^{n+1}\right), \tag{14}$$

$$\begin{aligned}\left(\frac{\partial U_k}{\partial x}\,\frac{\partial U_j}{\partial x}\right)_i^{n+1} &\doteq \left(\frac{\partial U_j}{\partial x}\right)_i^{n}\left(\frac{\partial U_k}{\partial x}\right)_i^{n+1} + \left(\frac{\partial U_k}{\partial x}\right)_i^{n}\left(\frac{\partial U_j}{\partial x}\right)_i^{n+1} - \left(\frac{\partial U_k}{\partial x}\,\frac{\partial U_j}{\partial x}\right)_i^{n}\\ &\doteq \frac{1}{(2\Delta x)^2}\Big[(-U_{j,i-1}^{n} + U_{j,i+1}^{n})(-U_{k,i-1}^{n+1} + U_{k,i+1}^{n+1}) + (-U_{k,i-1}^{n} + U_{k,i+1}^{n})\\ &\quad (-U_{j,i-1}^{n+1} + U_{j,i+1}^{n+1}) - (-U_{k,i-1}^{n} + U_{k,i+1}^{n})(-U_{j,i-1}^{n} + U_{j,i+1}^{n})\Big].\end{aligned}$$

(1[illegible])

The nonlinear coefficients, $A_k, \ldots, L_k$, are quasi-linearized by evaluating all these coefficients at time, t_n. This is known as "lagging" the coefficients. Then using an iterative updating procedure, these coeffieitns can be ultimately evaluated at t_{n+1} as required [9].

Coupling the discrete boundary conditions with the linearized set of implicit finite difference equations results in a three-by-three block-tridiagonal system of equations in the form $\hat{A}\,\hat{U} = \hat{R}$ where $\hat{A}$ is a $3(N-2) \times 3(N-2)$ sparse unsymmetric matrix, $\hat{U}$ and $\hat{R}$ are $3(N-2)$ vectors with N being the number of nodes in x-direction. This system of equations has been solved by MA28, a set of FORTRAN subroutines for the solution of sparse unsymmetric linear equations using a variant of Gaussian elimination. Efficiently using variable time steps, the running time of computation is minimized without detrimental effects on accuracy.

RESULTS AND DICUSSION

The evolution of pore pressure and temperature as functions of time for different concrete slab thicknesses at various depth-thickness ratios, $x/L = 1/20$, $1/4$, and $1/2$, are given in Figures 2 and 3. As can be seen from these figures, the responses of the pore pressure buildup and temperature in concrete slabs to the changes of the fire course, i.e., the change from the developing period to the following decay period, can be clearly identified. Circles are marked at those locations. Figure 2 shows that the pore pressure builds up in concrete slabs with

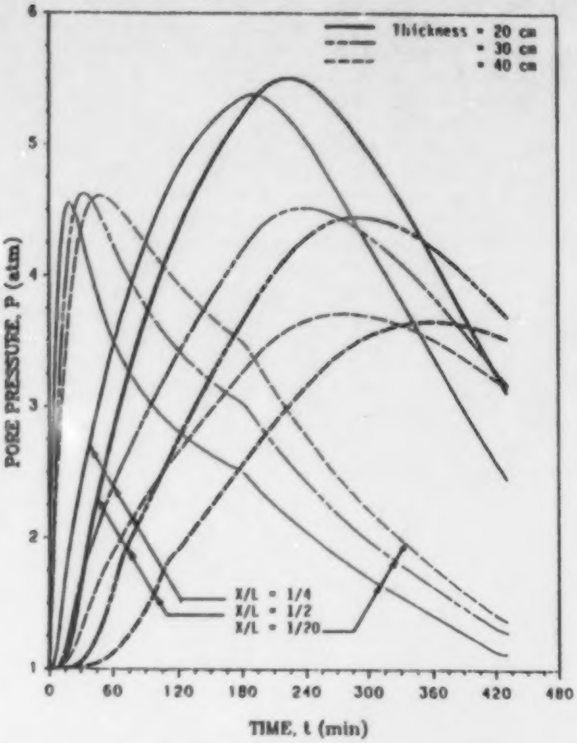

Fig.2 Influence of slab thickness on the pore pressure history

time evolution, across the heated regions. The pore pressure increases and reaches its maximum value as a result of higher heat flux and more accumulation of water vapor. The accumulation of vapor results in lower transport capacity. As the drying front moves towards the cooler regions (concrete slab center sections), the pore pressure tends to dissipate with time evolution during both periods of the fire exposure, i.e., the dry concrete zones are comparatively permeable.

At any depth-thickness ratio, x/L, of concrete slabs, the rate of pore pressure buildup is faster in the thinner concrete slabs than in the thicker ones. This continues until the pore pressure reaches maximum value. Thereafter, the pore pressure dissipates at higher rates in the thinner walls compared to those in thicker walls. In other words, the drying front in the thinner concrete walls is moving faster than in the thicker ones. In response to the whole fire course (developing and decay periods) the thinner the concrete wall, the faster the response of pore pressure buildup to these changes. From this figure, it has been found that the thickness has significant effect on the maximum values of the pore pressure attained in concrete slabs. In this aspect, the maximum pressure values achieved are higher in thinner concrete slabs than those in thicker ones. This is more pronounced in deeper zones of concrete slabs. Also, these results are substantiated by Fig. 4. The contribution of both convective and diffusive mechanisms in driving the moisture towards the fire exposed surface is more pronounced in deeper zones of thick walls. In the early stages of the fire exposure, the variation in the pore pressure is almost negligible in deeper zones of the thick walls. Therefore, the diffusive mechanism, driven by concrentration gradients is more dominant than the convective one. Later, as the pore pressure builds up in deeper zones, the convective mechanism, driven by pore pressure gradients, is more influential.

Fig. 3 exhibits the temperature response of concrete walls of different thicknesses, as a function of time, to the fire exposure. This trend of temperature response to the whole fire course, the developing period and following decay period, for a specific slab thickness at various depths was also seen in another investigation [7].

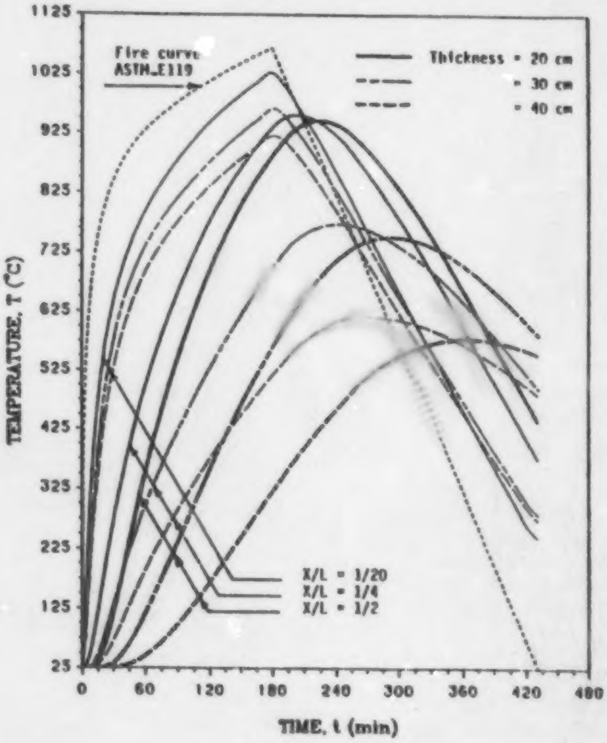

Fig.3 Influence of slab thickness on the temperature history

The rate of temperature change is faster in the vicinity of the exposed surface of concrete walls to fire than in deeper zones. In this aspect, beneath the surface, x/L = 1/20, the temperature reaches its maximum value during the developing period of fire exposure, while

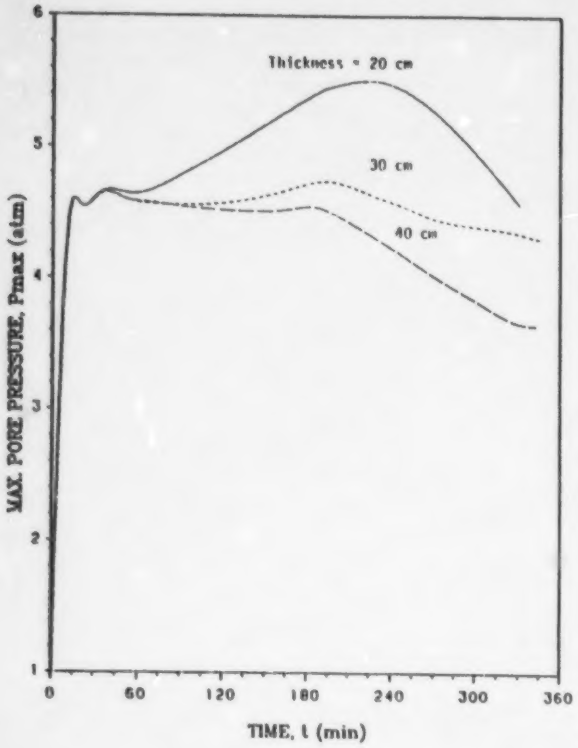

Fig.4 Influence of slab thickness on the maximum pore pressure history

in deeper zones, x/L = 1/4, and 1/2, the maximum values of the temperature attained occur throughout the decay period of the fire exposure. At a specific x/L, the thinner the concrete slab, the faster the rate of temperature rise and higher the maximum value of the temperature achieved. The rate of temperature rise in thinner concrete walls is higher than in thicker ones. This difference in temperature increases as x/L increases, i.e., the effect of concrete thickness on the temperature history is more pronounced in deeper zones. Fig. 4 shows the effect of the concrete wall thickness on the evolutive maximum pressures as a function of time. Again, this figure confirms the aforementioned results regarding the pore pressure buildup.

CONCLUSIONS

The numerical results reveal that the convective gaseous mass flow, driven by the pore pressure gradients, plays an important role in the transport phenomena throughout the developing period of the fire exposure and the following decay period. However, the diffusion mechanism is a more influential factor than the convective one in cooler regions of concrete walls. This contribution of both mechanisms is more pronounced in zones far from the exposed surface of thick walls.

The investigations demonstrate that the wall thickness has significant effects on both histories of the pore pressure buildup and of temperature in concrete walls throughout the whole fire course. This effect of delaying and reducing the pore pressure buildup and temperature rise in thicker concrete walls is more pronounced in deeper zones of these walls. In other words, as the results show for the thinner walls under fire, because of the rapid increases of pore pressure and temperature, the walls are more vulnerable to the damages in ruptures than the thicker ones. Thus, the model is capable of predicting the explosive spalling of concrete under fire.

REFERENCES

1. Sahota, M. S. and Pagni, P. G., Heat and Mass Transfer in Porous Media Subject to Fires, Int. J. Heat Mass Transfer 22, pp. 1069-1081, 1979.

2. Dayan, A. and Gluekler, E. L., Heat and Mass Transfer within an Intensely Heated Concrete Slab, Int. J. Heat Mass Transfer 25, pp. 1461-1467, 1982.

3. Bazant, Z. P. and Thonguthai, W., Pore Pressure in Heated Concrete Walls-Theoretical Prediction, Magazine of Concrete Research, Vol. 31, N107, pp. 67-76, 1979.

4. Dhatt, G., Jacquemier, M., and Kadje, C., Modeling of Drying Refractory Concete, Drying 86, Proc. of the 5th Int. Symp. on Drying, McGill University, pp. 94-104, 1986.

5. Harmathy, T. Z., Properties of Building Materials: Bases for Fire Safety Design, Design of Structures against Fire, Elsevier Applied Science Publishers, pp. 87-105, 1986.

6. Schneider, U. Properties of Materials at High Temperatures: Concrete, Dept. of Civil Eng., University of Kassel, Mönchebergstr. 7, D-3500 Kassel, Germany, 2nd Edition, June, 1986.

7. Lie, T. T., Rowe, T.J., and Lin, T. D., Residual strength of Fire-Exposed Reinforced Concrete Columns, Evaluation and Repair of Fire Damage to Concrete, American Concrete Institute, SP 92-9, pp. 153-174, 1986.

8. Lie, T. T., Fire-Temperature Relations, The SEPE Handbook of Fire Protection Engineering, Section 3, Ch. 5, pp. 3-(81-87), (JRC Paper No. 1579), 1988.

9. Huang, C. L. D. and Ahmed, Gamal N., Computational Solution for Heat and Mass Transfer in Concrete Slabs under Fire, Proc. of 6th Int. Conf. on Numerical Methods in Thermal Problems, Swansea, UK, pp. 960-970, July 3-7, 1989.

HEAT TRANSFER IN FORCED NON-NEWTONIAN FLUIDS WITH VISCOUS DISSIPATION PAST A HORIZONTAL FLAT PLATE

F.L. Bello-Ochende and C.D. Obiajunwa

Department of Mechanical Engineering, Faculty of Engineering and
Technology, University of Ilorin, Ilorin, Nigeria.

ABSTRACT

The problem of heat transfer in forced non-Newtonian fluids with viscous dissipation is considered. The retention of the viscous dissipation term in the energy transport equation appears to have rendered the problem intractable via similarity transformation. Hence, a numerical algorithm is presented, based on the use of two model velocity profiles postulated by Acrivos et al [1] and Leveque [2], to predict the dissipation effect on heat transfer. Since the region of interest is very thin, use is made of transformations, following Acrivos et al, that permit coordinate stretching in the appropriate direction. The energy transport equation is solved numerically using a forward-matching finite-difference scheme which is capable of automatic grid refinement near the leading edge. Local and mean Nusselt numbers are presented for a range of generalised Reynolds and Eckert numbers for a given Prandtl number for both pseudoplastic and dilatant fluids. When viscous dissipation is neglected, results compare well with that of Acrivos et al for the range, $0.25 \leq n \leq 1.75$, of the non-Newtonian parameter, n. Also, results indicate possible reductions of up to 26% in heat transfer rates below those which exclude viscous dissipation effects.

NOMENCLATURE

C_p	Specific heat at constant pressure, $^J/_{kg.k}$
E_c	Generalised Eckert number, $\mu u_\infty^{3-n} L_c^{n-1}/KC_p(T_\omega - T_\infty)$.
K	Consistency index.
L_c	Characteristic length of plate, m.
n	Non-Newtonian parameter.
N	Number of spatial divisions.
Nu_η	Local Nusselt number, $\eta Re^{\frac{1}{n+1}} \frac{\partial\theta}{\partial\xi}\Big\|_{\xi=0}$.
$\bar{N}u$	Mean Nusselt number, $\int_o^{\eta^*} Nu_\eta d\eta$
P	Dimensional pressure, N/m².
p^*	Non-dimensional pressure, $P/\rho u_\infty^2$
Pr	Generalised Prandtl number, $KC_p L_c^{1-n} u_\infty^{n-1}/\lambda$.
Re	Generalised Reynolds number, $\rho u_\infty^{2-n} L_c^n/K$.
T	Temperature, °k.
u,v	Local velocities in x-and y-directions respectively, m/s.
U,V	Normalised corresponding velocity components, u/u_∞ and $vRe^{\frac{1}{n+1}}/u_\infty$.
x,y	Horizontal and vertical coordinate axes respectively.

Greek Symbols

λ	Thermal conductivity of fluid, W/m.k.
β	Function of x and n.
δ_T	Dimensionless thermal boundary layer thickness.
η	Normalised horizontal coordinate, x/L_c.
μ	Dynamic viscosity of fluid.
τ_{xy}	Shear stress for the two-parameter equation of state, $K\left\|\frac{\partial u}{\partial y}\right\|^{n-1} \frac{\partial u}{\partial y}$, N/m².
θ	Dimensionless temperature potential, $\frac{T - T_\infty}{T_\omega - T_\infty}$.
ρ	Density of fluid, kg/m³.
ξ	Normalised vertical coordinate, $y\,Re^{\frac{1}{n+1}}/L_c$.

Subscripts

i,j	Nodal points.
ω	Wall values.
∞	Ambient conditions.

INTRODUCTION

The emergence of non-Newtonian fluids in industrial applications has stimulated, in recent times, the need to investigate the effect of temperature on the rheological properties of the fluids. The main reason for the renewed interest is probably because fluids such as molten plastics, pulp, slurries and emulsions, which do not conform with the classical Newtonian postulate that the stress tensor is proportional to the deformation tensor, are produced industrially in increasing quantities. These fluids are likely to be pumped and transported the same way as the common Newtonian fluids. Acrivos [3] was probably the first to conduct investigations on the heat transport phenomena in non-Newtonian fluids. Subsequently, numerous investigations [4 - 7] followed. In order to predict heat transfer rates, it is desirable to develop methods for calculating these rates of heat transfer to non-Newtonian fluids under various boundary constraints. These methods would facilitate optimal design of heat transfer equipment in areas of chemical, polymer, food processing and biomedical engineering.

In this work, the problem of heat transfer in forced non-Newtonian fluids with viscous dissipation is considered. The retention of the viscous dissipation term in the energy transport equation appears to render the problem intractable via similarity transformations. Hence, a numerical algorithm is presented, based on the use of two velocity profiles postulated by Acrivos et al and Leveque, to predict the effect of entropy generation, via viscous dissipation, on heat transfer in forced flow over a heated horizontal flat plate. Since the region of interest is very thin, use is made of transformations that permit coordinate stretching in the appropriate direction. A forward-matching finite-difference procedure is used to solve numerically the energy transport equation to determine the temperature field and the heat transfer coefficients. Results are presented for a range of generalized Reynolds, Prandtl and Eckert numbers for both pseudoplastic and dilatant fluids. When viscous dissipation is neglected, results compare well with those of Acrivos et al. for the range of non-Newtonian parameter considered. Also, predicted results indicate possible reductions of up to 26% in heat transfer rates below those which exclude viscous dissipation.

PROBLEM FORMULATION AND ANALYSIS

For a fluid passing by a submerged body, the viscous effect is significant only in the boundary layer adjacent to the body surface. Hence, boundary layer approximations can be invoked and applied to power-law fluids. Thus, if for simplicity constant fluid properties are assumed, the normalised conservation equations in the presence of dissipation function in the energy transport equation, may be cast in their normalised forms for the two-dimensional flow as,

Continuity Equation:

$$\frac{\partial U}{\partial \eta} + \frac{\partial V}{\partial \xi} = 0. \tag{1}$$

Streamwise Momentum Equation:

$$U\frac{\partial U}{\partial \eta} + V\frac{\partial U}{\partial \xi} = -\frac{\partial P^*}{\partial \eta} + D(n)\left|\frac{\partial U}{\partial \xi}\right|^{n-1} \frac{\partial^2 U}{\partial \xi^2}. \tag{2}$$

Energy Transport Equation:

$$U\frac{\partial \theta}{\partial \eta} + V\frac{\partial \theta}{\partial \xi} = J(n)\frac{\partial^2 \theta}{\partial \xi^2} + G(n)\left(\frac{\partial U}{\partial \xi}\right)^2. \tag{3}$$

where,

$$\begin{aligned} D(n) &= n\,Re^{\left(\frac{1-3n}{1+n}\right)} \\ J(n) &= Re^{\left(\frac{1-n}{1+n}\right)} \\ G(n) &= Ec \end{aligned} \tag{4}$$

The normalised boundary conditions are:

$$\begin{aligned} U\big|_{\xi=0} = V\big|_{\xi=0} = \theta\big|_{\xi=0} - 1 &= 0 \\ U\big|_{\xi=\delta_T} - 1 = V\big|_{\xi=\delta_T} = \theta\big|_{\xi=\delta_T} &= 0 \end{aligned} \tag{5}$$

At the stagnation point, $\eta = \xi = 0$

$$U - 1 = V = \theta = 0. \tag{6}$$

Following Acrivos et al, in the developing flow regime within the thin boundary layer, U admits a first term representation of the power series expansion in ξ. Thus,

$$U = \beta(\eta)\xi \tag{7}$$

where,

$$\beta(\eta) = \{C(n)\}^{\frac{1}{n}}\,\eta^{\frac{1}{n+1}} \tag{8}$$

and,

$$C(n) = \left(\frac{39}{280} \times \frac{1.5}{1+n}\right)^{\frac{n}{n+1}}. \tag{9}$$

Substituting the postulated form of U in eq. (7) into eq. (1) and integrating yields,

$$V = -\xi^2\{C(n)\}^{\frac{1}{n}}\,\eta^{-\frac{n}{n+1}}/2(n+1). \tag{10}$$

It is observed that the energy and momentum transport equations are uncoupled and each can therefore be solved independently. Substituting eq. (7) and eq. (10) into the normalised energy transport eq. (3) gives,

$$\beta(\eta)\xi\frac{\partial \theta}{\partial \eta} - \frac{\xi^2\{C(n)\}^{\frac{1}{n}}\,\eta^{-\frac{n}{n+1}}}{2(n+1)}\frac{\partial \theta}{\partial \xi} = J(n)\frac{\partial^2 \theta}{\partial \xi^2} + G(n)\{\beta(\eta)\}^2 \tag{11}$$

It is pertinent to note that eq. (11) is valid upstream of the location where $\eta = 1.0$. Downstream of this location, the Leveque model of the velocity profile is,

$$U = C^*\xi. \tag{12}$$

As a result, the energy transport equation downstream of $\eta = 1.0$ assumes the form

$$\{C(n)\}^{\frac{1}{n}}\frac{\partial \theta}{\partial \eta} = J(n)\frac{\partial^2 \theta}{\partial \xi^2} + G(n)\{C(n)\}^{\frac{2}{n}}. \tag{13}$$

However, at the location $\eta = 1.0$, the two velocity profiles as defined by eq. (7) and eq. (12) must be compatible so that,

$$C^* = \{C(n)\}^{\frac{1}{n}}. \tag{14}$$

Numerical Procedure

The thermal boundary layer thickness, δ_T^* at $\eta = 1.0$ can be estimated on the basis of mass flux conservation from,

$$\delta_T^* = \int_0^{\delta_T^*}\{C(n)\}^{\frac{1}{n}}\,\xi\,d\xi$$

to be,

$$\delta_T^* = 2/\{C(n)\}^{\frac{1}{n}}. \tag{15}$$

The mode of discretization of the domain starts with the division of δ_T^* at $\eta = 1.0$ into N equal parts of size $\Delta\xi$. Then, horizontal lines through these points are projected to meet or terminate at the hypothetical boundary layer edge at various points. From these points, vertical lines are drawn, and extended both ways, to terminate on the η-axis. The resulting picture of non-uniform discretization in the η-direction is shown in Fig. 1. Hence the grid lines are closely spaced near the leading edge and become progressively staggered downstream. This artifice for automatic grid refinement in computational regions where solution gradients are high has been utilized successfully by Bello-Ochende [8] and Bello-Ochende and Onumanyi [9] for different configurations or geometries.

Before commencement of numerical computations, the grid sizes, $\Delta\eta_{i,1}$ in the η-direction are computed, a priori, for any given set of parameters, from the following recurrence relations for downstream and upstream regions of the location $\eta_{N,1} = 1.0$.

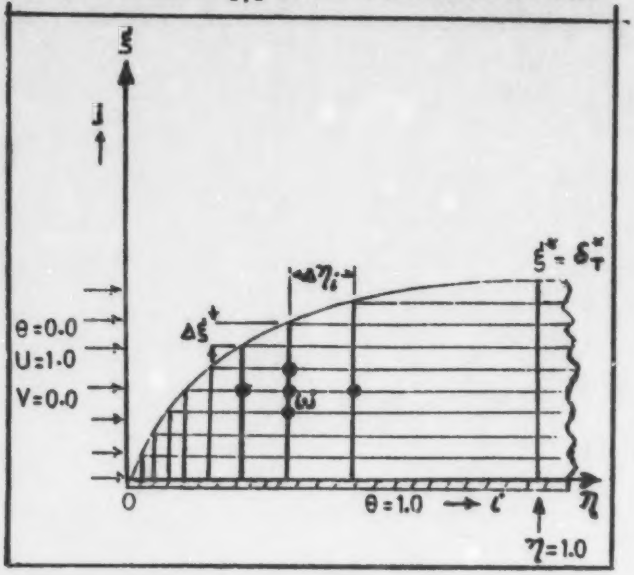

Fig.1. Schematic for coordinate system, boundary constraints and numerical grids.

(a) Region upstream of $\eta_{N,1} = 1.0$:

$$\eta_{I-1,1} = \eta_{I,1} - \frac{(J^*-1)(\Delta\xi)^3\{C(n)\}^{\frac{1}{n}}(\eta_{I,1})^{\frac{1}{n+1}}}{2AJ(n)} \qquad (16)$$

$$I = J^* = N,\ N-1,\ \ldots\ 1$$

$$\Delta\xi = \delta^*_{T/N}$$

where A is a constant greater than unity and subject to certain restriction on J(n) for dilatant fluids.

(b) Region downstream of $\eta_{N,1} = 1.0$

$$\eta_{I+1,1} = \eta_{I,1} + \frac{(J^*+1)(\Delta\xi)^3\{C(n)\}^{\frac{1}{n}}}{2AJ(n)} \qquad (17)$$

$$I = J^* = N,\ N+1,\ \ldots,\ N^*$$

where N^* may be fixed arbitrarily depending on how far, downstream of $\eta_{N,1} = 1.0$, it is wished to extend the computations. Having determined all the $\eta_{i,1}$s, the formal definition of $\Delta\eta_i$ is given as,

$$\Delta\eta_i = \eta_{i+1,1} - \eta_{i,1} \qquad (18)$$

$$i = 1,2,3,\ \ldots,\ N^*$$

and

$$\eta_{1,1} = 0.0.$$

Details of the discretised forms of the energy transport equations, computational algorithm and calculations of heat transfer results are available elsewhere [10], but are ommitted for the sake of brevity.

DISCUSSION OF RESULTS

In Figs. 2a and 2b present numerical results are shown and compare well with those predicted by Acrivos et al when viscous dissipation is neglected for low Reynolds number flows.

Figs. 3 and 4 illustrate the response of the local Nusselt numbers to changes in the viscous dissipation parameter, Ec. For strongly forced flows, the local Nusselt numbers decrease when Ec increases. For pseudoplastic fluids, at $\eta_{N,1} = 1.0$, maximum local Nusselt numbers are predicted. Downstream of $\eta_{N,1} = 1.0$. the local Nusselt numbers decrease sharply as Ec increases. For dilatant fluids, the local Nusselt numbers do not exhibit sharp decreases downstream of $\eta_{N,1} = 1.0$. Instead, the local Nusselt number approaches its maximum value asymptotically. The general decrease in the local Nusselt numbers with increases in Ec could be attributed to the reduced local temperature potentials between the isothermal plate and the neighbouring fluid whose temperature has been increased due to local frictional heating.

Fig.5 shows the plots of the mean Nusselt number against the power-law index, n. The mean Nusselt number decreases as both E_c and n increase. In conclusion, it is clear that viscous dissipation has a significant effect on heat transfer. For a given set of parameters, say Re, Pr and n, up to 26% reduction in heat transfer for Ec=0.0 is indicated for the range, $0 \leq Ec \leq 1.0$ considered.

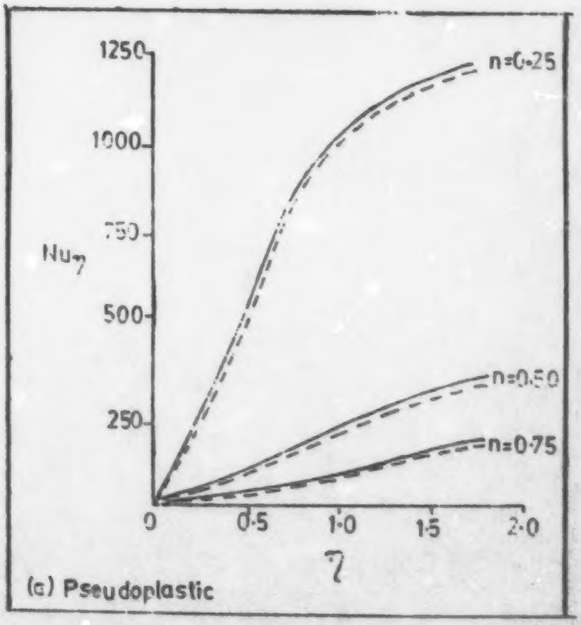

Fig.2a Streamwise Nusselt number variation for pseudoplastic fluids for Ec=0.0, Re=10^3 and Pr=10^2.

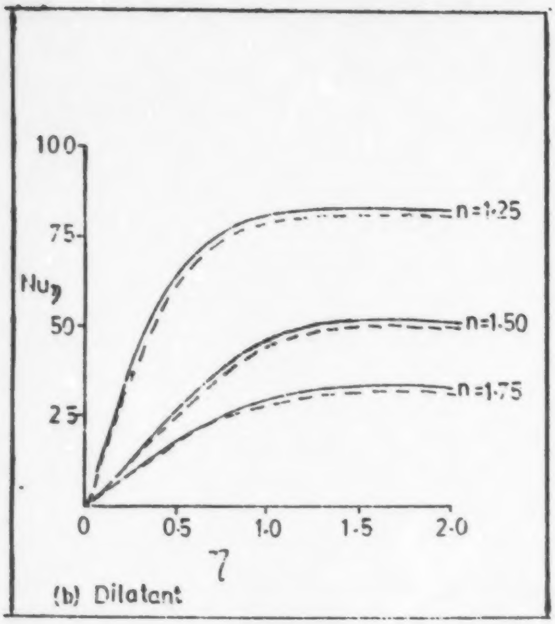

Fig.2b. Streamwise Nusselt number variation for dilatant fluids for Ec=0.0,Re=10^3 and Pr=10^2.

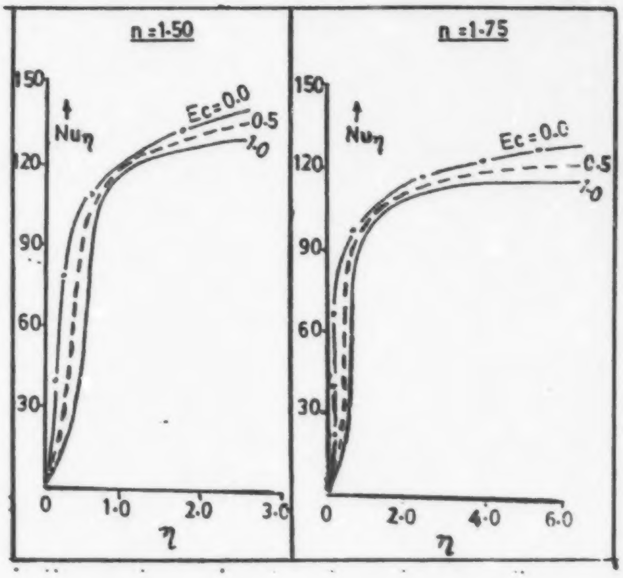

Fig.4. Effect of viscous dissipation on streamwise Nusselt numbers for dilatant fluids;Re=10^4 and Pr=10^2.

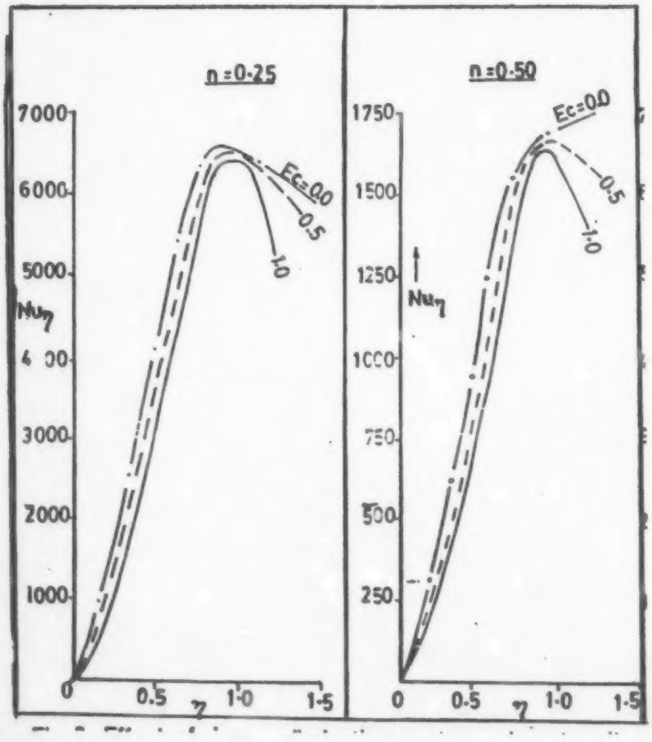

Fig.3. Effect of viscous dissipation on streamwise Nusselt numbers foe pseudoplastic fluids; Re=10^4 and Pr=10^2.

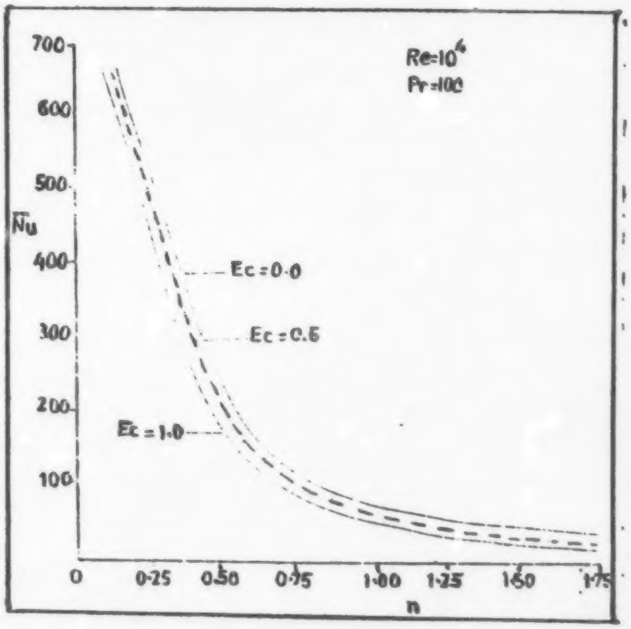

Fig.5. Mean Nusselt number vs. the non-Newtonian parameter.

ACKNOWLEDGEMENT

The lead author acknowledges the support of the University of Ilorin through the Senate Res. Grant,No.8.303.11 and the Computer Centre.

REFERENCES

1. Acrivos,A.,Shah,M.J.& Petersen,E.E., Momentum and Heat Transfer in Laminar Boundary-Layer Flows of Non-Newtonian Fluids Past External Surfaces, A.I.Ch.E.J.,Vol.6,No.2, pp.312-317,1960.
2. Leveque,M.A., Les Lois de la Transmission de Chaleur Par Convection, Annis Mines,Vol.13, pp. 201,1929.
3. Acrivos,A., A Theoretical Analysis of Laminar Natural Convection Heat Transfer to Non-Newtonian Fluids, A.I.Ch.E.J.,Vol.6,No,4, pp.584-590, 1960.
4. Lee,S.Y.& Ames,W.F., Similarity Solutions for Non-Newtonian Fluids, A.I.Ch.E.J., Vol.12,No,1, pp. 700-708,1966.
5, Mahalingam,R., Tilton,L.O. & Coulson,J.M., Heat Transfer in Laminar Flow of Non-Newtonian Fluids Chem, Eng. Sci.,Vol.30, pp.921-929,1975.
6. Some,A. & Chen,J.L.S., Free Convection of Non-Newtonian Fluids Over Non-Isothermal Two- Dimensional Bodies, Int.J. Heat Mass Transfer,Vol. 27,No.5, pp.791-794,1984.
7. Achwal,S.K. & Al-Harbi,D.K., Study of Transient Heat Transfer in Laminar Flow of a Fluid Over a Flat Plate, Int. Comm. Heat Mass Transfer,Vol.12, pp.269-275,1985.
8. Bello-Ochende,F.L., A Numerical Study of Natural Convection in Horizontal Elliptic Cylinders Rev. BrMec. Rio de Janeiro(Brazilian Journal of Mechanical Sciences),Vol.VII,No,4,pp.353-371,1985.
9. Bello-Ochende,F.L. & Onumanyi,P., Analysis of Transient Heat Transfer in a Triangular Region with a Corner Singularity, Mech. Res. Comm., Vol.14,nos.5/6, pp.403-406,1987.
10. Obiajunwa,C.D.,Effect of Viscous Dissipation on Laminar Non-Newtonian Fluid Flow Over a Heated Flat Plate, M.Eng. Thesis, Faculty of Engineering,and Technology, University of Ilorin, Ilorin Nigeria,1989.

STUDY OF FINNED HEAT TRANSFER UNDER THE CONDITION OF RADIATION AND CONVECTION

Yang Xiangxiang Li Liangbin

(Hua Qiao University, Quanzhou, Fujian, P. R. China)

ABSTRACT

A general differential equation for the heat transfer of trapezoidal fin is derived. By applying the 4th order Runge-Kutta integration scheme and Newton-Raphson iteration technique in numerical solution, the temperature distribution along the height of the fin is obtained. The influences of various parameters, including thermal conductivity, emissivity, temperature at the fin base, the height of the fin, and interfin spaces, on the finned heat transfer are analyzed.

NOMENCLATURE

K	thermal conductivity of fin material (W/m.K)
T_w	fin base temperature (K)
T_f	environmental media temperature (K)
h	heat exchange coefficient ($W/m^2.K$)
q_r	radiating heat exchange quantity of a fin (W/m^2)
B	effective radiation of a fin (W/m^2)
ε	emissivity of a fin
$dF_{dAy-dAy'}$	angle coefficient of two neighbouring fins' differential element surfaces dAy to dAy'
dF_{dAy-Ao}	angle coefficient of differential element surface on the fin to the environment

Non-dimensional parameters:

$N1 = \sin\theta$ $N2 = \cos\theta$ $N3 = tg\theta$

$N4 = \cos^2\theta$ $N5 = \frac{W - 2\delta_c}{H}$ $N6 = \delta_1/H$

$N7 = \frac{H.h}{K}$ $N8 = \frac{T_f}{T_w}$ $N9 = \varepsilon$

$N10 = \frac{H\sigma.Tw^3}{K}$ $N11 = \frac{H\sigma T_f^4}{KT_w}$ $N12 = \cos2\theta$

$N13 = \frac{\varepsilon}{1 - \varepsilon}$ $N14 = \frac{1}{\cos\theta}$

INTRODUCTION

Most of the heat exchangers were equipped with fins so as to enhance heat exchange. In a temperature of not so high, radiating heat transfer was neglected; however, in a higher temperature the effect of radiation has to be considered. As pointed out by literature[1], "When cooling a heater by natural convection in the air, even at room temperature, the heat exchange by radiation equivalents in the same order of magnitude to that by convection."

In view of this, the authors deal with finned heat transfer under the condition of radiation and convection. The trapezoidal straight fin was chosen from multifarious types of fins as representative owing to its easy of manufacturing and widely used in engineering. It was compared with the triagular and rectangular fins. The results are of practical value for engineering design.

ESTABLISHMENT OF A MATHEMATICAL MODEL

The following assumptions are given

for convenience of analysis:

1. A steady one-dimensional heat transfer;
2. the fin as a diffused grey body has a thermal conductivity and emissivity indifferent to the change of temperature;
3. the temperature of the fin changes with the height of the fin only;
4. the heat exchange coefficient of convection along the height of the fin is a constant.

The geometric dimension of trapezoidal fin is shown as Fig.1. Radiating heat exchange at the fin base is neglected for simplification. Thus the model of actual calculation follows the dotted line of Fig.1 .

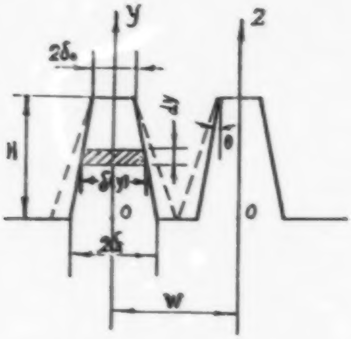

Fig.1 Trapezoidal fin

The mathematical description of the problem can be obtained from energy balance equation[2].

$$\frac{d}{dy}\left(\delta(y)\frac{dT}{dy}\right) = \frac{1}{K\cos\theta}\left[h(T - T_f) + q_r(y)\right] \qquad (1)$$

From the grey body heat radiation

$$q_r(y) = \frac{\varepsilon}{1-\varepsilon}\left[\sigma T^4(y) - B(y)\right] \qquad (2)$$

$$B(y) = \varepsilon\sigma T^4(y) + (1-\varepsilon)\left[\int_0^H B(y)\,dF_{dAy-dAy'} + \sigma T_f^4 dF_{dAy-Ao}\right] \qquad (3)$$

The boundary conditions are as follows

$y = 0$, $\quad T = T_w$

$y = H$, $\quad \frac{dT}{dy} = 0$

The angular coefficient in the above equations may be calculated in the light of literature[3-5].

let $X = \frac{Y}{H}$, $\quad Y = \frac{T(y)}{T_w}$ and $Z1 = \frac{dY}{dX}$.

The non-dimensional control differential equation (1) becomes

$$\frac{dZ1}{dX} = \frac{N2Z1 + u}{N6 - N3X} \qquad (4)$$

where

$u = N14(N7(Y - N8) + N13(N10Y^4 - u1)$

$u1 = (N9N10Y^4 + (1 - N9)N11.P)/$
$\quad [1 - 0.5(1 - N9)(1 - N4)A]$

The boundary condition becomes

$X = 0$, $\quad Y = 1$

$X = 1$, $\quad Z1 = 0$

This equation can be solved by adopting the 4th order Runge-Kutta integration scheme and Newton-Raphson iteration technique [6].

The value of $\left.\frac{dY}{dX}\right|_{X=0}$ can be solved by a known vertical temperature distribution along the height of the fin, and the heat transfer quantity Q can thus be solved.

RESULTS AND DISCUSSION

1. The temperature distribution along the fin height (Fig.2)

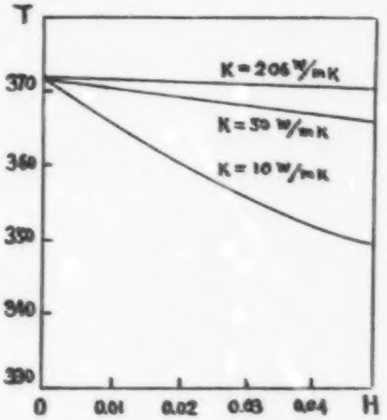

Fig.2 Temperature distribution in a fin

The temperature distribution along the fin height varies greatly when the thermal conductivity is rather small; however, it smoothes down gradually with the increase of thermal conductivity, and when the thermal conductivity becomes very large, the temperature gradient along the fin height approaches zero.

2. Heat exchange quantity Q varies with fin height (Fig.3)

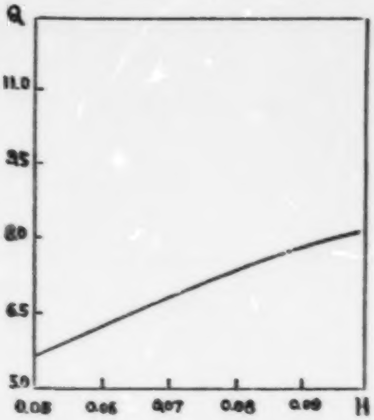

Fig.3 Q changes with H

As the fin increases in height, the heat exchange quantity increases greatly. Evidently, the heat exchange surface by convection increases with the increase of fin height.

3. Influence of interfin space W on the heat exchange quantity (Fig.4)

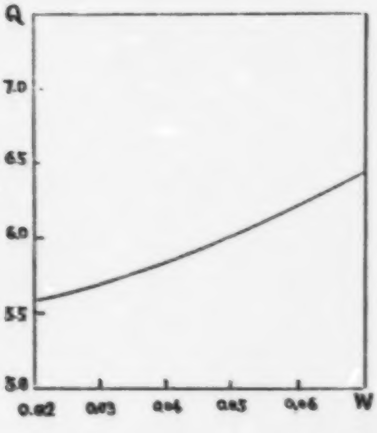

Fig.4 Q changes with W

The increase of W may lead to the enhancement of radiating heat exchange quantity due to the increase of angular coefficient of interfin walls and fins to the external environment. Therefore, Q increases correspondingly. Appropriate increase of W is advantageous to the radiating heat exchange, however, it limits the number of the fins to be installed in a certain breadth.

4. Influence of the thickness δ_i of the fin base on the heat exchange quantity Q (Fig.5)

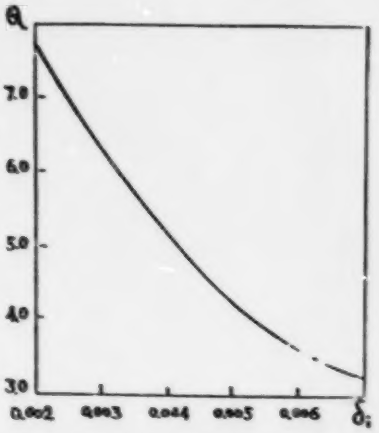

Fig.5 The fin keeps in constant volume, Q changes with δ_i

In case the fin keeps in constant volume, the fin height H decreases significantly with the increase of δ_i. The decrease of heat exchange area by convection leads to the corresponding decrease of finned heat exchange quantity Q.

5. Influence of environmental temperature T_f on heat exchange quantity Q (Fig.6)

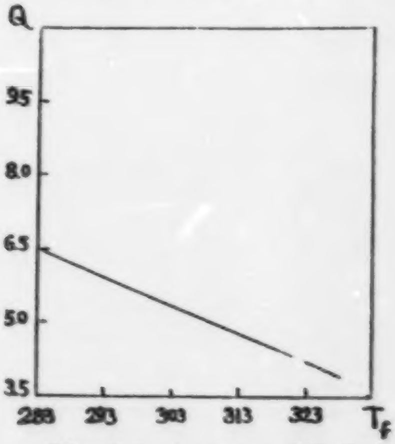

Fig.6 Q changes with T_f

Q decreases greatly with T_f. The increase of T_f leads to the decrease of temperature gradient and then corresponding decrease of heat exchange Q by convection and radiation.

6. Influence of the fin base temperature T_w on the heat exchange quantity Q (Fig.7)

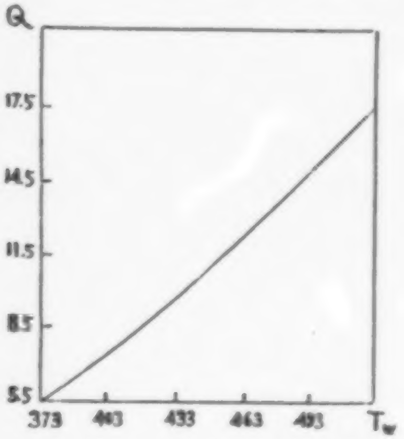

Fig.7 Q changes with T_w

Finned heat exchange quantity Q increases rapidly with the increase of the fin base temperature T_w. Evidently, the increase of T_w leads to the increase of temperature gradient, which causes the increase of heat exchange by convection and radiation.

7. Influence of emissivity ε on heat exchange quantity Q (Fig.8)

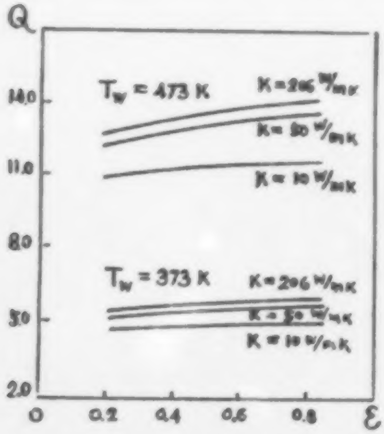

Fig.8 Q changes with ε

The higher the fin base temperature T_w, the greater the increase of finned heat exchange quantity Q with the increase of emissivity ε; if the fin base temperature being not so high, the finned heat exchange quantity Q changes with emissivity ε insignificantly, and different materials differ also insignificantly.

8. Influence of thermal conductivity K on heat exchange quantity Q (Fig.9)

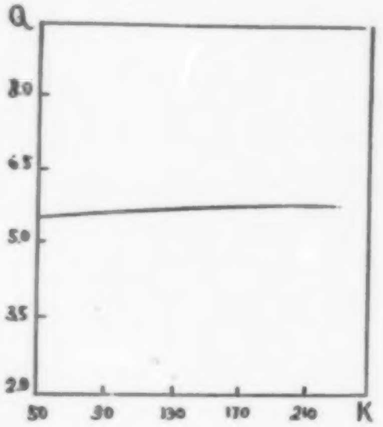

Fig.9 Q changes with K

The finned heat exchange quantity Q changes rather small when the thermal conductivity K increases. Evidently, it is inadvisable to enhance heat exchange quantity Q by manufacturing the fin with expensive material of high thermal conductivity.

9. A comparison of heat transfer in several fins with different cross section (Fig.10-11)

Fig.10 shows the ratio of heat exchange quantity of the trapezoidal fin Q_{tra} to that of rectangular fin Q_{rect} and the ratio of Q_{tra} to that of triangular fin Q_{tri} changes with thermal conductivity K. As prerequisites, they have similar volume or material consumption. It can be seen that the trapezoidal fin has a much greater heat exchange quantity than rectangular fin and increases with the increase of K; and the trapezoidal fin has a smaller heat exchange quantity than triangular fin and this difference does not significantly affect by K.

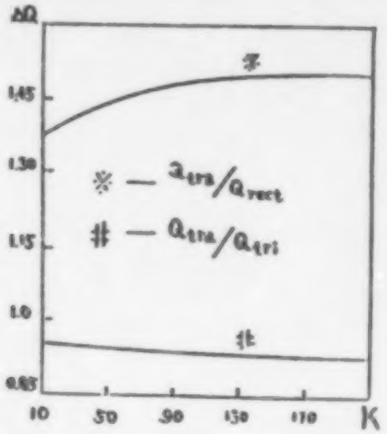

Fig.10 Heat transfer of the fins with different shapes

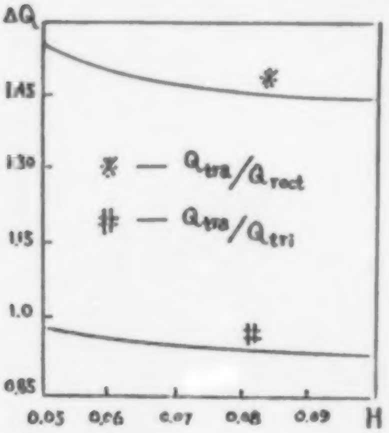

Fig.11 Heat transfer of the fins with different shapes

From Fig.11 it can be seen that the difference between Q_{tra} and Q_{tri} decreases with the increase of the height of fins; while Q_{tri} still greater than the heat exchange quantity of the fins with other cross section.

10. A comparison between heat transfer of trapezoidal fin by convection and radiation and that by convection alone (Fig.12)

It shows that under different thermal conductivity K, the ratio in percentage of radiating heat exchange quantity Q_r to heat exchange quantity by convection Q_c changes with the fin base temperature T_w. Q_r increases with the increase of T_w, so increases the percentage. Even if T_w = 373K, the ratio of Q_r to Q_c rises to 80.6 %. This shows quantitatively the necessity of considering radiating heat exchange in calculating finned heat transfer.

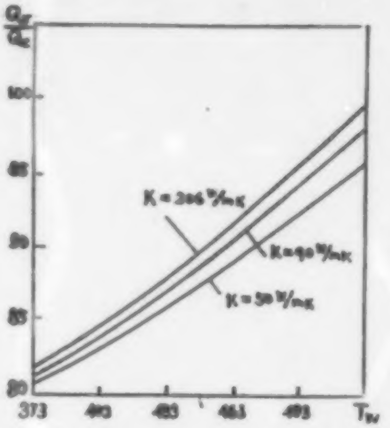

Fig.12 Q_r/Q_c changes with T_w

CONCLUSION

The following conclusion can be obtained by synthesis and analysis of the calculating results:

1. When cooling the fin in the air by natural convection, the influence of radiating heat exchange has to be considered.
2. Triangular fin has a better heat transfer than rectangular or trapezoidal fins. The trapezoidal fin with thinner fin tip, as manufacturing condition permitted, will intensify heat transfer.
3. When the temperature is not so high, it is inadvisable to adopt the material with high thermal conductivity.
4. To choose the fin with reasonable geometric dimension. It will intensify heat transfer.

It should be pointed out finally, the problem of variable thermal parameters and the optimization of heat transfer are worthy of further exploring.

REFERENCES

1. Zhang, Y. W. & Chen, Z. X., Numerical Calculation & Its Approximate Treatment of Finned Heat Transfer under the Condition of Radiation and Convection, Proc. China Thermophysics Conf, Chengdu, 1987.
2. Yang, X. X., A Study on Heat Transfer in the Fins of Variable Thermal Parameters and Variable Cross Section, J. of Hua Qiao Univ., Vol.7, pp.307-320, 1986.
3. Yang, X. R., et al., Manual of Angle Coefficient of Heat Exchange by Radiation , National Defence Industry, Pub. Co., 1982.
4. Sparrow, E. M. & Irvine, T. F., The Effectiveness of Radiating Fins with Mutual Irradiation, J. of Aerospace Sciences, No.1 0, 1961.
5. Sparrow, E. M. & Sises, R. D., Heat Transfer by Radiation,Higher Education Pub. Co., China, 1982.
6. Adams, J. A. & Rogers, D. F., Computer Analysis of Heat Transfer Theory, Science Publications, China, 1980.

ROTARY DRYER FOR FLASH DRYING PADDY IN DEVELOPING COUNTRIES

A.R. Elepaño and P.H. Oosthuizen

Mechanical Engineering Department
Queen's University
Kingston, Ontario, Canada

ABSTRACT

Experimental and numerical studies of a continuous flow rotary dryer for flash drying paddy are described. The dryer uses agro-waste as a heat source. The experimental study was done at the International Rice Research Institute (IRRI). Results showed that grain temperature should be limited to 100°C to prevent grain puffing. High temperature drying of grains with moisture content higher than 19% w.b. produced a product of acceptable quality. The throughput capacity and retention time of the paddy depend on the cylinder rotation speed, grain impurity and grain moisture content. Typical throughput capacity is 0.2 tons/hr at retention time of 4 min. A numerical model was developed for the dryer describing heat transfer from the fuel bed to the drying cylinder, from the cylinder to the paddy and the drying rate during the cooling process. Radiation dominates the heat transfer from the fuel bed to the cylinder. Temperature profile of the grain along the cylinder was predicted using finite element conduction model. At cylinder temperature of 150°C the grain temperature gradient is 36°C/m. The drying rate ranges from 2-3%/pass which is similar to that obtained in the experimental study.

NOMENCLATURE

c_p	Specific heat, kcal/kg-°C
E,F,n,Y	Constants
F_{1-2}	Radiation configuration factor
h	Convective heat transfer coefficient, kcal/m^2-hr-°C
k	Thermal conductivity, kcal/m-hr-°C
M	Moisture content, % w.b.
M_e	Equilibrium moisture content, % w.b.
M_o	Initial moisture content, % w.b.
MR	Moisture ratio = $(M-M_e)/(M_o-M_e)$
Pr	Prandtl number
Re	Reynolds number
RH	Relative humidity, %
T	Temperature, °C
Q	Steady-state heat transfer, W/m
V	Volumetric flow, m^3/hr
X	Proportionality constant
ρ	Density, kg/m^3
τ	Time
subscripts	
a	air
g	grain

INTRODUCTION

Paddy (i.e. rough rice) should be dried immediately upon harvest to prevent deterioration in the form of yellowing, moulding, germination and insect attack. With the introduction of short maturing varieties, farmers in developing countries now harvest twice or thrice a year. They normally dry their paddy by direct sundrying. However, with unreliable weather conditions during the wet season, they are faced with drying problems. Although there have been many efforts to develop mechanical drying methods suitable for small farmers, none of the resulting designs has achieved widespread acceptance. An appropriate dryer should be designed according to the needs of these farmers. It should be inexpensive, simple, robust and mobile.

Hall and Hall (1961), Chancellor (1968), Acasio and Belonio (1985) and Jeon et al. (1987) have studied conduction drying using high temperature for quick drying without significant loss in grain quality. Acasio and Belonio (1985) and Jeon et al. (1987) have noted the potential of using the method for partially drying paddy to its safe moisture content (below 19%) allowing it to be stored for several days until the weather is suitable for final drying to the desired final moisture content for milling.

The International Rice Research Institute (IRRI) has developed a high-temperature rotary dryer. The dryer provides a convenient facility for drying high moisture paddy and other grains. It also compliments the use of sundrying and/or other mechanical dryers for final drying.

This paper summarizes both the experimental work done at IRRI and the development of a numerical model of the dryer. The experimental study concentrated on the effects of various parameters (temperature, retention rate, etc.) on paddy quality and dryer efficiency. The effect of high-temperature drying on grain quality was also investigated by analyzing the quality of milled rice. The numerical investigation was done to evaluate both heat transfer mechanisms and drying rate of paddy. Results were then validated against the experimental results.

Design Features of the Dryer

The experimental rotary dryer is shown schematically in Fig. 1.

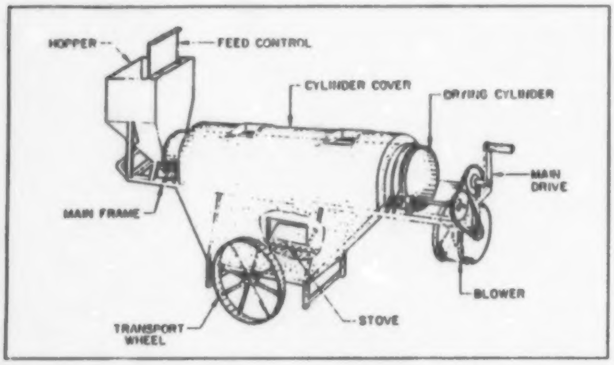

Fig. 1. Perspective view of the rotary dryer.

The main features of the dryer are:

Drying cylinder. The rotating cylinder has a diameter of 30 cm. and a length of 1.8 m. This is made out from empty oil drums fused together. Spiral lifting louvers were riveted over the smooth interior of the cylinder to prevent the grains from slipping. The sheet metal louvers also allow proper mixing of the grains resulting in uniform drying. A chain and sprocket combination is used for the main drive of the dryer. For ease in manual operation, a 1:60 gear ratio was used. The main drive can be modified by coupling a hand tractor engine.

Paddy to be dried is loaded into the hopper at one end of the drying cylinder. The hopper feeds the grains into the rotating cylinder. The rate of flow is controlled by a slide gate at the hopper outlet.

Stove/Furnace. The furnace is a simple enclosure provided with bottom grill and an access door at the bottom of the drying cylinder. Agro-waste such as coconut husks, rice straw, corn cobs and soybean stalks can be used as fuel for the dryer. These are burnt openly in the enclosure. Heat and cylinder temperature are controlled mainly through the rate of fuel supply to the furnace. Mud mixed with straw is used for insulating the furnace and the cylinder.

Auxiliary parts. Transport wheels are provided to enhance the mobility of the dryer. This enables the dryer to be moved from one drying area to another. An optional blower at the discharge end of the cylinder separates light impurities such as chaffs and immature grains from the paddy.

Cooling area. Since the grains have short retention time in the cylinder, a cooling area is necessary to hasten moisture removal from the hot discharged grains. Cooling and drying could be accomplished by either subjecting the grains to forced air, or by spreading them on perforated beds or simply placing them on a concrete floor.

Experimental Investigation

The experimental work was done at the Agricultural Engineering Department of IRRI. The dryer was evaluated taking into account the moisture reduction rate, dryer efficiency and milled rice quality at various temperatures, grain retention time and throughput capacity.

Cylinder and grain temperature. The cylinder temperature was measured by thermocouples placed on the inner surface of the cylinder with leads passing through a slip ring to a digital meter. The grain temperature was measured with an insulated cup having a thermocouple located at its centre. The cup is filled with grains at the discharge end.

Drying experiments were conducted at 100°C to 200°C cylinder temperatures which resulted in an outlet grain temperature of 60°C to 80°C. It was observed that grain puffing occurs when the grain temperature approaches 100°C, which for the experimental set-up, is attained at 250°C cylinder temperature.

Retention time and throughput capacity. Retention time is the time spent by the grain inside the drying cylinder. It depends on the initial moisture content of the grain, its purity and the speed of rotation of the cylinder. The dependency is shown in Fig. 2. Based on the typical working speed of a farmer, the cylinder was rotated at 6 rpm. Corresponding throughput capacity at different speeds is shown in Fig. 3.

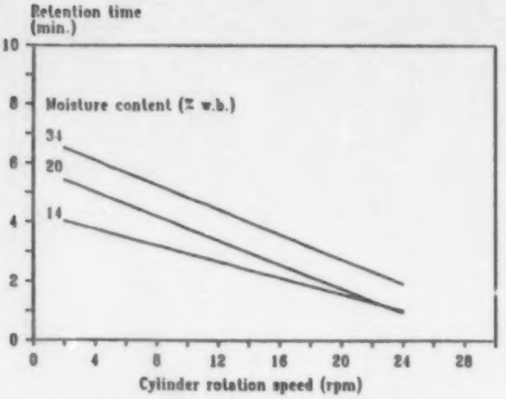

Fig. 2. Retention time of paddy at different initial moisture levels at various cylinder rotation speeds.

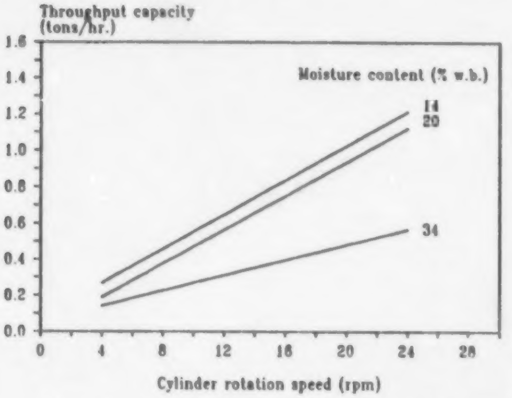

Fig. 3. Throughput capacity of the dryer at different initial moisture levels at various cylinder rotation speeds.

Drying rate. The moisture content of the paddy was measured with a resistance-type meter which was calibrated against oven technique. Freshly harvested paddy (IR-64 variety) having different moisture levels were collected. After heating the grains in the cylinder, they were spread across a wide concrete floor and mixed intermittently. Moisture contents were taken after heating and cooling of the grains. Table 1 shows the typical drying results. It will be noted that the drying rate per pass is faster at high moisture level. At low moisture content, the rate per pass is reduced since most of the surface moisture has already evaporated. Grains are intended to be dried to a moisture level of up to 19% w.b. where it is safe for storage for two weeks without significant deterioration.

Grain quality. The number of drying passes did not have any significant effect on the total milled rice recovery. However, the method used for final drying (i.e. sundrying or mechanical methods) was found to have a significant influence on the percentage of broken grains in the final product. This suggests that high temperature drying is possible provided the initial moisture content is high enough to avoid thermal stress to the grain. Moreover, the starch inside the grain is believed to have gelatinized during the drying process resulting in a flexible surface. This surface resists the forces of milling giving a product of less breakage. Table 2 shows the effect of high temperature drying on grain quality. The temperature results were obtained with a cylinder temperature of 150°C.

Table 1. Moisture content at various stages in the experimental study (% w.b.).

Run no.	1	2	3	4
Initial moisture content, % w.b.	34.0	30.0	26.0	22.0
After first pass	30.2	26.9	23.7	20.4
After second pass	27.1	24.6	21.8	19.8
After third pass	24.8	22.2	20.0	--

Table 2. Effect of pre-drying and method of final drying on milling recovery.

Pre-drying method	Final drying method	Percent milling recovery	Percent head rice	Percent broken rice	Whiteness degree
1 pass	Shade	71.9	67.9	4.0	32.0
2 passes	Dry	71.7	68.3	3.4	29.0
1 pass	Sundry	72.7	63.8	8.9	39.5
2 passes		72.0	63.4	8.7	40.0
1 pass	Mech.	71.8	65.3	6.5	40.0
2 passes	Dry	71.7	63.0	8.7	33.5
Sundried (control)		72.4	66.9	5.5	35.5

Dryer efficiency. The over-all thermal efficiency is the ratio of the heat required to evaporate the moisture removed to the total available fuel energy. The average overall thermal efficiency of the dryer was calculated to be about 20 percent.

Numerical Investigation

The numerical model considered three different sub-models of the drying process. The first model analyzes the heat transfer from the furnace to the cylinder. The second considered the transfer of heat from the rotating drying cylinder to the grains and the last predicted the moisture removal rate of the grains. Most of the parameters used in the study were taken from the experimental study. Meteorological data from IRRI were used to define atmospheric properties. Grain properties reported by Chung and Lee (1985) and Gupta (1985) were incorporated in the analysis. Parameters used in the models are given in Table 3.

Table 3. List of parameters.

I. Cylinder heating model
$Re = 10.0$
$Pr = 0.70$
$k_a = 45.6 \times 10^{-3}$ W/mK

II. Grain heating model
$k_g = 0.2655$ kcal/hr-m-°C
$\rho_g = 632$ kg/m^3
$c_{p-g} = 0.4705$ kcal/kg-°C
$h = 8.604$ kcal/hr-m^2-°C
$T_a = 35$ °C

III. Grain cooling model
$Re = 100.0$
$Pr = 0.7$
$RH = 70$ %
$T_a = 30$ °C

Cylinder heating model. Radiation and convection heat transfer are the mechanisms that dominate the transfer of heat to the cylinder. The fuel bed was considered to be a rectangular plate with combustion air passing through from the bottom and rising to the cylinder with insulation at the sides. The hot air passes around the cylinder and exhausts at the top portion of the cylinder.

Sparrow and Cess (1978) presented a graphical result of the radiation configuration factor in the case of a rectangular plate and cylinder of the same length. The computed F_{1-2} for the experimental set-up was 0.15. Convective heat transfer was computed using finite element method for forced convection flow. Results indicated that radiation dominates the heat transfer at 90% to 95% of the total heat transfer. Fig. 4 shows the variation of the total heat transfer with the fuel bed temperature at various cylinder temperatures. Cylinder temperatures of 100, 150, 200 and 250°C were considered. The cylinder temperature has no significant effect on the total heat transfer at the range considered.

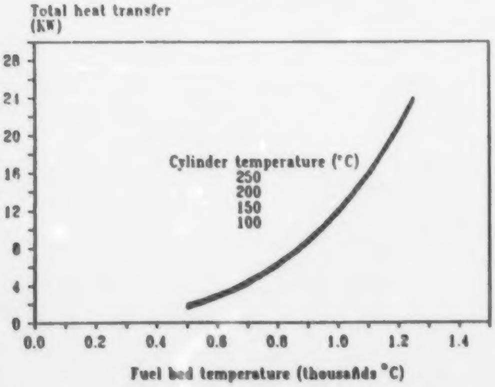

Fig. 4. Total heat transfer from fuel bed to cylinder at different cylinder temperatures and various fuel bed temperatures.

Grain heating model. The transfer of heat from the heated cylinder to the grains were considered to be essentially a steady state process. The following assumptions were made in the analysis:

- Grain properties are assumed to be constant.
- Conduction heat transfer is dominant in the system.
- Air inside the cylinder is stagnant and has constant temperature.
- Louvers have negligible effect on grain flow and heat transfer.
- Grains are thoroughly mixed and have uniform temperature across the lateral section.
- Since the retention time of the grains is short, the moisture reduction is negligible. Most of the drying is assumed to occur during the cooling period.

An analysis was done to find the heat transfer rate from a constant cylinder temperature to the grains in the cylinder. The cylinder is 30% filled with grains. Fig. 5 shows the results obtained using finite element method in solving Fourier's conduction law.

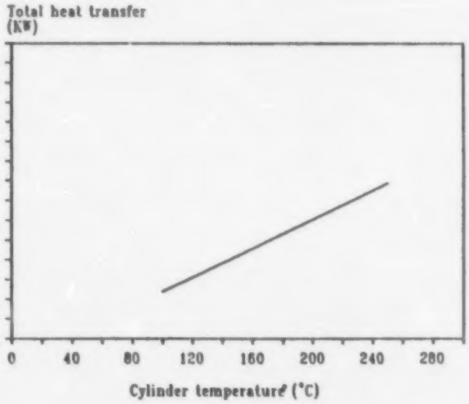

Fig. 5. Steady-state heat transfer rate in grain at various cylinder temperatures.

Combining results from the cylinder heating model and the grain heating model gives the variation of cylinder temperature with fuel bed temperatures. This variation is shown in Fig. 6.

Grain temperature along the cylinder was computed at various cylinder temperatures and longitudinal grain speeds. The governing equation is

$$Q = \rho c_p V \, dT/dz$$

Figs. 7 and 8 show the grain temperature variation for various cylinder temperatures and longitudinal grain speeds, respectively. The higher the cylinder temperature, the faster is the heating of the grains. For the experimental dryer with an effective cylinder length of 1.5 m. at 150°C

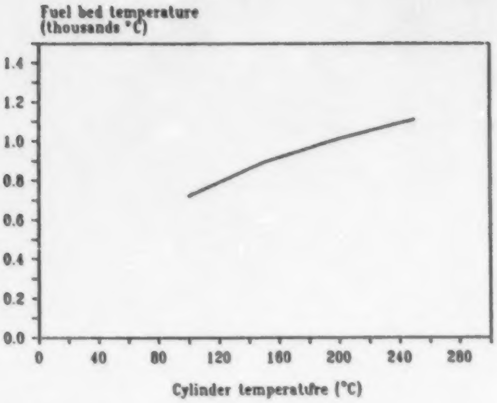

Fig. 6. Variation of fuel bed temperature at various cylinder temperatures.

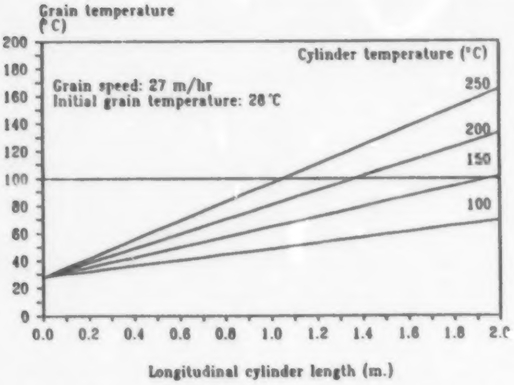

Fig. 7. Temperature profile of grains along the cylinder at various cylinder temperatures.

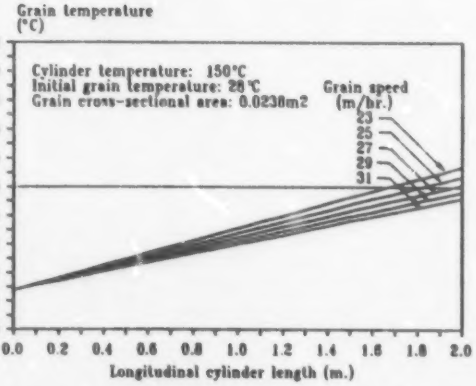

Fig. 8. Temperature profile of grains along the cylinder at various grain speeds.

cylinder temperature, the grain temperature is 80°C which is in the range for the experimental results. The same grain temperature can be achieved at higher cylinder temperature and shorter cylinder length.

The effect of longitudinal grain speed on grain temperature is not pronounced especially at the entrance of the cylinder. As expected, the higher the longitudinal grain speed or flow rate, the lower the discharge grain temperature.

Grain cooling model. This model computes for the drying rate of the grains after the heating process. The model computes the equilibrium moisture content at various grain temperatures and relative humidities based on Chung-Pfost equation

$$M_e = 100\left(\frac{\ln(RH/100)}{-E * (T+F)}\right)^{1/n}$$

where: $n = 2.4451$
$E = 0.00019187$
$F = 51.161$

The drying rate is then computed using the lumped transient moisture loss equation of the form

$$MR = (M-M_e)/(M_o-M_e) = \exp(-Xt^{Y})$$

The two equations were used to predict the moisture removal rate and the temperature decay of the grains after being discharged from the drying cylinder. The grains are assumed to be spread on a concrete floor at ambient temperature. Finite difference solution was adopted and results are presented in Fig. 9. The figure shows the drying rate at various passes in the dryer at different initial moisture contents. It will be noted that the drying rate is faster at higher moisture level. The analysis was limited to moisture contents of approximately 19% w.b. where respiration of the grains is greatly decreased.

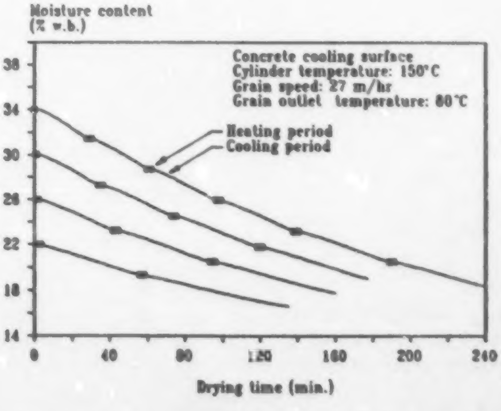

Fig. 9. Drying rate curves with heating and cooling periods.

This result gives an indication of the optimum cooling time of the grain. Turn around time for the drying process can be decreased resulting in a higher daily capacity of the dryer.

Table 4 shows the moisture content at various passes obtained by the numerical model. When these results are compared to the experimental results, the percentage difference ranges from 0.3 to about 20%. The difference increases as the moisture content decreases. The numerical model gives an acceptable drying rate at moisture content higher than 19% w.b. which is the target range of the study.

Table 4. Moisture content at various stages in the numerical model (% w.b.)

Run no.	1	2	3	4
Initial moisture content, % w.b.	34.0	30.0	26.0	22.0
After first pass	31.4[a](3.8)[b]	27.3(1.4)	23.2(3.9)	19.3(5.6)
After second pass	28.7(5.6)	24.5(0.3)	20.5(9.3)	16.6(19.1)
After third pass	26.0(4.5)	21.8(1.9)	17.8(12.4)	--

a = Predicted moisture content.
b = Percentage difference between numerical and experimental results.

CONCLUSION

The study indicates that rapid partial drying of paddy at temperature approaching 100°C can be carried out without producing unacceptable changes in grain quality. The cylinder temperature should be maintained below 250°C to ensure protection of the grain from possible breakage and puffing.

Numerical results and experimental results are similar. The heat transfer from the fuel bed to the cylinder is dominated by radiation at 90% to 95% of total heat transfer. The conduction model of the cylinder and grain heat transfer gave an indication of the temperature profile of the grains along the cylinder. The grain cooling model using the lumped transient moisture loss equation gave acceptable estimates of the drying rate of high moisture grains at various drying conditions. The model can be used to optimize the turn around period, thus increasing the efficiency of the drying process.

The dryer is an alternative technology for the partial drying of paddy which could answer the perennial problem of finding an appropriate drying facility for the humid tropics that is affordable to the small farmers.

REFERENCES

Acasio, U.A. & Belonio, A.T. 1985, Conduction drying of paddy with a rotary drum grain dryer, Proc. 6th Annual Workshop on Grain Post-harvest Technology, Indonesia, pp.72-81.

Agrawal, Y.C. & Singh, R.P. 1977, Thin-layer drying studies on short-grain rough rice, 1977 Winter meeting of the American Society of Agricultural Engineers, Paper No. 77-3531.

Chancellor, W.J. 1968, Characteristics of conducted heat drying and their comparison with those other drying methods, Trans. of ASAE, Vol. 11, No. 6.

Do-Sup Chung & Chong-Ho Lee. 1985, Physical and thermal properties of grains, Preserving Grain Quality by Aeration and In-store Drying (Proceedings of the international seminar held at Kuala Lumpur, Malaysia), Vol. 15, pp.53-66.

Gupta, C. 1985, Physical and engineering properties of rice grain and its by-product: their application in the design of rice processing machines, handling equipment and storage structures, Proc. 1985 ASEAN Technical Seminar on Post-harvest Technology, Manila, Philippines.

Hall, G.F. & Hall, C.W. 1961, Drying shelled corn by conduction heating, Trans. of ASAE, Vol. 42, No. 4.

Handbook of Heat Transfer Fundamentals. 1982, ed. Rohsenow, W.M., Hartnett, J.P. & Ganic, E.N. 2nd ed., p. 3.20, McGraw-Hill, New York.

Jeon, Y.W., Halos, L.S. & Elepaño, A.R. 1987, Design and performance evaluation of an IRRI pre-dryer, Proc. 10th ASEAN Technical Seminar on Grains Post-harvest Technology, Bangkok, Thailand.

Jindal V.K. & Obaldo, L.G. 1986, Rice husk-fired rotary dryer for disinfection and rapid drying of paddy, 9th Annual ASEAN Regional Seminar on Food and Feed Grains, Post Harvest Technology, Singapore.

Sparrow, E.M. & Cess, R.D. 1978, Radiation Heat Transfer, Augmented edition, Hemisphere Publishing Corp., Washington, D.C.

ASSISTING AND OPPOSING MIXED CONVECTIVE HEAT TRANSFER TO A CYLINDER IN A POROUS MEDIUM WITH FREEZING

P. H. Oosthuizen and J. T. Paul
Department of Mechanical Engineering
Queen's University
Kingston, Ontario, Canada K7L 3N6

ABSTRACT

Mixed free and forced convective heat transfer from a horizontal cylinder buried in a saturated porous medium with a vertical forced flow over the cylinder has been numerically considered. The cylinder surface is at a uniform temperature that is lower than the freezing temperature of the liquid with which the porous medium is saturated and freezing, therefore, occurs around the cylinder. The flow has been assumed to be steady, two-dimensional and laminar and the usual Darcy type assumptions have been adopted. The properties of the unfrozen liquid have been assumed constant except for the density change with temperature which gives rise to the buoyancy forces, this being treated using the Boussinesq approximation. The thermal conductivity of the frozen material has also been assumed constant but is, in general, not the same as the liquid conductivity. Freezing is assumed to occur at a single distinct known temperature. The governing equations expressed in terms of stream function and temperature, have been written in dimensionless form and solved using the finite element approach. Solutions have been obtained for a wide range of the governing parameters for both assisting and opposing flow. The effects of the governing parameters on the mean and local heat transfer rates from the cylinder have been examined.

NOMENCLATURE

B = the buoyancy parameter
c_f = specific heat of fluid
D' = cylinder diameter
g = gravitational acceleration
K = permeability
k_U = effective conductivity of unfrozen porous
= medium
k_F = effective conductivity of frozen porous medium
k_r = ratio of conductivity of frozen porous medium to
= that of unfrozen porous medium
Nu = local Nusselt number based on D'
$\overline{Nu}$ = mean Nusselt number based on D'
Nu_0 = Nusselt number that would exist with no ice
= under the same conditions
Pe = the Peclet number
p' = pressure
T' = temperature
T'_c = cylinder temperature
T'_F = liquid freezing temperature
T'_H = temperature of liquid in freestream ahead of
= cylinder
u' = velocity in x-direction
u'_0 = velocity of liquid in freestream ahead of cylinder
v' = velocity in y-direction
x' = coordinate in vertical direction
x = x' / D'
y' = coordinate in horizontal direction
y = y' / D'
β = coefficient of bulk expansion of fluid
δ = thickness of ice
θ = dimensionless temperature
θ_C = dimensionless cylinder temperature
θ_H = dimensionless liquid temperature
μ_f = viscosity of unfrozen liquid
ρ_f = density of unfrozen liquid
ψ = dimensionless stream function
ψ' = stream function

INTRODUCTION

Freezing in saturated porous media occurs in a number of practical situations. Examples occur in both the natural and artificial freezing of saturated soils, in some energy storage systems and in the transportation of some bulk materials. While the majority of these situations basically involve unsteady heat transfer, the position of the frost line changing with time, there are some situations of practical importance in which the heat transfer is essentially steady, examples occurring in the thawing of naturally frozen soils when structures are mounted in or on them and in some situations when pipes associated with a heat pump system are buried in the ground with a groundwater flow over them. In many such situations, although a forced velocity exists, its magnitude is so small that the buoyancy forces are important, i.e. the heat transfer is by mixed or combined free and forced convection. In order to gain some understanding of such flows, attention has here been given to the case of a horizontal cylinder buried in a saturated porous medium with a vertical forced flow over the cylinder. The forced flow ahead of the cylinder is at a uniform temperature that is higher than the freezing temperature of the liquid. The cylinder surface is at a uniform temperature that is lower than the freezing temperature of the liquid with which the porous medium is saturated and freezing, therefore, occurs around the cylinder. Both the case where the forced flow is vertically downwards, i.e. assisting mixed convective flow, and the case where the flow is vertically upwards, i.e. opposing mixed convective flow, have been considered.

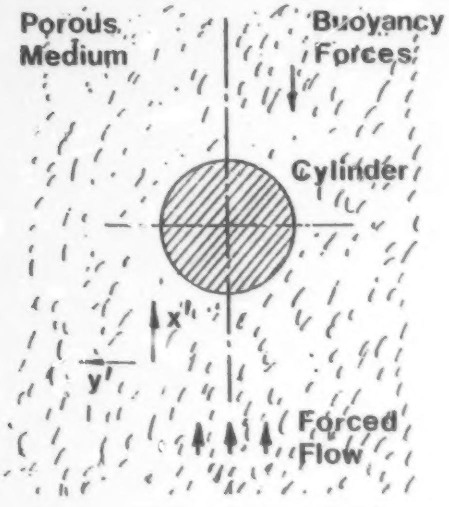

Fig. 1 Flow situation considered

There have been a number of previous studies of freezing in porous media under such conditions that the convective motion is important. Most of this work has, however, been concerned with unsteady heat transfer, the position of the frost line changing with time. Reviews of this work are given in, for example, papers by Frivik & Comini (1982), Goldstein & Reid (1978), Hashemi & Sliepcevich (1973), Takashi (1969) and Weaver & Viskanta (1985). Approximate numerical studies and experimental results for unsteady freezing on a cylinder in a porous medium with a forced flow over the cylinder are given in papers by Okada et al. (1978) and Okada (1980) and some of the results given in these studies for longer times can be compared with the present results for purely forced convection. The effects of free convective motion on steady state freezing in a porous medium filled cavity has been considered, for example, by Oosthuizen (1988), Bejan (1989) and Chellaiah and Viskanta (1989). Forced and mixed convective heat transfer from cylinders in a porous medium with no freezing has been considered in a number of studies, e.g. see Ming-Jer Huang et al. (1986), Oosthuizen (1987), Kuo-Ann Yih et al. (1984), and Cheng (1982). Free convective flow over a cylinder in a porous medium with has been considered by Fand et al. (1986), Merkin (1979) and Ingham (1987).

GOVERNING EQUATIONS AND SOLUTION PROCEDURE

In the unfrozen portion of the flow it has been assumed that the flow is two-dimensional and steady, and that the Darcy type assumptions apply. It has also been assumed that fluid properties are constant except for the density change with temperature which gives rise to the buoyancy forces, this effect being treated using the Boussinesq approximation. The flow has been assumed to be symmetrical about the vertical centre line of the cylinder and the forced flow ahead of the cylinder is assumed to have a uniform velocity and to be at a uniform temperature that is higher than the freezing temperature of the liquid. The cylinder is assumed to be cooled to a uniform temperature that is, in general, lower than the freezing temperature of the liquid.

In the frozen portion of the flow it is assumed that there is, of course, no fluid motion and that the effective thermal conductivity is constant but that this value is, in general, not the same as that for the unfrozen porous medium. It is also assumed that the liquid freezes at a single distinct temperature. It should be noted that because a steady state situation is being considered the freezing temperature alone determines the position of the frost line, i.e. the latent heat does not enter into the analysis.

Using the above assumptions, the governing equations for the unfrozen portion of the flow:

$$\frac{\partial u'}{\partial x'} + \frac{\partial v'}{\partial y'} = 0 \qquad (1)$$

$$\frac{\partial p'}{\partial x'} = - \frac{\mu_f u'}{K} \pm \beta g |(T' - T'_C)| \qquad (2)$$

$$\frac{\partial p'}{\partial y'} = - \frac{\mu_f v'}{K} \qquad (3)$$

$$u' \frac{\partial T'}{\partial x'} + v' \frac{\partial T'}{\partial y'} = \left(\frac{k}{\rho_f c_f} \right) \left(\frac{\partial^2 T'}{\partial x'^2} + \frac{\partial^2 T'}{\partial y'^2} \right) \qquad (4)$$

In eq. (2), the plus and minus signs in the buoyancy term refer to assisting and opposing flow respectively. In the equations, the superficial velocity is, of course, being used. The prime (') is used to denote dimensional quantities. The subscript, f, denotes fluid properties. The coordinate x' is measured in the direction of the forced flow. The boundary conditions on the solution are:

(i) On the surface of the cylinder:

$$T' = T'_C$$

(ii) For $y' = 0$:

$$\frac{\partial u'}{\partial y'} = 0 \quad , \quad \frac{\partial T'}{\partial y'} = 0$$

(iii) At large distances upstream of the cylinder:

$$u' = u'_0 \quad , \quad T' = T'_H$$

(iv) At large values of y':

$$u' = u'_0 \quad , \quad T' = T'_H$$

(v) At large distances downstream of the cylinder:

$$\frac{\partial u'}{\partial x'} = 0 \quad , \quad \frac{\partial T'}{\partial x'} = 0$$

The solution has been obtained by introducing the stream function defined as usual by:

$$u' = \frac{\partial \psi'}{\partial y'} \, , \quad v' = - \frac{\partial \psi'}{\partial x'} \qquad (5)$$

The following dimensionless variables are then defined:

$$\theta = (T' - T'_F)/(T'_H - T'_C)$$

$$x = x'/D' , \qquad y = y'/D' \qquad (6)$$

$$\psi = \psi'/(u'_0 D')$$

Because of the way in which the dimensionless temperature is defined, θ will be zero when the material is at the freezing point.

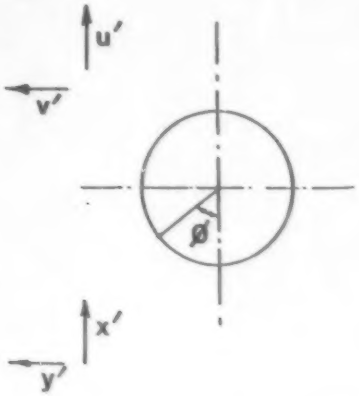

Fig. 2 Coordinate system used

In terms of these variables, the governing equations for the unfrozen material become:

$$\frac{\partial^2 \psi}{\partial x^2} + \frac{\partial^2 \psi}{\partial y^2} = \pm B \frac{\partial \theta}{\partial y} \qquad (7)$$

$$\frac{\partial \psi}{\partial y} \frac{\partial \theta}{\partial x} - \frac{\partial \psi}{\partial x} \frac{\partial \theta}{\partial y} = \left(\frac{\partial^2 \theta}{\partial x^2} + \frac{\partial^2 \theta}{\partial y^2} \right) / Pe \qquad (8)$$

In these equations, Pe is the Peclet number which is given by:

$$Pe = \frac{\rho_f u'_0 D' c_f}{k} \qquad (9)$$

and B is the buoyancy force parameter which is given by:

$$B = \frac{\beta g K \rho_f |(T'_H - T'_C)|}{\mu_f u'_0} \qquad (10)$$

In terms of the dimensionless variables, the boundary conditions on the solution are:

(i) On the surface of the cylinder:

$$\psi = 0, \quad \theta = \theta_C$$

(ii) For $y = 0$:

$$\psi = 0 \quad , \quad \frac{\partial T}{\partial y} = 0$$

(iii) At large distances upstream of the cylinder:

$$\psi = y, \quad \theta = 1 - \theta_C$$

(iv) At large values of y:

$$\psi = y, \quad \theta = 1 - \theta_C$$

(v) At large distances downstream of the cylinder:

$$\frac{\partial \psi}{\partial x} = 0 \quad , \quad \frac{\partial \theta}{\partial x} = 0$$

It has been noted that because of the way in which the dimensionless temperature, θ, is defined:

$$\theta_C = \theta_H - 1 \qquad (11)$$

The governing equations, subject to the boundary conditions discussed above, have been solved using the finite element method. The solution was obtained iteratively, the stream function being set equal to zero if the temperature was below the freezing point and the effective thermal conductivity being taken as either the frozen or unfrozen material value depending on whether the temperature was below or above zero. In this way continuity of heat flow across the frost line was ensured. The solution directly gives the local Nusselt number distribution along the surface of the cylinder, this local Nusselt number being defined by:

$$Nu = q D'/(T'_H - T'_C) k_U \qquad (12)$$

The mean Nusselt number, defined here as:

$$\overline{Nu} = \bar{q} D'/(T'_H - T'_C) k_U \qquad (13)$$

for the cylinder can then then be determined by integration of the local Nusselt number variations.

A number of calculations were undertaken to ensure that the results obtained were essentially independent of the grid size used and of the distances from the cylinder at which the boundary conditions were applied.

RESULTS AND DISCUSSION

The solution has as parameters:

- the dimensionless cylinder temperature (this determines the dimensionless temperature of the liquid ahead of the cylinder), θ_C
- the ratio of the thermal conductivity of the frozen material to that of the unfrozen material, k
- the Peclet number, Pe
- the buoyancy force parameter, B
- the direction of the buoyancy force relative to the forced flow, i.e. whether the flow is assisting or opposing

Solutions have been obtained for Peclet numbers of between 0 and 200 for conductivity ratios of between 1 and 2 for buoyancy force parameters of between 0 and 5 for various dimensionless cylinder temperatures between -0.6 and 0. The material is, of course, completely unfrozen when the dimensionless plate temperature is -1. The variations of mean and local Nusselt numbers have been considered.

The results for purely forced convection, i.e. for B = 0, will first be considered. The variation of the mean Nusselt number for this case with wall temperature and Peclet number is shown in Fig. 3. As the wall temperature is decreased and the thickness of the ice layer about the cylinder increases, the mean Nusselt number is decreased. An attempt has been made to correlate these results by assuming that:

$$Nu / Nu_0 = \text{function } (\theta_C) \tag{14}$$

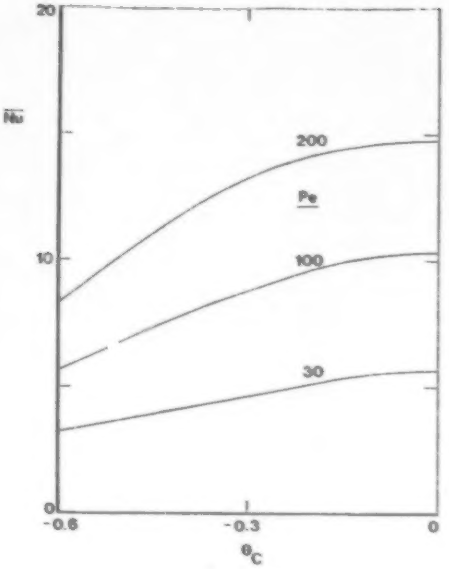

Fig. 3 **Variation of mean Nusselt number for forced convection with dimensionless wall temperature for various Peclet numbers for a conductivity ratio of 1.0.**

The results are presented in this way in Fig. 4. Good correlation of the results for all Peclet numbers is obtained.

The results for mixed convection will next be considered. Fig. 5 shows the variation of mean Nusselt number with buoyancy parameter for a fixed wall temperature and conductivity ratio. It will be seen that in assisting flow the Nusselt number is increased above the forced convective value while in opposing flow it is decreased below this forced convective value. The percentage decrease in the heat transfer rate in opposing flow under the circumstances being considered is somewhat greater than the percentage increase in the heat transfer rate in assisting flow. This is because as the heat transfer rate decreases the ice thickness tends to increase which causes a greater reduction in the heat transfer rate than the increase that results because of the decrease in ice thickness that occurs when the heat transfer rate is increased. The effect of the Peclet number on the results is more completely illustrated by the results given in Fig. 6 which shows the variation of mean Nusselt number with Peclet number for purely forced convection and for assisting and opposing flow for a buoyancy parameter of 2. As the Peclet number decreases and the heat transfer rate tends to be dominated by the thick ice layer the difference between the results in forced, assisting and opposing flows decreases. Again it will be noted that the decrease in heat transfer rate produced by the buoyancy forces in opposing flow tends to be greater than the increase produced by these forces in assisting flow. The effect of cylinder wall temperature on the mean Nusselt number is illustrated by the results given in Fig. 7 which shows the variation of mean Nusselt number with wall temperature for forced convection and for assisting and opposing flow for a buoyancy parameter of 2. As the wall temperature is decreased the effect of the buoyancy forces decreases because the ice layer has become thick and dominates the heat transfer process. The effect of the conductivity ratio on the results can be seen by comparing the results given in Fig. 8 which are for a conductivity ratio of 1.5 with the results given in Fig. 7 which are for a conductivity ratio of 1.0. The results for a dimensionless wall temperature of zero are of course independent of the conductivity ratio since no ice forms under these circumstances. As the wall temperature decreases the decrease in heat transfer rate is seen to increase with increasing conductivity ratio. Lastly, some typical local Nusselt number distributions are shown in Figs. 9 and 10.

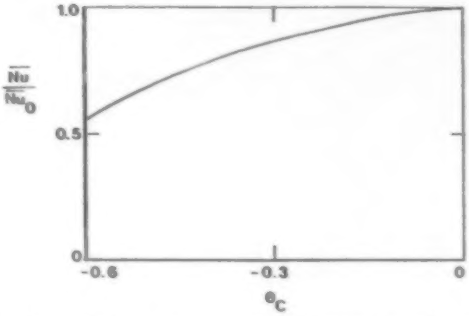

Fig. 4 **Correlation of mean heat transfer rate results**

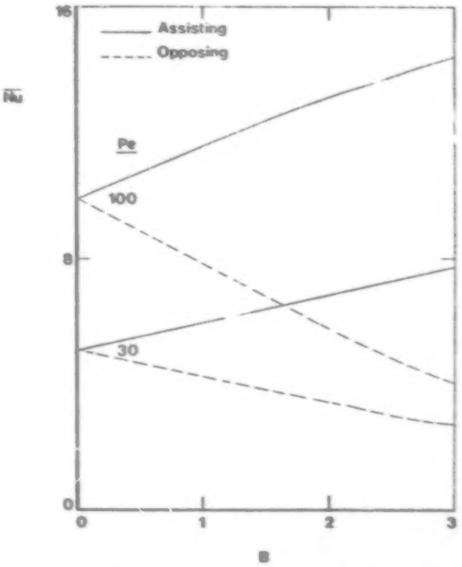

Fig. 5 **Variation of mean Nusselt number with buoyancy parameter for various values of the Peclet number for a dimensionless wall temperature of -0.2 and a conductivity ratio of 1.0.**

These results show that the major effect of the buoyancy forces on the local heat transfer rate occurs near the leading edge of the cylinder. in assisting flow the local heat transfer rate in this area is increased while in

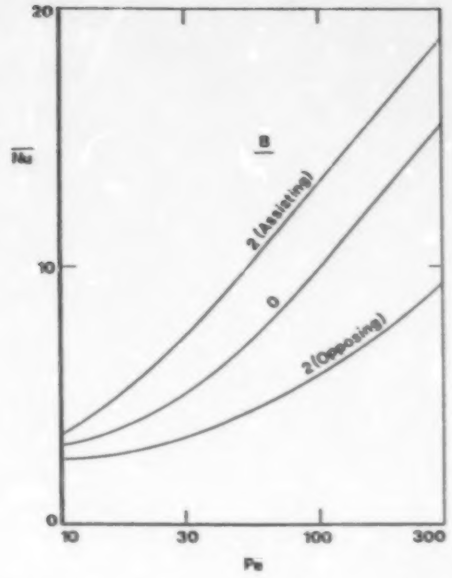

Fig. 6 Variation of mean Nusselt number with Peclet number for various values of the buoyancy parameter for a dimensionless wall temperature of -0.2 and a conductivity ratio of 1.0.

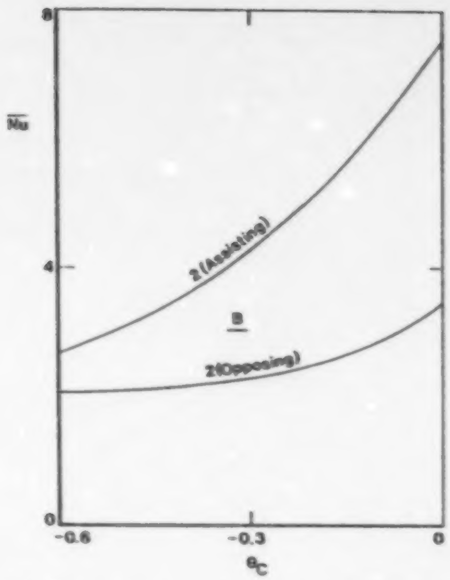

Fig. 8 Variation of mean Nusselt number with dimensionless wall temperature for various values of the buoyancy parameter for a Peclet number of 30 and a conductivity ratio of 1.5.

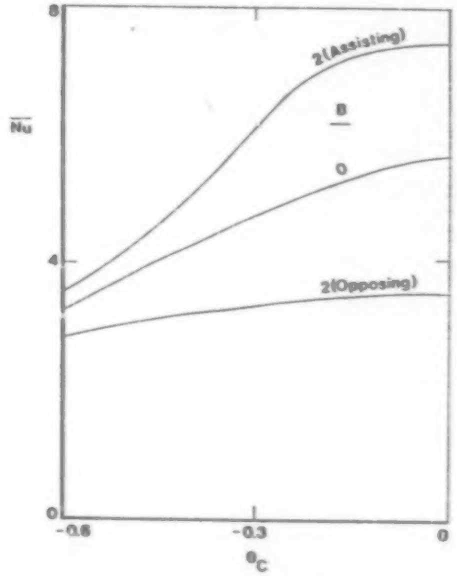

Fig. 7 Variation of mean Nusselt number with dimensionless wall temperature for various values of the buoyancy parameter for a Peclet number of 30 and a conductivity ratio of 1.0.

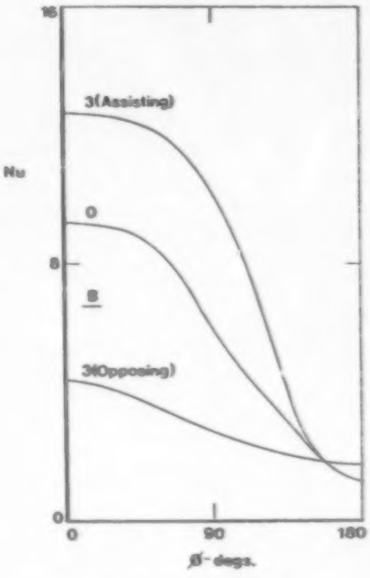

Fig. 9 Variation of local Nusselt number with angular position for various values of the buoyancy parameter for a Peclet number of 30, a dimensionless wall temperature of -0.2 and a conductivity ratio of 1.0.

opposing flow it is considerably decreased. It will also be seen that in opposing flow the buoyancy forces produce a small increase in the local heat transfer rate near the trailing edge of the cylinder.

CONCLUSIONS

The results obtained in the present study indicate that:

- the results for purely forced convection can be adequately correlated by using the form shown in eq. (14)
- the buoyancy forces increase the mean heat transfer rate in assisting flow and decrease it in opposing flow
- the major effect of the buoyancy forces on the local heat transfer rate distribution is near the leading edge of the cylinder

ACKNOWLEDGEMENTS

This work was supported by the Natural Sciences and Engineering Research Council of Canada.

REFERENCES

Bejan, A. 1989, Theory of Melting With Natural Convection in an Enclosed Porous Medium, ASME Journal of Heat Transfer , Vol. 111, pp. 407-415.

Chellaiah, S. & Viskanta R. 1989, Freezing of Water-Saturated Porous Media in the Presence of Natural Convection: Experiments and Analysis, ASME Journal of Heat Transfer , Vol. 111, pp. 425-432.

Cheng, P. 1982, Mixed Convection About a Horizontal Cylinder and a Sphere in a Fluid-Saturated Porous Medium, Int. J. Heat Mass Trans. , Vol. 25, pp. 1245-1247.

Fand, R. M., Steinberger, T. E. & Cheng, P. 1986, Natural Convection Heat Transfer from a Horizontal Cylinder Embedded in a Porous Medium, Int. J. Heat Mass Trans. Vol. 29, (1), pp. 119-133.

Frivik, P.E. & Comini, G. 1982, Seepage and Heat Flow in Soil Freezing, ASME Journal of Heat Transfer Vol. 104, pp. 323-328.

Goldstein, M.E. & Reid, R.L. 1978, Effect of Fluid on Freezing and Thawing of Saturated Porous Media, Proceedings, Royal Society of London , Ser. A, No. 364, pp. 45-73.

Hashemi, H.T. & Sliepcevich, C.M. 1973, Effect of Seepage Stream on Artificial Soil Freezing, ASCE Mechanics and Foundations Division Vol. 99, (1), pp. 267-289.

Ingham, B. D. 1987, Natural Convection about a Heated Horizontal Cylinder in a Porous Medium, J. Fluid Mech. , Vol. 184, 157-181.

Kuo-Ann Yih, Ming-Jer Huang & You-Li Chou 1984, Mixed Convection Flow over a Horizontal Cylinder or a Sphere Embedded in a Saturated Porous Medium, Proc. 4th Int. Conf. Appl. Num. Modelling pp. 704-710.

Merkin, J. H. 1979, Free Convection Boundary Layers on Axi-Symmetric and Two-Dimensional Bodies of Arbitrary Shape in a Saturated Porous Medium, Int. J. Heat Mass Trans. , Vol. 22, 1461-1462.

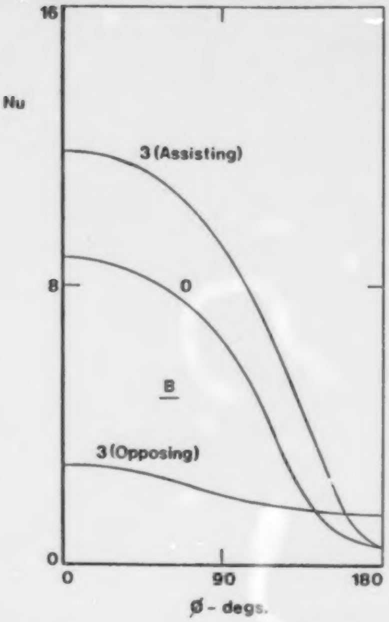

Fig. 10 Variation of local Nusselt number with angular position for various values of the buoyancy parameter for a Peclet number of 30, a dimensionless wall temperature of -0.2 and a conductivity ratio of 1.5.

Ming-Jer Huang, Kuo-Ann Yih, You-Li Chou & Cha'o-Kuang Chen 1986, Mixed Convection Flow over a Horizontal Cylinder or a Sphere Embedded in a Saturated Porous Medium, ASME J. Heat Trans. , Vol. 108, pp. 469-470.

Okada, M., Kimura, K. & Watanbe, I. 1978, Analysis of the Freezing Around a Chilled Pipe in Darcy Flow, Proc. 6th Int. Heat Trans. Conf. , Vol. 3, (EN-6), pp. 31-36.

Okada, M. 1980 Freezing Around Two Cooled Pipes in Darcy Flow, Heat Transfer-Japanese Research , Vol. 9, (3), pp. 54-69.

Oosthuizen, P. H. 1987, Mixed Convective Heat Transfer from a Cylinder in a Porous Medium Near an Impermeable Surface, Mixed Convective Heat Transfer-1987 , ASME HTD-84, pp. 75-82.

Oosthuizen, P.H. 1988, The Effects of Free Convection on Steady State Freezing in a Porous Medium-Filled Cavity, Proc. 1988 Nat. Heat Transfer Conf. , ASME HTD-96, Vol. 2, pp. 321-327.

Takashi, T. 1969, Influence of Seepage Stream on the Joining of Frozen Soil Zones in Artificial Soil Freezing, Special Report No. 103, Highway Research Board, pp. 273-286.

Weaver, J.R. & Viskanta, R. 1985, Freezing of Liquid Saturated Porous Media, Heat Transfer in Porous Media and Particulate Flows ASME HTD-46, pp. 1-8.

MODELLING OF AN INDIRECT NATURAL CONVECTIVE SOLAR RICE DRYER WITH A THERMAL STORAGE BED

P.H. Oosthuizen and H.M. Bashagur

Mechanical Engineering Department
Queen's University
Kingston, Ontario, Canada

ABSTRACT

A simple model of a natural convective solar rice dryer has been extended to include a packed thermal storage bed of small thickness. The system consists of a simple flat-plate collector and a drying chamber which contains the rice and storage beds.

When solar energy is available for collection, the air heated up inside the collector rises as a result of buoyancy and discharges into the drying chamber. It then passes through the storage bed which is located below the rice bed, heats up the rocks, resulting in sensible energy storage due to the heat capacity of the bed material. The air then passes through the rice bed and finally discharges to the outside. The model is based on the assumption that all minor pressure losses are negligible in comparison with the pressure drop across the storage and rice beds, so that the net buoyancy force balances these pressure drops across the storage and rice beds. It is assumed in calculating the drying rate that the air leaving the rice bed is saturated, which means that it is close to the ambient air temperature. The buoyancy effect above the rice is therefore assumed to be negligible in comparsion to that which occurs below the storage and rice beds.

The results obtained using the model show that little improvement in dryer performance results from the use of a storage bed.

1. INTRODUCTION

In many Third World countries rice is still dried by spreading it in a thin layer in the sun on a hard surface, i.e. by using sun drying. This method of solar drying is relatively rapid but does tends to incur quite high losses due to insect infestation, contamination of the rice and, at times, wind loss. These losses can be avoided by using an indirect natural convective dryer. However, the performance achieved with such dryers has not been very satisfactory. One reason for this is that such dryers do not store any energy. It has, therefore, been suggested that their performance could be improved by using a storage bed of the type indicated in Fig.1. In this study this has been numerically investigated.

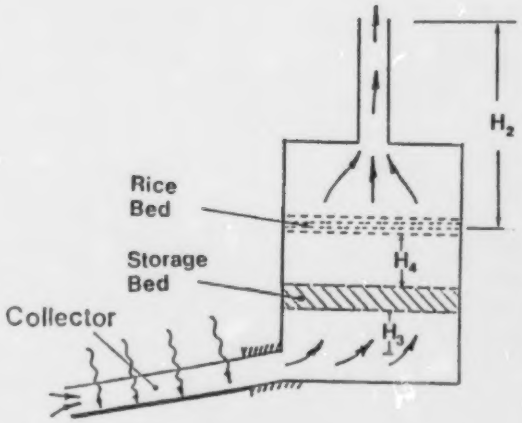

Figure 1 Typical Arrangement of an Indirect Natural Convective Solar Crop Dryer

2. GOVERNING EQUATIONS

In this model, the pressure drop across the storage bed and in the rice bed are being considered and all other pressure losses are assumed negligible in comparsion with these pressure losses.

Considering the above, the net buoyancy forces just balance the pressure drops across both the storage and the rice beds. Since the thickness of storage bed is so small and the rock diameters are assumed small, the storage bed pressure loss is treated in the same manner as the rice bed, i.e. by using a Darcy type model.

Hence assuming that the pressure drop in beds is proportional to the velocity of the air through storage bed, which by the assumptions would be equal to the velocity of the air through rice bed, it follows that:

$$\Delta P = U_d\,(t_r / K_r + t_s / K_s) \qquad (1)$$

Then the buoyancy force-pressure drop balance gives:

$$\beta g \rho \left[(T_a - T_b)(L\,\mathrm{Sin}\theta/2 + H_3) + (T_s - T_a) H_4 \right] = U_d (t_r / K_r + t_s / K_s) \qquad (2)$$

Since the air leaving the rice bed is close to the ambient air temperature, the buoyancy force term, that might occur above the rice bed has been neglected.

The instantaneous thermal efficiency, η for the flat plate solar collector is given by:

$$\eta = q_c / A_c\, q_i \qquad (3)$$

and the energy balance for the collector is given by:

$$q_c = \rho\, U_d\, A_d\, C_p\, (T_b - T_a) \qquad (4)$$

Equations 3 and 4 are sufficient to determine the temperature of the air leaving the collector.

The above equations contain the collector efficiency, η, as a variable. Assuming that the temperature rise along the collector is sufficiently small, so that a linear loss term can be assumed, then the efficiency takes the simple form:

$$\eta = A - B\,(T_p - T_a) / q_i \qquad (5)$$

Now, the rate of heat transfer between the collector plate and the air passing through the collector is given by:

$$h\,A_c (T_p - T_a) = A_c\, \eta\, q_i \qquad (6)$$

Equations 5 and 6 can then be combined to give:

$$\eta = A h / (B + h) \qquad (7)$$

Thus, the collector efficiency at which the dryer operates will depend on the value of h, which mainly depends on the mean air velocity through the collector and the buoyancy force in the collector.

If the value of the buoyancy force in the collector is considered to be small compared to that which occurs below storage and rice beds, then the flow of air along the collector follows laminar flow behavior. Therefore, the boundary layer assumptions can be applied, which indicate that the heat transfer coefficient h between the collector plate and the air passing through it is proportional to the square root of the Reynolds number based on the mean air velocity and the length of the collector. Thus,

$$NU_L = C\,(Re_L)^{0.5} \qquad (8)$$

Applying the continuity equation between the collector and drying chamber gives:

$$U_c\, a_c = U_d\, a_d \qquad (9)$$

From equations 8 and 9 it follows that:

$$h = C\,K_a (a_d / a_c)^{0.5} (Re)^{0.5} \qquad (10)$$

where Re is the Reynolds number based on the air velocity in drying chamber.

Equations 2 ,3 ,and 4 are sufficient to define the velocity of the air in drying chamber as follows:

$$Re^2 = (\beta g \rho^2/\mu^2) \left[L^4/K_a (H_3/L + \mathrm{Sin}\theta/2)(W/A_d) (\eta\, q_i K_a / C_p) + Re\, L\, (T_s - T_a) H_4 \right] \left[K_r\, K_s / (K_s t_r + K_r t_s) \right] \qquad (11)$$

This equation allows the air flow rate through the dryer, for any known insolation value, to be determined.

Since the collector efficiency is dependent on h, equation 7, and h depends on the induced velocity, equation 10, an iterative solution procedure must be used, starting by assuming value for the collector efficiency, η and the flow rate is calculated. This allows Re to be found and an improved η value can then be determined and the whole procedure repeated until convergence is achieved.

Before considering the drying process, the rate of change of storage bed temperature must be evaluated. This can be done by applying the energy balance on the storage bed, which gives:

$$\rho\, U_d A_d C_p (T_b - T_s) = M_s C_s\, dT_s/dt \qquad (12)$$

The enthalpy gain in the solar collector will be:

$$\dot{m}_a(h_b - h_a) = \eta\, q_i A_c \qquad (13)$$

and for the storage bed:

$$\dot{m}_a(h_a - h_b) = M_s C_s\, dT_s/dt \qquad (14)$$

Equations 13 and 14 give:

$$h_s = h_a + \eta\, q_i A_c / \dot{m}_a + (M_s C_s\, dT_s/dt)/\dot{m}_a \qquad (15)$$

Equation (12) defines the temperature of the air entering the rice bed. Since its initial moisture content is known from ambient conditions and assuming that the air leaving the rice bed is saturated, as shown diagramaticlly on a psychometeric chart in Fig.2, i.e. point c, the rate at which moisture removed can be found using

$$m_r\, dM/dt = \dot{m}_a(W_{out} - W_a) \qquad (16)$$

The calculation is ended when the moisture content has dropped to 12% which is close to the Equilibrium Moisture Content.

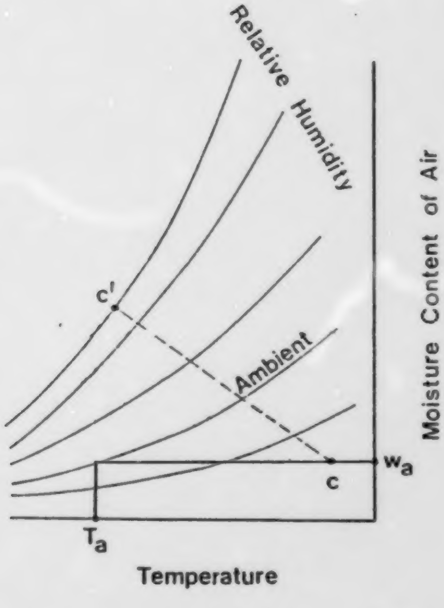

Figure 2. Conditions of the air in rice bed

3. COMPUTATIONAL PROCEDURE

A computer model of a natural convective solar rice dryer containing a storage bed based on the equations given in the previous section has been developed. Beside the dimensions of the dryer, this program requires as inputs, the rice bed loss factor, K_r, the storage bed loss factor, K_s, the rice density, ρ_r, the density of storage material, ρ_s, the collector performance parameters, A, B, and C, as well as the variations of the insolation, q, with time, and the relative humidity and the temperature of the ambient air, T_a.

In applying the model the following values have been assumed for these qualities:

$K_r = 0.0005\ m^2/P$
$K_s = 0.0007\ m^2/P$
$\rho_r = 600\ kg/m^3$
$A = 0.56$
$B = 4.31$
$C = 1.1$
$RH = 50\ \%$
$T_a = 30\ C^\circ$

The values of K_r and ρ_r are taken from [5], while the values of A, B, and C, are based on typical observed collector performance as indicated in Fig. 3, which is based on values given in [6]. The value of K_s is assumed.

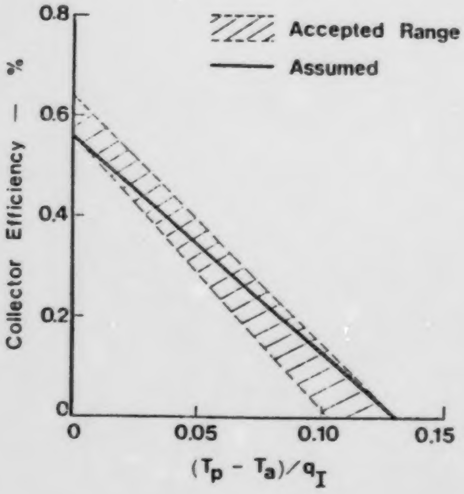

Figure 3. Assumed collector performance

With the above specified quantities and at each time at which q is specified, equations 1 through 11 can together be solved to give T_b, the mass flow rate through the dryer and the collector efficiency, η.

Depending on the value of T_b, the new storage temperature, $T_s(i+1)$, at the end of the time step is calculated, using equation 12. The drying rate, dM/dt, can then be calculated using equations 13 through 16.

Using the values of the drying rate so found, the variation of the rice moisture content, M, with time can be determined. This procedure is only applied until M has dropped to some specified minimum value which has been taken as 12 %.

4. RESULTS

The dimensions of the dryer used in the calculations are similar to those described by Bassey (1982) and Whitfield (1985). The collector was 0.7 × 0.7 m with a gap between the collector plate and the glass cover of about 40 mm. The dryer chamber was about 0.9 × 0.9 m in cross section.

The results obtained strongly suggests that the most important factors that limit the performance of the existing dryer were :

- The height of the storage bed above the collector outlet.
- The height of the rice bed above the storage bed.

In addition to the parameters mentioned above, the following fixed values were under taken :

Rice-bed thickness =40 mm
Storage bed thickness =60 mm
Density of the rocks = 2500 Kg/m^3
Specific heat of the rocks =0.88Kg/KJ C°
Ambient air temperature = 30 C°
Ambient relative humidity = 50 %
Initial rice moisture content = 30 %
Initial storage temperature is equal to the ambient air temperature. The insolation values used were the same as those given by Bassey (1982).

Before starting the drying process, the storage bed is charged continuously for 2-days, without loading the dryer with the rice, by the energy gained in the solar collector.
In this case a high flow rate would be expected, as a result of the increase in the buoyancy force term that would occur above storage bed. The calculations showed little improvement in the dryer performance as a result of this charging see Fig.4.

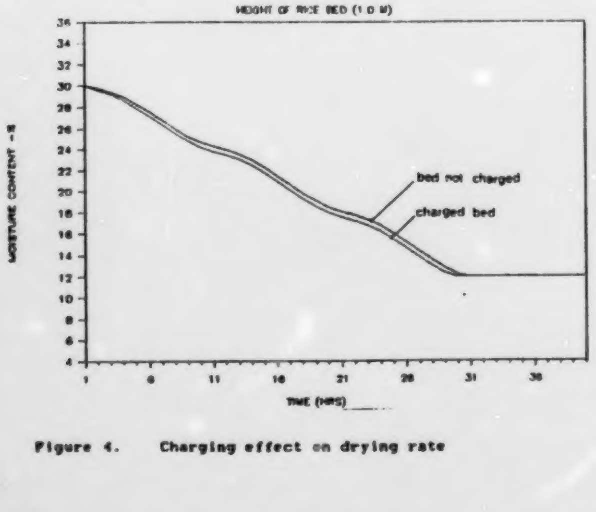

Figure 4. Charging effect on drying rate

Assuming, the dryer to be perfectly insulated,this stored energy could be used on cloudy days and at night, in this case the storage bed operates under discharging mode.

A study of the effect of the height of the storage bed above the collector outlet (H3) on dryer performance Fig. 5 , using the specified collector, showed significant improvement in dryer performance with increasing (H3) .

Figs. 6 through 10, show the effect of the height of the rice bed above the storage bed (H4), for different storage bed locations above collector outlet. A significant improvement in dryer performance with increasing (H4) up to value of 2 m was noted. However, little improvement in performance was found for (H4) values greater than 2 m .

However, a combination of 1.5 m storage bed to collector outlet height with 1.0 m rice to storage bed distance gives some improvement in performance over the natural convective rice dryer with no storage as shown in Fig. 11 .

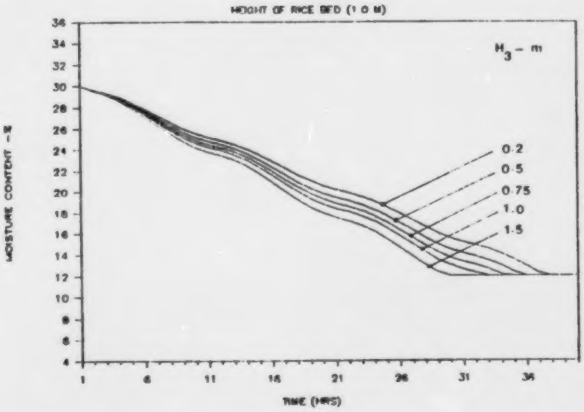

Figure 5. Effect of storage bed height on performance

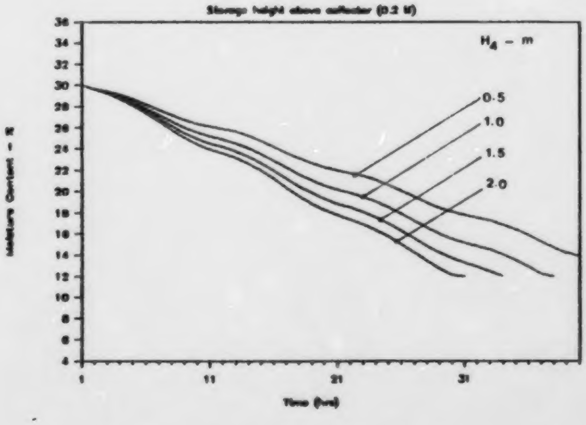

Figure 6. Effect of rice bed height on performance

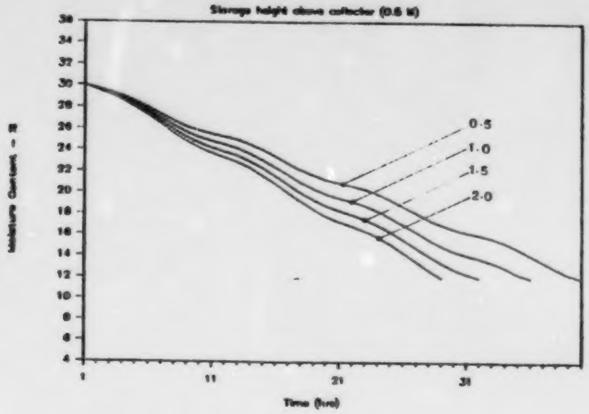

Figure 7. Effect of rice bed height on performance

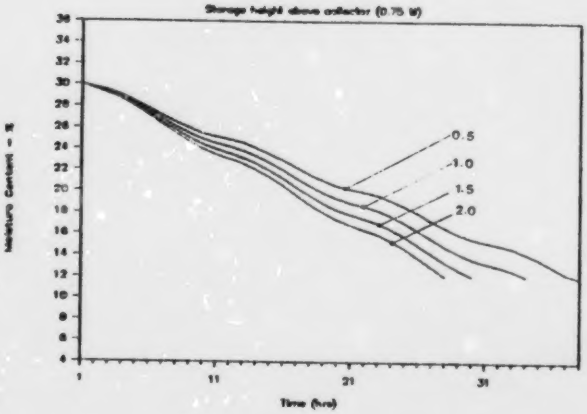

Figure 8. Effect of rice bed height on performance

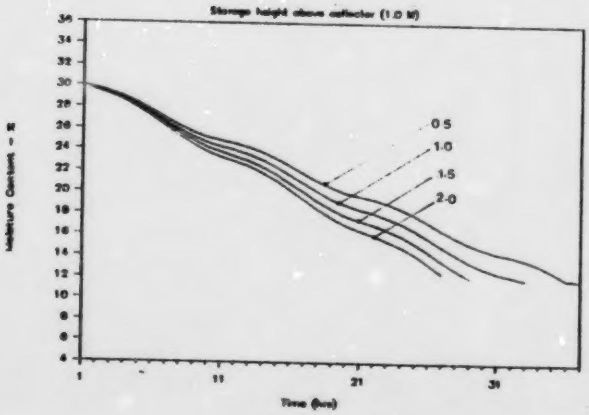

Figure 9. Effect of rice bed height on performance

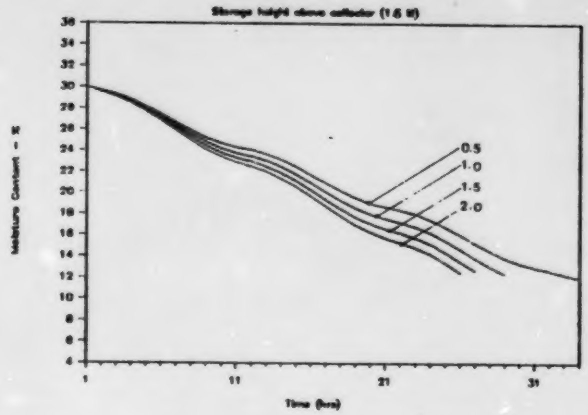

Figure 10. Effect of rice bed height on performance

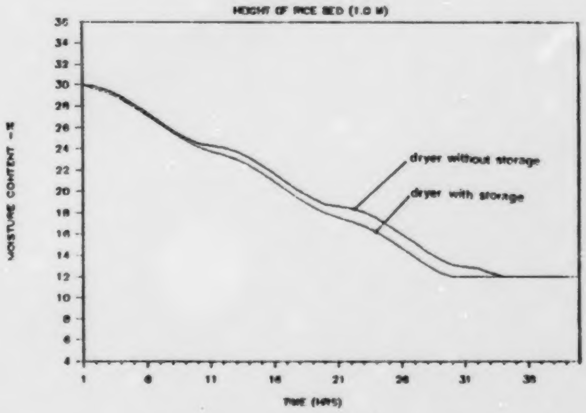

Figure 11. Comparison between performance of storage and non-storage dryers

5. CONCLUSIONS

The results given by the present analysis suggest the following:

The storage bed should be placed at least 1.0 m above the collector outlet.

The rice bed should be placed at a height of 1.0 m above the storage bed .

The sensible energy stored in the bed can roughly be used alone without any values for (q_1), for 2-days continuously with maximum 3% reduction in the rice moisture content.

The main conclusion is that a storage bed as described here does not produce much improvement in dryer performance.

6. ACKNOWLEDGEMENT

This study was supported by the International Development Research Center of Canada.

7. REFERENCES

1. Bassey, M. W. Potential Use and Performance of Indirect Free Convective Solar Crop Dryers in Sierra Leone, IDRC Report No.3-P-78-0113, 1982.
2. Whitifield, M. J. C. C., Limiting Performance and Potential of Free Convective Solar Crop Dryer in Sierra Leone, IDRC Report No.3-P-83-0107-01, 1985.
3. Oosthuizen, P. H. A Numerical Study of the Performance of Natural Convective Solar Rice Dryers. Presented at the Fifth International Drying Symposium, Cambridge, Massachusetts, 13-15, August 1986.
4. Oosthuizen, P. H., Preston, E.G.A., Bassey, M. Numerical Simulation of a Natural Convection Solar Rice Dryer. Proceedings of the 7th Miami International Conference on Alternative Energy Sources, Miami, Florida, 9-11, December 1985. pp.505-508.
5. Excell,R. H. B., Basic Design Theory for a Simple Solar Rice Dryer, Renewable Energy Review Journal, vol. 1, no. 2, pp. 1-14,1980.
6. Sayigh, A. A. M., The Technology of Flat Plate Collectors in Solar Energy Conversion -An Introductory Course, eds. A. E. Dixon and J. D. Leslie, pp.101-124, Pergamon Press, Toronto, 1969.

8. NOMENCLATURE

A,B - constants in collector equation
A_c - collector area
A_d - area of drying chamber
a_c - collector flow area
a_d - drying chamber flow area
b - collector gap size
C_p - specific heat of air
C_s - specific heat of the rocks
g - gravitational acceleration
H_3 - height of storage bed above collector outlet
H_4 - height of rice bed above storage bed
H_a - enthalpy of ambient air
H_b - enthalpy of air leaving the collector
H_s - enthalpy of air leaving storage bed

h - heat transfer coefficient between collector plate and air
K_r - rice bed pressure drop coefficient
K_s - storage bed pressure drop coefficient
K_a - thermal conductivity of air
L - lenght of collector
M - moisture content of rice on dry basis
m_r - mass of dry rice in bed

$\dot{m}_a$ - air mass flow rate through dryer

NU_L - hL/K_a

q_i - insolation

Re_L - $U_c L/\nu$

T_a - ambient air temperature
T_b - temperature of air leaving collector
T_p - temperature of collector plate
T_s - temperature of air leaving storage bed
t_r - thickness of rice bed
t_s - thickness of storage bed
U_d - mean air velocity in drying chamber
U_c - mean air velocity in collector
W - width of the collector
W_a - moisture content of air at ambient conditions
W_{out} - moisture content of air at exit of rice bed
β - bulk coefficient of expansion of air
ΔP - pressure drop across both rice and storage beds
η - collector efficiency
θ - angle of inclination of collector
μ - absolute viscosity
ρ - density of air
ρ_r - density of rice
ρ_s - density of rocks

Time Based Signal Analysis for the Detection of Intermittent and Impact Noise and Vibration

Jimi S.Y. Tjong
Ford Motor Company

Hugh W. Miller
Dr. Zygmunt Reif
Dr. Robert Gaspar
Mechanical Engineering Department
University of Windsor

ABSTRACT

This paper describes the use of time based signal analysis methods such as the energy envelope, time domain averaging and variance analysis. These methods are applied to analyze vibration signals that are semi periodic in nature i.e. the faults occasionally appear and disappear. These time based methods provide time histories of the change in a signal from moment to moment or from cycle to cycle and can reveal the cycle position and signal strength associated with the problem. Some examples of the application of these methods are also presented as applied to an internal combustion engine.

INTRODUCTION

With the advent of more stringent external noise legislation and the demand for lower interior noise levels, vehicle manufacturers are under increasing pressure to reduce the emitted noise from their engines. This paper describes time based signal analysis techniques which can be applied as a diagnostics tool for detection of faults which result in noise of internal combustion engines.

The potentials of signal analysis as a diagnostic tool have been recognized, it is the recent developments in computers which extend the capabilities of signal processing and hence the diagnostic capabilities.

Most rotating machines mainly generate repetitive signals roughly periodic in nature. The common method now use for analyzing these signals is based on decomposition into harmonic components. Many manufacturers produce efficient Fast Fourier Transform based analyzers for the above purpose. Another method is based on time domain averaging which is capable of extracting periodic components of the signals.

The time based signal processing techniques are extremely valuable because of their abilities to correlate the amplitude of the signals at corresponding angular positions. The variance analysis is based on a signal decomposition into periodic and non-periodic components. This method proves to be useful in detecting minor random effects associated with almost periodic signals. This is clearly illustrated by the use of variance analysis in detection of piston noise. Another method used is the energy envelope . Hilbert transform is a pricipal step in taking a time signal and calculating what is called an energy envelope. This envelope contains information about abrupt changes in signal energy content and hence it is well suited for the detection of signals that involve impacts.

SIGNAL PROCESSING TECHNIQUES

In the field of mechanical signature analysis, a complex signal is composed of three main components (a) the periodic, (b) the semi-periodic and finally (c) noise.

TIME DOMAIN AVERAGING (TDA)

Time domain averaging (TDA) is a powerful technique for extracting periodic components from a raw signal. It is accomplished by simply averaging several time traces, data point by data point, producing an average time trace. It is useful for detection of faults which occur consistently at a certain locations in a cycle. However, it is not necessarily useful in the detection of semi-periodic faults but it is an essential step in the process. A mathematical description of the TDA, including its properties as a filter in eliminating non cycle linked signals, is provided in the reference (1,2).

VARIANCE ANALYSIS

In the last section time domain averaging was described, which allows the extraction of periodic components which are always present in a signal. Other components, which are not always present but occur at specific positions in a cycle, are termed as semi-periodic. These types of signal can be valuable in detecting faults such as bearing defects, piston slap, and etc..
The mathematical development of the variance method can be found in reference (1) and examples of its use are presented in reference (2,3). The basic equations needed to perform this analysis are briefly described below:

$$AV(X(i)) = Y(i) = \frac{1}{m}\sum_{r=0}^{m-1} X(i)$$

$$Z(i) = VAR(X(i)) = AV\left((X(i) - Y(i))^2\right)$$

where

m = the number of traces collected

i = the index for vector data points

r = the index of a particular trace

$X(i)$ = the ith component of a vector X

$Y(i)$ = the average vector for all traces X

$Z(i)$ = the ith component of the variance vector

In these computations the removal of the periodic function is accomplished, and by squaring the result, the semi-periodic function information is exaggerated. This exaggeration protects the semi-periodic information from filtering out, while at the same time noise components converge to a specific constant value over the whole variance vector.

HILBERT TRANSFORM AND ENVELOPE DETECTION

The Hilbert transform is a principal step in taking a time signal and calculating what is called an energy envelope. This envelope contains information about abrupt changes in signal energy content. It is therefore well suited for the detection of signals that involve impacts or bursts. Mathematically, the Hilbert transform is formed from a transform of a real valued time series. If the Hilbert transform is added appropriately to the original time signal, it forms a complex value time series known as as analytic signal.

$$f_a(t) = f(t) + j\tilde{f}(t)$$

where

$f_a(t)$ = is the analytic signal

$f(t)$ = is the original time signal

$\tilde{f}(t)$ is the actual hilbert transform

The analytic signal has the following Fourier Transform properties

$$F(f_a(t)) = \left\{\begin{matrix} 2F(f(t)) \text{ for } f > 0 \\ F(f(t)) \text{ for } f = 0 \\ 0 \text{ for } f < 0 \end{matrix}\right\}$$

The rigorous mathematics which lead to these equations are described in reference (4).

These last equations suggest a method for the quick calculation of the Hilbert transform by using the Fast Fourier Transform (FFT). The time signal is first acquired and an FFT is performed on the signal. The parts of the FFT representing positive frequency values are increased by a factor of 2, except that which corresponds to a frequency of 0 which remains at its initial value. The parts of FFT representing the negative frequency values are set to 0. Then an Inverse FFT is performed, providing the analytic signal of which the Hilbert transform is the imaginary portion.

The energy envelope or the amplitude modulation curve, as it is sometimes called, is nothing more than the magnitude of the analytic signal.

MEASUREMENT SYSTEM

Time domain averaging , variance analysis and envelope detection techniques require that the beginning, end and each individual data point of the sampled signal be referenced to some event or time after / before an event. In this way, significant changes in the raw signal or processed time signal (TDA, variance and energy envelope traces) can be linked to specific events in a machine.
In an internal combustion engine, events are generally referenced to either crankshaft or camshaft angle. Furthermaore, data are usually collected for one complete engine cycle. The trigger event used in this measurement system is the firing of number 1 sparkplug of the engine. This generally occurs at a certain number of degrees

before top dead center of the piston's power stroke and this angle can be easily obtained by a device attached to the crankshaft itself. From here, it is simple to determine at what time after the firing of number 1 sparkplug the top dead center occurs, provided that the engine speed is kept constant.

Measurement data is obtained from accelerometers which were attached to the each cylinder wall of the engine block. The measurement system consists of transducers, a programmmable filter, an analyzer and an instrument controlller (computer) as illustrated in Figure 1. The data acquisition begins with transducers placed as described previously. The data passess through the filter where alias frequencies are removed. After triggering, the data is then collected by digital sampling of the analyzer. The digitized data is then transferred over an IEEE-488 interface to the computer and then stored on disk for permanent record. The computer controls the measurement system by setting the sampling rate, the total sampling time, the filter cutoff frequencies, activation of the trigger and systematic acquisition of the data. The system first averages data by continously transferring time traces and performing a point by point average (TDA). Then it acquires 25 separate time traces and stores this information with TDA on a disk. Post processing of these data is later carried out to obtain the variance and energy envelope data.

RESULTS AND DISCUSSIONS

At present, many engine manufacturers conduct a subjective analysis of piston noise, relying on the hearing capabilities of experienced engineers and technicians. This often complicates the process of correlating a signature analysis technique against piston noise. Two engines were analyzed using time domain averaging, variance analysis and energy envelope methods. Both these engines produced audible piston noise and could be very annoying at certain engine speed and load conditions.

Figure 2 and 3 show the TDA data of cylinder 6 and 5 respectively. Figure 4 and 5 show the variance data for cylinder 6 and 5 respectively. Figure 6 and 7 show the energy envelope data of cylinder 6 and 5 respectively. Figures 2 to 7 present all the data collected from engine number 1 where piston no.6 was the cause of the noise generated. In this case the piston noise occurs semi-periodically either in terms of amplitude or the time of occurrence. Consequently, the time domain averaging data will not show the noise. The Variance data as well as the energy envelope data show the significant difference between the cylinder no.6 and cylinder no. 5.

In the second engine, piston number 1 is grossly out of specification in dimensions. The noise generated by this piston occurs in one particular crank angle in the engine cycle but the amplitude of the noise varies from cycle to cycle. All the three methods i.e., time domain averaging, variance analysis and energy envelope analysis can be applied effectively in this case as illustrated by Figure 8 to 13.

CONCLUSIONS

The results indicate that the time based signal analysis techniques, such as the time domain averaging, variance analysis and the energy envelope analysis, provide valuable information on the relation between signal amplitude and rotational angle of machines. The combination of these techniques can be applied in analyzing most complex signals including periodic, semi periodic and transient types. Detailed information of such signals cannot be obtained by conventional spectral analysis techniques.

REFERENCES

1. Braun, S., Seth, S., 1977, Signature Analysis Methods and Apllications for Rotating Machines, ASME Publication 77-WA/AUT-5, 8 pages.

2. Braun, S., Seth, S., 1980, Analysis of Repetitive Mechanism Signatures, J. of Sound and Vibration, 70 (40), pp 513-526.

3. Seth, S., Field, N., 1984, Oil Pressure Signatures for Engine Lubrication System Monitoring, SAE Paper 840063, 8 pages.

4. Bendat, J., 1981, The Hilbert Transform and Applications to Correlation Measurements, Bruel and Kjaer Press.

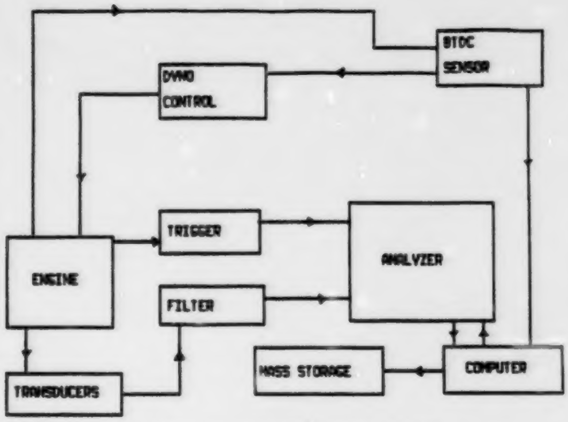
BTDC
SENSOR
DYNO
CONTROL
TRIGGER
ANALYZER
ENGINE
FILTER
MASS STORAGE
COMPUTER
TRANSDUCERS

Figure 1: The Measurement System

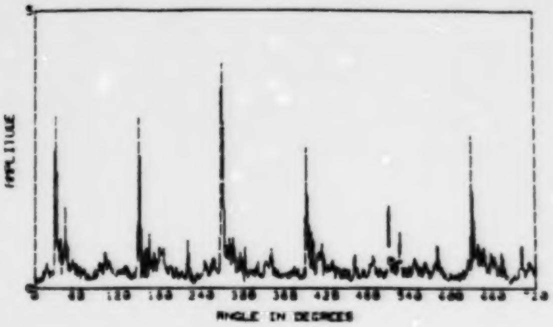

Figure 4: Variance Data, Cyl. No.6
Engine No.1

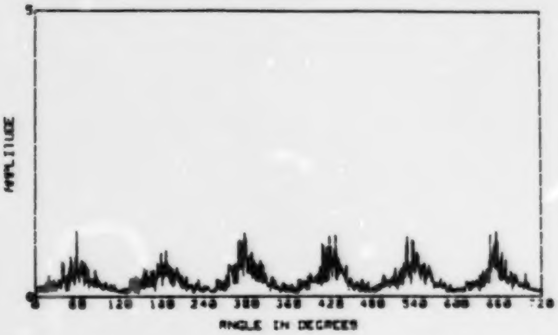

Figure 5: Variance Data, Cyl. No.5
Engine No.1

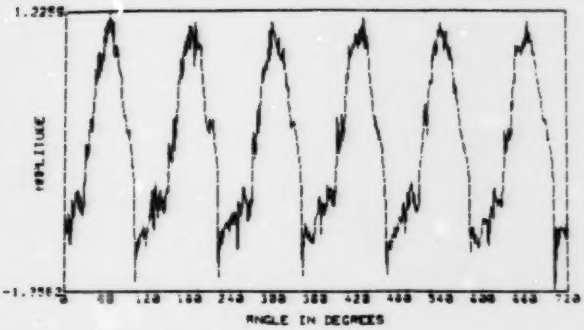

Figure 2: TDA Data, Cylinder No.6
Engine No.1

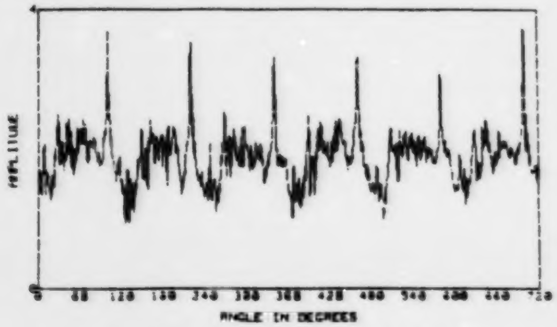

Figure 6: Energy Envelope Data, Cyl. No.6
Engine No.1

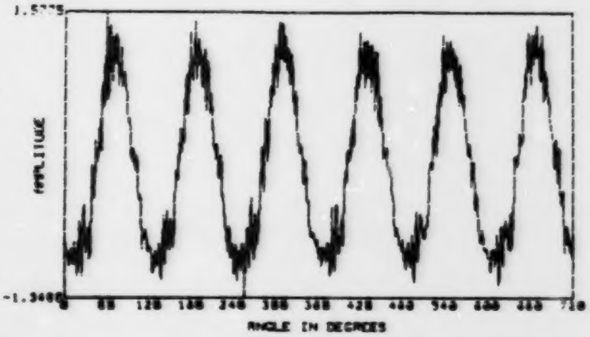

Figure 3: TDA Data, Cylinder No.5
Engine No.1

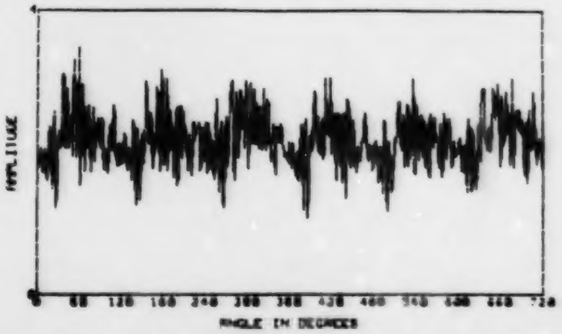

Figure 7: Energy Envelope Data, Cyl. No.5
Engine No.1

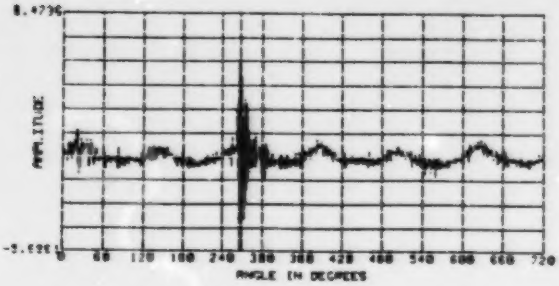

Figure 8: TDA Data,Cylinder No.1
Engine No.2

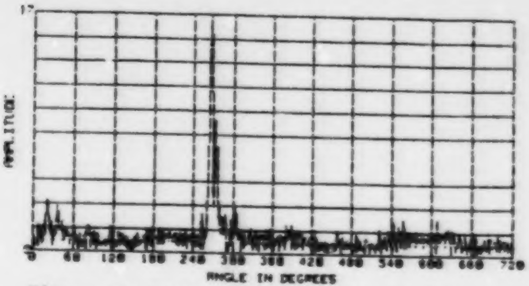

Figure 12: Energy Envelope Data,Cyl.No.1
Engine No.2

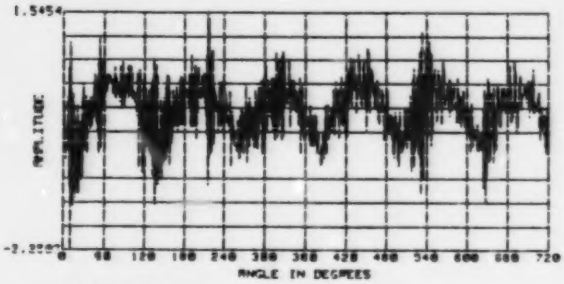

Figure 9: TDA Data,Cylinder No.4
Engine No.2

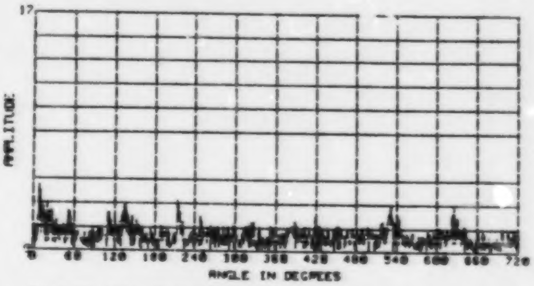

Figure 13: Energy Envelope Data,Cyl.No.4
Engine No.2

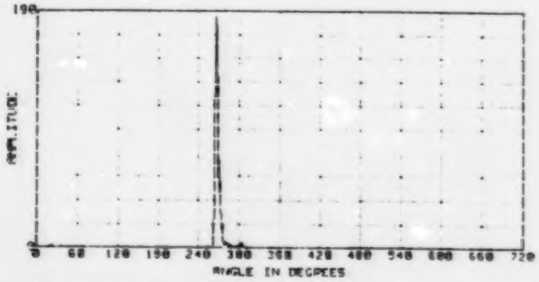

Figure 10: Variance Data,Cyl. No.1
Engine No.2

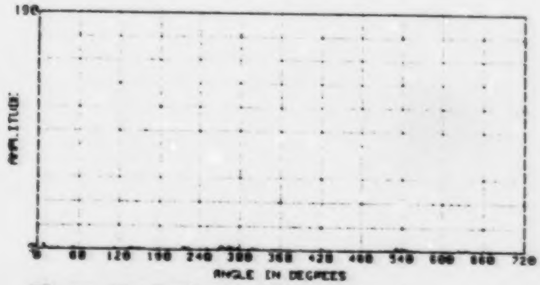

Figure 11: Variance Data,Cyl. No.4
Engine No.2

THE DETERMINATION OF MILLING CUTTER TOOL CONDITION USING VIBRATION SIGNALS

T.N.Moore,Associate Professor
J.Pei,Graduate Student

Department of Mechanical Engineering
Queen's University
Kingston, Ontario, Canada

Abstract

A necessary first step in the implementation of any automated, real-time diagnostic system is to identify measurement parameters and analysis techniques which will permit failure diagnosis to be performed reliably. This paper investigates the possibility of using vibration signals to detect failure of a multi-insert face mill. Tests were performed using a three-insert face mill to machine a standard workpiece. Cutting inserts with known amounts of edge fracture or wear were used, in various combinations, during the milling process. The resulting vibration signals, obtained both on the workpiece and the clamping fixture, were analysed to determine both the type and severity of insert failure that can be recognized using various signal analysis methods. It is shown that both edge fracture and wear can be detected, albeit with varying degrees of confidence.

1. Introduction

A major component of any effort to develop intelligent and flexible automation systems must be the concurrent development of automated, diagnostic systems to handle machinery maintenance and process control functions. In the short term such systems promise major gains in productivity and product quality. In the longer term, such diagnostic systems are one of the enabling technologies for the "lights out" factory.

An important element of the automated process control function is the real-time detection of cutting tool failure, including both wear and fracture mechanisms. The ability to detect such failures "on-line" would allow remedial action to be undertaken in a timely fashion, thus ensuring consistently high product quality and preventing potential damage to the process machinery.

Of all the metal removal processes employed in industry, by far the most prevelant are those of drilling and milling.

A number of researchers [1-3] have investigated the potential for on-line diagnosis of drill failure (particularly drill breakage) and several commercial systems are, in fact, presently available.

However, far less emphasis has been placed on the real-time detection of milling cutter failure. For this reason the present study will focus on milling operations, particularly that of face-milling.

2. Automated Tool Condition Monitoring

The basic premise of any automated, real-time tool condition monitoring system is that there exists either a directly measurable, or a derived parameter, which can be related to advancing tool wear and/or breakage. Obviously the most desirable monitoring system would be capable of detecting both types of failure successfully.

In the ideal case, the system should be able to detect levels of wear well below those at which the tool would have to be replaced, and should also be sensitive to relatively small changes in the level of wear. The latter characteristic would provide the system with the potential to "trend" the wear pattern and predict the amount of useful life left in the tool (allowable wear limit reached). With respect to tool fracture, the system should be able to detect both small fractures, "chipping" phenomena, and catastrophic failure of a tool. Althought prediction of such failures would be desirable, it is problematic whether this is a practical goal, at least in the near future. The number of variables which determine the actual occurrence of tool fracture together with their complex interactions, and in many instances their underlying stochastic nature, make reliable prediction capabilities, at best, a long-term prospect in tool monitoring systems.

System Characteristics

Figure 1 shows the block diagram of a generalized tool condition monitoring system [4].

In the "measurement" section the physical parameter (or possibly, parameters) of interest is converted to a form which is appropriate for further manipulation by the system (generally a digitized representation of an electric analog signal).

Within the "processing" section various techniques are implemented in order to suppress noise, compress information and emphasize important features of the acquired signals. Typical methods include analog or digital filtering, time domain averaging, Fourier transformation, parametric identification based on ARMA models, etc. Table 1 is adapted from Braun [4] and provides

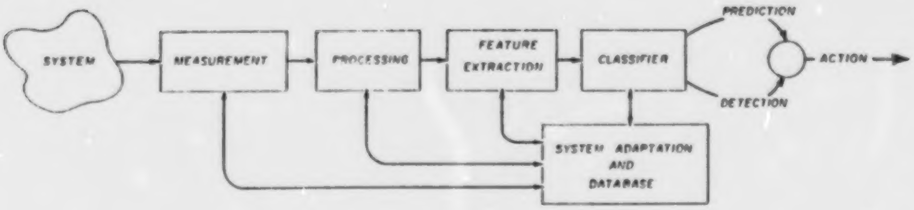

Fig. 1 Generalized Tool Condition Monitoring System.

a qualitative comparison of some processing techniques relative to their data reduction efficiency and pattern recognition value.

The purpose of the "feature extraction" section is to obtain a specific feature, or features, (often referred to as a feature vector) which can be used by the "classifier" to determine the specific type of failure and initiate appropriate corrective actions. Examples of features would include: total power of the signal, crest factor value, power in a particular frequency range, frequency of the maximum peak, amplitude of the maximum peak, the autoregressive parameters of the ARMA model, etc. If multiple features are employed they should be uncorrelated so that they provide independent indications of tool failure. When coupled with a hierarchical decision tree structure in the "classifier", such multiple feature vectors can greatly improve the reliability of the tool monitoring system.

The "adaptation and database" section should not only efficiently manage all data storage and manipulation requirements but also provide the system, to as great a degree as possible, with the ability to learn from experience.

Table 1 Relative Merits of Processing Techniques

Processing Technique	Data Reduction	Pattern Recognition
Time Domain		
Raw Signal	None	Variable
Filtered Signal	Poor	Variable to Good
Averaging	Medium	Good
Frequency Domain		
High Resolution Spectra	Medium	Good
Broad-Band Spectra	High	Variable to Poor
Amplitude Domain		
Probability Functions	Medium	Poor
Peak, r.m.s.	Extreme	Poor
Crest Factor, Kurtosis	Extreme	Variable
Cepstrum	Medium	*
Correlation	Medium	*
Variance	Medium	*
Moments	High	*

*Insufficient Experience

Measurement Parameters

Up to this time, the parameter(s) used to develop the feature vector is other than a direct measure of tool wear or breakage (although work by Lee and others [5] has begun to investigate this possibility) and is acquired during the actual machining process.

A number of parameters have been studied to determine their suitability as indicators of cutting tool failure including cutting forces [6-8], spindle motor current [9], acoustic emissions [10,11], cutting tool temperature [12] and noise [13]. These methods have achieved varying degrees of success.

An additional parameter which has a number of practical advantages is vibration. Accelerometers, the transducers most often used for the vibration measuring task, are small, rugged, reasonably inexpensive, and easily mounted near the cutting process. In addition, they are available with various sensitivities and frequency response ranges.

Research carried out by Mehta, Pandey and Chakravarti [14] and Grieshaber, Ramalingam and Frohrib [15] has indicated that vibration signals certainly could form the basis of a tool condition monitoring system for face-milling operations. However, this work was carried out for a single-tooth mill which is not particularly representative of the multi-insert face-mills actually employed in industry.

3. Objective

The objective of the present study, then, is to investigate the possibility of using vibration signals generated during interrupted face-milling to detect tool failure on multi-insert milling cutters.

This paper will report on the methodology and initial results of cutting tests employing inserts with known degrees of wear or breakage. Preliminary analyses of these signals in the time and frequency domains will also be presented. The results of more involved analyses and the development of strategies for automated recognition of these failure signals will be presented in future work.

4. Methodology

The experimental studies were carried out using a 3hp vertical milling machine. The cutting tool was a 3.81cm diameter, three insert, face-mill employing Carboloy TPG-322E grade 370 tungsten carbide cutting inserts. The "standard" workpiece was a mild steel plate with a length of 30.5cm, a height of 15.2cm, and a width of 1.3cm.

While cutting, the mill traversed the length of the workpiece performing an

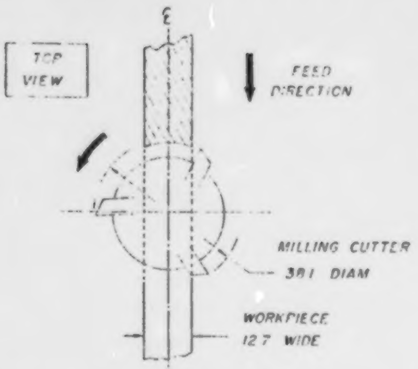
TOP VIEW
℄
FEED DIRECTION
MILLING CUTTER
38.1 DIAM
WORKPIECE
12.7 WIDE

Fig. 2 Schematic of Interrupted, Symmetric Milling Cut.

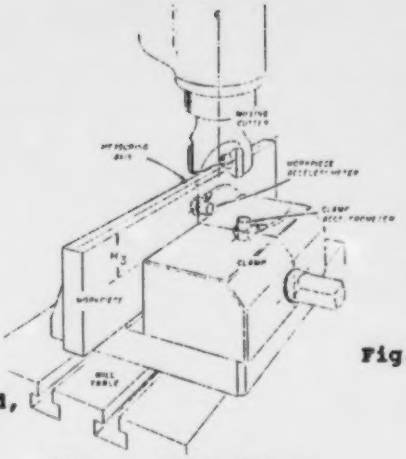
MILLING CUTTER
MEASURING AXIS
WORKPIECE ACCELEROMETER
CLAMP ACCELEROMETER
CLAMP
H3
WORKPIECE
MILL TABLE

Fig. 3 Test Set-up.

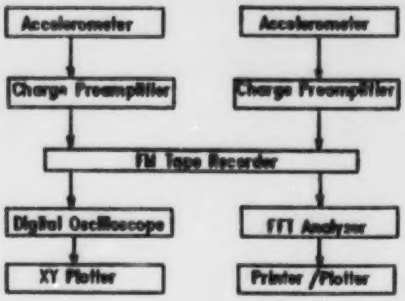
Accelerometer
Accelerometer
Charge Preamplifier
Charge Preamplifier
FM Tape Recorder
Digital Oscilloscope
FFT Analyzer
XY Plotter
Printer /Plotter

Fig. 4 Schematic of Measurement and Analysis System.

interrupted, symmetric cut. See Figure 2. The actual cutting conditions used are shown in Table 2.

The vibration generated during milling was measured at two locations: on the workpiece itself, and on the workpiece clamp (the more practical location from an industrial application point of view). The location of each accelerometer and its measurement axis is shown in Figure 3.

The vibration signals were tape recorded for later analysis in the laboratory. A schematic of the measurement/analysis system is shown in Figure 4.

Since it was recognized that changes in the structural dynamic characteristics of the machine-tool-workpiece system would introduce changes in the resulting vibration signal generated during milling, it was decided to minimize this effect as much as possible during the cutting experiments. This was done by fixing the three dimensions shown in Figure 5. Thus the tool-spindle projection, H1, the height of the table above the machine base, H2, and the height of the workpiece above the clamp, H3, were kept fixed during each cut.

Since it was desired to determine the potential for recognizing both wear and fracture failures of the milling inserts, two sets of tests were run.

The first series of tests consisted of milling cuts made using various combinations of worn and sharp inserts in the three-insert cutter. The worn inserts were obtained by machining a "wear block" under very light, and non-interrupted, machining conditions, thus achieving a slowly increasing amount of wear (flank wear on the insert) with minimal chance for edge chipping. If chipping did occur on an insert it was discarded. Once the desired flank wear had been obtained, the insert was put aside to be used subsequently in the actual interrupted face-milling tests performed on the standard workpiece.

Table 2 Cutting Conditions Used in Milling Tests

Depth of Cut	1.0 mm
Feed Rate	0.18 mm/tooth
Cutting Speed	180 m/min.
Engagement Angle	19.3

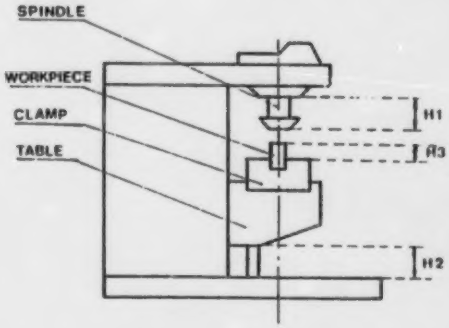
SPINDLE
WORKPIECE
CLAMP
TABLE
H1
H3
H2

Fig. 5 Dimensions Fixed During All Milling Tests.

In the second series of tests milling cuts were made using various combinations of "fractured" and sharp inserts in the three-insert cutter.

Due to the difficulty in obtaining controlled amounts of edge fracture during normal machining operations, it was decided to simulate fracture of the insert using electrical discharge machining to remove a controlled amount of the insert cutting edge. This is shown in Figure 6. The dimension, L, is used in this study to quantify the magnitude of the edge fracture.

Table 3 summarizes the magnitudes of wear and fracture used in the experiments. For each of these values, four cutter configurations were used, as shown in Table 4. Note that for a given configuration, if more than one failed insert was present, each had the same failure magnitude.

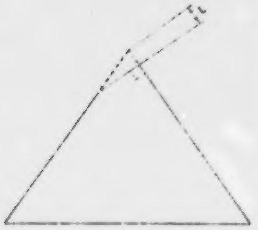

Fig. 6 Simulation of Insert Fracture.

Table 3 Summary of Failure Dimensions

mm / Insert	A	B	C	D	E	F	G	H
Dimension of Fractured Inserts	0.13	0.26	0.39	0.52	0.65	0.78	0.91	1.04
Dimension of Worn Inserts	0.13	0.26	0.39	0.52	0.65	0.78	-	-

Table 4 Milling Cutter Configurations

Insert / Configuration	No. 1	No. 2	No. 3
G1	Sharp	Sharp	Sharp
G2	Failed	Sharp	Sharp
G3	Failed	Sharp	Failed
G4	Failed	Failed	Failed
"Failed " indicates either worn or fractured, as appropriate			

5. Results

Although measurements were made both on the workpiece and on the clamp, only the latter will be presented in this paper. The measurements made on the workpiece were generally of greater magnitude and of slightly different spectral character, but indicated the same trends as those from the clamp location.

Whenever vibration measurements are to be used for diagnostic purposes it must be remembered that the vibration signal measured is actually the resultant of the vibrational energy generated by the process of interest (in this case, metal cutting by the mill's inserts) as modified by a "mechanical filter", that is, the machine-tool-fixture structural dynamics.

As such, it is necessary to be sure that all signals which are to be compared have, in fact, passed through the same "mechanical filter". In the present instance, this requires that the signal to be analyzed always be obtained during the same portion of the cutting cycle. This portion should be as short as possible, consistent with the time requirements of the analysis methods to be used. For this study the analyses were always undertaken using that portion of the vibration signal generated during the middle third of the cutting cycle.

Fractured Inserts

Time Domain Analysis

Figure 7 shows typical acceleration level versus time histories.

Figure 7(a) is for the case of three sharp inserts. Note that the engagement of each insert in the workpiece is clearly evident and that all engagements share similar characteristics, although they are by no means identical. This is consistent with recent work published by Johnston, Richter and Spiewak [16] which provided strong evidence that individual inserts on multi-insert cutters can have significantly diverse properties. Generally, however, the case of three sharp inserts would be easily recognizable from the data shown in Figure 7(a).

Figure 7(b) shows the resultant acceleration signal for the combination of two sharp inserts and one insert with a 0.39mm fracture. The sharp inserts produce signals consistent with those shown in Figure 7(a) while the fractured insert produces a significantly different output. The reduced output level for the fractured insert is a result of the much smaller depth of cut associated with this insert.

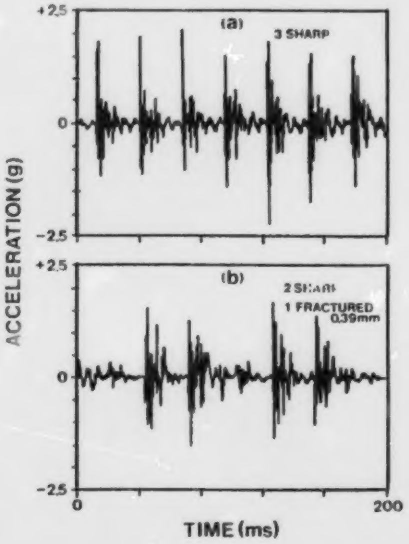

Fig. 7 Time Domain Data - Insert Fracture.

The results for other magnitudes of fracture and numbers of fractured inserts are basically the same. The presence of a fracture is readily detectable. It would seem from the time domain data available, that the use of either an "envelope detection" or a "threshold crossing" scheme would provide the ability to automate the detection of tool fracture in a multi-insert milling operation. However, it is not yet clear whether the time domain signal, on its own, can be used to reliably classify the actual magnitude of the fracture. This work remains to be done.

Frequency Domain Analysis

All frequency domain analyses discussed in this paper were obtained using eight ensemble averages and were calculated over a bandwidth of 0 to 20,000 Hz using 800 lines of resolution.

Figure 8 shows some typical frequency spectra for various tool conditions.

It is immediately apparent that, in general, fracture phenomena is indicated by an increase in the level of spectral components within the range of 10,000 to 17,000 Hz. A comparison of Figures 8(a) and 8(b) indicates a noticeable increase in the spectra around 11 kHz when a single insert fracture of 0.39mm is present. For two fractured inserts, Figure 8(c), the peak shifts to around 13.5 kHz. For the case of three fractured inserts, Figure 8(d), both the 13.5 kHz peak and an additional peak at about 17 kHz are apparent.

Comparing Figure 8(e) and 8(c) it is seen that, in general, increasing the size of the insert fracture results in an increase in the spectral peak associated with that failure condition. Unfortunately, a review of all the spectral data indicates that this increase in spectral peak does not always occur.

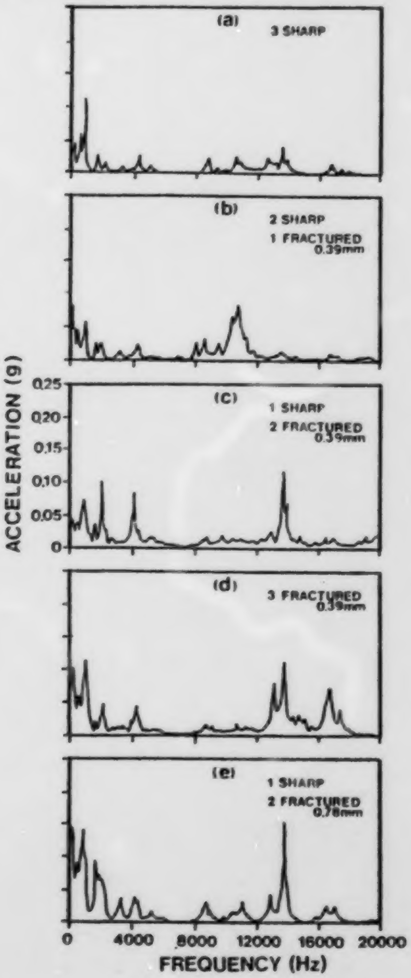

Fig. 8 Frequency Domain Data - Insert Fracture.

At the present time the eight ensembles used to obtain the spectral data are not synchronously averaged. That is, the data acquisition for the FFT analysis does not necessarily start at the same point on the cutter rotational cycle. Since the "data window" (the time required to obtain one set of data points) is significantly shorter than the time to complete one cutter revolution, it is possible that, in many instances, the data samples used for the FFT analyses do not contain information from the "failed" inserts. It may, therefore, be possible to improve the performance of the spectral data by utilizing a combination of synchronous averaging and delayed triggering to ensure that data representative of each insert in the cutter is obtained and processed.

Worn Inserts

Time Domain Analysis

The acceleration-time histories for the worn inserts do not, in general, produce the noticeably different engagement signals evident in the case of fracture (see Figure 7(b)). However, by processing the data in a slightly different manner it is possible to detect evidence of tool wear.

Figure 9 shows the amplitude probability density (APD) for several tool conditions. This distribution shows the percent of time a given level was present within the sample period. The data shown is for eight ensemble averages.

Figure 9(a) is for three sharp inserts. Note the essentially symmetric distribution.

For the combination of two sharp inserts and one with 0.65mm flank wear, see Figure 9(b), the APD is skewed to the left and its peak value is also shifted noticeably from its position for three sharp inserts.

Figure 9(c) shows the results for three inserts with 0.65mm flank wear. In this case the peak has decreased and shifted to the left and broadened significantly.

It thus seems possible that insert wear could be detected using such features as the location of the peak in the APD, the magnitude of the peak, and the area under specific segments of the distribution.

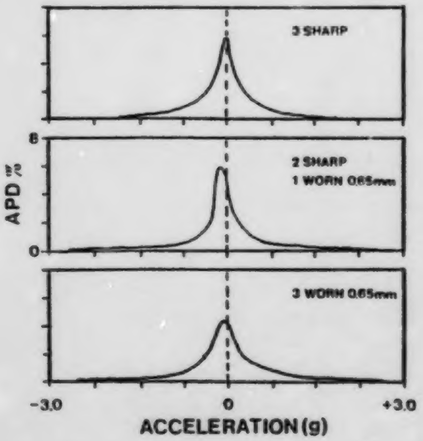

Fig. 9 Amplitude Probability Density - Insert Wear.

Frequency Domain Analysis

Typical results for worn inserts are shown in Figure 10.

As noted for fracture, the presence of insert wear results in a significant increase in the spectral components within the 10 kHz to 13 kHz band. The data shown is for 0.39mm flank wear but is representative of results obtained for all flank wear levels tested.

Although this would seem to indicate that the presence of flank wear could be detected using simple spectral analysis, it is not yet clear is the mehod would be sufficiently discriminating to permit reliable determination of the magnitude of flank wear. Also, at this time, specific features of the spectra have not been identified which would permit a distinction to be made between insert fracture and flank wear. It could perhaps be argued that this is not necessary if the severity of failure, either wear or fracture, could be determined with precision. These aspects of the problem remain to be addressed.

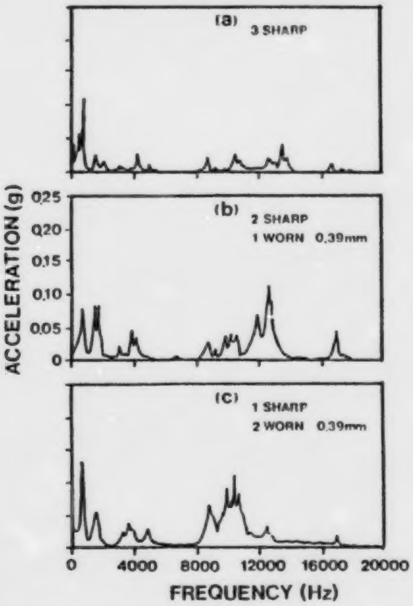

Fig. 10 Frequency Domain Data - Wear

6. Conclusions

This paper has presented preliminary results from a study undertaken to determine if vibration signals could be used to detect the failure (edge wear and fracture) of cutting inserts on a multi-insert face milling cutter.

It was shown that evidence of both tool fracture and flank wear can be found in both time and frequency domain analyses. However, it is also noted that when employing the simple analysis methods described in this paper, it is not possible to reliably determine the actual magnitude of the tool failure nor to distinguish between the type of failure (wear or fracture) that has occurred. Future work will attempt to identify processing methods which produce feature vectors capable of providing both quantitative measures of tool failure and unambiguous indication of the type of failure.

7. References

1. Braun, S. et. al., "Signature Analysis Applied to Drilling", ASME J. of Mechanical Design, Vol. 104, pp. 258-276, 1982.
2. Moore, T.N. and Reif, Z.F., "Detection of Tool Breakage Using Vibration Data", Society of Manufacturing Engineers, Manufacturing Engineering Transactions, pp. 45-50, 1985.
3. Reif, Z.F. and Chahine, J., "On-Line Monitoring of Tool Condition by Means of Vibration", Proc. 9th Engineering Applications of Mechanics Symposium, London, Ont., pp. 536-542, 1988.
4. Braun, S. ed., Mechanical Signal Analysis - Theory and Applications, 1986, Academic Press, London.
5. Lee, Y.H., Bandyopadhyay, P. and Kaminski, B., "Cutting Tool Wear Measurement Using Computer Vision", SME paper #MR86-934, 19p., 1986.
6. Altintas, Y., Yellowley, I. and Tlusty, J., "The Detection of Tool Breakage in Milling Operations", Journal of Engineering for Industry, Vol. 110, pp. 271-277, 1988.
7. Richter, F. and Spiewak, S.A., "A System for On-Line Detection and Prediction of Catastrophic Tool Failure in Milling", Proceedings of NAMRC XVII, pp. 137-143, 1989.
8. Lan, M.S. and Naerheim, Y. "In-Process Detection of Tool Breakage in Milling", ASME Winter Annual Meeting, Sensors and Controls for Manufacturing, PED Vol. 18, pp. 49-56, 1985.
9. Matsushima, K., Bertok, P. and Sata, T., "In-Process Detection of Tool Breakage by Monitoring the Spindle Current of a Machine Tool", ASME Winter Annual Meeting, Measurement and Control for Batch Manufacturing, pp. 145-154, 1982.
10. Ramalingam, S., Shi, T., Frohrib, D.A. and Moser, T., "Acoustic Emission Sensing with an Intelligent Insert and Tool Fracture Detection in Multi-Tooth Milling", Proceedings of NAMRC XVI, pp. 245-255, 1988.
11. Diei, E.N. and Dornfeld, D.A., "Acoustic Emission Sensing of Tool Wear in Face Milling", ASME J. of Engineering for Industry, Vol. 109, pp. 227-233, 1987.
12. Moshref, S.B., "Cutting Temperature as an Approach to On-Line Measurement of Tool Wear", Proceedings of NAMRC IX, pp. 28-31, 1981.
13. Lee, L.C., "A Study of Noise Emission for Tool Failure Prediction", J. Machine Tool Design and Research, Vol. 26, No. 2, pp. 205-215, 1986.
14. Mehta, N.K., Pandey, P.C. and Chakravarti, G., "An Investigation of Tool Wear and the Vibration Spectrum in Milling", Wear, Vol. 91, pp. 219-234, 1983.
15. Grieshaber, D., Ramalingam, S. and Frohrib, D., "On Real-Time Tool Fracture Monitoring in Milling", Proceedings of NAMRC XV, pp. 477-484, 1987.

THE ANALYSIS OF FAULT OCCURRENCES IN AN FMS

by

J. Jeswiet
Associate Professor
Department of Mechanical Engineering
Queen's University, Kingston, Ontario

ABSTRACT

This paper describes and discusses the operation of a Turning FMC* within an FMS* environment.The work reported is part of an ongoing study which was just completed at the MI-TNO in the Netherlands. The study was concerned with the possible use of FMS in a European manufacturing environment. One objective was the development of an SCS (Supervisory Control System) which could be used in an FMS for part order quantities as low as one. While development of the SCS software was being carried out other studies regarding tooling requirements, diagnostics, workholding and the general operation of such a system were also carried out. The paper discusses the Diagnostics/Operation study that was conducted.

The FMS consisted of a Turning FMC and a Machining FMC, with tooling centre, tool magazines and workpiece pallet systems.

The problems which occur with the introduction of revised manufacturer control system software are also illustrated.

INTRODUCTION

The modern technological environment is one in which a manufacturer needs to maintain a high machine utilization in order to remain profitable, especially with Flexible Manufacturing Systems (FMS). One of the ways of keeping machine utilization high is through the use of extensive and reliable diagnostic systems. Therefore the need for diagnostic systems in FMS and automation. However, extensive diagnostic systems do not yet exist in FMS's, in part because of the relative newness of this technology. This can be seen from some of the comments made in recent publications (1, 2, 3).

Diagnostic systems are used in a variety of industries such as the chemical, petrochemical and automotive industries, hence the idea of developing and using a diagnostic system is not a new one. The problems of developing a diagnostic system for an FMS system are different because FMS machinery runs sporadically and not all parts of the system are in continual use, especially in a small batch FMS production environment. This paper looks at how the overall system could be considered, not only the tool/workpiece volume where most research appears to be directed (4,5).

The work reported is part of an ongoing study which was just completed at the MI-TNO in the Netherlands. The study was concerned with the possible use of FMS in a European manufacturing environment. One objective was the development of an SCS (Supervisory Control System) which could be used in an FMS for part order quantities as low as one. While development of the SCS software was being carried out other studies regarding tooling requirements, diagnostics, workholding and the general operation of such a system were also carried out. This paper discusses the diagnostics/Operation study that was conducted.

The equipment used for this study consists of two, free standing FMC's, which are located at the MI-TNO at Apeldoorn in the Netherlands. The turning FMC is a Traub TNA480+FHS2 and the machining FMC is a MAHO MC50 (MFS50). Both have specially designed pallet systems.

FMS and UTILIZATION

The primary objective of FMS is the reduction of work in progress and faster response to the changing requirements of production (1). A corollary to this objective would be an idealistic requirement of 100% utilization. However, within

---

*FMS: Flexible Manufacturing System
FMC: Flexible Manufacturing Cell
MI-TNO: Metaalinstituut-TNO
TNO: Toegepast Natuurwetenschappelijk Onderzoek

the literature the trend appears to be a requirement of 97% utilization [defined as the number of pieces produced times the NC program running time relative to the total operating time (2)]. It should be noted that FMS's are usually manned operations, indeed few cases can be found in the literature where an FMS is completely unmanned for 24 hours. Just getting the system to run in an unmanned mode without problems for one back shift of 8 hours also appears to be a rare occurrence. But, as observed by Weck (6), manpower availability on weekends and holidays is always low and it is therefore important to be able to run in a completely unmanned mode for reonable lengths of time.

FMS cells are having problems being accepted in the machine tool industry because of cost and reliability and it has been suggested that more development is needed in this technology (7). It has also been observed (6) that not all problems associated with the introduction of small or medium sized manufacturing systems have yet been solved because of their complexity which gives reduced reliability and availability. It can be argued that one area for improvement in FMS is in diagnostics. Proper application of diagnostics will give more reliable FMS's and increase the amount of unmanned time available. Therefore the demands on FMS's, and their untended operation, makes the monitoring function for detecting abnormal occurrences increasingly important (8).

DIAGNOSTICS

An obvious point from which to begin is to define diagnostics in order to avoid any confusion.

Definition: (Oxford Dictionary).
"Diagnostic(n) symptom. Diagnose (v) determine nature of (disease). Diagnosis (n) identification of disease by means of symptoms." Obviously symptoms can require either immediate action or a more planned methodical reaction.

In machine diagnostics one considers the symptoms of a machine or a perceptible change in the system or its functions. Part and parcel of this is a diagnosis of what is occurring and what action must be taken, both long-term and short-term.

Diagnostic systems must be connected to monitoring devices. Without monitoring, either by humans or by sensors, there cannot be any diagnosis. Therefore monitoring and diagnosis go hand-in-hand so that one can call them Monitoring/Diagnostic systems or use the acronym, MD system; Monitoring: observation and detection of processes and faults; Diagnosis: interpretation of faults with corrections required to make repairs.

change in the system or its functions. Part and parcel of this is a diagnosis of what is occurring and what action must be taken, both long-term and short-term.

Diagnostic systems must be connected to monitoring devices. Without monitoring, either by humans or by sensors, there cannot be any diagnosis. Therefore monitoring and diagnosis go hand-in-hand so that one can call them Monitoring/Diagnostic systems or use the

CONTROL VOLUMES

The conventional approach to solving engineering problems is based upon the definition of the problem and the decomposition of the problem into smaller parts that can be solved individually. Therefore, if possible, it is desireable to develop a hierarchical structure to simplify an MD analysis. A method of dividing an FMS into control volumes (CV's), for purposes of determining where the most failures occur, was recently introduced (. Consider the Turning FMC shown in Figure 1, where the physical working area of the FMC can be subdivided

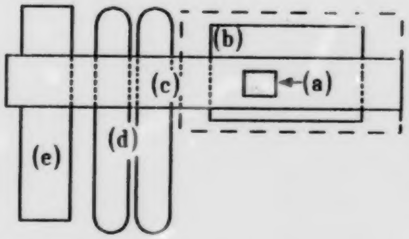

CV	Identification
(a)	Tool/workpiece interface
(b)	Machining volume
(c)	Robot volume
(d)	Workpiece pallet volume
(e)	Tool magazine volume
(f)	Gantry robot volume.
(t)	Tool preparation volume.
(p)	Software volume. 1) VAX, 8600 2) Microvax 3) PDP 11/23 4) Turning FMC controller - NC 5) Turning FMC controller - Robot 6) Machining FMC controller - NC 7) Machining FMC controller (PLC) - for pallet

Figure 1. Schematic of the different control volumes (CV's) for a Turning FMC.

into smaller volumes defined as Control Volumes (CV's). The Major divisions which occur in the Turning FMC are CV-(a) the tool/workpiece interface, CV-(b) the volume containing the machining area, CV-(c) the robot volume, CV-(d) the workpiece pallet volume, and CV-(e) the tool magazine volume. There can be additional CV's for an FMS giving additional regions where sensing must occur to keep a trouble free system. For instance, a small FMS could consist of a Turning FMC and a Machining FMC with a connecting gantry robot, as suggested by Noh et. al.(10). This would give an additional volume, CV-(f). Figure 2 illustrates the CV's that were used for the TNO FMS.

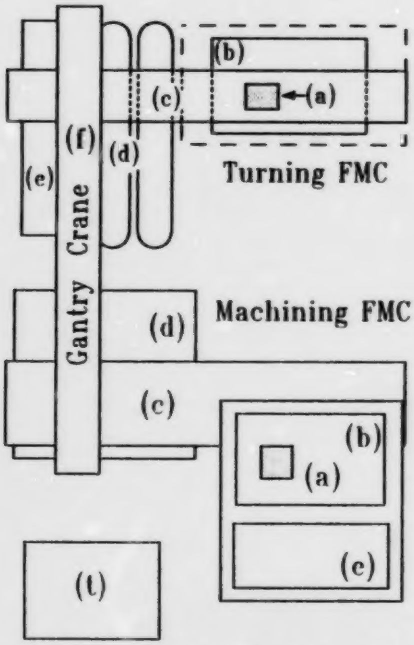
(b)
(a)
(c)
(f)
(d)
(e)
Turning FMC
Gantry Crane
Machining FMC
(d)
(c)
(b)
(a)
(c)
(t)

Figure 2. Schematic of the different control volumes (CV's) in the TNO FMS. The system at TNO does not have a gantry crane, AGV's were originally intended for this system.

Additional volumes which have an affect upon the analysis are: the tool preparation volume, CV-(t) and the software volume, CV-(p). The software volume is an abstract one, but it has been included because experience shows that many faults occur in software, especially during the start-up of a system that is supposedly market ready. Because software systems also have bugs the software volume has been subdivided into separate areas because the problems that do occur can usually be related to one of the volumes listed. For ease of identification the software volumes have been allocated to specific hardware within the system as shown in figure 3.

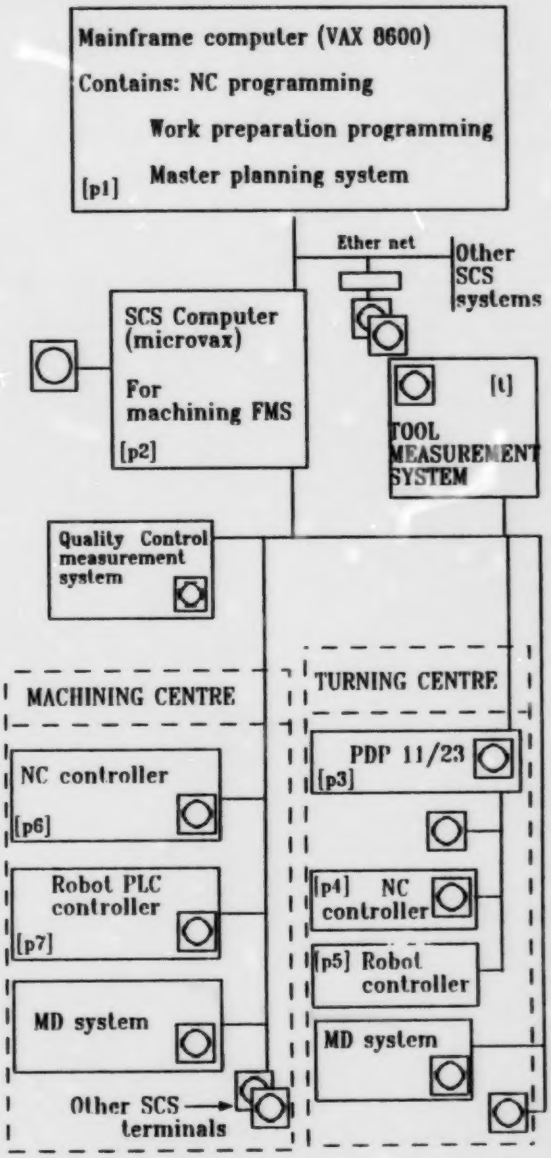
Mainframe computer (VAX 8600)
Contains: NC programming
Work preparation programming
Master planning system
[p1]
Ether net
Other SCS systems
SCS Computer (microvax)
For machining FMS
[p2]
[t]
TOOL MEASUREMENT SYSTEM
Quality Control measurement system
MACHINING CENTRE
TURNING CENTRE
NC controller
[p6]
PDP 11/23
[p3]
Robot PLC controller
[p7]
[p4] NC controller
[p5] Robot controller
MD system
MD system
Other SCS terminals

Figure 3. Computer control hierarchy showing the software volumes which are labelled as (p).

Our experience with machining and turning FMC's also shows that system failures that do occur will often include more than one volume. Therefore in setting up a fault analysis sheet for the turning and machining FMC's it was found that additional identification was needed for purposes of evaluating the systems. These were designated as follows:

σ = a fault detected by an existing sensor
ϕ = fault could be detected by a sensors
Ω = indicates a learning phase problem
τ = indicates a manufacturer problem
δ = software logic problem
R = repeating problem
α = system down for an extended period

Figure 4 shows the flow for recording information when the system is broken down into CV's with the fault designations. If one now sets up a simple check list, as shown in table 1, the different volumes where problems occur can be identified, including whether they are sensor related, manufacturer related or if they are a learning phase problem. Whenever a fault occurs in the system a check is assigned to the volume(s) associated with the problem. Because volumes overlap, a fault diagnosis will often be given more than one check. The data was accumulated in one year as shown in figure 5 which is a chart showing important dates in the life of the FMS project.

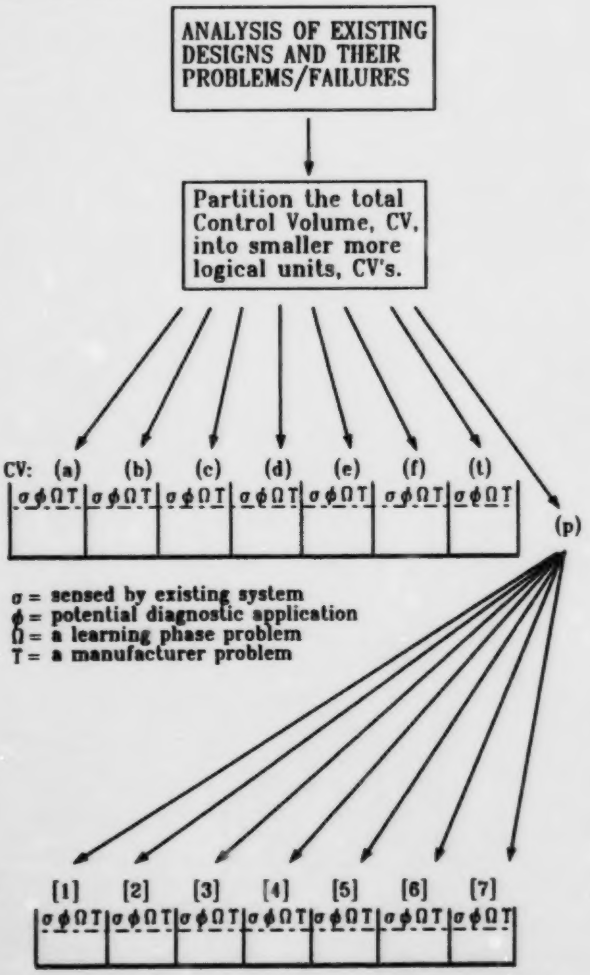
ANALYSIS OF EXISTING DESIGNS AND THEIR PROBLEMS/FAILURES
Partition the total Control Volume, CV, into smaller more logical units, CV's.
CV: (a) (b) (c) (d) (e) (f) (t)
σϕΩT σϕΩT σϕΩT σϕΩT σϕΩT σϕΩT σϕΩT
(p)
σ = sensed by existing system
ϕ = potential diagnostic application
Ω = a learning phase problem
T = a manufacturer problem
[1] [2] [3] [4] [5] [6] [7]
σϕΩT σϕΩT σϕΩT σϕΩT σϕΩT σϕΩT σϕΩT

Figure 4. Analysis of existing design with CV's.

At the beginning of the project the Turning FMC had a prototype software system which was under development for part of that time and therefore had many software problems during that stage of development. However, the learning/development period had been completed when formal recording of faults started. As can be observed in table 1, other problems which have to do with the design of the machine and the lack of adequate sensing started occurring and it can be seen that MD was becoming more applicable as the system was worn in. The introduction of a revised software package in mid-October increased the number of software faults dramatically. Figure 6 illustrates this dramatic increase. It can be seen that many of the faults can be attributed to the robot software volume, CV-(c). In this case the manufacturer claimed the system would run without very many problems, but this was not the case. Because of our involvement with the earlier software development, it could be observed that many of the old bugs had not been eliminated by the manufacturer.

Figure 6 illustrates more software problems that occurred after revised software from the robot equipment manufacturer was introduced. The time at which the revised robot control software was introduced can be observed by the dramatic increase in software problems in January, 1989 when it was introduced. This spike is even greater than the October spike. From the experience gained it can be seen that it took at least four to five months before all software problems which were related to the change were solved.

On several occasions the software was diagnosed as having a fault but this was later found to be an incorrect diagnosis on the part of the software diagnostic system. In fact, a control board was found to been defective in the robot control system and for some reason this continually appeared as a software diagnostic fault on the manufacturers software diagnostic system. This problem emphasized the need for a good software diagnostic system which can give trustworthy information.

The summations shown in table 1 indicate where problems are when dealing with: 1) a new FMS software system or 2) a more developed and better known system. One can expect that a similar type of pattern would emerge in industrial circumstances. Therefore with a competent MD system in place one can expect downtime to decrease in a long term operation.

There is no simple solution to identifying potential problem areas in each CV, but setting up a list of what can occur in each volume should allow for easier identification of areas where most potential problems occur. If a list is set up for each volume, as shown in table 1, it becomes immediately apparent that CV-(b) is an area of major concern. But this can be misleading because problems with the robot, CV-(c), can lead to resultant problems in CV-(b). For instance the housing containing the robot gripper may slip out of alignment and cause a tool to be out of position once placed by the robot in the turret head in CV-(b). Therefore areas where volume faults overlap must be examined critically.

Turning Centre Milestones

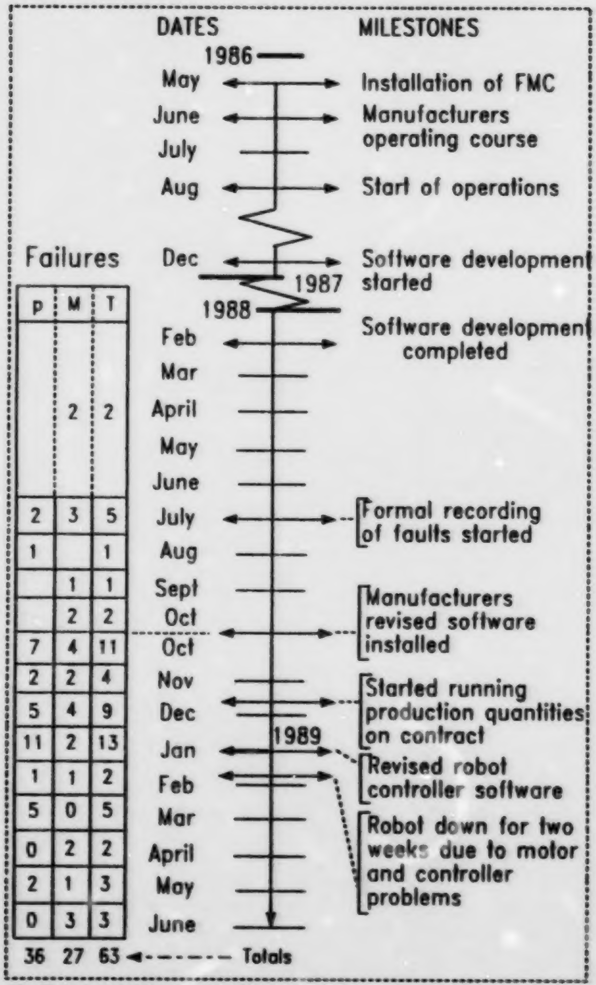
DATES
MILESTONES
1986
May
Installation of FMC
June
Manufacturers operating course
July
Aug
Start of operations
Dec
Software development started
1987
1988
Feb
Software development completed
Mar
April
May
June
July
Formal recording of faults started
Aug
Sept
Oct
Manufacturers revised software installed
Oct
Nov
Started running production quantities on contract
Dec
1989
Jan
Revised robot controller software
Feb
Mar
Robot down for two weeks due to motor and controller problems
April
May
June
Failures
p M T
2 2
2 3 5
1 1
1 1
2 2
7 4 11
2 2 4
5 4 9
11 2 13
1 1 2
5 0 5
0 2 2
2 1 3
0 3 3
36 27 63
Totals

T: Total number of failures
M: Number of mechanical failures
p: Number of software failures
* * *: New or revised software installed

Figure 5. A chart showing important dates, milestones, for recording events having an effect upon failures.

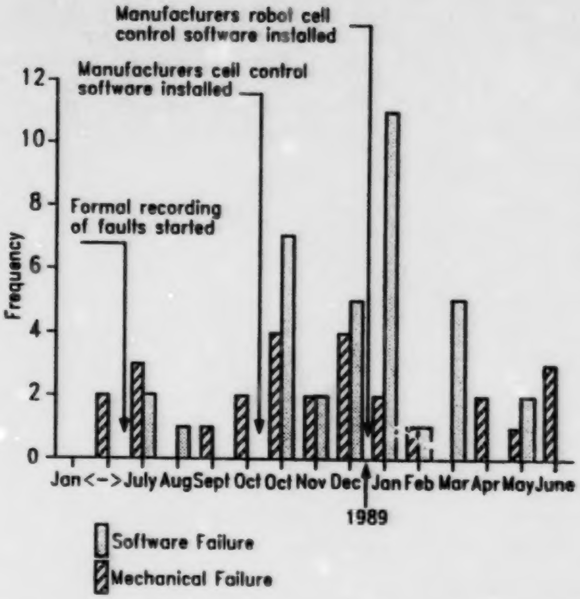

Figure 6. Comparison of Frequency of mechanical and software failure by month for the Turning FMC.

CONCLUSIONS

- A method has been introduced which can be used to analyze FMC's and FMS's for faults. Separating the system into control volumes gives a good overview of where the majority of the problms are concerning system breakdown. After a specific area has been identified it can then be broken down into CV's for further analysis.

- Most diagnostic research appears to be directed at the tool/workpiece interface. However, the data shows that most problems occur elsewhere in the system and that diagnostic research should be directed at other areas, such as the handling system if one wishes to improve the reliability of FMS's.

- In this project it was found that introducing a revised software package dramatically increased the shutdowns that occurred due to software problems. This could be a general as indicated in private conversations with several users.

- As a direct result of the previous finding, and although an obvious conclusion, one can conclude that a general rule regarding software should be: Once a software system is working successfully in industrial circumstances, do not make any software changes unless iron clad guarantees are included.

- Good simulation systems are needed for testing any revised software before it is introduced into an industrial environment. This needs a lot of attention if Flexible Manufacturing is to become more acceptable acceptable to medium and small size industries.

Table 1. A table of faults for the Turning FMC showing the volumes concerned and the reasons for failure.

Month		b	c	d	e	p	t	σ	Ω	τ	φ	δ	β	R	M
	1			1					1	1	1		1		1
	2			1						1			1		1
July 1988 →	3	1	1							1	1		1		1
	4		1					1		1			1	1	1
	5					1	1	1	1				1		
	6			1		1			1	1	1		1		
	7						1	1							1
Aug →	8					1				1		1	1		
Sept →	9	1					1			1			1		1
Oct →	10	1			1			1		1			1	1	1
	11						1			1			1		1
Revised cell control software installed															
	12					1				1			1		
	13					1				1		1	1		
	14					1				1		1	1		
	15					1				1			1		
	16		1		1			1					1		1
	17		1		1				1				1		1
	18					1			1	1			1		
	19					1				1		1	1		
	20					1				1		1	1		
	21	1	1							1	1		1		1
	22		1							1	1		1		1
Nov →	23	1								1			1		1
	24		1							1	1			1	1
	25					1				1			1		
	26			1		1			1	1	1	1	1	1	
Small part series production for industry															
Dec →	27	1			1	1			1	1	1	1	1		
	28	1	1						1	1	1		1		1
	29		1		1				1	1	1		1		1
	30					1				1			1		
	31					1				1			1		
	32			1		1				1		1	1	1	
	33	1								1	1				1
	34	1						1		1					1
Revised Robot control software installed															
	35		1			1		1							
Jan →	36					1	1			1			1		
	37			1		1				1		1	1		
	38				1	1				1		1	1		
	39					1				1		1	1		
	40				1	1				1		1	1		
	41					1				1		1	1		
	42			1		1				1		1	1		
	43			1		1				1		1	1		
	44					1	1			1		1	1		
	45		1							1			1	1	1
	46			1		1				1		1	1		
	47					1				1			1		
	48		1							1	1			1	1
Feb →	49		1			1				1	1			1	1
	50	1				1			1		1		1		
Mar →	51		1	1		1				1	1	1	1	1	
	52		1	1		1		1		1			1		
	53					1					1	1	1		
	54		1	1		1		1		1			1	1	
	55				1	1				1		1	1	1	
April →	56		1							1	1		1	1	1
	57		1							1	1		1	1	1
May →	58	1								1	1		1		1
	59		1			1				1	1		1	1	
	60					1	1			1			1	1	
June →	61		1					1		1					1
	62		1					1		1				1	1
	63		1					1		1			1	1	1
		12	22	11	8	37	7	12	10	56	20	19	54	18	27

- Much better diagnostic systems are needed to give a true evaluation of the problems which occur. In this project, the diagnostics provided for the operator, by the manufacturer, often did not indicate the true nature of the problem.

- In any mechanical design, in this case, the gantry robot indexing wrists, care should be taken when including surfaces in the design which depend upon friction, created by pressure to keep parts in a fixed position relative to each other. This was found to be a design fault which created problems on a regular basis and was the cause of some of the problems which occurred in volume (c) and (b).

ACKNOLEDGEMENTS

I would like to gratefully acknowledge the cooperation of the Metaalinstituut TNO, in the Netherlands, in allowing me to spend a sabbatical year working with their Experimental Flexible Manufacturing System. Without their excellent and unique facility this work would not have been possible. The support of NSERC Grant No. A 4960 is also gratefully acknowledged.

REFERENCES

- 1."Possible Pitfalls of FMS". G. Cullen. The FMS Magazine, IFS publications, 3(4),67, 1985.
- 2."Availability, performance and service of FMS". H. Hammer. The FMS Magazine, IFS publications, 5(4),180, 1987.
- 3."Developments in Flexible Turning". C. Haxby., The FMS Magazine, IFS publications 5(2),90, 1987.
- 4."A Critical Review of Sensors for Unmanned Machining". J. Tlusty and G.C. Andrews. Annals of CIRP vol. 32/2/1983, 563.
- 5."On-Line Machine and Process Diagnostics". R.L. Kegg. Annals of CIRP vol. 33/2/1984, 469.
- 6."Sensors, diagnostic methods and systems for application in manufacturing systems." M. Weck, Int. J of Materials and Product Technology, vol. 1, no. 2, 195, 1986.
- 7."Review of German FMS Reveals Shortcomings". W. Eversheim, K. Erkes, and H. Schmidt. The FMS Magazine, IFS Publications, 4 (3), 159, 1986.
- 8."Tool breakage Monitoring by Means of Fluctuations in Spindle Rotational Speed". S. Takata, T. Nakajima, J.H. Ahn, T. Sata. Annals of CIRP vol. 36/1/87, 49.
- 9."Monitoring and Diagnositics for FMS: Analyzing Two FMC's for faults". J. Jeswiet. 1989 transactions of SME/NAMRI, vol XVII, p. 325.
- 10."The Automatic Crane as a Material Transportation System in FMS". A. Noh, T. Isegane and K. Iwata. Annals of CIRP vol. 35/1/1986, 97.

NONISOTHERMAL METAL FLOW SIMULATIONS FOR THE DIE CASTING PROCESS.

C.A. Loong, V.V. Kappel, G. Salloum

Industrial Materials Research Institute
National Research Council Canada
75 de Mortagne, Boucherville, Québec J4B 6Y4

ABSTRACT

The general principles of nonisothermal flow are applied to the simulation for turbulent metal flow and rapid melt cooling encountered in the die casting process. Mathematical models of the material behavior, based on fluid mechanics and heat transfer, are used to predict the metal flow pattern during the die filling process. The calculations related to filling pressure, melt temperature profile and velocity distribution are based on a control volume approach. A practical method of flow simulation applicable within experimentally determined limits has been developed.

Simulation of the filling process is the principal part of a computer integrated die casting system. However, the system also covers other important functions such as material selection, die design, thermal analysis, process control and a detailed stress analysis of the casting, based on local material property variations, as predicted by the simulations.

The system ensures that all processing parameters are within permissible ranges. Similarly, it monitors any variations of the melt characteristics and reports deviations from the acceptable operating ranges defined for each alloy. Processing parameters, as well as product and die dimensions are optimized. Equal filling of multicavity dies or of a system with multiple gating can be achieved by modifying the feeding system through iterative balancing simulations. The design of the cooling channels is based on the thermal balance of the whole system, composed of the molten alloy, the die geometry and the different boundary conditions of the die.

The obstacles encountered in modeling and some practical ways or reducing the complexity of the problem are discussed. Experimental case studies are presented.

INTRODUCTION

Optimization of different stages of a manufacturing process requires coupling the analytical tools with the practical experience. This approach is being followed in the development of a computer integrated die casting system. The key part of the system is the simulation of flow of the liquid metal alloy into the die casting cavity. The application of the general principles of the coupled fluid flow and heat transfer is complex due to the turbulent nature of the flow [1,2]. In this work, a solid flow front propagation within the cavity is considered.

There are satisfactory techniques, using overall macroscopic balances to predict the relationships between pressure drop and volumetric flow through a control volume. These techniques are not by themselves directly suitable for analysis of the velocity or pressure distributions during the non-steady filling process. However, if we subdivide the system into control volumes and supply sufficient information on the flow distribution, we may use these techniques to solve the pressure and velocity distributions, while at the same time verifying the compatibility of the supplied information. This approach allows us to develop a practical method of flow simulation and use it within experimentally determined bounds.

MODELING OF THE TURBULENT AND NON-ISOTHERMIC FLOW

The cavity is divided into control volumes with specified flow entry and exit and the flow in each element is treated as a steady flow of an incompressible Newtonian fluid at constant temperature. The hydraulic resistances are then calculated applying the formulas [3] used in engineering flow analysis (Bernoulli equation) with certain adaptations. Following the isothermic calculations of each element, the heat losses during the total time of residence are calculated before proceeding to the next element. Relying on the high diffusivity of both, the metallic die and the liquid casting alloy, leave the thermal resistance at the die wall as a controlling factor for the calculations of the convective heat transfer at the die interface [4, 5].

MODELING OF THE CAVITY AND FEEDING SYSTEM

The simulation process begins with a three dimensional representation of the cast product with the feeding system, as shown in Figure 1. This representation is then used to produce a system of discrete flow elements. After all the modifications reflecting the optimization process have been applied, it serves then for semi-automatic die cavity and core design using solid modeling features.

The choice of a discretization method for the cavity will determine the speed of response of the interactive system as well as the time requirements for the preparation of the model. The method has to be simple to use and allow for the generation of a discrete model in a reasonably short time and provide a basis for simulation giving sufficient information about the process. At present the discretization is based on development of lay-flat pattern of the part, taking into account the changes of direction between the elements.

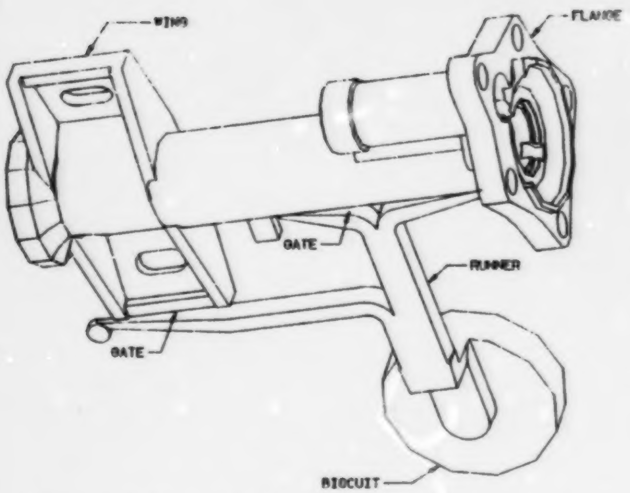

Figure 1: Solid model of an axle tube with feeding system.

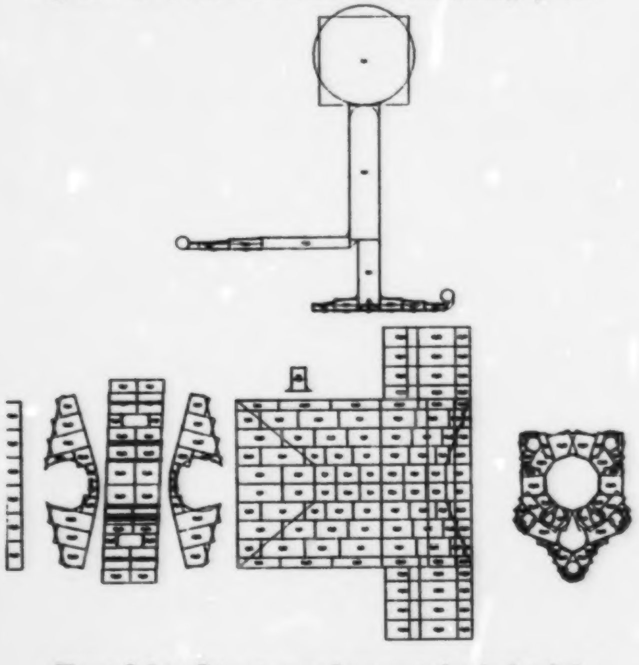

Figure 2: Lay-flat pattern and segmentation (axle tube).

Using the lay-flat pattern, the user determines the principal flow paths and divides them into flow elements, including the variations in section and direction (Figure 2). This requires a certain amount of practical experience and a good understanding of the die casting process. The results of first simulations provide for compatibility checks, followed by revisions in the flow paths scheme if necessary. During discretization, the system uses the information from the lay-flat pattern, to provide the necessary dimensions for the elements into which each flow path has to be broken. The density of the mesh, or the length of the elements, will depend mainly on the required detail for displaying the results and on changes in local geometry from one point to another. Hydraulic diameters of all the elements are calculated and modified by the system to account for the neighboring elements as well as for the changes in direction or cross section. This establishes the hydraulic resistances of the individual path elements. Presently, a new version based on the finite element method is under development.

SIMULATION OF THE FILLING PHASE

The flow front positions are generated starting from the entry point of the liquid metal, by comparing the hydraulic resistances of the flow elements in all parallel flow paths. The Darcy friction factors are established using the calculated mean velocities through the elements. A standard Darcy-Weisbach formula is then used in the calculation of the pressure drop [6] in each subdivided flow element. By comparing the total hydraulic resistances of the elements the stepwise progression of the flow front is predicted (Figure 3).

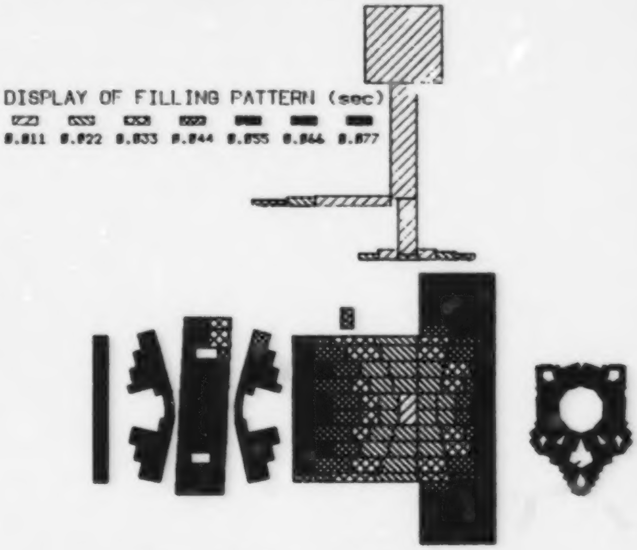

Figure 3: Filling pattern (axle tube).

Assuming that the die temperature is virtually constant during the short filling time, the melt temperatures at the exit of each element are calculated from the heat losses through the interface resistance, during the travel through the element. The new temperature is used for updating the material data, such as density and viscosity, before calculating the next element.

Special routines allow balancing simulations of single-cavity of multi-cavity dies. This is done by imposing an equal pressure drop in the branches of the system and by specifying the dimensions that may be modified to achieve a balanced system. Using similar pressure drop calculation as during the filling stage analysis, the system guides the user through the necessary iterations until sufficient precision in balancing has been reached.

During the simulation, the user may consult the stored information concerning the alloys, standard process parameters as well as a review of the parameters already in the system in order to make the use of the system simple and efficient and to reduce the chances of errors.

The results of the analysis are displayed during the simulation in a tabular form (Table 1), together with messages when any of the specified limits are exceeded. The post processing module also permits visualization of the specific results in a form of lay-flat pattern displays (as in Figure 3) or as graphs showing variation of a selected parameter with respect to either flow distance or time (Figures 4 and 5).

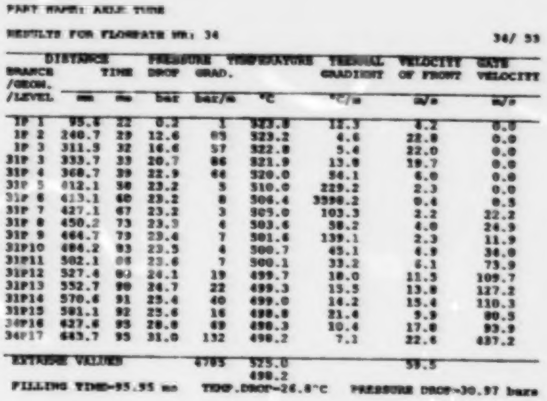

```
PART NAME: AXLE TUBE

RESULTS FOR FLOWPATH NR: 34                                              34/ 53
-------------------------------------------------------------------------------
         DISTANCE         PRESSURE  TEMPERATURE  THERMAL    VELOCITY    GATE
BRANCH          TIME  DROP  GRAD.               GRADIENT   OF FRONT    VELOCITY
/GEOM.
/LEVEL     mm    ms    bar   bar/m     °C         °C/m        m/s         m/s
-------------------------------------------------------------------------------
  1P 1    95.6   22    0.2      1    525.0        12.3         4.2         0.0
  1P 2   240.7   29   12.6     85    523.2         4.6        22.8         0.0
  1P 3   311.5   32   16.6     57    522.8         5.4        22.0         0.0
 31P 3   333.7   33   20.7     86    521.9        13.8        19.7         0.0
 31P 4   360.7   39   22.9     44    520.0        54.1         6.0         0.0
 31P 5   412.1   58   23.2      5    510.0       229.2         2.3         0.0
 31P 6   413.1   60   23.2      8    506.4      3590.2         0.4         0.5
 31P 7   427.1   67   23.2      3    505.0       103.3         2.2        22.2
 31P 8   450.2   73   23.3      4    503.6        58.2         4.0        24.9
 31P 9   464.7   79   23.4      7    501.6       139.1         2.3        11.9
 31P10   484.2   83   23.5      4    500.7        45.1         4.9        34.0
 31P11   502.1   86   23.6      7    500.1        33.2         6.1        73.9
 31P12   527.4   88   24.1     19    499.7        18.0        11.3       109.7
 31P13   552.7   90   24.7     22    499.3        15.5        13.8       127.2
 31P14   570.6   91   25.4     40    499.0        14.2        15.4       110.3
 31P15   581.1   92   25.6     16    498.8        21.4         9.9        80.5
 34P16   627.6   95   28.8     89    498.3        10.4        17.8        93.9
 34P17   643.7   95   31.0    132    498.2         7.1        22.6       437.2
-------------------------------------------------------------------------------
 EXTREME VALUES                4785  525.0                    59.5
                                     498.2
 FILLING TIME=95.55 ms   TEMP.DROP=26.8°C   PRESSURE DROP=30.97 bars
```

Table 1: Simulation results

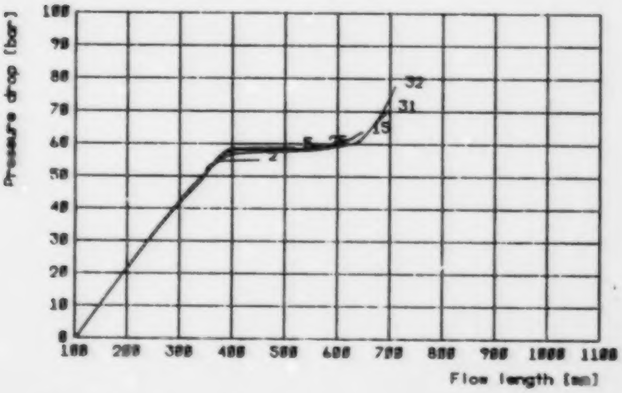

Figure 4: Display of calculated pressures vs flow length.

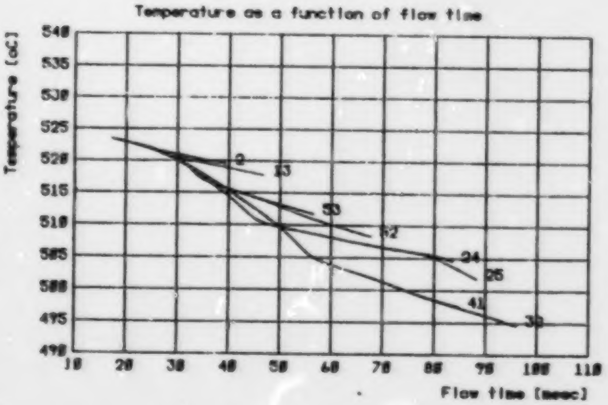

Figure 5: Display of calculated temperatures vs filling time.

To determine actual flow front propagation, partially filled casting were produced (Figures 6 and 7) and then compared to the graphic presentation of the simulation results (Figure 3). The contours of the partially filled casting were generally well predicted by the simulation.

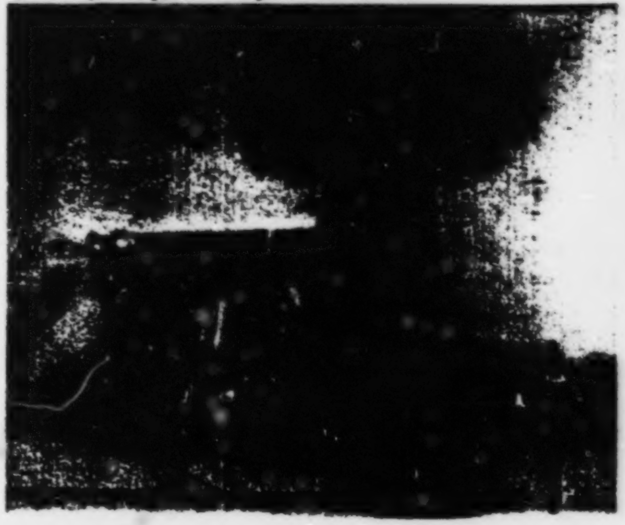

Figure 6: Partially filled axle tube casting.

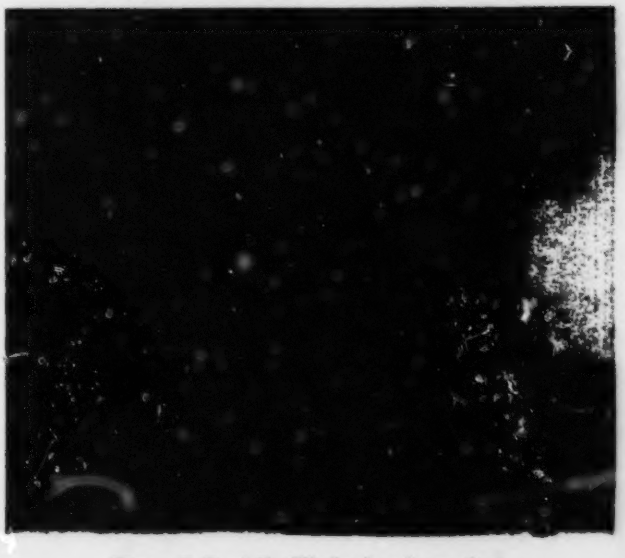

Figure 7: Partially filled axle tube casting.

The simulations can be repeated in order to optimize the casting parameters. These parameters were compared to the parameters optimized during a production in Table 2. and show good agreement.

The simulations of other simple and complex parts shown in Figures 8 and 9 were made and compared to the data obtained from production. An experimental program was undertaken to measure pressures, temperatures and velocities, as well as to observe flow fronts, defects in the cast product and any difficulties encountered during the casting process.

Comparison Parameters	Simulation Fast filling	 Optimum	 Slow filling	Production Min.	 Standard	 Max.
Short Shots (Filling Pattern)	Filling Pattern/ Wing and flange corners last to fill			Short Shots in agreement		
Filling Time (ms)	52	80	96		75	
Pressure to fill (psi)	2111	916	648		3150	3429
				intensification to 4000		
Temperature of Melt (F)		1022		1020	1027	1050
Gate Velocity (ips)	2204	1485	1237		1300	

Table 2: Production parameters vs simulated results.

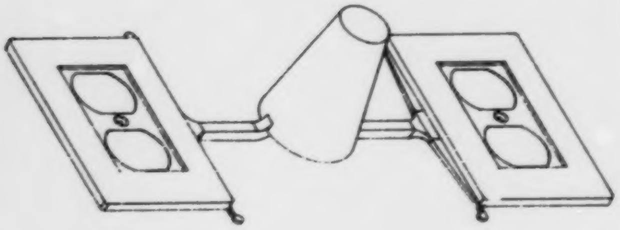

Figure 8: Wall plate

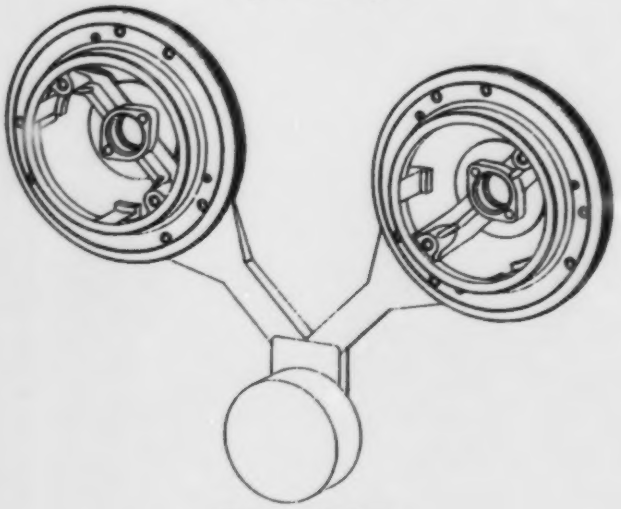

Figure 9: Bracket

CONCLUSIONS

The two dimensional modeling of the metal flow into a thin wall die cavity, using an engineering approach which takes account of all the geometry variations, gives an insight into the filling stage, provided it is used with judgment. It also forms the core element of an integrated system that covers all the phases of the die casting process, such as material selection, part design and die design, simulation of die filling and cooling, and analysis of the production parameters for the programmable controller. Based on the simulation, the product behavior can be evaluated and the design can be optimized before the dies are built. This results in reduction in lead time and lowering of re-tooling costs as well as in improved product quality.

ACKNOWLEDGMENTS

The authors would like to thank the Noranda Technology Centre, Parker White Metal Company and Eastern Die Casting for providing advice, samples and casting data related to this work. Special thanks are also due to Mr. Normand Nardini for his assistance in preparing the illustrations.

REFERENCES

Davis, A.J., Siauw, H., Significance of Metal Pressure in Hot Chamber Die Casting of Zinc , Part I - Theoretical Estimation of the Pressure Required to Inject Molten Zinc into Die Cavities SDCE 9th Int. Congress, Milwaukee, Wis., June 6-9, 1977.

Geiger, G.H., Poirier, D.R., Transport Phenomena in Metallurgy , Addison-Wesley, Reading, Mass., 1973.

Ho, K., Pehlke, R.D., Mechanism of Heat Transfer at a Metal-Mold Interface , AFS Transactions no. 84-61, 1984.

Murdock, J.W., Fluid Mechanics and its Applications . Houghton Mifflin, Boston, Mass., 1976.

Nelson, C.W., Nature of Heat Transfer at the Die Interface , SDCE 6th Int. Congress, Cleveland, Ohio, November 16-19, 1970.

Szekely, J., Fluid Flow Phenomena in Metals Processing . Academic Press, New York, 1979.

A FLEXIBLE INTERNAL DEFECT DETECTOR FOR 12 INCH PIPELINES

A. Teitsma

Pipetronix Division
International Pipeline Engineering Ltd.
450 Midwest Road
Scarborough, Ontario M1P 3A9

ABSTRACT

Most of the hundreds of thousands of kilometers of pipeline was designed without pipeline inspection in mind. This is especially true for smaller diameter lines where bends of one and a half diameters (or worse miter bends) are common and frequent. As well, small diameter pipelines tend to be made of seamless pipe presenting a rougher surface increasing wear and making defect detection difficult.

To allow "easy" passage of a 12 in. internal defect detector through frequent sharp bends a flexible version of the detector was designed and built. This paper describes the unique design features of the detector. These features should make the detector capable of passing through and detecting defects in most 12 in. lines. The design concepts are applicable to smaller diameter detectors.

INTRODUCTION

Optimal pipeline operation transports a product safely and reliable at low cost from source to destination. To ensure safe reliable operation the quality of an in service pipeline can best be determined by an in line inspection tool. Recent concerns about pipeline and environmental safety have resulted in more and more pipeline operators preparing for in line pipeline surveys. The most common defect in pipelines is corrosion. It is also the most worrisome because corrosion becomes progressively worse as a pipeline ages and about 25% of pipeline in the ground is more than 40 years old. The most commonly used method for finding corrosion as well as other metal loss defects is the flux leakage technique. Details of flux leakage inspection tools can be found elsewhere in these proceedings [1]. Briefly:

- saturate the pipe with a magnetic field,
- detect changes in the magnetic field at flaws.

Pipetronix has recently designed and built a 12 in. metal loss tool or pig as it is called by the industry (anything pushed through a pipeline by the product is called a pig). The 12 in. Magnescan inspection pig was built primarily to detect corrosion and one of the design specifications was that the pig woud distinguish interior defects (ID) from exterior defects. The method chosen was to build a module which detects only ID (internal defects). The main flux leakage detector is sensitive to both interior and exterior defects.

The 12 in. Magnescan tool consists of up to six modules: the metal loss detector which detects both interior and exterior defects, odometer-locate which measures distance along the pipeline and receives signals from transmitters at known locations, ID detector which detects only interior defects, recorder-electronics which processes electronic signals and stores all information collected during the pig run, battery and "pinger" which sends out a signal so the pig can be located if it gets stuck, a not infrequent phenomena in small diameter pipelines. Six sections were necessary because most of the hundreds of thousands of kilometers of pipeline in the ground was built without consideration for inspection. As a result for 12 in. pipeline 1 1/2 D right angle bends are common. Pipetronix's 12 in. Magnescan tool was designed to handle back to back 1 1/2 D right angle bends.

A common method for joining modules of a multi-segment pig is to use some form of universal joint. However a major disadvantage of joining multiple sections of an instrument by universal joints is that when pressure is applied to the rear, the instrument is likely to get stuck, an undesirable situation when running a pig in a pipeline. The six modules of the 12 in. pig are joined by flexible links consisting of a wire rope core surrounded by a urethane stiffner. This method of joining the modules allows some pressure to be applied to the rear of the string without jamming the pig. The modules themselves are rigid.

The ID section can also be flexible since the ID sensor is completely contained in the sensor heads, consisting of a pair of detection coils located between the outer poles of the magnetizer. The motivation in this case being to allow it to pass through more severe pipeline restrictions.

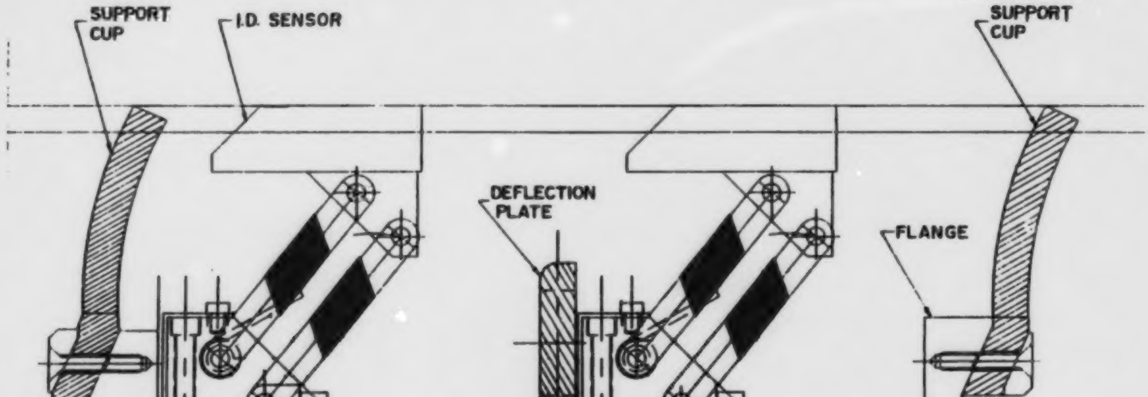

Figure no. 2: Cross-section of the flexible 12" I.D. detection section

A FLEXIBLE ID MODULE

The idea for a flexible ID module was an adaptation of the flexible links which join together the sections of the 12 in. Magnescan tool. For strength the core would consist of a wire rope. Urethane surrounding the rope would act as a stiffner. Supports for the parallel link sensor assemblies would also be of urethane. The flexible 12 in. ID module in figure 1 shows a schematic cross section of the ID module.

The final design of the ID section closely followed the original concept. The core consists of a 3/4 in. wire rope flared at the ends. This diameter, 1/8 in. greater than the flexible link core, increased the strength from 12,000 lb. to 17,000 lb. for the ID module. Wedges welded to the two end flanges secure the wire rope to the flanges. the major weakness in both the links and the flexible ID is embrittlement of the wire near the welds.

The wire rope core is surrounded by a 2 in. diameter urethane stiffner partly to ensure that the ID section is less flexible than the flexible links. The thickness of urethane might, at first, appear to make the body too stiff, however, rigidity is required to provide stable support for the sensors. Meanwhile loads, generated by pressure across the drive cups, can be up to 5600 lbs or more. At these loads the body of module becomes quite flexible in spite of the substantial amount of urethane.

As planned, the supports for the parallel link sensor mounts were also made of urethane. The supports were 4 in. in diameter. To prevent large flexibility changes along the module length and to prevent the body of the module from becoming too rigid, the supports were attached only at the front and rear, as shown in figure 1. Void space between the supports and the stiffner ensured that flexibility was determined by the stiffner alone. Teenuts embedded in the urethane supports provided attachment points for the parallel link sensor mounting assembly.

The parallel link assembly was developed about seven years ago. It has been unsurpassed in spite of many efforts to improve it. The assembly consists of a base and a pair of linkage arms which are free to pivot about the link pins as shown. The configuration keeps the face of the sensor parallel to the pipe surface at all deflections unlike most spring type arrangements which can cause some tilting. Stops restrict the upward travel of the sensor to prevent damage when inserting the module in the pipeline. The linkage allows enough slack for the sensors to follow contour variation due to pipe ovality. At an obstruction the sensor is moved down and away preventing sensor damage. The assembly was constucted to minimize sensor bounce at minor irregularities such as welds.

Sharp bends can cause severe depression of the sensor heads and could damage either the sensors or the parallel link assembly. To attempt to prevent such damage a deflector plate was added to the module. The deflector plate absorbs most excess pressure when the module rounds sharp bends. To add stiffnes to the deflector plate it is supported by the front face of the rear sensor mount assemblies.

The ID module is supported in the pipeline by front and rear support cups. Because the ID section is light no further support is required. The support cups provide no propulsion. Since many pipelines have a rough internal surfaces the support cups include hardened steel coil inserts to prevent excessive wear.

CONCLUSIONS

The ID module is a component of the 12 in. Magnescan inspection tool, one of a range of pigs varying in size from 12 in. in diameter to 48 in. in diameter developed by Pipetronix for in line inspection of pipelines. The hard diameter of the module is 8 in. and may be less because of the compressability of the urethane. At the time of writing, the flexible ID module had yet to be tested in a pipeline. Much of the technology it uses is identical to that of the rigid ID module in use. Its major innovation is its flexibility.

Flexibility has the obvious advantage

that the module should pass through all but the worst obstructions. For a 12 in. line the need for flexibility may not be great, but as Magnescan pigs for smaller diameter lines are developed by Pipetronix, flexibility may prove crucial.

ACKNOWLEDGEMENTS

We wish to thank Mr. H. S. Gram of Pipetronix for suggestions and working out details of the design. The 12 flexible ID module was built by Inspectech Ltd.

REFERENCES

1. Davies, L.A., Teitsma, A., "Design of Single Stage Pipeline Inspection Tools", Proceedings Tenth Symposium on Engineering Applications of Mechanics, 1990.

DESIGN OF SINGLE STAGE PIPELINE INSPECTION TOOLS

L.A. Davies and A. Teitsma

Pipetronix Division
International Pipeline Engineering Ltd.
450 Midwest Road
Scarborough, Ontario MIP 3A9

ABSTRACT

Good pipeline operation should include periodic inspection for pipeline corrosion and other defects. Inspection increases safety, prevents interruption of serivce, and is cost effective since repair or removal of defective sections of pipe can significantly extend the useful life of a pipeline.

The most common inspection method uses the magnetic flux leakage technique. The method requires a tool, propelled by the product flowing in the line, to travel through sections of pipeline up to several hundred miles long. Until recently, these tools were multiple stage tools. The tools were difficult to load and unload in many situations and could hang up on pipeline fixtures, interfering with pipeline operation.

Four years ago, we began the design and deployment of a series of single stage inspection tools ranging in size from 48 in. to 30 in. This paper discribes the single stage tool and the design criteria. Among the considerations were mechanical restrictions imposed by the magnetics, isolation of the electronics unit from shock and vibration, mechanical restrictions imposed by pipelines, and reliable operation over distances of hundreds of miles. Magnetic restrictions have, so far, placed a lower limit of 30 in. for single stage tools capable of passing through 3D bends.

INTRODUCTION

Optimal pipeline operation transports a product safely and reliable at low cost from source to destination. Two factors should be noted:

1) Efficient pipeline operation requires a pipeline free from defects which could force pipeline operation at reduced throughput or cause interruption of service due to line breaks.
2) Well publicized incidents have raised public awareness of pipeline safety and environmental impact.

Dealing with both factors requires knowledge of pipeline quality which can best be determined using an in line inspection tool.

Pipeline quality is partly determined by lack of defects. Defects can be introduced during manufacture (inclusions, laminations, hardspots), during construction (weld defects, gouges, dents), and during operation (third party damage, stress cracking, corrosion). Modern steels, manufacturing methods and construction practice have reduced the number of defects remaining after these stages. Better pipe coatings and better cathodic protection will reduce corrsion of new lines. But problems have not been eliminated and most of the pipe currently in service is old, with about one quarter being more than 40 years old. The most frequent defect in pipelines is corrosion.

To detect defects the most common in line inspection method uses the magnetic flux leakage technique. The essentials of this technique are:

- magnetically saturate the pipe

Figure no. I : Magnescan 48" inspection tool

- at flaws magnetic flux is forced out of the pipe
- use a sensor to detect the flux leakage at flaw locations

The inspection tool consisting of magnets, sensors electronics and a storage medium is known in the industry as a pig. The term pig is applied to a variety of tools used for inspection, cleaning, dewatering and sometimes product separation, which are pushed through a pipeline either by the product or by air depending upon the application.

Five years ago inspection pigs were configured as multi-stage tools. The minimum number of sections was two: a driver section which contained the electronics unit and a magnetic sensor section [1]. These pigs performed well but were difficult to load and occasionally hung up on pipeline fixtures. Because of pipeline industry interest and support Pipetronix started a research and develoment program culminating in the design and construction of the single stage Magnescan pig.

THE MAGNESCAN PIG

Design Specifications

The design of an inspection pig must consider restrictions imposed by existing pipelines. Some restrictions are too severe. Good design minimized the amount of in service pipeline which must be modified before it can be inspected. With this in mind Pipetronix developed the following specification for its Magnescan pig:

-pass through 3D bends
-pass through 10% bore restrictions
-by pass tees
-pass hinged Check Valves
-withstand 10g impact
-withstand velocities of 30 mph.
-low weight (e.g. maximum 6000lb. for the 48 in. pig)
-operate without mechanical failure for 500 miles

Design - 48 in. Magnescan Pig

The 48 in. Magnescan pig was designed to measure flaws in pipelines with wall thicknesses of 0.6 in. or less. The 48 in. was the first Magnescan tool designed and served as the prototype for smaller Magnescan inspection tools. The 48 in. pig is shown in Fig. 1: a schematic cross section is shown in Fig. 2.

The pig is entirely supported by twelve pairs of wheels which support and centre the pig in the pipeline. Neither the magnet assemblies nor the drive cups were designed to provide additional support. The initial wheel load is 900 lbs. Each pair of wheels supports up to 3000 lbs. The wheel springs consist of spring washers enclosed in a spring cylinder. The pig is driven through the line by pressure across the cups supplied by whatever product is being transported through the pipeline. The rear cup has by-pass holes through it so that, normally, the front cup is the drive cup. Without some by-pass the pressure on the rear cup tends to jam the pig sideways. Typical pressure differential across the drive cup are less than 1 lb. per square in. (the entire pig can be lifted by less than 4 lbs. per square in.). The rear cup serves to push the pig past areas such as tees where the product can by-pass the front cup. The front cup was designed to lift check valves or move aside any moveable object and to absorb a 10g impact.

The magnet assemblies were designed to maximize magnetic field induction into the pipe wall with the restriction that the design must be consistent with the mechanical design specifications. Experience has shown that the sensitivity of magnetic flux leakage tools increases with higher flux densities. Higher fluxes however are associated with larger heavier magnet assemblies. For example, the backing bar is solid steel and needs to have a large cross sectional area for good magnetic design. Magnet area must also be as large as possible. For the 48 in. pig an 8 in. by 1 3/4 in. backing bar was selected for both magnetic and mechanical reasons. The magnets were 8 in. by 8 in. ferrites with a

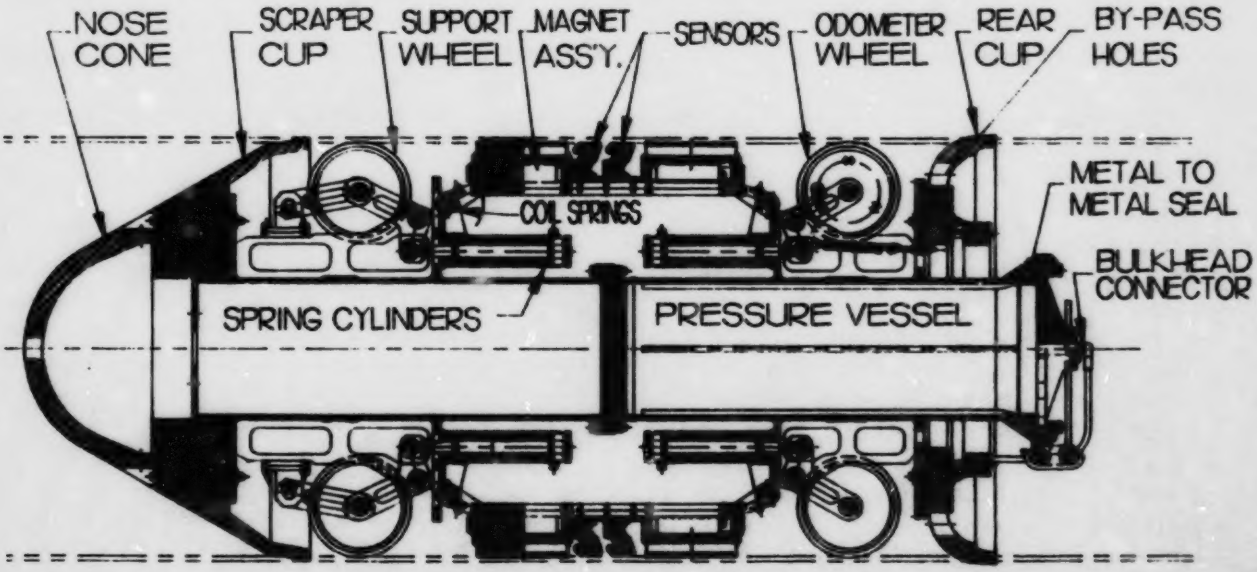

Figure no. 2: Cross-section of the Magnescan 48" flux leakage inspection pig flux density of 4 kilo gauss. Final weight was 275 lbs. per assembly. The magnet assemblies are held against the pipe wall by 400 lbs. generated by a set of custom designed 400 in lbs. coil springs.

Sensors are mounted on the magnet assembly between the two poles. The sensors use a "parallel link" system to maintain contact with the pipe wall. When a sensor hits an obstruction the link system moves the sensor down and away. The "parallel link" method has enough slack to allow the sensors to smoothly follow pipe contour changes. The parallel link mounting assembly, first developed seven years ago, has out performed all other sensor mounting methods in spite of many suggestions for "improvements".

The electronics unit, consisting of all electronics, the storage medium and power supplies, is contained in a pressure vessel which maintains an internal pressure of one atmosphere. The pressure vessel is the central component of the pig and serves as a base for mounting the components. The pressure vessel can withstand pressures greater than 2000 lbs. per sq. in. Access to the interior is through a metal to metal seal pressure tight door. A 100 pin Glenayre bulkhead connector rated at 5000 lbs. per sq. in. connects the electronics unit to the sensors.

The electronics unit is isolated from shock and vibration [1] by 3 sets of rubber wheels. Three sets are necessary to prevent a flexure vibration between the power suppliers and the data recorder. Inspection runs have shown that this simple system is adequate.

The weight of the tool was reduced by removing all excess metal including cut outs in load bearing structures where material did not add to load bearing capacity. Final weight of the tool was 6600 lbs., 600 lbs. over the weight specification. All other specifications were met.

For maintenance and shipping the tool is seated in the maintenance shipping stand. A gear wheel allows 360° rotation for assembly and disassembly. The wheel locks the pig in place when removal of magnet unbalances the tool.

Design -30 in. to 48 in. Magnescan Pigs

No important changes in the basic design were made for the smaller bore Magnescan pigs. As the diameter was reduced, the length to diameter ratio increased but all Magnescan tools have 3D bend capacity. The four basic pig sizes are 30 in.(eight pair of support wheels), 36 in. (eight pair of support wheels), 42 in. (ten pair of support wheels), and 48 in. (twelve pair of support wheels). Modification kits convert the 30 in. pig to 32 in. and 34 in., the 36 in. pig to 38 in. and 40 in., and the 42 in. pig to 44 in. and 46 in. All pigs smaller than 30 in. are multi-stage tools.

CONCLUSIONS

Simplicity is an inherent part of the Magnescan design. The tool features independent components for independent functions: support, propulsion and defect detection are each handled by independent component systems. The result is a series of tools which have, mechanically, operated without problems or breakdowns. Compared to multi-stage tools the Magnescan pig is compact, easy to handle, reliable and easy to maintain. The Magnescan inspection tool is unique in the oil and gas industry and the best in its class.

ACKNOWLEDGEMENTS

We wish to thank Mr. Corry Comello and Mr. Jeff Norman of Mecon Industries Ltd. for their valuable advice and suggestions. The 48 in. Magnescan tool was built by Mecon Industries Ltd.

REFERENCES

1.Moore, T.N., Mackintosh, D.D., and Teitsma, A., "Quantification of the Vibration Environment Experienced by Pipeline Inspection Tools", Proceedings Ninth Symposium on Engineering Applications of Mechanics, p.529, 1988.

A FRICTION SENSOR FOR SHEET METAL ROLLING

by

C. Nyahumwa, J. Jeswiet and T.N. Moore

Department of Mechanical Engineering
Queen's University, Kingston, Ontario

ABSTRACT

A sensor for measuring interface pressure in the roll gap has been designed with successful operation of the device in measuring interface friction in the cold rolling of aluminum. In order to be sure the friction measured at the interface is correct, the results are integrated across the billet surface and then multiplied be the torque arm and this quantity is compared to the input spindle torque that was measured during the experiment. These results were found to be within 5% of each other for reductions of 20% and 25%. The design of the sensor is described and the results are shown for reductions of 20% and 25%. The results are for the unlubricated rolling of aluminum.

INTRODUCTION

A sensor for the accurate measurement of interface friction in rolling has been developed at Queen's University at Kingston, Ontario. The development of this sensor has been a goal in this department for a considerable length of time, starting with Banerji and Rice (1), and followed with subsequent iterations by Jeswiet and Rice (2) and Britten and Jeswiet (3). Figure 1 illustrates the consecutive designs.

Although the design by Britten and Jeswiet (3) gave a frictional torque that was out by a factor of two for all reductions it did show that: 1) the neutral zone formed an arc across the roll face; A verification of earlier observations by Capus and Cockroft (4) who measured the change in direction of billet surface scratches before and after rolling, 2) the neutral zone increases in size with increasing reduction.

The sensor reported herein is similar in design to that of Britten and Jeswiet (3), but in this case it can measure the friction accurately.

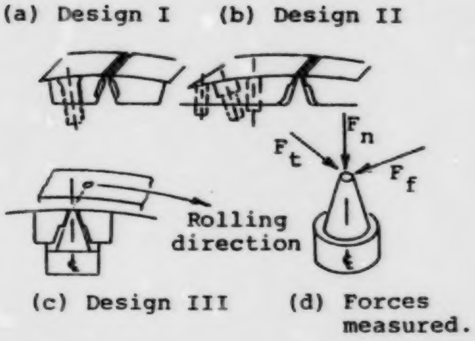
(a) Design I (b) Design II

(c) Design III (d) Forces measured.

Figure 1. The evolution of the pin type cantilever sensor as shown in (3). F_n: Normal Force. F_f: Friction force in the rolling direction. F_t : Friction force in direction transverse to rolling.

THE NEW FRICTION SENSOR DESIGN

An analysis of the sensor design III (3) indicated the gap between the active and sensing element and the filler block was too large. Calculations showed the gap should be smaller than the 0.076 mm gap used in design III, however it was virtually impossible to achieve better accuracy with the cone shaped design that had been used. Calculations showed the gap should be smaller than 0.038 mm. To meet the closer fit requirements and simplify the manufacturing procedure required for the sensor tip its shape was changed from a cone to a cylinder. The cone design required the fitting of one cone concentrically within another and then the fit of these within two cylindrical holes. Obtaining tolerances closer than those achieved with sensor design III was next to impossible.

The new sensor design is simpler because the tip of the cone now consists of two cylinders which are fit concentrically. Also, the whole unit can now be built outside the work roll and inserted into any location desired in the roll surface. The sensing unit has also been designed so that it can be ejected hydraulically if the need arises. Figures 2 shows details of the new sensor design.

The gauging technique and gauge layout method, established in earlier work, remains the same (5, 6). Also, because of the similarity of this sensor to the previous designs the calibration method was the same.

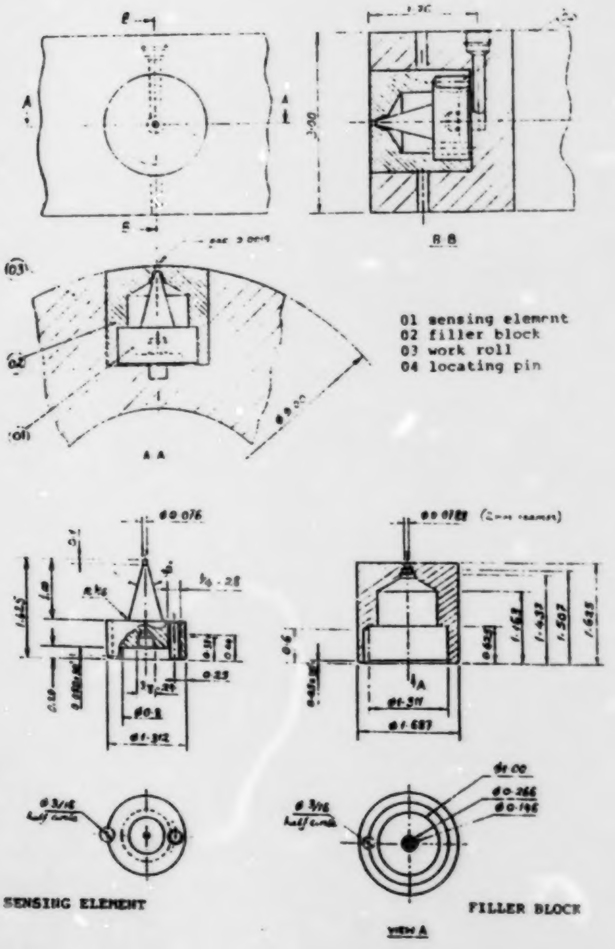

Figure 2. Drawings for the F/T/N sensor showing the sensing element and the final sensor assembly.

EXPERIMENTAL RESULTS

Rolling Conditions

Fifteen roll passes were made at 20% reduction and eight at 24.2%. The billets were 305 mm (12 inches) long with a cross-section of 16 mm (0.630 inches) wide and 6.25 mm ().25 inches) thick. the rolling speed was at 76.4 mm/s and the mill is two high with 230 mm (9 inch) diameter work rolls. Table 1 shows the data for both passes. For calculation purposes the average billet width is assumed as 16 mm 0.630 inches and the centre-line is assumed to be at 8 mm (0.315 inches).

Analysis of Friction Results

Figure 3 shows the results for five passes at 20% reduction. All the parameters measured are shown. From the top trace the bottom, the parameters measured are: F_f, through friction; N, normal force: F_t, transverse friction; RSF, Roll Separating Force; T_u, torque upper work roll; T_1, lower work roll.

Table 1. Experimental results for unlubricated cold rolling of 1100-H14 aluminum. Rolling speed 76.4 mm/s. For passes 20% and 24.2% reduction.

Pass no.	a [inches]	Entrance thickness [inches]	Exit width [inches]	Entrance thickness [inches]	Exit width [inches]	Reduction [%]	Spread [%]
32	0.211	0.236	0.190	0.657	0.688	19.5	4.7
33	0.300	"	0.190	0.654	0.684	19.5	4.6
34	0.481	"	"	0.645	0.679	19.5	5.3
36	0.245	"	"	0.635	0.667	19.5	5.0
37	0.330	"	0.188	0.606	0.643	20.3	6.1
38	0.517	"	0.189	0.651	0.679	19.9	4.3
39	0.546	"	0.188	0.635	0.667	19.9	5.0
40	0.039	"	0.189	0.632	0.663	20.3	4.9
41	0.177	"	"	0.645	0.679	20.3	5.3
42	0.618	"	0.188	0.624	0.654	20.3	4.8
43	0.324	"	"	0.630	0.660	20.3	4.8
44	0.214	"	"	0.651	0.681	20.3	4.6
45	0.184	"	"	0.608	0.642	20.3	5.6
46	0.580	"	"	0.624	0.656	20.3	5.1
53	0.306	"	0.179	0.621	0.665	24.2	7.1
54	0.512	"	0.178	0.636	0.679	24.5	6.8
55	0.051	"	0.178	0.625	0.670	24.5	7.2
56	0.108	"	0.179	0.650	0.693	24.2	6.6
57	0.241	"	0.179	0.649	0.689	24.2	6.2
58	0.520	"	0.180	0.649	0.690	23.7	6.3
59	0.371	"	0.179	0.653	0.696	24.2	6.6
60	0.061	"	0.179	0.649	0.691	24.2	6.5

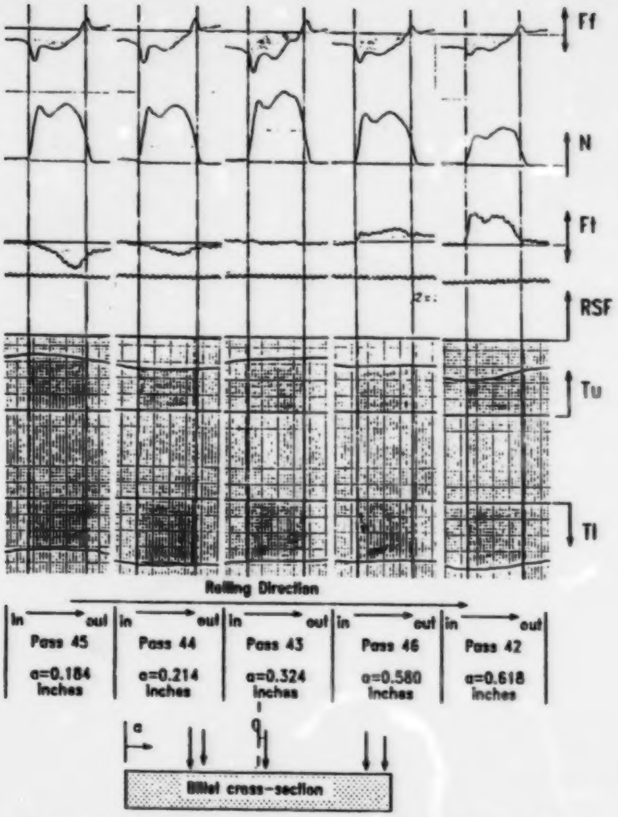

Figure 3. Results for five passes at 20% reduction, but at different distances of "a" from the billet edge. "a" is measured from the left hand edge of the billet.

It can be seen that the sensor detects an apparent friction force well before it enters the roll gap. There was some initial consternation about this. However, with the considerable amount of experience that has been developed with this sensor it was determined that temperature was not a factor. Testing revealed that the sensor gauges near the root of the sensing element along with movement of the sensor dummy gauges were the cause of the apparent friction force. However, comparisons of the frictional torque, which was calculated from the sensor friction forces shoed the results agreed with the input spindle torque that was measured. If these are equal then the friction force measured must be correct.

The parts of the experimental traces used for the calculation of frictional torque are shown shown in figure 3. These are shown by the shaded sections. For the results shown in the figure it can be seen that the transverse friction force is negligible close to the centre-line of rolling, as has been observed previously (3). As one progresses toward the billet edge the transverse friction increases to a maximum close to the billet edge. For the Normal force the maximum is along the billet centre-line and decreases to the billet edge.

The pass shown in figure 4 is useful in demonstrating how the friction torque is calculated from the experimental data.

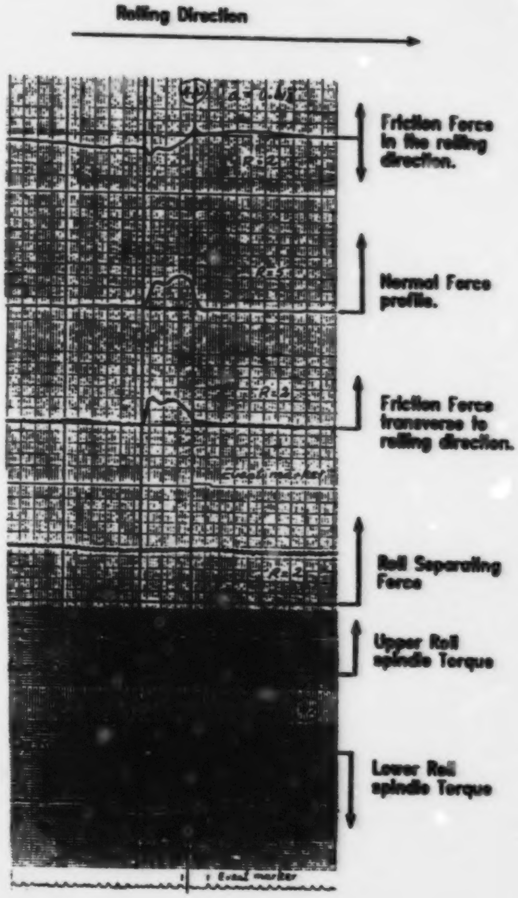

Figure 4. An example of the actual results for a 20% reduction and at a=0.618 inches. Pass 42.

The friction curve is first integrated along the arc of contact using intervals equal the sensor tip width of 1.98 mm (0.078 inches). This is illustrated in figures 5 and 6. This summaion differed depending upon the distance of the sensor from the centre-line of rolling. The summations for all the passes at the same reduction were then summed across the width of the billet using the same sensor width. This is shown in figure 7. A linear fit and quadratic fit were then tried with very negligible differences between the two. Therefore a linear fit was used.

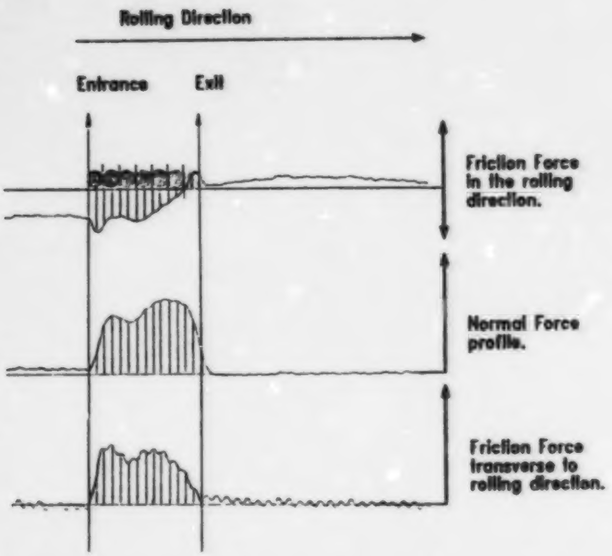

Figure 5. An illustration of pass 42 broken into two intervals, one sensor width and one half sensor width, along the rolling direction.

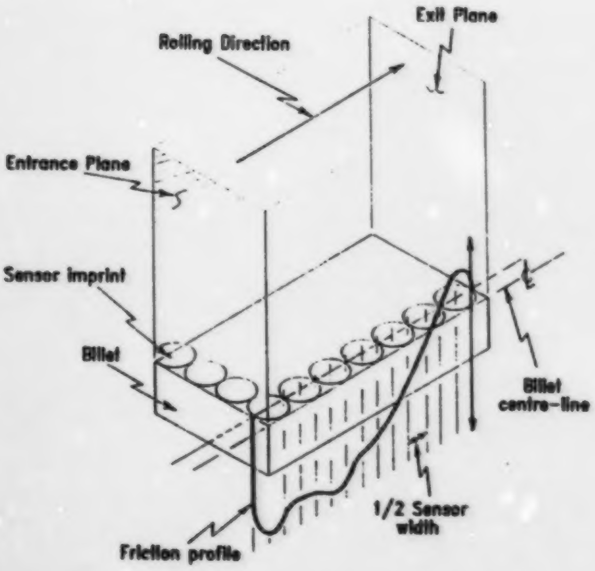
Exit Plane
Rolling Direction
Entrance Plane
Sensor imprint
Billet
Billet centre-line
1/2 Sensor width
Friction profile

Figure 6. An illustration of how the friction force is integrted across the billet arc of contact.

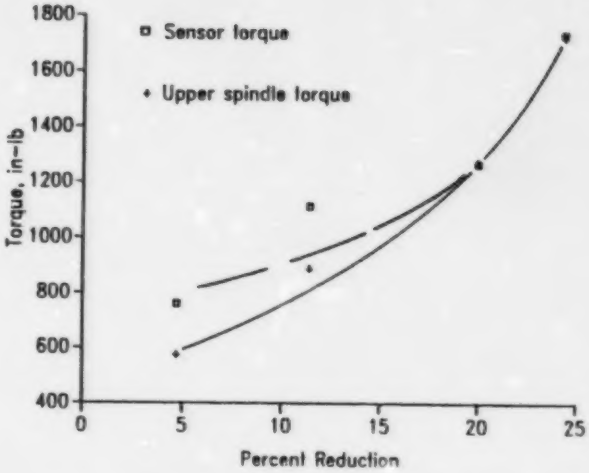

Figure 7. Friction sensor derived torque plotted versus the input torque measured at the upper spindle.

The total summation is then multiplied by the radius of the work roll giving the frictional torque. If the sensor is operating properly this frictional torque should be equal to the input spindle torque. It can be seen in the graph shown in figure 7 that this is indeed the case indicating the friction measured is correct. For example at 20% reduction the frictional torque is 1222 lb-inches and the shaft torque is 1273 lb-inches, results which are well within 5% of each other.

CONCLUSIONS

The latest design of the interface friction sensor provides an accurate measurement of the workroll/strip interface friction, as shown in the previous analysis. Verification of the friction torque with the input spindle torque shows the results to be within 5% of each other.

ACKNOWLEDGEMENTS

The authors gratefully acknowledge the support of the ALCOA Foundation grant 18961/24 and NSERC grant A 4960.

REFERENCES

1. "Experimental Determination of Normal Pressure and Friction Stress in the Roll Gap During Cold Rolling". A. Banerji and W.B. Rice. Annals of CIRP 2/1, pp53-54, 1972.
2. "The Design of a Sensor for Measuring Normal Pressure and Friction Stress in the Roll Gap During Cold Rolling". J. Jeswiet and W.B. Rice. 1982 SME/NAMRC-X transactions, p 3130
3. A Sensor for Measuring Normal Forces with Through and Transverse Friction Forces in the Roll Gap". D. Britten and J. Jeswiet. 1986 SME/NAMRC-XIV transactions. p 355.
4. "Relative Slip and Deformation During Cold Rolling". J.M. Capus and M.G. Cockroft. J. Inst. of Metals, vol 90, 1961, p 289.

DESIGN, DEVELOPMENT, AND TESTING OF A REAL-TIME IMPEDANCE CONTROL SYSTEM FOR DEBURRING OPERATION

Mohammad S. Ali, Mohammad Noori, and Janos Turi
Mechanical Engineering Department   Mathematical Sciences Department

Worcester Polytechnic Institute, Worcester, MA 01609, U.S.A.

ABSTRACT

Design, development and testing of a real-time active impedance control system for deburring are presented. This control system can simulate an active compliance including a mass, spring, and damper to accommodate the effects of normal interaction forces occurring during a deburring operation. This control system provides a bandwidth of 25.29 Hz. By on-line simulation of the mass, stiffness and damping parameters forthe impedance contoller, various behavior patterns of the controlled system are studied. Results are presented for actual deburring tests using both Force and Position Control strategies.

NOMENCLATURE

K_t = Motor torque constant (N.m / Amps.).
i = Motor current (Amps.).
J_e = Equivalent inertia = $J_m + J_s$ (Kg.m^2).
J_m = Motor's rotor inertia (Kg.m^2).
J_s = $M_s.r^2$ [the inertia on the motor's shaft equivalent to the mass of the slider (Kg.m^2)]
M_s = Slider mass (Kg).
r = Transformer modulus = $L/(2.\pi)$ (m/rad).
L = Lead of the screw (m/rev).
α = Angular acceleration of the motor shaft (rad/sec^2).
θ = Angular displacement of the motor shaft (rad).
F_{ext} = External normal load caused by the cutting process (N).
D = Mean diameter of the screw (m).
μ = Coefficient of friction.
2β = Included thread angle (rad) [21].
K_{fs} = Stiffness of the force sensor (N/m).
x = Displacement due to depth of cut = $r.\theta$ (m).

INTRODUCTION

During the process of manufacturing machine parts, irregularities, known as burrs, are often formed on the edges of surfaces. These burrs have to be removed to allow a perfect fit and to ensure safe and proper functioning of parts. Traditionally, manual deburring has been the only method available. Automation of deburring operation can improve the quality of parts while reducing the overall process cost.

In the majority of proposed efforts for automating deburring process [1-8], robotic deburring has been studied as a "trajectory-following" task. To satisfy prescribed geometric specifications however, one has to overcome the difficulty of controlling the contact force in the normal direction. This requires the incorporation of impedance into the control scheme. If the manipulator is modeled as a dynamic system with varying inertia, stiffness, and damping parameters its response to different kinds of input interaction forces can be controlled by changing these parametes. Position, i.e. high impedance, and force, i.e. low impedance, controls are considered as two forms of impedance control. The implementation of impedance control is discussed by Hogan [9,10,11]. Impedance control systems incorporating a linear stiffness have also been considered [12-15]. A controlled damping scheme has been described by Whitney [16]. The robustness issues of this approach for linear systems was addressed by Kazerooni [17].

In all these efforts [12-17] feedback from the end effector has been used to alter the robot path and to achieve the desired action. The disadvantages of this approach are discussed by Kazerooni [18]. As an alternative, Kazerooni [18] designed a controlled stiffness as an active Remote Center Compliance device with a bandwidth of 15 Hz.

The paper presens the first attempt in implementing the impedance control in its fullest form on an active mechanical manipulator (X-Y table). This manipulator can be attached to the robot arm to control the deburring process. The inertia, stiffness, and damping of this manipulator are simulated to produce different patterns of manipulator's response during the process. Several tests were performed on 4140 steel workpieces. Each workpiece was attached to the manipulator and has a step burr of 0.5 mm height which creates a force step input to the control system.

ANALYSIS OF THE PHYSICAL SYSTEM

All mechanical, dynamic, electric and hydraulic systems can be modelled using Bond Graph technique [19]. The physical system used in this work and its corresponding Bond Graph model are shown in Fig. 1 and Fig. 2 respectively. No normal interaction force is present between the deburring tool and the workpiece. Fig. 3 illustrates when the deburring operation begins. The algebraic equation of the torque required to move the slider in the same direction of the applied external load (F_{ext}) and to overcome the equivalent inertial and damping loads is :

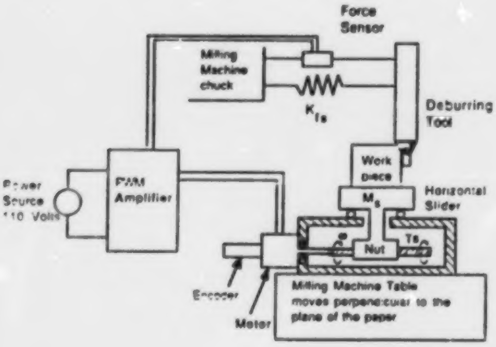
Force Sensor
Milling Machine chuck
K_{fs}
Deburring Tool
Work piece
Power Source 110 Volts
PWM Amplifier
M_s
Horizontal Slider
Nut
Ts
Encoder
Motor
Milling Machine Table moves perpendicular to the plane of the paper

Fig. 1 Schematic diagram of the test apparatus

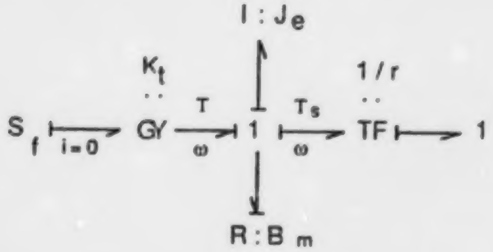
I : J_e
K_t
1 / r
S_f
i = 0
GY
T
ω
1
T_s
ω
TF
1
R : B_m

Fig. 2 Bond graph representation of Fig. 1

$$T = K_t . I = J_e . \alpha + B_m . \frac{d\theta}{dt} + F_{ext} . \frac{D}{2 . \cos\beta} . \frac{\pi . \mu . D - L}{\pi . D + \mu . L} \tag{1}$$

The F_{ext} exerted on the force sensor is

$$F_{ext} = - K_{fs} . x = - K_{fs} . \theta . (L/2 . \pi) = - K_{fs} . \theta . r \tag{2}$$

For simplicity β and μ are assumed to be negligible. Substiting F_{ext} from eq. 2 into eq. 1 gives:

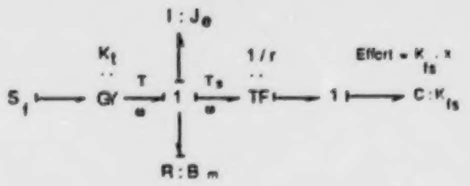
I : J_e
K_t
1 / r
Effort = K_{fs} . x
S_f
GY
T
ω
1
T_s
ω
TF
1
C : K_{fs}
R : B_m

Fig. 3 Bond graph representation at the instant the tool touchs the workpiece

$$T = K_t . I = J_e . \alpha + B_m . \frac{d\theta}{dt} + K_{fs} . r^2 . \theta \tag{3}$$

Eq. 3 in state-space is as follows:

$$\frac{dx}{dt} = Ax + Bu \tag{4}$$

Where:

$$x = \begin{bmatrix} \theta & \frac{d\theta}{dt} \end{bmatrix}^T , \quad B = \begin{bmatrix} 0 & \frac{K_t}{J_e} \end{bmatrix}^T , \quad u = i(t)$$

$$A = \begin{bmatrix} 0 & 1 \\ -\frac{K_{fs} r^2}{J_e} & -\frac{B_m}{J_e} \end{bmatrix}$$

The manipulator (X-Y table) described in this section cannot maintain a constant relative position or a constant force between the tool and the workpiece during a deburring process. Therefore, a complete impedence control imposed on the manipulator was developed to overcome this problem. The control strategy developed follows.

IMPLEMENTATION OF A FULL IMPEDANCE CONTROL

During deburring process it is difficult to predict the interaction forces between the tool and the workpiece. This is due to the random nature of physical characterstics of burrs and the vibration generated. Thus, there is a need for a manipulator which can reject or damp out these vibrations while keeping a constant force and/or maintaining a constant relative position between the workpiece and the tool. The manipulator should also sense any relatively big burr and respond to it with a fast yet stable response to satisfy the surface finish requirements.

Implementation of a full impedance control strategy on the physical system is achieved by including an impedance controller as an intermediate stage between the feedback signals and the feedforward signals to the amplifier. This controller will make the DC-Motor driven X-Y table simulate a spring-mass-dashpot system. The controller consists of hardware and software. The hardware consists of, a signal processing and conditioning unit, a data acquisition and control interface board, and a personal computer. The software developed for this controller, which represents the most important component of this strategy, has been described elsewhere [20].

The basic function of this on-line full impedance controller is to exert a simulated effort (torque) on the motor's shaft when the motor tries to move the slider away from the tool. Hence, this effort is applied at the time when the tool touches the workpiece. This simulated effort results from imposing a source of flow (angular speed of the motor shaft) on an artificial torsional vibrating system simulated by the software. By changing the dimensionless values of inertia, torsional spring, and damping parameters different kinds of dynamic behaviors can be imposed on the real system. Hence, the interaction force or the position of the tool relative to the workpiece can be controlled.

Fig. 4 shows a model of the artificial torsional vibrating system. Fig. 5 illustrates the Bond Graph representation of this system. As discussed in the previous section the source of flow represented by w in Fig. 4 is the result of the source of flow imposed on the tool holder. This source of flow can be represented by a bump on the workpiece, e.g., a simulated burr.

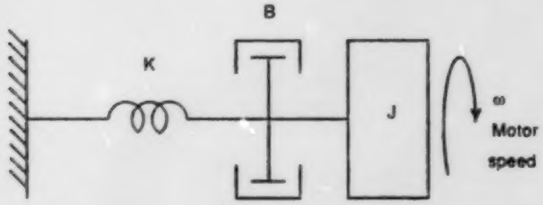

Fig.4 Model of the artificial tortional vibrating system

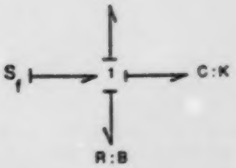

Fig. 5 Bond graph of Fig. 4

Fig. 6 shows a block diagram of the entire control system. In this figure θ_d represents a source of flow caused by a bump or a burr during the path following test or a deburring test [20].

EXPERIMENTAL STUDIES

The experiments are for evaluation of: 1) The bandwidth of the impedance control system; 2) The normal forces between the deburring tool and the workpiece-controller not present; and 3) The ability to do force and position control tests. Detailed description of other experiments are reported elsewhere [20].

Determination of the Bandwidth.

Sinusoidal forcing functions were used representing the force acting on the tool holder. The absolute value of the amplitude ratio between the speed and the force was evaluated at different input frequencies. Fig. 7 shows the frequency response curve for the control system. The bandwidth of the system, frequency corresponding to the point of intersection of the curve and horizontal line at -3 db, was 25.29 Hz.

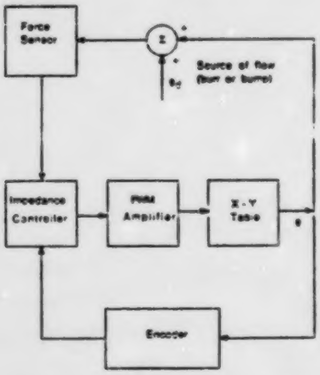

Fig. 6 Block diagram of the control system

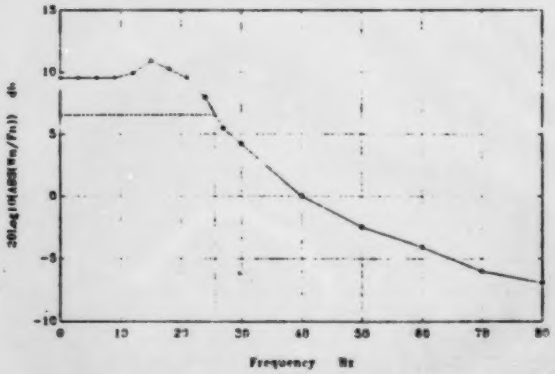

Figure 7 The frequency response for the control system

Deburring Without Impedance Controller

A deburring test was conducted on a straight edge 4140 steel workpiece with a bump of 0.5 mm height. The depth of cut was 0.254 mm (0.01 inch). The workpiece was fed at 5 mm/sec and the grinder was running at 20000 RPM. The control program was not used. The profile of the normal interaction forces during the deburring was studied. Fig. 8 shows a plot of the normal interaction forces present. It can be seen that the forces developed exceed the limit of the force sensor. Results from this study were later used in the impedance control software for changing the artificial stiffness of the slider.

Impedance Controlled Deburring Tests.

These tests were conducted to control the normal interaction forces between the deburring tool and the workpiece. The workpiece has a bump of 0.5 mm height to simulate a step burr. The depth of cut was 0.254 mm, feeding speed of the milling machine was 5 mm/sec and the grinder's speed was 20000 RPM. In

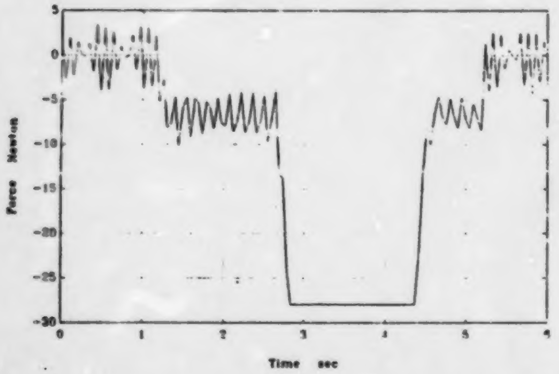

Figure 8 The normal forces between the tool and the workpiece during a deburring test without using the control program

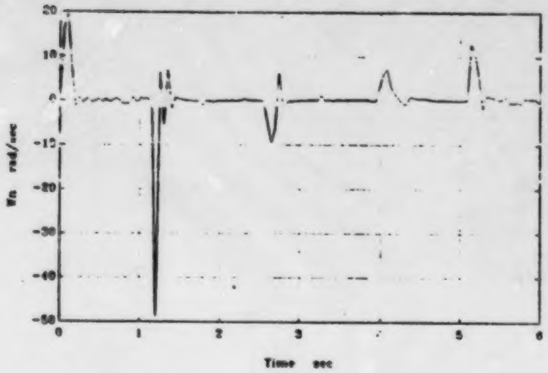

Figure 9a The system response (Motor angular speed) during force control test #1

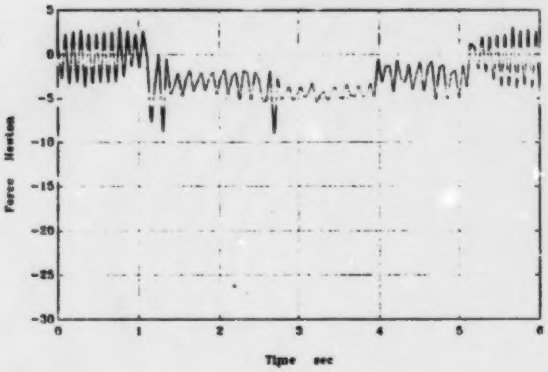

Figure 9b The normal forces between the tool and the workpiece during force control test #1

In case 1 a stiffness value of K=5, equivalent to a linear stiffness of 2936 N/m, and a damping coefficient of 0.1, equivalent to a linear damping of 58.7 N.sec/m were used in the program. Fig.'s 9a and 9b show the plots of the data collected for the corresponding test. In Fig. 9a the second jump in the speed is due to sudden increase in the interaction forces. This is when the deburring tool hits the workpiece to start the deburring process. Since the stiffness and the damping are small the overshoot of the response signal is high and it takes a relatively long time to settle down. The first jump in Fig. 9a is due to the effect of having the reference force in the program [20]. This represents the required force to be maintained between the deburring tool and the workpiece during the deburring process. The third jump results when the deburring tool hits the bump and another increase in the interaction forces is observed. The fourth jump occures when the deburring tool leaves the bump and returns to the original surface. The fifth jump is when the deburring tool leaves the surface of the workpiece. Other tests were also conducted in case 1 to examine the effect of increasing the damping coefficient on the overshoot of the system response (motor speed). Due to space limitations these results [20] are not shown.

In studies for case 2 higher values for stiffness were used, with a moderate value for damping. This was done in order to control the position of the work-piece relative to the deburring tool, and to study the effect of increasing the stiffness on the system behavior. With higher values of the stiffness used, more control on the position of the workpiece relative to the deburring tool was obtained. The value of the damping coefficient used was 1.5 and the stiffness was 150, equivalent to 88077 N/m. Fig.'s 10a and 10b show the results. Fig. 10b shows the effect of increasing the stiffness on the normal interaction forces during deburring process. The X-Y table behaves like a slider supported by a high stiffness spring and a moderate damping. The jump in the response signals was less than the one corresponding to the force control test. Other tests were also performed to study the effect of increasing the stiffness value [20]. The results are not reported herein.

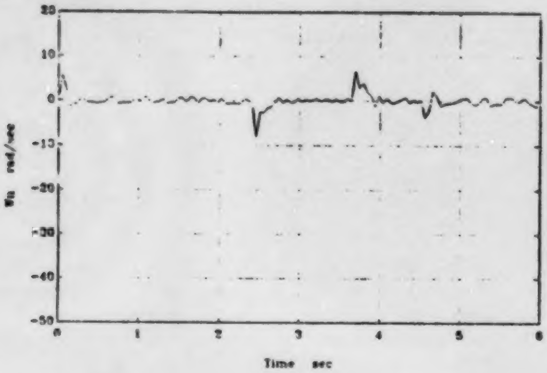

Figure 10a The system response (Motor angular speed) during position control test #1

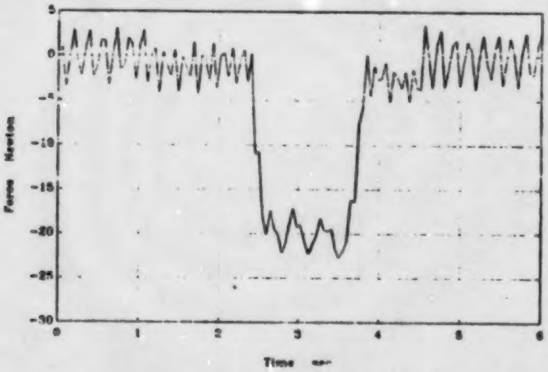

Figure 10b The normal forces between the tool and the workpiece during position control test #1

CONCLUSIONS AND RECOMMENDATIONS

Deburring process involves the interaction forces between the deburring tool and the workpiece. Ideally, the normal interaction forces and the position of the deburring tool relative to the workpiece should be maintained within a certain limit. The increase in the normal interaction forces due to deburring of a step burr should be accommodated during deburring process, rather than resisted. To do this, an impedance controller was developed and utilized. This controller simulates an inertial active system consisting of a mass, spring, and dashpot. This active system acts as a support for the slider. Position and Control strategies were achieved by simulating high and small stiffness values, respectively. The simulated dashpot in this system was used to reduce the overshoot of the system response and to increase the stability of the system. From the studies performed [20] it was found that the stability of the system was very sensitive to any slight increase or reduction in the mass parameter of the impedance controller. The bandwidth of the control system, using high sampling rate 500 samples/sec, was found experimentally to be 25.29 Hz. The sampling rate was limited and could not be increased because of the computation time involved.

Recommendations For Future Work

The principle idea of the impedance control manipulator developed in this work can be utilized in robotic deburring operations as an alternative to physical passive systems. If the robot can be taught to follow certain path of an intricate casted part, then a mini-impedance controlled manipulator can be attached to the arm of the robot to accommodate for the normal interaction forces during deburring of the part. To detect the removal of the burr special instruments such as a vision system can be installed on the robot arm. A better bandwidth, a higher sampling rate, and a wide range of stability of the system can be achieved if special devices were used to measure directly both the angular position of the motor shaft and the linear acceleration of the slider. Future work in this area includes optimizing the performance of the impedance controller developed in this work by using optimum control theory.

ACKNOWLEDGEMENTS

This work was partially supported by the National Science Foundation (Grant Number MSS-8707700). Authors would also like to thank Professor B. Seth, presently at Indian Institute of Technology, Bombay, India, for his valuable suggestions and encouragements at the early stage of this work.

REFERENCES

1. Abele, E.D. et al. 1984, Interactive Programming of Industrial Robots for Deburring, Proc. of 14th Int. Industrial Robot Symp., Minneapollis, Vol. 1.

2. Bopp, T. 1983, Robotic Finishing Applications: Polishing, Sanding,

Grinding, Proc. 13th Int. Industrial Robot Symp., Madison Vol. 1.

3. Gustaffson, L. 1983, Deburring with an Industrial Robot. Tech. Report, Society of Manufacturing Engineers.

4. Mortenson, A. 1983, Automatic Grinding, Proc. 13th Int. Industrial Robot Symp., Vol. 1.

5. Seltzer, D. 1982, Tactile Sensory Feedback for Difficult Robot Tasks, Proc. Robots VI Conf., Detroit, MI, March.

6. Thenander, R. 1983, Practical Examples of Deburring with ASEA Robot, Proc. 6th Ann. British Robot Assoc. Conf., Detroit, Mich., Vol. 1.

7. Warnecke, H.J. et al. 1980, Cleaning of Castings with Sensor Controlled Industrial Robots, Proc. 10th Industrial Robot Sump. , Vol. 1.

8. Williams, D.J. and Phillips, R.G. 1984, Robotic Deburring of Connecting Rod Liner Slots, Proc. 7th Ann. British Robotics Assoc. Conf., London, Vol. 1.

9. Hogan, N. 1983, Mechanical Impedance Control in Assistive Devices and Manipulators, pp 361-371, MIT Press, Cambridge.

10. Hogan, N. 1985, Impedance Control : An Approach to Manipulation, J.of Dynamic Systems, Measurements and Control., Vol. 107, pp 1-24.

11. Hogan, N. 1987, Stable Execution Of Contact Tasks Using Impedance Control, IEEE Technical paper No. CH2413-3/87/0000/1047, pp 1047-1054.

12. Paul, R. P., and Shimano, B. 1976, Compliance and Control, Proc. Joint Automatic Control Conference, San Francisco, pp. 694-699.

13. Andrews, R. J. 1981, Douli System : Design and Construction of a Manipulator and Controller for Research in Impedance Control, S.B. thesis, Massachusetts Institute of Technology, Cambridge, Mass.

14. Grunberg, D. B. 1983, Mechanical Impedance Control of Robotic Manipulators in Cartesian Coordinates, S.B./M.S. thesis, Massachusetts Institute of Technology, Cambridge, Mass.

15. Salisbury, J. K., Active Stiffness Conrol of a Manipulator in Cartesian Coordinates, Proc. 1986 IEEE Conference on Decision and Control. Albuquerque, New Mexico, Vol. 1, pp 95-100.

16. Whitney, D. E. 1971, Force Feedback Control of Manipulator Fine Motions, ASME J. of Dynamic Systems, Measurements and Control, June, pp. 91-97.

17. Kazerooni, H. 1985, A Robust Design Method for Impedance Control of Constrained Dynamic Systems, Ph.D. dissertation, Massachusetts Institute of Technology, Cambridge, Mass.

18. H. Kazerooni and J. Guo 1987, Direct-Drive, Active Compliant End-Effector (Active RCC), IEEE Technical Paper No. CH2413-3/87/0000/0758.

19. Rosenburg, R. and Karnopp, G. 1983, Introduction to Physical System Dynamics , McGraw-Hill, New York.

20. Ali, M. 1989, Design, Development, and Testing of a Real-Time Impedance Control system for Deburring Operation, M.S. thesis, Worcester Polytechnic Institute, Worcester, Mass.

21. Black, P.H. and Adams, O.E., 1968, Machine Design, McGraw-Hill, New York.

22. Ogata, K. 1970, Modern Control Engineering, Printice-Hall, Inc., Englewood Cliffs, New Jersey.

A DEXTERITY MEASURE FOR THE DESIGN EVALUATION OF REDUNDANT ROBOT MANIPULATORS

R. V. Mayorga * - B. Ressa ** - A. K. C. Wong *

* Dept. of Systems Design Engg., U. of Waterloo, Waterloo, Ont., Canada
** Advanced Robotics Dept., Tecnopolis/CSATA, Valenzano/Bari, Italy

1. Introduction

Due to the emerging importance of redundant manipulators several studies have been recently conducted attempting to establish some guidelines for their optimal design [6], [7], [16]; and also to perform a kinematic evaluation of some designs [8], [9], [17], [19], and [20]. In some of these studies ([6], [7], [16]) a valuable set of criteria consisting of: singularity avoidance; workspace optimization; kinematic simplicity; and mechanical constructability; are provided. However, they are subjective with respect to singularity avoidance. That is, it has been determined only the capability of singularity avoidance of some manipulators without providing a measure of this important property. Previous attempts to develop a measure for singularity avoidance and dexterity are based on establishing a performance index: derived from the singular value decomposition of the Jacobian matrix [8], [9], [17]; or from the square root of the determinant of the Jacobian matrix by its transpose [20].

Recently, Mayorga and Wong [12] have derived a local sufficiency criteria for singularity avoidance. It is shown in [12] that provided that at a time t_i the Jacobian matrix has full rank, if the norm of the Jacobian rate of change, with respect to time, is less than the inverse of the norm of the Jacobian pseudoinverse, then the rank of the Jacobian matrix is preserved at t_{i+1}. Based on this result, here it is easily shown that from the norm of the Jacobian rate of change matrix is possible to derive a lower bound for the ratio of the minimum singular value of the Jacobian over the maximum joint velocity, such that if satisfied rank preservation is insured in the entire time interval. Since the minimum singular value of any matrix is a measure of the distance to the set of all rank deficient matrices, the obtained lower bound represents in fact a dexterity measure for a robot manipulator. Here, this simple, but powerful, criteria is applied to evaluate the kinematic dexterity of 4 different designs of a HERA [5] redundant manipulator to be used in space operations. The selection of these designs is based on following the guidelines suggested in [7] and considering only some of the resultant manipulators capable to avoid all possible kind of internal singularities.

2. The Inverse Kinematics Problem

The concept of robot manipulators dexterity is intimately associated to the so-called inverse kinematics and singularities avoidance problems. For a given robot, at any instant of time, a configuration of the joints establishes a unique position and orientation of the end effector in the Cartesian space. Formally, let's consider a manipulator with n degrees of freedom and at any instant of time denote its joint variables by $\theta_i \equiv \theta_i(t)$; $i=1,2,\dots,n$. Also, let's define the manipulation variables describing the robot tasks by a vector of m variables $x_j \equiv x_j(t)$; $j=1,2,\dots,m$. Furthermore, specify $m \leq n$, that is, the case $m=n$ (nonredundant manipulator) and $m<n$ (redundant manipulator) are both considered. Finally, let $t \in [t_o, t_f]$, where t_o and t_f are the initial and final time of the task interval of time, and R^m and R^n be the m -dimensional and n -dimensional Euclidean spaces respectively, such that

$$x \equiv x(t) = \{x_1, x_2, \dots, x_m]^T \in R^m, \quad \theta \equiv \theta(t) = [\theta_1, \theta_2, \dots, \theta_n]^T \in R^n,$$

are related by

$$x(t) = f(\theta(t)). \tag{1}$$

In general, this relation is nonlinear and pointwise, hence an analytical inverse relationship cannot be easily obtained. Consequently, the inverse kinematics problem of finding a path $\theta(t)$ given a trajectory $x(t)$ is not a trivial one. Note that, at any instant of time the joint speeds in the configuration space and the corresponding end effector speed in the Cartesian space are related by the $(m\times n)$ Jacobian matrix given by:

$$J(\theta)\equiv J(\theta(t))=\partial f(\theta(t))/\partial\theta(t), \qquad (2)$$

that is, by differentiating Eq. (1) with respect to time and defining

$$\dot{x}\equiv\dot{x}(t)=dx(t)/dt,\ \dot{\theta}\equiv\dot{\theta}(t)=d\theta(t)/dt, \qquad (3)$$

then,

$$\dot{x}(t)=J(\theta(t))\dot{\theta}(t). \qquad (4)$$

From this equation, then it is possible to calculate a $\theta(t)$ path in terms of a prescribed trajectory $x(t)$. An approach to obtain at any $t\epsilon[t_o,t_f]$ a unique joint velocity vector $\dot{\theta}(t)$ for each velocity vector $\dot{x}(t)$ is by means of a Moore-Penrose [14] pseudoinverse. Let $m\leq n$ and at any $t_i\epsilon[t_o,t_f]$, $Rank[J(\theta(t_i))]=m$, then the pseudoinverse of $J(\theta(t_i))$ can be defined by:

$$J^{+}(\theta(t_i))=J(\theta(t_i))^{T}[J(\theta(t_i))\ J(\theta(t_i))^{T}]^{-1}. \qquad (5)$$

Therefore, at any $t_i\epsilon[t_o,t_f]$, a particular solution to Eq. (4) is given by:

$$\dot{\theta}(t_i)=J^{+}(\theta(t_i))\dot{x}(t_i). \qquad (6)$$

If for some $t_s\epsilon[t_o,t_f]$, $\theta(t_s)$ yields a rank deficient $J(\theta(t_s))$, i.e. $Rank[J(\theta(t_s))]<m$, then $J(\theta(t_s))$ is said to be singular, and the manipulator is said to be in a singular state or singular configuration.

As it is pointed out by Baillieul [1], the solution provided by Eq. (6) does not guarantee the generation of joint paths which for all $t\epsilon[t_o,t_f]$ avoid singular configurations. Fortunately, for redundant manipulators $(m<n)$ this problem can be further pursued by adding a null space vector to the right hand side of the Eq. (6) to obtain at any $t_i\epsilon[t_o,t_f]$ the general solution to Eq. (4) and given by:

$$\dot{\theta}(t_i) = J^{+}(\theta(t_i))\dot{x}(t_i) + [I-J^{+}(\theta(t_i))J(\theta(t_i))]v(t_i), \qquad (7)$$

where $v(t)$ is an arbitrary time varying vector of the same dimension as $\theta(t)$. However, the issue of specifying for all $t\epsilon[t_o,t_f]$, a priori the vector $v(t)$ such that $\theta(t)$ avoids singularities is still unsolved. Recently, several approaches for the proper selection of the vector $v(t)$ have been proposed. A. Ligeois [10] has suggested using $v(t)=\alpha\partial g(\theta)/\partial\theta$, where $g(\theta)$ is a performance index which is desired to be maximized instantaneously at each $t\epsilon[t_o,t_f]$, and α is a scalar function. T. Yoshikawa [20], Y. Nakamura and H. Hanafusa [13], follow a similar procedure, with the difference that $g(\theta)$ is considered to be a manipulatability measure $w(\theta)$. These approaches are based on the singular value decomposition at each $t\epsilon[t_o,t_f]$ of the Jacobian matrix [4], [20]. By considering the singular values $\sigma_1\geq\sigma_2\geq\ldots\sigma_m\geq0$, some manipulatability (dexterity) measures can be defined: (T. Yoshikawa [20]), $w(\theta)=[\det J(\theta)J(\theta)^{T}]^{1/2}$ $=\sigma_1\cdot\sigma_2\ldots\sigma_m$; (C.A. Klein [8]), $w(\theta)=\sigma_1/\sigma_m$, and $w(\theta)=\sigma_m$; which then can be further used to define a performance index. Note that these measures are relative; that is, they are appropiate for determining a best posture for a particular manipulator. Nevertheless, as pointed out by C. A. Klein [8], they cannot be used as an absolute guide for the design evaluation of different manipulators.

In the next section, the singularities avoidance approach recently developed in [12] is considered, and then the proposed dexterity measure is derived. This measure, besides being useful to detemine the best postures for a particular manipulator can also be used, unlike the ones given by Eqs. (8) and (9), as an absolute measure for the design evaluation of different redundant manipulators.

3. A Dexterity Measure

In this paper, the problem of avoiding (preventing) singularities is addressed as in [12]. First, let's introduce an additional notation: here the norm $\|\cdot\|$ stands for the p-norm $\|\cdot\|_p$, $p=1,2,\infty$ [14]. Now, note that for $t_i\epsilon[t_o,t_f]$; $J(\theta(t_{i+1}))=J(\theta(t_i))+\dot{J}(\theta(t_i))\Delta t+O(\Delta t^2)$, where, $\dot{J}(\theta(t_i))=d[J(\theta(t_i))]/dt$ and $O(\Delta t^2)$ is an $m\times n$ matrix representing second order terms. Let's define

$$\bar{J}(\theta(t_i))\equiv\dot{J}(\theta(t_i))\Delta t+O(\Delta t^2). \qquad (8)$$

Hence, the following theorem can be easily proved [12].

Theorem 1
Let $m\leq n$, and suppose that at $t_i\epsilon[t_o,t_f)$,
$Rank\{J(\theta(t_i))\}=m$. If

$$\|\, J^{+}(\theta(t_i))\,\|\ \|\,\bar{J}(\theta(t_i))\,\| < 1. \qquad (9)$$

Then

$$Rank\{J(\theta(t_{i+1}))\}=m.$$

Hence, given that at $t_i \epsilon [t_o, t_f]$, $Rank\{J(\theta(t_i))=m$, as long as Eq. (9) is satisfied a singular-free path can be obtained. Next, the following Corollaries can be easily proved and then the proposed dexterity measure can be derived.

Corollary 1
Let the assumptions of Theorem 1 be satisfied. Also let $p=2$, and σ_m be the smallest singular value of $J(\theta(t_i))$. If,

$$\|\ddot{J}(\theta(t_i))\| < \sigma_m, \tag{10}$$

then

$$Rank\{J(\theta(t_{i+1}))\}=m.$$

Proof:
From the Ineq. (10) $\|\ddot{J}(\theta(t_i))\|(1/\sigma_m)<1$. Now, ([4]) since $\|J^+(\theta(t_i))\|=(1/\sigma_m)$, then by Theorem 1 the result inmediately follows.

Note that both sides of the Ineq. (10) are related. However, by determining an upper bound for $\|\ddot{J}(\theta(t_i))\|$; thence, a lower bound for σ_m can be established to assure the rank preservation of $J(\theta(t_{i+1}))$. An easy way to obtain an upper bound for $\ddot{J}(\theta(t_i))$ is illustratred as follows. For convenience, let's drop the index t_i in the subsequent expressions, since $\dot{J}(\theta,\dot{\theta})$ is a linear function on $\dot{\theta}$ it can be decomposed in a sum of n matrices $(m \times n)$ $\hat{J}_i$ as follows:

$$\dot{J}(\theta,\dot{\theta})=\sum_{j=1}^{n}\hat{J}_j\dot{\theta}_j. \tag{11}$$

hence,

$$\|\dot{J}(\theta,\dot{\theta})\Delta t\|\leq\|\sum_{j=1}^{n}\hat{J}_j\dot{\theta}_j\Delta t\|\leq l\Delta t\sum_{j=1}^{n}\|\hat{J}_j\|, \tag{12}$$

where l is the maximum joint velocity. Now, notice that $\ddot{J}(\theta,\dot{\theta})=\sum_{j=1}^{n}[d\hat{J}_j/dt]\dot{\theta}_j$. But, each $[d\hat{J}_j/dt]$ can also be decomposed in a sum of n matrices $\ddot{J}_{jk}$. Then,

$$\|\ddot{J}(\theta,\dot{\theta})\Delta t^2\|\leq\|\sum_{j=1}^{n}[\sum_{k=1}^{n}\ddot{J}_{jk}\dot{\theta}_k]\dot{\theta}_j\Delta t^2\|\leq(l\Delta t)^2\sum_{j=1}^{n}\sum_{k=1}^{n}\|\ddot{J}_{jk}\|. \tag{13}$$

Therefore, from Eq. (9) and Ineqs. (12) and (13)

$$\|\ddot{J}(\theta,\dot{\theta})\|\leq l\Delta t\sum_{j=1}^{n}\|\hat{J}_j\|+(l\Delta t)^2\sum_{j=1}^{n}\sum_{k=1}^{n}\|\ddot{J}_{jk}\|\leq l(\alpha+\beta)\leq l(\alpha_{max}+\beta_{max}), \tag{14}$$

where $\alpha\equiv\Delta t\sum_{j=1}^{n}\|\hat{J}_j\|$, $\beta\equiv l\Delta t^2\sum_{j=1}^{n}\sum_{k=1}^{n}\|\ddot{J}_{jk}\|$, (15)

Corollary 2
Let the asumptions of Theorem 1 be satisfied. Also, let $p=2$; α and β as in Ineq. (15). If

$$\sigma_m/l > \alpha_{max}+\beta_{max}, \tag{16}$$

then

$$Rank\{J(\theta(t_{i+1}))\}=m.$$

Proof:
From Ineqs. (14) and (15), $\|\ddot{J}(\theta,\dot{\theta})\|<\sigma_m$; hence, by Corollary 1 the result inmediatly follows.

Therefore, as long as the Ineq. (16) is satisfied, a singular-free path is obtained. That is, Corollary 2 can be applied recursively in order to assure the rank preservation of $J(\theta)$ in the entire time interval $[t_o, t_f]$. Now, observe that the smallest singular value σ_m represents the distance to the set of all rank deficient matrices ([4], Pags. 19, 20) and that the Ineq. (25) establishes its proper lower bound to guarantee the rank preservation of $J(\theta)$ in the whole time interval. Since in Corollary 2 t_o, t_i, t_f, and $\theta(t_i)$ are considered arbitrary; hence, the value $\alpha_{max}+\beta_{max}$ can also be interpreted as a dexterity measure. That is, the smaller the (max) value given by (14) and (15), the easiest to comply with the Ineq. (16) in the whole time interval.

In practice it is desired/assumed that at any $t_i \epsilon [t_o, t_f]$ the joint velocities are bounded and piecewise continuous in t (i.e., $l\Delta t \rightarrow \delta$). Hence, for sufficiently small Δt the value β can be considered negligible. Therefore, for most practical cases, the value $l\alpha_{max}$ can be considered an appropiate lower bound for σ_m to assure the rank preservation of $J(\theta)$ in the entire time interval. Furthermore, since Δt is arbitrary, and $\|\hat{J}_j\|_2 \leq m\|\hat{J}_j\|_\infty$; $j=1,2,\ldots,n$; in practice, is sufficient to calculate $\sum_{j=1}^{n} \|\dot{J}_j\|_\infty \max$ to obtain a kinematic measure for a given manipulator. This value in fact represents an absolute measure; if a relative measure for a pariticular posture is desired, hence the value of α given by (15) should be used.

4. Geometries for a HERA redundant manipulator

In order to develop an efficient design for the HERA arm [5] as a redundant manipulator is convenient to consider the following approach. First, it is assumed that the HERA arm as a redundant manipulator is intended to perform the same tasks as the original design shown in Fig. 5. Hence, this design can be used as a reference and then the designs that result from augmenting it with some extra DOF can be analized. An appropiate criteria to conduct this study is the one recently proposed in [7]. Under this criteria the manipulators are evaluated according to: (a) Elimination of the internal singularities; (b) Optimization of workspace; (c) Kinematic simplicity; (d) Mechanical simplicity.

In this paper the emphasis of the study is placed on the singularities avoidance of each design. As pointed out in [6], since the addition of degrees of freedom also increases the number of internal singularities, the consideration of a 7 DOF design may be sufficient for this purpose. Among the possible designs that may satisfy the criteria shown above, the ones containing prismatic joints are neglected. Also, here the concept of kinematic simplicity is relaxed; that is, due to some constructive reasons, the three axes of the wrist joints may cross each other. Therefore, in agreement with these considerations the following resultant designs are selected.

G1

This is the first geometry that is considered and shown in Fig. 1. It differs from the original SMS design only by having a three DOF (roll, yaw and pitch) in the shoulder. This shoulder allows the avoidance of internal singularities and permits the optimization of the workspace. For this design the solution to the inverse kinematics problem may not be easy to obtain; however, this design is very appropiate. from a mechanical point of view, since the three shoulder actuators are not located in the same point of space.

G2

In this case (Fig. 2) the spheric joint in the shoulder is a roll-yaw-roll. This design provides the same advantages as the G1 design. Additionally, the simplification of the kinematics problem is achieved due to the presence of three joints with intersecting axes in the shoulder.

G3

In this case (Fig. 3) there is a roll-yaw in the shoulder, a pitch in the elbow and the forearm is split in two parts and joined with a yaw joint. Notice that the resultant design is symmetrical from this point of reference. This design although mechanically simpler than the G1 design, is kinematically more complex due to the additional link. With respect to the avoidance of internal singularities and the optimization of the workspace, this geometry presents the same capabilities as the previous designs.

G4

This design (Fig. 4) is similar to the previous design. the only difference is that the shoulder contains a pitch instead of a yaw. In this case the same comments for the G3 apply. That is, the same self-motion can be produced, and also a complex kinematics is present.

5. Design Evaluation

The proposed designs presented in Sec. 4 for a HERA arm as a redundant manipulator are evaluated in this section under the criteria derived in Sec. 3 and given by Eq. (16). For this purpose it is necessary to obtain an explicit expression for the matrices $J(\theta)$ and $\dot{J}(\theta,\dot{\theta})$. In order to generate the Jacobian matrix for each design first the link frames are assigned according to Craig's convention [3]. Then, for each case the corresponding link parameter table [3] is given as an input to a software package that uses the MAPLE symbolic computation language [15] to yield the entire (explicit form) Jacobian matix as follows:

$$J(\theta) = \begin{bmatrix} J_v \\ J_\omega \end{bmatrix}$$

Now, for convenience the indices θ an $\dot{\theta}$ are dropped in the subsequent expresions; let

$$\rho = \begin{bmatrix} p \\ \psi \end{bmatrix} = \dot{J}\dot{\theta} = \begin{bmatrix} \dot{J}_v\dot{\theta} \\ \dot{J}_\omega\dot{\theta} \end{bmatrix}, \qquad (17)$$

where, $p=[p_1,p_2,p_3]^T$ (in m/sec^2), and $\psi=[\psi_1,\psi_2,\psi_3]$ (in rad/sec^2). Notice that in general a consistent norm for the matrix $\dot{J}$ is given by

$$\|\dot{J}\| = \frac{\max}{\|\dot{\theta}\|_a=1}\{\|\dot{J}\dot{\theta}\|_b\} = \frac{\max}{\|\dot{\theta}\|_a=1}\{\|\rho\|_b\}, \tag{18}$$

where $\|\dot{\theta}\|_a$ is a norm on the joint speeds and $\|\rho\|_b$ is a norm (on accelerations) in the operational space. Hence, by specifying the limits λ_i; $i=1,2,\ldots,m$; in the operational space, a weighted ∞ norm for $\rho=\dot{J}\dot{\theta}$, can be defined by

$$\|\dot{J}\dot{\theta}\|_\infty = \|\rho\|_\infty = \max\{|\rho_i/\lambda_i|\};\ i=1,2,\ldots,m. \tag{19}$$

Here, $m=6$, $n=7$; so, it is convenient to specify $\lambda_i=\lambda_v$ for $i=1,2,3$ and $\lambda_i=\lambda_w$ for $i=4,5,6$. Then,

$$\|\dot{J}\dot{\theta}\|_\infty = \max\{|p_i/\lambda_v|, |\psi_i/\lambda_w|\};\ i=1,2,3. \tag{20}$$

Therefore,

$$\|\dot{J}\|_\infty = \max\{\|\dot{J}_v\|_\infty, \|\dot{J}_w\|_\infty\} = \frac{\max}{\|\dot{\theta}\|_\infty=1}\{\|\dot{J}_v\dot{\theta}\|_\infty, \|\dot{J}_w\dot{\theta}\|_\infty\},$$

$$= \frac{\max}{i=1,2,3}\{(1/\lambda_v)\sum_{j=1}^{n}(\dot{J}^2_{v(ij)})^{1/2},\ (1/\lambda_w)\sum_{j=1}^{n}(\dot{J}^2_{w(ij)})^{1/2}\}, \tag{21}$$

where $\dot{J}_{v(ij)}$ and $J_{w(ij)}$; $i=1,2,3$; $j=1,2,\ldots,7$; are the $i\ j$ elements of the $\dot{J}_v$ and $\dot{J}_w$ matrices respectively. Notice that $\|\dot{J}\|_\infty$ remains a function of θ. Observe that in this way it is possible to analyze, totally or separately, the effects that $\dot{J}_v$ and/or $\dot{J}_w$ have on $\|\dot{J}\|_\infty$.

For each HERA design the value $o_{max}/\Delta t$, that is, $\sum_{j=1}^{n}\|\hat{J}\|_\infty$max, is evaluated. In order to do so, first $\dot{J}$ is decomposed (in explicit form) as in Eq. (11), and in turn each $\hat{J}_j$; $j=1,2,\ldots,7$; is decomposed in a (3×7) $\hat{J}_{j/v}$ and (3×7) $\hat{J}_{j/w}$ (in explicit form) submatrices. Next, for each $\hat{J}_j$; $j=1,2,\ldots,7$ its corresponding $\|\hat{J}_{j/v}\|_\infty$ and $\|\hat{J}_{j/w}\|_\infty$ are calculated according to Eq. (21) obtaining their maximum values by careful examination (i.e. determining the appropiate θ values such that all the corresponding sin and/or cos terms take the maximum values), and by considering the ratio $\lambda_v/\lambda_w = 4$ (m/rad). Here, for convenience the index ∞ is dropped from $\|\cdot\|_\infty$ in the subsequent expressions. For each design the resultant maximum values for $\|\hat{J}_{j/v}\|$, $\|\hat{J}_{j/w}\|$, and $\|\hat{J}_j\|$ are shown in Table 1 In all cases, $\|\hat{J}_{7/v}\|=\|\hat{J}_{7/w}\|=\|\hat{J}_7\|=0.0$. Next, for each design the (total) values $\sum_{j=1}^{n}\|\hat{J}_{j/v}\|$max, $\sum_{j=1}^{n}\|\hat{J}_{j/w}\|$max, and $\sum_{j=1}^{n}\|\hat{J}_j\|$max are also computed and shown in Table 2

From the Table 2 it can be observed that the G4 design has the lowest $\sum_{j=1}^{n}\|\hat{J}_{j/v}\|$max (i.e. with respect to position) value, wheras the G1 design yields the lowest $\sum_{j=1}^{n}\|\hat{J}_{j/w}\|$max (i.e. with respect to orientation) value. However, overall (with respect to position and orientation) the G1 design possess the lowest $\sum_{j=1}^{n}\|\hat{J}_j\|$max. If the ratio λ_v/λ_w is halved; for each design, the value $\sum_{j=1}^{n}\|\hat{J}_{j/w}\|$max remains the same, wheras the value of each $\|\hat{J}_{j/v}\|$ is doubled; consequently, $\sum_{j=1}^{n}\|\hat{J}_{j/v}\|$max is doubled, and since the value for each $\|\hat{J}_j\|$ is changed, $\sum_{j=1}^{n}\|\hat{J}_j\|$max is altered. For this case again the G1 design produces the overall lowest value $\sum_{j=1}^{n}\|\hat{J}_j\|$max .

Observe that in [7] it is reported that the arm denominated Manipulator 8 (R-P-Y shoulder, R-P-R wrist) is equivalent to the Manipulator 7 (R-P-R shoulder, R-P-R wrist) and concluding in the superiority of the Manipulator 7 on mechanical reasons. In the same way it is possible to consider the G1 (R-Y-P shoulder, P-Y-R wrist) design equivalent to the G2 (R-Y-R shoulder, P-Y-R wrist) design; however, the Tables 1 and 1 show that there is a difference between these designs. That is, although a R-Y-P shoulder is equivalent to a R-Y-R shoulder, there is still a difference when the entire (i.e symmetric) geometry is considered. Furthermore, this difference is also observed by considering a design G5 made of a R-Y-P shoulder, Y elbow and P-Y-R wrist; and another one G6 consisting of a R-P-P shoulder, Y elbow, P-Y-R wrist. It is noticed that: with respect to position, the G6 design is better than the G1 and G5 although not as good as the G3 and G4; with respect to orientation and overall, the G6 is better than the G3 and G5, but worst than the G1. These results also show that, from a singularities point of view, a symmetric design (G3 and G5) may not be a good design after all. The results obtained are in agreement with the conclusions from the subjective study presented in [7]. However, here it has been possible to establish a quantitative difference, with respect to singularities avoidance, for the considered designs.

6. Conclusions

This paper has presented a dexterity measure, which can be used for the design evaluation of robot (redundant) manipulators. It has been shown that from the norm of the Jacobian rate of change matrix a lower bound for the ratio of the minimum singular value over the maximum joint velocity, can be obtained. Since the minimum singular value of any matrix is a measure of the distance to the set of all rank deficient matrices, this bound represents a dexterity measure for a robot manipulator.

The proposed criteria has been applied (in an absolute fashion) to evaluate the kinematic dexterity of five different designs of a HERA redundant manipulator to be used in space operations. The obtained results (i.e. the "best" design) are in agreement with the conclusions from previous subjective studies conducted for the design analysis of an industrial arm as a redundant manipulator.

Acknowledgment

This project was partially sponsored by a fellowship from the FORMEZ Italian agency.

References

[1] Baillieul J. "Kinematic Programming Alternatives For Redundant Manipulators", IEEE Intl. Conf. on Robotics and Automation, St. Louis Missouri, March 1985.

[2] Baker D. R., Wampler II C. W. "Some Facts Concerning The Inverse Kinematics of Redundant Manipulators", IEEE Intl. Conf. on Robotics and Automation, Raleigh N. C., March 31 - April 3, 1987.

[3] Craig J. J., "Introduction to Robotics Mechanics and Control", Addison Wesley Publishing Co. 1986.

[4] Golub G. H., Van Loan F., "Matrix Computations", North Oxford Academic, 1983.

[5] Hamann R. J., Hoogstraten J. A. "The Hermes Arm, Its Design and Verification", Proc. First European In-Orbit Operation Technology Symposium, Darmstadt, W. Germany, Nov. 1987.

[6] Hollerbach J. M., "Robots with Redundancy", Tutorial 2B, Related Characteristics Among Complex Robotic Systems, IEEE Int. Conf. on Robotics and Automation, Philadelphia PA, April 1988.

[7] Hollerbach J. M. "Evaluation of Redundant Manipulators Derived From The PUMA Geometry", The Winter Annual Meeting of the ASME, Miami Beach, Florida, Nov. 17-22, 1985.

[8] Klein C. A., "Use of Redundancy in the Design of Robotic Systems" The Robotics Research 2nd Int. Symposium, Eds. Hanafunsa H., and Inoue H., MIT Press, 1985.

[9] Kosuge K., Furuta K., "Kinematic and Dynamic Analysis of Robot Arm" IEEE Int. Conf. on Robotics and Automation, St. Louis, Missouri, Mar. 1985.

[10] Ligeois A. "Automatic Supervisory Control of the Configuration and Behaviour of Multibody Mechanisms", IEEE Trans., vol. SMC-7, No.12, pp. 868-871, Dec. 1977.

[11] Maciejewski A., Klein C., "Obstacle Avoidance for Kinematically Redundant Manipulators in Dynamically Varying Environments", Int. Int. Journal of Robotics Research, Vol. 4, No. 3, 1985.

[12] Mayorga R. V., Wong A. K. C., Ma K. S., "An Efficient Local Approach For The Optimal Path Generation of Robot Manipulators", Journal of Robotic Systems, Vol. 7, No. 1, Feb. 1990.

[13] Nakamura Y., Hanafusa H., "Task Priority Based Redundancy Control Of Robot Manipulators", The Robotics Research. 2nd Int. Symposium, Eds. H. Hanafusa, H. Inoue, MIT 1985.

[14] Stewart G. W., "Introduction To Matrix Computations", Academic Press, 1973.

[15] Symbolic Computation Group, University of Waterloo, "Maple Users Guide", WATCOM Publ. Ltd. Waterloo, Ont., 1985.

[16] Tesar D., Cleary K. R., "Decison Making Criteria for Redundant Manipulators, NATO ARW on Robots with Redundancy, Salo Lago de Garda, Italy, June 1988.

[17] Uchiyama M., Shimisu K., Hakomori K., "Performance Evaluation of Manipulators Using the Jacobian and its Application to Trajectory Planning", The Robotics Research, The 2nd Int. Symposium, Eds. Hanafusa H., Inoue H., MIT

Press 1985.

[18] Vidyasagar M., Spong M. W., "Robot Dynamics and Control", John Wiley and Sons, Inc.

[19] Wampler C. W., "Inverse Kinematics of a 7 DOF Manipulator", NATO ARW on Robots with Redundancy, Salo Lago di Garda, Italy, June 1988.

[20] Yoshikama T. "Manipulability and Redundancy Control of Robotic Mechanisms, IEEE Int. Conf. on Robotics and Automation, St. Louis Missouri, Mar. 1985.

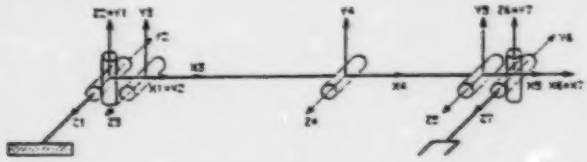

Figure 1: Geometry 1.

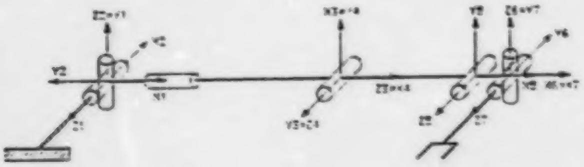

Figure 2: Geometry 2.

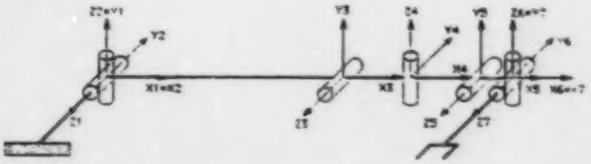

Figure 3: Geometry 3.

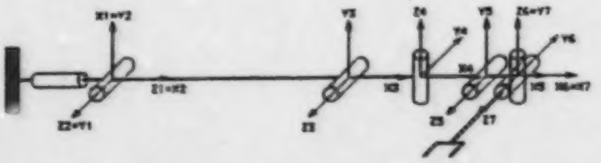

Figure 4: Geometry 4.

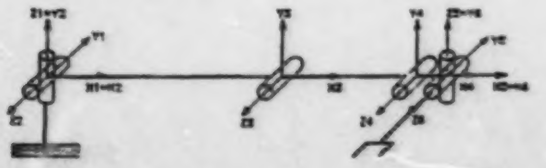

Figure 5: Original HERA geometry.

Table 1: Maximum norms.

	G1	*G2*	*G3*	*G4*
$\|\hat{J}_{1/v}\|$max	5.4	4.9	3.4	2.5
$\|\hat{J}_{1/\omega}\|$max	9.0	14.0	20.0	13.0
$\|\hat{J}_{1}\|$max	9.0	14.0	20.0	13.0
$\|\hat{J}_{2/v}\|$max	3.5	4.1	2.6	2.2
$\|\hat{J}_{2/\omega}\|$max	6.0	8.0	12.0	7.0
$\|\hat{J}_{2}\|$max	6.0	8.0	12.0	7.0
$\|\hat{J}_{3/v}\|$max	5.4	1.8	1.8	1.0
$\|\hat{J}_{3/\omega}\|$max	4.0	10.0	14.0	7.0
$\|\hat{J}_{3}\|$max	5.4	10.0	14.0	7.0
$\|\hat{J}_{4/v}\|$max	2.2	2.6	1.4	0.8
$\|\hat{J}_{4/\omega}\|$max	4.0	6.0	12.0	8.0
$\|\hat{J}_{4}\|$max	4.0	6.0	12.0	8.0
$\|\hat{J}_{5/v}\|$max	0.5	0.7	0.8	0.5
$\|\hat{J}_{5/\omega}\|$max	4.0	6.0	10.0	6.0
$\|\hat{J}_{5}\|$max	4.0	6.0	10.0	6.0
$\|\hat{J}_{6/v}\|$max	0.0	0.0	0.0	0.0
$\|\hat{J}_{6/\omega}\|$max	3.0	5.0	8.0	5.0
$\|\hat{J}_{6}\|$max	3.0	5.0	8.0	5.0

Table 2: Total sum of the maximum norms.

	G1	*G2*	*G3*	*G4*
$\sum_{j=1}^{n}\|\hat{J}_{j/v}\|$max	17.0	14.1	10.1	7.0
$\sum_{j=1}^{n}\|\hat{J}_{j/\omega}\|$max	30.0	49.0	76.0	46.0
$\sum_{j=1}^{n}\|\hat{J}_{j}\|$max	31.4	49.0	76.0	46.0

DYNAMIQUE DES MECANISMES ET ROBOTS MANIPULATEURS

Tian Bo WANG et Marc DAHAN

Laboratoire de Mécanique Appliquée
Route de Gray - 25030 BESANCON - France

RESUME

Pour établir l'équation du mouvement de chaînes articulées flexibles, nous utilisons la méthode des éléments finis et les équations de Lagrange. Nous montrons que l'assemblage des équations des éléments demande deux préparations préalables : le changement de repères et la transformation de déplacements nodaux. La méthode d'intégration pas à pas est utilisée pour la résolution numérique de l'équation non-linéaire du mouvement du mécanisme. Les résultats numériques permettent d'apprécier la validité de la méthode utilisée.

INTRODUCTION

L'étude cinéto-élastodynamique des mécanismes et l'étude dynamique des robots-manipulateurs déformables ont intéressé et intéressent beaucoup de chercheurs. Cependant, la plupart des auteurs ont restreint leur travail à l'étude plane de systèmes déformables [1,2,3,4,5]. D'autre part, les formules développées pour ces systèmes bidimensionnels ne peuvent être facilement modifiées pour s'adapter aux mécanismes spatiaux.

Dans ce travail, nous considérons une structure articulée tridimensionnelle dont les masses en mouvement sont réparties de manière pratiquement uniforme.

Pour la mise en place des équations du mouvement des éléments, nous proposons une méthode qui assure simultanément la compatibilité des déplacements, des vitesses et des accélérations en un noeud commun à différents éléments ; nombreux sont les auteurs qui ne tiennent compte que de la continuité des déplacements. Des résultats comparatifs et des graphiques font ressortir la validité des résultats obtenus.

EQUATION DU MOUVEMENT D'UN ELEMENT DEFORMABLE

L'élément considéré (fig. 1) est une poutre droite de section constante. Il est soumis à deux mouvements indépendants :

- d'une part l'élément considéré comme rigide est un grand mouvement, le mouvement du mécanisme porteur,
- d'autre part, l'élément considéré comme déformable est en petit mouvement, la vibration d'une structure élastique.

L'élément est étudié dans deux repères : le repère fixe de référence (O,x,y,z) et le repère lié à l'élément en mouvement (O_1,x_1,y_1,z_1) dont l'axe x_1 est parallèle à l'élément et dont les plans $x_1O_1y_1$ et $x_1O_1z_1$ sont des plans principaux d'inertie.

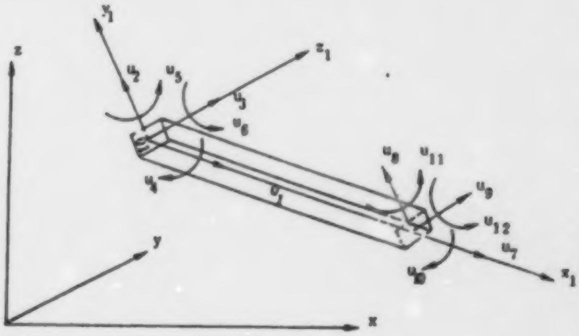

Figure 1

Les déplacements affectés à chaque noeud sont trois translations et trois rotations. On les note suivant la figure 1 :

$$U = (u_1,u_2,u_3,u_4,u_5,u_6,u_7,u_8,u_9,u_{10},u_{11},u_{12})^T . \quad (1)$$

Le vecteur déplacement U_i d'un point quelconque de la poutre est égal au produit

$$U_i = P.U, \quad (2)$$

avec

$$U_i = (u_x,u_y,u_z)^T .$$

P est une matrice de dimension 3 x 12 dont les termes sont donnés dans l'appendice.

Quand l'élément est considéré comme rigide, le grand mouvement, défini dans le repère (o,x,y,z), d'un point quelconque est déterminé par

$$X_1 = X_o + R.X_u \quad (3)$$

où $X_o = (x_o,y_o,z_o)^T$ définit le point O_1 dans le repère (O,x,y,z), R est la matrice de passage du repère (O,x,y,z) au repère (O_1,x_1,y_1,z_1) ; $X_u = (x_1,y_1,z_1)^T$ sont les coordonnées d'un point de l'élément dans le repère (O_1,x_1,y_1,z_1).

En envisageant à la fois le mouvement du mécanisme porteur et la vibration de l'élément déformable, le mouvement d'un point quelconque dans le repère (O,x,y,z) s'exprime par

$$X = X_1 + R.U_i \qquad (3)$$

et sa vitesse par

$$\dot{X} = \dot{X}_1 + \dot{R}U_i + R\dot{U}_i,$$

soit encore

$$\dot{X} = X_o + \dot{R}.X_u + \dot{R}PU + RP\dot{U}. \qquad (4)$$

On peut alors calculer l'énergie cinétique de l'élément

$$W_c = \frac{1}{2}\int_\Omega \rho\ (\dot{X})^T\ (\dot{X})\ d\Omega. \qquad (5)$$

Le grand mouvement n'affectant pas l'énergie élastique, elle a donc pour expression

$$W_e = \frac{1}{2}\int_\Omega U^T.Q^T.H.Q.U\ d\Omega. \qquad (6)$$

Les matrices Q et H sont détaillées dans l'appendice.

En reportant les expressions des énergies cinétiques et élastiques dans les équations de Lagrange, on obtient pour chaque élément du mécanisme, une équation du mouvement du type :

$$M_u.\ddot{U} + C_u.\dot{U} + K_u.U = Fu, \qquad (7)$$

avec

$$M_u = \int_\Omega \rho.P^T.P\ d\Omega,$$

$$C_u = 2\int_\Omega \rho.P^T.R^T.\dot{R}.P.d\Omega,$$

$$K_u = \int_\Omega \rho.P^T.R^T.\ddot{R}.P.d\Omega + \int_\Omega Q^T.H.Q\ d\Omega$$

$$F_u = \int_\Omega \rho.P^T.R^T.X_1\ d\Omega + Fe$$ (Fe représente les forces extérieures appliquées sur l'élément et ρ est la masse volumique de l'élément).

EQUATION DU MOUVEMENT DE SYSTEME

Dans eq.(7), les vecteurs U, $\dot{U}$ et $\ddot{U}$ sont définis dans le repère lié aux éléments correspondants. Pour formuler l'équation du système comportant plusieurs éléments, nous devons d'abord effectuer un changement de repères.

Entre le vecteur de déplacement nodal U exprimé et défini dans le repère lié à l'élément et celui Y exprimé et défini dans le repère fixe, nous avons la relation

$$U = A.Y \qquad (8)$$

avec

$$A = \begin{vmatrix} R^{-1} & & & O \\ & R^{-1} & & \\ & & R^{-1} & \\ O & & & R^{-1} \end{vmatrix}$$

Il en résulte pour la vitesse et l'accélération les expressions :

$$\dot{U} = \dot{A}Y + A\dot{Y} \qquad (9)$$

$$\ddot{U} = \ddot{A}Y + 2\dot{A}\dot{Y} + A\ddot{Y} \qquad (10)$$

Notons que certains auteurs [3,4] admettent pour la vitesse et l'accélération des expressions analogues :

$$\dot{U} = A\dot{Y} \qquad (11)$$

et

$$\ddot{U} = A\ddot{Y} \qquad (12)$$

Dans ces conditions, en assemblant les équations du mouvement des éléments pour établir l'équation du système, ils ne peuvent avoir la compatibilité des vitesses et des accélérations nodales. Cela se ressent sur la précision de la solution principalement quand la vitesse ou l'accélération du mécanisme sont élevées.

Si on reporte éq.(9) et éq.(10) dans éq.(7), on obtient :

$$My.\ddot{Y} + Cy.\dot{Y} + Ky.Y = Fy, \qquad (13)$$

avec

$$My = A^T.M_u.A$$

$$C_y = A^T.C_u.A + 2.A^T.M_u.\dot{A}$$

$$K_y = A^T.K_u.A + A^T.M_u.\ddot{A} + A^T.C_u.\dot{A}$$

$$F_y = A^T.F_u.$$

Pour toutes les liaisons actives ou pour les liaisons passives en bidimensionnel, on peut, après avoir fait le changement de repères, assembler toutes équations des éléments car les déplacements nodaux en un même noeud sont soit égaux, soit complètement indépendants. Par contre, pour les liaisons passives en tridimensionnel, certains termes du vecteur de déplacements nodaux, en un noeud commun à deux éléments, peuvent être dépendants. Pour les éliminer, nous avons dû introduire l'équation de transformation des déplacements nodaux qui s'écrit pour le ième élément du système

$$Y^{(i)} = T^{(i)}\ .\ V^{(i)}, \qquad (14)$$

$T^{(i)}$ est la matrice de transformation. A la différence de $Y^{(i)}$, les termes de $V^{(i)}$ sont soit égaux, soit indépendants.

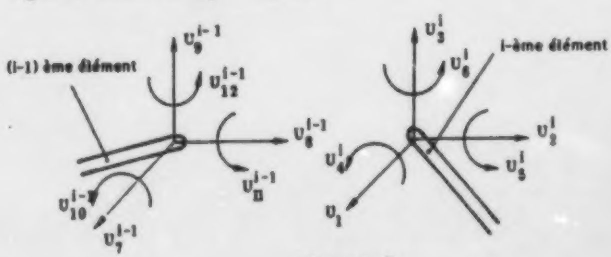

Figure 2.

A titre d'exemple, considérons la liaison rotoïde. Les déplacements nodaux à droite du (i-1)ème élément et les déplacements nodaux à gauche du ième élément sont définis dans fig.2.

Il est évident que nous avons trois égalités des déplacements suivant les trois axes :

$$y_7^{(i-1)}=y_1^{(i)},\ y_8^{(i-1)}=y_2^{i},\ y_9^{(i-1)}=y_3^{(i)}. \qquad (15)$$

Pour les déplacements angulaires $y_{10}^{(i-1)}$, $y_{11}^{(i-1)}$, $y_{12}^{(i-1)}$ et y_4^{i}, y_5^{i}, y_6^{i}, quatre sont indépendants, les deux autres peuvent s'exprimer en fonction des précédents. Par exemple, y_4^{i} et y_5^{i} s'expriment en fonction de

$y_{10}^{(i-1)}$, $y_{11}^{(i-1)}$, $y_{12}^{(i-1)}$ et $y_6^{(i)}$.

Dans ce cas, $V^{(i)}$ peut s'écrire

$$V^{(i)}=(y_1^{(i)},y_2^{(i)},y_3^{(i)},y_{10}^{(i-1)},y_{11}^{(i-1)},y_{12}^{(i1)}, \qquad (16)$$

$$y_6^{(i)},y_7^{(i)},y_8^{(i)},y_9^{(i)},y_{10}^{(i)},y_{11}^{(i)},y_{12}^{(i)})^T.$$

C'est un vecteur de dimension 13. La matrice de transformation $T^{(i)}$, de dimension (12x13), est donnée dans l'appendice.

D'après eq.(14), nous avons :

$$\dot{Y}^{(i)} = T^{(i)} \,.\, \dot{V} \qquad (17)$$

et $$\ddot{Y}^{(i)} = T^{(i)} \,.\, \ddot{V} \,. \qquad (18)$$

En reportant ces expressions dans eq.(13) nous obtenons pour le i-ème élément du système une équation sous la forme suivante :

$$M^{(i)}\ddot{V}^{(i)}+C^{(i)}.\dot{V}^{(i)}+K^{(i)} \,.\, V^{(i)} = F^{(i)}, \qquad (19)$$

avec

$$M^{(i)} = [T^{(i)}]^T \,.\, My^{(i)} \,.\, T^{(i)}$$

$$C^{(i)} = [T^{(i)}]^T \,.\, Cy^{(i)} \,.\, T^{(i)}$$

$$K^{(i)} = [T^{(i)}]^T \,.\, Ky^{(i)} \,.\, T^{(i)}$$

$$F^{(i)} = [T^{(i)}]^T \,.\, Fy^{(i)} \,.$$

Assemblant ces équations pour tous les éléments du système, on peut trouver l'équation du système :

$$M \,.\, \ddot{V} + C\dot{V} + KV = F. \qquad (20)$$

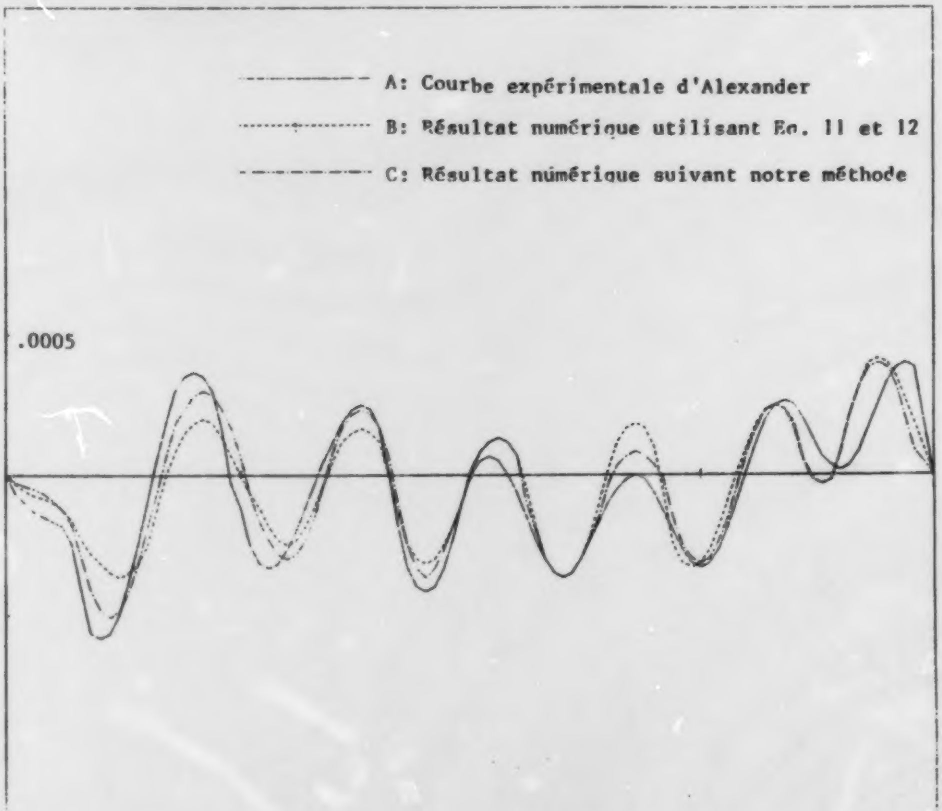

Figure 3.
ω= 400 tours/minute.

RESULTAT NUMERIQUE

La résolution de eq.(20) qui est une équation différentielle non-linéaire a été obtenue suivant une méthode d'intégration pas à pas [6]. Suivant cette technique, la réponse est calculée de proche en proche pour une suite de courts incréments de temps et on approche ainsi le comportement non-linéaire au moyen d'une séquence de systèmes linéaires successifs.

Reprenant le mécanisme plan utilisé par Alexander [1] pour effectuer un certain nombre d'essais expérimentaux, nous présentons dans les figures 3 et 4 les résultats numériques que nous avons obtenus (C) ainsi que ceux qui seraient obtenus en utilisant les eq.(11) et (12) (B).

Ces figures permettent, d'une part, de confirmer nos raisonnements et nos formules, d'autre part, de préciser nos réserves concernant les changements de repères qui n'assurent pas la continuité des vitesses et accélérations sur deux éléments voisins en un même noeud.

CONCLUSION

Nous avons présenté la modélisation de systèmes composés d'éléments déformables en négligeant l'effet de cisaillement et l'inertie due à un chargement axial.

Pour les systèmes dont les liaisons sont passives, le comportement en vibration ne doit être envisagé que si les vitesses des éléments du système sont élevées. Pour les systèmes à chaîne ouverte, dont les liaisons sont actives, les vibrations sont provoquées non seulement par les mouvements rapides des éléments du système mais aussi par le comportement des moteurs (actionneurs).

Cependant, les équations que nous avons développées dans cet article sont applicables à tous les systèmes articulés tridimensionnels, que ce soient des robots-manipulateurs ou des mécanismes à chaîne fermées.

REFERENCES

1. Alexander, R.M. & Lawrence, K.L., An Experimental Investigation of the Dynamic Response of an Elastic Mechanism, Engng for Ind., pp 268-274, 1974.

2. Bahgat, B.M. & Willmert, K.D., Finite Element Vibrational Analysis of Planar Mechanisms, Mech. and Machine Theory, Vol. 11, pp. 47-71, 1976.

3. Midha, A., Erdman, A.G. & Frohrib, D.A., Finite Element Approach to Mathematical Modeling of High-speed Linkages, Mech. and

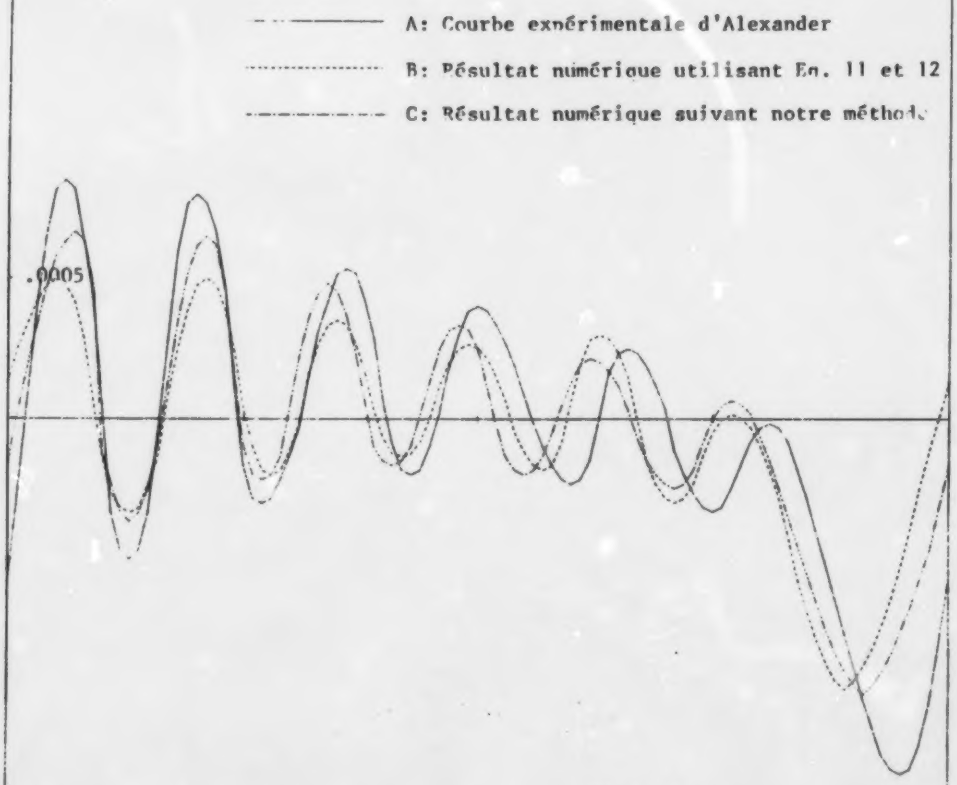

Figure 4.
ω= 400 tours/minute.

Machine Theory, vol. 13, pp. 603-616, 1978.

4. Nath, P.K & Ghosh, A., Kineto-elastodynamic Analysis of Mecanisms by Finite Element Method, Mech. and Machine Theory, Vol. 15, pp. 179-197, 1980.

5. Sunada, W. & Dubowsky, S., The Application of Finite Element Methods to the Dynamic Analysis of Flexible Spatial and Co-planar Linkage Systems, J. of Mech. Design, Vol. 103, pp. 643-651, 1981.

6. Wang, T.B, Synthèse et Etude Elasto-dynamique d'une Chaîne Fermée de Solides Articulés, Thèse, Université de Franche-Comté, Besançon, 1989.

APPENDICE

$$Q^T = \begin{bmatrix} -1 & 0 & 0 & 0 & 0 & 0 \\ 6(1-2\xi)\eta & 0 & 0 & 0 & 0 & 0 \\ 6(1-2\xi)\zeta & 0 & 0 & 0 & 0 & 0 \\ 0 & 0 & 0 & \xi l & 0 & -\eta l \\ (-4+6\xi)\zeta l & 0 & 0 & 0 & 0 & 0 \\ (4-6\xi)\eta l & 0 & 0 & 0 & 0 & 0 \\ 1 & 0 & 0 & 0 & 0 & 0 \\ 6(-1+2\xi)\eta & 0 & 0 & 0 & 0 & 0 \\ 6(-1+2\xi)\zeta & 0 & 0 & 0 & 0 & 0 \\ 0 & 0 & 0 & -\xi l & 0 & \eta l \\ (-2+6\xi)\zeta l & 0 & 0 & 0 & 0 & 0 \\ (2-6\xi)\eta l & 0 & 0 & 0 & 0 & 0 \end{bmatrix}.$$

$$P^T = \begin{vmatrix} 1-\xi & 0 & 0 \\ 6(\xi-\xi^2)\eta & 1-3\xi^2+2\xi^3 & 0 \\ 6(\xi-\xi^2)\zeta & 0 & 1-3\xi^2+2\xi^3 \\ 0 & -(1-\xi)\zeta l & (1-\xi)\eta l \\ (1-4\xi+3\xi^2)\zeta l & 0 & (-\xi+2\xi^2-\xi^3)l \\ (-1+4\xi-3\xi^2)\eta l & (\xi-2\xi^2+\xi^3)l & 0 \\ \xi & 0 & 0 \\ 6(-\xi+\xi^2)\eta & 3\xi^2-2\xi^3 & 0 \\ 6(-\xi+\xi^2)\zeta & 0 & 3\xi^2-2\xi^3 \\ 0 & -\xi\zeta l & \xi\eta l \\ (-2\xi+3\xi^2)\zeta l & 0 & (\xi^2-\xi^3)l \\ (2\xi-3\xi^2)\eta l & (-\xi^2+\xi^3)l & 0 \end{vmatrix}.$$

$\xi = \frac{x}{l}$.

$\eta = \frac{y}{l}$. l = longueur de l'élément.

$\zeta = \frac{z}{l}$.

$$H = \frac{E}{(1+\nu)(1-2\nu)} \begin{vmatrix} 1-\nu & \nu & \nu & 0 & 0 & 0 \\ \nu & 1-\nu & \nu & 0 & 0 & 0 \\ \nu & \nu & 1-\nu & 0 & 0 & 0 \\ 0 & 0 & 0 & \frac{1-2\nu}{2} & 0 & 0 \\ 0 & 0 & 0 & 0 & \frac{1-2\nu}{2} & 0 \\ 0 & 0 & 0 & 0 & 0 & \frac{1-2\nu}{2} \end{vmatrix}$$

E= module d'Young, ν= coefficient de Poisson.

$$T' = \begin{vmatrix} 1 & & & & & & & & & & & \\ & 1 & & & & & & & & & & \\ & & 1 & & & & & & & 0 & & \\ & & & 1 & & & & & & & & \\ & & & & 1 & & & & & & & \\ & & & -\frac{l'}{n'} & -\frac{m'}{n'} & & & & & & & \\ & & & \frac{l'}{n'} & \frac{m'}{n'} & 1 & & & & & & \\ & & & & & & 1 & & & & & \\ & & & & & & & 1 & & & & \\ & & 0 & & & & & & 1 & & & \\ & & & & & & & & & 1 & & \\ & & & & & & & & & & 1 & \\ & & & & & & & & & & & 1 \end{vmatrix}$$

l,m,n: cosinus directeurs de l'axe de la liaison rotoïde définis dans le repère fixe (O,x,y,z).

AN APPROACH FOR THE DESIGN AND DYNAMIC ANALYSIS OF LIGHT WEIGHT ROBOTIC MANIPULATORS USING FINITE ELEMENT METHOD

Ramachandran S. **Nagarajan T.** **Sivaprasad N.**

Dept. of Mechanical Engineering, Indian Institute of Technology
Madras 600 036, India.

ABSTRACT

Closed loop manipulators are preferred for better stiffness characteristics despite their limited work space. Present work aims at providing a design approach to lessen the problems faced by industrial engineers for design and dynamic analyses of light weight manipulators using Finite Element Method. Platform type manipulators having 6 SPS pairs of Stewart type and tetrahedron construction have been considered for the present analysis. 3D beam elements and triangular plate elements having 6 DOF per node have been used for modeling the manipulator structure. Direct stiffness formulation and consistent mass approach are used for developing Computer programs. Forces experienced during an assembly operation have been considered as load for the finite element model. Analyses have been carried out for optimization of weight based on the critical geometry of the manipulator using two different materials. Design details like dimensions of ball joints, links and actuator forces and torques have been presented. Resonant frequency which is to be taken care while the operation is being performed is predicted. Dynamic end effector deflections of the manipulators are compared by assuming a very small time step to simulate the actual working conditions.

NOMENCLATURE :

__Finite Element Parameters__ :

$[C]$	Global damping matrix
$\{F\}$	Global load vector
$\{F(t)\}$	Global time varying load vector
$[K]$	Global stiffness matrix $= [Kg]+[Kp]$
$[Kg]$	Global stiffness matrix of beam elements
$[Kp]$	Global Stiffness matrix of plate elements
$[M]$	Global mass matrix $=[M1]+[M2]$
$[M1]$	Mass matrix of beam elements
$[M2]$	Mass matrix of plate elements
$\{X\}$	Global displacement vector
$\{\dot{X}\}$	First derivative of global displacement vector
$\{\ddot{X}\}$	Second derivative of global displacement vector

__Link Parameters (pertaining to link i)__

A_i	Acceleration of link
F_i	Inertial force of link
I_i	Mass moment of inertia of link
T_i	Inertial torque of link
α_i	Angular acceleration of link
w_i	Angular velocity of link

INTRODUCTION

Robots designed with wider application potentials considering payload capacity and work space as main design factors, have a limitation on actuator speeds which are selected based on static load rating with a reasonable allowance for acceleration of links. Machine tool design practices followed till recently for robot manipulators design have resulted in heavy rigid structures. This approach allowed the designer to decouple the dynamic characteristics of the servo system and supporting structures, but necessitated the use of large actuators requiring more power. High operating speeds with heavy structures result in more inertial loads and hence complex control system designs. Light weight manipulators which create less inertial loads have an undesirable quality of large deflections. It is essential to study the dynamic performance of robots at early design stages since they work under severe unsteady dynamic conditions. Accuracy requirements have necessitated the use of multiloop spatial manipulators of closed loop type. Limitation on workspace of such manipulators does not deter their usage since they have high stiffness.

Finite element method is a useful stress analysis tool for industrial engineers. In the present work finite element method is used for analyzing robot structures with the following objectives:

a) To provide a design approach for a robot a mechanism
b) To optimize the design based on the critical geometry
c) To predict actuator drive requirements
d) To predict the end effector deflections under dynamic conditions

Forces experienced during an assembly task are used load vector based on the details presented in [1].

DESIGN PROCEDURE

A systematic approach is required for the design of manipulators which includes the determination of required degrees of freedoms (DOF), optimum linkage dimensions and design of other structural and control components.

Kinematic Synthesis

Robots are used for generating a path, motion or function over a range of operation within a specified tolerance. Initially, kinematic synthesis is done by assuming the links to be rigid to decide the cross section of links. In a high speed robot the designer either reduces the deflections of links in the structure or accounts for them in the design. Kinematic synthesis of a mechanism performed by eliminating the deflections at some specified accuracy points is inadequate since robots generate continuous paths and all the points are to be considered for synthesis. Manipulators having 6SPS pairs - Model I and one of tetrahedron type - Model II have been synthesized in [2,3]. Design of manipulators based on the proportions in [4] is made for the analysis.

Ball Joints

Motion of ball joints is always restricted practically due to physical dimensions. A ball joint assembly comprises of a ball head,a socket which houses the ball head and retainer rings to retain the ball in position. Dimensional details of ball joint assembly used for the present work are shown in Fig(1).

Link Design

Link dimensions are developed based on a layout of work piece and robot movement within the work space. Iteration techniques are used for arriving at a suitable link dimension. Computer aided design techniques are used for computing the optimum link dimensions To suit the ball joint dimensions, link diameter of 6 mm selected.

Platform Design

In a robot manipulator bottom platform is fixed to the ground and the top one to the end effector. 3 mm thick plate is used for the platform so that it is rigid enough not to deflect under load.

Actuator Design

Informations obtained from the analytic model decide the control system design. Resonant frequency, maximum velocity and acceleration of links are the main factors which influence the design of control system. Manipulator of Model I type will have the control effected at the prismatic pairs. Manipulator of Model II type will have control motors mounted at the bottom platform. Input forces and torques for the joint actuators which are required for sizing them are obtained from the finite element analysis.

Material Selection

Selection of material for the construction of a robot manipulator is an important factor especially for light weight constructions. Designer has to consider strength and stiffness, fatigue resistance, damping characteristics in the selection of materials. Several new advanced composite materials have potentially a significant role to play in the development of high speed robots. Choice of a material for the construction of a light weight manipulator is a difficult task since the design dimensions of the structure have complex relationships with the material properties.

Optimal Design

Optimization of the geometry of the manipulator is attempted in this work. Critical geometry of the manipulator is the geometry which has the minimum resonant frequency. Platform type manipulators designed based on the proportions available are analyzed for their critical geometries using finite element method.

KINETO-ELASTO-DYNAMIC ANALYSIS (KED)

KED is performed to ascertain that the dynamic stresses and dynamic deflections are within the specified tolerances. Excessive stresses and deflections impair the accuracy of the system. Methods involving rigid body dynamics provide only approximate informations about the dynamics of the system. Kineto-elasto-dynamic analysis can be performed in the following manner,

a) Using lumped mass
b) Using distributed mass

c) Using one link as elastic and other links as rigid
d) Assuming each link as a beam and using Euler-Bernoulli Theorem
e) Using assumed shape functions and Hermite polynomial expansions using Finite element method.

FINITE ELEMENT METHOD

Finite element formulation in general has stiffness matrix, mass matrix, damping matrix and load vector. Usually,finite element modeling is done by assuming the joints to have no clearances for simplifying the complexities involved in modeling the impact forces. Trigonometrical functions contained in the transformation matrices are computed from the kinematic analysis which enable the global characteristics of the mechanism of the manipulator be obtained before the application of boundary conditions such as allowable translations and rotations at the joints. In order to apply FEM to robotics the articulating system of the manipulator is modelled as instantaneous structures and the analysis is performed for small intervals of time, to simulate the exact working conditions. Mass and stiffness characteristics of the structure change continuously due to varying robot structure which is considered to be a structure in equilibrium at an instant of time under the action of various torques and forces. Damping matrix is not considered by many researchers since it requires a study of thermomechanical model constructed. However some researchers have assumed damping as a percentage of the mass and stiffness matrix. In the present work the effect of damping is not considered.

Kinematic Model

First step in performing the dynamic analysis is to perform a static analysis. A kinematic model of the manipulator specifying the pairs used at the joints and indicating their motions is made. Figs(2,3) show the physical models of the manipulator models I and II. Kinematic models of the manipulators are shown in Figs(4,5).

FE Model

Manipulators used for the analyses have been modelled using both 3D beam elements and triangular plate elements of FEM. Inner and outer elements of various pairs have separate degrees of freedoms(DOF) to account for joint clearances. Links of the manipulators have been modelled using 3D beam elements and plate elements are used for modeling the top and bottom platforms. Model I has 24 beam elements, 24 plate elements and 144 active DOF. DOF numbers 1 to 66 are specified only for the beam elements and DOF numbers 67 to 144 are common for both beam and plate elements. Model II has 30 beam elements and 12 plate elements. There are 69 active DOF for the model. DOF numbers 1 to 45 are specified only for the beam elements and DOF numbers 46 to 69 are common for both the elements. Beam elements have constant cross sectional properties and the plate elements have constant thickness. Figs(6,7) show the finite element models of the manipulators.

Analysis Procedure

Deflection analysis of the manipulator is performed is two stages. In the first stage the kinematic analysis is performed. For this purpose a deflection analysis is performed by solving the equation...

$$[K]\ \{X\} = \{F\} \qquad (1)$$

Global stiffness matrices of beam and plate elements are obtained by assembling the element stiffness matrices. The global stiffness matrix of the system is obtained by combining the global stiffness matrices of beam and plate elements. On obtaining the deflections of the robot structure corresponding to various DOF, the new co-ordinates of the links are computed and used for the subsequent analysis. Also, inertial forces and torques are computed from the displacements,velocities and accelerations of the links from the values in the appropriate DOF numbers by assuming a small time step using equations.....

$$Fi = mi \times ai \qquad (2)$$

$$Ti = Ii \times \alpha i + Ii \times wi^2 \qquad (3)$$

Input forces and torques are obtained by considering the forces experienced during an assembly task by solving equation (4) presented in the Appendix of the companion paper. By assuming a small time step, kineto-elasto-dynamic analysis is performed by the solution of the equation......

$$[M]\{\ddot{X}\}+[C]\{\dot{X}\}+[K]\{X\}=\{F(t)\} \qquad (4)$$

KED analysis is performed by assuming small time steps to near the exact working condition of the robot and is continued till the task is completed or for a specific period of time. In the present work the assembly task is assumed to be completed is a period of 2 secs with a time step of 0.05 sec. Resonant frequencies of vibration are computed using the equation ....

$$[M]\{\ddot{X}\}+[C]\{\dot{X}\}+[K]\{X\}=\{0\} \qquad (5)$$

Input torques and forces required at the joints are determined knowing the reaction forces experienced while inserting a peg in a hole. This is done for each load condition by restraining the elastic degrees of freedom at the initial end of the input pair locations. The computed input torque and force values are specified as loads for the finite element model in which the restrained degrees of freedom at the input end of input pair locations are allowed. Details of cross sections of elements and material used in the model are provided in Tables I.

COMPUTER PROGRAMS :

Computer programs in FORTRAN 77 coding for kinematic and dynamic analysis using FEM have been developed using SIEMENS 7580E system. Input details required for executing the programs have been presented in the companion paper. These programs have been developed based on the matrices presentedMin[4,5,6].

DISCUSSIONS

Based on the analysis of two type of manipulators the following conclusions are made

a) Actuator force values for Model I and torque values for Model II are presented in Figs(9,10) indicate that a constant force is required for the prismatic pairs of model I and time varying torques for the joint motors of Model II.

b) Analysis to determine the critical geometry of the manipulators which was performed by changing manipulator heights from 200 mm to 400 mm in steps of 50 mm and corresponding changes in link lengths indicates that Model II has the minimum resonant frequency at 400 mm height. Table II presents the resonant frequencies of the manipulators for the first three modes.

c) An analysis for the minimum weight of the manipulator structure is made using two different materials indicate that as much as 60% weight can be reduced when Aluminium is used. Light weight constructions when attempted should at the same time meet the specific requirements of the task.

d) End effector deflections are shown in Fig (10) for the two manipulators for the two materials considered and the one having minimum deflection will be used in tasks involving high accuracy. Load details used for the finite element models are shown in Fig(11).

CONCLUSION :

Kinematic pairs have been modelled as suggested in [4] and for modeling the platform manipulators plate elements along with beam elements have been used. Prediction of dynamic performance of a robot can be made using FEM and results obtained from other methods provide only approximate informations. This method is expected to be useful for industrial engineers for the design of robot manipulators and especially for light weight manipulators.

REFERENCES :

1. R.E.Gustavson., A theory for three dimensional mating of chamfered cylindrical parts, Trans.of ASME Journal of Mech,Trans and Autom in Design, June 1985, Vol.107,pp.112-122.

2. Hirochika Inouue.,Yuij Tsusaka.,Takeshi Fukuizumi.,Parallel Manipulator,Robotics Research, 3rd International Symposium, MIT Press, pp.321-327, 1988.

3. Alizade, R.I., Tagiyev, N. R., Kinematic Analysis of high class multiloop spatial mechanisms, Robots and Manipulators. pp.313-316.

4. Metha,Y.B., Bagci,C., Force and torque analysis of constrained space and plane mechanisms with offset links by Matrix Displacement Method, Mech.Mach Theory, Vol.9,pp.385-403,1974.

5. Rao,S.S., The finite element method in engineering, Pergamon Press, 1980, pp.382-395.

6. Ramachandran,S.,Nagarajan,T.,Sivaprasad, Estimation of resonant frequencies of platform type robotic manipulators using Finite element method, Proceedings of the Fifth IFToMM International Symposium on Linkages and Computer Aided Design Methods, Bucharest,Romania, July 6-11, 1989, pp.513-524.

TABLE I

Section Details and Material Properties

Material	E Kgf/sq.cm	G Kgf/sq.cm
Steel	2.10e06	1.15e06
Aluminium	0.70e06	0.35e06

Model I

1. 6 mm dia rod for elements 2,3,6,7,10,11 14,15,18,19,22,23.
2. 10 mm dia rod for elements 1,4,8,9,12, 13,16,17,20,21,24.
3. 3 mm thick plate elements for platforms

Model II

1. 6 mm dia rod for elements 2,3,4,5,8,9, 10,11,14,15,16,17
2. 10 mm dia rod for elements 1,4,8,9,12, 13,16,17,20,21,24.
3. 3 mm thick plate elements for platforms

Table II- Resonant Frequencies for 3 modes

Height mm	Mode	Material Steel	Material Aluminium
	Model I		
200	1	14.50	8.92
	2	15.20	16.80
	3	28.00	9.00
250	1	14.50	8.91
	2	15.20	16.80
	3	15.20	9.02
300	1	14.50	8.90
	2	18.90	16.70
	3	15.10	9.01
350	1	14.40	8.89
	2	18.90	16.70
	3	15.10	9.01
400	1	14.40	8.89
	2	15.20	16.70
	3	15.10	9.01
	Model II		
200	1	4.66	2.74
	2	5.17	3.13
	3	16.40	9.88
250	1	4.65	2.74
	2	5.16	3.13
	3	9.52	9.88
300	1	4.65	2.73
	2	5.15	3.12
	3	9.51	9.87
350	1	9.49	9.86
	2	5.14	3.12
	3	9.49	9.86
400	1	4.63	2.72
	2	5.13	3.12
	3	9.48	8.02

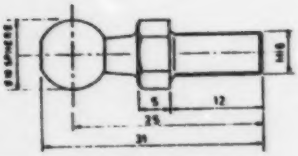
Ø10 SPHERE
M6
5
12
25
31

FIG.1a BALL HEAD

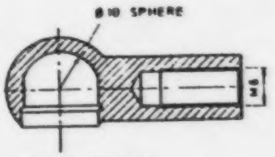
Ø10 SPHERE
M6

FIG.1b SOCKET

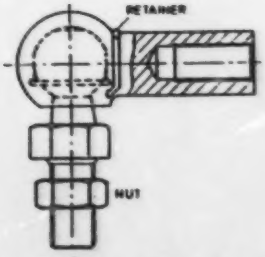
RETAINER
NUT

FIG.1 BALL JOINT ASSEMBLY

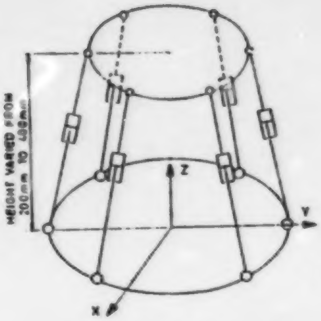
HEIGHT VARIED FROM 200mm TO 400mm
Z
Y
X

FIG.2 PHYSICAL MODEL OF 6 SPS MANIPULATOR MODEL 1.

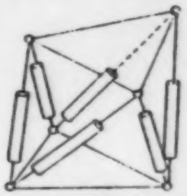

FIG.3 PHYSICAL MODEL OF 6 SPS MANIPULATOR MODEL 2

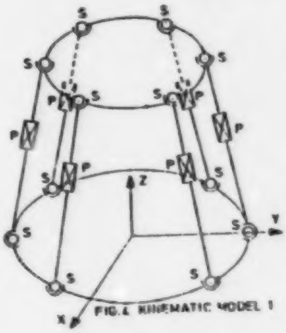

FIG.4 KINEMATIC MODEL 1

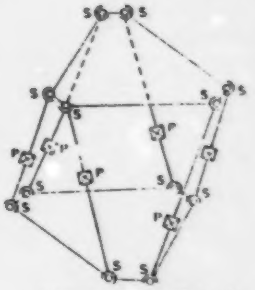

FIG.5 KINEMATIC MODEL 2

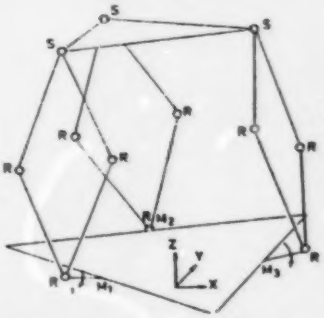
S
R
M1
M2
M3
Z
Y
X

FIG.6 KINEMATIC MODEL OF 2 WITH 9R AND 6S PAIRS (14)

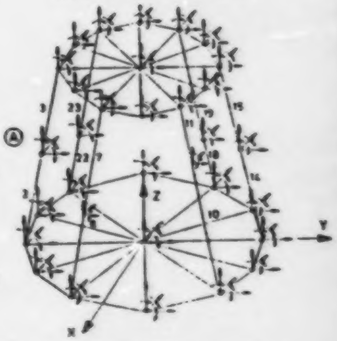

FIG.7 FINITE ELEMENT MODEL 1 (ELEMENT NUMBERS GIVEN)

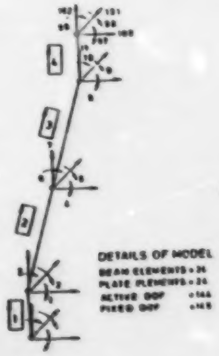
DETAILS OF MODEL
BEAM ELEMENTS = 26
PLATE ELEMENTS = 24
ACTIVE DOF = 144
FIXED DOF

FIG 7a DETAILS OF A (DOF NUMBERS GIVEN)

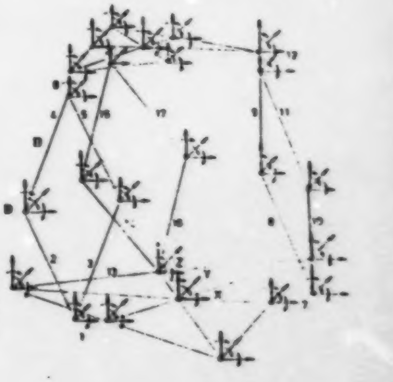

FIG.8 FINITE ELEMENT MODEL 2. (ELEMENT NUMBERS GIVEN)

DETAILS OF MODEL
BEAM ELEMENTS
PLATE ELEMENTS
ACTIVE DOF

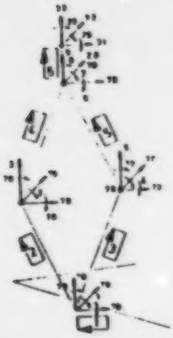

FIG. 9a DETAILS OF B DOF NUMBERS ARE METIONED IN FIG. OTHER DOF ARE FIXED DOF

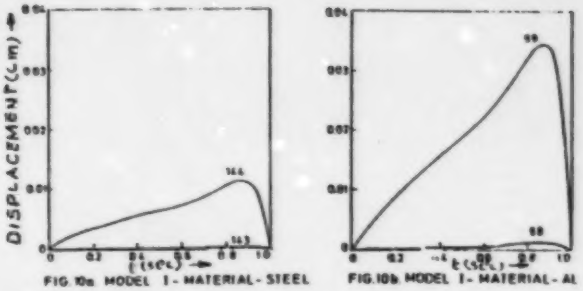

FIG. 10a MODEL I - MATERIAL - STEEL FIG. 10b MODEL I - MATERIAL - AL

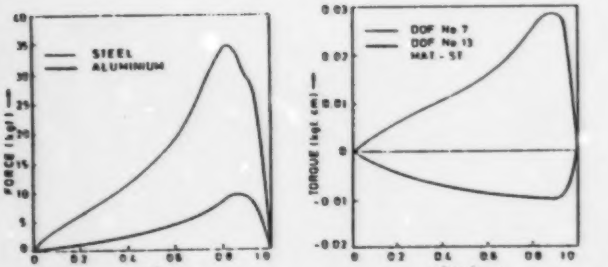

FIG 9a. INPUT FORCES - MODEL I FIG. 9b INPUT TORQUES - MODEL II

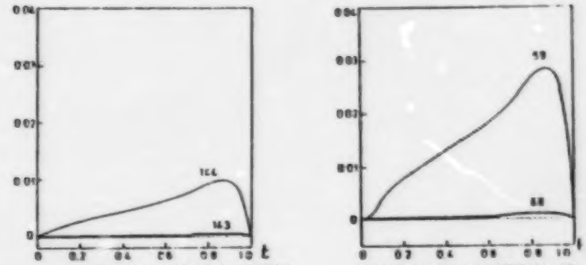

FIG 10c MODEL II - MATERIAL - STEEL FIG 10d MODEL II - MATERIAL - AL

FIG. 10. END EFFECTOR DISPLACEMENT

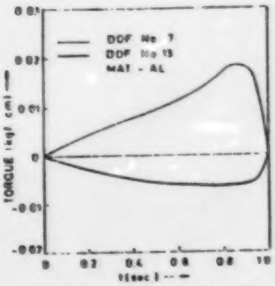

FIG. 9c. INPUT TORQUES - MODEL II

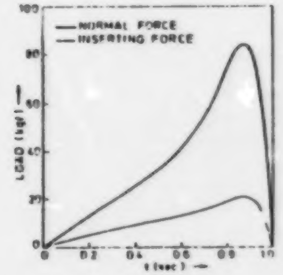

FIG. 11 LOAD DIAGRAM

FIG. 9 ACTUATOR INPUT PARAMETERS

ECONOMIC EVALUATION OF A CEMENT FLOOR FINISHING ROBOT

O. Moselhi, P. Fazio and S. Hason

Centre for Building Studies, Concordia Unversity
1455 de Maisonneuve Blvd. W., Montreal, Quebec, H3G 1M8

ABSTRACT

Construction automation has received considerable attention in recent years in an effort to overcome the problems of declining productivity, increasing labour costs, hazards in the workplace, and scarcity of skilled labour. However, since the construction industry has very little experience with robotics, there is little concensus regarding its use. This paper is part of a research effort aimed at identifying promising robotic applications in construction. Such applications are expected to exist when need and economic benefits are highest, and when technological and institutional resistance are lowest. The paper first identifies important constraints in the development and implementation of automation in construction. Next, the general benefits and costs of robot use in construction are identified. The paper presents what is believed to be the first economic analysis of an operational construction robot based on actual performance data. The analysis indicates that even at consevative robot efficiency values, the user incurs substantial benefits, and payback can be less than 18 months.

INTRODUCTION

Over the past fifty years, the construction industry has witnessed the application of a number of technological developments which have significantly changed almost every phase of the building process. First, mechanization brought raw power to virtually every operation from material handling to large scale assembly. Second, prefabrication of structural and architectural components enabled the application of factory-based mass production techniques, thus permitting further cost savings. Third, development of new materials made it easier and less costly to build. Fourth, and most recently, advances in microelectronics have enabled microprocessor control of construction equipment and have opened the door to on-site automation and robotics.

Construction automation and robotics first started to receive serious attention in 1983 as a result of Japanese and American interest [29]. Since then, research undertaken by over a dozen countries has produced various prototypes and commercially available systems for a number of applications, including structural steel erection, concreting, bricklaying, and interior wall erection [36, 38]. Canada, despite an excellent technological base in industrial automation and robotics [27], has yet no clear commitment to construction automation. This situation is expected to change as domestic and international pressures will increasingly force Canadian contractors to adopt robotic technologies in order to remain competitive both at home and abroad.

Recognizing the need for automation and robotics in the Canadian construciton industry, research currently undertaken at the Centre for Building Studies is aimed at identifying those applications that have the highest potential for automation. Such applications are expected to exist when need and economic benefits are highest, and when technological and institutional resistance are lowest. Within this established framework, this paper will examine the economic consequences of a robotic application selected through previous research by the authors [12,25, 26]. The paper first identifies important constraints in the development and implementation of automation in construction. Next, the general benefits and costs of robot use in construction are identified. Existing economic methods are reviewed, and an analysis of a commercially available system is performed.

IMPLEMENTATION CONSTRAINTS

Despite improvements in equipment, materials, techniques, and management, the construction industry has not experienced the same relative growth in productvity that has been achieved in other sectors of the economy. In fact, most estimates of construction productivity point to a slow growth rate [31, 37] or even a decline [11] when compared to other sectors. Whatever the case may be, productivity growth has certainly not been strong enough to offset escalating labour and material costs [10, 32]. The situation is further exacerbated by numerous forecasts of skilled labour shortages by the 1990's [7,18, 20].

Concerns over quality [34], and safety -the construction industry has more than double the average national accident rate, making it second only to forestry [6]-, are also strong motivators for introducing robots. The use of robots year round in Canada is expected to be an additional advantage since winter construction costs in major cities are approximately 25% greater than in the summer, and productivity of many trades drops by at least 20-30% when temperatures fall below 0°C or rise above 32°C [2]. Construction robots are also seen as important to the development of Canada's north, where it is estimated that 27% of the value of large energy-related projects will be spent, making it the second most important region in Canada in this respect [18].

In view of the issues just discussed, the need for automation and robotics in construction cannot be dismissed. Development and implementation of this technology is contingent however on a number of factors owing to unique product, market, and industry characteristics, and will therefore occur distinctly relative to manufacturing. Bearing these differences in mind, most researchers agree that the natural development of construction automation will at first involve the robotization of discrete tasks at the equipment level, followed by the combination of several activities by multitask machines, and will eventually result in the development of new methods or the redesign of traditional ones to facilitate full site automation [5,25,39]. Factors representing important constraints on the development of construction robotics are discussed here below.

Technological Constraints

Unlike many manufacturing applications, the operational environment in construction is largely unstructured and dynamic: Work is custom built with little standardization of output, actual dimensions of both parts and locations often vary from those specified on drawings, and there is virtually no process that is carried out at any single location. Operating in such an environment suggests the need for sophisticated mobility, sensory feedback, and adaptive control systems, with the added seemingly paradoxical requirement that the equipment must also be able to withstand harsh and hostile working conditions, i.e. out of doors, in dusty and cluttered spaces, and generally abusive manhandling. Most construction robots are therefore expected to be rugged vehicle-manipulator combinations [24,41], whose working space changes with the progress of the work, and whose travelling surface may be uneven, unlevel, and and/or unstable.

Despite considerable progress over the past decade, interaction with such a flexible environment requires technological capabilities which surpass the limits of existing technology. Most current robot programming methods, i.e. teach and on-line programming, allow minimal sensory integration and are impractical for applications involving low volume, complex, or non-repetitive tasks [8,14,22]. The development of off-line and task level programming languages, where the user provides a high level description of the task and lets the computer plan trajectories, movements, and sensor operations, is the key to truly intelligent robot systems [16].

Business Constraints

The different nature of the building market and the ensuing risks to construction firms make implementation of automation in construction more difficult that it is in manufacturing. Key features of the Canadian market have been analyzed in a previous study [12], and the portrait of the average Canadian construction firm which was obtained is one of a small, competitive, and highly leveraged firm, operating in a seasonal and cyclical industry, which, due to functionally segregated delivery and production systems, is highly specialized and has short term, project specific needs.

This type of environment, combined with the potentially long duration required for construction, makes any large capital investment risky. Consequnetly, for the average contractor to introduce robotic equipment it will have to be proven that its use will result in costs savings, improved delivery time, and thus increased profits. It is believed that robots "whose primary justification is quality improvement without increase in productivity need to overcome inherent disincentives in the building delivery process" [33].

Institutional Constraints

Implementation of automation may be further delayed by the heavily institutionalized regulatory and industrial relations systems in construction. Industry practitioners are subjected to perhaps more regulations, administered by more levels of government, than those in any other industry [9]. This regulatory framework hampers the industry's ability to innovate, and prevents it from using, within a reasonable amount of time, the most technically advanced systems and materials.

The construction industry is also unique in its industrial relations system, differing from the standard industrial relations system of other industries which is characterized by single union certification and single employer bargaining [1]. In most Canadian provinces today, mutli-employer associations negotiate on a province-wide basis with single trade or multi-trade union organizations. Although union membership varies by sector and province, it is estimated to be generally much stronger in Canada than in the U.S. [3]. In Quebec, a unique situation in North America exists, wherein all workers must belong to one of five recognized trade unions, all employers must belong to a provincial employer associaion, and settlements are extended by government decree over the whole province. The main effects of the decree system have been identified by a government study on deregulation as 1) restricting access of skilled workers and 2) impeding technological change [15].

ECONOMIC EVALUATION

Construction tasks are expected to have a high potential for automation when need and economic benefits outweigh technological barriers and institutional resistance. In order to evaluate automation potential in construction, a multicriteria Automation Index has been proposed [12], based on readily available information from the highly regulated construction industry in Québec, and supplemented by industry experience obtained through surveys. Within this model, economic evaluation provides the ability to compare the benefits of robotization with those of present construction methods.

A wide body of literature exists concerning the economic justification of robots in industrial applications [13,21,40]. The fact that the problem has been reduced to a 'cookbook' approach [23] further indicates that the issue is generally well understood. Most of these economic evaluation methods differ principally in the degree to which they allow for indirect benefits to be considered. Although essentially similar, the evaluation of construction robots deals with different economic variables. Table 1 summarizes direct and indirect benefits, and costs which must be considered in evaluating construction robots.

Due to very limited experience, few economic models exist for evaluating construction robots. Warsawski [41] was among the first to address this issue. In the absence of actual capital, operating, and maintenance cost data, he determined the value of a 'general purpose' construction robot as the present worth of direct labour savings less associated robot expenses. With the benefit of prototype designs for a dedicated sandblasting robot, Skibniewski [35] determined robot value for a 'typical project', and a yearly estimate was obtained by assuming a number of such projects per year. The two methods have been compared earlier by the authors [26], and found to yield significantly different results, suggesting that a closer assessment of economic variables is necessary. This paper presents what is believed to be the first economic analysis of an operational construction robot based on actual performance data.

EXAMPLE APPLICATION

As a preliminary investigation into the economic feasibility of construction robotics, an example application of a cement floor finishing robot is considered. The robot in question is commercially available in Japan, and its value is examined from the point of view of a Montreal based subcontractor, based on the assumption that the robot is purchased. The strength of construction unions and the harshness of the climate provide an interesting 'worst case' scenario.

The cement floor finishing process begins when the concrete has hardened, allowing approximately a 1/8 inch footprint indentation [30]. A walk-behind machine, known as a power trowel, consisting of four blades attached to a rotating shaft, is swept over the concrete surface. The process involves a first pass, called floating, and two or more successive passes, called troweling. Floating embeds coarse aggregate, removes humps and valleys, and compacts the concrete surface. Troweling is done after floating to producte a dense, smooth and hard surface. During floating, the blades are always kept flat, but are tilted during troweling to increase pressure on the surface. Although the time needed for initial hardening, and for setting after floating, is significantly affected by ambient temperature and humidity, it is not uncommon for crews to work, from initial pouring to final finishing, 12 hour shifts or more.

A general view of the robot is presented in Fig. 1. It consists of the main unit, remote control, power source, and cable reel. Normally the unit is operated automatically, although remote operation is possible. The dimensions of the area to be finished are input as well as the choice of a starting direction. The robot is designed so that the whole area can be covered by a series of transversal passes which are automatically calculated by the onboard computer. Touch sensors arranged around the main unit enable the robot to avoid obstacles. There are two rotating shafts of 4 blades each which rotate

Table 1: Benefits and Costs of Construction Robots

BENEFITS		COSTS
Direct Benefits	Indirect Benefits	
Labour Savings: Including vacation pay, fringe benefits, union contributions, and compensation premiums.	Increased Work Quality: May lead to less rework and repair, and and greater user satisfaction.	Capital Cost Set-up and dismantling
Extension of work: Robotization may enable comapny to handle more contracts, through increased efficiency.	Indirect Safety Savings: Includes delays of work, negative impact on productivity, reduced quality	On-site programming/ Supervision Maintenance
Reductions in the Cost of Compliance with Safety Regulations. Must be determined on a case by case basis, since some trades are responsible for setting up their own safety measures on site.	Reduction of Activity Duration: May be crucial, and lead to direct benefits if activity is critical and can be compressed.	Transportation Energy/fuel Training
Material Savings. May be significant, particularly in surface treatment operations.		Adaptation of work process to robot work
Auxiliary Equipment Savings: Such as scaffolding, hoists, lifts..		

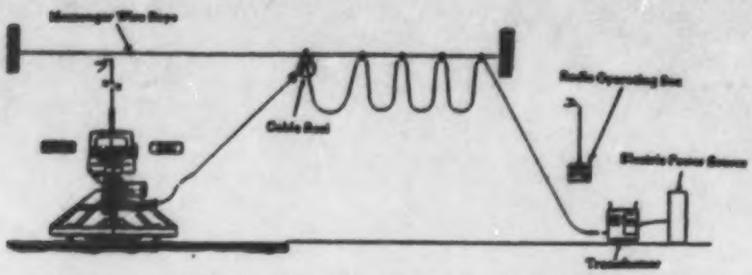

Figure 1: Cement Floor Finishing Robot Set-Up

in an opposite direction while pressing down with a force in proportion to the degree of hardening of the concrete. Extensive testing of the robot in Japan has indicated a finishing quality (surface flatness and roughness) equal or better than that achieved by a human operator, to the order of 0.05 mm surface denivellation or less [19].

The cost and benefits associated with the robot are identified in Table 2. Capital cost, maintenance cost, and design life data were obtained directly from the robot developer. For this particular robot, a design life of 5000 hours was roughly translated to an economic life of 4 years, based on the average number of hours worked by a human operator and considering the rugged operating conditions on site. Opportunity cost, i.e. the value of the next best opportunity foregone by purchasing the robot, is based on 10% return in any commercial bank. Cost of electric power and transportation are estimated based on similar characteristics of traditional movable construction equipment. Supervision cost is based on the cost of one qualified worker used in setting up and dismantling the robot, and in monitoring its performance. An escalation factor of 3% per annum is used to adjust all costs.

Labour savings are estimated by multiplying the average cost of a cement floor finisher (see Table 3) by the average number of working hrs/yr registered at the Quebec Construction Commission by that trade: In 1987 this figure amounted to 118 hrs/yr [28]. Use of the robot is estimated to increase the volume of work, i.e. working hrs/yr, by 5% annually. The salvage value at the end of economic life is assumed negligible. Other parameters used in the analysis inlcude: 12% minimum attractive rate of return; 50% combined federal and provincial tax rate; and the use of 100% accelerated depreciation for new high technology equipment, instead of 50% over two years for movable construction equipment (class 2)[1].

The last parameter to be considered is robot efficiency. Developers of cement floor finishing robots have indicated efficiencies ranging from 300 m^2/hr to 800 m^2/hr [17,19], depending on the model, but primarily on working conditions. When compared with the average productivity of a human operator, approximately 100 m^2/hr, the robot efficiency factor ranges from 3 to 8. However because of uncertainty about these values, and because of the rugged working conditions resulting from the harsh climate, a sensitivity analysis is performed over a conservative range of robot efficiency values, considering a lower bound value of 2.

The results obtained are summarized in Fig. 2, which shows the value of the floor finishing robot as a function of capital cost and robot

---

[1] The government of Quebec, in order to ensure competitiveness in the context of free trade, has introduced 100% accelerated depreciation for new high technology equipment. A discussion with a representative from the Ministry of Industry and Commerce has assured that this would apply to construction robots.

Table 2: Annual Benefits and Costs of a Floor Finishing Robot

ITEM	Year 0	Year 1	Year 2	Year 3	Year 4
Capital Cost	$ 50000.00				
Opportunity cost		$ 5000.00	$ 5500.00	$ 6050.00	$ 6655.00
Supervision cost		$ 28117.70	$ 30409.29	$ 32887.64	$ 35567.99
Maintenance cost		$ 5000.00	$ 5150.00	$ 5304.50	$ 5463.64
Electric Power cost		$ 1000.00	$ 1030.00	1060.90	$ 1092.73
Transportation cost		$ 1000.00	$ 1030.00	$ 1060.90	$ 1092.73
TOTAL COST	$ 50000.00	$ 40117.70	$ 43119.29	$ 46363.94	$ 49872.08
Labour Savings (efficiency = 2)		$ 56235.40	$ 60818.58	$ 65775.29	$ 71135.98
Labour Savings (efficiency = 2.5)		$ 70294.25	$ 76023.23	$ 82219.12	$ 88919.98
Labour Savings (efficiency = 3)		$ 84353.10	$ 91227.87	$ 9[illegible]562.94	$ 106703.90
Labour Savings (efficiency = 3.5)		$ 98411.95	$ 106432.50	$ 115106.70	$ 124487.90

Table 3: Hourly cost of a cement floor Finisher in Québec in 1987 [4]

ITEM	RATE
Wage rate	\$ 17.59/hr.
Vacations	\$ 1.76/hr.
Gross Salary	\$ 19.35/hr.
UI contributions	\$ 0.46/hr.
Quebec pension plan	\$ 0.36/hr.
Health insurance	\$ 0.62/hr.
Fringe benefits	\$ 1.08/hr.
Indemnity fund	\$ 0.02/hr.
Safety equipment	\$ 0.10/hr.
Quebec Construction Commission	\$ 0.15/hr.
Association of Building Contractors	\$ 0.02/hr.
Sub Total	\$ 22.16/hr.
Contribution to Quebec Health & Safety Commission	\$ 2.99/hr.
Total Hourly Labour Cost	\$ 25.15/hr.

effeciency. At the stated capital cost of \$50,000.00, the subcontractor begins to perceive a benefit when the robot's efficiency is at least 2 times that of a human operator. Clearly the robot's value is very sensitive with regards to the efficiency factor, increasing by \$23,840.00 with every 0.5 increase in that factor. Additionally, every \$1000.00 increase in capital cost decreases the robot's value to the subcontractor by approximately \$727.00. Fig. 3 shows the results of a classical benefit/cost analysis, i.e. disregarding depreciation and time value discounting, and indicates that break-even occurs at approximately 2.8, 1.6, 1.1, 0.85 years, when robot efficiency is respectively 2, 2.5, 3, and 3.5 times that of a human operator.

CONCLUSION

The use of robotics is an important development for Canada's evolving construction industry. The state of automation in construction and relevant issues affecting its acceptance are discussed. Construction tasks are expected to have a high potential for automation when need and economic benefits outweigh technological barriers and institutional resistance. The analysis indicates that at a conservative efficiency value of 3 times that of a human operator the robot user incurs substantial benefits. As technology becomes cheaper and the industry acquires more experience with robotics, the benefits of automation will become clearer, and robotic technology will provide an important edge to contractors who are continuously looking for cost effective construction methods.

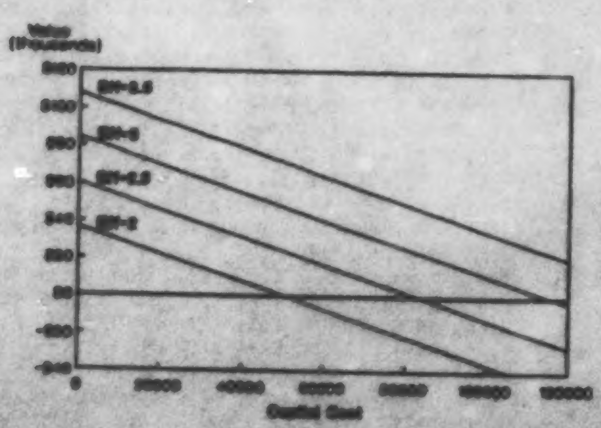

Figure 2: Robot Value vs Capital Cost

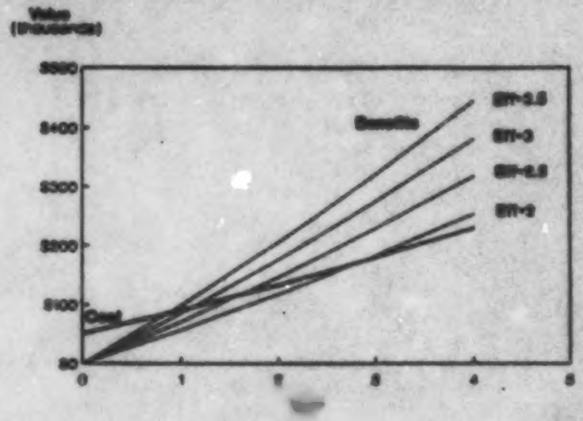

Figure 3: Break-even Analysis

ACKNOWLEDGEMENTS

The research described in this paper is being funded by the Natural Science and Engineering Research Council of Canada under grant No. A4430.

REFERENCES

[1] Adams, R.J., (1989). Industrial Relations Systems: Canada in Comparative Perspective. in Union-Management Relations in Canada, Anderson, J.C., Gunderson, M., Ponak, A. Eds., Addison-Wesley, pp. 437-464.

[2] Adrian, J.J., (1987). Construction Productivity Improvement. Elsevier, N.Y., pp. 167-179.

[3] Anderson, J.C., (1989). The Strategic Management of Industrial Relations in Union-Management Relations in Canada, Anderson, J.C., Guderson, M., Ponak, A., Eds., Addison-Wesley, pp. 99-124.

[4] Association des Entrepreneurs en Construction du Québec, (1988). Cout Horaire de la Main d'Oeuvre dans l'Industrie de la Constructon, Montréal, Canada.

[5] Bernold, E.B., (1987). Automation and Robotics in Construction: A challenge and a Change for an Industry in Transition. Proj. Man., pp. 155-160.

[6] Canadian Center for Occupational Health and Safety, (1988). Work Injury Statistics for Canada. Vol. XI, No. 1, pp. 6-7.

[7] Canadian Labour Market and Productivity Center, 1989). Apprenticeships in Construction Trades: Trends in the 1990's. CLMPC, Construction Sector Committee.

[8] Carter, Jr., C.F. (1985). The Role of robots in automating work. in Handbook of Ind. Rob., Nof, S. ed., John Wiley and sons, pp. 9-20.

[9] Construction Industry Development Council, (1984). Canada Constructs: Capital projects and Canadian Economic Growth in the Decades Ahead, Ottawa.

[10] Economic Council of Canada, (1973). Toward More Stable Growth in construction, Ottawa.

[11] Economic Council of Canada, (1986). The Bottom Line: Technology and Development. Ottawa.

[12] Fazio, P., et al., (1989). Automation Index for Evaluation of Robotics Implementation in Construction. Proc. 6th Int. Conf. on Robotics in Construction, San Francisco, June 6-8, pp. 317-324.

[13] Fleisher, G.A., (1982). A Generalized Methodology for Assessing the Economic Consequences of Acquiring Robots for Repetitive Operations. Proc. of the Annual Ind. Eng. Conf., pp. 130-139.

[14] Groover, M.P., et al., (1986). Industrial Robotics. McGraw-Hill.

[15] Groupe de Travail sur la Déreglementation, (1989). Reglementer Moins et Mieux. Les Publications Quebec, Quebec.

[16] Halpin, D.W., et al., (1987). Robotics Feasibility in the Construction Industry. Final Report, Dept. Constr. Eng. and Man., Nov.

[17] Kangari, R., Yoshida, T., (1989). Prototype Robotics in Construction Industry. J Const. Eng. and Man., Vol. 115, 2, June.

[18] Keys, B.A., Caskie, D.M., (1981). The Medium-term Employment Outlook: Construction Industry. The Labour Market Development Task Force, Canada Employment and Immigration Commission.

[19] Kikuchi, K. et al., (1988). Development and the Result of Practical Works of Concrete Floor Finishing Robot. Proc. 5th Int. Conf. on Robotics in Construction, Tokyo, June 6-8.

[20] Leslie, M., (1988). The Impact of Technology, Canadian Building, pp. 11-16, June.

[21] Lewis, A., et al., (1982). Investment Analysis for Robotic Applications. Pro. 13th Int. Symp. on Industrial Robots, pp. 4.128-4.141.

[22] Lozano-Pérez, T., (1985). Task-level Manipulator Programming. in Handbook of Industrial Robotics, Nof ed., John Wiley and Sons, pp. 404-418.

[23] Meyer, R.J., (1982). A Cookbook Approach to Robotics and Automotation Justification. Proc. Robots VI Conf., March 2-4.

[24] Moselhi, O., (1987). Automation and Robotics for Construction. Proc. 11th Canadian Cong. appl. Mech, Edmonton, Alb.

[25] Moselhi, O., (1988). Feasibility and Potential Implementation of Robots in Canadian Building Construction. Proc. 5th Int. Conf. on Robotics in Construction, Tokyo, June 6-8, pp. 229-238.

[26] Moselhi, O., Hason, S., (1989). Robotics in Construction: Implementation and Economic Evaluation. Can. J Civ. Eng., pp. 678-683, Oct.

[27] National Research Council of Canada. (1987). Advances in Cad/Cam and Robotics. Scrimgeour, J.H.C., and Vernadat, F. eds., Ottawa, May.

[28] Office de la Construction du Québec. (1987). Analyse de l'Industrie de la Construction au Québec, Québec, Canada.

[29] Okada, Y., (1988). Advanced Robot Technology Project in Japan. Proc. 5th Int. Conf. on Robotics in Construction, Tokyo, June, pp. 71-79.

[30] Peterson, C.O., (1986). Power Floating and Troweling. Concrete construction, Sept.

[31] Rakhra, A.S., (1988). Economic Considerations in the Construction Inudstry and the Issues Facing It. Institute for Research in Construction, pp. 11-32.

[32] Rose, J.b., (1979). A Canadian View of Labour Relations in Construction. Ind. Rel., Vol. 18, No. 2, pp. 156-172.

[33] Ruberg, K., Sander, D.M., (1987). Information and Knowledge for Building: A Role for Emerging Technologies in Advances in CAD/CAM and Robotics: NRC contributions. Scrimgeour, J.H.C., and Vernadat, F. eds., pp. 441-449, Canada.

[34] Sangrey, D.W., (1985). Quality and Reliability as Motivation for Construction Robotics. Proc. 2nd Int. Conf. on Robotics in Construction, Pittsburgh, Penn., June 24-26, pp. 31-39.

[35] Skibniewski, M.J., (1985). Engineering and Economic Analysis of Robotics Potential in Selected Construction Operations. Ph.D. Thesis, Dep. Civ. Eng., Carnegie-Mellon University, Pittsburgh, Penn., March.

[36] Skibniewski, M.J., Russel, J.S., (1989). Robotic Applications to Construction. Cost Eng., Vol. 31, No. 6 June, pp. 10-18.

[37] Stuber, G., (1984). The Slowdown in Productivity Growth in the 1975-1983 Period: A Survey of Possible Explanations. Bank of Canada Technical Reports, May.

[38] Suzuki, S., et al. Construction Robotics in Japan in Second Century of the Skyscaper, Council on Tall Buildings and Urban Habitat. Beddle, L.S. ed., Van Nostrand Reinhold, New York, pp. 507-552.

[39] Tucker, R.L., (1988). High Payoff Areas of Automation Applications. Proc. 5th Int. Conf. on Robotics in Construction, Tokyo, June 6-8, pp. 9-16.

[40] Van Blois, J.P., (1982). The Future of Robotic Justification. Proc. 13th Int. Symp. Ind. Robots, pp. 4.24-4.31.

[41] Warszawski, A., (1984). Application of Robotics to Building Construction. Report to the Dep. of Civ. Eng., Carnegie-Mellon University, Pittsurgh, Pen., June 1984.

THE OPERATION OF A GANTRY ROBOT IN A TURNING FMC

by

J. Jeswiet
Associate Professor
Department ofMechanical Engineering
Queen's University, Kingston, Ontario

ABSTRACT

This paper describes some of the problems encountered with a gantry robot which is an integral part of a Flexible Manufacturing Cell (FMC) and which is part of an on-going Flexible Manufacturing System (FMS) study at the MI-TNO in the Netherlands.

Robots are an integral part of a manufacturing system, either on a stand alone basis or as an integral part of a manufacturing cell, in this case an FMC. The gantry robot described in this paper is an integral part of a Turning FMC. It is the handling system for both the tools and the workpieces, thereby making the system flexible.

Conclusions are made regarding the mechanical design, the relative efficiency of the design and the software problems encountered.

INTRODUCTION

Robots do not operate on their own but are an integral part of manufacturing systems, either on a stand alone basis or as an integral part of a machine. In the former case one purchases a robot(s) and integrates it into the manufacturing system. In the latter case a robot(s) is an integral part of a Flexible Manufacturing Cell (FMC) or System (FMS). The robot discussed in this paper belongs to the latter.

In an on-going study (1) at MI-TNO in Apeldoorn in the Netherlands, two FMC's form the heart of a small FMS which is being tested for applicability in the metalworking industry with small part series requirements (from one to ten parts per order). The FMC's consist of a Turning FMC, TRAUB TNA480+FHS2 and a Machining FMC, MAHO MC50 (MFS50). Both have specially designed tool magazines and pallet systems but are also available on the market. It was a requirement of the study that market available equipment only be used. At the time of purchase both FMC's were the most up to date the manufacturers of this equipment could provide. Indeed, in the case of the Turning FMC, it was the first one of its type built by the manufacturer and was used for demonstrations to potential while the equipment was used in the research program at TNO. In this paper the performance of the gantry robot in the Turning FMC is examined.

THE TURNING FMC

The Turning FMC, see figure 1, consists of a CNC Turning centre, two workpiece pallet systems (32 positions per pallet conveyor), one tool magazine (128 positions) and a part/tool handling gantry Robot which is referred to as a Flexible Handling System (FHS). The FHS, see figure 2, consists of two, four degree of freedom robot arms, labelled P for parts handling and T for Tool handling. The two arms are fixed to each other and are propelled by the same NC controlled trolley. Each arm has two grippers, and in the case of P, it can handle two workpieces at one time. The two grippers on arm T are dedicated to two different functions: one gripper is for cutting tools and the other is for chucks only. In the case of arm P the grippers are mounted on an indexing head and are 180 degrees away from each other as shown in figure 3. The maximum load per gripper is 20 kilograms. Using these two arms the gantry robot provides the connection between the CNC Turning centre and the tool magazine and workpiece pallet conveyor.

ROBOT SPECIFICATIONS

The robot has a gantry configuration and is NC controlled. The three arm axes have DC servo drives and are continuous path controlled. The Robot controller is manufactured by Mitsubishi.

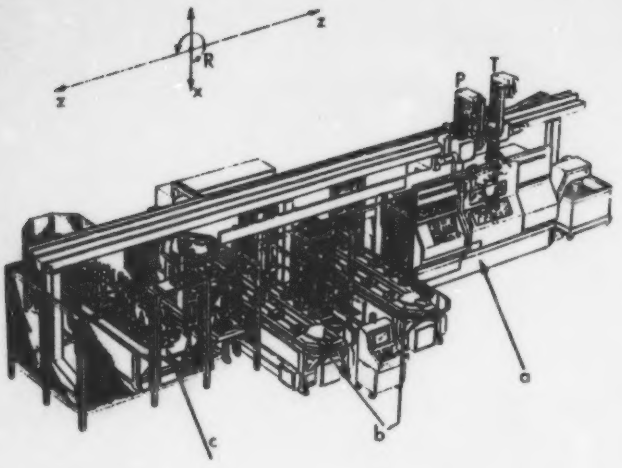

Figure 1. General overview of the Turning FMC at MI-TNO in the Netherlands. (a) CNC Turning centre, (b) Pallet conveyors, 32 positions per conveyor, (c) 128 positions per conveyor, (c) 128 position tool magazine.

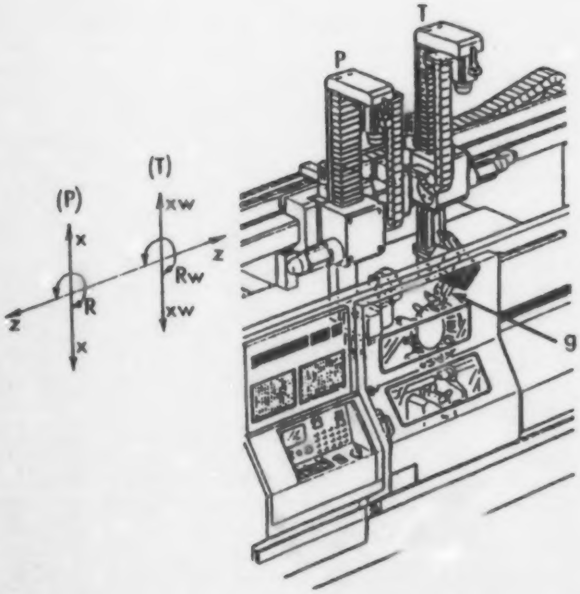

Figure 2. An illustration of Robot arms P and T with the coordinate axes, z, x and R. Arm T is shown loading the CNC turret. (g) is the gripper designated for handling cutting tools.

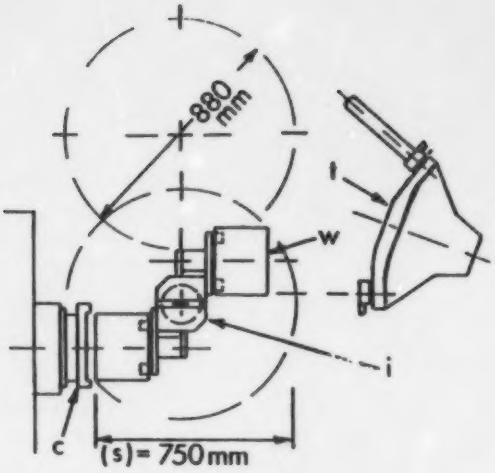

Figure 3. An illustration of the indexing head (i) which is mounted on Robot Arm P. It is shown handling two workpieces (w) one of which is being placed in the CNC chuck (c). The maximum workspace rotation radius is 880 mm. The CNC turret is indicated as (t).

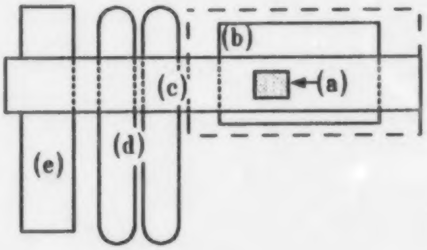

CV	Identification
(a)	Tool/workpiece interface
(b)	Machining volume
(c)	Robot volume
(d)	Workpiece pallet volume
(e)	Tool magazine volume
(f)	Gantry robot volume.
(t)	Tool preparation volume.
(p)	Software volume. 1) VAX, 8600 2) Microvax 3) PDP 11/23 4) Turning FMC controller - NC 5) Turning FMC controller - Robot 6) Machining FMC controller - NC 7) Machining FMC controller (PLC) - for pallet

Figure 4. Schematic of the different control volumes (CV's) for a Turning FMC.

The gripper on arm P is electric motor driven. Both gripper force and travel can be programmed. A built-in gripper traverse measurement device enables recording of the dimensions of the gripped workpiece. The jaw travel is programmable in steps of 0.1 mm and the maximum clamping force is 2000N. The grippers on arm T are simply open/close devices and are operated by springs and compressed air. They are mounted on an indexing head and are at right angles to each other. Both gripper indexing heads have a rotary motion of 0 to 270 degrees with a maximum indexing speed of 120 degrees per second. They can be position programmed to and accuracy of 0.01 degrees.

The gantry carriage has a maximum motion of 10 meters along the z axis. The maximum x-axis travel is 0.7 meters and both axes have a maximum programmable traverse rate of 60 m/min.

SYSTEM PROBLEMS

A system diagnostics program was introduced as part of the ongoing FMS study on July 1, 1988. In deciding which parts of the system were more important for diagnosis a simple method was set up as described in (2). This consisted of dividing the FMC into control volumes (CV's) as shown in figure 4. The results of this analysis indicate that vome (c), the FHS is a major problem area, as discussed in reference (3). In the first eight month period, the robot was involved in 27% of the 48 diagnostic problems that occurred. A diagnostic problem (a failure) is defined as a situation in which the system stops unexpectedly and an operator is required to get things started again. In three cases the FMC could not continue running at all and needed repairs.

Robot Problems - Mechanical

The robot had a variety of mechanical and software/hardware problems. The following is a description of some of the mechanical problems.

Problem 1. After only 4100 hours of operation the rollers on the arm trolley, shown in figure 5, had come loose and needed readjustment. Prior to readjustment the operator found that when heavy workpieces were transported arm P could be out of position by several millimeters requiring compensation in programming the end of arm position, with reference to the chuck position. Although readjustment may appear to be a relatively simple exercise it did cause more than one day of downtime which would be unacceptable in an industrial circumstance if unscheduled. This would have to be included in a regular maintenance check. However, considering this occurred after only six months of operation this frequency of maintenance would be too high for such a costly system.

Problem 2. The gripper indexing head, mentioned in the Robot specifications, contains a safety clutch which is meant to prevent damage to the robot arm if it encounters any obstructions. The principal parts concerned are shown schematically in figure 6. It can seen that friction at the surfaces labelled (a) prevents motion of the arm when not overloaded. The magnitude of the normal force required for the friction can be controlled by the tensioning pin that is shown in the diagram. When slp does occur, pin (B) is forced to move back so that it comes into the range of the electrical sensing element at (C). Although this is the expected manner of operation for the device it was found that for a very small amount of slip, giving a rotation of under 2 degrees for the indexing head, the sensor would not indicate any rotational movement had occurred. With normal use, it was found that after several months this amount of slip had occurred in the tooling arm T.

Because of slip on the gripper indexing head T, when a tool was transferred from the tool magazine to the turret, it did not slide properly into position. The indexing head and gripper must angle the tool at least 10 degrees when inserting the tool into the CNC turret. In several cases the angle was less than 10 degrees and the tool did not slide completely into position, thereby being out of position by 2.5 mm. in the z axis direction. If this had not been observed by the operator an out of tolerance set of parts would have been produced and alsc damage could have occurred to both the cutting tool and the chuck.

It appears the gripper clutch design is based on static load principles and may not have taken into account vibrations and temperature changes which can effect the interface friction resistance. A simple shear pin could provide a solution to this problem.

The two foregoing problems illustrate that when moving parts are involved care must be taken in the design. This is an age old problem in a new technology which occurred in several instances in this FMC.

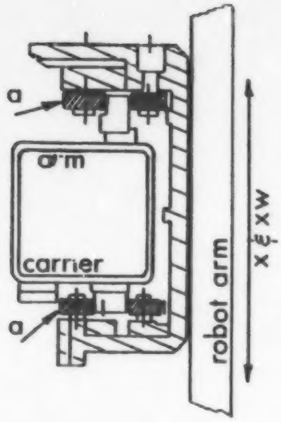

Figure 5. An illustration of the Robot arm carriage with the rollers (a) which needed readjustment. The vertical arm also had rollers for vertical axis, x-axis, motion, which also needed adjustments.

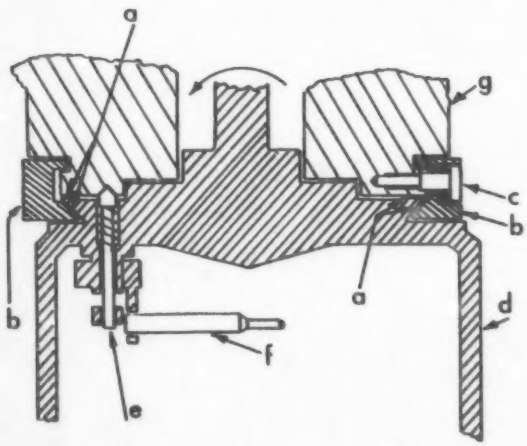

Figure 6. A drawing of the gripper indexing head surfaces which are under pressure and provide a clutch (slip) effect when overloaded at the surfaces labelled (a). (a) friction surfaces, (b) Compression/friction ring, (c) Tensioning screw, (d) rotating gripper housing, (e) Sensing pin, (f) Sensor, (g) fixed part of Robot arm T.

Robot Problems - Software/hardware

The computer is the major component, both hardware and software, which separates the Robot from other types of hardware automation. Thereforesome of the hardware/software problems which occurred will be considered.

Problem 3. The gantry Robot (FHS) is NC controlled. At one point in the program, over the course of more than six weeks, a variety of problems seemed to occur with the software concerned with controlling the z-axis. However, after a lot of analysis the problem was not found to be with the controller software but instead with the controller hardware board. Problems related to this were found to have occurred as early as 4132 hours of operation and the board was finally replaced at 4500 hours. A considerable amount of downtime was concerned with each failure. There are diagnostics in the software but in this case they were not of much use because continually indicated software problems whereas the problem really was in the hardware.

Problem 4. Software problems were a major problem in the whole FMC, and many of these could be related to the Robot controller. The CNC turning software appeared to be generally problem free. The Robot (FHS) software also seemed to be reasonably problem free until the introduction of revised manufacturer software in the middle of October 1988. At this point software problems increased dramatically far outweighing the mechanical problems that were being encountered. Figure 7 shows how dramatic the increase of software faults was relative to mechanical faults.

Problem 5. It was assumed the travelling cable which provided power to the robot arm trolley motors was a proven design. This was not the case because on several occasions the power cable failed and eventually had to be replaced.

System Design Problems.

The design of the FMC and integration of the CNC turning centre, with the Robot the tool magazine and pallet system also need to be redesigned. Consider figure 1 which shows the major elements of the FMC. In actual operation it was found the set-up times for a work order were much tool long because the tool magazine was located alongside the pallet conveyor system. Much shorter preparation times could have been achieved if the Turning CNC had been made the centrepoint of the system and the tool magazine had been physically located on the other side of the CNC.

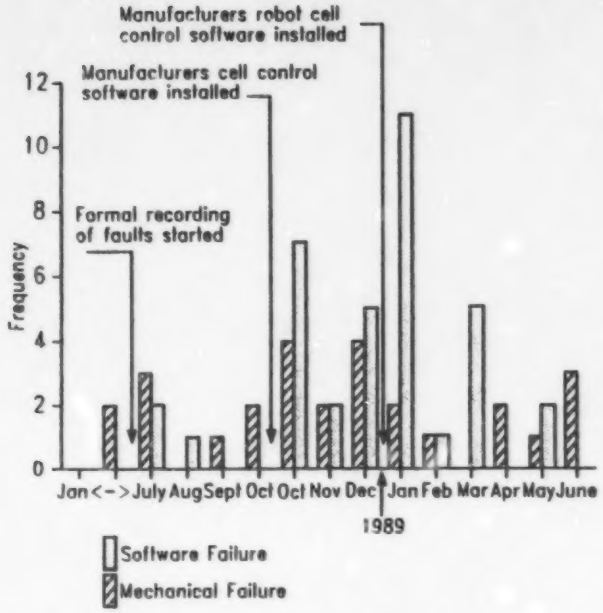

Figure 7. Comparison of Frequency of mechanical and software failure by month for the Turning FMC.

CONCLUSIONS

The concept of using a gantry Robot in this FMC seems to be a good one in general. However, considering some of the problems encountered one could reach the following conclusions:

- The tool magazine, pallet conveyor and CNC turning centre are not optimally located relative to each other for the most efficient performance of the robot as a part handling device.
- More efficient use could be made of the Robot arms if they were separated.
- In any mechanical design, including Robots, one must be very careful when designing in surface whic depend upon friction to keep the parts in a fixed position relative to each other.
- Much better diagnostic systems are needed to give a true evaluation of the problems in the system.
- Good simulation systems are needed for testing any revised software before it is installed in an industrial system.
- Once a software system is operating successfully in industrial circumstances do not make any software changes unless there are iron-clad guarantees the new software works properly.

The problems encountered so far in this study would not have been solved as quickly as they were without the presence of the highly skilled staff that was available. In this project there was a separate team for the development of the software for the supervisory control system (SCS). For the research and development on the FMS there was a group of seven which included technicians, engineers and a manager. Without all this highly skilled personnel the problems that arose would have taken much longer times to solve. This echoes the finding by Eversheim and Koch (3) that in spite of all automation, in the final analysis a manufacturing system is highly dependent upon the capability of its personnel. Also, if floor level automation is to increase there is a need for software systems which ease the burden of design as observed by Larin (4). This leads to the foregoing conclusion that reliable simulation systems are needed to check any new software design before it is implemented. Finally, if faster production speeds are an objective (5) then more efficient use must be made of the Robot in the system considered.

The foregoing are some of the findings of the on-going study at the MI-TNO into FMS. The gantry Robot which is part of this system has been considered in some detail with the foregoing conclusions. Further work is being done on this system with the development of an efficient Supervisory Control System (SCS) for the whole FMS of which the gantry robot forms a major part.

ACKNOWLEDGEMENTS

I would like to gratefully acknowledges the cooperation of the Metaalinstituut TNO, in the Netherlands in allowing me to spend a sabbatical year working with their flexible manufacturing system. The support of NSERC grant number A4960 is also gratefully acknowledged.

REFERENCES:

1. A.C. van Tol. TNO Researches FMS for the Metalworking Industry. The FMS Magazine, 6(2), p. 97, 1988.

2. J. Jeswiet. Monitoring and Diagnostics for FMS: Analyzing Two FMC's for Faults. SME/NAMRI transactions, May, 1989.

3. J. Jeswiet. The Performance of an FMC in an FMS Environment. CSME Mechanical Engineering Forum 1990.

4. W. Eversheim and L.F. Kok. Personnel in Flexible Manufacturing Systems - A Factor of Remainder Costs with High Responsibility for Costs. Manufacturing Systems, vol. 15, no. 2, p. 125, 1986.

5. D.J. Larin. Cell Control: What We have, What We'll need. Manufacturing Engineering, p. 41, January, 1989.

6. J. M. Martin. Cells Drive Manufacturing Strategy. Manufacturing Engineering, p. 49, January 1989.

ERROR ANALYSIS FOR THE AUTOMATIC VISUAL INSPECTION OF A 2D SHAPE WITH A LASER RANGE-FINDER CAMERA

Pierre McComber   Michel Galopin   Alain Paradis   Alain Royal

Ecole de technologie supérieure, Montréal, Qué.

ABSTRACT

Laser range-finder cameras are used in computer-controlled welding systems. This type of laser camera is well adapted to the harsh conditions associated with arc welding. Adaptive welding consists in choosing optimum welding parameters from an automatic visual recognition of the groove to be welded. A laser range-finder camera (Servot-Robot's Jupiter camera) is used to measure a 2D shape of a specific V-groove. The topology of the 2D shape defines the parameters to be evaluated and is known through appropriate dimensions. An algorithm is proposed to compute the means and variances of the various dimensions from the measured coordinates, processed as random variables. The vertices are first found from linear regression of the surface coordinates data. The shape dimensions are then computed from the vertices coordinates, using non-linear geometric equations. A two point estimate technique is used to calculate the means and variances of both the vertices coordinates and the shape dimensions. An example of an error analysis is provided for a V-groove shape, measured by the range finder camera.

INTRODUCTION

The role of automatic visual inspection systems is increasing in computer aided manufacturing (CAM) (Aleksander, 1983). Among its many applications, the laser range finder camera is used in computer-controlled welding systems. This type of laser camera is well adapted to the harsh conditions found in arc welding. Adaptive welding requires an adjustment of the welding parameters from an automatic visual inspection of the workpiece to weld. The camera scans the joint ahead of the welding torch, measuring the y and z coordinates of the work surface as it moves in the x direction. Therefore, adaptive welding requires the computation of the groove dimensions on different scans of the camera as it moves forward. The purpose of this paper is to present a method to determine the shape dimensions and the statistical errors from the measured range data of the camera, processed as random variables.

THE CAMERA AND ITS FEATURES

The laser range-finder camera is a Jupiter camera made by Servot-Robot (Rioux, 1986). The camera is based on a patented optical laser triangulation and relies on the synchronization of the projection and the detection of a spot of structured light. The basic elements are: a laser light source, a scanning mechanism to project the light spot onto the object surface and a position sensor, with a collecting lens looking off axis for the light spot. Trigonometric algebra is used to compute the distance from the projection and the detection direction.

Figure 1 shows a plot of the n points (y and z coordinates), obtained with the camera for a V-groove butt joint.

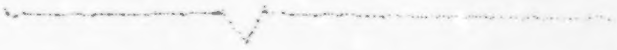

Fig. 1. Digital coordinate readings from the scanning of a V-groove butt joint.

This type of shape does not create shaded areas which are not seen by the laser spot. The measurement is based on the exact location of the maximum intensity of the deflected laser spot, on a row of CCD sensors. The variation of the light intensity must therefore be measured with high accuracy. For this purpose, the camera has a built-in automatic adjustment of the light intensity. Whenever the intensity of the spot changes, an automatic adjustment of the intensity scale is performed. This type of filtering temporarily decreases the accuracy, each time the intensity varies, due to a change in the direction of the inspected surface. This phenomenon can be observed near the vertices of the profile shown in Fig. 1.

When using the camera, there is an error due to surface roughness and an added error due to the changes in the orientation and the distance of the adjacent surfaces. Because of this feature of the range finder camera, the vertices cannot just be extracted from the data but rather have to be calculated. To make full use of the camera accuracy requires using all the measured points along the lines of a scan. The best fit of two adjacent lines gives the optimum coordinates y_j and z_j of the intersection points.

SHAPE MODEL FOR THE V-GROOVE

In order to compute the main features of the groove, e.g. the depth, the gap, the cross-section area, the automatic visual inspection system must compute parameters defining a shape model of the groove. A V-groove shape, with zero gap, is shown in Fig. 2. It includes four (4) line segments and five (5) vertices. The end points coordinates y_j and z_j of the line segments, set the geometry of the groove.

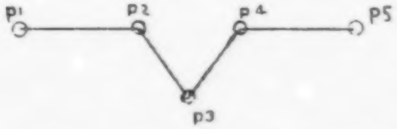

Fig. 2. A V-groove shape for welding thick plates.

The topology of the shape is established by a dimensioning scheme in which dimensions and tolerances are specified (Hillyard and Braid, 1978). These dimensions are usually the distances between the vertices and the angles between the straight lines. The visual inspection system verifies if the dimensions are within the specifications and measures the changes to be used for adaptive welding or in other applications.

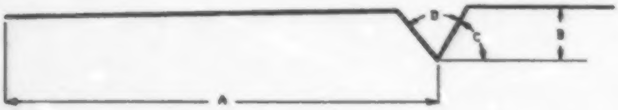

Fig. 3. The V-groove to be measured with one dimensioning scheme.

Figure 3 illustrates the shape of a V-groove with one of the many possible dimensioning schemes. The dimensions A, B, C and D are measured (see Fig. 3) and from the allowed tolerances on these quantities, the shape may be recognized and the shape parameters evaluated.

In this case, the distance of the groove from the end of the plate A, the depth of the groove B and the angles C and D, are the dimensions to be measured within appropriate statistical errors. These dimensions are related to the coordinates of the line intersections y_j and z_j, using the following equations.

$$z_1 = z_2 = z_4 \tag{1}$$

$$y_3 - y_1 = A \quad ; \quad z_3 - z_1 = B \tag{2}$$

$$y_4 = y_3 + (z_3 - z_1)/\tan(C) \tag{3}$$

$$y_2 = y_3 + (z_3 - z_1)/\tan(D + C) \tag{4}$$

Geometric equations are usually non-linear, making it more difficult to determine the statistical error of the camera readings in terms of these parameters. Other parameters, such as the groove cross-section area, can be related, in a similar way to the vertices coordinates.

STATISTICAL APPROACH TO THE COMPUTATION OF DIMENSIONS AND ERRORS

The camera visualizes a surface by a scan line whose points coordinates are processed as random variables. Once each line segment has been identified, linear regression is applied to find the intercept α and the slope β (Hines and Montgomery, 1980).

The computation procedure is as follows. The means of the points coordinates are first found:

$$\bar{y} = (\Sigma\, y_i)/n \quad ; \quad \bar{z} = (\Sigma\, z_i)/n \tag{5}$$

From these values, the quantities S_{yy} and S_{yz} are calculated:

$$S_{yy} = \Sigma\, (y_i - \bar{y})^2 \tag{6}$$

$$S_{yz} = \Sigma\, z_i\, (y_i - \bar{y}) \tag{7}$$

The least square estimates of the intercept α and the slope β are given by the following equations:

$$\bar{\beta} = S_{yz} / S_{yy} \tag{8}$$

$$\bar{\alpha} = \bar{z} - \bar{\beta}\, \bar{y} \tag{9}$$

Hence, the best line fit is:

$$z = \bar{\alpha} + \bar{\beta}\, y \tag{10}$$

The variances of β and α are given by the following equations:

$$V(\beta) = \sigma^2 / S_{yz} \qquad (11)$$

$$V(\alpha) = \sigma^2 \, (1/n + \bar{y}^2 / S_{yz}) \qquad (12)$$

where σ^2 is the variance of z:

$$\sigma^2 = (\Sigma z_i^2 - nz^2 - \beta S_{yz})/(n - 2) \qquad (13)$$

From the line parameters α_1, β_1 and α_2, β_2 of the two line segments, the intersections are calculated to find the shape vertices (y_j, z_j). The equations of the two regression lines are:

$$z = \alpha_1 + \beta_1 y \qquad (14)$$

$$z = \alpha_2 + \beta_2 y \qquad (15)$$

Therefore, the vertex coordinates are:

$$y = (\alpha_2 - \alpha_1) / (\beta_1 - \beta_2) \qquad (16)$$

$$z = \alpha_1 + \beta_1 y \qquad (17)$$

The shape dimensions are also related to the vertices coordinates, through the non-linear geometric eqs. (1) to (4). These functions are dependent on the random variables α and β.

The usual technique to calculate the error on functions of random variables, $Y = Y(X)$, is to use an approximation based on the Taylor series expansion, at the mean value of variable X. It requires the derivatives of the function with respect to each random variable. An easier approach, the point estimate method, has been proposed by Rosenblueth (1975).

This method derives the mean $\bar{Y}$ and the variance V(Y) of the dependent variable $Y = Y(X,)$ from the statistics of the independent variable X.

In the case of a two point estimate, the two X coordinates are:

$$X_+ = \bar{X} + \sigma_x \quad ; \quad X_- = \bar{X} - \sigma_x \qquad (18)$$

where $\bar{X}$ is the mean of the independent variable and σ_x its standard deviation. The two estimates of the function Y are therefore:

$$Y_+ = Y(X_+) \quad ; \quad Y_- = Y(X_-) \qquad (19)$$

The mean and variance of Y are then found from:

$$E(Y) = (Y_+ + Y_-) / 2 \qquad (20)$$

$$V(Y) = E(Y^2) - (E(y))^2 \qquad (21)$$

With four variables, which is the case here, the computations are made from the sixteen (16) combinations of the means of the variable, plus or minus the standard deviation. The intercept α and slope β are found for i = 1, 2, 3 and 4 with:

$$\alpha_{i\pm} = \bar{\alpha}_i \pm \sigma_{\alpha i} \qquad (22)$$

$$\beta_{i\pm} = \bar{\beta}_i \pm \sigma_{\beta i} \qquad (23)$$

Eqs. (22) and (23) are then used with eqs. (16) and (17) to give eight values of y_k and z_k, from which the mean and the variance of the vertices coordinates (y, z) are found:

$$E(y) = \Sigma y_k/8 \quad ; \quad E(z) = \Sigma z_k/8 \qquad (24)$$

$$V(y) = E(y^2) - (E(y))^2 \qquad (25)$$

$$V(z) = E(z^2) - (E(z)^2 \qquad (26)$$

The same approach is used to find the desired dimensions. The two point estimates of the vertices coordinates are:

$$y_{j\pm} = \bar{y}_j \pm \sigma_{yj} \qquad (27)$$

$$z_{j\pm} = \bar{z}_j \pm \sigma_{zj} \qquad (28)$$

Equations (24) to (26) for the mean and variance of the intersection points yield exact values, provided that α and β are random variables with gaussian distributions, because linear equations, eqs. (16) and (17) are used to find the vertices coordinates. However, the dimensions are usually obtained from non-linear equations. The two point estimate method is then accurate to the third order and is equivalent to a Taylor series truncated at the third derivative. The point estimate method presents the advantage of not having to calculate the derivatives of the non-linear function. A better accuracy could be obtained, if required, using more points for the mean and variance estimates.

EXAMPLE OF A STATISTICAL ESTIMATION OF THE SHAPE DIMENSIONS

The data y_i and z_i of the n points, as measured by a camera scan, are plotted in Fig. 1. These data, based on an appropriate calibration, are processed by the camera controller and are treated as random variables.

Step 1:

The points are grouped in different sets for each potential line segment. This is accomplished by comparing the slopes of the segments formed by adjacent points along the scan. Whenever a change in direction is detected, a new line segment is identified. Only the end points of these lines are memorized. Figure 4 shows the segments drawn between these end points.

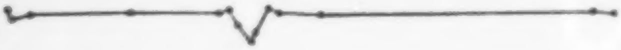

Fig. 4. Identification of the line segments from the scan data.

Step 2:

The length of each line segment is then computed. If the length is too short, the segment is not retained as part of the shape. The lines linking the remaining end points are drawn in Fig. 5.

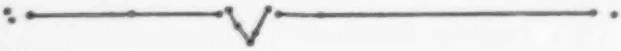

Fig. 5. The V-groove shape after the rejection the segments which are too short.

Step 3:

Adjacent line segments, having approximately the same slope, are then combined. Here, the shape is reduced to four segments, as shown in Fig. 6.

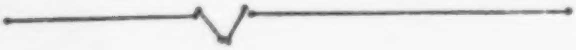

Fig. 6. The final four line segments defining the V-groove shape.

At this stage, the end points of the line segments do not coincide. The difference is significant and is related to the lower accuracy of the camera when the direction of the laser spot changes.

Step 4:

The next step is to compute the mean and the variance of intercept α and slope β for each of the lines, using eqs. (5) to (13). The intersections of each pair of adjacent lines are then calculated to yield the vertices, using eqs. (16) and (17). Equations (20) and (21) are used to find the mean and the variance of the vertices coordinates. The processed shape is shown in Fig. 7 and segments are drawn between the vertices as defined by their mean coordinates.

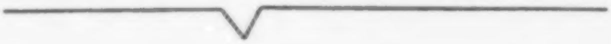

Fig. 7. Final shape after processing of the camera data.

Step 5:

Finally, the mean of the dimensions A, B, C and D and their variances are found, using a two point estimate of the coordinates based on eqs. (27) and (28).

Table 1 shows the results of these computations for the example described by Figs. 1 to 7.

Table 1

Mean and variance of the groove dimensions.

		MEAN	VARIANCE
Line slopes	1	1.8823E-02	1.1813E-03
β_i	2	-1.2436	1.5407E-03
	3	1.7956	2.0770E-03
	4	1.0038E-03	5.9922E-04
Intercepts	1	166.5541	0.2066
α_i (mm)	2	525.3802	0.6566
	3	-429.8072	0.9510
	4	174.1360	0.3471
Vertices	1	0.0000	0.0000
y_j (mm)	2	284.2274	0.7071
	3	314.2820	0.4759
	4	336.5292	0.6847
	5	792.0000	0.0000
z_j (mm)	1	166.5541	0.2067
	2	171.9037	0.8772
	3	134.5265	1.2390
	4	174.4743	1.2406
	5	174.9310	0.5829
Dimensions	A	314.2820	0.4759
A, B (mm)	B	38.9341	1.6383
C, D (degrees)	C	60.8862	2.8175E-02
	D	67.9162	3.1441E-02

CONCLUSIONS

A laser range-finder camera was used for the machine vision of a V-groove butt joint for arc welding. For this type of camera, the maximum error comes from the measurements of the vertices, due to the variation in the spot intensity where the direction of the surface changes. A higher accuracy is obtained by using all the data points to compute the means and variances of the vertices coordinates and the dimensions of the groove. The proposed algorithm computes the mean and the variance of the slope and the intercept of each line segments of the shape. The mean and the variance of the vertices coordinates are then calculated.

The shape dimensions are finally computed from the vertices coordinates, using the non-linear geometric equations. A two point estimate technique is used to calculate the means and the variances of these dimensions. The variance is a statistical measure of the camera reading error and can be compared with the acceptable tolerances of the shape model.

The results obtained for a V-groove butt joint indicate that the errors on the computed dimensions are small. This approach can be used for shape recognition as well as for the monitoring of the camera accuracy in automatic visual inspection of grooves for arc welding.

ACKNOWLEDGEMENTS

This research has been supported by NSERC grant A5413 and by the ETS-PSIR fund.

REFERENCES

Aleksander, I. 1983, Vision for Robots pp.1-234, Chapman & Hall, New-York.

Hillyard R.C. Braid I.C. 1978, Analysis of dimensions and tolerances in computer-aided mechanical design Computer-aided Design, Vol 10. pp.161-166.

Hines, W.W. Montgomery, D.C. 1980, Probability and Statistics in Engineering and Management Science, pp.359-386, John Wiley and Sons, New-York.

Rioux, M. 1986, Laser Range-Finder based on Synchronised Scanners, in Robot Sensors ed., A. Pugh, pp 175-190 Springer-Verlag, New-York.

Rosenblueth, E. 1975, Point Estimates for Probability Moments Proceedings of the National Academy of Science, Vol 72, no. 10, pp. 3812-3814.

COMPUTER GRAPHICS SIMULATION OF AN INDUSTRIAL ROBOT

Ali Meghdari

Sharif University of Technology*
Department of Mechanical Engineering
Tehran, Islamic Republic of Iran

Abstract:

This paper presents a three-dimensional graphic simulator for the PUMA-560 robot kinematics developed via the Core graphic package on the Sun workstation. The user can interactively teach and guide the robot to a specific position and orientation. During the teaching process, several intermediate positions may be saved as "VIA" points depending on the needs. After the teaching procedure, the robot motion may be replayed graphically through the recorded "VIA" points. Two menu items are used to control the graphic simulator. The main menu contains "RESET", "TEACH", "REPLAY", AND "QUIT". The sub menu is used to move the robot and change the viewing conditions. All the commands listed in the menu are driven by the input device, which is the mouse of the Sun workstation.

I. Introduction

Along with the evolution of the factory automation technology, interactive computer graphics simulation and "off-line" programming of industrial robots has attracted an increasing amount of attention in industry. Advanced robot simulation tools should be capable of simulation and displaying the motions of robot manipulators in the workspace, coordination with moving workpieces, and interactions with the environment (i.e. obstacles). Therefore, the key element in a simulation system is the application of computer graphics which allows motions to be displayed through computer graphical animation [1-2]. Since the robot arm and other workcell devices are represented graphically, the programmer can perform the programming and testing of a task without accessing the physical devices.

Teaching a robot with traditional "on-line" programming techniques is a time consuming process. Furthermore, the "on-line" method of robot programming requires the use of an actual robot which is physically put through its sequence of motions in the real environment. "Off-line" robot programming offers the potential to overcome many of these problems. Recent advances in computer technology have made interactive computer graphics a powerful and practical tool in every field, specially in the area of CAD/CAM [1-2]. A recent application of computer graphics to robotics is the simulation of the manipulator kinematics and off-line programming [3]. This will allow robots to remain on-line performing manufacturing tasks, while being programmed for other jobs. As a result, it will be easier to specify and develop optimum robot motion paths, program robots earlier in the product and tooling design cycle, and reduce the safety issues related to robots. Finally, off-line programming will accelerate trends towards fully utilized robot-based flexible manufacturing systems.

II. PUMA-560 Robot Kinematics and Motion Trajectory

II.1 Robot Kinematics

Any manipulator can be considered to consist of a chain of links connected together by either revolute or prismatic joints. One end of the chain is attached to a supporting base while the other end is relatively free and basically attached to an end effector which could be a multifingered hand, or a specialized articulated tool. By embedding a coordinated frame in each link of the manipulator, one can readily describe the relative position and orientation between these coordinate frames by means of the (4x4) Denavit Hartenberg Homogeneous transformations [6-7]. As described above a serial link manipulator is a sequence of interconnected rigid links by means of actuated joints. Therefore, an n degree of freedom manipulator will have n links and n joints. The base of the manipulator is known as link zero and is not considered as one of the n links, link one is connected to the base by joint one and there is no joint at the end of the final link.

In general, two links are connected by a "Lower Pair" joint (revolute, prismatic, or both). Therefore let us establish a joint axis (say the axis i-1) at the connection of the two links as shown in figure 1. Any link can be characterized by two numbers which define the relative location of the two axes in space;

---

* Part of this work was performed while serving the Los Alamos National Laboratory, Robotics & Automation Group, Los Alamos, N.M., U.S.A.

1) Link Length: the common normal distance between the axes which is unique, unless both axes are parallel (i.e. a_i for link i).
2) Link Twist: the angle between the axes in a plane perpendicular to the common normal (i.e. α_i for link i, this angle is measured from axis Z_{i-1} to axis Z_i in the right hand sense about X_i).

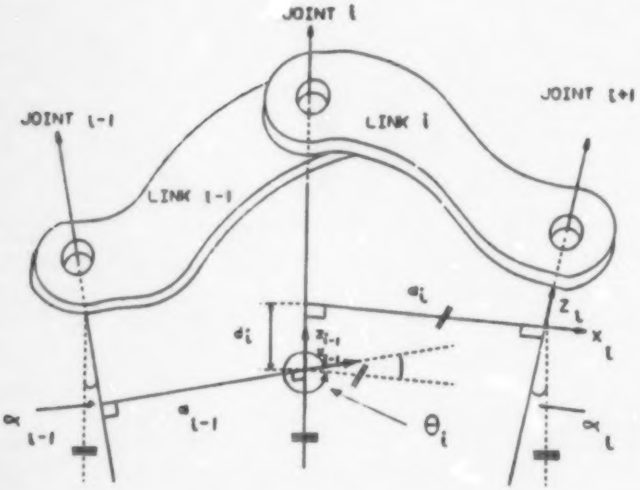

Fig. 1. Generalized manipulators link representation.

When two links are connected at the joint axis i-1, the relative position of the two such connected links is given by;

1) Link Offset: d_i which is the distance between the normals along the joint axis i-1, and
2) Joint Angle: θ_i which is the angle between the normals measured in a plane perpendicular to axis i-1 (this angle is measured from a_{i-1} to a_i in a right hand sense about Z_{i-1}).

The coordinate frames on the links are chosen as follows:

1) The Z_i coordinate is along the axis of motion (rotation) of the (i+1)th joint.
2) The X_i axis is in the direction of normal to both Z_i and Z_{i-1} axes, pointing away from the Z_{i-1} axis (such as to make a right hand coordinate with Z_i and Z_{i-1}).

The four parameters d_i, θ_i, a_i, and α_i constitute a minimally sufficient set to determine the kinematic configuration of each link of the robotic arm.

Note that for a plane revolute joint, generally d_i, a_i, and α_i are all constant while θ_i varies as link i rotates about the axis of joint i. On the other hand, for a prismatic joint θ_i, a_i, and α_i are constant while d_i varies as link i slides along the axis of joint i. Thus, for both cases a_i and α_i are generally constant and depend on the design of the robotic arm. For example when the joint axes of adjacent joints intersect, then the link length a_i is also zero (such as in the case of prismatic joints).

Once the Denavit-Hartenberg (D-H) coordinated system for each link is established, a homogeneous transformation matrix can be easily developed relating the ith coordinate frame to the (i-1)th coordinate frame by the following consecutive transformations:

1) Rotation about the Z_{i-1} axis by the angle θ_i to align the X_{i-1} and X_i axis; $\underset{\approx}{R}(Z_{i-1}, \theta_i) = \underset{\approx}{R}_1$.
2) Translation along the Z_{i-1} axis a distance d_i to bring the X_{i-1} and X_i axes into coincidence; $\underset{\approx}{T}(Z_{i-1}, d_i) = \underset{\approx}{T}_1$.
3) Translation along the X_i axis a distance a_i to bring the two origins into coincidence; $\underset{\approx}{T}(X_i, a_i) = \underset{\approx}{T}_2$.
4) Rotation about the X_i axis by an angle $_i$ to bring the two coordinate systems to completely coincide; $\underset{\approx}{R}(X_i, \alpha_i) = \underset{\approx}{R}_2$.

Thus the complete composite transformation of link i with respect to link i-1 (joint i with respect to joint i-1) is:

$$^{i-1}\underset{\approx}{A}_i = \underset{\approx}{R}_1\underset{\approx}{T}_1\underset{\approx}{T}_2\underset{\approx}{R}_2 =$$

$$= \begin{bmatrix} C\theta_i & -S\theta_i C\alpha_i & S\theta_i S\alpha_i & a_i C\theta_i \\ S\theta_i & C\theta_i C\alpha_i & -C\theta_i S\alpha_i & a_i S\theta_i \\ 0 & S\alpha_i & C\alpha_i & d_i \\ 0 & 0 & 0 & 1 \end{bmatrix} \qquad (1)$$

Where $C\theta_i = \mathrm{Cos}\theta_i$, $S\theta_i = \mathrm{Sin}\theta_i$, and for the case of prismatic joints a_i will be zero. Let us now obtain the kinematic equation for the PUMA-560 robot shown in figure 2. To describe the position and orientation of the robot, a reference coordinate frame is attached to each link. The local reference frame can be represented by a (4x4) homogeneous transformation matrix. For the PUMA-560, there exists six such transformation matrices (i.e. $^0\underset{\approx}{A}_1$ .... $^5\underset{\approx}{A}_6$) which are obtained by direct applications of equation (1) and Table 1 respectively.

Table 1. Table of Link Parameters of the PUMA-560 Robot.

Link i	θ_i	d_i	a_i	α_i
1	θ_1	0	0	-90°
2	θ_2	0	a_2	0
3	θ_3	d_3	a_3	90°
4	θ_4	d_4	0	-90°
5	θ_5	0	0	90°
6	θ_6	0	0	0

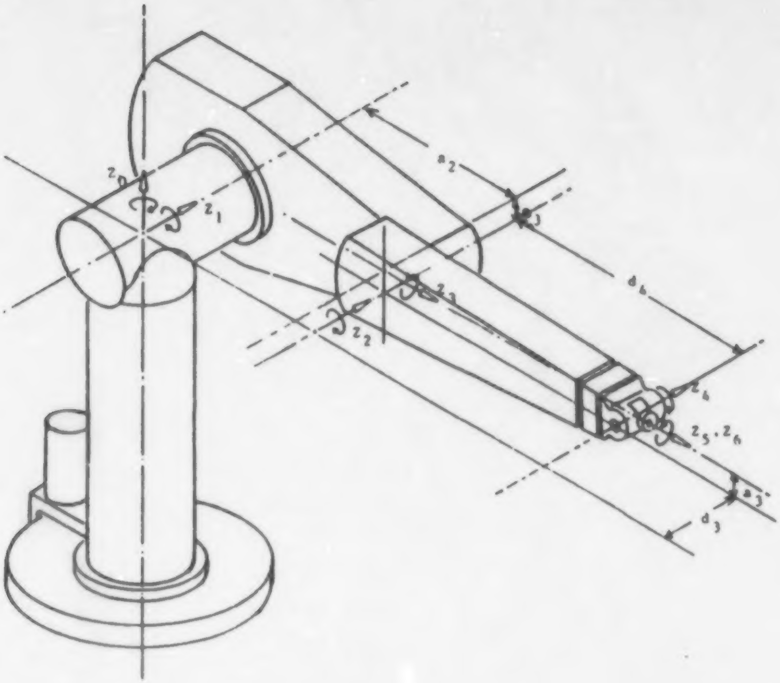

Fig. 2. Coordinate frames and link lengths for the PUMA arm.

Finally, the position and orientation of the PUMA-560 end effector with respect to base can be expressed by the following transformation ${}^0T_6$:

$$ {}^0\underset{=}{T}_6 = {}^0\underset{=}{A}_1\,{}^1\underset{=}{A}_2\,{}^2\underset{=}{A}_3\,{}^3\underset{=}{A}_4\,{}^4\underset{=}{A}_5\,{}^5\underset{=}{A}_6 = \begin{bmatrix} n_x & o_x & a_x & P_x \\ n_y & o_y & a_y & P_y \\ n_z & o_z & a_z & P_z \\ 0 & 0 & 0 & 1 \end{bmatrix} \qquad (2) $$

where:

$n_x = C_1[C_{23}(C_4C_5C_6-S_4S_6)-S_{23}S_5C_6]-S_1[S_4C_5C_6+C_4S_6]$
$n_y = S_1[C_{23}(C_4C_5C_6-S_4S_6)-S_{23}S_5C_6]+C_1[S_4C_5C_6+C_4S_6]$
$n_z = -S_{23}(C_4C_5C_6-S_4S_6)-C_{23}S_5C_6$
$o_x = C_1[-C_{23}(C_4C_5S_6+S_4C_6)+S_{23}S_5S_6]-S_1[-S_4C_5S_6+C_4C_6]$
$o_y = S_1[-C_{23}(C_4C_5S_6+S_4C_6)+S_{23}S_5S_6]+C_1[-S_4C_5S_6+C_4C_6]$
$o_z = S_{23}(C_4C_5S_6+S_4C_6)+C_{23}S_5S_6$
$a_x = C_1[C_{23}C_4S_5+S_{23}C_5]-S_1S_4S_5$
$a_y = S_1[C_{23}C_4S_5+S_{23}C_5]+C_1S_4S_5$
$a_z = -S_{23}C_4S_5+C_{23}C_5$
$P_x = C_1[d_4S_{23}+a_3C_{23}+a_2C_2]-S_1d_3$
$P_y = S_1[d_4S_{23}+a_3C_{23}+a_2C_2]+C_1d_3$
$P_z = d_4C_{23}-a_3S_{23}-a_2S_2$

As joint angles change, these matrices change accordingly. Given the local transformation matrices from link to link, the position and orientation of the gripper with respect to the base of the robot is obtained by successively multiplying these matrices in an appropriate order [6-8]. The final result is given by equation (2).

II.2 Robot Motion Trajectory

In most cases, the motion of a manipulator is considered as the motions of the gripper frame {G}, relative to the base frame {B}. Generally two types of motion schemes could be emulated between the "VIA" positions: 1) Joint Space Scheme, and 2) Cartesian Space Scheme. In the "Joint" space scheme, the motion trajectory is generated by interpolating the joint angles between the two successive "VIA" positions. Where as in the "Cartesian" space scheme, the motion trajectory is characterized by forcing the gripper to move along a straight line in the three-dimensional space. The generation of straight line motion is not as straight forward as that of the joint-interpolated motion. Instead of interpolating joint angles, it requires the angle-axis representation of transformation matrix for interpolation and inverse kinematics algorithm [6]. While the "Joint" motion scheme is always achievable, the "Cartesian" motion scheme is not always possible due to the physical constraints and singularities of the robot mechanism. Figures 3 and 4 display the wire-frame modeling of the PUMA-560 robot arm in joint-interpolated motion and straight line motion, respectively.

III. The Graphic Simulator

The Sun Core graphic package is used for the implementation of this graphic simulator [9]. Once the viewing conditions which include view

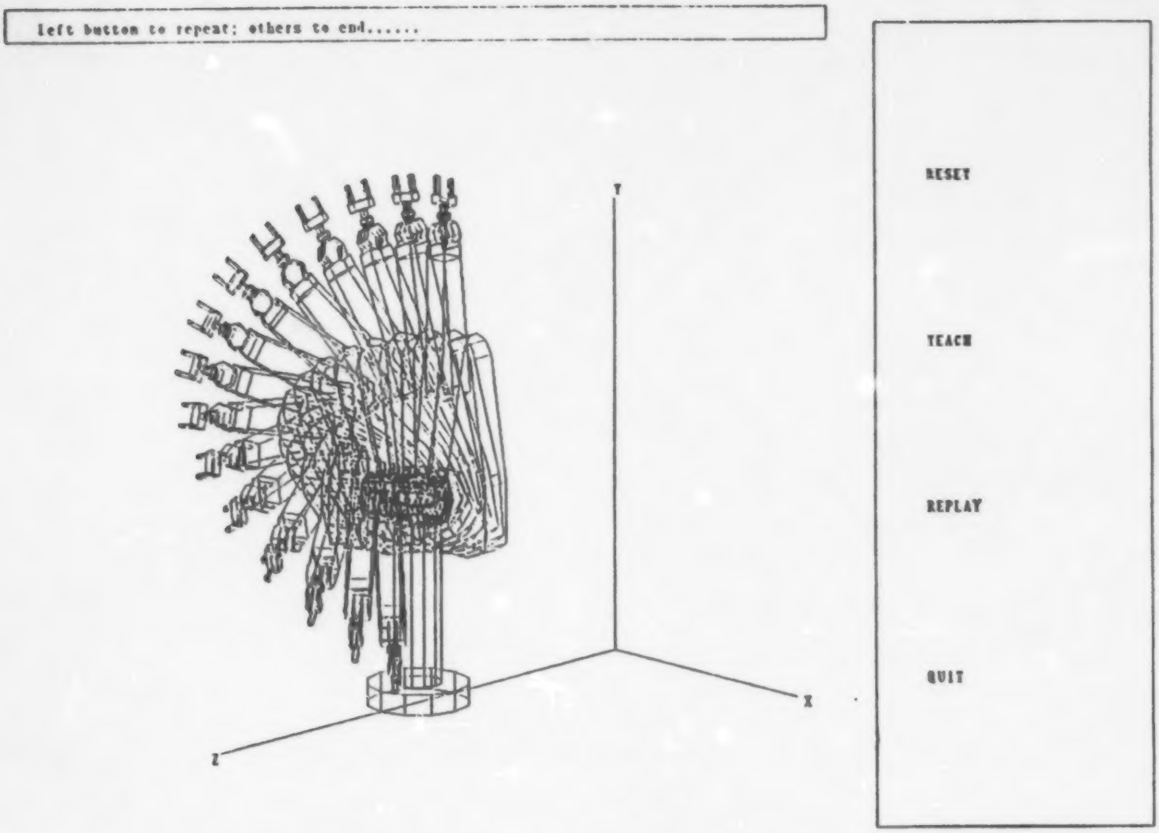
left button to repeat; others to end......

Fig. 3. Wire-frame modeling of the PUMA arm in joint-interpolated motion.

reference points, view plane normal, and window are set up, the output geometrical data for the PUMA robot can be displayed on the screen. Then Robotic movements are performed using the three-dimensional modeling transformations [2]. To enhance the editing capability, three viewing functions such as "viewing", "panning", and "zooming" have been implemented. The "viewing" function is able to change the relative viewing position around the robot. The "panning" function is used to move the robot image on the screen. And the "zooming" function provides the user the ability to observe the details of the displayed images. All the command functions are given via the mouse which is connected to the Sun workstation. Other input devices to the simulator include locator, valuator, and buttons.

To use the graphic simulator, the corresponding commands are written under two menus. A brief description of each command is given below:

* Main Menu

- RESET : reset the robot arm to its home position.
- TEACH : get into the sub-menu which includes all the commands needed to guide the robot to move.
- REPLAY : replay the guided motion.
- QUIT : quit and exit.

* Sub Menu

- Joint Scheme : set the motion between the "via" positions to be by joint-interpolated mode.
- Cartesian Scheme: set the motion between the "via" positions to be by straight-line mode.
- End : end the teaching mode and return to the main menu
- Pan : pan the robot image by giving a displacement vector
- View : change the reference view point along the circle which goes around the robot.

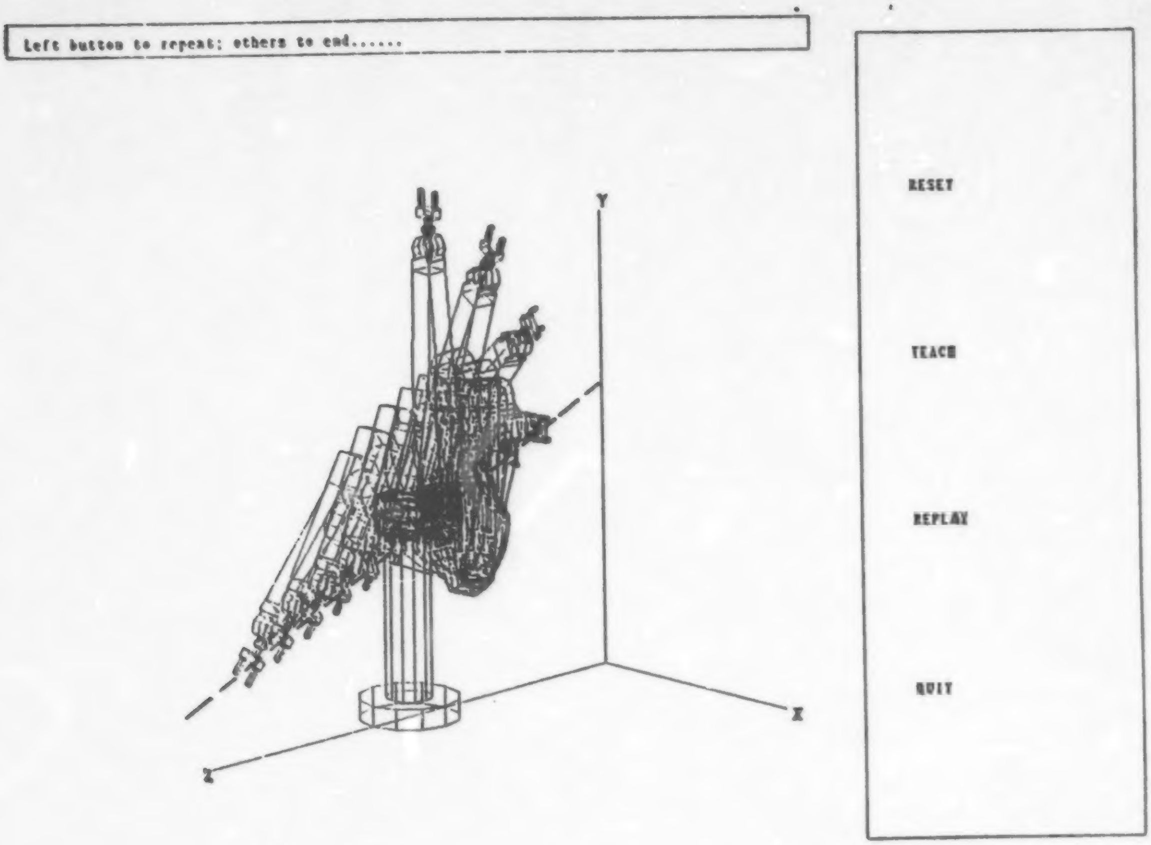
Left button to repeat; others to end......

Fig. 4. Wire-frame modeling of the PUMA arm in straight-line motion.

- Zoom : zoom the image of interest by defining a new window.
- Redraw : redraw the screen.
- Adjust : adjust the joint angle increment by using valuator (current increment value is displayed on screen)

1+ : command the 1st joint to move in positive angular direction with current increment value.

2+ : command the 2nd joint to move in positive angular direction with current increment value.

3+ : command the 3rd joint to move in positive angular direction with current increment value.

4+ : command the 4th joint to move in positive angular direction with current increment value.

5+ : command the 5th joint to move in positive angular direction with current increment value.

6+ : command the 6th joint to move in positive angular direction with current increment value.

Commands 1-, 2-, 3-, 4-, 5-, and 6- are the same as above except that motion is in a negative angular direction.

IV. Conclusions:

Computer graphics simulation of the PUMA-560 robot kinematics have been presented. Animation of motion together with displaying motion data provides an excellent way of visualizing robot motion and evaluating robot performance. This simulation program may be further developed to include various devices in a work cell such as tools, conveyors, fixtures, parts, NC machines, etc. Graphics-based simulation programs of this type are valuable to robot designers and users for applications in the industrial environment. The 35 pages simulation program written in "C" programming language may be obtained from professor Meghdari upon request.

__Acknowledgments__:

I would like to thank Dr. B.C. Chiou of the University of New Mexico for his valuable

comments on the program, and my wife, Shari Lin Meghdari, for the preparation of the typed manuscript.

References:

1. Hearn, D., & Baker, M., "*Computer Graphics*", Prentice Hall, Englewood Cliffs, New Jersey, 1986.

2. Foley J. D., & Van Dam A., "*Fundamentals of Interactive Computer Graphics*". Addison Wesley, 1982.

3. Ardayfio D. D., & Quiao D., "Kinematic Simulation of Novel Robotic Mechanisms Having Closed Kinematic Chains", *Proc. of the ASME Design Engineering Conference and Exhibit on Mechanical Vibration and Noise*, (85-DET-81), Cincinnati, Ohio, U.S.A., Sept. 10-15, 1985.

4. Meghdari A., "Dynamics Simulation Algorithms of Industrial Robots", submitted for publication to the *Amirkabir J. of Science & Engineering*, 1989.

5. Meghdari A., & Chiou B.C., "A Comparative Survey of Robot Manipulator Dynamics", *Proc. of the 9th Annual IEEE-ISE Conference & Symposium*, p.p. 50-58, Albuquerque, New Mexico, U.S.A., May 5-7, 1987.

6. Craig J. J., "*Introduction to Robotics: Mechanics and Control*". Addison Wesley, 1986.

7. Shahinpoor M., "*A Robot Engineering* Textbook". Harper & Row, 1987.

8. SunCore Programmer's Reference Manual, Sun *Microsystems Inc.*, 1986.

9. Crane C. D., Vora R., Tulenko, J. S., & Dalton, G. R., "Model Simulation for Robotic Control and Intelligence", *Proc. of the ANS Third Topical Meeting on Robotics and Remote Systems*, Sec. 11-3, pp. 1-6, Charleston, S.C., U.S.A., March 13-16, 1989.

CONTROL ALGORITHM FOR A PLANAR FIVE BAR MECHANISM USED AS ROBOTIC END EFFECTOR FOR PRECISION BUFFING OPERATION.

Satya Srinivas.V   Dr.T.Nagarajan

Department of Mechanical Engineering
Indian Institute of Technology Madras-600 036 INDIA

ABSTRACT:

Design and implementation of an on line control algorithm for continuous monitoring of precision buffing operation. A planar five bar mechanism is used as robotic end effector. Buffing operation is highly labour intensive and has to be performed at high speeds. Two problems have been dealt in this paper namely contour following andbuffing operation. Software compatible with MARK III controller is developed. Experimental work was performed with an on line force evaluation and inverse kinematics for positioning of end effector. Results for acrylic plastic, Hylem and Aluminium are presented to check the validity. Kinetoelastodynamic analysis using Finite Element Method was performed for above mechanism. Input control torques & end point positions which are evaluated by FEM analysis are presented.

INTRODUCTION:

Almost all commercial production robots perform as either a position or/and force control units. In operations such as buffing, deburring and other assembly processes one always comes across continuous variation of position and forces for different contours. For instance the buffing operation which has been dealt in this paper needs very accurate positioning and perfect force control.Components which need high surface finish especially after the deburring should be buffed so that we get the required surface finish and dimensional accuracy. Buffing operation encounters basically three problems:

(1). The operation is performed on almost finished components for a very high degree of surface finish so the process should be performed very carefully and at very high speeds. (2). For complicated shapes the end effector should be able to follow the contour always applying the thresold force required for the buffing operation. (3).When the tool is made of very smooth material continuous monitoring is required to examine the tool and workpiece contact condition.

The following control strategies are normally used for the end effector positioning:Ref [1]

(a). Hybrid force/position control:

This control is based on the position constraints that exist along the normal to a surface and the force constraints that are encountered along the surface. In this position and force control loops under different control laws (PID for position and PI for force) are used to control a manipulator. This requires an explicit description of workpiece in terms of position and forces.

(b). Joint Torque control.

This involves torque calculations for the individual motors to achieve position and force control. Here accurate knowledge of the model, arm dynamics, stiffness and friction are very essential. The practical viabiliaty of this method is yet to be proven.

(c).Sensor based control:

Required sensors are mounted and sensors measurements are compared with the required ones so that the difference can be used for giving the robot motion commands. This seems highly complicated and maintainance of this in industrial atmosphere can be difficult.

(d). Impedance control:

This models the manipulator as mass-spring-dashpot system with online control of the parameters inertia-stiffness-damping. Here continuous monitoring of force and position are made and stiffness can be varied electronically to form an active complaint end effector.

Contour following is a stable manoeuvre in which the robot end effector will tract a two dimensional path always remaining in contact with the part. geometrical knowledge of the path need not be available earlier to the operation.

In processes like buffing the forces are normally less and the material can be fragile so we should be able to accommodate the contact forces rather than use them just as feed back signals. If we do not control the operation according to the forces then end point position may exceed the desired tolerance or it may stall the process. In the buffing operation, robot end effector should be in position, to maintain the required threshold constant contact force. This force should be maintained for the required surface finish and dimensional accuracy. It is quite intuitive that such a system should have a small impedance (large complaince) in the tangential direction and large impedance(small complaince) in the normal direction. This algorithm involves sensing and accommodating the contact forces using simple position control software.

Direct drive five bar mechanism has been analysed by the Finite Element Method for the joint torques and the end effector deflections. Three dimensional beam elements having six degrees of freedom per node has been used for the modelling the geometry of the end effector considering the modelling of kinematic pairs located at the joints. Direct stiffness formulation and consistent mass approach has been considered in the finite element analysis. Finite element analysis provides accurate information of the torques for the joint motors mounted at kinematic pairs. Results of analysis such as joint input torques can used for design of drive motors. End effector position at every time step is computed and necessary corrections can be effected for the accurate positioning. Input control torques and end point positions can be theoretically evaluated by the Finite Element Program when the mechanism is mounted on a robot like XR100, SCARA .

The end effector mechanism that has been used can be considered to be as Direct Drive Arm(DDArm). Ref[2] Since DDArm has no gears between motors and joints it exhibits the following properties:no backlash, small friction and high mechanical stiffness. These properties differ from the serial ones which have high inertia loads, very sensitive to load changes or disturbances and also get heated fast. This leads to very accurate positioning ofthe buffing tool which is the premier requirement for the good edge following and high surface finish.

ARCHITECTURE & EXPERIMENTAL SET UP:

As shown in Fig(1) a planar five bar mechanism has been fabricated Ref[3]. An high speed DC motor is used for the buffing tool rotation. The design is made such that the tool along with the motor is very compact and can be very conveniently attached at the required point of the end effector.Two "PITTMAN DC Servo gearmotors" are used as the direct drives for the mechanism. These motors have been controlled by XR Series Mark III controller. Different materials have been chosen for the operation with surface roughness and edge profile as the case may be. The required software has been developed for the direct and inverse kinematics of the mechanism. Strain gauge based force sensors have been developed to measure orthogonal force components. The amplified signals (from carrier frequency amplifier) sent through the interfacing devices(analog to digital convertor) to PC AT-386, are used as the inputs to the control procedures.

CONTROL ALGORITHM:

Contour Following:

There are three components of the trajectory following: feed forward command initialization, movement or execution and feed forward command modification. All the three have to be performed for conventional trajectory planning. But here we initialize the movement and execute only.

Initially the work piece to be buffed is put in work volume of the parent robot to which the end effector is attached as shown in the Fig(2). Teach pendant can be used to describe the initial point of the operation using direct kinematics developed using geometrical equations shown in Appendix I. This calculates the coordinates of the end effector with the described angles of the drives. In fact even initialization can be done directly by sencing the forces,in which case end effector consumes more time to come in contact with the work piece Ref[4]. The tracking force F_r imposed by the component on the buffing tool is a resultant of normal force component F_n and the tangential force F_t Fig(3). These forces can be expressed in terms of the measured forces F_x and F_y by the equation (1).

$$\begin{bmatrix} F_x \\ F_y \end{bmatrix} = G \begin{bmatrix} F_n \\ F_t \end{bmatrix} \quad \ldots\ldots\ldots\ldots(i)$$

$$\text{where } G = \begin{bmatrix} -\mathrm{Sin}(\phi) & \mathrm{Cos}(\phi) \\ \mathrm{Cos}(\phi) & \mathrm{Sin}(\phi) \end{bmatrix}$$

ϕ is the angle between F_t and F_x

Inverse kinematics has been developed using the Denavit & Hartenberg (DH) matrix for the mechanism. Here DH Matrix analysis is performed with the product of matrices obtained for all joints being equated to identity matrix. Ref Appendix(II). Knowing the end effector co-ordinates the input angles are calculated. These angles are fed into the controller for the positioning of the end effector.

when the end effector starts its motion,position constraint is imposed in the normal direction and a force constraint in the tangential direction. For every small step of the end effector. The position co-ordinates,input angles are evaluated using the direct and inverse kinematics formulations. The contact forces, which are continuously monitored form the feed back signals. An on line computation can be performed for the threshold force that is required for the buffing operation depending on the surface finish required, material that is encountered at that instant and type of the tool. This can be changed continuously as per the conditions. The force components that act in the plane of operation can be used to evaluate the resultant force and the direction of the force that comes on the end effector. Thus the direction of the contact normal and the resultant force are evaluated at each instant. A check is made to see whether this force exceeds the threshold at that instant. If so then there should be alteration of the path of the end effector. This is achieved by choosing a point in the immediate vicinity of the present end effector position in the direction normal to the resultant of the force. Then inverse kinematics leads to the realocation of the end effector position and the process is continued until edge traversing is completed.

Buffing operation:

Buffing operation is also performed at the same time since the required contact force is always maintained. The force in the normal direction is continuously monitored and compared with the threshold Buffing force. When ever it deviates from the required value then end effector is moved away or nearer to the work piece using the inverse kinematics.This forms an open loop position control incorporating force feed back which accomodates the forces that are encountered in the operation.

Two dimensional beam elements having three degrees of freedom per node has been used for modelling the geometry of the end effector considering the modelling of kinematic pairs located at the joints. The FEM model that has been developed for this mechanism is shown in Fig(4). Direct stiffness formulation and consistent mass approach have been considered in the kinetoelastodynamics. Finite element analysis provides accurate information of the torques for the joint motors mounted at kinematic pairs. Results of analysis such as joint input torques can be used for design of drive motors. End effector position at every time step is computed and necessary corrections can be effected for the accurate positioning. Input control torques and end point positions can be theoretically evaluated by the Finite Element Program when the mechanism is mounted on a robot like XR100, SCARA.

RESULTS:

Experiments have been performed on three materials acrylic plastic,Nylem and aluminium.Fig(5a,b,c) shows the profile and the surface roughness before and after the operation. The operation is performed with soft felt buffing tool. Fig(6a,b,c) shows normal and tangential forces for two different feeds for all the three materials.Fig(7) shows the distance moved by the end effector for every step. The average speed of the buffing tool is 0.1215 cm/sec calculated on the basis of the total distance travelled by the tool is 14.5000mm and the time taken (12 Sec) for this travel. The resultant force and its direction are calculated. Fig(8a) shows normal and tangential forces when the feed is applied with out any operation.This shows that there is variation of force only in the normal direction where as in tangential direction it remains the same. When the operation is performed as shown in Fig(8b) we see force variation negligible in normal direction since it imposes only the position constraint. The tangential component varies considerable depending on the profile of the work piece. Fig(8c,d) shows the frequency spectrum just before the operation started with only the feed given and after completion of the process.

The forces that are got are used for the Finite Element Approach and the results are compared. The joint torques and end effector deflections that are calculated by this method are shown in the Fig(9). The error from the actual straight line is also investigated and which can indicate the picture of the work piece profile.

CONCLUSIONS:

Two problems have been tackled in this paper:contour following and buffing operation .One needs only one force sensor for both buffing operation in which metal removal is very less and the contour tracing by the end effector. In the case of duburring operation there is needof two force sensors one for the path following and other for stable metal removal.Ref[4].

The operation is performed using the planar five bar mechanism hence due to the mechanical considerations work space and path of operation are limited. Direct and inverse kinematics is performed for this mechanism alone assuming it as Direct drive manipulator. This can be attached on multiaxis robots such as Rhino RX 100, SCARA etc. Then kinematics both direct and inverse for the whole system has to be performed which gives it a stupendous accessibility of the work piece. Efforts are being made to run the Kinetoelastodynamic formulation with a pre and post processor online for the entire system.

APPENDIX(i):ref[5]

Direct kinematics: Refer fig(10)

O_a is the center of the axes.

The co-ordinates of the point C are given as (w.r.t AC)

$$X_c = r_a Cos(\theta) - a\ Cos(\theta+\lambda) \qquad \ldots\ldots(2)$$

$$Y_c = r_a Sin(\theta) + a\ Sin(\theta+\lambda) \qquad \ldots\ldots(3)$$

Co-ordinates of point c obtained w.r.t BC

$$X_c = d - r_b Cos(\alpha) + b\ Cos(\alpha+\beta) \qquad \ldots\ldots(4)$$

$$Y_c = r_b\ Sin(\alpha) + b\ Sin(\alpha+\beta) \qquad \ldots\ldots(5)$$

where λ & β are

$$Cos(\lambda) = \frac{1}{F^2+D^2}\left(EF \pm D\sqrt{D^2+F^2-E^2}\right) \quad \ldots(6)$$

where

$F=r_b\ \mathrm{Cos}(\theta+\alpha)-d\ \mathrm{Cos}(\theta)+r_a;$

$D=r_b\ \mathrm{Sin}(\theta+\alpha)-d\ \mathrm{Sin}(\theta);$

$$E=(1/2a)[a^2-b^2+r_a^2+r_b^2+d^2+2r_ar_b\mathrm{Cos}(\theta+\alpha)-2d(r_a\mathrm{Cos}(\theta)+r_b\mathrm{Cos}(\alpha))] \quad \ldots\ldots\ldots\ldots(7)$$

$$\mathrm{Cos}(\theta)=\frac{1}{J^2+K^2}\left(LJ \pm K\sqrt{K^2+J^2-L^2}\right) \quad \ldots(8)$$

where

$J=r_a\ \mathrm{Cos}(\theta+\alpha)-d\ \mathrm{Cos}(\theta)+r_b;$

$K=r_a\ \mathrm{Sin}(\theta+\alpha)-d\ \mathrm{Sin}(\theta);$

$$L=(1/2b)[a^2-b^2+r_a^2+r_b^2+d^2+2r_ar_b\mathrm{Cos}(\theta+\alpha)-2d(r_a\mathrm{Cos}(\theta)+r_b\mathrm{Cos}(\alpha))] \quad \ldots\ldots\ldots\ldots(9)$$

knowing the point c we get the coordinates of end effector point $R(X_r, Y_r)$ from the following equations

$$X_r=\frac{-U_2\pm\sqrt{U_2^2-4U_1U_3}}{2U_1};\quad Y_r=\frac{-Y_3-X_rY_1}{Y_2}$$

where $U_1=Y_2^2+Y_1^2; U_2=-2X_cY_2^2+2Y_3Y_1+2Y_1Y_2Y_c;$

$U_3=Y_2^2X_c^2+Y_3^2+2Y_cY_3Y_2-e^2Y_2^2;$

$Y_1=Y_c-Y_b; Y_2=X_b-X_c; Y_3=-Y_cX_b;$

Appendix(II):

Inverse kinematics of the closed loop planar five bar mechanism shown in fig(10). with (X_r, Y_r) as the end effector point the Denavit Hartenberg(DH) matrix is applied for the link RA and AU_a.

$$[A_1]=\begin{bmatrix} 1 & 0 & 0 & 0 \\ r_aC\theta & C\theta & -S\theta & 0 \\ r_aC\theta & S\theta & C\theta & 0 \\ 0 & 0 & 0 & 1 \end{bmatrix}$$

$$[A_2]=\begin{bmatrix} 1 & 0 & 0 & 0 \\ a\ C\theta_1 & C\theta_1 & -S\theta_1 & 0 \\ a\ C\theta_1 & S\theta_1 & C\theta_1 & 0 \\ 0 & 0 & 0 & 1 \end{bmatrix}$$

where $C\theta, S\theta$ denote $\mathrm{Cos}(\theta), \sin(\theta)$

$[A]=[A_1][A_2]$

$$[A]=\begin{bmatrix} 1 & 0 & 0 & 0 \\ r_aC\theta+aC(\theta+\theta_1) & 0 & 0 & 0 \\ r_aC\theta+aC(\theta+\theta_1) & 0 & 0 & 0 \\ 0 & 0 & 0 & 0 \end{bmatrix}$$

$$[A]\begin{bmatrix} 1 \\ X_1 \\ Y_1 \\ z_1 \end{bmatrix}=\begin{bmatrix} 1 \\ X_r \\ Y_r \\ z_r \end{bmatrix} \quad \ldots\ldots\ldots\ldots(10)$$

Equation (10) yields

$r_a\mathrm{Cos}(\theta)+a\ \mathrm{Cos}(\theta+\theta_1)=X_r$

$r_a\mathrm{Sin}(\theta)+a\ \mathrm{Sin}(\theta+\theta_1)=Y_r$

on simplification we have

$$2\ X_rr_a\mathrm{Cos}(\theta)+2Y_ra\ \mathrm{Sin}(\theta)=X_r^2+Y_r^2+r_a^2-a^2 \quad (11)$$

substituting cos & sin in terms of $\tan(\frac{\theta}{2})$ we solve for angle θ.

co-ordinates of point C are given by

$$Y_c=\frac{-z_5\pm\sqrt{z_5^2-4z_4z_6}}{2\ z_4};\quad X_c=\frac{z_3+Y_cz_2}{z_1}$$

where

$z_1=Y_r-Y_b;\ z_2=Y_r-Y_b;\ z_4=z_2^2+z_1^2;$

$z_3=-R_x(R_y-B_y)+R_y(R_x-B_x);$

$z_5=2z_3z_2-2R_xz_2z_1-2R_yz_1^2;$

$z_6=z_3^2+z_1^2R_x^2-2R_xz_1z_3+r_y^2z_1^2-e^2z_1^2;$

on the evaluation of the co-ordinates of the point C. With the assumption that U_a being shifted to U_b, DH Matrix is applied. This yeilds the equation

$$2\ X_cr_b\mathrm{Cos}(\alpha)+2Y_ra\ \mathrm{Sin}(\alpha)=X_c^2+Y_c^2+r_b^2-b^2..(12)$$

From the equations (11) & (12) we calculate the angles θ and α.

References:

1. F.M.Stepien,L.M.Sweet,C.Good,M.Tomizuka 1987 Control of tool/Workpiece Contact Force with application to Robotic Deburring in IEEE Jn. of Robotics and Automation Vol. RA-3,No.1, Feb 1987.
2. Haruhiko Asada & Kamal Youcef-Toumi 1984 Analysis and Design of a Direct Drive Arm with a Five bar link Parallel drive mechanism in Jn. of Dynamic Systems Measurements and Control Vol. 106 Sept 1984 pp 225-230.
3. H.Kazerooni 1988 Direct Drive Active Complaint End Effector(Active RCC) in IEEE Jounal of Robotics and Automation Vol.4, No. 3 June 1988 PP 324-333.
4. H.Kazerooni, 1988 Robotic Deburring of two-dimensional parts with unknown geometry Vol.7/ No. 4 Journal of Manufacturing systems.
5 C.H.An,C.G.Atkenson, J.M.Hollerbach Model based control of a robot manipulator. The MIT press.

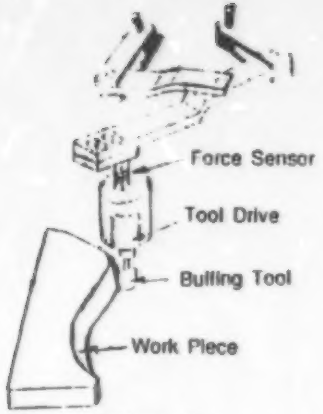
Force Sensor
Tool Drive
Buffing Tool
Work Piece

Fig. 1: Planar Five Bar Mechanism

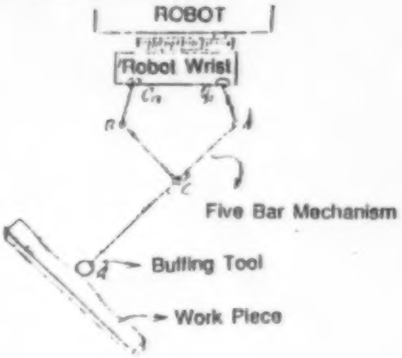
ROBOT
Robot Wrist
Five Bar Mechanism
Buffing Tool
Work Piece

Fig. 2

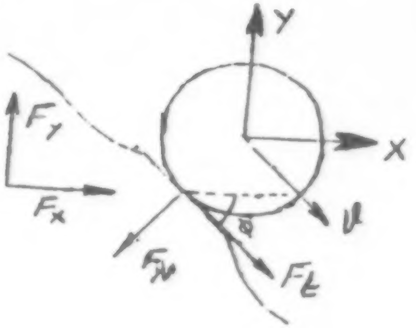
Y
X
F_Y
F_x
F_N
F_t
θ

Fig. 3

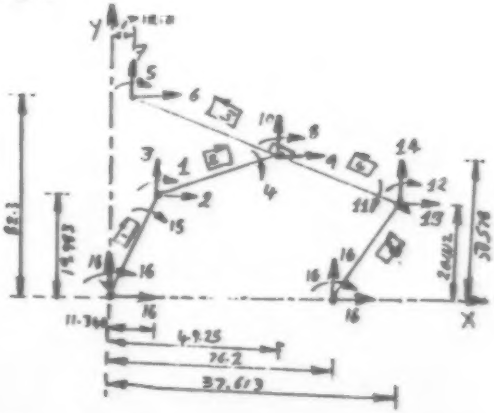
Y
X
1
2
3
4
5
6
7
8
9
10
11
12
13
14
15
16
19.983
26.482
58.574
49.25
76.2
37.613

Fig. 4: Finite Element Model

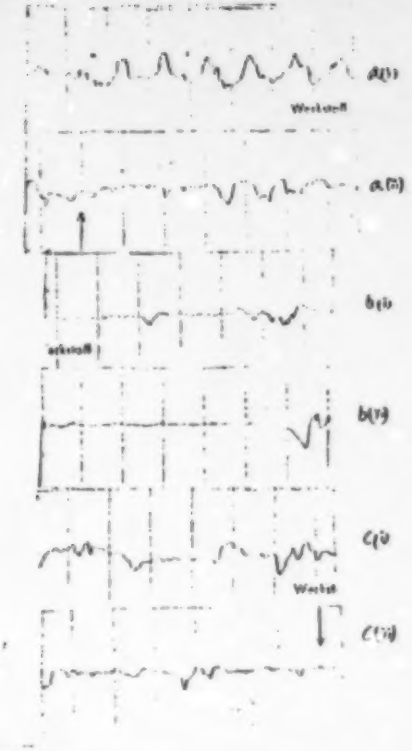

Fig. 5: (a) Acrylic Plastic
(b) Hylem Aluminium
(i) Before (ii) After

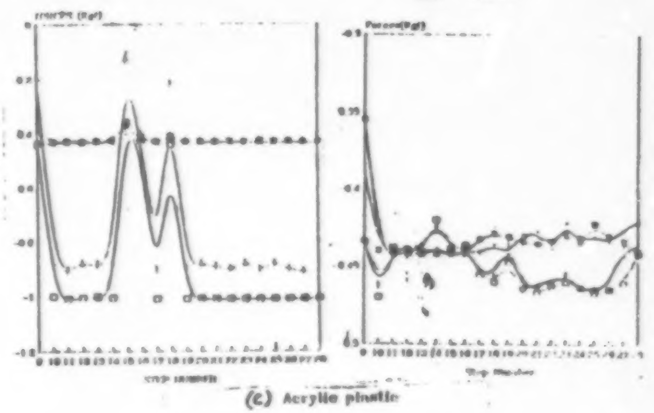

(c) Acrylic plastic

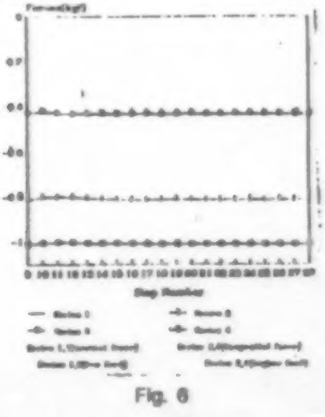

Fig. 6

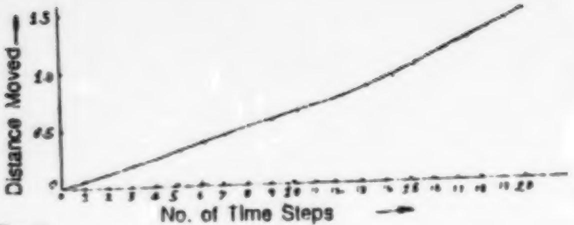

Fig. 7

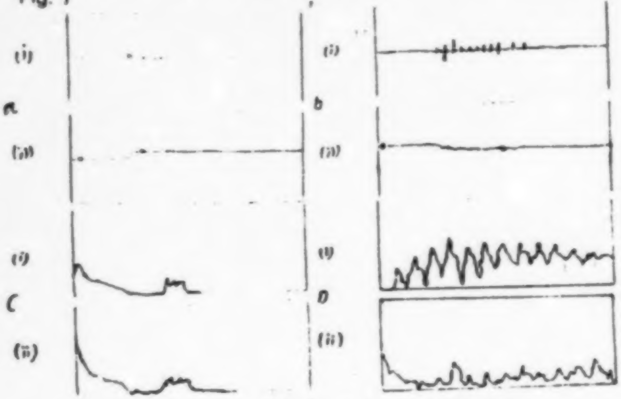

Fig. 8 (i) Tangential Force
(ii) Normal Force

Input Torques (Aluminium)

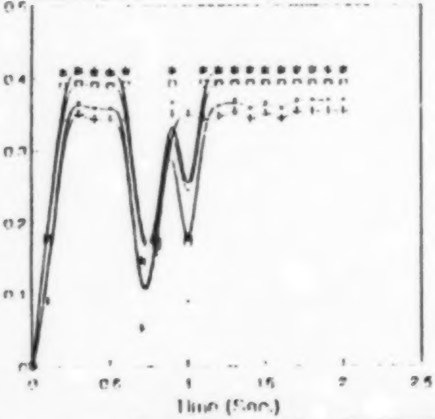

Input Torque (Acrylic Plastic)

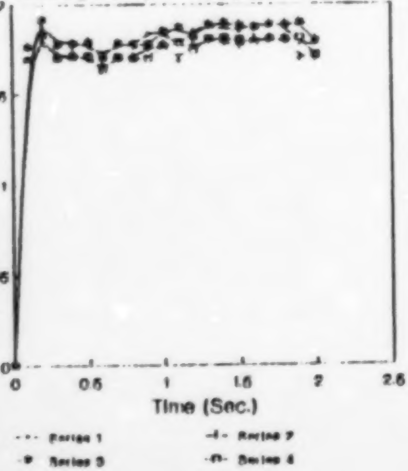

Fig. 9: Series 1,2 For Lower Feed
Series 3,4 For Higher Feed

Error Displacements (Aluminium)

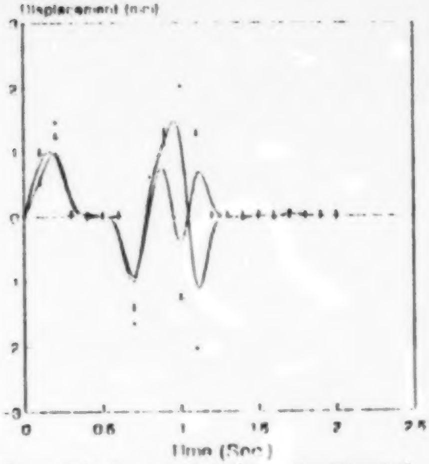

Error Displacements (Acrylic Plastic)

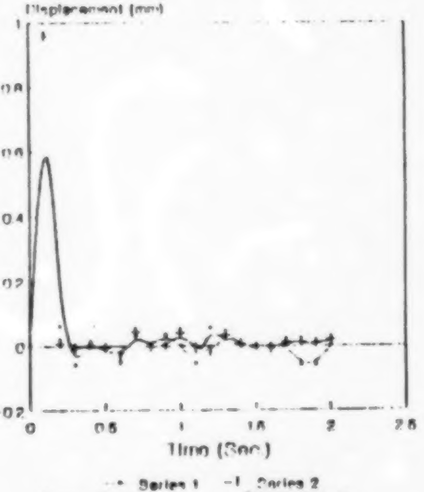

Lower Feed Higher Feed

Fig. 9

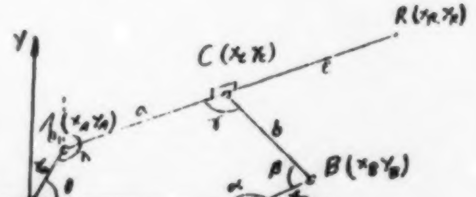
R (x_R, y_R)
Y
C (x_C y_C)
c
a
γ
b
A (x_A y_A)
θ
β
B (x_B y_B)
α
O_A
d
O_B
X

Fig. 10

THE TRANSPORTATION DEVELOPMENT CENTRE'S RAIL R&D PROGRAM RELATED TO HEAVY HAUL TRANSPORTATION

D.W. Dibble
W.S.C. McLaren
Transportation Development Centre
Policy and Coordination Group
Transport Canada

ABSTRACT

This paper describes selected rail transportation R&D projects that have been supported by the Transportation Development Centre (TDC) of Transport Canada.

Although Canadian railways are as technically advanced as other nations' railways, our rail haul distances for bulk commodities, e.g. coal, are generally much longer resulting in a competitive disadvantage. With this environment in mind, the focus of the paper is on technical R&D projects related to the improvement in efficiency and productivity of heavy haul unit train transportation of mineral commodities.

The technological developments that are described include: radial freight car truck development; rail grinding; aluminum coal car; and, fuelsaver.

The technological developments that are presented should result in future reductions in railway operating costs. Although the benefits are incremental in nature, they are important since railways in other countries are often aggressive in pursuing technological improvements and the competitiveness of Canadian mineral products depends on keeping pace with new developments.

INTRODUCTION

The Transportation Development Centre (TDC) is a component of the Research and Development Directorate of Transport Canada's Policy and Coordination Group. Located in Montreal, TDC maintains a core of technological expertise and R&D project management capability, contracting out projects to a variety of performing organizations, mostly in the private sector. TDC's R&D program covers all modes of transportation. The objectives of the R&D program derive from federal and departmental priorities and policies for transportation.

The activities described in this paper cover both past and current R&D projects related to mineral transportation by rail.

HISTORY OF TDC R&D IN RAIL TRANSPORTATION

Over the years since the formation of TDC in 1970, the priorities have changed, but Rail has been a consistent component of the TDC R&D program from the start. It was the introduction of the 100-ton car in the early 70's which resulted in TDC first being involved in R&D related to rail transportation. The 100-ton car, though attractive from an economic standpoint, resulted in severe deterioration of track structure, particularly in curves, and triggered the formation of a North American wide government-industry program known as the Track Train Dynamics Program (TTD). TDC was represented on the Steering Committee of the TTD its completion in 1985.

In the early 80's, under the auspices of the Railway Advisory Board, a proposal to Transport Canada resulted in the five-year augmented rail research program, sponsored by TDC and involving funding and cooperative effort from industry. Under this program, a number of significant research projects were undertaken, some of which are described in this paper.

The Railway Advisory Board has played an important role in the coordination of Canadian industry/government R&D in the rail freight sector in past years. The Board has recently been reconstituted as the Railway Research Advisory Board and will provide a forum for those interested in railway research.

Today TDC's rail R&D depends to a significant degree on support received through the Panel for Energy Research and Development (PERD) of Energy Mines and Resources Canada. Transport Canada's priorities lie in safety and the TDC-funded portion of the rail program focuses on support to our regulatory function and support for safety-related technology development.

FREIGHT CAR TRUCK DEVELOPMENT

The Problem

The 3-piece freight car truck consists of wheelsets, sideframes and a bolster. The truck was conceived more than 50 years ago as a suspension and guidance system for freight cars of approximately 30 tons. Today, this same truck (with many refinements but no major design change) is expected to support and guide cars of 100 tons and more at higher speeds in longer and heavier trains. As a result of this dramatic change, truck curving performance has deteriorated, stability problems have increased, and truck-related costs have escalated to represent up to 10% of all railway expenditures. In 1983, CP Rail alone estimated truck-related costs in excess of $100 million.(1)

Standard 3-piece trucks cannot provide satisfactory curving performance without excessive flange forces. These forces accelerate wheel and rail wear and increase fuel consumption. Trucks exhibit dynamic lateral instability (hunting) that limits the top speed for lightly loaded and empty cars to less than 50 mph, causes damage to car bodies and lading, and promotes track gauge and alignment problems. Costs related to truck damage stem from out-of-service time for cars and track caused by on-line failures, truck maintenance, repairs to track structure due to truck-related damage, and derailments caused by truck-related failures.

Research and Development

The challenge was to improve truck performance by using technology that: could be applied to existing trucks and new trucks; was reasonably inexpensive; did not complicate maintenance procedures; and did not significantly increase the weight of trucks.

The R&D investigations concluded that curving performance and dynamic stability could be substantially improved on existing trucks. Predictions for improved truck performance included: extended wheel life, possibility of similar extensions to rail life, and stability up to 80 mph on tangent track.

Solutions

DR-1/DR-2 Truck

CN Rail Research, in cooperation with Dresser Transportation, Dofasco and TDC, developed a steering assembly based on a design by Mr. H. List. The assembly could be incorporated into a new truck design or retrofitted to existing trucks to facilitate radial steering. It featured two, C-shaped steering arms connected to the wheelsets and to each other through a pivot at the centre of the truck and resilient elastomeric pads mounted between the roller-bearing adapter and the side-frame.

The steering arms offer sufficient interaxle lateral stiffness to maintain sideframe alignment thus reducing parallelogramming. The elastomeric pads allow controlled longitudinal movement of the axles which, in turn, permits radial alignment of the wheels through curves.

Existing 100-ton freight car trucks, equipped with the C-arms and pads, entered service testing in 1978. These trucks were known as DR-1. Subsequently, an over the bolster version of the DR-1, called the DR-2, was developed to accommodate truck-mounted brake systems similar to those found on CP Rail coal cars.

Both trucks are in service with railroads in Canada and the U.S. including CN Rail, CP Rail, Burlington Northern (BN) and Norfolk Southern. The DR-2 is also being tested by railroads in India and Egypt.

Framed-Braced Trucks

An alternative truck design was developed by UTDC Inc. of Kingston in 1980 under the sponsorship of TDC and the Ontario ministries of Transportation and of Northern Affairs.

The frame-braced truck design uses diagonal rods attached through resilient, centre-bonded bushings to brackets welded to the sideframes. This arrangement provides sufficient shear stiffness to prevent parallelogramming. Elastomeric pads mounted at the bearing adapters are used to facilitate yaw control. The design can be incorporated into new truck designs or retrofitted to conventional 3-piece trucks.

The truck is in both intermodal and heavy haul service with railroads in Canada and the US including CP Rail, BN, Norfolk Southern, Union Pacific, Trailer Train and CSX Transportation.

Truck Evaluation Program

Initially, laboratory and short-term in-service performance evaluations were performed on the new truck designs by CN and CP Rail in cooperation with TDC. As experience was gained, small numbers of the most promising designs were placed in revenue service to quantify the expected benefits. For purposes of comparison, control cars equipped with standard 3-piece freight car trucks were placed in service at the same time. All test cars were fitted with new wheels and the new wheel profiles were recorded.

Periodic wheel and rail profile measurements and angle-of-attack measurements, which determine the radial position of the wheelset in a curve, were taken to quantify curving performance; train rolling resistance was measured to determine energy impact; wheel removal statistics were monitored over large populations of trucks; the effect of self-steering on other truck components was determined; and high-speed tangent track tests were performed to quantify the critical or hunting speed of the trucks and determine the safe operating speed.

Benefits

Reduction of wheel wear, particularly flange wear, was the first and most obvious benefit derived from the use of radial trucks. The dramatic results, obtained from CP Rail, indicate that radial truck wheels exhibited approximately 25% of the flange wear and 70% of the tread wear that developed on the control cars. These are two of the factors that led to improved wheel-set economics for cars equipped with radial axle trucks.

The Association of American Railroads (AAR), at the Transportation Test Center, conducted rolling resistance and energy consumption tests on frame-braced and conventional three-piece trucks for the Burlington Northern Railroad.

It was determined that frame-braced trucks would result in savings of 0.8 lbs./ton on tangent track, representing a 36% reduction from the value of 2.13 lbs./ton obtained for the conventional trucks. For curved track, the frame-braced truck had a resistance of 0.4 lbs./ton/degree in both empty and loaded conditions which represents a reduction of 50% in curve resistance for conventional trucks.

With the use of the BN Train Energy Model, the fuel requirements of both empty and loaded, conventional truck equipped and frame-braced equipped unit trains were calculated for a 1600-mile round trip. The results for the frame-braced unit train indicated savings of 269 US gallons of fuel (5.3%) in the empty movement and 709 US gallons (11%) in the loaded movement. The total round trip savings were 978 US gallons or 8.5% of total fuel consumption.(2)

The Witness Groove Method, a rail wear measurement tool developed by the National Research Council (NRC) to determine rail wear after only a few passages of a train, indicated that on dry track the radial trucks produced rail wear savings of approximately 25% compared to standard trucks. This represents a substantial increase in rail life. For example, rail located on a tight curve and subjected to heavy loadings may have a useful life of only 5 to 7 years. Use of radial axle trucks can extend this life by about 2 years. The number of years of extra life depends on the curvature of the track and the tonnage and volume of traffic.

The cost of a standard truck is about $8,500. The incremental cost for a radial axle truck(either as a retrofit or as additional cost on a new truck) is about $2,500 to $3,500 depending on the type of truck. This increased capital cost is the prime reason that railroads have taken a conservative approach to investing in this new equipment. Because the life of freight cars (including the trucks) generally averages 30 to 35 years, the railroads want to be convinced that the initial capital investment is justified by the benefits.

Because the measurable benefits are greatest for heavy haul railroads, they have been the first to make significant investments in radial axle trucks. In Western Canada, CN and BC Rail are jointly operating approximately 800 cars equipped with DR-1 radial axle trucks in unit coal trains. CP Rail is currently conducting a large-scale evaluation program in its Pacific Region using a 100-car unit coal train equipped with radial trucks. In addition, a new unit coal train, equipped with the DR-2 radial trucks, has recently started operation.

RAIL GRINDING

Background

With the growth in the 1970's of unit trains comprised of 100-ton cars, rail damage, particularly in curves, increased dramatically. In order to extend rail life, the use of alloy and/or heat treated rail was introduced, heavier rail (132 lb. and 136 lb.) was installed, the use of rail gauge face lubricators was improved and continuous welded rail was substituted for jointed rail.

When lubricant is applied to the gauge face of the rail, the wear rate decreases. When the wear rate recedes below a certain value, the fatigue limit of the rail surface is reached before it can be worn away by the rubbing contact between the wheel and the rail. Numerous surface contact fatigue cracks appear and are manifested as head checks, shelly spots, flaking and corrugations. Providing the corrugations are removed periodically by grinding, a longer rail life can be achieved with gauge face lubrication than without it.

Corrective Grinding

The conventional or traditional approach up until recently has simply been to grind the top surface of the rail at infrequent intervals to remove defects. This grinding approach, conducted after corrugations have developed, constitutes a corrective method of grinding. The typical corrective grinding criteria require rail to be ground when corrugations reach a depth of 0.020". In order to make the rail flat, several passes are made with a large grinding train. Although the grinding normally removes the corrugations, many cracks are left in the valleys of the original corrugations. As these cracks are connected to the surface, their growth will continue with the passage of the next train resulting in the early appearance of shelly spots, flakes and corrugations.

Profile Grinding

Considerable success has been achieved through a process known as rail profile grinding. In this process, the grinding train is used to modify the profile of the head of the rail in order to change the geometry of the wheel/rail contact so that wheel treads contact the rail near the centre of the head. This results in a decrease in the high contact stresses that occur in the gauge and field corners of the rail. Since the contact fatigue stresses are reduced, this leads to a decrease in shelling and corrugation development.

It was the development and use of profile grinding by the mining railroads of Australia and their reports of its benefits at subsequent Heavy Haul conferences that triggered interest on the part of Canadian and American railways. As the Australian lines are built and operated much like North American railways with similar equipment and axle loads, their experience has been applied to our operations. Profile grinding in Canada and the U.S. is used primarily to control corrugations on the low rail in curves and control gauge corner contact fatigue on the high rail of the curves to avoid spalling and shelling.

Preventative Grinding

Although carefully conducted rail profile grinding will reduce the rate of growth of corrugations and extend rail life, it will not by itself eliminate the formation of corrugations. In the absence of other action, corrugations will form and must be removed by grinding. Laboratory research undertaken by the Western Laboratory of the National Research Council has shown that by combining rail profile grinding with frequent but light grinding cycles, along with full lubrication, the life of rail can be extended significantly. Although only a minimal amount of metal is removed, this technique eliminates the tiny rail-head cracks before they can spread or even initiate and, at the same time, maintains the correct head profile.

Field trials of the preventive grinding technique are being run by CN Rail, CP Rail and BC Rail. It has been reported that Burlington Northern is using this technique on their main coal route handling 150 MGT. A comparison between corrective and preventive grinding is as follows:

	Corrective	Preventive
Grinding Period	20 MGT	8 MGT
Size of train (no. of stones)	88-120	30-44
Speed of grinding	3 mph	8 mph
Passes/year	4.5	8
Metal removed/year	0.013"	0.004"
Metal removed/year	0.060"	0.032"

Not all rail would be ground at the same frequency: tangent track would be ground every 24 MGT; mild curve track every 16 MGT and sharp curve track every 8 MGT. This would provide a projected rail life of 2250 MGT, 1500 MGT and 750 MGT respectively. These figures, compared to corrective grinding, represents approximately a threefold increase in rail life. (3,4,5)

ALUMINUM COAL CAR

Description

The gross weight of coal cars used in Canada today is limited to 263,000 lb. by railway standards. The payload capacity of a car is 263,000 lb. less the tare weight of the car. The 100-ton car is based on a tare weight of 63,000 lb. leaving 200,000 lb. for payload. Actual tare weights of cars currently in coal service in Canada are less than the nominal 63,000 lb. The lightest of the steel cars is the CP Rail bathtub gondola which has a tare weight of 53,000 lb. One alternative to achieve a reduction in the tare weight of the coal car is to substitute the steel for aluminum. The target for the tare weight of the aluminum coal car is between 43,000 lb. and 44,000 lb. The difference of 9 to 10,000 lb. can be replaced with payload and for a given transportation requirement in terms of tons of coal delivered will result in fewer trains/trips needed to deliver the commodity. The savings in variable operating costs of these trains represents the return on the investment in aluminum cars.

Since such tare weight improvements appear very attractive, it is interesting to speculate why aluminum coal cars are not extensively used in Canada today. In fact, interest in aluminum cars is developing; in recent years, 85% of new coal car purchases in the U.S. have been aluminum. In fact, the purchasers of most U.S. coal cars are the electric utilities.

There have been attempts in Canada to introduce aluminum coal cars, but these have not been successful and have impeded, rather than accelerated, their introduction. There are, therefore, risks involved in embarking on another attempt. Nonetheless there are valid reasons for expecting that the chances of achieving success are much improved this time. One reason is that there now exists, as a result of previous work, reliable information on longitudinal train forces experienced in service. The observed fatigue problems of these earlier attempts have now been explained in terms of these forces. In addition, to overcome the problems of these cars, revised structural components have been developed.

Test Program

It is expected that an aluminum coal car of improved design will be constructed and tested in service for a period of two years: first, in standard unit-train operation, i.e. normal couplers and then in rigid train operation. The testing will enable the various design improvements to be assessed. In addition, the load environment will be established and the fatigue life of the car estimated. Recommendations for further design changes will be made if warranted.

Benefits

The underlying benefits of the aluminum coal car are such that a successful service testing experience will provide the confidence needed by the railway industry to procure aluminum coal cars in future procurements on an equal footing with proven steel car designs.

FUELSAVER

Background

Fuel costs represent a substantial portion of the railways' operating expenses. For this reason, various techniques are used to reduce locomotive fuel consumption. One such system being supported by TDC, the Fuelsaving Device, is being developed by DSL Dynamic Sciences Ltd. in cooperation with the Quebec North Shore & Labrador Railway (QNS&L).

This system is designed to reduce unnecessary fuel consumption due to idling of the locomotive and to using excess power in a train consist. The system permits a more fuel efficient management of the locomotive.

Description

The fuel saving control system allows the locomotive engine to be completely stopped when the locomotive is not needed for work, whether the unit is stationary or in a multiple unit consist in mainline service.

Engine water-jacket temperature is monitored and maintained between 100 °F and 130 °F by periodically restarting the engine automatically. The system also continually monitors the status of engine control equipment and sets alarms in the event of failure of critical components.

Single Locomotive Operation

The engineman can select one of two possible modes of operation for the locomotive fuel saving system:

Normal: The system would be set to "normal" mode when the locomotive is required for work. In this mode the system continues to be active but does not cycle the engine on and off.

Cycle: This mode is used when the locomotive is not needed for work. In this mode the engine is normally turned off. When the engine coolant temperature falls below 100 °F the engine is automatically started and runs until the engine coolant temperature reaches 130 °F. The engine continues to turn off and on in this way as long as the "cycle" mode is selected.

Locomotives in Multiple-Unit Operation

When a locomotive equipped with a fuel-saver system is used in a consist its status ie, lead unit, trail unit, etc. is selected by the engineman at the start of the journey. Thereafter, the engineman can remotely select through the trainline and/or Locotrol Control Unit, the mode of operation of each locomotive in the consist.

System Control

The system is controlled by a ruggedized, microprocessor-based main control unit.

This unit is mounted in the main locomotive electrical cabinet and controls all aspects of the locomotive fuel saving system. The consist control panel supports features related to the excess of power in the consist. It permits the selective shut-down of locomotive units in the consist. Selected units are automatically isolated and cycled, ready to be recalled any time they are required. This unit is mounted in or beside the locomotive control stand so that it is easily accessible by the engineman.(6)

Test Results

The fuel saving system is installed on the entire locomotive fleet of QNS&L but is only fully operational, at present, on approximately 75% of the fleet. As system training for the locomotive enginemen has not been completed, the fuel savers are currently used only when the locomotives are in the various yards - shop maintenance personnel have been fully trained on the use of the system and they set the locomotives in the cycle mode whenever locomotives are in the yard for maintenance or other reasons.

Extensive data on the performance of the fuel saver have been collected for yard operation since November 1988. The on-board computer (part of the fuel saver's microprocessor) records various parameters whenever the system is in the cycle mode. Parameters recorded include:

- total time in fuel saving mode,
- total engine stopped time,
- number of automatic starts,
- total idling time (normally stays in idle for 1 minute after each start),
- total time in throttle 4 (engine is run in this throttle position to quickly warm up the engine) and,
- number of starts initiated by the auto-drain temperature switch (one of the sensors that is monitored by the microprocessor).

Preliminary results indicate that the fuel saver system is functioning very well. In ambient temperature conditions that ranged between -9 °C and -26 °C the use of the fuel-saver saved between 3.5 US gal/hr. and 4.0 US gal/hr. compared to normal consumption if the locomotive had been left in idle for the same period of time.

The final report describing the results of the full program is expected to be available in the Spring of 1990.

CONCLUSIONS

The technological developments presented should result in either continued or future reductions in railway operating costs. Although the benefits are incremental in nature, they are important since railways in other countries are often aggressive in pursuing technological improvements and the competitiveness of Canadian mineral products depends on keeping pace with new developments.

It is expected that with the revitalization of the Railway Research Advisory Board a more active industry-government co-operative railway research program will result which will assist Canadian railways to remain competitive.

REFERENCES

1. Bartley, G.W., "Problem Definition", Proceedings of the Conference on the Economics and Performance of Freight Car Trucks, October 1983.

2. Rownd, K.C., et al, "Rolling Resistance Characterization Test of Frame-Braced and Conventional Three-Piece Trucks", AAR, R-723, April 1989.

3. Kalousek, Dr. J., "Rail Wear and Contact Fatigue Model Utilizing Lubrication and Grinding to Extend Rail Life", Proceedings of the Seminar on Rail Freight R&D, June 1986.

4. Maughan, R.G., "Rail Transportation of Coal in Western Canada", Transportation Development Centre, May 1988, TP 9316E.

5. Shedd, T., "Profile Grinding is Cost Effective", Modern Railroads, May 1989.

6. Levesque, G., "DSL Fuelsaving Device", Proceedings of the Seminar on Rail Freight R&D, June 1986.

OPTIMISATION OF ROAD VEHICLE POWER SYSTEMS

A.S.Davies

Fuels and Lubricants Laboratory
National Research Council of Canada

ABSTRACT

Reciprocating, internal combustion engines, operating on fossil derived fuels are almost universally utilised for road transportation around the world. The potential for improvements to vehicle operating efficiency and the reduction of harmful pollutants with such fuels is reviewed.

Vehicles that stop and restart frequently, deliver relatively poor fuel economy and exhaust emissions levels, by comparison with the near steady state operating conditions which are typical of highway cruising conditions.

The power required to accelerate a vehicle greatly exceeds the power required to maintain typical cruising speeds; also the engine is usually required to operate at speed and loads far removed from the ideal.

During stop/start driving conditions, typical of City driving; the majority of the mechanical energy transmitted from the engine, through the transmission, is converted into kinetic energy (in the form of vehicle speed); much of this energy is ultimately converted into heat and lost to the atmosphere, when the service brakes are applied,

In 1986 tests were conducted by the National Research Council of Canada using a conventional diesel powered city bus, of 1984 manufacture, which was operated according to a standard test driving cycle. The tests showed that 81% of the fuel consumed during a complete stop-start cycle, was consumed during the acceleration portion of the cycle.

During the acceleration, the vehicle, as a system was 53% efficient at converting the engine generated energy into vehicle motion; 42% of the total mechanical energy generated by the diesel engine, over the cycle was ultimately dissipated in the brakes,during the deceleration. The overall fuel efficiency of the vehicle during this driving cycle was found to be less than 8%

In the late 1970's, restrictions in the world fuel supply spurred many investigators to seek practical methods of vehicle energy conservation.

A team at the National Research Council of Canada, evaluated the alternatives, and identified the concept of regenerative braking, using a hydraulic accumulator based system, as having the most immediate potential, in addition to the basic vehicle improvements, which the manufacturers continue to pursue.

A regenerative power system was subsequently designed and constructed, and was installed on a 35 ft , Ontario Bus Industries, ORION I city bus. Very significant fuel and emissions reductions, have been attained with the prototype.

INTRODUCTION

The most prolific power source for road vehicles up to this time, is based on the reciprocating engine, consuming a fossil derived hydrocarbon fuel. Reciprocating engines appear in many forms, including 2 and 4 stroke, gasoline and diesel, with direct and indirect fuel injection, combustion systems.

These engines,together with the associated fuel and transmission systems, have gained widespread acceptance on account of their reliability, high power to weight ratio, low cost; their operational safety and their ease of use, which includes refuelling and starting. But perhaps the most significant features that these engines have in common, are their easy and rapid startability, together with their wide operating speed and load range; including their ability to provide for rapid transitions. These latter, features are extremely valuable, in road vehicles, where the engine speed and load requirement varies considerably depending upon the driving conditions,which might range from high traffic density, in-town conditions, to hill climbing situations (perhaps heavily laden and towing a trailer) or they might require highway cruising.

However,regardless of the particular type of reciprocating engine, the fuel economy and production of toxic exhaust emissions is optimal within a much narrower range of operation than that typically utilised in vehicle operation.

Figure 1 illustrates for a typical Diesel engine, how the Specific Fuel Consumption varies with engine speed and load, and shows the potential for maximising the economy of operation if the speed and load range can be restricted. [Specific Fuel Consumption is a measure of an engine's fuel efficiency, in terms of the quantity of fuel required to produce a given quantity of mechanical energy; typical units are grams (fuel) per kW-hr engine output energy.]

Curves may also be constructed for the emissions of pollutants such as CO, CO_2, HC, NO_x and particulates. The engine operation may then be optimised for a combination of fuel efficiency and exhaust emissions, by (**open** loop) control of the transmission ratio and engine parameters such as ignition timing and fuel mixture etc.

In figure 2, using the same base data as used in figure 1, the data is redrawn to show the variation of actual fuel consumption, with engine power. Here a direct relationship between engine power and fuel consumption is seen, with engine speed having a relatively minor influence.

The conclusion to be drawn from this figure, typical for reciprocating internal combustion engines, is that reduction of a vehicle's power requirement offers the greatest potential, for fuel consumption reduction.

Methods to reduce the power requirement of road vehicles include vehicle weight reduction, reduction of power losses within engine and transmission, and the reduction of road and aerodynamic drag. Developments in these areas continue to be actively pursued by vehicle and component manufacturers.

The level of activity directed at improving the efficiency of the reciprocating engine, is in 1990 still intense, 114 yrs after the invention of the 4 stroke Otto cycle (spark ignited gasoline) engine and 92 years after the invention of the Diesel engine.

Current developments include the use of low friction, high temperature materials; multiple valves per cylinder; turbo and super-charging; microprocessor controlled fuel injection, and, for Diesel engines; high pressure fuel injection operating at pressures around 1500 bar. Variable valve timing is currently available on at least one production gasoline engine.

With the advent of automotive microelectronics and appropriate sensors, it is now feasible to exercise closed loop control of both engine and transmission, in order to obtain optimal economy, power and emissions performance from the entire power train, under transient operating conditions.

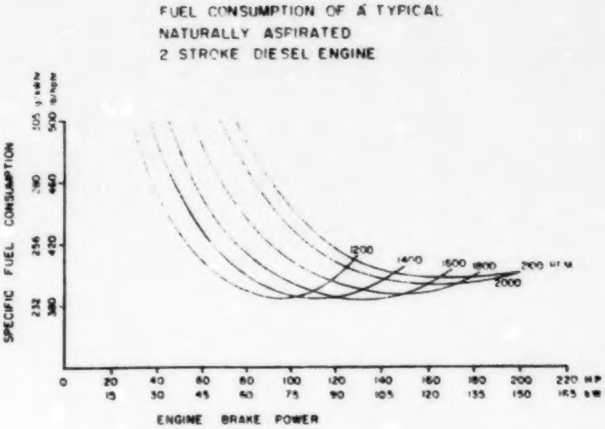

Fig. 1 TYPICAL DIESEL SPECIFIC FUEL CONSUMPTION MAP

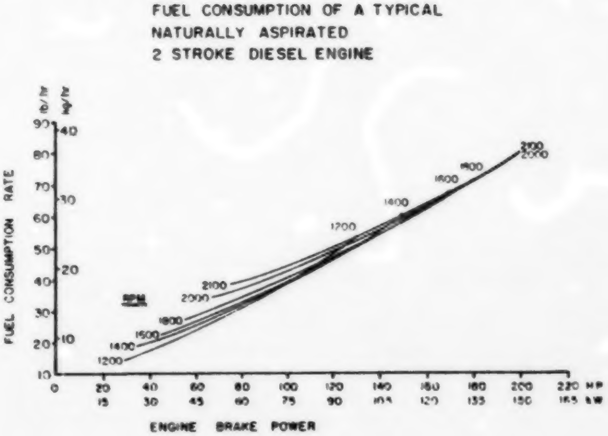

Fig. 2 TYPICAL DIESEL FUEL CONSUMPTION versus POWER

Added to these developments, is the search for alternative fuels with which to operate these engines; these are targeted to reduce the reliance on oil reserves and to reduce the levels of toxic exhaust emissions and carbon dioxide. Potential alternatives subject to R & D around the world include the alcohols methanol and ethanol, natural gas and hydrogen.

More radical alternatives are also being sought, such as electric vehicles powered by improved batteries or fuel cells; and gas turbine engines with extensive use of ceramic components to elevate the operating temperatures and efficiencies [1]* The performance level of internal combustion engines in general,and of the reciprocating variants in particular, cannot currently be approached let alone exceeded,by even the most advanced alternatives, in terms of power density, the energy density of the fuels, and the available operating speed and power range.

The durability of the current Diesel engine (which in the case of Heavy Duty truck engines, are expected to exceed 400,000 miles between major overhauls); together with the thermal efficiency of these engines, (up to 40%), cannot yet be matched, but form obvious targets for the ongoing automotive gas turbine developments such as the AGT 100 [General Motors ,Allison Division] and AGT 101 [Garret] [1]

However, the improvement of reciprocating engines by the ongoing engine developments will certainly continue and can profitably be supplemented by optimisation of the conditions over which the engines are required to operate. As discussed above there are gains to be made by restricting the speed and the power requirement for the engine.

RESTRICTING ENGINE SPEED RANGE

Due to the wide range of speed required by road vehicles, it is customary to employ multiple speed transmissions, typically 3 to 5 ratios on passenger vehicles, and 10 to 18 ratios on heavy commercial vehicles. Extending this concept to provide more than 20 ratios or a continuously variable transmission, would provide obvious advantages to all road vehicles.

Such transmission systems are being actively developed today,[2] [3] [4] [5] [6] but few have as yet been realised on a production basis, and of those in production today, none are applicable to heavy commercial vehicles.

REDUCTION OF ENGINE POWER REQUIREMENT

A common feature of most transmissions being researched today, is the absence of a slipping coupling such as the hydrodynamic torque converter. This will eliminate the large power losses that occur during vehicle acceleration and ultimately reduce the power required of the engine.

A power requirement feature, particularly demanding of energy in the city vehicle, is the acceleration / deceleration cycle. The power required to accelerate a vehicle greatly exceeds the power required to cruise (i.e. maintain a constant and moderate speed) In stop/start driving conditions, mechanical energy generated by the engine (obtained from the fuel energy at 20 to 30 % efficiency), is, during the acceleration phase, converted to kinetic energy of the vehicle. During deceleration, this kinetic energy is converted into heat at the friction brakes, and ultimately lost to the atmosphere.

The quantity of kinetic energy possessed by a vehicle travelling at 48 km / h is equivalent to an elevation of 9.14 m. (30 mph = 30 ft elevation.)

Tests conducted by the TRRC [7] showed that in a conventional city bus equipped with an automatic transmission and torque converter, the efficiency of the vehicle in converting engine power to vehicle energy was 53% Also, during a 30 mph standard driving cycle, comprising a 48 km/h [30 mph] maximum speed,and with a stop at each 322 m [1/5 mile]; the friction brakes are required to dissipate 42% of the total energy generated by the engine - fig 3.

The overall efficiency of fuel usage is assessed as:-

Engine η x vehicle/transmission η x (1 - energy dissipated during braking)

say .25 x .53 x (1-.42) = 7.7 %

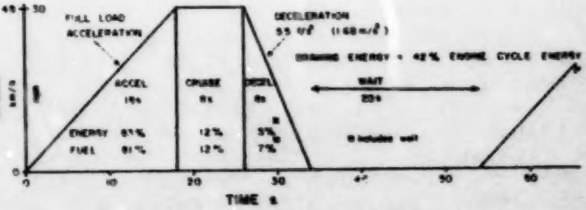

Fig. 3 ENERGY & FUEL BALANCE FOR 30 mph BUS CYCLE

---

* Numbers in parentheses refer to references listed at the end of the paper.

A Regenerative Power Train avoids much of the energy loss, by capturing and storing the vehicle, mechanical energy during deceleration, and reapplying the stored energy during the subsequent vehicle acceleration. In applications where the vehicle power requirement is determined by a desired acceleration level, an engine of lower power can be employed in a vehicle incorporating a regenerative braking system.

A team at the National Research Council was applied to design,construct and evaluate a regenerative power system which was installed on a conventional city bus.[8 & 9] figs 4 & 5.

Independently and over a similar time span, regenerative braking systems evolved at MAN in Germany [10] , Volvo in Sweden [11 & 12] , The Technical University of Denmark [13], Leyland Vehicles in the U.K. [14] and Mitsubishi Motors in Japan [15]

EVALUATION PROCEDURE.

Tests were conducted on a substantially level, 3.0 km (1.86 mile) oval test track.

The City Business District (CBD) and Arterial Phase (AP) of the D.O.T. (Washington) "Transit Coach Design Operating Duty Cycle", [16, 17] were utilised fig 6.

In addition, a 48 km/h (30 mph) phase was used, as earlier studies [8] had determined that the regenerative power train system should be optimised for speeds in the range 32 to 48 km/h (20 to 30 mph)

The bus was subsequently evaluated for its exhaust emissions performance, again by comparison with the standard vehicle.[16]

EMISSIONS ASSESSMENT - TEST PROCEDURE

Emissions testing was conducted at the SouthWest Research Institute, using a chassis dynamometer equipped with inertia discs,simulating the vehicle mass.

The bus was operated according to the CBD phase of the Advanced Design Bus Drive cycles, using a service level deceleration of 5.5 ft/s^2 (1.68 m/s^2 ,and a 10 second idle period between successive cycles[17]

Emissions were constantly sampled over a 2 mile run of the cycle. The cycle average fuel economy was determined by the carbon balance technique, using emissions measurements of HC CO and CO_2

To facilitate comparison, the bus was tested in two configurations; firstly with the Regenerative Power Train operational, and secondly, as a standard vehicle. [Mechanical drives to the regenerative system completely disconnected.]

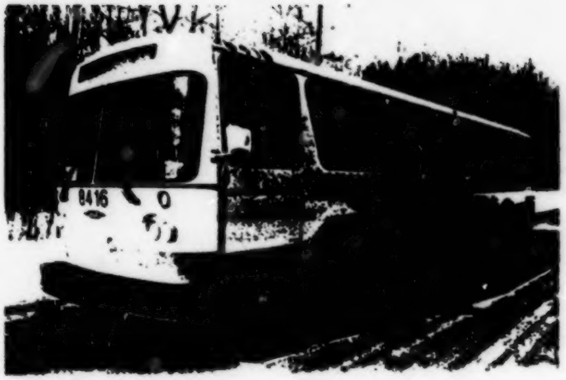

Fig. 4 ORION I CITY BUS

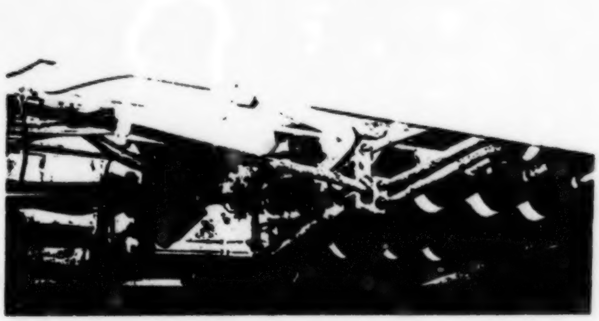

Fig. 5 REGENERATIVE POWER TRAIN INSTALLATION

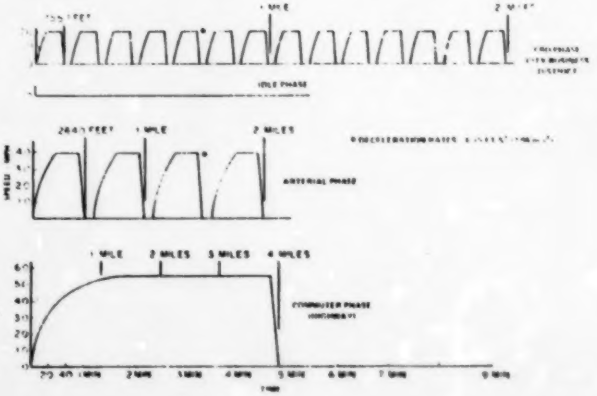

Fig. 6 ADVANCED DESIGN BUS - TEST DRIVING CYCLES

In practice, the Regenerative Power Train would add some 2000 lbs to the vehicle weight, this was reflected in the total inertia weights utilised on the dynamometer.

ANALYTICAL PROCEDURES

Total hydrocarbons and NO_x were determined over each test cycle by integration of the diluted exhaust gas concentrations obtained using the Constant Volume Sampling (CVS) technique.

Concentrations of CO and CO_2 were determined from CVS dilute exhaust sample bags.

NO_x was reduced 19 percent somewhat in line with the percentage improvement in fuel economy ; particulate and CO emissions were more strongly influenced, with reductions of 27 and 60 per cent , respectively. HC emissions were the least affected with a reduction of 8 percent.

Utilising the different sensitivities demonstrated, the results were extrapolated in accordance with the expected performance of a production regenerativa power train system - fig 7.

CONCLUSIONS.

For road vehicles, due to their advantageous performance abilities,the reciprocating internal combustion engine will continue to provide the motive power for the foreseeable future, consuming fossil derived hydrocarbon fuels.

Small but continuous improvements in engine efficiency and emissions performance are foreseen, together with the usage of alternative fuels.

Power train improvements will permit more efficient operation of the engines; principal amongst the improvements anticipated by the author are the adoption of microelectronic control for mechanical clutches (and probable elimination of the torque converter), transmissions providing continuously variable ratios, and regenerative braking concepts.

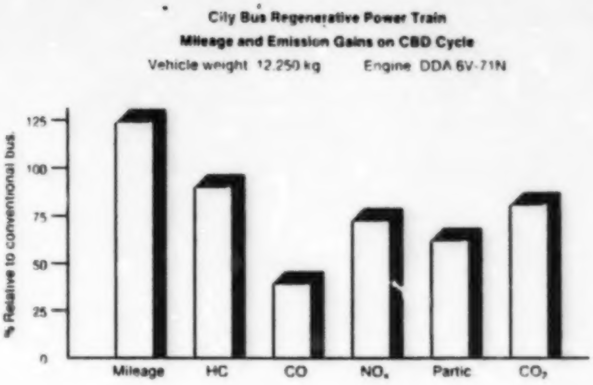

Fig. 7 EXHAUST EMISSIONS AFTER ENERGY REGENERATION

REFERENCES.

1. Proceedings of the Twenty-Fourth Automotive Technology Development Contractors Coordination Meeting. Dearborn, Michigan October 1986 SAE Publication P 197

   G.L.Boyd et al., A Technology Development Summary of the AGT101 Advanced Gas Turbine Program.

   H.E.Helms et al., AGT 100 Advanced Gas Turbine Technology Development Project

2. Society of Automotive Engineers, Automotive Engineering Vol 95, No.1 November 1987 (Ford CVT)

3. Hagin.F and Martini.S ,Conference of the Electric Vehicle Development Group. London,September 1981 (MAN ,Split power, Continuously Variable Transmission)

4. Kerr,J.J, and Ferguson R.J. The Binary Logic Incremental Transmission, Mechanism and Machine Theory **18** (5), 357-361 (1983)

5. New Scientist ,August 13 1987 p.33 (Perbury traction CVT)

6. R.J.Ferguson and J.R.G.Morrison. The Efficiency of the 64-Ratio Ker-Train Transmission. Society of Automotive Engineers SAE 861287

7. A.S.Davies. Fuel Economy and Emissions Potential of a City Bus, Regenerative Power Train. Society of Automotive Engineers S.A.E 872267

8. A.S.Davies and W.S.Heggie Predicting the Retardation Performance of Vehicles Equipped with Hydro-Pneumatic Energy Storage Systems. S.A.E. 859261 20th IECEC Conference, Miami,August 1985

9. W.S.Heggie and A.S.Davies. The Development and Testing of a Regenerative Diesel-Hydraulic Power Train for the Urban Bus. B.H.R.A. Conference. University of Bath, Sept.1986.

10. F.Hagin and P.Merker Drive systems with brake energy recovery. U.S.Dept. of Energy 5th International Automotive Propulsion Systems Symposium,April 1980

11. L.Hammerstrom VTS Hydrostatic Transmission Experiences from the first field test. International Symposium Advanced & Hybrid Vehicles, University of Strathclyde, Sept.1984.

12. C.H.Curtis. Energy storage systems for public service vehicles. Integrated Engine Transmission Systems Symposium. Institution of Mechanical Engineers/ University of Bath July 1986

13. P.Buchwald,G.Christensen,H.Larsen and P.Sunn Pedersen. Improvement of Citybus Fuel Economy Using a Hydraulic Hybrid Propulsion System - A Theoretical and Experimental Study. Society of Automotive Engineers SAE 790305

14. H.W.Hahn Improving the overall efficiency of trucks and buses Institution of Mechanical Engineers,London. December 1983.

15. N.Nakazawa et al. Development of a Braking Energy Regeneration System for City Buses Society of Automotive Engineers SAE 872265

16. A.S.Davies. The Reduction of City Bus Exhaust Emissions by Means of a Regenerative Power Train. Society of Automotive Engineers S.A.E 890267

17. Baseline Advanced Design Transit Coach Specifications. Department of Transportation,Urban Mass Transportation Administration, Washington, D.C., April 1977

ÉTUDE DE LA STABILITÉ DES VÉHICULES ARTICULÉS PAR LA MÉTHODE DE LYAPUNOV

Mustapha Khan   Paul Bourassa   Milan Brezina

Département de génie mécanique
Université de Sherbrooke
Sherbrooke (Québec)

RÉSUMÉ

La stabilité dynamique d'un véhicule articulé du type tracteur-remorque est étudiée en se basant sur une approche qualitative du problème. L'application de la méthode de Lyapunov et l'optimisation d'une fonction quadratique de Lyapunov nous permettent non seulement de trouver un domaine de stabilité, mais aussi d'avoir le plus grand domaine possible correspondant au type de fonctions choisies. L'intégration numérique sert enfin comme moyen de vérification des résultats obtenus.

1. INTRODUCTION

L'évolution économique et ses besoins de plus en plus importants en transporteurs lourds ont imposé, au cours des dernières années, l'utilisation de véhicules ayant des espaces de chargement de plus en plus vastes et des capacités de charge de plus en plus grandes. Cette mutation s'est effectuée malgré que les problèmes qui affectent ce type de véhicules ne sont pas parfaitement cernés.

Ces problèmes se manifestent souvent par des mouvements importants d'oscillations latérales (snaking), lorsque le système est perturbé à certaines vitesses critiques, ainsi que par des accidents catastrophiques du type "tête à queue" (jack-knife).

Malgré le caractère non linéaire du mouvement des véhicules articulés, leur stabilité a été étudiée en considérant autant le modèle linéaire que le modèle non linéaire. Les études basées sur un modèle linéarisé Jindra [1], Ellis [2], Mikulcik [3], ont donné des résultats qui concordent bien avec l'expérience à condition que les perturbations considérées aient des amplitudes assez faibles pour que le système reste au voisinage de son équilibre dynamique.

Pour les études basées sur des modèles non linéaires, on peut distinguer deux catégories différentes: 1) les études qui considèrent de faibles perturbations autour des points d'équilibres, Eke et Kane [4], Eshlman [5]. Ces études donnent de très bons résultats concernant les situations étudiées mais ne peuvent rien conclure concernant des perturbations plus importantes. 2) les études qui s'intéressent à des perturbations quelconques, Singh [6] et [7], Sachs et Chou [8]. Singh [6], utilise l'intégration numérique des équations de mouvement pour déterminer le domaine de stabilité du véhicule. Dans [7], il utilise la théorie de Lyapunov pour retrouver le domaine de stabilité et arrive à la conclusion que ce domaine est plus petit que celui obtenu par intégration numérique. Cette constatation est due au fait que Singh [7] utilise la fonction simple de Lyapunov $V(X) = 1/2 \{X\}^T[I] \{X\}$ et non une fonction optimale. Sach et Chou, par contre, optimisent le domaine de stabilité d'une automobile en considérant seulement deux degrés de liberté du mouvement.

Dans ce travail, on va essayer d'établir le domaine de stabilité d'un véhicule articulé "tracteur remorque" en utilisant la méthode de Lyapunov en prenant comme fonction de Lyapunov la forme quadratique $V(X) = \{X\}^T[Q] \{X\}$ et en essayant d'optimiser la matrice définie positive [Q].

2. MODÉLISATION

Comme la majorité des systèmes mécaniques, les véhicules articulés sont formés d'un très grand nombre de masses, ressorts, et amortisseurs qui donnent à ses véhicules une nature très complexe et très difficile à modéliser et à étudier à cause de leur nombre de degrés de liberté très élevé. Dans le modèle considéré (Fig. 1), et qui a déjà fait ses preuves dans les études précédentes, le système tracteur-remorque est représenté par deux unités reliées entre elles par un axe vertical. On considère que ce système circule à une vitesse constante sur une route horizontale, uniforme et ayant un rayon de courbure constant. En quelque sorte, les seuls mouvements considérés sont l'avance du véhicule, son déplacement latéral, et le lacet des deux unités; alors que le tangage, le roulis, ainsi que les différents mouvements dus à la suspension sont négligés dans notre modèle. Les différentes données utilisées dans ce travail sont présentées dans le tableau 1. (Ellis [9]).

TABLEAU 1

Masse du tracteur $M_T = 2713$ kg
Masse de la remorque $M_R = 9045$ kg
Moment d'inertie du tracteur = $I_T = 4040$ kg.m^2
Moment d'inertie de la remorque = $I_R = 47440$ kg.m^2
$b_1 = 1.15$ m $b_2 = 1.60$ m $b_3 = 1.20$ m
$b_4 = 4.5$ m $b_5 = 1.5$ m
$c_{11} = c_{21} = -103600$ N/rad, $c_{31} = c_{41} = -305500$ N/rad
$c_{51} = c_{61} = -256400$ N/rad

c_{i2} est donné par: $\left.\frac{\partial F_i}{\partial \alpha_i}\right|_{\alpha = \alpha_m} = 0 \Rightarrow \quad c_{i2} = -c_{i1}/(3\alpha_m^2)$

avec $\alpha_m = 0.15$ rad

3. DÉRIVATION DES ÉQUATIONS DE MOUVEMENT

Pour faciliter la dérivation de ces équations, on attache au centre de gravité c du tracteur un repère $(c, \vec{X}, \vec{Y}, \vec{Z})$ et au centre de gravité c_1 de la remorque un repère $(c_1, \vec{X}_1, \vec{Y}_1, \vec{Z}_1)$. Pour écrire les équations de mouvement, on va appliquer à chacune des unités du système la $2^{\text{ème}}$ loi de Newton et le théorème du moment dynamique exprimé dans le repère associé à l'unité considérée.

$$\sum \vec{F}_T = M_T \, \vec{a}_c \tag{1}$$

$$\sum \vec{M}_c = \frac{d}{dt}(\vec{H}_c) \tag{2}$$

$$\sum \vec{F}_R = M_R \, \vec{a}_{c1} \tag{3}$$

$$\sum \vec{M}_{c1} = \frac{d}{dt}(\vec{H}_{c1}) \tag{4}$$

En tenant compte du fait que le point 0_1 appartient aux deux unités, on peut écrire l'équation de contrainte suivante:

$$\vec{V}_{o1/c} + \vec{V}_c = \vec{V}_{o1/c1} \quad \vec{V}_{c1} \tag{5}$$

La combinaison des cinq équations précédentes et en considérant que la vitesse d'avance V_x est constante ($\dot{V}_x = 0$), et que les forces longitudinales (motrices et de freinage) s'annulent entre elles, nous pouvons écrire les équations de mouvement de ce système sous la forme:

$$\begin{aligned}(M_T + M_R)\dot{V}_y - M_R b_3 \dot{\omega}_1 - M_R b_4 \dot{\omega}_2 \cos\gamma = \\ -(M_T + M_R)V_x\omega_1 + M_R b_4 \omega_2^2 \sin\gamma \\ +(F_1 + F_2)\cos\delta + (F_3 + F_4) + (F_5 + F_6)\cos\gamma\end{aligned} \tag{6}$$

$$\begin{aligned}-M_R b_3 \dot{V}_y + (I_T + M_R b_3^2)\dot{\omega}_1 + M_R b_3 b_4 \dot{\omega}_2 \cos\gamma \\ = M_R b_3 V_x \omega_1 - M_R b_3 b_4 \omega_2^2 \sin\gamma + b_1(F_1 + F_2)\cos\delta \\ -b_2(F_3 + F_4) - b_3(F_5 + F_6)\cos\gamma + c_f\end{aligned} \tag{7}$$

$$\begin{aligned}-M_R b_4 \dot{V}_y \cos\gamma + M_R b_3 b_4 \dot{\omega}_1 \cos\gamma + (I_R + M_R b_4^2)\dot{\omega}_2 \\ = M_R b_4 V_x \omega_1 \cos\gamma - M_R b_4 V_y \omega_1 \sin\gamma \\ + M_R b_3 b_4 \omega_1^2 \sin\gamma - (b_4 + b_5)(F_5 + F_6) - c_f\end{aligned} \tag{8}$$

L'angle γ entre les deux unités est donné à partir de l'équation:

$$\dot{\gamma} = \omega_1 = \omega_2 \tag{9}$$

Les équations (6) - (9) donnent les équations de mouvement de notre système.

3.1 Les forces latérales:

Les équations des forces latérales F_i sont données par la forme empirique proposée par Ellis [9]:

$$F_i = c_{i1} \, \alpha_i + c_{i2} \, \alpha_i^3 \qquad (i = 1, 2, \ldots, 6) \tag{10}$$

Les valeurs des c_{i1} et c_{i3} sont données pour le véhicule considéré dans le Table I.

Les angles de glissement α_i sont reliés aux vitesses latérales et longitudinales des roues et aux angles de bracage δ_i par la relation:

$$\operatorname{tg}(\alpha_i + \delta_i) = \frac{Vy_i}{Vx_i} \tag{11}$$

En sachant que les angles de glissement restent toujours petits, on peut écrire:

$$\alpha_i + \delta_i = \frac{Vy_i}{Vx_i} \Rightarrow \alpha_i = \frac{Vy_i}{Vx_i} - \delta_i \tag{12}$$

Vu que les roues arrières du tracteur et les roues de la remorque sont fixes,

$\delta_2 = \delta_3 = 0$

et

$\delta_1 = \delta =$ angle de bracage,

et on peut écrire:

$$\alpha_1 = \alpha_2 = \frac{V_y + b_1\omega_1}{V_x} - \delta \tag{13}$$

$$\alpha_3 = \alpha_4 = \frac{V_y - b_2\omega_1}{V_x} \tag{14}$$

$$\alpha_5 = \alpha_6 = \frac{V_x \sin\gamma + (V_y - b_3\omega_1)\cos\gamma - (b_4 + b_5)\omega_2}{V_x \cos\gamma - (V_y - b_3\omega_1)\sin\gamma}$$

Lorsque le véhicule est en équilibre dynamique

$(V_y - b_3 \, \omega_1) \sin\gamma << V_x \cos\gamma$

et γ est petit $\Rightarrow \sin\gamma = \gamma$

d'où

$$\alpha_5 = \alpha_6 = \frac{V_y - b_3\omega_1 - (b_4 + b_5)\,\omega_2 + V_x\,\gamma}{V_x} \tag{15}$$

L'utilisation des équations (13) - (15) dans (10) et en posant:

$(V_y, \omega_1, \omega_2, \gamma) = (Q_1, Q_2, Q_3, Q_4)$

et $\quad f_1 = F_1 + F_2, \; f_2 = F_3 + F_4, \; f_3 = F_5 + F_6$

on peut écrire:

$$f_1 = \frac{c_{11}+c_{21}}{V_x}(Q_1 + b_1Q_2 - V_x\delta) + \frac{c_{12}+c_{22}}{V_x^3}(Q_1 + b_1Q_2 - V_x\gamma)^3 \qquad (16)$$

$$f_2 = \frac{c_{31}+c_{41}}{V_x}(Q_1 - b_2Q_2) + \frac{c_{32}+c_{42}}{V_x^3}(Q_1 - b_2Q_2)^3 \qquad (17)$$

$$f_3 = \frac{c_{51}+c_{61}}{V_x}[Q_1 - b_3Q_2 - (b_4 + b_5)\,Q_3 + V_xQ_4]$$

$$+ \frac{c_{52}+c_{62}}{V_x^3}[Q_1 - b_3Q_2 - (b_4 + b_5)Q_3 + V_xQ_4]^3 \qquad (18)$$

L'utilisation de ces trois dernières équations dans les équations (6) - (9) et en considérant γ et δ petits, on peut écrire, en négligeant c_f:

$$\begin{bmatrix} (M_T + M_R) & -M_Rb_3 & -M_Rb_4 & 0 \\ -M_Rb_3 & (I_T + M_Rb_3^2) & M_Rb_3b_4 & 0 \\ -M_Rb_4 & M_Rb_3b_4 & (I_R + M_Rb_4^2) & 0 \\ 0 & 0 & 0 & 1 \end{bmatrix} \begin{Bmatrix} \dot{Q}_1 \\ \dot{Q}_2 \\ \dot{Q}_3 \\ \dot{Q}_4 \end{Bmatrix} =$$

$$\begin{Bmatrix} -(M_T + M_R)V_xQ_2 + M_Rb_4Q_3^2Q_4 + (f_1 + f_2 + f_3) \\ M_Rb_3V_xQ_2 - M_Rb_3b_4Q_2^2Q_4 + b_1f_1 - b_2f_2 - b_3f_3 \\ M_Rb_4V_xQ_2 - M_Rb_4Q_1Q_2Q_4 + M_Rb_3b_4Q_1^2Q_4 \\ \qquad\qquad - (b_4 + b_5)f_3 \\ Q_2 - Q_3 \end{Bmatrix}$$

$$= \begin{Bmatrix} F_1(Q) \\ F_2(Q) \\ F_3(Q) \\ F_4(Q) \end{Bmatrix} \qquad (19)$$

ou sous forme plus compacte:

$$[A]\,\{\dot{Q}\} = \{F(Q)\} \qquad (20)$$

ou bien

$$\{\dot{Q}\} = [A]^{-1}\{F(Q)\} = \{G(Q)\} \qquad (21)$$

4. RÉPONSE DU VÉHICULE

Si le véhicule décrit par l'équation (21) est soumis à une perturbation quelconque qui donne aux variables (Q_1, Q_2, Q_3, Q_4) les grandeurs q_1, q_2, q_3, q_4), il peut répondre de plusieurs façons différentes dépendamment des valeurs respectives de q_1, q_2, q_3, q_4. Ces réponses peuvent, soit le ramener à nouveau vers l'équilibre dynamique, soit amplifier le déséquilibre initial.

Sur les figures 2 et 3, on retrouve deux réponses différentes du véhicule. Sur la figure 2, on remarque qu'au bout de 4 secondes, le véhicule retrouve sa stabilité dynamique, alors que sur la figure 3, on remarque que le véhicule a subi une perte de stabilité caractérisée par une augmentation dangereuse de l'angle γ entre les deux unités qui ne peut donner lieu qu'à un tête à queue (jack-knife) certain.

Les valeurs vers lesquelles convergent les courbes de la figure 2 sont les coordonnées de l'un des points d'équilibre donnés par la solution de l'équation:

$$\{\dot{Q}\} = \{G(Q)\} = \{0\} \qquad (22)$$

5. ANALYSE QUALITATIVE

Dans cette section, on peut traiter deux aspects de la stabilité des véhicules articulés. La stabilité de ces véhicules au voisinage immédiat des points d'équilibre donnés par la résolution de l'équation (22), et la recherche des frontières du domaine de stabilité autour des points d'équilibre stables.

5.1 Stabilité au voisinage des points d'équilibre

Pour (Q_1, Q_2, Q_3, Q_4) $\in R^4$, on peut trouver plusieurs ensembles de points vérifiant l'équation (22). Ces ensembles de points représentent les lieux d'équilibre dynamique du véhicule appelés communément les "points singuliers".

Pour déterminer l'état du véhicule au voisinage de ces points, on peut utiliser le développement de Taylor pour écrire l'équation (21) sous la forme:

$$\{\dot{y}\} = [B]\,\{y\} + \{H(y)\} \qquad (23)$$

où: $y_i = Q_i - Q_{io}$ ($i = 1, 2, \ldots 4$)
avec (Q_{10}, Q_{20}, Q_{30}, Q_{40}) sont les coordonnées du point singulier considéré.

$$[B] = \begin{bmatrix} \dfrac{\partial G_1(Q)}{\partial Q_1} & \text{———} & \dfrac{\partial G_1(Q)}{\partial Q_4} \\ \vdots & & \vdots \\ \dfrac{\partial G_4(Q)}{\partial Q_1} & \text{———} & \dfrac{\partial G_4(Q)}{\partial Q_4} \end{bmatrix}_{(Q_1,\ldots Q_4) = (Q_{10},\ldots,Q_{40})} \qquad (24)$$

et H(y) contient les termes d'ordre supérieur ou égal à 2.

Au voisinage des points d'équilibre vérifiant l'équation (22), le système (23) peut être approximé par sa partie linéaire:

$$\{\dot{y}\} = [B]\{y\} \tag{25}$$

dont la solution est donnée par [10]:

$$\{y(t)\} = e^{[B]t}\{c\} \tag{26}$$

pour que cette solution soit stable, il faut que la matrice [B] ait des valeurs propres dont les parties réelles sont toutes négatives. Cette notion est résumée par la théorème suivant:

Théorème I (principe de la $1^{ère}$ approximation ou $1^{ère}$ méthode de Lyapunov):
soit {q} un point d'équilibre du système autonome décrit par l'équation (23). Si:

$$\lim_{\|y\| \to 0} \frac{\|H(y)\|}{\|y\|} = 0$$

et si, les valeurs propres du système linéarisé $\{\dot{y}\} = [B]\{y\}$ possèdent des parties réelles négatives, le système (23) possède une stabilité asymptotique au voisinage de {q}.

Sur le tableau 2, on peut retrouver des points d'équilibre dynamique obtenus à partir de la résolution de l'équation (22) avec (Q_1, Q_2, Q_3, Q_4) variant de (-9, -9, -9, -∏) à (9, 9, 9, ∏). Parmi tous ces points, le seul qui est stable est le 4è pour lequel les valeurs propres de [B] ont toutes des parties réelles négatives. Ces résultats sont obtenus pour une vitesse d'avance V_x = 75 km/h et un angle de bracage $\delta = 3°$.

5.2 Domaine de stabilité

Comme il est bien connu, il n'existe aucune technique qui permet de déterminer les frontières du domaine de stabilité asymptotique pour le système d'ordre n donné par l'équation (23):

$$\{\dot{y}\} = \{f(y)\} = [B]\{y\} + \{H(y)\}$$

autour du point d'équilibre stable du tableau 2.

Plusieurs auteurs ont utilisé les possibilités offertes par la 2è méthode de Lyapunov pour estimer le domaine de stabilité optimal du système considéré. Cette méthode est résumée par le théorème suivant:

Théorème II: Lasalle et Lefschetz [11]

Le point d'équilibre {y} = {0} possède une stabilité asymptotique s'il existe une fonction scalaire V(y), appelée fonction de Lyapunov, ayant des dérivées partielles continues à l'intérieur d'un domaine Ω contenant le point {y} = {0}, et telle que:

1°) $V(y) > 0 \qquad \forall\,(\{y\} \neq \{0\}) \in \Omega$
2°) $V(0) = 0$
3°) $\dot{V}(y) < 0 \qquad \forall\,(\{y\} \neq \{0\}) \in \Omega$
4°) $\dot{V}(0) = 0$

TABLEAU 2

Coordonnées du point d'équilibre	Valeurs propres de [B] correspondante	État du système
- 3.7453; - 2.1768 - 2.1768; - 0.9753	0.3969 ± (13.1469) i 19.5271; 28.0152	instable
- 0.1493; 0.2348 0.2348; - 0.1300	- 9.4396 ± 7.0468 i 6.6216; - 2.1857	instable
4.5416; - 2.6870 - 2.6870; - 1.6294	88.1529; - 15.6744 43.1915; 2.1882	instable
- 0.1356; 0.2335 0.2335; 0.0183	- 9.3513 ± 7.1676 i - 1.5816 ± 2.8100 i	stable
4.1859; - 0.5744 - 5744; - 0.7246	- 9.8756; 25.8373 17.1070; -2.2293	instable
6.7451; 0.5146 0.5146; 0.1650	42.4181; 12.9346 - 2.9032; 15.5440	instable
5.5900; 2.5961 2.5961; 1.0409	3.0514 ± 13.9298 i 21.2061; 29.0811	instable
- 4.2342; 2.3819 2.3819; 1.4867	71.6647; - 11.3714 38.8615; 2.0399	instable
- 0.1049; + 0.2308 0.2308; 0.3720	- 9.4436 ± 7.1138 i 13.1854; - 2.7719	instable

Chin [12] présente plusieurs méthodes qui ont été utilisées par les différents chercheurs pour générer la fonction de Lyapunov du système autonome (23), soit:

$$\{\dot{y}\} = [B]\{y\} + \{H(y)\} \qquad (27)$$

où [B] est une matrice stable.

Pour les besoins de notre travail on a utilisé une fonction quadratique de la forme:

$$V(y) = \{y\}^T [P] \{y\} \;;\; [P] \text{ symétrique} \qquad (28)$$

dont le domaine de stabilité correspondant est donné par:

$$\{y\}^T [P] \{y\} < V_m,\ V_m > 0 \qquad (29)$$

avec

$$V_m = (\min V(y) \text{ avec } \{y\} \in \Omega) \qquad (30)$$

et où

$$\Omega = (\{y\} \,/\, \dot{V}(y) = 0,\ \{y\} \neq 0) \qquad (31)$$

à cause de la symétrie de [P], on peut écrire:

$$\dot{V}(y) = \{\dot{y}\}^T [P] \{y\} + \{y\}^T [P] \{\dot{y}\} \qquad (32)$$

L'utilisation de (27) dans (32) permet d'écrire:

$$\dot{V}(y) = -\{y\}^T [Q] \{y\} + 2\{y\}^T [P] \{H(y)\} \qquad (33)$$

avec

$$[Q] = -\left([B]^T [P] + [P][B]\right) \qquad (34)$$

Donc pour [Q] donnée, le problème est réduit à trouver [P] en résolvant l'équation (34) puis à minimiser la fonction suivante:

$$\left.\begin{array}{l} \min \ V(y) \\ \text{avec} \\ \dot{V}(y) = 0 \end{array}\right\} \qquad (35)$$

La résolution de ce système contraint, par la méthode des multiplicateurs de Lagrange, nous permet de trouver l'estimé correspondant à [Q] du domaine de stabilité dont le volume est proportionnel à celui de l'hypersphère $\{y\}^T [P] \{y\} = V_m$, ce volume:

$$\text{VOL} = \pi \left(\frac{V_m^{\,n}}{\text{DET}(P)} \right)^{1/2} \qquad (36)$$

Donc pour optimiser le domaine Ω, il suffit de trouver la matrice [Q] qui donne le plus grand volume (36) tout en vérifiant le système (35).

5.3 Méthode de génération des matrices [Q]

Dans notre travail on a pris:

$$[Q] = [T][T]^T \qquad (37)$$

où [T] est une matrice triangulaire inférieure qu'on écrit sous la forme:

$$[T] = \begin{bmatrix} T_1 & 0 & 0 & 0 \\ T_5 & T_2 & 0 & 0 \\ T_8 & T_6 & T_3 & 0 \\ T_{10} & T_9 & T_7 & T_4 \end{bmatrix} \qquad (38)$$

On sait qu'il n'existe aucune méthode systématique pour générer de telles matrices [T], alors en partant de la matrice $[T_o] = [I]$ on a procédé de la façon suivante:

1°) On prend T_1 variable, et en gardant $T_j (j > 1)$ constants on recherche la meilleure valeur T_{01} de T_1 qui respecte le théorème II et qui maximise le volume donné par (36).

2°) En prenant $T_1 = T_{01}$ on fait varier T_2 tout en gardant $T_j (j > 2)$ constants, on calcule T_{02}, la meilleure valeur de T_2.

3°) On poursuit la procédure avec les autres éléments de [T] jusqu'à l'obtention de $[T_o]$, la matrice qui maximise le volume donné par (36).

4°) En prenant la matrice $[T_o]$ comme matrice initiale, on recommence les procédures de 1°) à 3°) pour essayer d'obtenir la matrice $[T_o]_{opt}$ qui maximise l'estimé du domaine Ω.

La recherche est arrêtée lorsqu'un passage de 1°) à 3°) n'arrive plus à améliorer le volume (36) davantage.

5.4 Résolution de l'équation matricielle de Lyapunov

Pour pouvoir calculer le volume donné par (36), il faut être capable de résoudre l'équation (34), appelée l'équation matricielle de Lyapunov. Plusieurs méthodes sont disponibles, Barnett et Storey [13]. Dans notre travail, on a préféré transformer cette équation en un système d'équations linéaires de la forme:

$$[A_K]\{PV\} = -\{QV\} \qquad (39)$$

avec

$$[A_K] = [B]^T \otimes [I] + [I] \otimes [B]^T \qquad (40)$$

où ⊗ dénote le produit de Kronecker.

et:

$$\{PV\} = \begin{Bmatrix} P(1,1) \\ \cdot \\ \cdot \\ P(1,n) \\ P(2,1) \\ \cdot \\ \cdot \\ P(2,n) \\ \cdot \\ \cdot \\ P(n,n) \end{Bmatrix} \quad \text{et} \quad \{QV\} = \begin{Bmatrix} Q(1,1) \\ \cdot \\ \cdot \\ Q(1,n) \\ Q(2,1) \\ \cdot \\ \cdot \\ Q(2,n) \\ \cdot \\ \cdot \\ Q(n,n) \end{Bmatrix} \qquad (41)$$

et trouver $[PV]$ sous la forme:

$$[PV] = -[A_K]^{-1}\,[QV] \qquad (42)$$

Le domaine de stabilité obtenu en suivant cette procédure est représenté sur la figure 4, dans l'espace $(Q_1, Q_2, \dot{Q}_4)$. La valeur de Q_4 est considérée constante et égale à la valeur correspondant au point stable du Tableau 2.

Vu la difficulté de représenter le domaine continu en entier, on a préféré représenter des coupes de ce dernier par différents plans parallèles au plan (Q_1, Q_2). Ces plans sont représentés par les différentes valeurs données à $\dot{Q}_4$.

6. CONCLUSION

L'objectif de cette étude était de déterminer les frontières du domaine de stabilité d'un véhicule articulé en fonction des données initiales. L'étude démontre l'existence d'un tel domaine. Des opérations d'intégration numériques ultérieures ont montré qu'il existait, à l'extérieur du domaine de la figure 4, d'autres points stables. Cette constatation nous permet d'affirmer la possibilité d'existence d'autres fonctions de Lyapunov qui donneraient une meilleure estimé du domaine de stabilité que celle utilisée ici. Donc, une étude exaustive des différentes familles de fonctions définies positives s'impose.

De plus, le choix d'un angle de bracage et d'une vitesse d'avances constantes représente une simplification qui peut être altérée par une intervention du conducteur. Cette intervention pourrait être bénéfique dans certaines situations, mais elle ne peut apporter aucune possibilité de correction dans des situations comme celle représentée sur la figure 3.

Finalement, l'optimisation du domaine de stabilité d'un véhicule, en fonction de la vitesse, des dimensions du véhicule, et de sa charge peut être une bonne solution d'avenir des problèmes de ces véhicules.

BIBLIOGRAPHIE

[1] Jindra, F., Tractor and Semi-Trailer Handling, Automobile Engineer, October 1963, pp. 438-446.

[2] Ellis, J.R., The Ride and Handling of Semi-Trailer Articulated Vehicles, Automobile Engineer, December 1966, pp. 523-529.

[3] Miculcik, E.C., Stability Criteria for Automobile-Trailer Combinations, Vehicle System Dynamics, Vol. 9, pp. 281-289, 1980.

[4] Eke, F.O. & Kane, T.R., A Nonliear Study of the Steady-State Turning Behavior of Car-Trailer System, SAE/SP-80/463, 1980.

[5] Eshleman, R.L. & Dsia, S.D., Articulated Vehicle Handling, IITRI Report, Chicago, 1972.

[6] Singh, M., Stability Bounds of Tractor-Semi-trailer, Vehicle System Dynamics, Vol. 9, pp. 69-86, 1980.

[7] Singh, M., On the Theory of Dynamic Stability of Motor Vehicle Carriers, Ph.D. Thesis, Wayne State University, Detroit, August 1978.

[8] Sach, H.K. & Chou, C.C., On the Stability in the Sense of Liapunov of a Rubber Tire Vehicle, Transactions of ASME, Journal of Dynamic Systems, Measurement and Control, June 1976, pp. 180-185.

[9] Ellis, J.R., Vehicle Dynamics, London Business Books Limited, 1969.

[10] Bronson, R., Theory and Problems of Differential equations, McGraw-Hill, 1973.

[11] Lasalle, J. & Lefschetz, S., Stability by Lyapunov's Direct Method with Applications, Academic Press, 1961.

[12] Chin, P.S.M., Generalized Integral Method to Derive Lyapunov Functions for Nonlinear Systems, International Journal of Control, Vol. 46, No. 3, pp. 933-943, 1987.

[13] Barnett, S. & Storey, C., Matrix Methods in Stability Theory, Thomas Nelson and Sons, 1970.

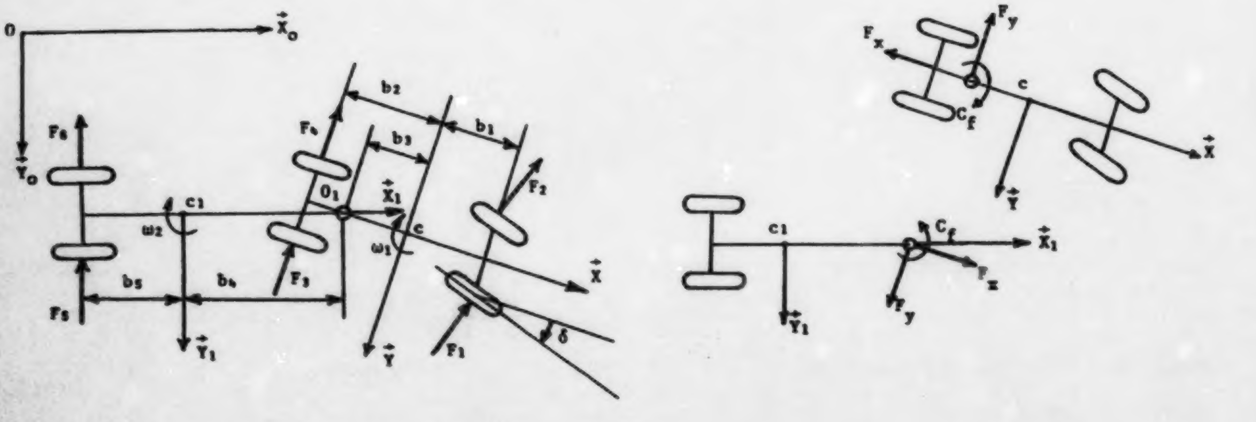

FIG. 1: REPRESENTATION SCHEMATIQUE DU VEHICULE

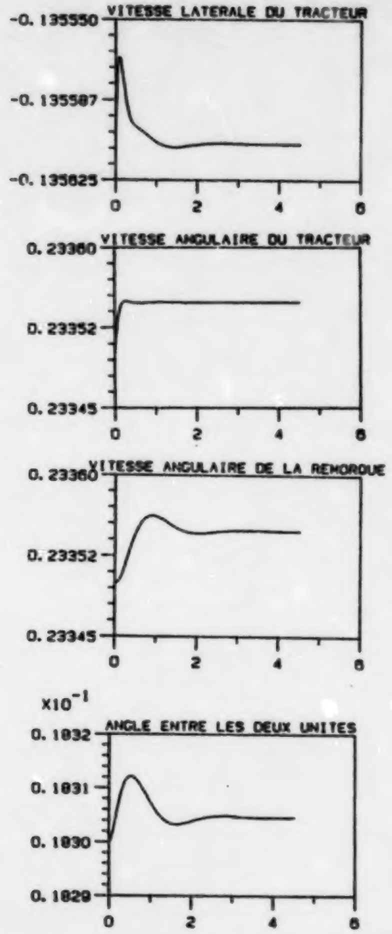

FIG. 2 : REPONSE STABLE DU VEHICULE A UNE FAIBLE PERTURBATION

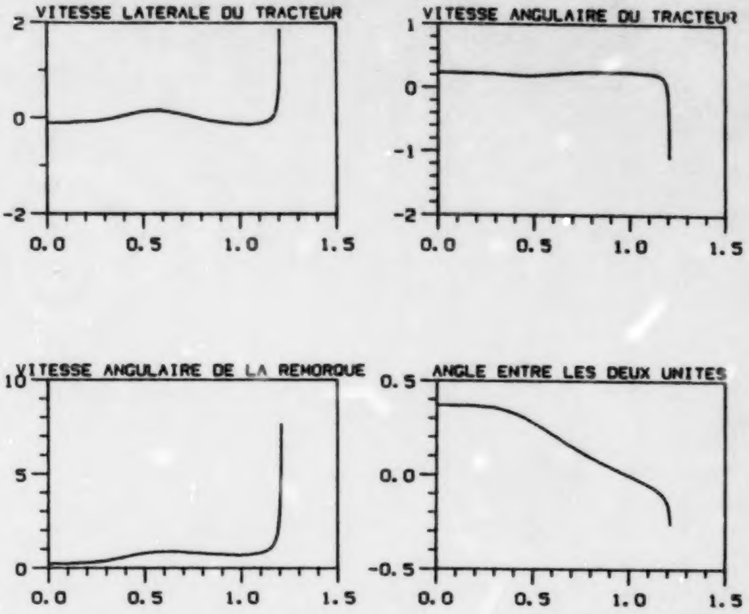

FIG. 3 : REPONSE INSTABLE DU VEHICULE A UNE FAIBLE PERTURBATION

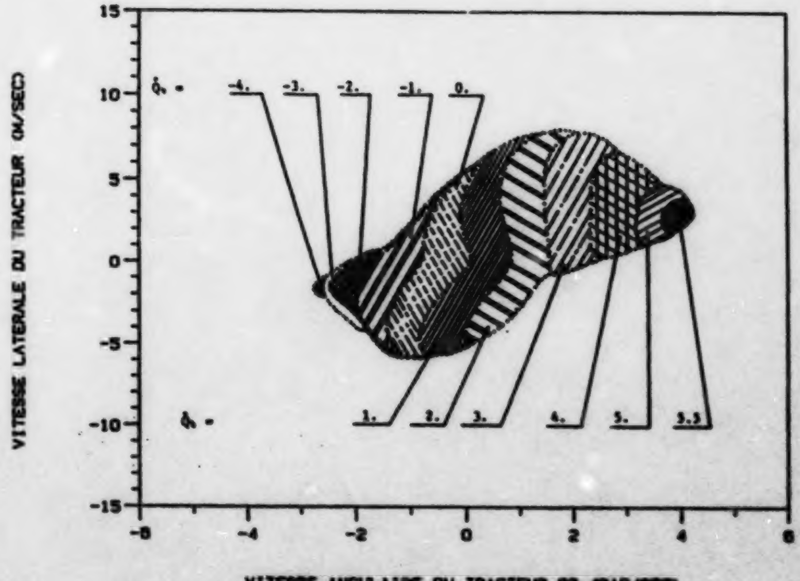

FIG. 4 : DOMAINE DE STABILITE DANS L'ESPACE (Q1, Q2, Q̇4)

DYNAMIC PERFORMANCE OF LOGGING TRUCKS

M. El-Gindy and J.H.F. Woodrooffe

Vehicle Dynamics Laboratory
National Research Council of Canada

ABSTRACT

This paper presents the results of a study of rollover and directional stability of four selected log-hauling truck configurations, namely, tractor/pole trailer; tractor-jeep/pole trailer; tractor/triaxle trailer; and tractor/quadaxle trailer. The effects on vehicle performance of standard-width (2.44 m) tandem-axle 6.7 m wheelbase tractor and extended-width (2.59 m) tridem-axle 6.0 m wheelbase tractor with air lift pusher-axle have been examined. Because of the unique design features of these vehicles it was necessary to develop three new linear yaw plane mathematical models to predict their directional behaviour in both the time and frequency domains. The vehicle's static rollover behaviour was analyzed with UMTRI's Static Roll Model. The vehicle congfigurations examined in this study have been evaluated against the performance criteria of rollover threshold, transient response time, understeer coefficient, high speed offtracking, and rearward amplification.

INTRODUCTION

The logging industry must often transport long payloads (logs) through sharply curved, narrow, offroad paths as well as on highways. To meet these requirements, special types of articulated vehicles have been developed in various parts of Canada and the United States. These types of vehicles consist of standard highway tri-axle tractors (6.7 m wheelbase) and one or more articulated units (jeep, pole, tri-axle or quadaxle trailers). The load acts as a link joining the tractor or a jeep at a turntable (or fifth wheel) to the trailer at its turntable. These vehicle configurations have certain unique design features, i.e. not seen on conventional highway commercial articulated heavy vehicles.

Recent demands to increase the productivity of logging vehicles have raised interest in making use of tridem-axle tractors in place of the conventional tandem-axle tractors. Although tridem tractors would clearly give an advantage of higher payloads, there were concerns about the possible degradation they could cause to the rollover threshold and directional stability of the overall vehicle. This subject was of considerable interest to the National Research Council because of the complexity of the vehicles from a modelling point of view, that would require detailed and high level analysis. At the request of the Forest Engineering Research Institute of Canada (FERIC), the Vehicle Dynamics Laboratory of NRC has analytically examined the influence on rollover threshold and directional dynamics of using an extended-width (2.59 m) 6.0 m wheelbase tridem-axle tractor with a pusher-axle, in both the lowered and raised positions, in place of the conventional standard-width (2.44 m) 6.7 m tandem-axle tractor. Due to the vehicles' unique design features, it was necessary to develop three new linear yaw plane mathematical models [1] to examine the time histories and the frequency responses of these vehicles. These new computer simulation models permit the examining of different tractor configurations in various ways [1,2].

Because of the logging vehicles' unique design features, geometrical analysis of various vehicle configurations has been developed. This geometrical analysis was fundamentally important from the standpoint of solving the equations of motion developed in this study to represent the proposed tridem vehicle configurations. The major differences between these vehicles and the conventional commercial articulated vehicles are:

1. The number of the articulated points is equal to the number of vehicle elements, while in the case of the conventional vehicles of n articulated units the number of the articulation points is n - 1.

2. Due to the increased number of articulation points, one of the articulated vehicle units (usually the trailer or dolly) must have a variable length drawbar usually achieved by a sliding action.

The objectives of this study are to assess and compare the effect of 6.7 m and 6.0 m wheelbase tandem-axle and tridem-axle tractors on the roll and directional stability of four selected log hauling truck configurations, namely, tractor/pole trailer; tractor-jeep/pole trailer; tractor/triaxle trailer; and tractor/quadaxle trailer.

To achieve the objectives of this study, the following analytical methods have been performed [1].

- Geometrical analysis.
- Static rollover threshold analysis.
- Time histories of yaw plane response to steering input.
- Frequency response analysis.

COMPUTER SIMULATION MODELS

This section outlines the computer simulation models developed or adopted to predict the directional behaviour and rollover threshold of various vehicle configurations.

Static Roll Model

The static roll model [3,4,5] was developed by the Univeristy of Michigan's Transportation Research Institute (UMTRI) for calculating the rollover threshold of articulated vehicles during steady turning manoeuvres. The basic assumptions and features of this model are:

1. The roll angles of the sprung mass and axles are small, such that the small angle assumptions $\sin \alpha = \alpha$ and $\cos \alpha = 1.0$ hold.

2. The articulated angles are small, such that the influence of the articulation angle on roll response can be neglected.

3. The total vertical load carried by each composite axle is assumed to remain constant during the rollover process. In order to accommodate any pitching motion that might take place during rollover, the sprung masses are permitted to take up different vertical deflections at each of the three axle locations.

The model contains a fairly detailed description of suspension and tire properties (such as vertical, lateral and overturning stiffness), such that an accurate prediction of the steady-turning rollover threshold is possible. A single computer run is sufficient to compute the roll response of the vehicle over the entire range of lateral acceleration levels up to the rollover threshold.

New NRC Yaw Plane Computer Simulation Models

Three new linear yaw plane mathematical models have been developed in this study for determining the directional behaviour of the proposed log hauling and conventional commercial vehicles. Computer programs based on these models were then developed using UMTRI's subroutines library. These programs are used for studying the following aspects of a vehicle's directional stability and performance:

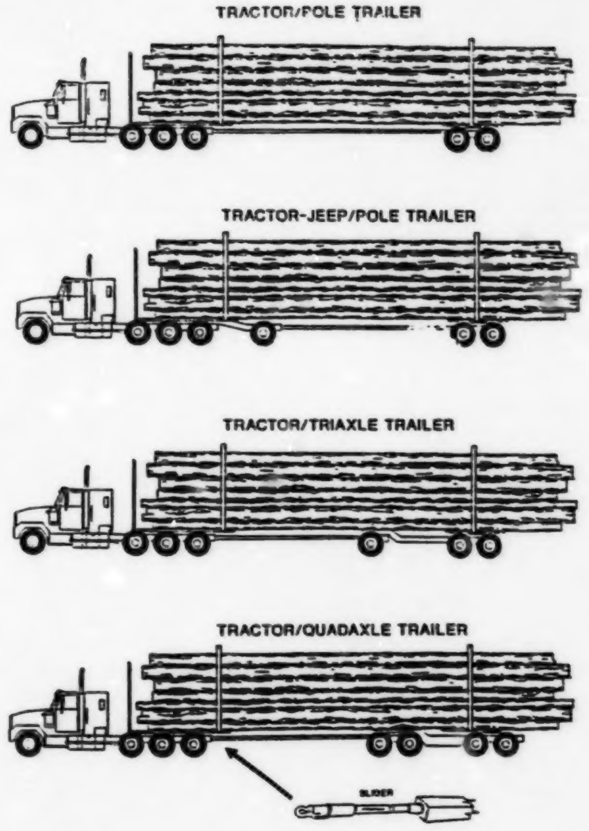

Fig. 1 Vehicle configurations

1. Transient and steady-state turning response of each of the vehicle's elements to steering input (time histories analysis).

2. Frequency response of the vehicle, i.e. its directional response to sinusoidal steer inputs over a range of steering frequencies.

The new mathematical models are designed for the analysis of the following vehicle configurations (see Fig. 1).

- Tractor-pole trailer
- Tractor-jeep/pole trailer
- Tractor/triaxle (quadaxle) trailer

The models permit the analysis of a tractor or truck with up to four axles. One of the models' features is their ability to handle (forced) steering on any of the vehicle's tridem group axles [1,2].

In the models' equations of motion, the roll dynamics of the vehicle are not taken into account and the vehicle is assumed to travel at constant forward speed. The degrees of freedom permitted in the models are therefore limited to lateral and yawing motion of tractor and the following articulated units, all in a horizontal plane.

METHOD OF EVALUATION

The evaluation of the vehicles' rollover and directional dynamics will be based on five selected performance criteria. For each criterion a suggested preliminary value will represent the expected safe limit. These criteria are used in various places throughout the balance of this report, and are defined as follows:

1. Rollover Threshold

The definition of this criterion is: The lateral acceleration level achieved just prior to one group of composite axles on one side of the vehicle completely lifting off the ground (observed minimum value is 0.25 g).

2. Transient Response Time

The definition of this criterion is: The time required to reach 90% of the vehicle's steady-state lateral acceleration at highway speed (90 km/h) resulting from a rapid ramp-step steering input of maximum 1 degree and a steering rate of 5 deg/sec. The acceptable range of the response time is dependent upon personal and external factors affecting the driver. (Suggested range is from 0.3 to 1.7 sec.)

3. Understeer Coefficient

The definition of this criterion is: The dividend of (wheelbase/turn radius - front wheel steer angle) divided by (steady-state lateral acceleration) at the tractor centre of gravity. Negative values indicate understeering and positive values indicate oversteering characteristics. The values are not dependent on the lateral acceleration level due to the linearization of the yaw plane models. The values are valid for low level lateral acceleration (less than 0.2 g). (Suggested range is from -0.4 to zero.)

4. Highspeed Offtracking Indicator

The definition of this criterion is: The dividend of the articulation angle or sum of articulation angles of the joined vehicle units divided by the dimensionless path curvature of the tractor (path curvature - wheelbase/steady state turning radius) at speed of 90 km/h and front wheel steer angle of 1 degree. (Suggested range is from zero to 2.5 deg.)

5. Rearward Amplification

The definition of this criterion is: The ratio between the peaks of the lateral acceleration of the payload centre of gravity and the tractor centre of gravity during sinusoidal steering manoeuvres. (Suggested range is from 1 (or less) to 2.)

Presented in the next section are the results obtained from the NRC yaw plane computer simulation programs developed in this study for predicting the directional response to steering input for 12 vehicle configurations with tandem-axle and tridem-axle tractors.

RESULTS

Rollover Threshold

Fig. 2 shows the predicted rollover threshold of tractor/pole trailer, tractor/triaxle trailer and tractor/quadaxle trailer with standard-width (2.44 m) 6.7 m tandem-axle tractor and extended-width (2.59 m) 6.0 tridem-axle tractor equipped with an air lift pusher-axle in both the lowered and raised positions. It can be noted that:

1. For the tractor/pole trailer configuration, the extended-width vehicle (2.59 m width across tires) with a pusher-axle down (P. Down) and a 6.0 m wheelbase tractor shows a slighly better rollover threshold than the standard-width vehicle (2.44 m) with a 6.7 m wheelbase tandem-axle tractor. However, the rollover threshold is noticeably worse (reduced by 10.3%) when the pusher-axle of the tridem-axle 6.0 m tractor is lifted (P. Up), which is often done to improve the tractive effort (by placing more load on the drive tandem axles).
2. The tractor/triaxle trailer configurations show a lower rollover threshold than that of the tractor/pole trailer. The tractor/quadaxle configurations show a lower rollover threshold than that of the tractor/triaxle trailer configurations. The primary reason for the reduction of the rollover threshold is the increased payload weight, hence the raised payload centre of gravity height, with the overall vehicle width, track, and suspension spread remaining the same for both the standard-width and extended-width vehicles. The lowest rollover threshold (unacceptably low at less than 0.25 g) is shown by the standard-width 6.7 m tandem-axle tractor/quadaxle trailer. The rollover threshold of this vehicle can be improved when the extended-width 6.0 m

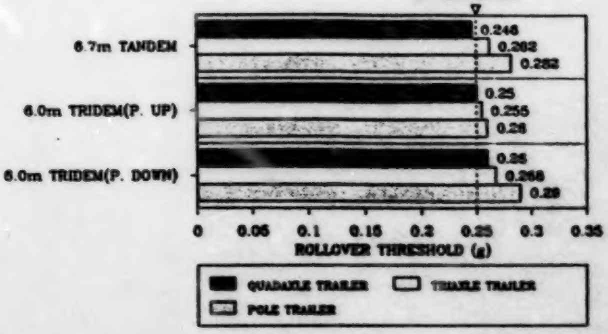

Fig. 2 Influence of tractor type on rollover threshold

tridem-axle tractor is used with its pusher-axle down.

The study of the rollover threshold of various vehicle configurations reveals that:

1. The overall width of log-hauling vehicles that incorporate a standard-width (2.44 m) 6.7 m tandem-axle tractor should be extended from 96 in (2.44 m) to 102 in (2.59 m) in order to improve their rollover stability.

2. The extended-width 6.0 m tridem-axle tractor exhibits satisfactory rollover stability with the pole trailer and the triaxle trailer but not with the quadaxle trailer.

Transient Response Time

Fig. 3 shows the calculated transient response time for various vehicle configurations. It can be noted that:

1. The increased number of axles of the tractor/quadaxle trailer and its high weight and yaw moments of inertia cause the transient response time to be higher than the other vehicle configurations in all cases. The largest response time (above the acceptable limit of 1.7 sec) occurs with the 6.7 m tandem-axle tractor/quadaxle trailer, largely because of the vehicle's high equivalent damping level in the plane of motion.

2. The transient response time is lowest for the tractor-jeep/pole trailer. This indicates quick response during rapid steering manoeuvres, which implies that drivers must be careful and sensitive when steering this vehicle in severe manoeuvres.

3. Lifting the pusher-axle of the 6.0 m tridem-axle tractor does not significantly influence the response time.

In general, the tractor/quadaxle trailer response time can be improved, i.e. reduced to an acceptable level by replacing the 6.7 m tandem-axle tractor with the 6.0 m tridem axle tractor. (The pusher-axle may be lowered or raised.)

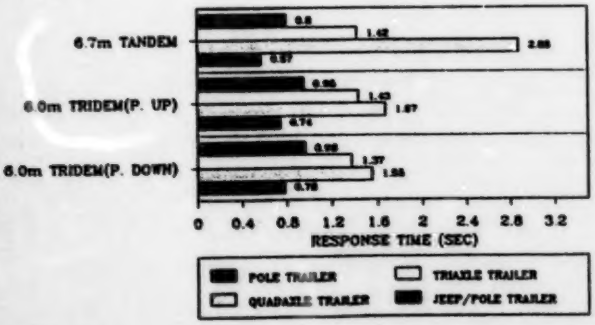

Fig. 3 Influence of tractor type on the transient response time

Understeer Coefficient

Fig. 4 shows the calculated understeer coefficients for various vehicle configurations. It can be noted that:

1. The understeer level of the 6.0 m tridem-axle tractor-jeep/pole trailer is, regardless of whether its pusher-axle is in the lowered or raised position, much higher than that of the 6.7 m tandem-axle tractor.

2. All other vehicles exhibit reasonable understeering levels (i.e. higher than -4.0 deg) except for the 6.7 m tandem-axle tractor/quadaxle trailer which shows slight oversteering characteristics (0.29 deg).

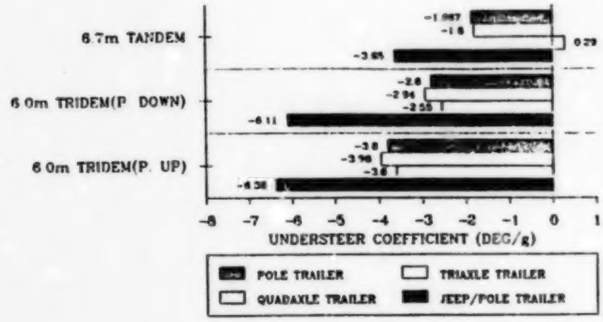

Fig. 4 Influence of tractor type on the understeer coefficient

These results show some cause for concern about using a 6.0 m tridem-axle tractor with the jeep/pole trailer because of its high understeering level; they support the previous concern about the 6.7 m tandem-axle/quadaxle trailer due to its over-steering.

Highspeed Offtracking

Fig. 5 shows the predicted offtracking indicator for various vehicle configurations. It can be noted that:

1. The highspeed offtracking is highly related to the vehicle's understeer level. However, vehicles with a high understeer level, namely, the tractor-jeep/pole trailer configurations, show low offtracking; while vehicles with a low understeer level (or even oversteering) namely, the tractor/quadaxle trailers, show the highest values of offtracking.

2. Tractor/pole trailer and tractor/triaxle trailer configurations show reasonable offtracking levels connected to the tandem-axle 6.7 m standard-width tractor and the tridem-axle 6.0 m extended-width tractor, with the pusher-axle in either the raised or lowered position.

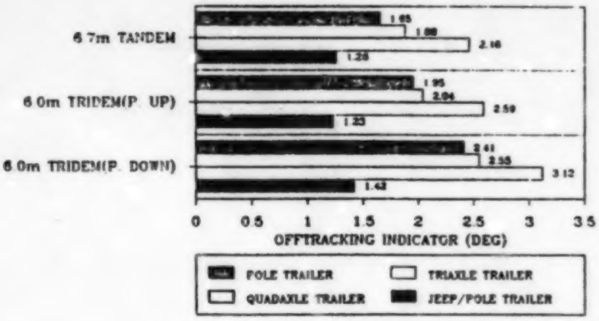

Fig. 5 Influence of tractor type on the high speed offtracking

Rearward Amplification

Fig. 6 shows the peak lateral acceleration rearward amplification at the payload centre of gravity for various vehicle configurations. These results were obtained from the "frequency response method". It can be noted that

1. The highest rearward amplifications are shown by the tractor-jeep/pole trailer configurations, mainly because the front bunk's turntable is located on the jeep with considerable distance between it and the tractor/jeep joint. In the cases of other vehicle configurations, the front bunk's turntable is directly located on the tractor frame, which results in lower rearward amplification at their payload centres of gravity.

2. The lowest rearward amplifications are obtained from tractor/pole trailer configurations, owing to a relatively shorter distance between the tractor's centre of gravity and the payload's centre of gravity.

In general, the vehicle configurations with standard-width or extended-width tractors show reasonable rearward amplifications, i.e. less than 2.

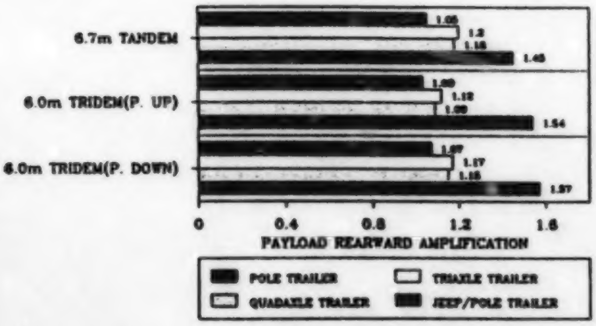

Fig. 6 Influence of tractor type on the payload rearward amplification

CONCLUSIONS

1. The log-hauling trucks examined in this study exhibit low rollover thresholds due to their high payload centres of gravity. This unwanted tendency can be overcome to some extent by increasing the vehicles' overall width without increasing the payload weight and adding extra axles, for example, by replacing the tandem-axle tractor with a tridem-axle tractor.

2. The general performance of the tractor/pole trailer and tractor/triaxle trailer vehicle configurations are acceptable, and are safer than the tractor/quadaxle trailer and tractor-jeep/pole trailer configurations.

3. Using an extended-width 6.0 m tridem-axle tractor with an air lift pusher-axle (to allow a higher payload) can provide a vehicle with directional behaviour very close to that of vehicles using a 6.7 m tandem-axle tractor when the configuration is either that of a tractor/pole trailer or tractor/quadaxle trailer. At the same time, using a 6.0 m tractor in a tractor-jeep/pole-trailer or tractor/quadaxle trailer configuration can result in degrading their overall performance.

REFERENCES

1. El-Gindy, M. and Woodrooffe, J.H.F., Study of Rollover Threshold and Directional Stability of Log Hauling Trucks, NRC Technical Report, TR-VDL-002, January 1990.

2. El-Gindy, M., Directional Behaviour of a Log-Hauling Truck with a Tridem-axle Tractor, CSME Mechanical Engineering Forum 1990.

3. Winkler, C.D., Mallikarjunarao, C. and MacAdam, C.C. Analytical Test Plan: Part I - Description of Simulation Models, Parametric Analysis of Heavy Truck Dynamic Stability, The University of Michigan Transportation Research Institute, April, 1981.

4. Wong, J.Y. and El-Gindy, M. Computer Simulation of Heavy Vehicle Dynamic Behaviour. User's Guide to the UMTRI Models, Technical Report No. 3, Vehicle Weights and Dimensions Study, Roads and Transportation Association of Canada, June 1985.

5. El-Gindy, M. and Hosamel-deen, Y.H. Sensitivity Parametric Analysis of UMTRI Static Roll Model. Int. J. of Vehicle Design, Vol. 10, No. 2, pp. 187-209, 1989.

FREE VIBRATION ANALYSIS OF SIMPLY SUPPORTED RECTANGULAR PLATES WITH INTERNAL POINT SUPPORTS

D.J. Gorman and H.L. Ohman

Department of Mechanical Engineering
University of Ottawa, Ottawa, Canada K1N 6N5

ABSTRACT

An interest in the free vibration frequencies and mode shapes of rectangular plates resting on point supports has arisen in connection with design of electronic circuit boards, solar panels, and other industrial problems. In this paper the problem of a rectangular plate with simple support on the edges and arbitrarily located rigid point supports on the lateral surfaces is investigated. It is shown how highly accurate analytical type solutions are obtained for this family of problems. It is also shown how the analysis may be slightly modified in order to take care of the effects of local added masses.

NOMENCLATURE

a,b	plate edge lengths
D	plate flexual rigidity
M	attached local mass
M_r	ratio of attached mass to mass of plate
P	harmonic concentrated driving force
P^*	dimensionless concentrated driving force $= -2Pb^3/Da^2$
u,v	dimensionless co-ordinates of driving force
u^*	=1-u
v^*	=1-v
W	plate lateral displacement
x,y	co-ordinates along plate
ξ, η	dimensionless co-ordinates, $\xi = x/a$, $\eta = y/b$
ϕ	plate aspect ratio = b/a
λ^2	eigenvalue $(= \omega a^2 \sqrt{\rho/D})$
ω	circular frequency of vibration
ρ	mass of plate per unit area

INTRODUCTION

A growing interest in the establishment of free vibration frequencies and mode shapes of rectangular plates, with various edge conditions and internal point supports, has developed in connection with the vibration analysis of solar collector panels and electronic circuit boards. In both cases it is desired to arrange the point supports so as to shift plate natural frequencies out of the range of frequencies where harmonic excitation is anticipated. Failure to achieve this can result in highly undesirable vibration of electric components attached to the circuit boards and in all cases a serious shortening of the fatigue life of the plate assembly.

In this paper the effect of arbitrarily distributed "rigid" point supports on the free vibration frequencies and mode shapes of simply supported rectangular plates is investigated. Since, as will be shown, it is very easy to extend the anlysis to also take into account the effects on vibration of concentrated masses attached to the plate, this extension of the analysis is described as well.

The term " rigid" point support refers to support at a point, of the type usually provided by screw type fastener, or local welds. Such support, in this paper, is modelled mathematically by utilizing a local cluster of four discrete point supports. Each discrete point support forbids plate lateral motion at its point of application. It does not itself, however, oppose rotation of the plate and imparts no moment to it. To achieve "rigid" point support of the type provided by fastening screws and washers, 4 discrete point supports are utilized, one at each end of mutualy perpendicular diameters running across the surface of the washer to be simulated and parallel to the edges of the plate. While each discrete point support prohibits plate lateral displacement, only, the combination of the pairs of supports prohibits rotation of the plate in ether of the above mentioned two directions. It is found that excellent simulation of screw fastener support, or local spot weld support, is thereby achieved.

The objective of this paper is to give a concise and clear description of the mathematical procedure employed and to present the results of some representative frequency and mode shape studies.

MATHEMATICAL PROCEDURE

We begin by reviewing briefly the solution for steady state vibration of a rectangular plate with simple support along all edges and driven by a concentrated harmonic force acting on its lateral surface. Such a plate is represented schematically in Fig.1. The first solution to this problem was described by Nowacki [1]. Here, reference will be made to the solution as presented in Ref.[2].

The plate is considered to be divided into two rectangular portions by the solid line running through the point of application of the harmonic force (Fig.1). The amplitude of vibration of the upper and lower segments of the plate are represented by the functions $W_1(\xi,\eta)$ and $W_2(\xi,\eta)$, respectively. It is known that a solution for the function $W_1(\xi,\eta)$ can be written in the form proposed by *Lévy* as

$$W_1(\xi,\eta) = \sum_{m=1}^{\infty} Y_m(\eta) \sin m\pi\xi \tag{1}$$

Furthermore, because of the boundary conditions it follows that $Y_m(\eta)$ can be written as,

$$Y_m(\eta) = A_m \sinh \beta_m \eta + B_m \sin \gamma_m \eta$$

or (2)

$$Y_m(\eta) = A_m \sinh \beta_m \eta + B_m \sinh \gamma_m \eta$$

where, $\beta_m = \phi\sqrt{\lambda^2 + (m\pi)^2}$, $\gamma_m = \phi\sqrt{\lambda^2 - (m\pi)^2}$, or $\gamma_m = \phi\sqrt{(m\pi)^2 - \lambda^2}$, whichever is real. The first expression of Eqn.(2) is utilized if $\lambda^2 > (m\pi)^2$. Here λ^2 is the dimensionless frequency (eigenvalue) as defined in the Nomenclature. A_m and B_m are constants to be determined. A solution similar to that of Eqns. (1) and (2), involving the constants C_m and D_m, is written for the function $W_2(\xi,\eta)$.

In order to obtain the response of the plate to the concentrated harmonic excitation force it is necessary to solve for the unknown constants above. For any value of m, four sets of equations can be written involving the four unknown constants. These equations are performed through the enforcement of continuity across the common boundary separating the two plate segments. Three of these equations involve enforcement of continuity of, displacement, slope and bending moment at the boundary. A fourth arises because of the need to enforce the condition of dynamic equilibrium at the interface of segments. To achieve this we represent the amplitude of driving force by the Dirac Delta function. This function in turn, is expanded in a sine series as utilized in Eqn.(1), it is required that each term in this distributed driving force must be in equilibrium with the vertical edge reactions at the boundaries of the two plate segments.

With the four equations, as discussed above, available the unkown coefficients, and hence the plate response, can be written as a function of the amplitude of the excitation force and the dimensionless frequency (eigenvalue) λ^2. Expressions for the coefficients A_m,B_m etc., are reproduced here for convenience [2]. They are, for $\lambda^2 > (m\pi)^2$

$$A_m = \frac{P^* \sin m\pi u \sinh \beta_m v^*}{(\beta_m^2 + \gamma_m^2)\beta_m \sinh \beta_m}$$

$$B_m = \frac{-P^* \sin m\pi u \sin \gamma_m v^*}{(\beta_m^2 + \gamma_m^2)\gamma_m \sin \gamma_m}$$

$$C_m = \frac{P^* \sin m\pi u \sinh \beta_m v}{(\beta_m^2 + \gamma_m^2)\beta_m \sinh \beta_m}$$

$$D_m = \frac{-P^* \sin m\pi u \sin \gamma_m v}{(\beta_m^2 + \gamma_m^2)\gamma_m \sin \gamma_m}$$

and, for $\lambda^2 < (m\pi)^2$

$$A_m = \frac{P^* \sin m\pi u \sinh \beta_m v^*}{(\beta_m^2 - \gamma_m^2)\beta_m \sinh \beta_m}$$

$$B_m = \frac{-P^* \sin m\pi u \sinh \gamma_m v^*}{(\beta_m^2 - \gamma_m^2)\gamma_m \sinh \gamma_m}$$

$$C_m = \frac{P^* \sin m\pi u \sinh \beta_m v}{(\beta_m^2 - \gamma_m^2)\beta_m \sinh \beta_m}$$

$$D_m = \frac{-P^* \sin m\pi u \sinh \gamma_m v}{(\beta_m^2 - \gamma_m^2)\gamma_m \sinh \gamma_m}$$

where all symbols are as defined in the Nomenclature.

With solution available for the rectangular plate driven by a harmonic concentrated force, we are in a position to investigate problems related to "rigid"-point supported plates. Let us suppose we wish to analyse the free vibration of simply supported plate with rigid point support at four chosen locations as indicated in Fig.2. To achieve this end we require 16 separate solutions of type discussed above, each with a driving concentrated harmonic force at one of the discrete point support locations indicated in the Figure. In the analytical procedure employed all 16 of these solutions are superimposed, one-upon-the-other. Because of the linearity of the problem superposition of these solutions is mathematically legitimate.

Free vibration eigenvalues of the plate are obtained by establishing those values of the parameters λ^2 which permits a nontrivial solution for the driving force amplitudes P_1^*, P_2^*, ..., etc., subject to the condition that net displacement of the superimposed solutions equals zero at the location of each of the 16 discrete driving force locations. To achieve this end we construct an eigenvalue matrix of the type shown schematically in Fig. 3. In this schematic representation we consider a superposition of five individual solutions, only, in the interest of conserving space.

The symbols δ_1, δ_2, etc., in the Figure, symbolize the net displacement at driven point 1, 2, etc., on the plate. Each element in the first row of the matrix, when multiplied by the force amplitude P^* immediately above it, represents the contribution of that particular driven plate solution to net plate displacement at the driven point 1. In fact, the i, j element represents the contribution to driven point i, of the solution pertaining to a plate driven at point j. The 5 x 5 schematic matrix represents, therefore, a set of five simultaneous algebraic equations relating the driving amplitudes P_1^*, P_2^*, etc.

It will be appreciated that an eigenvalue matrix of this type is easily generated on a digital computer once the coordinates of the driven points are prescribed. The values, u,v, u^* and v^*, will be different for each force-driven solution. They will be determined once the driving points are specified.

Computation of Eigenvalues and Mode Shapes

Returning briefly to the simply supported plate of Fig.2 it is seen that 16 x 16 matrix would be required to analyse its free vibration motion. Eigenvalues are obtained by following established procedures. A trial value is selected for the parameter λ^2, well below the first mode eigenvalue. The matrix associated with this trial value is generated. The determinant of the matrix is computed and stored. The value of λ^2 is augmented, and the procedure repeated until the determinant undergoes a change in sign. The eigenvalue, the value of λ^2 for which the determinant vanishes, is then obtained by standard means. Following obtaining of the first (fundamental) eigenvalues the procedure is repeated in order to obtain the desired higher eigenvalues.

In order to obtain mode shapes, one of the driving force amplitudes, P^* is set equal to unity. A solution for the remaining driving force amplitudes is then obtained from the set of simultaneous algebraic equations. With this information available, the mode shape, comprised of sum of all the force driven solutions can be obtained and plotted.

Matrix Modifications Required to Handle Attached Masses

Consider the simply supported plate of Fig.4 with a localized mass M attached at the dimensionless co-ordinates u, and v. This mass will exert a harmonic inertia force on the plate which opposes motion and whose amplitude equals $M\omega^2 aW(u,v)$, where, $W(u,v)$ is the net plate dimensionless displacement at the co-ordinates u, v. It is easily shown that so far as the plate is concerned it experiences a local harmonic force acting in the direction of displacementof the plate and with dimensionless amplitude

$$P^* = -2\phi^4 M_r \lambda^4 W(u,v) \tag{3}$$

Denoting the contributions to displacement at the point u, v, due to the driving forces, P_1^*, P_2^*, etc., associated with the discrete point supports as $P_1^* W_1(u,v)$, $P_2^* W_2(u,v)$, etc., it follows from Eqn. (3) that we may write

$$P^*Q = P_1^* W_1(u,v) + P_2^* W_2(u,v) + ... + P^* W_M(u,v) \tag{4}$$

where the last term relates to dispalcement related to inertia force associated with the added mass, only, and

$$Q = \frac{-1}{2\phi^4 M_R \lambda^4} \tag{5}$$

Eqn.(4) may be rewritten as,

$$P_1^* W_1(u,v) + P_2^* W_2(u,v) + ... + P^* \{W_M(u,v) - Q\} = 0 \tag{6}$$

Examination of Eqn.(6) reveals how to prepare eigenvalue matrices when, in addition to discrete point supports acting on the plate, we have local attached masses. We should begin by considering all locations of discrete point supports and attached masses as though they were locations of discrete point supports. Let us say the N'th location of interest is, in fact, the location of an attached mass. We should then return to the element N.N. of the matrix and modify it as indicated in Eqn.(6), i.e., we should subtract from this element the appropriate quantity Q.

PRESENTATION OF RESULTS

The free vibration behaviour of two simply supported rectangular plates of aspect ratio 1.5 was studied. The first plate, designated plate " A", was given rigid point support at four symmetrically distributed locations lying on the plate diagonals and dimensionless distance U from the ends of plate. Plate "B" was also given rigid point support at four symmetrically distributed locations but these locations always lay along two lines running parallel to the long edges of the plate and one quarter of the length in from these edges. They also were located dimensionless distance u from the short edges of the plate.

Traces of the first four eigenvalues vs. dimensionaless distance u are presented in Figure 5 and 6 for the above two plates. It is seen that in each case the eigenvalues are very sensitive to support location. In each case the lowest eigenvalue is seen to peak at values of U equal to about 0.32. This observation will be of interest to designers who wish to keep the fundamental mode frequency as high as possible. It is observed here, as well as in almost all other calculations carried out , that there is considerable crossing over of mode lines beyond values of U equal to about 0.25.

First four eigenvalues for plate A and B are tabulated in Tables 1 and 2 for various values of the parameter u.

Three dimension mode shape plots for plates A and B are presented in Figure 7. These plots correspond to eigenvalues taken from Tables 1, and 2, respectively. These mode shapes permit the designer to establish the high acceleration regions of any plate for any mode. Circuit board designers will wish to place delicate electronic gear in locations where these high accelerations can be avoided.

SUMMARY

By superimposing the basic solutions for a simply supported rectangular plate driven by a harmonic concentrated force it has been possible to perform a highly accurate free vibration analysis of the same type of plate given rigid point support at numerous arbitrary locations. It is shown how the analysis is easily modified to take care of additional attached masses. It is believed that the analytical technique described here will play a valuable role in the design of certain electronic circuit boards, solar panels, and other industrial design problems. The mathematical model is simple in nature and highly accurate analytical type results are readily achievable.

REFERENCES

1. Nowacki, W., *Dynamics of Elastic Systems*, Chapman and Hall, London, 1963.
2. D.J. Gorman *Free Vibration Analysis of Rectangular Plates*, New York: Elsevier/North Holland Inc., 1982.

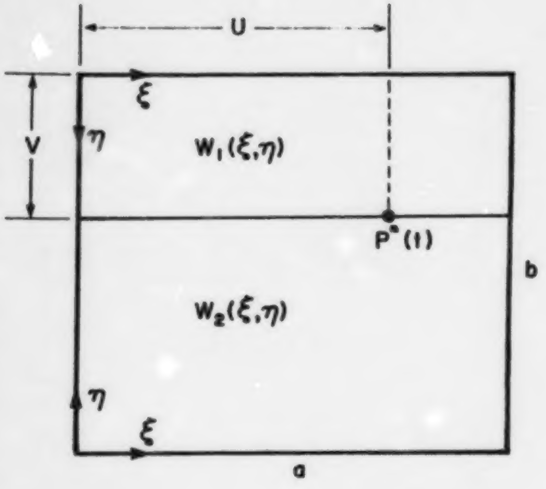
U
V
ξ
η
$W_1(\xi,\eta)$
$P^*(t)$
b
$W_2(\xi,\eta)$
η
ξ
a

Fig. 1 SIMPLY SUPPORTED RECTANGULAR PLATE DRIVEN BY CONCENTRATED HARMONIC DRIVING FORCE $P^*(t)$.

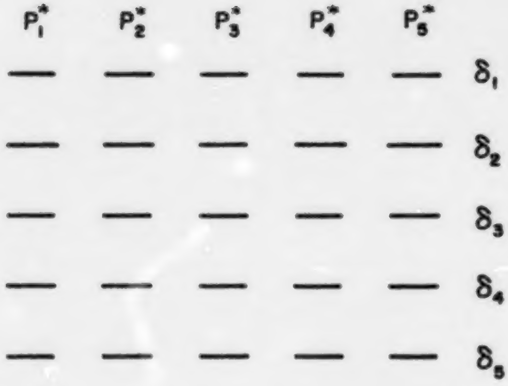
P_1^*
P_2^*
P_3^*
P_4^*
P_5^*
δ_1
δ_2
δ_3
δ_4
δ_5

Fig. 3 SCHEMATIC REPRESENTATION OF FIVE - BY - FIVE EIGENVALUE MATRIX.

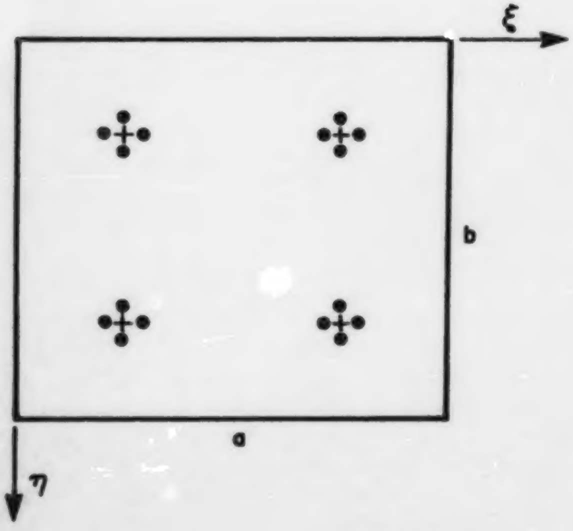

Fig. 2 SIMPLY SUPPORTED RECTANGULAR PLATE WITH FOUR RIGID POINT SUPPORTS. DISCRETE POINT SUPPORTS ARE INDICATED BY SOLID DOTS.

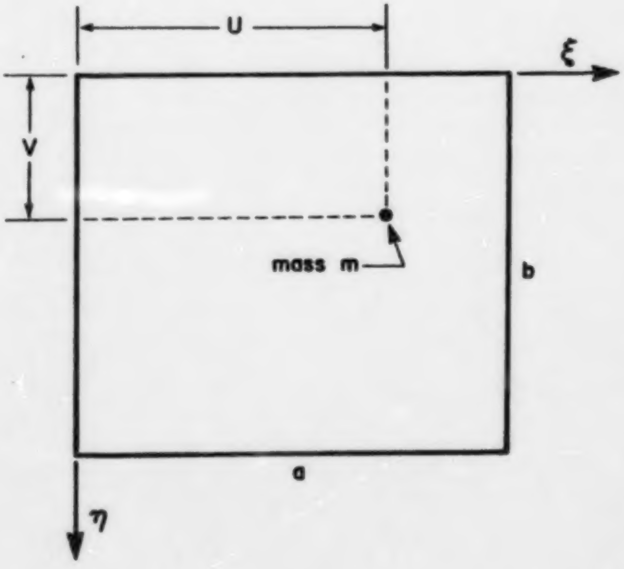
U
ξ
V
mass m
b
a
η

Fig. 4 SIMPLY SUPPORTED RECTANGULAR PLATE WITH LOCAL MASS m ATTACHED.

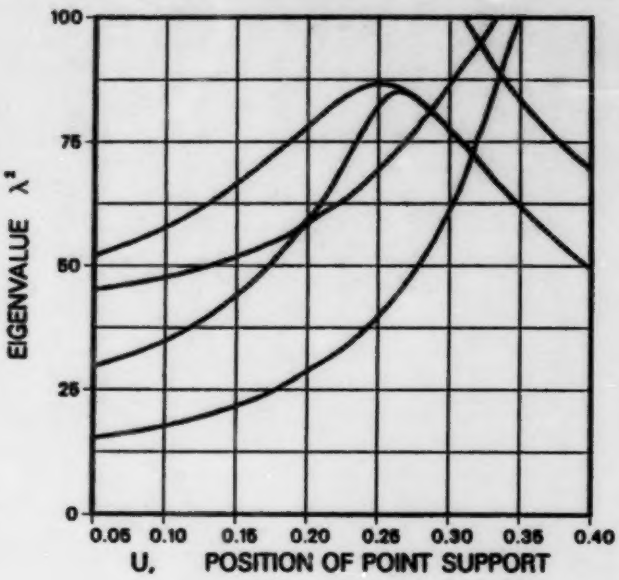

Fig. 5 FIRST FOUR EIGENVALUES vs. SUPPORT POSITION FOR PLATE "A".

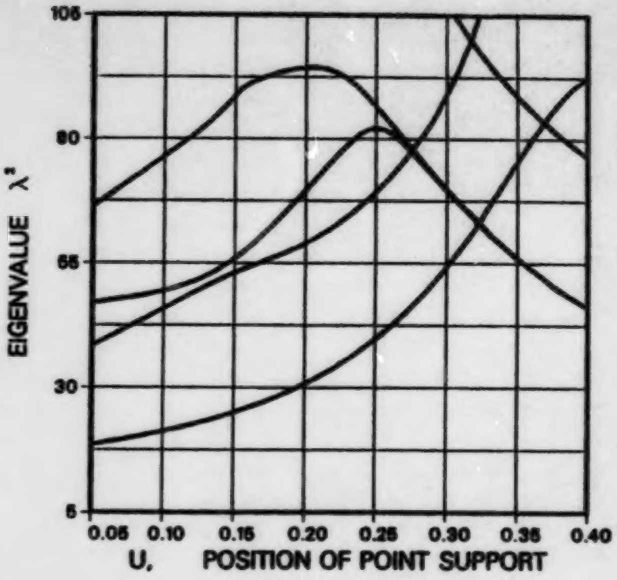

Fig. 6 FIRST FOUR EIGENVALUES vs. SUPPORT POSITION FOR PLATE "B".

Table 1 First Four Eigenvalues Computed for Plate "A"

	Mode			
u	1	2	3	4
.05	29.63	45.14	52.01	15.31
.10	17.71	34.84	47.71	57.71
.15	21.77	43.98	51.80	66.42
.20	28.35	58.34	59.02	77.75
.25	39.64	69.10	81.90	86.25
.30	60.85	86.14	77.19	76.98
.35	61.62	61.71	83.06	83.29
.40	49.16	49.21	69.05	69.51

Table 2 First Four Eigenvalues Computed for Plate "B"

	Mode			
u	1	2	3	4
.05	18.51	38.28	47.07	66.21
.10	21.20	45.76	49.40	76.28
.15	25.00	53.01	55.79	88.43
.20	30.69	58.87	69.32	94.01
.25	39.64	69.10	81.90	86.25
.30	54.01	69.31	69.58	88.65
.35	55.77	55.89	88.40	88.47
.40	45.75	45.97	76.26	76.30

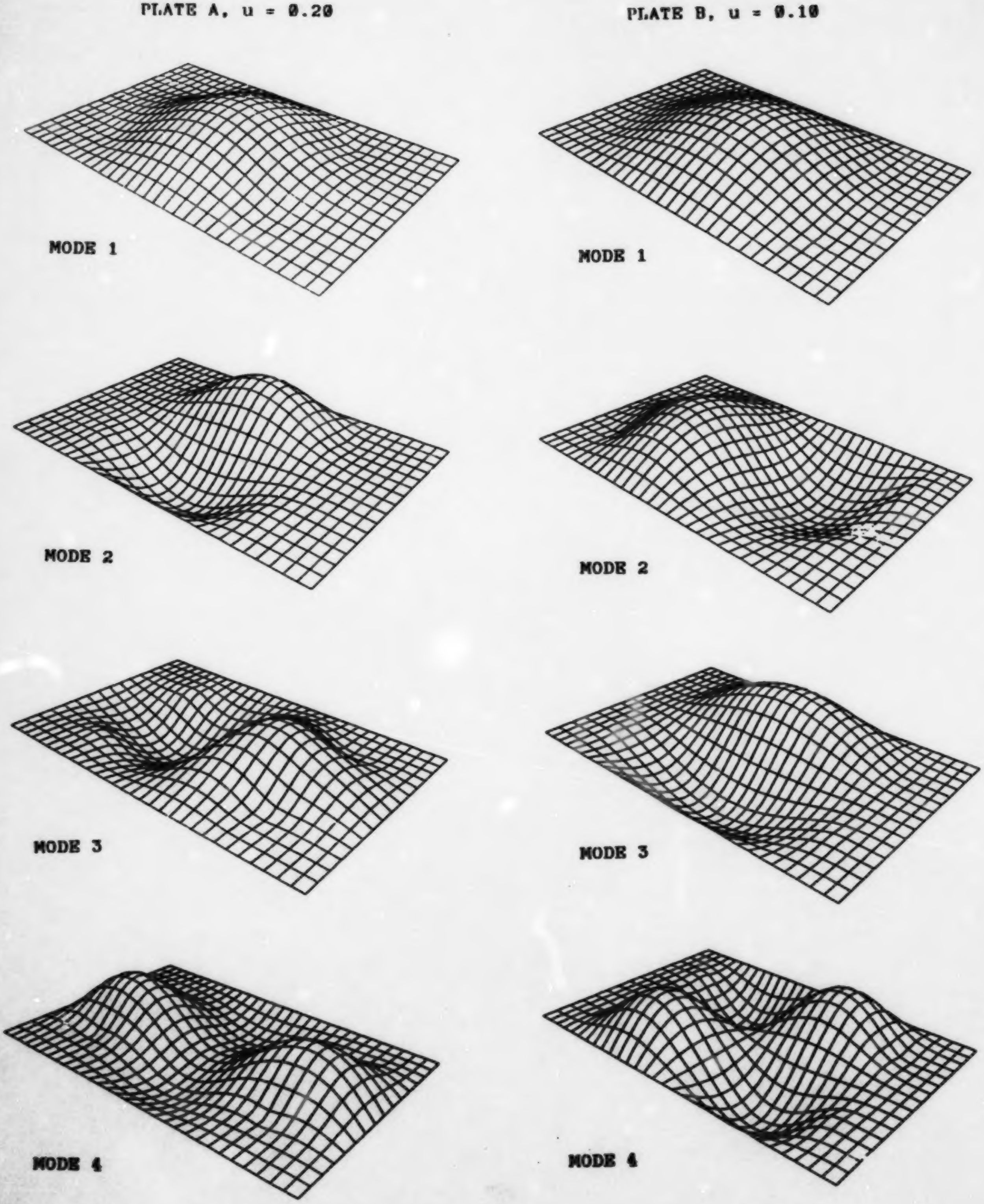
PLATE A, u = 0.20
PLATE B, u = 0.10
MODE 1
MODE 1
MODE 2
MODE 2
MODE 3
MODE 3
MODE 4
MODE 4

Fig. 7 TYPICAL MODE SHAPES FOR RECTANGULAR PLATES OF ASPECT RATIO, (b/a), = 1.5.

A MODIFIED LÉVY TYPE SOLUTION
FOR THE FREE VIBRATION ANALYSIS OF SIMPLY SUPPORTED ISOSCELES TRIANGULAR PLATES

H.T. Saliba

Associate Professor
Dept. of Mech. Eng.
Lakehead University, Thunder Bay, Ont.

ABSTRACT

The Lévy-type solution, traditionally associated with the problem of bending of rectangular plates with at least two opposite edges simply supported, is applied to the title problem. The solution is discussed in detail for the symmetric vibration modes of the plate. Reference is made to the author's published work on the problem of simply supported right triangular plates and how it relates to the anti-symmetric vibration modes of the present problem. The advantages of this method over existing highly accurate but more intricate superposition solutions are discussed while virtually total agreement with their results is indicated.

NOMENCLATURE

a	plate dimension in x direction.
b	plate dimension in y direction.
D	flexural rigidity of plate, $= Eh^3/12(1-\nu^2)$.
E	Youngs modulus of plate material.
h	plate thickness.
K	number of terms used in solution.
K^*	upper limit for first summation of solution.
W	plate lateral displacement divided by side length a.
η	distance along y axis divided by side length b, = y/b.
λ^2	eigenvalue, $= \omega a^2\sqrt{\rho/D}$.
ν	Poisson's ratio of plate material.
ξ	distance along plate x axis divided by side length a, = x/a.
ρ	mass of plate per unit area.
ϕ	plate aspect ratio, = b/a.
ω	circular frequency of plate vibration.

INTRODUCTION

In the year 1820, Navier presented a paper to the French Academy of Sciences on the solution of bending of simply supported rectangular plates by double trigonometric series. This solution is sometimes called the forced solution. At the turn of the century, in 1899, a solution by single Fourier series was introduced by Lévy[1].

Although Lévy's method which uses a single trigonometric series is more general than Navier's solution, it does not have an entirely general character since in its original form it can only be applied to rectangular plate vibration problems where at least two opposite edges are simply supported. However, it has been shown that by making use of the superposition techniques[2-4], this Lévy-type solution is readily employed to solve not only rectangular plate vibration problems of all possible combinations of classical boundary conditions, but also to analyze numerous rectangular plates with non-classical type boundary conditions. Furthermore, the superposition techniques have been extended to the solution of triangular plates[5], as well as trapezoidal plates[6,7]. However, it is the objective of the present paper to show how the Lévy-type solution is applied directly to obtain simple, yet highly accurate, solutions for simply supported non-rectangular plates by requiring the boundary conditions to be satisfied along oblique lines in the plane of rectangular plates instead of the outer edges. As an example, the solution of the simply supported isosceles triangular plate is discussed.

THE GOVERNING DIFFERENTIAL EQUATION

The correct differential equation governing the pure bending of plates subjected to lateral static loading is presented with detailed derivation by Timoshenko[8], and is written as

$$\frac{\partial^4 W(x,y)}{\partial x^4} + \frac{2\partial^4 W(x,y)}{\partial x^2 \partial y^2} + \frac{\partial^4 W(x,y)}{\partial y^4} = \frac{q(x,y)}{D}. \quad (1)$$

where $q(x,y)$ is the applied static loading.

The governing differential equation for the free vibration of rectangular plates is obtained by replacing the lateral force $q(x,y)$ of eq. (1) by the inertial force and by introducing the time variable parameter t as follows:

$$\frac{\partial^4 W(x,y,t)}{\partial x^4} + \frac{2\partial^4 W(x,y,t)}{\partial x^2 \partial y^2} + \frac{\partial^4 W(x,y,t)}{\partial y^4} + \frac{\rho}{D}\frac{\partial^2 W(x,y,t)}{\partial t^2} = 0. \quad (2)$$

By replacing $W(x,y,t)$ by its equivalent $W(x,y)T(t)$ (separable variables), it can be shown that $T(t) = A\sin(\omega t + \alpha)$. And eq. (2) can be written as

$$\frac{\partial^4 W(x,y)}{\partial x^4} + \frac{2\partial^4 W(x,y)}{\partial x^2 \partial y^2} + \frac{\partial^4 W(x,y)}{\partial y^4} - \frac{\omega^2 \rho W(x,y)}{D} = 0. \quad (3)$$

In its dimensionless form, eq. (3) can be written as

$$\frac{\partial^4 W(\xi,\eta)}{\partial \xi^4} + \frac{2\partial^4 W(\xi,\eta)}{\phi^2 \partial \xi^2 \partial \eta^2} + \frac{\partial^4 W(\xi,\eta)}{\phi^4 \partial \eta^4} - \lambda^4 W(\xi,\eta) = 0. \quad (4)$$

or,

$$\frac{\partial^4 W(\xi,\eta)}{\partial \eta^4} + \frac{2\phi^2 \partial^4 W(\xi,\eta)}{\partial \eta^2 \partial \xi^2} + \frac{\phi^4 \partial^4 W(\xi,\eta)}{\partial \xi^4} - \phi^4 \lambda^4 W(\xi,\eta) = 0. \quad (5)$$

THE LÉVY TYPE SOLUTION

M. Lévy suggested taking a solution in the form of a series[1]. And the Lévy-type solution of eq. (5) would be

$$\lim_{k \to \infty} W(\xi,\eta) = \sum_{m=1}^{k} Y_m(\eta) \sin(m\pi\xi). \quad (6)$$

By substituting this solution in eq. (5) and rearranging we get

$$\frac{d^4 Y_m(\eta)}{d\eta^4} - 2\phi^2 (m\pi)^2 . \frac{d^2 Y_m(\eta)}{d\eta^2} + \phi^4 [(m\pi)^4 - \lambda^4] Y_m(\eta) = 0. \quad (7)$$

The solution of eq. (7) depends on whether $\lambda^2 - (m\pi)^2$ is negative or positive. If $\lambda^2 > (m\pi)^2$ then

$$Y_m(\eta) = A_m \cosh \beta_m \eta + B_m \sinh \beta_m \eta + C_m \sin \gamma_m \eta + D_m \cos \gamma_m \eta. \quad (8)$$

and if $\lambda^2 < (m\pi)^2$ then

$$Y_m(\eta) = A_m \cosh \beta_m \eta + B_m \sinh \beta_m \eta + C_m \sinh \gamma_m \eta + D_m \cosh \gamma_m \eta. \quad (9)$$

where, $\beta_m = \phi\sqrt{\lambda^2 + (m\pi)^2}$, and $\gamma_m = \phi\sqrt{\lambda^2 - (m\pi)^2}$ or $\gamma_m = \phi\sqrt{(m\pi)^2 - \lambda^2}$, whichever is real. And where A_m, B_m, C_m and D_m are constants to be determined by means of prescribed boundary conditions.

THE SIMPLY SUPPORTED ISOSCELES TRIANGLE

Consider the triangular plate of Fig. 1. The plate is simply supported along all three edges. In view of the symmetry of the plate about the η axis, which coincide with the central axis of the full plate, physical considerations dictate that all possible free vibration modes must be symmetric or anti-symmetric with respect to this axis. Although not necessary, dealing with each of these two families of vibration modes separately makes the solution of the problem somewhat easier to follow. It also makes it possible to easily identify the eigenvalues and classify them accordingly (i.e. symmetric and anti-symmetric). Furthermore, it allows us to take advantage of the symmetry of the plate and thereby to concentrate the analysis on only half of the full plate. We start by investigating the family of symmetric modes first.

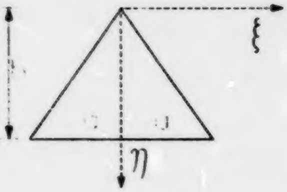

Figure 1. Simply supported isosceles triangular plate

Symmetric Modes

Attention is now focused on Fig. 2. The figure shows a rectangular plate of dimensions (a x b). Symmetry conditions are assumed along the edge $\xi = 0$, and are simulated by what is termed here as slip shear conditions (i.e. zero slope and zero vertical edge reaction). This is represented in the figure by the two adjacent small circles about the edge. In view of the simple support conditions along the two opposite edges $\eta = 1$ and $\eta = 0$, the Lévy-type solution for this plate is written as

$$\lim_{k \to \infty}(\xi,\eta) = \sum_{m=1}^{k} Y_m(\xi) \sin(m\pi\eta). \quad (10)$$

where,

$$Y(\xi) = A_m \cosh \beta_m \xi + B_m \cos \gamma_m \xi + C_m \sinh \beta_m \xi + D_m \sin \gamma_m \xi.$$

or if $\phi^2\lambda^2 < (m\pi)^2$ then,

$$Y(\xi) = A_m \mathit{coch} \beta_m \xi + B_m \cosh \gamma_m \xi + C_m \sinh \beta_m \xi + D_m \sinh \gamma_m \xi.$$

and where $\beta_m = \frac{1}{\phi}\sqrt{\phi^2\lambda^2 + (m\pi)^2}$, and $\gamma_m = \frac{1}{\phi}\sqrt{\phi^2\lambda^2 - (m\pi)^2}$ or $\gamma_m = \frac{1}{\phi}\sqrt{(m\pi)^2 - \phi^2\lambda^2}$ whichever is real. In view of the slip shear conditions along the symmetry axis of the original plate, $\xi = 0$, we have $C_m = D_m = 0$. Therefore,

$$Y_m(\xi) = A_m \cosh \beta_m \xi + B_m \cos \gamma_m \xi.$$

or if $\phi^2 \lambda^2 < (m\pi)^2$,

$$Y_m(\xi) = A_m \cosh \beta_m \xi + B_m \cos \gamma_m \xi.$$

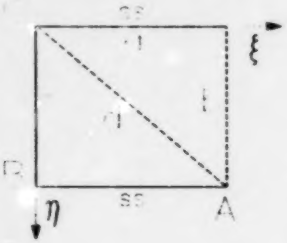

Figure 2. Rectangular plate used in the solution of symmetric modes.

The two remaining coefficients A_m and B_m are now obtained by enforcing the prescribed boundary conditions along the remaining edge which, normally, would have been the edge $\xi = 1$. However since our interest here lies in the triangle ABC and not the full rectangular plate, it is necessary to enforce the simple support conditions along the diagonal segment AC which represent the hypotenuse of the right triangle of interest. These conditions are the zero lateral displacement and zero bending moment about the diagonal d.

Satisfaction of the Boundary Conditions

It is clearly seen that the boundary conditions along the two edges $\xi = 0$ and $\eta = 1$ are automatically satisfied. However, conditions along the third edge $\xi = \eta$ remain to be satisfied. We first look at the zero lateral displacement condition. The displacement along this edge may be written as

$$W(\xi,\xi) = \sum_{m=1}^{k^*} (A_m \cosh \beta_m \xi + B_m \cos \gamma m \xi) \sin(m\pi\xi)$$
$$+ \sum_{k^*+1}^{\infty} (A_m \cosh \beta_m \xi + B_m \cosh \gamma_m \xi) \sin(m\pi\xi)$$
$$= 0. \qquad (11)$$

If we expand each term of the above series in an appropriate Fourier series, we could impose the constraint that the sum of the coefficients before each of the Fourier trigonometric functions must be zero. Therefore, let

$$I = 2\int_0^1 \cosh \beta_m \xi \sin m\pi\xi \sin n\pi\xi \, d\xi.$$

which leads to $I = EX1 + EX2$, where

$$EX1 = \frac{\beta_m \cos(m\pi - n\pi) \sinh \beta_m}{\beta_m^2 + (m\pi - n\pi)^2}$$

$$EX2 = -\frac{\beta_m \cos(m\pi + n\pi) \sinh \beta_m}{\beta_m^2 + (m\pi + n\pi)^2}.$$

Now let

$$II = 2\int_0^1 \cos \gamma_m \xi \sin m\pi\xi \sin n\pi\xi.$$

which leads to $II = EX3 + EX4$, where for $\gamma_m^2 \neq (m\pi - n\pi)^2$

$$EX3 = \frac{\gamma_m \sin \gamma_m \cos(m\pi - n\pi)}{\gamma_m^2 - (m\pi - n\pi)^2}$$

and for $\gamma_m^2 \neq (m\pi + n\pi)^2$

$$EX4 = \frac{\gamma_m \sin \gamma_m \cos(m\pi + n\pi)}{(m\pi + n\pi)^2 - \gamma_m^2}.$$

Finally, let

$$III = 2\int_0^1 \cosh \gamma_m \xi \sin m\pi\xi \sin n\pi\xi \, d\xi.$$

which upon integration leads to $III = EX5 + EX6$, where

$$EX5 = \frac{\gamma_m \cos(m\pi - n\pi) \sinh \gamma_m}{\gamma_m^2 + (m\pi - n\pi)^2}$$

$$EX6 = -\frac{\gamma_m \cos(m\pi + n\pi) \sinh \gamma_m}{\gamma_m^2 + (m\pi + n\pi)^2}.$$

Requiring the sum of the coefficients before each of the Fourier trigonometric functions to be zero leads to

$$A_m(EX1 + EX2) + B_m(EX3 + EX4) = 0, \qquad (12\text{-}a)$$

or if $\phi^2 \lambda^2 < (m\pi)^2$,

$$A_m(EX1 + EX2) + B_m(EX5 + EX6) = 0. \qquad (12\text{-}b)$$

We next look at the condition of zero moment. The bending moment equation about any line in the plane of a plate was given by Timoshenko[8]. It is reproduced here in its dimensionless form as follows:

$$\frac{M_n b^2}{aD} = -\left[\theta_1 \phi^2 \frac{\partial^2 W}{\partial \xi^2} + \theta_2 \frac{\partial^2 W}{\partial \eta^2} + \theta_3 \phi \frac{\partial^2 W}{\partial \xi \partial \eta}\right] \qquad (13)$$

where,

$$\theta_1 = \cos^2 \alpha + \nu \sin^2 \alpha.$$

$$Q_2 = \sin^2\alpha + \nu\cos^2\alpha,$$

$$Q_3 = (1-\nu)\sin 2\alpha,$$

and where α is the angle between the normal to the line and the ξ axis. It is seen from Eq. (13) that the following derivatives for each term of the involved series are required.

$$\frac{\partial^2 h}{\partial \xi^2} = [A_m\beta_m^2\cosh\beta_m\xi - B_m\gamma_m^2\cos\gamma_m\xi]\sin(m\pi\xi)$$

$$or = [A_m\beta_m^2\cosh\beta_m\xi + B_m\gamma_m^2\cosh\gamma_m\xi]\sin(m\pi\xi)$$

$$\frac{\partial^2 h}{\partial \eta^2} = -(m\pi)^2[A_m\cosh\beta_m\xi + B_m\cos\gamma_m\xi]\sin(m\pi\xi)$$

$$or = -(m\pi)^2[A_m\cosh\beta_m\xi + B_m\cosh\gamma_m\xi]\sin(m\pi\xi)$$

$$\frac{\partial^2 h}{\partial \xi\partial \eta} = (m\pi)[A_m\beta_m\sinh\beta_m\xi - B_m\gamma_m\sin\gamma_m\xi]\cos(m\pi\xi)$$

$$or = (m\pi)[A_m\beta_m\sinh\beta_m\xi + B_m\gamma_m\sinh\gamma_m\xi]\cos(m\pi\xi)$$

where η has been replaced by its equivalent term ξ. Following the previously established procedure, it is seen that the first two derivatives can be expressed in terms of $FN1$ through $FN6$. However, the third derivative which is a mixed derivative, needs to be expanded in the same Fourier sine series as above so that it can be combined with the first two term of eq. (13). Now let

$$I = 2\int_0^1 \sinh\beta_m\xi\cos(m\pi\xi)\sin n\pi\xi\, d\xi.$$

Performing the integrations, one gets $I = Y1 + Y2$, where,

$$Y1 = -\frac{(m\pi - n\pi)\cos(m\pi + n\pi)\sinh\beta_m}{\beta_m^2 + (m\pi + n\pi)^2},$$

$$Y2 = \frac{(m\pi - n\pi)\cos(m\pi - n\pi)\sinh\beta_m}{\beta_m^2 + (m\pi - n\pi)^2}.$$

And let

$$II = 2\int_0^1 \sin\gamma_m\xi\cos m\pi\xi\sin n\pi\xi\, d\xi.$$

then $II = Y3 + Y4$, where for $\gamma_m^2 \neq (m\pi + n\pi)^2$,

$$Y3 = \frac{(m\pi + n\pi)\cos(m\pi + n\pi)\sin\gamma_m}{\gamma_m^2 - (m\pi + n\pi)^2}$$

and for $\gamma_m^2 \neq (m\pi - n\pi)^2$,

$$Y4 = \frac{(m\pi - n\pi)\cos(m\pi - n\pi)\sin\gamma_m}{(m\pi - n\pi)^2 - \gamma_m^2}.$$

Finally, we let

$$III = 2\int_0^1 \sinh\gamma_m\xi\cos m\pi\xi\sin n\pi\xi\, d\xi.$$

then $III = Y5 + Y6$, where

$$Y5 = -\frac{(m\pi + n\pi)\cos(m\pi + n\pi)\sinh\gamma_m}{\gamma_m^2 + (m\pi + n\pi)^2},$$

$$Y6 = \frac{(m\pi - n\pi)\cos(m\pi - n\pi)\sinh\gamma_m}{\gamma_m^2 + (m\pi - n\pi)^2}.$$

Now let

$$A11N = Q_1\phi^2\beta_m^2(FN1 + FN2),$$

$$A12N = -Q_1\phi^2\gamma_m^2(FN3 + FN4),$$

or if $\phi^2\lambda^2 < (m\pi)^2$,

$$A12N = Q_1\phi^2\gamma_m^2(FN5 + FN6),$$

$$A13N = -Q_2(m\pi)^2(FN1 + FN2),$$

$$A14N = -Q_2(m\pi)^2(FN3 + FN4),$$

or if $\phi^2\lambda^2 < (m\pi)^2$,

$$A14N = -Q_2(m\pi)^2(FN5 + FN6),$$

$$A15N = Q_3\phi(m\pi)\beta_m(Y1 + Y2),$$

$$A16N = -Q_3\phi(m\pi)\gamma_m(Y3 + Y4),$$

or if $\phi^2\lambda^2 < (m\pi)^2$,

$$A16N = Q_3\phi(m\pi)\gamma_m(Y5 + Y6).$$

The condition of zero moment about the edge, $\eta = \xi$, is now satisfied by requiring the sum of the coefficients before each of the Fourier trigonometric functions to be zero. This leads to

$$-A_m(A11N + A13N + A15N) + B_m(A12N + A14N + A16N)] = 0. \qquad (14)$$

Eq. (12) and eq. (14) represent a set of 2K homogeneous algebraic equations with 2K unknowns, where K is the number of terms in the Fourier series expansion. For non-trivial solution, the determinant of the coefficient matrix of these equations is required to vanish, leading to the determination of the eigenvalues and consequently to the eigenvectors.

Anti-Symmetric Modes

For anti-symmetric vibration modes, the central axis, $\xi = 0$, in Fig. 1 is a nodal line. Therefore, the half plate can be analyzed as a simply supported right triangular plate of dimensions (a x b) as shown in Fig. 3. The solution of which has already been discussed by this author in connection with the solution of the simply supported right triangular plate[9].

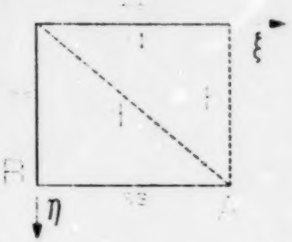

Figure 3. Rectangular plate used in the solution of anti-symmetric modes.

CONCLUDING REMARKS

In view of the simplicity of the solution and the fact that it has been made available to the reader, it is felt that the presentation of lengthy tables of results would not be desirable here. However, if required, using the information provided herein and in Reference [9], the reader could easily write a small computer program to generate the numerical data pertaining to any particular application. In doing so, the reader should keep in mind that for good convergence, the problem should be formulated such that the aspect ratio b/a is always greater than or equal to unity, where b is always the length of the side along which the boundary conditions are adjusted to ensure the simple support conditions along the diagonal d, as shown in Fig. 1. However, it is felt appropriate here to give the reader an indication of the accuracy and the degree of convergence to be expected when using this method.

The exact eigenvalues of some particular cases can be found. One such case is the particular case of the 45°.90°.45° isosceles triangle. It can easily be shown that the eigenvalues for this particular triangle can be obtained from the known exact solution of the simply supported square plate. In the case of symmetric modes, the first three eigenvalues are $5\pi^2/2$, $13\pi^2/2$ and $17\pi^2/2$. And in the case of anti-symmetric modes, these are $5\pi^2$, $13\pi^2$ and $17\pi^2$. In both cases, the exact eigenvalues were obtained with only six term expansions, leading to a coefficient matrix of 12 x 12. This represent considerable saving and apparent economical advantage over the previously used superposition method, where the size of the coefficient matrix is considerably larger[5].

ACKNOWLEDGEMENT

The author wishes to acknowledge the financial support of the Natural Science and Engineering Research Council of Canada.

REFERENCES

1. M. Lévy, 1899 C.R. Acad. Sci., 129, 535-539. Sur l'equilibre elastiqe d'une plaque rectangulaire.
2. D.J. Gorman, 1982 Free Vibration Analysis of Rectangular Plates. New York: Elsevier/North-Holland, Inc.
3. H.T. Saliba, 1984 Journal of Sound and Vibration 94(3), 381-395. Free vibration analysis of rectangular cantilever plates with symmetrically distributed point supports along the edges.
4. H.T. Saliba, 1988 Journal of Sound and Vibration 127(1), 77-89. Free vibration analysis of rectangular cantilever plates with symmetrically distributed lateral point supports.
5. D.J. Gorman, 1983 Journal of Sound and Vibration 89(1), 107-118. A highly accurate analytical solution for free vibration analysis of simply supported right triangular plates.
6. H.T. Saliba, 1986 Journal of Sound and Vibration 110(1), 87-97. Free vibration analysis of simply supported symmetrical trapezoidal plates.
7. H.T. Saliba, 1988 Journal of Sound and Vibration 126(2), 237-247. Transverse free vibration of fully clamped symmetrical trapezoidal plates.
8. S. Timoshenko and S. Woinowsky-Krieger, Theory of Plates and Shells, 2nd ed., McGrow-Hill Book Company, New York, 1959.
9. H.T. Saliba, 1990 Journal of Sound and Vibration 138(3), 000-000. Transverse free vibration of simply supported right triangular thin plates: a highly accurate simplified solution.

Free Vibration of a Thick-walled Vessel

D. Redekop
Department of Mechanical Engineering
University of Ottawa
Ottawa, Ontario, Canada
K1N 6N5

ABSTRACT

The free vibration of a thick-walled steel cylindrical vessel closed by hemispherical heads is considered. The theory is presented for the determination of natural frequencies and mode shapes for the special case of axisymmetric and longitudinally symmetric vibrations. Consideration can then be restricted to one half of the domain, i. e. to half of a cylindrical shell and one head. Separate series solutions are written for each of these components. The constants and coefficients of the series are available for the satisfying of boundary and continuity conditions. Determination of these unknowns is by solution of a triple eigenvalue problem, for which an iterative procedure is proposed. Publication of numerical results is reserved for a future communication.

INTRODUCTION

Geometrically complicated vessels are used in the space and power industries. Determination of the vibration characteristics of such vessels has been considered by a number of authors [1-7]. Shell membrane and bending theories have been used, as well as the finite element method (FEM). Consideration has been restricted so far to thin-walled vessels.

Thick-walled vessels are finding increased application in industry, particularly as design pressures are increased. Satisfactory analysis of such vessels requires the use of the three-dimensional theory of elastodymanics [8]. Several applications of this theory have already been made [8-10], but the geometries considered have been simple ones, consisting of a single shell component only.

In this study a three-dimensional method of analysis is used to solve a thick-walled vessel problem involving two components (Fig. 1). The necessary theory for determining the natural frequencies and mode shapes is presented. Full specification of the series expansions to be adopted for each component is given. It is shown that to determine all series parameters a triple eigenvalue problem must be solved. The paper concludes with details of a proposed iterative solution to this problem.

GOVERNING EQUATIONS

The governing equations of the three-dimensional linear theory of elastodynamics are the Navier equations [8] which may be expressed as

$$(\hat{\lambda} + 2\hat{\mu}) \nabla \nabla \cdot \mathbf{u} - \hat{\mu} \nabla \times \nabla \times \mathbf{u} = \hat{\rho} \ddot{\mathbf{u}} \qquad (1)$$

where $\mathbf{u}$ is the displacement vector, $\hat{\lambda}, \hat{\mu}$ are the Lame parameters, $\hat{\rho}$ the mass density, $\ddot{\mathbf{u}}$ indicates the second derivative of $\mathbf{u}$ with respect to the time t, and ∇ the gradient operator. Body forces and temperature variations are neglected and the material is assumed to be homogeneous and isotropic.

The Navier equations are identically satisfied [8] if the displacement vector is computed from the Helmholtz potentials Φ, Ψ, χ using

$$\mathbf{u} = \mathbf{L} + \mathbf{M} + \mathbf{N} \qquad (2)$$

where

$$\begin{aligned} \mathbf{L} &= \nabla \Phi \\ \mathbf{M} &= \nabla \times \mathbf{w} \Psi \mathbf{e}_3 \\ \mathbf{N} &= l \nabla \times \nabla \times \mathbf{w} \chi \mathbf{e}_3 \end{aligned} \qquad (3)$$

and l is a length factor, w an arbitrary function to make the wave equation separable, and $\mathbf{e}_3$ a unit vector in the 3rd coordinate direction. The Helmholtz potentials must satisfy

$$\begin{aligned} c_1^2 \nabla^2 \Phi &= \ddot{\Phi} \\ c_2^2 \nabla^2 \Psi &= \ddot{\Psi} \\ c_2^2 \nabla^2 \chi &= \ddot{\chi} \end{aligned} \qquad (4)$$

where

$$c_1 = [\hat{\lambda} + 2\hat{\mu}/\hat{\rho}]^{1/2}, \; c_2 = [\hat{\lambda}/\hat{\rho}]^{1/2} \qquad (5)$$

and ∇^2 is the Laplacian operator. Quantities c_1 and c_2 are respectively the irrotational and equivoluminal wave velocities, and in eq. (2) L represents the irrotational contribution to u, while M and N the equivoluminal contributions.

Series expansions are written to eq. (4) for each shell component in terms of underterminined constants and coefficients. Components of the stress dyadic σ are then obtained using stress-strain relations. The undetermined quantities are adjusted to satisfy for each shell component, on the inner and outer surface, the boundary conditions

$$\sigma \bullet \mathbf{n} = 0 \qquad (6)$$

and to satisfy, on the common surface of connection, the conditions of displacement and stress continuity

$$\mathbf{u}^{I} = \mathbf{u}^{II}$$
$$\sigma^{I} \bullet \mathbf{n}^{I} = \sigma^{II} \bullet \mathbf{n}^{II} \qquad (7)$$

In equations (6-7) **n** is the outward normal vector, and the superscripts refer to components I (cylinder) and II (sphere), meeting at this surface. The solution for the cylinder must also satisfy on the longitudinal plane of symmetry, $z = 0$, the following conditions

$$u_z = 0, \ \sigma_{rz} = 0 \qquad (8)$$

EIGENFUNCTIONS FOR THE CYLINDER

The series expansion for the cylinder must satisfy the homogeneous boundary conditions

$$\sigma_{rr}(\rho_i,\zeta,t) = 0, \ \sigma_{rr}(\rho_o,\zeta,t) = 0, \qquad (9)$$
$$\sigma_{rz}(\rho_i,\zeta,t) = 0, \ \sigma_{rz}(\rho_o,\zeta,t) = 0$$

and the conditions on the longitudinal plane of symmetry

$$\sigma_{rz}(\rho,0,t) = 0, \ u_z(\rho,0,t) = 0 \qquad (10)$$

Here

$$\rho = r/a, \ \zeta = z/a$$
$$\rho_i = r_i/a, \ \rho_o = r_o/a \qquad (11)$$
$$a = (r_i + r_o)/2$$

where r, z are circular cylindrical coordinates (Fig. 2), and r_i, r_o represent respectively the inside and outside radii of the cylinder.

Considering eqs. (2-4) and (9-10) the set of axisymmetric displacement components may be taken as [8]

$$\begin{aligned} \frac{u_r}{a} &= (\alpha\rho)^{-1}[a_1 u_1^{(1)}(\alpha\rho) + a_2 u_1^{(2)}(\alpha\rho) + a_5 l u_3^{(1)}(\beta\rho) \\ &\quad + a_6 l u_3^{(2)}(\beta\rho)] \cosh \gamma\zeta \ e^{-i\omega t} \qquad (12) \\ \frac{u_z}{a} &= a^{-1}[a_1 w_1^{(1)}(\alpha\rho) + a_2 w_1^{(2)}(\alpha\rho) + a_5 l w_3^{(1)}(\beta\rho) \\ &\quad + a_6 l w_3^{(2)}(\beta\rho)] \sinh \gamma\zeta \ e^{-i\omega t} \end{aligned}$$

where a_1, a_2, a_5, a_6 are integration constants and

$$\alpha^2 = (a\omega/c_1)^2 - \gamma^2, \ \beta^2 = (a\omega/c_2)^2 - \gamma^2 \qquad (13)$$

Quantity γ is the axial decay coefficient while ω is the frequency. The displacement coefficient functions appearing in eq. (12) are given by

$$\begin{aligned} u_1^{(i)}(\alpha\rho) &= \alpha\rho C_{-1}^{(i)}(\alpha\rho) \\ u_3^{(i)}(\beta\rho) &= \pm i\gamma\beta\rho C_{-1}^{(i)}(\beta\rho) \\ w_1^{(i)}(\alpha\rho) &= \pm i\gamma C_o^{(i)}(\alpha\rho) \qquad (14) \\ w_3^{(i)}(\beta\rho) &= \beta^2 C_o^{(i)}(\beta\rho) \end{aligned}$$

where the constant i on the right hand members is the imaginary unity. The cylinder functions $C_n^{(i)}$, $i = 1, 2$ are appropriate solutions of the equations

$$\rho^2 \frac{d^2 x}{d\rho^2} + \rho \frac{dx}{d\rho} + [(a\omega/c)^2 - \gamma^2]\rho^2 x = 0 \qquad (15)$$

and $C_{-n}^{(i)} = -C_n^{(i)}$. For convenience the solutions to eq. (15) may be taken as as the functions $V_n, \dot{W}_n$ used in refs. [11-12].

The stress components (Fig. 2) are then given by [8]

$$\begin{aligned} \frac{\sigma_{rr}}{2\hat{\mu}} &= \rho^{-2}[a_1 t_{11}^{(1)}(\alpha\rho) + a_2 t_{11}^{(2)}(\alpha\rho) + a_5 l t_{13}^{(1)}(\beta\rho) \\ &\quad + a_6 l t_{13}^{(2)}(\beta\rho)] \cosh \gamma\zeta \ e^{-i\omega t} \\ \frac{\sigma_{\theta\theta}}{2\hat{\mu}} &= \rho^{-2}[a_1 t_{21}^{(1)}(\alpha\rho) + a_2 t_{21}^{(2)}(\alpha\rho) + a_5 l t_{23}^{(1)}(\beta\rho) \\ &\quad + a_6 l t_{23}^{(2)}(\beta\rho)] \cosh \gamma\zeta \ e^{-i\omega t} \qquad (16) \\ \frac{\sigma_{zz}}{2\hat{\mu}} &= \rho^{-2}[a_1 t_{31}^{(1)}(\alpha\rho) + a_2 t_{31}^{(2)}(\alpha\rho) + a_5 l t_{33}^{(1)}(\beta\rho) \\ &\quad + a_6 l t_{33}^{(2)}(\beta\rho)] \cosh \gamma\zeta \ e^{-i\omega t} \\ \frac{\sigma_{rz}}{2\hat{\mu}} &= \rho^{-2}[a_1 t_{51}^{(1)}(\alpha\rho) + a_2 t_{51}^{(2)}(\alpha\rho) + a_5 l t_{53}^{(1)}(\beta\rho) \\ &\quad + a_6 l t_{53}^{(2)}(\beta\rho)] \sinh \gamma\zeta \ e^{-i\omega t} \end{aligned}$$

where

$$\begin{aligned} t_{11}^{(i)}(\alpha\rho) &= (-k_2^2\rho^2/2 + \gamma^2\rho^2)C_o^{(i)}(\alpha\rho) - \alpha\rho C_{-1}^{(i)}(\alpha\rho) \\ t_{13}^{(i)}(\beta\rho) &= (\pm i\gamma)[-\beta^2\rho^2 C_o^{(i)}(\beta\rho) - \beta\rho C_{-1}^{(i)}(\beta\rho)] \\ t_{21}^{(i)}(\alpha\rho) &= (-k_2^2\rho^2/2 + k_1^2\rho^2)C_o^{(i)}(\alpha\rho) + \alpha\rho C_{-1}^{(i)}(\alpha\rho) \\ t_{23}^{(i)}(\beta\rho) &= (\pm i\gamma)\beta\rho C_{-1}^{(i)}(\beta\rho) \qquad (17) \\ t_{31}^{(i)}(\alpha\rho) &= (\alpha^2\rho^2 - k_2^2\rho^2/2)C_o^{(i)}(\alpha\rho) \\ t_{33}^{(i)}(\beta\rho) &= (\pm i\gamma)(\beta\rho)^2 C_o^{(i)}(\beta\rho) \\ t_{51}^{(i)}(\alpha\rho) &= (\pm i\gamma\rho)\alpha\rho C_{-1}^{(i)}(\alpha\rho) \\ t_{53}^{(i)}(\beta\rho) &= \frac{1}{2\rho}(\beta^2\rho^2 - \gamma^2\rho^2)\beta\rho C_{-1}^{(i)}(\beta\rho) \end{aligned}$$

and

$$k_1^2 = (a\omega/c_1)^2, \ k_2^2 = (a\omega/c_2)^2 \qquad (18)$$

Enforcing the boundary conditions eq. (9) leads to four homogeneous equations in a_1, a_2, a_5, a_6. For non-trivial solution the determinant of these equations must be zero, i. e. $D_I = 0$, or

$$\begin{vmatrix} t_{11}^{(1)}(\alpha\rho_i) & t_{11}^{(2)}(\alpha\rho_i) & t_{13}^{(1)}(\beta\rho_i) & t_{13}^{(2)}(\beta\rho_i) \\ t_{51}^{(1)}(\alpha\rho_i) & t_{51}^{(2)}(\alpha\rho_i) & t_{53}^{(1)}(\beta\rho_i) & t_{53}^{(2)}(\beta\rho_i) \\ t_{11}^{(1)}(\alpha\rho_o) & t_{11}^{(2)}(\alpha\rho_o) & t_{13}^{(1)}(\beta\rho_o) & t_{13}^{(2)}(\beta\rho_o) \\ t_{51}^{(1)}(\alpha\rho_o) & t_{51}^{(2)}(\alpha\rho_o) & t_{53}^{(1)}(\beta\rho_o) & t_{53}^{(2)}(\beta\rho_o) \end{vmatrix} = 0 \qquad (19)$$

For a specified (trial) value of ω this equation may be solved for the decay coefficients γ_m, $m = 1, 2, \ldots$ The equation is nonlinear and is solved for the γ_m using the complex form of the Muller method [13]. Starting values required in this iterative procedure may be found through an aymptotic representation of (19).

Corresponding to each γ_m found using this procedure the constants a_1, a_2, a_5, a_6 may be solved for in terms of one of the constants, say a_6, relabelled d_m. When the solution for γ_m is complex two independent real solutions are obtained by separating the real and imaginary parts. Combining all solutions, the displacement and stress components, automatically satisfying the homogeneous boundary conditions (9), and the symmetry conditions (10), can be written in the form

$$
\begin{aligned}
\frac{u_r}{a} &= \Sigma d_n u_{rn} \\
\frac{u_z}{a} &= \Sigma d_n u_{zn} \\
\frac{\sigma_{rr}}{2\hat{\mu}} &= \Sigma d_n \sigma_{rrn} \qquad (20)\\
\frac{\sigma_{\theta\theta}}{2\hat{\mu}} &= \Sigma d_n \sigma_{\theta\theta n} \\
\frac{\sigma_{zz}}{2\hat{\mu}} &= \Sigma d_n \sigma_{zzn} \\
\frac{\sigma_{rz}}{2\hat{\mu}} &= \Sigma d_n \sigma_{rzn}
\end{aligned}
$$

where the summations are for $n = 1, 2, ..., N_c$. The N_c accounts for possible multiplicity of eigenfunctions for a single γ_m arising from a complex solution.

EIGENFUNCTIONS FOR THE SPHERE

The series expansion for the sphere must satisfy the homogeneous boundary conditions

$$
\begin{aligned}
\tau_{RR}(\xi_i, \phi, t) = 0,\ \tau_{RR}(\xi_o, \phi, t) = 0 \qquad (21)\\
\tau_{R\phi}(\xi_i, \phi, t) = 0,\ \tau_{R\phi}(\xi_o, \phi, t) = 0
\end{aligned}
$$

and the following conditions

$$\tau_{\phi\phi}, \tau_{R\phi} \longrightarrow 0 \qquad (22)$$

at $\phi = 0$. Here

$$\xi = R/a,\ \xi_i = R_i/a,\ \xi_o = R_o/a \qquad (23)$$

Quantities R, ϕ are the radial and polar coordinates (Fig. 2) of an axisymmetric spherical system and R_i, R_o are the inside and outside radii of the sphere.

Considering eqs. (2-4) and (21-22) the set of axisymmetric displacement components may be taken as [8]

$$
\begin{aligned}
\frac{v_R}{a} &= (a\xi)^{-1}[A_1 U_1^{(1)}(\kappa\xi) + A_2 U_1^{(2)}(\kappa\xi) + A_5 l U_3^{(1)}(\lambda\xi) \\
&\quad + A_6 l U_3^{(2)}(\lambda\xi)] P_\nu e^{-i\omega t} \qquad (24)\\
\frac{v_\phi}{a} &= (a\xi)^{-1}[A_1 V_1^{(1)}(\kappa\xi) + A_2 V_1^{(2)}(\kappa\xi) + A_5 l V_3^{(1)}(\lambda\xi) \\
&\quad + A_6 l V_3^{(2)}(\lambda\xi)] \frac{dP_\nu}{d\phi} e^{-i\omega t}
\end{aligned}
$$

where A_1, A_2, A_5, A_6 are integration constants and

$$\kappa = a\omega/c_1,\ \lambda = a\omega/c_2 \qquad (25)$$

and ω is again the frequency. Function $P_\nu = P_\nu(\cos\phi)$ is the Legendre function of order ν and argument $\cos\phi$. It is regular at $\phi = 0$. Quantity ν represents the decay coefficient in the ϕ direction.

The displacement coefficient functions appearing in eq. (24) are given by

$$
\begin{aligned}
U_1^{(i)}(\kappa\xi) &= \nu z_\nu^{(i)}(\kappa\xi) - \kappa\xi z_{\nu+1}^{(i)}(\kappa\xi) \\
U_3^{(i)}(\lambda\xi) &= \nu(\nu+1) z_\nu^{(i)}(\lambda\xi) \qquad (26)\\
V_1^{(i)}(\kappa\xi) &= z_\nu^{(i)}(\kappa\xi) \\
V_3^{(i)}(\lambda\xi) &= (\nu+1) z_\nu^{(i)}(\lambda\xi) - \lambda\xi z_{\nu+1}^{(i)}(\lambda\xi)
\end{aligned}
$$

The functions $z_\nu^{(i)}(x)$ appearing in these coefficients are given by

$$
\begin{aligned}
z_\nu^{(1)}(x) &= (\pi/2x)^{1/2} J_{\nu+1/2}(x) \qquad (27)\\
z_\nu^{(2)}(x) &= (\pi/2x)^{1/2} Y_{\nu+1/2}(x)
\end{aligned}
$$

with $x = \kappa\xi$ or $\lambda\xi$. Quantities $J_{\nu+1/2}(x)$ and $Y_{\nu+1/2}(x)$ are Bessel functions of the first and second kind of order $\nu + 1/2$ and argument x. The derivative of P_ν appearing in eq. (21) and below is given by

$$\frac{dP_\nu}{d\phi} = \nu \cot\phi P_\nu - \frac{\nu}{\sin\phi} P_{\nu-1} \qquad (28)$$

The stress components (Fig. 2) are then given by [8]

$$
\begin{aligned}
\frac{\tau_{RR}}{2\hat{\mu}} &= \xi^{-2}[A_1 T_{11}^{(1)}(\kappa\xi) + A_2 T_{11}^{(2)}(\kappa\xi) + A_5 l T_{13}^{(1)}(\lambda\xi) \\
&\quad + A_6 l T_{13}^{(2)}(\lambda\xi)] P_\nu e^{-i\omega t} \qquad (29)\\
\frac{\tau_{\phi\phi}}{2\hat{\mu}} &= \xi^{-2}[A_1 \{T_{21}^{(1)}(\kappa\xi) P_\nu - \hat{T}_{21}^{(1)}(\kappa\xi) \cot\phi \frac{dP_\nu}{d\phi}\} \\
&\quad + A_2 \{T_{21}^{(2)}(\kappa\xi) P_\nu - \hat{T}_{21}^{(2)}(\kappa\xi) \cot\phi \frac{dP_\nu}{d\phi}\} \\
&\quad + A_5 l \{T_{23}^{(1)}(\lambda\xi) P_\nu - \hat{T}_{23}^{(1)}(\lambda\xi) \cot\phi \frac{dP_\nu}{d\phi}\} \\
&\quad + A_6 l \{T_{23}^{(2)}(\lambda\xi) P_\nu - \hat{T}_{23}^{(2)}(\lambda\xi) \cot\phi \frac{dP_\nu}{d\phi}\}] e^{-i\omega t} \\
\frac{\tau_{\theta\theta}}{2\hat{\mu}} &= \xi^{-2}[A_1 \{T_{31}^{(1)}(\kappa\xi) P_\nu + \hat{T}_{31}^{(1)}(\kappa\xi) \cot\phi \frac{dP_\nu}{d\phi}\} \\
&\quad + A_2 \{T_{31}^{(2)}(\kappa\xi) P_\nu + \hat{T}_{31}^{(2)}(\kappa\xi) \cot\phi \frac{dP_\nu}{d\phi}\} \\
&\quad + A_5 l \{T_{33}^{(1)}(\lambda\xi) P_\nu + \hat{T}_{33}^{(1)}(\lambda\xi) \cot\phi \frac{dP_\nu}{d\phi}\} \\
&\quad + A_6 l \{T_{33}^{(2)}(\lambda\xi) P_\nu + \hat{T}_{33}^{(2)}(\lambda\xi) \cot\phi \frac{dP_\nu}{d\phi}\}] e^{-i\omega t} \\
\frac{\tau_{R\phi}}{2\hat{\mu}} &= \xi^{-2}[A_1 T_{41}^{(1)}(\kappa\xi) + A_2 T_{41}^{(2)}(\kappa\xi) + A_5 l T_{43}^{(1)}(\lambda\xi) \\
&\quad + A_6 l T_{43}^{(2)}(\lambda\xi)] P_\nu e^{-i\omega t}
\end{aligned}
$$

where

$$
\begin{aligned}
T_{11}^{(i)}(\kappa\xi) &= (\nu^2 - \nu - (\lambda\xi)^2/2) z_\nu^{(i)}(\kappa\xi) + 2\kappa\xi z_{\nu+1}^{(i)}(\kappa\xi) \\
T_{13}^{(i)}(\lambda\xi) &= (\nu^2 + \nu)[(\nu - 1) z_\nu^{(i)}(\lambda\xi) - \lambda\xi\, z_{\nu+1}^{(i)}(\lambda\xi)] \\
T_{21}^{(i)}(\kappa\xi) &= (-\nu^2 - (\lambda\xi)^2/2 + (\kappa\xi)^2) z_\nu^{(i)}(\kappa\xi) - \kappa\xi z_{\nu+1}^{(i)}(\kappa\xi) \\
\hat{T}_{21}^{(i)}(\kappa\xi) &= z_\nu^{(i)}(\kappa\xi) \qquad (30)\\
T_{23}^{(i)}(\lambda\xi) &= -(\nu^2 + \nu)[\nu z_\nu^{(i)}(\lambda\xi) - \lambda\xi z_{\nu+1}^{(i)}(\lambda\xi)] \\
\hat{T}_{23}^{(i)}(\lambda\xi) &= (\nu + 1) z_\nu^{(i)}(\lambda\xi) - \lambda\xi z_{\nu+1}^{(i)}(\lambda\xi) \\
T_{31}^{(i)}(\kappa\xi) &= (\nu - (\lambda\xi)^2/2 + (\kappa\xi)^2) z_\nu^{(i)}(\kappa\xi) - \kappa\xi z_{\nu+1}^{(i)}(\kappa\xi) \\
\hat{T}_{31}^{(i)}(\kappa\xi) &= z_\nu^{(i)}(\kappa\xi) \\
T_{33}^{(i)}(\lambda\xi) &= (\nu^2 + \nu) z_\nu^{(i)}(\lambda\xi) \\
\hat{T}_{33}^{(i)}(\lambda\xi) &= (\nu + 1) z_\nu^{(i)}(\lambda\xi) - \lambda\xi z_{\nu+1}^{(i)}(\lambda\xi) \\
T_{41}^{(i)}(\kappa\xi) &= (\nu - 1) z_\nu^{(i)}(\kappa\xi) - \kappa\xi z_{\nu+1}^{(i)}(\kappa\xi) \\
T_{43}^{(i)}(\lambda\xi) &= (\nu^2 - 1 - (\lambda\xi)^2/2) z_\nu^{(i)}(\lambda\xi) + \lambda\xi z_{\nu+1}^{(i)}(\lambda\xi)
\end{aligned}
$$

Enforcing the boundary conditions (21) leads to four homogeneous equations in A_1, A_2, A_5, A_6. For non-trivial solution the determinant of these equations must be zero, i. e. $D_{II} = 0$ or

$$\begin{vmatrix} T_{11}^{(1)}(\kappa\xi_i) & T_{11}^{(2)}(\kappa\xi_i) & T_{13}^{(1)}(\kappa\xi_i) & T_{13}^{(2)}(\kappa\xi_i) \\ T_{41}^{(1)}(\kappa\xi_i) & T_{41}^{(2)}(\kappa\xi_i) & T_{43}^{(1)}(\kappa\xi_i) & T_{43}^{(2)}(\kappa\xi_i) \\ T_{11}^{(1)}(\kappa\xi_o) & T_{11}^{(2)}(\kappa\xi_o) & T_{13}^{(1)}(\kappa\xi_o) & T_{13}^{(2)}(\kappa\xi_o) \\ T_{41}^{(1)}(\kappa\xi_o) & T_{41}^{(2)}(\kappa\xi_o) & T_{43}^{(1)}(\kappa\xi_o) & T_{43}^{(2)}(\kappa\xi_o) \end{vmatrix} = 0 \qquad (31)$$

For a specified (trial) value of ω this equation may be solved for the decay coefficients ν_m , $m = 1, 2, ...$ As in the case for the cylinder this eigenvalue equation is non-linear and may be solved for the ν_m by the complex form of the Muller method. Starting values for the iterations may be found by an asymptotic solution of eq. (31).

Corresponding to each ν_m found by this method, the constants A_1, A_2, A_5, A_6 may be solved in terms of one of the constants, say A_6, relabelled D_m. When the solution for ν_m is complex two independent real solutions are obtained by separating the real and imaginary parts. Combining all solutions, the displacement and stress components for the sphere, automatically satisfying the homogeneous boundary conditions (21) and the regularity conditions (22) are given by

$$\begin{aligned} \frac{v_R}{a} &= \Sigma D_n v_{Rn} \\ \frac{v_\phi}{a} &= \Sigma D_n v_{\phi n} \\ \frac{\tau_{RR}}{2\hat{\mu}} &= \Sigma D_n \tau_{RRn} \qquad (32) \\ \frac{\tau_{\phi\phi}}{2\hat{\mu}} &= \Sigma D_n \tau_{\phi\phi n} \\ \frac{\tau_{\theta\theta}}{2\hat{\mu}} &= \Sigma d_n \tau_{\theta\theta n} \\ \frac{\tau_{R\phi}}{2\hat{\mu}} &= \Sigma d_n \tau_{R\phi n} \end{aligned}$$

where the summations are for $n = 1, 2, \ldots, N_s$.

CONTINUITY CONDITIONS

The solutions presented above for the cylinder and sphere are completely determinate except for the constants $d_n; n = 1, 2, \ldots, N_c$ and $D_n; n = 1, 2, \ldots, N_s$ and the frequency ω. The constants and frequency are determined by enforcing the conditions of continuity (7) on the surface of connection of the sphere and cylinder.

The scalar form of the equations (7) are

$$\begin{aligned} &u_r - v_R = 0, \; u_z + v_\phi = 0 \qquad (33) \\ &\sigma_{zz} - \tau_{\phi\phi} = 0, \; \sigma_{rz} + \tau_{R\phi} = 0 \end{aligned}$$

The displacement and stress components are given by eqs. (20) and (32) in terms of non-orthogonal eigenfunctions, requiring a least squares solution for the unknown constants. Substituting the expansions (20) and (32) into the integral I over the surface of connection

$$I = \int [\frac{(u_r - v_R)^2}{a^2} + \frac{(u_z + v_\phi)^2}{a^2} + \frac{(\sigma_{zz} - \tau_{\phi\,\phi})^2}{(2\hat{\mu})^2} + \frac{(\sigma_{rz} + \tau_{R\phi})^2}{(2\hat{\mu})^2}] dA \qquad (34)$$

and differentiating with respect to each of the constants d_n, D_n, in turn, leads to a homogeneous set of $N_c + N_s$ equations for the $N_c + N_s$ unknown constants. Setting the determinant D_{III} of the matrix of the coefficients in these equations to zero yields the frequency equation

$$D_{III} = 0 \qquad (35)$$

from which ω is determined.

An iterative procedure is proposed for determining the frequency ω and decay coefficients γ_m and ν_m from eqs. (19), (31), and (35). A trial value for ω is assumed and then corresponding sets of values γ_m and ν_m are found from eqs. (19) and (31). These values of γ_m and ν_m are used to define the eigenfunctions of eqs. (20) and (35). An improved solution for ω is then calculated by solving eq. (35). Upon convergence of ω the constants d_n, D_n may be solved in terms of one constant. Corresponding mode shapes can then be determined with the aid of eqs. (20) and (32).

CONCLUSION

A theoretical solution has been presented for determining the free vibration characteristics of a thick-walled cylindrical vessel closed by hemispherical heads. The solution is restricted to axisymmetric and longitudinally symmetrical vibrations. Solution characterists and numerical results will be presented in a future publication.

ACKNOWLEDGEMENT

This study was supported by a grant from the Natural Sciences and Engineering Research Council of Canada.

REFERENCES

1. Singh, A. V. and Kumar, V., Free vibration of cylindrical shells closed by a torispherical head, CANCAM'89, Ottawa, pp. 98-99, 1989.
2. Tavakoli, M. S. and Singh, R., Eigensolutions of joined-hermetic shell structures using the state space method, J. Sound and Vibration, Vol. 100, pp. 97-123, 1989.
3. Sheinman, I., Analysis of shells of revolution under earthquake motion, Nucl. Eng. Des., Vol. [illegible], pp. 249-262, 1986.
4. Irie, T., Yamada, G. and Muramoto, Y., Free vibration of joined conical-cylindrical shells, J. Sound and Vibration, Vol. 95, pp. 31-39, 1984.
5. Kalnins, A. and Godfrey, D. A., Seismic analysis of thin shell structures, Nucl. Eng. Des., Vol. 27, pp. 68-76, 1974.
6. Zudans, Z., Dynamic response of shell type structures subjectd to impulsive mechanical and thermal loadings, Nucl. Eng. Des., Vol. 3, pp. 117-137, 1966.

7. Saunders, H. and Paslay, P. R. Inextensional vibrations of a sphere-cone shell combination, J. Acoustical Soc. Am., Vol. 31, pp. 579-583, 1959.

8. Eringen, A. C. and Suhubi, E. S., *Elastodynamics*, Academic Press, New York, 1975.

9. Singal, R. K. and Williams, K., A theoretical and experimental study of vibrations of thick circular cylindrical shells and rings, J. Vibration, Stress and Reliability in Design, Vol. 110, pp. 533-537, 1988.

10. Armenakas, A. E., Gazis, D. C. and Herrmann, G., *Free Vibrations of Circular Cylindrical Shells*, Pergamon, New York, 1969.

11. Balabanov, L. M., Homogenous solutions and fulfillment of boundary conditions at the ends in the equilibrium problem for a thick walled isotropic cylinder, Mech. Sol., Vol. 3, Part 1, pp. 65-68, 1968.

12. Redekop, D., Homogeneous eigenfunction method applied to the elasticity problem of a pressure vessel with a hemispherical head, Nucl. Eng. Des., Vol. 40, pp. 369-382, 1977.

13. Muller, D. E., A method for solving algebraic equations using an automatic computer, Math. Tables Aids Comput., Vol. 10, pp. 208-215, 1956.

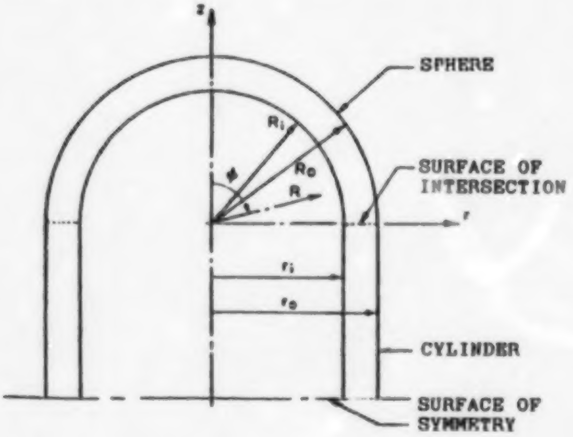
z
SPHERE
R_i
R_o
R
ϕ
SURFACE OF INTERSECTION
r
r_i
r_o
CYLINDER
SURFACE OF SYMMETRY

Fig. 1 Axisymmetric thick-walled vessel.

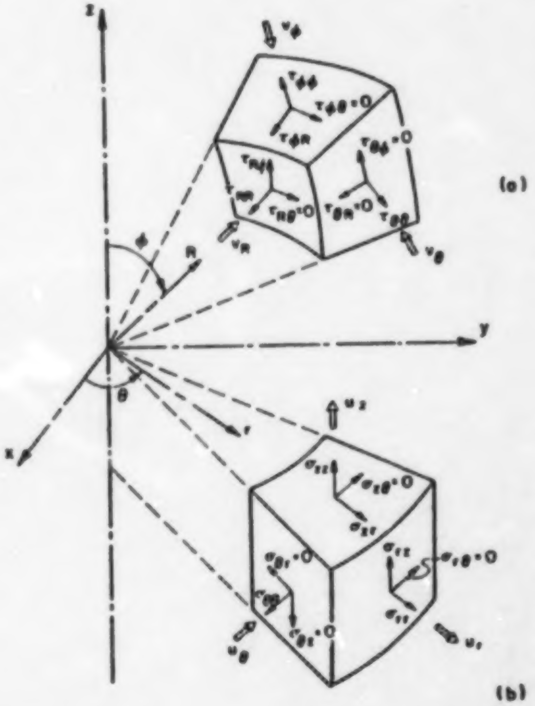
z
u_ϕ
$\tau_{\phi\phi}$
$\tau_{\phi\theta}=0$
$\tau_{\phi R}$
$\tau_{\theta\phi}=0$
$\tau_{R\phi}$
τ_{RR}
$\tau_{R\theta}=0$
$\tau_{\theta R}=0$
$\tau_{\theta\theta}$
u_R
u_θ
(a)
ϕ
R
y
θ
r
x
u_z
σ_{zz}
$\sigma_{z\theta}=0$
σ_{zr}
$\sigma_{\theta r}=0$
σ_{rz}
$\sigma_{r\theta}=0$
$\sigma_{\theta\theta}$
$\sigma_{\theta z}=0$
σ_{rr}
u_θ
u_r
(b)

Fig. 2 Displacement and stress components (a) sphere, (b) cylinder.

NONLINEAR PARAMETRIC VIBRATION OF FULLY CLAMPED RECTANGULAR PLATES

S.D. Yu and D.J. Gorman

Department of Mechanical Engineering
University of Ottawa, Ottawa, Canada K1N 6N5

ABSTRACT

Nonlinear vibration of fully clamped rectangular plates subjected to periodic inplane excitations is investigated in this paper. The Galerkin principle and double Fourier expansion technique are employed to reduce the *von Kármán* partial differential equations into a set of coupled nonlinear ordinary differential equations with periodic coefficients which can be solved by well developed analytical methods. The method of superposition is successfully used to find the exact eigenvalues and normalized eigenfunctions of plate free lateral vibration. Asymptotic solutions of the nonlinear equations for single mode vibration of the plate are given by the perturbation method. Numerical calculations are performed on the fully clamped rectangular plate with aspect ratio $\phi = 1.5$.

INTRODUCTION

The earliest work on the nonlinear parametric vibration of rectangular plates was given by Bolotin [1]. An experimental study on nonlinear parametric response of simply supported rectangular plates was conducted by Somerset and Evan-Iwanowski [2] and [3]. A few other papers concerning effects of nonlinearities on instable regions and nonlinear response of rectangular plates can be found in more recent survey articles by Ibrahim [4] and by Yamada and Irie [5].

Reviewing the literature, one finds that almost all previous work on nonlinear parametric vibration of plates was limited to simply supported plates. This is mostly because eigenvalues and eigenfunctions for simply supported plates are analytically available. To begin a research on plates with other boundary conditions one may meet great difficulty in obtaining accurate eigenvalues and analytical eigenfuctions. Another difficulty in analysing nonlinear vibrations of plates is how to find analytical solutions of the coupled *von Kármán* nonlinear partial differential equations.

Fortunately, the first problem can now be solved by using the method of superposition proposed by Gorman [6]. With this method one can obtain accurate eigenvalues and analytical eigenfunctions of rectangular plates with any classical boundary conditions and even more complex supports, such as point-supports, line-supports, attached concentrated masses, distributed elasticity, etc.

In this paper, the Galerkin principle is employed to construct the solution of plate lateral displacement. A double Fourier expansion technique is used to expand the inhomogeneous function in the *von Kármán* equations into a set of Fourier sine series. Following this procedure, the governing partial differential equations are reduced to a set of coupled nonlinear ordinary differential equations with periodic coefficients. Solutions of these equations can then be obtained to the desired degree of accuracy by several approximation techniques.

DERIVATION OF DIFFERENTIAL EQUATIONS

The governing differential equations of large amplitude vibration of plates subjected to inplane periodic loads, according to Timoshenko [7], are

$$\nabla^4 W + \frac{\rho}{D}\frac{\partial^2 W}{\partial t^2} = \frac{h}{D}\left(\frac{\partial^2 F}{\partial y^2}\frac{\partial^2 W}{\partial x^2} + \frac{\partial^2 F}{\partial x^2}\frac{\partial^2 W}{\partial y^2} - 2\frac{\partial^2 F}{\partial x \partial y}\frac{\partial^2 W}{\partial x \partial y}\right) \tag{1}$$

$$\nabla^4 F = E\left[\left(\frac{\partial^2 W}{\partial x \partial y}\right)^2 - \frac{\partial^2 W}{\partial x^2}\frac{\partial^2 W}{\partial y^2}\right] \tag{2}$$

Considering the transformation $x = a\xi$, $y = b\eta$, $\omega^* t = \tau$, $W(x,y,t) = h\tilde{W}(\xi,\eta,\tau)$ and $F(x,y,t) = P_{cr}h\tilde{F}(\xi,\eta,\tau)$, where ω^* is the natural frequency of the plate first mode vibration; P_{cr}, the critical compression load of the plate, equals $P_{cr} = \frac{\kappa D}{a^2}$. One rewrites Eqs.(1) and (2) as

$$\frac{\partial^4 \tilde{W}}{\partial \xi^4} + \frac{2}{\phi^2}\frac{\partial^4 \tilde{W}}{\partial \xi^2 \partial \eta^2} + \frac{1}{\phi^4}\frac{\partial^4 \tilde{W}}{\partial \eta^4} + \lambda^{*4}\frac{\partial^2 \tilde{W}}{\partial \tau^2} =$$

$$\sigma\left[\frac{\partial^2 \tilde{F}}{\partial \eta^2}\frac{\partial^2 \tilde{W}}{\partial \xi^2} + \frac{\partial^2 \tilde{F}}{\partial \xi^2}\frac{\partial^2 \tilde{W}}{\partial \eta^2} - 2\frac{\partial^2 \tilde{F}}{\partial \xi \partial \eta}\frac{\partial^2 \tilde{W}}{\partial \xi \partial \eta}\right] \tag{3}$$

$$\frac{\partial^4 \tilde{F}}{\partial \xi^4} + \frac{2}{\phi^2}\frac{\partial^4 \tilde{F}}{\partial \xi^2 \partial \eta^2} + \frac{1}{\phi^4}\frac{\partial^4 \tilde{F}}{\partial \eta^4} = \delta\left[\left(\frac{\partial^2 \tilde{W}}{\partial \xi \partial \eta}\right)^2 - \frac{\partial^2 \tilde{W}}{\partial \xi^2}\frac{\partial^2 \tilde{W}}{\partial \eta^2}\right] \tag{4}$$

where

$$\sigma = \frac{\kappa h^2}{b^2}$$

$$\delta = \frac{12a^4(1-\nu^2)}{\kappa h^2 b^2}$$

$$\lambda^{*2} = \omega^* a^2 \sqrt{\rho/D}$$

The coupled non-dimensional equations (3) and (4) determine the behaviour of plate large amplitude vibration due to inplane time-varying parametric loads. Mathematically there are no existing solutions for them. We here employ the Galerkin principle to seek the solution of $W(\xi,\eta,\tau)$ in the form

$$W(\xi,\eta,\tau) = \sum_{l=1}^{\infty} f_l(\tau)\Phi_l(\xi,\eta) \tag{5}$$

where $\Phi_l(\xi,\eta)$ are a set of normalized dimensionless eigenfunctions of the plate lateral free vibration, orthogonal and complete on the square domain D surrounded by the four lines $\xi = 0$, $\xi = 1$, $\eta = 0$ and $\eta = 1$.

Assume that the plate considered is under uniform compression in the ξ and η directions. The applied inplane force intensities $P_\xi(\tau)$ and $P_\eta(\tau)$ are sinusoidally time-varying functions independent of the plate deflections and of the coordinates ξ and η. Hence it is reasonable to divide the Airy function into two parts. It is written as

$$\tilde{F}(\xi,\eta,\tau) = \tilde{F}_1(\xi,\eta,P_\xi,P_\eta,\tau) + \tilde{F}_2(\xi,\eta,W,\tau) \tag{6}$$

The function $\tilde{F}_1(\xi,\eta,P_\xi,P_\eta,\tau)$ pertaining to applied inplane forces, consists of general solutions of the homogeneous equation of Eqn.(4). Considering the boundary conditions for the Airy function along the four clamped edges, one can write $\tilde{F}_1$ as

$$\tilde{F}_1 = -[\frac{b^2 P_\xi^*}{2h^2 P_{cr}}\varphi(\tau)\eta^2 + \frac{a^2 P_\eta^*}{2h^2 P_{cr}}\psi(\tau)\xi^2] \tag{7}$$

where

$$\varphi(\tau) = \cos(\frac{\theta_1}{\omega^*}\tau) = \cos(\theta_1^*\tau)$$

$$\psi(\tau) = \cos(\frac{\theta_2}{\omega^*}\tau) = \cos(\theta_2^*\tau)$$

P_ξ^* and P_η^* are amplitudes; θ_1 and θ_2 the excitation frequencies of the applied sinusoidal inplane forces.

The second part of Airy function $\tilde{F}_2(\xi,\eta,W,\tau)$ can be obtained by seeking a particular solution of the inhomogeneous equation (4). Inserting Eqn.(5) into Eqn.(4), we obtain

$$\frac{\partial^4 \tilde{F}}{\partial\xi^4} + \frac{2}{\phi^2}\frac{\partial^4 \tilde{F}}{\partial\xi^2\partial\eta^2} + \frac{1}{\phi^4}\frac{\partial^4 \tilde{F}}{\partial\eta^4} =$$

$$\sum_{i=1}^{\infty}\sum_{j=1}^{\infty}\delta f_i f_j[\frac{\partial^2\Phi_i}{\partial\xi\partial\eta}\frac{\partial^2\Phi_j}{\partial\xi\partial\eta} - \frac{\partial^2\Phi_i}{\partial\xi^2}\frac{\partial^2\Phi_j}{\partial\eta^2}] \tag{8}$$

Generally, it is difficult to obtain analytical solutions of the above inhomogeneous equation. Fortunately, with the superposition method, one can always acquire the analytical form of solution for the lateral displacement of the plate. Considering the continuous differentiability of functions $\Phi_i(\xi,\eta)$ together with the boundary conditions, it is evident that functions $\Psi_{ij}(\xi,\eta)$, defined by

$$\Psi_{ij}(\xi,\eta) = \frac{\partial^2\Phi_i}{\partial\xi\partial\eta}\frac{\partial^2\Phi_j}{\partial\xi\partial\eta} - \frac{\partial^2\Phi_i}{\partial\xi^2}\frac{\partial^2\Phi_j}{\partial\eta^2}$$

can be expanded into a double sine series which is uniformly convergent over the whole domain D. They are written as,

$$\Psi_{ij}(\xi,\eta) = \sum_{m=1}^{\infty}\sum_{n=1}^{\infty} a_{ijmn}\sin m\pi\xi \sin n\pi\eta \tag{9}$$

where,

$$a_{ijmn} = 4\int_0^1\int_0^1 \Psi_{ij}(\xi,\eta)\sin m\pi\xi \sin n\pi\eta d\xi d\eta$$

$$(i,j,m,n = 1,2,...)$$

Fourier coeficients a_{ijmn} can be found analytically and numerically. Inserting the above expressions into Eqn.(8), we obtain the following particular solution,

$$\tilde{F}_2 = \sum_{i,j,m,n=1}^{\infty} \frac{\delta a_{ijmn}}{[(m\pi)^2 + (\frac{n\pi}{\phi})^2]^2} f_i f_j \sin m\pi\xi \sin n\pi\eta \tag{10}$$

The Airy function which satisfies the governing equation and the boundary conditions, can now be written as

$$\tilde{F}(\xi,\eta,\tau) = -[\frac{b^2 P_\xi^*}{2h^2 P_{cr}}\varphi(\tau)\eta^2 + \frac{a^2 P_\eta^*}{2h^2 P_{cr}}\psi(\tau)\xi^2] +$$

$$\sum_{i=1}^{\infty}\sum_{j=1}^{\infty}\sum_{m=1}^{\infty}\sum_{n=1}^{\infty} \frac{\delta a_{ijmn}}{[(m\pi)^2 + (\frac{n\pi}{\phi})^2]^2} f_i f_j \sin m\pi\xi \sin n\pi\eta \tag{11}$$

We next investigate the solution of Eqn.(3). Inserting Eqs. (5) and (11) into Eqn. (3), multiplying the two sides of the newly obtained equation by $\Phi_k(\xi,\eta)$, and then integrating two sides of the equation over the square domain D, a set of ordinary differential equations on the generalized coordinates f_k is obtained by making use of the orthogonality of the plate eigenfunctions and the following relation

$$\frac{\partial^4\Phi_k(\xi,\eta)}{\partial\xi^4} + \frac{2}{\phi^2}\frac{\partial^4\Phi_k(\xi,\eta)}{\partial\xi^2\partial\eta^2} + \frac{1}{\phi^4}\frac{\partial^4\Phi_k(\xi,\eta)}{\partial\eta^4} = \lambda_k^4\Phi_k(\xi,\eta)$$

They are written as

$$\frac{d^2 f_k}{d\tau^2} + \bar{\omega}_k^2 f_k + \sum_{l=1}^{\infty}[\varphi(\tau)\mu_{kl}^{\xi} + \psi(\tau)\mu_{kl}^{\eta}]f_l + \sum_{i,j,l=1}^{\infty}\gamma_{kijl} f_i f_j f_l = 0 \tag{12}$$

(k=1,2,3,...)

where

$$\bar{\omega}_k = \omega_k/\omega^*$$

$$\lambda_k^2 = \omega_k a^2\sqrt{\rho/D}$$

$$\mu_{kl}^{\xi} = \frac{a^2 P_\xi^*}{D\lambda^{*4}}\int_0^1\int_0^1 \Phi_k(\xi,\eta)\frac{\partial^2\Phi_l}{\partial\xi^2}d\xi d\eta$$

$$\mu_{kl}^{\eta} = \frac{a^2 P_\eta^*}{D\phi^2\lambda^{*4}}\int_0^1\int_0^1 \Phi_k(\xi,\eta)\frac{\partial^2\Phi_l}{\partial\eta^2}d\xi d\eta$$

$$\gamma_{kijl} = \frac{12(1-\nu^2)}{\phi^4\lambda^{*4}}\sum_{m,n=1}^{\infty}\frac{\pi^2 a_{ijmn}}{[(m\pi)^2 + (\frac{n\pi}{\phi})^2]^2}\{\int_0^1\int_0^1$$

$$[n^2\frac{\partial^2\Phi_l}{\partial\xi^2} + m^2\frac{\partial^2\Phi_l}{\partial\eta^2}]\sin m\pi\xi\sin n\pi\eta +$$

$$2mn\frac{\partial^2\Phi_l}{\partial\xi\partial\eta}\cos m\pi\xi\cos n\pi\eta]\Phi_k d\xi d\eta\}$$

ANALYSIS OF PLATE FREE VIBRATION AND PARAMETERS IN THE GOVERNING EQUATIONS

In this part, we will use the superposition method developed by Gorman to obtain the accurate eigenvalues, normalized analytical eigenfunctions of the plate free lateral vibration and parameters appearing in the governing equations (12).

As there are no general analytical expressions for the natural frequencies and mode shapes of rectangular plates except plates with at least one pair of opposite edges simply supported, one has to investigate each particular case of support by using the method of superposition.

Theoretical Analysis

Consider the plate of dimensions $b \times a$ fully clamped along the four rectilinear edges. It is verified that solution for the plate can be obtained by superimposing solutions for each building block. Because of space limit, reader are suggested to refer to [6] for understanding of the concept of the superposition method. Only solutions and results will be presented in the following text.

Four building blocks are used in this analysis. One can easily write *Lévy* type solutions for those building blocks. They are

$$W_1(\xi,\eta) = \sum_{m=1}^{K_m^*} E_m(\theta_{11m}\frac{\sinh\beta_m\eta}{\sinh\beta_m} + \theta_{13m}\frac{\sin\gamma_m\eta}{\sin\gamma_m})\sin m\pi\xi$$
$$+ \sum_{m=K_m^*+1}^{\infty} E_m(\theta_{22m}\frac{\sinh\beta_m\eta}{\sinh\beta_m} + \theta_{23m}\frac{\sinh\gamma_m\eta}{\sinh\gamma_m})\sin m\pi\xi \tag{13}$$

$$W_2(\xi,\eta) = \sum_{n=1}^{K_n^*} E_n(\theta_{11n}\frac{\sinh\beta_n\xi}{\sinh\beta_n} + \theta_{13n}\frac{\sin\gamma_n\xi}{\sin\gamma_n})\sin n\pi\eta$$
$$+ \sum_{n=K_n^*+1}^{\infty} E_n(\theta_{22n}\frac{\sinh\beta_n\xi}{\sinh\beta_n} + \theta_{23n}\frac{\sinh\gamma_n\xi}{\sinh\gamma_n})\sin n\pi\eta \tag{14}$$

$$W_3(\xi,\eta) = \sum_{p=1}^{K_p^*} E_p(\theta_{11p}\frac{\sinh\beta_p\eta^*}{\sinh\beta_p} + \theta_{13p}\frac{\sin\gamma_p\eta^*}{\sin\gamma_p})\sin p\pi\xi$$
$$+ \sum_{p=K_p^*+1}^{\infty} E_p(\theta_{22p}\frac{\sinh\beta_p\eta^*}{\sinh\beta_p} + \theta_{23p}\frac{\sinh\gamma_p\eta^*}{\sinh\gamma_p})\sin p\pi\xi \tag{15}$$

$$W_4(\xi,\eta) = \sum_{q=1}^{K_q^*} E_q(\theta_{11q}\frac{\sinh\beta_q\xi^*}{\sinh\beta_q} + \theta_{13q}\frac{\sin\gamma_q\xi^*}{\sin\gamma_q})\sin q\pi\eta$$
$$+ \sum_{q=K_q^*+1}^{\infty} E_q(\theta_{22q}\frac{\sinh\beta_q\xi^*}{\sinh\beta_q} + \theta_{23q}\frac{\sinh\gamma_q\xi^*}{\sinh\gamma_q})\sin q\pi\eta \tag{16}$$

where $\xi^* = 1 - \xi$, $\eta^* = 1 - \eta$.

Numerical Results

To obtain the eigenvalues and analytical eigenfunctions one must force those solutions to fulfil exactly the boundary conditions. It is required that net slopes along the four rectilinear edges should be zero. Suppose K terms are taken in series for the analytical solutions of all building blocks. Satisfaction of the boundary conditions will result in a set of 4K algebraic equations relating the coefficients E_m, E_n, E_p, E_q. These algebraic equations containing 4K unknowns give an eigenvalue matrix of dimensions $4K \times 4K$. Eigenvalues are obtained by searching for those values of λ^2 which cause the determinant of the matrix to vanish. Eigenfunctions are then readily obtained by summing the contribution of each building block, as shown in Eqns. (13), (14), (15) and (16), to the displacement. Normalisation of eigenfunctions can be obtained by requiring the dimesionless form $\Phi_k(\xi,\eta)$ of the eigenfunctions $\Phi_k(x,y)$ to satisfy

$$\int_0^1\int_0^1 \Phi_k(\xi,\eta)\Phi_k(\xi,\eta)d\xi d\eta = 1 \tag{17}$$

k=1,2,3...)

Investigations have been carried on to ensure convergence in computing eigenvalues, eigenfunctions and coefficients appearing in the governing differential equations. Results are found to be very satisfactory when 30 terms are used in the computations. Calculations of those parameters are performed on fully clamped rectangular plates with aspect ration $\phi = 1.5$. Values are presented in Table 1. The tabulated values of μ_{kk}^{ξ} are divided by $a^2P_\xi^*/D$, and γ_{kkkk} are given for Poisson's ratio $\nu = 0.333$. The type of mode (T.O.M.) in the third column of the table indicates the symmetry or antisymmetry of mode with respect to plate central axes $\xi$and η. The first character pertains to ξ axis, and the second pertaining to η axis. For example, S-A represents the mode symmetrical with respect to ξ axis, and antisymmetric with respect to η axis. Taking advantage of this mode classification, a large amount of unnecessary computations will be left out in running our Fortran code.

SOLUTIONS AND CONCLUSIONS

There are several well-developed techniques which can handle the solutions of Eqns.(12) (see [8], [9], and [10]). In the present paper, only single mode vibration analysis of the plate subjected to time-varying compresion in the x direction is given. Detail work toward complete analysis of plate nonlinear parametric vibrations will soon appear in publications. It is mentioned here that there is no essen-

Table 1 Parameters Computed for Fully Clamped Plate with Aspect Ratio $\phi = 1.5$

k	λ_k^2	t.o.m.	$\bar{\omega}_k^2$	$\bar{\mu}_{kk}$	γ_{kkkk}
1	27.005	S-S	1.000	-12.47	1.118
2	41.704	A-S	2.385	-12.02	5.413
3	66.124	S-A	5.996	-46.71	6.031
4	66.522	S-S	6.068	-11.59	17.59
5	79.805	A-A	8.733	-45.75	16.67
6	100.81	A-S	13.94	-11.30	44.39
7	103.13	S-A	14.58	-44.99	34.16
8	125.30	S-S	21.53	-118.3	28.27
9	136.08	A-A	25.39	-44.31	69.96
10	138.64	A-S	26.36	-104.6	56.87

tial difficulty in extending this work to plates with any other boundary conditions if one masters the principle of the method of superposition and and procedures proposed in this paper.

In the case of single mode vibration, $f_i(\tau) = 0$ (i= 1, 2, ..., k-1, k+1, ...), Eqns.(12) are reduced to a series of uncoupled nonlinear equations with time-varying coefficients, which can be solved independently. They are written as,

$$\frac{d^2 f_k}{d\tau^2} + \bar{\omega}_k^2 f_k + \mu_{kk}^{\xi}\varphi(\tau) f_k + \gamma_{kkkk} f_k^3 = 0 \qquad (18)$$

where numerical results for parameters in Eqns. (18) are presented in Table 1; k pertains to the order of plate vibration mode, $k_{max} = 10$.

Assuming that P_ξ^* is much less than the critical load P_{cr}, and the lateral deflection of plate is much less than the plate geometries, Eqn.(18) can be asymptotically solved by the method of averaging. Detailed derivation is omitted. Interested readers may refer to [9]. The stationary amplitude of the plate dynamic response to the parametric excitation when principal resonance takes place can be written as,

$$A_k = \sqrt{\frac{4}{3\gamma_{kkkk}}[(\frac{\theta_1^*}{2})^2 - \bar{\omega}_k^2 \pm \frac{1}{2}\mu_{kk}^{\xi}]} \qquad (19)$$

Table 2 presents dimensionless amplitude values for various values of P_ξ^* when the parametric excitation frequency θ_1^* is near to $2\bar{\omega}_k$. Because the nonlinear coefficients γ_{kkkk} are positive for the first ten vibration modes, amplitude-frequency charts for those modes present hard-spring characteristics, i.e., jumping frequencies are always larger than the critical resonant frequencies $2\bar{\omega}_k$. Actually, the amplitude can not increase indefinitely with the excitation frequency because damping exists in any real system, and it will restrain the growth of amplitude. Detailed analysis of this topic can be found in either [8] or [9].

Considering the Galerkin expansion (5) and nondimensional transformation, we can easily obtain the global response of the plate single mode vibration. They are written as,

$$W(x, y, t) = h f_k(t)\Phi_k(x, y) \qquad (20)$$

where h is the plate thickness. Fig. 1 shows the first mode nonlinear vibration of the fully clamped plate . It is observed that boundary conditions along the four rectilinear edges are well satisfied.

Table 2 Values of A_k for Various Excitation Amplitudes

	$\alpha = P_\xi^*/P_{cr}$					
Mode	0.01	0.10	0.20	0.30	0.40	0.50
1	2.085	6.594	9.326	11.42	13.19	14.75
2	0.930	2.942	4.161	5.096	5.885	6.579
3	1.737	5.495	7.771	9.518	10.99	12.29
4	0.507	1.603	2.267	2.776	3.206	3.584
5	1.034	3.271	4.626	5.665	6.542	7.314
6	0.315	0.996	1.409	1.726	1.992	2.228
7	0.717	2.266	3.205	3.924	4.532	5.067
8	1.277	4.039	5.712	6.996	8.078	9.032
9	0.497	1.571	2.222	2.722	3.143	3.514
10	0.847	2.678	3.787	4.638	5.356	5.988

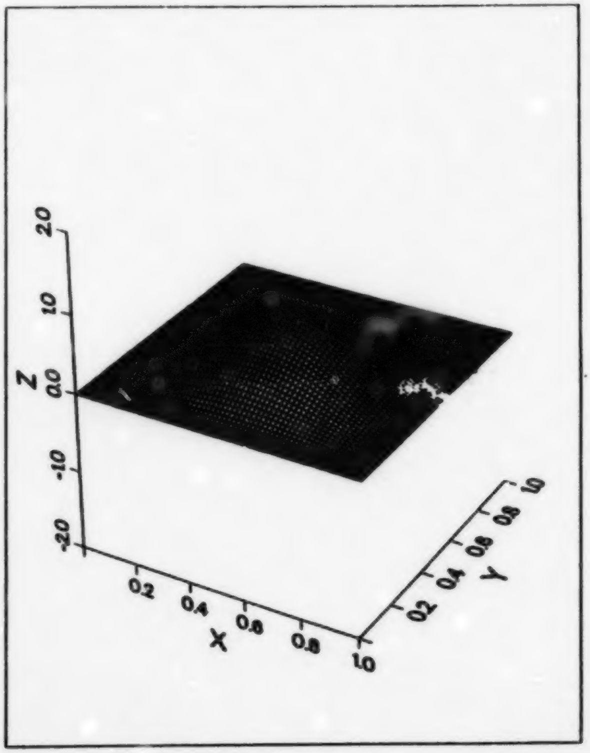

Fig. 1 First Mode Vibration of a Fully Clamped Plate

In order to convince other interested researchers that procedures proposed in this paper work extremely well in nonlinear vibration anlysis of plates. Calculations are also performed on square plate, so that we can compare our results with a few data on buckling of the square plate available in the literature. By simply setting the plate aspect ratio equal 1.0 in our Fortran code , we obtain the following results with six digit accuracy:

$$\lambda_1^2 = 35.9852; \quad \tilde{\mu}_{11} = -12.3497\;; \quad \gamma_{1111} = 2.88433.$$

Buckling load of the fully clamped square plate can be easily obtained from Eqn.(18). As is well known, when the vibratory frequency $\bar{\omega}_1^2 - \mu_{11}^{\xi}$ equals zero, in linear case the response of the plate increases indefinitely with time. We say that this is the case of buckling. The plate will lose its static stability when the inplane load is beyond the critical compression load which causes the vibratory frequency to vanish. Following this way, we obtain

$$P_{cr} = \frac{D\lambda_1^4}{a^2 \mid \tilde{\mu}_{11} \mid} \tag{21}$$

Substituting computed values of parameters into Eqn.(21), we get

$$P_{cr} = \frac{104.856D}{a^2} = \frac{10.624D\pi^2}{a^2} \tag{22}$$

Using the energy method, Chajes [11] obtained the critical load

$$P_{cr} = \frac{10.67D\pi^2}{a^2} \tag{23}$$

Lévy [12], using an infinite series for w, obtained the following critical load:

$$P_{cr} = \frac{10.07D\pi^2}{a^2} \tag{24}$$

Values of critical load obtained by our method is only a little less than Chajes', and not quite higher than *Lévy*'s. Normally, the energy method gives upper bound of the problem. *Lévy*'s result was achieved in 1942. As computing facilities were so poor at that time, the claimed accurate result, of course, is questionable. It can be believed that result given in this paper is the accurate one.

To authors' knowledge, the present paper, for the first time, successfully investigates the nonlinear parametric vibrations of fully clamped rectangular plates by using the superposition method together with other techniques. It is verified that the method of superposition works extremely well in finding eigenvalues and eigenfunctions of plate lateral vibration which are indispensable to this research. Also results given in this paper can be directly used to obtain buckling compression load and post-buckling behavior.

REFERENCES

1. V.V. Bolotin *Dynamic Stability of Elastic Systems*, Holden Day (1964).
2. J.H. Somerset and R.M. Evan-Iwanowski "Experiments on the Large Amplitude Parametric Vibrations of Rectangular Plates", *Developments in Theoretical and Applied Mechanics*, Vol.3, Pergamon Press Ltd., London, pp331-335(1966).
3. J.H. Somerset and R.M. Evan-Iwanowski "Influence of Nonlinear Inertia on the Parametric Response of Rectangular Plates", *Int. J. Nonlinear Mechanics*, Vol.2, pp217-232(1967).
4. R.A. Ibrahim "Parametric Vibration: Current Problems (1)", *Shock and Vibration Digest*, pp41-57 (1978)
5. G. Yamada and T. Irie "Plate Vibration Research in Japan", *Appl. Mech. Rev.*, Vol.40, No. 7, pp879-892(1987).
6. D.J. Gorman *Free Vibration Analysis of Rectangular Plates*, New York: Elsevier/North Holland Inc. (1982).
7. S. Timeshenko and S. Woinowski-Krieger *Theory of Plates and Shells*, McGraw-Hill Book Company, Second Edition, New York, pp415-418(1959)
8. A.H. Nayfeh and D.T. Mook *Nonlinear Oscilations*, John Wiley & Sons, New York, 1979.
9. N.N. Bogoliubov and Y.A. Mitropolsky *Asymptoptic Methods in the Theory of Non-Linear Oscilations*, Gordon & Breach Science Publishers, Inc., New York, 1961.
10. C.S. Shu "On the Parametric Excitation of a Dynamic System Having Multiple Degrees of Freedom", *Journal of Appl. Mech., Trans. of ASME*, Vol.30, pp367-372(1963).
11. A. Chajes *Principles of Structural Stability Theory*, Prentice Hall, Inc., Englewood Cliffs, New Jersey, 1974.
12. S. Levy "Buckling of Rectangular Plates with Built-in Edges", *Journal of Appl. Mech., Trans. of ASME*, Vol.9, 1942.

"On the Design of Vehicle Engine Cooling Systems"

S. F. Bloomer* T. E. Base** H. N. Charles*

*Siemens-Bendix Automotive Electronics, Cooling Products, Chatham, Ontario
**Department of Mechanical Engineering, The University of Western Ontario, London, Ontario

ABSTRACT

In the paper a computer aided approach to the design of a vehicle engine cooling system will be introduced and in particular calculations to determine the air flow distribution through a radiator due to an axial flow fan placed in an arbitrary position downstream of the radiator. The position of the cooling fan and the non-uniform distribution of air flow through the fan all contribute to the nonuniformity of the air flow through the radiator and a possible reduction in the radiator cooling efficiency. An algorithm was developed based on three dimensional potential flow theory to model the flow field between the radiator and the fan including the upstream suction or inflow of the axial flow fan. In the analysis for a particular radiator-fan combination a factor was calculated which related the actual heat transfer from the radiator to the theoretical heat transfer value based on uniform flow over the complete radiator surface. Experimental tests on various radiator-fan assemblies were also conducted in the Siemens Automotive Ltd. laboratory to determine velocity distributions through the radiator for a particular axial flow fan position. The experimental results verified the validity of the theoretical modelling technique.

INTRODUCTION

The paper is concerned with automobile engine cooling systems. With the introduction of electric motor driven radiator cooling fans instead of direct engine driven fans, the fan is now independent of the engine position. As a result the fan-radiator cooling system may be positioned in any convenient position in proximity to the engine. At the same time with the new automobile designs the space available for engine cooling systems has been reduced.

The performance analysis of axial flow fans was discussed previously by Base et al. (1988) and also details of automobile cooling systems are presented by Klaus Dieter Emmenthal (1986). A finite element method of solution based on the collocation method or "Weissinger's Lifting Line Theory" was developed. This method had previously been used successfully to predict wing loading for fixed airfoil studies. The fan blade was divided up into quadrilateral shaped four node surface elements and three dimensional 'bound' vortices were positioned at the quarter chord point of each element. The collocation or control points, where the boundary condition of "no flow" through the fan blade was satisfied, were positioned at the three-quarter chord point of each finite element. Figure 1 shows an axial flow fan divided into finite elements for analysis. Starting with the potential flow analytical computer solution for the axial flow fan the various real effects for an automobile cooling fan were then added to the computer model. These real effects included the radiator pressure prop, fixed ring, shroud effects, tip clearance and hub effects. One important aspect of the software program was that details of the axial flow velocity distribution through the fan with varying radial position were possible to be determined. Table I presents a typical output from the software program. In the following the characteristics of various automobile radiators will be discussed and finally a method to predict the velocity distribution of cooling air through a radiator to aid in local heat transfer. Calculations will be presented.

Radiation Pressure Drop Characteristics and its effects on the performance of the axial flow fan.

In the analysis of axial flow fans suitable for the cooling of an automobile radiator an expression to represent the variation of the pressure drop across the radiator with the mean velocity of air flowing through the radiator is well represented by the following equation.

$$\Lambda p_{RAD} = \Lambda_r U^{b_r}$$

where Λ_r and b_r are constants.

A software program was written based on regression analysis so that from a set of experimental results a best fit curve could be obtained for the corresponding Λ_r and b_r values. For example, for eight radiators tested the range of values of Λ_R and b_R were as follows:

$$12.5 \leq \Lambda_r \leq 20.9$$

$$1.50 \leq b_r \leq 1.64$$

In this analysis the units of the velocity were m/s and the units of pressure were Pascal.

A typical plot of the pressure drop with velocity for a radiator suitable for an automobile cooling system is shown in figure 2.

When an axial flow fan and radiator are placed in tandem position the volume flow through the fan is reduced. The start in any analysis is to determine the design point for the axial flow fan radiator assembly. This was achieved by applying the Newton-Ralphson technique to the radiator and fan performance data. Figures 3 and 4 show a typical curve used to determine the design point for the fan. Figure 3 shows the fan characteristics in "U.S." units and it may be noted the good agreement between experimentally measured values and the computer software prediction. Figure 4 shows the radiator and fan characteristics superimposed in order to determine the system design point. In this analysis the velocity distribution through the radiator was assumed to be uniform. In general this is not the case.

The axial velocity distribution across a radiator

To determine the velocity distribution across a radiator due to the suction created by an axial flow fan placed downstream of a radiator three dimensional potential flow theory was initially used. Three dimensional potential flow theory was developed for a potential line doublet. The line doublet is similar to a two dimensional point doublet in that it can be considered to consist in this case, of a potential sink in close proximity to a source. The only difference is that this effect occurs along a line. By replacing the fan disc by concentric potential line doublets it was possible to create the upstream suction effect of the fan and also the downstream blowing effect. The "couple of the doublet was directly proportional to the local air velocity through the fan at that particular radius. The elemental doublet expression for the axial velocity component for the configuration shown is:

$$w = \frac{\mu \, \delta\xi}{4\pi r^3} \left(\frac{3yz}{r^2} \right)$$

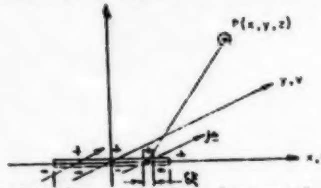

where

μ is the 'couple' of the doublet $\delta\xi$ is the elemental length of the doublet x,y,z are field points

and $$r^2 = x^2 + y^2 + z^2$$

The radiator was divided into rectangular shaped elements and the potential velocity through the radiator at the centre of each element was then calculated. It was then possible to determine the velocity distributed through the radiator for a particular fan position and fan characteristics. Table II shows the output from the software program with the mean velocity in m/s through each element indicated. Fig. 5 shows the velocity distribution across the radiator for various fan positions.

Heat Transfer Calculations

Once the distribution of air flow through the radiator was obtained it was now possible, using typical heat transfer correlations to determine the heat transfer characteristics of a radiator - fan assembly. Figure 6 shows the heat transfer variation with velocity. Table III shows a typical software program output including the outlet air temperature from the radiator element effectiveness and element coolant temperatures for a radiator fan assembly.

Discussion

A four part study has been made to aid in the design of automobile engine cooling systems. First a software program based on a finite element method was used to determine the characteristics of an axial flow fan when the flow was restricted by a radiatior. Secondly the pressure drop characteristics of a radiator with varying axial flow distribution were studied. Thirdly, a method based on three dimensional potential flow theory was used to determine the velocity distribution across the face of the radiation for a particular axial flow fan position. Finally, the airflow analysis was used in heat transfer calculations.

Conclusions

The various software program outputs were tested by comparing predicted values of airflows and airflow distribution across the radiator with experimental values. In general good agreement was achieved, particularly with the air flow comparisons. In conclusion, the integrated software packages provides a very useful tool for design of automobile engine cooling systems.

References

Base, T. E., Charles, H.N., and Bloomer, S. F. "Design of Axial Flow Fans Suitable for Automobile Cooling Systems", Ninth Sym. on Engineering Applications, U.W.O. May, 1988. pp.454 - 462

Klaus-Dieter Emmenthal "Engine Cooling system" Chap. 9, Aerodynamics of Road Vehicles. Ed. Wolf-Heinrich Hudro - pub. Butterworth, London.

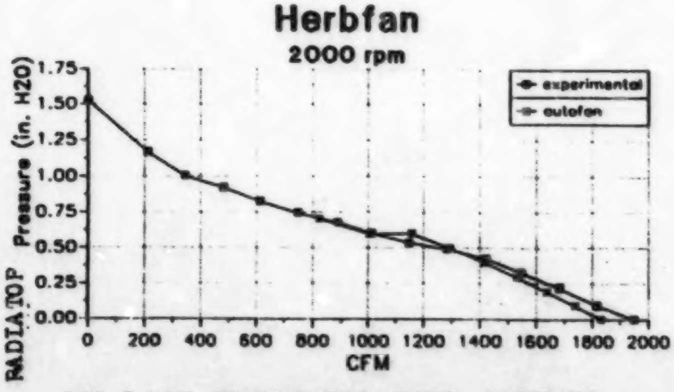

FIG.3 FAN PERFORMANCE CURVE: RADIATOR PRESSURE DROP VERSUS VOL. FLOW

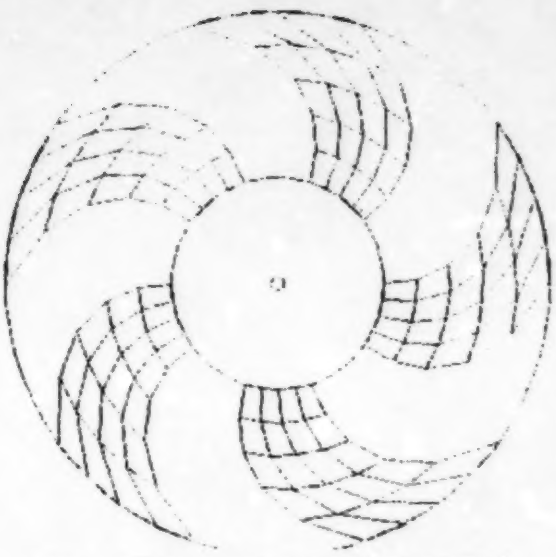

FIG.1 AXIAL FLOW FAN DIVIDED INTO FINITE ELEMENTS

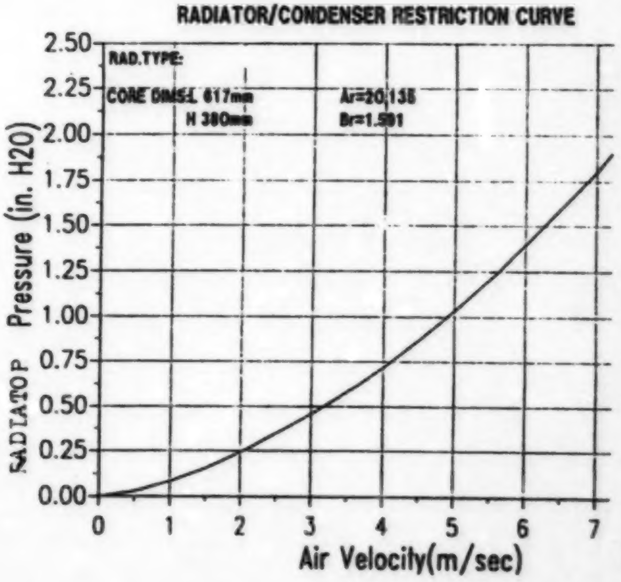

FIG.2 VARIATION OF PRESSURE DROP ACROSS A RADIATOR WITH FLOW VELOCITY.

TABLE 1 TYPICAL OUTPUT FROM "AUTOFAN" SOFTWARE PROGRAM

```
FAN BLADE GEOMETRY ****************

RADIUS RADIUS     CHORD      BLADE      CAMBER     POSN.OFLOCAL
NUMBER METRES     (MM)    ANGL.(DEGS) PERCENT    MAX.CAMBR  SOLDTY
   1   0.07900  69.07369  25.37427   0.06636    0.49987   0.97409
   2   0.09158  66.66079  23.91493   0.05652    0.49974   0.81090
   3   0.10686  66.72768  19.10411   0.05555    0.62670   0.69569
   4   0.12331  67.77754  17.07407   0.06663    0.62749   0.61234
   5   0.14121  72.13601  16.75574   0.05795    0.50028   0.56928
   6   0.15893  81.12605  16.74690   0.03821    0.37401   0.56870
   7   0.17454  94.95789  14.10678   0.01025    0.12450   0.60611
   8   0.18696 111.62404  14.77501   0.00385    0.12435   0.66518
   9   0.19800 130.80099  12.31587   0.00728    0.12670   0.73597

 OVERALL SOLIDITY OF FAN=     0.66792

 FIRST MOM.  SOLIDITY OF FAN=     0.67077

 SECOND MOM. SOLIDITY OF FAN=     0.63391


                              BLADE SHAPE DATA

          NUMBER OF BLADES   7
          BLADE SHAPE COORDINATES ARE SPECIFIED BY 9 RADII AND 9 CHORD LINES

          RADIUS VALUES IN MM
            79.00   91.58  106.86  123.31  141.21  158.93  174.54  186.96  198.00

          ANGLE VALUES IN DEGREES
                   Leading Edge
  Radius      1       2       3       4       5       6       7       8       9




                   Trailing Edge

          HEIGHT VALUES IN MM
                   Leading Edge
  Radius      1       2       3       4       5       6       7       8       9




                   Trailing Edge

                           FAN PERFORMANCE -(INCLUDING FIXED RING EFFECT)

 HEIGHT OF FIXED RING IN "MM" =      30.0

                              BLADE ELEMENT CHARACTERISTICS

          ELEMENT   ANGLE OF    TAN(FI)     LIFT      DRAG    AXIAL INFLOW   ROTAT. INFLOW  BLD.ELA.EFFIC.
             #      INCIDENCE              COEFF.    COEFF.     FACTOR          FACTOR
          -------   ---------   -------    ------    ------   ------------   -------------
             1       20.5293    0.0719     0.6191    0.2318     0.1550          0.1528        0.04954
             2       17.2227    0.0750     0.5178    0.1605     0.1484          0.0972        0.05522
             3       13.7377    0.0761     0.4123    0.1008     0.1394          0.0612        0.06256
             4       12.4887    0.0774     0.3710    0.0822     0.1488          0.0524        0.07176
             5       12.2863    0.0781     0.3663    0.0798     0.1794          0.0596        0.08741
             6       11.7775    0.0813     0.3625    0.0756     0.2123          0.0682        0.10561
             7       10.4769    0.0869     0.7524    0.2364     0.2307          0.0686        0.08205
             8        9.6803    0.0781     0.8354    0.1694     0.2787          0.0904        0.14321

             ** NO RADIATOR **
                                                      AXIAL FLOW VELOCITY DISTRIBUTION THROUGH FAN
 RPM=SPEED OF FAN IN REVS. PER MINUTE
 CFM=VOLUME FLOW IN CU. FT. PER MINUTE.(REF. 15 DEGS.C)   RADIUS(MM)      AXIAL FLOW(M/S)
 RAM=RAM AIR SPEED IN METRES PER SEC.
 NOTE:ALL PRESSURES ARE RECORDED IN INCHES OF WATER **   ----------      ----------
 PLENUM=TOTAL PRESSURE FAR UPSTREAM OF FAN.                85.29300          6.73717
 DPFAN=PRESSURE RISE ACROSS THE FAN = (P3-P2)              99.22150          6.45123
 P1=STATIC PRESSURE IMMEDIATELY UPSTREAM OF RADIATOR      115.08550          6.05740
 P3=STATIC PRESSURE DOWNSTREAM BUT NEAR TO THE FAN        132.26201          6.46844
 HP= FAN POWER REQUIRED IN HORSE POWER                    150.06850          7.79866
 WATTS=FAN POWER REQUIRED IN WATTS                        166.73300          9.22931
 TH.COEF.=FAN THRUST COEFF.                               180.74850         10.07842
 TO.COEF.=FAN TORQUE OR POWER COEFF.                      192.47900         12.11468
 FL.COEF.=FAN FLOW COEFF.
 EFFIC=FAN IDEAL EFFICIENCY                            ------------------------------

          RPM  I  CFM  I  RAM  I PLENUM I DPFAN I  P1   I  P3  I   HP  I WATTS I TH COEF I TO COEF I FL COEF I EFFIC.

          2000  1821.4    0.000   0.000   0.847  -0.171   0.675   0.345 257.677   0.084   0.024   0.168   0.392
```

EFFECT ON AIRFLOW DISTRIBUTION OF FAN POSITION RELATIVE TO RADIATOR.

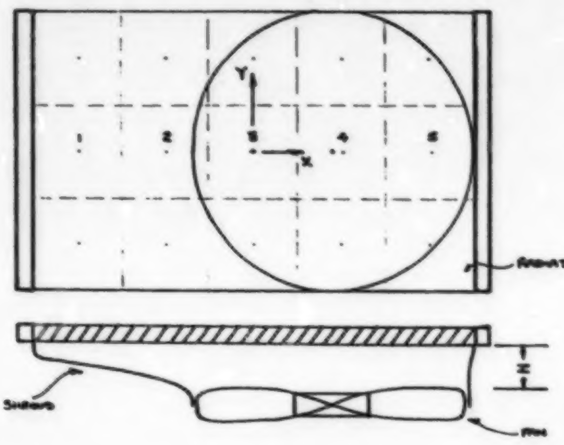

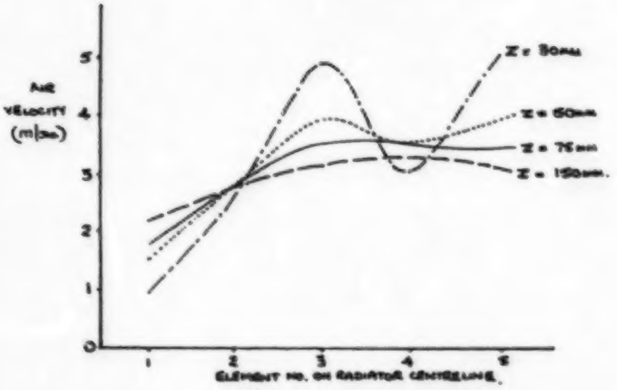

FIG. 5 VELOCITY DISTRIBUTION ACROSS A
A RADIATOR :FAN ASSEMBLY

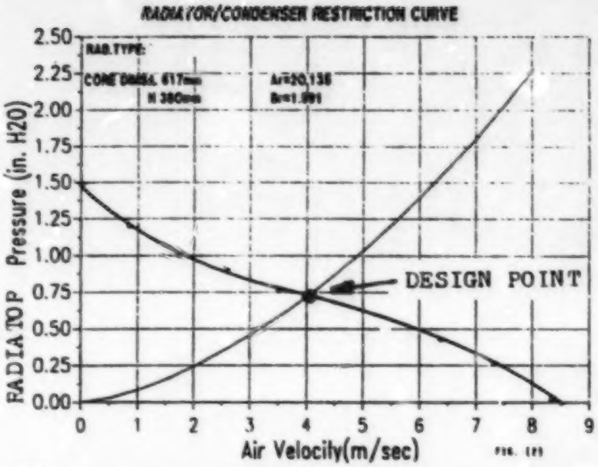

FIG.4 RADIATOR AND FAN DATA SUPERIMPOSED:
DESIGN POINT

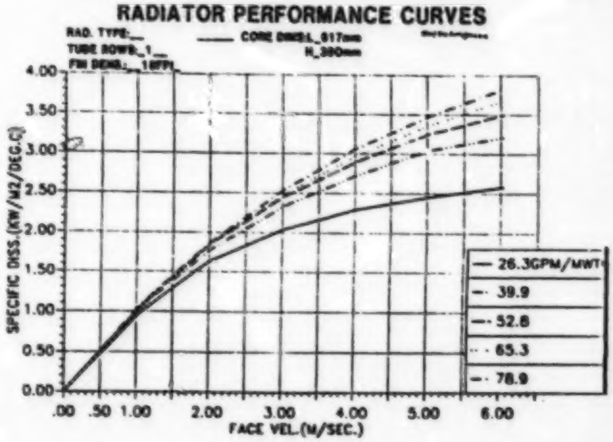

FIG.6 HEAT TRANSFER FROM RADIATOR

FAN: HERBFAN

RAD SIZE: H = 380.0mm W = 600.0 mm
Ar = 18.358 Br = 1.696
ELEMENT GRID: 3 VERTICAL, 5 HORIZONTAL

FAN OFFSET: X = 110.0mm Y = 0.0mm
FAN CLEARANCE: 30.0 mm FROM RAD TO FAN

2.18	4.72	2.35	1.52	0.94
4.89	3.16	4.70	2.67	1.07
2.18	4.72	2.35	1.52	0.94

UNIFORM FLOW: Q = 1341. CFM
Ps = 0.416 in. H20

DISTRIBUTED FLOW: Q = 1286. CFM
Ps = 0.451 in. H20

FLOW LOSS = 4.1 %

FAN: HERBFAN

RAD SIZE: H = 380.0mm W = 600.0 mm
Ar = 18.358 Br = 1.696
ELEMENT GRID: 3 VERTICAL, 5 HORIZONTAL

FAN OFFSET: X = 110.0mm Y = 0.0mm
FAN CLEARANCE: 50.0 mm FROM RAD TO FAN

2.62	3.91	2.77	1.97	1.36
3.95	3.52	3.92	2.73	1.50
2.62	3.91	2.77	1.97	1.36

UNIFORM FLOW: Q = 1341. CFM
Ps = 0.416 in. H20

DISTRIBUTED FLOW: Q = 1317. CFM
Ps = 0.431 in. H20

FLOW LOSS = 1.8 %

TABLE II TYPICAL OUTPUT FROM SOFTWARE PROGRAM THAT PREDICTS THE VELOCITY DISTRIBUTION ACROSS A RADIATOR

```
TOTAL CFM  1338.58
COOLANT OUTLET TEMPERATURE(DEG.C)  120.93
MEAN AIR TEMP.BETWEEN RAD.AND CONDENSER(DEG.C)   59.36
MEAN AIR OUTLET TEMP.(DEG.C)  113.08
RADIATOR EFFECTIVENESS  0.786
AMBIENT AIR TEMP.(DEG.C)  46.90


COOLANT FLOW DIRECTION--->--->---

 ____________________________________________________________________________
| ( 1 , 1 )     | ( 1 , 2 )     | ( 1 , 3 )     | ( 1 , 4 )     | ( 1 , 5 )     |
|               |               |               |               |               |
| V= 2.620      |    3.910      |    2.770      |    1.970      |    1.360      |
|               |               |               |               |               |
|SD= 2.563      |    3.324      |    2.517      |    1.894      |    1.347      |
|               |               |               |               |               |
| Q= 2.729      |    3.450      |    2.547      |    1.881      |    1.319      |
|_______________|_______________|_______________|_______________|_______________|
| ( 2 , 1 )     | ( 2 , 2 )     | ( 2 , 3 )     | ( 2 , 4 )     | ( 2 , 5 )     |
|               |               |               |               |               |
| V= 3.950      |    3.520      |    3.920      |    2.730      |    1.500      |
|               |               |               |               |               |
|SD= 3.576      |    3.056      |    3.331      |    2.487      |    1.473      |
|               |               |               |               |               |
| Q= 3.790      |    3.147      |    3.337      |    2.430      |    1.414      |
|_______________|_______________|_______________|_______________|_______________|
| ( 3 , 1 )     | ( 3 , 2 )     | ( 3 , 3 )     | ( 3 , 4 )     | ( 3 , 5 )     |
|               |               |               |               |               |
| V= 2.620      |    3.910      |    2.770      |    1.970      |    1.360      |
|               |               |               |               |               |
|SD= 2.563      |    3.324      |    2.517      |    1.894      |    1.347      |
|               |               |               |               |               |
| Q= 2.729      |    3.450      |    2.547      |    1.881      |    1.319      |
|_______________|_______________|_______________|_______________|_______________|




 RAD.AIR OUTLET            RAD.ELEMENT           ELEMENT COOLANT
   TEMP(DEG.C)             EFFECTIVENESS           IN TEMP(DEG.C)

T( 1 , 1 )=119.70        E( 1 , 1 )=0.881        TCI( 1 , 1 )=128.00
T( 1 , 2 )=110.34        E( 1 , 2 )=0.763        TCI( 1 , 2 )=126.48
T( 1 , 3 )=112.54        E( 1 , 3 )=0.819        TCI( 1 , 3 )=124.55
T( 1 , 4 )=114.60        E( 1 , 4 )=0.868        TCI( 1 , 4 )=123.13
T( 1 , 5 )=115.48        E( 1 , 5 )=0.897        TCI( 1 , 5 )=122.08
T( 2 , 1 )=114.89        E( 2 , 1 )=0.812        TCI( 2 , 1 )=128.00
T( 2 , 2 )=111.04        E( 2 , 2 )=0.780        TCI( 2 , 2 )=125.88
T( 2 , 3 )=108.53        E( 2 , 3 )=0.763        TCI( 2 , 3 )=124.12
T( 2 , 4 )=110.80        E( 2 , 4 )=0.821        TCI( 2 , 4 )=122.26
T( 2 , 5 )=113.91        E( 2 , 5 )=0.888        TCI( 2 , 5 )=120.90
T( 3 , 1 )=119.70        E( 3 , 1 )=0.881        TCI( 3 , 1 )=128.00
T( 3 , 2 )=110.34        E( 3 , 2 )=0.763        TCI( 3 , 2 )=126.48
T( 3 , 3 )=112.54        E( 3 , 3 )=0.819        TCI( 3 , 3 )=124.55
T( 3 , 4 )=114.60        E( 3 , 4 )=0.868        TCI( 3 , 4 )=123.13
T( 3 , 5 )=115.48        E( 3 , 5 )=0.897        TCI( 3 , 5 )=122.08
```

TABLE III TYPICAL OUTPUT FROM SOFTWARE PROGRAM THAT PREDICTS THE RADIATOR HEAT TRANSFER

AUTHOR INDEX

Ahmed, G.N. 255
Ali, M.S. 327
Anderson, R.J. 95
Aydemir, N.H. 163
Balafoutis, C.A. 55, 85
Base, T.E. 433
Bashagur, H.M. 285
Basile, S. 49
Bassey, M.W. 115
Bello-Ochende, F.L. 181, 261
Benmeddour, A. 157
Bindzi, I. 61
Birk, A.M. 191
Bloomer, S.F. 433
Bouak, F. 157
Bourassa, P. 395
Brezina, M. 395
Bryant, J.T. 17
Caohuu, T. 21
Carscallen, W.E. 199
Chan, J.D. 21
Charles, H.N. 433
Chidley, D.B. 191
Cooke, T.D.V. 17
Dahan, M. 341
Davies, A.S. 389
Davies, L.A. 317
Dibble, D.W. 383
Ebadian M.A. 207, 249
Elepaño, A.R. 273
El-Gindy, M. 403
Fang, Z. 145
Fazio, P. 353
Galanis, N. 243
Galopin, M. 365
Gaspar, R.G. 49, 291
Goheen, K.R. 73
Gorman, D.J. 409, 427
Haque, I. 79
Hason, S. 353
Héon, K. 151
Hrycak, P. 175, 225
Huang, C.L.D. 255
Jeswiet, J. 303, 321, 359
Kallel, F. 243
Kappel, V.V. 309
Kaya, D.M. 175
Khan, M. 395
Kirtley, C. 43
Kizhatil, R.K. 121
Kuhn, D.C.S. 129, 169
Laneville, A. 151, 157
Latouf, B.K. 49
Liangbin, L. 267
Lieh, J. 79
Loong, C.A. 309
Massé, B. 151
Mayorga, R.V. 333
Mbengue, H.M. 115
McBride, I. 17
McComber, P. 365
McLaren, W.S.C. 383
Meghdari, A. 371
Miller, H.W. 291
Montasser, W. 141
Moore, T.N. 297, 321
Moselhi, O. 353
Munro, S.D. 27
Nagarajan, T. 67, 347, 377
Naylor, D. 237
Nguyen, L.T. 27, 33, 39
Noori, M. 327
Nowak, E.S. 231
Nyalumwa, C. 321
Obiajunwa, C.D. 261
Ogunleye, I.O. 181
Ohman, H.L. 409
Oosthuizen, P.H. 169, 187, 273
.... 279, 285
Paradis, A. 365
Paraschivoiu, I. 145
Patel, R.V. 55, 85
Paul, J.T. 279
Pei, J. 101, 109, 297
Phillips, T.W. 27, 33, 39
Pichora, D.R. 11
Popov, G. 135
Quiet, R.C. 95
Ramachandran, S. 67, 347
Rao, D.R. 33
Redekop, D. 421
Reif, Z.F. 1, 291
Rémy, H. 21
Ressa, B. 333
Richard, M.J. 61
Royal, A. 365
Saliba, H.T. 415
Salloum, G. 309
Sandman, D.J. 225
Sankar, S. 135

Sankar, T.S. 135
Seshadri, R. 121
Sethi, S. 175
Showole, R.A. 213, 231
Sivaprasad, N. 67, 347
Small, C.F. 11
Snel, J.L. 33
Srinivas V., S. 377
Srinivasan, R 73
Tarasuk, J.D. 213, 237
Teitsma, A. 313, 317
Tjong, J.S.Y. 291
Tong, P.C.C. 187
Tsouras, K.E. 225
Tuan, C.H. 21
Turi, J. 327
Venart, J.E.S. 163
Vittecoq, P. 157
Wang, J. 219
Wang, T.B. 341
Wei, C. 175
Whiting, P. 129, 169
Wong, A.K.C. 333
Woodrooffe, J.H.F. 403
Wyss, U.P. 17
Xiangxiang, Y. 267
Xue, L. 101, 109
Yang, G. 207, 249
Yu, S.D. 427
Yu, Y. 91
Zhang, H. 219